

# Handbook of advanced dielectric, piezoelectric and ferroelectric materials

Synthesis, properties and  
applications

Edited by Zuo-Guang Ye



Handbook of advanced dielectric,  
piezoelectric and ferroelectric materials

## Related titles:

### *Materials for energy conversion devices*

(ISBN 978-1-85573-932-1)

The term 'electroceramic' is used to describe ceramic materials that have been specially formulated with specific electrical, magnetic or optical properties. Electroceramics are of increasing importance in many key technologies including: microelectronics, communications and energy conversion. This innovative book is the first comprehensive survey of major new developments in electroceramics for energy conversion devices. It presents current research from leading innovators in the field.

### *Nanolithography and patterning techniques in microelectronics*

(ISBN 978-1-85573-93-4)

Currently, surface patterning is achieved by means of optical lithographic techniques. However, as industry moves towards the fabrication of devices with size features of 100 nm or less, the technological community is looking for alternative approaches to materials fabrication at the nanoscale. By using nanolithography, scientists can drive patterning currents through surfaces while building a 3-D structure from a series of patterned layers. Electron-induced chemical lithography can create ultra-high resolution templates for the site-selective immobilisation of molecules to form functional, hierarchically organised structures. This new book concentrates on state-of-the-art nanolithographic methods with a particular emphasis on polymer research.

### *Nanostructure control of materials*

(ISBN 978-1-85573-933-8)

Nanotechnology is an area of science and technology where dimensions and tolerances in the range of 0.1–100 nm play a critical role. Nanotechnology has opened up new worlds of opportunity encompassing precision engineering as well as electronics, electromechanical systems and mainstream biomedical applications in areas as diverse as gene therapy, drug delivery and novel drug discovery techniques. Nanostructured materials present exciting opportunities for the manipulation of structure and properties at the nanoscale. The ability to engineer novel structures at the molecular level has led to unprecedented opportunities for materials design. This new book provides detailed insights into the synthesis/structure and property relationships of nanostructured materials. A valuable book for materials scientists, mechanical and electronic engineers and medical researchers.

Details of these and other Woodhead Publishing materials books, as well as materials books from Maney Publishing, can be obtained by:

- visiting our web site at [www.woodheadpublishing.com](http://www.woodheadpublishing.com)
- contacting Customer Services (e-mail: [sales@woodhead-publishing.com](mailto:sales@woodhead-publishing.com); fax: +44 (0) 1223 893694; tel.: +44 (0) 1223 891358 ext.130; address: Woodhead Publishing Ltd, Abington Hall, Abington, Cambridge CB21 6AH, England)

If you would like to receive information on forthcoming titles, please send your address details to: Francis Dodds (address, tel. and fax as above; e-mail: [francisd@woodhead-publishing.com](mailto:francisd@woodhead-publishing.com)). Please confirm which subject areas you are interested in.

Maney currently publishes 16 peer-reviewed materials science and engineering journals. For further information visit [www.maney.co.uk/journals](http://www.maney.co.uk/journals)

# Handbook of advanced dielectric, piezoelectric and ferroelectric materials

Synthesis, properties and  
applications

---

Edited by  
Zuo-Guang Ye

**Woodhead Publishing and Maney Publishing  
on behalf of  
The Institute of Materials, Minerals & Mining**

**CRC Press  
Boca Raton Boston New York Washington, DC**

**WOODHEAD PUBLISHING LIMITED**  
Cambridge England

Woodhead Publishing Limited and Maney Publishing Limited on behalf of  
The Institute of Materials, Minerals & Mining

Woodhead Publishing Limited, Abington Hall, Abington  
Cambridge CB21 6AH, England  
www.woodheadpublishing.com

Published in North America by CRC Press LLC, 6000 Broken Sound Parkway, NW,  
Suite 300, Boca Raton, FL 33487, USA

First published 2008, Woodhead Publishing Limited and CRC Press LLC  
© 2008, Woodhead Publishing Limited  
The authors have asserted their moral rights.

This book contains information obtained from authentic and highly regarded sources. Reprinted material is quoted with permission, and sources are indicated. Reasonable efforts have been made to publish reliable data and information, but the authors and the publishers cannot assume responsibility for the validity of all materials. Neither the authors nor the publishers, nor anyone else associated with this publication, shall be liable for any loss, damage or liability directly or indirectly caused or alleged to be caused by this book.

Neither this book nor any part may be reproduced or transmitted in any form or by any means, electronic or mechanical, including photocopying, microfilming and recording, or by any information storage or retrieval system, without permission in writing from Woodhead Publishing Limited.

The consent of Woodhead Publishing Limited does not extend to copying for general distribution, for promotion, for creating new works, or for resale. Specific permission must be obtained in writing from Woodhead Publishing Limited for such copying.

Trademark notice: Product or corporate names may be trademarks or registered trademarks, and are used only for identification and explanation, without intent to infringe.

British Library Cataloguing in Publication Data

A catalogue record for this book is available from the British Library.

Library of Congress Cataloging in Publication Data

A catalog record for this book is available from the Library of Congress.

Woodhead Publishing ISBN 978-1-84569-186-8 (book)

Woodhead Publishing ISBN 978-1-84569-400-5 (e-book)

CRC Press ISBN 978-1-4200-7085-9

CRC Press order number: WP 7085

The publishers' policy is to use permanent paper from mills that operate a sustainable forestry policy, and which has been manufactured from pulp which is processed using acid-free and elementary chlorine-free practices. Furthermore, the publishers ensure that the text paper and cover board used have met acceptable environmental accreditation standards.

Project managed by Macfarlane Production Services, Dunstable, Bedfordshire, England  
(e-mail:macfarl@aol.com)

Typeset by Replika Press Pvt. Ltd. India

Printed by TJ International Limited, Padstow, Cornwall, England

## Contributor contact details

---

(\* = main contact)

### Editor

Zuo-Guang Ye  
Department of Chemistry  
Simon Fraser University  
8888 University Drive  
Burnaby  
BC, V5A 1S6  
Canada

E-mail: zye@sfu.ca

### Chapter 1

Pengdi Han\*, Jian Tian and  
Weiling Yan  
H. C. Materials Corporation  
479 Quadrangle Drive  
Suite-E  
Bolingbrook, IL 60440  
USA

E-mail: p-han1@uiuc.edu;  
han@hcmat.com

### Chapter 2

L-C Lim  
Department of Mechanical  
Engineering  
National University of Singapore  
9 Engineering Drive  
Singapore 117576  
and  
Microfine Materials Technologies  
Pte Ltd  
10 Bukit Batok Crescent  
#06-02 The Spire  
Singapore 658079

E-mail: mpelimlc@nus.edu.sg

### Chapter 3

Wesley S Hackenberger\*, Jun Luo,  
Xiaoning Jiang, Kevin A Snook  
and P W Rehrig  
TRS Technologies Inc.  
2820 E. College Avenue  
State College, PA 16801  
USA

Shujun Zhang and Tom R ShROUT  
Materials Research Institute  
Pennsylvania State University  
University Park, PA 16802  
USA

E-mail: wes@trstechnologies.com;  
jun@trstechnologies.com

#### Chapter 4

Sung Min Rhim  
Humanscan Co. Ltd  
Ansan-si  
Kyunggi-do 425-110  
Korea

Min Chul Shin and Sang-Goo Lee\*  
IBULe Photonics Co. Ltd  
7-39 Songdo-dong  
Yeonsu-gu  
Incheon 406-840  
Korea

E-mail: Sanggoo7@ibule.com

#### Chapter 5

Shujun Zhang\* and Thomas R  
ShROUT  
Materials Research Institute  
Pennsylvania State University  
University Park, PA 16802  
USA

Jun Luo  
TRS Technologies Inc.  
2820 E. College Avenue  
State College, PA 16801  
USA

David W Snyder  
Electro-Optics Center  
Pennsylvania State University  
Freeport, PA 16229  
USA

E-mail: tshROUT@psu.edu;  
soz1@psu.edu

#### Chapter 6

Ho-Yong Lee  
Department of Materials Science  
and Engineering  
Sunmoon University  
Asan 336-708  
Korea

and  
Ceracomp Co. Ltd  
3F-3309  
Chungnam Techno Park  
Cheonan  
Chungnam 330-816  
Korea

E-mail: hlee@sunmoon.ac.kr;  
hlee@ceracomp.com

#### Chapter 7

Yonghong Bing  
Department of Chemistry  
University of Washington  
Box 351700  
Seattle  
Washington, 98195-1700  
USA

E-mail: bingy@u.washington.edu

Z-G Ye  
Department of Chemistry  
Simon Fraser University  
Burnaby  
BC, V5A 1S6  
Canada

E-mail: zye@sfu.ca

## Chapter 8

Yohachi (John) Yamashita\* and  
Yasuharu Hosono  
Toshiba R&D Center  
1 Komukai Toshiba-cho  
Saiwaiku  
Kawasaki 212-8582  
Japan

E-mail:  
yohachi.yamashita@nifty.ne.jp;  
yohachi.yamashita@toshiba.co.jp

## Chapter 9

Wenwu Cao  
Materials Research Institute  
Pennsylvania State University  
University Park, PA 16802  
USA

E-mail: cao@math.psu.edu

## Chapter 10

Satoshi Wada  
Materials Science and Technology  
Interdisciplinary Graduate School  
of Medical and Engineering  
University of Yamanashi  
4-4-37 Takeda  
Kofu  
Yamanashi 400-8510  
Japan

E-mail: swada@yamanashi.ac.jp;  
swada@ceram.titech.ac.jp

## Chapter 11

Dragan Damjanovic,\* Matthew  
Davis and Marko Budimir  
EPFL STI IMX LC  
MXD 236  
Station 12  
1015 Lausanne  
Switzerland

E-mail: dragan.damjanovic@epfl.ch

## Chapter 12

V Hugo Schmidt\* and R R Chien  
Department of Physics  
Montana State University  
Bozeman, MT 59717  
USA



Chi-Shun Tu  
Department of Physics  
Fu Jen Catholic University  
Taipei 242  
Taiwan

E-mail:  
schmidt@physics.montana.edu;  
039611@mail.fju.edu.tw;  
chien@physics.montana.edu

### Chapter 13

T Liu and C S Lynch\*  
The George W. Woodruff School of  
Mechanical Engineering  
The Georgia Institute of  
Technology  
Atlanta, GA 30332-0405  
USA

E-mail:  
christopher.lynch@me.gatech.edu  
tl79@mail.gatech.edu;  
lynch.admin@me.gatech.edu

### Chapter 14

Jean-Michel Kiat\* and Brahim  
Dkhil  
Laboratoire Structures Propriétés et  
Modélisation des Solides  
Ecole Centrale Paris  
CNRS-UMR8580  
Grande Voie des Vignes  
92295 Châtenay-Malabry Cedex  
France

Jean-Michel Kiat\*  
Laboratoire Léon Brillouin  
CE Saclay CNRS-UMR12  
91991 Gif-Sur-Yvette Cedex  
France

E-mail: kiat@spms.ecp.fr

### Chapter 15

Miguel Alguero,\* Jesús Ricote,  
Pablo Ramos and Ricardo Jiménez  
Instituto de Ciencia de Materiales  
de Madrid (CSIC)  
Cantoblanco  
28049 Madrid  
Spain

E-mail: malguero@icmm.csic.es

Julie Carreaud, Jean-Michel Kiat  
and Brahim Dkhil  
Laboratoire Structures Propriété et  
Modélisation des Solides  
Ecole Centrale Paris  
92295 Châtenay-Malabry Cedex  
France

Jean Michel-Kiat  
Laboratoire Léon Brillouin  
CE Saclay  
91191 Gif-Sur-Yvette Cedex  
France

Janez Holc and Marija Kosec  
Institute Jozef Stefan  
Jamova 39  
1000 Ljubljana  
Slovenia

## Chapter 16

K Uchino,\* J H Zheng, Y Gao, S Ural, S-H Park, N Bhattacharya  
International Center for Actuators  
and Transducers  
Pennsylvania State University  
University Park, PA 16802  
USA

K Uchino  
Micromechatronics Inc.  
Pennsylvania State College  
PA 16803  
USA

S Hirose  
Faculty of Engineering  
Yamagata University  
Yonezawa  
Japan

E-mail: kenjiuchino@psu.edu

## Chapter 17

Hong Wang\* and Xi Yao  
Electronic Materials Research  
Laboratory  
Xi'an Jiaotong University  
Xi'an 710049  
China

E-mail: hwang@mail.xjtu.edu.cn

## Chapter 18

J F Scott  
Centre for Ferroics  
Earth Sciences Department  
Cambridge University  
Cambridge CB2 3EQ  
UK

E-mail: jsco99@esc.cam.ac.uk

## Chapter 19

Igor A Kornev\*, B-K Lai, I Naumov, I Ponomareva, Huaxiang Fu and L Bellaiche  
Physics Department  
University of Arkansas  
Fayetteville, AR 72701  
USA

Igor A Kornev  
Mads Clausen Institute  
University of Southern Denmark  
Denmark

E-mail: ikornev@uark.edu  
laurent@uark.edu

## Chapter 20

Izabela Szafraniak-Wiza\*  
Poznan University of Technology  
Institute of Materials Science and  
Engineering  
M. Skłodowska-Curie Sq. 5  
60-965 Poznan  
Poland

E-mail: izaszaf@sol.put.poznan.pl

Marin Alexe and Dietrich Hesse  
Max Planck Institute of  
Microstructure Physics  
Weinberg 2  
06120 Halle (Saale)  
Germany

E-mail: hesse@mpi-halle.de  
malexe@mpi-halle.de

## Chapter 21

Vladimir Ya. Shur  
Ferroelectric Laboratory  
Ural State University  
Lenin Ave, 51  
Ekaterinburg 620083  
Russia

E-mail: Vladimir.shur@usu.ru

## Chapter 22

C Elissalde\* and M Maglione  
ICMCB-CNRS  
University of Bordeaux 1  
87 Av Dr Schweitzer  
33608 Pessac cedex  
France

E-mail: elissald@icmcb-  
bordeaux.cnrs.fr

## Chapter 23

I Vrejoiu,\* D Hesse and M Alexe  
Max Planck Institute of  
Microstructure Physics  
Weinberg 2  
06120 Halle (Saale)  
Germany

E-mail: malexe@mpi-halle.mpg.de;  
vrejoiu@mpi-halle.mpg.de

## Chapter 24

Weiguang Zhu\*  
School of Electrical and Electronic  
Engineering  
BLK S2, B2a-03  
Nanyang Technological University  
50 Nanyang Avenue  
Singapore 639798

Zhihong Wang  
Micromachines Centre  
School of Mechanical and  
Aerospace Engineering  
Nanyang Technological University  
50 Nanyang Avenue  
Singapore 639798

E-mail: ewzhu@ntu.edu.sg;  
EZHWang@ntu.edu.sg

Jianmin Miao  
Micromachines Centre  
School of Mechanical and  
Aerospace Engineering  
Nanyang Technological University  
50 Nanyang Avenue  
Singapore 639798

## Chapter 25

B Noheda\*  
Zernike Institute for Advanced  
Materials  
University of Groningen  
Nijenborgh 4  
9747AG Groningen  
The Netherlands

G Catalan  
Department of Earth Sciences  
University of Cambridge  
Cambridge CB2 3EQ  
UK

E-mail: [b.noheda@rug.nl](mailto:b.noheda@rug.nl);  
[gcat05@esc.cam.ac.uk](mailto:gcat05@esc.cam.ac.uk)

## Chapter 26

T Kimura  
Department of Applied Chemistry  
Faculty of Science and Technology  
Keio University  
3-14-1 Hiyoshi  
Kohoku-ku  
Yokohama 223-8522  
Japan

E-mail: [kimura@applc.keio.ac.jp](mailto:kimura@applc.keio.ac.jp)

## Chapter 27

Tadashi Takenaka  
Faculty of Science and Technology  
Tokyo University of Science  
Yamazaki 2641  
Nada, 278-8510  
Japan

E-mail: [tadashi@ee.noda.tus.ac.jp](mailto:tadashi@ee.noda.tus.ac.jp)

## Chapter 28

Keshwaree Babooram  
Department of Chemistry and  
Biochemistry  
Laurentian University  
Sudbury  
Ontario, P3E 2C6  
Canada  
E-mail: [kbabooram@laurentian.ca](mailto:kbabooram@laurentian.ca)

Zuo-Guang Ye\*  
Department of Chemistry  
Simon Fraser University  
888 University Drive  
Burnaby  
BC, V5A 1S6  
Canada

E-mail: [zye@sfu.ca](mailto:zye@sfu.ca)

## Chapter 29

Kenji Toda\* and Mineo Sato  
Graduate School of Science and  
Technology  
Center for Transdisciplinary  
Research  
Niigata University  
8050 Ikarashi 2-nocho  
Niigata 950-2181  
Japan

E-mail: [ktoda@eng.niigata-u.ac.jp](mailto:ktoda@eng.niigata-u.ac.jp);  
[inorg@gs.niigata-u.ac.jp](mailto:inorg@gs.niigata-u.ac.jp)

## Chapter 30

Annie Simon\* and Jean Ravez  
Institut de Chimie de la Matière  
Condensée de Bordeaux ICMCB-  
CNRS  
University Bordeaux 1  
87 Avenue du Dr Schweitzer  
33608 Pessac Cedex  
France

E-mail: [simon@icmcb-bordeaux.cnrs.fr](mailto:simon@icmcb-bordeaux.cnrs.fr)

## Chapter 31

Y N Qin and S Q Zhu\*  
National Laboratory of Solid  
State Microstructures  
Department of Physics  
Nanjing University  
Nanjing 210093  
China

E-mail: [zhusn@nju.edu.cn](mailto:zhusn@nju.edu.cn);  
[yqqin@nju.edu.cn](mailto:yqqin@nju.edu.cn);  
[zhusn\\_hk@yahoo.com.cn](mailto:zhusn_hk@yahoo.com.cn)

## Chapter 32

Takaaki Tsurumi\* and Takakiyo  
Harigai  
Graduate School of Science and  
Engineering  
Tokyo Institute of Technology  
2-12-1 Ookayama  
Meguro  
Tokyo 152-8552  
Japan.

E-mail: [ttsurumi@ceram.titech.ac.jp](mailto:ttsurumi@ceram.titech.ac.jp);  
[satomi.ii@ceram.titech.ac.jp](mailto:satomi.ii@ceram.titech.ac.jp)

## Chapter 33

Yuji Noguchi\* and Masaru  
Miyayama  
Research Center for Advanced  
Science and Technology  
The University of Tokyo  
4-6-1 Komaba  
Meguro-ku  
Tokyo 153-8904  
Japan

Yuji Noguchi  
SORST, Japan Science and  
Technology Corporation (JST)  
4-1-8 Honcho  
Kawaguchi-shi  
Saitama 332-0012  
Japan

E-mail: [ynoguchi@crm.rcast.u-tokyo.ac.jp](mailto:ynoguchi@crm.rcast.u-tokyo.ac.jp)

# Introduction

---

Research and development in dielectric, piezoelectric and ferroelectric materials has advanced at an unimaginable rate in the past decade, driven mainly by three factors:

1. new forms of materials have been prepared in a multitude of sizes (e.g. buck single crystals and ceramics, nano-structured films, tubes, wires and particles) by a variety of techniques (e.g. melt growth, physical deposition and to soft chemical synthesis),
2. novel and intricate structural and physical properties have been discovered in these materials (e.g. morphotropic phase boundary and related phenomena, domain engineering under fields, effects of nanostructures and superlattices), and
3. the extraordinary potential offered by these materials to be used in the fabrication of a wide range of high-performance devices (such as sensors, actuators, medical ultrasonic transducers, micro electromechanical systems (MEMS), microwave tuners, ferroelectric non-volatile random access memories (FeRAM), electro-optical modulators, etc.).

It was based on these three themes that this book has been conceived, in order to provide an up to date account of the state-of-the-art in this rapidly growing field.

The book is organized under eight main topics. Part I covers high strain, high performance piezo- and ferroelectric single crystals. This area has thrived with the (re)discovery of the extremely large piezoelectric strains and very high electromechanical coupling factors in the single crystals of the solid solutions between a lead magnesium (zinc) niobate relaxor and lead titanate ferroelectric. The outstanding performance of these crystals makes them the primary candidates for the next generation of electromechanical transducers for a broad range of applications, e.g. powerful undersea sonar systems, high-resolution ultrasonic imaging. Materials synthesis and property specification are discussed, along with their implications to devices. New materials systems with high Curie temperature and high piezoelectric performance are presented as a beacon for future development. On the other

hand, the development of piezocrystals has generated many perplexing issues, whose resolution is important to our fundamental understanding and for the technological applications of the materials. Of particular interest are the mechanism of high piezoelectric response and the enhancement of materials performance by domain engineering, and the morphotropic phase boundary and related phenomena. Together, they naturally constitute the topics of the following two sections.

Field-induced effects and domain engineering are described in Part II. A full set of materials properties and the domain engineering principles are presented for ferroelectric single crystals. Excellent piezoelectric properties are realized in conventional materials, such as barium titanate crystals, by appropriate domain-wall engineering. The enhancement of piezoelectric performance in perovskite crystals is demonstrated to arise from the various kinds of instabilities induced thermally, chemically, electrically and mechanically. Since the mechanism of high-piezoelectric response is associated with the rotation of the polarization directions by an appropriate electric field, the examination of complex domain structures and the phase energies of the relaxor ferroelectric single crystals provides a better understanding of the complex phenomenon.

Part III deals with the morphotropic phase boundary and its related phenomena, in which the complex structural features of relaxors and the related MPB systems are presented and analyzed in greater detail. Furthermore, the size effects on the macroscopic properties are also discussed.

Part IV is dedicated to high power piezoelectrics and microwave dielectrics and their applications. Current and future applications often require piezoelectrics to be driven to highest amplitude. Therefore, understanding of the loss mechanisms and heat generation is crucial for designing low-loss and high-power piezoelectric materials. As excellent microwave dielectrics, bismuth-based pyrochlore ceramics appear to be promising for tunable devices with low loss.

Part V explores nanoscale piezo- and ferroelectric materials. Great potential for device applications has emerged recently, mostly because of the capability to make nanostructured ferroelectrics. These materials have in turn ushered in new challenges both in the understanding of fundamental issues such as domains and domain engineering, and in the fabrication of materials in the forms of nanocrystals or 3D nano-composites.

Equally important is Part VI, which follows up along the lines of low-dimensional materials with piezo- and ferroelectric films. The ability to produce near-perfect, single-crystalline thin films and high-quality thick films has paved the road to device applications such as FeRAM and MEMS. The domain structure and polarizations specific to ferroelectric thin films are treated under symmetry engineering.

Non-conventional processing techniques and new materials are presented in Part VII. The preparation of textured or grain orientation-controlled materials has vastly improved the piezo- and ferroelectric properties of perovskite-based materials, making them more suitable for applications in electronic devices. New soft chemical routes have led to the formation of ferroelectrics and relaxors in the forms of nanoparticles, thin films and ceramics at low temperature (even room temperature), with enhanced properties.

Lastly, in Part VIII, we focus on some novel physical properties of dielectric and ferroelectric superlattices and their applications, as well as the complex structure-property relations of bismuth layer-structured single crystals.

This book is aimed to serve as a comprehensive reference to a broad spectrum of graduate students, academic researchers, development scientists, materials producers, device designers and applications engineers who are working in, or are interested in moving into, the fascinating field of advanced dielectric, piezoelectric and ferroelectric materials research and development.

The publication of this book would not have been possible without the help and support from many people. I thank all the authors for their knowledgeable contributions which I am sure will be highly valued by the readers. Their enthusiasm, dedication, hard work and cooperation in the making of this book were invaluable. I thank several anonymous referees for helping me review some of the chapters. I thank Wallace Smith and Carl Wu of the US Office of Naval Research for their constant support. Many of my colleagues here at Simon Fraser have lent me their encouragement that is much appreciated. I also thank the members of my research group and my family for their understanding and support.

It has also been a great pleasure to work with the competent and patient editorial staff at Woodhead Publishing Limited in Cambridge. In particular, I thank Rob Sitton, the Commissioning Editor, who initiated the project and brought it to fruition, and Ian Borthwick, the Publications Co-ordinator, who, as the main contact person throughout the project, effectively ensured the communication among the authors, the publisher and the editor, to allow the timely completion of all the chapters. Special thanks also go to Laura Bunney, the Project Editor, Melanie Cotterell, the Product Delivery Manager, and Francis Dodds, the Editorial Director.

Zuo-Guang Ye  
Department of Chemistry and  
4D LABS  
Simon Fraser University  
Burnaby, British Columbia  
Canada



# Bridgman growth and properties of PMN–PT-based single crystals

---

P HAN, J TIAN and W YAN  
H. C. Materials Corporation, USA

## 1.1 Introduction

### 1.1.1 Background

Continual development in acoustic transduction devices has been made since the end of World War II. This progress came about largely due to the availability of improved materials. The example of PZT (lead zirconate titanate) piezoelectric ceramics is well known. Recently, progress in the growth and characterization of PMN–PT (lead magnesium niobate–lead titanate)-based piezoelectric crystals has promoted the development of the next generation of acoustic transduction devices.

The recent shift in focus from blue water to littoral operations for the US Navy has placed additional requirements on sonar systems. New materials of high energy density and improved properties are needed for enhanced sonar transduction performance. Material property improvements include:

- increased strain to enhance acoustic source level;
- increased electromechanical coupling to broaden bandwidth;
- increased energy density to reduce transducer weight and give higher efficiencies;
- reduced hysteresis to produce greater thermal stability;
- increased sensibility to improve signal/noise ratio.

A breakthrough was announced at the Piezoelectric Crystal Planning Workshop<sup>1</sup> sponsored by the Office of Naval Research in May 1997. Single crystals of PZN–PT (lead zinc niobate–lead titanate) and PMN–PT near MPB (morphotropic phase boundary) compositions exhibit extraordinary piezoelectric properties, namely, electrical field-induced strains exceeding 1%, and electromechanical coupling exceeding 90% (compared with 0.1% and 70–75%, respectively, in the state-of-the-art PZT piezoceramics)<sup>2,3</sup>. These perovskite relaxor ferroelectric crystals have opened up new opportunities not only in current acoustic transduction devices, where traditional PZT

ceramics are used, but also in exploration of new applications, such as medical ultrasonics, non-destructive detection, marine seismic exploration and energy harvesting. These new crystals of giant-piezoelectric properties will enable “revolutionary” developments for the next generation of acoustic transduction devices. Thus, there is an urgent need to develop crystal-growth techniques for the fabrication of large, high-quality piezoelectric crystals at industrial scale.

### 1.1.2 Challenges in the growth of large PMN–PT crystals

It is a great challenge to develop a cost-effective method for the growth of the high-strain piezocrystals of large sizes (75–100 mm (3–4 inches) in diameter by 150–200 mm (6–8 inches) in length, and high quality. Generally speaking, the difficulties found when growing large-sized crystals of lead-containing materials are their complex thermodynamic behavior and special physical properties. For example, common problems include incongruent melting and low thermal conductivity. The incongruent melting means that crystals cannot be grown from stoichiometric melts. The low thermal conductivity affects the transport of latent heat released during the crystallization process, thereby causing interface instability, defects, inclusions and phase segregation, etc. The difficulties here stemmed from a basic discrepancy between theoretical predictions and experimental data on the congruent behavior and the perovskite precipitation characteristics for the MPB solid solution systems associated with PT.

In addition, solid-state phase transformations commonly occur on cooling to room temperature that lead to twinning and possible cracking problems. Furthermore, the growth of lead-containing crystals at high temperatures encounters more special technical barriers, including:

- corrosion of container materials – platinum crucibles are attacked by lead-containing melt at temperatures above 1300°C, leading to severe leakage;
- high volatility of toxic PbO from the melt at high temperatures;
- difficulties in controlling compositional homogeneity for multi-component systems due to the compositional segregation.

The critical problems enumerated above make the growth of large PMN–PT crystals for commercialization a challenging task.

### 1.1.3 Growth of PMN–PT crystals from stoichiometric melt using the Bridgman method

PMN–PT is a binary solid solution of lead magnesium niobate (PMN) and lead titanate (PT). It can be represented by the formula  $(1-x)[\text{Pb}(\text{Mg}_{1/3}\text{Nb}_{2/3}\text{O}_3)]-x[\text{PbTiO}_3]$ . PMN–PT has the  $\text{ABO}_3$  perovskite structure and an MPB

where the structure changes from rhombohedral to tetragonal at  $x \sim 0.34$ – $0.35$ . To obtain crystal samples, the high-temperature solution (flux) growth as a ‘universal’ method has been widely used for a variety of complex oxide compounds including the perovskite relaxor ferroelectric materials. In the 1990s millimeter-sized crystals of PMN–PT were grown from high-temperature solution with  $\text{PbO/B}_2\text{O}_3$  as the flux<sup>4</sup>. Recently, inch-sized ( $\sim 25$  mm) PMN–PT crystals with improved quality have been successfully grown using the flux growth method<sup>5–8</sup> and a modified flux growth, the so-called ‘solution-Bridgman’ method<sup>9</sup>. However, the growth rate and crystal size of the above crystal growth methods were limited and not suitable for commercial production. To suppress the evaporation of the volatile melt component  $\text{PbO}$ , crystal growth of PMN–PT under high pressure (80 atm Ar with 1% oxygen)<sup>10</sup> was demonstrated using a vertical Bridgman furnace. It confirmed that lead evaporation was significantly reduced even for the unsealed crucible, but the crystal quality was degraded due to inclusions such as voids and Mg–Si–O-rich impurities. A possible reason is that high pressure also influenced the interface dynamic process, leading to the occurrence of constitutional supercooling.

It has been well known that the most straightforward and economical way of growing high-quality large crystals is the Bridgman<sup>11</sup>–Stockbarger<sup>12</sup> method, which normally freezes stoichiometric melt without flux: a molten ingot is gradually crystallized from one end to the other. However, the stoichiometric melt growth of the single crystals of  $\text{ABO}_3$  perovskite relaxor ferroelectric materials is suitable only for systems that satisfy the following essential criteria: (i) the system is congruent melting and/or (ii) in the compositional phase diagram there must exist a window from which the perovskite as the primary phase (instead of the pyrochlore phase of the same chemical composition) can be directly crystallized from the melt. Unfortunately, most of the known MPB systems associated with PT ( $\text{PbTiO}_3$ ) are incongruent and thus no window exists in the phase diagrams for the perovskite phase to crystallize first. As a result, these perovskite crystals cannot be grown from stoichiometric melts. Fluxes or mineral agents must be used for the crystal growth to avoid interference from unexpected nuclei of the non-perovskite phases.

Perovskite PMN melts congruently at  $1320^\circ\text{C}$ <sup>13</sup> and perovskite PT melts congruently at  $1285^\circ\text{C}$ . Thus, both end compounds of the PMN–PT binary system are congruent-melting perovskite phases. This implies that PMN–PT is more likely to form the perovskite phase, instead of the parasitic pyrochlore phase, than the other MPB binary solid solutions such as PZN–PT (PZN melts incongruently). Since the first experimental report in 1997<sup>14,15</sup> on the melt growth of high-quality PMN–PT crystals from stoichiometric melt (without flux) in sealed platinum crucibles using a modified Bridgman furnace, more efforts<sup>16–19</sup> have been made to the melt growth of the PMN–PT-based

crystals; however, undesired compositional segregations were encountered<sup>13</sup>. At the present time, <001>-seeded PMN–PT crystals of 75 mm (3 inch) diameter and 200 mm (8 inch) length (6 kg each boule) have been commercially manufactured using the multi-crucible vertical Bridgman method<sup>20</sup>.

In the following sections, the details of the melt growth of PMN–PT-based crystals using the Bridgman method developed at the H. C. Materials Corporation are described. The physical properties are systematically characterized and discussed in the context of domain engineering and elasto-piezo-dielectric tensor concepts, which are important for the appropriate selection of crystal cut directions and vibration modes.

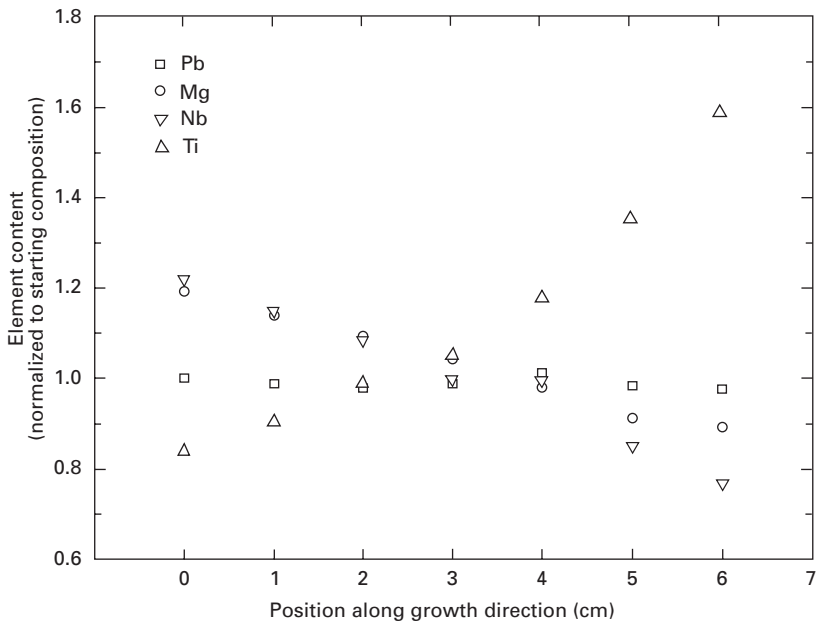
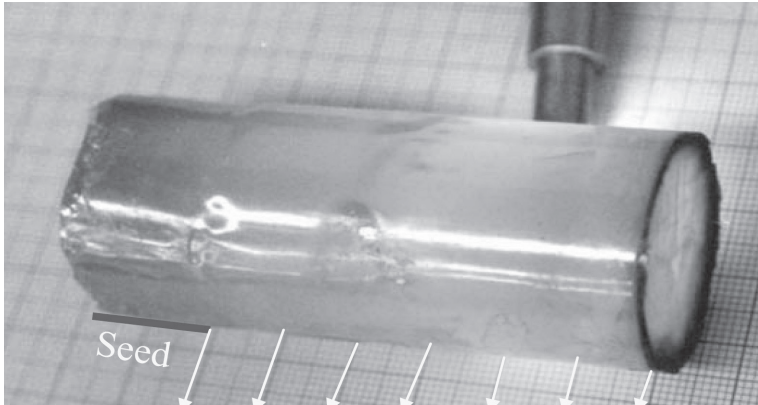
## 1.2 Crystal growth

### 1.2.1 Phase equilibrium

A prerequisite for growing PMN–PT crystals is the detailed knowledge of the high-temperature phase equilibrium of the binary solid solution. There are limited data about the PMN–PT phase diagram. As mentioned above, only congruent melting at 1320 °C for perovskite PMN and 1285 °C for PT was known. In 1999, we reported the results of the compositional segregation (Fig. 1.1) based on ICP (induction coupled plasma spectroscopy, accuracy better than 0.5%) analysis of a PMN–31%PT single crystal<sup>16</sup>. The growth parameters are: seeding [210], growth rate 0.8 mm/h, temperature gradient 20 °C/cm, and maximum temperature 1365 °C. The effective segregation coefficient is estimated ~85% for PT. The result of the crystal growth from stoichiometric melt indicated that the phase equilibrium diagram may be a typical binary solid solution system. In 2003, the first high-temperature phase diagram of the PMN–PT binary system was reported<sup>19</sup>. A combination of all available data, provides a phase equilibrium diagram, as proposed in Fig. 1.2. This phase diagram is accurate enough as the guidance for the thermal process control during crystal growth and it has been successfully used in the PMN–PT crystal growth.

### 1.2.2 Platinum crucible leakage and lead oxide chemistry

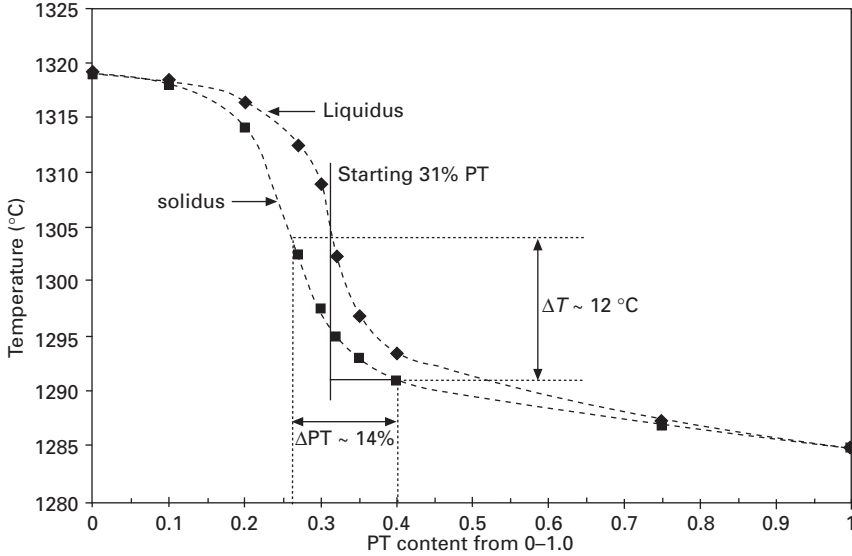
A suitable container/crucible for the lead-containing melt is one of the essential requirements for PMN–PT crystal growth at the maximum temperature up to 1370 °C for a few hundred hours. Several materials such as iridium (Ir), platinum (Pt)/rhodium (Rh) alloy, Pt/gold (Au) alloy and pure platinum have been tried. Pure platinum has been proven to be the best crucible material. It is chemically stable, so does not contaminate the melt. However, the operating temperature is over the safety temperature limit of 1300 °C in air for Pt



1.1 ICP analysis of a PMN-PT crystal boule.

metal. Thus, it is probable that the platinum crucible could be attacked by lead-containing melt, especially at temperatures above 1350°C. The crucible leakages due to PbO attack pose a serious threat to crystal growth. After systematic investigations, we have found that there are two main reasons leading to the crucible leakage.

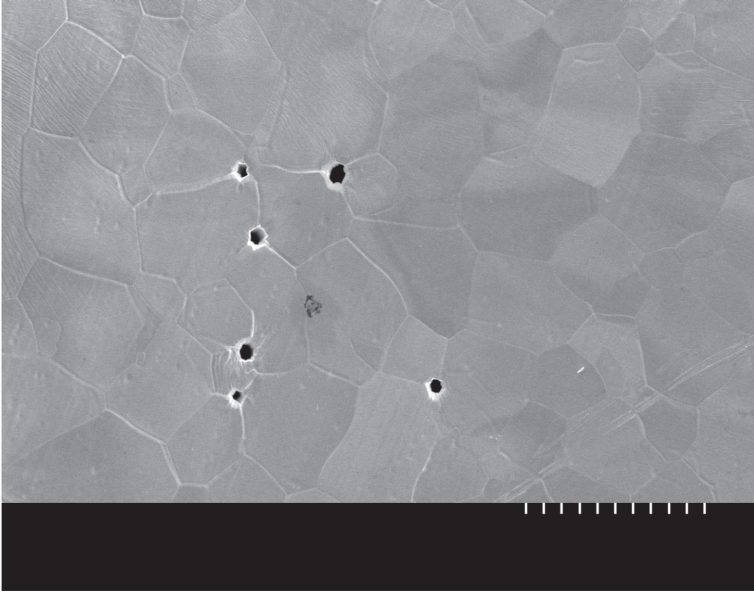
First the purity and the quality of the platinum crucible are not high enough. During crystal growth at high temperatures platinum grains grow to up to sub-millimeter sizes and some of the large grains can penetrate the wall of the crucible. As the platinum grains grow, impurities in the platinum metal



1.2 Suggested phase equilibrium diagram of PMN-PT binary system.

can be segregated and expelled into the tri-junctions of platinum grains. The lead-containing melt, acting as a strong flux, would ‘eat’ (dissolve) the impurities and thus form micro-holes in the platinum crucible wall (Fig. 1.3).

Second, the chemical behavior of lead oxides before melting is complex<sup>21</sup>. The commercial lead oxide (PbO) generally contains some  $Pb_3O_4$ . To understand the influence of the chemical reaction on the platinum corrosion, TGAs (thermal gravity analyses) on PbO and  $Pb_3O_4$  powders were performed in conjunction with X-ray diffraction for phase identifications. Figure 1.4 clearly indicates that PbO absorbed oxygen in the temperature range from 430 to 520 °C to form  $Pb_3O_4$  (or  $PbO_{1.1/3}$ ). Above 600 °C, the  $PbO_{1.1/3}$  released one-third of the oxygen and returned to PbO. So, one can imagine the following scenario: if (i) some free PbO exists in the chemical batch loaded in a platinum crucible and (ii) the temperature of the crucible in the furnace is hotter at the upper segment, i.e. the heating rate of the upper crucible is faster than the lower part, then oxygen deficiency inside the sealed crucible will occur when the temperature at the lower segment of the crucible ramps up to around 520 °C. If the temperature of the upper segment increases over the liquidus temperature of PbO 888 °C, some PbO may be reduced to form micrometer drops of lead metal. The reduced lead immediately forms alloy with platinum, which has a much lower melting point than platinum or lead and thus causes crucible leakage. To avoid the leakage of platinum crucible, the following measures are suggested:

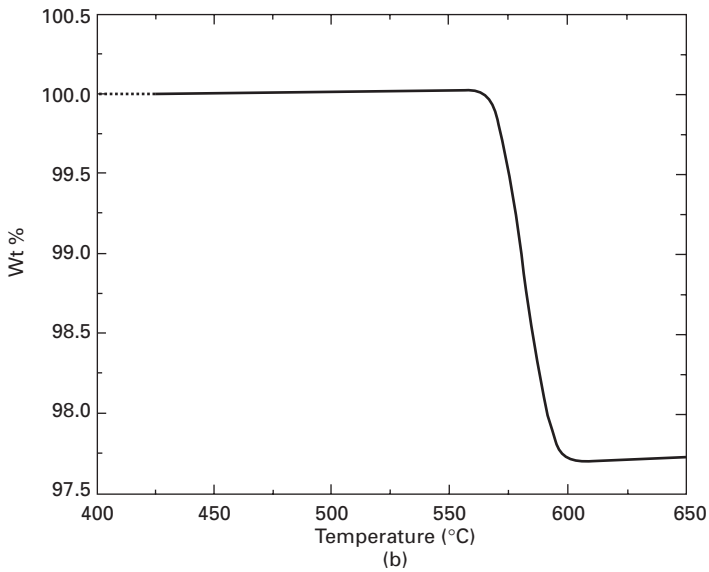
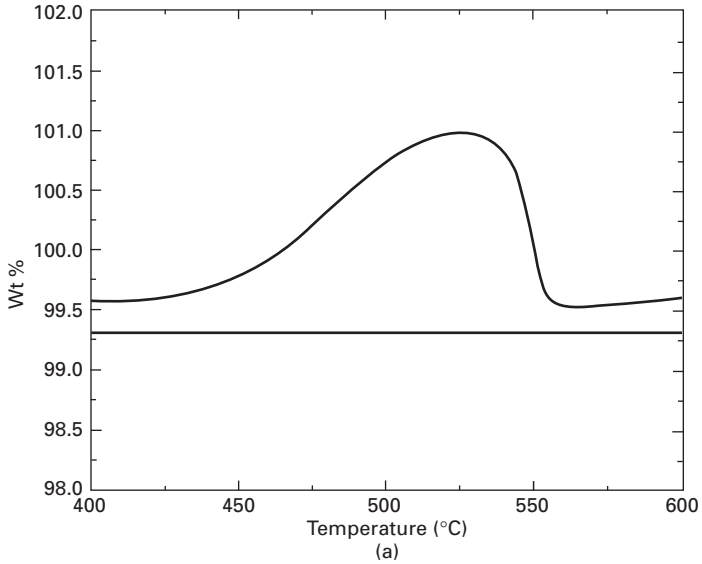


1.3 SEM image of 10–40  $\mu\text{m}$  holes at the tri-junctions of platinum grains in the wall of platinum crucible after crystal growth at 1350  $^{\circ}\text{C}$  for 150 h.

- Use high purity platinum for the crucibles.
- Use  $\text{Pb}_3\text{O}_4$  instead of  $\text{PbO}$  as starting raw chemicals.
- Sinter the mixture of raw chemicals to eliminate the free  $\text{PbO}$  in the precursor for crystal growth in any manner, such as a typical ceramic process.

### 1.2.3 Apparatus for crystal growth

The Bridgman growth method is the most straightforward and inexpensive way to grow large crystals of high quality. In order to fabricate PMN–PT crystals of large size and high quality, cost effectively two major modifications have been made to our growth system. First, a multi-crucible approach was taken. Second, to suppress the effect of compositional segregation, a zone-leveling<sup>22–24</sup> configuration was adopted by narrowing the hot zone of the furnace chambers. A Bridgman crystal-growth system with a multi-crucible configuration is given in Fig. 1.5(a). The growth furnace has five chambers; each has three zones: upper, hot and lower. A platinum crucible is placed in a ceramic buffer tube assembly on a levitation mechanism that controls the moving rate of the crucible. A master computer system is used to control the temperature, crucible moving rate and data acquisition. Five crystal boules can be obtained from one run (Fig. 1.5(b)). The typical growth parameters

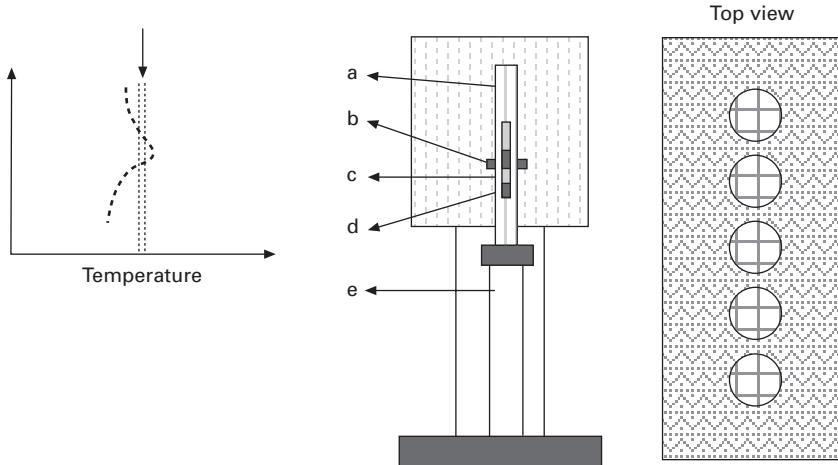


1.4 (a) PbO starts to absorb oxygen to form  $Pb_3O_4$  at 430°C.  $Pb_3O_4$  reaches maximum at 520°C.  $Pb_3O_4$  releases oxygen and forms PbO as temperature continues to ramp up. (b)  $Pb_3O_4$  releases oxygen and forms PbO above 600°C.

are: the maximum temperature 1365°C, temperature gradient 20°C/cm, and growth rate 0.4 mm/h.

The crystal-growth systems have been scaled up to grow 75 mm (3 inch) diameter crystals. Figure 1.6 shows the progress of crystal growth from 50



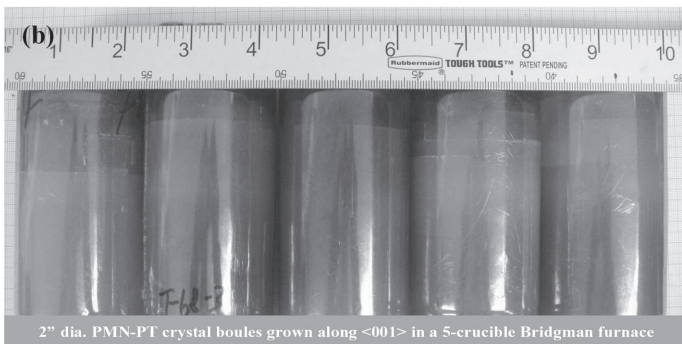


**Crystal-growth system**

a. Ceramic tube liner; b. Heater; c. Crucible; d. Seed; e. Levitation mechanism.

**US patent 6,972,730 B2**

(a)

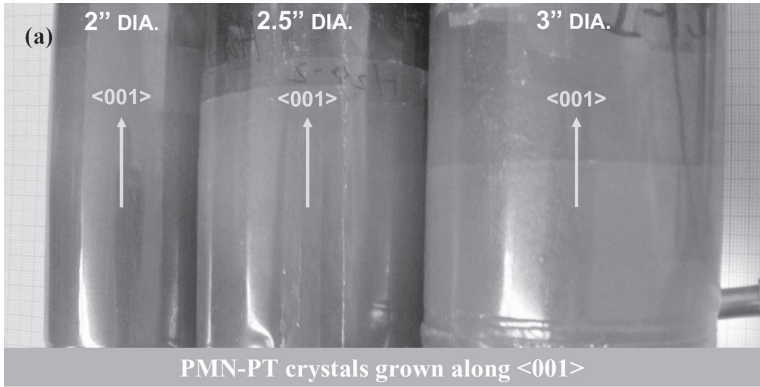


(b)

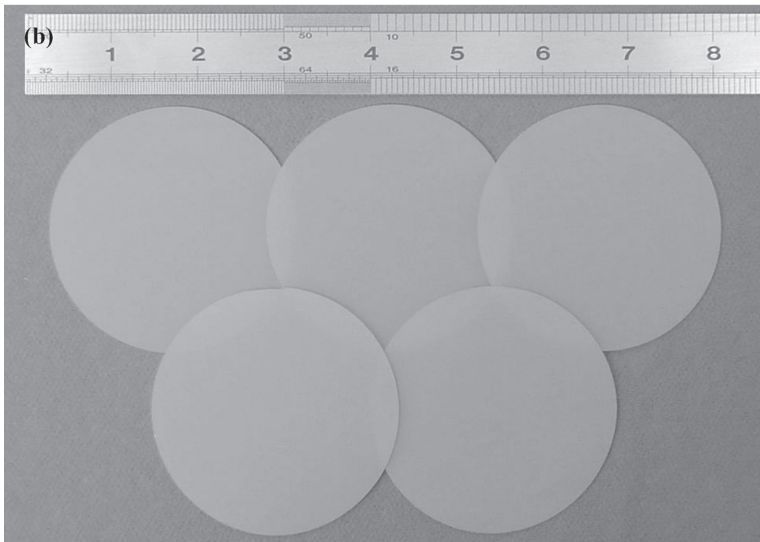
1.5 (a) Multi-crucible Bridgman growth system and (b) as-grown PMN-PT crystal boules with 50 mm (2 inch) diameter by  $\langle 001 \rangle$  seeding. There are some (001) cracks perpendicular to the growth direction in the vicinity of MPB. However, the useful segments are crack-free.

to 75 mm (2 to 3 inch) diameters. The system can deliver the following crystal-growth conditions:

- Maximum hot-zone temperature 1600 °C.
- Temperature gradient near liquid-solid interface 10–20 °C/cm.
- Furnace temperature programmable with control accuracy better than  $\pm 0.1$  °C at 1500 °C.
- Crucible moving rate controlled by a stepping motor.



(a)



(b)

1.6 Crystal growth capacity scaled up: (a) <001>-seeded PMN-PT crystal boules from 50 to 75 mm (2-3 inch) diameter (b); 75 mm (3-inch) diameter (001) wafers of PMN-PT single crystal.

- A data acquisition system monitors all parameters.
- A uninterruptible power supply (UPS) protects the control system.
- A standby natural gas electrical generator protects against power black-out.

#### 1.2.4 Procedures of crystal growth

The normal crystal-growth procedures are listed below:

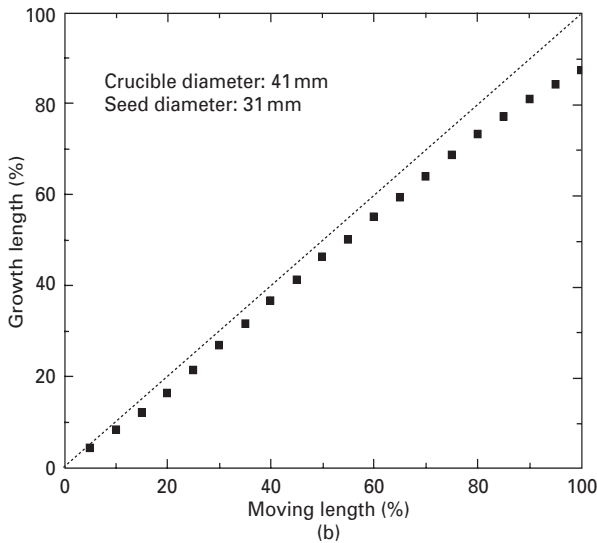
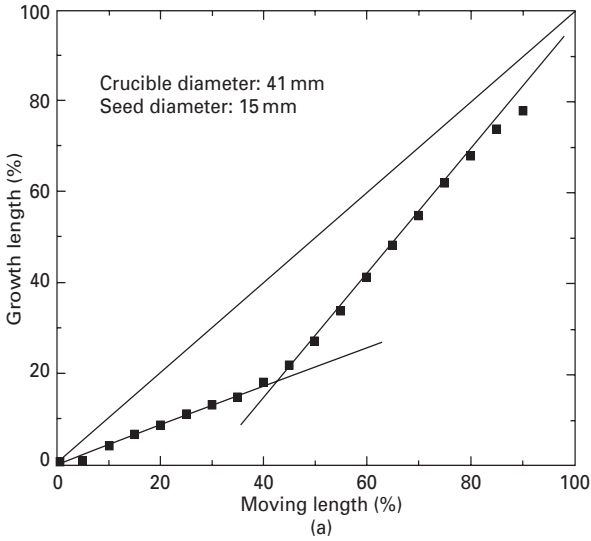
- Prepare the precursors free of PbO.
- Place a <001> seed of PMN–PT crystal at the bottom of the platinum crucible, load the precursor into the crucible, and seal the top of the crucible with a platinum lid.
- Assemble the loaded crucible into a ceramic buffer tube and fill the gap between the crucible and the ceramic tube with alumina or zirconia powders.
- Load the assembly into the corresponding chamber in the growth furnace and adjust the vertical position to the initial growth site in the chamber.
- Heat up the furnace to 1350–1370 °C at a rate of 100 °C/h to melt the loaded precursors.
- Soak for 2–8 h at the melting temperature, then start crystal growth by moving down the assembly at a rate of 0.4–0.8 mm/h.
- When crystal growth is complete, ramp down the furnace temperature at a rate of 60 °C/h to room temperature.
- Unload the crucible.

### 1.2.5 Interface control

General speaking, one of the key parameters of the Bridgman crystal growth is the precise control of the shape and position of liquid/solid interface. The interface shape can be controlled to be flat or a little convex to the melt side. However, it is difficult to keep a constant crystal-growth rate by holding the furnace temperature unchanged. In other words, the growth rate drifts (non-linear) to some degree due to the so-called ‘end-effect’ caused by the limited crucible length. Experimental results indicated that the shorter the crucible the stronger the end-effect, and that the smaller diameter of the seed, the more severe the end-effect. Figure 1.7(a) and 1.7(b) illustrate the difference in the end-effects for the same crucible diameter and length but different seed diameters. It is clear that the smaller-diameter seed shows a larger drift in growth rate. This end-effect strongly affects crystal quality and property uniformity. In the worst case, the acceleration of the growth rate (Fig. 1.7a) may cause constitutional supercooling that disturbs the steady growth, leading to inclusions, micro-cracks and even unexpected nuclei.

## 1.3 Imperfection

In the early stage of the crystal growth, there were several typical macro-defects such as inclusions, voids and cracks. After modification and optimization of furnace structure and growth parameters these defects were eliminated. In addition, the compositional homogeneity was improved by zone leveling and by increasing growth length.



1.7 The influence of end-effect on growth rate for different seed diameters. Small-diameter seed leads to a stronger non-linear growth rate at a constant crucible moving rate.

However, some special imperfections related to domain structures need to be better understood. One is the oxygen deficiency in as-grown PMN-PT crystals. The crystal becomes dark gray instead of light yellow. Although the dark gray color can be bleached by post-annealing (e.g. 600 °C for 10 h, in air) the domain structures remain cloudy and irregular and the physical

properties vary from the normal state. It is difficult to observe the detailed domain structure using transmission electron microscopy (TEM) because domain changes during sample preparation. Another one is the line defect, dislocations that were observed on (111), (211) and (001) faces by chemical etching<sup>25</sup>. So far, there have been few reports on the influence of dislocation density and dislocation orientations on piezoelectric properties.

Both defects mentioned above impact piezoelectric properties that depend on the domain structure. It is almost certain that these types of defect play a role as domain wall pinning centers to modulate or to control the domain structure. Thus, physical properties would vary from the normal state.

## 1.4 Property characterization

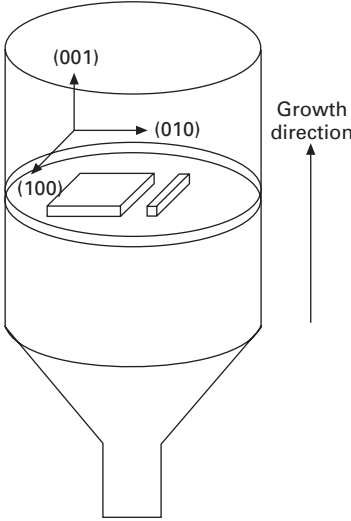
For a PMN–PT crystal grown from stoichiometric melt, PT content increases along the length of the crystal due to compositional segregation. Since properties of PMN–PT crystals are closely related to the composition<sup>27</sup>, variations in piezoelectric properties are expected along the growth direction<sup>28</sup>. This section reports on the systematic characterization of property variations, and their interrelationships for a whole PMN–31%PT crystal boule grown by a normal Bridgman method<sup>29</sup>.

### 1.4.1 Specimen preparation

To characterize property variations along the growth direction of PMN–PT crystals, two types of specimen were prepared (Fig. 1.8). (i) Crystal plates of  $7 \times 7 \times 0.7 \text{ mm}^3$  (17 pieces) and (ii) crystal bars of  $7 \times 0.7 \times 0.7 \text{ mm}^3$  (17 pieces) were sectioned from one crystal boule. All of the six faces of the plates and bars were oriented within  $0.5^\circ$  of the {001} planes. To ensure relative compositional homogeneity within a specimen, the large faces of the crystal plates, and the length direction of the crystal bars, were chosen to be normal to the growth direction  $\langle 001 \rangle$ . In addition, so as to minimize compositional differences between plates and bars, each plate had a corresponding bar sectioned from the same location within the wafer (Fig. 1.8).

### 1.4.2 Poling

Crystal specimen surfaces were ultrasonically cleaned before deposition of gold electrodes by sputtering (Hummer 8 Coater, Anatech). Plates were poled in the thickness direction ( $\langle 001 \rangle$ ), and bars along their length ( $\langle 100 \rangle$ ). The poling field was  $\sim 5 \text{ kV/cm}$ , and the poling current was monitored to completeness at room temperature. All of the properties were determined at room temperature 24h after poling.



1.8 Orientation of crystal plates and bars.

### 1.4.3 Instruments and methods

#### *Dielectric properties*

The dielectric constant  $K$  of crystal plates was calculated from geometry and capacitance measurements<sup>30</sup> (HP 4294A, Agilent Technologies) at different frequencies, according to

$$K = \frac{1}{\epsilon_0} \frac{d}{A} C \quad 1.1$$

where  $K$  is the free ( $K_{33}^T$ , 1 kHz) or clamped ( $K_{33}^S$ , 5 MHz) dielectric constant,  $\epsilon_0$  is the permittivity of free space,  $d$  is the specimen thickness,  $A$  is the electrode area and  $C$  is the capacitance.

#### *Piezoelectric properties*

The longitudinal piezoelectric charge coefficient  $d_{33}$  for crystal plates was measured on a Berlincourt-type quasi-static  $d_{33}$  meter (0.25 N, 110 Hz; model ZJ-3B, Institute of Acoustic, Chinese Academy of Science). Values for the longitudinal piezoelectric voltage coefficient  $g_{33}$  were calculated, according to<sup>31</sup>:

$$g_{33} = \frac{d_{33}}{(\epsilon_0 K_{33}^T)} \quad 1.2$$

Stable  $d_{33}$  values for the bars were not obtained from the meter (to be discussed later). Instead, the values were calculated from  $k_{33}$ ,  $s_{33}^E$  and  $K_{33}^T$  (see below).

### Elastic properties

Elastic constants were calculated from resonance measurements on the bars. The frequencies for the maximum resistance  $f_p$  and maximum conductance  $f_s$  of the crystal bars were determined on the impedance analyzer. The short-circuit compliance  $s_{33}^E$  was calculated, according to<sup>32,33</sup>.

$$s_{33}^E = \frac{1}{4\rho f_p^2 l^2} \frac{1}{1 - k_{33}^2} = s_{33}^D \frac{1}{1 - k_{33}^2} \quad 1.3$$

where  $\rho$  is the crystal density (8.2 g/cm<sup>3</sup>),  $l$  is the bar length (7 mm) and  $k_{33}$  is the electromechanical coupling factor for the longitudinal vibration.

### Electromechanical coupling

The rod extensional electromechanical coupling factor  $k_{33}$  (longitudinal excitation) was determined by one of two methods depending on specimen geometry. For the crystal plates, the coupling factor  $k_{33,Calc}$  was estimated from the free and clamped dielectric constants<sup>34</sup>:

$$k_{33,Calc}^2 = 1 - \frac{K_{33}^S}{K_{33}^T} \quad 1.4$$

For the crystal bars, the coupling factors  $k_{33}$  and  $k_{31}$  (transverse excitation) were determined from the aforementioned resonance frequencies  $f_p$  and  $f_s$ <sup>32,33</sup>.

$$k_{33}^2 = \frac{\pi}{2} \frac{f_s}{f_p} \tan \left( \frac{\pi}{2} \frac{f_p - f_s}{f_p} \right) \quad 1.5$$

### $d_{33}$ and $g_{33}$ calculations

From the values of  $k_{33}$ , and  $s_{33}^E$  obtained for crystal bars and  $K_{33}^T$  from crystal plates,  $d_{33}$  was calculated according to<sup>32</sup>:

$$d_{33,Calc} = k_{33} \sqrt{s_{33}^E} \sqrt{K_{33}^T} \quad 1.6$$

The more accurate  $K_{33}^T$  values obtained from crystal plates were used in the  $d_{33,Calc}$  calculation. The width-to-thickness ratio was 10:1 for plates compared with 1:10 for bars. Similarly, the corresponding piezoelectric voltage coefficient  $g_{33,Calc}$  was calculated from Eq. (1.2).

#### 1.4.4 Property variations

As mentioned above, the PT content for melt-grown crystals increases along the growth direction due to compositional segregation. Accordingly, the

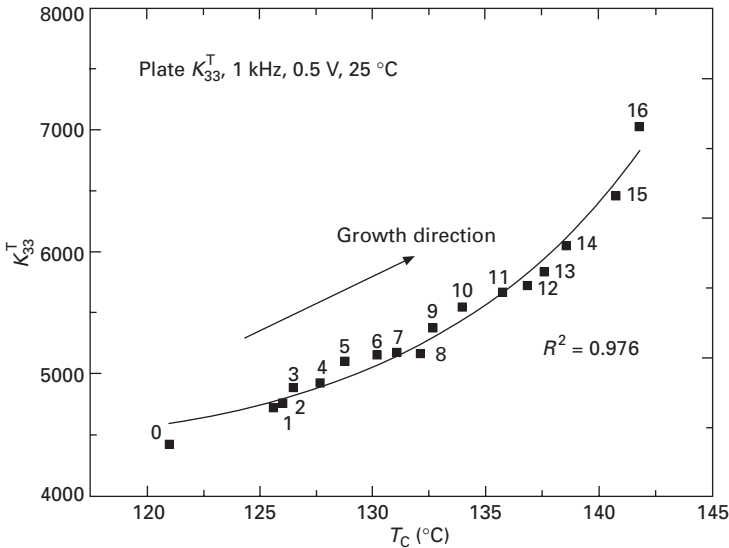
ferroelectric–paraelectric transition temperature ( $T_C$ ) increases with increasing PT content<sup>35,36</sup>. Thus  $T_C$  can be used as an indicator for the composition of PMN–PT specimens<sup>37</sup>. In this section,  $T_C$  is reported as the temperature for maximum  $K_{33}^T$ .

### *Dielectric constant*

Figure 1.9 illustrates the dependence of  $K_{33}^T$  at room temperature on PT content, as judged from  $T_C$  data. Specimen 0 was close to the base of the crystal and specimen 16 was close to the MPB. The subsequent specimens, 1 through 15, encompass the compositional range commonly used in piezoelectric applications. For this set of specimens,  $T_C$  increased from 121 to 142 °C, which corresponded to a PT range of 26.5–32%.  $K_{33}^T$  increased from 4400 to 7000 at room temperature with increasing PT content.

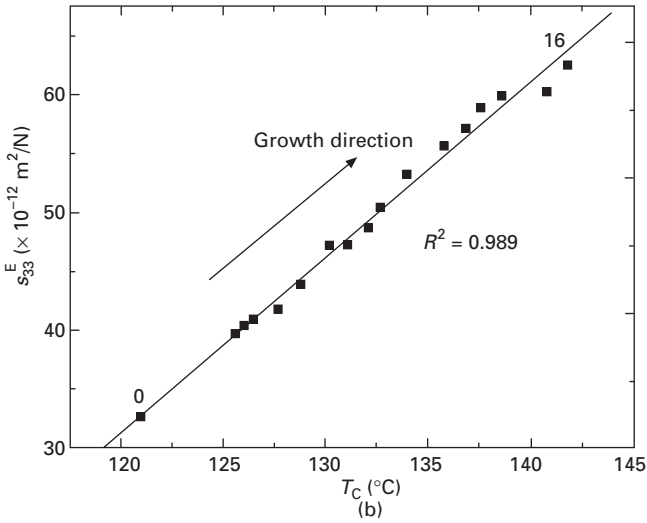
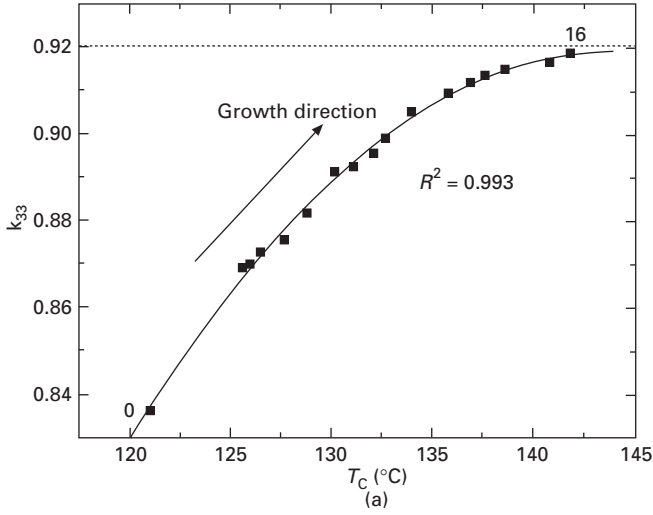
### *Electromechanical coupling factor and elastic compliance*

$k_{33}$  and  $s_{33}^E$  values obtained for the crystal bars increased slightly with increasing  $T_C$  (Fig. 1.10). For example,  $k_{33}$  increased from 0.84 to 0.92 (9.5%) as  $T_C$  increased from 121 °C to 142 °C (i.e., 26.5% to 32% PT), with the majority of  $k_{33}$  values greater than 0.87 (Table 1.1), even though  $K_{33}^T$  and  $d_{33}$  increased significantly. In addition,  $k_{33}$  appeared to approach an asymptotic value of



1.9 Dielectric properties for specimens selected along the growth direction.





1.10 (a) Measured coupling factor and (b) calculated compliance for bars selected along the crystal growth direction.

$\sim 0.92$ . The calculated values of  $k_{33}$  for plates from  $K_{33}^T$  and  $K_{33}^S$  data (Eq. (1.4)) exhibited a similar trend to the  $k_{33}$  values obtained from the bars by the resonance method (Eq. (1.5)) (Table 1.1). The data obtained by calculation and measurements ( $\bar{k}_{33, \text{Calc}} = 0.921$  and  $\bar{k}_{33} = 0.896$ , respectively) are in good agreement ( $< 3\%$ ), giving confidence to the two independent methods of determination for  $k_{33}$ .

The  $s_{33}^E$  values obtained for crystal bars by the resonance method (Eq. (1.3)) increased significantly from  $32.6 \times 10^{-12} \text{ m}^2/\text{N}$  to  $62.6 \times 10^{-12} \text{ m}^2/\text{N}$ , as

**Table 1.1** Coupling factors for bars and plates (as determined by resonance and dielectric measurements, respectively)

Specimen no.	$T_C(^{\circ}\text{C})$	$k_{33}(\text{bar})$	$k_{33}(\text{plate})$
0	121.0	0.836	0.887
1	125.6	0.869	0.904
2	126.0	0.870	0.907
3	126.5	0.873	0.908
4	127.7	0.875	0.911
5	128.8	0.882	0.914
6	130.2	0.891	0.915
7	131.1	0.892	0.916
8	132.1	0.896	0.916
9	132.7	0.899	0.921
10	134.0	0.905	0.925
11	135.8	0.910	0.927
12	136.9	0.912	0.929
13	137.6	0.913	0.932
14	138.6	0.915	0.935
15	140.8	0.917	0.939
16	141.8	0.919	0.944
Average	n/a	0.896	0.921

$T_C$  increased from 121 to 142 °C (i.e. 26.5% PT to 32% PT). There was a strong linear dependence of  $s_{33}^E$  on the PT content near the MPB (Fig. 1.10 b).

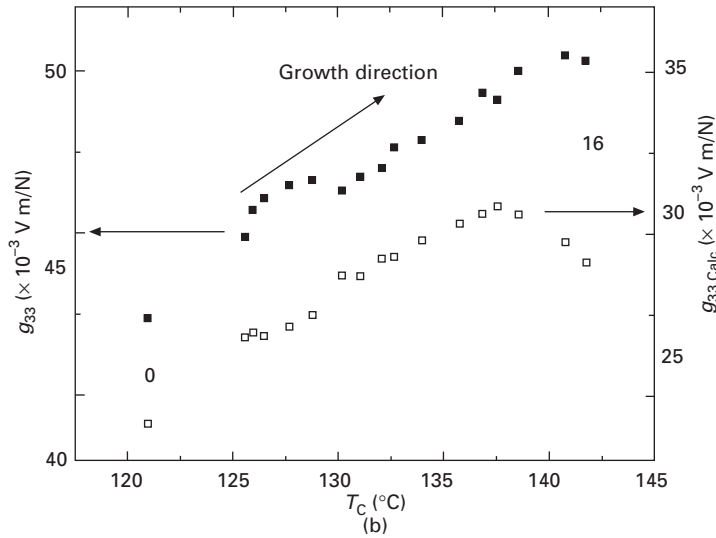
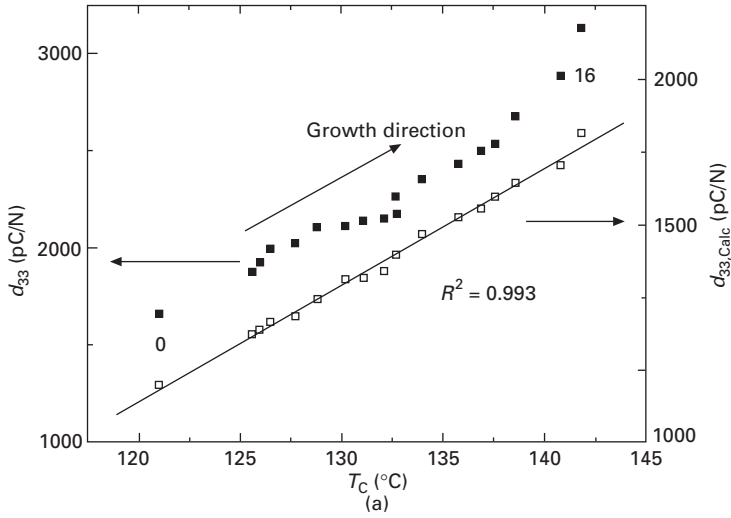
### $d_{33}$ and $g_{33}$

Both (a) the measured  $d_{33}$  values obtained on the plates and (b) the calculated  $d_{33,Calc}$  values for bars and plates (Section 1.3.3) show a strong dependence on PT content (Fig. 1.11b). The values for the directly measured  $d_{33}$  increased from 1660 to 3140 pC/N (by ~90%). The calculated  $d_{33,Calc}$  values increased from 950 to 1820 pC/N, a similar increase of ~90%. There was a strong linear dependence of  $d_{33}$  with  $T_C$ , and thus PT content. Recall that the  $k_{33}$  values were relatively constant in this MPB region.

Figure 11(b) illustrates slight changes in  $g_{33}$  from 42 to  $50 \times 10^{-3}$  V m/N. By comparison, the calculated  $g_{33,Calc}$  values increased initially from 24 to  $31 \times 10^{-3}$  V m/N, but then decreased to  $29 \times 10^{-3}$  V m/N at the  $T_C$  of 142 °C (to be discussed later). The measured values for  $g_{33}$  approached a steady value of  $\sim 50 \times 10^{-3}$  V m/N. By contrast,  $g_{33,Calc}$  reached a maximum value of  $31 \times 10^{-3}$  V m/N at a  $T_C$  of 137 °C.

### Elastic properties and electromechanical coupling

Figure 1.12 illustrates the relationship between  $s_{33}^E$  and  $k_{33}$ . Data are presented with y-axis variable of  $k_{33}^2$  (i.e., energy conversion efficiency) and x-axis



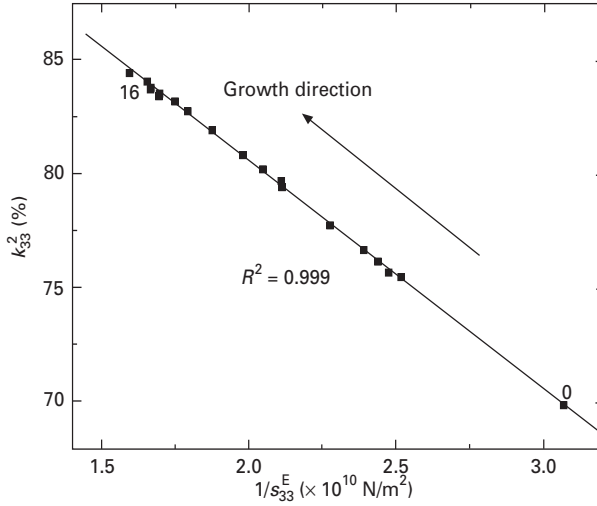
1.11 Comparison of measured and calculated piezoelectric properties for selected plates.

variable of  $1/s_{33}^E$  (related to stiffness). The values of  $s_{33}^E$  and  $k_{33}$  increase with PT content along the growth direction, as indicated by the arrow.

### 1.4.5 Interrelationship of properties

#### Measured and calculated $d_{33}$ and $g_{33}$

The  $d_{33}$  values obtained from the PIEZO  $d_{33}$  meter for the plate specimens are higher than the corresponding calculated  $d_{33,Calc}$  values by an average of



1.12 Relationship between longitudinal energy conversion efficiency and reciprocal compliance.

66% (Fig. 1.11a). Since the calculations of  $d_{33,Calc}$  use parameters obtained from standard geometries (i.e. bars for  $k_{33}$  and  $s_{33}^E$ , plates for  $K_{33}^T$ ),  $d_{33,Calc}$  is considered closer to the true  $d_{33}$  value. The measured values for bars on the PIEZO meter were not reproducible and varied with the applied pre-force, especially for compositions with higher  $T_C$  (closer to the MPB). This was attributed to the larger stresses resulting from the smaller cross-sectional area of the bar ( $0.49 \text{ mm}^2$ ). A larger applied stress (e.g.  $>2 \text{ MPa}$  for a  $1 \text{ N}$  pre-force) may lead to non-linear contributions to  $d_{33}$  [381]. Such effects would be more evident for more compliant specimens closer to the MPB (i.e., higher  $T_C$ ).

$g_{33,Calc}$  was calculated from  $d_{33}$  and  $K_{33}^T$  Eq.(2), where the  $d_{33}$  values were obtained from two different methods and  $K_{33}^T$  was measured only for crystal plates. Consequently,  $g_{33,Calc}$  had two corresponding sets of values (Fig. 1.11b), with  $g_{33,Calc}$  closer to the true values for the reasons discussed above.

#### Covariation of $K_{33}^T$ and $d_{33}$

The results show that both  $d_{33}$  (Fig. 1.11a) and  $K_{33}^T$  (Fig. 1.9) increase significantly ( $>80\%$  and  $>50\%$ , respectively) with a relatively small change in composition (i.e. 4% change in PT content). The increasing trend in both  $d_{33}$  and  $K_{33}^T$  can be attributed to changes in stress-induced and field-induced polarization  $P_3^{30}$ , where:

$$P_i = d_{ijk} T_{jk} \quad 1.7$$

and

$$P_i = \varepsilon_0 \chi_{ij} E_j \quad 1.8$$

Thus, the dielectric susceptibility  $\chi_{33}^T$  is essentially equivalent to  $K_{33}^T$  ( $K_{33}^T = 1 + \chi_{33}^T$ ) for high- $K$  materials ( $K_{33}^T > 4000$  for PMN–PT); therefore,

$$P_i = d_{ijk} T_{jk}; \varepsilon_0 K_{ij} E_j \quad 1.9$$

and it is clear from Eq. (1.9) that both  $d_{33}$  and  $K_{33}^T$  would change in the same sense with displaced polarization  $P_3$ .

Equation (1.6) further explains why  $d_{33}$  exhibits a greater variation (>80%) than  $K_{33}^T$  (>50%). Both  $k_{33}$  and  $s_{33}^E$  increase with  $T_C$  (Fig. 1.10). In addition,  $s_{33}^E$  shows a larger increase than  $K_{33}^T$  (Fig. 1.9) for the same composition and  $T_C$  range (121–142 °C). As a result, the product of  $\sqrt{s_{33}^E}$  and  $\sqrt{K_{33}^T}$  gives a larger relative increase with  $T_C$ , compared with  $K_{33}^T$  ( $\equiv \sqrt{K_{33}^T} \sqrt{K_{33}^T}$ ). Thus, the triple product of  $k_{33}$  (which increases with  $T_C$ ) with  $\sqrt{s_{33}^E}$  and  $\sqrt{K_{33}^T}$ , i.e.,  $d_{33, \text{Calc}} = k_{33} \sqrt{s_{33}^E} \sqrt{K_{33}^T}$ , should have a larger relative increase than  $K_{33}^T$  alone. This is indeed observed in the  $T_C$  range of 121–142 °C (i.e. near the MPB).

Bokov and Ye<sup>39</sup> have suggested that the superior  $d_{33}$  values for PMN–PT crystals before the MPB were due to the large dielectric response ( $K_{33}^T$ ). Our results confirm that an increase in  $K_{33}^T$  is important for an increase in  $d_{33}$ , but  $k_{33}$  and  $s_{33}^E$  are also important. For example, softening in the vicinity of the MPB increases  $s_{33}^E$  and gives rise to enhanced dielectric and piezoelectric displacements, as discussed before.

### *Small increase in the piezoelectric voltage coefficient*

In contrast to the relatively large increases in  $d_{33}$  and  $K_{33}^T$  with  $T_C$  (and PT content),  $g_{33}$  shows a weaker dependence on  $T_C$  (Fig. 1.11b). This is expected from Eq. (1.2), where  $d_{33}$  and  $K_{33}^T$  share similar offsetting increasing trends with  $T_C$ . Specifically,  $g_{33}$  can be derived from Eqs. (1.2) and (1.6) as:

$$g_{33} = \frac{k_{33} \sqrt{s_{33}^E}}{\sqrt{K_{33}^T}} \quad 1.10$$

Similar to the discussion on  $d_{33}$  (above), the relative increases in  $s_{33}^E$  and  $K_{33}^T$  are of the same magnitude. Therefore, the resulting  $g_{33}$  exhibits a weak dependence on  $T_C$  (and PT content).

The decrease in  $g_{33, \text{Calc}}$  for the two specimens with the highest  $T_C$  (Fig. 1.11b) can now be considered in terms of the changes in  $k_{33}$ ,  $s_{33}^E$  and  $K_{33}^T$  in Eq. (1.10):  $k_{33}$  approaches a constant value as  $T_C$  increases,  $s_{33}^E$  increases with a linear dependence, and  $K_{33}^T$  exhibits an exponential increase with  $T_C$ . Therefore, as the composition changes towards the MPB, the exponential

increase in  $K_{33}^T$  out-competes the combined increase in  $k_{33}$  and  $s_{33}^E$ , thus resulting in a net decrease in  $g_{33,Calc}$ , as observed.

### *Mechanical softening and property enhancement*

Property variations occur along the growth direction in PMN–PT crystals with composition towards the MPB. Both  $k_{33}$  and  $s_{33}^E$  increase with  $T_C$  (PT content) (Fig. 1.12). These trends are attributed to an increasing softening that occurs as the composition approaches the MPB (35% PT), where a phase transformation occurs to the tetragonal state. Softening at phase transformations is considered an important factor for induced displacements and the superior properties for  $K_{33}^T$ ,  $d_{33}$  and  $k_{33}$ .

The reported anisotropies in property coefficients for PMN–PT single crystals corroborate our argument that mechanical softening is important for piezoelectric enhancement<sup>40</sup>. For stress-induced displacements, superior piezoelectric properties occur along the softest direction. For the compositions reported above, the lowest value of the Young's modulus (largest elastic compliance) was along  $\langle 001 \rangle$ .

### *Implications for applications*

The property variations along the growth direction for PMN–PT crystals have important implications for device applications. The superior and variable  $d_{33}$  and  $K_{33}^T$  values enable a wide selection of piezoelectric and impedance parameters for design considerations. A most important factor is that  $k_{33}$  remains relatively high and stable ( $k = 0.87\text{--}0.92$ ) over a wide range of  $d_{33}$  and  $K_{33}^T$  values. This allows for the design of devices that do not significantly affect the energy conversion efficiency or signal transmission bandwidth. Experimental results also indicate the voltage coefficient is not superior to PZT ceramics. For example, the  $g_{33}$  of PMN–PT crystals ( $24 \sim 31 \times 10^{-3} \text{ V m/N}$ ) is similar to that of PZT ( $20 \sim 27 \times 10^{-3} \text{ V m/N}$ ). Thus, it would appear not to be particularly beneficial to use PMN–PT for voltage generation. Instead, the design should take advantage of the superior  $d_{33}$  and  $k_{33}$  coefficients of PMN–PT crystals.

Since the property variations occur along the growth direction, it is advantageous to choose crystals grown along preferred crystallographic directions for specific excitation modes. This is particularly true when in-plate homogeneity is critical. Specifically, a  $\langle 001 \rangle$ -seeded crystal offers the best homogeneity for a (001) plate, where the longitudinal extension mode is used. Similarly, a  $\langle 011 \rangle$ -grown crystal is best for (011) plates where the transverse extension mode is desired. The direction of crystal growth becomes increasingly important for larger crystal plates. For example, consider a (001) plate 50 mm in length, sectioned from a  $\langle 011 \rangle$  crystal, where the plate

length direction is  $45^\circ$  to the growth direction. The two ends of the plate are  $>35$  mm apart along the growth direction. For the current melt-growth method, such a distance would allow for significant chemical segregation to occur, with associated property variations along the length of the plate. Therefore, it is preferable to use PMN–PT crystals grown along certain crystallographic directions for specific applications.

## 1.5 Optimization of cut directions

The piezoelectric properties of PMN–PT crystals are anisotropic, i.e. direction dependent. To optimize piezoelectric performance for each vibration modes, we topologically surveyed the maximum piezoelectric  $d$  coefficient through theoretical calculation and experimental verification<sup>26</sup>. The survey has led to discoveries of new cut directions that maximize piezoelectric  $d$  coefficients for all of the possible symmetric domain configurations and all of the vibration modes of PMN–PT crystals.

### 1.5.1 Method

To calculate the piezoelectric coefficients using the matrices for equilibrium properties of the 32 crystal classes<sup>41</sup> we assume that the elasto-piezo-dielectric matrices are applicable not only to the original  $3m$  single-domain PMN–PT crystals but also to the domain-engineered crystals with  $4mm$  ( $\langle 001 \rangle$  poling) or  $mm2$  ( $\langle 011 \rangle$  poling) multi-domain symmetric configurations (see Fig. 1.17 on page 35). Coordinate rotations were applied on all of these three domain symmetries. The maximum piezoelectric coefficients were calculated based on the measured independent matrix values in the original coordinates and verified experimentally in the rotated coordinates.

The fundamental of the transformation law is that the components of a tensor are the components of a physical quantity, which should retain its identity however the axes may be changed. The transformation of piezoelectric coefficients by changing coordinate system is represented by the following equation<sup>42</sup>:

$$d'_{ijk} = \sum a_{il}a_{jm}a_{kn}d_{lmn} \quad 1.11$$

where  $d_{lmn}$  is the piezoelectric coefficient in the original coordinate system,  $d'_{ijk}$  is the piezoelectric coefficient in the new rotated coordinate system, and  $a_{il}$ ,  $a_{jm}$  and  $a_{kn}$  are the components of the transformation matrix.

The coordinate rotation was defined in the following way: rotation was first made by angle  $\phi$  around the  $z$ -axis, then around the new  $x$ -axis by angle  $\theta$ , and finally around the new  $z$ -axis by angle  $\Psi$ <sup>[43]</sup>. All of the rotations were counterclockwise. The piezoelectric coefficients after the rotation in the three-dimensional space were derived as functions of the independent piezoelectric

coefficients in the original coordinate system and the rotated Euler angles ( $\varphi$ ,  $\theta$ ,  $\Psi$ ) using tensor calculations.

The coordinates were selected as follows: for the  $3m$  symmetry,  $[111]$  as  $z$ -axis,  $[1-10]$  as  $x$ -axis and  $[11-2]$  as  $y$ -axis; for  $mm2$  symmetry,  $[011]$  as  $z$ -axis,  $[100]$  as  $x$ -axis, and  $[01-1]$  as  $y$ -axis; for  $4mm$  symmetry,  $[001]$  as  $z$ -axis,  $[100]$  as  $x$ -axis, and  $[010]$  as  $y$ -axis. To obtain the independent piezoelectric coefficients, three sets of specimens of PMN–31%PT crystal ( $3m$ ,  $mm2$  and  $4mm$ ) were prepared to cope with the scattering of the measurements due to PT content variations. Independent piezoelectric coefficients of the three engineered domain systems were directly measured using a modified Berlincout meter with homemade adaptors, with the measurement error within  $\pm 5\%$ .

## 1.5.2 Results and discussion

### $\langle 001 \rangle$ poling

A symmetrical multi-domain configuration is formed with macroscopic tetragonal symmetry ( $4mm$ ) after poling along  $\langle 001 \rangle$ . This  $4mm$  symmetrical domain structure only has three independent piezoelectric coefficients,  $d_{15} = d_{24}$ ,  $d_{31} = d_{32}$  and  $d_{33}$ .

The calculation on the  $4mm$  multi-domain was not presented in this section because it has already been well described in the literature<sup>44</sup>. The maximum of  $d_{33}$  is in the  $\langle 001 \rangle$  direction (see Fig. 1.16 on page 33).

### $\langle 111 \rangle$ poling

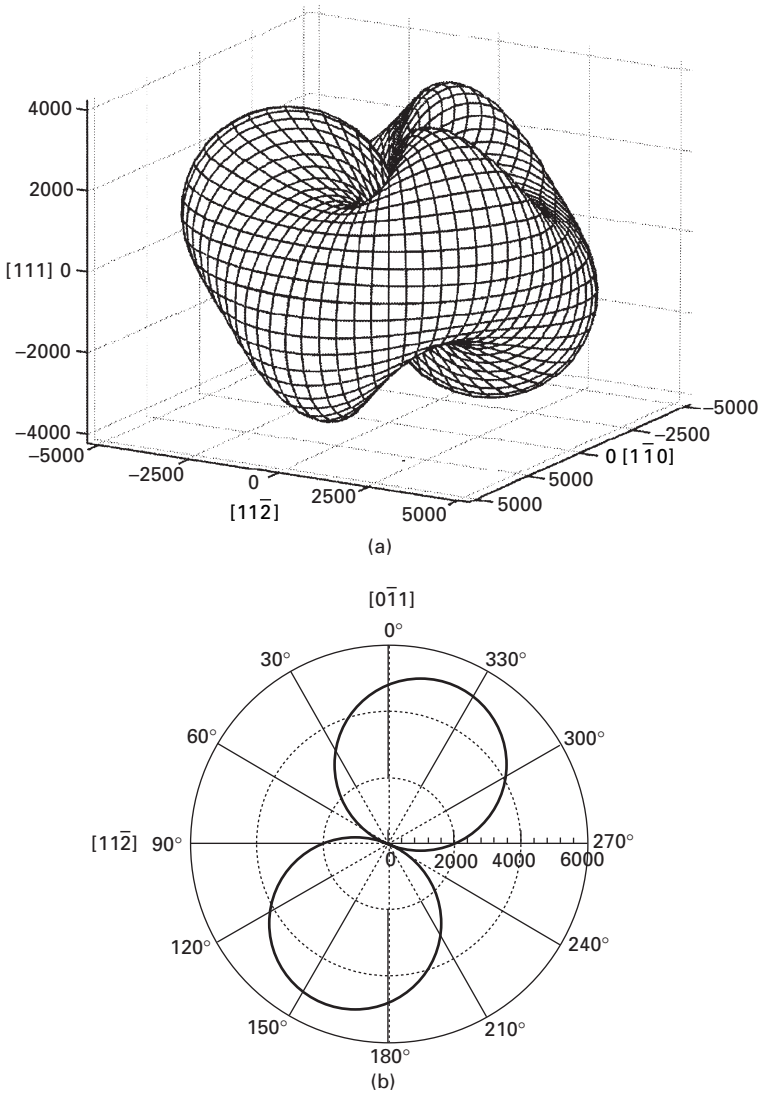
A single domain PMN–PT crystal ( $3m$ ) can be obtained by completely poling along the  $\langle 111 \rangle$  direction. The single domain crystal has four independent piezoelectric coefficients:  $d_{15}$  ( $= d_{14}$ ),  $d_{16}$  ( $= d_{21}/2 = -d_{22}/2$ ),  $d_{31}$  ( $= d_{32}$ ) and  $d_{33}$ . The representation surface of the shear piezoelectric coefficient  $d_{15}$  was then calculated (Fig. 1.13). The amplitude of the surfaces represents the absolute value of the  $d_{15}$  in that orientation.

The maximum value of  $d_{15}$  of 5190 pC/N is in the direction of  $\theta$  of  $337.5^\circ$  and  $\varphi$  of  $0^\circ$  ( $zxt-22.5^\circ$ ). The maximum amplitude of  $d_{15}$  ( $-5190$  pC/N) was found at  $\theta$  of  $157.5^\circ$  and  $\varphi$  of  $0^\circ$  ( $xzt 157.5^\circ$ ). The maximum  $d_{15}$  value in the rotated coordinate is approximately 1.1 times the original value. In particular, the cross-talk from  $d_{16}$  is eliminated. In contrast, strong crosstalk between  $d_{15}$  (4800 pC/N) and  $d_{16}$  (1975 pC/N) exists before the rotation of  $22.5^\circ$ .

### $\langle 011 \rangle$ poling

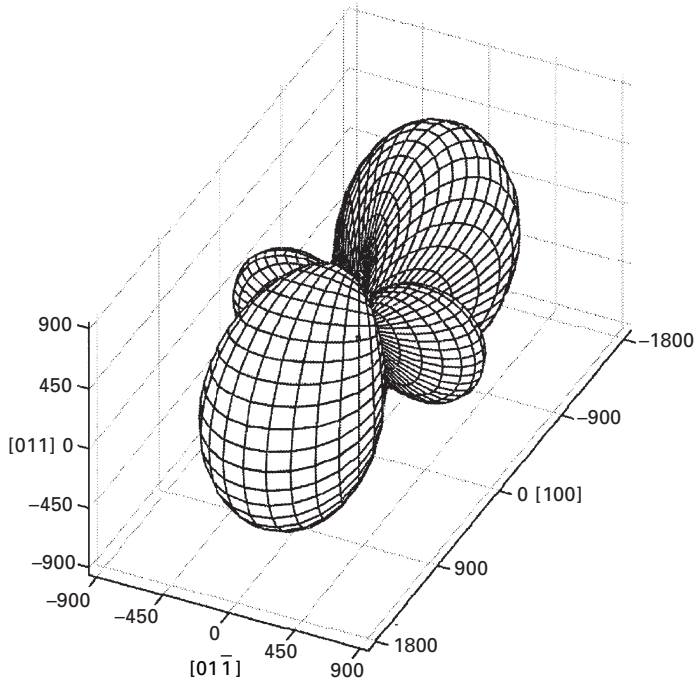
When poling along the  $\langle 011 \rangle$ , a symmetric multi-domain configuration is formed with macroscopic orthorhombic symmetry ( $mm2$ ). The piezoelectric



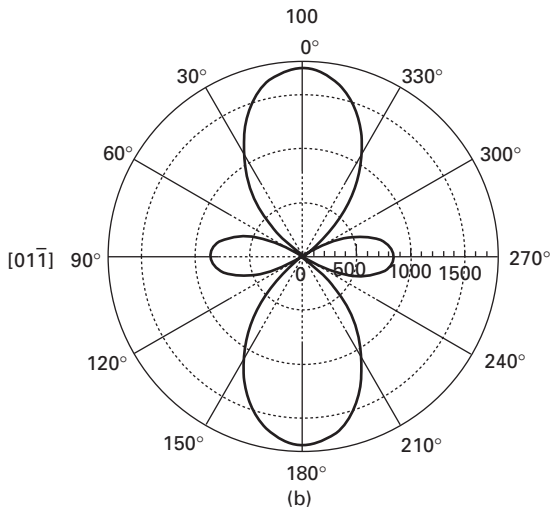


1.13 (a) Three-dimensional plot of the piezoelectric representation surface of  $d_{15}$  for a rhombohedral single-domain PMN-PT crystal. (b) Cross-section of the piezoelectric representation surface in the  $(110)$  plane.

matrices of ferroelectric crystals with orthorhombic symmetry have five independent piezoelectric coefficients:  $d_{15}$ ,  $d_{24}$ ,  $d_{31}$ ,  $d_{32}$  and  $d_{33}$ . The representation surface of the transverse piezoelectric coefficient  $d_{31}$  was calculated (Fig. 1.14). The direction of the largest  $d_{31}$  ( $-1750 \text{ pC/N}$ ) is in  $\theta = 0^\circ$  or  $180^\circ$  and  $\varphi = 0^\circ$ , whereas  $d_{32}$  has a positive value of approximately half or the  $d_{31}$ .



(a)

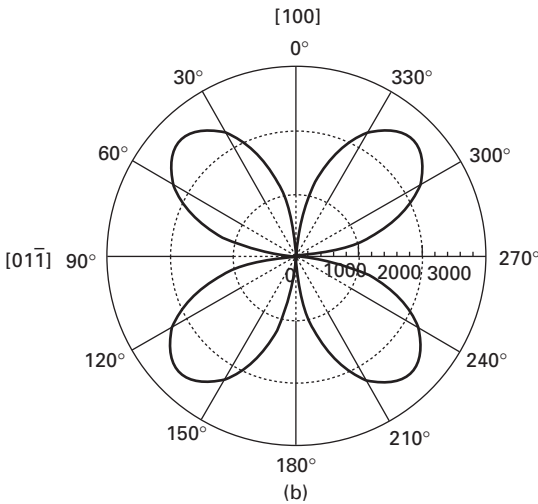
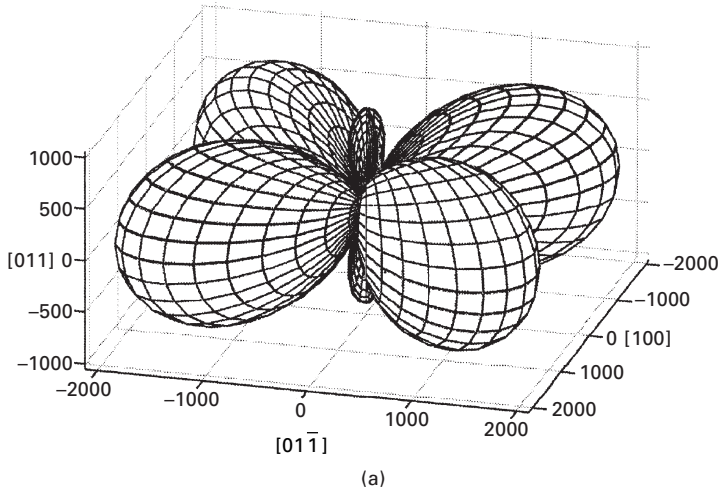


(b)

1.14 (a) Three-dimensional plot of the piezoelectric representation surface of  $d_{31}$  for a PMN-PT crystal with  $mm2$  symmetric multi-domain. (b) Cross-section of the piezoelectric representation surface in the (011) plane.

The shear piezoelectric coefficient  $d_{36}$  is a dependent tensor and is zero in the original coordinate. To explore the maximum value of  $d_{36}$  in a rotated coordinate system, the representation surface of the  $d_{36}$  was calculated (Fig. 1.15). The maximum  $d_{36}$  ( $\pm 2600$  pC/N) was obtained in the direction of  $\theta$  of  $0^\circ$  and  $\varphi$  of  $\pm 45^\circ$  ( $zxt \pm 45^\circ$ ) or  $\pm 225^\circ$ . The  $d_{36}$  rotated about  $z$ -axis can be expressed as:

$$d_{36} = -2d_{31}\sin(\varphi)\cos(\varphi) + 2d_{32}\sin(\varphi)\cos(\varphi) \quad 1.12$$



1.15 (a) Three-dimensional plot of the piezoelectric representation surface of the  $d_{36}$  for a PMN-PT crystal with  $mm2$  symmetric multi-domain. (b) Cross-section of the piezoelectric representation surface in the (011) plane.

Thus, the maximum amplitude of  $d_{36}$  equals  $\pm(d_{32}-d_{31})$  at  $\varphi = \pm 45^\circ$  or  $\pm 225^\circ$ , which is the sum of the absolute values of  $d_{31}$  and  $d_{32}$ . From the application point of view, it is impressive that  $d_{36}$  can be re-poled (poling electrode = working electrode) in addition to the large piezoelectric coefficient.

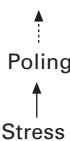
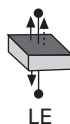
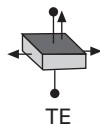

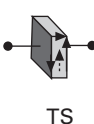
To verify the above maximum values based on the theoretical calculation, four sets of specimens were prepared according to the rotation angles where the maximum  $d$  values occur. The experimental data confirm the calculated results (Table 1.2), suggesting that the piezoelectric matrices of the 32 symmetric classes are applicable to the domain-engineered PMN-PT crystals with  $4mm$  or  $mm2$  multi-domain symmetric configurations.

### 1.6 Conclusions and future trends

The modified Bridgman growth method has been successfully applied to the growth of large PMN-PT crystals (76 mm in diameter  $\times$  200 mm long) on an industrial scale. Based on the conventional crystal growth method, two major modifications have been made: multi-crucible configuration and zone leveling. These successful developments in the crystal growth techniques have led to the cost-effective manufacture of large PMN-PT crystals. The technical progresses that have been made during the crystal-growth investigations include: (1) the understanding of the reason for platinum crucible corrosion by lead-containing melt and knowing how to reduce the leakages during crystal growth; (2) the optimization of the furnace structure and growth parameters to increase the crystal perfection; and (3) the  $\langle 001 \rangle$  seeding method that significantly improves the property uniformity of the (001) crystal wafer.

The piezoelectric properties were systematically characterized. The database of the physical properties of PMN-PT crystals has been documented. It has

Table 1.2 New cut directions to optimize piezoelectric performance

Vibration mode	Longitudinal extension	Transverse extension	Longitudinal shear	Transverse shear
 <p>Poling ↑ Stress</p>	 <p>LE</p>	 <p>TE</p>	 <p>LS</p>	 <p>TS</p>
Symmetry	$4mm$	$mm2$	$mm2$	$3m$
Cut direction	$zxt\ 0^\circ$	$zxt\ 0^\circ$	$zxt\ \pm 45^\circ$	$xzt\ -22.5^\circ$
Calculated (value 31% PT)	$d_{33}$ 2000 pC/N	$d_{31}$ -1750 pC/N	$d_{36}$ 2600 pC/N	$d_{15}, d_{16}$ 5190, 0 pC/N
Measured value (31% PT)	$d_{33}$ 200 pC/N	$d_{31}$ -1750 pC/N	$d_{36}$ 2520 pC/N	$d_{15}, d_{16}$ 5300, 60 pC/N

been determined that the most useful composition of the PMN–PT is in the range of 26.5–32% PT, which corresponds to a  $T_C$  range of 121–142 °C. The majority of properties improved along the growth direction towards the MPB. In the useful composition range,  $d_{33}$  increased by > 80%,  $K_{33}^T$  by >50%, and  $s_{33}^E$  by >90%. By contrast, the  $k_{33}$  and  $g_{33}$  values were less sensitive (<20%) to changes in composition.

The representation surfaces of the piezoelectric charge coefficient ( $d_{ij}$ ) were calculated for the <001>-, <011>- and <111>-poled PMN–PT crystals and experimentally verified. It was discovered that the  $zxt \pm 45^\circ$  cut for the <011>-poled PMN–PT crystal gives a unique re-poleable shear piezoelectric coefficient  $d_{36}$  up to 2600 pC/N. It was also found that an extraordinarily high shear piezoelectric coefficient  $d_{15}$  up to 5190 pC/N for the single domain crystal ( $3m$ ) occurred in the  $xzt 22.5^\circ$  cut. The highest  $d_{31}$  of –1750 pC/N in the  $zxt 0^\circ$  cut was obtained in the <011>-poled crystals.

The achievements in the crystal growth and characterization of PMN–PT crystals have built the foundation for the development of the next generation of acoustic transduction devices. The future trends for the PMN–PT based piezoelectric crystals lie largely in engineering developments that enhance production yields and reduce costs by enlargement of crystal dimensions, i.e. larger diameters (100 mm, 4 inches, or beyond) and longer length. Further progress in the improvement of compositional segregation (e.g. by continuous top-feeding Bridgman method<sup>45</sup>) is important for commercialization. In addition, to broaden applications, the physical properties of PMN–PT-based crystals need to be improved, in particular, the thermal stability and electrical coercive field. To paraphrase, hardening of PMN–PT based crystals must be developed using the Bridgman method. A straightforward approach is through compositional modifications of a PMN–PT binary system with a third component, such as PIN (lead indium niobate) or PYbN (lead ytterbium niobate), to form a ternary MPB system. H. C. Materials has demonstrated the feasibility of growing 50 mm (2-inch) diameter crystals of PYbN–PMN–PT (15/50/35) and PIN–PMN–PT (26/43/31) using the Bridgman method<sup>46</sup>. Both crystals show higher developing temperatures above 110 °C and larger coercive field of 5~6 kV/cm compared with PMN–PT crystals (85~95 °C and 2 kV/cm, respectively). It is expected that the success in the fabrication of large-sized piezoelectric single crystals with modified compositions using the Bridgman method will lead to omni-applications of these crystals in acoustic transduction devices.

## 1.7 Appendix

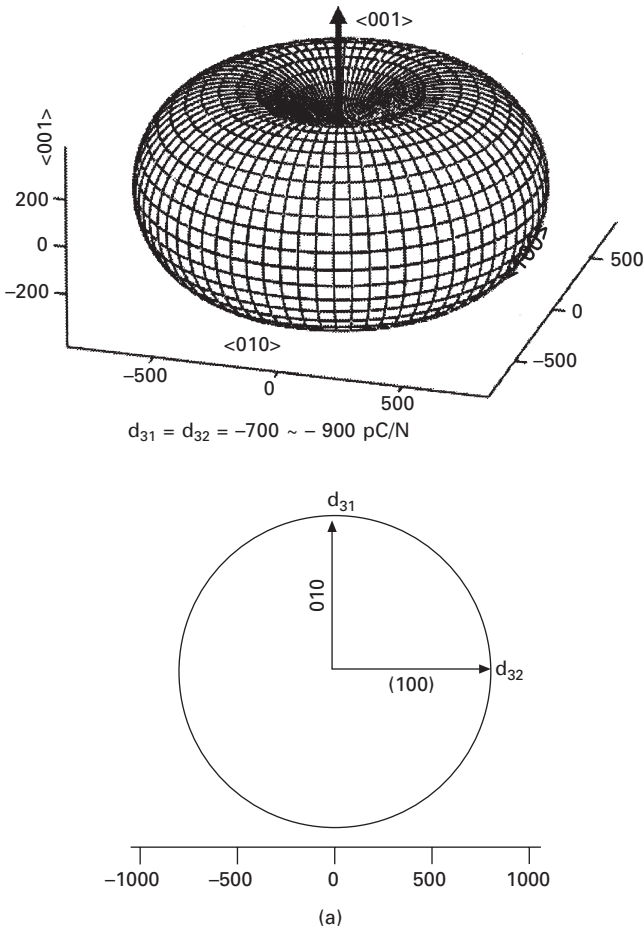
The following data are very useful for the device designer to select PMN–PT crystals correctly and to use the giant piezoelectric property effectively. The physical properties of the crystals strongly depend on the cut directions and

Table 1.3 Property comparisons between <001>-poled 33-mode, and <011>-poled 31-mode

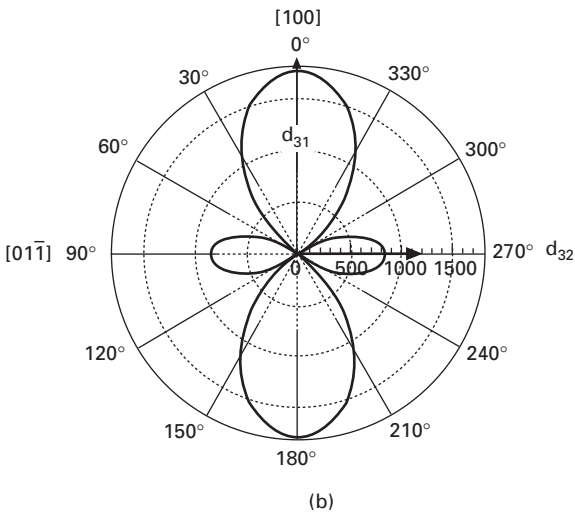
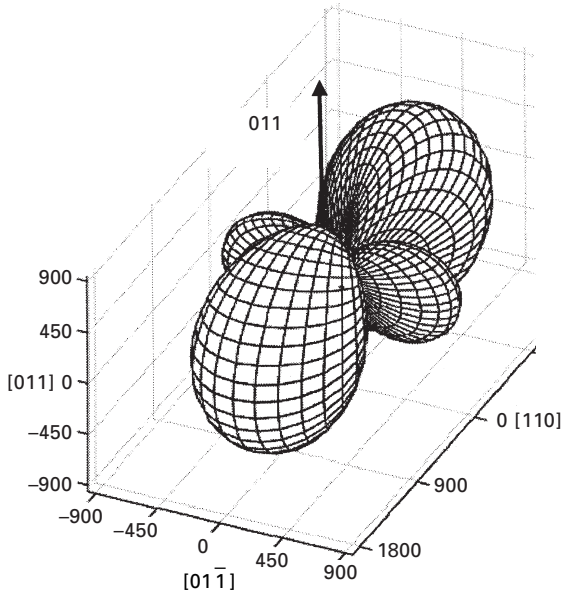
<001>-poled 33-mode			<011>-poled 31-mode				
Property		Type A	Type B	Property	Type A	Type B	
$K_3^T$		5000	6500	$K_3^T$	3200	4600	
$\tan\delta$		0.0040	0.0060	$\tan\delta$	0.0035	0.0024	
$d_{33}$	[pC/N]	1600	2400	$d_{31}$	[pC/N]	-1100	-1750
$d_{31}$	[pC/N]	-580	-900	$d_{32}$	[pC/N]	301	564
$k_{33}$		0.88	0.91	$k_{31}$		0.69	0.90
$s_{33}^E$	[ $10^{-12}$ m <sup>2</sup> /N]	38	60	$s_{11}^E$	[ $10^{-12}$ m <sup>2</sup> /N]	53	84
$s_{33}^D$	[ $10^{-12}$ m <sup>2</sup> /N]	9.8	12	$s_{11}^D$	[ $10^{-12}$ m <sup>2</sup> /N]	26	30
$g_{31}$	[ $10^{-3}$ V m/N]	32	37	$g_{31}$	[ $10^{-3}$ V m/N]	-34	-38
$E_c$ coercive	[kV/cm]	2.5	2.3	$E_c$ coercive	[kV/cm]	4.5	4.0
Depoling	[°C]	93	85	Depoling	[°C]	95	85
Acoustic imp.	mrayl	28	277	Acoustic imp.	mrayl	32	30
<001>				<001>			

vibration modes. Three symmetric poling directions provide totally different piezoelectric properties like different materials even though the crystals have same chemical compositions. The chemical composition, i.e. PT content, also impacts on the physical properties. It can be seen in the property table below. Type A and B crystals sorted by compositions are 28% PT and 31% PT respectively.

The data and information in Table 1.3 and Figs 1.16 and 1.17 are a brief summary of the most important physical properties of the PMN–PT crystals.

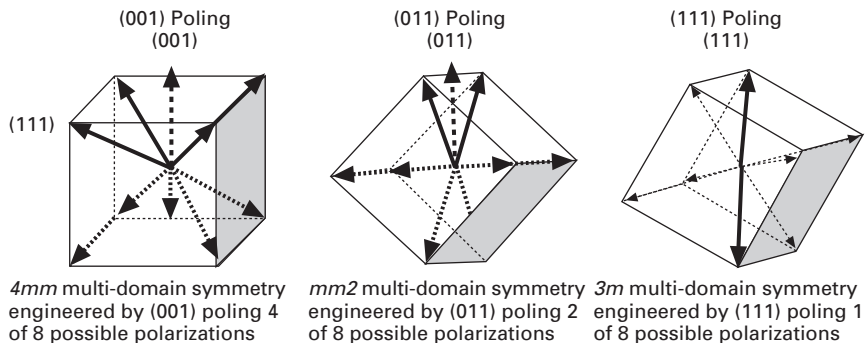


1.16 Anisotropic difference between <001>-poled 31-mode and <011>-poled 31-mode: (a) 3D plot of  $d_{31}$  for <001> poled PMN–PT (left), 2D plot, Z-cut (right); (b) 3D plot of  $d_{31}$  for <110> poled PMN–PT (left), 2D plot, Z-cut (right).



1.16 (Continued)





1.17 Domain states engineered in three configurations.

## 1.8 References

1. The US Navy 'Piezoelectric Crystal Planning Workshop', Washington Dulles Airport Marriott, May 14–16, 1997.
2. S.-E. Park and T.R. Shrout, 'Ultrahigh strain and piezoelectric behavior in relaxor based ferroelectric single crystals', *J. Appl. Phys.*, **82**, 1804–1881 (1997).
3. S.-E. Park and T.R. Shrout, 'Characteristics of relaxor-based piezoelectric single crystals for ultrasonic transducers', *IEEE Trans. UFFC*, **44**, 1140–1147 (1997).
4. T.R. Shrout, Z.P. Chang, N. Kim, and S. Markgraf, 'Dielectric behavior of single crystals near the  $(1-x)\text{Pb}(\text{Mg}_{1/3}\text{Nb}_{2/3})\text{O}_3-x\text{PbTiO}_3$  morphotropic phase boundary', *Ferroelectric Lett.*, **12**, 63–69 (1990).
5. P.M. Bridenbaugh, J. Rottenberg and G.M. Loiacono, 'Single crystal growth of PMN–PT solid solutions', US Navy 'Piezoelectric Crystal Planning Workshop', Washington Dulles Airport Marriott, May 14–16, 1997.
6. M. Dong and Z.G. Ye, 'High-temperature solution growth and characterization of the piezo-/ferroelectric  $(1-x)\text{Pb}(\text{Mg}_{1/3}\text{Nb}_{2/3})\text{O}_3-x\text{PbTiO}_3$  [PMNT] single crystals' *J. Crystal Growth*, **209**, 81–90 (2000).
7. D.R. Gabbe, 'Top-seeded solution growth of PMN–PT single crystals', US Navy Workshop on Acoustic Transduction Materials and Devices, at Baltimore, MA, May 14–16, 2001.
8. L.C. Lim, 'Flux growth of large-size high homogeneity PMN–PT single crystals', US Navy Workshop on Acoustic Transduction Materials and Devices, at State College, PA, May 6–8, 2003.
9. K. Harada, S. Shimadzu, T. Kobayashi, S. Saitoh and Y. Yamashita, 'Crystal growth and electrical properties of  $\text{Pb}[(\text{Zn}_{1/3}\text{Nb}_{2/3})_{0.91}\text{Ti}_{0.09}]\text{O}_3$  single crystals produced by solution Bridgman method', *J. Am. Cer. Soc.*, **81**, 2785–2873 (1998).
10. R. Soundararajan, R.N. Das, R. Tjossem, A. Bandyopadhyay, K.G. Lynn, E.E. Eisser and J. Lazaroff, 'Growth and characterization of single-crystal lead magnesium niobate-lead titanate via high-pressure vertical Bridgman method', *J. Mater.*, **9–12**, 605–619 (2004).
11. P.W. Bridgman, 'Certain physical properties of single crystals of tungsten, antimony, bismuth, tellurium, cadmium, zinc, and tin', *Proc. Am. Acad. Arts Sci.*, **60**, 305–383 (1925).

12. D.C. Stockbarger, 'Production of large single crystals of lithium fluoride', *Rev. Sci. Instr.*, **7**, 133–136 (1936).
13. Z.G. Ye, P. Tissot and H. Schmid, 'Pseudo-binary  $\text{Pb}(\text{Mg}_{1/3}\text{Nb}_{2/3})\text{O}_3\text{-PbO}$  phase diagram and crystal growth of  $\text{Pb}(\text{Mg}_{1/3}\text{Nb}_{2/3})\text{O}_3[\text{PMN}]$ ', *Mat. Res. Bull.*, **25**, 739–748, (1990).
14. H. Luo, G. Shen, P. Wang, X. Le, and Z. Yin, 'Study of new piezoelectric material-relaxor ferroelectric single crystals', *J. Inorg. Mater.*, **12**, 768 (1997).
15. G. Xu, H. Luo, G. Shen, Q. Le, W. Zhong, H. Xiu and Z. Yin, 'Growth and properties of tetragonal single crystal PMN-PT', The Eleventh Chinese Conference on Crystal Growth and Materials, Chang-Chuen, Applied Chemistry Institute, Chinese Academy of Sciences, September 7–13, 1997.
16. P. Han, 'Growth and characterization of large PMN-PT crystals', US Navy Workshop on Acoustic Transduction Materials and Devices, at State College, PA, April 13–15, 1999.
17. P.M. Bridenbaugh, J. Rottenberg and G. Ruland, 'Single crystal growth of PMN-PT', US Navy Workshop on Acoustic Transduction Materials and Devices, at State College, PA, April 13–15, 1999.
18. S.G. Lee, R. Monteiro, M.C. Custodio and R.S. Feigelson, 'Growth of PMN and PMN-PT by the vertical Bridgman method', US Navy Workshop on Acoustic Transduction Materials and Devices, at State College, PA, April 13–15, 1999.
19. K.T. Zawilski, M. Custodio, C. Claudia, R.C. DeMattei, S.G. Lee, R.G. Monteiro, H. Odagawa and, R.S. Feigelson, 'Segregation during the vertical Bridgman growth of lead magnesium niobate-lead titanate single crystals', *J. Crystal Growth*, **258**, 353–367 (2003).
20. P. Han and J. Tian, 'Progress in growth of 3-inch diameter PMN-PT crystals', US Navy Workshop on Acoustic Transduction Materials and Devices, The Penn State Conference Center, State College, PA, 9–11 May, 2006.
21. J.S. Nordyke, *Lead in the World of Ceramics*, The American Ceramic Society, Inc. Columbus, OH 43214. (1984).
22. W.G. Pfann, *Zone Melting*, 2nd edn, Wiley, New York (1966).
23. P. Han, 'Hybrid Stockbarger zone-leveling melting method for directed crystallization and growth of single crystals of lead magnesium niobate-lead titanate (PMN-PT) solid solutions and related piezocrystals', US Patent 6942730 B2 (Nov., 2001).
24. P. Han, Final Report (HCM0012, 1999), Contract No. N00014-98C-0414, Project title: 'Growth of large-sized relaxor ferroelectric single crystals'.
25. P. Han, 'Recent development of fabrication of PMN-PT piezocrystals: crystal manufacturing and domain engineering, US Navy Workshop on Acoustic Transduction Materials and Devices, The Penn State Conference Center, State College, PA, 6–8 May, 2003.
26. P. Han, W. Yan, J. Tian, X. Huang and H. Pan, 'Cut directions for the optimization of piezoelectric coefficients of lead magnesium niobate-lead titanate ferroelectric crystals', *Appl. Phys. Lett.*, **86**, 052902 (2005).
27. X.Y. Zhao, B.J. Fang, H. Cao, Y.P. Guo and H.S. Luo, 'Dielectric and piezoelectric performance of PMN-PT single crystals with compositions around the MPB: influence of composition, poling field and crystal orientation', *Mater. Sci. Engr. B Solid State Mater. for Adv. Tech.*, **96**, 254–262 (2002).
28. H. Cao, B.J. Fang, H.Q. Xu and H.S. Luo, 'Effects of segregation on composition and dielectric and piezoelectric properties of  $\text{Pb}(\text{Mg}_{1/3}\text{Nb}_{2/3})\text{O}_3\text{-38\%PbTiO}_3$  single crystal', *J. Inorg. Mater.*, **18**, 50–56 (2003).

29. J. Tian, P. Han and D. Payne, 'Measurements along the growth direction of PMN-PT crystals: dielectric, piezoelectric, and elastic properties', *IEEE Trans. UFFC*, vol 54, no. 9, 1895–1902, September (2007).
30. A.J. Moulson and J.M. Herbert, *Electroceramics*, 2nd edn. Wiley, Hoboken, NJ (2003).
31. Piezoelectric and Ferroelectric Crystals Committee, 'IRE Standards on Piezoelectric Crystals: Measurements of Piezoelectric Ceramics, 1961', *Proc. IRE*, 1161–1169 (1961).
32. Standards Committee of the IEEE Ultrasonics, Ferroelectrics, and Frequency Control Society, '*IEEE Standard on Piezoelectricity*', IEEE, New York, 1–66 (1987).
33. Y. Li, Z. Qin, and Z. Zhou, *Measurement of Piezoelectric and Ferroelectric Materials*, 1st edn, Science Press, Beijing (1984).
34. IEEE, 'IRE Standards on Piezoelectric Crystals: Determination of the Elastic, Piezoelectric, and Dielectric Constants – The Electromechanical Coupling Factor, 1958', *Proc. IRE*, 764–778 (1958).
35. T.R. Shrout, Z.P. Chang, N.C. Kim, and S. Markgraf, 'Dielectric behavior of single-crystals near the  $(1 - x)\text{Pb}(\text{Mg}_{1/3}\text{Nb}_{2/3})\text{O}_3 - x\text{PbTiO}_3$  morphotropic phase-boundary', *Ferroelectrics Lett. Sect.*, **12**, 63–69 (1990).
36. D. Zekria, V.A. Shuvaeva and A.M. Glazer, 'Birefringence imaging measurements on the phase diagram of  $\text{Pb}(\text{Mg}_{1/3}\text{Nb}_{2/3})\text{O}_3 - \text{PbTiO}_3$ ', *J. Phys. -Condensed Matter*, **17**, 1593–1600 (2005).
37. J. Tian, 'Measurements along the growth direction for PMN–PT crystals: dielectric, piezoelectric, and mechanical properties', MS Thesis, University of Illinois at Urbana-Champaign, Urbana (2006).
38. D. Viehland, J.F. Li, E. McLaughlin, J. Powers, R. Janus and H. Robinson, 'Effect of uniaxial stress on the large-signal electromechanical properties of electrostrictive and piezoelectric lead magnesium niobate lead titanate ceramics', *J. Appl. Phys.*, **95**, 1969–1972 (2004).
39. A.A. Bokov and Z.G. Ye, 'Universal relaxor polarization in  $\text{Pb}(\text{Mg}_{1/3}\text{Nb}_{2/3})\text{O}_3$  and related materials', *Phys. Rev. B*, **66**, 064103 1–9 (2002).
40. D. Viehland and J.F. Li, 'Young's modulus and hysteretic losses of  $0.7\text{Pb}(\text{Mg}_{1/3}\text{Nb}_{2/3})\text{O}_3 - 0.3\text{PbTiO}_3$ : single versus polycrystalline forms', *J. Appl. Phys.*, **94**, 7719–7722 (2003).
41. W.G. Cady, *Piezoelectricity*, McGraw-Hill, New York (1946).
42. J.F. Nye, *Physical Properties of Crystals*, Clarendon Press, Oxford (1957).
43. H. Goldstein, *Classical Mechanics*, 2nd edn, Addison-Wesley, Reading, MA, (1980).
44. R. Zhang, B. Jiang and W. Cao, 'Orientation dependence of piezoelectric properties of single domain  $0.67\text{Pb}(\text{Mg}_{1/3}\text{Nb}_{2/3})\text{O}_3 - 0.33\text{PbTiO}_3$  crystals', *Appl. Phys. Lett.*, **82**, 3737–3739 (2003).
45. M. Sugimoto, 'Magnetic spinel single crystals by Bridgman technique', *Crystals, Growth, Properties and Applications*, ed (C.J.M. Rooijmans) Springer-Verlag, Berlin, Heidelberg, New York (1978).
46. J. Tian and P. Han, 'Growth and property characterization of lead magnesium niobate–lead titanate based single crystals', US Navy Workshop on Acoustic Transduction Materials and Devices, The Penn State Conference Center, State College, PA, 15–17 May, 2007.

## Flux growth and characterization of PZN–PT and PMN–PT single crystals

L - C LIM, National University of Singapore and Microfine Materials Technologies Pte Ltd, Singapore

### 2.1 Introduction

Relaxor single crystals, notably single crystals of solid solutions of  $\text{Pb}(\text{Zn}_{1/3}\text{Nb}_{2/3})\text{O}_3\text{--PbTiO}_3$  (PZN–PT) and  $\text{Pb}(\text{Mg}_{1/3}\text{Nb}_{2/3})\text{O}_3\text{--PbTiO}_3$  (PMN–PT), have been studied extensively in recent years due to their extremely high dielectric and piezoelectric constants compared with state-of-the-art lead zirconate titanate (PZT) ceramics. They are candidate materials for new high-performance piezo-devices such as medical ultrasound imaging probes (Saitoh *et al.*, 1994, 1999; Lopath *et al.*, 1996; Gururaja *et al.*, 1999; Ritter *et al.*, 2000; Oakley and Zipparo, 2000; Rhim *et al.*, 2002, 2005; Michau *et al.*, 2002; Cheng *et al.*, 2003; Marin-Franch *et al.*, 2004; Chen and Panda, 2005), sonars for underwater communications (Powers *et al.*, 2000; Tressler and Howarth, 2000, 2003; Park and Hackenberger, 2002; Marin-Franch *et al.*, 2004), high-authority sensors and actuators (Wlodkowski *et al.*, 2000, 2001; Park and Hackenberger, 2002; Shipps and Deng, 2003), etc.

Unlike PZT materials, PZN–PT and PMN–PT single crystals can be grown with relative ease from either high-temperature solution and/or congruent melt. The growth of relaxor single crystals was pioneered by the Russian scientists in the late 1950s, who successfully synthesized monocrystals of  $\text{Pb}(\text{Ni}_{1/3}\text{Ta}_{2/3})\text{O}_3$  (PNiT),  $\text{Pb}(\text{Mg}_{1/3}\text{Ta}_{2/3})\text{O}_3$  (PMT),  $\text{Pb}(\text{Co}_{1/3}\text{Nb}_{2/3})\text{O}_3$  (PCoN) and  $\text{Pb}(\text{Zn}_{1/3}\text{Nb}_{2/3})\text{O}_3$  (PZN) by the solution growth technique with  $\text{PbO}$  flux (Myl'nikova and Bokov, 1959, 1962; Bokov and Myl'nikova, 1961). In the late 1960s, Nomura and co-workers (Nomura *et al.*, 1969; Yokomizo *et al.*, 1970) succeeded in growing single crystals of PZN–PT solid solution of the entire composition range. Since then, there have been only a few reports on the growth of PMN single crystals using the same flux (Bonner and Van Uitert, 1967; Afanas'ev *et al.*, 1977; Setter and Cross, 1980; Petrovskii *et al.*, 1984).

In the early 1980s, Kuwata *et al.* (1981, 1982) performed a series of measurements and found that PZN–9%PT samples poled along the [001] crystal axis exhibited anomalously large piezoelectric coefficients and

electromechanical coupling factors ( $d_{33} = 1500$  pC/N and  $k_{33} = 0.92$ ). There followed a period of little research activity in this area. In 1990, Ye *et al.* (1990) reported a systematic study on the growth of PMN single crystal with PbO flux, who also noted that addition of 5 wt%  $B_2O_3$  promoted the formation of the pyrochlore phase. On the other hand, ShROUT *et al.* (1990) reported the successful synthesis of PMN-PT single crystal with PbO +  $B_2O_3$  complex fluxes.

In the mid-1990s, systematic studies of flux growth of PZN-PT single crystals using the high-temperature flux technique have been carried out by two separate groups in Pennsylvania State University and Toshiba Research Center, respectively (Mulvihill *et al.*, 1996; Park *et al.*, 1996, 1997; Kobayashi *et al.*, 1997, 1998; Saitoh *et al.*, 1999). By then, the size of the crystals obtained was sufficiently large to enable a detailed property evaluation of the materials and for device exploitation. In 1994, Saitoh *et al.* published the first patent of medical ultrasonic probe made of PZN-PT single crystal of improved sensitivity and bandwidth. In 1996 and 1997, Park and ShROUT (1997a, b, c) published a series of papers confirming the superior dielectric and piezoelectric properties of single crystals of PZN-PT and PMN-PT systems. Their works have created a renewed interest worldwide in growing large-size relaxor-PT single crystals and in their applications in various piezo devices and systems. More recent works related to flux growth of PZN-PT single crystal include that of Gentil *et al.* (2000), Kumar *et al.* (2000), Zhang *et al.* (2000), Sentailler *et al.* (2002), Xiao *et al.* (2002), Dabkowski *et al.* (2004), Lim and Rajan (2004), Benayad *et al.* (2004) and Babu *et al.* (2006), while similar studies but for PMN-PT crystals were performed by Park *et al.* (1998), Dong and Ye (1999), Jiang *et al.* (2001), Fan *et al.* (2003), Lim *et al.* (2005) and Kania *et al.* (2005).

The size of PZN-PT and PMN-PT single crystals produced by the conventional flux growth technique remained relatively small, being <20 mm typically. In order to growth large PZN-PT single crystals, other flux growth techniques have been explored. These include the solution Bridgman growth technique by Shimanuki *et al.* (1998), Harada *et al.* (1998, 2001), Matsushita *et al.* (2002), Fang *et al.* (2002), Xu *et al.* (2002, 2003, 2005) and Babu *et al.* (2006). In addition, the top-seeded solution growth technique has also been attempted (Bonner and Van Uitert, 1967; Park *et al.*, 1998; Chen and Ye, 2001a,b; Karaki *et al.*, 2002a; Bertram *et al.*, 2003; Benayad *et al.*, 2004), while Fang *et al.* (2001) reported the growth of PZN-9%PT single crystal directly from melt. At the time of writing, the largest flux-grown PZN-PT single crystals measure about 3 inches (76.2 mm) in diameter, and were produced by the solution Bridgman growth method with a bottom-supported Pt crucible (Matsushita *et al.*, 2002).

As for PMN-PT, the growth of this crystal from congruent melts has been experimented by contemporary researchers and crystal growers recently.

PMN–PT single crystals of 50–76 mm or larger in diameter and more than 100 mm in boule length have been successfully grown by several groups (Lee *et al.*, 1999; Zhu and Han, 1999; Luo *et al.*, 2000a,b; Xu *et al.*, 2000, 2001; Sentailler *et al.*, 2002; Wan *et al.*, 2004; Shin *et al.*, 2004; Nicoara *et al.*, 2005).

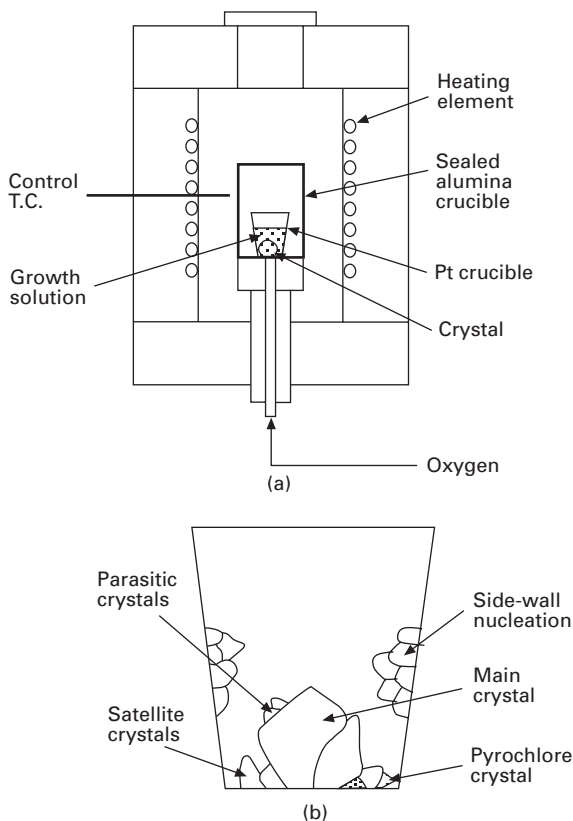
Despite the extensive efforts made in the flux growth of PZN–PT and PMN–PT and the melt-growth of PMN–PT single crystals, currently grown PZN–PT and PMN–PT single crystal are plagued with a host of problems. One of the major issues has been compositional segregation in the grown crystals. This has led to large scatter in measured dielectric and electromechanical properties reported by various research groups as well as within individual groups (Luo *et al.*, 2000a,b; Xu *et al.*, 2000, 2001a,b; Sentailler *et al.*, 2002; Karaki *et al.*, 2002b; Guo *et al.*, 2003; Zawilski *et al.*, 2003; Shin *et al.*, 2004; Wan *et al.*, 2004; Nicoara *et al.*, 2005). Developing ways of growing large high-homogeneity PZN–PT and PMN–PT single crystals is thus one of the major challenges faced by scientists and researchers before these crystals find wide spread applications.

This chapter describes the results of flux growth of PZN–PT and PMN–PT single crystals performed in the author's laboratory over the past seven years (Kumar and Lim, 2000; Lim, 2004; Lim and Rajan, 2004; Rajan *et al.*, 2005; Lim *et al.*, 2005). The flux growth mechanisms of PZN–PT and PMN–PT single crystals and the effects of flux and crystal compositions and growth conditions on the quality of grown crystals are described and discussed. Large single crystals ( $\geq 35$  mm edge length for PZN–PT and  $\geq 25$  mm PMN–PT) of improved homogeneity have been successfully grown by an improved flux growth technique which promotes (001) layer growth of the crystals. The properties of the crystals obtained were evaluated and the results are presented and discussed.

## 2.2 Flux growth of PZN–PT and PMN–PT single crystals

Figure 2.1 shows the typical set-up (a) and growth result (b) of high-temperature flux growth of PZN–PT and PMN–PT single crystals. The most commonly used fluxes for the growth of PZN–PT and PMN–PT single crystals are PbO (or  $\text{Pb}_3\text{O}_4$ ) and complex fluxes consisting of a mixture of PbO and  $\text{B}_2\text{O}_3$ , respectively, with the solute-to-flux mole ratios varying from 0.55:0.45 to 0.30:0.70.

The component oxide powders, of 99.95% or higher purity, are weighed to desired proportions and then mixed thoroughly. The charge mixture may be loaded directly into the Pt crucible, although pre-calcined charge has also been commonly used. Then, the Pt crucible is covered with the lid and further placed in a sealed alumina crucible assembly, as shown in Fig. 2.1(a),



2.1 Schematics showing (a) set-up for flux growth of lead-based relaxor single crystals from high temperature via spontaneous nucleation and (b) typical growth results.

to contain potential PbO loss during the crystal growth run. The assembly is placed in the crystal growth furnace, which is often equipped with a local cooling arrangement to eliminate unwanted nucleation. Techniques used for local point cooling include the use of a thin metal rod (Shimanuki *et al.*, 1998; Harada *et al.*, 1998, 2001; Matsushita *et al.*, 2002; Babu *et al.*, 2006), metal wire (Chen and Ye, 2001; Karaki *et al.*, 2002a) and controlled stream of gas flow (Kobayashi *et al.*, 1997, 1998; Saitoh *et al.*, 1999; Kumar and Lim, 2000; Benayad *et al.*, 2004; Dabkowski *et al.*, 2004).

The crucible assembly with the charge is then heated to high temperature, typically between 1150 and 1250 °C, and held for a sufficiently long period of up to 10h to melt and homogenize the solution. Then, the assembly is cooled at a controlled rate, typically in the range of 0.5–1.5 °C/h, to start the crystal growth process.

When perfect single-crystal nucleation is initiated in the middle of the

base of the Pt crucible, the crystal will grow in a stress-free manner with minimum constraints and is totally protected by the PbO-rich solution. The latter is important because most relaxor-PT systems, in particular PZN-PT, are unstable at high temperatures even in PbO-rich vapour environments (Jang *et al.*, 1992; Wakiya *et al.*, 1995; Lim *et al.*, 2002). The entire crystal growth run may last for one to several weeks. Depending on the crystal type, slow cooling is stopped after the growth temperature reaches about 800–1000 °C, whereupon the assembly is cooled at a fast rate to room conditions. It has also been common practice to use gradually increasing cooling rate in the slow cooling stage (Mulvihill *et al.*, 1996; Saitoh *et al.*, 1999; Zhang *et al.*, 2000; Fan *et al.*, 2003; Babu *et al.*, 2006), in order to achieve a more constant crystal growth rate. This, however, requires the knowledge of the ternary phase diagram of the material systems concerned. Although relevant ternary phase diagrams remain unavailable to date, binary phase diagrams for the PMN-PbO system and for the (PZN-9%PT)-PbO system have been reported by Ye *et al.* (1990) and Dong and Ye (2001), respectively.

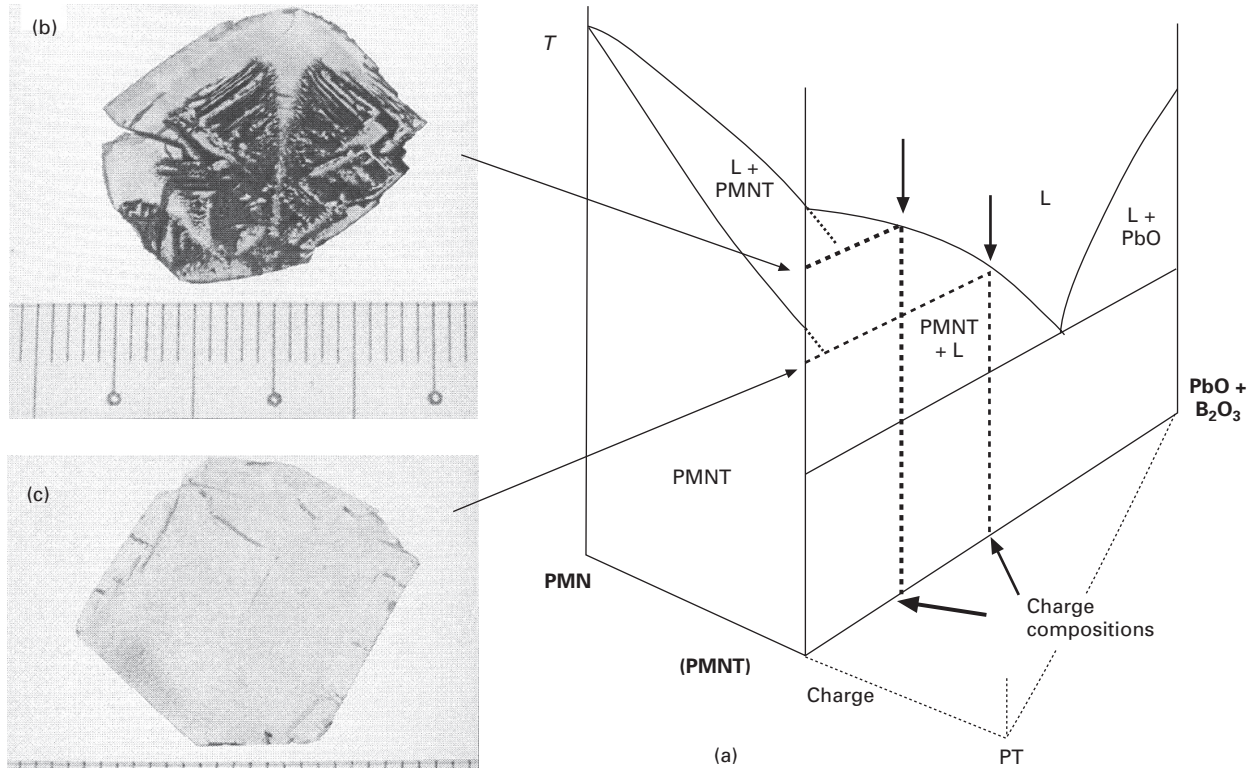
At the conclusion of the crystal growth run, the crystal is retrieved from the remaining solidified flux by leaching in boiling concentrated nitric acid. It has also been common practice to decant the remaining flux solution by flipping over the alumina crucible assembly at the end stage of the cooling process. This, however, must be executed with care because the crystal may crack due to thermal shock, especially for large crystals.

## 2.3      Effect of flux composition

PbO melts at 886 °C and the PbO-B<sub>2</sub>O<sub>3</sub> mixture has a relatively low eutectic point of 493 °C. They are commonly used fluxes in the growth of PZN-PT and PMN-PT single crystals. Being an end element of the final compound, the use of PbO in the growth of PZN-PT and PMN-PT is advantageous in that introduction of foreign ions can be avoided.

PbO melt has a reasonably low viscosity and high solubility for complex oxides. However, its major drawbacks include its toxicity, volatility above 1100 °C and a tendency to corrode platinum above 1300 °C. Lead oxide (PbO) with additives of Pb<sub>3</sub>O<sub>4</sub> may also be used. The addition of Pb<sub>3</sub>O<sub>4</sub> assures an oxidizing atmosphere during crystallization and it has been reported that this may help promote the stability of the perovskite phase during the crystal growth (Park and ShROUT, 1997a; Dong and Ye, 1999; Kania *et al.*, 2005). The addition of B<sub>2</sub>O<sub>3</sub> not only helps lower the crystallization temperature of the relaxor-PT system but also increases the viscosity of the solution. Both of these effectively prevent the loss of PbO through volatilization during the crystal growth run, which is desirable for the growth of certain relaxor-PT single crystals of relatively high solution temperature, such as the PMN-PT system.





2.2(a) A hypothetical phase diagram of the  $PMN-PT-(PbO + B_2O_3)$  system. The vertical sections of  $PMN-PT$  single crystals grown with insufficient  $B_2O_3$  and sufficient  $B_2O_3$  in  $PbO$ -based fluxes are given in (b) and (c), respectively.

The flux composition strongly affects the outcome of the crystal growth. For instance, our experience has shown that, on the one hand, the addition of  $B_2O_3$  to PbO flux promotes the formation of the pyrochlore phase in the PZN–PT system, on the other hand, a suitable amount of  $B_2O_3$  flux is needed in the growth of PMN–PT to ensure a good growth result.

In addition to flux composition, an appropriate flux-to-solute ratio is essential in relaxor–PT single crystal growth. Figure 2.2(a) gives a hypothetical phase diagram of the PMN–PT–PbO( $B_2O_3$ ) system, which serves to illustrate the importance of flux composition and content in PMN–PT growth (Lim, 2004; Lim *et al.*, 2005). This figure shows that when nil or insufficient  $B_2O_3$  is present in the solution, the grown PMN–PT crystals always contain a large amount of flux inclusions, especially in the initially grown part of the crystals (Fig. 2.2b). This can be attributed to the high crystallization temperature associated with the growth solution, such that the crystallization temperature is higher than the solidus of the binary PMN–PT system (Fig. 2.2a). Under the said conditions, phase separation is expected; the solidified mass is thus a mixture of a low-PT solid phase and a high-PT liquid phase.

The problem of phase-separated flux inclusion can be avoided by increasing the flux content in the starting charge to ensure that crystal growth takes place predominantly below the solidus of the corresponding binary relaxor–PT system. This is shown schematically in Fig. 2.2(a). A vertical section of a PMN–30%PT single crystal grown under such a condition is shown in Fig. 2.2(c). The obtained crystal is free of flux inclusions and fully dense.

The above results show that appropriate flux compositions and correct solute-to-flux mole ratios play a critical role in relaxor–PT single crystal growth. This is especially so for the growth of relaxor–PT single crystals of high PT content, such as PMN–PT. As will be shown below, although typical solute-to-flux ratios of 0.55:0.45 to 0.30:0.70 have been quoted, it may be necessary to fine-tune the ratio based on the PT content in the solution to ensure good crystal growth results.

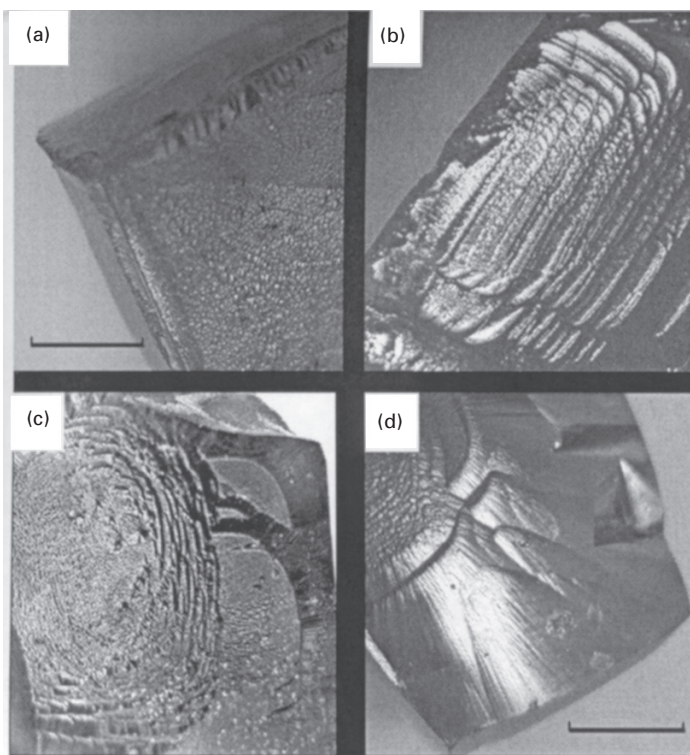
## 2.4      **Growth of relaxor single crystals of low PT contents: PZN–(4–7)%PT**

The PZN– $x$ PT system has a morphotropic phase boundary at  $x \approx 0.09$ – $0.10$  (Kuwata *et al.*, 1981; La-Orauttapong *et al.*, 2002). PZN–PT single crystals of PT contents less than 8 mol% are sought after due to their reasonably good thermal stability and excellent dielectric and piezoelectric properties after poling. Compared with PMN–PT crystals, the growth of PZN–(4–7)%PT single crystals appears to be much less complicated due to its lower PT contents.

The flux used for the growth of PZN–PT single crystals was PbO. Typical solute-to-flux mole ratio used was 0.55:0.45. When the degree of

supersaturation in the solution is low (i.e. at low cooling rates), the growth of PZN-PT single crystals starts by nucleation at  $\langle 111 \rangle$  corners followed by spreading down adjacent  $\langle 001 \rangle$  edges and (001) crystal faces, as evidenced in Fig. 2.3(a). This is typical of crystal growth from solution of simple ionic salts (Van Hook, 1961), suggesting that PZN-PT-PbO solutions with  $\leq 7$  mol%PT must be composed of simple ions. This remains so even when the PT content in the solution is close to the morphotropic phase boundary composition, i.e. about 9–10 mol% PT.

With an increased degree of supersaturation in the solution, growth of respective single crystals via nucleation at  $\langle 001 \rangle$  edges and on  $\{001\}$  faces becomes feasible, as evidenced in Fig. 2.3(b) and (c). The growth remains faceted in nature until the supersaturation is sufficiently high to promote profuse nucleation and growth on  $\{001\}$  faces. When this occurs, (001) growth facets are gradually replaced with smooth, non-crystallographic crystal faces. An example of such is shown in Fig. 2.3(d).

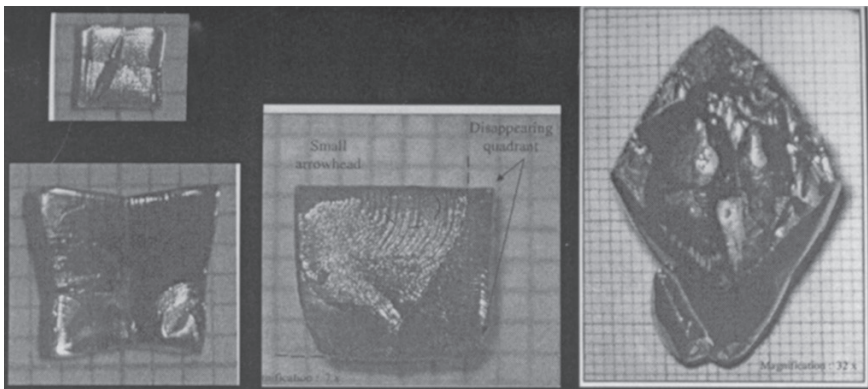


2.3 (a) Natural (001) growth faces in flux-grown PZN-(4–9)%PT. (b) and (c) Nucleation of (001) layer growth at  $\langle 001 \rangle$  edges and (001) faces, respectively. (d) Non-crystallographic crystal faces produced by a fast cooling rate.

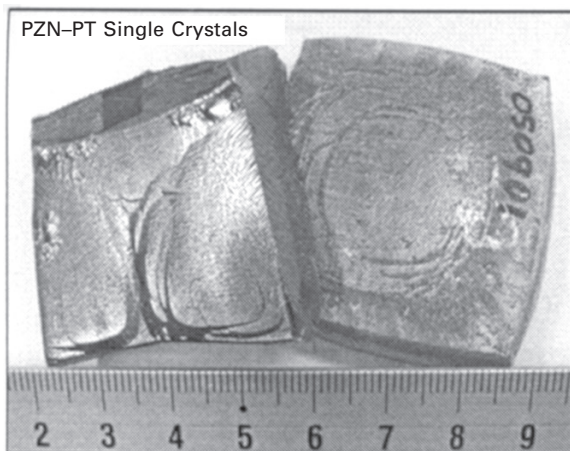
When first nucleated, PZN–PT single crystals are close to cubic in shape (Kumar and Lim, 2000; Lim and Rajan, 2004). With favourable isotherms in the solution, preferential nucleation at a certain or given [111] corner is promoted such that the corner nucleation rate outpaces the spreading rate onto adjacent {001} crystal faces. As a result, the small cube-shaped crystal would evolve into various shapes as it grows, as shown in Fig. 2.4.

It is evident that one could engineer the isotherms in the solution to control [111] corner nucleation while promoting (001) layer growth. The crystal growth process in this case will be dominated by the layer growth on certain (001) crystal planes. Since each (001) layer represents a layer of material grown within a given time interval, and hence of reduced solute segregation, wafers cut parallel to the prevalent (001) layer growth plane would show improved homogeneity in composition. Besides, should the crystal growth occur in an equilibrium or near-equilibrium condition, such as with suitably low cooling and hence growth rates, compositional uniformity between wafers can also be enhanced.

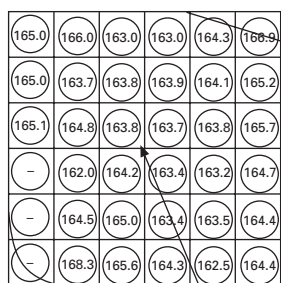
Figure 2.5 shows two PZN–PT single crystals grown using the above scheme. As-grown PZN–PT single crystals are translucent and light yellow to brownish-yellow in colour and exhibit prominent (001) facets. Wafers of 0.4 mm thickness were sliced from the crystals and the distribution of Curie temperature ( $T_C$ ) were determined by means of the array dot electrode technique (Kumar *et al.*, 2003). Figure 2.6(a) shows the distribution of  $T_C$  within an as-cut wafer, while Fig. 2.6(b) gives the statistical distribution obtained from more than 140 trimmed wafers of >20 mm edge length. These figures show that for PZN–PT single crystals of <7 mol% PT grown under optimal conditions, the compositions of the crystals were fairly uniform such that  $\Delta T_C < \pm 2^\circ\text{C}$  for most part (>75% in volume) of the crystal. This corresponds to  $< \pm 0.5$



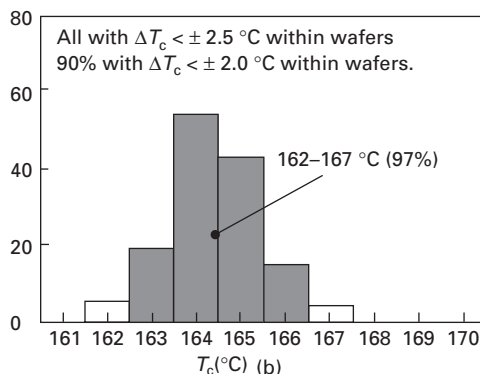
2.4 Evolution from (a) near-cubic to (b) star-shaped, (c) arrowhead-shaped and (d) spearhead-shaped crystal due to fast growth along certain <111> directions promoted by favorable isotherms in the solution.



2.5 Two large PZN-PT single crystals grown from PbO flux.



(a)



2.6 Compositional uniformity check of flux-grown PZN-(6-7)%PT single crystals: (a) distribution of Curie temperature ( $T_c$ ) within an as-cut wafer determined by the array dot electrode technique, the separation between the dot electrodes is 5 mm; (b) statistical distribution of  $T_c$  obtained from more than 140 wafers of >20mm edge length prepared from about 10 single crystals grown in the present work.

mol% PT variations in the crystals. The above results show that for relaxor-PT single crystals of low PT contents, the improved flux growth technique is a viable means of producing large crystals of high compositional homogeneity.

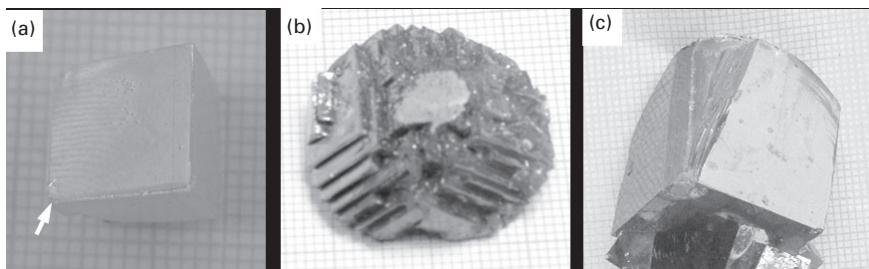
## 2.5 Flux growth of relaxor single crystals of high PT contents: PMN-(28-34)% PT

PMN-yPT system has a morphotropic phase boundary at  $y \approx 0.33-0.35$  (Choi *et al.*, 1989; Noblanc *et al.*, 1996). Small PMN-PT single crystals (of

a few millimetres edge length) can be readily grown from PbO-based fluxes. They generally exhibit clear (001) growth facets, as shown in Fig. 2.7(a). However, it may not be as straightforward when growing large PMN–PT single crystals, because the high PT content of the system produces significant complications to the flux growth of this material. Our experience has shown that the growth of PMN–PT single crystals with pure PbO flux often produced undesirable results (Lim, 2004; Lim *et al.*, 2005). Thus, PbO + B<sub>2</sub>O<sub>3</sub> complex fluxes were used instead. Even so, the growth results depended sensitively on the B<sub>2</sub>O<sub>3</sub> content in the PbO solution, as will be detailed below.

First of all, as described earlier in Fig. 2.2, when there is nil or insufficient B<sub>2</sub>O<sub>3</sub> in the solution, phase-separated flux inclusions are common features in flux-grown PMN–PT crystals (Fig. 2.2b). With sufficient B<sub>2</sub>O<sub>3</sub> in the PbO flux to bring the crystallization temperature below the solidus of the binary PMN–PT system, the phase-separated flux inclusion problem can be successfully avoided (Fig. 2.2c). Even so, the amount of B<sub>2</sub>O<sub>3</sub> was found to significantly affect the compositional segregation of the crystal (Lim, 2004; Lim *et al.*, 2005). For instance, measurements of  $T_C$  distributions from wafers cut from as-grown PMN–PT crystals showed that with less-than-optimum amounts of B<sub>2</sub>O<sub>3</sub> in PbO flux, the variations within wafers were acceptable (i.e.  $\Delta T_C \leq \pm 3.0^\circ\text{C}$ ) but were too large even between adjacent cuts of wafers (of about 0.5 mm thickness). On the other hand, with higher-than-optimum amounts of B<sub>2</sub>O<sub>3</sub>, the reverse was observed instead.

The amount of B<sub>2</sub>O<sub>3</sub> in PbO flux also affects the growth mechanism of PMN–PT crystals. Figures 2.7(b) and (c) show the general morphologies of large PMN–PT single crystals (i.e. those  $\geq 20$  mm edge length) grown in the present work. Although all crystals exhibit apparent (001) growth facets,



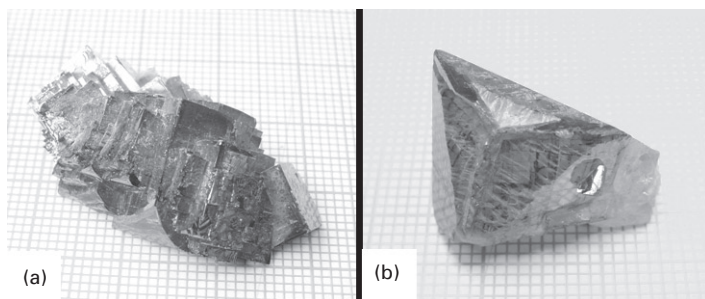
2.7 Different (001) growth morphologies in flux-grown PMN–30%PT single crystals: (a) small cubic-shaped crystal of prominent (001) facets of up to 10 mm edge length produced from PbO-based fluxes. Note the evidence of  $\langle 111 \rangle$  corner nucleation (arrowed) followed by  $\langle 011 \rangle$  edge and (001) layer growth; (b) (001) platelet growth in large crystals ( $>20$  mm edge length) produced from pure PbO flux; (c) microscopic (001) layer growth in large crystals ( $>20$  mm edge length) produced from PbO-based flux containing  $>5$  mol% B<sub>2</sub>O<sub>3</sub>.

those grown without or with insufficient  $B_2O_3$  in the PbO flux have a platelet morphology (Fig. 2.7b). An obvious change from (001) platelet growth to microscopic (001) layer growth is evident even with a few mol% of  $B_2O_3$  (i.e. about 5 mol%) added to the PbO flux (Fig. 2.7c).

Figure 2.8 shows the change in nucleation mechanism during growth from solution with increasing  $B_2O_3$  content, revealed by deliberately increasing the cooling rate at the later stage of the crystal growth run. Apparently, with a low  $B_2O_3$  content in the PbO flux, the (001) layer growth is initiated via the nucleation and growth of (001)-oriented crystal blocks on the (001) growth facets (Fig. 2.8a). On the other hand, with sufficient  $B_2O_3$  addition, (001) layer growth occurs through  $\langle 111 \rangle$  corner nucleation followed by spreading down the adjacent  $\langle 001 \rangle$  edges and (001) faces (Fig. 2.8b).

The above observations suggest that ionic complexes formed in the high temperature solution of PMN-PT-PbO( $B_2O_3$ ) system play an important role in the growth of PMN-PT single crystals. Owing to the strong affinity between  $Ti^{4+}$  and  $O^{2-}$  ions and the substantial amount of PT present in the PMN- $y$ PT system studied ( $y = 0.28-0.34$ ), it is likely that  $Ti^{4+}$  and  $O^{2-}$  ions may form various large ionic complexes or clusters (possibly with some covalent nature) in the solution. The growth of PMN-PT with insufficient  $B_2O_3$  addition is thus controlled by cluster growth of  $Ti^{4+}-O^{2-}$  based complexes. Owing to the lower diffusivity of the latter in the solution, as opposed to other simpler ions, the adjacent solution becomes enriched with  $Ti^{4+}-O^{2-}$  complexes, leading to a significant increase in the PT content of successively grown layers as the crystal grows in size.

On the other hand, owing to the strong  $B^{3+}-O^{2-}$  bonds and the valency difference, addition of  $B_2O_3$  helps modify the nature of the  $Ti^{4+}-O^{2-}$ -based complexes in the solution. With sufficient  $B_2O_3$  in the PbO flux, a change



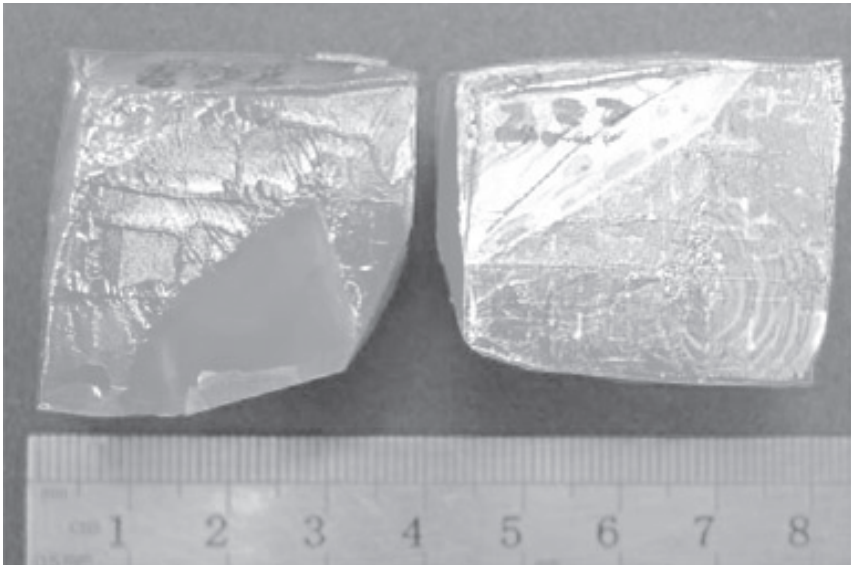
2.8 Different nucleation mechanisms in flux growth of PMN-PT single crystals, revealed by higher cooling rates near the end of the growth runs: (a) cluster nucleation on (001) facets with less-than-optimum amounts of  $B_2O_3$  in PbO flux; (b)  $\langle 111 \rangle$  corner and  $\langle 001 \rangle$  edge nucleation and growth with near-optimum amounts of  $B_2O_3$  in PbO flux.

from the cluster nucleation on (001) faces (Fig. 2.8a) followed by platelet growth (Fig. 2.7a) to  $\langle 111 \rangle$  corner and  $\langle 001 \rangle$  edge nucleation (Fig. 2.8b) followed by microscopic (001) layer growth (Fig. 2.7b) takes place.

Since the corner and edge nucleation mechanisms are favoured in the growth of ionic crystals from solutions of simple ions (Van Hook, 1961), the addition of  $B_2O_3$  must have helped break up existing  $Ti^{4+}-O^{2-}$ -based complexes into simpler or smaller ones comprising, possibly,  $Ti^{4+}$ ,  $B^{3+}$  and  $O^{2-}$  ions. This, in turn, gives rise to a change in the crystal growth mechanism observed. Note also that when this occurs, the diffusivity of the simpler or smaller ionic complexes in the solution is substantially enhanced. This, in turn, would lead to reduced compositional gradients in the grown crystal.

Figure 2.9 shows two large PMN–PT single crystals grown from optimal fluxes of  $PbO + zB_2O_3$ , where  $z \geq 0.10$ . The colour of as-grown PMN–PT crystals varies from brownish-to-greenish yellow. High-quality crystals are translucent when viewed against the light. Unlike PZN–PT single crystals, the surfaces of as-grown PMN–PT crystals often show characteristic  $\langle 001 \rangle$  domain wall traces criss-crossing one another at right angles (Fig. 2.9, see also Section 2.6.8).

$T_C$  mapping was obtained with the array dot-electrode technique from successive (001) wafers cut from a number of large ( $\geq 25$  mm edge length) PMN–PT crystals, grown at relatively slow cooling rates of  $\leq 0.8^\circ C/h$  to ensure that the growth condition is near equilibrium (Lim, 2004; Lim *et al.*, 2005). Figure 2.10(a) shows the wafers cut from one of such crystal which

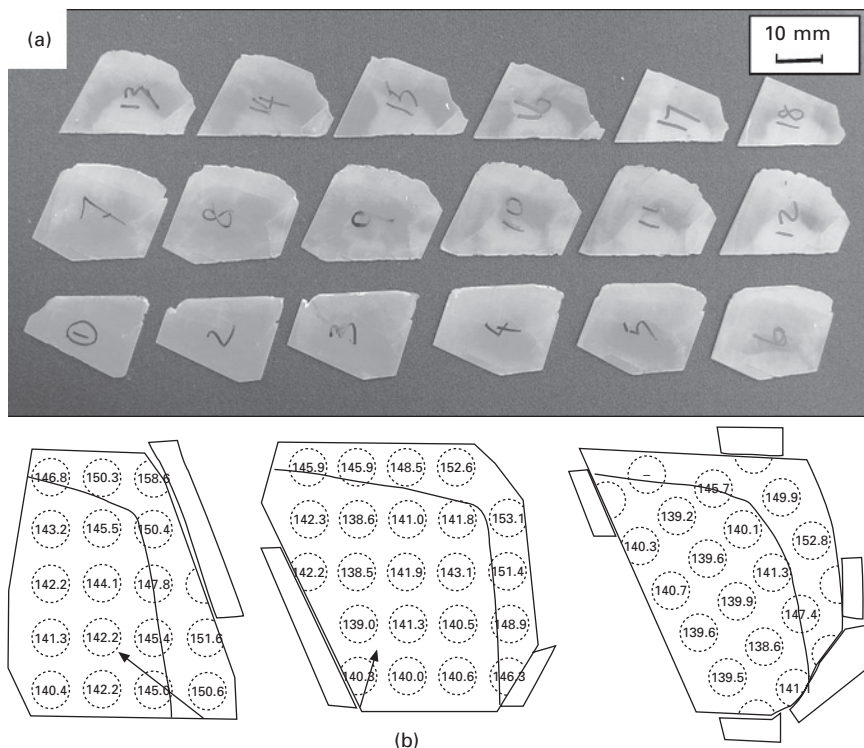


2.9 Two large PMN–PT single crystals grown from  $PbO + B_2O_3$  complex fluxes.



was grown from a starting charge composition of 34 mol% PT. Figure 2.10(b) gives the  $T_C$  distribution in three selected wafers, i.e. W3, W9 and W12. It shows that the  $T_C$  distribution is fairly uniform over a large part of the wafers adjacent to the base of the crystal, i.e. adjacent to the nucleation point (arrowed in Fig. 2.10b). The  $T_C$  values for this part of the crystal vary around  $140 \pm 3^\circ\text{C}$ , corresponding to a composition of about PMN-32% PT. The PT content in this uniform part of the grown crystal is thus about 2 mol% less than that in the initial charge.

Figure 2.10(b) further shows that the  $T_C$  values for the outer part of the wafers, hence the crystal, increases appreciably. This implies that although the initial part of the grown crystal has a relatively uniform PT content, the outer part shows a steep increase in PT content. Similar observations were also made for the two other crystals grown with the same initial charge composition of 34%PT, of which one was grown under a much lower cooling rate of about  $0.2^\circ\text{C/h}$ .



2.10 Mapping of ferroelectric phase transition temperature: (a) 0.5mm thick wafers sliced parallel to the prevalent (001) layer growth plane of a grown PMN-PT crystal; (b)  $T_C$  distributions in wafer nos. W3, W9 and W12 shown in (a). The dot electrodes are 5 mm in centre-to-centre separation.

Since the composition remains relatively uniform over a large initial portion of the grown crystals which is independent of the growth rate used, flux growth of PMN–PT crystals from optimum PbO–B<sub>2</sub>O<sub>3</sub> fluxes is likely to occur under equilibrium or near-equilibrium conditions, at least during the initial to intermediate stage of the growth. Furthermore, since the difference between the PT content in the initial charge and the grown crystal is not affected by the growth rate used, it is likely that this difference, i.e. about 2.0 mol% PT, is retained in the solution to maintain the equilibrium of the complex flux formation reaction. This being the case, one can anticipate that the grown crystal always has a lower PT content than the charge, regardless of the initial charge composition and the growth rate. This holds as long as equilibrium is attained for the complex flux reaction.

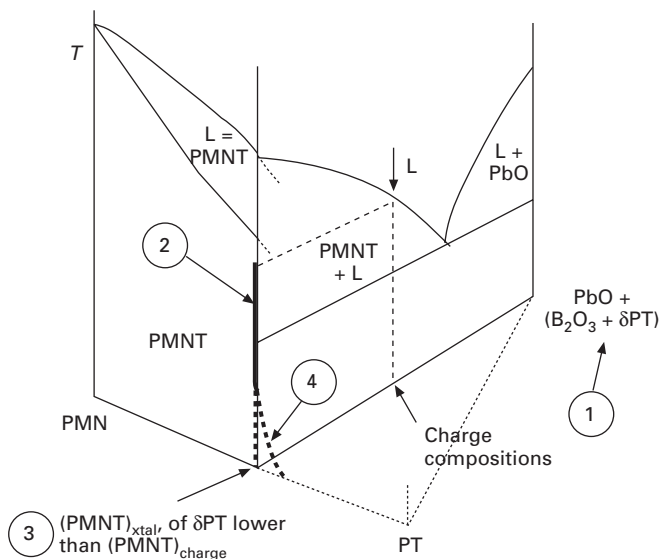
The above hypothesis was checked by altering the charge composition to 30% and 32% PT while maintaining the optimum B<sub>2</sub>O<sub>3</sub> content in the flux. Our aim was to grow PMN–28%PT and PMN–30% PT crystals as our intended crystal compositions. After the growth, examination of the distribution of  $T_C$  of the wafers cut from the grown crystals revealed that the crystals were indeed of 28% PT ( $T_C \approx 125^\circ\text{C}$ ) and 30% PT ( $T_C \approx 135^\circ\text{C}$ ) as per the experimental plan. The  $T_C$  values of the flux-grown PMN–PT single crystals agree reasonably well with those obtained by Choi *et al.* (1989) and Noblanc *et al.* (1996) on PMN–PT ceramics of controlled compositions.

The above result confirms that the actual fluxes for the growth of PMN–PT are indeed complex fluxes of  $\text{PbO} + z(\text{B}_2\text{O}_3 + \delta\text{PT})$ , where  $\delta$  is a function of B<sub>2</sub>O<sub>3</sub> content in the flux. Furthermore, it suggests that with the established complex flux, the growth path is nearly vertical under equilibrium or near-equilibrium growth conditions. This is illustrated schematically in Fig. 2.11.

The present work shows that with optimum B<sub>2</sub>O<sub>3</sub> content in the flux, such that the large ionic complexes are broken up into simpler ions, high uniformity PMN–PT single crystals can be grown with PbO-based fluxes when the growth is allowed to proceed in a near-equilibrium manner. However, as the growth temperature reduces, the ratio of B<sub>2</sub>O<sub>3</sub>-to-PT in the solution increases appreciably and the B<sup>3+</sup>-based ionic complexes may reform in the solution. When this happens, the viscosity of the solution would increase considerably. The (001) layer growth may then become kinetics-controlled. As a result, the uniformity in the crystal composition degrades accordingly, and the PT content increases appreciably in the last-to-grow part of the crystal. This is illustrated schematically in Fig. 2.11.

## 2.6 Other commonly encountered problems

In addition to phase-separated flux inclusions and compositional segregation problems discussed above, other commonly encountered problems during flux growth of PZN–PT and PMN–PT single crystals include multiple



**2.11 Modified phase diagram and growth path for flux growth of PMN-PT single crystals from PbO-B<sub>2</sub>O<sub>3</sub>-based fluxes.** The actual flux should be  $PbO + z(B_2O_3 + \delta PT)$ , because a fixed amount of PT, determined by the amount of B<sub>2</sub>O<sub>3</sub> in the flux, is needed to maintain the equilibrium of the complex flux formation reaction in the solution (marked '1' in the figure). The growth path is relatively vertical at sufficiently high growth temperatures under near-equilibrium growth conditions (marked '2'). As a result, the composition of the initial part of the grown crystal is about 2 mol%PT less than that of the initial charge (marked '3'). The growth path deviates from the vertical line at low growth temperatures when the growth becomes kinetics controlled, as indicated by the dashed curve (marked '4').

nucleation at the cooling point, formation of satellite and parasitic crystals, side-wall nucleation, flux trappings, cracks, PT-rich surface layer. They are briefly described below (see also Fig. 2.1b).

### 2.6.1 Multiple nucleation and satellite crystals

The use of local point cooling arrangement in flux growth does not always guarantee single crystal nucleation and growth. Instead, multiple crystal nucleation at the intended cooling point is common. Even if single crystal nucleation is successful, satellite crystals may nucleate later in the course of slow cooling, destroying an otherwise perfect crystal growth run. Under less controlled conditions, the situation could be a lot worse and the end result is crystals many millimetres in size. The problem of satellite crystal formation has been traced to limited convection in the solution coupled with a high

cooling rate. Such problems can be alleviated, to a large degree, by improving the point cooling arrangement and lowering the cooling rate used.

### 2.6.2 Parasitic crystals

Unlike satellite crystals which nucleate at the periphery of the main crystal at the base of the Pt crucible, parasitic crystals nucleate and grow onto the main growing crystal. The cause for the formation of parasitic crystals is the same as for satellite crystals except that a higher degree of supersaturation is required for their formation. Similar to satellite crystals, the formation of parasitic crystals can be suppressed by lowering the cooling rate.

### 2.6.3 Side-wall nucleation

In conventional flux growth of relaxor–PT single crystals, profuse spontaneous nucleation on the Pt crucible wall along the meniscus ring often occurs later in the crystal growth run (Mulvihill *et al.*, 1996; Park *et al.*, 1997; Kumar *et al.*, 2000, Zhang *et al.*, 2000). Although this may not affect the quality of the main crystal growing from the base of the Pt crucible, it deprives the latter of solute that is needed to feed its growth. Suppression of side-wall nucleation is crucial for the growth of large relaxor–PT single crystals by the flux growth technique. Side-wall nucleation can be eliminated by ensuring the top surface of the solution always experiences a temperature greater than that of the bottom of the crucible (Lim *et al.*, 2004, 2005; Babu *et al.*, 2006).

### 2.6.4 Pyrochlore crystals

Pyrochlore crystals were observed when inappropriate flux compositions and/or flux-to-solute ratios were used. They are fairly common features when the crystal growth run is allowed to proceed to a much lower temperature, say, <900 °C. Under the said condition, the solution becomes exceedingly enriched in PbO flux, giving rise to conducive conditions for their formation. They are also found when point nucleation has failed such that a pool of solution is trapped inside the inner periphery of a ring of interconnected satellite crystals. They may also form when the crystallization rate is too high such that the crystal formed may contain a high degree of imperfections. When this occurs, there is a tendency for the defect-containing crystal to transform to the pyrochlore phase during the subsequent slow-cooling stage. Formation of pyrochlore crystals can be avoided when the crystal growth conditions are carefully controlled to ensure that they are not far from ideal and when satellite crystal formation has been avoided. Ending the crystal growth run at a higher temperature also helps in this regard. The use of B<sub>2</sub>O<sub>3</sub> in PbO flux should be avoided in the growth of PZN–PT as it promotes the

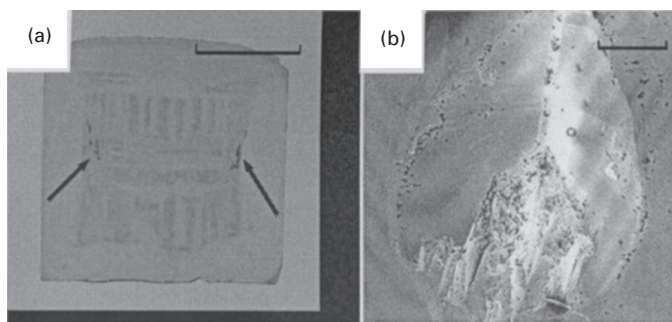
formation of the pyrochlore phase. This agrees with the findings of earlier researchers (Bokov and Myl'nikova, 1961; Gentil *et al.*, 2000; Yamashita, quoted in Zhang *et al.*, 2000) although Zhang *et al.* (2000) reported a different result.

### 2.6.5 Flux trappings

Even with optimal flux composition such that the problem of phase-separated flux inclusion problem is avoided, as-grown relaxor-PT single crystals may also contain abundant flux inclusions. An example is given in Fig. 2.12(a). It should be noted that under normal growth conditions, multiple growth sectors often operate concurrently on a given crystal. At sufficiently high growth rates, the boundaries where such growth sectors meet are potential sites for flux trapping. When uncontrolled nucleation and growth on (001) crystal faces occurs due to a high degree of supersaturation in the solution, the flux can be easily trapped at the growth front of the solidifying solid. A vivid example of such is given in Fig. 2.12(b).

### 2.6.6 Cracks

Relaxor single crystals are brittle and crack easily. A large as-grown single crystal of relaxor compositions may crack along its periphery if it experiences mild thermal shock during the crystal growth or retrieval process. When satellite and/or parasitic crystals are present, the stress concentrations associated with anisotropic thermal expansion produced by cooling may also induce cracking of the larger crystal, which often initiates at the apex of the smaller embedded crystal. The presence of pyrochlore crystals is another main cause for crack formation, due probably to the large difference in thermal expansion coefficients between the perovskite PZN-PT and the non-perovskite pyrochlore



2.12 Trapping of flux (a) at growth sector boundary (arrowed) and (b) at the growth front at high growth rates in PZN-9%PT.

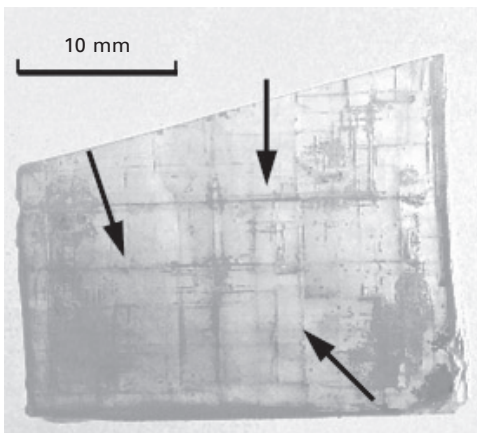
phase during cooling. Cracks in relaxor-PT single crystals may or may not be crystallographic, especially for periphery cracks, which at times can assume a smooth hemispherical shape. Crystal cracking problems can be largely eliminated by avoiding the pyrochlore phase and the formation of satellite and parasitic crystals during the crystal growth, and by handling the crystal with care to avoid unnecessary thermal and/or mechanical shock.

### 2.6.7 Pt inclusions

Although not always, Pt inclusions were at times observed in flux-grown PMN-PT single crystals produced in our laboratory. They often manifested as a shining deposit layer on the surface of internal cracks and/or growth sector boundaries. Their presence may be attributed to the presence of  $B_2O_3$  in the solution and the higher growth solution temperature used in this case. In contrast, Pt inclusions were seldom detected in the growth of PZN-PT single crystal when pure PbO flux and a significantly lower solution temperature were employed.

### 2.6.8 PT-rich surface layer with fragile domain walls

As described in Section 2.5, severe segregation occurs at the later stage of flux growth of PMN-PT single crystals. When growing PMN-PT single crystals of near-morphotropic phase boundary compositions, this may lead to the formation of a tetragonal-rich surface layer. This layer is manifested by the characteristic long and straight  $\langle 100 \rangle$  domain wall traces criss-crossing one another at right angles. As shown in Fig. 2.13. When viewed against the



2.13 PT-rich surface layer with prominent but fragile (001) domain walls (arrowed) in an as-grown PMN-30%PT single crystal.

light, some of these domain walls are highly reflective, suggesting that they may be cracked. Those intact walls remain fairly fragile and are potential sites of cracking during subsequent crystal cutting and polishing. Similar surface layer and characteristic domain walls were seldom observed in flux-grown PZN-PT single crystals when the starting charge composition was kept below 8 mol% PT.

## 2.7 Properties of flux-grown PZN-PT and PMN-PT single crystals

PZN- $x$ PT and PMN- $y$ PT single crystals with  $x = 4.5\text{--}8.0\%$  and  $y = 28\text{--}32\%$ , being the final crystal composition determined using their Curie temperatures (cf. works of Kuwata *et al.*, 1981; Shrout *et al.*, 1990; Noblanc *et al.*, 1996), were sliced and diced into  $[100]^L/[010]^W/[001]^T$   $k_{31}$ - and  $k_t$ -plates and  $k_{33}$ -bars, of  $7^L \times 2^W \times 0.5^T$  mm<sup>3</sup>,  $5^L \times 5^W \times 0.5^T$  mm<sup>3</sup> and  $3^L \times 3^W \times 9^T$  mm<sup>3</sup> in dimensions, respectively. To check the effect of length orientation on  $k_{31}$  properties,  $[110]^L/[1-10]^W/[001]^T$   $k_{31}$ -plates were also prepared. As for  $[011]$ -poled samples,  $k_{32}$ -mode plates of  $9.0^L \times 3.0^W \times 0.5^T$  mm<sup>3</sup> in dimensions were diced from  $(011)$  wafers with two different length orientations, i.e.  $[100]^L/[0-11]^W/[011]^T$  and  $[0-11]^L/[100]^W/[011]^T$ . The samples were coated with nichrome-gold/palladium electrodes on appropriate faces. To establish the optimum poling fields for both the plate and bar samples, the samples were poled progressively in silicone oil at room temperature from 0.2 to 2.0 kV/mm for the  $k_{31}$ - (or  $k_{32}$ -) and  $k_t$ -plates and from 0.2 to 0.5 kV/mm for the  $k_{33}$ -bars. After each poling step, the dielectric constant ( $K^T$ , measured at 1 kHz) and electromechanical coupling factors ( $k_{33}$ ,  $k_{31}$ ,  $k_{32}$  and  $k_t$ , measured with the resonance technique) were determined using an Agilent 4294 impedance network analyzer and the piezoelectric coefficients ( $d_{33}$ ,  $d_{31}$  and  $d_{32}$ ) were obtained with a Berlincourt-type meter. The poling field giving the best property values was taken as the optimum poling condition. X-ray diffraction studies and polarized light microscopy were carried out to identify the phases present in the poled crystals (Shanthi *et al.*, 2005b; Rajan *et al.*, 2007).

For  $[001]$ -poled PZN-4.5%PT and PMN-28%PT single crystals, which are compositionally far from the MPBs, the poled domain structure is largely rhombohedral (Kuwata *et al.*, 1981; Shrout *et al.*, 1990; La-Orautapong *et al.*, 2002; Lu *et al.*, 2002; Noheda *et al.*, 2002; Rajan *et al.*, 2007). The poled properties of these crystals are given in columns 2 and 3 of Table 2.1. Such crystals show respectable properties with  $K^T \approx 5000$ ,  $d_{33} \approx 2200$  pC/N,  $d_{31} \approx -(1000\text{--}1100)$  pC/N,  $k_{33} \approx 0.90\text{--}0.92$ ,  $k_{31} \approx 0.50$  for PZN-4.5%PT; and  $K^T \approx 4500\text{--}5000$ ,  $d_{33} \approx 2000$  pC/N,  $d_{31} \approx -1000$  pC/N,  $k_{33} \approx 0.90\text{--}0.92$ ,  $k_{31} \approx 0.50$  for PMN-28%PT. Most interestingly, insignificant degradation of properties was observed when the above crystals were poled to 2.0 kV/mm. Crystals of the above two compositions are thus ideal for high field applications. For

Table 2.1 Properties of flux-grown [001]-poled PZN-PT and PMN-PT single crystals (poled at 0.7–0.8kV/mm for  $k_{31}$ - and  $k_t$ - plates and 0.4–0.6 kV/mm for  $k_{33}$ -bars)

Properties	Optimallypoled					Over-poled	
	PZN-4.5%PT	PMN-28%PT	PZN-(6-7)%PT	PMN-30%PT	PZN-8%PT	PZN-8%PT	PMN-32%PT
$T_c$ (°C)	≈156	≈125	≈164	≈135	≈170	≈170	≈145
$T_{DP}$ (°C)	≈ 110	≈ 95	≈ 100	≈ 85	≈90	70–80	≈ 80
$K^T$	4500–5500	4500–5500	6800–8000	7500–9000	5500–6500	3300–4500	4500–5500
$\tan\delta$	<0.01	<0.01	<0.01	<0.01	<0.01	<0.01	<0.01
$k_{33}$	0.90–0.92	0.90–0.92	0.92–0.94	0.92–0.94	0.92–0.94	0.88–0.91	0.91–0.94
$k_t$	0.50–0.52	0.55–0.58	0.52–0.53	0.58–0.62	0.53–0.57	0.53	0.57–0.60
$k_{31}$ [110] <sup>L</sup>	–	–	0.80–0.85	0.80–0.85	–	–	0.79–0.81
( $d_{31}$ in pC/N)	–	–	–(1100–1400)	(–900)	–	–	–(750–1000)
$d_{33}$ (pC/N)	2000–2500	1900–2100	2500–3000	2200–2500	2500–2900	1800–2200	1600–1800
$d_{31}$ [010] <sup>L</sup>	–1140	–(900–1100)	–(1400–1800)	–(1100–1400)	–	–	–(350–800)
(pC/N)	( $k_{31}$ ≈ 0.50)	( $k_{31}$ ≈ 0.55)	( $k_{31}$ ≈ 0.50)	( $k_{31}$ ≈ 0.50)	–	–	( $k_{31}$ ≈ 0.50)

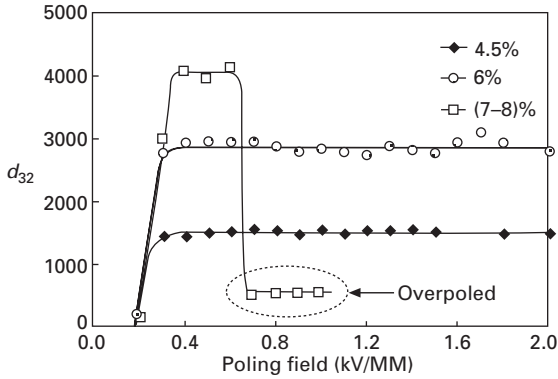


[011]-poled single crystal plates of  $[100]^L$  length, we obtained  $K^T \approx 3000$ ,  $d_{32} \approx -1400$  pC/N and  $k_{31} = 0.88$  for PZN-4.5%PT, which again show negligible sign of property degradation on being poled to 2.0 kV/mm.

Columns 4 and 5 of Table 2.1 give the properties of [001]-poled PZN-(6–7)%PT and PMN-30%PT in the optimally poled state, which are 3–4 mol%PT away from the MPBs but have a predominantly rhombohedral domain structure (Lim and Rajan, 2004; Rajan *et al.*, 2004, 2005, 2007; Lim *et al.*, 2005; Shanthi *et al.*, 2005a). They exhibit extremely high dielectric and electromechanical properties, with  $K^T \approx 6800$ –8000,  $d_{33} \approx 2800$  pC/N,  $d_{31} \approx -(1400$ –1800) pC/N,  $k_{33} \approx 0.93$ –0.94,  $k_{31} [110]^L \approx 0.80$ –0.85;  $k_t \approx 0.50$ –0.55 for PZN-(6–7)%PT; and  $K^T = 7500$ –9000,  $d_{33} = 2200$ –2500 pC/N,  $d_{31} = -(1100$ –1400) pC/N,  $k_{33} \approx 0.92$ –0.94,  $k_{31} [110]^L \approx 0.80$ –0.85;  $k_t \approx 0.58$ –0.62 for PMN-(30–31)%PT.

As for [011]-poled crystals, superior dielectric and piezoelectric properties were obtained for the  $[100]^L$ -length cut samples, with  $K^T \approx 4800$ ,  $d_{32} = -3000$  pC/N and  $k_{32} = 0.91$  for PZN-6%PT and  $K^T \approx 5000$ –6000,  $d_{32} = -(3200$ –4000) pC/N and  $k_{32} = 0.92$ –0.96 for PZN-7%PT. These properties pertain to the optimally poled samples. Our X-ray and polarized light microscopy studies further revealed that the superior dielectric and piezoelectric properties of the [011]-optimally poled PZN-PT can be attributed to the presence of 10–15% of orthorhombic phase among a rhombohedral matrix in the material (Rajan *et al.*, 2007). This observation indicates that the coexistence of both rhombohedral and a metastable phase is responsible for the superior piezoelectric properties of relaxor-PT single crystals, despite the metastable phase being a minor phase.

As described above, PZN-PT and PMN-PT may become over-poled at high poling fields with significant amounts of induced monoclinic or orthorhombic phase in the material (Rajan *et al.*, 2005; Shanthi *et al.*, 2005a). This is especially pronounced for [011]-poled crystals of compositions close to the morphotropic phase boundary (Shanthi *et al.*, 2005a; Rajan *et al.*, 2007). The [011] poling responses of PZN-PT single crystals of different compositions are given in Fig. 2.14. It shows that when optimally poled, the measured properties of  $k_{32}$  plates are much superior to the [001]-poled plates. For instance, [011]-optimally poled PZN-7%PT exhibits  $d_{32} \approx -4000$  pC/N, which compares favourably to the value of  $-1800$  pC/N for [001]-poled crystals. When poled above 0.6 kV/mm, however, PZN-7%PT single crystal plates become over-poled and their  $d_{32}$  values drop to  $-(600$ –700) pC/N instead. For [011]-poled crystal, the overpoled structure corresponds to a predominantly orthorhombic state (Lu *et al.*, 2001, 2002; Priya *et al.*, 2002; Guo *et al.*, 2002a,b; Shanthi *et al.*, 2005a,b; Rajan *et al.*, 2007). The last two columns of Table 2.2 give the measured properties of PZN-7%PT and PMN-32%PT in the over-poled state. It is evident that the over-poled properties are much inferior to those of the optimally poled samples.



2.14 Transverse piezoelectric coefficients ( $d_{32}$ ) of [011]-poled PZN-PT single crystals of different PT contents as functions of poling field. The actuating length direction is along the [100] crystal direction.

Table 2.2 Properties of [100]<sup>l</sup>-oriented flux-grown [011]-poled PZN-PT and PMN-PT single crystals

Property	Optimally-poled			Over-poled	
	PZN-6%PT	PMN-30%PT	PZN-7%PT	PZN-7%PT	PMN-32%PT
Poling field (kV/mm)	1.0–2.0	1.0–2.0	0.4–0.5	0.6–2.0	0.3–2.0
$K^T$	4200–5200	5500–6000	5000–6000	1700–1800	3500–4000
$\tan\delta$	<0.01	<0.01	<0.01	<0.01	<0.01
$k_{32}$	0.90–0.93	0.90–0.94	0.92–0.96	0.65–0.70	0.70–0.75
$d_{32}$ (pC/N)	–(2700–3200)	–(2100–2600)	–(3200–4000)	–(500–700)	–(250–500)

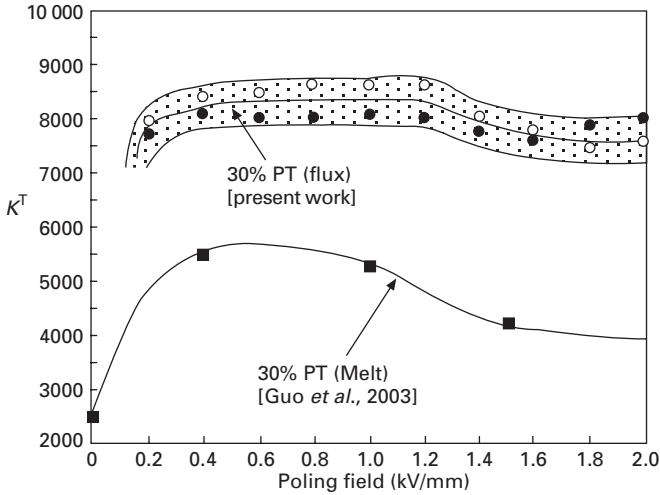
Another interesting observation made by us is that, the threshold poling field above which over-poling sets is sample geometry dependent (Rajan *et al.*, 2005, 2007). For instance,  $k_{33}$  bars become over-poled at significantly lower fields than  $k_{31}$  or  $k_{32}$  plates. Although different sample geometries may impose different mechanical constraints during poling, it is also possible that processing-induced defects in the  $k_{33}$  bars, which are more difficult to prepare, could produce undesired field concentrations in their vicinities, leading to local over-poling at lower fields.

## 2.8 Comparison with reported property values

The dielectric and piezoelectric properties of differently poled PZN-PT single crystals have been reported by earlier workers; for example see, Table 1 of

Lim and Rajan (2004). The reported values, however, show significant variations both among different research groups and within individual groups. The property variations are most significant for crystals of near MPB composition. For instance, the poled dielectric constant ( $K^T$ ) and piezoelectric coefficients ( $d_{33}$  and  $d_{31}$ ) of PZN-(8-9.5)%PT single crystals show deviations of 25% or higher from the average values. It is evident from the present work that, in addition to possible compositional segregation within the samples, the reported low property values of PZN-(8-9)%PT single crystals and the associated variations are likely the result of global or local overpoling. This is especially so for samples poled by means of the field cooling technique (Kuwata *et al.*, 1982; Park and Shrout, 1997a,c; Saitoh *et al.*, 1998; Shimanuki *et al.*, 1998; Hosono *et al.*, 2002). In such a poling technique, the crystal was heated to above the Curie temperature. The desired poling field was then applied and the crystal was allowed to cool to room temperature under field. More recently, complete sets of data for [001]-poled PZN-4.5%PT, PZN-7%PT and PZN-8%PT have been reported by Yin *et al.* (2000) and R. Zhang *et al.* (2001, 2002, 2003a). Although the poling conditions used were not detailed in their works, their values agree reasonably with the optimally poled values reported in the present work. They also performed the measurement on the transverse properties of [011]-poled PZN-4.5%PT and PZN-8%PT single crystals (R. Zhang *et al.*, 2004). However, their [011]-poled property values are much inferior to those obtained in the present work.

Even larger variations in reported property values have been noted in PMN-PT single crystals; see, for example, Table 3 of Rajan *et al.* (2007). This crystal can be grown from either PbO-based solutions or melt. Due to the higher PT content present, PMN-PT crystals display higher compositional variations in the as-grown state. As shown in Section 2.5, for flux-grown PMN-PT crystals, the PT content in the first-grown uniform-composition portion is typically 2 mol% PT less than that in the initial charge. Equally significant or larger compositional variations have been reported in melt-grown PMN-PT single crystals (Luo *et al.*, 2000a,b; Xu *et al.*, 2001b; Karaki *et al.*, 2002b; Park and Hackenberger, 2002; Zawilski *et al.*, 2003; Shin *et al.*, 2004). Despite the above, only the initial charge compositions have been quoted in most reported works. This could have contributed to the inconsistency in the property values reported. Furthermore, due to their lower rhombohedral to tetragonal transformation temperature and coercive field, PMN-PT single crystals of near MPB compositions are more susceptible to overpoling than are PZN-PT crystals (Shanthi *et al.*, 2005a,b). This is especially so for melt-grown PMN-PT crystals. Figure 2.15 compares the poling responses of flux-grown and melt-grown PMN-30%PT single crystals, the latter data being extracted from Fig. 2.4 of Guo *et al.* (2003). It is evident that the properties of melt-grown PMN-PT single crystals correspond more to the overpoled



2.15 Dielectric constant as functions of poling field for flux- and melt-grown PMN–30%PT single crystals poled in the [001]-thickness direction at room temperature. The data for melt-grown PMN–30%PT are taken from Fig. 4 of Guo *et al.* (2003).

behaviours of their flux-grown counterparts. As explained in Section 2.5, large ionic clusters are present in the melt of relaxor ferroelectrics, especially those with high PT content. This may result in an increased amount of crystal defects in the grown crystals which, in turn, may result in their inferior properties and overpoling resistance. The above suggests that one should use the reported property values for PMN–PT single crystals with caution. Furthermore, it is highly desirable to quote the growth technique used, the measured Curie temperature (or actual composition) of the test samples, and the poling condition employed in future reporting of property values of relaxor single crystals.

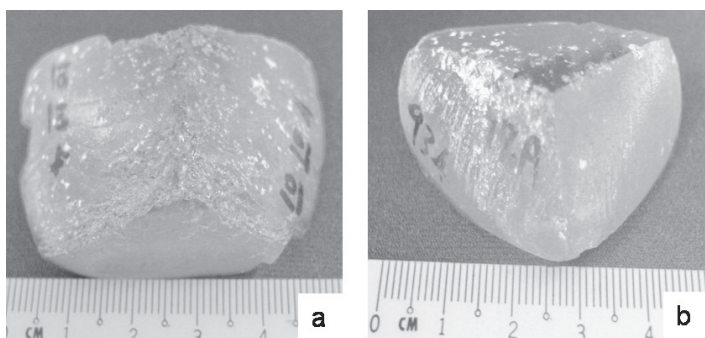
## 2.9 Future trends

Despite their excellent dielectric and piezoelectric properties, commercialization of PZN–PT and PMN–PT single crystals still faces a number of hurdles before their widespread uses can be realized. In addition to reported inconsistency in composition and properties, two other major obstacles are the high crystal cost and the lack of full material property matrices of crystals of different compositions and orientation cuts needed for device design and simulation purposes.

As shown in the present work, flux-grown PZN– $x$ PT single crystals of low PT contents (i.e.  $x \leq 0.07$ ) show good crystal homogeneity and significantly superior piezoelectric properties. Building on the experience gained so far,

our next step is to grow PZN-PT single crystals of larger sizes, say, >50 mm edge length, using the high-temperature flux technique to help reduce crystal cost. Another interesting aspect in this regard is to control the growth direction to yield crystals of the desired growth orientation to maximize its usage rate. This may be done by carefully engineering the isotherms of the solution and the growth programme. Two PZN-PT single crystals, one engineered for [110]-oriented growth and the other for [111]-oriented growth, are shown in Fig. 2.16(a) and (b), respectively. The [110]-growth crystals are ideal for making [011]-poled sensors and actuators while the [111]-oriented crystals for making [111] shear sensors.

The possibility of growing relaxor single crystals of higher use temperature and/or coercive field including crystal doping is also being studied. The plan is to stay with relaxor crystals of low PT contents, notably PZN-PT-based crystals. The growth and characterization of Fe, Co, Mn and/or F doped PZN-PT single crystals have recently been attempted by contemporary researchers with encouraging results. These works show that doping can be used to advantage to alter the Curie and rhombohedral to tetragonal phase transition temperatures (Priya *et al.*, 2001, 2003; S.J. Zhang *et al.*, 2003, 2004; Zhu and Yan, 2001; Kobor *et al.*, 2005a) and to impart a hardening effect to the crystal, i.e. to increase the coercive field, mechanical quality factor and vibration velocity (Priya *et al.*, 2001, 2002, 2003; S.J. Zhang *et al.*, 2003, 2004; Kobor *et al.*, 2005a,b). However, the effects of doping on the dielectric constants and piezoelectric coefficients of PZN-PT single crystals remain unclear as conflicting results are reported by various groups (Priya *et al.*, 2001; S.J. Zhang *et al.*, 2003, 2004; Kobor *et al.*, 2005a,b). Doping has also been used to alter the photoreflective, photovoltaic and pyroelectric properties of PZN-PT (Sato *et al.*, 2004) and PMN-PT single crystals (Tang *et al.*, 2006; Tu *et al.*, 2006).



2.16 (a) [110]-oriented and (b) [111]-oriented PZN-PT single crystals produced by the high-temperature flux growth technique, in contrast to [001]-oriented crystals in Fig. 2.5.

As for property characterization, our current effort has been to perform detailed and reliable measurements as well as using the matrix transformation technique to generate full property matrices of PZN–PT single crystals of different compositions and orientation cuts. Works in progress include the construction of full property matrices of [111]-poled single-domain and of [001]- and [011]-poled multi-domain PZN–(6–7)%PT single crystals. Such property matrices are important not only for modelling work in the design of piezoelectric devices but also in fundamental research in understanding how the phases and domain structures may affect the properties of domain-engineered relaxor single crystals. The results will be published elsewhere. It is of interest to see how the results compare with the measured properties matrices of Yin *et al.* (2000) and R. Zhang *et al.* (2001, 2002, 2003a,b, 2004a) and the deduced property values of Damjanovic *et al.* (2003) and Zhang and Cao (2004).

## 2.10 Conclusions

While the solutions of relaxor single crystals of low PT content, such as PZN– $x$ PT with  $x \leq 0.09$ , are made of simple ions, those of high PT content, such as PMN– $y$ PT with  $y \geq 0.25$ , contain large ionic complexes. For the former crystal compositions, large (>30 mm edge length), high-quality single crystals can be reproducibly grown by the high-temperature flux technique, by implementing appropriate measures to induce single-point nucleation, applying a slow cooling rate to ensure near-equilibrium growth conditions and engineering the isotherms in the solution to promote controlled (001) layer growth. For PZN– $x$ PT with  $x \leq 0.07$ , the variation of Curie temperature of the grown crystals can be controlled to within  $\pm 2^\circ\text{C}$ , corresponding to  $\Delta x \leq \pm 0.005$ . On the other hand, due to the large ionic complexes in the solution, the growth of PMN– $y$ PT single crystals of near morphotropic phase boundary compositions ( $0.28 < y < 0.34$ ) requires very careful control of the flux composition and growth conditions. Even so, flux- (and melt-) grown PMN–PT crystals suffer from more severe compositional variations, often with a PT-rich outer layer. Flux growth of PZN– $x$ PT single crystals with  $x \leq 0.07$  thus shows promises for large-scale growth for commercial ends.

The measurements have shown that the dielectric and piezoelectric properties of flux-grown PZN–(6–7)%PT and PMN–(28–30)%PT single crystals are superior to similar crystals but of compositions either too far from or too close to the morphotropic phase boundaries. The results further show that poling can induce monoclinic and/or orthorhombic phases which, when present in small quantities, are responsible for the superior dielectric and electromechanical properties observed. When present in sufficient quantity, such as in overpoled PZN–PT and PMN–PT single crystals, the induced metastable monoclinic and/or orthorhombic phases would lead to property

degradation of the material. It is thus advantageous to stay adequately away from the MPB compositions in order to avoid overpoling induced property variation and degradation during processing and/or use of PZN-PT and PMN-PT single crystals. Our results also show that flux-grown PZN-PT single crystals exhibit superior dielectric and piezoelectric properties to flux-grown PMN-PT single crystals, and that the latter show improved properties compared to their melt-grown counterparts.

## 2.11 Acknowledgements

The author gratefully acknowledges the financial and technical support received from the NUS, A\*Star, DSTA, NICOP/ONR and Microfine Materials Technologies Pte Ltd. Most of the results reported in this work are taken from the theses research of K.K. Rajan and M. Shanthi.

## 2.12 References and further reading

- Afanas'ev I I, Bereznoi A A, Bushneva S and Prokof'ev S V (1977), 'Growing crystals of lead magnoniobate and magnetantalate', *Sov J Opt Technol*, **44**, 613–615.
- Babu J B, Madeswaran G, Prakash C and Dhanasekaran R (2006), 'Growth, structural phase transition and ferroelectric properties of  $\text{Pb}[(\text{Zn}_{1/3}\text{Nb}_{2/3})_{0.91}\text{Ti}_{0.09}]\text{O}_3$  single crystals', *J Cryst Growth*, **292**, 399–403.
- Benayad A, Kobor D, Lebrun L, Guiffard B and Guyomar D (2004), 'Characteristics of  $\text{Pb}[(\text{Zn}_{1/3}\text{Nb}_{2/3})_{0.955}\text{Ti}_{0.045}]\text{O}_3$  single crystals versus growth method', *J Cryst Growth*, **270**, 137–144.
- Bertram R, Reck G and Uecker R (2003), 'Growth and correlation between composition and structure of  $(1-x)\text{Pb}(\text{Zn}_{1/3}\text{Nb}_{2/3})\text{O}_3-x\text{PbTiO}_3$  near the morphotropic phase boundary', *J Cryst Growth*, **253**, 212–220.
- Bokov V A and Myl'nikova I E (1961), 'Ferroelectric properties of monocrystals of new perovskite compounds', *Sov Phys – Solid State*, **2**, 2428–2432.
- Bonner W A and Van Uitert L G (1967), 'Growth of single crystals of  $\text{Pb}_3\text{MgNb}_2\text{O}_9$  by the Kyropoulos technique', *Mat Res Bull*, **2**, 131–134.
- Chen J and Panda R (2005), 'Review: commercialization of piezoelectric single crystals for medical imaging applications', *Proc. 2005 IEEE Ultrasonics Symp*, 235–240.
- Chen W and Ye Z-G (2001a), 'Top seeded solution growth and characterization of piezo-/ferroelectric  $(1-x)\text{Pb}(\text{Zn}_{1/3}\text{Nb}_{2/3})\text{O}_3-x\text{PbTiO}_3$  single crystals', *J Cryst Growth*, **233**, 503–511.
- Chen W and Ye Z-G (2001b), 'Top-cooling-solution-growth and characterization of piezoelectric  $0.955\text{Pb}(\text{Zn}_{1/3}\text{Nb}_{2/3})\text{O}_3-0.045\text{PbTiO}_3$  [PZNT] single crystals', *J Mater Sci*, **36**, 4393–4399.
- Cheng K C, Chan H L W, Choy C L, Yin Q, Luo H and Yin Z (2003), 'Single crystal PMN-0.33PT/epoxy 1-3 composites for ultrasonic transducer applications', *IEEE Trans UFFC*, **50**, 1177–1183.
- Choi S W, Shrout T R, Jang S J and Bhalla A S (1989), 'Dielectric and pyroelectric properties in the  $\text{Pb}(\text{Mg}_{1/3}\text{Nb}_{2/3})\text{O}_3-\text{PbTiO}_3$  system', *Ferroelectrics*, **100**, 29–38.
- Dabkowski A, Dabkowska H A, Greedan J E, Ren W and Mukherjee B K (2004), 'Growth

- and properties of single crystals of relaxor PZN–PT materials obtained from high-temperature solution', *J Cryst Growth*, **265**, 204–213.
- Damjanovic D, Budimir M, Davis M and Setter N (2003), 'Monodomain versus polydomain piezoelectric response of  $0.67\text{Pb}(\text{Mg}_{1/3}\text{Nb}_{2/3})\text{O}_3$ – $0.33\text{PbTiO}_3$  single crystals along non-polar directions', *Appl Phys Lett*, **83**, 527–529.
- Dong M and Ye Z-G (1999), 'High-temperature solution growth and characterization of the piezo-/ferroelectric  $(1-x)\text{Pb}(\text{Mg}_{1/3}\text{Nb}_{2/3})\text{O}_3$ – $x\text{PbTiO}_3$  [PMNT] single crystals', *J Cryst Growth*, **209**, 81–90.
- Dong M and Ye Z-G (2001), 'High-temperature thermodynamic properties and pseudo-binary phase diagram of the  $\text{Pb}(\text{Zn}_{1/3}\text{Nb}_{2/3})_{0.91}\text{Ti}_{0.09}\text{O}_3$ – $\text{PbO}$  system', *Jpn J Appl Phys*, **40**, 4604–4610.
- Fan H, Zhao L, Tang B, Tian C and Kim H-E (2003), 'Growth and characterization of PMNT relaxor-based ferroelectric single crystals by flux method', *Mater Sci Eng B*, **99**, 183–186.
- Fang B, Luo H, Xu H, He T and Yin Z (2001), 'Growth of  $\text{Pb}[(\text{Zn}_{1/3}\text{Nb}_{2/3})_{0.91}\text{Ti}_{0.09}]\text{O}_3$  single crystals directly from melt', *Jpn J Appl Phys*, **40**, L1377–L1379.
- Fang B-J, Xu H Q, He T-H, Luo H-S and Yin Z-W (2002), 'Growth mechanism and electrical properties of  $\text{Pb}[(\text{Zn}_{1/3}\text{Nb}_{2/3})_{0.91}\text{Ti}_{0.09}]\text{O}_3$  single crystals by a modified Bridgman method', *J Cryst Growth*, **244**, 318–326.
- Gentil S, Robert G, Setter N, Tissot P and Rivera J-P (2000), 'Growth and properties of transparent  $\text{Pb}(\text{Zn}_{1/3}\text{Nb}_{2/3})\text{O}_3$ – $\text{PbTiO}_3$  single crystals with a cubic habitus', *Jpn J Appl Phys*, **39**, 2732–2735.
- Guo Y, Luo H, Xu H, Wang P and Yin Z (2002), 'Field-induced orthorhombic phase in relaxor-based ferroelectric single crystals  $\text{Pb}(\text{Mg}_{1/3}\text{Nb}_{2/3})\text{O}_3$ – $\text{PbTiO}_3$ ', *Ferroelectrics*, **281**, 79–86.
- Guo Y, Luo H, Ling D, Xu H, He T and Yin Z (2003), 'The phase transition sequence and the location of the morphotropic phase boundary region in  $(1-x)[\text{Pb}(\text{Mg}_{1/3}\text{Nb}_{2/3})\text{O}_3$ – $x\text{PbTiO}_3$  single crystal', *J Phys Condens Matter*, **15**, L77–L82.
- Gururaja T R, Panda R K, Chen J and Beck H (1999), 'Single crystal transducers for medical imaging applications', in *Proc. 1999 IEEE Ultrasonics Symp*, 969–972.
- Harada K, Shimanuki S, Kobayashi T, Saitoh S and Yamashita Y (1998), 'Crystal growth and electrical properties of  $\text{Pb}[(\text{Zn}_{1/3}\text{Nb}_{2/3})_{0.91}\text{Ti}_{0.09}]\text{O}_3$  single crystals produced by solution Bridgman method', *J Am Ceram Soc*, **81**, 2785–2788.
- Harada K, Hosono Y, Yamashita Y and Miwa K (2001), 'Piezoelectric  $\text{Pb}[(\text{Zn}_{1/3}\text{Nb}_{2/3})_{0.91}\text{Ti}_{0.09}]\text{O}_3$  single crystals with a diameter of 2 inches by the solution Bridgman method supported on the bottom of a crucible', *J Cryst Growth*, **229**, 294–298.
- Hosono Y, Harada K, Kobayashi T K, Itsumi K, Izumi M, Yamashita Y and Ichinose N (2002), 'Dielectric and piezoelectric properties of  $0.93\text{Pb}(\text{Zn}_{1/3}\text{Nb}_{2/3})\text{O}_3$ – $0.07\text{PbTiO}_3$  piezoelectric single crystals for medical array transducers', *Jpn J Appl Phys*, **41**, 7084–7088.
- Jang H M, Oh S H and Moon J H (1992), 'Thermodynamic stability and mechanisms of formation and decomposition of perovskite  $\text{Pb}(\text{Zn}_{1/3}\text{Nb}_{2/3})\text{O}_3$  prepared by the  $\text{PbO}$  flux method', *J Am Ceram Soc*, **75**, 82–88.
- Jiang X, Tang F, Wang J T and Chen T-P (2001), 'Growth and properties of PMN–PT single crystals', *Physica C*, **364–365**, 678–683.
- Kania A, Slodczyk A and Ujma Z (2005), 'Flux growth and characterization of  $(1-x)\text{PbMg}_{1/3}\text{Nb}_{2/3}\text{O}_3$ – $x\text{PbTiO}_3$  single crystals', *J Cryst Growth*, **289**, 134–139.
- Karaki T, Nakamoto M and Adachi M (2002a), 'Top-seeded solution growth of  $\text{Pb}[(\text{Zn}_{1/3}\text{Nb}_{2/3})_{0.93}\text{Ti}_{0.07}]\text{O}_3$  single crystals', *Jpn J Appl Phys*, **41**, 6997–6999.



- Karaki T, Adachi M, Hosono Y and Yamashita Y (2002b), 'Distribution of piezoelectric properties in  $\text{Pb}[(\text{Mg}_{1/3}\text{Nb}_{2/3})_{0.7}\text{Ti}_{0.3}]\text{O}_3$  single crystal', *Jpn J Appl Phys*, **41**, L402–L404.
- Kobayashi T, Shimanuki S, Saitoh S and Yamashita Y (1997), 'Improved growth of large lead zinc niobate titanate piezoelectric single crystals for medical ultrasonic transducers', *Jpn J Appl Phys*, **36**, 6035–6038.
- Kobayashi T, Saitoh S, Harada K, Shimanuki S and Yamashita Y (1998), 'Growth of large and homogeneous PZN-PT single crystals for medical ultrasonic array transducers', in Colla E, Damjanovic D and Setter N (eds), *Proc ISAF'98*, IEEE, Piscataway, NJ, 235–238.
- Kobor D, Lebrun L, Sebald G and Guyomar D (2005a), 'Characterisation of pure and substituted  $0.955\text{Pb}(\text{Zn}_{1/3}\text{Nb}_{2/3})\text{O}_3-0.045\text{PbTiO}_3$ ', *J Cryst Growth*, **275**, 580–588.
- Kobor D, Albareda a, Perez R, Garcia J, Lebrun L and Guyomar D (2005b): 'Dielectric and mechanical nonlinearities of <001> oriented pure and doped single crystals of PZN-4.5PT', *J Phys D Appl Phys*, **38**, 2258–2264.
- Kumar F J, Lim L C, Chilong C and Tan M J (2000), 'Morphological aspects of flux grown  $0.91\text{Pb}(\text{Zn}_{1/3}\text{Nb}_{2/3})\text{O}_3-0.09\text{PbTiO}_3$  crystals', *J Cryst Growth*, **216**, 311–316.
- Kumar F J, Lim L C, Lim S P and Lee K H (2003), 'Non-destructive evaluation of large-area PZN-8%PT single crystal wafers for medical ultrasound imaging probe applications', *IEEE Trans UFFC*, **50**, 203–209.
- Kuwata J, Uchino K and Nomura S (1981), 'Phase transitions in  $\text{Pb}(\text{Zn}_{1/3}\text{Nb}_{2/3})\text{O}_3-\text{PbTiO}_3$  system', *Ferroelectrics*, **37**, 579–582.
- Kuwata J, Uchino K and Nomura S (1982), 'Dielectric and piezoelectric properties of  $0.91\text{Pb}(\text{Zn}_{1/3}\text{Nb}_{2/3})\text{O}_3-0.09\text{PbTiO}_3$  single crystals' *Jpn J Appl Phys*, **21**, 1298–1302.
- La-Orautapong D, Noheda B, Ye Z-G, Gehring PM, Toulouse J, Cox D E and Shirane G (2002), 'Phase diagram of the relaxor ferroelectric  $(1-x)\text{Pb}(\text{Zn}_{1/3}\text{Nb}_{2/3})\text{O}_3-x\text{PbTiO}_3$ ', *Phys Rev B*, **65**, 144101.
- Lee S G, Monteiro R G, Fiegelson R S, Lee H S, Lee M and Park S-E (1999), 'Growth and electrostrictive properties of  $\text{Pb}(\text{Mg}_{1/3}\text{Nb}_{2/3})\text{O}_3$  crystals', *Appl Phys Lett*, **74**, 1030–1032.
- Lim L C (2004), 'Flux growth of  $\text{Pb}(\text{Zn}_{1/3}\text{Nb}_{2/3})\text{O}_3-\text{PbTiO}_3$  and  $\text{Pb}(\text{Mg}_{1/3}\text{Nb}_{2/3})\text{O}_3-\text{PbTiO}_3$  single crystals', in Trolier-McKinstry S, Cross L E and Yamashita Y (eds), *Piezoelectric Single Crystals and their Application*, Pennsylvania State University, State College, PA, 117–137.
- Lim L C and Rajan K K (2004), 'High-homogeneity high-performance flux-grown  $\text{Pb}(\text{Zn}_{1/3}\text{Nb}_{2/3})\text{O}_3-(6-7)\%\text{PbTiO}_3$  single crystals', *J Cryst Growth*, **271**, 435–444.
- Lim L C, Liu R and Kumar F J (2002), 'Surface breakaway decomposition of perovskite  $0.91\text{PZN}-0.09\text{PT}$  during high-temperature annealing', *J Am Ceram Soc*, **85**, 2817–2826.
- Lim L C, Shanthi M, Rajan K K and Lim C Y H (2005), 'Flux growth of high-homogeneity PMN-PT single crystal and their property characterization', *J Cryst. Growth*, **282**, 330–342.
- Lopath P D, Park S-E, Shung K K and ShROUT T R (1996), 'Ultrasonic transducers using piezoelectric single crystal perovskites', in Kulwicki M B, Amin A and Safari A (eds), *Proc. ISAF'96*, IEEE, Piscataway, NJ, 543–546.
- Lu Y, Jeong D-Y, Cheng Z-Y, Zhang Q M, Luo H-S, Yin Z-W and Viehland D (2001), 'Phase transitional behaviour and piezoelectric properties of the orthorhombic phase of  $\text{Pb}(\text{Mg}_{1/3}\text{Nb}_{2/3})\text{O}_3-\text{PbTiO}_3$  single crystals', *Appl Phys Lett*, **78**, 3109–3111.
- Lu Y, Jeong D-Y, Cheng Z-Y, ShROUT T and Zhang Q M (2002), 'Phase stabilities of

- “morphotropic” phases in  $\text{Pb}(\text{Zn}_{1/3}\text{Nb}_{2/3})\text{O}_3\text{-PbTiO}_3$  single crystals’, *Appl Phys Lett*, **80**, 1918–1920.
- Luo H, Xu G, Xu H, Wang P and Yin Z (2000a), ‘Compositional homogeneity and electrical properties of lead magnesium niobate titanate single crystals grown by a modified Bridgman technique’, *Jpn J Appl Phys*, **39**, 5581–5585.
- Luo H, Xu G, Xu H, Wang P and Yin Z (2000b), ‘The effect of segregation during the growth of relaxor ferroelectric PMNT single crystals’, in Streiffer S K, Gibbons B J and Tsurumi T (eds), *Proc ISAF’00*, vol. 1, IEEE, Piscataway, NJ, 667–670.
- Marin-Franch P, Cochran S and Kirk K (2004), ‘Progress towards ultrasound applications of new single crystal materials’, *J Mater Sci*, **15**, 715–720.
- Matsushita M, Tachi T and Echizenya K (2002), ‘Growth of 3-in single crystals of piezoelectric  $\text{Pb}[(\text{Zn}_{1/3}\text{Nb}_{2/3})_{0.91}\text{Ti}_{0.09}]\text{O}_3$  by the supported solution Bridgman method’, *J Cryst Growth*, **237–239**, 853–857.
- Michau S, Mauchamp P and Dufait R (2002), ‘Single crystal-based phased array for transoesophageal ultrasound probe’, *Proc. 2002 IEEE Ultraonics Symp.*, 1269–1272.
- Mulvihill M L, Park S E, Risch G, Li Z, Uchino K and Shrout T (1996), ‘The role of processing variables in the flux growth of lead zinc niobate–lead titanate relaxor ferroelectric single crystals’, *Jpn J Appl Phys*, **35**, 3984–3990.
- Myl’nikova I E and Bokov V A (1959), *Kristallografiya*, **4**, 443 [in Russian].
- Myl’nikova I E and Bokov V A (1962), ‘Growth and electrical properties of monocystals of  $\text{Pb}_3\text{NiNb}_2\text{O}_9$  and  $\text{PbMgNb}_2\text{O}_9$ ’, in Shubnikov A V and Sheftal N N (eds), *Growth of Crystals*, vol. 3, Consultants Bureau, New York, 309–315.
- Nicoara I, Nicoara D, Marin C and Ostrogorsky A G (2005), ‘Directional solidification of  $\text{PMN}_{0.65}\text{PT}_{0.35}$  ferroelectric crystals at 1 and 7 atm’, *J Cryst Growth*, **274**, 118–125.
- Noblañc O, Gaucher P and Calvarin G (1996), ‘Structural and dielectric studies of  $\text{Pb}(\text{Mg}_{1/3}\text{Nb}_{2/3})\text{O}_3\text{-PbTiO}_3$  ferroelectric solid solutions around the morphotropic boundary’, *J Appl Phys*, **79**, 4291–4297.
- Noheda B, Cox D E, Shirane G, Gao J and Ye Z G (2002), ‘Phase diagram of relaxor ferroelectric  $\text{Pb}(\text{Mg}_{1/3}\text{Nb}_{2/3})\text{O}_3\text{-PbTiO}_3$  system’, *Phys Rev B*, **66**, 054104.
- Nomura S, Takahashi T and Yokomizo Y (1969), ‘Ferroelectric properties in the system  $\text{Pb}(\text{Zn}_{1/3}\text{Nb}_{2/3})\text{O}_3\text{-PbTiO}_3$ ’, *Jpn J Appl Phys*, **27**, 262.
- Oakley C G and Zipparo M J (2000), ‘Single crystal piezoelectrics: a revolutionary development for transducers’, *Proc. 2000 IEEE Ultrasonics Symp.*, 1157–1167.
- Park C S, Lim K Y, Choi D Y and Chung S J (1998), ‘Crystal growth of  $\text{PbMg}_{1/3}\text{Nb}_{2/3}\text{O}_3$  and  $\text{PbZn}_{1/3}\text{Nb}_{2/3}\text{O}_3$  and structural studies on the ordering’, *J Kor Phys Soc*, **32**, S974–S977.
- Park S E and Hackenberger W (2002), ‘High performance single crystal piezoelectrics: applications and issues’, *Curr Opin Solid State Mater Sci*, **6**, 11–18.
- Park S E and Shrout T R (1997a), ‘Ultrahigh strain and piezoelectric behaviour in relaxor based ferroelectric single crystals’, *J Appl Phys*, **82**, 1804–1811.
- Park S E and Shrout T R (1997b), ‘Characteristics of relaxor-based piezoelectric single crystals for ultrasonic transducers’, *IEEE Trans UFFC*, **44**, 1140–1147.
- Park S E and Shrout T R (1997c), ‘Relaxor based ferroelectric single crystals for electromechanical actuators’, *Mater Res Innovat*, **1**, 20–25.
- Park S E and Shrout T R (1997d), ‘Relaxor based ferroelectric single crystals with high piezoelectric performance’ in *Proc 8th US-Japan Seminar on Dielectric and Ferroelectric Ceramic Thin Films*, 11–13 October, 1997, Plymouth, MA, 235–241.
- Park S E, Mulvihill M L, Lopath P D, Zipparo M and Shrout T R (1996), ‘Crystal growth and ferroelectric related properties of  $(1-x)\text{Pb}(\text{A}_{1/3}\text{Nb}_{2/3})\text{O}_3\text{-xPbTiO}_3$  ( $\text{A} = \text{Zn}^{2+}, \text{Mg}^{2+}$ ),

- in Kulwichi B M, Amin A and Safari A (eds), *Proc ISAF '96*, vol. 1, IEEE, Piscataway, NJ, 79–82.
- Park S-E, Mulvihill M L, Risch G and Shrout T R (1997), 'The effect of growth condition on dielectric properties of  $\text{Pb}(\text{Zn}_{1/3}\text{Nb}_{2/3})\text{O}_3$  crystal', *Jpn J Appl Phys*, **36**, 1154–1158.
- Petrovskii G T, Bonder I A, Andreev E M and Keroleva N (1984), 'Formation of single crystals of the perovskite like ferroelectric PMN', *Inorg Mater*, **20**, 924–928.
- Powers J M, Moffett M B and Nussbaum F (2000), 'Single crystal naval transducer development', in Streiffer S K, Gibbons B J and Tsurumi T (eds), *Proc ISAF'00*, vol. 1, IEEE, Piscataway, NJ, 351–354.
- Priya S and Uchino K (2003), 'High power resonance characteristics and dielectric properties of Co-substituted  $0.92\text{Pb}(\text{Zn}_{1/3}\text{Nb}_{2/3})\text{O}_3-0.08\text{PbTiO}_3$  single crystal', *Jpn J Appl Phys*, **42**, 531–534.
- Priya S, Uchino K and Viehland D (2001), 'Crystal growth and piezoelectric properties of Mn-substituted  $\text{Pb}(\text{Zn}_{1/3}\text{Nb}_{2/3})\text{O}_3$  single crystal', *Jpn J Appl Phys*, **40**, L1044–L1047.
- Priya S, Uchino K and Viehland D (2002), 'Fe-substituted  $0.92\text{Pb}(\text{Zn}_{1/3}\text{Nb}_{2/3})\text{O}_3-0.08\text{PbTiO}_3$  single crystals: a "hard" piezocrystal', *Appl Phys Lett*, **81**, 2430–2432.
- Priya S, Ryu J, Cross L E, Uchino K and Viehland D (2002a), 'Investigation of the ferroelectric orthorhombic phase in the  $\text{Pb}(\text{Zn}_{1/3}\text{Nb}_{2/3})\text{O}_3-\text{PbTiO}_3$  system', *Ferroelectrics*, **274**, 121–126.
- Rajan K K, Ng Y S, Zhang J and Lim L C (2004), '[001]-poled PZN-(6–7)%PT  $k_{31}$ -actuators – effects of initial domain structure, length orientation and poling conditions', *Appl Phys Lett*, **85**, 4136–4138.
- Rajan K K, Zhang M J and Lim L C (2005), 'Optimum compositions for  $\text{Pb}(\text{Zn}_{1/3}\text{Nb}_{2/3})\text{O}_3-\text{PbTiO}_3$  single crystal for high-performance applications', *Jpn J Appl Phys*, **44**, 264–266.
- Rajan K K, Shanthi M, Chang W S, Jin J and Lim L C (2007), 'Dielectric and piezoelectric properties of [001] and [011]-poled relaxor ferroelectric PZN-PT and PMN-PT single crystals', *Sensors and Actuators A*, **133**, 110–116.
- Rhim S M, Jung H, Kim S and Lee S-G (2002), 'A 2.6 MHz phased array ultrasonic probe using  $0.67\text{Pb}(\text{Mg}_{1/3}\text{Nb}_{2/3})\text{O}_3-0.33\text{PbTiO}_3$  single crystal grown by the Bridgman method', *Proc 2002 IEEE Ultrasonics Symp*, 1143–1148.
- Rhim S M, Jung H, Jun J S and Hwang JS (2005), 'A 6.0 MHz 0.15 mm pitch phased array ultrasonic probe using PMN-PT single crystal', *Proc 2005 IEEE Ultrasonics Symp*, 219–222.
- Ritter T, Geng X, Shung K K, Lopath P D, Park S-E and Shrout T R (2000), 'Single crystal PZN-PT-polymer composites for ultrasound transducer applications', *IEEE Trans UFFC*, **47**, 792–800.
- Saitoh S, Izumi M, Shimanuki S, Hashimoto S and Yamashita Y (1994), 'Ultrasonic Probe', US Patent No. 5,295,487, March 22, 1994.
- Saitoh S, Kobayashi T, Harada K, Shimanuki S and Yamashita Y (1998), 'A 20 MHz single-element ultrasonic probe using  $0.91\text{Pb}(\text{Zn}_{1/3}\text{Nb}_{2/3})\text{O}_3-0.09\text{PbTiO}_3$  single crystal', *IEEE Trans UFFC*, **45**, 1071–1076.
- Saitoh S, Takeuchi T, Kobayashi T, Harada K, Shimanuki S and Yamashita Y (1999), 'A 3.7 MHz phased array probe using  $0.91\text{Pb}(\text{Zn}_{1/3}\text{Nb}_{2/3})\text{O}_3-0.09\text{PbTiO}_3$  single crystal', *IEEE Trans UFFC*, **46**, 414–421.
- Santailler J L, Ferrand B, Damjanovic D, Couchaud M, Dusserrer P, Budimir M, Mibord S and Abad T (2002), 'Growth and characterisation of piezoelectric PZN-PT 91/11

- and PMN–PT 66/34 single crystals for ultrasonic transducers’, in White G and Tsurumi T (eds), *Proc ISAF’02*, IEEE, Piscataway, NJ, 443–446.
- Sato Y, Abe S, Fujimura, R, Ono H, Oda K, Shimura T and Kuroda K (2004), ‘Photorefractive effect and photochromism in the Fe-doped relaxor ferroelectric crystal  $\text{Pb}(\text{Zn}_{1/3}\text{Nb}_{2/3})\text{O}_3\text{–PbTiO}_3$ ’, *J Appl Phys*, **96**, 4852–4855.
- Setter N and Cross L E (1980), ‘Flux growth of lead scandium tantalate  $\text{Pb}(\text{Sc}_{0.5}\text{Ta}_{0.5})\text{O}_3$  and lead magnesium niobate  $\text{Pb}(\text{Mg}_{1/3}\text{Nb}_{2/3})\text{O}_3$  single crystals’, *J Cryst Growth*, **50**, 555–556.
- Shanthi M, Hoe K H, Lim C Y H and Lim L C (2005a), ‘Overpoling-induced property degradation in  $\text{Pb}(\text{Mg}_{1/2}\text{Nb}_{2/3})\text{O}_3\text{–PbTiO}_3$  single crystals of near-morphotropic phase boundary compositions’, *Appl Phys Lett*, **86**, 262908.
- Shanthi M, Chia S M and Lim L C (2005b), ‘Overpoling resistance of [011]-poled  $\text{Pb}(\text{Mg}_{1/2}\text{Nb}_{2/3})\text{O}_3\text{–PbTiO}_3$  single crystals’, *Appl Phys Lett*, **87**, 202902.
- Shimanuki S, Saitoh S and Yamashita Y (1998), ‘Single crystal of the  $\text{Pb}(\text{Zn}_{1/3}\text{Nb}_{2/3})\text{O}_3\text{–PbTiO}_3$  system grown by the vertical Bridgman method and its characterization’, *Jpn J Appl Phys*, **37**, 3382–3385.
- Shin M C, Chung S J, Lee S-G and Feigelson R S (2004), ‘Growth and observation of domain structure of lead magnesium niobate-lead titanate single crystals’, *J Cryst Growth*, **263**, 412–420.
- Shippy J C and Deng K (2003), ‘A miniature vector sensor for line array applications’, *IEEE Oceans Conf. Record*, **5**, 2367–2370.
- Shrout T R, Chang Z P, Kim N and Markgraf S (1990), ‘Dielectric behaviour of single crystals near the  $(1-x)\text{Pb}(\text{Mg}_{1/3}\text{Nb}_{2/3})\text{O}_3\text{–}(x)\text{PbTiO}_3$  morphotropic phase boundary’, *Ferroelectric Lett*, **12**, 63–69.
- Tang Y, Luo L, Jia Y, Luo H, Zhao X, Xu H, Lin D, Sun J, Meng X, Zhu J and Es-Soumi M (2006), ‘Mn-doped  $0.71\text{Pb}(\text{Mg}_{1/3}\text{Nb}_{2/3})\text{O}_3\text{–}0.29\text{PbTiO}_3$  pyroelectric crystals for uncooled infrared focal plane arrays applications’, *Appl Phys Lett*, **89**, 162906.
- Tressler J F and Howarth T R (2000), ‘Cymbal drives utilizing relaxor-based ferroelectric single crystal materials’, in Streiffer S K, Gibbons B J and Tsurumi T (eds), *Proc ISAF’00*, vol. 1, IEEE, Piscataway, NJ, 561–564.
- Tressler J F, Howarth T R and Huang D (2003), ‘A comparison of the underwater acoustic performance of single crystal vs. piezoelectric ceramic based cymbal projectors’, *IEEE Oceans Conf. Record*, **5**, 2372–2379.
- Tu C S, Chien R R, Wang F-T, Schmidt V H and Han P (2004), ‘Phase stability after an electric-field poling in  $\text{Pb}(\text{Mg}_{1/3}\text{Nb}_{2/3})_{1-x}\text{Ti}_x\text{O}_3$  crystals’, *Phys Rev B*, **70**, 220103.
- Tu C S, Wang F-T, Chien R R, Schmidt V H, Hung C-M and Tseng C-T (2006), ‘Dielectric and photovoltaic phenomena in tungsten-doped  $\text{Pb}(\text{Mg}_{1/3}\text{Nb}_{2/3})_{1-x}\text{Ti}_x\text{O}_3$  crystal’, *Appl Phys Lett*, **88**, 032902.
- Van Hook A (1961), *Crystallization: Theory and Practice*, Reinhold Publishing Corporation, New York, 73.
- Wakiya N, Ishizawa N, Shinozaki K and Mizutani N (1995), ‘Thermal stability of  $\text{Pb}(\text{Zn}_{1/3}\text{Nb}_{2/3})\text{O}_3$  (PZN) and consideration of stabilization conditions of perovskite type compounds’, *Mater Res Bull*, **30**, 1121–1131.
- Wan X, Wang J, Chan H L W, Choy C L, Luo H and Yin Z (2004), ‘Growth and optical properties of  $0.62\text{Pb}(\text{Mg}_{1/3}\text{Nb}_{2/3})\text{O}_3\text{–}0.38\text{PbTiO}_3$  single crystals by a modified Bridgman technique’, *J Cryst Growth*, **263**, 251–255.
- Wlodkowski P, Deng K, Kahn M and Chase M (2000), ‘The development of mesoscale accelerometers with single crystal piezoelectric materials’, in Streiffer S K, Gibbons B J and Tsurumi T (eds), *Proc ISAF’00*, vol. 1, IEEE, Piscataway, NJ, 565–567.

- Wlodkowski P, Deng K and Kahn M (2001), 'The development of high-sensitivity, low-noise accelerometers utilizing single crystal piezoelectric materials', *Sensors and Actuators A*, **90**, 125–131.
- Xiao J, Hang Y, Wan S, Zhu X, Zhou S, Huang W, Tian Y and Yin S (2002), 'Characterization of 0.92Pb(Zn<sub>1/3</sub>Nb<sub>2/3</sub>)O<sub>3</sub>-0.08PbTiO<sub>3</sub> crystals grown from high-temperature solutions', *J Cryst Growth*, **242**, 355–361.
- Xu G, Luo H, Wang P, Xu H and Yin Z (2000), 'Ferroelectric and piezoelectric properties of novel relaxor ferroelectric single crystal PMNT', *Chin Sci Bull*, **45**, 491–495.
- Xu G, Luo H, Guo Y, Gao Y, Xu H, Qi Z, Zhong W and Yin Z (2001), 'Growth and piezoelectric properties of Pb(Mg<sub>1/3</sub>Nb<sub>2/3</sub>)O<sub>3</sub>-PbTiO<sub>3</sub> crystals by the modified Bridgman technique', *Solid State Comm*, **120**, 321–324.
- Xu J, Fan S, Lu B, Tong J and Zhang A (2002), 'Seeded growth of relaxor ferroelectric single crystals Pb[(Zn<sub>1/3</sub>Nb<sub>2/3</sub>)<sub>0.91</sub>Ti<sub>0.09</sub>]O<sub>3</sub> by the vertical Bridgman method', *Jpn J Appl Phys*, **41**, 7000–7002.
- Xu J, Tong J, Shi M, Wu A and Fan S (2003), 'Flux Bridgman growth of Pb[(Zn<sub>1/3</sub>Nb<sub>2/3</sub>)<sub>0.93</sub>Ti<sub>0.07</sub>]O<sub>3</sub> piezocrystals', *J Cryst Growth*, **253**, 274–279.
- Xu J, Wu X, Tong J, Shi M and Qian G (2005), 'Two-step Bridgman growth of 0.91Pb(Zn<sub>1/3</sub>Nb<sub>2/3</sub>)O<sub>3</sub>-0.09PbTiO<sub>3</sub> single crystals', *J Cryst Growth*, **280**, 107–112.
- Ye Z-G, Tissor P and Schmid H (1990), 'Pseudo-binary Pb(Mg<sub>1/3</sub>Nb<sub>2/3</sub>)O<sub>3</sub>-PbO phase diagram and crystal growth of Pb(Mg<sub>1/3</sub>Nb<sub>2/3</sub>)O<sub>3</sub> PMN]', *Mater Res Bull*, **25**, 739–748.
- Yin J, Jiang B and Cao W (2000), 'Elastic, piezoelectric and dielectric properties of 0.955Pb(Zn<sub>1/3</sub>Nb<sub>2/3</sub>)O<sub>3</sub>-0.045PbTiO<sub>3</sub> single crystal with designed multidomains', *IEEE Trans UFFC*, **47**, 285–291.
- Yokomizo Y, Takahashi T and Nomura S (1970), 'Ferroelectric properties in the system Pb(Zn<sub>1/3</sub>Nb<sub>2/3</sub>)O<sub>3</sub>-PbTiO<sub>3</sub>', *J Phys Soc Japan*, **28**, 1278–1284.
- Zawilski K T, Custodio M C C, DeMattei R C, Lee S-G, Monteiro R G, Odagawa H and Feigelson R S (2003), 'Segregation during the vertical Bridgman growth of lead magnesium niobate-lead titanate single crystals', *J Cryst Growth*, **258**, 353–367.
- Zhang L, Dong M and Ye Z-G (2000), 'Flux growth and characterization of the relaxor-based Pb[(Zn<sub>1/3</sub>Nb<sub>2/3</sub>)<sub>1-x</sub>Ti<sub>x</sub>]O<sub>3</sub> [PZNT] piezocrystals', *Mater Sci Eng B*, **78**, 96–104.
- Zhang R and Cao W (2004), 'Transformed material coefficients for single-domain 0.67Pb(Mg<sub>1/3</sub>Nb<sub>2/3</sub>)O<sub>3</sub>-0.33PbTiO<sub>3</sub> single crystals under differently defined coordinate systems', *Appl Phys Lett*, **85**, 6380–6382.
- Zhang R, Jiang B and Cao W (2001), 'Elastic, piezoelectric and dielectric properties of multidomain 0.67Pb(Mg<sub>1/3</sub>Nb<sub>2/3</sub>)O<sub>3</sub>-0.33PbTiO<sub>3</sub> single crystals', *J Appl Phys*, **90**, 3471–3475 (see also *Proc. 2001 IEEE Ultrasonic Symp.*, p. 1101).
- Zhang R, Jiang B, Cao W and Amin A (2002), 'Complete set of material constants of 0.93Pb(Zn<sub>1/3</sub>Nb<sub>2/3</sub>)O<sub>3</sub>-0.07PbTiO<sub>3</sub> domain engineered single crystal', *J Mater Sci Lett*, **21**, 1877–1879.
- Zhang R, Jiang B and Cao W (2003a), 'Complete set of properties of 0.92Pb(Zn<sub>1/3</sub>Nb<sub>2/3</sub>)O<sub>3</sub>-0.08PbTiO<sub>3</sub> single crystal with engineered domains', *Mater Lett*, **57**, 1305–1308.
- Zhang R, Jiang B and Cao W (2003b), 'Single-domain properties of 0.67Pb(Mg<sub>1/3</sub>Nb<sub>2/3</sub>)O<sub>3</sub>-0.33PbTiO<sub>3</sub> single crystals under electric field bias', *Appl Phys Lett*, **85**, 6380–6382.
- Zhang R, Jiang B and Cao W (2004), 'Superior  $d_{32}$  and  $k_{32}$  coefficients in 0.955Pb(Zn<sub>1/3</sub>Nb<sub>2/3</sub>)O<sub>3</sub>-0.045PbTiO<sub>3</sub> and 0.92Pb(Zn<sub>1/3</sub>Nb<sub>2/3</sub>)O<sub>3</sub>-0.08PbTiO<sub>3</sub> single crystals poling along [011]', *J Phys Chem Solids*, **65**, 1083–1086.

- Zhang S J, Lebrun L, Jeong D Y, Randall C A, Zhang Q M and Shrout T R (2003): 'Growth and characterisation of Fe-doped  $\text{Pb}(\text{Zn}_{1/3}\text{Nb}_{2/3})\text{O}_3\text{-PbTiO}_3$  single crystals', *J Appl Phys*, **93**, 9257–9262.
- Zhang S J, Lebrun L, Randall C A and Shrout T R (2004): 'Growth and electrical properties of (Mn,F) co-doped  $0.92\text{Pb}(\text{Zn}_{1/3}\text{Nb}_{2/3})\text{O}_3\text{-}0.08\text{PbTiO}_3$  single crystal', *J Cryst Growth*, **267**, 204–212.
- Zhu D M and Han P D (1999), 'Thermal conductivity and electromechanical property of single-crystal lead magnesium niobate titanate', *Appl Phys Lett*, **75**, 3868–3870.
- Zhu W and Yan M (2001), 'Effect of Mn-doping on the morphotropic phase boundary of PZN-BT-PT system', *J Mater Sci Lett*, **20**, 1527–1529.

## Recent developments and applications of piezoelectric crystals

---

W S HACKENBERGER, J LUO, X JIANG,  
K A SNOOK and P W REHRIG, TRS Technologies USA  
and S ZHANG and T R SHROUT,  
Pennsylvania State University, USA

### 3.1 Introduction

Piezoelectric single crystals based on  $\text{Pb}(\text{Mg}_{1/3}\text{Nb}_{2/3})_{1-x}\text{Ti}_x\text{O}_3$  (PMN–PT) and  $\text{Pb}(\text{Zn}_{1/3}\text{Nb}_{2/3})_{1-x}\text{Ti}_x\text{O}_3$  (PZN–PT) offer large improvements in piezoelectric strain and electromechanical coupling coefficient for actuator and transducer applications [1, 2]. Over the past several years, much work has been done to demonstrate the advantages crystals can provide for a variety of military and domestic applications, including medical ultrasound transducers, naval sonar transducers, high-precision actuators for adaptive optics and many other potential applications [2–8]. Currently, crystal growers are focusing on PMN–PT single crystal because it can be grown by solidification from a melt using the Bridgman method. Although growth of PMN–PT by the Bridgman method has already achieved larger crystals and resulted in cost reductions over flux growth, refinement of Bridgman is ongoing, including increased crystal diameter, increased longitudinal and radial uniformity, reduction of defects and  $\langle 001 \rangle$ -oriented growth. Further cost reductions and uniformity improvements are also expected by applying zone melting growth to level the composition along the crystallization direction in this solid-state solution system.

In this chapter, the progress at TRS on the crystal growth of relaxor piezoelectric single crystals is presented with the emphasis on Bridgman and zone-melting growth of PMN–PT. Meanwhile the dynamic performance under different frequency and electric bias conditions is discussed to provide useful information for device design, in which the low ferroelectric–ferroelectric phase transition temperature and low coercive field of single crystals are the main issues. The broad range of actuator and transducer applications developed or under development at TRS are reviewed, showing that much higher performance over the conventional piezoelectric ceramics have been demonstrated. Future trends in crystal growth and applications are discussed briefly as well.

## 3.2 Crystal growth and characterization of relaxor piezoelectrics

### 3.2.1 Flux growth of PMN–PT and PZN–PT

PMN–PT and PZN–PT crystals were initially grown by the flux method, which demonstrated ultra-high piezoelectric coefficients and strain levels with low hysteresis, leading to a new era of relaxor ferroelectric materials studies [2, 9]. In this process, oxide raw materials including high-purity  $\text{Pb}_3\text{O}_4$ ,  $\text{MgCO}_3$  (or  $\text{ZnO}$ ),  $\text{Nb}_2\text{O}_5$  and  $\text{TiO}_2$  were weighed according to the desired molar ratio with excess  $\text{Pb}_3\text{O}_4$  as a flux. The mixed powders were usually loaded into a platinum crucible, which was sealed to minimize  $\text{PbO}$  volatilization from the solution. The crystallization process was driven by slow cooling ( $1\text{--}5^\circ\text{C}/\text{h}$ ) after the solution was held at soak temperature ( $1100\text{--}1200^\circ\text{C}$ ) for several hours in the furnace. Although high-quality PMN–PT and PZN–PT crystals have been grown from flux for quite a long time, limitations such as small crystal size, slow crystal growth rate and complicated post-growth processing make flux growth unattractive for large-scale commercial production of these crystals. The exploration of effective crystal growth technologies for relaxor piezoelectric single crystals has been pursued extensively. This section reviews the recent progress at TRS on Bridgman and zone-melting growth of relaxor piezoelectric crystals.

### 3.2.2 Recent progress in Bridgman growth of PMN–PT crystal

It has been shown that PMN–PT has a more stable perovskite phase and exhibits less of a tendency to form the parasitic pyrochlore phase compared with PZN–PT [10, 11]. Pre-synthesizing PMN–PT and using sealed Pt crucibles to prevent volatilization of  $\text{PbO}$  above  $1250^\circ\text{C}$ , PMN–PT single crystals have been grown directly from the melt using the Bridgman method [12, 13]. Compared with flux growth, the Bridgman technique can grow large single crystal boules along specific crystallographic orientations with much higher efficiency, which can potentially reduce the cost of PMN–PT crystal to be competitive with high-quality piezoelectric ceramics used in high-end applications.

Through several years' effort on raw material synthesis, crystal growth orientation control and crystal diameter enlargement, significant progress has been made in Bridgman growth of PMN–PT. High-quality and large PMN–PT crystals without macro-defects have been successfully grown along different crystallographic orientations, including  $\langle 111 \rangle$ ,  $\langle 110 \rangle$  and  $\langle 001 \rangle$ . Since PMN–PT crystal exhibits the highest piezoelectric response along the  $\langle 001 \rangle$  orientation [2], successful and repeatable  $\langle 001 \rangle$ -oriented growth



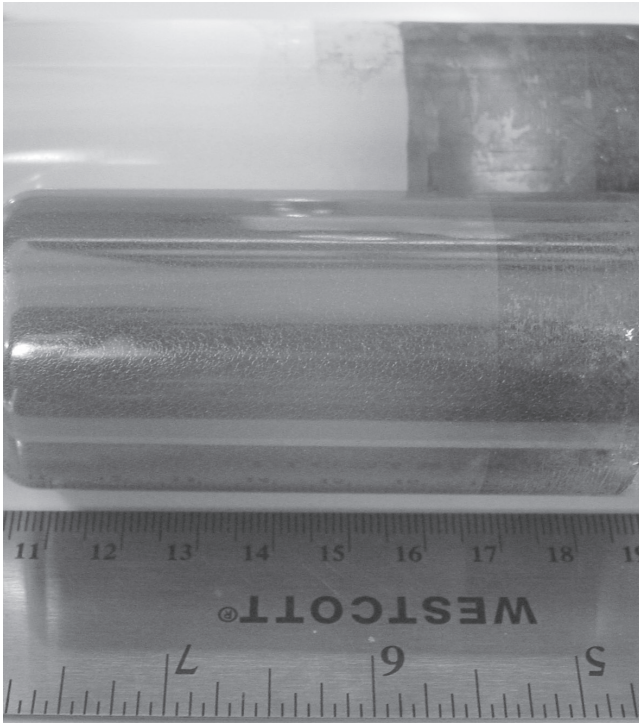
produces highly uniform (001) wafers for the first time, regardless of the axial composition segregation, and greatly facilitates crystal element fabrication. By scaling-up crystal size, the cost of PMN–PT crystals has been reduced by several times in recent years.

Owing to the large difference in melting point and density between each oxide, especially between PbO ( $T_m = 886^\circ\text{C}$ ,  $\rho = 9.53\text{ g/cm}^3$ ) and MgO ( $T_m = 2852^\circ\text{C}$ ,  $\rho = 3.58\text{ g/cm}^3$ ), it is usually difficult to get a homogeneous perovskite phase by directly mixing the oxides without the presence of a minor amount of the pyrochlore phase [10]. Pre-synthesized PMN–PT using a modified columbite precursor method has been proved to be the most efficient way to eliminate the pyrochlore phase [4].

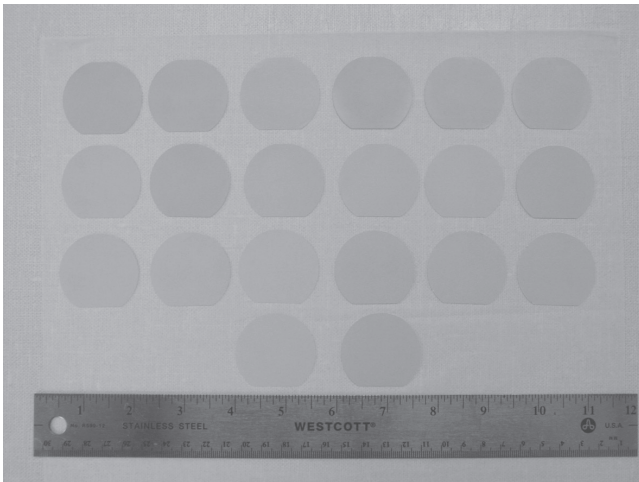
Crystal growth is usually performed in either straight or tapered Pt crucibles. After the oriented PMN–PT crystal seed and synthesized PMN–PT powder or ceramic pellets are charged into the Pt crucible, it is sealed with a Pt lid to prevent the PbO evaporation at high temperature. Resistance-heated multi-zone furnaces with soaking temperature higher than  $1380^\circ\text{C}$  and the axial temperature gradient larger than  $20^\circ\text{C/cm}$  are used for the growth. Several thermocouples are usually placed touching the Pt crucible to monitor the melt temperature during the growth. Unidirectional solidification is accomplished by slowly lowering the Pt crucible through the temperature gradient with a translation speed less than  $2\text{ mm/h}$ .

Large PMN–PT crystals roughly along the  $\langle 111 \rangle$  orientation can usually be grown by the self-seeded Bridgman process (growth without the presence of a single crystal seed), since  $\langle 111 \rangle$  is the fastest growth direction. By developing seeded Bridgman growth and applying different growth speeds with precise temperature profile control, high quality PMN–PT crystals along all the three major crystallographic orientations,  $\langle 111 \rangle$ ,  $\langle 110 \rangle$  and  $\langle 001 \rangle$ , have been successfully grown with no major obstacles. Figure 3.1 shows the crystal boules grown along  $\langle 001 \rangle$ , which are usually  $40\text{--}50\text{ mm}$  in diameter and about  $100\text{ mm}$  in length with light green color. Also shown are macro-defect-free (001) wafers cut from these boules.

To evaluate the composition distributions in Bridgman grown crystals, long bar-shape samples were cut from each boule and the main elements, Pb, Mg, Nb and Ti in the PMN–PT system were profiled quantitatively along the boules by electron probe micro-analysis (EPMA). Except for Pb, all other elements exhibited compositional segregation during growth, with effective segregation coefficients of Nb and Mg larger than 1 while that of Ti is smaller than 1. Figure 3.2 compares the composition profile (Ti concentration) in  $\langle 111 \rangle$ - and  $\langle 001 \rangle$ -oriented crystal boules grown under similar conditions and shows no significant difference in composition gradient between growth directions. The composition profiles of Ti were simulated by a well-established equation used for describing the compositional segregation behavior in solid solution systems during the normal solidification process [15]:

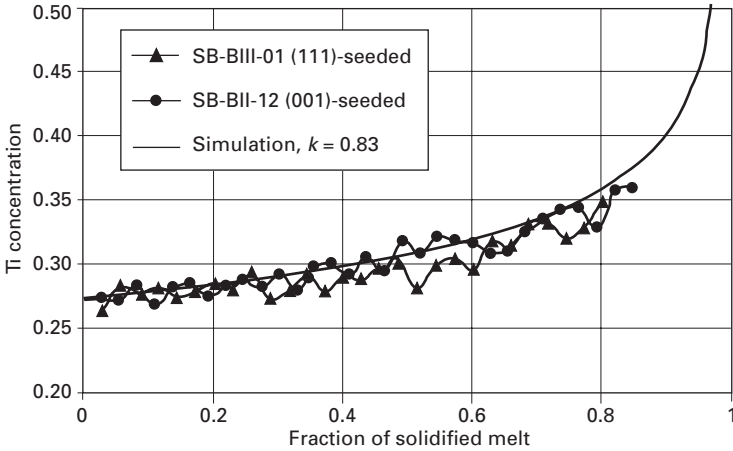


(a)



(b)

3.1 Photographs of crystal boules grown along  $\langle 001 \rangle$  (a) and macro-defect-free (001) wafers (b) cut from them.

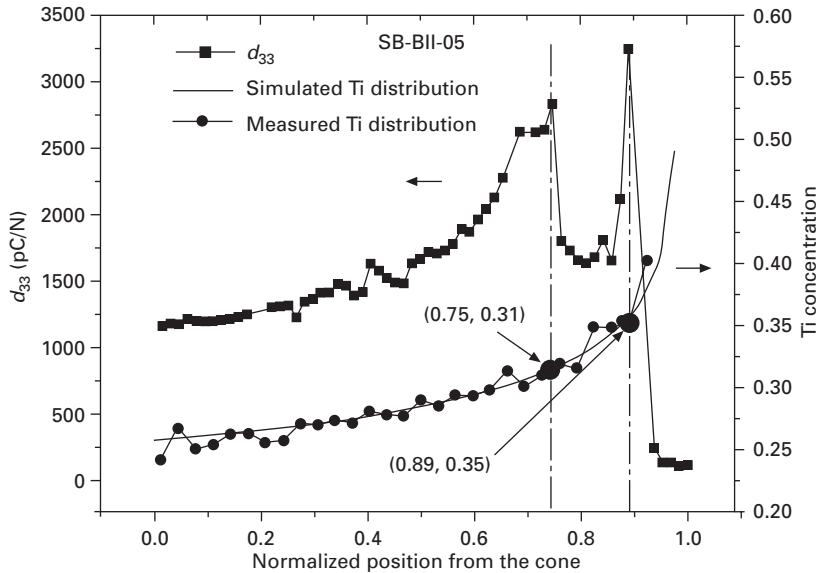


3.2 Composition profiles of Ti in <111>- and <001>-oriented crystal boules.

$$c_s = k_e c_0 (1 - g)^{k_e - 1} \quad 3.1$$

where  $k_e$  is effective segregation coefficient,  $C_s$  and  $C_0$  are the solute concentration in the crystal and the starting melt, and  $g$  is the solidified fraction. By simulation, the estimated effective segregation coefficients of Ti in these two runs were both around 0.83.

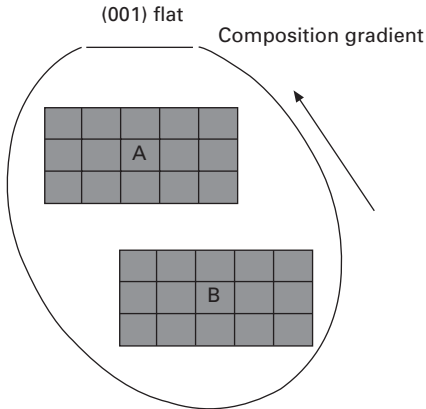
By observing the double side polished slices cut along the PMN–PT crystal growth direction, usually three different regions can be identified in each boule by the change of transparency and spontaneous domain structure. In the lower part of the boule, where crystallization occurred first, the crystal is semi-transparent and uniform with no visible ferroelectric domains. In the middle part, the crystal is very cloudy due to light scattering by large and irregular-shaped visible domains. In the upper part, the crystal becomes suddenly quite transparent with only  $90^\circ$  and  $180^\circ$  domains observed. Long bars have been cut along the growth direction from as-grown boules and then sliced into small squares or rectangular plates with the large pair of faces in (001) and with the aspect ratio between width (length) and thickness larger than 10:1. These plates were poled (10 kV/cm at room temperature) and the piezoelectric coefficient ( $d_{33}$ ) was measured individually by direct observation of strain as a function of electric field using a modified Sawyer–Tower circuit and linear variable differential transducer (LVDT) driven by a lock-in amplifier (Stanford SR830). For the longitudinal variation of  $d_{33}$  along the whole boule usually two peaks show up around the two boundaries between the three parts of the boule. Figure 3.3 compares the piezoelectric property ( $d_{33}$ ) variation with the composition distribution measured by EPMA, which shows the region between these two peaks roughly corresponds to a



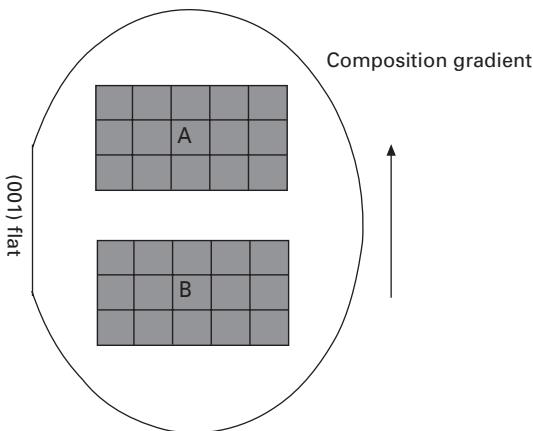
3.3 Comparison of piezoelectric coefficient variation with Ti concentration distribution along the same PMN-PT boule.

PT ( $\text{PbTiO}_3$ ) concentration of 31–35% (15–20% of the total boule length), and is basically consistent with the broad MPB region between rhombohedral and tetragonal phases proposed by Guo *et al.* [16,17]. Studies show that the mixed phases, including metastable ferroelectric monoclinic ( $\text{FE}_m$ ) and ferroelectric orthorhombic ( $\text{FE}_o$ ) phases, are possibly present in this region [16–18].

(001) wafers sliced from  $\langle 111 \rangle$ -,  $\langle 110 \rangle$ - and  $\langle 001 \rangle$ -oriented PMN-PT crystal boules have been cut into  $5 \times 5 \times 0.5 \text{ mm}^3$  plates so that the variation of piezoelectric and dielectric properties within the wafers cut from differently oriented boules could be evaluated (see Fig. 3.4). Piezoelectric coefficient,  $d_{33}$ , was measured by the same strain vs. electric field measurement as mentioned above. Meanwhile, dielectric constant,  $K$ , was measured by a Hewlett Packard 4194 impedance analyzer. For the wafers cut from  $\langle 111 \rangle$ - and  $\langle 110 \rangle$ -oriented boules, two rectangular areas, which have all of their edges along [001], were selected to evaluate property uniformity. Area A and B are the same size ( $25 \times 15 \text{ mm}^2$ ); however, A is closer to the morphotropic phase boundary (MPB) than B, since the slice was cut inclined to the crystal growth direction. As shown in Table 3.1, in both  $\langle 111 \rangle$ - and  $\langle 110 \rangle$ -oriented growth, area B has higher property uniformity than area A in both  $d_{33}$  and  $K$ . Comparison of the A (or B) areas between the  $\langle 111 \rangle$ - and  $\langle 110 \rangle$ -oriented growth shows that the latter obviously has better uniformity. Very high-property uniformity has been achieved in (001) wafers of  $\langle 001 \rangle$ -oriented



(001) wafer with an (001) flat inclined to the axis  
Growth orientation: (111)  
(a)



(001) wafer with an (001) flat on the side  
Growth orientation: (110)  
(b)

### 3.4 The cutting of (001) wafer and $d_{33}$ mode plates from the boules with different orientations.

growth (cut perpendicular to the growth direction). The coefficient variation in a whole (001) wafer was no more than  $\pm 2\%$  for both piezoelectric coefficient and dielectric constant, which shows significant advantage of the  $\langle 001 \rangle$ -oriented growth.

In summary, large high-quality PMN–PT crystals along the  $\langle 111 \rangle$ -,  $\langle 110 \rangle$ - and  $\langle 001 \rangle$ -orientations have been successfully grown by the seeded Bridgman method. A broad MPB region covering 15–20% of the whole length of the boule was identified with PT concentration from 31% to 35%, by characterization of longitudinal variation of both piezoelectric properties

Table 3.1 Property uniformity in (001) wafers

(001) Wafer from	SB-BIII-01 <111>-boule				SB-BIII-11 <110>-boule				SB-BIII-08 <001>-boule	
	A		B		A		B		Whole	
Property	<i>K</i>	<i>d</i> <sub>33</sub> (pC/N)	<i>K</i>	<i>d</i> <sub>33</sub> (pC/N)	<i>K</i>	<i>d</i> <sub>33</sub> (pC/N)	<i>K</i>	<i>d</i> <sub>33</sub> (pC/N)	<i>K</i>	<i>d</i> <sub>33</sub> (pC/N)
Average	6523	1974	5619	1700	5695	2298	5463	1993	5888	1889
Std dev.	711	156	168	104	293	141	293	96	117	31
Coef. var.%	±10.9	±7.9	±3.0	±6.1	±5.2	±6.2	±5.4	±4.8	±2.0	±1.6
Max. var.%	±23.3	±18.2	±5.1	±12.0	±9.9	±11.9	±8.3	±7.4	±3.8	±3.7

Coefficient variation = standard deviation/average

Maximum variation = (maximum-minimum)/(2×average)

and composition. Lateral uniformity analysis indicates that the property variation is not only strongly related to the growth direction, but also to the sample cutting direction. Cutting perpendicular to the composition gradient, which is always along the crystal growth direction, will give much less property variation. Since (001) wafers cut from <001>-oriented boules are perpendicular to the composition gradient, less than  $\pm 2\%$  variation of both the piezoelectric and dielectric properties has been achieved for (001) wafers cut from <001> grown boules.

### 3.2.3 Innovative zone-melting growth of PMN–PT crystal

Although the Bridgman method is a very promising technique, the composition segregation issue has to be addressed for commercial production of PMN–PT crystal. Since PMN–PT is a complete solid solution system as shown by its high-temperature phase diagram, it inevitably exhibits an inhomogeneous composition distribution along crystal boules grown by Bridgman method [12], resulting in variation of dielectric and piezoelectric properties along the growth orientation. Even though the composition variation along the growth direction can be restrained to some degree by applying higher growth rate and a lower axial temperature gradient across the solid–liquid interface, it can never be eliminated due to the thermodynamic nature of the solid solution system [12]. The existence of such a composition and property variation is one of the main disadvantages of Bridgman growth. As mentioned before, PMN–PT exhibits the highest piezoelectric response along the <001> orientation [2]. Although the <001>-oriented Bridgman growth can produce desirable (001) wafers with very high lateral uniformity in each wafer, it cannot eliminate the wafer-to-wafer variation, resulting in only about one-third of the length in each boule with the required PT composition range with desired piezoelectric and dielectric properties and a reasonable property variation (typically  $\pm 3$  to  $5\%$ ).

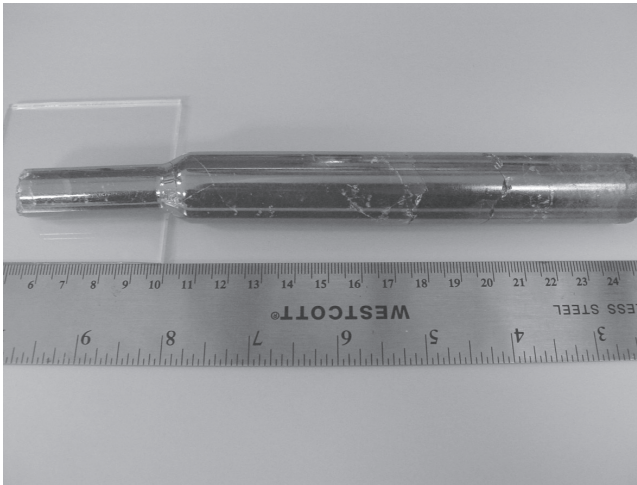
Owing to the inevitable composition segregation in Bridgman growth, alternative crystal growth techniques have to be sought to further improve the longitudinal composition uniformity along the growth direction and to extend the portion of as-grown boules which has optimal piezoelectric properties. Zone leveling, a type of zone-melting methods, which has been shown to produce a uniform, or level, distribution of solute in polycrystals and single crystals in many applications [19] has been proposed as an alternative method to prevent composition segregation in PMN–PT crystal growth [10].

In single-pass zone leveling, the composition distribution along the solidification direction can be described by the following equation [19]:

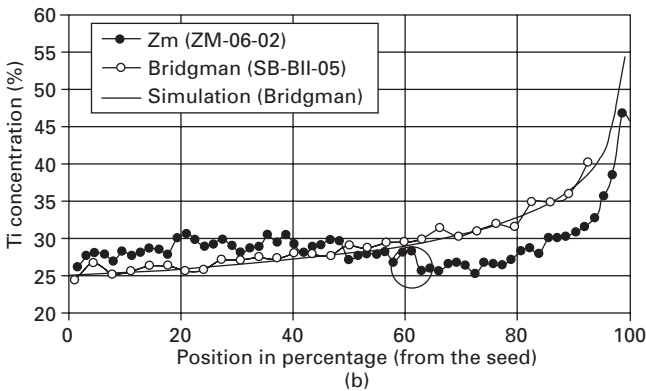
$$c_s = c_0(1 - (1 - k_e)e^{-k_e g/l}) \quad 3.2$$

where  $g$  is the distance from the point at which the first solid freezes and  $l$  is the length of melting zone. The equation is valid in all but the last melting zone. Theoretically, zone leveling can produce a flat composition distribution except for the initial and ending regions.

The zone melting growth of PMN–PT crystals was initially demonstrated in an RF induction heated furnace by self-seeded and  $\langle 111 \rangle$ -seeded growth [20]. Recently,  $\langle 110 \rangle$ -oriented PMN–PT single crystals have also been grown by a modified zone melting process in a three-zone resistance heated furnace. One of the boules grown by this modified zone melting method is shown in Fig. 3.5(a) and the Ti concentration along the growth direction in this boule



(a)



(b)

3.5 Photo of a boule grown by a modified zone melting method (a) and Ti concentration along the growth direction in this boule in comparison with that in a boule grown by Bridgman method (b).



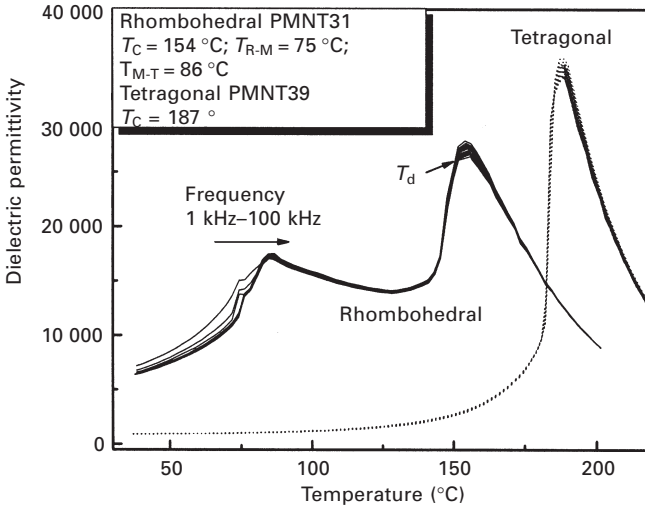
analyzed by EPMA is presented in Fig. 3.5(b) and compared with that in a boule grown by Bridgman method. It is apparent from the data that the zone melting method improved the longitudinal composition uniformity of the boule by leveling the Ti concentration in the middle part of the boule. The circled area in Fig. 3.5b corresponds to the location of the crucible where minor leakage of the melt occurred, which might be the cause of the sharp decrease of Ti concentration in the same area. Although preliminary studies have been carried out to explore the feasibility of zone melting growth of PMN–PT crystal, more effort is needed before it becomes competitive to the well-developed Bridgman growth method.

### 3.3 Dynamic performance of piezoelectric crystals with frequency and dc bias

Piezoelectric single crystals used in electromechanical devices are in many cases exposed to high electric field, high dynamic stress, high frequency or any combination of these. For PMN–PT single crystals, use is limited to less than 90° due to a strongly curved MPB, and a dc bias field must often be used to prevent depoling for high ac drive applications. So it is desirable to get detailed information about the dielectric and piezoelectric behavior under different frequency and dc bias fields.

#### 3.3.1 Dielectric behavior with frequency

The frequency dependence of dielectric permittivity as a function of temperature for [001] oriented  $0.69\text{Pb}(\text{Mg}_{1/3}\text{Nb}_{2/3})\text{O}_3\text{--}0.31\text{PbTiO}_3$  (PMNT31) and  $0.61\text{Pb}(\text{Mg}_{1/3}\text{Nb}_{2/3})\text{O}_3\text{--}0.39\text{PbTiO}_3$  (PMNT39) single crystals has been characterized in the frequency range of 100 Hz to 100 kHz (Fig. 3.6). Several dielectric anomalies below  $T_C$  are observed in Fig. 3.6 for rhombohedral PMNT31 and only one peak is found at  $T_C$  for tetragonal PMNT39. The two dielectric anomalies in the low temperature range, around 75 and 86 °C, correspond to ferroelectric phase transitions between rhombohedral and monoclinic phases and monoclinic and tetragonal phases, respectively [21]. The dielectric peak located at 154 °C is the temperature of maximum dielectric permittivity ( $T_C$ ) of PMNT31 crystals. It is also observed that frequency dispersion of dielectric permittivity occurs when the temperature is below 86 °C and over 151 °C, while the dielectric permittivity is frequency independent in the temperature range 86–151 °C. A transition between the normal ferroelectric and relaxor states is indicated by the appearance of a frequency dispersive shoulder slightly below the  $T_C$  and an abrupt disappearance of the frequency dispersion at a lower temperature. This temperature is described as  $T_d \sim 151$  °C in Fig. 3.6, which reflects the decay of a macrodomain state to a microdomain state driven by thermal agitation [23–23], while no evident

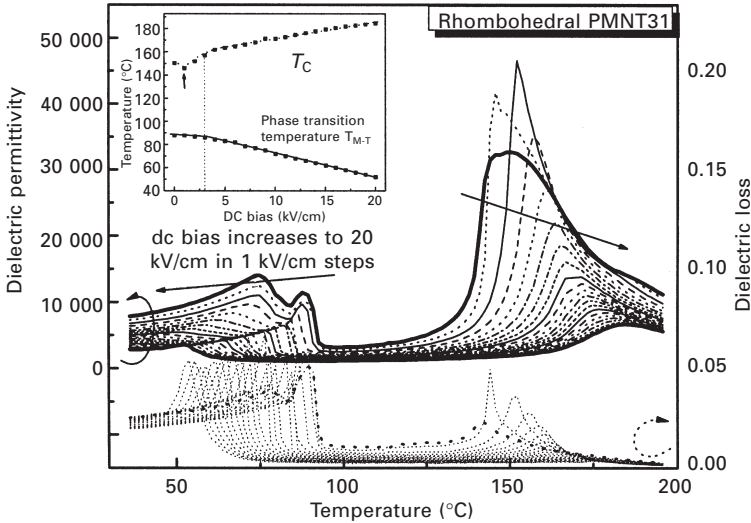


3.6 Frequency dependence of dielectric properties as a function of temperature for [001] oriented rhombohedral PMNT31 and tetragonal PMNT39 crystals, measured on a zero-field-heating run.

frequency-dependent dielectric behavior was found for tetragonal PMNT39, with a  $T_C$  around 187°C.

### 3.3.2 Dielectric behavior with dc bias

Figure 3.7 shows the dielectric permittivity and dielectric loss as a function of temperature for [001] oriented and poled PMNT31 single crystals that are measured on heating at 100kHz frequency with an applied field [24]. The dc bias is increased from 0 to 20 kV/cm in 1kV/cm incremental steps. As shown in Fig. 3.7, when the dc bias is larger than 1kV/cm, the maximum dielectric permittivity peak becomes sharper and higher then subsequently lowers and becomes more diffuse while also shifting to higher temperature with further increases in bias. This is in good agreement with other reports [21, 25, 26]. It should be noted that when the dc bias is small (~1 kV/cm), the  $T_C$  is found to shift to lower temperature, and then increases when dc bias is above 1kV/cm and increases linearly when dc bias is over 3kV/cm (as depicted in the small inset figure). The ferroelectric phase transition temperatures  $T_{R-M}$  and  $T_{M-T}$  are found to shift to lower temperature with increasing dc bias. The dielectric peak at the rhombohedral to monoclinic phase transition becomes more diffuse and broad when the dc bias is larger than 4kV/cm, implying the coexistence of the rhombohedral and monoclinic phases under this condition because of compositional fluctuations. It will disappear when the dc bias is over 10kV/cm and only the electric-field-induced monoclinic phase is observed at room temperature. Figure 3.8 displays

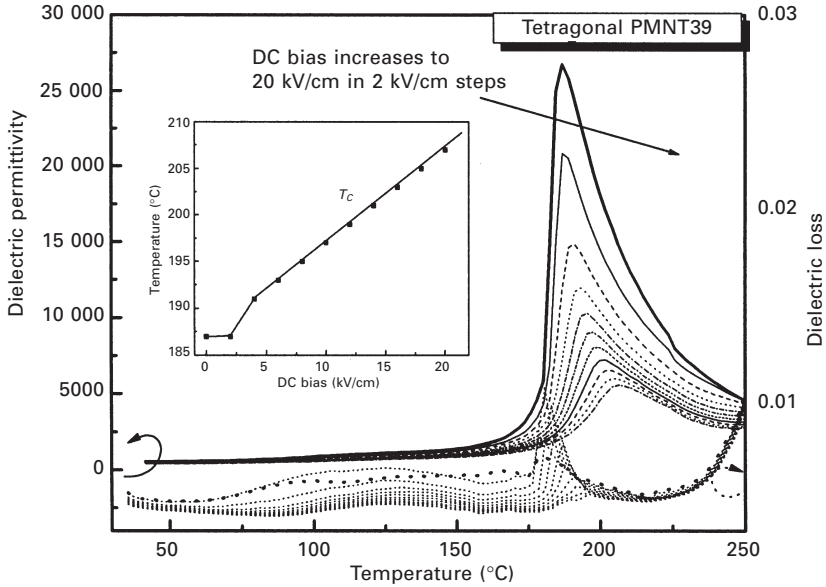


3.7 dc bias field dependence of dielectric permittivity and dielectric loss as a function of temperature for [001] oriented PMNT31 single crystals (measured at frequency of 100 kHz during heating). The thick lines in the figures are dielectric property without dc bias. The small inset shows the  $T_C$  and  $T_{M-T}$  as a function of dc bias (after ref. 24).

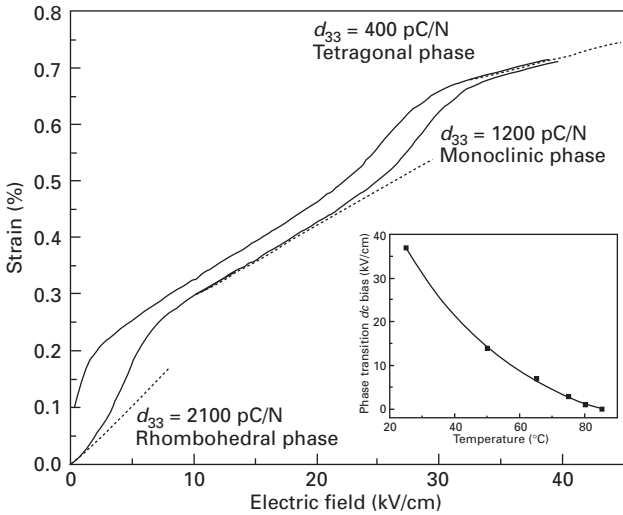
the dielectric permittivity and dielectric loss as a function of temperature for [001] oriented and poled PMNT39 tetragonal single crystals, measured at 100 kHz frequency during field-heating as the dc bias increases from 0 to 20 kV/cm in 2 kV/cm incremental steps. The dielectric permittivity peaks are found to lower and broaden. The  $T_C$  is found to be 187 °C when the dc bias is around 2 kV/cm, which is the same value as that without dc bias, then shifts to higher temperature with increasing dc bias. Similar phenomena were observed in other compositions in the PMNT system such as PMNT26 crystals [27] and PMNT10 ceramics [28]. It has also been reported recently [29] that PMNT single crystals with PT content lower than 40%, at small biases, in contrast to usual ferroelectrics,  $T_C$  remains practically unchanged or even decreases with electric field, up to a certain threshold bias (which is considered to be the magnitude of the random field), above which  $T_C$  increases. This behavior can be well explained when considering a first-order phase transition at the relaxor-ferroelectric phase boundary as well as the quenched random fields and random bonds model [29, 30].

### 3.3.3 Piezoelectric behavior with dc bias

Figure 3.9 shows the unipolar strain as a function of electric field for a PMNT31 crystal, in which it can be seen that the crystal transforms from the



3.8 dc bias field dependence of dielectric permittivity and dielectric loss as a function of temperature for [001] oriented PMNT39 single crystal (measured at frequency of 100 kHz during heating). The thick lines in the figures are dielectric behavior without dc bias. The small inset exhibits the  $T_c$  as a function of dc bias.



3.9 Unipolar electric field dependence of the strain response for a PMNT31 crystal measured up to 40 kV/cm field. The small inset shows dc bias fields for monoclinic to tetragonal phase transition at different temperatures (after ref. 31).

rhombohedral phase to the monoclinic phase, and then to the tetragonal phase with increasing electric field. The piezoelectric coefficient  $d_{33}$  is calculated from the various slopes to be 2100 pC/N for the rhombohedral phase, 1200 pC/N for the monoclinic phase, and 400 pC/N the electric-field-induced tetragonal phase. The small inset figure in Fig. 3.9 shows the dc bias field required for the monoclinic to tetragonal phase transition as a function of temperature for PMNT31 single crystals. It exhibits an exponential decay tendency with increasing temperature for the transformation fields, which suggests that upon heating, the polarization vector moves more easily toward the [001] orientation under the applied dc bias [31, 32].

### 3.4 Single crystal piezoelectric actuators

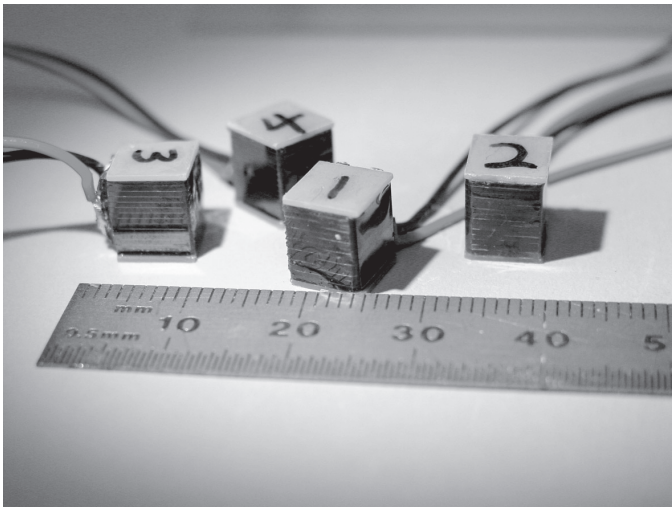
Piezoelectric actuations have been used extensively in a broad range of applications including precision positioning control, active damping control, adaptive optics and adaptive structures for flap control [33–37]. Many different types of piezoelectric actuators have been developed, including in-plane actuators (or plate actuators), stack actuators, benders, flextensional actuators, and piezo-motors. In-plane actuation mostly adopts the ‘31’ mode to generate motion in plane. Its enhancement has been achieved by utilizing inter-digital electrodes because of the low transverse piezoelectric coefficient ( $d_{31}$ ) compared with the longitudinal counterpart ( $d_{33}/d_{31} \sim 2$  for most piezo materials). Stack actuators are featured with amplified stroke (each layer stroke times the number of layers) and high blocking force. Benders and flextensional actuators such as ‘Moonie’, ‘Cymbal’, ‘Thunder’ and ‘HYBAS’ are well known with low profile and large stroke because of amplification mechanisms. Piezomotors based on the difference of static and dynamic friction or vibration modes are used for both rotary and linear motion control with high resolution and position set-hold at power-off. All these piezoelectric actuators based on piezoelectric ceramics are available on the market; however, single crystal piezoelectric actuators with higher energy density compared with their ceramic counterpart are still in the development stage partially because of the limited availability of materials. Single crystal piezoelectrics based on PZN–PT or PMN–PT exhibit large increases in strain over conventional piezoelectric ceramics due to the ability to orient the crystals along a preferred high-strain crystallographic direction. Due to a unique ferroelectric domain configuration, the crystals’ piezoelectric strain remains nearly hysteresis-free up to levels of  $\sim 0.5$  to  $0.6\%$  depending on the crystal composition [37]. Furthermore, the crystals have been found to retain appreciable piezoactivity to temperatures as low as 20 K, an important attribute for many cryogenic actuation applications [38]. In this section, a couple of single crystal piezoelectric actuators developed at TRS for deformable mirror, rotorcraft flap control and cryogenic actuation applications are reported.

### 3.4.1 PMN–PT single crystal stack actuators for deformable mirrors

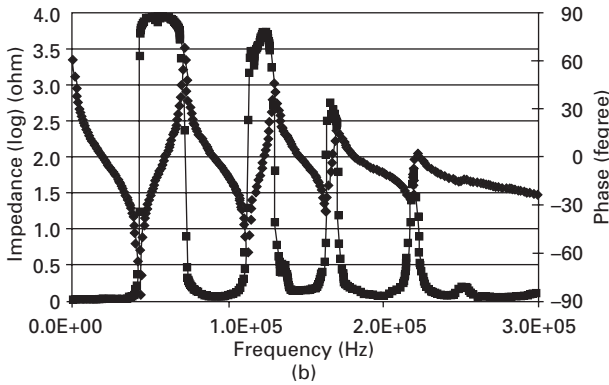
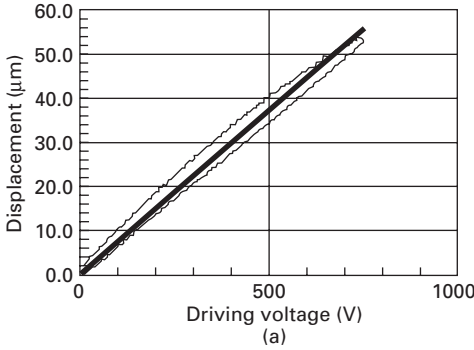
Figure 3.10 shows a picture of some PMN–PT stack actuators developed at TRS. The displacement output of a stack actuator is equal to  $n*d_{33}*V$ , where  $n$  is the total number of layers,  $d_{33}$  is the longitudinal piezoelectric coefficient and  $V$  is the driving voltage. It is known that  $d_{33}$  of PMN–PT single crystal is about 3–5 times of PZT ceramics, which means that PMN–PT single crystal stack actuators are expected to yield 3–5 times the stroke of PZT ceramic stack actuator under the same driving condition, or, the total length of PMN–PT single crystal stack actuators is 1/5–1/3 of that of PZT ceramic stacks if the same output stroke is required. This characteristic of single crystal actuators is very attractive to deformable mirror applications for either weight reduction or stroke improvement.

Figure 3.11 (a) shows the displacement vs. electric voltage for a typical 40-layer PMN–PT stack actuator (~ 21 mm long), where good linearity between displacement and driving voltage is observed. Over 50  $\mu\text{m}$  stroke is obtained with a driving field of 14 kV/cm. Figure 3.11(b) shows the impedance and phase vs. frequency of a 30-layer stack actuator (~ 16 mm long). The results from resonant measurements suggest fast response and highly efficient actuation when single crystals are used.

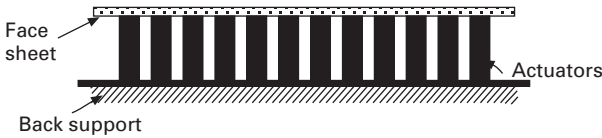
Figure 3.12 shows schematically a deformable mirror (DM) structure with stack actuators. Full aperture modeling for a 127 mm (5 inch) mirror with 289 single crystal stack actuators ( $5 \times 5 \times 21 \text{ mm}^3$ ) has been investigated.



3.10 Photograph of some single crystal stack actuators fabricated by TRS.



3.11 Stack actuator characterization: (a) displacement vs. voltage of a PMN-PT single crystal stack ( $5 \times 5 \times 21 \text{ mm}^3$ ); (b) impedance and phase vs. frequency of a 30-layer stack ( $5 \times 5 \times 16 \text{ mm}^3$ ).



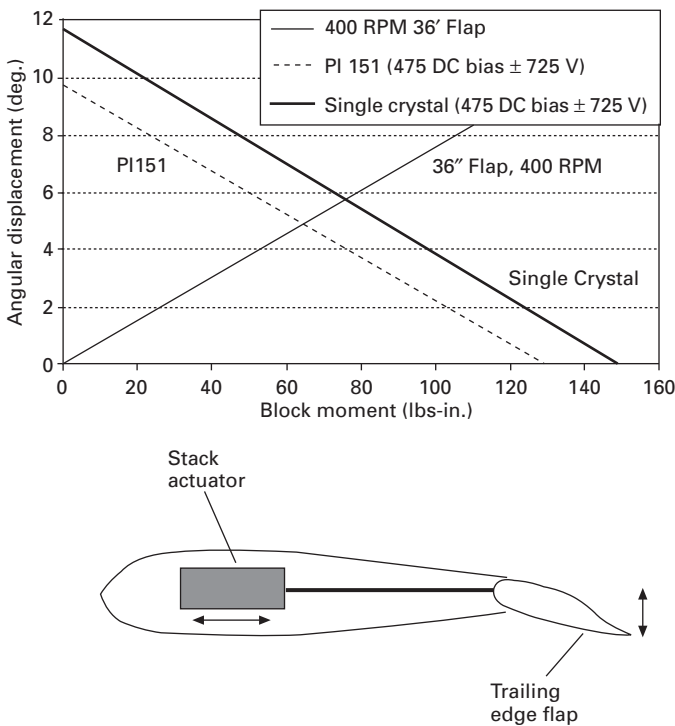
3.12 Schematic of a deformable mirror with stack actuators.

The input surface has a  $20 \mu\text{m}$  focus error with a PV of  $39.93 \mu\text{m}$ , and an RMS error of  $11.52 \mu\text{m}$ . After correction, the PV is  $0.52 \mu\text{m}$ , and the RMS error is  $0.07 \mu\text{m}$ , which is very promising since no DM has been developed for such a large focus error correction ( $>30\lambda$  for  $632.8 \text{ nm}$  wave). The required stroke is from  $-24.45 \mu\text{m}$  to  $13.01 \mu\text{m}$ , and the force is from  $1.16 \text{ N}$  to  $3.49 \text{ N}$ . Thus, both stroke and force are within the single crystal stack actuator's capability. Compared with currently available electrostrictive or piezoceramic DMs, which are used for low stroke wavefront correction ( $5\text{--}10 \mu\text{m}$ ), single crystal piezoelectric DMs are promising for large stroke correction and also

for cryogenic wavefront correction due to the excellent cryogenic properties of single crystal actuators [4, 38].

### 3.4.2 Single crystal actuators for rotorcraft flap control

Single crystal piezoelectric actuators for rotorcraft flap control have drawn attention because of the fact that single crystal piezoelectrics have high strain energy density [5, 34]. As an example, comparison between single crystal stack actuators and commercially available PZT stacks (PI 151) has been investigated for full scale flap control. Figure 3.13 shows the free angle displacement vs. blocking force for PI 151 and PMN-PT single crystal actuators. The required angle displacement-blocking force line for a rotor in hover at 400 RPM actuating a 915 mm (36 in) flap is given in Fig. 3.13 as reference. A flap displacement increase of 16% is reached using PMN-PT single crystal actuators compared with those obtained for the 2X-frame actuator using a commercially available ceramic stacked actuator. PI 151



3.13 Free angular displacement/block force diagram for single crystal and PI 151 ceramic stack actuators for trailing edge flap control. The relationship between displacement and force for a rotor in hover at 400 RPM actuating a 36 in. flap is given as reference.

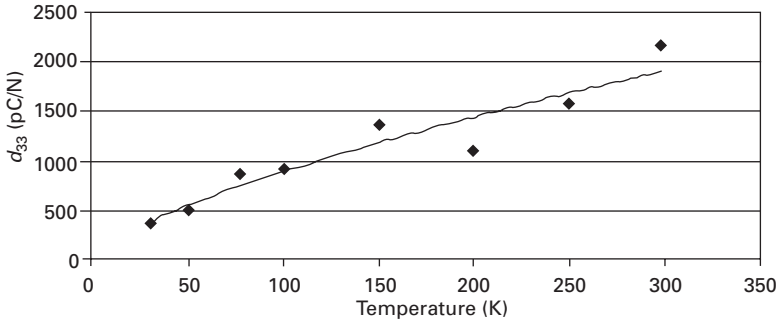


stack actuators would provide approximately  $5^\circ$  flap deflection output, while single crystal stack actuators would provide  $5.8^\circ$ . Therefore, when driving both actuators at their maximum capability, the single crystal stack actuator will provide flap deflections  $0.8^\circ$  higher than PI 151. This would allow the actuator system to withstand higher aerodynamic force conditions, or to maintain those with a simpler amplification mechanism. More comparison between single crystal and PZT actuators with various configurations including tube actuators, shear actuators and benders for flap control can be found in ref. [5].

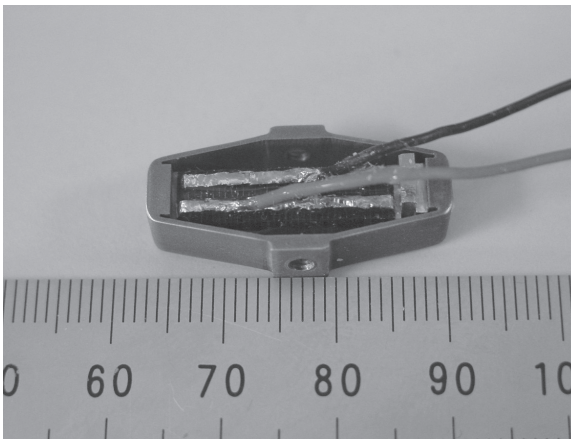
### 3.4.3 Single crystal piezoelectric actuators for cryogenic actuation

Precise cryogenic actuation is required in many NASA space applications [35]. Some recent research efforts have reported on magnetostrictive cryogenic actuation with superconducting coils by Energen, ferroelectric cryogenic rod (or stack) actuators using ceramics by Xinetics, and single crystal stack actuators and single crystal in-plane cryogenic actuators by TRS. Among them, the superconducting technology does not yet allow mature magnetostrictive cryogenic actuation, and the fabrication process, cost and volume of actuators are not comparable with its piezoelectric counterpart. Piezoelectric actuation is well known for its high-precision displacement control, high force output, quick response, low power consumption and low profile. However, most piezoelectric materials lose 75% of their piezoelectric performance at temperatures less than 77 K, giving rise to extremely small strain and actuation at cryogenic temperatures [35]. Fortunately, the recently invented single crystal piezoelectrics exhibit significantly higher piezoelectric performance at both room temperature and cryogenic temperatures [4], e.g.  $d_{33}$  of single crystal piezoelectrics (PMN-PT or PZN-PT) at 30 K is about equal to the  $d_{33}$  of PZT-5A at room temperature, indicating promising cryogenic actuation using single crystal piezoelectrics.

PMN-PT stack actuators, flexensional actuators and a piezomotor were developed for cryogenic actuation. Figure 3.14 shows  $d_{33}$  vs. temperature for a  $5 \times 5 \times 4 \text{ mm}^3$  single crystal stack actuator. It is noticed that the effective  $d_{33}$  at 30 K is about 400 pC/N. The single crystal flexensional actuator (Fig. 3.15) retained >60% of its room temperature stroke at 75 K. For the cryogenic linear motor test, we placed the PMN-PT single crystal piezoelectric motor into a chamber full of liquid nitrogen. A thermo-couple was used to monitor the chamber's temperature. Experimental measurements showed that at  $-200^\circ\text{C}$ , the motor still worked properly with a slightly decreased speed [5]. All these results suggest that single crystal piezoelectric actuators hold importance for cryogenic actuation applications.



3.14 Cryogenic  $d_{33}$  of a PMN-PT stack actuator.



3.15 Cryogenic displacement of a flextensional actuator.

## 3.5 Single crystal piezoelectric transducers

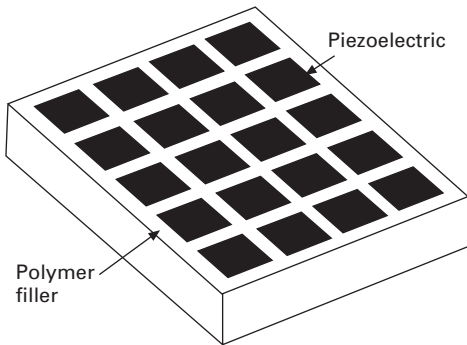
### 3.5.1 Medical transducers

Ultrasound transducers first began their use in medical investigation in the first half of the twentieth century, and their reach has since broadened extensively past the original gastrointestinal, obstetric and cardiac imaging performed in the 1950s. The quality of imaging has greatly improved, providing quantitative measurements of the developing fetus, as well as investigation of blood flow and tumor detection. Data processing techniques have given rise to Doppler and power Doppler imaging, harmonic imaging and elastography. These, in combination with increased insonifying frequencies, have opened new applications in ophthalmology, intravascular imaging, dermatology and orthopedics.

Nearly all medical imaging transducers operate using a plate design, where array elements are patterned from a piezoelectric plate that is located between

acoustic matching layers and a backing layer. The piezoelectric material provides the conversion between the electrical and acoustic domains. The bulk of commercial systems utilize the ceramic PZT, which offers relatively high width extensional ( $k'_{33}$ ) electromechanical coupling for array transducers. Many of these piezoelectrics, however, are not ideal for pulse-echo operation because they exhibit a low ‘figure of merit’  $g_h d_h$ , due to the low charge coefficient  $d_h (= d_{33} + 2d_{31})$  and the high permittivity of the piezoelectric material. Composites provide a partial solution to this problem. In particular, composites utilizing 1–3 connectivity, as shown in Fig. 3.16, provide the highest coupling (longitudinal length extensional,  $k_{33}$ ) and therefore have the greatest potential for high bandwidth [6, 8]. An increase in the hydrostatic parameters is observed, as shown in Table 3.2, as well as a decrease in mechanical  $Q$  which allows for better detection of sharp pulses.

Single crystals offer further advantages for medical imaging, through their increased anisotropy. The electromechanical coupling of PZN–PT and PMN–PT single crystals is as high as 94% in the  $\langle 001 \rangle$ , which can be utilized in the composite structure. The resulting wide bandwidth, over 130% [6], can be used for a variety of applications including sub-harmonic or second harmonic imaging, Doppler and coded excitation for increased penetration.



3.16 Piezoelectric–polymer composite exhibiting 1–3 connectivity.

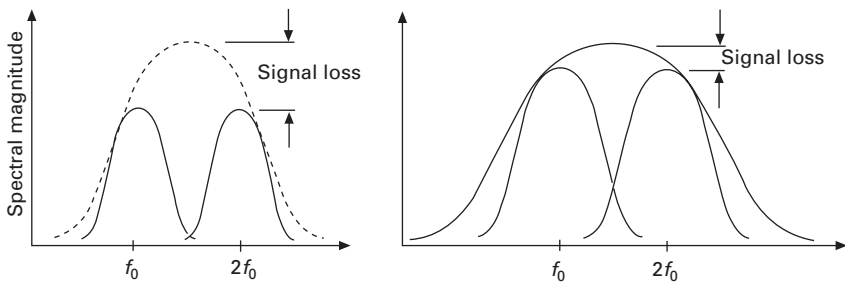
Table 3.2 Comparison of hydrostatic coefficients for pulse-echo operation of PZT and PMN-PT materials

Piezoelectric	Relative permittivity	$g_h$ (V m/N)	$d_h$ (pC/N)	$d_h g_h$ (nm <sup>2</sup> /N)
PZT ceramic	1800	0.0025	40	100
PZT 1–3 composite	54	0.056	27	1536
PMN–PT single crystal	4436	0.002	80	160
PMN–PT composite	340	0.037	111	4115

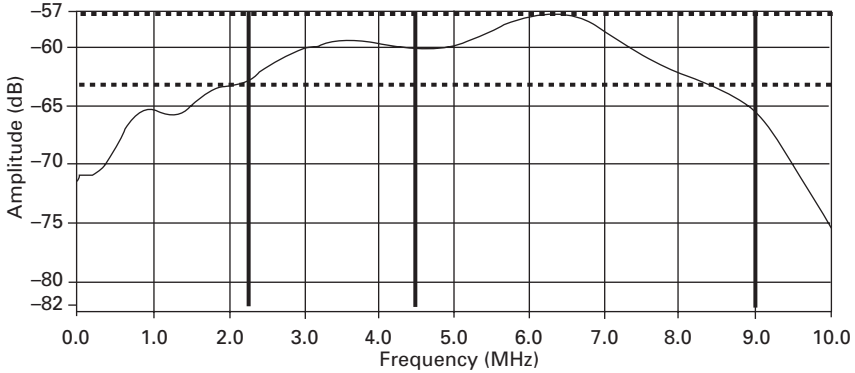
The increase in  $d_h$  also outweighs the increase in permittivity, providing a figure of merit more than three times that of PZT composite [39, 40]. This directly improves the signal to noise ratio, providing either deeper penetration or lower excitation amplitudes. This is particularly important in emerging high-frequency ultrasound imaging applications in areas such as ophthalmology, dermatology, intravascular ultrasound, small animal imaging and laparoscopic procedures. Attenuation in tissues is highly dependent on frequency, and is currently one of the primary limitations in imaging systems above 5–10 MHz.

Imaging resolution is proportional to pulse length, which is dependent upon both frequency and bandwidth. However, higher frequency imaging is limited in depth by attenuation, which is also proportional to frequency. Harmonic imaging provides a solution by transmitting at one frequency and receiving at a harmonic of that frequency, resulting in a high frequency signal that only travels half the distance of a traditional pulse-echo signal. Bandwidth is important in achieving adequate signal-to-noise ratio (SNR) for both the transmitted and received signals, as illustrated in Fig. 3.17.

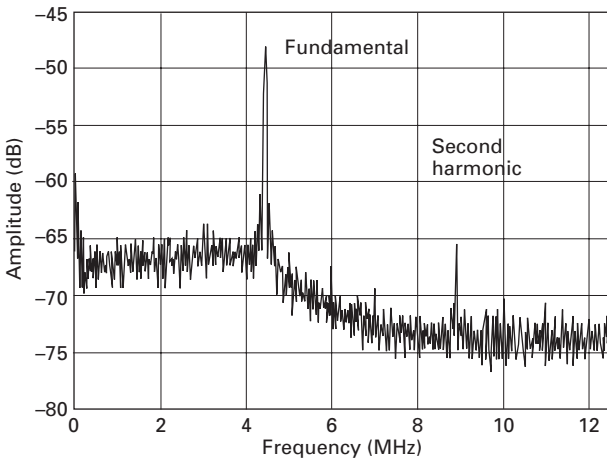
A 4.9 MHz transducer utilizing single crystal was made to minimize this signal loss. A single element transducer with an aperture of 18 mm and 56% volume fraction was manufactured. Utilization of two matching layers and heavy backing helped to improve bandwidth to 132%, as shown in Fig. 3.18. Measurement of a harmonic signal was performed using an excitation signal consisting of a 64-cycle, sinusoidal tone burst at 4.5 MHz. Sonazoid microbubbles in a water bath were excited, and acted as the fundamental and harmonic echo source. Acquisition was performed at 25 MHz, and the signals were averaged. From the spectrum shown in Fig. 3.19, it can be seen that the second harmonic (at 9 MHz) was only 17.5 dB down from the fundamental signal.



3.17 Comparison of transducer bandwidth (dotted line) effect on power available at fundamental and harmonic frequencies (solid lines). Wider bandwidth provides less loss in signal generation and reception while also allowing for wider bandwidth in each frequency range.



3.18 Frequency spectrum from harmonic imaging transducer, based on impulse response.

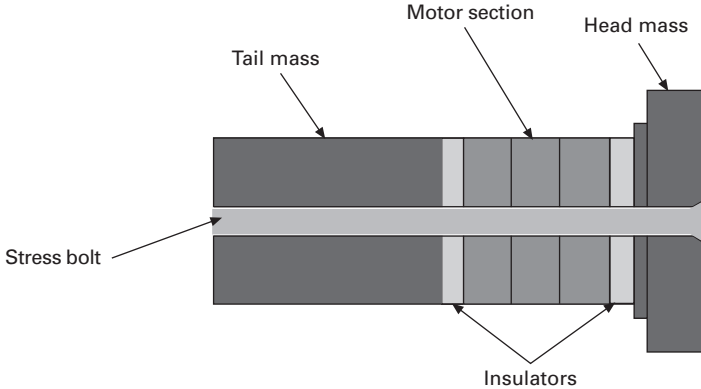


3.19 Spectrum showing fundamental and harmonic echoes from Sonazoid obtained using single crystal transducer excited at 4.5 MHz.

### 3.5.2 Sonar transducers

Sonar applications require significantly more demanding acoustic performance characteristics and environmental considerations. Sonar systems have ranges from meters to kilometers, thus even at low-frequency operation of 2–500 kHz, high acoustic source levels are often used. Additionally, the variations in temperature, hydrostatic pressure and the chemistry of seawater complicate construction and performance standardization.

Tonpizl transducers (pistons with head and tail masses) are standard in sonar applications operating near 100 kHz or below. Figure 3.20 shows the general design of a tonpizl element, of which a series are generally used to



3.20 Cross-section of typical tonpiliz transducer.

form an array. The stress bolt along the length is applied to prevent tension in the piezoelectric. The motor section consists of piezoelectric rings connected mechanically in series and electrically in parallel. An approximation to the resonance frequency of such a system is given as [41]:

$$\omega_s^2 = \frac{E_e A}{l} \cdot \frac{M_1 + M_2}{M_1 M_2} \quad 3.3$$

where  $E_e$  is the Young's modulus of the piezoelectric material,  $A$  is area of the stack,  $l$  is length, and  $M_1$  and  $M_2$  are the masses of the head and tail, respectively. It should be noted that the effective Young's modulus of the stack, including stress bolt and joints, provides a more exact approximation.

Exploration in both the military and industrial sectors is shifting towards small, unmanned systems utilizing a wider array of sonar detectors and sources. As detection technology becomes more sophisticated, there has also been an increase in the complexity of towed sonar arrays. Both of these applications have seen an increased demand for both larger bandwidth devices, as well as smaller packages that maintain current drive capabilities.

For these reasons, there has been a move towards single crystal ferroelectrics. In particular, the effective Young's modulus is approximately one-quarter that of traditional Navy Type III ceramics, resulting in a comparable decrease in stack length when maintaining the frequency, as can be seen in Eq. 3.3. The length of the piezoelectric stack is also generally larger than the width, which allows the overall stack to operate in a near-33 mode. The high effective  $k_{33}$  of 90% results in a high bandwidth comparable to current piezoelectric-magnetostrictive hybrid transducers. A high source level is achievable with single crystal due to its high  $d_{33}$  of 2200 pC/N. The large strain results in high acoustic power relative to ceramic materials, and the low dielectric losses (below 0.01) provide efficient transfer of energy between the transducer and system.

Single crystal PZN–PT and PMN–PT are ‘soft’ materials and can depole under high fields due to their low coercive fields (less than 0.4 MV/m). The majority of high-field ac excitation is done under bias to eliminate depoling effects. Under bias, these materials offer significantly higher energy densities ( $= k_{33}^2 e_{33}^T E_{\text{rms}}^2$ ) than Type III ceramics. PMN–PT shows an energy density of 8.7 kJ/m<sup>3</sup> compared with 0.6 kJ/m<sup>3</sup> for the ceramic [7]. Given higher energy densities, much lower power is necessary for operation. Untethered vehicles such as unmanned underwater vehicles (UUVs) for underwater oil or mineral mining, cable inspection, oceanographic research or defense can benefit from longer deployment schedules and greater coverage. Other sonar applications include sonobuoys, towed arrays and hull-mounted sonar.

### 3.6 Conclusions and future trends

By seeded Bridgman growth, TRS has successfully grown large, high quality PMN–PT crystals along  $\langle 111 \rangle$ -,  $\langle 110 \rangle$ - and  $\langle 001 \rangle$ -orientations. Lateral uniformity analysis indicates that the property variation in Bridgman-grown crystals is strongly related not only to the growth direction, but also to the sample cutting direction. Cutting perpendicular to the composition gradient, which is always along the crystal growth direction, will give much less property variation. Since (001) wafers cut from  $\langle 001 \rangle$ -oriented boules are perpendicular to the composition gradient, less than  $\pm 2\%$  variation of both the piezoelectric and dielectric properties has been achieved in the whole wafer. However, for PMN–PT solid solution system, the composition segregation inevitably exists in Bridgman growth, resulting in an inhomogeneous composition distribution and the variations of dielectric and piezoelectric properties along the growth orientation. It was demonstrated that zone-melting growth is an effective technique to level the composition variation and improve the property uniformity along the growth direction.

Currently, the Bridgman method is becoming a mature technique to produce large PMN–PT crystals. In the future, the crystal growth techniques, such as the modified zone-melting or the continuous feeding Bridgman growth [42], which potentially reduce or even eliminate the composition segregation in the as-grown crystals, should be further developed. Adapting these techniques to large PMN–PT crystal growth can further improve the wafer-to-wafer uniformity and reduce the cost of crystal production.

Device design based on PMN–PT piezoelectric crystal often involve high electric field, high frequency, high temperature or any combination of these. DC bias also must often be applied to keep the crystal from depoling. It was found that, for PMN–33%PT crystals, frequency dispersion of dielectric permittivity occurs when the temperature is below 86 °C and over 151 °C, while the dielectric permittivity is frequency independent in the temperature range of 86–151 °C. A transition between the normal ferroelectric and relaxor

states is indicated by the appearance of a frequency dispersive shoulder slightly below the  $T_c$  and an abrupt disappearance of the frequency dispersion at lower temperature range. No evident frequency-dependent dielectric behavior was found for tetragonal PMNT39. It is evident that the  $T_c$  of PMN–PT crystals increases with external DC bias field, while the ferroelectric phase transition,  $T_{rf}$ , shifts downward, limiting the temperature usage range of the crystals.

Based on the full study of piezoelectric and dielectric properties, TRS has demonstrated the merit of PMN–PT crystal over conventional PZT ceramics for several types of crystal-based actuators for adaptive optics and cryogenic actuations. TRS has also demonstrated the merits of crystals for high sensitivity and broadband sonar and medical transducer applications. It is also realized that the main obstacles for the broad range of applications of PMN–PT crystals are its low  $T_c$ ,  $T_{rf}$  and  $E_c$ . The new generation electric devices demand the development of high-performance crystals for expanded operating domains, such as high temperature, high drive field and/or high drive stress. Composition modification of PMN–PT crystal by A-site or B-site substitution can be a feasible approach for industry to enhance the performance and expand the operating domains of PMN–PT, since the melt growth techniques developed for pure PMN–PT crystal growth can be adapted to these materials with further optimization. New binary or ternary systems, which have stable perovskite phase so that the crystals can be directly grown from their melt, should also been explored for high-temperature applications.

### 3.7      References

- 1 Service R F, 'Shape-changing crystals get shiftier', *Science*, 1997 **275** 1878.
- 2 Park S E, and Shrout T R, 'Ultrahigh strain and piezoelectric behavior in relaxor based ferroelectric single crystals', *J. Appl. Phys.*, 1997 **82** 1804–8.
- 3 Rehrig P W, Hackenberger W S, Jiang X, Shrout T R, Zhang S J, and Speyer R, 'Status of piezoelectric single crystal growth for medical transducer applications', *2003 IEEE Ultrasonics Symposium* (766-9) 2003.
- 4 Jiang X N, Rehrig P W, Hackenberger W S, Moore J, Chodimella S, and Patrick B, 'Single crystal piezoelectric actuators for advanced deformable mirrors', *ASME Proceedings of Adaptive Materials and Systems*, Anaheim, CA, 2004.
- 5 Jiang X N, Rehrig P W, Hackenberger W S, Smith E, Dong S, Viehland D, Moore J, and Patrick B, 'Advanced piezoelectric single crystal based actuators', *Proc. SPIE* 2005, **5761**, 253–262.
- 6 Ritter T, Geng X, Shung K K, Lopath P D, Park S-E, and Shrout T R, 'Single crystal PZN–PT–polymer composites for ultrasound transducer applications', *IEEE Trans. Ultra. Ferro. Freq. Contr.* 2000 **47**(4) 792–800.
- 7 Powers J M, Moffett M B, and Nussbaum F, 'Single crystal naval transducer development', *IEEE Symp. App. Ferro.* 2000 **1**, 351, 354.
- 8 Hackenberger W S, Jiang X, Rehrig P W, Geng X, Winder A, and Forsberg F, 'Broad band single crystal transducer for contrast agent harmonic imaging', *Proc. IEEE Ultrason. Symp.*, 2004.



- 9 Kuwata J, Uchino K, and Nomura S, 'Dielectric and piezoelectric properties of  $0.91\text{Pb}(\text{Zn}_{1/3}\text{Nb}_{2/3})\text{O}_3-0.09\text{PbTiO}_3$  single crystals', *Jpn J. Appl. Phys.*, 1982 **21** 1298–1302.
- 10 Zawilski K T, Claudia M, Custodio C, Demattei R C, Lee S-G, Monteiro R G, Odagawa H, and Feigelson R S, 'Segregation during the vertical Bridgman growth of lead magnesium niobate single crystals', *J. Crystal Growth*, 2003 **258** 353–67.
- 11 Dong M, and Ye Z-G, 'High temperature solution growth and characterization of piezo-/ferroelectric PMNT single crystals', *J. Crystal Growth*, 2000 **209** 81–90.
- 12 Luo H, Xu G, Wang P, and Yin Z, 'Growth and characterization of relaxor ferroelectric PMNT single crystals', *Ferroelectrics*, 1999 **231** 685–90.
- 13 Luo H, Xu G, Xu H, Wang P, and Yin Z, 'Compositional homogeneity and electrical properties of lead magnesium niobate titanate single crystals grown by a modified Bridgman technique', *J. Appl. Phys., Part 1*, 2000 **39(9B)** 5581–5.
- 14 Swartz S L, and Shrout T R, 'Fabrication of perovskite lead magnesium niobate', *Mater. Res. Bull.*, 1982 **17** 1245–50.
- 15 Zhang K C and Zhang L H, *Science and Technology of Crystal Growth*, vol. I, 2nd edn, Science Press, Beijing, China, 1997, p. 413–16.
- 16 Guo Y, Luo H, Ling D, Xu H, He T, and Yin Z, 'Effect of a bias field on the dielectric properties of  $0.69\text{Pb}(\text{Mg}_{1/3}\text{Nb}_{2/3})\text{O}_3-0.31\text{PbTiO}_3$  single crystals with different orientations', *J. Phys.: Condens. Matter* 2003 **15** L77.
- 17 Guo Y, Luo H, Chen K, Xu H, and Yin Z, 'Effect of composition and poling field on the properties and ferroelectric phase-stability of  $\text{Pb}(\text{Mg}_{1/3}\text{Nb}_{2/3})\text{O}_3-\text{PbTiO}_3$  crystals', *J. Appl. Phys.* 2002 **92** 6134–8.
- 18 Davis M, Damjanovic D and Setter N, 'Electric-field-, temperature-, and stress-induced phase transitions in relaxor ferroelectric single crystals', *Phys. Rev. B*, 2006 **73** 014115.
- 19 Pfann W G, *Zone Melting*, 2nd edn, Wiley, New York, 1966, pp. 8–27.
- 20 Zawilski K T, DeMattei R C, and Feigelson R S, 'Zone leveling of lead magnesium niobate-lead titanate crystals using RF heating', *J. Crystal Growth*. 2005 **277** 393–400.
- 21 Han J P and Cao W W, 'Electric field effects on the phase transitions in [001] oriented  $(1-x)\text{PMN}-x\text{PT}$  single crystals with compositions near the morphotropic phase boundary', *Phys. Rev. B.*, 2006 **68** 134102.
- 22 Zhao X Y, Wang J, Peng Z, Chew K H, Chan H L W, Choy C L, and Luo H S, 'Electric field effect on polarization and depolarization behavior of the (001) oriented relaxor-based  $0.7\text{PMN}-0.3\text{PT}$  single crystal', *Physica B*, 2003 **339** 68–73.
- 23 Yao X, Chen Z L, and Cross L E, 'Polarization and depolarization behavior of hot-pressed lead lanthanum zirconate titanate ceramics', *J. Appl. Phys.* 1983 **54** 3399–403.
- 24 Zhang S J, Luo J, Shanta R, Snyder D W, and Shrout T R, 'Modified PMN–PT single crystals for high temperature application', submitted to ISAF 2006.
- 25 Zhao X Y, Wang J, Chan H L W, Choy C L, and Luo H S, 'Effect of a bias field on the dielectric properties of  $0.69\text{PMN}-0.31\text{PT}$  single crystals with different orientations', *J. Phys.: Condens. Matter*, 2003 **15** 6899–908.
- 26 Prosandeev S A, Raevski I P, Emelyanov A S, Colla E V, Dellis J L, Marssi M El, Kapphan S P, and Jastrabik L, 'Nontrivial dependence of dielectric stiffness on bias field in relaxors and dipole glasses', *J. Appl. Phys.*, 2005 **98** 014103.
- 27 Zhang S J, Shrout T R, Luo J, and Rehrig P W, Unpublished.

- 28 Viehland D, Jang S J, and Cross L E, 'Local polar configurations in lead magnesium niobate relaxors', *J. Appl. Phys.*, 1991 **69** 414–19.
- 29 Raevski I P, Prosandeev S A, Emelyanov A S, Raevskaya S I, Colla E V, Viehland D, Kleemann W, Vakhrushev S B, Dellis J L, Marssi M El, and Jastrabik L, 'Bias-field effect on the temperature anomalies of dielectric permittivity in PMN–PT single crystals', *Phys. Rev. B.*, 2005 **72** 184104.
- 30 Gui H, Gu B L, and Zhang X W, 'Dynamics of the freezing process in relaxor ferroelectrics', *Phys. Rev. B.*, 1995 **52** 3135–42.
- 31 Zhang S J, Luo J, Xia R, Rehrig P W, Randall C A, and Shrout T R, 'Field-induced piezoelectric response in  $\text{Pb}(\text{Mg}_{1/3}\text{Nb}_{2/3})\text{O}_3$ – $\text{PbTiO}_3$  single crystals', *Solid State Commun.*, 2006 **137** 16–20.
- 32 Ren W, Liu S F, and Mukherjee B K, 'Piezoelectric properties and phase transitions of  $\langle 001 \rangle$  oriented PZN–PT single crystals', *Appl. Phys. Lett.*, 2002 **80** 3174–6.
- 33 K. Uchino, *Piezoelectric Actuators and Ultrasonic Motors*, Kluwer Academic Pub, Boston 1997.
- 34 F. Straub, V. Anand, and D. Domzalski, *Development of a Piezoelectric Actuator for Trailing Edge Flap Control of Full Scale Rotor Blades*, Institute of Physics and Publishing, Smart Materials and Structures, 10, 25–34, 2001.
- 35 NASA JWST Cryogenic Actuator Activities, <http://ngst.gsfc.nasa.gov/hardware/text/actuatoractivities.html>.
- 36 Langlois M P, Angel J P R, Lloyd-Hart M, Miller S, and Angeli G, 'High order adaptive optics system with a high density spherical membrane deformable mirror', *SPIE Proceedings* 1999.
- 37 Park S E, and Shrout T R, 'Relaxor based ferroelectric single crystals for electromechanical actuators', *Mat. Res. Innovat.*, 1997 **1** 20–25.
- 38 Paik D S, Park S E, Hackenberger W S, and Shrout T R, 'Dielectric and piezoelectric properties of perovskite materials at cryogenic temperatures', *J. Mater. Sci.*, 1998 **34** 469–473.
- 39 Moulson A J, and Herbert J M, *Electroceramics: Materials, Properties, Applications*, Chapman & Hall, New York, 1990.
- 40 Xu Z, Chen F, Xi Z, Li Z, Cao L, Feng Y and Yao X, 'The studies of single crystal PMN–PT68/32/polymer 1–3 composites', *Ceramics Inter.*, 2004 **30** 1777–80.
- 41 Stansfield D, *Underwater Electroacoustic Transducers*, Bath University Press and Institute of Acoustics, Bath, 1991.
- 42 Mitsuyoshi M, Yoshihito T, and Yosuke I, 'Development of large diameter piezo-single crystal PMN–PT with high energy conversion efficiency', JFE Technical Report, No. 06, pp 46–53, October 2005.

## Piezoelectric single crystals for medical ultrasonic transducers

---

S M RHIM, Humanscan Co. Ltd, Korea and M C SHIN  
and S - G LEE, IBULe Photonics Co. Ltd, Korea

### 4.1 Introduction

Medical ultrasound imaging technique has progressed considerably in the recent years. With the improvement of ultrasound image resolution and a low device price compared with computer tomography (CT), magnetic resonance imaging (MRI) and X-ray imaging systems, the market share of ultrasound imaging system is gradually increasing.<sup>1</sup> The applications of medical ultrasonic imaging span a wide frequency range, from 1.5 to 30 MHz, depending on the organs to be imaged. For abdominal, obstetric and cardiological applications, the frequency range is from 2 to 5 MHz. For pediatric and peripheral vascular applications, the range is from 5 to 7.5 MHz. For imaging small objects such as the eye and for many other emerging applications, such as intracardiac and intravascular imaging, the frequency range is from 10 to 30 MHz.<sup>2</sup>

Ultrasound imaging technology has a long history since its modest beginnings in the 1950s and the image quality of medical ultrasound has improved vastly with linear and phased array transducer designs replacing the mechanical 2D transducer used in the 1980s. There are many ultrasound imaging systems using new technology with such advanced features as compounded imaging, second harmonic imaging, contrast agents, color flow Doppler and 3D imaging.

To improve the ultrasound imaging quality, many technologies have been used for transducer fabrication, such as multilayer, piezo-material/polymer composite,<sup>3</sup> single crystal, multi-row, fine pitch, and cMUT (capacitive microfabricated ultrasound transducer).<sup>4</sup> Some technologies have already been used for commercialized transducers and the ultrasound image quality has progressed considerably because of this advanced technology; some new technologies are still being developed for commercialization as cMUT.

Among these technologies, the single crystal transducer has directly benefited from the recent development of relaxor-based materials. In 1997, Park and Shrout<sup>5</sup> reported that  $(1 - x)\text{Pb}(\text{Zn}_{1/3}\text{Nb}_{2/3})\text{O}_3 - x\text{PbTiO}_3$  (PZN-PT)

and  $(1 - x)\text{Pb}(\text{Mg}_{1/3}\text{Nb}_{2/3})\text{O}_3 - x\text{PbTiO}_3$  (PMN–PT) single crystals exhibited very high piezoelectric coefficients ( $d_{33} > 2000$  pC/N) and strain levels (0.6%) with little hysteresis when crystals are poled along the  $\langle 001 \rangle$  direction. As a result, these materials have great potential for use in both actuator and transducer applications.<sup>5–8</sup> These materials have excellent piezoelectric properties near the morphotropic phase boundary (MPB) where the solid solution changes structure from rhombohedral to tetragonal, near the composition of 35% PT ( $x = 0.35$ ).

In this chapter, an overview of the growth of PMN–PT single crystal and the characterization of PMN–PT single crystals will be presented first. Then, the disadvantages of  $\text{Pb}(\text{Zr}_{1-x}\text{Ti}_x)\text{O}_3$  (PZT) ceramics will be compared to the advantages of PMN–PT single crystals. Finally, the commercialization of PMN–PT single crystal transducers and the future of single crystal transducers will be discussed in detail.

## 4.2 Piezoelectric single crystals

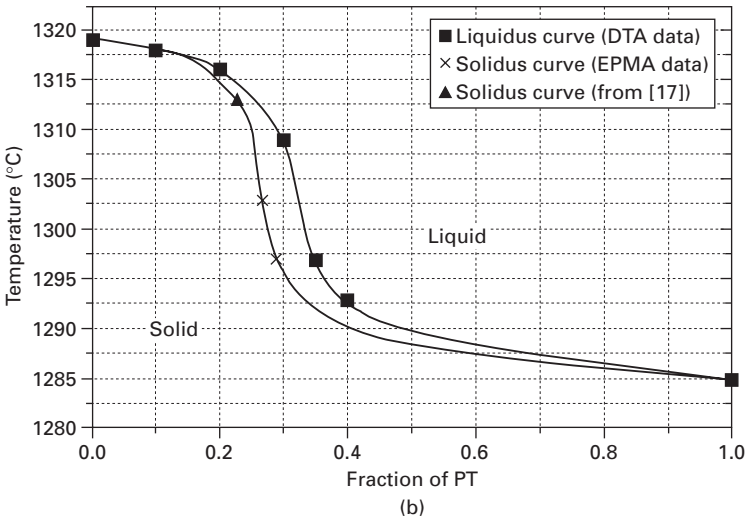
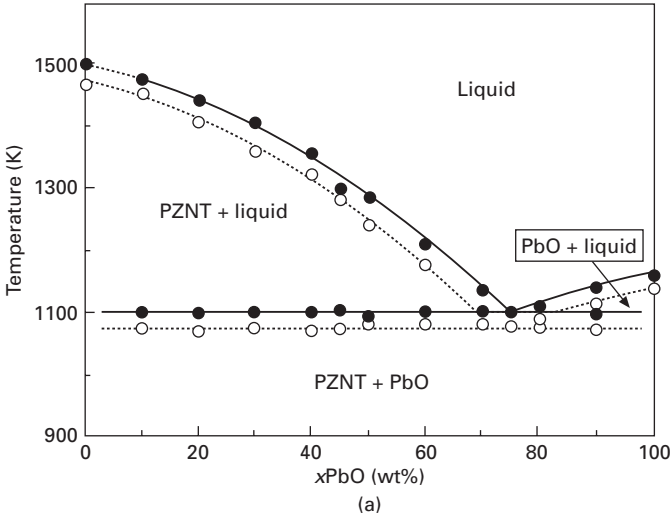
Single crystals of the solid solutions between complex lead perovskites and lead titanate, with the general formula  $\text{Pb}(\text{B}_1\text{B}_2)\text{O}_3 - \text{PbTiO}_3$  ( $\text{B}_1 = \text{Mg}^{2+}$ ,  $\text{Zn}^{2+}$ ,  $\text{Ni}^{2+}$ ,  $\text{Sc}^{3+}$ , etc.;  $\text{B}_2 = \text{Nb}^{5+}$ ,  $\text{Ta}^{5+}$ , etc.), have been extensively studied since Kuwata *et al.* reported the extremely high piezoelectric properties in PZN–PT.<sup>7</sup> Among these single crystals, PZN–PT and PMN–PT exhibit an ultra-high piezoelectric constant,  $d_{33}$ , and a very large electromechanical coupling factor,  $k_{33}$ , when the crystals are poled along the  $\langle 001 \rangle$  direction which is different with the spontaneous polarization direction of  $\langle 111 \rangle$  in comparison with those of PZT ceramics.<sup>5</sup> Such excellent properties make them attractive for both actuator and ultrasonic transducer applications.

### 4.2.1 Crystal growth

Because of the instability of perovskite PZN phase, it is difficult to synthesize pure PZN–PT ceramic powder by solid-state reaction under normal conditions. Therefore, PZN–PT crystal growth is performed with the component oxides and the PbO flux. In contrast, PMN–PT ceramic powder can be synthesized by the columbite method<sup>9</sup> and PMN–PT crystals can be grown from the melt. Lee *et al.* first suggested the use of the Bridgman technique with sealed Pt crucibles as an attractive alternative to flux growth.<sup>10</sup> Some of the defects (e.g. dendrites, inclusions and voids) found in the PMN–PT crystals grown by directly melting the component oxides can be caused by melt inhomogeneity.<sup>11–16</sup> It may be difficult to form a homogeneous PMN–PT melt from the component oxides because of the large differences in the melting temperature and the density. For example, MgO is not only more refractory than PbO ( $T_{\text{m-MgO}} = 2852$  °C,  $T_{\text{m-PbO}} = 886$  °C), but it is also much

lighter ( $\rho_{\text{MgO}} = 3.58 \text{ g/cm}^3$ ,  $\rho_{\text{PbO}} = 9.53 \text{ g/cm}^3$ ). In order to avoid melt homogeneity problems, it is desirable to pre-synthesize charge material.

An accurate high-temperature phase diagram is very important for the growth of large single crystals. Thermogravimetric/differential thermal analysis (TG/DTA) was used to obtain a high-temperature phase diagram. A complete pseudo-binary phased diagram between PZNT91/9 and PbO was established by Dong and Ye.<sup>17</sup> The typical eutectic behavior is shown in Fig. 4.1(a). This phase diagram helps to grow PZN-PT single crystals by the solution Bridgman



4.1 High-temperature phase diagram of the PZNT-PbO<sup>17</sup> and PMN-PT<sup>18</sup> pseudo-binary systems.

Table 4.1 Melting points of the  $(1 - x)\text{PMN}-x\text{PT}$  system

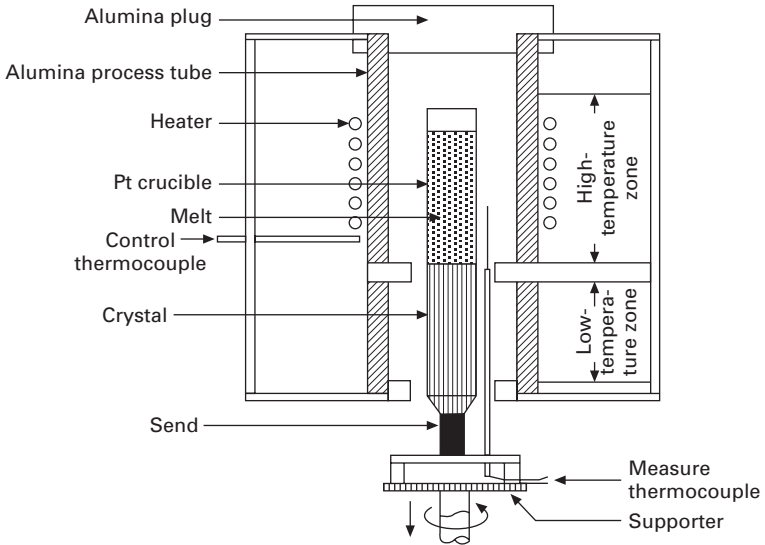
Composition ( $x$ )	Melting point ( $^{\circ}\text{C}$ )	Notes
0.00	1320 <sup>19,20</sup>	Both used sealed Pt crucibles and arrived at the same value
	1319 <sup>18</sup>	DTA using sealed Pt crucibles
0.10	1318 <sup>18</sup>	DTA using sealed Pt crucibles
0.20	1316 <sup>18</sup>	DTA using sealed Pt crucibles
0.30	1296 <sup>21</sup>	DTA using unsealed Pt crucibles in air
	1309 <sup>18</sup>	DTA using sealed Pt crucibles
0.32	1271, 1288 <sup>22</sup>	DTA of flux grown crystal in unsealed Pt pans under $\text{N}_2$ atmosphere (two values were from the two peaks observed)
0.35	1288 <sup>21</sup>	DTA using unsealed Pt crucibles in air
	1297 <sup>18</sup>	DTA using sealed Pt crucibles
0.40	1284 <sup>21</sup>	DTA using unsealed Pt crucibles in air
	1293 <sup>18</sup>	DTA using sealed Pt crucibles
1.00	1285 <sup>18</sup>	DTA using sealed Pt crucibles
	1285 <sup>23</sup>	Phase diagram study using sealed Pt crucibles

method. The melting points of PMN–PT observed by DTA are given in Table 4.1. The measured melting points decreases incrementally from  $x = 0$  (1319  $^{\circ}\text{C}$ ) to  $x = 1.0$  (1285  $^{\circ}\text{C}$ ). These results are very helpful in estimating where the initial solid–liquid interface position would be during seeding, and in preventing complete melting of the seed or powdered charge. After growth, the actual initial interface position could be estimated through either optical inspection or composition measurements. A pseudo-binary phased diagram between PMN and PT was proposed by Zawilski *et al.*, as shown in Fig. 4.1(b).<sup>18</sup>

The growth of large PZN–PT and PMN–PT single crystals has mostly been carried out using the following four methods: flux (using PbO flux), Bridgman, solution Bridgman (using PbO flux) and abnormal grain growth.

A schematic diagram of Bridgman growth system is shown in Fig. 4.2. The growth was generally carried out in either tapered Pt crucibles with seed pockets or straight-walled Pt crucibles. In order to prevent the component volatilization and to control the atmosphere, the crucible was sealed with a lid by welding. The crucible preparation is very important in the Bridgman growth of PMN–PT since PbO-containing melts can attack Pt at elevated temperatures. Leaks of any size can be a problem, and large leaks can ruin an experiment.

During growth, a vapor-filled region formed above the melt because the charges, which are composed of packed powder, shrink on melting. Pressure built up in this region at growth temperatures, and the upper ~2–3 cm of the crucibles typically swelled by several millimeters. The swelling did not usually affect the growth results. However, small amounts of red/orange



4.2 Schematic diagram of a Bridgman growth system.

materials were often deposited at the top of the crucibles, indicating some leakage. The furnace gradient at the growth interface was  $\sim 20^\circ\text{C}/\text{cm}$ . The thermocouple was welded on the side of the crucible near the bottom to control the position of the initial growth interface. Unidirectional solidification was accomplished through either furnace or crucible translation. Typical translation rates of  $0.1\sim 1\text{ mm/h}$  were used.

After growth, the crystals were slowly cooled down to room temperature to prevent cracking. Particular care was taken in the  $200^\circ\text{C}$  to room temperature range (cooling rate of  $5^\circ\text{C}/\text{h}$ ) where the material undergoes a phase transition from cubic to tetragonal or rhombohedral phase (depending on composition). The crucibles were not reusable, as the grown crystals could not be removed without cutting away the crucible. The grown crystals had smooth and shiny surfaces on which the grain structure of the Pt crucible was imprinted.

#### 4.2.2 Characterization of the grown crystals

The Ti concentration increases along the growing direction. The Ti concentration profile is very similar to the classic shape of the unidirectional solidification of a completely mixed melt with no diffusion in the solid. The equation describing the concentration profile of a system for the case of complete mixing is<sup>24</sup>:

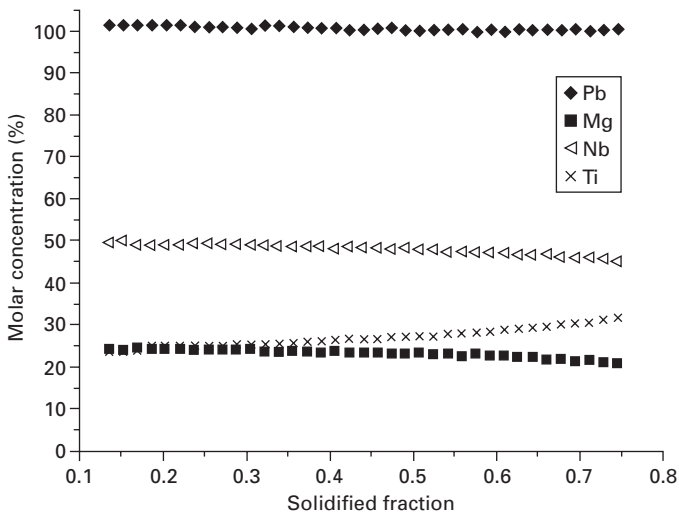
$$C = kC_0(1 - f)^{(k-1)} \quad 4.1$$

where  $C$  is the concentration in the solid,  $k$  is the effective segregation coefficient,  $C_0$  is the initial melt concentration and  $f$  is the fraction of the original melt that has solidified. Figure 4.3 shows compositional variation in PMN–PT single crystal.<sup>25</sup> From the logarithmic plot, the effective distribution coefficient ( $k$ ) was estimated about 0.82 for  $C_0 = 30\%$  in Fig. 4.3. These results are very similar to those reported by Zawilski *et al.*<sup>18</sup>

Figure 4.4 shows the X-ray diffraction (XRD) patterns obtained from different positions of a PMN–PT single grown crystal, with the characteristic tetragonal peak splitting taking place at higher Ti concentrations, in accordance with the composition analysis. Therefore, because of the segregation, from the bottom to the top of the crystal, the phase symmetry gradually changes from rhombohedral to tetragonal with increasing Ti contents.

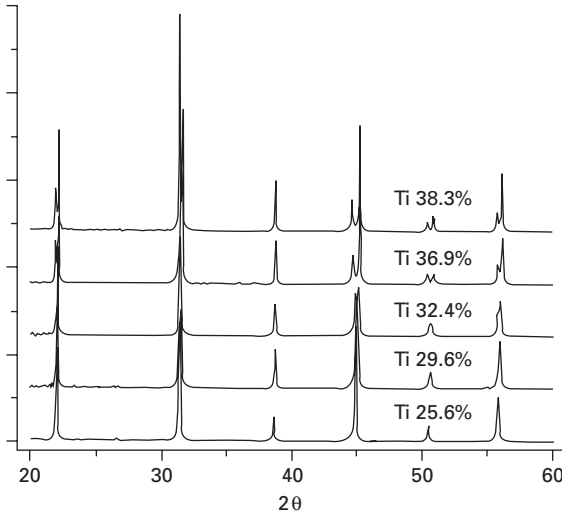
The polarization directions of domains are different between the rhombohedral and tetragonal phases. Each phase has a specific domain structure. Figures 4.5 and 4.6 show the domain configurations of the rhombohedral and tetragonal PMN–PT crystals, respectively, observed by optical microscopy, surface etching and scanning force microscopy (SFM).<sup>25</sup> In the rhombohedral phase, both regular tire-track patterns and irregular fingerprint patterns were observed on the as-grown crystal plates. The tire-track patterns were composed of  $\{1\ 0\ 0\}$  and  $\{1\ 1\ 0\}$  domain walls. The irregular fingerprint patterns were antiparallel domains. In the tetragonal crystals, three different types of etching area were observed. These patterns consisted of  $180^\circ$  domains and  $90^\circ$   $\{1\ 1\ 0\}$  domain boundary.

The best piezoelectric response was found in the rhombohedral PZN–PT



4.3 Compositional variations along the axial direction of a PMN–PT crystal grown by the Bridgman method





4.4 XRD pattern from different vertical locations in a grown PMN-PT crystal.

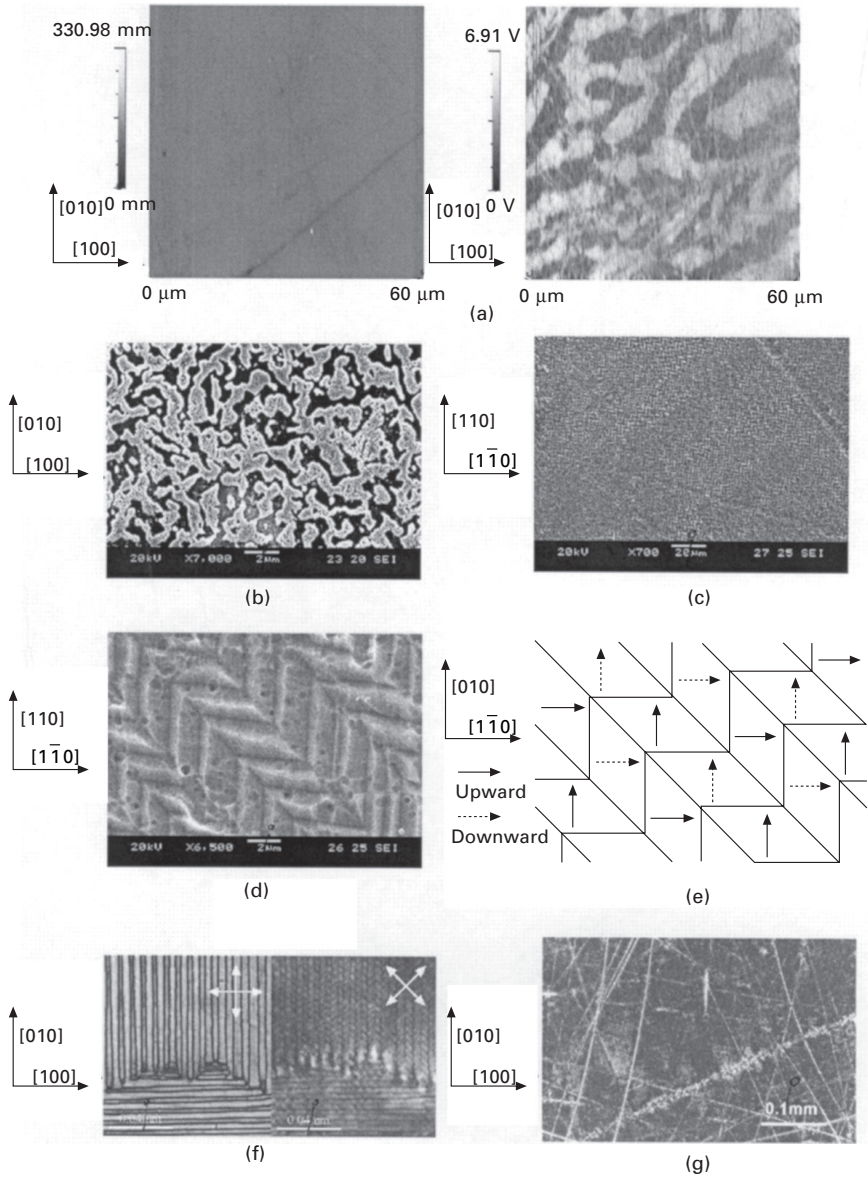
and PMN-PT single crystals poled long the  $\langle 001 \rangle$  direction,<sup>5</sup> which is different from spontaneous polarization direction. The  $\langle 001 \rangle$  poled crystals show a macroscopic 4mm symmetry and excellent piezoelectric properties. It is also very important to have a complete set of elastic, piezoelectric and dielectric constants. The data can be obtained by using a combined method involving both pulse-echo and impedance resonance techniques.<sup>26</sup> A complete set of data for  $\langle 001 \rangle$  poled rhombohedral PMN-PT single crystals is given in Table 4.2.

The uniformity of the crystals is very important for the performance of transducer. It can be checked by measuring the chemical composition of the crystal wafer and the dielectric and piezoelectric properties of the elements of N channel, as shown in Fig. 4.7.

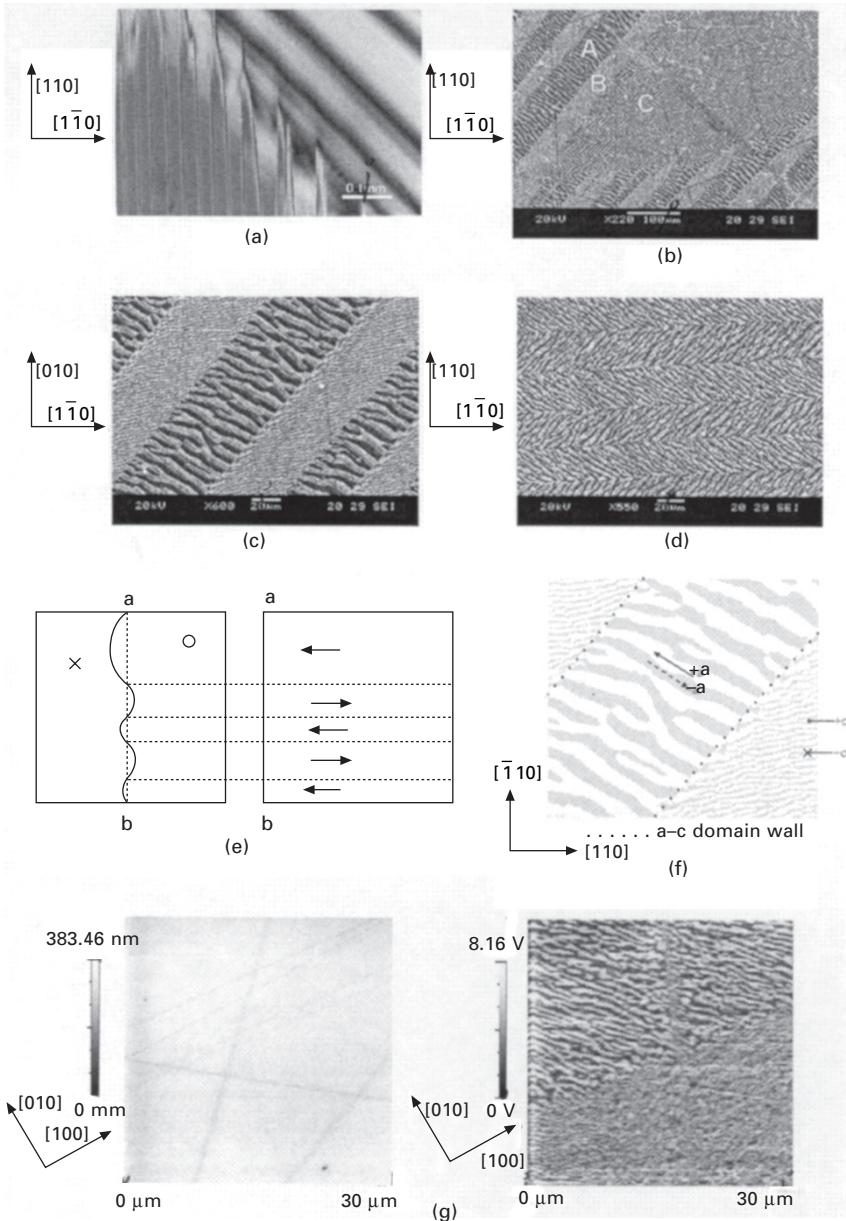
## 4.3 Single crystal transducers

### 4.3.1 Single crystals versus conventional PZT ceramics

One key method of improving ultrasound imaging is to increase the performance of ultrasonic transducer. The vast majority of ultrasonic transducers utilize polycrystalline piezoelectrics based on the composition  $\text{Pb}(\text{Zr}_{1-x}\text{Ti}_x)\text{O}_3$  (PZT). These materials bring the benefit of relatively high electromechanical coupling factor and piezoelectric constant and, therefore, display improved probe bandwidth and sensitivity. Recent ultrasonic arrays for medical imaging system are made from piezoelectric ceramics, such as PZT-5A, PZT-5H, etc.



4.5 Domain patterns of rhombohedral single crystal (PMN-25.6%PT) observed at room temperature: (a) by SFM in the piezoresponse mode (topology (left) and piezoresponse (right) are displayed); (b) fingerprint pattern (180° domain wall) observed by SEM after etching; (c) tire-track pattern (71° or 109° domain wall); (d) magnification of (c); (e) spatial configuration of (d); (f) domain pattern under a polarizing microscope; and (g) domain pattern under a polarizing microscope after heat treatment.<sup>25</sup>



4.6 Domain patterns of tetragonal PMN-PT (PMN-38%PT) single crystals at room temperature: (a) polarizing micrograph; (b) etching pattern consisting of three different types of etching area; (c) etching pattern of  $a$ - $c$  domains; (d) etching pattern of  $a$ - $a$  domains; (e) size relation between  $a$ -domains and  $c$ -domains; (f) spatial configuration of (d); and (g) piezoelectric mode SFM scan on (0 0 1)-oriented platelet: topology (left) and normal piezoresponse (right) are displayed.<sup>25</sup>

Table 4.2 Elastic, dielectric, and piezoelectric data set of rhombohedral PMN-PT crystals

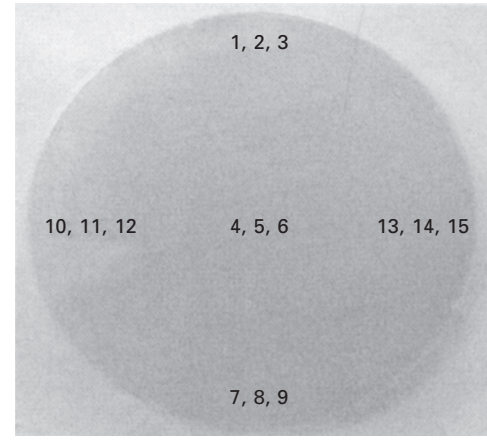
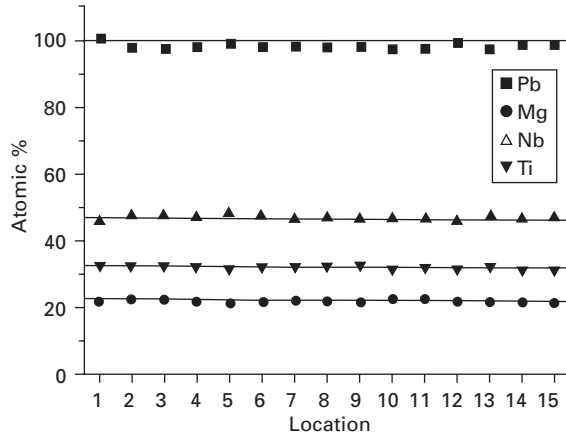
	Properties	Values		Properties	Values
1	$\epsilon_3^T (\epsilon_0)$	6110	10	$k_{31}$	0.51
2	$\epsilon_1^T (\epsilon_0)$	1717	11	$k_{15}$	0.31
3	$d_{33}(10^{-12} \text{ C/N})$	1658	12	$k_t$	0.58
4	$d_{31}(10^{-12} \text{ C/N})$	-894	13	$s_{11}^E (10^{-12} \text{ m}^2/\text{N})$	56.2
5	$d_{15}(10^{-12} \text{ C/N})$	150.6	14	$s_{12}^E (10^{-12} \text{ m}^2/\text{N})$	-22.1
6	$g_{33}(10^{-3} \text{ V m/N})$	30.6	15	$s_{13}^E (10^{-12} \text{ m}^2/\text{N})$	-29.7
7	$g_{31}(10^{-3} \text{ V m/N})$	-16.5	16	$s_{33}^E (10^{-12} \text{ m}^2/\text{N})$	60.6
8	$d_{15}(10^{-3} \text{ V m/N})$	9.9	17	$s_{44}^E (10^{-12} \text{ m}^2/\text{N})$	15.2
9	$k_{33}$	0.92	18	$s_{66}^E (10^{-12} \text{ m}^2/\text{N})$	16.3

Because of the small array element sizes, a very high relative dielectric constant and high coupling factor are necessary in modern ultrasonic array applications. The most important parameters in ultrasonic array are  $k_{33}$ ,  $d_{33}$  and  $g_{33}$ . The piezoelectric coefficient  $d_{33}$  measures the strain developed per applied field and is a measure of the effectiveness of the material as a driver or transmitter. The constant  $g_{33}$  is the electric field generated per applied stress and is a measure of the effectiveness when used as a receiver. The materials with higher coupling coefficients  $k_{33}$  can give better bandwidths and pulse response in medical applications.<sup>27</sup>

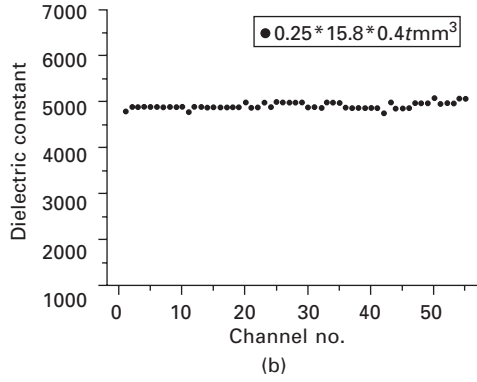
To overcome the disadvantages of conventional PZT ceramics, the multilayer/polymer composite technology is introduced into transducers.<sup>28</sup> The current performance status of a multilayer/polymer composite transducer is almost the same as a normal single crystal transducer using a single layer, but it is very difficult for a multilayer/polymer composite PZT transducer to get high manufacturing yields.

The piezoelectric properties of PZT ceramics have shown little improvement over the past two decades. On the other hand, the PZN-PT and PMN-PT single crystals exhibit an ultra-high piezoelectric constant,  $d_{33}$ , and a very large electromechanical coupling factor,  $k_{33}$ , in comparison with those of PZT ceramics, making them attractive for both actuator and ultrasonic transducer applications.

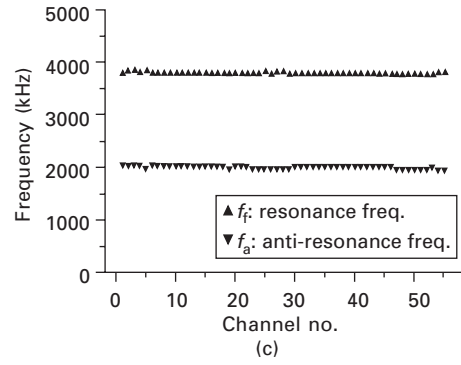
Many research results concerning medical transducers using single crystals have been reported since the mid-1990s.<sup>28-31</sup> Saitoh *et al.* reported the first images of B-mode and color Doppler images obtained by 3.5 MHz 96 channels phased array made from a PZN-PT single crystal.<sup>32</sup> The two-way sensitivity of PZN-PT transducer is 6 dB higher than that of conventional PZT transducer and -6 dB fractional bandwidth is 30% broader. Because the dielectric constant



(a)



(b)



(c)

4.7 Uniformity of PMN-PT single crystals: (a) composition variation check; (b) dielectric constant; and (c) resonance, anti-resonance frequencies for elements of N-channel.

*Table 4.3* Mechanical and electrical properties of piezoelectric single crystals and PZT ceramics

Properties	PZT-5H	3203HD <sup>(1)</sup>	PZT-5K <sup>(2)</sup>	PZN-7%PT	PMN-33%PT
Density [kg/m <sup>3</sup> ]	7500	7800	8200	8200	8000
Dielectric constant at 1 kHz	3400	3800	6200	6500	5500
Dielectric loss [%]	2	2.4	2	<1	<1
Curie temperature [°C]	190	225	160	167	140
$k_{33}$	0.75	0.75	0.75	0.94	0.93
$k'_{33}$	0.68	0.69	0.63	0.83	0.83
$k_t$	0.505	0.55		0.55	0.63
$d_{33}$ [pC/N]	593	650	870	2400	2000

(1) CTS Co. Ltd. (<http://www.ctscorp.com>).

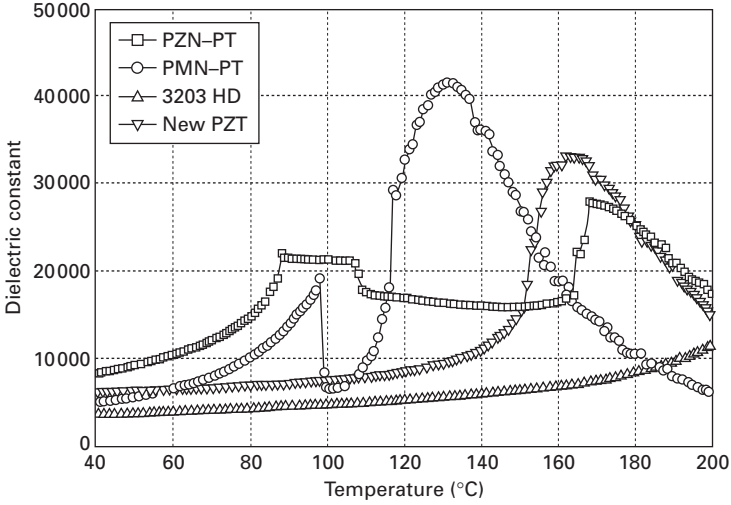
(2) Morgan Electroceramics Co., Ltd (<http://www.morganelectroceramics.com>).

of the current PZT (>6000) is higher than that of previous PZT (<4000) and is similar to that of single crystals, at the present, the sensitivity of single crystal transducer is almost the same as PZT. Table 4.3 compares the mechanical and electrical properties of the piezoelectric single crystals and PZT ceramics. Although the dielectric constant of new PZT is higher than that of PMN-PT single crystals, the coupling factor of new PZT ceramics is lower than that of single crystals. Therefore, the performance of the transducer using new PZT is lower than that of a single crystal transducer.

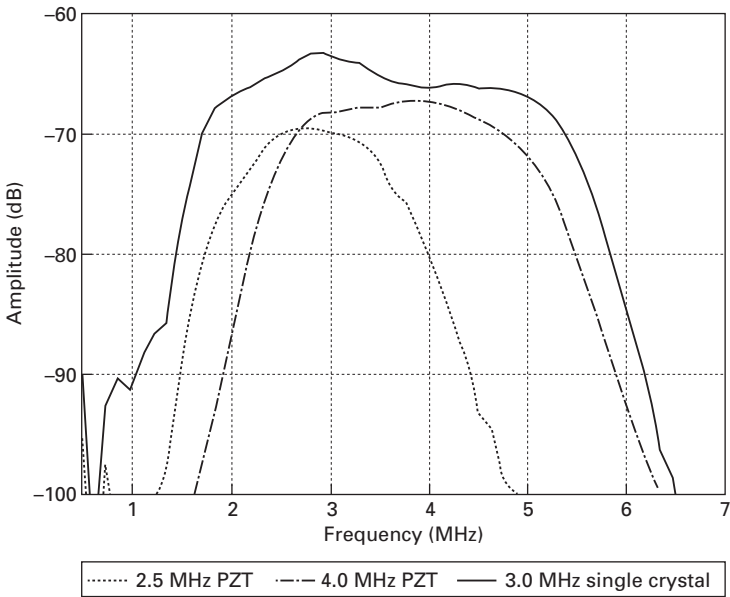
Because the electromechanical coupling factor of single crystals is higher than that of PZT ceramics, the fractional bandwidth of single crystal transducers is broader than that of PZT transducers. However, the Curie temperature of single crystal is lower than that of PZT. The low Curie temperature can cause depoling during the fabrication processes such as curing the bonding epoxy, electrical connection, dicing process and so on. Figure 4.8 shows the temperature dependence of the dielectric constant of a single crystal and a PZT ceramic. To overcome this problem, a great deal of effort has been put into increasing the Curie temperature of the PMN-PT and PZN-PT crystals and into searching for new materials with a higher  $T_C$ .<sup>33</sup>

#### 4.3.2 Commercialization of single crystal transducers

The major advantage of single crystal transducers is broad bandwidth and high sensitivity compared with PZT ceramic transducer. One single crystal



4.8 Temperature dependence of dielectric constant of PMN-PT, PZN-PT, and PZTs.



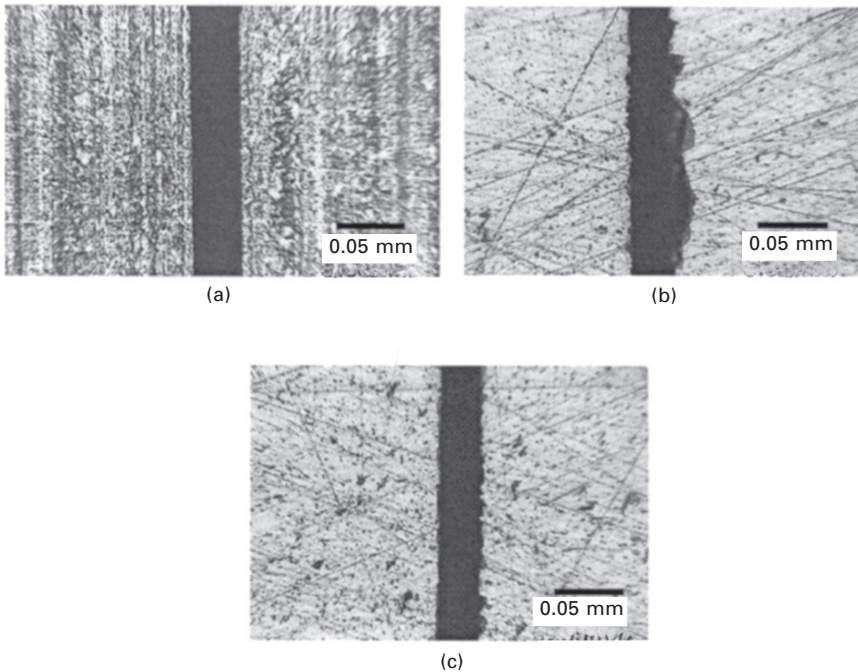
4.9 Frequency spectra of 2.5 and 4 MHz PZT transducers vs. a 3 MHz single crystal transducer.

transducer with broad bandwidth can substitute two different frequency PZT transducers. Figure 4.9 gives the frequency spectra of 2.5 and 4 MHz PZT transducers and a 3 MHz single crystal transducer, indicating this advantage

of single crystal transducer with a broader bandwidth. The 3 MHz single crystal transducer was commercialized by Humanscan in 2003.<sup>34</sup>

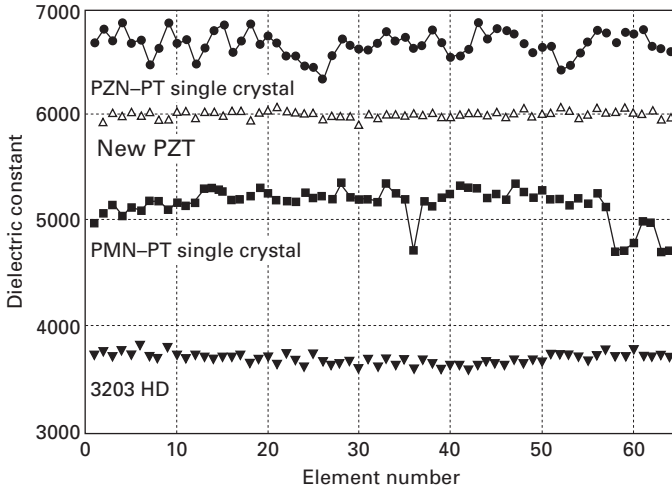
The process of transducer fabrication using single crystals differs from that using PZT. There are many steps required for making transducers, including acoustic stack fabrication, layer bonding, dicing, electrical connection, acoustic lens fabrication and so on. Among these processes, the dicing process for single crystal is appreciably different from that for PZT ceramics. Figure 4.10 shows diced elements of ordinary PZT, PMN–PT single crystal using conventional PZT dicing process, and PMN–PT prepared using an optimized dicing process. The element width is 120  $\mu\text{m}$  and the kerf is 35  $\mu\text{m}$ . When a conventional PZT dicing process is used on a single crystal, considerable chipping occurs. A soft bonded and small grit size blade is necessary for single crystal. The dicing speed and temperature control are also the most important parameters for the dicing of single crystal.

Single crystals have low-frequency constants and, therefore, to make the same frequency transducer, the single crystal has to be thinner than PZT ceramic. The relatively low mechanical strength of single crystal is a serious problem in making a high-frequency ( $>7$  MHz) transducer. Another problem for single crystal transducers is the composition uniformity across the wafer.



4.10 Diced element of (a) PZT; (b) PMN–PT single crystal using PZT process; and (c) PMN–PT single crystal using optimized process.



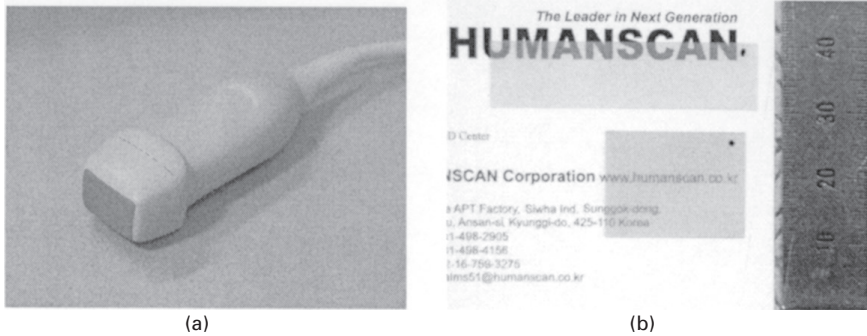


4.11 Uniformity of dielectric constant of PMN-PT and PZN-PT crystals and two PZT ceramics.

Figure 4.11 shows the dielectric constant variation of 64 channels of PMN-PT, PZN-PT and two PZT transducers. The variation of the dielectric constant of the single crystal element is larger than that of PZT ceramics, but the uniformity of single crystal has been improved compared with previous results.<sup>35</sup> Because poor uniformity of single crystals is a serious problem in the commercialization of transducers, useful and accurate non-destructive inspection methods is developed such as using optical methods and dot electrodes.<sup>36</sup> At the present, for the evaluation of uniformity of a single crystal, the values of the dielectric constant, Curie temperature and composition ratio are used.

### Phased array

Phased array transducers using single crystals have been studied during the last 10 years.<sup>30, 32, 37-39</sup> Figure 4.12(a) shows a 2.6 MHz 64 channel phased array presented at the 2003 IEEE UFFC conference<sup>37</sup> and Fig. 4.12(b) shows a PMN-PT single crystal used in phased array and linear array. The crystal thickness of 3.0 MHz phased array is 0.4 mm and that of the 7.5 MHz linear array is 0.13 mm. Because the fractional bandwidth of single crystal transducers is broader than that of PZT transducers, harmonic mode imaging exhibits some advantages, which include a better lateral resolution, lower sidelobes and less noise in the near field than conventional ultrasound imaging. However, the price paid is a slightly worse axial resolution resulting from a reduced bandwidth.<sup>40</sup> Therefore, single crystal transducers having broad fractional



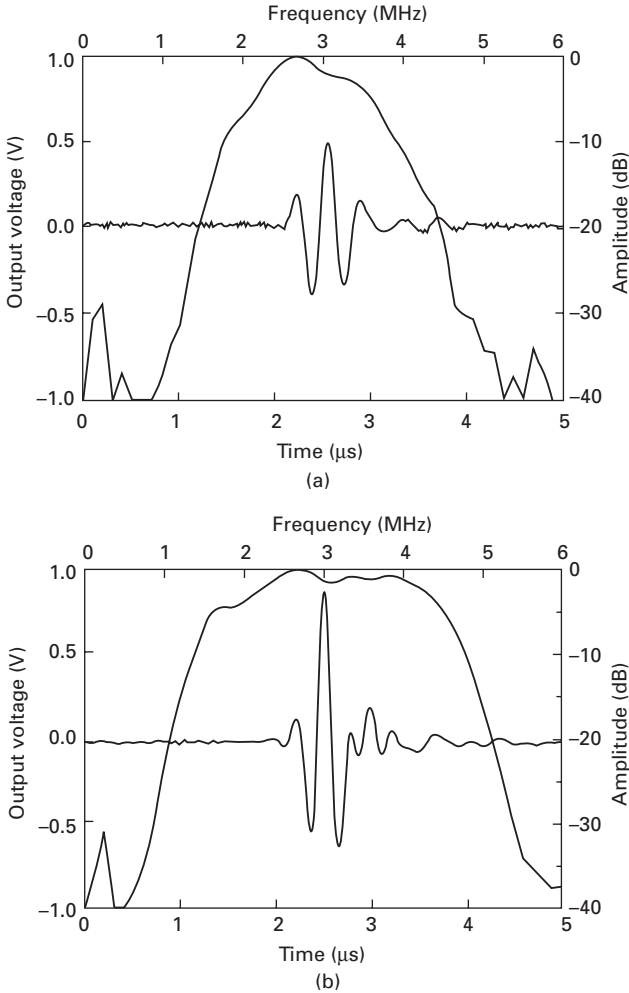
4.12 (a) 2.6 MHz 64 channel phased array using PMN–PT single crystal and (b) PMN–PT single crystal used in phased array and linear array.

bandwidth are more suitable for harmonic imaging, especially in cardiac applications.

The current PZT transducer has a limited bandwidth of the order of 80%. However, the PMN–PT single crystal transducer shows about 100% fractional bandwidth. Because the sensitivity of the single crystal transducer is higher than that of the PZT transducer, the color Doppler performance of single crystal transducer is better. The sensitivity of the PMN–PT transducer is 5 dB higher than that of PZT transducer. Figure 4.13 shows a two-way spectrum from phased array using PZT ceramics and PMN–PT single crystals. Harmonic mode cardiac images using PZT transducers and PMN–PT single crystal transducer are shown in Fig. 4.14. Figure 4.15 shows color Doppler mode images of the four chamber view of an adult heart using PZT and PMN–PT transducers.

#### *High-frequency linear array*

Attenuation of ultrasound in a transducer may occur because waves have been scattered by finite-size grains or by dislocations in a solid. Another cause of attenuation is the unequal thermal conduction and expansion of neighboring grains due to their axes being rotated with respect to each other. For these reasons, single crystals exhibit much lower sound attenuation at high frequencies than the same materials in polycrystalline form.<sup>41</sup> Since single crystal has a lower frequency constant than PZT ceramics, if the frequency is the same, the thickness of single crystal is thinner than that of PZT. In the case of 7.5 MHz linear array, the thickness of PZT is about 180  $\mu\text{m}$ , while that of single crystal is 130  $\mu\text{m}$ . Moreover, because single crystal has a low mechanical strength, cracks occur easily during the dicing process. Figure 4.16 shows a B-mode image and a color Doppler image using a PMN–PT linear array.



4.13 Two-way spectrum of phased array using (a) conventional PZT and (b) PMN-PT single crystal.

*Fine pitch phased array*

The state-of-the-art transducers call for smaller and smaller elements, such as fine pitch array, to improve image quality. A fine pitch increases element directivity for spatial compounding and reduces harmonic frequency grating lobe levels.

A 2.5 MHz phased array with a fine pitch (170 μm) using triple layer PZT and three matching layers was reported.<sup>42</sup> According to recent research results, the sensitivity of triple layer PZT phased array is almost the same as that of single layer single crystal phased array.<sup>43</sup> The 6 MHz phased array with a

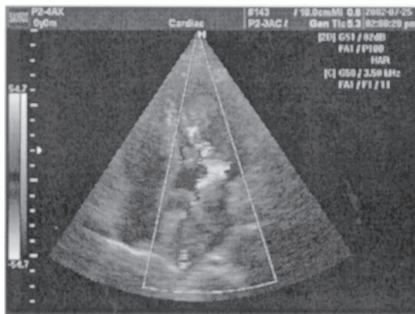


(a)

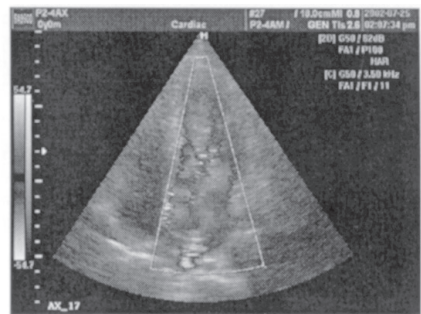


(b)

4.14 Harmonic mode images using (a) PZT and (b) PMN-PT single crystal transducer.



(a)

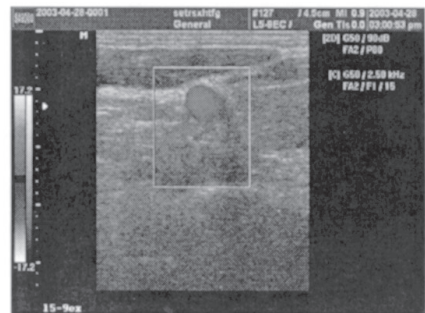


(b)

4.15 Color Doppler mode images of (a) PZT and (b) PMN-PT single crystal transducer.



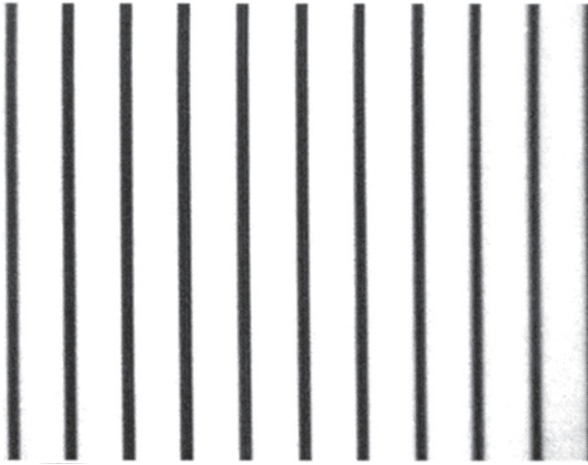
(a)



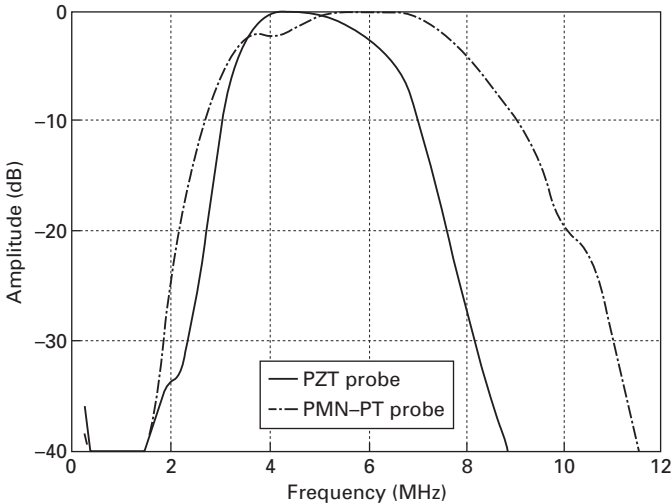
(b)

4.16 (a) B-mode image and (b) Doppler image of 7.5MHz linear array using PMN-PT single crystal.

fine pitch (150  $\mu\text{m}$ ) using PMN–PT single crystal was announced.<sup>43</sup> Figure 4.17 shows a diced element surface having 0.15 mm pitch and 0.03 mm kerf using PMN–PT single crystal. Figure 4.18 gives the frequency spectra of PZT and PMN–PT probes, respectively. The  $-6\text{dB}$  low-frequency and high-frequency edges of PZT probe are about 3.3 and 6.7 MHz, respectively. The low edge of the PMN–PT probe (3.0 MHz) is similar to, but the high-frequency edge is about 2 MHz higher than that of the PZT probe. This means that it is



4.17 Diced element surface having 0.15 mm element pitch and 0.03 mm kerf.



4.18 Frequency spectra of a PZT probe vs. a PMN–PT probe.

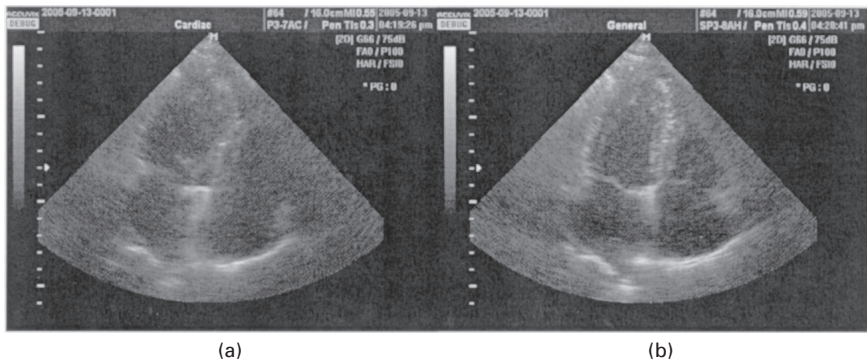
possible for the PMN–PT probe to use a lower Tx frequency (the center frequency of induced pulse on the probe from the imaging system) for better penetration. This is very useful for harmonic imaging especially in cardiac application. If the Tx frequency is lower, the Rx frequency (the center frequency of received pulse by the probe from the human body) of harmonic component is higher, resulting in a better resolution. Therefore, a broad bandwidth enhances both penetration and resolution.

Table 4.4 gives a summary of pulse echo characteristics of PZT and PMN–PT single crystals after averaging all of the elements. The center frequencies of the PMN–PT probe are slightly higher than that of the PZT probe. The echo amplitude of the PMN–PT probe is about 2 dB higher than that of the PZT probe. The –6 dB fractional bandwidth of the PMN–PT probe is about 30% broader than that of the PZT ceramic probe.

Figure 4.19 shows B-mode harmonic images of PZT and PMN–PT single crystal probes using ACCUVIX XQ (Medison Co., Ltd). The system settings of the both cases are the same except the Tx frequency. The Tx voltages of both are the same and the Tx frequencies are slightly different because the bandwidths of the two probes are different. The B-mode sensitivity of the PMN–PT probe is higher than that of the PZT ceramic probe and the contrast and resolution of the PMN–PT probe are also better than those of the PZT

Table 4.4 Summary of pulse echo characteristics of PZT and PMN–PT probes

Properties	Relative sensitivity [dB]	Center frequency [MHz]	–6 dB bandwidth [%]	–20 dB bandwidth [%]	–6 dB ringdown [ $\mu$ s]	–20 dB ringdown [ $\mu$ s]
PZT	0	5.0	68	94	0.312	0.736
PMN–PT	+2.1	5.9	98	130	0.189	0.462



4.19 Comparison of harmonic B-mode images of 6MHz phased array with a fine pitch (150 $\mu$ m) (a) PZT probe vs. (b) PMN–PT probe.

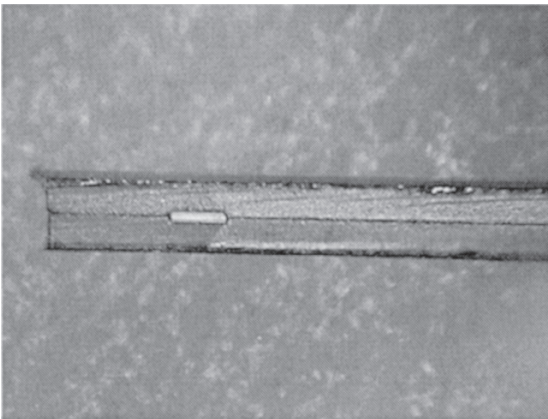
probe. These results are consistent with the two-way pulse echo data in Table 4.4. If the system condition optimization can be done, the image quality of the PMN–PT probe will be even better.

### 4.3.3 Future of medical ultrasound transducer using single crystal

#### *Multilayer single crystal probe*

The electrical impedance mismatch between the small elements and the cable or system is somewhat serious, especially for low center frequency ( $< 4$  MHz) applications. In the case of a fine pitch transducer ( $150\text{--}200\ \mu\text{m}$ ), the electrical impedance of the element is about  $800\text{--}1000\ \Omega$  and this can result in a significant mismatch to the cable and system ( $50\text{--}100\ \Omega$ ). A typical solution to this electrical mismatch problem is to use buffer electronics or a multilayer structure to reduce the electrical impedance of the element. The electrical impedance of a 3 MHz phased array using a double PMN–PT single crystal is only 25% of a single layer PMN–PT phased array.<sup>42</sup> Figure 4.20 shows the cross-section of a double PMN–PT single crystal wafer. Each layer thickness of the double layer is 0.2 mm and the total thickness is 0.4 mm. Table 4.5 summarizes the electrical properties of PZT ceramics, single layer PMN–PT and double layer PMN–PT single crystals.

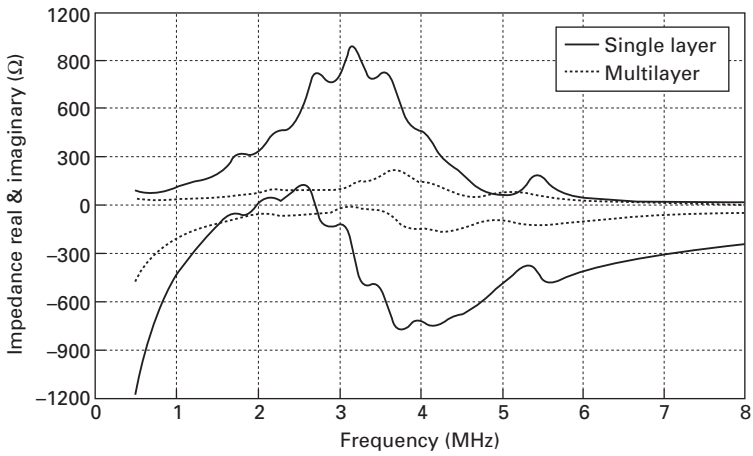
Figure 4.21 shows the electrical impedance of single layer and double layer PMN–PT phased array elements. The impedance at 3 MHz of the double layer PMN–PT phased array is very close to the impedance of the cable with  $85\ \Omega$ . This means that the sensitivity loss of a double layer PMN–PT phased array is much smaller than that of a single layer PMN–PT phased array. Figures 4.22 and 4.23 show the B-mode harmonic image and color Doppler



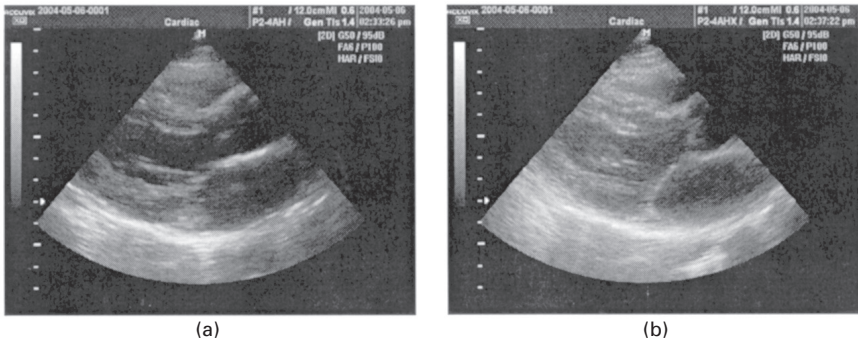
4.20 Cross-section of a double layer PMN–PT single crystal.

Table 4.5 Measured electrical properties of PZT ceramics, and single layer and double layer PMN-PT single crystals

Properties		PZT	Single layer PMN-PT	Double layer PMN-PT
Density	[kg/m <sup>3</sup> ]	7800	8000	8000
$K_3^T$		3800	5500	24 860
$K_3^s$		1250	1100	6390
tan $\delta$		2	<1	<1
$k'_{33}$		0.74	0.82	0.862
$v'_L$	[m/s]	4118	3180	2848
Z	[MRayls]	32.1	25.6	23.0

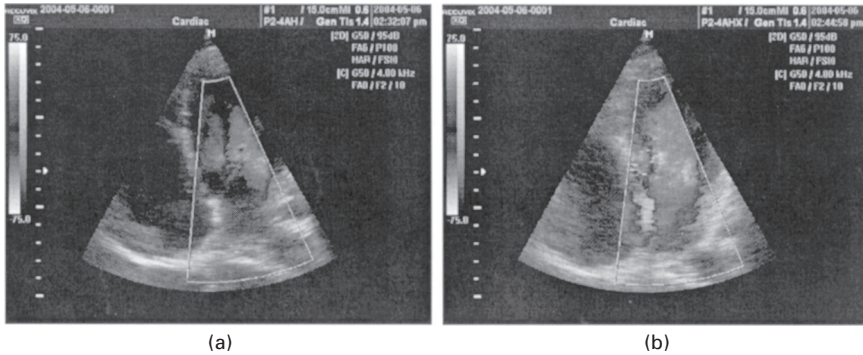


4.21 Electrical impedance of single layer and multilayer PMN-PT phased array elements.



4.22 Comparison of harmonic B-mode images of 3MHz phased array acquired by (a) a single layer PMN-PT probe and (b) a double layer PMN-PT probe.





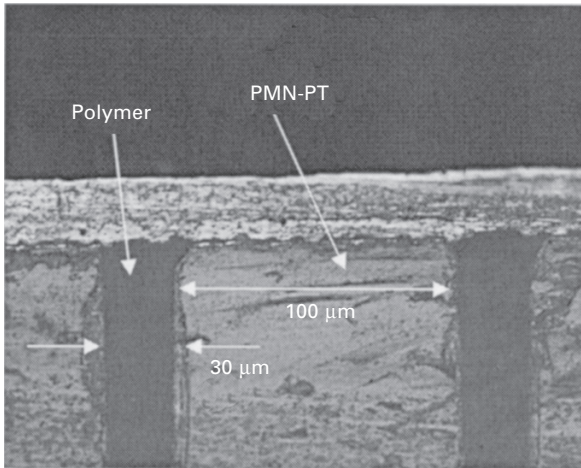
4.23 Color Doppler mode images of 3 MHz phased array acquired by (a) a single layer PMN-PT probe and (b) a double layer PMN-PT probe.

image of single layer PMN-PT and multi-layer PMN-PT probes, respectively. The B-mode and color Doppler sensitivity of the multilayer PMN-PT probe is higher than that of the single layer PMN-PT probe. Because of the lower electrical impedance of the double layer PMN-PT single crystal, a higher sensitivity is obtained compared with the single layer PMN-PT single crystal. This means that the heat generation on the double layer PMN-PT probe surface is reduced when the same voltage is applied to the probe.

#### *Multilayer/polymer composite single crystal phased array*

To produce a better image, broader bandwidth and higher sensitivity are required. To increase the bandwidth, the piezomaterial/polymer composite is one of the solutions. In the case of PZT ceramics, the electromechanical coupling factor of PZT/polymer composite is higher than that of PZT ceramics only because of the decreasing stiffness of ceramics. However, the dielectric constant of the PZT/polymer composite is lower than that of PZT ceramics because of the polymer having a low dielectric constant. If the dielectric constant is low, the electrical impedance is high and then the sensitivity is also low because of the electrical impedance mismatch between element and cable. Therefore, we have to increase the dielectric constant in order to increase the sensitivity of the probe.

Figure 4.24 shows the cross-section of a multilayer PMN-PT single crystal/polymer composite wafer with 80% single crystal volume fraction. Table 4.6 summarizes the mechanical and electrical properties of PZT ceramics, and single layer and multilayer/polymer composite PMN-PT single crystals. The clamped dielectric constant of the multilayer/polymer composite PMN-PT single crystal is almost four times that of 3203HD PZT ceramics. The electromechanical coupling factor of the PMN-PT single crystal/polymer



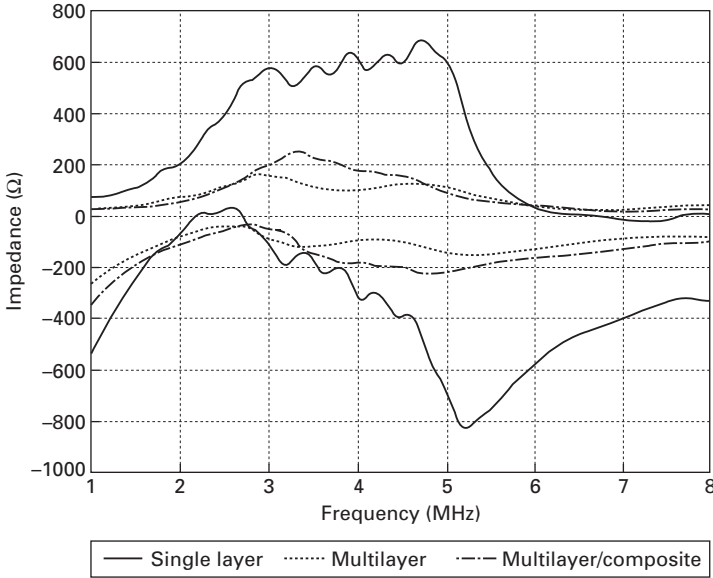
4.24 Cross-section of a multi-layer PMN-PT/polymer composite wafer.

Table 4.6 Electrical and mechanical properties of 3203HD PZT ceramics, and multilayer and multilayer/polymer composite PMN-PT single crystals

Properties	3203HD	Single layer	Multilayer/composite
Density [kg/m <sup>3</sup> ]	7800	8000	8000
$K_3^T$	3800	5500	11500
$K_3^s$	1250	1100	4000
$\tan\delta$ [%]	2	<1	<1
$k'_{33}$	0.74	0.82	0.82
$v_l$ [m/s]	4100	3200	2700
$Z$ [MRayls]	32	26	19

composite is almost the same as that of the single layer PMN-PT single crystal. Moreover, the acoustic impedance of the multilayer/polymer composite PMN-PT is much lower than that of PZT and the single layer PMN-PT single crystal. This means the acoustic impedance mismatch between piezomaterial and human body is improved and it is possible to use comparably low acoustic impedance matching layer with about 6–7 MRayls, compared with that of ceramic with about 8–10 MRayls.

Figure 4.25 shows the electrical impedance (without cable) of the elements of single layer, multilayer, and multilayer/polymer PMN-PT single crystal. The electrical impedance of the multilayer/polymer at 3.5 MHz is only 40% of that of the single layer PMN-PT single crystal. Figure 4.26 shows the frequency spectra and waveforms of single layer, multilayer and multilayer/polymer composite PMN-PT single crystal probes. The -6 dB bandwidth and sensitivity of multilayer/polymer composite PMN-PT probe is about



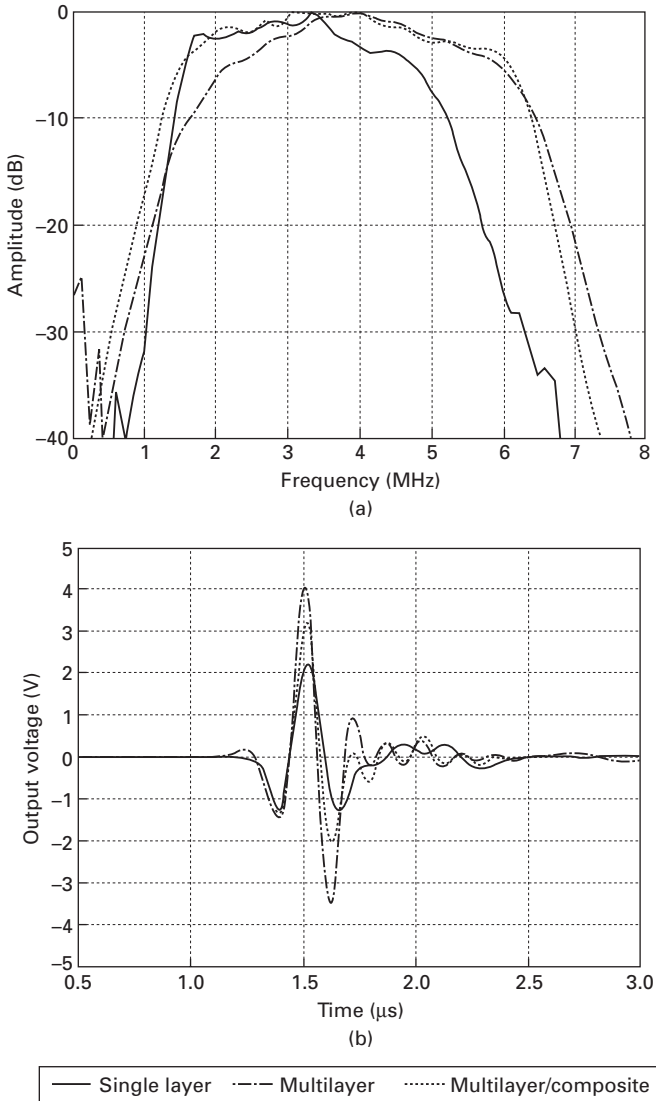
4.25 Electrical impedance (without cable) of the elements of single layer, multi-layer, and multi-layer/polymer PMN-PT single crystals.

20% broader and 3 dB higher than those of the single layer PMN-PT probe, respectively. The measured acceptance angle of the multilayer/polymer PMN-PT probe matches well the theoretical value.

#### 4.4 Conclusions and future trends

The excellent piezoelectric properties of the single crystal improved the performance of ultrasonic medical transducers. To provide better image quality of recent imaging systems, the number of channels is increased and the mismatch between probe and cable or system should be increased. To reduce this electrical impedance mismatch, high dielectric materials and the multilayer technique are being developed by many researchers. In particular, the multilayer technique is very useful for a multi-row probe that is used for multi-focusing and 3D image. However, the bandwidth of the multi-row probe is narrower than the normal 1D probe because of the complicated electrical connection. However, broad bandwidth is necessary for harmonic imaging in phased array and when a single crystal is used for a multi-row probe, we can obtain a bandwidth as broad as that using a normal 1D probe.

In recent years the capacitive microfabricated ultrasound transducer (cMUT) has undergone intensive development and created interest as an alternative to conventional piezoelectric ultrasound probes. Moreover, the cMUT has advantages over a 2D array for 3D imaging and smart probe for SOC (system-



4.26 (a) Frequency spectra and (b) waveforms of single layer, multi-layer, and multi-layer/polymer PMN-PT single crystal probes.

on-chip) or POC (point-of-care). Even though many things need to be improved for commercialization, especially low sensitivity comparing with the normal probe, cMUT has a very attractive future as a medical ultrasound probe.

## 4.5 References

1. R. E. McKeighen, 'Design guidelines for medical ultrasonic arrays', *Proc SPIE*, 1998 **3341**(01) 2–18.
2. T. R. Gururaja, 'Piezoelectrics for medical ultrasonic imaging', *Am Ceram Soc Bull*, 1994 **73**(5) 50–5.
3. D. M. Mill, and S. W. Smith, 'Multi-layered PZT/polymer composites to increase signal-to-noise ratio and resolution for medical ultrasound transducers', *IEEE Trans Ultrason Ferroelect Freq Contr*, 1999 **46**(4) 961–71.
4. G. Caliano, R. Carotenuto, V. Foglietti, A. Caronti, A. Iula, and M. Pappalardo, 'Design, fabrication and characterization of a capacitive micromachined ultrasonic probe for medical imaging', *IEEE Trans Ultrason Ferroelect Freq Contr*, 2005 **52**(12) 2259–69.
5. S-E. Park, and T. R. Shrout, 'Ultrahigh strain and piezoelectric behavior in relaxor based ferroelectric single crystals', *J Appl Phys*, 1997 **82**(4) 1804–11.
6. R. F. Service, 'Materials science: shape-changing crystals get shiftier', *Science*, 1997 **275**(5308) 1878.
7. J. Kuwata, K. Uchino, and S. Nomura, 'Dielectric and piezoelectric properties of  $0.91\text{Pb}(\text{Zn}_{1/3}\text{Nb}_{2/3})\text{O}_3-0.09\text{PbTiO}_3$  single crystal', *Jpn J Appl Phys Part 1*, 1982 **21**(9) 1298–302.
8. Y. Yamashita, Y. Hosono, K. Harada, and N. Yasuda, 'Present and future of piezoelectric single crystals and the importance of B-site cations for high piezoelectric response', *IEEE Trans Ultrason Ferroelect Freq Contr*, 2002 **49**(2) 184–92.
9. S. L. Swartz, and T. R. Shrout, 'Fabrication of perovskite lead magnesium niobate', *Mater Res Bull*, 1982 **17**(10), 1245–50.
10. S.-G. Lee, H. S. Lee, R. G. Monteiro, M. Lee, and R. S. Feigelson, 'Growth of lead magnesium niobate single crystals by the Bridgman method', AACG/West Sixteenth Conference on Crystal Growth and Epitaxy, June 7–10, 1998.
11. H. Luo, G. Xu, H. Xu, P. Wang, and Z. Yin, 'Compositional homogeneity and electrical properties of lead magnesium niobate titanate single crystals grown by a modified Bridgman technique', *Jpn J Appl Phys Part 1*, 2000 **39**(9B) 5581–5.
12. G. Xu, H. Luo, H. Xu, Z. Qi, and Z. Yin, 'Dendrite growth observed in  $\text{Pb}(\text{Mg}_{1/3}\text{Nb}_{2/3})\text{O}_3-\text{PbTiO}_3$  single crystals prepared by the Bridgman process', *Jpn J Appl Phys Part 2*, 2001 **40**(4B) L396–7.
13. G. Xu, H. Luo, H. Xu, Z. Qi, P. Wang, W. Zhong, and Z. Yin, 'Structural defects of  $\text{Pb}(\text{Mg}_{1/3}\text{Nb}_{2/3})\text{O}_3-\text{PbTiO}_3$  single crystals grown by a Bridgman method', *J Crystal Growth*, 2001 **222**(1/2) 202–8.
14. G. Xu, H. Luo, Y. Guo, Y. Gao, H. Xu, Z. Qi, W. Zhong, and Z. Yin, 'Growth and piezoelectric properties of  $\text{Pb}(\text{Mg}_{1/3}\text{Nb}_{2/3})\text{O}_3-\text{PbTiO}_3$  crystals by the modified Bridgman technique', *Solid State Commun*, 2001 **120**(7/8) 321–4.
15. G. Xu, H. Luo, P. Wang, H. Xu, and Z. Yin, 'Ferroelectric and piezoelectric properties of novel relaxor ferroelectric single crystals PMNT', *Chinese Sci Bull*, 2000 **45**(6) 491–5.
16. H. Luo, G. Xu, P. Wang, and Z. Yin, 'Growth and characterization of relaxor ferroelectric PMNT single crystals', *Ferroelectrics*, 1999 **231** 97–102.
17. M. Dong, and Z.-G. Ye, 'High temperature thermodynamic properties and pseudo-binary phase diagram of the  $\text{Pb}(\text{Zn}_{1/3}\text{Nb}_{2/3})_{0.91}\text{Ti}_{0.09}\text{O}_3-\text{PbO}$  system', *Jpn J Appl Phys Part 1*, 2001 **40**(7) 4604–10.

18. K. T. Zawilski, M. Claudia, C. Custodio, R. C. DeMattei, S-G. Lee, R. G. Monteiro, H. Odagawa, and R. S. Feigelson, 'Segregation during the vertical Bridgman growth of lead magnesium niobate–lead titanate single crystals', *J Crystal Growth* 2003 **258**(3/4) 353–67.
19. S.-G. Lee, R. G. Monteiro, R. S. Feigelson, H. S. Lee, and M. Lee, S-E. Park, 'Growth and electrostrictive properties of  $\text{Pb}(\text{Mg}_{1/3}\text{Nb}_{2/3})\text{O}_3$  crystals', *Appl Phys Lett*, 1999 **74**(7) 1030–32.
20. Z-G. Ye, P. Tissot, and H. Schmid, 'Pseudo-binary  $\text{Pb}(\text{Mg}_{1/3}\text{Nb}_{2/3})\text{O}_3$ – $\text{PbO}$  phase diagram and crystal growth of  $\text{Pb}(\text{Mg}_{1/3}\text{Nb}_{2/3})\text{O}_3$  [PMN]', *Mater Res Bull*, 1990 **25**(6) 739–48.
21. H. Luo, G. Xu, H. Xu, P. Wang, and Z. Yin, 'Compositional homogeneity and electrical properties of lead magnesium niobate titanate single crystals grown by a modified Bridgman technique', *Jpn J Appl Phys Part 1*, 2000 **39**(9B 527) 5581–5.
22. Z.-G. Ye, M. Dong, and Y. Yamashita, 'Thermal stability of the  $\text{Pb}(\text{Zn}_{1/3}\text{Nb}_{2/3})\text{O}_3$ – $\text{PbTiO}_3$  [PZNT91/9] and  $\text{Pb}(\text{Mg}_{1/3}\text{Nb}_{2/3})\text{O}_3$ – $\text{PbTiO}_3$  [PMNT68/32] single crystals', *J. Crystal Growth*, 2000 **211**(1–4) 247–51.
23. S. Fushimi, and T. Ikeda, 'Phase equilibrium in the system  $\text{PbO}$ – $\text{TiO}_2$ – $\text{ZrO}_2$ ', *J Am Ceram Soc*, 1967 **50**(3) 129–32.
24. W. G. Pfann, *Zone Melting*, 2nd edn, New York, Wiley, 1966.
25. M. C. Shin, S. J. Chung, S.-G. Lee, and R. S. Feigelson, 'Growth and observation of domain structure of lead magnesium niobate–lead titanate single crystals', *J Crystal Growth*, 2004 **263**(1–4) 412–20.
26. H. Cao, V. H. Schmidt, R. Zhang, W. Cao, and H. Luo, 'Elastic, piezoelectric, and dielectric properties of  $0.58\text{Pb}(\text{Mg}_{1/3}\text{Nb}_{2/3})\text{O}_3$ – $0.42\text{PbTiO}_3$  single crystal', *J Appl Phys*, 2004 **96**(1) 549–54.
27. Frost & Sullivan, 'The World Medical Diagnostic Ultrasound Imaging Equipment Market', www.frost.com, 2001.
28. D. M. Mill and S. Smith, 'Multi-layer composite hybrid transducer for medical ultrasound', *Proc IEEE Ultrason Symp*, 2000 **2** 1153–6.
29. S-E. Park and T. R. Shrout, 'Characteristics of relaxor-based piezoelectric single crystal for ultrasonic transducers', *Proc IEEE Ultrason Symp*, 1996 **2** 935–42.
30. S. Saitoh, T. Takeuchi, T. Kobayashi, K. Harada, S. Shimanuki, and Y. Yamashita, 'A 3.5 MHz phased array probe using  $0.91\text{Pb}(\text{Zn}_{1/3}\text{Nb}_{2/3})\text{O}_3$ – $0.09\text{PbTiO}_3$  single crystal', *Proc IEEE Ultrason Symp*, 1998 **2** 1847–50.
31. S. Saitoh, T. Kobayashi, K. Harada, S. Shimanuki, and Y. Yamashita, 'A 20 MHz single-element ultrasonic probe using  $0.91\text{Pb}(\text{Zn}_{1/3}\text{Nb}_{2/3})\text{O}_3$ – $0.09\text{PbTiO}_3$  single crystal', *IEEE Trans Ultrason Ferroelec Freq Cont*, 1998 **45**(4) 1071–6.
32. S. Saitoh, T. Takeuchi, T. Kobayashi, K. Harada, S. Shimanuki, and Y. Yamashita, 'A 3.7 MHz Phased array probe using  $0.91\text{Pb}(\text{Zn}_{1/3}\text{Nb}_{2/3})\text{O}_3$ – $0.09\text{PbTiO}_3$  single crystal', *IEEE Trans Ultrason Ferroelec Freq Contr*, 1999 **46**(20) 414–21.
33. Y. Hosono, Y. Yamashita, H. Sakamoto, and N. Ichinose, 'Large piezoelectric constant of high-Curie-temperature  $\text{Pb}(\text{In}_{1/2}\text{Nb}_{1/2})\text{O}_3$ – $\text{Pb}(\text{Mg}_{1/3}\text{Nb}_{2/3})$ – $\text{PbTiO}_3$  ternary single crystal near morphotropic phase boundary', *Jpn J Appl Phys Part 2*, 2002, L1240–L1242.
34. <http://humanscan.co.kr>
35. S. Michau, P. Mauchamp, and R. Dufait, 'Single crystal-based phased array for transoesophageal ultrasound probe', *Proc IEEE Ultrason Symp*, 2002 **2** 1269–72.
36. F. J. Kumar, L-C. Lim, S. P. Lim, and K. H. Lee, 'Nondestructive evaluation of

- large-area PZN-8%PT single crystal wafers for medical ultrasound imaging probe applications', *IEEE Trans Ultrason Ferroelect Freq Contr*, 2003 **50**(3) 203–9.
37. S. M. Rhim, H. Jung, S. Kim, and S-G. Lee, 'A 2.6MHz phased array ultrasonic probe using  $0.67\text{Pb}(\text{Mg}_{1/3}\text{Nb}_{2/3})\text{O}_3$ - $0.33\text{PbTiO}_3$  single crystal grown by the Bridgman method', *Proc IEEE Ultrason Symp*, 2002 **2** 1143–8.
  38. S. Saitoh, T. Kobayashi, K. Harada, S. Shimanuki, and Y. Yamashita, 'Forty-channel phased array ultrasonic probe using  $0.91\text{Pb}(\text{Zn}_{1/3}\text{Nb}_{2/3})\text{O}_3$ - $0.09\text{PbTiO}_3$  single crystal', *IEEE Trans Ultrason Ferroelect Freq Contr*, 1999 **46**(1) 152–7.
  39. M. Zipparo, C. Oakley, W. Hackenberger, and L. Hackenberger, 'Single crystal composites, transducer, and array', *Proc IEEE Ultrason Symp*, 1999 **2** 965–8.
  40. K. K. Shung, 'Introduction to Harmonic Imaging', NIH newsletter 3rd issue 6, 2002.
  41. G. S. Kino, *Acoustic Waves*, New Jersey, Prentice Hall Inc., 1987.
  42. X. Ming Lu, and T. L. Proulx, 'Single crystal vs. PZT ceramics for medical ultrasound applications', *Proc IEEE Ultrason Symp*, 2005 **1** 227–30.
  43. S. M. Rhim, H. Jung, J. S. Jung, and J. S. Hwang, 'A 6.0MHz 0.15 mm pitch phased array ultrasonic probe using PMN-PT Single crystal', *Proc IEEE Ultrason Symp*, 2005 **1** 219–22.

## High-performance, high- $T_C$ piezoelectric crystals

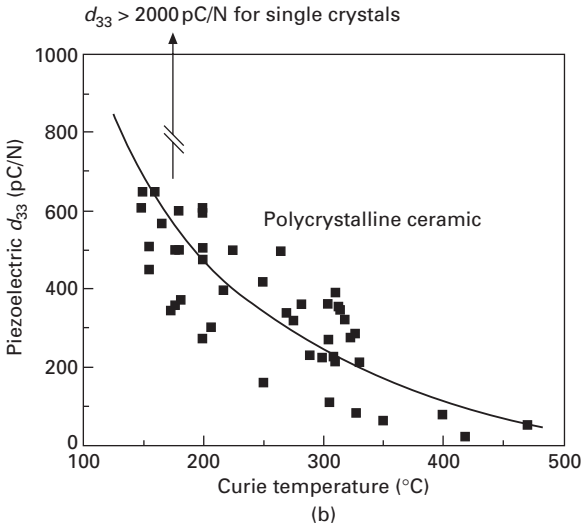
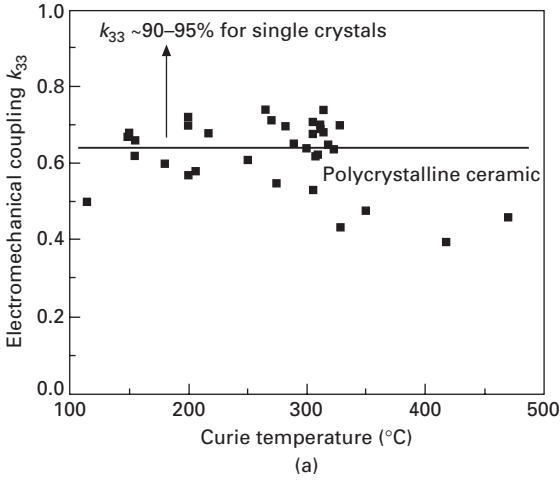
S J Z H A N G, Pennsylvania State University, USA, J L U O,  
TR S Technologies, Inc., USA, and D W S N Y D E R and  
T R S H R O U T, Pennsylvania State University, USA

### 5.1 Introduction

Relaxor-based single crystals, such as  $\text{Pb}(\text{Zn}_{1/3}\text{Nb}_{2/3})\text{O}_3\text{-PbTiO}_3$  (PZNT) and  $\text{Pb}(\text{Mg}_{1/3}\text{Nb}_{2/3})\text{O}_3\text{-PbTiO}_3$  (PMNT), have been recently found to offer significantly high performance, with electromechanical coupling ( $k_{33} > 90\%$ ) and piezoelectric coefficients ( $d_{33} > 2000$  pC/N) that outperform the PZT polycrystalline ceramics ( $k_{33} \sim 75\%$ ,  $d_{33} \sim 400\text{--}600$  pC/N), as shown in Fig. 5.1, making them promising candidates for medical ultrasonics, sonar transducers and solid-state actuators.<sup>1–7</sup> However, their relatively low Curie temperature ( $T_C \sim 130\text{--}170$  °C) will limit their applications in transducers in which thermal stability is anticipated in terms of dielectric and piezoelectric property variation and depolarization as a result of postfabrication processes. These usage will be further restricted by  $T_{R-T}$  – the rhombohedral to tetragonal phase transformation temperature, which is significantly lower than the Curie temperature  $T_C$ , owing to a strongly curved morphotropic phase boundary (MPB). As can be seen in Fig. 5.2, a generic phase diagram for relaxor–PT single crystal systems depicting a strongly curved MPB, showing the  $T_{R-T}$  is far below the Curie temperature, especially at the MPB composition, where the high piezoelectric property is expected.

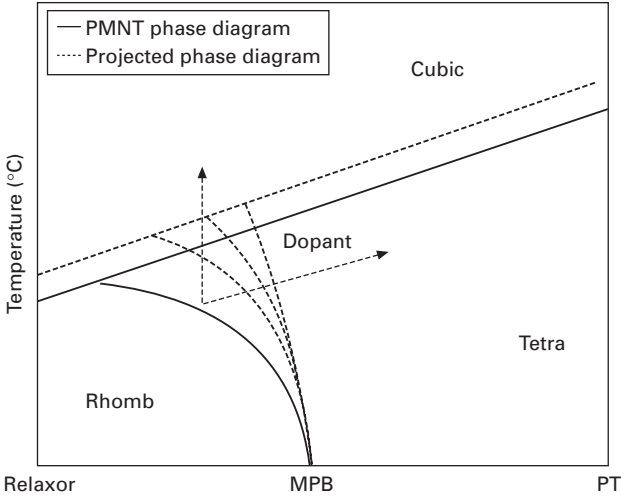
In addition to the thermal environments, piezoelectric crystals used in electromechanical devices are subjected to an electric field and/or mechanical stress, usually the external factors will deteriorate the piezoelectric properties stability owing to the field and/or stress and/or temperature-induced rhombohedral (or monoclinic) phase to tetragonal phase transformation.<sup>8,9</sup> Figure 5.3 shows the electromechanical coupling factor  $k_{33}$  of 0.67PMN–0.33PT (abbreviated PMNT33; the same notation is used throughout the chapter) crystals as a function of electric field and temperature, in which one can see that the coupling factor increases slightly with increasing temperature, and then drops sharply when the crystal in the electric field or thermally induced tetragonal phase.<sup>9</sup> Figure 5.4 gives the piezoelectric coefficient  $d_{33}$  as a function of temperature and dc bias, exhibiting the same tendency as



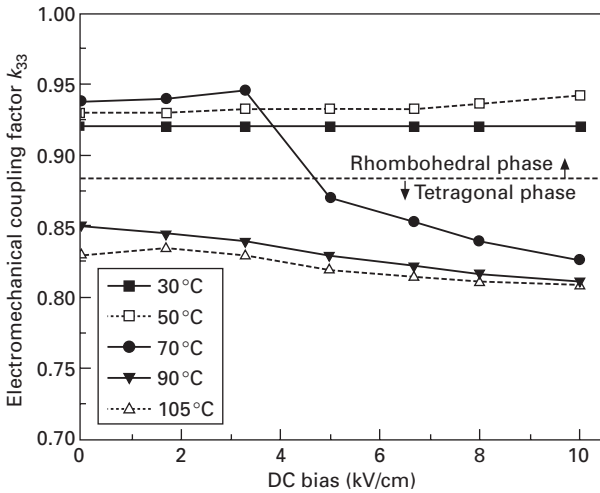


5.1 Electromechanical coupling  $k_{33}$  and piezoelectric  $d_{33}$  of relaxor-PT single crystals, compared with polycrystalline piezoelectric ceramics as a function of Curie temperature; the crystal systems exhibit significantly higher values.

that observed for electromechanical coupling factor. The phase transition is found to occur at 5 kV/cm DC bias when the temperature is around 70 °C, while it is only 2 kV/cm at 90 °C, indicating the piezoelectric behavior depends strongly on both temperature and electric field. As shown in Fig. 5.5, the ferroelectric phase transition temperature (usage temperature range, above which the piezoelectric activity degrades owing to the phase transformation) for rhombohedral PMNT single crystals, decreases with



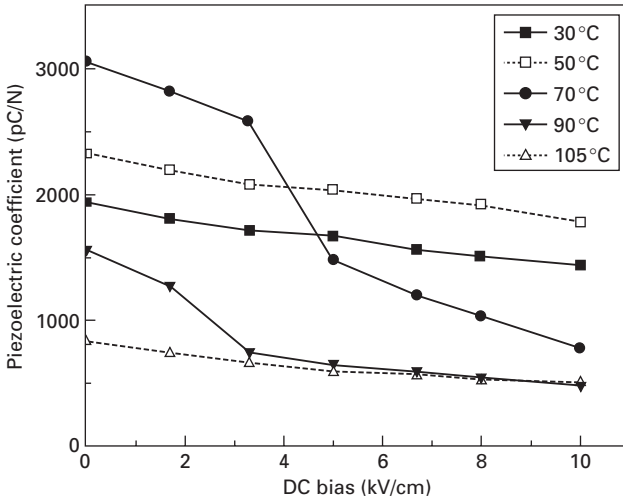
5.2 A generic phase diagram for relaxor-PT crystal systems, depicting a strongly curved MPB; the dotted line is the projected phase diagram for modified systems.



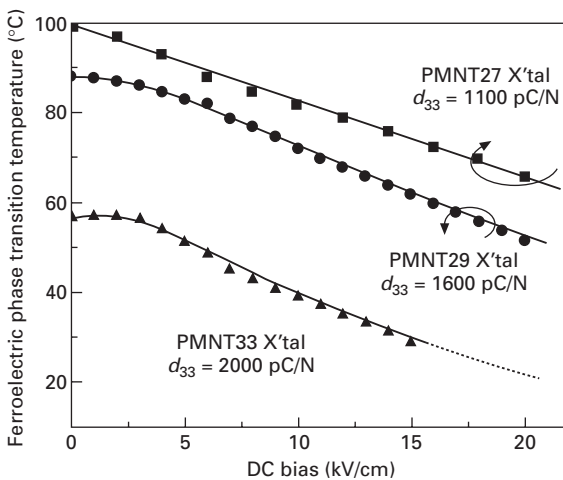
5.3 Electromechanical coupling factor  $k_{33}$  as a function of temperature and dc bias for PMNT33 crystals (after ref. 9).

increasing dc bias field.<sup>10</sup> Figure 5.6 gives the phase diagram of the PMNT system as a function of dc bias, in which the tetragonal phase region is found to be expanded with increasing dc bias, further limiting the usage temperature range for applications.<sup>10</sup>

Higher  $T_C$  with straightening MPB compositions is desirable and projected

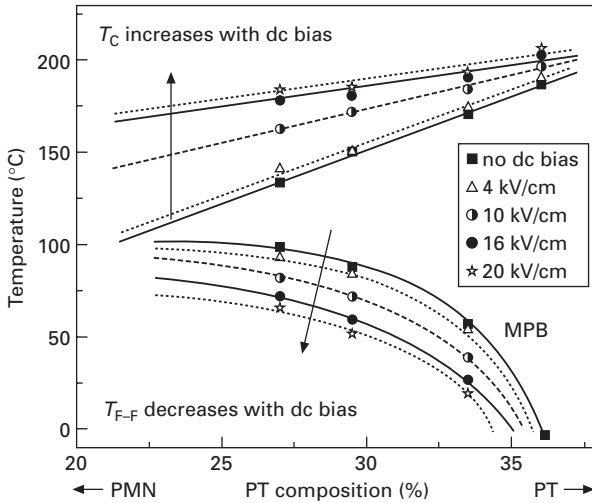


5.4 Piezoelectric coefficient as a function of temperature and dc bias for PMNT33 single crystals.



5.5 The ferroelectric phase transition temperature for the rhombohedral PMNT single crystals as a function of bias (after ref. 10).

in the PMNT systems, as shown in Fig. 5.2, which will broaden the application temperature usage range by 10–20 °C. Among all the relaxor–PT systems,  $\text{Pb}(\text{In}_{1/2}\text{Nb}_{1/2})\text{O}_3\text{--PbTiO}_3$  (PINT),  $\text{Pb}(\text{Sc}_{1/2}\text{Nb}_{1/2})\text{O}_3\text{--PbTiO}_3$  (PSNT) or their ternary systems with PMN end member were found to possess relative high Curie temperatures near the MPB composition. For these systems,  $T_C$  is in the order of 260–310 °C, but  $T_{R-T}$  is in the range of only 50–120 °C,<sup>11–30</sup>



5.6 Phase diagram for the PMNT single crystals under different dc bias fields (after ref. 10).

their poor performance at elevated temperature is still a barrier in many applications.

In this chapter, three approaches were used to enhance the temperature usage range of rhombohedral single crystal perovskites. First, A- or B-site dopant modifications ( $\sim 1\text{--}5\text{ mol}\%$ ) were made to the PMNT system to examine the effect on the MPB curvature. This approach was selected because of the commercial availability of PMNT single crystals using Bridgman growth. Second, crystal growth and characterization of compositions based on PSNT and PINT systems, with emphasis on the  $\text{Pb}(\text{Yb}_{1/2}\text{Nb}_{1/2})\text{O}_3\text{--PbTiO}_3$  (PYNT) systems, which having the highest  $T_C$  over  $330\text{ }^\circ\text{C}$  among the relaxor-PT systems.<sup>31–39</sup> Third, the crystal growth of new bismuth based  $\text{BiScO}_3\text{--PbTiO}_3$  perovskites, which offers significantly higher  $T_C$ s on the order of  $400\text{ }^\circ\text{C}$ , greatly increasing the temperature range for transducer applications.<sup>40–47</sup>

For applications that require even higher temperatures ( $>400\text{ }^\circ\text{C}$ ), for example: the operation of probes within Venus's  $450\text{ }^\circ\text{C}$  atmosphere, coal-fired electric generation plants or the nuclear plants could benefit from high-temperature sensors for health monitoring of furnace components and reactor systems.<sup>48</sup> Considering the Curie temperature for most perovskite systems is lower than  $500\text{ }^\circ\text{C}$ , this chapter will present an introduction of non-perovskite piezoelectric single crystals, including  $\text{LiNbO}_3$ ,  $\text{La}_3\text{Ga}_5\text{SiO}_{14}$ ,  $\text{GaPO}_4$  and  $\text{ReCa}_4\text{O}(\text{BO}_3)_3$  (Re = rare earth element) piezoelectric crystals, for the potential of application at ultra-high temperature.

## 5.2 Background on the growth of relaxor-PT single crystals

Relaxor ferroelectrics are generally lead-based perovskite compounds with the general formula  $\text{Pb}(\text{B}_I\text{B}_{II})\text{O}_3$ , where  $\text{B}_I$  and  $\text{B}_{II}$  are two different ionic species. Myl'nikova and Bokov firstly reported the growth of relaxor single crystals in the late 1950s and single crystals of  $\text{Pb}(\text{Mg}_{1/3}\text{Nb}_{2/3})\text{O}_3$  (PMN),  $\text{Pb}(\text{Zn}_{1/3}\text{Nb}_{2/3})\text{O}_3$  (PZN),  $\text{Pb}(\text{Ni}_{1/3}\text{Nb}_{2/3})\text{O}_3$  (PNN),  $\text{Pb}(\text{Co}_{1/3}\text{Nb}_{2/3})\text{O}_3$  (PCN) were successfully grown by the solution growth technique.<sup>49–51</sup> PZNT single crystals were obtained by the flux method and reported in 1982<sup>52</sup> and in 1989, Shrout *et al.* successfully synthesized single crystals in the PMNT system from high-temperature solution.<sup>53</sup> In the late 1990s, systematic studies on the flux growth (including the modified flux-Bridgman method) of large size PZNT single crystals and Bridgman growth of PMNT crystals were carried out.<sup>54–71</sup> For the growth of PZNT crystals, common fluxes are  $\text{PbO}$  ( $\text{Pb}_3\text{O}_4$ ) and/or a mixture of  $\text{PbO}$  and  $\text{B}_2\text{O}_3$ .<sup>69–71</sup> It was also reported that PZNT crystals can be obtained by top-seeded solution techniques but with less success because of lead evaporation.<sup>72,73</sup> In order to reduce the defects in the PMNT crystals grown by the modified Bridgman method, which include macroscopic inclusions and the composition uniformity, seeded single crystals oriented along the crystallographic directions [001], [110] and [111] were applied during the growth. It was found that good quality PMNT single crystals could be obtained when grown along [111] and [110] directions, but were difficult to grow along the [001] direction because of the anisotropic growth rate, where the [111] direction was found to be more competitive.<sup>60,66,67</sup> Other crystal fabrication techniques, such as solid-state single crystal growth (SSCG), may provide 'single crystal-like' ceramics of the PMNT system as a cost-effective means to further achieve market dominance.<sup>74</sup>

## 5.3 Modification of PMNT single crystals

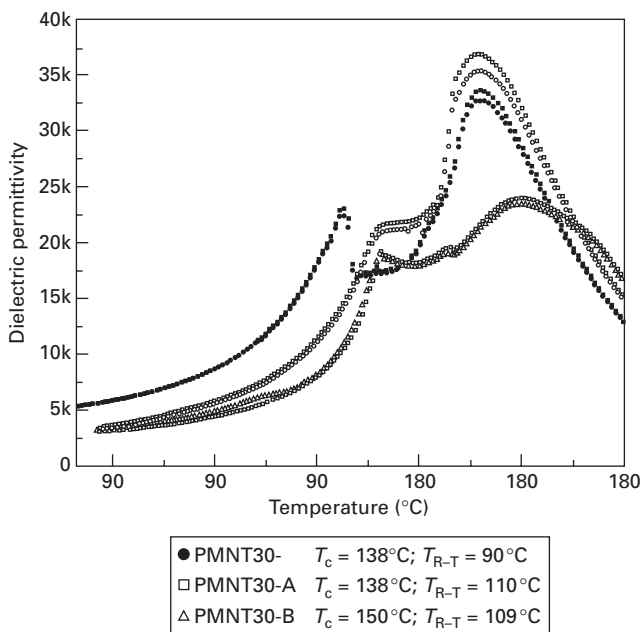
It has been known for some time that there is a correlation between the Curie temperature of perovskite  $\text{ABO}_3$  ferroelectrics and the Goldschmidt tolerance factor. The tolerance factor  $t$  for a perovskite is given by the expression:<sup>75</sup>

$$t = \frac{r_a + r_o}{\sqrt{2}(r_b + r_o)}$$

where  $r_a$  is the ionic radius of A site cations,  $r_b$  is the ionic radius of B site cations and  $r_o$  is the ionic radius of oxygen (perovskite stability is maximized for tolerance factors between 0.8 and 1.05). A correlation between the end member tolerance factor and the Curie temperature of the MPB composition

was proposed based on the data known for the  $\text{ABO}_3\text{-PbTiO}_3$  solid solution systems.<sup>76</sup> As the tolerance factor decreases, the Curie temperature of the MPB composition increases. According to this assumption, A-site cations with smaller ionic radius (when compared with the  $\text{Pb}^{2+}$  ionic radius) or B-site cations with larger ionic radius (when compared with the  $\text{Ti}^{4+}$  ionic radius) were selected as the doping elements for the modifications of the PMNT systems and the preliminary results show that the doping on the A site or B site can enhance the usage temperature range of PMNT30 by 10–20 °C at a doping level of 1–5 mol%.

As shown in Fig. 5.7, the Curie temperature of an A-site modified PMNT30 crystal was found to keep constant while the ferroelectric phase transition increased by 15 °C when compared with the pure counterpart, meanwhile, both the Curie temperature and ferroelectric phase transition temperatures for a B-site modified PMNT30 were found to shift upward by 10–15 °C when compared with the pure crystals. The piezoelectric coefficient for both A-site and B-site modified crystals were found to exhibit comparable values of 1200–1800 pC/N, with slightly improved coercive field.<sup>10</sup>



5.7 Dielectric property as a function of temperature for A- or B-site modified PMNT30, measured at 1, 10 and 100 kHz frequencies, compared with the pure counterpart.

## 5.4 Relaxor–PT systems with high Curie temperature

Table 5.1 lists most of the lead-based relaxor–PT systems, among which the  $\text{Pb}(\text{Sc}_{1/2}\text{Nb}_{1/2})\text{O}_3\text{--PbTiO}_3$  (PSNT),  $\text{Pb}(\text{In}_{1/2}\text{Nb}_{1/2})\text{O}_3\text{--PbTiO}_3$  (PINT) and  $\text{Pb}(\text{Yb}_{1/2}\text{Nb}_{1/2})\text{O}_3\text{--PbTiO}_3$  (PYNT) were found to possess relative high Curie temperatures near their MPB compositions.<sup>39,77–79</sup> Henceforth, numerous researchers focused on single crystals of these binary systems or ternary systems with PMN, in order to achieve high performance over a wide temperature usage range.<sup>11–39</sup>

PSNT single crystals with MPB compositions were successfully grown by the high-temperature solution method, as reported by Yamashita and coworkers<sup>11,15</sup> and Bing and Ye.<sup>12–14</sup> PSNT33 crystals were reported to possess a high Curie temperature of  $T_C \sim 206^\circ\text{C}$ ,  $30\text{--}50^\circ\text{C}$  higher than PMNT and PZNT systems; however, the electromechanical coupling factor and dielectric constant were found to be only  $k_{33} = 72\%$  and 960, respectively, due to the poor quality of the crystals. Ternary systems  $\text{Pb}(\text{Sc}_{1/2}\text{Nb}_{1/2})\text{O}_3\text{--Pb}(\text{Mg}_{1/3}\text{Nb}_{2/3})\text{O}_3\text{--PbTiO}_3$  (PSMNT)<sup>23,24</sup> and  $\text{Pb}(\text{Sc}_{1/2}\text{Nb}_{1/2})\text{O}_3\text{--Pb}(\text{Zn}_{1/3}\text{Nb}_{2/3})\text{O}_3\text{--PbTiO}_3$  (PSZNT)<sup>28,29</sup> were grown by the flux method or solution Bridgman method. A  $T_C$  of  $\sim 200^\circ\text{C}$  with a dielectric constant of about 2600 were found for the grown single crystals, but no piezoelectric properties was reported. Moreover, it was found to be difficult to grow PSNT crystals directly from the melt due to the poor perovskite stability; only small crystals with dimension in the order of few millimeters could be obtained.

Single crystals of PINT and their electromechanical properties were investigated and reported in last few years.<sup>16–22</sup> PINT28 crystals were grown by the high-temperature solution method and the Curie temperature was reported to be  $260^\circ\text{C}$  with the ferroelectric phase transition temperature

Table 5.1 Morphotropic phase boundaries in perovskite  $\text{Pb}(\text{B}_i\text{B}_{ii})\text{O}_3\text{--PT}$  systems

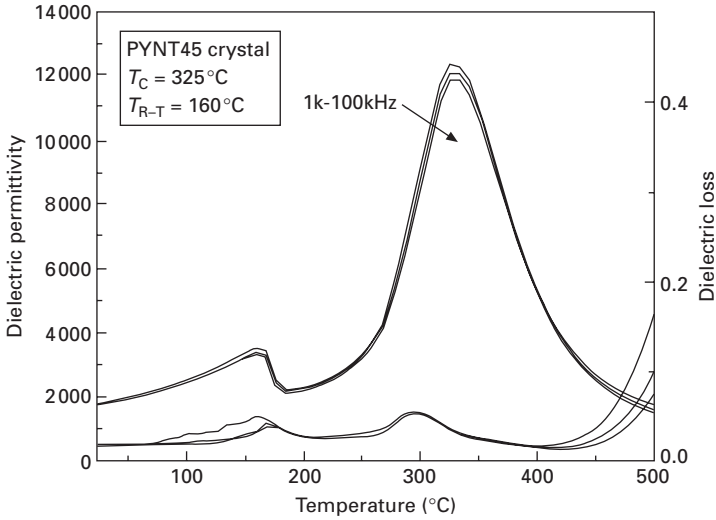
Binary system	PT content on MPB	$T_C$ ( $^\circ\text{C}$ ) at MPB	$T_{R-T}$ ( $^\circ\text{C}$ ) at MPB
$(1-x)\text{Pb}(\text{Zn}_{1/3}\text{Nb}_{2/3})\text{O}_3\text{--}x\text{PbTiO}_3$ (PZNT)	$x \cong 0.09$	$\sim 180$	95
$(1-x)\text{Pb}(\text{Mg}_{1/3}\text{Nb}_{2/3})\text{O}_3\text{--}x\text{PbTiO}_3$ (PMNT)	$x \cong 0.33$	$\sim 150$	80
$(1-x)\text{Pb}(\text{Ni}_{1/3}\text{Nb}_{2/3})\text{O}_3\text{--}x\text{PbTiO}_3$ (PNNT)	$x \cong 0.40$	$\sim 130$	/
$(1-x)\text{Pb}(\text{Co}_{1/3}\text{Nb}_{2/3})\text{O}_3\text{--}x\text{PbTiO}_3$ (PCNT)	$x \cong 0.38$	$\sim 250$	/
$(1-x)\text{Pb}(\text{Sc}_{1/2}\text{Nb}_{1/2})\text{O}_3\text{--}x\text{PbTiO}_3$ (PSNT)	$x \cong 0.43$	$\sim 260$	100
$(1-x)\text{Pb}(\text{Sc}_{1/2}\text{Ta}_{1/2})\text{O}_3\text{--}x\text{PbTiO}_3$ (PSTT)	$x \cong 0.45$	$\sim 205$	/
$(1-x)\text{Pb}(\text{Fe}_{1/2}\text{Nb}_{1/2})\text{O}_3\text{--}x\text{PbTiO}_3$ (PFNT)	$x \cong 0.07$	$\sim 140$	/
$(1-x)\text{Pb}(\text{In}_{1/2}\text{Nb}_{1/2})\text{O}_3\text{--}x\text{PbTiO}_3$ (PINT)	$x \cong 0.37$	$\sim 320$	120
$(1-x)\text{Pb}(\text{Yb}_{1/2}\text{Nb}_{1/2})\text{O}_3\text{--}x\text{PbTiO}_3$ (PYNT)	$x \cong 0.50$	$\sim 360$	160
$(1-x)\text{Pb}(\text{Mg}_{1/2}\text{W}_{1/2})\text{O}_3\text{--}x\text{PbTiO}_3$ (PMWPT)	$x \cong 0.55$	$\sim 60$	/
$(1-x)\text{Pb}(\text{Co}_{1/2}\text{W}_{1/2})\text{O}_3\text{--}x\text{PbTiO}_3$ (PCWPT)	$x \cong 0.45$	$\sim 310$	/

$T_{R-T}$  around 100 °C. The electromechanical coupling factor in sliver mode  $k'_{33}$  was found to be 78% and the longitudinal one was estimated to be 85% at room temperature, which was almost independent of temperature up to 200 °C.<sup>17,18</sup> The enhanced temperature stability of a PINT crystal may be ascribed to the crystal's composition located away from its MPB as well as its high  $T_C$ .<sup>19</sup> The same research group also reported the growth of PINT crystals by the solution Bridgman method. The composition of the grown crystals was found to vary along the growth direction owing to the composition segregation – the same issue encountered in Bridgman-grown PMNT crystals. The  $T_C$  and  $T_{R-T}$  were found to be 300 °C and 120 °C, respectively, for PINT31 crystals.<sup>20</sup> PINT single crystals were also grown directly from the melt using the modified Bridgman method and reported to possess high piezoelectric coefficients  $d_{33} \sim 2000$  pC/N with an electromechanical coupling  $k_{33} \sim 94\%$ , comparable to the PMNT and PZNT systems, while exhibiting a higher  $T_C$  of 200 °C, but no information about the temperature usage range (i.e.  $T_{R-T}$ ) of this crystal was reported.<sup>22</sup> Single crystals in the ternary  $\text{Pb}(\text{In}_{1/2}\text{Nb}_{1/2})\text{O}_3\text{-Pb}(\text{Mg}_{1/3}\text{Nb}_{2/3})\text{O}_3\text{-PbTiO}_3$  (PIMNT) system were also grown using the solution and/or modified Bridgman techniques, a transition temperature on the order of 200 °C with dielectric constant of  $\sim 4000$  and piezoelectric coefficient  $d_{33}$  of  $\sim 2000$  pC/N were reported, however, low ferroelectric phase transitions,  $T_{R-T}$ , on the order of 80–110 °C were observed. Furthermore, large compositional segregation was found along the crystal boules, similar to that found in PINT and PMNT systems.<sup>16</sup>

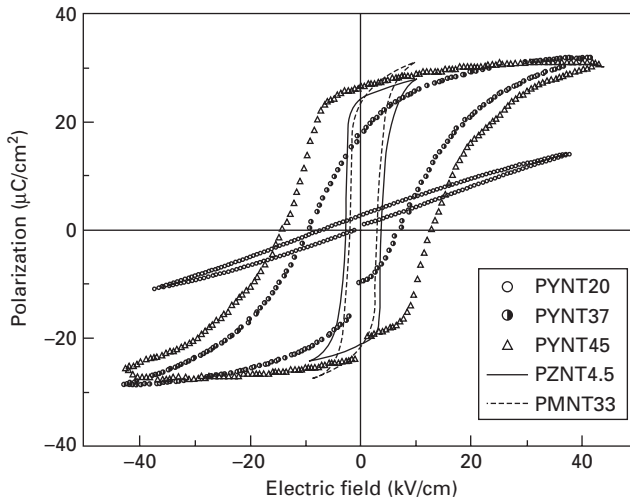
PYNT with the MPB composition (PT content around 50%) was found to possess a  $T_C$  of  $\sim 360$  °C, the highest among all the lead-based relaxor-PT systems (see Table 5.1) and similar to commercial PZT5A ceramics. Piezoelectric single crystals in the PYNT system were grown using the flux method. Perovskite PYNT solid solutions were prepared using the 'columbite process', which consists of presynthesis of the B-site precursor  $\text{YbNbO}_4$  prior to reaction with  $\text{PbO}$  and  $\text{TiO}_2$ , in order to stabilize the perovskite phase.<sup>33,35,80,81</sup> Figure 5.8 presents the dielectric permittivity and dielectric loss for [001] oriented PYNT45 crystals, in which one can see that there are two dielectric anomalies, located at 325 °C and 160 °C, corresponding to the Curie temperature  $T_C$  and the rhombohedral to tetragonal phase transition temperature  $T_{R-T}$ , respectively. The increased  $T_{R-T}$  temperature gives a broadened temperature usage range and also stabilizes the property temperature dependence as reported.<sup>34</sup>

Bipolar polarization loops were measured on [001] oriented PYNT single crystals with various PT contents at 1 Hz and  $\pm 40$  kV/cm electric field. As shown in Fig. 5.9, the shape of the P-E hysteresis loops changes from slim to square with increasing PT content, revealing that the PYNT single crystals transfer from relaxor-like behavior to normal ferroelectric behavior with increasing PT content. The polarization hysteresis measured at 1 Hz and





5.8 Dielectric properties as a function of temperature for the PYNT45 single crystal, measured at 1, 10 and 100 kHz. (after ref. 34).

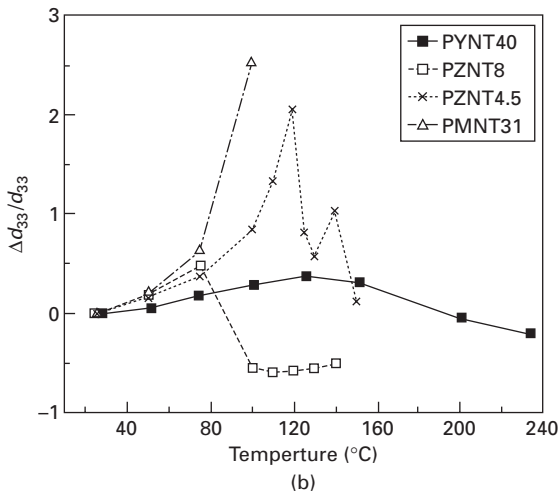
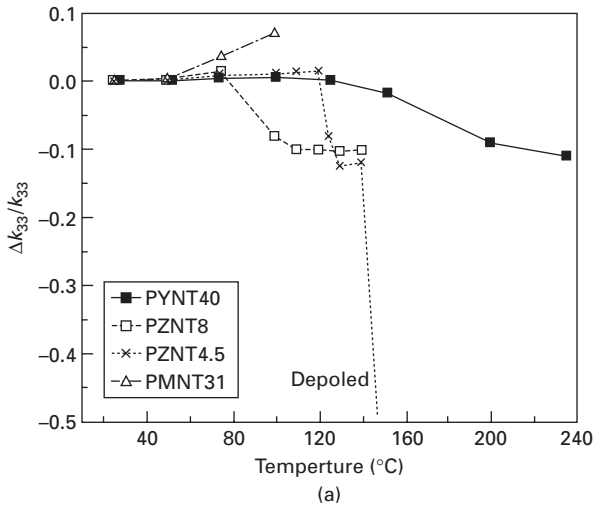


5.9 Polarization hysteresis for the PYNT single crystals with PT content at 0.20, 0.37 and 0.46, respectively, and compared to PZNT4.5 and PMNT33 crystals.

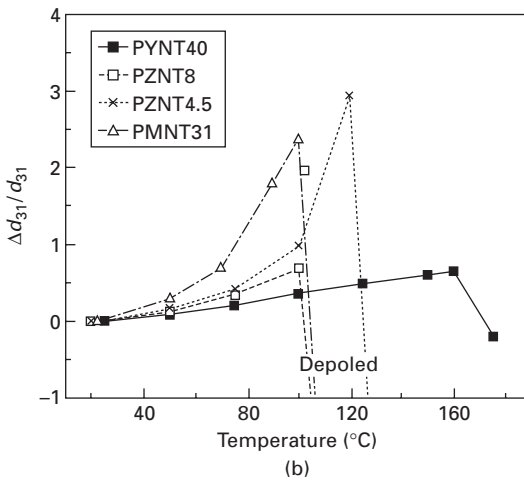
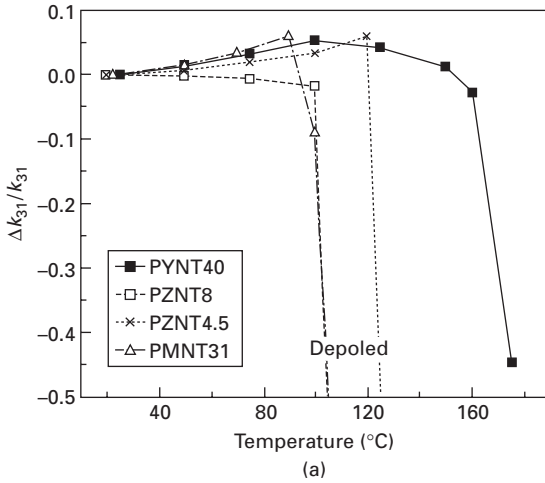
$\pm 10 \text{ kV}/\text{cm}$  field for PZNT4.5 and PMNT33 single crystals were also given in Fig. 5.9 for comparison. The coercive field was found to be  $\sim 13 \text{ kV}/\text{cm}$  for PYNT46, much higher than those of the PZNT and PMNT crystals (which are found to be 3.5 and 2.2  $\text{kV}/\text{cm}$ , respectively).<sup>35</sup>

Figures 5.10 – 5.12 show the electromechanical and piezoelectric properties

as a function of temperature for the PYNT40 single crystals, which are compared with PZNT and PMNT crystals, where  $k_{ij}$  are the electromechanical coupling factors and  $d_{ij}$  are the piezoelectric coefficients, for longitudinal mode ( $ij = 33$ ), lateral mode ( $ij = 31$ ) and shear mode ( $ij = 15$ ) samples, respectively.  $\Delta k/k$  represents the variation of the electromechanical coupling factor at high temperature when compared with room temperature value, while  $\Delta d/d$  gives the variation of the piezoelectric coefficients. It was observed that the values remain nearly constant for all the single crystals until their



5.10 Relative change of longitudinal electromechanical and piezoelectric properties as a function of temperature for different relaxor-PT systems.

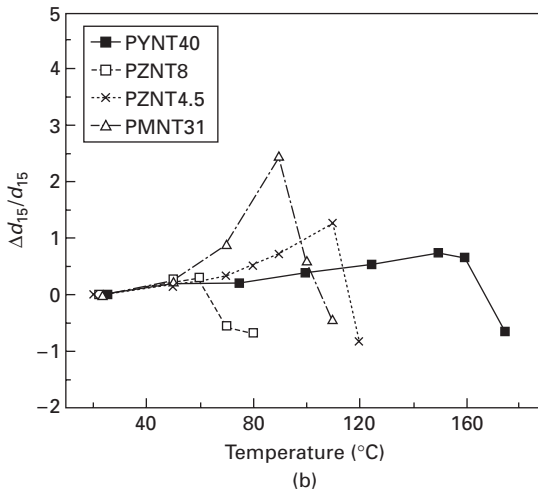
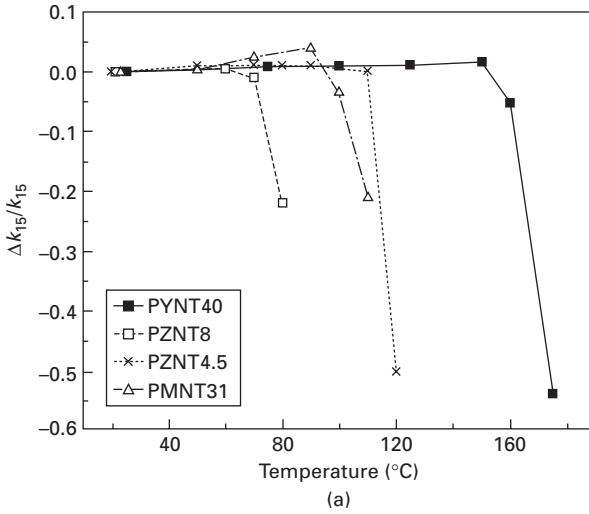


5.11 Relative change of lateral electromechanical and piezoelectric properties as a function of temperature for different relaxor-PT systems.

$T_{R-T}$  temperature, which was around 160 °C for PYNT40, nearly double the upper temperature usage limit compared to PMNT crystals. In addition, the electromechanical and piezoelectric properties of PYNT crystals are comparable to those of the PZNT and PMNT crystals.

## 5.5 High $T_C$ bismuth-based perovskite single crystals

Based on the above Sections 5.3 and 5.4, we can see that the A-site or B-site modifications on the PMNT single crystals can only increase the  $T_C$  and



5.12 Relative change of shear electromechanical and piezoelectric properties as a function of temperature for different relaxor-PT systems.

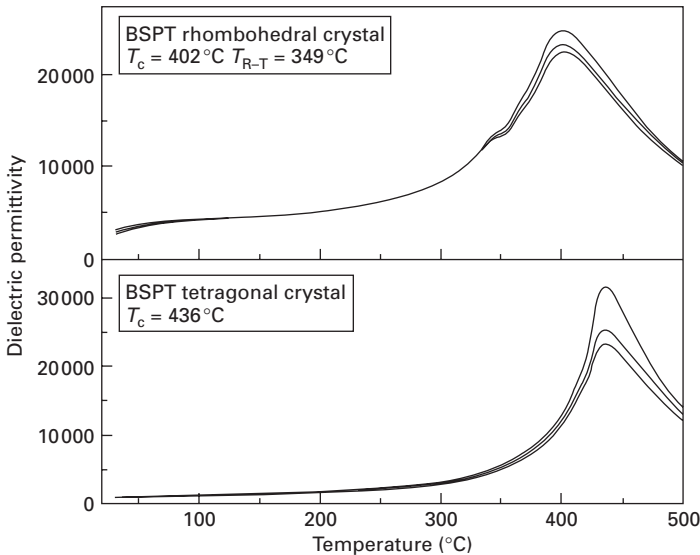
$T_{R-T}$  modestly by 10–20 °C. Of significant potential are crystals near the MPB composition in the PYNT system, with a  $T_C > 330$  °C, even though  $T_{R-T}$  was found to be only half that value at ~160 °C, the result of a strongly curved MPB. The usage range of the lead based relaxor-PTs are still significantly lower than that of PZT-based ceramics.

Recently, a new perovskite system  $(1-x)\text{BiScO}_3-x\text{PbTiO}_3$  (BSPT) with MPB ( $x = 0.64$ ) between the rhombohedral and tetragonal structures, was found to possess a Curie temperature around ~450 °C (100 °C higher than the

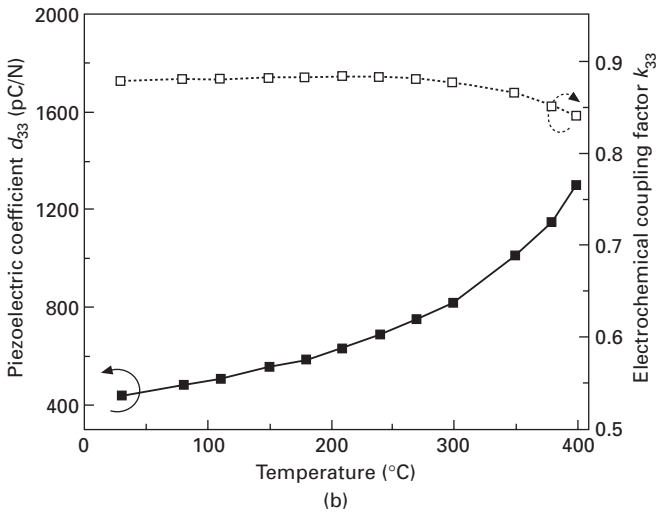
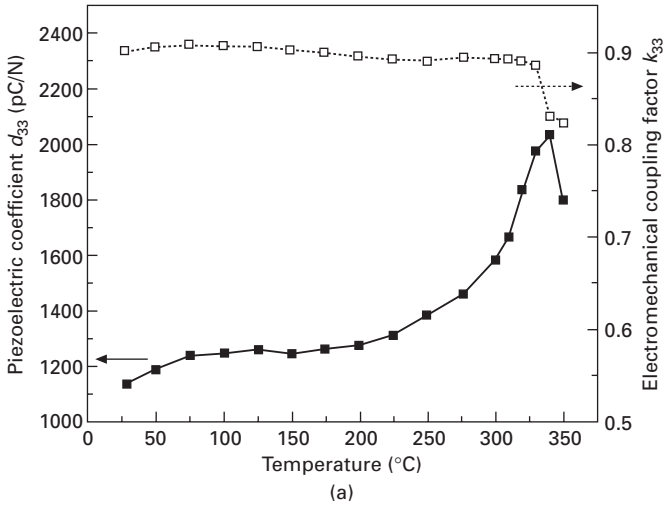
commercial PZT5A materials) with comparable piezoelectric properties ( $\sim 460$  pC/N) in polycrystalline ceramics.<sup>76,82,83</sup> Single crystals of BSPT were grown and the addition of  $\text{BaTiO}_3$  was used to aid in stabilizing the perovskite phase. The characterization of the BSPT single crystals with different PT content has been reported.<sup>40–47</sup>

Figure 5.13 shows the dielectric permittivity as a function of temperature for rhombohedral BSPT57 and tetragonal BSPT66 crystals. Two dielectric anomalies were observed in the curves of the BSPT57 crystals, revealing a  $T_{R-T}$  of  $349^\circ\text{C}$  and a  $T_C$  of  $402^\circ\text{C}$ ,<sup>46</sup> both much higher than the lead based relaxor-PT systems. For tetragonal BSPT66 crystals, however, only one peak at  $436^\circ\text{C}$  was found and believed to be associated with the  $T_C$ .<sup>44</sup> This  $T_C$  was found to be more than  $20^\circ\text{C}$  lower when compared with the reported values for the tetragonal crystals<sup>43</sup> and ceramics,<sup>82</sup> due to the  $\text{BaTiO}_3$  additive. It was observed from Fig. 5.13 that the BSPT crystals exhibit a very flat dielectric constant curve in the temperature range from room temperature to  $300^\circ\text{C}$ .

The temperature dependence of the piezoelectric and electromechanical properties of the rhombohedral BSPT57 and tetragonal BSPT66 crystals for longitudinal mode are shown in Fig. 5.14(a) and (b), respectively. It was found that the  $k_{33}$  value for the BSPT57 crystal was 90% at room temperature and kept constant to  $330^\circ\text{C}$ , close to its  $T_{R-T}$ . The piezoelectric coefficient



5.13 Dielectric properties as a function of temperature for BSPT57 rhombohedral crystals and BSPT66 tetragonal crystals, measured at 1, 10 and 100 kHz frequencies, respectively.



5.14 Electromechanical and piezoelectric properties as a function of temperature for rhombohedral (a, after ref. 46) and tetragonal (b, after ref. 44) BSPT crystals.

was about 1150 pC/N at room temperature, gradually increasing to 2050 pC/N at 330 °C before dropping to 1800 pC/N at 340 °C because of the  $T_{R-T}$  phase transformation.<sup>46</sup> The  $k_{33}$  value for the tetragonal BSPT66 crystals was found to be 88% at room temperature, decreasing slightly to 84% at 400 °C, decreasing due to depoling when the temperature approached its Curie temperature. The  $d_{33}$  value increased from 450 pC/N at room temperature to 1300 pC/N at 400 °C, showing a similar tendency as observed in the rhombohedral BSPT crystals.<sup>44</sup>

Table 5.2 summarizes the detailed dielectric and piezoelectric properties of different single crystal systems, in which one can see that the BSPT system possesses both higher  $T_C$  and  $T_{R-T}$  temperatures when compared with other relaxor–PT systems. Figure 5.15 presents the coercive fields as a function of Curie temperature, in which it is found the coercive field increases linearly with increasing  $T_C$ , indicating systems with higher Curie temperature possess the potential higher acoustic of power (higher coercive field). Figure 5.16 shows the overall temperature usage range for the various relaxor–PT systems, including PZNT, PMNT, PSNT, PINT and PYNT, compared with BSPT system. As shown, the strongly curved MPB limits the temperature usage range of these systems far less than  $T_C$ . Of particular promising are crystals in the bismuth-based BSPT system, with  $T_C$  in the order of 450 °C and  $T_{R-T}$  of 350 °C.

In order to carry on the theoretical and practical studies of the BSPT system, it is necessary to know the full set of material constants of the crystals. The material constants of the rhombohedral BSPT57<sup>42</sup> and tetragonal BSPT66 crystals<sup>44</sup> are compared with PZNT<sup>44,84</sup> and PMNT33<sup>85</sup> systems and given in Tables 5.3 and 5.4.

## 5.6 Non-perovskite piezoelectric single crystals

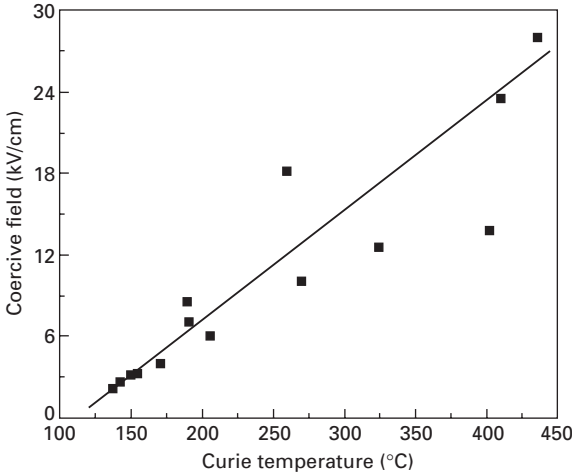
Quartz is one of the earliest piezoelectric materials used in electronic devices and can be grown by hydrothermal technique. The dielectric constant and piezoelectric coefficient were found to be 4.5 and 2 pC/N, respectively. Although piezoelectric  $\alpha$ -quartz has a transition temperature of 573 °C, its usage temperature is normally limited to 350 °C, above which the crystal structure is subject to twinning, destroying its piezoelectric properties. Lithium niobate (LiNbO<sub>3</sub>-LN) can be grown from the melt directly using the Czochralski pulling method. It was reported to possess a Curie temperature of 1150 °C, with a dielectric constant and a piezoelectric coefficient of about 25 and 6 pC/N, respectively.<sup>86</sup> One of the advantages of LN crystals compared with the perovskite systems is the large piezoelectric voltage coefficient, due to the inherently low dielectric constant (for example,  $g_{15} = 91 \times 10^{-3}$  V m/N, three or four times higher when compared with most with the perovskite single crystals). The application temperature range for the LN crystals is limited to 650 °C due to its low resistivity.<sup>86</sup>

Langasite (La<sub>3</sub>Ga<sub>5</sub>SiO<sub>14</sub>, LGS) crystals and its isomorphs (such as langanite and langatite, to name a few) can be grown using the Czochralski method<sup>87,88</sup> and have been actively investigated because of high-temperature bulk acoustic wave (BAW) and surface acoustic wave (SAW) applications.<sup>89</sup> Langasite family crystals do not undergo any phase transformations up to their melting temperatures around 1470 °C, which makes the usage temperature range much broader. The dielectric constants and piezoelectric coefficients are

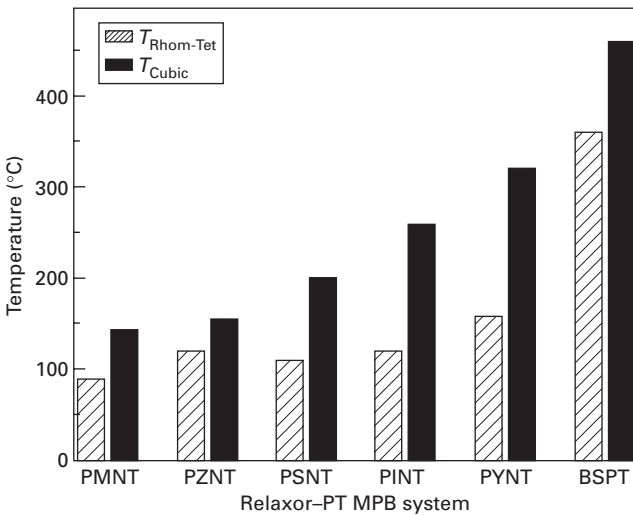
Table 5.2 Detailed dielectric and piezoelectric properties of various single crystals

Crystal	$T_C$ (°C)	$T_{R-T}$ (°C)	$E_c$ (kV/cm)	$\frac{\epsilon_{33}^T}{\epsilon_0}$	$d_{33}$ (pC/N)	$k_{33}$ (%)	$d_{31}$ (pC/N)	$k_{31}$ (%)	Ref.
PMNT31	143	90	2.5	5100	2000	90	-750	80	37
PMNT31-A	138	110	2.2	3600	1400	89	/	/	/
PMNT31-B	150	110	3.1	4800	1500	90	/	/	10
PZNT4.5	155	120	3.2	4400	2100	90-91	-900	83	37
PZNT8	170	100	4	6000	2500	93	-1300	89	37
PZNT12	190	/	8.5	870	576	86	-217	52	44
PSNT33	206	/	6	960	/	72	/	/	11
PINT28	260	100	18	1500	700	85	/	/	17-19
PINT34	200	<100	/	5000	2000	94	/	/	22
PIMNT	191	55	7	3630	1950	~88	/	/	24
PYNT40	270	168	10	2700	1200	88	-500	76	37
PYNT45	325	160	12.5	2000	2000	88-90	-550	78	38
BSPT57	402	349	13.7	3000	1200	90	-560	77	42,46
BSPT58	410	357	23.5	3200	1400	91	-670	80	41
BSPT66	436	/	28	820	440	88	-162	52	44





5.15 Coercive field as a function of Curie temperature for various relaxor-PT single crystals.



5.16 Temperature usage range of various single crystal piezoelectrics (after ref. 45).

found to be in the range of 18~25 and 5~8 pC/N, respectively.<sup>90-92</sup> Gallium orthophosphate ( $GaPO_4$ ) crystal was firstly studied in France,<sup>93</sup> after which, the application of  $GaPO_4$  as a piezoelectric crystal was investigated. The crystals can be grown using hydrothermal technique and presently are produced commercially in autoclaves. It was reported to possess a high  $d_{11}$  value of 4.5 pC/N and a low dielectric constant of ~6. Compared with quartz crystals,

Table 5.3 Measured and derived elastic compliance constants  $s_{ij}$ (10<sup>-12</sup> m<sup>2</sup>/N) and elastic stiffness constants  $c_{ij}$ (1010 N/m<sup>2</sup>) for the rhombohedral BSPT57 and tetragonal BSPT66 crystals, compared with PZNT and PMNT33 single crystals

Crystal	$s_{11}^E$	$s_{12}^E$	$s_{13}^E$	$s_{33}^E$	$s_{66}^E$	$s_{11}^D$	$s_{12}^D$	$s_{13}^D$	$s_{33}^D$	$s_{66}^D$
BSPT57	38.0	-12.2	-25.4	60.0	24.4	27.9	-22.3	-2.9	10.2	24.4
BSPT66	13.5	-2.7	-11.3	34.0	21.0	9.8	-6.3	-1.5	7.3	21.0
PZNT4.5	82.0	-28.5	-51.0	108.0	15.9	61.5	-49.0	-9.0	20.6	15.9
PZNT8	87.0	-13.1	-70.0	141.0	15.4	55.8	-44.2	-8.2	18.5	15.4
PZNT12	22.4	-3.5	-21.0	58.0	27.9	16.3	-9.7	-4.8	14.9	27.9
PMNT33	69.0	-11.1	-55.7	119.6	15.2	44.0	-34.0	-4.1	11.1	15.2
Crystal	$c_{11}^E$	$c_{12}^E$	$c_{13}^E$	$c_{33}^E$	$c_{66}^E$	$c_{11}^D$	$c_{12}^D$	$c_{13}^D$	$c_{33}^D$	$c_{66}^D$
BSPT57	12.6	10.6	9.9	10.0	4.1	15.4	11.6	8.9	12.5	4.1
BSPT66	18.6	12.4	10.3	9.8	4.8	20.2	14.0	7.1	16.6	4.8
PZNT4.5	11.1	10.2	10.1	10.5	6.3	11.3	10.4	9.5	13.5	6.3
PZNT8	11.5	10.5	10.9	11.5	6.5	11.8	10.8	10.0	14.3	6.5
PZNT12	15.2	11.4	9.7	8.7	3.6	15.4	11.6	8.9	12.5	3.6
PMNT33	11.5	10.3	10.2	10.3	6.6	11.7	10.5	9.0	17.4	6.6

*Table 5.4* Piezoelectric coefficients,  $d_{ij}$ (pC/N),  $e_{ij}$  (C/m<sup>2</sup>),  $g_{ij}$  (10<sup>-3</sup> Vm/N) and  $h_{ij}$ (10<sup>8</sup> V/m), electromechanical coupling factors  $k$  and dielectric constants  $\epsilon$  ( $\epsilon_0$ ) for the rhombohedral BSPT57 and tetragonal BSPT66 crystals, compared to PZNT and PMNT33 crystals.

Crystal	$T_C$ (°C)	$E_C$ (kV/cm)	$\epsilon_{33}^T$	$\epsilon_{33}^S$	$k_{33}$	$k_{31}$	$k_{31}$ (45°)	$k_t$
BSPT57	402	13	3000	460	0.91	0.52	0.73	0.56
BSPT66	436	28	820	160	0.88	0.52	0.60	0.64
PZNT4.5	155	3.2	5200	1000	0.91	0.50	0.83	0.50
PZNT8	170	4	7700	984	0.94	0.60	0.89	0.45
PZNT12	190	8.5	870	220	0.86	0.52	0.58	0.55
PMNT33	160	2	8200	680	0.94	0.59	/	0.50

Crystal	$d_{33}$	$d_{31}$	$e_{33}$	$e_{31}$	$g_{33}$	$g_{31}$	$h_{33}$	$h_{31}$
BSPT57	1150	-520	13.6	-6.6	43.3	-19.5	33.4	-16.2
BSPT66	440	-162	9.8	-4.7	60.6	-22.3	69.7	-33.3
PZNT4.5	2000	-970	15.0	-3.7	44.0	-21.0	17.0	-4.3
PZNT8	2890	-1455	15.4	-5.1	42.4	-21.3	17.7	-5.8
PZNT12	576	-217	8.6	-1.9	74.9	-28.2	44.1	-9.6
PMNT33	2820	-1330	20.3	-3.9	38.8	-18.4	33.7	-5.9

GaPO<sub>4</sub> possesses nearly all the advantages of quartz, but also possess higher electromechanical coupling and has thermally stable physical properties up to 950 °C, at which temperature an irreversible transformation into a cristobalite-like phase occurs.<sup>94-98</sup>

Oxyborate crystals ReCa<sub>4</sub>O(BO<sub>3</sub>)<sub>3</sub> (Re = rare earth elements), including GdCOB, YCOB and LaCOB, can be grown from the melt by using the Czochralski method. This family of crystals was extensively studied for non-linear optical or laser applications due to its large transparency range, reasonable non-linear optical coefficient and high damage threshold.<sup>99</sup> The dielectric constants and piezoelectric coefficients were reported to be in the range of 10–15 and 2–9 pC/N, while the electromechanical coupling factor is in the range of 10–17%.<sup>100-105</sup> As observed in the langasite family of crystals, no phase transformation was found to occur prior to its melting temperature ~1500 °C, making the oxyborate crystals promising materials for ultra-high-temperature applications.

## 5.7 Summary

The applications of commercially available PMNT piezoelectric single crystals may be limited by their strongly curved MPB, so it is desirable to obtain crystals with a broader temperature usage range. This chapter introduced various types of high-temperature piezoelectric crystals, with an emphasis on the perovskite ferroelectric systems.

The preliminary results show that A-site or B-site modifications on PMNT single crystals obtain only modest increase ( $\sim 10\text{--}20^\circ\text{C}$ ) in the ferroelectric phase transition. The modification level is controlled at lower than 5 mol% in order to obtain pure perovskite phase. The growth of various relaxor-PT systems were explained by several research groups, but with little success due to the following reasons: either no significant improvement (only up to  $30^\circ\text{C}$  when compared with PMNT crystals) of the ferroelectric phase transition temperature (such as PIN-PMN-PT and PSN-PMN-PT systems), which is the major factor limiting the application temperature range; or it is very hard to grow large crystals and no successful Brigman growth was achieved due to the inferior perovskite stability (like PYNT system, which will form pyrochlore phase or decomposed to PbO at high temperature). Bismuth-based perovskite system, BSPT, was found to have excellent temperature stability, comparable piezoelectric performance, and significantly enhanced usage temperature range when compared to other lead-based perovskite single crystals. But it is difficult to obtain large crystals and hard to control the crystal quality because there are two volatile compositions, PbO and  $\text{Bi}_2\text{O}_3$ , in the material.

Compared with the perovskite MPB single crystals, non-perovskite piezoelectric crystals were found to possess very low piezoelectric and dielectric properties, but their much better temperature-independent properties and much wider usage temperature range make this kind of crystals employable where stable piezoelectric responses at ultra-high temperatures are required. Large piezoelectric voltage coefficients are expected in these crystals because of the ultra-low dielectric constant. Usually these piezoelectric crystals have very low symmetry – for example, the langasite family and  $\text{GaPO}_3$  belong to 32 group, and the oxyborate family belongs to m group – which make it very hard to find suitable orientations for the practical applications. The high resistivity should also be considered in the ultra-high-temperature sensor or actuator applications because of the length of time that a charge can be maintained within a sensor or actuator is proportional to the RC time constant.

## 5.8     Future trends

The future trend for high-temperature piezoelectric single crystals may be focused on two issues, first, how to raise the Curie temperature and/or the usage temperature range of the ferroelectric single crystals? Three approaches are discussed in this chapter, in which the bismuth-based solid solution is very promising owing to the lower tolerance factor, when compared with their lead-based counterparts, and supposed to have higher Curie temperature in the MPB composition based on the tolerance factor. Second, how to commercialize the crystals, which includes how to get large, high-quality crystals and how to reduce the production cost? Owing to perovskite unstable

and/or high-temperature decomposition for many of the lead-based and bismuth-based solid solution, it is difficult to grow the crystal from melt directly. So it is important to select suitable flux compositions in the high-temperature solution or flux Bridgman growth methods. Also, the solid-state conversion crystal growth method has the advantage of low-cost and composition control (homogeneous composition), which is also a feasible solution to obtain large size single crystals.

## 5.9 Acknowledgment

The work was supported by ONR and NIH under #P41-RR11795.

## 5.10 References

- 1 Park S E and Shrout T R, 'Ultrahigh strain and piezoelectric behavior in relaxor based ferroelectric single crystals', *J. Appl. Phys.*, 1997 **82** 1804–11.
- 2 Park S E and Hackenberger W, 'High performance single crystal piezoelectrics: applications and issues', *Curr. Opin. in Sol. Stat. Mat. Sci.*, 2002 **6** 11–18.
- 3 Park S E and Shrout T R, 'Characteristics of relaxor-based piezoelectric single crystals for ultrasonic transducers', *IEEE Trans. Ultrason. Ferroelect. Freq. Contr.*, 1997 **44** 1140–47.
- 4 Zhang S J, Lebrun L, Liu S F, Rhee S, Randall C A and Shrout T R, 'Piezoelectric shear coefficients of  $\text{Pb}(\text{Zn}_{1/3}\text{Nb}_{2/3})\text{O}_3$ - $\text{PbTiO}_3$  single crystals', *Jpn. J. Appl. Phys.*, 2002 **41** L1099–102.
- 5 Park S E and Shrout T R, 'Relaxor based ferroelectric single crystals for electro-mechanical actuators', *Mater. Res. Innovat.*, 1997 **1** 20–25.
- 6 Zhang R, Jiang B, Jiang W H and Cao W W, 'Anisotropy in domain engineered  $0.92\text{Pb}(\text{Zn}_{1/3}\text{Nb}_{2/3})\text{O}_3$ - $0.08\text{PbTiO}_3$  single crystal and analysis of its property fluctuations', *IEEE Trans. Ultrason. Ferro. Freq. Contr.*, 2002 **49** 1622–7.
- 7 Dammak H, Renault A E, Gaucher P, Thi M P and Calvarin G, 'Origin of the giant piezoelectric properties in the [001] domain engineered relaxor single crystals', *Jpn. J. Appl. Phys.*, 2003 **42** 6477–82.
- 8 Davis M, Damjanovic D and Setter N, 'Electric-field-, temperature-, and stress-induced phase transitions in relaxor ferroelectric single crystals', *Phys. Rev. B*, 2006 **73** 014115 (1–16).
- 9 Zhang S J, Luo J, Xia R, Rehrig P W, Randall C A and Shrout T R, 'Field-induced piezoelectric response in  $\text{Pb}(\text{Mg}_{1/3}\text{Nb}_{2/3})\text{O}_3$ - $\text{PbTiO}_3$  single crystals', *Solid State Commun.*, 2006 **137** 16–20.
- 10 Zhang S J, Luo J, Shanta R, Snyder D W and Shrout T R, 'Modified  $\text{Pb}(\text{Mg}_{1/3}\text{Nb}_{2/3})\text{O}_3$ - $\text{PbTiO}_3$  single crystals for high temperature application', *Proceedings of 15<sup>th</sup> IEEE-ISAF*, NC, Sunset beach, July 31–August 2, ed. A Gruverman, 261–4, 2006.
- 11 Yamashita Y and Harada K, 'Crystal growth and electrical properties of lead scandium niobate lead titanate binary single crystals', *Jpn. J. Appl. Phys.*, 1997 **36** 6039–42.
- 12 Bing Y H and Ye Z G, 'Effects of chemical compositions on the growth of relaxor ferroelectric  $\text{Pb}(\text{Sc}_{1/2}\text{Nb}_{1/2})\text{O}_3$ - $\text{PbTiO}_3$  single crystals', *J. Cryst. Growth*, 2003 **250** 118–25.

- 13 Bing Y H and Ye Z G, 'Synthesis, phase segregation and properties of piezo-/ferroelectric  $\text{Pb}(\text{Sc}_{1/2}\text{Nb}_{1/2})\text{O}_3\text{-PbTiO}_3$  single crystals', *J. Cryst. Growth*, 2006 **287** 326–9.
- 14 Bing Y H and Ye Z G, 'Effects of growth conditions on the domain structure and dielectric properties of  $\text{Pb}(\text{Sc}_{1/2}\text{Nb}_{1/2})\text{O}_3\text{-PbTiO}_3$  single crystals', *Mater. Sci. and Eng. B*, 2005 **120** 72–5.
- 15 Yamashita Y and Shimanuki S, 'Synthesis of lead scandium niobate–lead titanate pseudo binary system single crystals', *Mater. Res. Bull.*, 1996 **31** 887–95.
- 16 Guo Y, Luo H, He T and Yin Z, 'Peculiar properties of a high Curie temperature  $\text{Pb}(\text{In}_{1/2}\text{Nb}_{1/2})\text{O}_3\text{-PbTiO}_3$  single crystal grown by the modified Bridgman technique', *Solid Stat. Commun.*, 2002 **123** 417–20.
- 17 Yasuda N, Ohwa H, Kume M, Hayashi K, Hosono Y and Yamashita Y, 'Crystal growth and electrical properties of lead indium niobate–lead titanate binary single crystal', *J. Cryst. Growth*, 2001 **229** 299–304.
- 18 Yasuda N, Ohwa H, Kume M and Yamashita Y, 'Piezoelectric properties of a high Curie temperature  $\text{Pb}(\text{In}_{1/2}\text{Nb}_{1/2})\text{O}_3\text{-PbTiO}_3$  binary system single crystal near a morphotropic phase boundary', *Jpn. J. Appl. Phys.*, 2000 **39** L66–8.
- 19 Yasuda N, Ohwa H, Hasegawa D, Hosono H, Yamashita Y, Iwata M and Ishibashi Y, 'Dielectric and piezoelectric properties of lead indium niobate lead titanate single crystal with high Curie temperature near morphotropic phase boundary', *Ferroelectrics*, 2002 **270** 247–52.
- 20 Yasuda N, Mori N, Ohwa H, Hosono Y, Yamashita Y, Iwata M, Maeda M, Suzuki I and Ishibashi Y, 'Crystal growth and some properties of lead indium niobate–lead titanate single crystals produced by solution Bridgman method', *Jpn. J. Appl. Phys.*, 2002 **41** 7007–10.
- 21 Yasuda N, Ohwa H, Hasegawa D, Hayashi K, Hosono Y, Yamashita Y, Iwata M and Ishibashi Y, 'Temperature dependence of piezoelectric properties of a high Curie temperature  $\text{Pb}(\text{In}_{1/2}\text{Nb}_{1/2})\text{O}_3\text{-PbTiO}_3$  binary system single crystal near a morphotropic phase boundary', *Jpn. J. Appl. Phys.*, 2000 **39** 5586–8.
- 22 Guo Y, Luo H, He T, Pan X and Yin Z, 'Electric field induced strain and piezoelectric properties of a high Curie temperature  $\text{Pb}(\text{In}_{1/2}\text{Nb}_{1/2})\text{O}_3\text{-PbTiO}_3$  single crystal', *Mater. Res. Bull.*, 2003 **38** 857–64.
- 23 Hosono Y, Harada K, Yamashita Y, Dong M and Ye Z G, 'Growth, electric and thermal properties of lead scandium niobate–lead magnesium niobate–lead titanate ternary single crystals', *Jpn. J. Appl. Phys.*, 2000 **39** 5589–92.
- 24 Hosono Y, Yamashita Y, Sakamoto H and Ichinose N, 'Crystal growth of  $\text{Pb}(\text{In}_{1/2}\text{Nb}_{1/2})\text{O}_3\text{-Pb}(\text{Mg}_{1/3}\text{Nb}_{2/3})\text{O}_3\text{-PbTiO}_3$  and  $\text{Pb}(\text{Sc}_{1/2}\text{Nb}_{1/2})\text{O}_3\text{-Pb}(\text{Mg}_{1/3}\text{Nb}_{2/3})\text{O}_3\text{-PbTiO}_3$  piezoelectric single crystals using the solution Bridgman method', *Jpn. J. Appl. Phys.*, 2003 **42** 6062–7.
- 25 Hosono Y, Yamashita Y, Sakamoto H and Ichinose N, 'Growth of single crystals of high Curie temperature  $\text{Pb}(\text{In}_{1/2}\text{Nb}_{1/2})\text{O}_3\text{-Pb}(\text{Mg}_{1/3}\text{Nb}_{2/3})\text{O}_3\text{-PbTiO}_3$  ternary systems near morphotropic phase boundary', *Jpn. J. Appl. Phys.*, 2003 **42** 5681–6.
- 26 Yamashita Y, Harada K, Hosono Y, Natsume S and Ichinose N, 'Effects of B-site ions on the electromechanical coupling factors of  $\text{Pb}(\text{B}'\text{B}'')\text{O}_3\text{-PbTiO}_3$  piezoelectric materials', *Jpn. J. Appl. Phys.*, 1998 **37** 5288–91.
- 27 Hosono Y, Yamashita Y, Sakamoto H and Ichinose N, 'Large piezoelectric constant of high Curie temperature  $\text{Pb}(\text{In}_{1/2}\text{Nb}_{1/2})\text{O}_3\text{-Pb}(\text{Mg}_{1/3}\text{Nb}_{2/3})\text{O}_3\text{-PbTiO}_3$  ternary single crystal near morphotropic phase boundary', *Jpn. J. Appl. Phys.*, 2002 **41** L1240–2.

- 28 Ichinose N, Saigo Y, Hosono Y and Yamashita Y, 'Crystal growth and electrical properties of high  $T_C$  relaxor-PbTiO<sub>3</sub> system single crystals', *Ferroelectrics*, 2001 **261** 205–12.
- 29 Ichinose N, Saigo Y, Hosono Y and Yamashita Y, 'Preparation and dielectric properties of high  $T_C$  relaxor-based single crystals', *Ferroelectrics*, 2002 **267** 311–16.
- 30 Duan Z Q, Xu G S, Wang X F, Yang D F, Pan X M and Wang P C, 'Electrical properties of high Curie temperature (1-x)Pb(In<sub>1/2</sub>Nb<sub>1/2</sub>)O<sub>3</sub>-xPbTiO<sub>3</sub> single crystals grown by the solution Bridgman technique', *Solid State Commun.*, 2005 **134** 559–63.
- 31 Shrout T R, Eitel R E, Zhang S J, Randall C A, Alberta E and Rehrig P W, 'Recent developments in transition temperature perovskite crystals', *IEEE Ultrasonic Symposium*, Honolulu, 2003 774–77.
- 32 Yasuda N, Ohwa H, Kume M, Hosono Y, Yamashita Y, Ishino S, Terauchi H, Iwata M and Ishibashi Y, 'Crystal growth and dielectric properties of solid solutions of Pb(Yb<sub>1/2</sub>Nb<sub>1/2</sub>)O<sub>3</sub>-PbTiO<sub>3</sub> with a high Curie temperature near a morphotropic phase boundary', *Jpn. J. Appl. Phys.*, 2001 **40** 5664–77.
- 33 Zhang S J, Rehrig P W, Randall C A and Shrout T R, 'Crystal growth and electrical properties of Pb(Yb<sub>1/2</sub>Nb<sub>1/2</sub>)O<sub>3</sub>-PbTiO<sub>3</sub> perovskite single crystals', *J. Cryst. Growth*, 2002 **234** 415–20.
- 34 Zhang S J, Priya S, Furman E, Shrout T R and Randall C A, 'A random-field model for polarization reversal in Pb(Yb<sub>1/2</sub>Nb<sub>1/2</sub>)O<sub>3</sub>-PbTiO<sub>3</sub> single crystals', *J. Appl. Phys.*, 2002 **91** 6002–6.
- 35 Zhang S J, Rhee S, Randall C A and Shrout T R, 'Dielectric and piezoelectric properties of high Curie temperature single crystals in the Pb(Yb<sub>1/2</sub>Nb<sub>1/2</sub>)O<sub>3</sub>-PbTiO<sub>3</sub> solid solution series', *Jpn. J. Appl. Phys.*, 2002 **41** 722–26.
- 36 Zhang S J, Lebrun L, Rhee S, Randall C A and Shrout T R, 'Shear mode piezoelectric properties of Pb(Yb<sub>1/2</sub>Nb<sub>1/2</sub>)O<sub>3</sub>-PbTiO<sub>3</sub> single crystals', *Appl. Phys. Lett.*, 2002 **81** 892–94.
- 37 Zhang S J, Lebrun L, Rhee S, Randall C A and Shrout T R, 'Dielectric and piezoelectric properties as a function of temperature for Pb(Yb<sub>1/2</sub>Nb<sub>1/2</sub>)O<sub>3</sub>-PbTiO<sub>3</sub> single crystals', *Proceedings of 13<sup>th</sup> IEEE-ISAF*, NJ, Piscataway, 2002 455–58.
- 38 Zhang S J, Lebrun L, Randall C A and Shrout T R, 'High Curie temperature, high performance perovskite single crystals in the Pb(Yb<sub>1/2</sub>Nb<sub>1/2</sub>)O<sub>3</sub>-PbTiO<sub>3</sub> and BiScO<sub>3</sub>-PbTiO<sub>3</sub> systems', in R. Gue *et al.* (eds) *Morphotropic Phase Boundary Perovskites, High Strain Piezoelectrics and Dielectric Ceramics actions* OH, Westerville, 2001 85–93.
- 39 Yamashita Y, 'Large electromechanical coupling factors in perovskite binary material system', *Jpn. J. Appl. Phys.*, 1994 **33** 5328–31.
- 40 Zhang S J, Randall C A and Shrout T R, 'Dielectric and piezoelectric properties of BiScO<sub>3</sub>-PbTiO<sub>3</sub> crystals with morphotropic phase boundary composition', *Jpn. J. Appl. Phys.*, 2004 **43** 6199–203.
- 41 Zhang S J, Randall C A and Shrout T R, 'Electromechanical properties in rhombohedral BiScO<sub>3</sub>-PbTiO<sub>3</sub> single crystals as a function of temperature', *Jpn. J. Appl. Phys.*, 2003 **42** L1152–4.
- 42 Zhang S J, Randall C A and Shrout T R, 'Characterization of perovskite piezoelectric single crystals of 0.43BiScO<sub>3</sub>-0.57PbTiO<sub>3</sub> with high Curie temperature', *J. Appl. Phys.*, 2004 **95** 4291–5.
- 43 Zhang S J, Lebrun L, Rhee S, Eitel R E, Randall C A and Shrout T R, 'Crystal growth and characterization of new high Curie temperature BiScO<sub>3</sub>-PbTiO<sub>3</sub> single crystals', *J. Cryst. Growth*, 2002 **236** 210–16.

- 44 Zhang S J, Randall C A and Shrout T R, 'Dielectric, piezoelectric and elastic properties of tetragonal  $\text{BiScO}_3\text{-PbTiO}_3$  single crystal with single domain', *Solid State Commun.*, 2004 **131** 41–45.
- 45 Zhang S J, Randall C A and Shrout T R, 'Recent developments in high Curie temperature perovskite single crystals', *IEEE Trans. Ultrason. Ferro. Freq. Cont.*, 2005 **52** 564–69.
- 46 Zhang S J, Randall C A and Shrout T R, 'High Curie temperature piezocrystals in the  $\text{BiScO}_3\text{-PbTiO}_3$  perovskite system', *Appl. Phys. Lett.*, 2003 **83** 3150–52.
- 47 Shrout T R, Zhang S J, Eitel R, Stringer C and Randall C A, 'High performance, high temperature perovskite piezoelectrics', *Proceedings of 14<sup>th</sup> IEEE-ISAF*, NJ, Piscataway, 2004 126–29.
- 48 Schulz M J, Sundaresan M J, McMichael J, Clayton D, Sadler R and Nagel B, 'Piezoelectric materials at elevated temperature', *J. Intell. Mater. Struct.*, 2003 **14** 693–705.
- 49 Lim L C, 'Flux growth of  $\text{Pb}(\text{Zn}_{1/3}\text{Nb}_{2/3})\text{O}_3\text{-PbTiO}_3$  and  $\text{Pb}(\text{Mg}_{1/3}\text{Nb}_{2/3})\text{O}_3\text{-PbTiO}_3$  single crystals', in *Piezoelectric Single Crystals and Their Applications*, Ed. Trolrier-McKinstry S, Cross L and Yamashita Y, Pennsylvania State University, 2004 117.
- 50 Myl'nikova I E and Bokov V A, 'Some dielectric properties of single crystals of  $\text{Pb}_3\text{NiNb}_2\text{O}_3$ ', *Kristallografiya*, 1959 **4** 433–34.
- 51 Bokov V A and Myl'nikova I E, 'Ferroelectric properties of monocrystals of new perovskite type compounds', *Soviet Physics – Solid State*, 1961 **2** 2428–32.
- 52 Kuwata J, Uchino K and Nomura S, 'Dielectric and piezoelectric properties of  $0.91\text{Pb}(\text{Zn}_{1/3}\text{Nb}_{2/3})\text{O}_3\text{-}0.09\text{PbTiO}_3$  single crystals', *Jpn. J. Appl. Phys.*, 1982 **21** 1298–302.
- 53 Shrout T R, Chang Z, Kim N and Markgraf S, 'Dielectric behavior of single crystals near the  $\text{Pb}(\text{Mg}_{1/3}\text{Nb}_{2/3})\text{O}_3\text{-PbTiO}_3$  morphotropic phase boundary', *Ferroelectric Lett. Sec.*, 1990 **12** 63–69.
- 54 Park S E, Mulvihill M L, Risch G and Shrout T R, 'The effect of growth conditions on the dielectric properties of  $\text{Pb}(\text{Zn}_{1/3}\text{Nb}_{2/3})\text{O}_3$  single crystals', *Jpn. J. Appl. Phys.*, 1997 **36** 1154–58.
- 55 Zhang S J, Lebrun L, Jeong D Y, Randall C A, Zhang Q M and Shrout T R, 'Growth and characterization of Fe-doped  $\text{Pb}(\text{Zn}_{1/3}\text{Nb}_{2/3})\text{O}_3\text{-PbTiO}_3$  single crystals', *J. Appl. Phys.*, 2003 **93** 9257–62.
- 56 Zhang S J, Lebrun L, Randall C A and Shrout T R, 'Growth and electrical properties of (Mn,F) co-doped  $0.92\text{Pb}(\text{Zn}_{1/3}\text{Nb}_{2/3})\text{O}_3\text{-}0.08\text{PbTiO}_3$  single crystal', *J. Cryst. Growth*, 2004 **267** 204–12.
- 57 Zhang S J, Lebrun L, Randall C A and Shrout T R, 'Orientation dependence properties of modified tetragonal  $0.88\text{Pb}(\text{Zn}_{1/3}\text{Nb}_{2/3})\text{O}_3\text{-}0.12\text{PbTiO}_3$  single crystals', *Phys. Stat. Sol. (a)*, 2005 **202** 151–57.
- 58 Ye Z G, Tissor P and Schmid H, 'Pseudo-binary  $\text{Pb}(\text{Mg}_{1/3}\text{Nb}_{2/3})\text{O}_3\text{-PbO}$  phase diagram and crystal growth of  $\text{Pb}(\text{Mg}_{1/3}\text{Nb}_{2/3})\text{O}_3$ ', *Mat. Res. Bull.*, 1990 **25** 739–48.
- 59 Dong M and Ye Z G, 'High temperature solution growth and characterization of the piezo-/ferroelectric  $\text{Pb}(\text{Mg}_{1/3}\text{Nb}_{2/3})\text{O}_3\text{-PbTiO}_3$  single crystals', *J. Cryst. Growth*, 2000 **209** 81–90.
- 60 Rehrig P W, Hackenberger W S, Jiang X N, Shrout T R, Zhang S J and Speyer R, 'Status of piezoelectric single crystal growth for medical transducer applications', *IEEE Ultrasonics Symposium*, Honolulu, 2003 766–69.
- 61 Fang B J, Xu H Q, He T H, Luo H S and Yin Z, 'Growth mechanism and electrical



- properties of  $\text{Pb}(\text{Zn}_{1/3}\text{Nb}_{2/3})\text{O}_3\text{-PbTiO}_3$  single crystals by a modified Bridgman method', *J. Cryst. Growth*, 2002 **244** 318–26.
- 62 Fang B J, Luo H S, Xu H, He T and Yin Z, 'Growth of  $\text{Pb}(\text{Zn}_{1/3}\text{Nb}_{2/3})\text{O}_3\text{-PbTiO}_3$  single crystals directly from melt', *Jpn. J. Appl. Phys.*, 2001 **40** L1377–79.
- 63 Harada K, Hosono Y, Yamashita Y and Miwa K, 'Piezoelectric  $\text{Pb}(\text{Mg}_{1/3}\text{Nb}_{2/3})\text{O}_3\text{-PbTiO}_3$  single crystals with a diameter of 2 inches by the solution Bridgman method supported on the bottom of a crucible', *J. Cryst. Growth*, 2001 **229** 294–98.
- 64 Matsushita M, Tachi T and Echizenya K, 'Growth of 3 inch single crystals of piezoelectric  $\text{Pb}(\text{Mg}_{1/3}\text{Nb}_{2/3})\text{O}_3\text{-PbTiO}_3$  by the supported solution Bridgman method', *J. Cryst. Growth*, 2002 **237–9**, 853–57.
- 65 Han P, Yan W, Tian J, Huang X and Pan H, 'Cut directions for the optimization of piezoelectric coefficients of lead magnesium niobate–lead titanate ferroelectric crystals', *Appl. Phys. Lett.*, 2005 **86** 052902.
- 66 Luo H, Xu G, Xu H, Wang P and Yin Z, 'Compositional homogeneity and electrical properties of lead magnesium niobate titanate single crystals grown by a modified Bridgman technique', *Jpn. J. Appl. Phys.*, 2000 **39** 5581–85.
- 67 Xu G, Luo H, Guo Y, Gao Y, Xu H, Qi Z, Zhong W and Yin Z, 'Growth and piezoelectric properties of  $\text{Pb}(\text{Mg}_{1/3}\text{Nb}_{2/3})\text{O}_3\text{-PbTiO}_3$  crystals by the modified Bridgman technique', *Solid State Commun.*, 2001 **120** 321–24.
- 68 Shanthi M, Hoe K H, Lim C Y H and Lim L C, 'Overpoling induced property degradation in  $\text{Pb}(\text{Mg}_{1/3}\text{Nb}_{2/3})\text{O}_3\text{-PbTiO}_3$  single crystals of near morphotropic phase boundary compositions', *Appl. Phys. Lett.*, 2005 **86** 262908.
- 69 Lim L C and Rajan K K, 'High homogeneity high performance flux-grown  $\text{Pb}(\text{Zn}_{1/3}\text{Nb}_{2/3})\text{O}_3\text{-PbTiO}_3$  single crystals', *J. Cryst. Growth*, 2004 **271** 435–44.
- 70 Rajan K K, Ng Y S, Zhang J and Lim L C, '[001] poled  $\text{Pb}(\text{Zn}_{1/3}\text{Nb}_{2/3})\text{O}_3\text{-PbTiO}_3$   $k_{31}$  actuators: effects of initial domain structure, length orientation, and poling conditions', *Appl. Phys. Lett.*, 2004 **85** 4136–38.
- 71 Kumar F J, Lim L C, Chilong C and Tan M J, 'Morphological aspects of flux grown  $\text{Pb}(\text{Zn}_{1/3}\text{Nb}_{2/3})\text{O}_3\text{-PbTiO}_3$  crystals', *J. Cryst. Growth*, 2000 **216** 311–16.
- 72 Chen W and Ye Z G, 'Top seeded solution growth and characterization of piezo/ferroelectric  $\text{Pb}(\text{Zn}_{1/3}\text{Nb}_{2/3})\text{O}_3\text{-PbTiO}_3$  single crystals', *J. Cryst. Growth*, 2001 **233** 503–11.
- 73 Karaki T, Nakamoto M and Adachi M, 'Top-seeded solution growth of  $\text{Pb}(\text{Zn}_{1/3}\text{Nb}_{2/3})\text{O}_3\text{-PbTiO}_3$  single crystals', *Jpn. J. Appl. Phys.*, 2002 **41** 6997–99.
- 74 Lee H Y, 'Solid-state single crystal growth (SSCG) method: a cost-effective way of growing piezoelectric single crystals', in *Piezoelectric Single Crystals and Their Applications*, Ed. Trolier-McKinstry S, Cross L E and Yamashita Y, Pennsylvania State University, 2004 160.
- 75 Goldschmidt V M, 'Die Gesetze der Krystallochemie', *Naturwissenschaften*, 1926 **14** 477–85.
- 76 Eitel R, Randall C A, Shrout T R, Rehrig P, Hackenberger W and Park S E, 'New high temperature morphotropic phase boundary piezoelectrics based on  $\text{Bi}(\text{Me})\text{O}_3\text{-PbTiO}_3$  ceramics', *Jpn. J. Appl. Phys.*, 2001 **40** 5999–6002.
- 77 Randall C A, Eitel R E, Stringer C, Song T H, Zhang S J and Shrout T R, 'High performance, high temperature perovskite piezoelectric ceramics', in *Piezoelectric Single Crystals and Their Applications*, Ed. Trolier-McKinstry S, Cross L E and Yamashita Y, Pennsylvania State University, 2004 346.
- 78 Landolt-Bornstein, *Ferroelectrics and Related Substances*, Ed. K.H. Hellwege and A.M. Hellwege, Berlin, Heidelberg, New York, Springer-Verlag, Vol. 16, 1981.

- 79 Zhang S J, Randall C A and Shrout T R, 'Recent developments in high temperature piezoelectric single crystals', *Recent Res. Devel. Crystal Growth* 2005 **4** 167–86.
- 80 Swartz S L and Shrout T R, 'Fabrication of perovskite lead magnesium niobate', *Mater. Res. Bull.*, 1982 **17** 1245–50.
- 81 Zhang S J, Randall C A and Shrout T R, 'Characterization of high Curie temperature piezocrystals in doped  $\text{Pb}(\text{Yb}_{1/2}\text{Nb}_{1/2})\text{-PbTiO}_3$  system', in K.M. Nair (ed.) *Ceramic Materials and Multilayer Electronic Devices*, Nashville, TN, 2003 149–56.
- 82 Eitel R, Randall C A, Shrout T R and Park S E, 'Preparation and characterization of high temperature perovskite ferroelectrics in the solid solution  $\text{BiScO}_3\text{-PbTiO}_3$ ', *Jpn. J. Appl. Phys.*, 2002 **41** 2099–104.
- 83 Eitel R E, Zhang S J, Shrout T R, Randall C A and Levin I, 'Phase diagram of the perovskite system  $\text{BiScO}_3\text{-PbTiO}_3$ ', *J. Appl. Phys.*, 2004 **96** 2828–31.
- 84 Zhang R, Jiang B, Jiang W H and Cao W W, 'Complete set of properties of 0.92Pb  $(\text{Mg}_{1/3}\text{Nb}_{2/3})\text{O}_3\text{-0.08PbTiO}_3$  single crystal with engineered domains', *Mater. Lett.*, 2003 **57** 1305–8.
- 85 Zhang R, Jiang B and Cao W W, 'Elastic, piezoelectric and dielectric properties of multidomain 0.67Pb  $(\text{Mg}_{1/3}\text{Nb}_{2/3})\text{O}_3\text{-0.33PbTiO}_3$  single crystals', *J. Appl. Phys.*, 2001 **90** 3471–75.
- 86 Shrout T R, Eitel R E and Randall C A, 'High performance, high temperature perovskite piezoelectric ceramics', *Piezoelectric Materials in Devices*, Switzerland, Lausanne, 2002 413–32.
- 87 Takeda H, Shimamura K, Kohno T and Fukuda T, 'Growth and characterization of  $\text{La}_3\text{Nb}_{0.5}\text{Ga}_{5.5}\text{O}_{14}$  single crystals', *J. Cryst. Growth*, 1996 **169** 503–08.
- 88 Kawanaka H, Takeda H, Shimamura K and Fukuda T, 'Growth and characterization of  $\text{La}_3\text{Ta}_{0.5}\text{Ga}_{5.5}\text{O}_{14}$  single crystals', *J. Cryst. Growth*, 1998 **183** 274–77.
- 89 Dvoesherstov M Yu, Petrov S G, Cherednik V I and Chirimanov A P, 'New optimal orientations for surface acoustic waves in langasite, langanite and langatate piezoelectric crystals', *Technical Phys.*, 2002 **47** 1032–37.
- 90 Ogi H, Nakamura N, Sato K, Hirao M and Uda S, 'Elastic, anelastic and piezoelectric coefficients of langasite: resonance ultrasound spectroscopy with laser-Doppler interferometry', *IEEE Trans. Ultrason. Ferro. Freq. Control*, 2003 **50** 553–60.
- 91 Bohm J, Chilla E, Flannery C, Frohlich H J, Hauke T, Heimann R B, Hengst M and Straube U, 'Czochralski growth and characterization of piezoelectric single crystals with langasite structure: LGS, LGN and LGT II. Piezoelectric and elastic properties', *J. Cryst. Growth*, 2000 **216** 293–98.
- 92 Adachi M, Kimura T, Miyamoto W, Chen Z, Kawabata A, 'Dielectric, elastic and piezoelectric properties of  $\text{La}_3\text{Ga}_5\text{SiO}_{14}$  single crystals', *J. Korean Phys. Soc.*, 1998 **32** S1274–77.
- 93 Philippot E, Ibanez A, Goiffon A, Cochez M, Zarka A, Capell B, Schwartzel J and Detaint J, 'A quartz-like material: gallium phosphate  $\text{GaPO}_4$ ; crystal growth and characterization', *J. Cryst. Growth*, 1993 **130** 195–208.
- 94 Cochez M, Foulon J D, Ibanez A, Goiffon A, Philippot E, Capelle B, Zarka A, Schwartzel J and Detaint J 'Crystal growth and characterizations of a quartz like material:  $\text{GaPO}_4$ ', *J. de Phys IV*, 1994 **4** 183–88.
- 95 Reiter C, Krempl P, Thanner H, Wallnofer W and Worsch P, 'Material properties of  $\text{GaPO}_4$  and their relevance for applications', *Ann. Chim. Sci. Mat.*, 2001 **26** 91–94.
- 96 Krempl P, Krispel F and Wallnofer W, 'Industrial development and prospects of  $\text{GaPO}_4$ ', *Ann. Chim. Sci. Mat.*, 1997 **22** 623–26.

- 97 Reiter C, Thanner H, Wallnofer W and Krempl P, 'Properties of  $\text{GaPO}_4$  thickness shear resonators', *Ann. Chim. Sci. Mat.*, 1997 **22** 633–36.
- 98 Krempl P, Schleinzer G, Wallnofer W, 'Gallium phosphate,  $\text{GaPO}_4$ : a new piezoelectric crystal material for high temperature sensorics', *Sensors and Actuators A*, 1997 **61** 361–3.
- 99 Zhang S J, Cheng Z X and Chen H C, 'A new oxyborate crystal,  $\text{GdCa}_4\text{O}(\text{BO}_3)_3$ : defects and optical properties', *Defect and Diffusion Forum*, 2000 **186–187** 79–106.
- 100 Wang J, Hu X, Yin X, Song R, Wei J, Shao Z, Liu Y, Jiang M, Tian Y, Jiang J and Huang W, 'Growth, defects and properties of  $\text{GdCOB}$  and  $\text{Nd}:\text{GdCOB}$  crystals', *J. Mater. Res.*, 2001 **16** 790–96.
- 101 Takeda H, Sako H, Shimizu H, Kodama K, Nishida M, Nakao H, Nishida T, Okamura S, Shikida T and Shiosakit, 'Growth and characterization of lanthanum calcium oxoborate  $\text{LaCa}_4\text{O}(\text{BO}_3)_3$  single crystals', *Jpn. J. Appl. Phys.*, 2003 **42** 6081–85.
- 102 Shimizu H, Kodama K, Takeda H, Nishida T, Shikida T, Okamura S, Shiosaki T, 'Evaluation of material constants and temperature properties in lanthanum calcium oxoborate  $\text{LaCa}_4\text{O}(\text{BO}_3)_3$  single crystals', *Jpn. J. Appl. Phys.*, 2004 **43** 6716–20.
- 103 Shimizu H, Nishida T, Nishida M, Takeda H and Shiosaki T, 'Dielectric, elastic and piezoelectric constants of lanthanum calcium oxoborate single crystals with monoclinic structure of point group  $m'$ ', *Jpn. J. Appl. Phys.*, 2005 **44** 7059–63.
- 104 Nishida T, Shimizu H and Shiosaki T, 'Theoretical calculation of the surface acoustic wave characteristics of  $\text{GdCOB}$  single crystals', *J. Alloys Compounds*, 2006 **408–412** 577–81.
- 105 Markiewicz E, Pawlaczyk C, Klos A, Hofman W and Pajaczowska A, 'Temperature behavior of piezoelectric gadolinium calcium oxoborate  $\text{GdCa}_4\text{O}(\text{BO}_3)_3$  crystal', *Phys. Stat. Solidi A*, 2006 **203** 372–78.

## Development of high-performance piezoelectric single crystals by using solid-state single crystal growth (SSCG) method

H Y LEE, Sunmoon University and Ceracomp Co. Ltd, Korea

### 6.1 Introduction

Some piezoelectric single crystals such as  $\text{Pb}(\text{Mg}_{1/3}\text{Nb}_{2/3})\text{O}_3\text{-PbTiO}_3$  (PMN-PT),  $\text{Pb}(\text{Zn}_{1/3}\text{Nb}_{2/3})\text{O}_3\text{-PbTiO}_3$  (PZN-PT), and  $\text{Ba}(\text{Ti,Zr})\text{O}_3$  (BZT) are known to exhibit remarkable piezoelectric properties.<sup>1-3</sup> Lead-based piezoelectric PMN-PT and PZN-PT single crystals were reported to have piezoelectric coefficients ( $d_{33}$ ) higher than 2000 pC/N and electromechanical coupling factors ( $k_{33}$ ) higher than 0.9.<sup>1,2</sup> It was also demonstrated that the lead-free  $\text{Ba}(\text{Ti,Zr})\text{O}_3$  single crystals with appropriate amounts of Zr also have a  $k_{33}$  of about 0.9 and a  $d_{33}$  higher than 1000 pC/N. Because of their extraordinary piezoelectric properties, it is expected that a breakthrough in piezoelectric applications will be possible in the near future.

PMN-PT and PZN-PT single crystals have usually been fabricated by the flux method and the Bridgman technique.<sup>4-10</sup> The flux method is a simple and low-cost technique, but is limited because of crystal quality and quantity. The Bridgman technique has a good reproducibility, but requires sophisticated and expensive equipment and may have a problem providing composition homogeneity. These methods are suitable for growing bulk single crystals, but are not easily transferable to large-scale manufacturing. The solid-state single crystal growth (SSCG) technique has been developed as an alternative crystal growth method that offers advantages over the conventional melt methods such as the flux method and the Bridgman technique.<sup>11,12</sup>

In the SSCG process, a small single crystal seed is diffusion-bonded to a polycrystalline body and grows by consuming fine matrix grains to become a large single crystal after long annealing of crystal growth step. This process was referred to as solid-state single crystal growth because it does not involve complete melting of major components. Since this process is basically the same as a normal sintering process, it is not only cost-effective but also suitable to mass production of single crystals. Especially, the SSCG method is useful for single crystal growth of materials with high melting temperature, destructive phase transitions, volatile components, and incongruent melting.

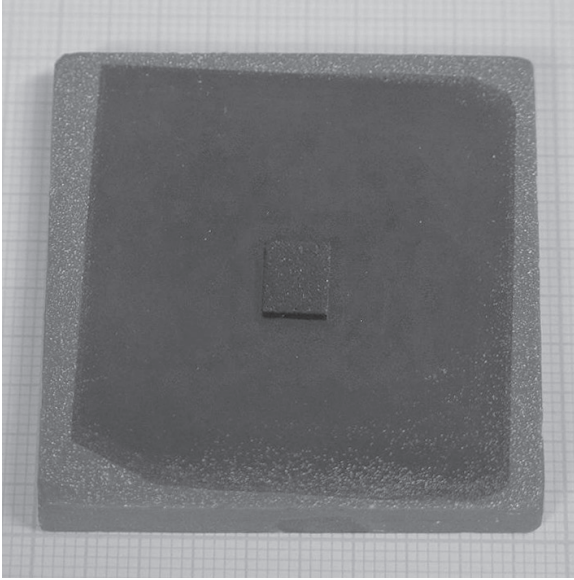
As an alternative crystal growth method, several research groups have already studied and developed the SSCG method, e.g. NGK in Japan developed the SSCG method to produce ferrite single crystals.<sup>13,14</sup> The SSCG method was also proved to be feasible for BaTiO<sub>3</sub> single crystals.<sup>15–18</sup> As an alternative to the Bridgman method, the SSCG technique has been intensively studied for growth of PMN–PT single crystals.<sup>19,20</sup>

In this chapter I report that piezoelectric single crystals of Ba(Ti,Zr)O<sub>3</sub>, PMN–PT (undoped, Fe-doped, and Mn-doped), and PMN–PZT have been successfully fabricated by the SSCG method. The dielectric and piezoelectric properties of the grown crystals have also been characterized. These results shows that the SSCG technique can be applied to the growth of Ba(Ti,Zr)O<sub>3</sub>, PMN–PT, and relaxor–PZT single crystals and can also be used for development of new high-performance piezoelectric single crystals which are difficult to fabricate by conventional single crystal growth techniques.

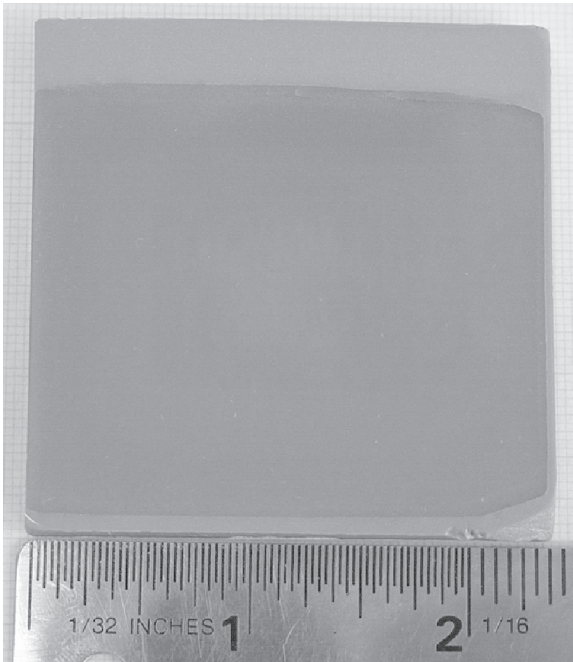
## 6.2 Solid-state crystal growth (SSCG) process

The abnormal grain growth (AGG, also referred to as discontinuous grain growth or exaggerated grain growth) during sintering of polycrystalline ceramics has been extensively studied. During AGG, a few grains grow much faster than surrounding fine matrix grains so that the microstructure exhibits a bimodal distribution of grain size. Abnormal grains usually grow until they impinge each other. This suggests the possibility of single crystal growth by controlling AGG. If it is possible to control the nucleation of abnormal grains in a polycrystalline material, AGG can be used to grow a single crystal in a polycrystalline material. In the SSCG process a small single crystal seed can be used to control the nucleation of abnormal grains effectively. By using a seed crystal with known crystallographic orientation, the crystallographic orientation of the growing single crystal can be easily predetermined.

Figure 6.1 shows the solid-state growth of a (100) Ba(Zr<sub>0.1</sub>Ti<sub>0.9</sub>)O<sub>3</sub> (BZT) seed crystal in a Ba(Zr<sub>0.1</sub>Ti<sub>0.9</sub>)O<sub>3</sub> ceramic. Before the annealing of crystal growth, a small (100) BZT single crystal was placed on the top of the BZT ceramic. During the heat treatment, the small (100) BZT seed crystal grew from the top to the bottom of the Ba(Zr<sub>0.1</sub>Ti<sub>0.9</sub>)O<sub>3</sub> ceramic and thus a Ba(Zr<sub>0.1</sub>Ti<sub>0.9</sub>)O<sub>3</sub> single crystal of  $\sim 40 \times 40 \times 8 \text{ mm}^3$  formed in the BZT ceramics. The grown single crystal, i.e. the region swept by the seed crystal during the heat treatment, is clearly discerned from the appearance of the specimen compared with the remaining polycrystalline region. During the growth of the (100) seed crystal, the {100} planes of the grown single crystal were always well developed. Figure 6.2 shows a polished surface of a (100) BZT single crystal larger than  $50 \times 50 \times 10 \text{ mm}^3$ , which was grown in a BZT ceramic. The seed crystal on the grown Ba(Zr<sub>0.1</sub>Ti<sub>0.9</sub>)O<sub>3</sub> crystal was ground off after the SSCG process.

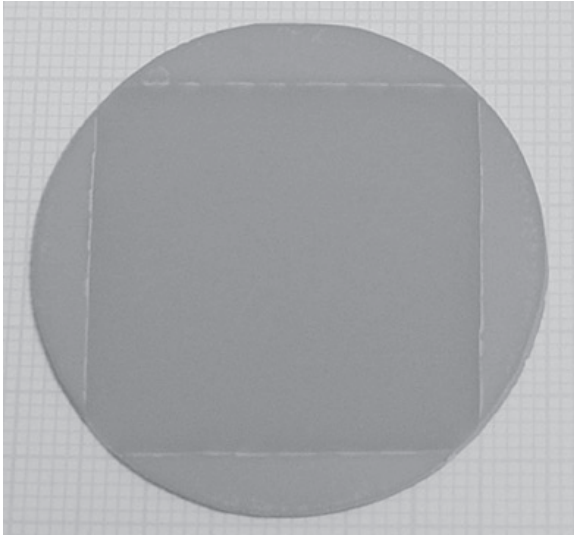


6.1 SSCG of BZT: growth of a (100) BZT seed crystal in a BZT ceramic.

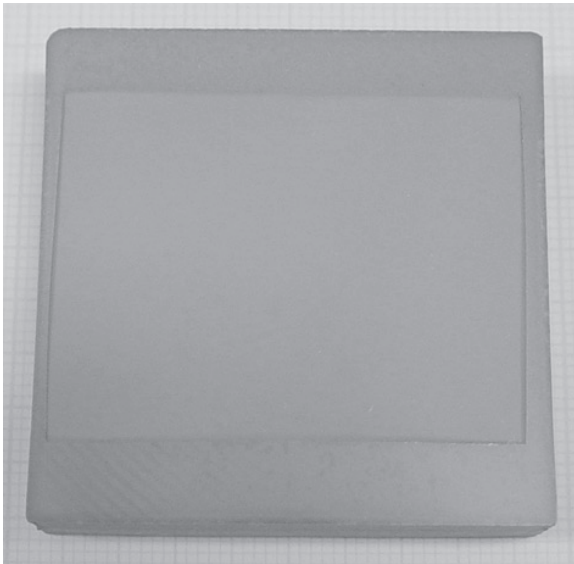


6.2 A BZT single crystal, bigger than  $50 \times 50 \times 10 \text{ mm}^3$  in size, grown by the SSCG technique.

Figure 6.3 shows the polished surfaces of (a) 70PMN–30PT and (b) PMN–PZT single crystals grown by the SSCG process. Before the annealing of crystal growth, a  $\text{Ba}(\text{Zr}_{0.1}\text{Ti}_{0.9})\text{O}_3$  single crystal was placed on the top of the ceramic. During the heat treatment, the BZT seed crystals grew into the (a)



(a)

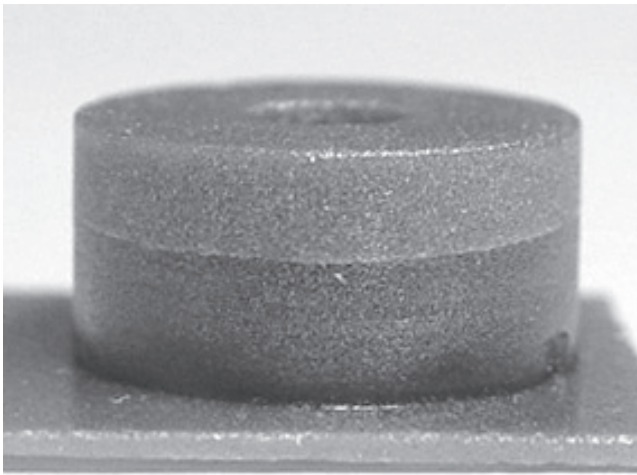


(b)

6.3 Polished surfaces of (a) 70PMN–30PT and (b) PMN–PZT single crystals grown by SSCG process.

70PMN–30PT and (b) PMN–PZT ceramics, respectively. In spite of the difference in chemical composition between the seed crystals and the ceramics, the BZT seed crystals were chemically stable in the Pb-based ceramics and thus acted as an effective seed single crystal. These results demonstrate that piezoelectric single crystals of BZT, PMN–PT, and PMN–PZT with sizes up to 40 or 50 mm could be successfully fabricated by the simple SSCG process.

One of the advantages of the SSCG method is that the net shape crystal growth is possible, because the melting of ceramic precursors does not occur during the crystal growth process. Figure 6.4 shows the growth of a ring-shaped BZT single crystal. First a ring-shaped BZT powder compact was prepared by uni-axial pressing of BZT powder and sintered. After the sintering



(a)



(b)

**6.4** Growth of a ring-shaped BZT single crystal from a BZT seed crystal at the bottom (a) and two BZT single crystal rings grown by SSCG technique without mechanical drilling process (b).



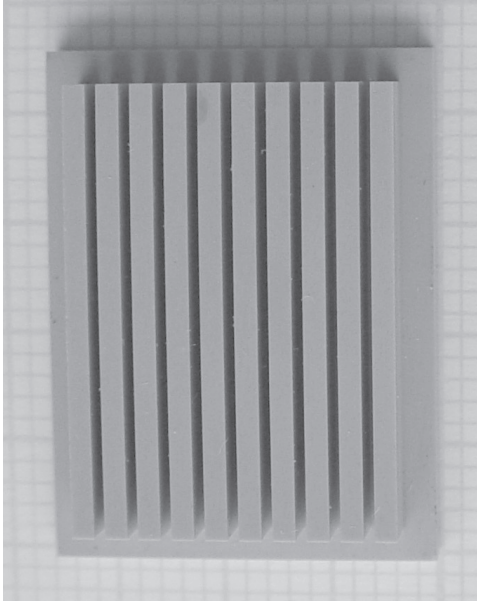
the ring-shaped BZT ceramic was placed on the top of a (100) BZT single crystal seed and then heat-treated, as shown in Fig. 6.4(a). Figure 6.4(a) shows the growth of a BZT single crystal from the seed crystal to the ring-shaped ceramic. Since the shape of the growing BZT single crystal was the same as that of the BZT ceramic, ring-shaped BZT single crystals were successfully fabricated without mechanical machining of single crystal blocks after the crystal growth step, as shown in Fig. 6.4(b). As another example of the net shape crystal growth, Figure 6.5 shows the growth of a PMN–PT single crystal from a PMN–PT ceramic which was mechanically machined in a 2–2 composite form before the crystal growth step. Instead of difficult machining of brittle PMN–PT single crystals, the sintered PMN–PT ceramics were diced as shown in Fig. 6.5(a) and heat-treated for the crystal growth. By using this technique piezoelectric single crystals can be prepared in a 1–3 or 2–2 composite form, while avoiding the mechanical machining steps of brittle single crystals.

## 6.3 Dielectric and piezoelectric properties of BZT, PMN–PT, and PMN–PZT single crystals

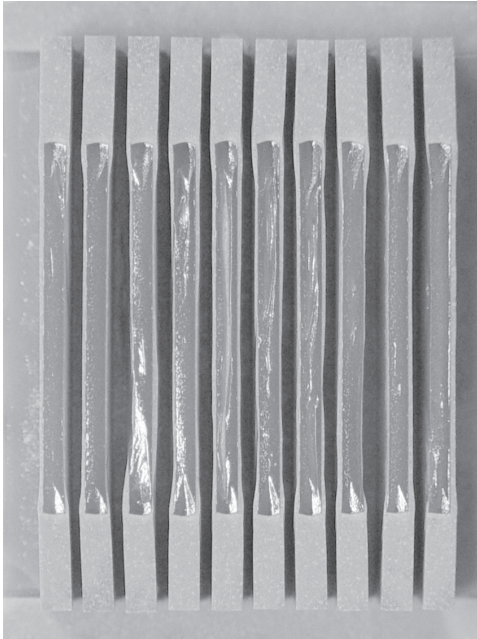
### 6.3.1 SSCG Ba(Zr,Ti)O<sub>3</sub> single crystals

The addition of Zr in BaTiO<sub>3</sub> decreases the Curie temperature (the cubic–tetragonal phase transition temperature,  $T_C$ ), but increases the tetragonal–orthorhombic transition temperature ( $T_{OT}$ ) and the orthorhombic–rhombohedral transition temperature ( $T_{RO}$ ).<sup>21</sup> Therefore, it is possible to stabilize any of the four phases (tetragonal, orthorhombic, rhombohedral, or cubic) at room temperature by adding appropriate amounts of Zr.<sup>21</sup> When the orthorhombic or rhombohedral phase is stabilized at room temperature, the resulting single crystals show high piezoelectric properties and are promising candidates for high-performance and non-lead piezoelectrics.<sup>3</sup>

Figure 6.6 shows the variation of dielectric constant ( $K_3^T$ ) with temperature of the (001) single crystal plates of BaTiO<sub>3</sub>, Ba(Zr<sub>0.05</sub>Ti<sub>0.95</sub>)O<sub>3</sub>, Ba(Zr<sub>0.075</sub>Ti<sub>0.925</sub>)O<sub>3</sub> and Ba(Zr<sub>0.1</sub>Ti<sub>0.9</sub>)O<sub>3</sub>. The (001) BaTiO<sub>3</sub> single crystal did not show any phase transition at temperatures between room temperature and its Curie temperature. In the curve of Ba(Zr<sub>0.05</sub>Ti<sub>0.95</sub>)O<sub>3</sub> single crystal, one phase transition ( $T_{OT}$ ) between tetragonal phase and orthorhombic phase was observed in the measurement temperature range. The Ba(Zr<sub>0.075</sub>Ti<sub>0.925</sub>)O<sub>3</sub> and Ba(Zr<sub>0.1</sub>Ti<sub>0.9</sub>)O<sub>3</sub> single crystals showed two peaks of the orthorhombic–tetragonal ( $T_{OT}$ ) and rhombohedral–orthorhombic ( $T_{RO}$ ) phase transitions. Since the Ba(Zr<sub>0.075</sub>Ti<sub>0.925</sub>)O<sub>3</sub> single crystal had rhombohedral phase at room temperature and its  $T_{RO}$  was close to room temperature, their dielectric and piezoelectric properties were characterized. Table 6.1 shows the measured dielectric and piezoelectric properties of Ba(Zr<sub>0.075</sub>Ti<sub>0.925</sub>)O<sub>3</sub> single crystals.

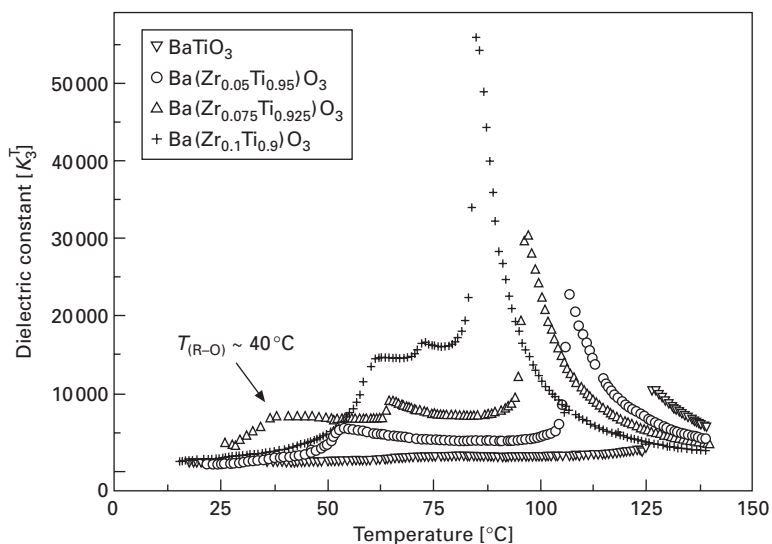


(a)



(b)

6.5 A PMN-PT polycrystalline ceramic prepared for fabrication of 2-2 composite (a) and growth of a PMN-PT single crystal in a 2-2 composite form from a BZT seed crystal at the bottom (b).



6.6 Variation of dielectric constant (at 1 kHz) with temperature:  $\text{BaTiO}_3$ ,  $\text{Ba}(\text{Zr}_{0.05}\text{Ti}_{0.95})\text{O}_3$ ,  $\text{Ba}(\text{Zr}_{0.075}\text{Ti}_{0.925})\text{O}_3$  and  $\text{Ba}(\text{Zr}_{0.1}\text{Ti}_{0.9})\text{O}_3$  single crystals.

Table 6.1 Dielectric and piezoelectric properties of  $\text{Ba}(\text{Zr}_{0.075}\text{Ti}_{0.925})\text{O}_3$  single crystals

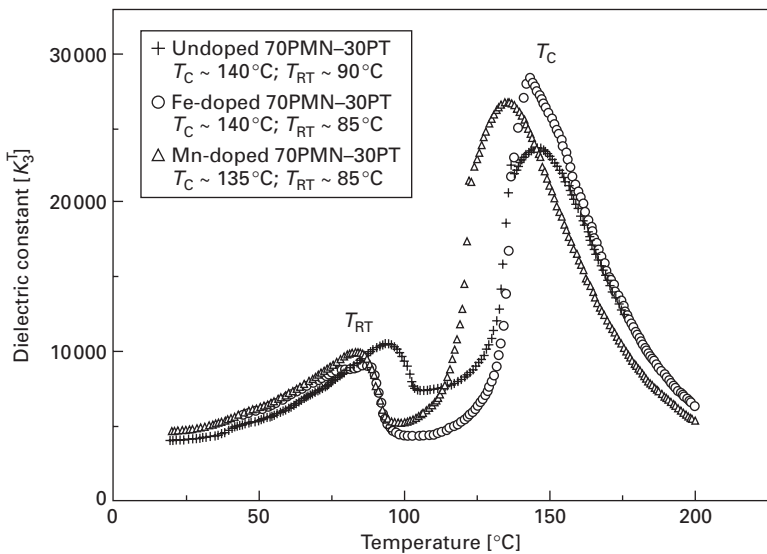
$K_3^T$		4000
$\tan \delta$		> 0.01
$k_{33}$		0.9
$d_{33}$	[pC/N]	1150
$S_{33}^D$	$[\times 10^{-12} \text{ m}^2/\text{N}]$	7.5
$S_{33}^E$	$[\times 10^{-12} \text{ m}^2/\text{N}]$	45
$Y_{33}$	[GPa]	25
$N_{33}$	[Hz m]	1050
$Q_m$		20

Compared with other  $\text{Ba}(\text{Zr}_x\text{Ti}_{1-x})\text{O}_3$  single crystals with different values of  $x$ , the  $\text{Ba}(\text{Zr}_{0.075}\text{Ti}_{0.925})\text{O}_3$  single crystals were found to exhibit better piezoelectric properties (because they are rhombohedral at room temperature and close to the phase boundary between rhombohedral and orthorhombic phases). The measured electromechanical coupling factor ( $k_{33}$ ) and piezoelectric coefficient ( $d_{33}$ ) were about 0.9 and 1050 pC/N, respectively. These results confirm that rhombohedral  $\text{Ba}(\text{Zr}_x\text{Ti}_{1-x})\text{O}_3$  single crystals with appropriate values of  $x$  are promising candidates for high-performance and non-lead piezoelectrics.<sup>3</sup>

### 6.3.2    SSCG PMN–PT single crystals

Following the discovery of the outstanding piezoelectric properties of PMN–PT and PZN–PT single crystals, a great deal of effort has been put in the growth of these crystals by either the flux method or the Bridgman method.<sup>4–10</sup> In the flux method it is difficult to grow large and oriented single crystals, which are necessary for commercial applications. Material loss due to the vaporization of volatile PbO is another disadvantage of the flux method. Feigelson<sup>7</sup> first suggested that the Bridgman method could be used to grow PMN–PT single crystals with sealed Pt crucibles as an alternative to flux growth. However, the Bridgman method presents several problems in the crystal growth of PMN–PT crystals with composition near the morphotropic phase boundary (MPB) composition, including: compositional variation along the growth direction and leak of Pt crucibles.<sup>7,8,10</sup> In order to overcome these problems, several options such as the modified Bridgman method and the zone leveling method were suggested. Among them the SSCG method is one of promising techniques for growing chemically uniform PMN–PT single crystals, because complete melting of major components is not necessary. In particular, for the growth of chemically uniform single crystals of more complicated compositions such as doped PMN–PT, or relaxor–PMN–PT, the SSCG technique has advantages over the conventional crystal growth methods.

Figure 6.7 shows the variation of dielectric constant ( $K_3^T$ ) with temperature of (001) single crystal plates of undoped 70PMN–30PT, Fe-doped PMN–PT, Mn-doped PMN–PT,



6.7 Variation of dielectric constant (at 1 kHz) with temperature: undoped 70PMN–30PT, Fe-doped 70PMN–30PT, and Mn-doped 70PMN–30PT single crystals.

**Table 6.2** Dielectric and piezoelectric properties of (a) undoped 70PMN–30PT, (b) Fe-doped 70PMN–30PT, and (c) Mn-doped 70PMN–30PT single crystals grown by the SSCG process

	(001) PMN–30PT	(001) Fe-doped PMN–30PT	(001) Mn-doped PMN–30PT
$K_3^T$	5000	4850	3700
$\tan \delta$	> 0.01	> 0.02	> 0.02
$T_C$ [°C]	140	140	135
$T_{RT}$ [°C]	90	85	85
$k_{33}$	0.9	0.91	0.89
$d_{33}$ [pC/N]	1500	1450	1080
$S_{33}^D$ [ $\times 10^{-12}$ m <sup>2</sup> /N]	10.7	10.2	9.5
$S_{33}^E$ [ $\times 10^{-12}$ m <sup>2</sup> /N]	54	60	46
$Y_{33}$ [GPa]	19	17	22
$N_{33}$ [Hz m]	840	800	900
$Q_m$	35	40	30

and Mn-doped PMN–PT, grown by the SSCG technique (see Fig. 6.3a). The undoped 70PMN–30PT single crystal has a Curie temperature ( $T_C$ ) of  $\sim 140^\circ\text{C}$  and a transition temperature between rhombohedral and tetragonal phases ( $T_{RT}$ ) of  $\sim 90^\circ\text{C}$ .  $T_C$  and  $T_{RT}$  of Fe-doped PMN–PT single crystals were  $140^\circ\text{C}$  and  $85^\circ\text{C}$ , respectively. Mn-doped PMN–PT single crystals show a  $T_C$  of  $135^\circ\text{C}$  and a  $T_{RT}$  of  $90^\circ\text{C}$ . Table 6.2 shows the measured dielectric and piezoelectric properties of undoped 70PMN–30PT, Fe-doped PMN–PT, and Mn-doped single crystals. These results show that the SSCG technique has been successfully applied to the fabrication of undoped as well as doped PMN–PT single crystals.

### 6.3.3 SSCG PMN-PZT single crystals

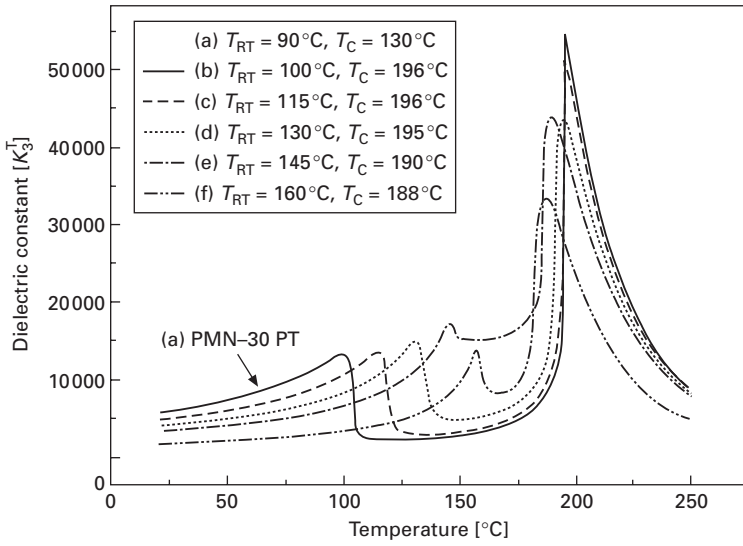
The excellent piezoelectric properties ( $k_{33} > 0.9$ ;  $d_{33} > 2000$  pC/N) of PMN–PT and PZN–PT single crystals make it possible to develop the next generation electromechanical devices such as ultrasonic transducers and actuators. However, their disadvantages such as low  $T_C$ ,  $T_{RT}$ , and  $E_C$  limit their use in general piezoelectric applications. Therefore piezoelectric single crystals with high  $T_C$ ,  $T_{RT}$ , and  $E_C$  are desired and are being developed for more general applications. Several research groups have already reported growth and properties of high  $T_C$  piezoelectric crystals of relaxor–PT systems, such as  $\text{Pb}(\text{Sc}_{1/2}\text{Nb}_{1/2})\text{O}_3\text{–PbTiO}_3$  (PSN–PT),<sup>22</sup>  $\text{Pb}(\text{Yb}_{1/2}\text{Nb}_{1/2})\text{O}_3\text{–PbTiO}_3$  (PYbN–PT),<sup>23</sup>  $\text{Pb}(\text{In}_{1/2}\text{Nb}_{1/2})\text{O}_3\text{–PbTiO}_3$  (PIN–PT),<sup>24</sup>  $\text{BiScO}_3\text{–PbTiO}_3$  (BS–PT),<sup>25</sup> and PIN–PMN–PT.<sup>26,27</sup> Owing to high vapor pressure of PbO melt, however, the conventional growth processes of flux and Bridgman methods have critical limitations such as a complicated growth process, and chemically inhomogeneous crystals, resulting in low yield and high cost. Some expensive

raw materials such as  $\text{In}_2\text{O}_3$  and  $\text{Sc}_2\text{O}_3$  will also increase the production cost.

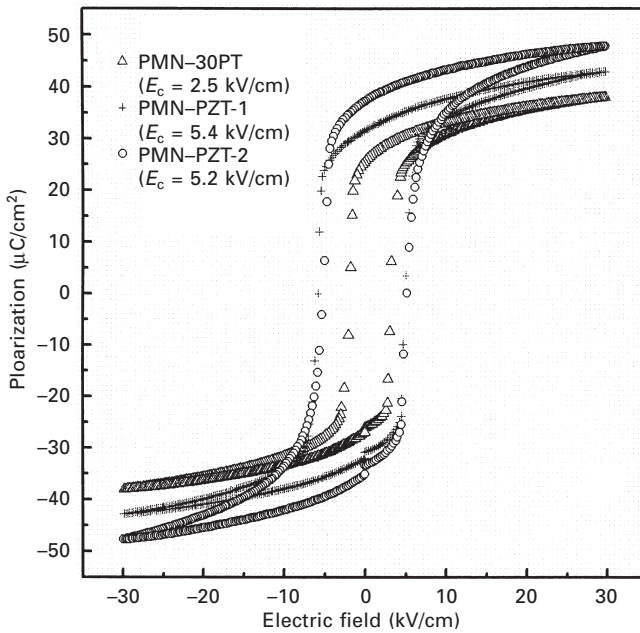
PZT ceramics have been the mainstay for high-performance piezoelectric applications. Compositionally PZT ceramics lie near the MPB between the tetragonal and rhombohedral phases and the MPB compositions exhibit anomalously high dielectric and piezoelectric properties. Relaxor–PZT ceramics have a wide range of MPB compositions depending on the ratio of relaxor/PZ/PT, as well as the type of relaxors. Therefore, it is expected that relaxor–PZT single crystals will have a wide range of dielectric and piezoelectric properties, and some relaxor–PZT single crystals will show much better properties than relaxor-PT single crystals such as PMN–PT, PZN–PT, and PIN–PT, if relaxor–PZT materials could be grown in single crystal form. In contrast to relaxor-PT crystal growth, PZT and relaxor–PZT cannot be readily grown in bulk single crystal form because of incongruent melting behavior of PZT. During incongruent melting of PZT, PZT decomposes to a liquid and a solid phase  $\text{ZrO}_2$ . The solid phase  $\text{ZrO}_2$  in the liquid phase prevents continuous growth of PZT single crystals. Attempts to grow single crystals of PZT and relaxor–PZT only resulted in crystallites too small to allow adequate property measurements. Therefore, in order to grow large PZT or relaxor–PZT single crystals, a melting step of PZT should be avoided in the crystal growth process.

In the PMN–PZ–PT system near the MPB compositions, the  $T_C$  and  $T_{RT}$  of PMN–PZT single crystals vary with the ratio of PMN/PZ/PT approximately in the ranges of  $150^\circ\text{C} < T_C < 350^\circ\text{C}$  and  $50^\circ\text{C} < T_{RT} < 300^\circ\text{C}$ . Therefore, by adjusting the composition and achieving chemical uniformity, PMN–PZT single crystals of high  $T_C$  and  $T_{RT}$  can be obtained. As shown in Fig. 6.3(b), a chemically homogeneous and fully dense PMN–PZT single crystal was grown by the SSCG technique. Figure 6.8 shows the possibility of controlling  $T_C$  and  $T_{RT}$  of PMN–PZT single crystals by changing the ratio of PMN/PZ/PT. In Fig. 6.8, the Curie temperatures of all PMN–PZT single crystals are approximately  $200^\circ\text{C}$ ; however, their  $T_{RT}$  varies from  $100^\circ\text{C}$  to  $160^\circ\text{C}$  depending on the ratio of PMN:PZ:PT. This result shows that PMN–PZT single crystals of high  $T_C$  and  $T_{RT}$  can be fabricated and their  $T_C$  and  $T_{RT}$  can be controlled.

Figure 6.9 shows the polarization curves of (001) single crystal plates of PMN–30PT and PMN–PZT with electric field. The coercive electric field ( $E_C$ ) of (001) PMN–PZT single crystal plates was higher than  $5\text{ kV/cm}$ , which is almost twice as high as that of a (001) PMN–30PT single crystal plate. In Table 6.3 the measured dielectric and piezoelectric properties of PMN–PZT single crystals are summarized. Among the PMN–PZT single crystals near the MPB, PMN–PZT-1 single crystals showed very well-balanced dielectric and piezoelectric properties with  $T_C \approx 200^\circ\text{C}$ ,  $T_{RT} \approx 100^\circ\text{C}$ ,  $(K_3^T) \approx 6000$ ,  $k_{33} \approx 0.92$ ,  $d_{33} \approx 2000$ , and  $E_C \approx 5\text{ kV/cm}$ . The  $d_{32}$  of (011)/ $\langle 100 \rangle$  PMN–PZT-1 single crystal plates reached about  $1900\text{ pC/N}$ .



6.8 Variation of dielectric constants (at 1 kHz) of PMN-PZT single crystals with temperature.



6.9 Plots of polarization vs. electric field: (a) PMN-30PT, (b) PMN-PZT-1, and (c) PMN-PZT-2.

**Table 6.3** Dielectric and piezoelectric properties of PMN–PZT single crystals grown by the SSCG process

	(001) PMN–PZT-1	(001) PMN–PZT-2	(001) PMN–PZT-3	(001) PMN–PZT-4	(001) PMN–PZT-5
$K_3^T$	6000	5000	4200	3500	3000
$\tan \delta$	> 0.01	> 0.01	> 0.01	> 0.01	> 0.01
$T_C$ [°C]	200	200	195	190	190
$T_{RT}$ [°C]	100	115	130	145	160
$k_{33}$	0.92	0.92	0.9	0.9	0.89
$d_{33}$ [pC/N]	2000	1750	1450	1250	1000
$d_{32}(011)/<100>$ pC/N	1900	1700	1400	1100	850

## 6.4 Conclusions and future trends

The SSCG method has been applied to the growth of high-performance piezoelectric single crystals such as Ba(Zr,Ti)O<sub>3</sub>, PMN–PT, and PMN–PZT. In the case of Ba(Zr,Ti)O<sub>3</sub> solid solution, the single crystals grew up to 50 mm in lateral dimension. Rhombohedral Ba(Zr<sub>0.075</sub>Ti<sub>0.925</sub>)O<sub>3</sub> single crystals exhibit a  $k_{33}$  of about 0.9 and a  $d_{33}$  of about 1000 pC/N at room temperature and are thus promising candidates for high-performance and lead-free piezoelectrics. The undoped, Fe-doped, and Mn-doped 70PMN–30PT single crystals were produced by SSCG. The doping does not make their single crystal growth process more complicated and thus chemically uniform doped PMN–PT single crystals were successfully grown by the SSCG process. The PMN–PZT single crystals with different ratios of PMN/PZ/PT as well as different  $T_{RT}$  were fabricated by SSCG. By changing the ratios of PMN/PZ/PT in the PMN–PZ–PT system, the dielectric and piezoelectric properties of PMN–PZT single crystals could be easily controlled.

It was demonstrated in this chapter that the SSCG method is a very effective way of producing high-performance piezoelectric single crystals such as BaTiO<sub>3</sub>, Ba(Ti,Zr)O<sub>3</sub>, PMN–PT, and PMN–PT–PZ. Up to now, the SSCG technique has been the only way for growth of large relaxor–PZT single crystals. Therefore, the SSCG process will provide a breakthrough in the fabrication of high-performance piezoelectric single crystals, especially the high  $T_C$  relaxor–PZT single crystals.

## 6.5 References

1. S. E. Park, T. R. Shrout, 'Ultrahigh strain and piezoelectric behavior in relaxor based ferroelectric single crystal,' *Journal of Applied Physics* **82** (4) 1804–1811 (1997).
2. S. E. Park, T. R. Shrout, 'Characteristics of relaxor-based piezoelectric single crystals for ultrasonic transducer,' *IEEE Trans on Ultrasonics, Ferroelectrics, and Frequency Control Special Issues on Ultrasonic Transducer* **44** (5) 1140–1146 (1997).



3. P. W. Rehrig, S. E. Park, S. Trolier-McKinstry, G. L. Messing, B. Jones, T. R. Shrout, 'Piezoelectric properties of zirconium-doped barium titanate single crystals grown by templated grain growth,' *Journal of Applied Physics* **86** (3) 1657–1661 (1999).
4. T. R. Shrout, Z. P. Chang, N. Kim, S. Markgraf, 'Dielectric behavior of single crystal near the  $(1-x)\text{Pb}(\text{Mg}_{1/3}\text{Nb}_{2/3})\text{O}_3-x\text{PbTiO}_3$  morphotropic phase boundary,' *Ferroelectrics Letters* **12** 63–69 (1990).
5. M. Dong, Z. G. Ye, 'High-temperature solution growth and characterization of the piezo-/ferroelectric  $(1-x)\text{Pb}(\text{Mg}_{1/3}\text{Nb}_{2/3})\text{O}_3-x\text{PbTiO}_3$  [PMNT] single crystals,' *Journal of Crystal Growth* **209** 81–90 (2000).
6. X. Jiang, F. Tang, J. T. Wang, T. P. Chen, 'Growth and properties of PMN-PT single crystals,' *Physica C* **364–365** 678–683 (2001).
7. R. S. Feigelson, 'Growth of large single crystals of relaxor ferroelectrics under controlled conditions,' *Piezoelectric Crystal Planning Workshop*, Washington, DC, May 14–16 (1997).
8. S. G. Lee, R. G. Monteiro, R. S. Feigelson, H. S. Lee, M. Lee, S. E. Park, 'Growth and electrostrictive properties of  $\text{Pb}(\text{Mg}_{1/3}\text{Nb}_{2/3})\text{O}_3$  crystals,' *Applied Physics Letters* **74** (7) 1030–1032 (1999).
9. G. Xu, H. Luo, H. Xu, Z. Qi, P. Wang, W. Zhong, Z. Yin, 'Structural defects of  $\text{Pb}(\text{Mg}_{1/3}\text{Nb}_{2/3})\text{O}_3-\text{PbTiO}_3$  single crystals grown by a Bridgman method,' *Journal of Crystal Growth* **222** 202–208 (2001).
10. K. T. Zawilski, M. C. C. Custodio, R. C. DeMattei, S. G. Lee, R. G. Monteiro, H. Odagawa, R. F. Feigelson, 'Segregation during the vertical Bridgman growth of lead magnesium niobate–lead titanate single crystals,' *Journal of Crystal Growth* **258** 353–367 (2003).
11. T. M. Heo, J. B. Lee, D. H. Kim, H. Y. Lee, N. M. Hwang, J. K. Park, U. J. Chung, D. Y. Kim, 'Solid-state single crystal growth of  $\text{BaTiO}_3$  and PMN-PT,' in *Morphotropic Phase Boundary Perovskites, High Strain Piezoelectrics, and Dielectric Ceramics*, *Ceramic Transactions*, Wiley, Indianapolis **136** 211–218 (2003).
12. H.-Y. Lee, 'Solid state single crystal growth (SSCG) method: a cost-effective way of growing piezoelectric single crystals,' pp. 160–177 in *Piezoelectric Single Crystals and Their Application*, Edited by S. Trolier McKinstry, Y. Yamashita and L. E. Cross Penn State University, State College, (2004).
13. S. Matsuzawa, S. Mase, 'Method for producing a single crystal ferrite,' US Patent No. 4339301 (1982).
14. K. Kugimiya, K. Hirota, K. Matsuyama, 'Process for producing single crystal ceramics,' US Patent No. 4900393 (1990).
15. T. Yamamoto, T. Sakuma, 'Fabrication of barium titanate single crystals by solid-state grain growth,' *Journal of the American Ceramic Society* **77** (4) 1107–1109 (1994).
16. Y. S. Yoo, M. K. Kang, J. H. Han, H. Kim, D. Y. Kim, 'Fabrication of  $\text{BaTiO}_3$  single crystals by using exaggerated grain growth method,' *Journal of the European Ceramic Society* **17** 1725–1727 (1997).
17. P. W. Rehrig, G. L. Messing, S. Trolier-McKinstry, 'Templated grain growth of barium titanate single crystals,' *Journal of the American Ceramic Society* **83** (11) 2654–2660 (2000).
18. H. Y. Lee, J. S. Kim, D. Y. Kim, 'Fabrication of  $\text{BaTiO}_3$  single crystals using secondary abnormal grain growth,' *Journal of the European Ceramic Society* **20** 1595–1597 (2000).

19. T. Li, A. M. Scotch, H. M. Chan, M. P. Harmer, 'Single crystals of  $\text{Pb}(\text{Mg}_{1/3}\text{Nb}_{2/3})\text{O}_3$ -35 mol%  $\text{PbTiO}_3$  from polycrystalline precursors,' *Journal of the American Ceramic Society* **81** (1) 244-248 (1998).
20. A. Khan, F. A. Meschke, T. Li, A. M. Scotch, H. M. Chan, M. P. Harmer, 'Growth of  $\text{Pb}(\text{Mg}_{1/3}\text{Nb}_{2/3})\text{O}_3$ -35 mol%  $\text{PbTiO}_3$  single crystals from (111) substrates by seeded polycrystal conversion,' *Journal of the American Ceramic Society* **82** (11) 2958-2962 (1999).
21. B. Jaffe, W. R. Cook, H. Jaffe, *Piezoelectric Ceramics*, Academic Press, London and New York (1971).
22. Y. H. Bing, Z. G. Ye, 'Synthesis, phase segregation and properties of piezo-/ferroelectric  $(1-x)\text{Pb}(\text{Sc}_{1/2}\text{Nb}_{1/2})\text{O}_3$ - $x\text{PbTiO}_3$  single crystals,' *Journal of Crystal Growth* **287** 326-329 (2006).
23. S. Zhang, P. W. Rehrig, C. Randall, T. R. Shrout, 'Crystal growth and electrical properties of  $\text{Pb}(\text{Yb}_{1/2}\text{Nb}_{1/2})\text{O}_3$ - $\text{PbTiO}_3$  perovskite single crystals,' *Journal of Crystal Growth* **234** 415-420 (2002).
24. N. Yasuda, H. Ohwa, M. Kume, K. Hayashi, Y. Hosono, Y. Yamashita, 'Crystal growth and electrical properties of lead indium niobate-lead titanate binary single crystal,' *Journal of Crystal Growth* **229** 299-304 (2001).
25. S. Zhang, L. Lebrun, S. Rhee, R. E. Eitel, C. A. Randall, T. R. Shrout, 'Crystal growth and characterization of new high Curie temperature  $(1-x)\text{BiScO}_3$ - $x\text{PbTiO}_3$  single crystals,' *Journal of Crystal Growth* **236** 210-216 (2002).
26. Y. Hosono, Y. Yamashita, H. Sakamoto, N. Ichinose, 'Large piezoelectric constant of high-Curie-temperature  $\text{Pb}(\text{In}_{1/2}\text{Nb}_{1/2})\text{O}_3$ - $\text{Pb}(\text{Mg}_{1/3}\text{Nb}_{2/3})\text{O}_3$ - $\text{PbTiO}_3$  ternary single crystal near morphotropic phase boundary,' *Japanese Journal of Applied Physics* **41** (11A) L1240-L1242 (2002).
27. Y. Hosono, Y. Yamashita, H. Sakamoto, N. Ichinose, 'Dielectric and piezoelectric properties of  $\text{Pb}(\text{In}_{1/2}\text{Nb}_{1/2})\text{O}_3$ - $\text{Pb}(\text{Mg}_{1/3}\text{Nb}_{2/3})\text{O}_3$ - $\text{PbTiO}_3$  ternary ceramic materials near the morphotropic phase boundary,' *Japanese Journal of Applied Physics* **42** (2A) 535-538 (2003).

# Piezo- and ferroelectric $(1-x)\text{Pb}(\text{Sc}_{1/2}\text{Nb}_{1/2})\text{O}_3-x\text{PbTiO}_3$ solid solution system

---

Y-H BING and Z-G YE,  
Simon Fraser University, Canada

## 7.1 Introduction

Single crystals of the solid solutions between the relaxor ferroelectrics  $\text{Pb}(\text{Mg}_{1/3}\text{Nb}_{2/3})\text{O}_3$  (PMN) and  $\text{Pb}(\text{Zn}_{1/3}\text{Nb}_{2/3})\text{O}_3$  (PZN), and the normal ferroelectric  $\text{PbTiO}_3$  (PT), namely, PMN–PT and PZN–PT, have attracted a great deal of attention over the past years because of their high dielectric constant and extraordinary piezoelectric properties, with a strain levels exceeding 1% and an electromechanical coupling factor  $k_{33} > 90\%$  (Park and Shrout, 1997; Kuwata *et al.*, 1981), which outperform the state-of-the-art PZT-based piezoceramics (with 0.1% and 70–75%, respectively). The electromechanical performance of these crystals makes them the materials of choice for the next generation of acoustic transducers.

An intense program of materials development and device demonstrations has been undertaken under the sponsorships of the US Defense Advanced Research Projects Agency and the Office of Naval Research, which has advanced the materials technology to the level of prototype quantities/costs and confirmed the considerable potential – enhanced device sensitivity, source level, bandwidth and compactness – originally envisioned for Navy SONAR devices (Cross, 2004; Park and Shrout, 2002; Yamashita *et al.*, 2002). On the other hand, a wide range of advanced applications based on these innovative piezocrystals is also being actively pursued in the civilian sectors, including medical ultrasonic diagnostics and therapy, active machine tool control and vibration suppression (see Chapters 3 and 4). For example, the excellent properties of the piezocrystals used in the medical ultrasonic imaging system have resulted in dramatic improvements in the efficiency, sensitivity and bandwidth of the ultrasound transducers (Philips, 2004; Chen and Panda 2004).

However, there are several issues regarding future applications of the PMN–PT and PZN–PT crystals. One of them is a low Curie temperature ( $T_C < 160^\circ\text{C}$ ) and especially an even lower depoling temperature ( $T_{\text{MPB}} < 100^\circ\text{C}$ ) in these crystals because of the presence of a morphotropic phase

boundary (MPB). The low  $T_{\text{MPB}}$  and  $T_{\text{C}}$  cause the materials to be depoled easily, reduce the thermal stability of dielectric and piezoelectric properties, limit the acoustic power and the temperature range of operation of the devices and also make the device fabrication processing more difficult (Park and Shrout, 2002; Yamashita *et al.*, 2002). These drawbacks would significantly reduce the piezoelectric response and thereby diminish the performance of the transducer devices. Therefore, high temperature stability is necessary for applications in many areas.

To solve these issues, active studies have been pursued on several compounds with higher  $T_{\text{C}}$ . Piezoelectric single crystals of  $(1-x)\text{Pb}(\text{Yb}_{1/2}\text{Nb}_{1/2})\text{O}_3-x\text{PbTiO}_3$  solid solution were grown using a flux technique and the electromechanical properties were reported by Zhang *et al.* (2002a,b). The Curie temperature of the grown crystals lies in the range of 300–400 °C. The piezoelectric coefficient  $d_{33}$  is high and reaches approximately 2500 pC/N for the  $\langle 001 \rangle$ -oriented PYN–46%PT single crystals. The system of  $(1-x)\text{BiScO}_3-x\text{PbTiO}_3$  with MPB compositions was synthesized in the form of ceramics with a Curie temperature of 430 °C and a  $d_{33}$  of 450 pC/N at a composition of  $x = 0.64$  (Eitel *et al.*, 2001). The  $(1-x)\text{BiScO}_3-x\text{PbTiO}_3$  single crystals were grown using a flux method. The Curie temperature of rhombohedral crystals was found to be about 404 °C, with a rhombohedral–tetragonal phase transition temperature around 350 °C (Zhang *et al.*, 2003). Single crystals of  $(1-x)\text{Pb}(\text{In}_{1/2}\text{Nb}_{1/2})\text{O}_3-x\text{PbTiO}_3$  and their electromechanical properties were also reported with a  $T_{\text{C}}$  around 320 °C and a  $d_{33}$  of 400 pC/N (Yasuda *et al.*, 1999, 2000a,b).

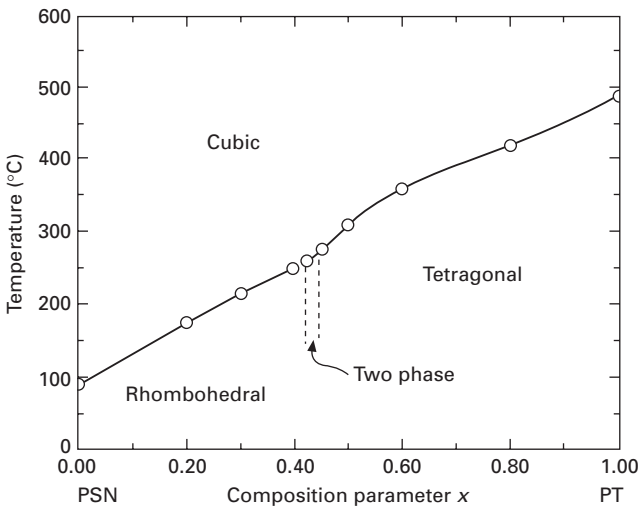
Despite the above encouraging results, continued research on other new MPB systems of high  $T_{\text{C}}$  piezoelectric materials in the form of ceramics and single crystals constitutes an important area of investigation for the future development of high-temperature transducers operating at temperatures much higher than room temperature. The solid solution of  $(1-x)\text{Pb}(\text{Sc}_{1/2}\text{Nb}_{1/2})\text{O}_3-x\text{PbTiO}_3$  has emerged as an interesting system to study and exploit because it shows the existence of an MPB with a Curie temperature  $T_{\text{C}} > 200$  °C.

The solid solution of  $(1-x)\text{Pb}(\text{Sc}_{1/2}\text{Nb}_{1/2})\text{O}_3-x\text{PbTiO}_3$  [ $(1-x)\text{PSN}-x\text{PT}$ ] is formed between the relaxor  $\text{Pb}(\text{Sc}_{1/2}\text{Nb}_{1/2})\text{O}_3$  and the normal ferroelectric  $\text{PbTiO}_3$ .  $\text{Pb}(\text{Sc}_{1/2}\text{Nb}_{1/2})\text{O}_3$  (PSN) was first synthesized in the form of ceramics by Smolenskii *et al.* (1959). This compound has the perovskite structure and its Curie temperature is  $T_{\text{C}} = 90$  °C. Single crystals of PSN were grown using the flux method with  $\text{PbO}$  or  $\text{PbO}-\text{B}_2\text{O}_3$  as flux (Yanagisawa *et al.*, 1998). The study of the  $(1-x)\text{PSN}-x\text{PT}$  binary system was first reported by Tennery *et al.* (1968) based on the experiments on ceramic specimens. Very high peak values (about 26 000) of dielectric constant, with the peak value of loss in the order of 0.05 to 0.08, were observed at  $x = 0.20$ . The rhombohedral symmetry was assigned for the composition  $x < 0.425$  and tetragonal for  $x > 0.45$  at room temperature. In the range of  $0.425 \leq x \leq 0.45$ , a mixture of

rhombohedral and tetragonal phases was proposed. The piezoelectric radial coupling coefficient ( $k_p$ ) was studied as a function of  $x$  and the maximum value of  $k_p = 0.46$  was observed with  $x = 0.425$ , which falls into the region of two-phase coexistence. A preliminary phase diagram was established by means of dielectric measurements and a two-phase region corresponding to the composition around  $x = 0.425$  with a Curie temperature around  $260^\circ\text{C}$  was roughly sketched (Fig. 7.1).

After Tennery's work, only few studies were carried out on the  $(1-x)\text{PSN}-x\text{PT}$  compounds. Yamashita (1994a) reported the large electromechanical coupling factors of  $k_p = 71\%$ ,  $k_{33} = 77\%$ , and a piezoelectric coefficient  $d_{33} = 450$  pC/N for the  $(1-x)\text{PSN}-x\text{PT}$  ceramics and the Nb-doped  $(1-x)\text{PSN}-x\text{PT}$  ceramics with  $x = 0.43$ . Later, Yamashita *et al.* (1996, 1997) reported the crystal growth and electrical properties of the  $(1-x)\text{PSN}-x\text{PT}$  single crystals grown by a flux method using  $\text{PbO}-\text{B}_2\text{O}_3$  as the solvent. The chemical analysis revealed that the composition of the crystals is in the range of 0.33 to 0.35, which is different from the initially weighed MPB composition of  $x = 0.42$ . The  $\langle 001 \rangle$ -oriented crystal showed a dielectric constant peak of 60 000 at the  $T_C$  of  $206^\circ\text{C}$ , a remnant polarization  $P_r = 26$   $\mu\text{C}/\text{cm}^2$ , a coercive field  $E_C = 6$  kV/cm and a coupling factor  $k_{33} = 72\%$ .

Nevertheless, there are several issues concerning the growth of  $(1-x)\text{PSN}-x\text{PT}$  crystals that have not been resolved. Because of the very high melting point,  $T_m > 1425^\circ\text{C}$  (Yanagisawa *et al.*, 1998) of the solid solution system, difficulties were encountered in the growth. Consequently, the dielectric and piezoelectric properties of the  $(1-x)\text{PSN}-x\text{PT}$  crystals have not been fully



7.1 Original temperature vs. composition phase diagram for the  $(1-x)\text{Pb}(\text{Sc}_{1/2}\text{Nb}_{1/2})\text{O}_3-x\text{PbTiO}_3$  system (after Tennery *et al.*, 1968).

studied and exploited owing to the poor quality and the significant composition fluctuations of the crystals grown previously.

On the other hand, there are several fundamental issues regarding the  $(1-x)\text{PSN}-x\text{PT}$  system in general that remain to be understood. First, the MPB region of the solid solution is not yet clearly defined. The preliminary phase diagram in Fig. 7.1 only sketched the region of two-phase coexistence, lacking detailed information on phase symmetry and phase components. A more complex MPB was found in the PZT system (Jaffe *et al.*, 1971; Noheda *et al.*, 1999), and then in the PZN–PT (Kuwata *et al.*, 1981; La-Orauttapong *et al.*, 2002) and PMN–PT systems (Choi *et al.*, 1989; Sing and Pandey, 2001; Ye *et al.*, 2001; Noheda *et al.*, 2002). It is expected that the phase diagram of the  $(1-x)\text{PSN}-x\text{PT}$  system should show similar features, with the presence of an MPB region with a curved upper boundary, the complexity of the phase components and the presence of low symmetry phase(s). Recently, Haumont *et al.* (2003) proposed a modified  $(1-x)\text{PSN}-x\text{PT}$  phase diagram based on the analysis of X-ray and neutron diffraction data. In this phase diagram, the rhombohedral symmetry was confirmed as a ground state for  $x \leq 0.26$ , while the pure tetragonal symmetry was observed for  $x \geq 0.55$ . A new monoclinic phase was deduced for  $0.37 < x < 0.43$ . However, the information for upper boundary of the MPB is missing and no additional anomaly except the one for  $T_C$  was found in the permittivity measurements as a function of temperature, which would be associated with the phase transition of the monoclinic phase. It is well known that two anomalies were detected in the PMN–PT (Shrout *et al.*, 1990) and PZN–PT (Kuwata *et al.*, 1981) systems from the measurements of the dielectric permittivity upon cooling, corresponding to the two transitions: one is the transition from the paraelectric to the ferroelectric tetragonal phase at  $T_C$ , the other is the transition from the tetragonal to the ferroelectric rhombohedral or monoclinic phase. Such MPB behaviour is also expected to occur in the  $(1-x)\text{PSN}-x\text{PT}$  system.

This chapter describes the synthesis, structure, morphotropic phase diagram, and properties of the  $(1-x)\text{Pb}(\text{Sc}_{1/2}\text{Nb}_{1/2})\text{O}_3-x\text{PbTiO}_3$  solid solution ceramics (Section 7.2), and the growth and characterization of  $\text{Pb}(\text{Sc}_{1/2}\text{Nb}_{1/2})\text{O}_3$  and  $(1-x)\text{Pb}(\text{Sc}_{1/2}\text{Nb}_{1/2})\text{O}_3-x\text{PbTiO}_3$  single crystals (Selections 7.3 and 7.4).

## 7.2 Synthesis, structure, morphotropic phase diagram and properties of the $(1-x)\text{Pb}(\text{Sc}_{1/2}\text{Nb}_{1/2})\text{O}_3-x\text{PbTiO}_3$ solid solution ceramics

In this section, we describe the systematic study of the  $(1-x)\text{PSN}-x\text{PT}$  solid solution in the form of ceramics with compositions within the morphotropic phase boundary (MPB) region ( $0.35 \leq x \leq 0.50$ ), in terms of structure and physical properties. The morphotropic phase diagram has been discussed

with the presence of the newly discovered monoclinic phases, providing a better understanding of the complex MPB behaviour and phase components. This information is useful for the preparation of the  $(1-x)\text{PSN}-x\text{PT}$  single crystals for high  $T_C$  piezoelectric applications.

### 7.2.1 Synthesis of the $(1-x)\text{Pb}(\text{Sc}_{1/2}\text{Nb}_{1/2})\text{O}_3-x\text{PbTiO}_3$ ceramics

Analogue to the synthesis of PMN ceramics proposed by Swartz and Shrout (1982), the perovskite PSN and  $(1-x)\text{PSN}-x\text{PT}$  ceramics free from pyrochlore phases were prepared based on the wolframite precursor method (Yamashita, 1993, 1994b; Adachi *et al.*, 1994, 1995). The important steps we used for synthesis of the  $(1-x)\text{PSN}-x\text{PT}$  ceramics are described here.

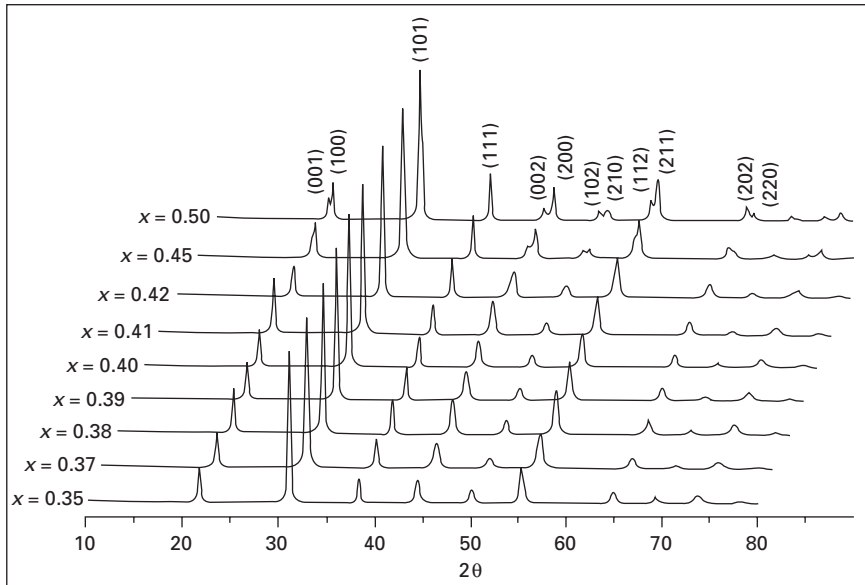
Considering that the evaporation of PbO is significantly accelerated when the temperature is higher than 950 °C, the calcination of the  $(1-x)\text{PSN}-x\text{PT}$  powder takes place at temperatures below 900 °C and the mixture is reacted in a closed atmosphere by placing it into an alumina crucible sealed with an alumina lid.

Our experimental results show that the  $(1-x)\text{PSN}-x\text{PT}$  solid solution obtained by the calcination process is not always free of pyrochlore phase. The appearance of the pyrochlore phase is attributed to the relatively low reaction temperature (< 900 °C) and to the partial loss of PbO, both favouring the formation of the pyrochlore phase. Therefore, 2–5% excess of PbO out of total chemical weight is generally added to the mixture prior to the calcining processing and the weight loss of the mixture is monitored after calcining and sintering.

The pellets of  $(1-x)\text{PSN}-x\text{PT}$  are sintered in a PbO-rich environment at 1270–1280 °C for 6 to 8 h. The resulting  $(1-x)\text{PSN}-x\text{PT}$  ceramics show a shrinkage of about 13% in diameter on the average. The formation of a clean perovskite phase free of pyrochlore phase is verified by the powder X-ray spectra.

### 7.2.2 Structural analysis and X-ray spectra of the $(1-x)\text{Pb}(\text{Sc}_{1/2}\text{Nb}_{1/2})\text{O}_3-x\text{PbTiO}_3$ ceramics

X-ray diffraction (XRD) (Philips, Cu K $\alpha$  radiation) was performed on the  $(1-x)\text{PSN}-x\text{PT}$  ceramic pellets of the compositions  $x = 0.35, 0.37, 0.38, 0.39, 0.40, 0.41, 0.42, 0.45,$  and  $0.50$ , that were annealed at high temperature; the spectra are shown in Fig. 7.2. All the ceramics show a clean perovskite phase free of impurities. The tetragonal splits are visible for the composition  $x = 0.45$  and these splits become more clear for the composition  $x = 0.50$ . Upon further decrease of the PT content ( $x < 0.45$ ), a broadened peak with



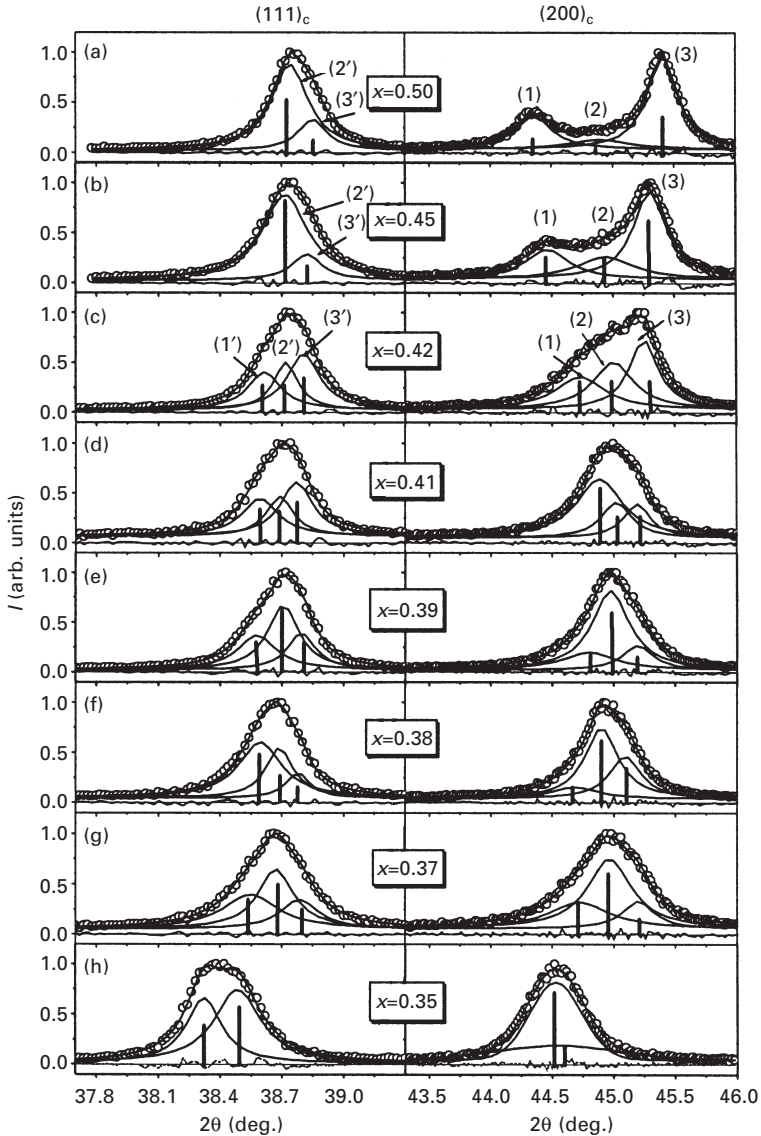
7.2 X-ray spectra of the  $(1-x)\text{Pb}(\text{Sc}_{1/2}\text{Nb}_{1/2})\text{O}_3-x\text{PbTiO}_3$  ceramics with compositions around the MPB.

asymmetrical profile appears for the cubic (200), (210) and (112) reflections, which is an indication of the decrease in the structural symmetry.

More detailed analysis is presented in Fig. 7.3 for the pseudocubic  $(111)_c$  and  $(200)_c$  reflections. It is concluded that the major phase adopts the tetragonal symmetry for  $x = 0.50$  (Fig. 7.3a), with the presence of an additional weak (minority) phase of different symmetry. The steady growth of the second phase is clearly revealed in  $x = 0.45$  (Fig. 7.3b), in which the tetragonal phase is still recognized as the major phase. However, for  $x = 0.42$  (Fig. 7.3c), the tetragonal splitting of  $(200)_c$  becomes less clear, giving rise to a broadened complex reflection profile, which can be fitted into three peaks. According to the theoretically calculated characteristic splitting for the different phases, peaks (1') and (3') on the  $(111)_c$  reflection and peaks (1)–(3) on the  $(200)_c$  reflection indicate the presence of a monoclinic phase, which has become the major phase in  $x = 0.42$ . This monoclinic phase is mixed with some amount of the tetragonal phase which corresponds to peak (2') on  $(111)_c$  and peaks (1) and (3) on  $(200)_c$  that overlap with two of the monoclinic peaks. This mixture of monoclinic and tetragonal phases is also found for the compositions of  $x = 0.41$  to 0.37 (Fig. 7.3d–g), in which both the  $(111)_c$  and  $(200)_c$  reflections show qualitatively the similar features to  $x = 0.42$ .

As  $x$  decreases to 0.35 (Fig. 7.3h), the  $(111)_c$  reflection can be fitted into two peaks that are significantly shifted to lower angles, while the  $(200)_c$  reflection can be well defined by a single peak (plus a broad peak due to





7.3 Pseudocubic  $(111)_c$  and  $(200)_c$  reflections (open circles) of  $(1-x)\text{Pb}(\text{Sc}_{1/2}\text{Nb}_{1/2})\text{O}_3-x\text{PbTiO}_3$  with composition  $x = 0.35, 0.37, 0.38, 0.39, 0.41, 0.42, 0.45,$  and  $0.50$  at room temperature, and the deconvolution of the peak profile with different phase components. The fitting profile, the curves after deconvolution and the residues of the fitting results are shown together. The vertical lines indicate the peak positions after deconvolution of the peak profile with approximate intensity ratios. The pseudocubic reflections  $(111)_c$  and  $(200)_c$  were fitted to a Lorentzian function. One exception is for the  $(200)_c$  reflection of  $x = 0.35$ , which was fitted by a Gaussian function. The diffracted intensities were normalized with respect to the maximum of peak intensity in the entire spectrum.

background diffusion) of Gaussian function. The two distinct peaks for  $(111)_c$  and the dominant peak for  $(200)_c$  are the signature of the rhombohedral symmetry, indicating the formation of the  $R3m$  phase for  $x = 0.35$ .

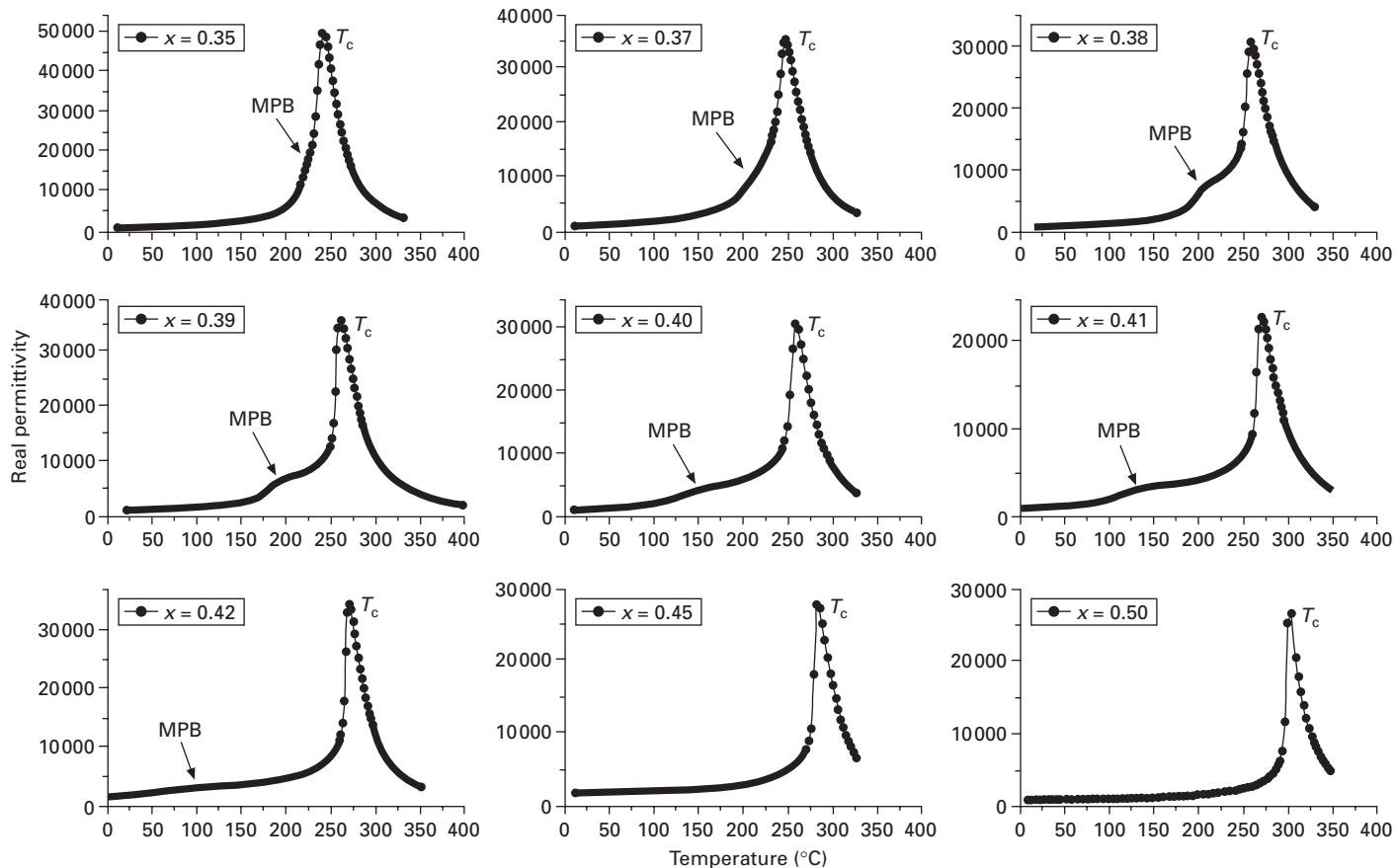
Based on the above analysis, we conclude that the solid solution of  $(1-x)\text{PSN}-x\text{PT}$  with compositions in the MPB region exhibits a complex phase mixture with the monoclinic phase that appears as the major phase for  $0.37 \leq x \leq 0.42$ , and a small amount of the tetragonal phase. This observation is in agreement with the report by Haumont *et al.* (2003), who evidenced a monoclinic phase (of  $Pm$  or  $Cm$  symmetry) as the ground state combined with some amount of the tetragonal phase for the composition  $x = 0.43$ .

### 7.2.3 Dielectric properties

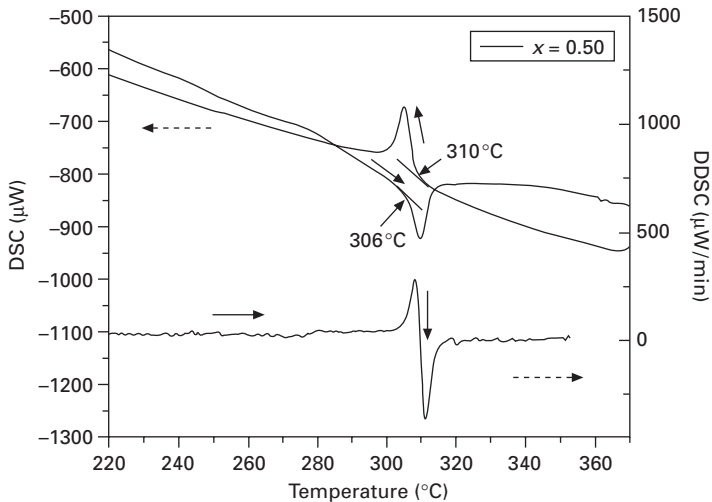
The dielectric permittivity as a function of temperature at various frequencies (from 10 to 100 kHz) was measured from 400 °C down to 10 °C at 2–3 °C intervals for the  $(1-x)\text{PSN}-x\text{PT}$  ceramics with the compositions  $x = 0.35, 0.37, 0.38, 0.39, 0.40, 0.41, 0.42, 0.45,$  and  $0.50$  by means of an Alpha High Resolution Dielectric/Impedance Analyzer (NovoControl). The real permittivity is shown in Fig. 7.4 for the frequency  $f = 100$  kHz. The spectral features depend on the compositions. For  $x = 0.45$  and  $x = 0.50$ , only one anomaly appears at  $T_C \approx 286$  °C and  $T_C \approx 305$  °C, respectively, corresponding to the phase transition from the paraelectric cubic to the ferroelectric tetragonal phase. For the compositions of  $0.35 \leq x \leq 0.42$ , however, the permittivity spectrum clearly shows two anomalies. In addition to the sharp peak at  $T_C$ , another shoulder-like anomaly appears at a lower temperature, named  $T_{\text{MPB}}$ , indicating a second transition from the ferroelectric tetragonal phase into another ferroelectric phase(s). As Ti content decreases,  $T_C$  moves to a lower temperature, while  $T_{\text{MPB}}$  shifts to a higher temperature. The two anomalies are nearly merged for  $x = 0.35$ . The appearance of  $T_{\text{MPB}}$  and the associated phase transition in  $(1-x)\text{PSN}-x\text{PT}$  indicate the typical features of the morphotropic phase boundary behaviour, as previously observed in the PZT, PMN–PT, and PZN–PT systems (Kuwata *et al.*, 1981; Shrout *et al.*, 1990; Noheda *et al.*, 1999; Ye *et al.*, 2001; Ohwada *et al.*, 2003).

### 7.2.4 Thermal analysis by differential scanning calorimetry (DSC)

The temperature dependences of the heat flow of the  $(1-x)\text{PSN}-x\text{PT}$  ceramics ( $x = 0.35, 0.37, 0.38, 0.39, 0.40, 0.41, 0.42, 0.45,$  and  $0.50$ ) were measured on a differential scanning calorimeter (DSC6200, Seiko Exstar). Figure 7.5 shows the DSC measurement for the  $0.50\text{PSN}-0.50\text{PT}$  ceramics as an example. Thermal anomalies with an endothermic peak on heating and an exothermic peak on cooling are observed. The thermal events show an onset temperature



7.4 Real permittivity of the  $(1-x)\text{Pb}(\text{Sc}_{1/2}\text{Nb}_{1/2})\text{O}_3-x\text{PbTiO}_3$  ceramics as a function of temperature for the compositions  $x = 0.35, 0.37, 0.38, 0.39, 0.40, 0.41, 0.42, 0.45,$  and  $0.50$  at the frequency  $f = 100$  kHz.



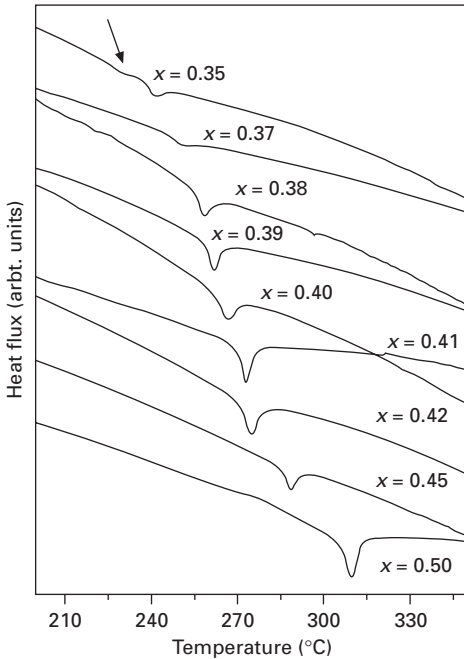
7.5 DSC measurement of  $0.50\text{Pb}(\text{Sc}_{1/2}\text{Nb}_{1/2})\text{O}_3\text{-}0.50\text{PbTiO}_3$  ceramics as a function of temperature on heating and cooling.

of  $306^\circ\text{C}$  upon heating and  $310^\circ\text{C}$  upon cooling, indicating a normal thermal hysteresis. The peak temperature is in good agreement with the permittivity peak temperature of  $0.50\text{PSN-}0.50\text{PT}$  ( $304^\circ\text{C}$ ). The same measurements and analysis were performed on the ceramic samples of different compositions, as shown in Fig. 7.6 for the heating data.

The thermal events detected by the DSC measurements indicate a structural phase transition for all the samples studied. The temperature of the phase transition is in good agreement with the Curie temperature  $T_C$  obtained by the permittivity measurements. An additional weak anomaly is observed on the low-temperature side of the major DSC peak for  $x = 0.35$ , which corresponds to the morphotropic phase transition temperature  $T_{\text{MPB}}$  observed in the dielectric permittivity measurements. This transition should appear in some other compositions, but the thermal events are too weak to be detected.

### 7.2.5 Morphotropic phase diagram of the $(1-x)\text{Pb}(\text{Sc}_{1/2}\text{Nb}_{1/2})\text{O}_3\text{-}x\text{PbTiO}_3$ solid solution system

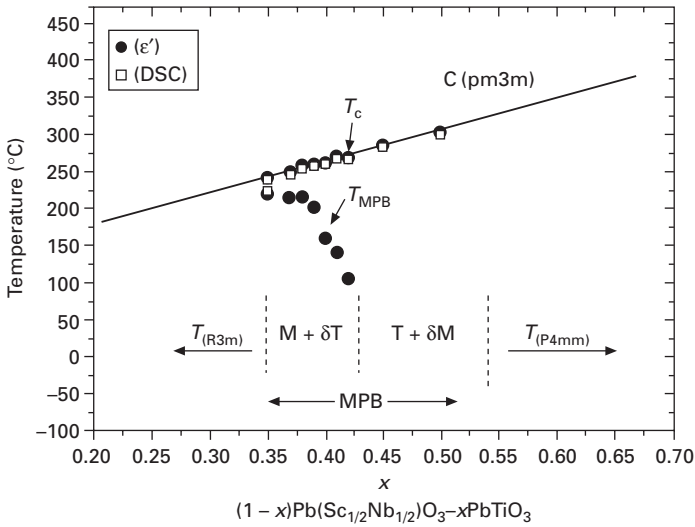
Based on the above XRD, DSC, and dielectric results, a phase diagram for the solid solution of  $(1-x)\text{PSN-}x\text{PT}$  is established with more details in and around the MPB, as shown in Fig. 7.7. The para-/ferroelectric phase transition temperature  $T_C$  is in good agreement with the data previously reported by Tennery *et al.* (1968). The most important feature of this phase diagram is that the MPB region is identified as a mixture of the monoclinic (M) phase



7.6 DSC measurements for the  $(1-x)\text{Pb}(\text{Sc}_{1/2}\text{Nb}_{1/2})\text{O}_3 - x\text{PbTiO}_3$  ceramics with compositions of  $x = 0.35, 0.37, 0.38, 0.39, 0.40, 0.41, 0.42, 0.45,$  and  $0.50$ .

the (majority) and some of the tetragonal (T) phase for  $0.35 < x < 0.42$  at or around room temperature. With  $x$  increasing from 0.42 to 0.50, the T phase becomes the major phase, with the monoclinic phase persisting in a small amount. Therefore, as the PT content ( $x$ ) increases, the  $(1-x)\text{PSN}-x\text{PT}$  solid solution undergoes a sequence of structural changes from the rhombohedral (R) phase ( $x \leq 0.35$ ), to the monoclinic (M) phase mixed with a small amount of the tetragonal phase ( $+\delta\text{T}$ ) ( $0.35 < x < 0.45$ ), then to the tetragonal T phase mixed with a small amount of the monoclinic phase ( $+\delta\text{M}$ ) ( $0.45 \leq x \leq 0.50$ ) and finally to the pure tetragonal (T) phase ( $x > 0.50$ ). (Note that the pure tetragonal phase was observed by Haumont *et al.* (2003) for  $x \geq 0.55$  only.)

More importantly, in Fig. 7.7, the morphotropic phase boundary region is well defined by a curved upper limit, which indicates the temperatures of the morphotropic phase transition  $T_{\text{MPB}}$ . Upon cooling through  $T_{\text{MPB}}$ ,  $(1-x)\text{PSN}-x\text{PT}$  transforms from a tetragonal phase into either a mixture of the monoclinic and the tetragonal phases (for  $0.37 \leq x \leq 0.42$ ) or to the rhombohedral phase (for  $0.35 \leq x < 0.37$ ). The curvature of the MPB upper limit indicates the dependence of the morphotropic phase transition temperature on the composition. Interestingly, the  $(1-x)\text{PSN}-x\text{PT}$  compositions of  $0.35 \leq x \leq 0.39$  exhibit both a higher  $T_{\text{MPB}}$  ( $> 175^\circ\text{C}$ ) and a higher  $T_{\text{C}}$  ( $> 200^\circ\text{C}$ ) than



7.7 Phase diagram for the  $(1-x)\text{Pb}(\text{Sc}_{1/2}\text{Nb}_{1/2})\text{O}_3-x\text{PbTiO}_3$  solid solution around its MPB established based on the results of this work. Solid circles are the boundary between the tetragonal phase (at high temperature) and  $M + \delta T$  phase(s) at low temperature, which represents the upper limit of the MPB region with the monoclinic phase in majority.

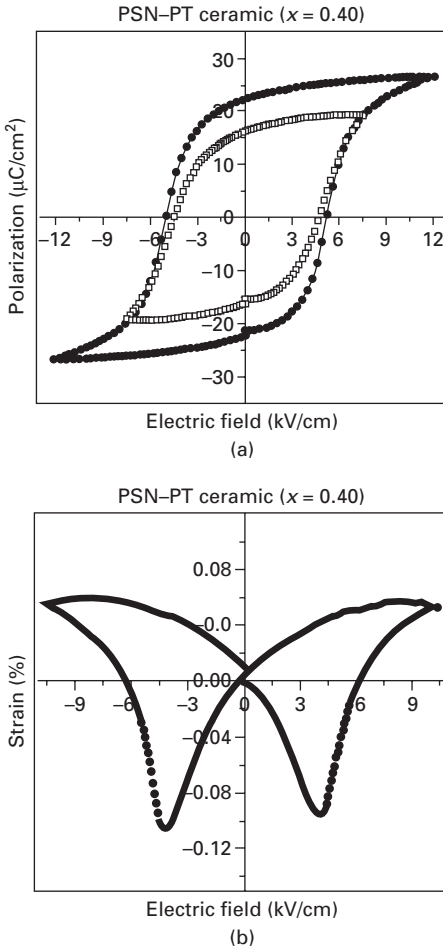
the PMN–PT and PZN–PT systems, making them a more interesting relaxor-based material system for high-temperature piezoelectric applications.

### 7.2.6 Ferroelectric and piezoelectric characterizations

The ferroelectricity of the  $(1-x)\text{PSN}-x\text{PT}$  samples of MPB compositions is confirmed by polarization–electric field hysteresis loops displayed at room temperature. Typical hysteresis loops for 0.60PSN–0.40PT at different applied electric fields ( $\pm 7.5$  kV/cm and  $\pm 12$  kV/cm) are shown in Fig. 7.8(a). The remnant polarization reaches  $P_r \approx 22 \mu\text{C}/\text{cm}^2$  under a drive field of  $E \approx \pm 12$  kV/cm with a coercive field of  $E_C \approx 5$  kV/cm.

Figure 7.8(b) shows the variation of strain as a function of bipolar electric field for the same sample. It displays a symmetric ‘butterfly’ loop, resulting from the bipolar ferroelectric switching behaviour. A peak-to-peak strain value of 0.15% is obtained at  $E = \pm 10$  kV/cm.

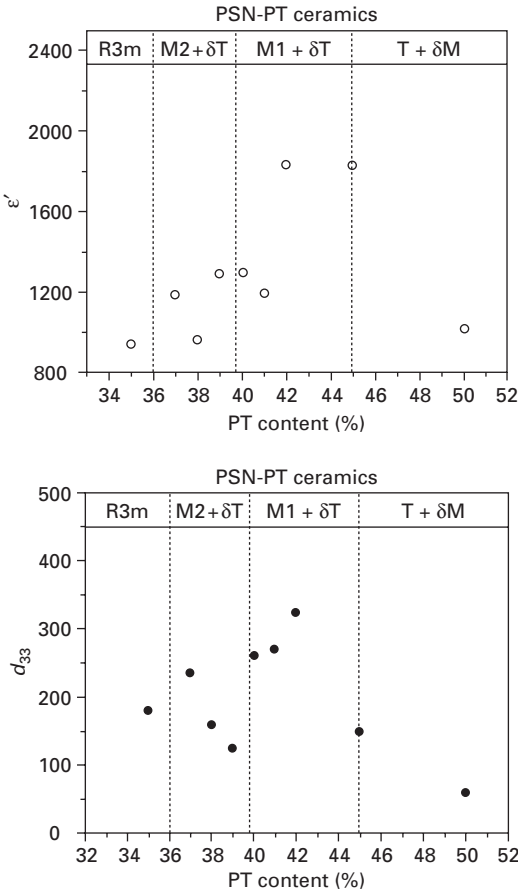
The dielectric constants and the piezoelectric coefficients  $d_{33}$  at room temperature are plotted as a function of compositions and shown in Fig. 7.9. The areas of different phase components are marked to highlight the composition and phase dependence of the properties. It can be seen that the highest values of  $\epsilon'$  and  $d_{33}$  appear in the ceramics of compositions within the MPB region.



7.8 Typical hysteresis loops (a) and strain-electric field variation (b) for  $0.60\text{Pb}(\text{Sc}_{1/2}\text{Nb}_{1/2})\text{O}_3-0.40\text{PbTiO}_3$  ceramics under a bipolar drive (solid circle:  $\pm 12$  kV/cm; open square:  $\pm 7.5$  kV/cm).

### 7.3 Growth of relaxor ferroelectric $\text{Pb}(\text{Sc}_{1/2}\text{Nb}_{1/2})\text{O}_3$ and $(1-x)\text{Pb}(\text{Sc}_{1/2}\text{Nb}_{1/2})\text{O}_3-x\text{PbTiO}_3$ single crystals

This section describes the growth of relaxor ferroelectric PSN and  $(1-x)\text{PSN}-x\text{PT}$  solid solution single crystals and Section 7.4 describes the characterization of the physical properties of the grown crystals.



7.9 Room temperature dielectric constants and piezoelectric coefficients  $d_{33}$  as a function of composition and phase component for the  $(1-x)\text{Pb}(\text{Sc}_{1/2}\text{Nb}_{1/2})\text{O}_3-x\text{PbTiO}_3$  ceramics. R stands for the rhombohedral  $R3m$  phase; M1: the monoclinic  $Pm$  phase; M2: the monoclinic  $Cm$  phase; and T: the tetragonal  $P4mm$  phase.

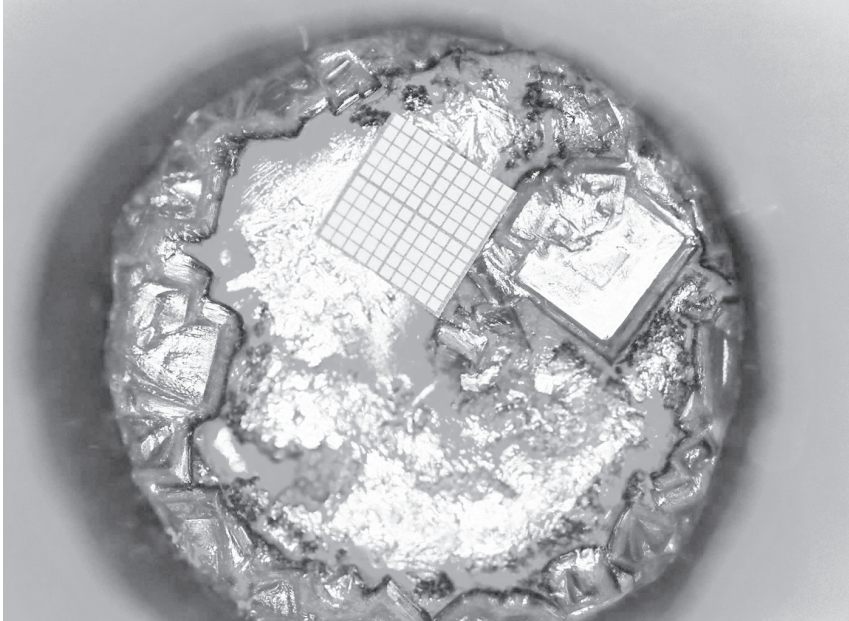
### 7.3.1 Crystal growth

Because of the high melting points of PSN and  $(1-x)\text{PSN}-x\text{PT}$  ( $>1400^\circ\text{C}$ ), the use of a flux is necessary for the crystal growth in order to lower the temperature limits. Previous work has revealed that the mixture of  $(\text{PbO} + \delta\text{B}_2\text{O}_3)$  is an effective solvent for the growth of the PMN-PT and PZN-PT piezocrystals because it combines the advantage of both the borate and the PbO solvent (Dong and Ye, 2000; Zhang *et al.*, 2000). Therefore, similar flux composition and growth conditions are applied for the growth of PSN and  $(1-x)\text{PSN}-x\text{PT}$ . Table 7.1 lists the melting points of PSN (Yanagisawa *et al.*, 1998),  $\text{PbTiO}_3$  (Eisa *et al.*, 1980), PbO (Geller and Bunting 1937), and



*Table 7.1* Melting points of  $\text{Pb}(\text{Sc}_{1/2}\text{Nb}_{1/2})\text{O}_3$  (PSN),  $\text{PbTiO}_3$ ,  $\text{PbO}$ , and  $\text{B}_2\text{O}_3$

Compounds	Melting point (°C)
PSN	1425
$\text{PbTiO}_3$	1285
$\text{PbO}$	886
$\text{B}_2\text{O}_3$	450



*7.10* Top-view of an as-cooled crucible from growth of  $(1-x)\text{Pb}(\text{Sc}_{1/2}\text{Nb}_{1/2})\text{O}_3-x\text{PbTiO}_3$  single crystals, showing the growth by spontaneous nucleation around the crucible walls.

$\text{B}_2\text{O}_3$  (Levin, 1966). It can be seen that the melting point of PSN is much higher than PT, a character that is very similar to the PMN–PT binary system. As a result, a similar phase segregation problem is expected in the grown  $(1-x)\text{PSN}-x\text{PT}$  crystals, as described in the following sections.

A double crucible setup (Dong and Ye, 2000) was used for the crystal growth. From the spontaneous nucleation process upon slow cooling from 1180 to 1000 °C, most of the crystals were nucleated and grown on the bottom and walls of the crucibles (Fig. 7.10), probably because of heat dissipation through the walls of the container. The X-ray powder diffraction shows that the grown crystals exhibit a pure perovskite phase.

### 7.3.2 Growth mechanism

During the growth of PSN and  $(1-x)$ PSN- $x$ PT crystals, the crystals of the pyrochlore phase of the  $\text{Pb}_{1.5}\text{Nb}_2\text{O}_{6.5}$ -type appeared in several growth trials. Interestingly, the formation of the pyrochlore phase was found to depend on the chemical compositions and the lower limit of growth temperature, below which the crystallization process is stopped (Bing and Ye, 2003). It is concluded that a higher portion of flux vs. solute and a larger ratio of PbO vs.  $\text{B}_2\text{O}_3$  help stabilize the perovskite phase down to a lower temperature. A higher amount of  $\text{B}_2\text{O}_3$  in the flux may favour the formation of the pyrochlore phase. In other words, the pyrochlore phase may be more stable over a wider temperature range if the flux is richer in  $\text{B}_2\text{O}_3$ . By carefully selecting the PSNT/flux and PbO/ $\text{B}_2\text{O}_3$  ratios in the solution, it is possible to obtain the perovskite  $(1-x)$ PSN- $x$ PT crystals in a certain temperature range without a pyrochlore phase.

In the growth by spontaneous nucleation, an appropriate supersaturation is required to trigger the formation of the nuclei. On the other hand, the habit of the crystal strongly depends on the growth parameters, e.g. the degree of supersaturation, the temperature profile and the chemical composition (Chernov, 1984). Especially when the growth takes place in polycomponent systems, such as [(PSN-PT) + flux] in this case, a distribution constant  $k$  for a given component can reflect the growth mechanisms. Usually, at slow rates of growth, the effective distribution coefficient  $k_{\text{eff}}$  can be expressed as (Laudise, 1970):

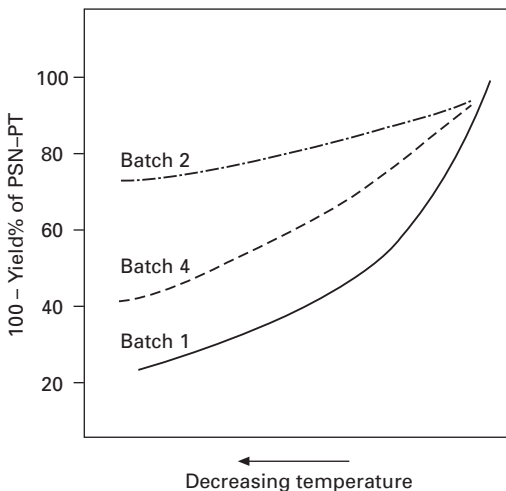
$$k_{\text{eff}} = \frac{C_{\text{s(act)}}}{C_{\text{l(act)}}} \quad 7.1$$

where  $C_{\text{s(act)}}$  and  $C_{\text{l(act)}}$  are the actual concentrations of the products in the form of the solid and liquid. The value of  $k_{\text{eff}}$  depends on the growth rate, the diffusion constant for the materials in the melt, and the width of the diffusion layer. For polycomponent systems,  $k_{\text{eff}}$  can be greater or less than 1. The closer is  $k_{\text{eff}}$  to the unity, the easier the component would get into the bulk. From this point of view,  $k_{\text{eff}}$  is a very important parameter for the crystal growth in a solid solution compound. As we will see later, the value of  $k_{\text{eff}}$  is closely related to the segregation problem in  $(1-x)$ PSN- $x$ PT.

The morphology of the  $(1-x)$ PSN- $x$ PT crystals is affected by a number of factors, including the shape and the size of the container and the chemical ratio between flux and products. The  $(1-x)$ PSN- $x$ PT crystals show a pseudo-cubic form when grown on the crucible bottom, but a distorted form when grown on the walls. The 'ribbon'-like cellular structure was observed in the growing crystals, arising from severe constitutional supercooling conditions occurring during the growth. This happens when the solid/liquid interface of growth cannot adjust itself to keep in a planar surface shape, necessary for a stable growth (Laudise, 1970).

Appropriate ratios of PSNT/flux and  $\text{PbO}/\text{B}_2\text{O}_3$  must be kept to maintain a stable growth. It was found that an increase in the portion of  $\text{B}_2\text{O}_3$  can lower the temperature coefficient of solubility. However, if the level of  $\text{B}_2\text{O}_3$  is too high in the solution, the so-called skeletons or faceted growth will appear, because the crystal is grown under an unstable boundary due to the convex form of solid/liquid interface. The unstable growth is mainly caused by the concentration difference between the corner and the center of the growing cubic crystals (Saito, 1996). The growth may become less stable when the feed is markedly deficient, and the fluctuation in the saturation at the different parts becomes too large to keep a constant normal growth rate over the flat surface. By adding the necessary amount of solute, i.e. by increasing the concentration of  $(1-x)\text{PSN}-x\text{PT}$  in the solution, a more uniform distribution of driven force is established to allow a stable growth (Lawson and Nielsen, 1958; Chernov, 1984).

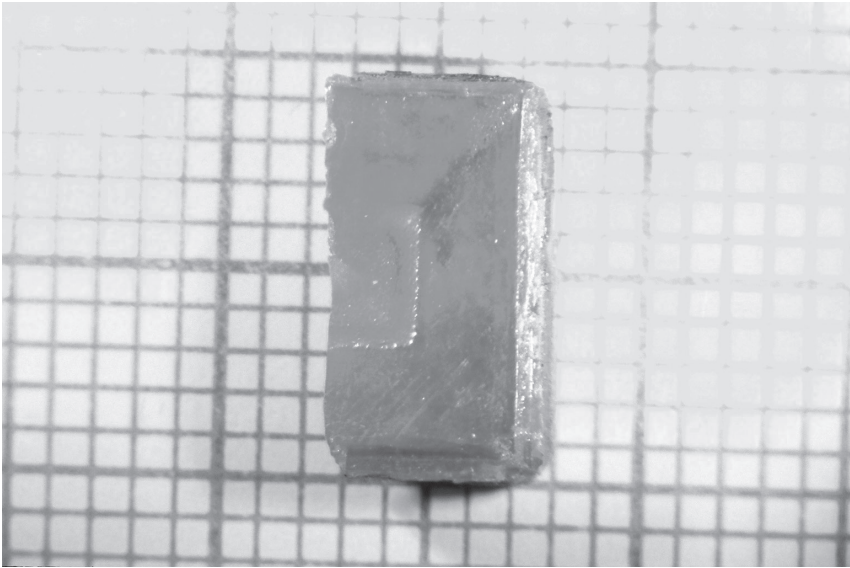
For the growth of  $(1-x)\text{PSN}-x\text{PT}$  solid solution crystals, the above discussion can be depicted by the schematic plot of (100–yield per cent) of the grown  $(1-x)\text{PSN}-x\text{PT}$  single crystals vs. temperature, as shown in Fig. 7.11. The yields (percentages) of the crystallized  $(1-x)\text{PSN}-x\text{PT}$  perovskite crystals were calculated from the ratios of the amount (weight) of the grown  $(1-x)\text{PSN}-x\text{PT}$  crystals over that of the charged nominal  $(1-x)\text{PSN}-x\text{PT}$  powder in the stoichiometric composition in the selected batches and are listed in Table 7.2. Analysis of these data shows that the yields of  $(1-x)\text{PSN}-x\text{PT}$  crystals during the growth are affected by the PSNT/flux and  $\text{PbO}/\text{B}_2\text{O}_3$  ratios. Increasing the portion of  $\text{B}_2\text{O}_3$  in the flux composition in Batch 2,



7.11 Schematic variation of (100–yield%) of the grown  $(1-x)\text{Pb}(\text{Sc}_{1/2}\text{Nb}_{1/2})\text{O}_3-x\text{PbTiO}_3$  single crystals vs. temperature.

*Table 7.2* Summary of the various growth parameters and the yields of the grown  $(1-x)\text{Pb}(\text{Sc}_{1/2}\text{Nb}_{1/2})\text{O}_3-x\text{PbTiO}_3$  single crystals for selected trials

Batch	Ratio of PSNT/ flux (mol%)	Ratio of PbO/ $\text{B}_2\text{O}_3$ (mol%)	Yields of grown PSNT crystals (%)
1	15/85	75/25	$85 \pm 5$
2	15/85	70/30	$22 \pm 2$
3	25/75	70/30	$64 \pm 2$
4	25/75	70/30	$62 \pm 2$



7.12 Crystal of  $(1-x)\text{Pb}(\text{Sc}_{1/2}\text{Nb}_{1/2})\text{O}_3-x\text{PbTiO}_3$  solid solution exhibiting the pseudo-cubic morphology.

while keeping the same ratio of PSNT/flux as in Batch 1, results in a significant reduction of the percentage yields in the same temperature interval, corresponding to a relatively flat temperature curve. Increasing the ratio of PSNT/flux in Batch 4, while keeping the same ratio of PbO/ $\text{B}_2\text{O}_3$  as in Batch 2, increases the yields of  $(1-x)\text{PSN}-x\text{PT}$  crystals and hence the slope of its temperature variation. Therefore, by changing the chemical compositions, the solubility of  $(1-x)\text{PSN}-x\text{PT}$  can be appropriately adjusted to achieve a more stable growth.

Based on the analysis of crystal growth mechanism (Bing and Ye, 2003), the growth parameters were optimized, which has resulted in a significant improvement both in the morphology and the quality of the grown  $(1-x)\text{PSN}-x\text{PT}$  crystals. Figure 7.12 shows a crystal that exhibits pseudo-cubic

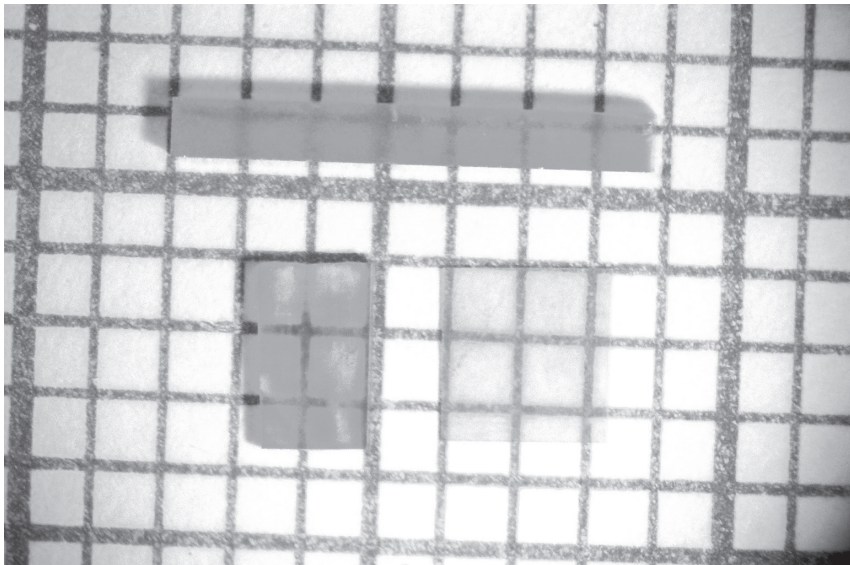
morphology, indicating that an appropriate saturation was achieved at the solid/liquid interface and remained almost constant during the growth.

## 7.4 Properties of $\text{Pb}(\text{Sc}_{1/2}\text{Nb}_{1/2})\text{O}_3$ and $(1-x)\text{Pb}(\text{Sc}_{1/2}\text{Nb}_{1/2})\text{O}_3-x\text{PbTiO}_3$ single crystals

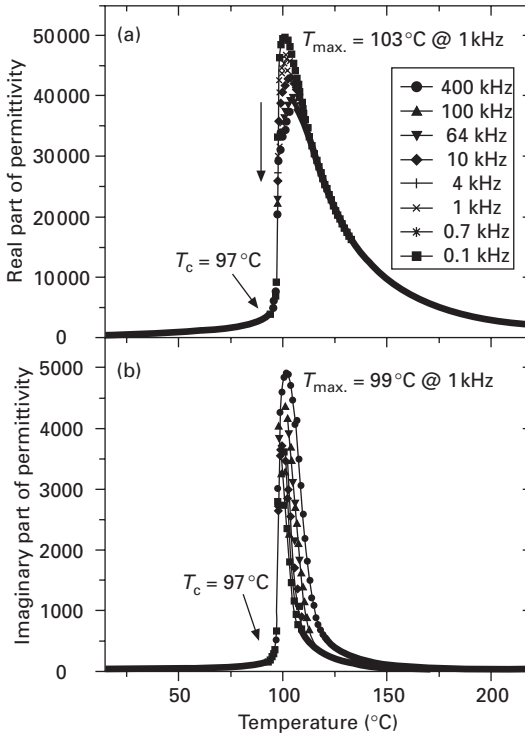
This section describes the dielectric, ferroelectric and piezoelectric properties and the optical domain structure of the PSN and  $(1-x)\text{PSN}-x\text{PT}$  single crystals. Figure 7.13 shows the typical samples used for those characterizations. The  $(001)_{\text{cub}}$ -oriented platelets were mirror polished for optical measurements first and then sputtered with gold layers for the subsequent dielectric and ferroelectric measurements. The rod sample was used for piezoelectric resonance measurements.

### 7.4.1 Dielectric properties of $\text{Pb}(\text{Sc}_{1/2}\text{Nb}_{1/2})\text{O}_3$ crystals

The PSN crystals studied exhibit the typical character of a disordered structure, similar to that reported for the disordered PSN ceramics with a stoichiometric Pb content (Chu *et al.*, 1994). Figure 7.14 shows the temperature dependences



7.13 Typical crystal samples of  $(1-x)\text{Pb}(\text{Sc}_{1/2}\text{Nb}_{1/2})\text{O}_3-x\text{PbTiO}_3$  used for electrical and optical measurements (the  $(001)_{\text{cub}}$ -oriented plate sample for dielectric, ferroelectric and optical measurements, the  $(001)_{\text{cub}}$ -oriented rod sample used for piezoelectric resonance measurements).

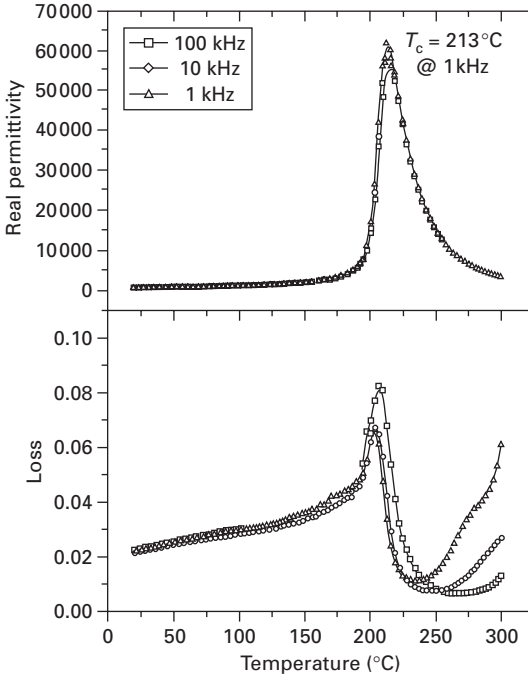


7.14 Real (a) and imaginary (b) parts of permittivity of  $\text{Pb}(\text{Sc}_{1/2}\text{Nb}_{1/2})\text{O}_3$  single crystals, as a function of temperature (upon cooling) at different frequencies.

of the real and imaginary parts of dielectric permittivity for a (001)-oriented PSN crystal measured at different frequencies. Upon cooling, a maximum permittivity was observed at temperature  $T_{\text{max}}$ , which is  $103^\circ\text{C}$  for the real part and  $99^\circ\text{C}$  for the imaginary part (at 1 kHz). It shows frequency dispersion with  $T_{\text{max}}$  shifting to a high temperature as frequency increases, suggesting the typical relaxor ferroelectric behaviour. A remarkable sharp drop of the permittivity can be observed in both real and imaginary parts at the same temperature  $T_c = 97^\circ\text{C}$ , accompanied by a strong attenuation of the frequency dispersion. This sharp decrease in dielectric permittivity immediately below  $T_{\text{max}}$  corresponds to the spontaneous relaxor to ferroelectric phase transition, which is consistent with that reported for PSN ceramics (Chu *et al.*, 1994).

#### 7.4.2 Dielectric properties of $(1-x)\text{Pb}(\text{Sc}_{1/2}\text{Nb}_{1/2})\text{O}_3-x\text{PbTiO}_3$ crystals

Figure 7.15 shows the temperature dependence of the real permittivity (dielectric constant,  $\epsilon'$ ) at various frequencies of a  $(001)_{\text{cub}} (1-x)\text{PSN}-x\text{PT}$



7.15 Real dielectric permittivity and loss of a  $(001)_{\text{cub}}$ -oriented  $(1-x)\text{Pb}(\text{Sc}_{1/2}\text{Nb}_{1/2})\text{O}_3-x\text{PbTiO}_3$  single crystal with nominal composition  $x = 0.425$ .

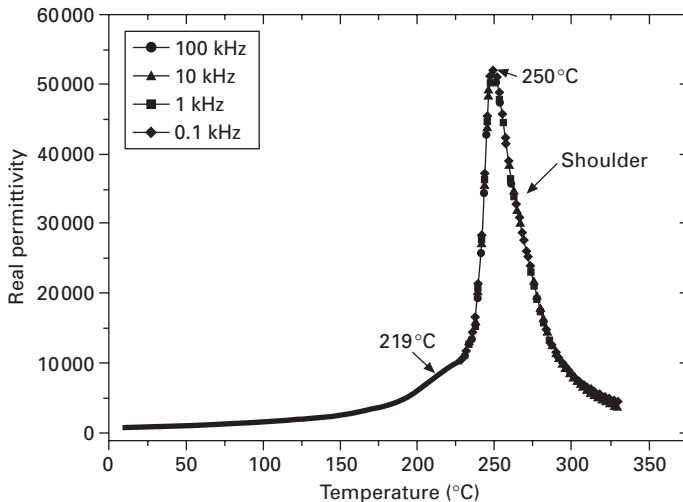
crystal platelet with nominal composition at  $x = 0.425$ , measured from  $300\text{ }^\circ\text{C}$  down to  $10\text{ }^\circ\text{C}$  at  $2\text{--}3\text{ }^\circ\text{C}$  intervals in the frequency range from 10 to 100 kHz. The dielectric constant shows a sharp peak at  $T_{\text{max}} = 213\text{ }^\circ\text{C}$ , corresponding to the ferroelectric Curie temperature  $T_{\text{C}}$ , with a very high maximum value of 60 000. No frequency dispersion is found near  $T_{\text{max}}$ , suggesting a normal ferroelectric behaviour.

It can be seen from the measured transition temperature that the actual composition (estimated to be  $x \approx 0.28$ ) of the grown  $(1-x)\text{PSN}-x\text{PT}$  single crystals differs significantly from the nominal composition ( $x = 0.425$ ). This suggests that a severe phase (or composition) segregation occurs during the crystallization of the solid solution compound. This problem was encountered in the growth of PMN-PT crystals, as well as in many other solid solution systems. The high-temperature phase diagram of the PMN-PT solid solution has recently been established (Gao, 2003). It quantitatively describes the separation of the solidus and liquidus lines which is the origin of the segregation problem. Since the melting point of PSN ( $>1425\text{ }^\circ\text{C}$ ) is higher than that of  $\text{PbTiO}_3$ , we can expect a qualitatively similar phase segregation phenomenon to appear, giving rise to the same trend, i.e. the composition of the grown

$(1-x)\text{PSN}-x\text{PT}$  crystals should contain a lower concentration of  $\text{PbTiO}_3$  than the nominal composition.

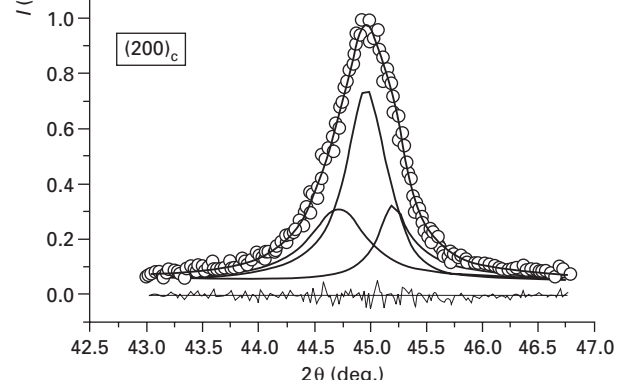
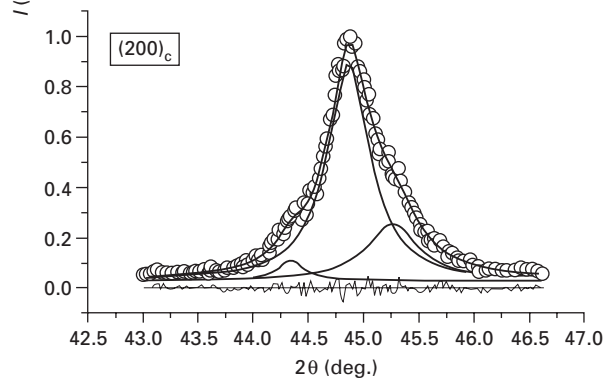
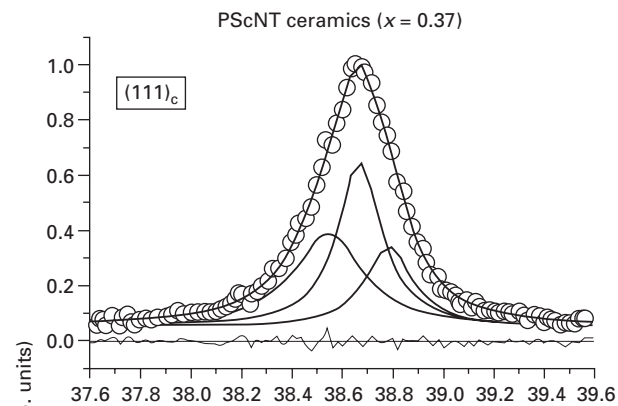
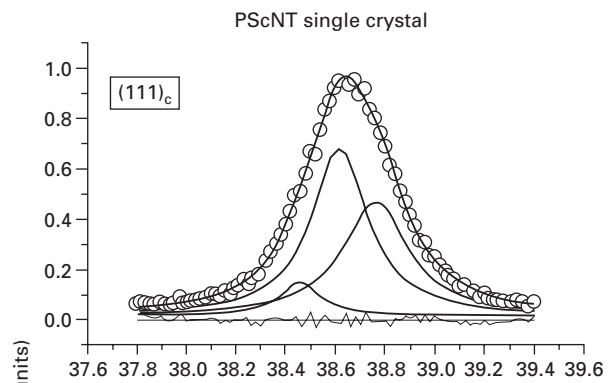
Based on the qualitatively estimated phase segregation trend, the  $(1-x)\text{PSN}-x\text{PT}$  crystals with compositions within the MPB region have been grown from an adjusted nominally charged composition. Figure 7.16 shows the dielectric permittivity measured on the  $(1-x)\text{PSN}-x\text{PT}$  crystals with nominal composition of  $x = 0.51$  upon cooling. It reveals two anomalies at  $T_C = 250^\circ\text{C}$  and  $T_{\text{MPB}} = 219^\circ\text{C}$ , respectively, which are typical of the MPB behaviour of the ferroelectric solid solutions. According to the  $T_C$ -composition relationship shown in the MPB phase diagram of Fig. 7.7, the actual composition of this  $(1-x)\text{PSN}-x\text{PT}$  crystal is located at  $x = 0.37$ . Therefore, the effective phase segregation coefficient is found to be  $k = 0.73$ . Such a smaller-than-unity coefficient indicates that the Ti concentration in the grown crystals is indeed lower than in the liquid of the loaded composition (Eq. 7.1), which is consistent with the estimated phase segregation trend. Similar segregation behavior has been reported for the PMN-PT system (Luo *et al.*, 2000; Zawilski *et al.*, 2003).

In order to investigate the phase symmetry of this MPB crystal in detail, the powder X-ray profiles of the pseudocubic  $(111)_{\text{cub}}$  and  $(200)_{\text{cub}}$  reflections of this crystal are analyzed using the Lorentzian fitting procedure and the results are shown in Fig. 7.17 together with the experimental data from the  $(1-x)\text{PSN}-x\text{PT}$  ceramic with composition at  $x = 0.37$ . Both the  $(111)_{\text{cub}}$  and  $(200)_{\text{cub}}$  reflections can be well fitted with three peaks. The phase analysis of



7.16 Variation of the real part of permittivity of  $(1-x)\text{Pb}(\text{Sc}_{1/2}\text{Nb}_{1/2})\text{O}_3-x\text{PbTiO}_3$  single crystals with composition within the MPB, as function of temperature, measured upon cooling.





(a)

(b)

7.17 Analysis of the X-ray profiles of  $0.63\text{Pb}(\text{Sc}_{1/2}\text{Nb}_{1/2})\text{O}_3-0.37\text{PbTiO}_3$  single crystals and ceramics (open circles: experiment data; solid lines: fitting results).

the MPB crystal in Fig. 7.17(a) indicates that a monoclinic phase is present as the major phase which is mixed with a small amount of the tetragonal phase. Comparing the XRD data and fitting results of the crystals with those of the 0.63PSN–0.37PT ceramics (Fig. 7.17b), it can be seen that the phase symmetry and phase components of both samples are in good agreement with each other, confirming the MPB composition and phase behavior of the grown crystals.

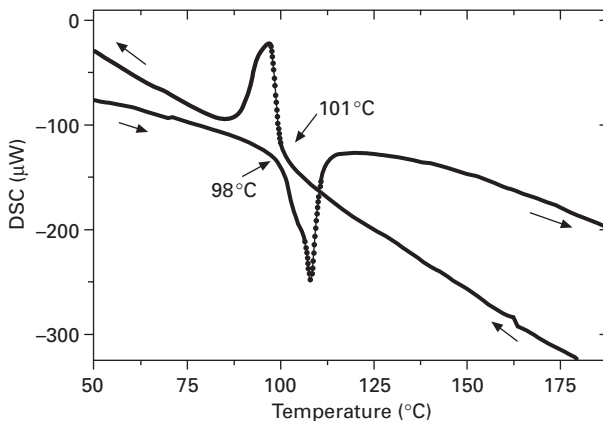
The phase transition of the MPB crystal at  $T_C$  appears as a sharp peak without frequency dispersion. This suggests that as the Ti content increases to 37%, the crystal behaves like a normal ferroelectric with a non-dispersive and sharp phase transition. A slight ‘shoulder-like’ anomaly was observed at about 265 °C for all frequencies in Fig. 7.16, which could be due to the nucleation of precursor domains of the ferroelectric phase (Bing and Ye, 2005).

#### 7.4.3 Calorimetric analysis of $\text{Pb}(\text{Sc}_{1/2}\text{Nb}_{1/2})\text{O}_3$ crystals

Differential scanning calorimetry (DSC) analysis was carried out on PSN crystals. As shown in Fig. 7.18, PSN exhibits a sharp anomaly at 98 °C in the variation of heat flow as a function of temperature, indicating a structure phase transition. This temperature is in good agreement with the temperature  $T_C$  at which the sharp decrease in dielectric permittivity occurs.

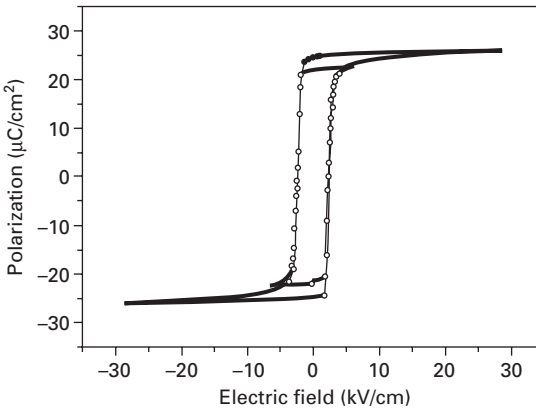
#### 7.4.4 Ferroelectricity

Well-developed ferroelectric hysteresis loops are displayed under the moderate bipolar electric field for the  $(001)_{\text{cub}}$ -oriented PSN and  $(1-x)\text{PSN}-x\text{PT}$  crystals

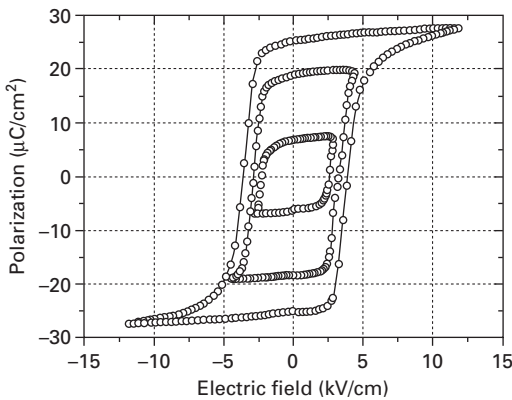


7.18 Differential scanning calorimetry (DSC) measurements of  $\text{Pb}(\text{Sc}_{1/2}\text{Nb}_{1/2})\text{O}_3$  single crystals, upon heating and cooling.

at room temperature, as shown in Fig. 7.19, indicating the ferroelectricity. In PSN, the saturation of the polarization is achieved at an electric field of  $\pm 18$  kV/cm with a maximum polarization of  $25 \mu\text{C}/\text{cm}^2$  and a relatively small coercive electric field of  $E_C \approx 2.5$  kV/cm. Such a hysteresis loop with almost vertical lines and flat electric field dependence indicates a sharp switching of macrodomains and a fairly stable domain state when the electric field is removed. In  $(1-x)\text{PSN}-x\text{PT}$  ( $x = 0.425$ ), the saturation of the polarization is achieved at an electric field of  $\pm 10$  kV/cm. The remnant polarization reaches  $P_r \approx 25 \mu\text{C}/\text{cm}^2$  under a bipolar drive of  $E = \pm 12$  kV/cm with a coercive electric field of  $E_C \approx 4$  kV/cm, slightly larger than that of the PSN crystals.



(a)



(b)

7.19 Polarization vs. electric field (P-E) loops for a  $(001)_{\text{cub}}$ -oriented  $\text{Pb}(\text{Sc}_{1/2}\text{Nb}_{1/2})\text{O}_3$  crystal (a) and  $(1-x)\text{Pb}(\text{Sc}_{1/2}\text{Nb}_{1/2})\text{O}_3-x\text{PbTiO}_3$  ( $x = 0.425$ ) crystal (b) at room temperature, indicating the ferroelectricity.

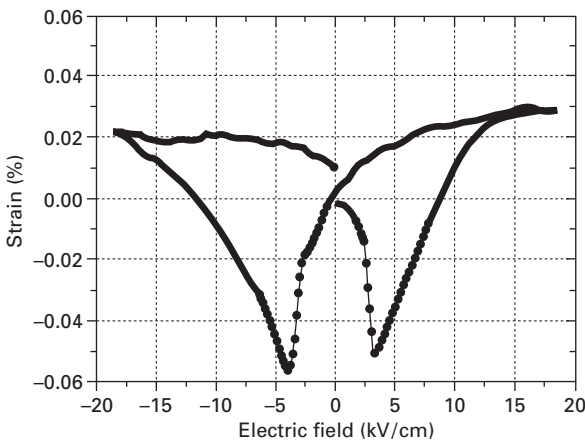
### 7.4.5 Piezoelectricity

Figure 7.20 shows the strain–electric field relation for the  $(001)_{\text{cub}}$ -oriented  $(1-x)\text{PSN}-x\text{PT}$  ( $x = 0.425$ ) sample under a bipolar drive. A peak-to-peak strain value of 0.07% has been reached at  $E \approx \pm 18 \text{ kV/cm}$ .

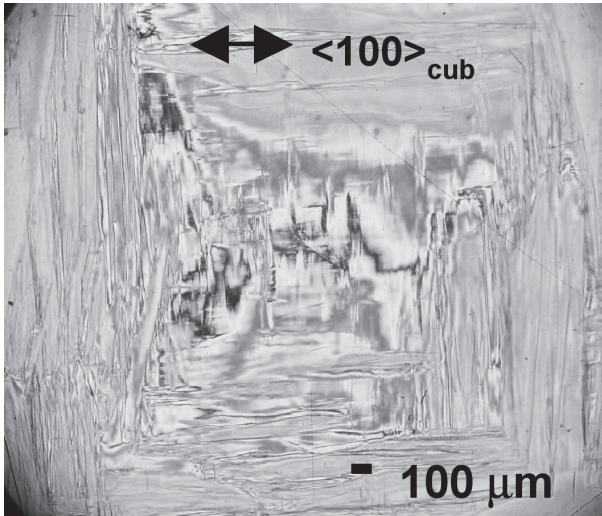
The longitudinal electromechanical coupling factor  $k_{33}$  was determined by the measurements of the resonance ( $f_r$ ) and antiresonance ( $f_a$ ) frequencies for a  $(001)_{\text{cub}}$ -oriented  $(1-x)\text{PSN}-x\text{PT}$  crystal rod. The rod sample is prepoled along the  $\langle 100 \rangle_{\text{cub}}$  length direction by applying an electric field of 20 kV/cm at a temperature above 150 °C, and then cooled to room temperature with the electric field kept on. The typical profile of the resonance ( $f_r$ ) and antiresonance ( $f_a$ ) frequencies at room temperature gives rise to the values of the longitudinal electromechanical coupling factor  $k_{33}$  in the range of 73–80%. The  $d_{33}$  values measured by Berlincourt  $d_{33}$  meter are found in the range of 300–500 pC/N.

### 7.4.6 Domain structure

The domain structure and its evolution as a function of temperature in the  $(001)_{\text{cub}}$ -oriented PSN single crystals and the  $(001)_{\text{cub}}$ -oriented  $(1-x)\text{PSN}-x\text{PT}$  single crystals with different compositions have been observed and examined by cross polarized light microscopy (Olympus BX60) in a temperature range between  $-180^\circ\text{C}$  and  $250^\circ\text{C}$ . Figure 7.21 shows a typical domain pattern in the  $(001)_{\text{cub}}$  PSN plate. The domain pattern at room temperature is composed of fine birefringent domains, indicating a macro-domain state. When the sample was rotated in such a way that the  $\langle 001 \rangle_{\text{cub}}$ .



7.20 The bipolar strain vs. electric field for the  $(001)_{\text{cub}}$ -oriented  $(1-x)\text{Pb}(\text{Sc}_{1/2}\text{Nb}_{1/2})\text{O}_3-x\text{PbTiO}_3$  ( $x = 0.425$ ) single crystal.



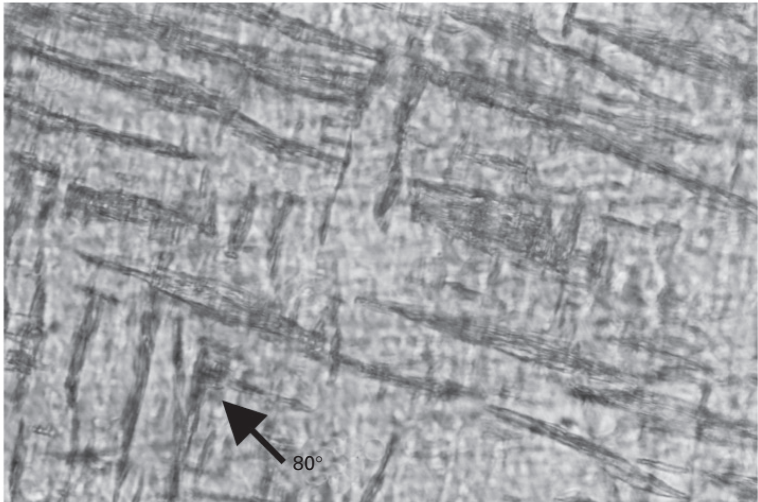
7.21 Domain structure of the  $(001)_{\text{cub}}$ -oriented  $\text{Pb}(\text{Sc}_{1/2}\text{Nb}_{1/2})\text{O}_3$ —single crystals under cross polarized light microscopy at room temperature.

direction of crystal forms an angle of  $45^\circ$  with the directions of the polarizer (namely  $45^\circ$  position hereafter), most areas of the crystal became dark, indicating a rhombohedral symmetry at room temperature as the major phase. A sharp phase transition can be observed upon heating with a full extinction at any angles with respect to the crossed polarizers, which is in agreement with the cubic symmetry. The birefringent domains reappear upon cooling through  $T_C$ .

In the  $(1-x)\text{PSN}-x\text{PT}$  crystals, the long-range ferroelectric states are evidenced by distinct birefringent domains. However, the crystals with different dielectric  $T_{\text{max}}$  show very different domain patterns. The domain patterns for the crystals grown from two different nominal compositions that show the different dielectric  $T_{\text{max}}$  are shown in Fig. 7.22. The crystal with a dielectric  $T_{\text{max}}$  around  $210^\circ\text{C}$  (estimated to be  $x \approx 0.26$ ) exhibits birefringent domains (Fig. 7.22 a) with a fine structure and is in full extinction when the crystal is at the  $45^\circ$  position, indicating a rhombohedral symmetry at room temperature. On the other hand, the crystal that shows a dielectric maximum at  $243^\circ\text{C}$  (with  $x \approx 0.36$ ) displays spindle-like domains (Fig. 7.22 b). The crystals with composition close to or within MPB show only partially extinction while the other parts remain birefringent in a particular position. Such a complex domain structure indicates the coexistence of multiple phases of different symmetry, reflecting the nature of the MPB.



(a) 100 μm



(b) 10 μm

7.22 Domain structure of the  $(001)_{\text{cub}}$ -oriented  $(1-x)\text{Pb}(\text{Sc}_{1/2}\text{Nb}_{1/2})\text{O}_3-x\text{PbTiO}_3$  crystals, which show the different dielectric maximums: (a)  $T_{\text{max}} = 210^\circ\text{C}$  (estimated to be  $x \approx 0.26$ ) and (b)  $T_{\text{max}} = 243^\circ\text{C}$  (estimated to be  $x \approx 0.36$ ), observed at room temperature under cross polarized light microscopy.

## 7.5 Concluding remarks and future trends

In this chapter we present the revised MPB phase diagram of the  $(1-x)\text{Pb}(\text{Sc}_{1/2}\text{Nb}_{1/2})\text{O}_3-x\text{PbTiO}_3$  [ $(1-x)\text{PSN}-x\text{PT}$ ] solid solution system, and describe the optimized growth process and the characterization of the  $(1-x)\text{PSN}-x\text{PT}$  single crystals with composition in the morphotropic phase boundary (MPB) region.

The solid solution of  $(1-x)\text{PSN}-x\text{PT}$  with compositions within the MPB region ( $0.35 \leq x \leq 0.50$ ) has been synthesized in the pure perovskite phase by an improved two-step wolframite precursor method. The MPB phase diagram of the solid solution system has been established by means of dielectric measurements, differential scanning calorimetry (DSC) and X-ray structural analysis. It shows an MPB region, in which a complex phase mixture is proposed with the presence of a monoclinic phase. The materials of MPB compositions typically exhibit two phase transitions at  $T_C$  and  $T_{\text{MPB}}$ , respectively, as revealed by the dielectric anomalies. The increasing substitution of the  $\text{Ti}^{4+}$  ion for the complex  $(\text{Sc}_{1/2}\text{Nb}_{1/2})^{4+}$  ions gives rise to an increase in  $T_C$  and a decrease in  $T_{\text{MPB}}$ .

If we compare the MPB phase diagram of the  $(1-x)\text{PSN}-x\text{PT}$  solid solution with those of the PZT, PZN-PT, and PMN-PT systems, we can see that the phase diagrams of all these solid solutions show some common features, such as the curvature of the MPB upper limit boundary and the presence of an intermediate lower symmetry phase acting as a bridge connecting the rhombohedral (R) and the tetragonal (T) phases. Interestingly, the dielectric and piezoelectric properties are enhanced in the materials of the MPB compositions. Therefore, the establishment of the phase diagram of the  $(1-x)\text{PSN}-x\text{PT}$  solid solution with the monoclinic symmetry lying between the R-phase and the T-phase gives another example of MPB system, useful for understanding the MPB behaviour and the high electromechanical response in these materials, and for developing new piezoelectric crystals for a wide temperature range of applications.

Perovskite PSN and  $(1-x)\text{PSN}-x\text{PT}$  single crystals with composition near the MPB have been grown by an improved flux method. The growth conditions were optimized in terms of the chemical compositions and discussed in the light of thermodynamics and kinetics of crystal growth. It is found that the morphology, the quality, and the chemical and physical properties of the grown crystals are affected by the growth conditions, such as the ratios of PSNT/flux and  $\text{PbO}/\text{B}_2\text{O}_3$ . By adjusting the chemical and thermal parameters, optimum growth conditions have been found, which lead to the growth of  $(1-x)\text{PSN}-x\text{PT}$  single crystals of good quality and of medium size.

The characterization of the piezoelectric properties of the  $(1-x)\text{PSN}-x\text{PT}$  crystals shows that the bipolar strain value and the longitudinal electromechanical coupling factor  $k_{33}$  are comparable with those of PZT

ceramics. Even though these properties are lower than those reported in the PMN–PT and PZN–PT single crystals of the MPB composition, the  $T_C$ , and especially  $T_{MPB}$ , of the  $(1-x)PSN-xPT$  crystals are much higher than those in the PMN–PT and PZN–PT crystals, which represents an attractive feature of this complex system. The rather mediocre piezoelectric performance of the  $(1-x)PSN-xPT$  crystals could be attributed to the fact that the actual composition of the grown crystals departed from the charged MPB one as a result of phase segregation, and also the complexity of the phase mixture.

Future investigation of the  $(1-x)PSN-xPT$  crystals should focus on the further improvement of crystal growth, the minimization of composition segregation and the adjustment of the MPB composition, so as to improve the piezoelectric properties. It is expected that upon optimization of the MPB composition and properties, the  $(1-x)PSN-xPT$  single crystals can constitute a new resource of high piezoelectric crystals with high  $T_C$  and high  $T_{MPB}$ , potentially useful for a wide range of electromechanical transducer applications.

## 7.6 Acknowledgements

This work was supported by the US Office of Naval Research (Grant No. N00014-1-06-0166) and the Natural Science and Engineering Research Council of Canada (NSERC).

## 7.7 References

- Adachi M, Miyabukuro E, and Kawabata A, (1994), 'Preparation and properties of  $Pb[(Sc_{1/2}Nb_{1/2})_{0.575}Ti_{0.425}]O_3$  ceramics', *Jpn. J. Appl. Phys.*, **33**, 5420–5422.
- Adachi M, Toshima T, Takahashi M, Yamashita Y, and Kawabata A, (1995), 'Preparation and properties of niobium-doped  $Pb[(Sc_{1/2}Nb_{1/2})_{0.58}Ti_{0.42}]O_3$  ceramics using hot isostatic pressing', *Jpn. J. Appl. Phys.*, **34**, 5324–5327.
- Bing Y-H, and Ye Z-G, (2003), 'Effects of chemical compositions on the growth of relaxor ferroelectric  $Pb(Sc_{1/2}Nb_{1/2})_{1-x}Ti_xO_3$  single crystals', *J. Crystal Growth*, **250**, 118–125.
- Bing Y-H, and Ye Z-G, (2005), 'Effects of growth conditions on the domain structure and dielectric properties of  $(1-x)Pb(Sc_{1/2}Nb_{1/2})O_3-xPbTiO_3$  single crystals', *Mater. Sci. Eng. B*, **120**, 72–75.
- Chen J, and Panda R, (2004), *PureWave Crystal Technology – White Paper*, Philips.
- Chernov A A, (1984), *Modern Crystallography III*, Berlin, Heidelberg, Springer-Verlag.
- Choi S W, Shrout T R, Jang S J, and Bhalla A S, (1989), 'Dielectric and pyroelectric properties in the  $Pb(Mg_{1/3}Nb_{2/3})O_3-PbTiO_3$  system', *Ferroelectrics*, **100**, 29–38.
- Chu F, Reaney I M, and Setter N, (1994), 'Investigation of relaxors that transform spontaneously into ferroelectrics', *Ferroelectrics*, **151**, 343–348.
- Cross L E, (2004), 'Lead-free at last', *Nature*, **432**, 24–25.
- Dong M, and Ye Z-G, (2000), 'High-temperature solution growth and characterization of the piezo-/ferroelectric  $(1-x)Pb(Mg_{1/3}Nb_{2/3})O_3-xPbTiO_3$  [PMNT] single crystals', *J. Cryst. Growth*, **209**, 81–90.



- Eisa M A, Abadir M F, and Gadalla A M, (1980), 'The system  $\text{TiO}_2\text{-PbO}$  in air', *Trans. J. Br. Ceram. Soc.*, **79**[4], 100–104.
- Eitel R E, Randall C A, Shrout T R, Rehrig P W, Hackenberger W, and Park S-E, (2001), 'New high temperature morphotropic phase boundary piezoelectrics based on  $\text{Bi}(\text{Me})\text{O}_3\text{-PbTiO}_3$  ceramics', *Jpn. J. Appl. Phys.*, **40**, 5999–6002.
- Gao J, (2003), M.Sc. Thesis, 'Synthesis and Phase Diagrams of the  $\text{Pb}(\text{Mg}_{1/3}\text{Nb}_{2/3})\text{O}_3\text{-PbTiO}_3\text{-PbO}$  System', Simon Fraser University, BC, Canada.
- Geller R F, and Bunting E N, (1937), 'The system  $\text{PbO-B}_2\text{O}_3$ ', *J. Research Nat. Bur. Standards*, **18**[5], 585–593.
- Haumont R, Dkhil B, Kiat J M, Al-Barakaty A, Dammak H, and Bellaiche L, (2003), 'Cationic-competition-induced monoclinic phase in high piezoelectric  $(\text{PbSc}_{1/2}\text{Nb}_{1/2}\text{O}_3)_{1-x}(\text{PbTiO}_3)_x$  compounds', *Phys. Rev. B*, **68**, 014114.
- Jaffe B, Cook W R, and Jaffe H, (1971), *Piezoelectric Ceramics*, London, Academic Press.
- Kuwata J, Uchino K, and Nomura S, (1981), 'Phase transitions in the  $\text{Pb}(\text{Zn}_{1/3}\text{Nb}_{2/3})\text{O}_3\text{-PbTiO}_3$  system', *Ferroelectrics*, **37**, 579–582.
- La-Orautapong D, Noheda B, Ye Z-G, Gehring P M, Toulouse J, Cox D E, and Shirane G, (2002), 'Phase diagram of the relaxor ferroelectric  $(1-x)\text{Pb}(\text{Zn}_{1/3}\text{Nb}_{2/3})\text{O}_3-x\text{PbTiO}_3$ ', *Phys. Rev. B*, **65**, 144101.
- Laudise R A, (1970), *The Growth of Single Crystals*, New Jersey, Prentice-Hall Inc.
- Lawson W D, and Nielsen S, (1958), *Preparation of Single Crystal*, London, Butterworths Scientific Publications.
- Levin E M, (1966), *J. Research Nat. Bur. Standards*, **70A**[1], 12.
- Luo H, Xu G, Xu H, Wang P, and Yin Z, (2000), 'Compositional homogeneity and electrical properties of lead magnesium niobate titanate single crystals grown by a modified Bridgman technique', *Jpn. J. Appl. Phys.*, **39**, 5581–5585.
- Noheda B, Cox D E, Shirane G, Gonzalo J A, Cross L E, and Park S-E, (1999), 'A monoclinic ferroelectric phase in the  $\text{Pb}(\text{Zr}_{1-x}\text{Ti}_x)\text{O}_3$  solid solution', *Appl. Phys. Lett.*, **74**, 2059–2061.
- Noheda B, Cox D E, Shirane G, Gao J, and Ye Z-G, (2002), 'Phase diagram of the ferroelectric relaxor  $(1-x)\text{PbMg}_{1/3}\text{Nb}_{2/3}\text{O}_3-x\text{PbTiO}_3$ ', *Phys. Rev. B*, **66**, 054104.
- Ohwada K, Hirota K, Rehrig P W, Fujii Y, and Shirane G, (2003), 'Neutron diffraction study of field-cooling effects on the relaxor ferroelectric  $\text{Pb}[(\text{Zn}_{1/3}\text{Nb}_{2/3})_{0.92}\text{Ti}_{0.08}]\text{O}_3$ ', *Phys. Rev. B*, **67**, 094111.
- Park S E, and Hackenberger W, (2002), 'High performance single crystal piezoelectrics: applications and issues', *Curr. Opin. Solid State & Mater. Sci.* **6**, 11–18.
- Park S E, and Shrout T R, (1997), 'Ultrahigh strain and piezoelectric behavior in relaxor based ferroelectric single crystals', *J. Appl. Phys.*, **82**, 1804–1811.
- Philips, (2004), *Press Release*, 18 October, [http://www.medical.philips.com/main/news/content/file\\_649.html](http://www.medical.philips.com/main/news/content/file_649.html)
- Saito Y, (1996), *Statistical Physics of Crystal Growth*, Singapore, World Scientific.
- Shrout T R, Chang Z P, Kim M, and Markgraf S, (1990), 'Dielectric behavior of single crystals near the  $(1-x)\text{Pb}(\text{Mg}_{1/3}\text{Nb}_{2/3})\text{O}_3\text{-PbTiO}_3$  morphotropic phase boundary', *Ferroelectric Lett.*, **12**, 63–69.
- Sing A K, and Pandey D, (2001), 'Structure and the location of the morphotropic phase boundary region in  $(1-x)[\text{Pb}(\text{Mg}_{1/3}\text{Nb}_{2/3})\text{O}_3]-x\text{PbTiO}_3$ ', *J. Phys.: Condens. Matter.*, **13**, L931–L936.
- Smolenskii G A, Isupov V A, and Agranovskaya A I, (1959), 'New ferroelectrics of complex composition of the type  $\text{A}_2^{2+}(\text{B}_I^{3+}\text{B}_{II}^{5+})\text{O}_6$ ', *Sov. Phys. Solid State*, **1**, 150–151.

- Swartz S L, and Shrout T R, (1982), 'Fabrication of perovskite lead magnesium niobate', *Mater. Res. Bull.*, **17**, 1245–1250.
- Tennery V J, Hang K W, and Novak R E, (1968), 'Ferroelectric and structural properties of the  $\text{Pb}(\text{Sc}_{1/2}\text{Nb}_{1/2})_{1-x}\text{Ti}_x\text{O}_3$  system', *J. Am. Ceram. Soci.*, **51**(12), 671–674.
- Yamashita Y, (1993), 'Improved ferroelectric properties of niobium-doped  $\text{Pb}[(\text{Sc}_{1/2}\text{Nb}_{1/2})\text{Ti}]\text{O}_3$  ceramic material', *Jpn. J. Appl. Phys.*, **32**, 5036–5040.
- Yamashita Y, (1994a), 'Large electromechanical coupling factors in perovskite binary material system', *Jpn. J. Appl. Phys.*, **33**, 5328–5331.
- Yamashita Y, (1994b), 'Piezoelectric properties of niobium-doped  $[\text{Pb}(\text{Sc}_{1/2}\text{Nb}_{1/2})_{1-x}\text{Ti}_x]\text{O}_3$  ceramics material near the morphotropic phase boundary', *Jpn. J. Appl. Phys.*, **33**, 4652–4656.
- Yamashita Y, and Hardada K, (1997), 'Crystal growth and electrical properties of lead scandium niobate–lead titanate binary single crystals', *Jpn. J. Appl. Phys.*, **36**, 6039–6042.
- Yamashita Y, and Shimanuki S, (1996), 'Synthesis of lead scandium niobate–lead titanate pseudo binary system single crystals', *Mater. Res. Bull.*, **31**(7), 887–895.
- Yamashita Y, Hosono Y, Harada K, and Ye Z.-G, (2002), 'Relaxor ferroelectric crystals – recent development and applications', in *Piezoelectric Materials in Devices*, N. Setter (Editor), N. Setter, Lausanne, pp. 455–466.
- Yanagisawa K, Rendon-Angeles J C, Kanai H, and Yamashita Y, (1998), 'Determination of the melting point of lead scandium niobate', *J. Mater. Sci. Lett.*, **17**, 2105–2107.
- Yasuda Y, Ohwa H, Ito K, Iwata M, and Ishibashi Y, (1999), 'Dielectric properties of the  $\text{Pb}(\text{In}_{1/2}\text{Nb}_{1/2})\text{O}_3$ – $\text{PbTiO}_3$  single crystal', *Ferroelectrics*, **230**, 115–120.
- Yasuda Y, Ohwa H, Kume M, and Yamashita Y, (2000a), 'Piezoelectric properties of a high Curie temperature  $\text{Pb}(\text{In}_{1/2}\text{Nb}_{1/2})\text{O}_3$ – $\text{PbTiO}_3$  binary system single crystal near a morphotropic phase boundary', *Jpn. J. Appl. Phys.*, **39**, L66–L68.
- Yasuda Y, Ohwa H, Hasegawa H, Hayashi K, Hosono Y, Yamashita Y, Iwata M, and Ishibashi Y, (2000b), 'Temperature dependence of piezoelectric properties of a high Curie temperature  $\text{Pb}(\text{In}_{1/2}\text{Nb}_{1/2})\text{O}_3$ – $\text{PbTiO}_3$  binary system single crystal near a morphotropic phase boundary', *Jpn. J. Appl. Phys.*, **39**, 5586–5588.
- Ye Z-G, Noheda B, Dong M, Cox D E, and Shirane G, (2001), 'Monoclinic phase in the relaxor-based piezoelectric/ferroelectric  $\text{Pb}(\text{Mg}_{1/3}\text{Nb}_{2/3})\text{O}_3$ – $\text{PbTiO}_3$  system', *Phys. Rev. B*, **64**, 184114.
- Zawilski K T, Claudia M, Custodio C, DeMattei R C, Lee S-G, Monteiro R G, Odagawa H, and Feigelson R S, (2003), 'Segregation during the vertical Bridgman growth of lead magnesium niobate–lead titanate single crystals', *J. Cryst. Growth*, **258**[3–4], 353–367.
- Zhang L, Dong M, and Ye Z-G, (2000), 'Flux growth and characterization of the relaxor-based  $\text{Pb}[(\text{Zn}_{1/3}\text{Nb}_{2/3})_{1-x}\text{Ti}_x]\text{O}_3$  [PZNT] piezocrystals', *Mater. Sci. Eng. B*, **78**, 96–104.
- Zhang S J, Rehrig P W, Randall C A, and Shrout T R, (2002a), 'Crystal growth and electrical properties of  $\text{Pb}(\text{Yb}_{1/2}\text{Nb}_{1/2})\text{O}_3$ – $\text{PbTiO}_3$  perovskite single crystals', *J. Cryst. Growth*, **234**, 415–420.
- Zhang S J, Randall C A, and Shrout T R, (2002b), 'Dielectric and piezoelectric properties of high Curie temperature single crystals in the  $\text{Pb}(\text{Yb}_{1/2}\text{Nb}_{1/2})\text{O}_3$ – $x\text{PbTiO}_3$  solid solution series', *Jpn. J. Appl. Phys.*, **41**, 722–726.
- Zhang S J, Randall C A, and Shrout T R, (2003), 'High Curie temperature piezocrystals in the  $\text{BiScO}_3$ – $\text{PbTiO}_3$  perovskite system', *Appl. Phys. Lett.*, **83**, 3150–3152.

# High Curie temperature piezoelectric single crystals of the $\text{Pb}(\text{In}_{1/2}\text{Nb}_{1/2})\text{O}_3\text{-Pb}(\text{Mg}_{1/3}\text{Nb}_{2/3})\text{O}_3\text{-PbTiO}_3$ ternary materials system

Y J YAMASHITA and Y HOSONO,  
Toshiba R & D Center, Japan

## 8.1 Introduction

During the past 50 years barium titanate ( $\text{BaTiO}_3$ , BT) and lead zirconate titanate ( $\text{Pb}(\text{Zr,Ti})\text{O}_3$ , PZT) have become well established as the preferred ferroelectric materials for a wide variety of ferroelectric devices such as capacitors and piezoelectric actuators. However, in the past two decades, relaxor materials with the general formula  $\text{Pb}(\text{B}'\text{B}'')\text{O}_3$  where  $\text{B}'$  is a low-valence cation, e.g.  $\text{Mg}^{2+}$ ,  $\text{Ni}^{2+}$ ,  $\text{Zn}^{2+}$ ,  $\text{In}^{3+}$ , or  $\text{Sc}^{3+}$ , and  $\text{B}''$  is a high-valence cation, e.g.  $\text{Nb}^{5+}$ ,  $\text{Ta}^{5+}$ , or  $\text{W}^{6+}$ , have been investigated for applications such as multilayer ceramic capacitors and electrostrictive devices. In recent years, a new approach to the development of piezoelectric materials based on  $\text{PbZrO}_3$ -free, relaxor-lead titanate (PT) systems has attracted particular attention (Kuwata *et al.*, 1982, Shrout *et al.*, 1990, Harada *et al.*, 1998). The advantage of relaxor-PT piezoelectric materials compared with conventional PZT, as shown in Table 8.1, is the ease with which piezoelectric single crystals (PSCs) of MPB compositions can be grown.

In particular,  $\text{Pb}[(\text{Zn}_{1/3}\text{Nb}_{2/3})_{0.91}\text{Ti}_{0.09}]\text{O}_3$  (PZNT 91/9) and  $\text{Pb}(\text{Mg}_{1/3}\text{Nb}_{2/3})_{0.68}\text{Ti}_{0.32}]\text{O}_3$  (PMNT 68/32) binary PSCs are well known because they have an extremely large electromechanical coupling factor in longitudinal mode  $k_{33} > 90\%$ , and a large piezoelectric constants,  $d_{33} > 2000$  pC/N, along the [001] axis. Various applications, such as those in medical transducers, actuators, and undersea sonars, have been proposed which would exploit these excellent properties. The authors have already reported on the growth of large PZNT 91/9 PSC by the solution Bridgman method (Harada *et al.*, 1998) and the fabrication of a 3.7 MHz phased-array probe using PZNT 91/9 PSC has been reported, as well as its pulse echo characteristics and the final imaging quality (Saitoh *et al.*, 1999).

However, these binary system PSCs have some disadvantages that must be overcome. Although large PZNT and PMNT PSCs near the MPB are grown by the solution-Bridgman method or the pure Bridgman method with diameters of more than 80 mm, and good dielectric and piezoelectric properties

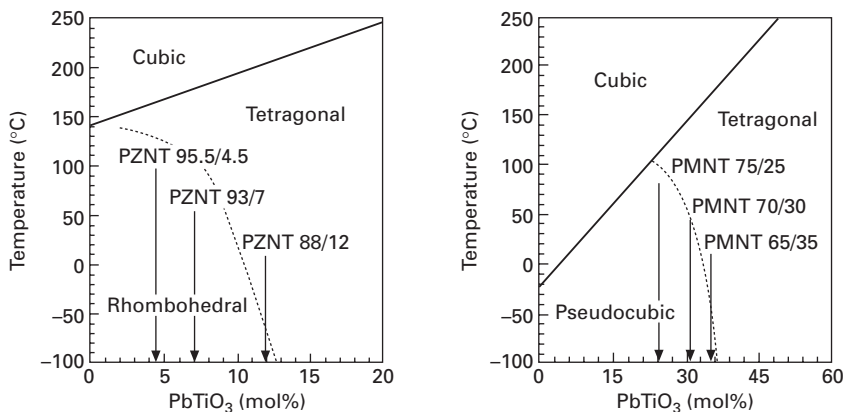
Table 8.1 Relaxor materials, high  $T_C$  materials and their MPBs with lead titanate

Relaxor materials	Abbrev.	$T_C$ K (°C)	$\epsilon_{\max}$	Structure	Ferro.	Ti @ MPB (mol%)	$T_C$ @MPB K (°C)
$\text{Pb}(\text{B}^{2+}_{1/3}\text{B}^{5+}_{2/3})\text{O}_3$							
$\text{Pb}(\text{Cd}_{1/3}\text{Nb}_{2/3})\text{O}_3$	PCdN	273 (0)	8 000	PC	F	28	653 (380)
$\text{Pb}(\text{Zn}_{1/3}\text{Nb}_{2/3})\text{O}_3$	PZN	413 (140)	22 000	R	F	9–10	448 (175)
$\text{Pb}(\text{Mg}_{1/3}\text{Nb}_{2/3})\text{O}_3$	PMN	263 (–10)	18 000	PC	F	30–33	428 (155)
$\text{Pb}(\text{Ni}_{1/3}\text{Nb}_{2/3})\text{O}_3$	PNN	153 (–120)	4 000	PC	F	28–33	403 (130)
$\text{Pb}(\text{Mn}_{1/3}\text{Nb}_{2/3})\text{O}_3$	PMnN	153 (–120)	4 000	PC	F	30–35	403 (130)
$\text{Pb}(\text{Co}_{1/3}\text{Nb}_{2/3})\text{O}_3$	PCoN	175 (–98)	6 000	M	F	33	523 (250)
$\text{Pb}(\text{Mg}_{1/3}\text{Ta}_{2/3})\text{O}_3$	PMgT	175 (–98)	7 000	PC	F	30?	373 (100)
$\text{Pb}(\text{B}^{3+}_{1/2}\text{B}^{5+}_{1/2})\text{O}_3$							
$\text{Pb}(\text{Yb}_{1/2}\text{Nb}_{1/2})\text{O}_3$	PYbN	553 (280)	150	M	AF	50	633 (360)
$\text{Pb}(\text{In}_{1/2}\text{Nb}_{1/2})\text{O}_3$	PIN	363 (90)	550	M	F	37	593 (320)
$\text{Pb}(\text{Sc}_{1/2}\text{Nb}_{1/2})\text{O}_3$	PSN	363 (90)	38 000	R	F	42	533 (260)
$\text{Pb}(\text{Fe}_{1/2}\text{Nb}_{1/2})\text{O}_3$	PFN	385 (112)	12 000	R	F	??	413 (140)
$\text{Pb}(\text{Sc}_{1/2}\text{Ta}_{1/2})\text{O}_3$	PST	299 (26)	28 000	R	F	45	478 (205)
Others							
* $\text{PbZrO}_3$	PZ	513 (240)	3 000	O	AF	47	633 (360)
$(\text{Pb},\text{La})(\text{Zr},\text{Ti})\text{O}_3$	PLZT	<623 (<350)	30 000	R, T	F, AF	35–47	<623 (<350)
$\text{BiScO}_3$	BS	>673 (>350)	<1 000	R	F	64	723 (450)
$\text{BiInO}_3$	BlIn	>973 (>700)	<1 000	R	F?	70	843 (570)
$\text{PbTiO}_3$	PT	763 (490)	9 000	T	F		

C: Cubic, M: Monoclinic, O: Orthorhombic, PC: Pseudocubic, PY: Pyrochlore, R: Rhombohedral, T: Tetragonal, AF: Antiferroelectrics, F: Ferroelectrics.

have been confirmed, they have a relatively low  $T_C$  of approximately 140–175 °C (Luo *et al.*, 1999, 2000). In particular, the low  $T_C$  prevents their use in more general applications. Moreover, they have phase transition temperatures from the rhombohedral to the tetragonal phase at around 50–80 °C, which is referred to as  $T_{RT}$  (Hosono *et al.*, 2002a). Figure 8.1 shows the schematic phase diagrams of the PZNT and PMNT solid solution systems. The PZNT 91/9 and PMNT 70/30 PSC near the morphotropic phase boundary (MPB) consist mainly of rhombohedral phases at room temperature and have excellent dielectric and piezoelectric properties. The dielectric and piezoelectric properties of PZNT and PMNT PSCs change at temperatures above  $T_{RT}$  because of the phase transformation (Feng *et al.*, 2004, 2006; Yamashita *et al.*, 2004a). The coupling factor of the rectangular bar mode,  $k_{33}$ , decreases sharply at  $T_{RT}$  and then decreases gradually towards the  $T_C$ . Therefore, it is necessary to design the compositions of piezoelectric PSCs based on a consideration of the requirements of the specific application so as to achieve the optimum balance between piezoelectric properties and thermal stability. However, it is difficult in either the PZNT or PMNT binary systems to raise  $T_{RT}$  and  $T_C$  simultaneously, as shown in Fig. 8.1. In general, when the  $T_C$  increases, the  $T_{RT}$  decreases. Therefore, designing crystal compositions with high  $T_{RT}$  and  $T_C$  is difficult in these binary PSCs (Yamashita *et al.*, 2004c).

On the other hand, the growth and electrical properties of some relaxor-PT PSCs with high  $T_C$  have been reported, such as  $(1-x)\text{Pb}(\text{In}_{1/2}\text{Nb}_{1/2})\text{O}_3-x\text{PbTiO}_3$  (PINT) (Yasuda *et al.*, 1999, 2001) and  $(1-x)\text{Pb}(\text{Yb}_{1/2}\text{Nb}_{1/2})\text{O}_3-x\text{PbTiO}_3$  (PYNT) PSCs (Zhang *et al.*, 2002) with  $T_C > 250$  °C. Although the crystals show high  $T_C$ , the crystal qualities are poor, the PSC sizes are small and the piezoelectric properties are inferior to those of PZNT and PMNT PSCs. The present authors reported crystal growth and electrical properties



8.1 Schematic PZNT and PMNT phase diagrams near the MPB.

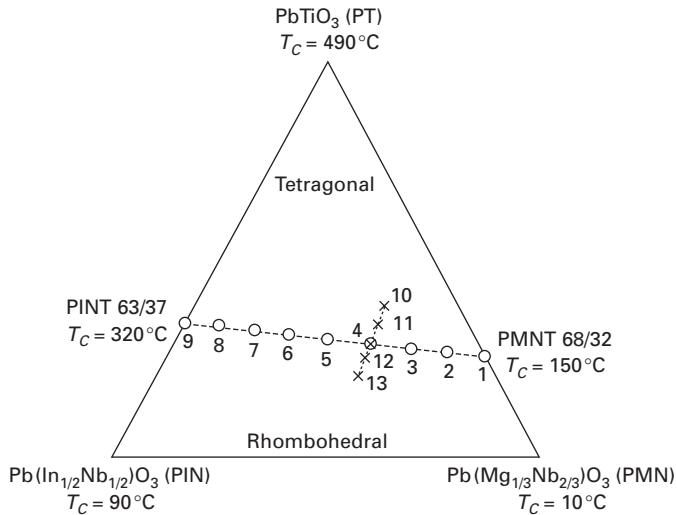
of  $(1-x)\text{Pb}(\text{Sc}_{1/2}\text{Nb}_{1/2})\text{O}_3-x\text{PbTiO}_3$  (PSNT) PSCs (Yamashita and Shimanuki 1996). PSNT has a relatively high  $T_C$  ( $>200^\circ\text{C}$ ); however, it has two major limitations: a high melting point of  $1420^\circ\text{C}$  and a high raw-material cost. Thus, the authors focused on PINT 63/37, which has a high Curie temperature,  $T_C = 320^\circ\text{C}$ , and a relatively low melting point of  $1294^\circ\text{C}$ , as a candidate substitute material for PMNT 68/32 (melting point of  $1271^\circ\text{C}$ ) (Hosono *et al.*, 2000). Because the two melting points are similar, the crystal growth of  $x\text{Pb}(\text{In}_{1/2}\text{Nb}_{1/2})\text{O}_3-y\text{Pb}(\text{Mg}_{1/3}\text{Nb}_{2/3})-z\text{PbTiO}_3$  (PIMNT100x/100y/100z) should be possible. Moreover, it was assumed that the line connecting the MPB compositions of PMNT 68/32 and PINT 63/37 is the MPB composition of the PIMNT ternary system. Therefore, the  $T_C$  of the PIMNT ternary system can be controlled from  $150$  to  $320^\circ\text{C}$  at MPB compositions where it is expected to exhibit good dielectric and piezoelectric properties.

In this chapter, the synthesis and evaluation of PIMNT ternary ceramics are first described. An excellent electromechanical coupling factor,  $k_p = 67\%$ , a relatively high Curie temperature,  $T_C = 197^\circ\text{C}$ , and a good perovskite stability of the PIMNT 16/51/33 ceramics near the MPB have been confirmed (Hosono, 2003a). Crystal growth in the PIMNT ternary system by the Bridgman method will be discussed along with the compositional variation and the dielectric and piezoelectric properties.

## 8.2 PIMNT ceramics

In this section, the physical and electrical properties of PIMNT 100x/100y/100z ceramics near the morphotropic phase boundary (MPB) are presented. We focus on the compositions of the PIMNT ternary system, which are on the straight line connecting the MPBs of the PIMNT 0/68/32 (PMNT68/32) and PIMNT 63/0/37 (PINT63/37) binary systems. The purpose of this work was to study in detail the dielectric and piezoelectric properties of the PIMNT ternary ceramic system in the vicinity of the MPB, and to determine a ceramic material with good piezoelectric properties and a moderate  $T_C$  of around  $200^\circ\text{C}$ .

Figure 8.2 shows the compositions of the samples synthesized in the PIMNT ternary system. Nine compositions along the MPB line and five compositions across the MPB line were prepared. The details of the ceramic sample preparation procedure have been reported in previous papers (Hosono *et al.*, 2002b, 2003a). Figure 8.3 shows X-ray diffraction (XRD) patterns for PIMNT 100x/100y/100z ceramics. As shown in the figure, all ceramic samples had a single phase perovskite structure without any trace of pyrochlore. The result indicates that the perovskite structure is very stable in the PIMNT system. Fired PIMNT 25/43/32 indicated a rhombohedral (R) phase, whereas PIMNT 23/41/36 had a tetragonal (T) phase. However, compositions along the MPB, PIMNT 8/59/33 to PIMNT 56/8/36, showed three different peaks

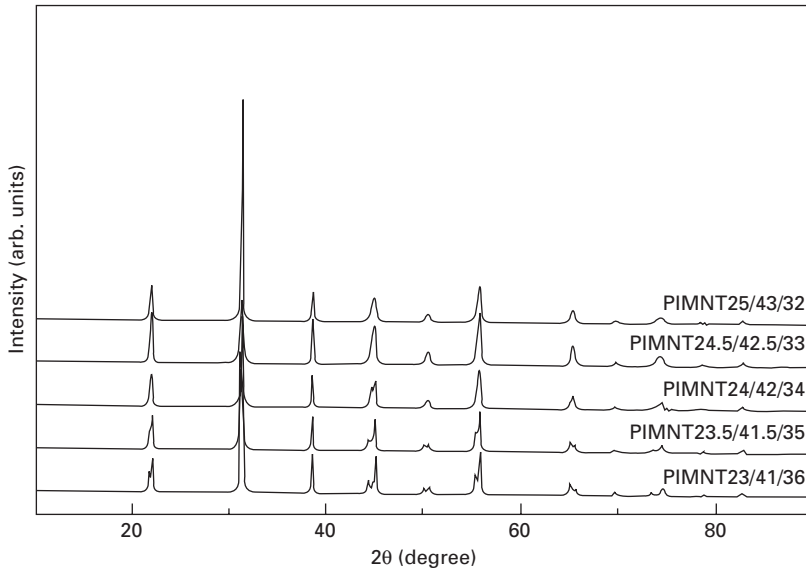
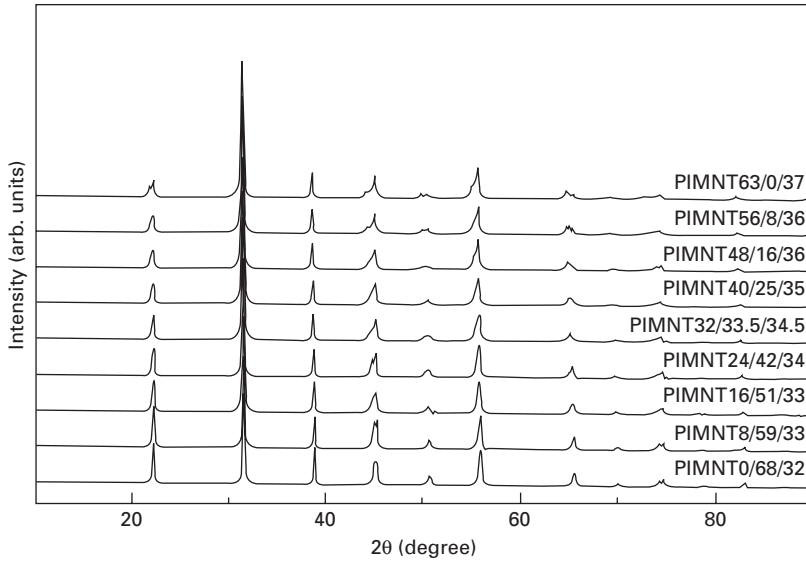


8.2 PIN-PMN-PT ternary system phase diagram.

at around 45 degrees, representing a mixture of the rhombohedral and tetragonal phases. Hence, the MPB is an almost linear, narrow region between the MPBs of the PIMNT 0/68/32 (PMNT 68/32) and PIMNT 63/0/37 (PINT 63/37) binary systems.

Figure 8.4 shows the dielectric properties of PIMNT  $100x/100y/100z$  ceramics along the MPB measured at 100 kHz. The composition, PIMNT 0/68/32, showed a large dielectric constant maximum of 47 480. The dielectric constant maximum decreased as the PIN content increased. This is due to the low dielectric constant maximum of PIMNT 63/0/37. The dependence of  $T_C$  as a function of PIN ( $x$ ) is shown in Fig. 8.5. The  $T_C$  varied from 160 to 320 °C almost linearly as the PIN content increased. This result suggests that the  $T_C$  of the MPB composition in the PIMNT system can be controlled, leading to the realization of excellent piezoelectric properties.

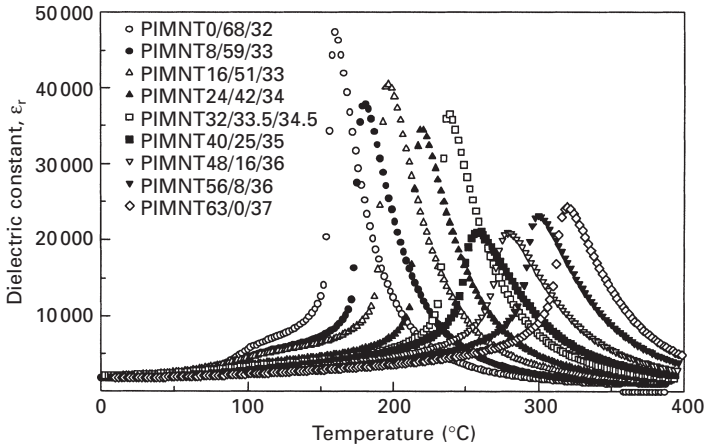
Figure 8.6 shows the electromechanical coupling factor planar mode,  $k_p$ , for PIMNT ceramics along the MPB. The largest value of the electromechanical coupling factor planar mode  $k_p = 67.6\%$  was observed for PIMNT 24/42/34. The  $k_p$  values of the PIMNT ternary ceramics were slightly higher than those of the end member MPB compositions at PIMNT 0/68/32 and PIMNT 63/0/37. The compositions with high  $k_p$  showed low  $\epsilon_{33}^T/\epsilon_0$ . A high piezoelectric constant,  $d_{33} = 510$  pC/N, was found at PIMNT 0/68/32 and PIMNT 16/51/33. The high  $d_{33}$  values are due to their high dielectric constants and large coupling factors. Two compositions with moderate  $T_C$  of around 200 °C were PIMNT 16/51/33 and PIMNT 24/42/34. The former composition, with  $T_C = 197$  °C, showed  $\epsilon_{33}^T/\epsilon_0 = 2400$ ,  $k_p = 67.1\%$  and  $d_{33} = 510$  pC/N and the latter one with  $T_C = 219$  °C showed  $\epsilon_{33}^T/\epsilon_0 = 2120$ ,  $k_p = 67.6\%$  and



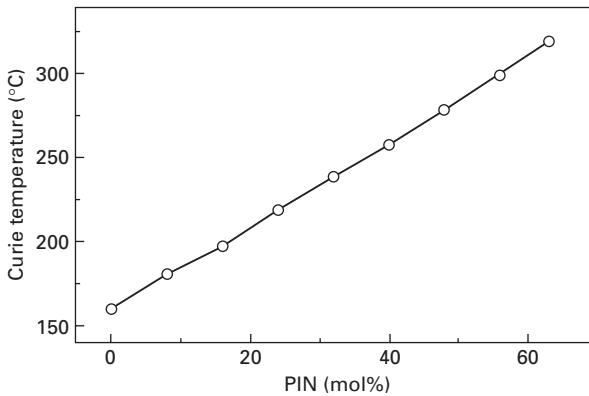
8.3 X-ray diffraction of the PIN-PMN-PT ternary ceramics system near the MPB.

$d_{33} = 505$  pC/N. The obtained electrical properties are excellent for high  $T_C$  piezoelectric materials. The high  $d_{33}$  values and reasonable  $T_C$  of PIMNT ceramic materials make them good candidates to replace conventional PZT ceramics in various piezoelectric applications. Tables 8.2 and 8.3 summarize all the electrical properties of the PIMNT ceramics along and across the MPB.



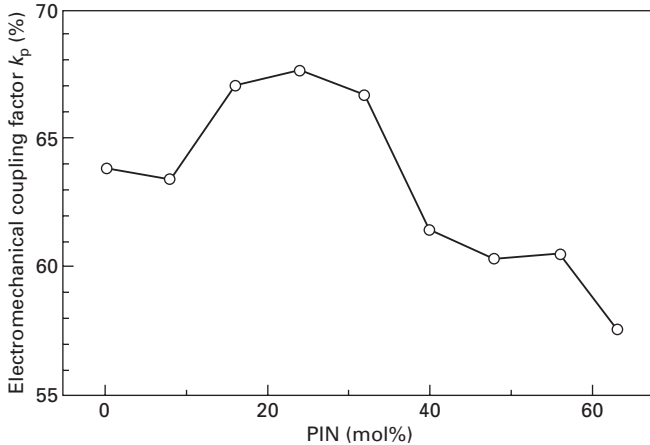


8.4 Dielectric constant as a function of temperature measured at  $f = 1.0$  kHz of the PIN-PMN-PT ternary ceramics system near the MPB.



8.5 Curie temperature  $T_c$  of the PIN-PMN-PT ceramics ternary system near the MPB.

The ceramic samples across the MPB were used to confirm that the line connecting the MPBs of PIMNT 0/68/32 and PIMNT 63/0/37 is the MPB of the PIMNT ternary system. The peak post-poling dielectric constant at room temperature reached 3890 at PIMNT 23/41/36. This compound had a low coupling factor,  $k_p = 60.5\%$ , and was slightly tetragonal phase. On the other hand, compositions on the rhombohedral side had high coupling factors,  $k_p > 65\%$ , but low dielectric constants,  $\epsilon_{33}^T/\epsilon_0 < 2000$ . PIMNT 24/42/34 (on the line connecting the MPBs of PIMNT 0/68/32 and PIMNT 63/0/37) showed the highest coupling factor and a moderate dielectric constant as mentioned above. Therefore, the MPB of the PIMNT ternary system is an almost linear, narrow region between the MPBs of PIMNT 0/68/32 and PIMNT 63/0/37.



8.6 Electromechanical coupling factor planar mode  $k_p$  of the PIN-PMN-PT ternary ceramics system near the MPB.

The PIMNT material system has a more stable perovskite structure than PZNT or PMNT ceramics. The raw-material cost of  $\text{In}_2\text{O}_3$  is lower than that of the  $\text{Sc}_2\text{O}_3$  which is used for PSNT. The PIMNT materials have reasonably high  $k_p$  and  $d_{33}$ . A high  $T_C$  ranging from 180 to 240 °C is also attractive compared with that of PZNT 91/9 ( $T_C = 175$  °C) or PMNT 70/30 ( $T_C = 145$  °C). The material system may have a high coercive field  $E_c$ , which is closely related to  $T_C$ . PIMNT materials are suitable for use in high- $T_C$  PSC applications if crystals of high quality and reasonable size are obtained.

### 8.3 PIMNT single crystals grown by the flux method

In this section, PIMNT piezoelectric single crystals (PSCs) grown by the conventional flux method and their dielectric and piezoelectric properties are presented. An excellent electromechanical coupling factor,  $k_p = 67\%$ , a relatively high Curie temperature,  $T_C = 197$  °C, and good perovskite stability of the PIMNT 16/51/33 and PIMNT 24/42/34 ceramics near the MPB have been confirmed. Therefore, PIMNT ternary PSCs with MPB compositions are expected to have excellent piezoelectric properties, as well as a high  $T_C$  (> 200 °C). However, to date there have been no reports on the synthesis of ternary PSCs that consist of six elements, Pb, In, Mg, Nb, Ti and O. The purpose of this work is to investigate the possibility of growing PIMNT ternary PSCs with good enough quality and size near the MPB and to characterize their properties.

High-purity chemicals (higher than 99.9%),  $\text{PbO}$ ,  $\text{In}_2\text{O}_3$ ,  $\text{MgO}$ ,  $\text{Nb}_2\text{O}_5$  and  $\text{TiO}_2$  (Kojundo Chemical Lab. Co., Ltd, Saitama, Japan), were used as

Table 8.2 Dielectric and piezoelectric properties of PIMNT 100x/100y/100z ceramics along the MPB

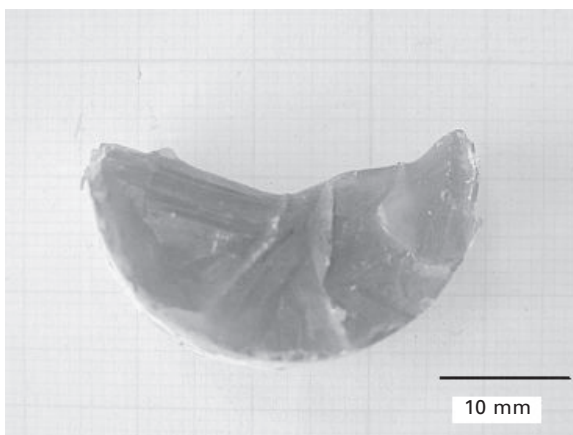
Sample #	Composition	$T_C$ (°C)	$\epsilon_r/\epsilon_0$	$\epsilon_{33}^T/\epsilon_0$	$\epsilon_{max}$	$k_p$ (%)	$d_{33}$ (pC/N)
1	PIMNT0/68/32	160	1830	2320	47 480	63.8	510
2	PIMNT8/59/33	181	1800	2230	37 880	63.4	500
3	PIMNT16/51/33	197	2080	2400	40 460	67.1	510
4	PIMNT24/42/34	219	2010	2120	34 430	67.6	505
5	PIMNT32/33.5/34.5	239	2140	2160	36 520	66.7	495
6	PIMNT40/25/35	258	1840	2130	21 000	61.4	430
7	PIMNT48/16/36	279	1840	2120	20 890	60.3	430
8	PIMNT56/8/36	300	1870	2440	23 110	60.5	440
9	PIMNT63/0/37	320	1800	2450	24 190	57.7	435

Table 8.3 Dielectric and piezoelectric properties of PIMNT ceramics across the MPB

Sample #	Composition	$T_C$ (°C)	$\epsilon_r/\epsilon_0$	$\epsilon_{33}^T/\epsilon_0$	$\epsilon_{max}$	$k_p$ (%)	$d_{33}$ (pC/N)
10	PIMNT 23/41/36	231	2630	3890	32 860	60.5	550
11	PIMNT 23.5/41.5/35	223	2670	2560	35 710	62.1	515
4	PIMNT 24/42/34	219	2010	2120	34 430	67.6	505
12	PIMNT 24.5/42.5/33	211	1740	1910	35 250	65.3	465
13	PIMNT 25/43/32	213	1660	1850	35 720	66.8	465

starting materials. A flux composition of 80 mol% PbO–20 mol% B<sub>2</sub>O<sub>3</sub> was selected for PSC synthesis. The flux and the precalcined PIMNT powder were lightly mixed in a plastic bag without any solvent. The selected ratio was 50 PIMNT 16/51/33 : 40 PbO : 10 B<sub>2</sub>O<sub>3</sub> (mol%). The mixture (100 g) was placed in a 20 cm<sup>3</sup> platinum crucible with a lid after twice premelting at 1000 °C for 1 h. The Pt crucible was placed in 100 cm<sup>3</sup> and 300 cm<sup>3</sup> Al<sub>2</sub>O<sub>3</sub> double crucibles with lids to prevent the evaporation of lead oxide and possible damage to the furnace. The crucible was placed in a computer-controlled electric furnace. The temperature was increased to 1230 °C and maintained for 5 h before being slowly reduced to 850 °C at 1.2 °C/h. After cooling to room temperature at a rate of 100 °C/h, the crucibles were weighed to determine the weight loss of the contents during heat treatment. After the crystal growth, the contents were rinsed in boiling 50% acetic acid for 24 h to separate the PSCs from the residual flux. The PbO–B<sub>2</sub>O<sub>3</sub> flux caused negligible damage to the Pt crucible and the weight losses due to PbO evaporation were less than 1.4% for the temperature profile described above. Crystals in the crucibles were visible to the naked eye.

Figure 8.7 shows the top view of the PIMNT crystal obtained by the flux method. This large yellowish brown crystal was obtained at the top of the contents. The crystal structure was studied by X-ray diffraction (XRD) after pulverizing some of the crystals. The grown crystals showed a single phase perovskite structure. PIMNT wafers with (001) faces were sliced from the crystals. The wafers have no serious inclusions, but consist of transparent and opaque areas. A rectangular plate (9 mm × 7 mm × 0.4 mm) was used for electrical measurements. Au/Cr electrodes were sputtered on both sides of the test specimen. The specimen was poled by applying an electrical field of

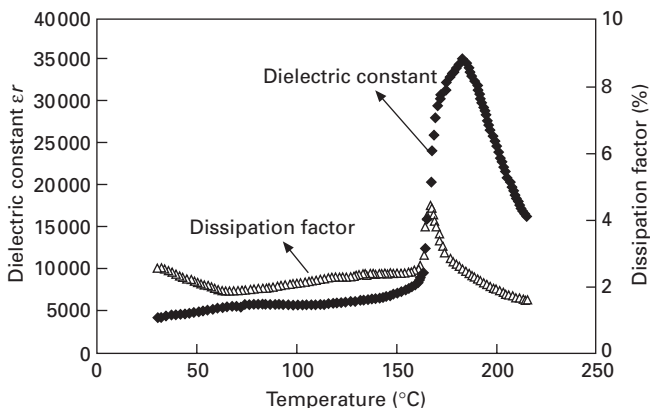


8.7 The PIMNT 16/51/33 PSC near the MPB composition prepared by the flux method.

1 kV/mm for 10 min at room temperature. The electrical capacitance and dielectric loss were measured at 1 kHz using a computer-controlled impedance analyzer (HP4192A). The temperature dependence of dielectric properties was measured at 1 kHz using the same measurement system in a temperature range of 30 to 220 °C. The piezoelectric constant,  $d_{33}$ , was measured using a  $d_{33}$  meter (Institute of Acoustics Academia Sinica, Model ZJ-3D).

Figure 8.8 shows the dielectric properties of one of the PIMNT PSCs with a maximum dielectric constant at 187 °C, indicating a  $T_C$  that is about 40 °C higher than that of the PMNT 68/32 PSC. The broad peak of the dielectric constant at around  $T_C$  is due to the scatter of the  $T_C$  resulting from the compositional variation in the crystal. A small peak of the dielectric constant is observed near 50 °C, which is considered to be the phase-transition temperature,  $T_{RT}$ , from the rhombohedral to the tetragonal phase. This indicates that the PSC is in the rhombohedral phase at room temperature. This result agrees with the XRD pattern without split peaks. The  $T_{RT}$  of the obtained crystal was slightly lower than expected from the same ceramics value. In order to increase the  $T_{RT}$ , the composition should be shifted slightly towards that of the rhombohedral phase by reducing the Ti content or increasing the  $\text{Pb}(\text{In}_{1/2}\text{Nb}_{1/2})\text{O}_3$  content. The room-temperature dielectric constant,  $\epsilon_{33}^T/\epsilon_0$ , and dielectric loss factor after poling were 3100 and 0.8%, respectively. The piezoelectric constant,  $d_{33} = 2200$  pC/N, is extremely large and the value is comparable to those of the PZNT 91/9 and PMNT 70/30 PSCs. The  $d_{33}$  value of PINT 72/28 PSC with a high Curie temperature,  $T_C > 250$  °C, is 700 pC/N. Therefore, the  $d_{33}$  value of the PIMNT crystal is one of the highest values reported so far for any piezoelectric material with a  $T_C > 185$  °C.

In conclusion, PIMNT 16/51/33 PSCs of high quality were synthesized by the flux method. The crystals show a large piezoelectric constant,  $d_{33} = 2200$  pC/N, with  $T_C = 187$  °C (Hosono *et al.*, 2002b).



8.8 Dielectric constant and dissipation factor of the PIMNT 16/51/33 PSC near the MPB composition prepared by the flux method.

## 8.4 PIMNT and PSMNT single crystals grown by the Bridgman method

In this section, PIMNT and  $\text{Pb}(\text{In}_{1/2}\text{Nb}_{1/2})\text{O}_3$ – $\text{Pb}(\text{Mg}_{1/3}\text{Nb}_{2/3})\text{O}_3$   $\text{PbTiO}_3$  (PSMNT) piezoelectric single crystals (PSCs) grown by the Bridgman method, and the dielectric and piezoelectric properties of these crystals are discussed. As mentioned above, the present authors investigated the ceramics and PSCs of the PIMNT ternary system and reported that the PIMNT PSCs showed the highest piezoelectric constant among piezoelectric materials with a Curie temperature of higher than 185 °C (Hosono *et al.*, 2003a,b,c). Moreover, we reported that PSMNT ceramics, a ternary system similar to PIMNT, exhibited a large coupling factor,  $k_p = 70\%$ , and piezoelectric constant,  $d_{33} = 680$  pC/N, with a high Curie temperature,  $T_C = 207$  °C, which is slightly superior to those of PIMNT ceramics (Yamashita and Shimanuki, 1996). Therefore, PSMNT PSCs are also expected to show excellent piezoelectric properties if high-quality crystals are obtained. However, the crystal growth of PSMNT ternary system is very difficult because of the high melting point of  $\text{Pb}(\text{Sc}_{1/2}\text{Nb}_{1/2})\text{O}_3$  (1420 °C) (Yamashita and Shimanuki, 1996).

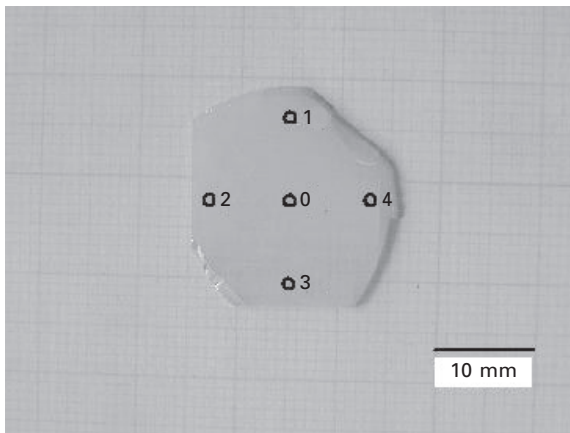
The purpose of this work was to grow large and high-quality PIMNT and PSMNT PSCs using the solution Bridgman method and to investigate the compositional variation of the obtained crystals in order to select a promising candidate piezoelectric material with high  $T_{RT}$  and  $T_C$ . Moreover, the electrical properties of PIMNT PSCs grown by the Bridgman method are reported and compared with those of PZNT and PMNT binary PSCs.

High-purity chemicals (better than 99.9%),  $\text{PbO}$ ,  $\text{In}_2\text{O}_3$ ,  $\text{Sc}_2\text{O}_3$ ,  $\text{MgO}$ ,  $\text{Nb}_2\text{O}_5$  and  $\text{TiO}_2$  (Kojundo Chemical Lab. Co., Ltd, Japan) were used as starting materials. PIMNT 16/51/33 and PSMNT 16/49/35 were selected as crystal compositions, which are on the MPB lines. In order to compare crystal growth, similar compositions were used. After wet-mixing the raw materials using a plastic ball mill with 5 mm diameter  $\text{ZrO}_2$  balls for 24 h, the slurry was dried in an oven. Calcining was performed at 850 °C for 2 h. The precalcined PIMNT (PSMNT) powders and flux were lightly mixed in a plastic bag without any solvent. The flux used for the crystal growth was  $\text{PbO}$ – $\text{B}_2\text{O}_3$ . The ratio selected was 50 PIMNT (PSMNT) : 40  $\text{PbO}$  : 10  $\text{B}_2\text{O}_3$  (mol%). A mixture weighing 245 g was placed in a 25 mm diameter, 150 mm long, 0.35 mm thick Pt crucible after one premelt at 1000 °C. The Pt crucible was driven down through the hot zone at a speed of 0.4 mm/h after maintaining it at 1250 °C for 5 h. After the crystal growth, the crucibles were weighed to determine the weight loss of the contents during the heat treatment. The Pt crucibles were stripped off using a pair of nippers to observe the features of the solidified contents.

The Pt crucible suffered negligible damage and the weight losses due to  $\text{PbO}$  evaporation were less than 2% for the temperature profile described

above. The  $\text{PbO-B}_2\text{O}_3$  flux is very effective for preventing evaporation of  $\text{PbO}$ . A large PIMNT PSC was found on the bottom of the crucible and many small crystals were observed on the sides of the crucible. The features of the solidified content are very similar to those of the PZNT system. On the other hand, the solidified content of PSMNT boule differed considerably from that of PIMNT. It had an opaque yellow area of ceramic-like material at the bottom side and many crystals of medium size over the opaque area. Although the crucible was kept in the highest temperature zone for 5 h before starting the cooling, the raw materials at the bottom of the crucible did not melt sufficiently. The holding time should be longer in order to melt the raw materials into the flux completely. The XRD patterns of two parts of the solidified contents were investigated; the opaque area mainly consists of a perovskite structure but with a small portion of pyrochlore. The crystalline area consists of a single perovskite phase.

The solidified content of PIMNT was rinsed in boiling 80% acetic acid for 12 h to separate the PSC from the residual flux. The crystal was 25 mm in diameter and 30 mm in length, and its weight was 109.1 g, which is equal to approximately 44.4% of the raw materials. The morphology of the crystal indicates that a single nucleation event occurred on the bottom of the crucible and the crystal grew in the [111] direction. The crystal obtained was sliced along the (001) plane after its orientation was determined from Laue X-ray diffraction patterns. Nineteen wafers 0.5 mm in thickness were obtained and lapped to about 0.36 mm in thickness. The PIMNT wafers were numbered in ascending order from the part of the crystal grown near the crucible bottom (the initial part). Figure 8.9 shows one of the wafers obtained from PIMNT PSC prepared by the Bridgman process. Some wafers cut from the bottom



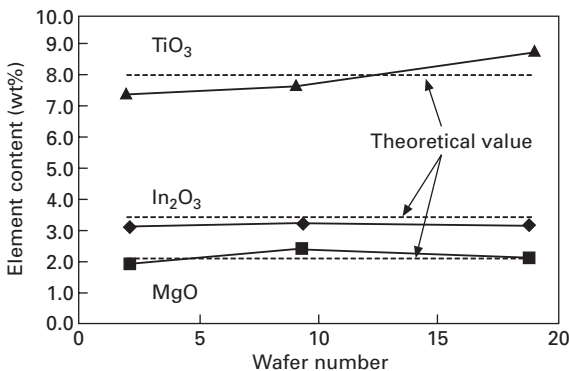
8.9 The PIMNT 16/51/33 PSC wafer near the MPB composition prepared by the solution Bridgman method and EPMA measurement points.

side contained some inclusions. The quality of the wafers improves from the initial part to the end of the crystal. Six wafers were selected from the initial (Nos. 1 and 2), middle (Nos. 8 and 9) and end parts (Nos. 18 and 19) for evaluation of the compositional variations and electrical properties.

The compositional variation of the PIMNT wafers was evaluated using an electron probe microanalyzer (EPMA, Shimadzu Corp., Model V6). Five measurement points in the form of a cross were set as shown in Fig. 8.9. The distance between neighboring points was 8 mm. Three wafers were selected from the initial (No. 2), middle (No. 9) and end (No. 19) of the PIMNT PSC for the compositional analysis. Table 8.4 lists the average of five points for the EPMA results and the theoretical values of the starting material: PIMNT 16/51/33. Figure 8.10 shows the EPMA results among the three wafers. The Ti content increased gradually from the initial part to the end part. Luo *et al.* (2000) reported the same behavior for PMNT PSCs. On the other hand, the In/Mg ratios of the three wafers were almost the same as the theoretical value. The PIMNT ternary system consists of four elements for the B-site (In, Mg, Nb and Ti) in the perovskite structure. Those elements have combinations such as  $(\text{In}_{1/2}\text{Nb}_{1/2})^{4+}$ ,  $(\text{Mg}_{1/3}\text{Nb}_{2/3})^{4+}$  and  $\text{Ti}^{4+}$  in the crystal in

Table 8.4 EPMA results of three wafers cut from the PIMNT 16/51/33 PSC

Wafer number	PbO (wt%)	$\text{In}_2\text{O}_3$ (wt%)	MgO (wt%)	$\text{Nb}_2\text{O}_5$ (wt%)	$\text{TiO}_2$ (wt%)
2 (initial)	70.21	3.17	1.93	17.42	7.51
9 (middle)	69.59	3.23	2.37	17.65	7.76
19 (end)	69.39	3.16	2.14	17.54	8.81
Theoretical value of PIMNT 16/51/33	69.03	3.43	2.12	17.26	8.15



8.10 EPMA result of the PIMNT 16/51/33 PSC wafers near the MPB composition prepared by the solution Bridgman method.



order to compensate for the charges. If the In/Mg ratio differs considerably in the crystal, obtaining a homogeneous crystal is very difficult. However, the In/Mg ratio is relatively constant in the PIMNT crystal. This is the key to obtaining a homogeneous PSC in the ternary system. Moreover, some wafers had yellowish brown and black areas. In the black area, the Pb content was slightly higher than that in the yellowish brown area.

The solidified content of PSMNT was cut lengthwise to evaluate the compositional variation because the crystals were multinucleated. The crystal structure was studied by X-ray diffraction after pulverizing some parts of the solidified content. Compositional variation of the PSMNT crystals was evaluated using an (EPMA, Shimadzu Corp., Model V6). The surface of the solid was lapped to a mirror finish for the measurement. Nine measurement points, which were designated by the irradiating spots, were set; five points (Nos. 3 to 7) are on the crystal. The distance between neighboring points was 5 mm.

The measured Pb contents were slightly higher than the theoretical values. The reason is an excess flux (PbO) inclusion within the crystal measurement area. Although the Sc content gradually decreased from the top to the bottom portion, the Mg content increased. Therefore, the Sc/Mg ratio changed considerably in the same crystal. Moreover, similar to the case of the PMNT and PIMNT PSCs, the Ti content increased from the bottom to the top of the crystals in the solidified content. Because of the large compositional variations for Sc, Mg and Ti, it is very difficult to obtain a homogeneous crystal by the conventional Bridgman process. These results of crystal growth and compositional analysis suggest that the PIMNT PSC system offers an advantage in terms of crystal growth in that it is easier to grow than the PSMNT PSC.

Rectangular plates cut from three PIMNT wafers (Nos. 1, 8 and 18) were used for electrical measurements. Au/Cr electrodes were sputtered on both sides of the test specimen. The dielectric constants and dielectric losses before and after poling were measured at 1 kHz using an impedance analyzer (HP4192A). Sliver transducer for coupling factor,  $k'_{33}$ , measurement was obtained by dicing with a dicing saw (DISCO, Model DAD-2H/6T). The dicing pitch and wheel thickness were 0.22 mm and 0.05 mm, respectively. The sliver transducers were poled after dicing by applying an electric field of 1 kV/mm at room temperature. The coupling factors  $k'_{33}$  were calculated using equation (8.1) after measuring the impedance curve using a network spectrum analyzer (HP4195A):

$$k_t, k'_{33} = \frac{\pi}{2} \cdot \frac{f_s}{f_p} \tan \left[ \frac{\pi}{2} \cdot \frac{(f_p + f_s)}{f_p} \right] \quad (8.1)$$

where  $f_p$  is the parallel resonance frequency and  $f_s$  is the series resonance frequency.

Temperature dependence of the dielectric properties of the PIMNT PSCs (Wafer Nos. 1, 8 and 18) selected from the initial, middle and end parts of the crystal were measured. The Curie temperature,  $T_C$ , varied from 181 to 196 °C with increasing wafer number. The  $T_C$  of the end part is approximately 15 °C higher than that of the initial part of the crystal. The results of the EPMA indicate that the Ti content increases from the initial part to the end of the crystal. Therefore, this variation of  $T_C$  must be due to the increase of  $\text{PbTiO}_3$  ( $T_C = 490$  °C) in the crystal. Peaks in the dielectric constant are observed below 100 °C in Nos. 1 and 8, probably due to the phase transition from the rhombohedral to tetragonal phases. This result indicates that the crystals show the rhombohedral phase at room temperature. On the other hand, a small peak is observed in No. 18 at approximately 30 °C. Therefore, the crystal must be near the MPB composition. In order to raise the  $T_{RT}$ , the composition needs to be shifted slightly into the rhombohedral phase field by decreasing the Ti content in the crystal.

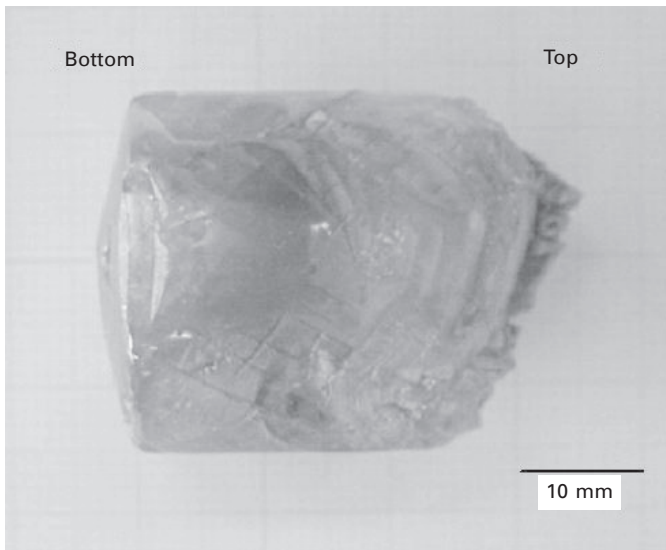
Table 8.5 lists the dielectric and piezoelectric properties of the PIMNT PSCs at the initial, middle and end parts. The dielectric constants of the plate transducers,  $\epsilon_{33}^T/\epsilon_0$ , were ranged from 1480 to 4400 at room temperature. The end part, No. 18, showed low  $\epsilon_{33}^T/\epsilon_0$  because it belongs to the MPB composition near the tetragonal region at room temperature. Generally, the  $\epsilon_{33}^T/\epsilon_0$  of the piezoelectric material belonging to the tetragonal phase is small along the [001] direction. A maximum piezoelectric constant,  $d_{33} = 1950$  pC/N, was observed in the middle part, No. 8, which is almost the same as that of the crystal obtained by the flux method. The maximum coercive field,  $E_C = 8.9$  kV/mm, which is approximately twice that of PMNT 70/30, was observed in the end part, on wafer No. 18.  $E_C$  increases with increasing  $T_C$ . The remanent polarizations,  $P_r$ , of the three wafers show almost the same

Table 8.5 Electrical properties of three wafers cut from the PIMNT 24/42/34 PSC

	Wafer No. 1	Wafer No. 8	Wafer No. 18
Crystal part	Initial	Middle	End
Dielectric constant $\epsilon_{33}^T/\epsilon_0$	4400	3630	1480
Phase-transition temp. $T_{RT}$ (°C)	91	55	–
Curie temp. $T_C$ (°C)	181	191	196
Coupling factor $k_t$ (%)	54.7	61.2	62.9
Piezoelectric const. $d_{33}$ (pC/N)	1350	1950	1550
Remanent polarization $P_r$ ( $\mu\text{C}/\text{cm}^2$ )	39.3	38.2	39.4
Coercive field $E_c$ (kV/cm)	4.4	7.0	8.9
Coupling factor $k'_{33}$ (%)	64.7	80.3	83.6
Frequency const. $N_{33}^f$ (Hz m)	1610	1110	1000

values. The end part, No. 18, also exhibits a large value because it belongs to the MPB composition very near the tetragonal region. The coupling factors sliver mode,  $k'_{33}$ , which are important for phased array probes, were measured using sliver transducers obtained by dicing, as mentioned above. Observation by microscope revealed no serious cracking and chipping on the sides of the sliver transducers diced from Nos. 8 and 18, but some cracks on the sides of the transducers diced from No. 1. The reason for the cracking and chipping is thought to be that the crystal quality of No. 1 was inferior to the others. Therefore, very clear impedance behaviors and high  $k'_{33}$  values were observed in the sliver transducers of Nos. 8 and 18. Moreover, they had high-frequency constants,  $N'_{33}r = 1000\text{--}1100\text{ Hz m}$ . On the other hand, the  $k'_{33}$  values of the sliver transducers cut from No. 1 were lower than the other ones. The low  $k'_{33}$  may be attributable to the poor crystal quality.

After the first crystal growth of the PIMNT 16/42/34, second crystal growth was carried out with PIMNT 24/42/34 (Hosono *et al.*, 2004) to increase  $T_{RT}$ . Figure 8.11 shows the PIMNT 24/42/34 PSC produced by the solution Bridgman process. A large size,  $20 \times 20 \times 0.5\text{ mm}^3$ , and a good quality of the wafer were obtained. The chemical composition of the pulverized powder of some PSCs is slightly different from that of the charged composition. The PbO ratio was a little higher than that of the charged composition because the PbO flux or PbO inclusion might be included in the crystal samples. The PIMNT ternary system consists of four elements for the B-site (In, Mg, Nb and Ti) in the perovskite structure. Those B-site elements show three

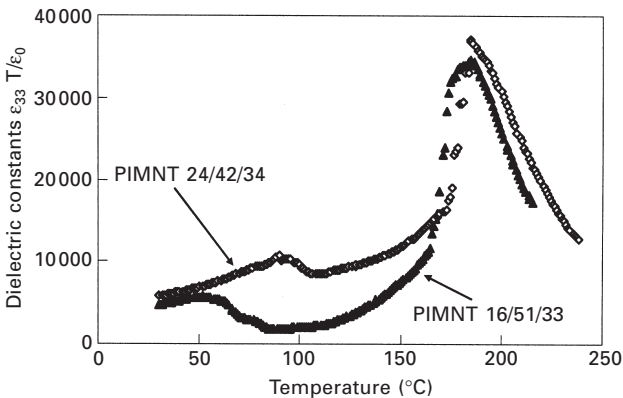


8.11 The PIMNT 24/42/34 PSC near the MPB composition prepared by the solution Bridgman method.

combinations, namely  $(\text{In}_{1/2}\text{Nb}_{1/2})^{4+}$ ,  $(\text{Mg}_{1/3}\text{Nb}_{2/3})^{4+}$  and  $\text{Ti}^{4+}$ , in the crystal in order to compensate electrons. Therefore, the  $\text{Pb}(\text{In}_{1/2}\text{Nb}_{1/2})\text{O}_3$  and  $\text{Pb}(\text{Mg}_{1/3}\text{Nb}_{2/3})\text{O}_3$  show rhombohedral phase but the  $\text{PbTiO}_3$  shows tetragonal phase. The PIMNT ternary system changes the phase as a function of its composition and the charged composition of the PIMNT 24/42/34 is around the morphotropic phase boundary (MPB). A ratio, defined as  $(\text{In}_2\text{O}_3 + \text{MgO})/\text{TiO}_2$ , between  $(\text{In}_2\text{O}_3 + \text{MgO})$  content regarded as the rhombohedral phase and  $\text{TiO}_2$  content regarded as the tetragonal phase is 0.37 for the crystal composition and 0.35 for the charged composition, respectively. This means that the PIMNT PSC obtained this time consists of a composition which shows the rhombohedral phase.

Figure 8.12 shows the temperature dependence of the dielectric constants of poled plate transducers of PIMNT 24/42/34 and PIMNT 16/51/33 PSC measured at 1 kHz. Small peaks of the dielectric constant are observed at 50–90 °C, corresponding to the phase-transition temperature,  $T_{\text{RT}}$ . The  $T_{\text{RT}}$  and  $T_{\text{C}}$  of PIMNT 24/42/34 and PIMNT 16/51/33 PSC were 89 and 184 °C and 52 and 181 °C, respectively. The  $T_{\text{RT}}$  of PIMNT 24/42/34 PSC was about 40 °C higher than that of the PIMNT 16/51/33 PSC, whereas the  $T_{\text{C}}$  of the PIMNT 24/42/34 PSC was almost the same as that of the PIMNT 16/51/33 PSC. The  $T_{\text{C}}$  of the PIMNT 24/42/34 PSC was slightly lower than we expected because the  $(\text{In}_2\text{O}_3 + \text{MgO})/\text{TiO}_2$  ratio was lower than that of charged composition for the crystal growth. This means that the PIMNT PSC has low PT content, which shows high  $T_{\text{C}}$  of 490 °C. The  $T_{\text{C}}$  (= 219 °C) of the PIMNT 24/42/34 ceramic has been confirmed in a previous report (Hosono *et al.*, 2003).

Table 8.6 lists the dielectric and piezoelectric properties of the PZNT 93/7, PMNT 70/30, PIMNT 24/42/34 and the ideal PSC for medical transducers.



8.12 Dielectric properties of the PIMNT 24/42/34 and PIMNT 16/51/33 PSC.

**Table 8.6** Electrical properties of the obtained and the ideal PSCs for medical array transducers

	PZNT 93/07	PMNT 70/30	PIMNT 24/42/34	Ideal PSC
Free dielectric constant $\epsilon_{33}^T/\epsilon_0$	4000	5500	4900	>4000
Clamped dielectric constant $\epsilon_{33}^S$	600	1200	1000	>1000
Phase-transition temp. $T_{RT}$ (°C)	92	89	89	>100
Curie temp. $T_C$ (°C)	165	145	184	>180
Coupling factor $k_{31}$ (%)	58	50	70	<60
Coupling factor length mode $k_{33}$ (%)	95	93	(90)	>88
Piezoelectric const. $d_{33}$ (pC/N)	2400	2200	2200	>1500
Coercive field $E_c$ (kV/cm)	5	3.0	6.8	>6
Coupling factor sliver mode $k'_{33}$ (%)	82	82	80	>80
Frequency const. $N'_{33}r$ (Hz m)	900	1180	1200	>1180
PSC size (mm)	50	70	25	>50

The dielectric constant after poling,  $\epsilon_{33}^T/\epsilon_0$ , of the PIMNT 24/42/34 was 4900 at room temperature, which is almost the same value as that of PMNT 70/30. High dielectric constant of the piezoelectric material is very important for the ultrasonic medical array transducer application. Recently, the capacitance of the array transducer is becoming smaller, because the element size of the array transducer is becoming smaller as the number of channels increases. In order to match electrical impedance between a tiny piezoelectric element and a coaxial cable, higher dielectric constant, which means larger capacitance, is required. A large piezoelectric constant,  $d_{33} = 2200$  pC/N, was observed in the PIMNT 24/42/34 PSC, which is almost the same as that of the PZNT 93/7 and the PMNT 70/30 PSC. In ultrasonic applications, few waveforms of pulse voltage are applied to the transducer. Therefore, the stability of the piezoelectric properties when the inverse pulse voltage is applied to the transducer is important for the relaxor-PSC with relatively low  $T_C$ . The  $E_C$  of the PIMNT PSC was 6.9 kV/mm, which is around 1.5 times larger than that of the PMNT 67/33 PSC.

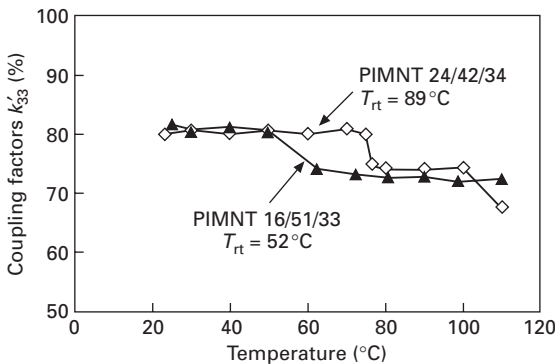
The coupling factors,  $k'_{33}$ , which are important for the phased array probe, were measured using sliver transducers obtained by dicing. Observation by microscopy revealed no serious cracking and chipping on the sides of the sliver transducers diced from the plane transducer. The transducer showed very clear impedance behavior and high  $k'_{33}$  value of around 80%, which is almost the same as those of the PZNT 91/9 and PMNT 70/30 PSCs. Moreover, it had high-frequency constant,  $N'_{33}r = 1200$  Hz m, which is as high as that of PMNT 70/30 PSC. The frequency constant,  $N'_{33}r$ , is expressed by the following equation:

$$N'_{33}r = 2 \times f_s \times d \quad 8.2$$

where  $f_s$  is series resonance frequency and  $d$  is thickness of the transducer.

As indicated by the equation, high-frequency constant means a thicker transducer can be used in order to vibrate the transducer at the same frequency. Therefore, piezoelectric material with high-frequency constant is promising for the high-frequency applications.

Next, the temperature dependence of  $k'_{33}$  was measured using the sliver transducers of the PIMNT 24/42/34 and PIMNT 16/51/33 PSCs. The phase-transition temperatures,  $T_{RT}$ , the Curie temperatures,  $T_C$ , and the coupling factors,  $k'_{33}$ , at room temperature of the PIMNT 24/42/34 and PIMNT 16/51/33 PSCs used for the measurement were 89 °C, 184 °C and 80%, and 52 °C, 181 °C, 82%, respectively. The  $T_{RT}$  and  $T_C$  values were measured using poled plate transducers before dicing to the sliver transducers. The  $k'_{33}$  values are almost the same as each other. Figure 8.13 shows the temperature dependence of the  $k'_{33}$  of the PIMNT 24/42/34 and PIMNT 16/51/33 PSCs. The  $k'_{33}$  decreased in a step-like manner from 50 to 80 °C, which is similar to the behavior of PZNT PSCs we reported in the past (Hosono *et al.*, 2002a). The authors think that the  $k'_{33}$  exhibits a step-like decrease near the  $T_{RT}$  because PIMNT PSC starts to transform from the rhombohedral to tetragonal phase at those temperatures, and the directions of spontaneous polarizations also change. Therefore, the degradation temperature of  $k'_{33}$  was in agreement with the  $T_{RT}$  measured using the poled PIMNT PSC, as in the case of the PZNT PSCs. Because the transducer may be heated to around 70 °C, thermal stability of piezoelectric properties is very important in the medical transducer application. Although the  $k'_{33}$  of the PIMNT 16/51/33 PSC decreased at about 50 °C, the  $k'_{33}$  of the PIMNT 24/42/34 PSC hardly changed until 70 °C. This result indicates that the PIMNT 24/42/34 PSC had not only excellent piezoelectric properties but also that those properties had good thermal stability due to its high  $T_{RT}$ . Moreover, it had good voltage-proof nature due to its high  $T_C$ . Therefore, the PIMNT 24/42/34 PSC may be



8.13 Temperature dependence of the  $k'_{33}$  of the PIMNT 24/42/34 and PIMNT 16/51/33 PSC.

the best composition of the piezoelectric material for the medical array transducer application. In particular, the large coercive fields and high-frequency constants make the PIMNT 24/42/34 PSC useful for high-frequency transducer and multi-layer transducer applications.

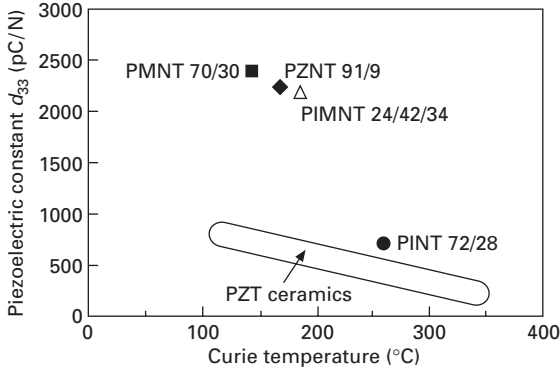
In summary, crystal growth of PIMNT and PSMNT ternary systems was investigated by the solution Bridgman method using a PbO–B<sub>2</sub>O<sub>3</sub> flux. The results obtained are as follows:

- A large PIMNT PSC of 25 mm in diameter and 30 mm in length was obtained by driving the crucible at a speed of 0.4 mm/h from 1250 to 900 °C. On the other hand, PSMNT PSCs were multinucleated under the same growth conditions.
- The results of EPMA revealed that the Ti content gradually increased during the growth in PIMNT and PSMNT PSCs. However, the In/Mg ratio was constant in the PIMNT PSC, whereas the Sc/Mg ratio varied considerably in the PSMNT PSC.
- The Curie temperature,  $T_C$ , of the PIMNT crystal ranged from 181 to 196 °C from the initial part to the end part, which is in agreement with the EPMA results.
- Excellent dielectric and piezoelectric properties were confirmed in the crystal with  $T_{RT} = 89$  °C and  $T_C = 184$  °C: dielectric constant,  $\epsilon_{33}^T/\epsilon_0 = 4900$ , piezoelectric constant,  $d_{33} = 2200$  pC/N, coercive field of  $E_c = 6.8$  kV/cm, coupling factor,  $k'_{33} = 80\%$  and frequency constant,  $N'_{33r} = 1200$  Hz m.

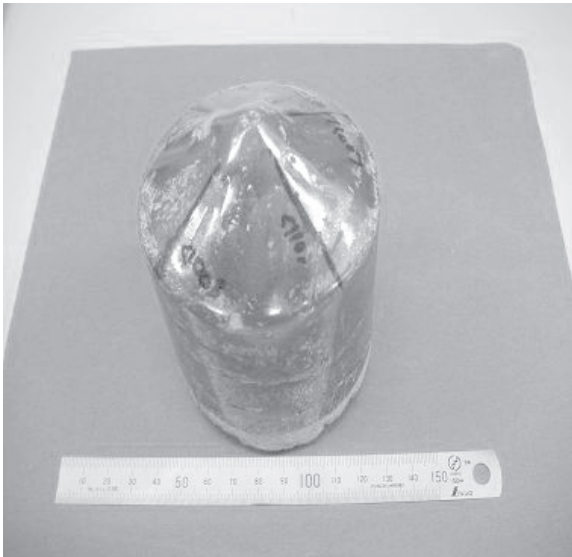
It was confirmed that crystal growth in the PIMNT system was easier than in the PSMNT system. Moreover, the compositional variation of the PIMNT PSC was smaller than that in PSMNT PSC. Finally, the obtained PIMNT PSC exhibited good dielectric and piezoelectric properties as well as a high  $T_{RT}$  and  $T_C$ .

Figure 8.14 shows the relationship between the Curie temperature,  $T_C$ , and piezoelectric constants,  $d_{33}$ , of relaxor–PT PSCs and PZT ceramics. The  $d_{33}$  values of relaxor–PT PSCs are larger than those of PZT ceramics, particularly PMNT 70/30, PZNT 91/9 and PIMNT 24/42/34. PINT 72/28, which has a high  $T_C$  of 260 °C, shows lower  $d_{33}$  than those of other PSCs. The low  $d_{33}$  may be due to the poor crystal quality and the high  $T_C$ . Because little  $d_{33}$  data on relaxor–PT PSCs with  $T_C$  over 200 °C has been reported, the relationship between  $T_C$  and  $d_{33}$  is unclear.

In this study, the starting material selected was the PIMNT 16/51/33 and PIMNT 24/42/34, which falls on the compositional line connecting the MPB compositions of the PMNT 68/32 ( $T_C = 150$  °C) and PINT 63/37 ( $T_C = 320$  °C). The  $T_C$  of the PIMNT ternary system with MPB compositions can be controlled from 150 to 320 °C. Therefore, if the composition of PIMNT PSCs is designed carefully with an optimum balance between the piezoelectric



8.14 Piezoelectric constants as a function of Curie temperature of several relaxor-PT single crystals and PZT ceramics.



8.15 Large, 80 mm in diameter PMN–PIN–PT PSC produced by the Bridgman process. (Courtesy of JFE Minerals Co. of Japan.)

properties, high  $T_{RT}$  and high  $T_C$ , PIMNT PSCs may become excellent candidates for applications such as medical imaging, non-destructive testing and actuators. Figure 8.15 shows recent progress of the PSC growth of the PIN–PMN–PT produced by JFE Mineral Co., Chiba, Japan, by the Bridgman process. The crystal diameter is 80 mm, the length is 80 mm and the weight is 2.2 kg ([http://www.jfe-mineral.co.jp/e\\_mineral/seihin/eseihin034.html](http://www.jfe-mineral.co.jp/e_mineral/seihin/eseihin034.html)).



## 8.5 Future trends

Ultrasonic array transducers are applied in medical echo diagnostic ultrasound systems. Frequencies used for these applications are 2–20 MHz. The typical cardiac transducer operates at a center frequency of 2–4 MHz and makes use of a piezoelectric material plate with a size of  $15 \times 25 \text{ mm}^2$ . The key to achieve this is the performance of the piezoelectric material, which transmits and receives the echo ultrasound. High dielectric constant ( $\epsilon_{33}^T/\epsilon_0 > 3500$ ) PZT5H ceramics have been mostly used for this application in decades. However, recent research has focused on obtaining greater sensitivity and broader bandwidth, and new transducers such as piezoelectric composites have been studied.

PSCs of PZNT 91/9 and PMNT 70/30 have a large  $d_{33}$  ( $>2000 \text{ pC/N}$ ) and  $k_{33}$  ( $>92\%$ ),  $k'_{33}$  ( $>80\%$ ) and  $g_{33}$  ( $>60 \times 10^{-3} \text{ V m/N}$ ), values far larger than those obtained for any PZT ceramic specimens. This is one reason that intensive research on medical transducers has been conducted in various parts of the world during the last 10 years. After the initial reports and presentations by Toshiba in the early 1990s several organizations in the USA, South Korea and China, entered the field. Saitoh *et al.* (1999b) reported the first images of B-mode and Doppler-mode obtained by using PZNT91/09 PSC for cardiac transducers operating at 3.5 MHz with 96 channels. The echo amplitude of the PZNT probe is about 6 dB higher than that of the PZT probe, and the frictional bandwidth is 30% wider. This means that both the penetration and the resolution of the PZNT probe are superior to those of conventional PZT probes. Large coupling factor  $k'_{33}$  ( $>82\%$ ), dielectric constant after poling ( $\epsilon_{33}^T/\epsilon_0 > 3000$ ) and low acoustic impedance  $Z_{33} < 24$  ( $\times 10^6 \text{ kg/m}^2\text{s}$ ) make the PZNT 91/9 PSC an excellent transducer material for medical diagnostic applications. At present, the size of PZNT, PMNT and PIMNT PSC is sufficient for various applications. However, the quality and uniformity of these crystals within and between the wafers larger than 50 mm in diameter, as well as among lots and among manufacturers, are still insufficient (Yamashita *et al.*, 2004c). Although it is usually easy to grow PSCs in [111] or [110] directions, it is very difficult to grow them in the [001] direction, but [001] wafers are used for medical transducers. There is always some inhomogeneous  $\text{TiO}_2$  distribution within wafers. This is one of the causes of large scattering of  $k_{33}$ ,  $d_{33}$  and dielectric constant within wafer. In addition, the manufacture of high-frequency, i.e. more than 7 MHz, PSC transducers that requires thin thickness plate (less than  $150 \mu\text{m}$ ), is very difficult because of the low-frequency constant and low mechanical strength of PSC. The present cost of PSC wafers is more than 10 times that of PZT ceramics. Other drawbacks are temperature instability, mechanical properties, chipping by dicing, matching layers/electrode/PSC bonding strengths, low clamped dielectric constant, low  $E_c$ , de-poling, low production yield, etc.

However, the PIMNT PSC introduced in this chapter can solve most of these shortcomings.

The Bridgman and solution Bridgman processes and the TSSG process are well-established PSC growth processes. However, these processes have several shortcomings, such as Pt crucible cost and composition inhomogeneity. In order to resolve these shortcomings, a new approach has been studied. Solid-state crystal growth (SSCG) (Lee *et al.*, 2000; Lee, 2004) and templated crystal growth (TCG) processes have many advantages over conventional PSC processes and they are expected to reduce the cost of homogeneous relaxor PSCs for mass production in the near future. In addition, utilizing the domain engineering (Wada *et al.*, 2005) which revealed through PSC research, the ceramic BaTiO<sub>3</sub> piezoelectric properties are also drastically improved by Takahashi *et al.* (2006a,b). Therefore, it is plausible that PIMNT materials may become the predominant materials for sophisticated, performance-oriented piezoelectric products in the near future. To that end, research on methods of evaluating PSC wafer quality and uniformity using non-destructive processes is an urgent task. Improvement in the uniformity of capacitance, electromechanical coupling factor  $k_{33}$  and piezoelectric constant  $d_{33}$  within and between wafers is also a major task for crystal growers. Detailed basic research to determine the mechanism accounting for the scattering of electrical properties should be conducted from the viewpoints of composition, domain structure and defect chemistry.

Finally, research on new PSC, ceramic materials and technology to solve all the present problems is essential. From the application aspect, a new dicing process that prevents cracking and deteriorating of PSC is also necessary in order to make fine pitch, high-frequency array transducers. A conformation of scalability which indicates the size dependency of physical, dielectric and piezoelectric properties of small size less than 1.0 mm<sup>2</sup> is required to design fine size piezoelectric medical array transducers.

## 8.6 Conclusions

Piezoelectric ceramics and PSCs in the  $x\text{Pb}(\text{In}_{1/2}\text{Nb}_{1/2})\text{O}_3-y\text{Pb}(\text{Mg}_{1/3}\text{Nb}_{2/3})\text{O}_3-z\text{PbTiO}_3$  (PIMNT100 $x$ /100 $y$ /100 $z$ ) ternary system have been investigated in order to develop new piezoelectric materials with high Curie temperature,  $T_C$ .

The PIMNT PSCs have been grown using a PbO–B<sub>2</sub>O<sub>3</sub> flux both by the conventional flux method and by the solution Bridgman method. The largest crystal size obtained is 25 mm in diameter and 30 mm in length. Although the Ti content gradually increased along the length of the grown crystal, the In/Mg ratio was almost constant.

The obtained PIMNT 24/42/34 crystal shows excellent electrical properties in the (001) plane, e.g. a dielectric constant ( $\epsilon_{33}^T/\epsilon_0 = 4900$ ), piezoelectric

constant  $d_{33} = 2200$  pC/N, coupling factor sliver mode  $k'_{33} = 80\%$ , which are almost the same as those of the PZNT 91/9 and PMNT 68/32 PSCs. However, PIMNT has a high phase transition temperature  $T_{RT} = 89^\circ\text{C}$  and Curie temperature  $T_C = 184^\circ\text{C}$ . Moreover, it has a large coercive field  $E_C = 6.8$  kV/cm due to the high  $T_{RT}$ ,  $T_C$ , and a high frequency constant  $N'_{33}r = 1200$  Hz m. The high  $T_C$ , large coercive field and high frequency constant of the PIMNT PSCs make them promising candidates for medical transducers and actuators which require a stable temperature performance. In order to utilize the piezoelectric crystals for medical array transducers application, a conformation of scalability of physical, dielectric and piezoelectric properties is necessary.

## 8.7 References

- Feng Z, Zao X and Luo H (2004), Composition and orientation dependence of phase configuration and dielectric constant tenability in poled  $\text{Pb}(\text{Mg}_{1/3}\text{Nb}_{2/3})\text{O}_3\text{-PbTiO}_3$  crystals, *J. Phys. Condens. Matter*, **16**, 6771–6778.
- Feng Z, Zao X and Luo H (2006), Composition and orientation dependence of dielectric and piezoelectric properties in poled  $\text{Pb}(\text{Mg}_{1/3}\text{Nb}_{2/3})\text{O}_3\text{-PbTiO}_3$  crystals, *J. Appl. Phys.*, **100**, 024104, 1–5.
- Harada K, Shimanuki S, Kobayashi T, Saitoh S and Yamashita Y (1998), Crystal growth and electrical properties of  $\text{Pb}[(\text{Zn}_{1/3}\text{Nb}_{2/3})_{0.91}\text{Ti}_{0.09}]\text{O}_3$  single crystals produced by solution Bridgman method, *J. Am. Ceram. Soc.*, **81**, 2785–2788.
- Hosono Y, Harada K, Yamashita Y, Dong M and Ye Z G (2000), Growth, electric and thermal properties of lead scandium niobate–lead magnesium niobate–lead titanate ternary single crystals, *Jpn. J. Appl. Phys.*, **39**, 5589–5592.
- Hosono Y, Harada K, Kobayashi T, Itsumi K, Izumi M, Yamashita Y and Ichinose N (2002a), Dielectric and piezoelectric properties of  $0.93\text{Pb}(\text{Zn}_{1/3}\text{Nb}_{2/3})\text{O}_3\text{-}0.07\text{PbTiO}_3$  piezoelectric single crystals for medical array transducers, *Jpn. J. Appl. Phys.*, **41**, 7084–7088.
- Hosono Y, Yamashita Y, Sakamoto H and Ichinose N (2002b), Large piezoelectric constant of high-Curie-temperature  $\text{Pb}(\text{In}_{1/2}\text{Nb}_{1/2})\text{O}_3\text{-Pb}(\text{Mg}_{1/3}\text{Nb}_{2/3})\text{-PbTiO}_3$  ternary single crystal near morphotropic phase boundary, *Jpn. J. Appl. Phys.*, **41**, L1240–L1242.
- Hosono Y, Yamashita Y, Sakamoto H and Ichinose N (2003b), Dielectric and piezoelectric properties of  $\text{Pb}(\text{In}_{1/2}\text{Nb}_{1/2})\text{O}_3\text{-Pb}(\text{Mg}_{1/3}\text{Nb}_{2/3})\text{O}_3\text{-PbTiO}_3$  ternary ceramic materials near the morphotropic phase boundary, *Jpn. J. Appl. Phys.*, **42**, 535–538.
- Hosono Y, Yamashita Y, Sakamoto H and Ichinose N (2003b), Growth of single crystals of high-Curie-temperature  $\text{Pb}(\text{In}_{1/2}\text{Nb}_{1/2})\text{O}_3\text{-Pb}(\text{Mg}_{1/3}\text{Nb}_{2/3})\text{O}_3\text{-PbTiO}_3$  ternary systems near morphotropic phase boundary, *Jpn. J. Appl. Phys.*, **42**, 5681–5686.
- Hosono Y, Yamashita Y, Sakamoto H and Ichinose N (2003c), Crystal growth of  $\text{Pb}(\text{In}_{1/2}\text{Nb}_{1/2})\text{O}_3\text{-Pb}(\text{Mg}_{1/3}\text{Nb}_{2/3})\text{O}_3\text{-PbTiO}_3$  and  $\text{Pb}(\text{Sc}_{1/2}\text{Nb}_{1/2})\text{O}_3\text{-Pb}(\text{Mg}_{1/3}\text{Nb}_{2/3})\text{O}_3\text{-PbTiO}_3$  piezoelectric single crystals using the solution Bridgman method, *Jpn. J. Appl. Phys.*, **42**, 6062–6067.
- Hosono Y, Yamashita Y, Hirayama K and Ichinose N (2004), Dielectric and piezoelectric properties of  $\text{Pb}[(\text{In}_{1/2}\text{Nb}_{1/2})_{0.24}(\text{Mg}_{1/3}\text{Nb}_{2/3})_{0.42}\text{Ti}_{0.34}]\text{O}_3$  single crystals, *Jpn. J. Appl. Phys.*, **44**, 7037–7041.

- Kuwata J, Uchino K and Nomura S (1982), Dielectric and piezoelectric properties of  $0.91\text{Pb}(\text{Zn}_{1/3}\text{Nb}_{2/3})\text{O}_3\text{-}0.09\text{PbTiO}_3$  single crystals, *Jpn. J. Appl. Phys.*, **21**, 1298–1301.
- Lee H Y, Kim J S and Kim D Y (2000), Fabrication of  $\text{BaTiO}_3$  single crystals using secondary abnormal grain growth, *J. Eur. Ceram. Soc.*, **83**(11), 1595–1597.
- Lee H Y (2004), Solid state single crystal growth (SSCG) method: a cost-effective way of growing piezoelectric single crystals, in Trolrier-McKenstry S, Cross L E and Yamashita Y, *Piezoelectric Single Crystals and Their Applications*, State College, Pennsylvania State University, 160–177.
- Luo H, Xu G, Xu G, Wang P and Yin Z (1999), Growth and characterization of relaxor ferroelectric PMNT single crystals, *Ferroelectrics*, **231**, 97–102.
- Luo H, Xu G, Xu H, Wang P and Yin Z (2000), Compositional homogeneity and electrical properties of lead magnesium niobate titanate single crystals prepared by the modified Bridgman technique, *Jpn. J. Appl. Phys.*, **39**, 5581–5585.
- Saitoh S, Takeuchi T, Kobayashi T, Harada K, Shimanuki S and Yamashita Y (1999a), A 3.7 MHz phased array probe using  $0.91\text{Pb}(\text{Zn}_{1/3}\text{Nb}_{2/3})\text{O}_3\text{-}0.09\text{PbTiO}_3$ , *IEEE Trans. Ultrason., Ferroelect., Freq. Control*, **46**, 414–421.
- Saitoh S, Takeuchi T, Kobayashi T, Harada K, Shimanuki S and Yamashita Y, (1999b) An improved phased array ultrasonic probe using  $0.91\text{Pb}(\text{Zn}_{1/3}\text{Nb}_{2/3})\text{O}_3\text{-}0.09\text{PbTiO}_3$  single crystal, *Jpn. J. Appl. Phys.*, **38**, 3380–3384.
- Shrout T R, Chang Z P, Kim N and Markgraf S (1990), Dielectric behavior of single crystals near the  $(1-x)\text{Pb}(\text{Mg}_{1/3}\text{Nb}_{2/3})\text{O}_3\text{-}(x)\text{PbTiO}_3$  morphotropic phase boundary, *Ferroelectric Letters*, **12**, 63–67.
- Takahashi H, Numamoto Y, Tani J, Matsuta K, Qiu J and Tsurekawa S (2006a), Lead-free barium titanate ceramics with large piezoelectric constant fabricated by microwave sintering, *Jpn. J. Appl. Phys.*, **45** (2006) L30.
- Takahashi H, Numamoto Y, Tani J, Matsuta K, Qiu J and Tsurekawa S (2006b), Piezoelectric properties of  $\text{BaTiO}_3$  ceramics with high performance fabricated by microwave sintering, *Jpn. J. Appl. Phys.*, **45**, 7405–7408.
- Wada S, Yako K, Kanemoto H and Tsurumi T (2005), Enhanced piezoelectric properties of barium titanate single crystals with different engineered domain sizes, *J. Appl. Phys.*, **98**, 014109,
- Yamashita Y and Shimanuki S, (1996), Synthesis of lead scandium niobate–lead titanate binary system single crystals, *Mat. Res. Bull.*, **7**, 887–895.
- Yamashita Y, Harada K, Tao H and Ichinose N, (1996), Piezoelectric properties of  $\text{Pb}(\text{Sc}_{1/2}\text{Nb}_{1/2})\text{O}_3\text{-Pb}(\text{Mg}_{1/3}\text{Nb}_{2/3})\text{O}_3\text{-PbTiO}_3$  ternary ceramic materials near the morphotropic phase boundary, *Integrated Ferroelectrics*, **13**, 1–3.
- Yamashita Y, Hosono Y and Ye Z G (2004a), Recent development trend of piezoelectric single crystals: a review, *Trans. Mater. Resear. Soc. Jpn.*, **29**[4] 1059–1066.
- Yamashita Y, Hosono Y and Ichinose N (2004b), Dielectric and piezoelectric properties of  $\text{Pb}(\text{In}_{1/2}\text{Nb}_{1/2})\text{O}_3\text{-Pb}(\text{Mg}_{1/3}\text{Nb}_{2/3})\text{O}_3\text{-PbTiO}_3$  ternary materials with high Curie temperatures, in Trolrier-McKenstry S, Cross L E and Yamashita Y, *Piezoelectric Single Crystals and Their Applications*, State College, Pennsylvania State University, 323–345.
- Yamashita Y, Hosono Y, Harada K and Ye Z G (2004c), Relaxor ferroelectric crystals – recent development and application, in Setter N (ed.), *Piezoelectric Materials in Devices*, Lausanne, EPFL, 455–466.
- Yasuda N, Ohwa H, Ito K, Iwata M and Ishibashi Y (1999), Dielectric properties of the  $\text{Pb}(\text{In}_{1/2}\text{Nb}_{1/2})\text{O}_3\text{-PbTiO}_3$  single crystal, *Ferroelectrics*, **230**, 115–120.

- Yasuda N, Ohwa H, Kume M, Hayashi K, Hosono Y and Yamashita Y (2001), Crystal growth and electrical properties of lead indium niobate–lead titanate binary single crystal, *J. Cryst. Growth*, **229**, 299–304.
- Zhang S, Rhee S, Randall C A and Shrout T R (2002), Dielectric and piezoelectric properties of high Curie temperature single crystals in the  $\text{Pb}(\text{Yb}_{1/2}\text{Nb}_{1/2})\text{O}_3-x\text{PbTiO}_3$  solid solution series, *Jpn. J. Appl. Phys.*, **41**, 722–726.

## Full-set material properties and domain engineering principles of ferroelectric single crystals

W C A O, The Pennsylvania State University, USA

### 9.1 Introduction

Relaxor ferroelectric materials have demonstrated superior dielectric properties and they can form solid solutions with ferroelectric materials to produce larger piezoelectric response. The investigation of relaxor-based ferroelectric ceramics and single crystals began in the 1960s.<sup>1,2</sup> Interesting electromechanical phenomena were observed in  $0.91\text{Pb}(\text{Zn}_{1/3}\text{Nb}_{2/3})\text{O}_3-0.09\text{PbTiO}_3$  single crystals in the 1980s, which can produce high electromechanical coupling coefficient of  $k_{33} > 90\%$  when being poled along [001] of cubic phase direction.<sup>3</sup> The phenomena were further explored in the late 1990s when better and larger crystals were fabricated.<sup>4,5</sup> It was demonstrated that single crystals  $(1-x)\text{Pb}(\text{Mg}_{1/3}\text{Nb}_{2/3})\text{O}_3-x\text{PbTiO}_3$  (PMN-PT) and  $(1-x)\text{Pb}(\text{Zn}_{1/3}\text{Nb}_{2/3})\text{O}_3-x\text{PbTiO}_3$  (PZN-PT) poled along [001] of cubic phase coordinates can produce very large piezoelectric coefficient ( $d_{33} > 2000$  pC/N) and very high electromechanical coupling coefficient ( $k_{33} > 90\%$ ).<sup>4,5</sup> With the improvement of fabrication techniques, the size of the crystals and the compositional uniformity have now met the requirements for practical applications. The method of intentionally off-polar direction poling to produce desired domain patterns in order to obtain large piezoelectric response is referred as ‘domain engineering’.

In order to use computer simulations to design devices that can utilize these advanced piezoelectric crystals, one must know the complete set of material parameters for input in the design software. For such a purpose, it is insufficient to know only the  $d_{33}$  and  $k_{33}$  coefficients since the materials are very anisotropic. An accurate, complete set of material properties can provide useful comparison among different composition crystals in order to select the best crystals for particular applications. In addition, such complete information is also needed for theoretical analysis to understand the fundamental principle of domain engineering method and to find the physical origin of such super-large  $d_{33}$  and  $k_{33}$  coefficients in domain engineered crystals.

There are two critical issues involved in the property characterization of these multi-domain single crystals. First, because the material properties are anisotropic, we must identify the effective symmetries of these multi-domain systems in order to define the material constant matrices. Unlike single domain single crystals, for which the macroscopic symmetry is the same as the microscopic crystal symmetry, the macroscopic symmetry of a domain engineered single crystal is the effective symmetry of the engineered domain patterns, which can be very different from the crystal symmetry. Because several energetically degenerated domain states exist in the structure and several domain wall orientations are allowed, the engineered domain patterns can be quite complicated and the symmetries of such patterns need to be analyzed for different combinations of domains and domain walls.

The second issue is the self-consistency of the full matrix data. Based on symmetry analysis, there are only a fixed number of independent material constants for a given symmetry. Therefore, one must be able to correlate the data from different types of measurements using symmetry constraints and constitutive relations. Experimental measurements showed that material properties could be substantially different for different geometry samples of the same composition because the domain patterns being generated are strongly influenced by the geometry and boundary conditions. In addition, uncertainties of some derived quantities can be very large due to the unstable nature of some constitutive relations. Unstable relations refer to those mathematical formulas that can enlarge the error through error propagation as discussed in more details below.

In this chapter, we will discuss these two issues and provide a collection of full-set property data for PMN–PT and PZN–PT single crystals that have been measured up to date. The chapter is arranged as follows: in Section 9.2, the challenges involved in the characterization of these domain engineered crystals are discussed and the methodologies used to overcome these difficulties are described. In Section 9.3, a list is provided of available full set material properties, including [001] and [011] direction poled PZN–PT and PMN–PT multi-domain single crystals in the rhombohedral phase, as well as single domain rhombohedral and tetragonal phase PMN–PT single crystals. In Section 9.4, the correlation between single domain and multi-domain data is described and the orientation effect that constitutes the basic principle of domain engineering is discussed briefly. Section 9.5 provides some general remarks for using domain engineering methods to enhance the functional properties of ferroelectric materials.

## 9.2 Technical challenges and characterization methods

### 9.2.1 Effective symmetries of multi-domain single crystal systems

Theoretically speaking, different domain states are energetically degenerated in the ferroelectric phase. However, if two or more domains are put together they can form interesting domain configurations depending on domain wall orientations as well as their relative volume ratios.

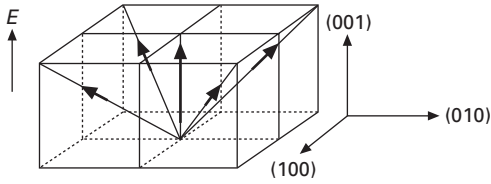
In multi-domain crystals, the effective macroscopic symmetry is determined by the spatial distribution of domains, not by the lattice structure. Domain pattern symmetry describes the collective microstructure of domains and domain walls, while the permissible domains and domain walls depend on the underlying crystal lattice symmetry of the ferroelectric phase and its relationship with the symmetry of the paraelectric phase. Hence, crystal symmetry and domain pattern symmetry are interrelated but quite different. There is an interesting hierarchical relationship: the symmetry of the crystal structure determines the domain structure, while the symmetry of the domain structure determines the macroscopic symmetry of the multi-domain crystal. It is interesting to note that the effective domain pattern symmetry could be either higher or lower than the symmetry of the unit cell.<sup>6–8</sup>

The domain engineered PMN–PT and PZN–PT crystals that can give large electromechanical properties are all in the rhombohedral phase with the symmetry group  $3m$ . Microscopically, the dipole in each unit cell in the rhombohedral phase is formed along one of the eight body diagonal directions of the paraelectric cubic unit cell at the ferroelectric phase transition. To be consistent with the convention in this community, we always use the cubic coordinates to label the poling field direction for the multi-domain rhombohedral phase crystals.

An initially proposed configuration of the [001] poled rhombohedral phase PMN–PT and PZN–PT single crystals is given in Fig. 9.1, in which the multi-domain configuration is made of four different domains of equal volume fractions divided by cross-intersecting (charged) domain walls oriented along [100] and [010].<sup>4</sup> This configuration has an effective domain pattern symmetry of tetragonal  $4mm$ . However, optical and electron microscope images of such domain patterns have rarely been reported in the literature. In fact, some reports found that the observed domain walls are oriented in the  $\langle 110 \rangle$  family instead of the  $\langle 100 \rangle$  family.<sup>9</sup> Therefore, researchers also propose monoclinic  $m$  symmetry for the underlying crystal structure for these crystals with compositions near the morphotropic phase boundary (MPB), which will allow the  $\langle 110 \rangle$  oriented domain walls.<sup>9</sup>

There is also some experimental evidence on the non-equivalence of the [100] and [010] directions in many domain engineered crystals, which implies





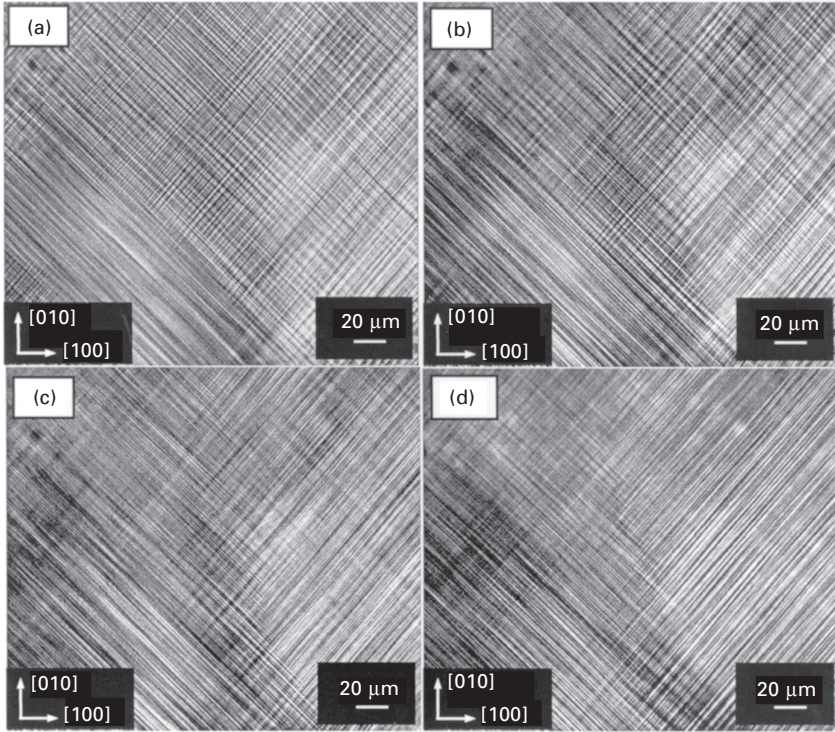
9.1 Possible domain configuration and associated polarization orientation in a [001] poled PMN-PT single crystal of rhombohedral phase.

that the effective symmetry of the multi-domain structure can be lower than tetragonal  $4mm$ .<sup>10</sup> For rhombohedral  $3m$  symmetry crystals, the existence of  $\langle 110 \rangle$  family domain walls implies that the domains form  $109^\circ$  twins in the multi-domain structure. Therefore, locally, the effective symmetry of the domain pattern is orthorhombic  $mm2$ , or even lower.<sup>10</sup> Such a symmetry difference cannot be detected by the measurement of  $d_{33}$  alone because the piezoelectric  $d_{33}$  coefficient will be the same for both symmetries.

The physical origin for the preference of  $109^\circ$  twins over  $71^\circ$  twins in the rhombohedral phase is due to the lesser elastic deformation involved in the  $109^\circ$  twinning with respect to the original cubic structure. The difficulty caused by the  $\langle 110 \rangle$  family walls is that it is not possible to create a tetragonal  $4mm$  symmetry domain pattern using only  $109^\circ$  twins like what is illustrated for the case of  $\langle 100 \rangle$  family walls as shown in Fig. 9.1.

This puzzle might be explained by the result of an optical study of domain patterns in the  $0.68\text{Pb}(\text{Mg}_{1/3}\text{Nb}_{2/3})\text{O}_3-0.32\text{PbTiO}_3$  (PMN-32%PT) system.<sup>11</sup> By focusing an optical polarizing microscope at different depth, it was found that the local domain patterns only involve 2-variant twins instead of 4-variant crosshatched domain structures shown in Fig. 9.1. The twins are interwoven along [001] to form a 3D structure that can be easily mistaken as intersecting twin sets because of the finite focal depth of the microscope. This situation is shown clearly in Fig. 9.2. In Fig. 9.2(a), one can see two intersecting domain wall sets in the upper right corner with wall orientations in  $[110]$  and  $[1\bar{1}0]$ , while the lower left corner has a patch of twin structure with walls along  $[1\bar{1}0]$ . From Fig. 9.2(b) to 9.2(d), the focal point is moved deeper into the thickness direction, one can see that the upper right corner gradually becomes a twin set with domain walls along  $[110]$  while the lower left corner showing a crosshatched domain pattern in Fig. 9.2(d).

The twin cluster size is about  $20\ \mu\text{m}$  in these pictures. Therefore, strictly speaking, the local domain pattern symmetry for this crystal, in the size of  $20\ \mu\text{m}$  or less, is orthorhombic  $mm2$ , which is basically a twin band consisting of two types of domains with  $109^\circ$  domain walls. There is a transition region between layers with mixed domain clusters as we move along the [001]



9.2 Domain structures of a PMN–32%PT single crystal observed by focusing at different depths. From (a) to (d), the focusing depth gradually increases along  $[001]$ .

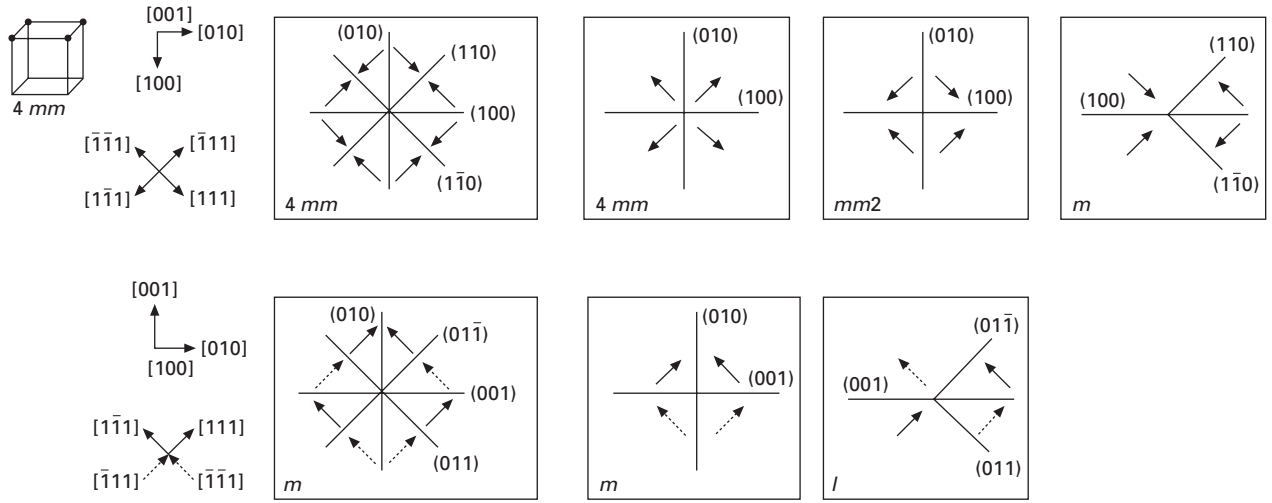
direction, which looks like crosshatched domain pattern with intersecting domain walls oriented in  $[110]$  and  $[1\bar{1}0]$ . In terms of the 3D structure as a whole, the effective symmetry for such interwoven domain patterns is tetragonal  $4mm$ , but only in the average sense. Such interwoven domain patterns provide a reconciliation of the  $\langle 110 \rangle$  family walls observed optically and the rhombohedral crystal symmetry from the x-ray diffraction (XRD) results. Considering the two end members of the solid solution systems, PMN–PT and PZN–PT are tetragonal and rhombohedral, respectively, it is more reasonable to assume a slightly distorted rhombohedral phase rather than a true monoclinic symmetry for the solid solution near the MPB composition. The rhombohedral symmetry is also in agreement with the theoretical results from Landau–Devonshire theory for a ferroelectric with perovskite crystal structure.<sup>12</sup>

There are two main differences of this interwoven structure with the proposed domain structure shown in Fig. 9.1, although both structures have the effective domain pattern symmetry of tetragonal  $4mm$ . First, the domain

wall orientations in Fig. 9.2 are in  $[110]$  and  $[1\bar{1}0]$  instead of  $[100]$  and  $[010]$  shown in Fig. 9.1. Second, the interwoven structure does not have translational symmetry in any given  $(001)$  plane like the structure showing in Fig. 9.1. In other words, the effective  $4mm$  symmetry of the interwoven structure is only in a statistical sense; there is no domain superlattice in this structure. Both types of domain structures, however, are tetragonal  $4mm$  in the macroscopic sense, so the  $[001]$  poled PMN–PT and PZN–PT crystals can be treated as having tetragonal  $4mm$  symmetry for the purpose of macroscopic property characterization.

In more rigorous analysis, the volume ratios and the inclusion of different types of permissible domain walls in the domain pattern will also change the effective symmetry of the multi-domain structure.<sup>13,14</sup> Based on group theoretical analysis, one can derive the average symmetry of a multi-domain system when given the number of variants involved in the domain pattern.<sup>6–8</sup> For the  $[001]$  poled rhombohedral phase crystals, there are four possible domain states remaining after poling. There are also different permissible domain walls, both charged and non-charged types, which divide these domains. If we consider the walls together with the four domain states while forming the domain patterns, more domain patterns can be generated. The effective domain pattern symmetries can be as high as tetragonal  $4mm$  and as low as triclinic of  $I$ .<sup>14</sup> This situation is illustrated in Fig. 9.3. The four remaining domain states after poling along  $[001]$  are represented by the four dots on the unit cell at the upper left corner. The average domain pattern symmetry without the involvement of domain walls is tetragonal  $4mm$ . However, if we are putting in the permissible domain walls, many interesting domain patterns can be formed. As shown in the figure, there are two patterns having tetragonal  $4mm$  symmetry, one pattern having orthorhombic  $mm2$  symmetry, three patterns having monoclinic  $m$  symmetry and one pattern having triclinic  $I$  symmetry.<sup>14</sup>

The complication of the domain pattern symmetry directly affects the complete set of material property characterization because the geometry of the samples affects the boundary conditions, while the boundary conditions directly regulate the domain pattern formation. Hence, the resulting anisotropy of the domain pattern can be different for different geometry samples, which will lead to large property variation from sample to sample. Because the full-set material properties must be obtained from measurements on several samples owing to the large number of independent constants to be determined, such sample to sample variation will cause inconsistencies among data collected from different geometry samples. Therefore, with this symmetry consideration in mind, we must use fewer samples with similar geometries. In addition, it is important to maintain the same boundary conditions when measuring the full-set material constants if possible.



9.3 Possible symmetries of domain patterns made of the four remaining domain states plus permissible domain walls for a rhombohedral symmetry crystal. The patterns are illustrated looking down from [001] and the solid arrows are tilting up while the dashed arrows are tilting down.

### 9.2.2 Factors affecting self-consistency of full-set data

Different methods are used to obtain the complete set of material properties. The most commonly used characterization method for piezoelectric materials is the resonance method. The principle of this technique is described in detail by Berlincourt *et al.* and in the IEEE standard for piezoelectricity.<sup>15,16</sup> However, practical utilization of the resonance method for these multi-domain systems produced several challenges. First of all, the multi-domain structures produced in these crystals depend on sample geometry as described in Section 9.2.1, while the resonance method requires different geometry samples in order to isolate different modes. Therefore, the change of domain patterns in different geometry samples makes it impossible to get self-consistent property data.

Second, the derived constants could have very large errors because some of the constitutive relations contain large error amplification factors. For example, the most obvious error amplification factor is  $1/(1 - k_{33}^2)$ , which can be very large since  $k_{33}$  ranges from 0.90 to 0.96 in these crystals. Detailed analysis revealed that the error amplification factor in some derived quantities could be more than 100!<sup>17</sup> To illustrate the errors produced by unstable mathematical formulas, let us look at the relative errors in the derived piezoelectric strain constants  $e_{33}$  and  $e_{31}$  caused by the relative errors of  $c_{33}^E$  and  $c_{13}^E$ . The error amplification factor ranges from 7.6 to 125 as shown in Table 9.1 for five different compositions of PMN–PT and PZN–PT crystals. The amplitude of error amplification for single crystal BaTiO<sub>3</sub> is also listed in the table for comparison. One can see that the formulas for BaTiO<sub>3</sub> are fairly stable.

The third challenge is the presence of chemical inhomogeneity in these crystals. The composition variation from one end to the other of a 2" long (50 mm) crystal boule could be as large as 5–10%. Because the material properties are extremely sensitive to composition variation in these crystals, particularly near the MPB composition, slight compositional variation from sample to sample would totally destroy the self-consistency of the complete data set.

Therefore, in order to get self-consistent full-set material constants, it is important to reduce the number of samples, ensure composition uniformity in the samples used, avoid too much geometry difference among different samples and try to avoid using unstable formulas for derived quantities. To meet these challenges, a systematic procedure has been developed over the past few years, which utilizes both ultrasonic as well as resonance methods in an effort to obtain the maximum number of measurements from the least number of samples.<sup>18</sup>

The property variation due to compositional fluctuation becomes serious for compositions near the MPB because the desired piezoelectric properties

*Table 9.1* The ratios of relative errors of  $e_{33}$  and  $e_{31}$  to the relative errors of  $c_{12}$ ,  $c_{13}$  and  $c_{33}$  for PZN-4.5%PT, PZN-7%PT, PZN-8%PT, PMN-30%PT, PMN-33%PT and BaTiO<sub>3</sub>

	PZN-4.5%PT	PZN-7.0%PT	PZN-8.0%PT	PMN-30%PT	PMN-33%PT	BaTiO <sub>3</sub>
$\left(\frac{\Delta e_{31}}{e_{31}}\right) \bigg/ \left(\frac{\Delta c_{12}^E}{c_{12}^E}\right)$	21.5	54.2	52.5	39.2	59.6	2.3
$\left(\frac{\Delta e_{31}}{e_{31}}\right) \bigg/ \left(\frac{\Delta c_{13}^E}{c_{13}^E}\right)$	43.8	112	109	82.6	125.1	4.9
$\left(\frac{\Delta e_{33}}{e_{33}}\right) \bigg/ \left(\frac{\Delta c_{33}^E}{c_{33}^E}\right)$	14.9	17.9	19.2	7.6	15.2	3.9
$\left(\frac{\Delta e_{33}}{e_{33}}\right) \bigg/ \left(\frac{\Delta c_{13}^E}{c_{13}^E}\right)$	28.7	34.4	36.3	14.3	30.1	7.2

exist only in the rhombohedral phase, not in the tetragonal phase. The piezoelectric properties reach their peaks at the MPB composition, then drastically decrease when the PT content is increased beyond the MPB. On the rhombohedral side of the phase diagram, although the change in the electromechanical coupling coefficient  $k_{33}$  among different compositions is not so drastic, other properties, such as the piezoelectric  $d_{33}$  coefficient, show a severe decrease. The property changes with composition on the tetragonal side are much more pronounced.

### 9.2.3 Experimental procedure and error analysis

The ultrasonic pulse-echo method is another classic technique for material property characterization, which has been widely used for the measurements of elastic properties in solids and for the study of phase transitions involving the softening of Brillouin zone center acoustic phonons. However, for piezoelectric materials, people are more likely to use the resonance technique since it is easier and less involved with instrumentation. On the other hand, the passive nature of the ultrasonic technique has a unique advantage: it does not suffer from mode coupling when two or more dimensions of the sample are similar, while mode coupling makes the resonance technique unusable for such cases because the shifting of the resonance peaks. Therefore, there is no need to use high aspect ratio samples in ultrasonic measurements for mode isolation. In addition, one can get several measurements from one crystal since ultrasonic wave velocities along different crystal orientations involve different combinations of elastic and piezoelectric coefficients, and the shear and longitudinal waves also give independent measurements in a given propagation direction.

For [001] poled PMN–PT and PZN–PT crystals, the effective macroscopic symmetry is tetragonal  $4mm$  as discussed in Section 9.2.1. There are a total of 11 independent material constants needed to fully describe the system: 6 elastic, 3 piezoelectric and 2 dielectric constants. Using the ultrasonic pulse-echo method, the phase velocities of longitudinal and shear waves can be measured along the three pure mode directions: [100], [001] and [110]. Since shear waves can have their displacements parallel or perpendicular to the poling direction, one can obtain eight independent velocities in these three pure mode directions. The relationships between the velocities and the elastic stiffness constants for a tetragonal symmetry single crystal are given in Table 9.2. It can be seen that there is more than one way to determine  $c_{44}^D$  and  $c_{12}^E$ , which can provide some consistency checks.

In addition to the ultrasonic measurements, two length-extensional and one thickness resonance measurement can be used to obtain the corresponding electromechanical coupling coefficients  $k_{33}$ ,  $k_{31}$  and  $k_t$ , as well as elastic compliances  $s_{11}^E$ ,  $s_{33}^D$  and the elastic stiffness  $c_{33}^D$ . The dielectric measurements

**Table 9.2** Relationships between phase velocities and elastic constants for a system with tetragonal  $4mm$  symmetry. They apply to the multi-domain PMN-PT and PZN-PT single crystals poled in [001]

$v$	$v_1^{[001]}$	$v_s^{[001]}$	$v_l^{[100]}$	$v_{sL}^{[100]}$	$v_{sl}^{[100]}$	$v_l^{[110]}$	$v_{sL}^{[110]}$	$v_{sl}^{[110]}$
$\rho v^2$	$c_{33}^D$	$c_{44}^E$	$c_{11}^E$	$c_{66}^E$	$c_{44}^D$	$\frac{1}{2}(c_{11}^E + c_{12}^E + 2c_{66}^E)$	$\frac{1}{2}(c_{11}^E - c_{12}^E)$	$c_{44}^D$

at low frequencies, generally at 1 kHz, can give the dielectric constants  $\epsilon_{11}^T$  and  $\epsilon_{33}^T$ . The piezoelectric strain constant  $d_{33}$  may also be checked by the quasi-static method using a  $d_{33}$  meter. Combining all the above-mentioned measurements, the following material constants can be directly obtained:  $c_{11}^E, c_{12}^E, c_{44}^E, c_{66}^E, c_{33}^D$  and  $c_{44}^D; s_{11}^E$  and  $s_{33}^D; \epsilon_{11}^T$  and  $\epsilon_{33}^T; d_{33}$  as well as the coupling coefficients  $k_{33}, k_{31}$  and  $k_t$ . Altogether 14 constants can be obtained directly from 17 independent measurements. This provides consistency checks and, more importantly, the flexibility to throw out unreliable measurements since there are only 11 independent coefficients to be determined for the  $4mm$  symmetry.

In order to illustrate the concept of error propagation, let us look at a few examples using the data of PMN-30%PT as numerical inputs. For tetragonal symmetry, there are six independent elastic stiffness constants  $c_{\alpha\beta}^E$ . However,  $c_{33}^E$  and  $c_{13}^E$  cannot be directly measured. The quantity  $c_{33}^E$  may be obtained from the measured  $c_{33}^D$  and  $k_t$  by using the relation

$$c_{33}^E = c_{33}^D (1 - k_t^2) \tag{9.1}$$

The errors in the measurements of  $c_{33}^D$  and  $k_t$  will propagate to the calculated  $c_{33}^E$ ,

$$\frac{\Delta c_{33}^E}{c_{33}^E} = \frac{\Delta c_{33}^D}{c_{33}^D} + 2 \left( \frac{\Delta k_t}{k_t} \right) \left( \frac{k_t^2}{1 - k_t^2} \right) \tag{9.2}$$

Equation (9.2) says that the error of calculated  $c_{33}^E$  comes from two sources, the relative error of  $k_t$  and  $c_{33}^D$ . Because the relative error of  $k_t$  is only 1.1%, and the relative error of  $c_{33}^D$  from the ultrasonic measurement is about 0.9% for a 5 mm thick sample, the relative error of  $c_{33}^D$  from Eq. (9.1) is about 2.0% at the most. Therefore, such formulas are stable.

In order to determine  $c_{13}^E$ , we can use the following formula:

$$c_{13}^E = - \frac{s_{13}^E (c_{11}^E + c_{12}^E)}{s_{33}^E} \tag{9.3}$$

which requires  $s_{13}^E$  and  $s_{33}^E$  to be determined first. The IEEE standard on piezoelectricity suggests calculating  $s_{33}^E$  from the measured  $s_{33}^D$  and  $k_{33}$  by the following relation:



$$s_{33}^E = \frac{s_{33}^D}{1 - k_{33}^2} \quad 9.4$$

In this case, the relative error of  $s_{33}^E$  is given by

$$\frac{\Delta s_{33}^E}{s_{33}^E} = \frac{\Delta s_{33}^D}{s_{33}^D} + 2 \left( \frac{\Delta k_{33}}{k_{33}} \right) \left( \frac{k_{33}^2}{1 - k_{33}^2} \right) \quad 9.5$$

For a [001] poled PMN–30%PT the measured electromechanical coupling coefficient  $k_{33} = 0.92$ , then  $2k_{33}^2/(1 - k_{33}^2) = 11.0$ . Hence, if there was 0.5% error in the measured  $k_{33}$ , the calculated  $s_{33}^E$  would have more than 5.5% error. Considering the relative error of  $s_{33}^D$  could reach 0.9%, the relative error of  $s_{33}^E$  could be larger than 6.4%. Although this error level is still acceptable, we need to remember that the reliability of  $s_{33}^E$  is not as high as the directly measured quantities.

The other way to get  $s_{33}^E$  is from quasi-statically measured  $d_{33}$  using the formula

$$s_{33}^E = \frac{d_{33}^2}{\epsilon_{33}^T k_{33}^2} \quad 9.6$$

In this case, the relative error of the calculated  $s_{33}^E$  is given by

$$\frac{\Delta s_{33}^E}{s_{33}^E} = 2 \frac{\Delta d_{33}}{d_{33}} + \frac{\Delta \epsilon_{33}^T}{\epsilon_{33}^T} + 2 \left( \frac{\Delta k_{33}}{k_{33}} \right) \quad 9.7$$

which depends only on the relative errors of  $k_{33}$  and  $d_{33}$ . Considering the worst scenario, the relative error of calculated  $s_{33}^E$  from Eq. (9.6) is only about 2.7%. Obviously, for piezoelectric materials with large  $k_{33}$  it is better to use Eq. (9.6) instead of Eq. (9.4) to determine  $s_{33}^E$ .

After obtaining  $c_{33}^E$  and  $s_{33}^E$ ,  $s_{13}^E$  can be calculated by

$$s_{13}^E = -\sqrt{\frac{s_{33}^E (s_{33}^E c_{33}^E - 1)}{2(c_{11}^E + c_{12}^E)}} \quad 9.8$$

Finally, the constant  $c_{13}^E$  can be calculated from Eq. (9.3). Up to this point, all six independent elastic stiffness constants under constant electric field have been determined. Since the elastic compliance matrix is the inverse of the elastic stiffness matrix, all six independent elastic compliance constants  $s_{\lambda\mu}^E$  can be easily determined. The measured  $s_{11}^E$  from the resonance bar can be used as a consistency check.

The piezoelectric stress constant  $d_{31}$  is readily obtained from the measured quantities

$$d_{31} = -\sqrt{\epsilon_{33}^T s_{11}^E k_{31}^2} \quad 9.9$$

From the measured  $c_{44}^E$  and  $c_{44}^D$ , the electromechanical coupling coefficient  $k_{15}$  can be determined

$$k_{15}^2 = \left( 1 - \frac{c_{44}^E}{c_{44}^D} \right) \quad 9.10$$

The possible error of  $k_{15}$  determined depends on the ratio of  $c_{44}^E/c_{44}^D$ :

$$\frac{\Delta k_{15}}{k_{15}} = \frac{1}{2} \left( \frac{\Delta c_{44}^D}{c_{44}^D} + \frac{\Delta c_{44}^E}{c_{44}^E} \right) \left( \frac{c_{44}^E}{c_{44}^E - c_{44}^D} \right) \quad 9.11$$

If the ratio  $c_{44}^E/c_{44}^D > \frac{2}{3}$ , the error term  $[(\Delta c_{44}^D/c_{44}^D) + (\Delta c_{44}^E/c_{44}^E)]$  will be magnified. For a [001] poled PMN–30%PT single crystal  $c_{44}^E/(c_{44}^D - c_{44}^E) = 10.1$ , therefore, the term  $[(\Delta c_{44}^D/c_{44}^D) + (\Delta c_{44}^E/c_{44}^E)]$  will be magnified by a factor of 5. The shear piezoelectric coefficient  $d_{15}$  can be calculated by

$$d_{15}^2 = \frac{\varepsilon_{11}^T k_{15}^2}{c_{44}^E} = \varepsilon_{11}^T \left( \frac{1}{c_{44}^E} - \frac{1}{c_{44}^D} \right) \quad 9.12$$

The piezoelectric stress constant  $e_{ij}$  can be derived from the corresponding formulas:

$$e_{31} = d_{31}(c_{11}^E + c_{12}^E) + d_{33}c_{13}^E \quad 9.13$$

$$e_{33} = 2d_{31}c_{13}^E + d_{33}c_{33}^E \quad 9.14$$

$$e_{15} = d_{15}c_{44}^E \quad 9.15$$

For a [001] poled PMN–30%PT single crystal, the estimated error of  $e_{31}$  caused by the uncertainties of  $c_{12}^E$  and  $c_{13}^E$  alone is given by

$$\frac{\Delta e_{31}}{e_{31}} = 39.2 \left( \frac{\Delta c_{12}^E}{c_{12}^E} \right) + 82.6 \left( \frac{\Delta c_{13}^E}{c_{13}^E} \right) \quad 9.16$$

This means that a very small change in  $c_{12}^E$  and  $c_{13}^E$  will lead to very large uncertainties in the derived value of  $e_{31}$ . Also, the error of  $e_{33}$  caused by  $c_{33}^E$  and  $c_{13}^E$  alone can be estimated by

$$\frac{\Delta e_{33}}{e_{33}} = 7.6 \left( \frac{\Delta c_{33}^E}{c_{33}^E} \right) + 14.3 \left( \frac{\Delta c_{13}^E}{c_{13}^E} \right) \quad 9.17$$

From Eqs. (9.16) and (9.17), the calculated values of  $e_{31}$  and  $e_{33}$  are very sensitive to the changes of  $c_{12}^E$  and  $c_{13}^E$  when  $d_{33}$  and  $d_{31}$  are very large, hence they are not very stable formulas. Interestingly, the reverse is not true, i.e., the change in the value of  $e_{31}$  has very little influence on the values of

$c_{12}^E$  or  $c_{13}^E$ . Overall, the derived piezoelectric strain constants  $e_{ij}$  are less reliable than the piezoelectric stress constants  $d_{ij}$ ; therefore, one must assign less weight for  $e_{ij}$  coefficients when performing data analysis to get the self-consistent set of material constants. General guidelines in obtaining reliable data are as follows:

- Energy conservation demands the electromechanical coupling coefficients to be always less than 1. Thus, large piezoelectric constants  $d_{i\lambda}$  demand large dielectric permittivity  $\epsilon_{ij}$ . After a full set of constants has been determined, the electromechanical coupling coefficients can be calculated using these constants and none of them should be larger than 1.
- For  $4mm$  symmetry crystals, the elastic compliances  $s_{12}^E$  and  $s_{13}^E$  must be negative and the volume compressibility must be positive, i.e.  $2s_{11}^E + 2s_{12}^E + 4s_{13}^E + s_{33}^E > 0$ .
- The elastic strain energy of crystals should be positively definite. For  $4mm$  symmetry crystals this requires  $c_{44}^E > 0$ ,  $c_{66}^E > 0$ ,  $c_{11}^E > |c_{12}^E|$  and  $(c_{11}^E + c_{12}^E)c_{33}^E > 2(c_{13}^E)^2$ . Also, the condition  $(s_{11}^E + s_{12}^E)s_{33}^E > 2(s_{13}^E)^2$  needs to be satisfied.
- From similar arguments as in the above point  $d_{31}$  must be negative for  $4mm$  symmetry crystals when  $d_{33}$  is positive. For the same reason,  $e_{31}$ ,  $g_{31}$  and  $h_{31}$  should all be negative. For the orthorhombic [011] poled crystals,  $d_{33}$  and  $d_{31}$  can be both positive, but  $d_{32}$  must be very negative.

### 9.3 Complete set material properties for a few compositions of PMN–PT and PZN–PT single crystals

Using the experimental procedure described in Section 9.2, a few complete sets of material properties have been obtained for domain engineered  $0.955\text{Pb}(\text{Zn}_{1/3}\text{Nb}_{2/3})\text{O}_3-0.045\text{PbTiO}_3$  [PZN–4.5%PT],<sup>19</sup>  $0.93\text{Pb}(\text{Zn}_{1/3}\text{Nb}_{2/3})\text{O}_3-0.07\text{PbTiO}_3$  [PZN–7%PT],<sup>20</sup>  $0.92\text{Pb}(\text{Zn}_{1/3}\text{Nb}_{2/3})\text{O}_3-0.08\text{PbTiO}_3$  [PZN–8%PT],<sup>21</sup>  $0.70\text{Pb}(\text{Mg}_{1/3}\text{Nb}_{2/3})\text{O}_3-0.30\text{PbTiO}_3$  [PMN–30%PT]<sup>22</sup> and  $0.67\text{Pb}(\text{Mg}_{1/3}\text{Nb}_{2/3})\text{O}_3-0.33\text{PbTiO}_3$  [PMN–33%PT]<sup>23</sup> single crystals. The results are listed in Tables 9.3, 9.4, 9.5, 9.6 and 9.7, respectively. All multi-domain systems are treated as having effective tetragonal  $4mm$  symmetry following the arguments given in Section 9.2.1.

#### 9.3.1 PZN–PT multidomain crystals poled along [001]

From Tables 9.3, 9.4, and 9.5, we can clearly see property changes in different compositions of PZN–PT crystals poled along [001]. The effective piezoelectric coefficient  $d_{33}$  is the most important parameter for transducer and sensor

Table 9.3 Measured and derived full-set material properties of PZN-4.5%PT single crystal poled along [001]

**Density:**  $\rho = 8310 \text{ kg/m}^3$

**Elastic stiffness constants:**  $c_{\lambda\mu}$  ( $10^{10} \text{ N/m}^2$ )

$c_{11}^{E^*}$	$c_{12}^E$	$c_{13}^E$	$c_{33}^E$	$c_{44}^{E^*}$	$c_{66}^{E^*}$	$c_{11}^D$	$c_{12}^D$	$c_{13}^D$	$c_{33}^{D^*}$	$c_{44}^{D^*}$	$c_{66}^D$
11.10	10.20	10.10	10.526	6.40	6.30	11.28	10.38	9.38	13.48	6.70	6.30

**Elastic compliance constants:**  $s_{\lambda\mu}$  ( $10^{-12} \text{ m}^2/\text{N}$ )

$s_{11}^{E^*}$	$s_{12}^E$	$s_{13}^E$	$s_{33}^E$	$s_{44}^E$	$s_{66}^E$	$s_{11}^D$	$s_{12}^D$	$s_{13}^D$	$s_{33}^{D^*}$	$s_{44}^D$	$s_{66}^D$
81.63	-29.48	-50.04	105.5	15.63	15.87	61.36	-49.75	-8.08	18.65	14.93	15.87

**Piezoelectric constants:**  $e_{i\lambda}$  ( $\text{C/m}^2$ ),  $d_{i\lambda}$  ( $10^{-12} \text{ C/N}$ ),  $g_{i\lambda}$  ( $10^{-3} \text{ V m/N}$ ),  $h_{i\lambda}$  ( $10^8 \text{ V/m}$ )

$e_{15}$	$e_{31}^*$	$e_{33}^*$	$d_{15}$	$d_{31}$	$d_{33}^*$	$g_{15}$	$g_{31}$	$g_{33}$	$h_{15}$	$h_{31}$	$h_{33}$
8.87	-3.76	15.39	139	-966	2000	5.05	-20.98	43.44	3.38	-4.70	19.22

**Dielectric constants:**  $\epsilon_{ij}(\epsilon_0)$ ,  $\beta_{ij}(10^{-4}/\epsilon_0)$  **Electromechanical coupling constants:**  $k$

$\epsilon_{11}^S$	$\epsilon_{33}^S$	$\epsilon_{11}^{T^*}$	$\epsilon_{33}^{T^*}$	$\beta_{11}^S$	$\beta_{33}^S$	$\beta_{11}^T$	$\beta_{33}^S$	$k_{15}$	$k_{31}^*$	$k_{33}^*$	$k_t^*$
2961	904	3100	5200	3.38	11.06	3.23	1.92	0.217	0.498	0.907	0.468

\* Directly measured properties.

Table 9.4 Measured and derived full-set material properties of PZN-7.0% PT single crystal poled along [001]

**Density:**  $\rho = 8350 \text{ kg/m}^3$

**Elastic stiffness constants:**  $c_{\lambda\mu}$  ( $10^{10} \text{ N/m}^2$ )

$c_{11}^E$	$c_{12}^E$	$c_{13}^E$	$c_{33}^E$	$c_{44}^E$	$c_{66}^E$	$c_{11}^D$	$c_{12}^D$	$c_{13}^D$	$c_{33}^{D*}$	$c_{44}^{D*}$	$c_{66}^D$
11.30	10.30	10.50	10.91	6.30	7.10	11.37	10.37	10.03	14.03	6.80	7.10

**Elastic compliance constants:**  $s_{\lambda\mu}$  ( $10^{-12} \text{ m}^2/\text{N}$ )

$s_{11}^E$	$s_{12}^E$	$s_{13}^E$	$s_{33}^E$	$s_{44}^E$	$s_{66}^E$	$s_{11}^D$	$s_{12}^D$	$s_{13}^D$	$s_{33}^{D*}$	$s_{44}^D$	$s_{66}^D$
85.87	-14.13	-69.02	142.0	15.87	14.08	56.74	-43.25	-9.64	20.91	14.71	14.08

**Piezoelectric constants:**  $e_{k\lambda}$  ( $\text{C/m}^2$ ),  $d_{k\lambda}$  ( $10^{-12} \text{ C/N}$ ),  $g_{k\lambda}$  ( $10^{-3} \text{ V m/N}$ )  $h_{k\lambda}$  ( $10^8 \text{ V/m}$ )

$e_{15}$	$e_{31}$	$e_{33}$	$d_{15}$	$d_{31}$	$d_{33}^*$	$g_{15}$	$g_{31}$	$g_{33}$	$h_{15}$	$h_{31}$	$h_{33}$
11.09	-2.29	15.06	176	-1204	2455	6.63	-24.19	49.32	4.51	-3.14	20.69

**Dielectric constants:**  $\epsilon_{ij}$  ( $\epsilon_0$ ),  $\beta_{ij}$  ( $10^{-4}/\epsilon_0$ ) **Electromechanical coupling constants:**  $k$

$\epsilon_{11}^S$	$\epsilon_{33}^S$	$\epsilon_{11}^T$	$\epsilon_{33}^T$	$\beta_{11}^S$	$\beta_{33}^S$	$\beta_{11}^T$	$\beta_{33}^T$	$k_{15}$	$k_{31}^*$	$k_{33}^*$	$k_t^*$
2779	822.5	3000	5622	3.598	12.16	3.33	1.78	0.271	0.582	0.923	0.471

\* Directly measured properties.

Table 9.5 Measured and derived full-set material properties of PZN–8.0% PT single crystal poled along [001]

**Density:**  $\rho = 8315 \text{ kg/m}^3$

**Elastic stiffness constants:**  $c_{\alpha\beta}$  ( $10^{10} \text{ N/m}^2$ )

$C_{11}^E$	$C_{12}^E$	$C_{13}^E$	$C_{33}^E$	$C_{44}^E$	$C_{66}^E$	$C_{11}^D$	$C_{12}^D$	$C_{13}^D$	$C_{33}^{D*}$	$C_{44}^{D*}$	$C_{66}^D$
11.50	10.50	10.90	11.51	6.34	6.50	11.80	10.80	10.00	14.25	6.76	6.50

**Elastic compliance constants:**  $s_{\alpha\beta}$  ( $10^{-12} \text{ m}^2/\text{N}$ )

$S_{11}^E$	$S_{12}^E$	$S_{13}^E$	$S_{33}^E$	$S_{44}^E$	$S_{66}^E$	$S_{11}^D$	$S_{12}^D$	$S_{13}^D$	$S_{33}^{D*}$	$S_{44}^D$	$S_{66}^D$
86.89	-13.11	-69.87	141.0	15.77	15.38	55.84	-44.16	-8.19	18.52	14.79	15.38

**Piezoelectric constants:**  $e_{k\lambda}$  ( $\text{C/m}^2$ ),  $d_{k\lambda}$  ( $10^{-12} \text{ C/N}$ ),  $g_{k\lambda}$  ( $10^{-3} \text{ V m/N}$ ),  $h_{k\lambda}$  ( $10^8 \text{ V/m}$ )

$e_{15}$	$e_{31}^*$	$e_{33}^*$	$d_{15}$	$d_{31}$	$d_{33}^*$	$g_{15}$	$g_{31}$	$g_{33}$	$h_{15}$	$h_{31}$	$h_{33}$
10.06	-5.09	15.45	158.6	-1455	2890	6.18	-21.34	42.39	4.18	-5.84	17.72

**Dielectric constants:**  $\epsilon_{ij}$  ( $\epsilon_0$ ),  $\beta_{ij}$  ( $10^{-4}/\epsilon_0$ ) **Electromechanical coupling constants:**  $k$

$\epsilon_{11}^S$	$\epsilon_{33}^S$	$\epsilon_{11}^T$	$\epsilon_{33}^T$	$\beta_{11}^S$	$\beta_{33}^S$	$\beta_{11}^T$	$\beta_{33}^T$	$k_{15}$	$k_{31}^*$	$k_{33}^*$	$k_t^*$
2720	984	2900	7700	3.68	10.16	3.45	1.30	0.249	0.598	0.932	0.438

\* Directly measured properties.

Table 9.6 Measured and derived full-set material properties of PMN-30%PT single crystal poled along [001]

**Density:**  $\rho = 8038 \text{ kg/m}^3$

**Elastic stiffness constants:**  $c_{\lambda\mu}$  ( $10^{10} \text{ N/m}^2$ )

$c_{11}^{E^*}$	$c_{12}^E$	$c_{13}^E$	$c_{33}^E$	$c_{44}^{E^*}$	$c_{66}^{E^*}$	$c_{11}^D$	$c_{12}^D$	$c_{13}^D$	$c_{33}^{D^*}$	$c_{44}^{D^*}$	$c_{66}^D$
11.71	10.30	10.10	10.74	7.14	6.60	11.76	10.35	9.51	17.41	7.77	6.60

**Elastic compliance constants:**  $s_{\lambda\mu}$  ( $10^{-12} \text{ m}^2/\text{N}$ )

$s_{11}^{E^*}$	$s_{12}^E$	$s_{13}^E$	$s_{33}^E$	$s_{44}^E$	$s_{66}^E$	$s_{11}^D$	$s_{12}^D$	$s_{13}^D$	$s_{33}^{D^*}$	$s_{44}^D$	$s_{66}^D$
51.98	-18.94	-31.05	67.66	14.01	15.15	39.72	-31.20	-4.66	10.83	12.87	15.15

**Piezoelectric constants:**  $e_{i\lambda}$  ( $\text{C/m}^2$ ),  $d_{i\lambda}$  ( $10^{-12} \text{ C/N}$ ),  $g_{i\lambda}$  ( $10^{-3} \text{ V m/N}$ ),  $h_{i\lambda}$  ( $10^8 \text{ V/m}$ )

$e_{15}$	$e_{31}^*$	$e_{33}^*$	$d_{15}$	$d_{31}$	$d_{33}^*$	$g_{15}$	$g_{31}$	$g_{33}$	$h_{15}$	$h_{31}$	$h_{33}$
13.58	-2.41	27.07	190.3	-920	1981	5.97	-13.32	28.68	4.64	-2.19	24.60

**Dielectric constants:**  $\varepsilon_{ij}(\varepsilon_0)$ ,  $\beta_{ij}(10^{-4}/\varepsilon_0)$  **Electromechanical coupling constants:**  $k$

$\varepsilon_{11}^S$	$\varepsilon_{33}^S$	$\varepsilon_{11}^{T^*}$	$\varepsilon_{33}^{T^*}$	$\beta_{11}^S$	$\beta_{33}^S$	$\beta_{11}^T$	$\beta_{33}^T$	$k_{15}$	$k_{31}^*$	$k_{33}^*$	$k_t^*$
3308	1243	3600	7800	3.02	8.05	2.78	1.28	0.285	0.486	0.916	0.618

\* Directly measured properties.

Table 9.7 Measured and derived full-set material properties of PMN–33%PT single crystal poled along [001]

**Density:**  $\rho = 8060 \text{ g/m}^3$

**Elastic stiffness constants:**  $c_{\alpha\beta}$  ( $10^{10} \text{ N/m}^2$ )

$c_{11}^E$	$c_{12}^E$	$c_{13}^E$	$c_{33}^E$	$c_{44}^E$	$c_{66}^E$	$c_{11}^D$	$c_{12}^D$	$c_{13}^D$	$c_{33}^{D*}$	$c_{44}^{D*}$	$c_{66}^D$
11.50	10.30	10.20	10.38	6.90	6.60	11.69	10.49	9.05	17.31	7.70	6.60

**Elastic compliance constants:**  $s_{\alpha\beta}$  ( $10^{-12} \text{ m}^2/\text{N}$ )

$s_{11}^E$	$s_{12}^E$	$s_{13}^E$	$s_{33}^E$	$s_{44}^E$	$s_{66}^E$	$s_{11}^D$	$s_{12}^D$	$s_{13}^D$	$s_{33}^{D*}$	$s_{44}^D$	$s_{66}^D$
70.15	-13.19	-55.96	119.6	14.49	15.15	45.60	-37.74	-4.11	10.08	12.99	15.15

**Piezoelectric constants:**  $e_{i\lambda}$  ( $\text{C/m}^2$ ),  $d_{i\lambda}$  ( $10^{-12} \text{ C/N}$ ),  $g_{i\lambda}$  ( $10^{-3} \text{ V m/N}$ ),  $h_{i\lambda}$  ( $10^8 \text{ V/m}$ )

$e_{15}$	$e_{31}^*$	$e_{33}^*$	$d_{15}$	$d_{31}$	$d_{33}^*$	$g_{15}$	$g_{31}$	$g_{33}$	$h_{15}$	$h_{31}$	$h_{33}$
10.08	-3.39	20.40	146.1	-1335	2820	10.31	-18.39	38.84	7.94	-5.64	33.94

**Dielectric constants:**  $\epsilon_{ij}(\epsilon_0)$ ,  $\beta_{ij}(10^{-4}/\epsilon_0)$  **Electromechanical coupling constants:**  $k$

$\epsilon_{11}^S$	$\epsilon_{33}^S$	$\epsilon_{11}^{T*}$	$\epsilon_{33}^{T*}$	$\beta_{11}^S$	$\beta_{33}^S$	$\beta_{11}^T$	$\beta_{33}^T$	$k_{15}$	$k_{31}^*$	$k_{33}^*$	$k_t^*$
1434	679	1600	8200	6.97	14.73	6.25	1.22	0.322	0.592	0.95	0.633

\* Directly measured properties.



applications. It increases as the composition gets closer to the MPB and reaches 2890 pC/N for PZN–8%PT. Beyond 8%PT, the crystals will be in the tetragonal phase and the  $d_{33}$  value drastically decreases. The  $d_{31}$  coefficient follows the same trend as  $d_{33}$  and reaches the highest value of –1455 pC/N for PZN–8%PT. On the other hand, the shear piezoelectric coefficient  $d_{15}$  (~ 160 pC/N) does not change much with composition and is also rather small compared with that of other known piezoelectric materials. The dielectric constant  $\epsilon_{33}$  increases with PT content from the rhombohedral phase side of the phase diagram toward the MPB composition and reaches a peak value of 7700 for PZN–8%PT at room temperature, but the  $\epsilon_{11}$  (~3000) value seems to be insensitive to the compositional change. One may also notice that the electromechanical coupling coefficients  $k_{33}$ ,  $k_{31}$ ,  $k_{15}$  and  $k_t$  are not as sensitive to compositional change in the PZN–PT system. Although the  $k_{33}$  value is very high compared with other known piezoelectric materials, the  $k_t$  value is slightly less than that of soft Pb(Ti, Zr)O<sub>3</sub> (PZT5H) ceramics and the  $k_{15}$  value is also rather small compared with that of PZT. In other words, the [001] poled crystals are only advantageous for piezoelectric devices based on  $k_{33}$  and  $k_{31}$  modes.

### 9.3.2 PMN–PT multidomain crystals poled along [001]

Tables 9.6 and 9.7 are properties of two compositions of [001] poled PMN–PT domain engineered crystals. One can clearly see much more pronounced property degradation compared with that of the PZN–PT system when the composition is away from the MPB. From PMN–33%PT to PMN–30%PT, the piezoelectric constant  $d_{33}$  is reduced from 2820 to 1981 pC/N and the  $d_{31}$  is reduced from –1335 to –920 pC/N, respectively.

One may notice that the elastic stiffness constants  $c_{\lambda\mu}$  change very little among different compositions. But the elastic compliance constants  $s_{\lambda\mu}$  change noticeably with composition. Moreover, it seems that the superior piezoelectric properties of these systems are directly related to the large  $s_{33}^E$  value, which is much larger than that of PZT ceramics and also becomes larger when the composition gets closer to the MPB.

When the PT composition is more than 39% in the PMN–PT system, the crystal will be in the tetragonal phase. In order to get a complete picture of the composition influence to the material properties, the material properties of 0.58Pb(Mg<sub>1/3</sub>Nb<sub>2/3</sub>)O<sub>3</sub>–0.42PbTiO<sub>3</sub> [PMN–42%PT] are listed in Table 9.8.<sup>24</sup> It is clearly demonstrated that the piezoelectric properties become much worse in this single domain single crystal with tetragonal crystallographic symmetry. The piezoelectric properties of tetragonal PMN–PT crystal are even worse than regular PZT ceramics. There is a very strong dielectric anisotropy with the dielectric constant  $\epsilon_{11}^T > 8600$  but  $\epsilon_{33}^T$  only ~660.

Table 9.8 Measured and derived full-set material properties of PMN-42%PT single domain single crystal poled along [001]

**Density:**  $\rho = 8100 \text{ kg/m}^3$

**Elastic stiffness constants:**  $c_{\alpha\beta}$  ( $10^{10} \text{ N/m}^2$ )

$c_{11}^E$	$c_{12}^E$	$c_{13}^E$	$c_{33}^E$	$c_{44}^E$	$c_{66}^E$	$c_{11}^D$	$c_{12}^D$	$c_{13}^D$	$c_{33}^{D*}$	$c_{44}^{D*}$	$c_{66}^D$
17.51	8.51	8.3	10.5	2.85	8.0	17.7	8.7	7.18	16.99	8.05	8.0

**Elastic compliance constants:**  $s_{\alpha\beta}$  ( $10^{-12} \text{ m}^2/\text{N}$ )

$s_{11}^E$	$s_{12}^E$	$s_{13}^E$	$s_{33}^E$	$s_{44}^E$	$s_{66}^E$	$s_{11}^D$	$s_{12}^D$	$s_{13}^D$	$s_{33}^{D*}$	$s_{44}^D$	$s_{66}^D$
9.43	-1.68	-6.13	19.21	35.09	12.5	8.02	-3.10	-2.08	7.64	12.42	12.5

**Piezoelectric constants:**  $e_{i\lambda}$  ( $\text{C/m}^2$ ),  $d_{i\lambda}$  ( $10^{-12} \text{ C/N}$ ),  $g_{i\lambda}$  ( $10^{-3} \text{ V m/N}$ ),  $h_{i\lambda}$  ( $10^8 \text{ V/m}$ )

$e_{15}$	$e_{31}^*$	$e_{33}^*$	$d_{15}$	$d_{31}$	$d_{33}^*$	$g_{15}$	$g_{31}$	$g_{33}$	$h_{15}$	$h_{31}$	$h_{33}$
37.5	-2.1	12.2	131	-91	260	17.23	-15.57	44.5	13.87	-9.16	53.22

**Dielectric constants:**  $\epsilon_{ij}(\epsilon_0)$ ,  $\beta_{ij}(10^{-4}/\epsilon_0)$  **Electromechanical coupling constants:**  $k$

$\epsilon_{11}^S$	$\epsilon_{33}^S$	$\epsilon_{11}^T$	$\epsilon_{33}^T$	$\beta_{11}^S$	$\beta_{33}^S$	$\beta_{11}^T$	$\beta_{33}^T$	$k_{15}$	$k_{31}^*$	$k_{33}^*$	$k_t^*$
3054	259	8627	660	3.27	38.61	1.16	15.15	0.8	0.39	0.78	0.62

\* Directly measured properties.

### 9.3.3 PZN–PT multi-domain crystals poled along [011]

Domain patterns in these domain engineered single crystals can be manipulated by off-polar direction poling, and the poling field does not have to be applied along [001]. In fact, if the optimized properties are  $d_{32}$  or  $d_{15}$ , [011] direction poled crystals can be better than [001] direction poled crystals. This can be seen from the complete set of properties characterized on a [011] poled PZN–7%PT crystal system.<sup>25</sup> For the [011] direction poled crystals, the effective domain pattern symmetry is orthorhombic  $mm2$ , so that 17 independent coefficients must be measured to form the complete data set.<sup>26</sup> From Table 9.9 we can see that the [011] direction poled crystal has much superior  $d_{32}$  (–1460 pC/N) with the electromechanical coupling coefficients  $k_{32}$  reaching 0.87. Although the  $d_{31}$  value of [001] poled crystals can also reach –1400 pC/N, their  $k_{31}$  values are less than 0.58. Therefore, the [011] poled crystals are superior in transverse mode piezoelectric device applications. In addition, the [011] direction poled crystals have a very large shear piezoelectric coefficient  $d_{15}$  (>1800 pC/N), while the shear piezoelectric coefficient of [001] poled crystals is much smaller ( $d_{15} < 180$  pC/N).

## 9.4 Correlation between single domain and multi-domain properties and the principle of property enhancement in domain engineered ferroelectric single crystals

In order to understand the principles of property enhancement through the domain engineering process, it is necessary to find the correlation between single domain properties and multi-domain properties. There are two main contributions from multi-domain structures that do not exist in single domain systems. One is the domain wall contribution, as often mentioned in ceramic piezoelectric materials, and the other is the orientation effect.

A full set of data had been obtained for single domain single crystal PMN–33%PT,<sup>27</sup> which has rhombohedral  $3m$  symmetry. There are altogether 12 independent material constants to fully describe the crystal: 6 elastic, 4 piezoelectric and 2 dielectric constants. In order to define the property matrix and find the correlations to the multi-domain data, we must define the coordinate system of the rhombohedral phase with respect to the cubic phase coordinates. As illustrated in Fig. 9.4, if we use the subscript ‘r’ to represent the rhombohedral phase, their relationships with cubic coordinate systems are:

$$[100]_r \leftrightarrow [1\bar{1}0], [010]_r \leftrightarrow [11\bar{2}], [001]_r \leftrightarrow [111]$$

Here the conversions between the cubic and the tetragonal coordinate systems are different from those used in reference 27 therefore, some signs of the constants listed in Table 9.10 are different from those given

Table 9.9 Complete set of material coefficients of PZN-7%PT single crystal poled along [011]

**Density:**  $\rho = 8350 \text{ kg/m}^3$

**Elastic stiffness coefficients:**  $c_{\lambda\mu} (10^{10} \text{ N/m}^2)$

$c_{11}^E$	$c_{12}^E$	$c_{13}^E$	$c_{22}^E$	$c_{23}^E$	$c_{33}^E$	$c_{44}^E$	$c_{55}^E$	$c_{66}^E$
14.5	15.32	12.67	18.02	15.00	14.10	6.47	0.34	7.10
$c_{11}^D$	$c_{12}^D$	$c_{13}^D$	$c_{22}^D$	$c_{23}^D$	$c_{33}^D$	$c_{44}^D$	$c_{55}^D$	$c_{66}^D$
17.40	21.16	11.43	29.82	12.50	14.63	6.54	0.41	7.10

**Elastic compliance coefficients:**  $s_{\lambda\mu} (10^{-12} \text{ m}^2/\text{N})$

$s_{11}^E$	$s_{12}^E$	$s_{13}^E$	$s_{22}^E$	$s_{23}^E$	$s_{33}^E$	$s_{44}^E$	$s_{55}^E$	$s_{66}^E$
67.52	-60.16	3.36	102.00	-54.47	62.02	15.45	291.55	14.08
$s_{11}^D$	$s_{12}^D$	$s_{13}^D$	$s_{22}^D$	$s_{23}^D$	$s_{33}^D$	$s_{44}^D$	$s_{55}^D$	$s_{66}^D$
59.40	-35.38	-16.17	26.30	5.16	15.05	15.30	245.99	14.08

**Piezoelectric coefficients:**  $e_{i\lambda} (\text{C/m}^2)$ ,  $d_{i\lambda} (10^{-12} \text{ C/N})$ ,  $g_{i\lambda} (10^{-3} \text{ V m/N})$  and  $h_{i\lambda} (10^8 \text{ V/m})$

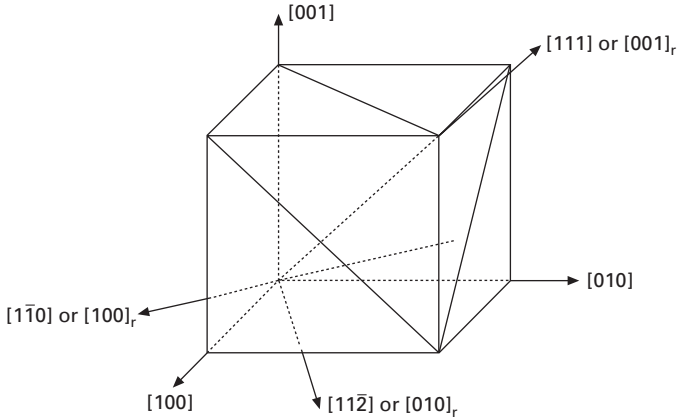
$e_{15}$	$e_{24}$	$e_{31}$	$e_{32}$	$e_{33}$
6.25	3.24	-8.64	-17.44	3.69
$d_{15}$	$d_{24}$	$d_{31}$	$d_{32}$	$d_{33}$
1823	50	478	-1460	1150
$g_{15}$	$g_{24}$	$g_{31}$	$g_{32}$	$g_{33}$
24.99	3.03	16.98	-51.85	40.84
$h_{15}$	$h_{24}$	$h_{31}$	$h_{32}$	$h_{33}$
1.02	1.98	-33.53	-67.65	14.33

**Dielectric coefficients:**  $\epsilon_{ij} (\epsilon_0)$  and  $\beta_{ij} (10^{-4}/\epsilon_0)$

$\epsilon_{11}^S$	$\epsilon_{22}^S$	$\epsilon_{33}^S$	$\epsilon_{11}^T$	$\epsilon_{22}^T$	$\epsilon_{33}^T$
6953	1847	291	8240	1865	3180
$\beta_{11}^S$	$\beta_{22}^S$	$\beta_{33}^S$	$\beta_{11}^T$	$\beta_{22}^T$	$\beta_{33}^T$
1.44	5.42	34.34	1.21	5.36	3.14

**Electromechanical coupling coefficients:**  $k$

$k_{15}$	$k_{24}$	$k_{31}$	$k_{32}$	$k_{33}$	$k_t$
0.40	0.10	0.35	0.86	0.87	0.19



9.4 The rhombohedral coordinates defined for PMN-0.33PT and their relationship to the cubic coordinates.

Table 9.10 Measured and derived material properties of single domain PMN-33%PT single crystal poled along [111]

<b>Elastic stiffness constants:</b> $c_{\lambda m}$ ( $10^{10}$ N/m <sup>2</sup> )							
$c_{11}^E$	$c_{12}^E$	$c_{13}^E$	$c_{14}^E$	$c_{33}^E$	$c_{44}^E$	$c_{66}^E$	
20.12	7.36	11.50	-4.15	17.12	2.90	6.38	
$c_{11}^D$	$c_{12}^D$	$c_{13}^D$	$c_{14}^{D^*}$	$c_{33}^{D^*}$	$c_{44}^{D^*}$	$c_{66}^{D^*}$	
20.43	7.62	10.32	-3.87	21.94	5.63	6.41	
<b>Elastic compliance constants:</b> $s_{\lambda \mu}$ ( $10^{-12}$ m <sup>2</sup> /N)							
$s_{11}^E$	$s_{12}^E$	$s_{13}^E$	$s_{14}^E$	$s_{33}^E$	$s_{44}^E$	$s_{66}^E$	
62.16	-53.85	-5.58	166.24	13.34	510.98	232.02	
$s_{11}^D$	$s_{12}^D$	$s_{13}^D$	$s_{14}^D$	$s_{33}^{D^*}$	$s_{44}^{D^*}$	$s_{66}^{D^*}$	
9.39	-3.94	-2.57	9.15	6.97	30.33	26.65	
<b>Piezoelectric coefficients:</b> $e_{i\lambda}$ (C/m <sup>2</sup> ), $d_{i\lambda}$ ( $10^{-12}$ C/N), $g_{i\lambda}$ ( $10^{-3}$ V m/N) and $h_{i\lambda}$ ( $10^8$ V/m)							
$e_{15}^*$	$e_{22}^*$	$e_{31}$	$e_{33}$	$d_{15}$	$d_{22}$	$d_{31}^*$	$d_{33}^*$
7.52	-0.78	-2.88	11.83	4100	-1340	-90	190
$g_{15}$	$g_{22}$	$g_{31}$	$g_{33}$	$h_{15}$	$h_{22}$	$h_{31}$	$h_{33}$
11.72	-3.83	-1.59	3.35	36.38	-3.78	-9.94	40.78
<b>Dielectric constants:</b> $\epsilon_{ij}(\epsilon_0)$ and $\beta_{ij}(10^{-4}/\epsilon_0)$							
$\epsilon_{11}^{S^*}$	$\epsilon_{33}^S$	$\epsilon_{11}^T$	$\epsilon_{33}^T$	$\beta_{11}^S$	$\beta_{33}^S$	$\beta_{11}^T$	$\beta_{33}^T$
233	328	3950	640	42.84	30.53	2.53	15.63
<b>Electromechanical coupling constants <math>k</math> and density <math>\rho</math></b>							
$k_{15}$	$k_{31}^*$	$k_{33}^*$	$k_t^*$	$\rho$ (kg/m <sup>3</sup> )			
0.70	0.15	0.69	0.47	8060			

\* Directly measured properties.

in reference 27. Detailed explanation of the coordinate transformation has been described by Zhang and Cao.<sup>28</sup> The full-set single domain material properties were measured under a bias field along the polar direction [111]

to ensure that the crystals are always in the single domain state because the single domain state seems less stable than the multi-domain state. One must note that the application of a bias electric field will cause some property change since most properties are field dependent.

The measured complete set of material properties under bias for the PMN–33%PT single domain single crystal is given in Table 9.10.<sup>27,28</sup> One can find many interesting facts from the single domain data set in comparison with the multi-domain data set of the same composition given in Table 9.7. The electromechanical coupling coefficient  $k_{33}$  and the piezoelectric constant  $d_{33}$  for single-domain PMN–33%PT single crystals are only 69% and 190 pC/N, respectively. These values are much smaller than those of domain engineered PMN–33%PT single crystals. However, the shear piezoelectric constant  $d_{15}$  of single domain PMN–33%PT single crystals reaches 4100 pC/N even under bias, which is much larger than that of multi-domain PMN–33%PT single crystals. There is also a report of  $d_{15}$  value for the single domain PMN–PT systems as high as 7000 pC/N without bias.<sup>29</sup> This means that part of the  $d_{15}$  value in the single domain state has been converted to effective  $d_{33}$  in the domain engineered crystals.

To see this conversion from the orientation effect, we can perform matrix rotation using the single domain data given in Table 9.10. The transformations of the dielectric constants piezoelectric constants and elastic compliance from one orientation to another can be performed based on their matrix definitions. Let  $\{\mathbf{b}_i\}$  and  $\{\mathbf{b}_i^*\}$  ( $i = 1, 2, 3$ ) be orthonormal bases representing the original and rotated coordinates, respectively. The component  $a_{ij}$  of the transformation matrix  $A$  is given by

$$a_{ij} = \mathbf{b}_i^* \cdot \mathbf{b}_j \tag{9.18}$$

In the Voigt notation, the material constants in the rotated coordinate system can be calculated by<sup>30</sup>

$$\boldsymbol{\epsilon}^* = A\boldsymbol{\epsilon}A^t \tag{9.19}$$

$$\mathbf{d}^* = A\mathbf{d}N^t \tag{9.20}$$

$$\mathbf{s}^* = N\mathbf{s}N^t \tag{9.21}$$

where  $A^t$  and  $N^t$  represent the transpose of matrices  $A$  and  $N$ , respectively, with the matrix  $N$  given by

$$N = \begin{bmatrix} a_{11}^2 & a_{12}^2 & a_{13}^2 & a_{12}a_{13} & a_{11}a_{13} & a_{11}a_{12} \\ a_{21}^2 & a_{22}^2 & a_{23}^2 & a_{22}a_{23} & a_{21}a_{23} & a_{21}a_{22} \\ a_{31}^2 & a_{32}^2 & a_{33}^2 & a_{32}a_{33} & a_{31}a_{33} & a_{31}a_{32} \\ 2a_{21}a_{31} & 2a_{22}a_{32} & 2a_{23}a_{33} & a_{22}a_{33} + a_{23}a_{32} & a_{21}a_{33} + a_{23}a_{31} & a_{21}a_{32} + a_{22}a_{31} \\ 2a_{11}a_{31} & 2a_{12}a_{32} & 2a_{13}a_{33} & a_{12}a_{33} + a_{13}a_{32} & a_{11}a_{33} + a_{13}a_{31} & a_{11}a_{32} + a_{12}a_{31} \\ 2a_{11}a_{21} & 2a_{12}a_{22} & 2a_{13}a_{23} & a_{12}a_{23} + a_{13}a_{22} & a_{11}a_{23} + a_{13}a_{21} & a_{11}a_{22} + a_{12}a_{21} \end{bmatrix} \tag{9.22}$$

The electromechanical coupling factor  $k_{33}^*$  in the rotated orientation is then given by

$$k_{33}^* = \frac{d_{33}^*}{\sqrt{s_{33}^* \epsilon_{33}^*}} \quad 9.23$$

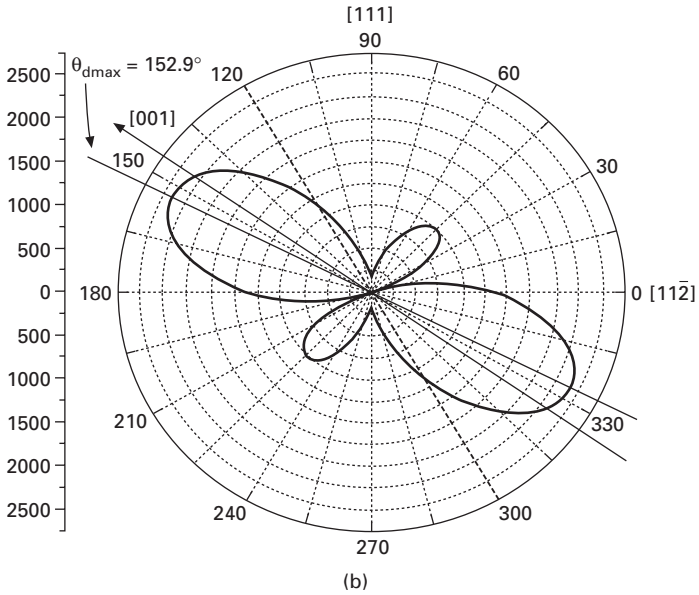
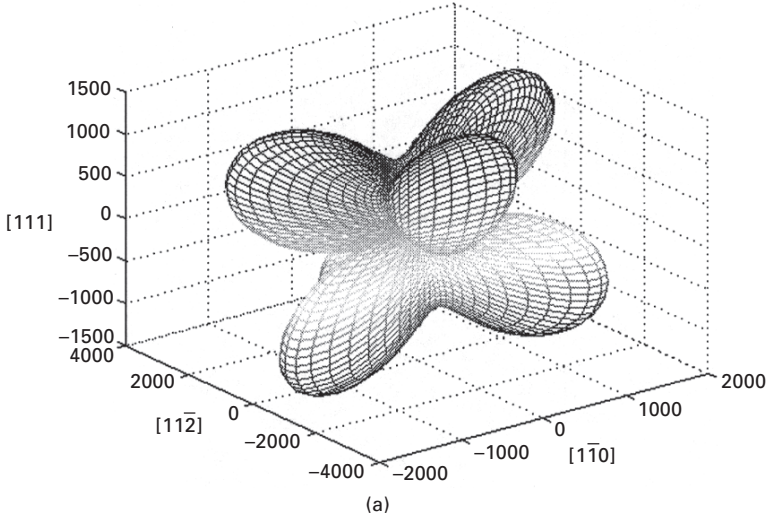
Because we are particularly interested in the  $d_{33}^*$  and  $k_{33}^*$  for these crystals, their rotated values are plotted in Figs 9.5 and 9.6, respectively. In both figures, (a) is the orientational dependence of the amplitude in 3D and (b) is a particular 2D cross section of (a). The distance between the origin and a point on the surface in Figs 9.5(a) and 9.6(a) or a point on the curve in Figs 9.5(b) and 9.6(b) represents the absolute value of the constant in the corresponding direction. The maximum values of  $d_{33}^*$  and  $k_{33}^*$  can be obtained in the  $63.0^\circ$  and  $70.8^\circ$  directions, respectively, from the dipolar direction, in which the maximum effective piezoelectric constant  $d_{33}^*$  reaches 2411 pC/N and the electromechanical coupling factor  $k_{33}^*$  reaches 0.94. In fact, if one uses the single domain data set to directly calculate the properties along [001] ( $54.74^\circ$  from the dipolar direction), the effective values are  $d_{33}^* = 2316$  pC/N and  $k_{33}^* = 0.93$ , which are almost the same as those directly measured values for multi-domain PMN–33%PT single crystals. The effective  $d_{15}^*$  along the [001] direction decreases to 134 pC/N, which is very close to the measured  $d_{15}^* = 143$  pC/N in the multi-domain system. Such a good match is quite amazing considering the single domain data were measured under bias, while the bias field can cause some properties to degrade, particularly the  $d_{15}$  value.

As shown in Fig. 9.5(b) and 9.6(b), in terms of the rhombohedral coordinates, the maximum value of effective  $d_{33}$  occurs in the directions  $152.9^\circ$  and  $332.9^\circ$ , respectively, from the  $[010]_r$  of the rhombohedral coordinates while the maximum value of  $k_{33}$  occurs in directions  $160.8^\circ$  and  $340.8^\circ$ , respectively, from the  $[010]_r$ . One can also see that these two quantities do not change significantly with orientation near their maximum values, particularly the  $k_{33}^*$  value; therefore, the [001] direction poled crystals can give almost the optimum electromechanical coupling coefficient  $k_{33}$  and piezoelectric coefficient  $d_{33}$ .

The calculated values are based purely on the property rotation. Hence, we may conclude that the main portion of the superior effective  $d_{33}$  in the multi-domain state comes from the orientational conversion of the super-large shear piezoelectric constant  $d_{15}$  of the single domain state.

## 9.5 Summary

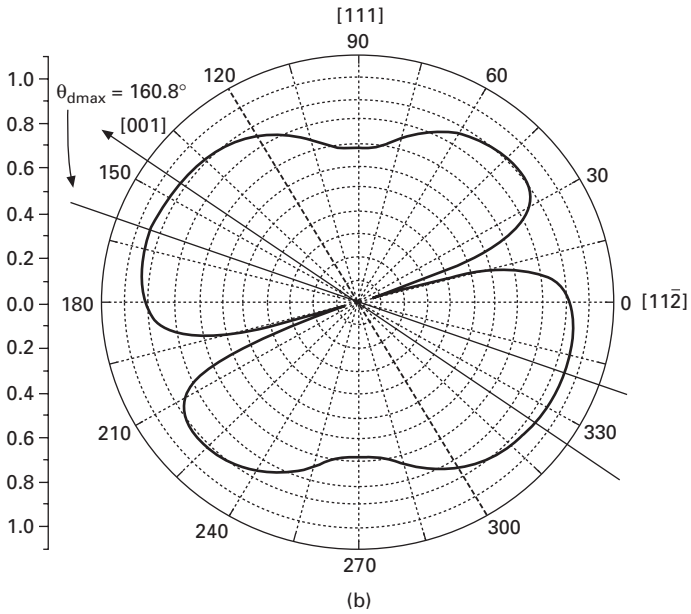
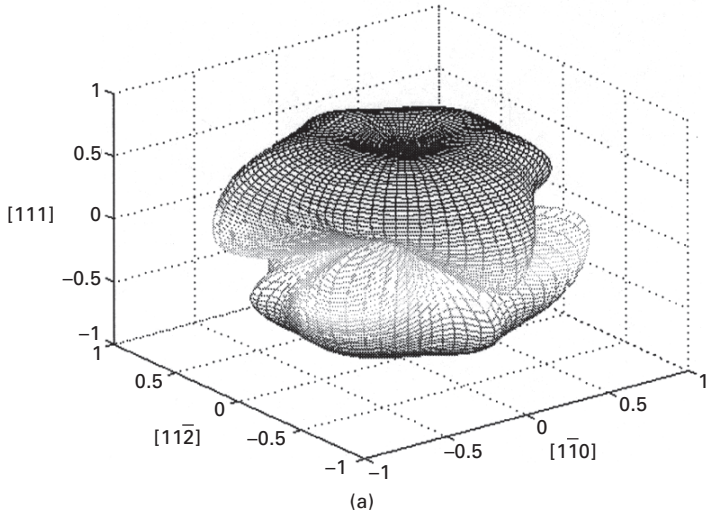
The intensive research on domain engineered PMN–PT and PZN–PT single



9.5 (a) Orientational dependence of piezoelectric constant  $d_{33}$  (in units of  $10^{-12}$  C/N). (b) The cross-section of (a) in the  $[112]$ - $[111]$  plane.

crystals in recent years not only has given us a new category of piezoelectric materials that could lead to a new generation of electromechanical devices, it has also produced a new physical means to enhance functional properties





9.6 (a) Electromechanical coupling coefficient  $k_{33}$ . (b) The cross-section of (a) in the  $[112]$ – $[111]$  plane.

of ferroelectric materials. The basic idea of domain engineering of ferroelectric crystals is to re-direct the field-induced displacement of a certain mode to other modes through the manipulation of domain structures. Such domain manipulation is different from the conventional sense of increasing ‘extrinsic contributions’, which refers to the additional electromechanical activities

produced by the movement of domain walls. Here, the domain patterns form a new class of mesoscopic structures that have their own symmetries and their unique properties, which can be quite different from the properties of the underlying crystal structure. Obviously, not all ferroelectric crystals can be ‘domain engineered’ to achieve high piezoelectric properties. At least one of the piezoelectric coefficients in the single domain state must be very large in order for the re-directing scheme to work.

Another fundamental principle for domain engineering is to use domain interactions to create structural instabilities. It is known that the lattices in the domain wall regions are distorted. When high domain wall density is introduced in the crystal, they could lower the phase transition temperature since the domain walls are natural nucleation sites to induce phase transitions. The piezoelectric and dielectric properties can become very large due to such domain pattern-induced instabilities.

Domain pattern formation not only depends on the characteristics poling field, such as the field level, direction and duration time, but also depends on the environment temperature and boundary conditions of the sample. Considering the unique feature of domain engineered crystals, the characterization work must be conducted with extreme care. Not all the traditional characterization methods can give reasonable values since some of them will cause the change of domain patterns, which in turn leads to property changes. It is also important to understand the error propagation mechanism and develop ways to reduce the measurement errors when the system has very large piezoelectric coefficients and high electromechanical coupling coefficients.

## 9.6 References

1. H. Ouchi, K. Nagano and S. Hayakawa, ‘Piezoelectric properties of  $\text{Pb}(\text{Mg}_{1/3}\text{Nb}_{2/3})\text{O}_3\text{-PbTiO}_3$  solid solution ceramics’, *J. Am. Ceram. Soc.*, **48**, pp. 630–635 (1965).
2. S. Nomura, T. Takahashi and Y. Yokomizo, ‘Ferroelectric properties in the system  $\text{Pb}(\text{Zn}_{1/3}\text{Nb}_{2/3})\text{O}_3\text{-PbTiO}_3$ ’, *J. Phys. Soc. Jpn.*, **27**, pp. 262–267 (1969).
3. J. Kuwata, K. Uchino and S. Nomura, ‘Dielectric and piezoelectric properties of  $0.91\text{Pb}(\text{Zn}_{1/3}\text{Nb}_{2/3})\text{O}_3\text{-}0.09\text{PbTiO}_3$  single crystals’, *Jpn. J. Appl. Phys.*, **21**, pp. 1298–1320 (1982).
4. S. E. Park and T. R. Shrout, ‘Ultrahigh strain and piezoelectric behavior in relaxor based ferroelectric single crystals’, *J. Appl. Phys.*, **82**, pp. 1804–1811 (1997).
5. S. E. Park and T. R. Shrout, ‘Characteristics of relaxor-based piezoelectric single crystals for ultrasonic transducers’, *IEEE Trans. UFFC*, **44**, pp. 1140–1147 (1997).
6. J. Fousek, D. B. Litvin and L. E. Cross, ‘Domain geometry engineering and domain average engineering of ferroics’, *J. Phys. Condens. Matter*, **13**, L33–38 (2001).
7. J. Fuksa and V. Janovec, ‘Macroscopic symmetries and domain configurations of engineered domain structures’, *J. Phys. Condens. Matter*, **14**, pp. 3795–3812 (2002).

8. D. Hatch, H. T. Stokes and W. Cao, 'Allowed mesoscopic point group symmetries in domain average engineering of perovskite ferroelectric crystal', *J. Appl. Phys.*, **94**, pp. 5220–5227 (2003).
9. Z. G. Ye and M. Dong, 'Morphotropic domain structures and phase transitions in relaxor-based piezo-/ferroelectric  $(1-x)\text{Pb}(\text{Mg}_{1/3}\text{Nb}_{2/3})\text{O}_3-x\text{PbTiO}_3$  single crystals', *J. Appl. Phys.*, **87**, pp. 2312–2319 (2000).
10. J. Yin and W. Cao, 'Effective macroscopic symmetries and materials properties of multi-domain PZN–PT single crystals', *J. Appl. Phys.*, **92**, pp. 444–448, (2002).
11. J. Han and W. Cao, 'Interweaving domain configurations in [001] poled rhombohedral phase  $0.68\text{Pb}(\text{Mg}_{1/3}\text{Nb}_{2/3})\text{O}_3-0.32\text{PbTiO}_3$  single crystals' *Appl. Phys. Lett.*, **83**, pp. 2040–2042 (2003).
12. A. F. Devonshire, 'Theory of barium titanate', *Phil. Mag.*, **40**, pp. 1040–1050 (1949).
13. J. Erhart and W. Cao, 'Effective symmetry and physical properties of twinned perovskite ferroelectric crystals', *J. Mater. Res.*, **16**, pp. 570–577 (2001).
14. J. Erhart and W. Cao, 'Permissible symmetries of multi-domain configurations in perovskite ferroelectric crystals', *J. Appl. Phys.*, **94**, pp. 3436–3445 (2003).
15. D. A. Berlincourt, D. R. Curran and H. Jaffe, 'Piezoelectric and piezomagnetic materials and their function in transducers', in *Physical Acoustics*, ed. W. P. Mason, vol **1**, Part A, Academic Press, New York, pp. 169–267 (1964).
16. IEEE Standard on Piezoelectricity, ANSI/IEEE STD 1987 (1987).
17. S. Zhu, B. Jiang and W. Cao, 'Characterization of piezoelectric materials using ultrasonic and resonant techniques', *Proceedings of SPIE*, **3341**, pp. 154–162 (1998).
18. W. Jiang, R. Zhang, B. Jiang and W. Cao, 'Characterization of piezoelectric materials with high piezoelectric and electromechanical coupling coefficients', *Ultrasonics*, **41**, pp. 55–63 (2003).
19. J. Yin, B. Jiang and W. Cao, 'Elastic, piezoelectric and dielectric properties of  $0.955\text{Pb}(\text{Zn}_{1/3}\text{Nb}_{2/3})\text{O}_3-0.045\text{PbTiO}_3$  single crystal with designed multi-domains', *IEEE Trans. UFFC*, **47**, pp. 285–291 (2000).
20. R. Zhang, B. Jiang, W. Cao and A. Amin, 'Complete set of material constants of  $0.93\text{Pb}(\text{Zn}_{1/3}\text{Nb}_{2/3})\text{O}_3-0.07\text{PbTiO}_3$  domain engineered single crystal', *J. Mater. Sci. Lett.*, **21**, pp. 1877–1879 (2002).
21. R. Zhang, B. Jiang, W. Jiang and W. Cao, 'Complete set of properties of  $0.92\text{Pb}(\text{Zn}_{1/3}\text{Nb}_{2/3})\text{O}_3-0.08\text{PbTiO}_3$  single crystal with engineered domains', *Mater. Lett.*, **57**, pp. 1305–1308 (2003).
22. R. Zhang, B. Jiang and W. Cao, 'Elastic, dielectric and piezoelectric coefficients of domain engineered  $0.70\text{Pb}(\text{Mg}_{1/3}\text{Nb}_{2/3})\text{O}_3-0.30\text{PbTiO}_3$  single crystal', *AIP Conference Proceedings*, **626**, pp. 188–197 (2002).
23. R. Zhang, B. Jiang and W. Cao, 'Elastic, piezoelectric and dielectric properties of multi-domain  $0.67\text{Pb}(\text{Mg}_{1/3}\text{Nb}_{2/3})\text{O}_3-0.33\text{PbTiO}_3$  single crystal', *J. Appl. Phys.*, **90**, pp. 3471–3475 (2001).
24. H. Cao, V. Hugo Schmidt, R. Zhang, W. Cao and H. S. Luo, 'Elastic, piezoelectric and dielectric properties of  $0.58\text{Pb}(\text{Mg}_{1/3}\text{Nb}_{2/3})\text{O}_3-0.42\text{PbTiO}_3$  single crystal', *J. Appl. Phys.*, **96**, pp. 549–554 (2004).
25. R. Zhang, B. Jiang, W. Jiang and W. Cao, 'Complete set of elastic, dielectric and piezoelectric coefficients of  $0.93\text{Pb}(\text{Zn}_{1/3}\text{Nb}_{2/3})\text{O}_3-0.07\text{PbTiO}_3$  single crystal poled along [011]', *Appl. Phys. Lett.*, **89**, pp. 242908-1–242908-3 (2006).
26. J. F. Nye, *Physical Properties of Crystals*, Oxford University Press, London (1957).

27. R. Zhang, B. Jiang and W. Cao, 'Single-domain properties of  $0.67\text{Pb}(\text{Mg}_{1/3}\text{Nb}_{2/3})\text{O}_3-0.33\text{PbTiO}_3$  single crystals under electric field bias', *Appl. Phys. Lett.*, **82**, pp. 787–789 (2003).
28. R. Zhang and W. Cao, 'Transformed material coefficients for single domain  $0.67\text{Pb}(\text{Mg}_{1/3}\text{Nb}_{2/3})\text{O}_3-0.33\text{PbTiO}_3$  single crystal under differently defined coordinate systems', *Appl. Phys. Lett.*, **85**, pp. 6380–6382 (2004).
29. E. A McLaughlin and H. C. Robinson, 'Shear mode properties of single crystal ferroelectrics', *J. Acoust. Soc. Am.*, **114**, pp. 2322 (2003).
30. W. G. Cady, in *Piezoelectricity*, Dover Publications, Inc., New York (1964).
31. R. Zhang, B. Jiang and W. Cao, 'Orientation dependence of piezoelectric properties of single domain  $0.67\text{Pb}(\text{Mn}_{1/3}\text{Nb}_{2/3})\text{O}_3-0.33\text{PbTiO}_3$  Crystals', *Appl. Phys. Lett.*, **82**, pp. 3737–3739 (2003).

# Domain wall engineering in piezoelectric crystals with engineered domain configuration

S W A D A, University of Yamanashi, Japan

## 10.1 Introduction

Domain configurations in ferroelectric materials can determine ferroelectric and related properties such as piezoelectricity, pyroelectricity and dielectricity. Thus, one of the most interesting investigations for ferroelectric-related applications is the control of the desirable domain configuration. This technique is called domain engineering. Domain engineering is the most important technique to obtain enhanced ferroelectric-related properties for conventional ferroelectric materials. To date, the following domain engineering techniques have been proposed and established:

- The inhibited domain wall motion by the acceptor doping into  $\text{Pb}(\text{Ti}, \text{Zr})\text{O}_3$  (PZT) ceramics, i.e. ‘hard’ PZT; the hard PZT ceramics are used for the piezoelectric transformer application.<sup>1</sup>
- The enhanced domain wall motion by the donor doping into PZT ceramics, i.e. ‘soft’ PZT; the soft PZT ceramics are used for the actuator application.<sup>1</sup>
- The induction of a periodic domain-inverted structure into lithium tantalate ( $\text{LiTaO}_3$ ) and lithium niobate ( $\text{LiNbO}_3$ ) single crystals; and this device is used for the surface acoustic wave application<sup>2,3</sup> and the non-linear optical application.<sup>4,5</sup>
- Recently, for the T-bit memory application, the writing and reading techniques of nanodomain on a  $\text{LiTaO}_3$  single crystal plate were reported by Cho and coworkers,<sup>6,7</sup> and for the 3D photonic crystal application, the writing and etching techniques of nanodomain of a  $\text{LiNbO}_3$  single crystal plate were reported by Kitamura and coworkers.<sup>8</sup>

These are very important domain engineering techniques, and through their use enhanced ferroelectric-related properties and new properties can be expected.

Among these domain engineering techniques, the one using crystallographic anisotropy of the ferroelectric single crystals is known as engineered domain configuration.<sup>9–11</sup> This engineered domain configuration can induce enhanced

piezoelectric properties in ferroelectric single crystals. However, there are still many unknowns such as the mechanism of the enhanced property. In particular, it is very important to find the most suitable engineered domain configuration for the piezoelectric applications. In this study, various engineered domain configurations were induced in  $\text{BaTiO}_3$  single crystals, and their piezoelectric properties were investigated as a function of (1) the crystal structure, (2) the crystallographic orientation and (3) the domain size (domain wall density). Moreover, for the tetragonal  $\text{BaTiO}_3$  crystals with engineered domain configurations, it has recently been found that the piezoelectric properties significantly improved with decreasing domain size (domain wall density).<sup>12,13</sup> These results suggest that the domain walls in the engineered domain configuration could contribute significantly to the piezoelectric properties. In this chapter, it is suggested that a significant contribution of domain wall region to piezoelectric, elastic and dielectric properties, and engineered domain configurations can be very helpful to fix the domain wall region in piezoelectric crystals, i.e. to prepare a composite between (a) a distorted domain wall region and (b) a normal tetragonal domain region. Thus, an increase in the volume fraction of the distorted domain wall region can result in crystals with ultra-high piezoelectric properties.

## 10.2 History of engineered domain configuration

The engineered domain configuration was initially found in  $\text{Pb}(\text{Zn}_{1/3}\text{Nb}_{2/3})\text{O}_3\text{-PbTiO}_3$  (PZN-PT) single crystals. In  $[001]_c$  oriented rhombohedral PZN-PT single crystals, ultra-high piezoelectric activities were reported by Park and coworkers<sup>9,14,15</sup> and Kuwata *et al.*<sup>16,17</sup> with a strain over 1.7%, a piezoelectric constant  $d_{33}$  over 2500 pC/N, a electromechanical coupling factor  $k_{33}$  over 93% and a hysteresis-free strain vs. electric field behavior. The  $(1-x)\text{PZN-xPT}$  single crystals with  $x < 0.08$  have rhombohedral  $3m$  symmetry at room temperature, and their polar directions are  $[111]_c$ .<sup>16,17</sup> However, the unipolar electric field (E-field) drive along the  $[111]_c$  direction showed a large hysteretic strain vs. E-field behavior, a low  $d_{33}$  of 83 pC/N and a low  $k_{33}$  of 38%. To explain the above strong anisotropy in piezoelectric properties, *in situ* domain observation was carried out using  $[111]_c$  and  $[001]_c$  oriented pure PZN and 0.92PZN-0.08PT single crystals.<sup>10,11</sup> The result showed that when the E-field was applied along the  $[001]_c$  direction, a very stable domain structure appeared, and domain wall motion was undetectable under dc-bias, resulting in the hysteresis-minimized strain vs. electric-field behavior.

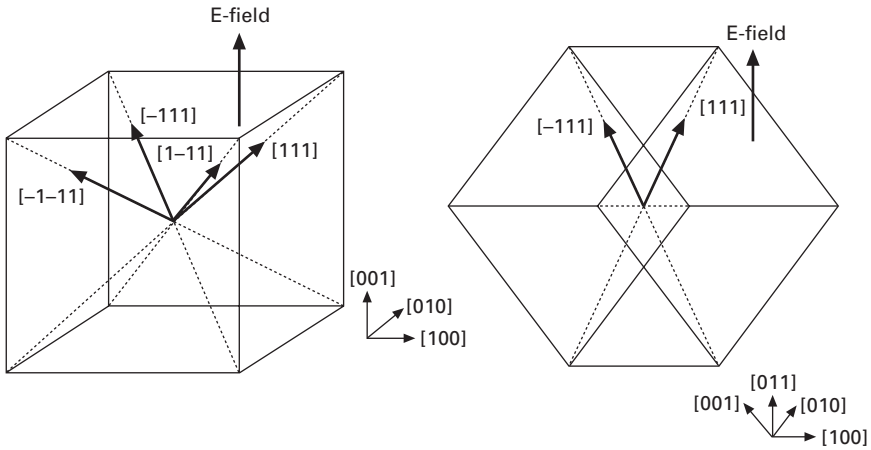
The  $[001]_c$  poled  $3m$  crystals have four equivalent domains with four polar vectors along the  $[111]_c$ ,  $[-111]_c$ ,  $[1-11]_c$  and  $[-1-11]_c$  directions because of their polar directions being along  $\langle 111 \rangle_c$ . Therefore, the components of each polar vector along the  $[001]_c$  direction are completely equal with each other, so that each domain wall cannot move under the E-field drive along

the  $[001]_c$  direction owing to the equivalent domain energy changes.<sup>9-11,14,15</sup> This suggests the possibility of controlling the domain configuration in single crystals using the crystallographic orientation, and the appearance of a new technology in the domain engineering field. Thus, this special domain structure in ferroelectric single crystals using the crystallographic orientation was called the engineered domain configuration.<sup>9-11</sup>

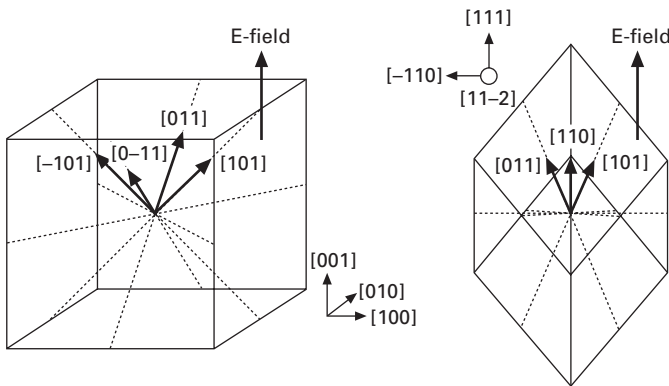
### 10.3 Effect of engineered domain configuration on piezoelectric property

The engineered domain configuration is expected to possess the following five features in terms of piezoelectric performance: (1) hysteresis-free strain vs. E-field behavior owing to the inhibition of domain wall motion, (2) higher piezoelectric constant along a non-polar direction owing to the easy tilt of a polar vector by the E-field, (3) change of macroscopic symmetry in crystals with engineered domain configuration,<sup>10,11</sup> (4) complex contribution of other high shear piezoelectric constants such as  $d_{15}$ , and (5) contribution of non-180° domain wall region to piezoelectric properties. Features (1) to (4) can be useful for both single-domain and multi-domain crystals while feature (5) is expected only for multi-domain crystals. The engineered domain configuration is defined as the domain structure composed of some equivalent polar vectors along the E-field drive direction. Therefore, the engineered domain configuration is basically multi-domain, and many kinds of engineered domain configurations are possible depending on (a) the crystal structure and (b) the crystallographic orientation.<sup>18</sup>

For the rhombohedral  $3m$  ferroelectric crystal with the polar directions of  $\langle 111 \rangle_c$ , when the E-field is applied along the  $[001]_c$  and  $[110]_c$  directions, the two types of the engineered domain configurations formed are shown in Fig. 10.1. For the orthorhombic  $mm2$  ferroelectric crystal with the polar directions of  $\langle 110 \rangle_c$ , when the E-field is applied along the  $[001]_c$  and  $[111]_c$  directions, two kinds of the engineered domain configurations are formed, as shown in Fig. 10.2. Moreover, for the tetragonal  $4mm$  ferroelectric crystal with the polar directions of  $\langle 001 \rangle_c$ , when the E-field is applied along  $[111]_c$  and  $[110]_c$  directions, two kinds of the engineered domain configurations are formed, as shown in Fig. 10.3. In general, most of the practical ferroelectric materials belong to the rhombohedral  $3m$ , orthorhombic  $mm2$  or tetragonal  $4mm$  symmetry. Therefore, in this section, only these three crystal structures will be considered as the conventional engineered domain configurations. On the other hand, in each of the three crystal structures, three different crystallographic directions of  $[001]_c$ ,  $[110]_c$  and  $[111]_c$  can be considered in order to induce the above engineered domain configurations. However, it is expected that the  $[110]_c$  poled  $3m$  and  $4mm$  ferroelectric crystals may exhibit a much smaller influence on the ferroelectric-related properties than the



10.1 Schematic model of the engineered domain configurations for the [001]- and [011]-poled rhombohedral  $3m$  ferroelectric crystals.



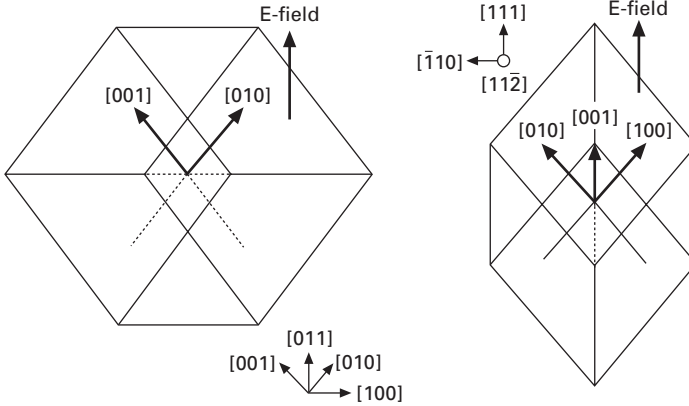
10.2 Schematic model of the engineered domain configurations for the [001]- and [111]-poled orthorhombic  $mm2$  ferroelectric crystals.

$[001]_c$  poled  $3m$  and  $mm2$  ferroelectric crystals and the  $[111]_c$  poled  $mm2$  and  $4mm$  ferroelectric crystals. This is because the engineered domain configuration in the  $[110]_c$  poled  $3m$  and  $4mm$  ferroelectric crystals is composed of just two kinds of polar vectors. Thus, in this section, only the two kinds of the crystallographic directions of  $[001]_c$  and  $[111]_c$  will be considered.

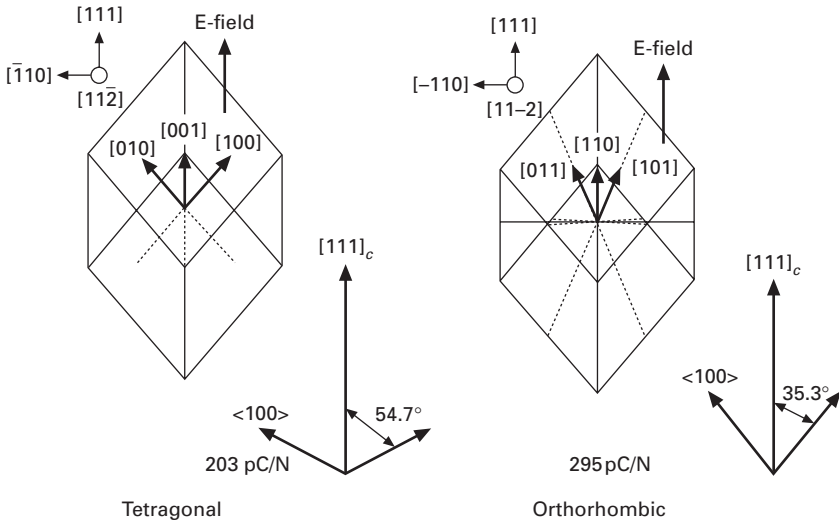
### 10.4 Crystal structure and crystallographic orientation dependence of $BaTiO_3$ crystals with various engineered domain configurations

If the concept of engineered domain configuration for PZN–PT single crystals could be applied to other ferroelectric crystals, enhanced piezoelectric properties





10.3 Schematic model of the engineered domain configurations for the [011]- and [111]-poled tetragonal  $4mm$  ferroelectric crystals.

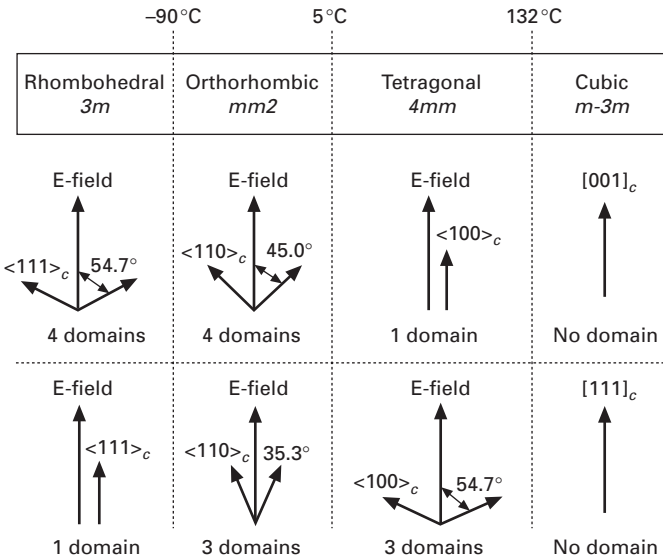


10.4 Two engineered domain configurations for the  $[111]_c$  poled (a) tetragonal and (b) orthorhombic  $\text{BaTiO}_3$  single crystals.

would be expected for lead-free ferroelectrics.  $\text{BaTiO}_3$  single crystal is one of the typical lead-free ferroelectrics and has the tetragonal  $4mm$  symmetry at room temperature.<sup>19</sup> The piezoelectric properties were investigated using the  $[111]_c$  oriented tetragonal  $\text{BaTiO}_3$  single crystals, as shown in Fig. 10.4.<sup>20–22</sup> It should be noted that the piezoelectric constant  $d_{33}$  was directly measured from the strain vs. E-field curves. Two kinds of engineered domain configurations were formed, i.e. (a) the  $[111]_c$  poled tetragonal engineered domain configuration and (b) the  $[111]_c$  poled orthorhombic

engineered domain configuration (Fig. 10.4). This is because for the tetragonal BaTiO<sub>3</sub> crystals, the higher E-field drive over 10 kV/cm along the [111]<sub>c</sub> direction led to the E-field induced phase transition from the tetragonal 4mm to orthorhombic mm2 phase. The original d<sub>33</sub> below 10 kV/cm was 203 pC/N while the d<sub>33</sub> in the induced phase above 10 kV/cm reached 295 pC/N. It is known that the d<sub>33</sub> value of the [001]<sub>c</sub> poled tetragonal BaTiO<sub>3</sub> single crystals was 90 pC/N.<sup>19</sup> Therefore, the d<sub>33</sub> of the [111]<sub>c</sub> poled tetragonal BaTiO<sub>3</sub> was almost twice, and the d<sub>33</sub> of the [111]<sub>c</sub> poled orthorhombic BaTiO<sub>3</sub> was almost three times, as large as that of the [001]<sub>c</sub> poled tetragonal BaTiO<sub>3</sub>.<sup>20,22</sup>

We must consider the difference between the d<sub>33</sub> values of 203 and 295 pC/N. As shown in Fig. 10.4, both the [111]<sub>c</sub> poled tetragonal and orthorhombic engineered domains were composed of three kinds of domains, but the angle θ between the polar direction and the E-field direction were quite different, i.e. θ = 54.7° for the d<sub>33</sub> of 203 pC/N, while θ = 35.3° for the d<sub>33</sub> of 295 pC/N. It is very important to clarify whether this angle θ is effective for the piezoelectric performance or not. Thus, the piezoelectric properties of BaTiO<sub>3</sub> single crystals were investigated as a function of the crystallographic orientations of [001]<sub>c</sub> and [111]<sub>c</sub>, and the crystal structures of tetragonal, orthorhombic and rhombohedral phases, as shown in Fig. 10.5.<sup>20,22</sup> The temperature was changed from -100 to 200 °C. It should be noted that the piezoelectric properties were measured by two kinds of methods, i.e. (a) measurement under a high E-field over 100 V/cm (estimation of piezoelectric



10.5 Expected domain configurations for the [111]<sub>c</sub> and [001]<sub>c</sub> poled BaTiO<sub>3</sub> single crystals with three kinds of the crystal structures.

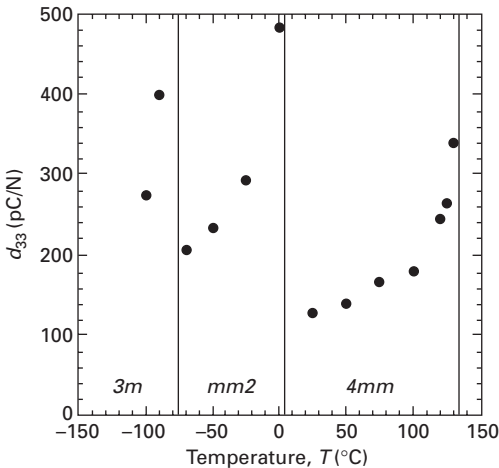
constants from the strain vs. E-field curves) and (b) resonance–antiresonance measurement under a low ac E-field below 10 V/cm (estimation of piezoelectric properties from the impedance vs. frequency curves).

### 10.4.1 Piezoelectric properties measured under high E-field

#### *[001]<sub>c</sub> oriented BaTiO<sub>3</sub> single crystals*

Under high E-fields, the strain vs. E-field curves of the  $[001]_c$  oriented BaTiO<sub>3</sub> single crystals were measured from  $-100$  to  $200$  °C.<sup>18,21</sup> On the basis of the slope of the strain behaviors over 20 kV/cm, the piezoelectric constant  $d_{33}$  was calculated directly, as shown in Fig. 10.6. It should be noted from Fig. 10.6 that for the  $[001]_c$  oriented orthorhombic BaTiO<sub>3</sub> single crystals, the maximum  $d_{33}$  of 500 pC/N was obtained at 0 °C. This is a very large value that is almost comparable to that of PZT ceramics. The  $d_{33}$  of the  $[001]_c$  poled orthorhombic BaTiO<sub>3</sub> single crystals was much higher than that of the  $[001]_c$  poled rhombohedral BaTiO<sub>3</sub> single crystals. When the E-field was applied along the  $[001]_c$  direction, two kinds of engineered domain configurations could be formed, i.e. (a) the  $[001]_c$  poled orthorhombic BaTiO<sub>3</sub> crystal with four equivalent domains and a  $\theta$  of 45.0° and (b) the  $[001]_c$  poled rhombohedral BaTiO<sub>3</sub> crystal with four equivalent domains and a  $\theta$  of 54.7°.

It was expected that if the number of the equivalent domains constructing the engineered domain configuration is the same, the smaller angle  $\theta$  can

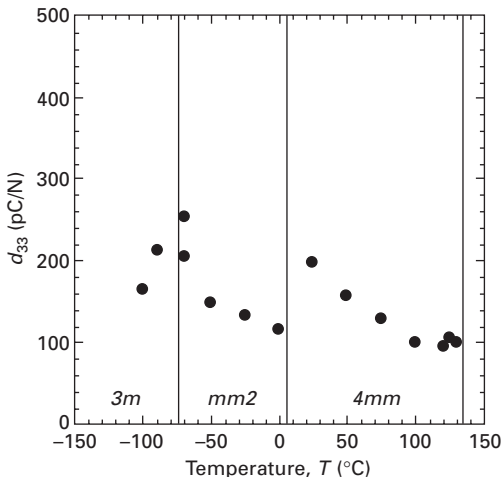


10.6 Relationship between the  $d_{33}$  and temperature for the  $[001]_c$  oriented BaTiO<sub>3</sub> single crystals from  $-100$  to  $150$  °C.

cause larger piezoelectric properties. The result in Fig. 10.6 supported the above hypothesis. Therefore, when the E-field was applied along the  $[001]_c$  direction of  $\text{BaTiO}_3$  single crystals, the orthorhombic phase was very important for the higher piezoelectric performance.

### $[111]_c$ oriented $\text{BaTiO}_3$ single crystals

The strain vs. E-field curves of the  $[111]_c$  oriented  $\text{BaTiO}_3$  single crystals were also measured from  $-100$  to  $200$  °C.<sup>18,21</sup> On the basis of the slope of the strain behaviors below  $10$  kV/cm, the piezoelectric constant  $d_{33}$  was calculated and shown in Fig. 10.7. The strain vs. E-field curves at  $25$  °C underwent discontinuous changes owing to two kinds of the E-field induced phase transitions, i.e. (1) the first transition from tetragonal to orthorhombic phase around  $4\text{--}6$  kV/cm and (2) the second transition from orthorhombic to rhombohedral phase around  $30$  kV/cm.<sup>20–22</sup> In Fig. 10.7, it should be noted that for the  $[111]_c$  oriented orthorhombic  $\text{BaTiO}_3$  single crystals, the maximum  $d_{33}$  of  $260$  pC/N was obtained at  $-70$  °C. As mentioned above, the  $d_{33}$  of the  $[111]_c$  poled orthorhombic  $\text{BaTiO}_3$  crystal over  $10$  kV/cm was  $295$  pC/N at  $25$  °C (Fig. 10.4). We believe that this discrepancy in  $d_{33}$  ( $35$  pC/N) may be caused by the temperature difference. Moreover, in Fig. 10.7, the  $d_{33}$  ( $-74$  °C) of the  $[111]_c$  poled orthorhombic  $\text{BaTiO}_3$  single crystals was higher than that ( $20$  °C) of the  $[111]_c$  poled tetragonal  $\text{BaTiO}_3$  single crystals. In Fig. 10.5, when the E-field was applied along the  $[111]_c$  direction, two kinds of the engineered domain configurations could be obtained, i.e. (a) the  $[111]_c$  poled orthorhombic  $\text{BaTiO}_3$  crystal with the three equivalent domains and  $\theta$



10.7 Relationship between the  $d_{33}$  and temperature for the  $[111]_c$  oriented  $\text{BaTiO}_3$  single crystals from  $-100$  to  $150$  °C.

of  $35.3^\circ$  and (b) the  $[111]_c$  poled tetragonal  $\text{BaTiO}_3$  crystal with the three equivalent domains and  $\theta$  of  $54.7^\circ$ . Therefore, it was confirmed that when the number of the equivalent domains constructing the engineered configuration is the same, a smaller angle  $\theta$  can cause larger piezoelectric properties. Therefore, when the E-field was applied along  $[111]_c$  direction of  $\text{BaTiO}_3$  single crystals, the orthorhombic phase was also very important for the higher piezoelectric performance.

*Crystal structure and crystallographic orientation for the best engineered domain configuration in  $\text{BaTiO}_3$  single crystals*

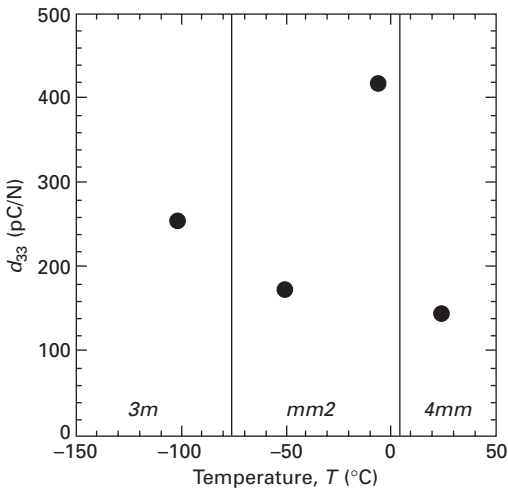
The above discussions suggested that of the factors that can be responsible for the piezoelectric performance, the following two are the most important: (1) the number of the equivalent domains constructing the engineered domain configuration and (2) the angle  $\theta$  between the polar direction and the E-field direction.<sup>18</sup> Based on Fig. 10.5, we use the piezoelectric constants in Figs 10.6 and 10.7 to check these factors. As mentioned above, when the number of the equivalent domains constructing the engineered domain configuration was the same, the smaller angle  $\theta$  caused larger piezoelectric properties. Next, the role of the number of the equivalent domains constructing the engineered domain configuration can be clarified by comparing the  $[001]_c$  poled rhombohedral  $\text{BaTiO}_3$  crystal that had four equivalent domains and  $\theta$  of  $54.7^\circ$  with the  $[111]_c$  poled tetragonal crystal that had three equivalent domains and the same  $\theta$  of  $54.7^\circ$ . The  $d_{33}$  of the  $[001]_c$  poled rhombohedral  $\text{BaTiO}_3$  crystal was about 400 pC/N, which is twice as high as that of the  $[111]_c$  poled tetragonal  $\text{BaTiO}_3$  crystal (about 200 pC/N). This suggests that the effect of the number of the equivalent domains on the piezoelectric properties is significantly larger than that of  $\theta$ .<sup>18</sup> This observation is confirmed by comparing the  $[001]_c$  poled orthorhombic  $\text{BaTiO}_3$  crystal that had four equivalent domains and a  $\theta$  of  $45.0^\circ$  with the  $[111]_c$  poled orthorhombic  $\text{BaTiO}_3$  crystal had three equivalent domains and a  $\theta$  of  $35.3^\circ$ : the  $d_{33}$  of the former was twice as high as that of the latter.<sup>18</sup>

The above discussion indicates a new direction to obtain the best engineered domain configuration for the piezoelectric application. The first step is to identify the engineered domain configuration with the largest number of equivalent domains. For the normal perovskite-type ferroelectric single crystals, only the  $[001]_c$  poled orthorhombic and rhombohedral crystals can satisfy this requirement. The second step is to find the engineered domain configurations with the smallest angle  $\theta$ . For the normal perovskite-type ferroelectric single crystals, only the  $[001]_c$  poled orthorhombic crystals can satisfy the second request. Therefore, the best engineered domain configuration for the piezoelectric application can be found in the  $[001]_c$  poled orthorhombic single crystals. From this reasoning, potassium niobate ( $\text{KNbO}_3$ ) crystals

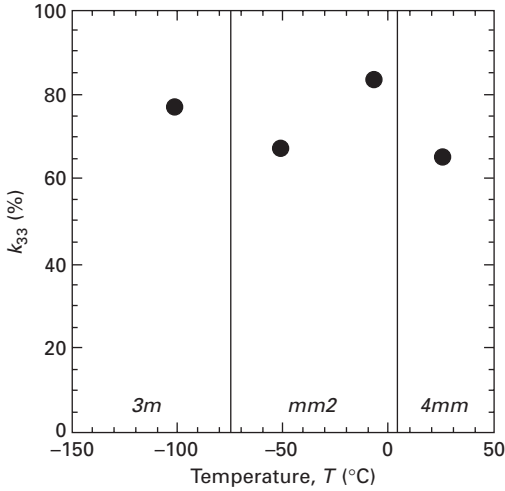
appear to be one of the promising candidates with ferroelectric orthorhombic symmetry.<sup>23</sup>

### 10.4.2 Piezoelectric properties measured under low ac E-field

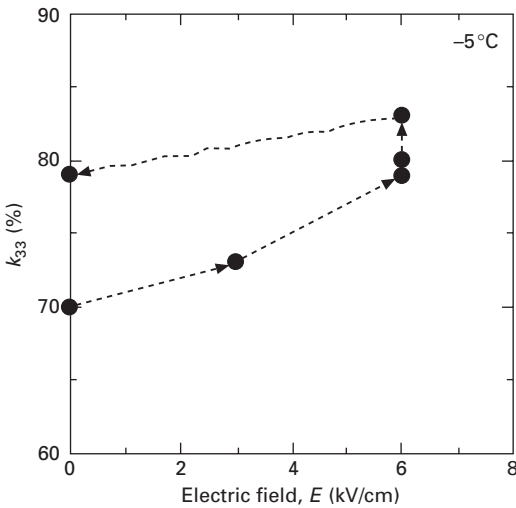
It was shown in the previous section that the high piezoelectric properties can be realized in the  $[001]_c$  poled orthorhombic and rhombohedral  $\text{BaTiO}_3$  crystals. Using the IEEE resonance technique, other piezoelectric properties such as the electromechanical coupling factor and dielectric constant were measured for the  $[001]_c$  oriented  $\text{BaTiO}_3$  crystals.<sup>18,21</sup> Figures 10.8 and 10.9 show the  $d_{33}$  and  $k_{33}$  vs. temperature curves of the  $[001]_c$  oriented  $\text{BaTiO}_3$  crystals, respectively, which were measured using a low ac E-field of 1 V/cm and a high dc E-field of 6 kV/cm. As expected, the  $[001]_c$  poled orthorhombic  $\text{BaTiO}_3$  crystals exhibited the maximum  $d_{33}$  of 415 pC/N and  $k_{33}$  of 85% at  $-5^\circ\text{C}$ . These values were much higher than those of PZT ceramics. Figure 10.10 shows the dc E-field dependence of  $k_{33}$  at  $-5^\circ\text{C}$  using a low ac E-field of 1 V/cm. Before poling treatment (start point),  $k_{33}$  was just 70%, and during the poling treatment at 6 kV/cm,  $k_{33}$  increased to 85%. After poling treatment (final point),  $k_{33}$  still kept a high value of 79%. This result suggested that poling treatment is very important for high piezoelectric properties. On the other hand, Figs 10.11 and 10.12 show the  $d_{31}$  and  $k_{31}$  vs. temperature curves of the  $[001]_c$  oriented  $\text{BaTiO}_3$  crystals. As expected, the  $[001]_c$  poled orthorhombic  $\text{BaTiO}_3$  crystals exhibited the maximum  $d_{31}$  of  $-280$  pC/N and  $k_{31}$  of 65% at  $0^\circ\text{C}$ .



10.8 Relationship between the  $d_{33}$  and temperature for the  $[001]_c$  oriented  $\text{BaTiO}_3$  single crystals from  $-100$  to  $25^\circ\text{C}$ .

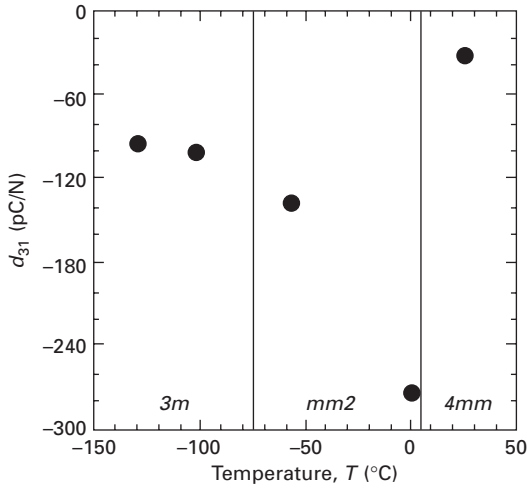


10.9 Relationship between  $k_{33}$  and temperature for the  $[001]_c$  oriented  $\text{BaTiO}_3$  single crystals from  $-100$  to  $25^\circ\text{C}$ .

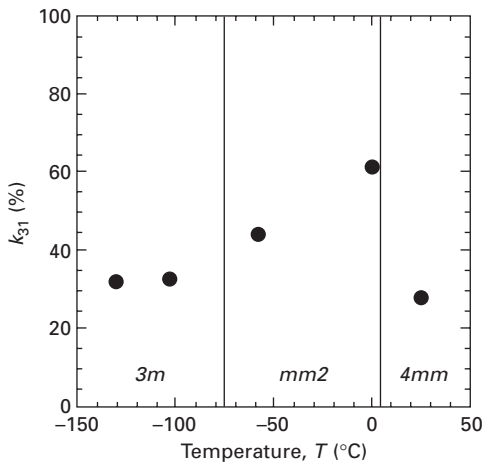


10.10 Relationship between the  $k_{33}$  and E-field for the  $[001]_c$  oriented  $\text{BaTiO}_3$  single crystals measured at  $-5^\circ\text{C}$ . Arrows indicate poling procedure.

The above results indicated that for the  $\text{BaTiO}_3$  single crystals, the combination of the orthorhombic  $mm2$  phase and the  $[001]_c$  crystallographic direction exhibited the best piezoelectric properties. It is well known that the  $[001]_c$  poled tetragonal  $\text{BaTiO}_3$  crystals show a  $d_{33}$  of 90 pC/N and a  $k_{33}$  of 56%.<sup>19</sup> Therefore, the introduction of the best engineered domain configuration



10.11 Relationship between the  $d_{31}$  and temperature for the  $[001]_c$  oriented  $\text{BaTiO}_3$  single crystals from  $-100$  to  $25^{\circ}\text{C}$ .



10.12 Relationship between the  $k_{31}$  and temperature for the  $[001]_c$  oriented  $\text{BaTiO}_3$  single crystals from  $-100$  to  $25^{\circ}\text{C}$ .

into the  $\text{BaTiO}_3$  crystals resulted in a five-fold increase in  $d_{33}$  and a 1.5-fold increase in  $k_{33}$ . Moreover, if the  $[001]_c$  poled orthorhombic single crystals could be obtained at room temperature, we would expect much higher piezoelectric properties. Thus, as mentioned previously,  $\text{KNbO}_3$  may exhibit a higher potential for piezoelectric applications because of its orthorhombic  $mm2$  phase at room temperature.<sup>23</sup>



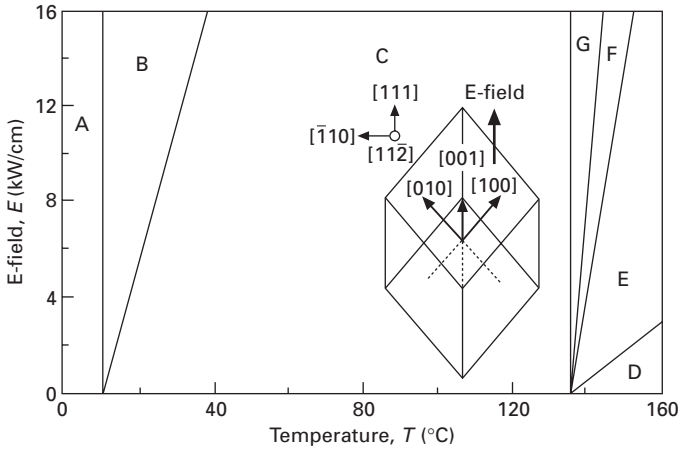
## 10.5 Domain size dependence of BaTiO<sub>3</sub> crystals with engineered domain configurations

BaTiO<sub>3</sub> single crystals have a tetragonal  $P4mm$  phase at room temperature. To induce an engineered domain configuration in the tetragonal crystals, the E-field should be applied along the  $[111]_c$  direction. The piezoelectric measurements showed that the  $d_{33}$  of the  $[111]_c$  poled tetragonal BaTiO<sub>3</sub> crystal with the engineered domain configuration was almost 203 pC/N,<sup>20</sup> and this value was more than twice as large as the 90 pC/N of the  $[001]_c$  poled BaTiO<sub>3</sub> single-domain crystal.<sup>19</sup> On the other hand, the  $d_{33}$  of the  $[001]_c$  poled rhombohedral PZN–PT crystal with the engineered domain configuration was almost 30 times as large as the 83 pC/N of the  $[111]_c$  poled PZN–PT single-domain crystal.<sup>15</sup> To explain the origin of this huge difference, we consider the domain size, i.e. the domain wall density, for the engineered domain configuration. This is because the domain structure of the  $[001]_c$  poled PZN–PT crystal was composed of the fiber-like domains with a domain length of 130  $\mu\text{m}$  and a domain width of around 1  $\mu\text{m}$ <sup>10,11</sup> while that of the  $[111]_c$  poled BaTiO<sub>3</sub> crystal was made of a very coarse domain with a wide domain width of 300–400  $\mu\text{m}$ .<sup>20</sup> This result suggested that a non-180° domain wall region could contribute to piezoelectric properties significantly owing to its strained region with gradient changing lattice structures. Thus, when the fine domain structure is induced in the  $[111]_c$  poled tetragonal BaTiO<sub>3</sub> crystals with the engineered domain configuration, it is possible to obtain a much enhanced piezoelectric property. Therefore, the piezoelectric properties of BaTiO<sub>3</sub> single crystals were investigated as a function of domain size, i.e. domain wall density. In particular, in the  $[111]_c$  oriented tetragonal BaTiO<sub>3</sub> crystals with an engineered domain configuration, the domain size dependence on E-field and the temperature were investigated in detail.

### 10.5.1 Domain size dependence on E-field and temperature

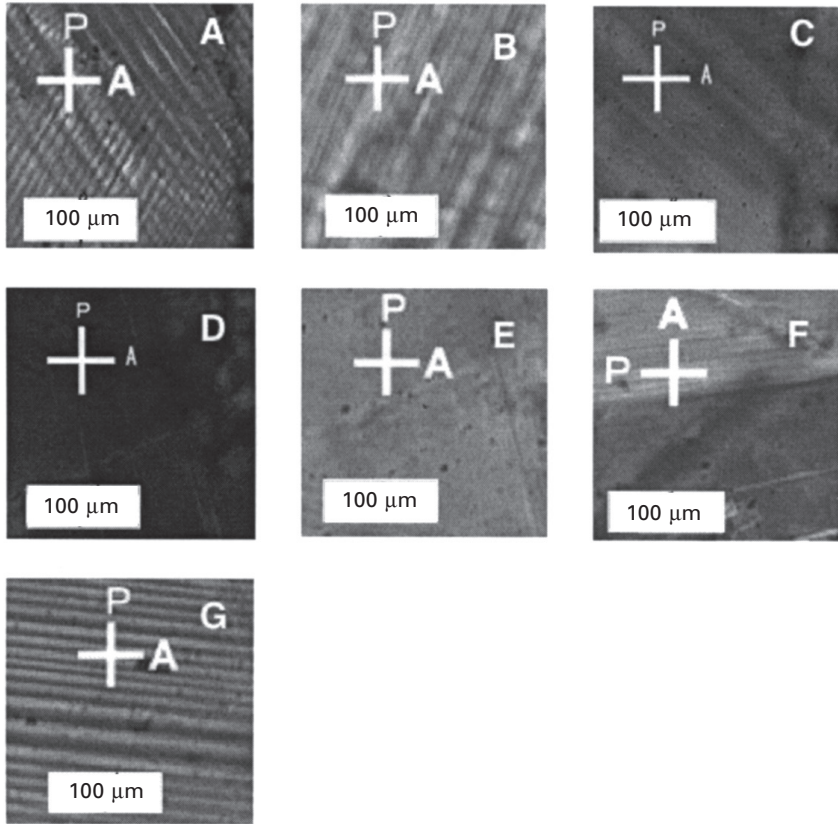
To understand domain size dependence on E-field and temperature for the  $[111]_c$  oriented BaTiO<sub>3</sub> crystals, the domain structures were observed at various temperatures from 0 to 200 °C and various E-fields from 0 to 16 kV/cm. Prior to any domain observation, the BaTiO<sub>3</sub> crystals were heated to 160 °C, and then cooled to the observation temperatures at a cooling rate of 0.4 °C/min without E-field. At the constant temperature, the dc E-fields were applied along the  $[111]_c$  direction very slowly.

Figure 10.13 shows the domain size dependence on the E-field and temperature for the  $[111]_c$  oriented BaTiO<sub>3</sub> crystals with the engineered domain configuration. Figure 10.14 shows the typical domain structures observed in the corresponding regions A to G presented in Fig. 10.13 (P and



10.13 Schematic domain configuration map as a function of temperature and E-field along the  $[111]_c$  direction for the  $[111]_c$  oriented  $\text{BaTiO}_3$  single crystals with the engineered domain configuration. Areas A through G stand for a region with different domain configurations related to Fig. 10.14, respectively.

A indicate the crossed polarizer and analyzer). In Fig. 10.13, the 'A' and 'B' regions were assigned to the orthorhombic  $mm2$  phase. At 25 °C, the dc E-field drive along the  $[111]_c$  direction for the tetragonal  $\text{BaTiO}_3$  crystals resulted in the E-field induced phase transition from  $4mm$  to  $mm2$ , and this result was consistent with previous reports.<sup>18,20–22</sup> Figure 10.14(A) and (B) shows that these domain structures were composed of the fine domains. The fine domains in the 'A' region were induced by a normal phase transition from the tetragonal phase to the orthorhombic phase without E-field. On the other hand, the fine domains in the 'B' region resulted from the E-field induced phase transition from the tetragonal to orthorhombic phase. Thus, when the E-field was removed, the domain structure in the 'B' region easily returned to the normal tetragonal domain configuration as shown in Fig. 10.14(C). Thus, the fine domain structure in the 'A' and 'B' regions cannot exist at room temperature without the E-field. The 'C' region was assigned to the tetragonal  $4mm$  symmetry. The poling treatment in this region changed the domain structure slightly, but the observed domain walls were all completely assigned to  $90^\circ$  domain walls of the  $\{110\}_c$  planes as shown in Fig. 10.14(c).<sup>24</sup> The 'D' region was assigned to the optical isotropic state with the cubic  $m-3m$  symmetry as shown in Fig. 10.14(D). However, the 'E' region was very unclear and abnormal. The same brightness in the 'E' region under crossed-polarizers suggested that this domain state was not optical isotropic, but an anisotropic state.<sup>25</sup> When the E-field was applied along the  $[111]_c$  direction for the cubic  $m-3m$  symmetry, it is expected that the cubic  $m-3m$  symmetry could be



10.14 Various domain configurations in (A) the 'A' region, (B) the 'B' region, (C) the 'C' region, (D) the 'D' region, (E) the 'E' region, (F) the 'F' region and (G) the 'G' region as shown in Fig. 10.13. P and A on each graph indicate the crossed polarizer and analyzer.

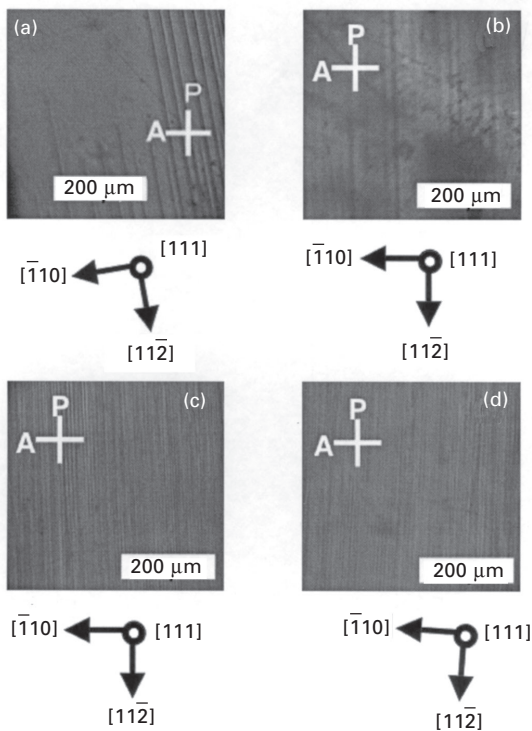
slightly distorted to become rhombohedral or monoclinic. However, at present, the origin of this birefringence is unknown. In the 'F' region, the coexistence of the bright state without the domain walls and the fine domain state was observed. In the 'G' region, only the fine domain structure was clearly observed, all the domain walls of which were assigned to  $90^\circ$  of the  $\{110\}_c$  planes.

In the 'A', 'B', 'C' and 'D' regions, these symmetries were assigned on the basis of some reports.<sup>18,20-22</sup> However, there is no information about the 'E', 'F' and 'G' regions. Thus, these symmetries were measured using the *in situ* Raman scattering measurement, which was combined with the polarizing microscopic observation. As a result, the change from 'D' to 'G' by E-field was assigned to an E-field induced phase transition from the cubic to tetragonal phase.<sup>26</sup>

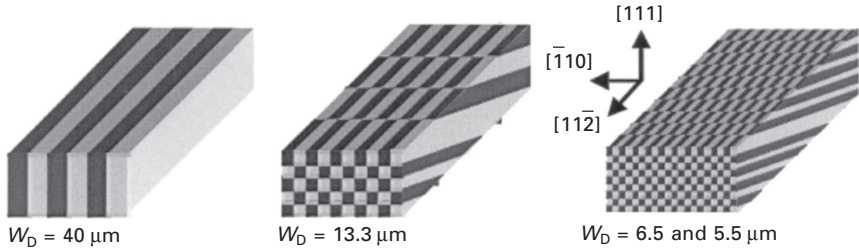
### 10.5.2 Domain size dependence of the piezoelectric property using 31 resonators

On the basis of the result of the domain size dependence on the E-field and temperature, various kinds of domain size were induced in the  $[111]_c$  oriented  $\text{BaTiO}_3$  single crystals with the engineered domain configuration. The engineered domain  $\text{BaTiO}_3$  crystal with a large domain size was poled at just below the Curie temperature ( $T_C$ ) while that with the finer domain size was poled at just above  $T_C$ . Figure 10.15 shows the  $\text{BaTiO}_3$  single crystals with four kinds of domain sizes, i.e. (a) over  $40\ \mu\text{m}$ , (b) of  $13.3\ \mu\text{m}$ , (c) of  $6.5\ \mu\text{m}$  and (d) of  $5.5\ \mu\text{m}$ . All of the domains observed in Fig. 10.15 were assigned to  $90^\circ$  domain walls of  $\{110\}_c$  planes. The domain configurations for all the resonators prepared in this study were composed of the same  $90^\circ$  domain walls,<sup>24</sup> and the difference between these domain configurations was just domain size, i.e. domain wall density, as shown in Fig. 10.16.

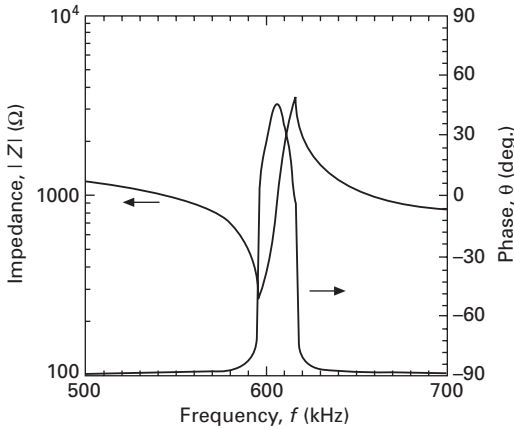
Using these 31 resonators with the different domain sizes, the piezoelectric properties were measured at  $25^\circ\text{C}$  by a conventional resonance–antiresonance



10.15 Engineered domain configurations of the  $[111]_c$  oriented  $\text{BaTiO}_3$  single crystals with the different average domain sizes of (a) greater than  $40\ \mu\text{m}$ , (b)  $13.3\ \mu\text{m}$ , (c)  $6.5\ \mu\text{m}$  and (d)  $5.5\ \mu\text{m}$ .

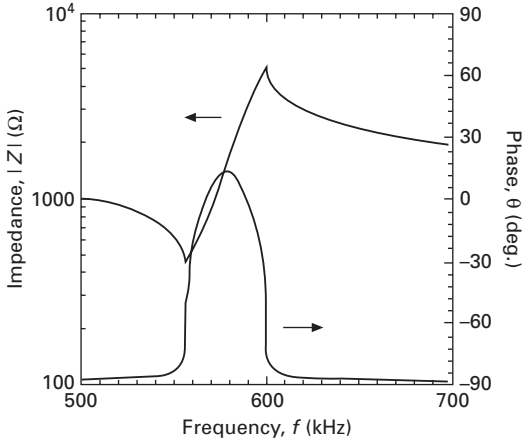


10.16 Schematic 31 resonators composed of the engineered domain configuration with different domain sizes.



10.17 Frequency dependence of the impedance and phase for the  $[111]_c$  oriented  $\text{BaTiO}_3$  single crystals with an average domain size of greater than  $40 \mu\text{m}$ , measured at  $25^\circ\text{C}$ .

method<sup>27</sup> using a weak ac E-field of  $125 \text{ mV/mm}$ . Figures 10.17 and 10.18 show the frequency dependence of the impedance and the phase for the 31 resonators with a domain size over  $40 \mu\text{m}$  and that with a domain size of  $6.5 \mu\text{m}$ , respectively. If the poling treatment is completely successful, the phase between resonance and antiresonance frequencies should be close to  $+90^\circ$ . However, in these figures, the maximum phase angle was only  $+50^\circ$  and  $+15^\circ$ , respectively. These low phase angles suggested an insufficient poling treatment. Using these resonance and antiresonance frequencies, the piezoelectric-related constants were estimated. Table 10.1 shows the domain size dependence of the properties using these 31 resonators. The  $d_{31}$  of the  $[001]_c$  oriented  $\text{BaTiO}_3$  single-domain crystal was reported as  $-33.4 \text{ pC/N}$  while the effective  $d_{31}$  of the  $[111]_c$  oriented  $\text{BaTiO}_3$  single-domain crystal calculated using the  $d_{33}$  of  $90 \text{ pC/N}$ ,  $d_{31}$  of  $-33.4 \text{ pC/N}$  and  $d_{15}$  of  $564 \text{ pC/N}$  reported by Zgonik *et al.*<sup>19</sup> was  $-62 \text{ pC/N}$ . On the other hand, the  $d_{31}$  of the  $[111]_c$  poled  $\text{BaTiO}_3$  single crystal with a domain size over  $40 \mu\text{m}$  was estimated



10.18 Frequency dependence of the impedance and phase for the  $[111]_c$  oriented  $\text{BaTiO}_3$  single crystals with an average domain size of  $6.5\ \mu\text{m}$ , measured at  $25^\circ\text{C}$ .

to be  $-97.8\ \text{pC/N}$  while that of the  $[111]_c$  poled  $\text{BaTiO}_3$  single crystal with a domain size of  $6.5\ \mu\text{m}$  was found to be  $-180\ \text{pC/N}$ . In particular, the 31 resonator with a domain size of  $5.5\ \mu\text{m}$  showed much higher  $d_{31}$  of  $-230\ \text{pC/N}$  and  $k_{31}$  of  $47.5\%$  than those ( $d_{31}$  of  $-171\ \text{pC/N}$  and  $k_{31}$  of  $34.4\%$ ) reported for soft PZT ceramics.<sup>1</sup> Therefore, the  $[111]_c$  oriented engineered domain  $\text{BaTiO}_3$  crystal exhibit much higher piezoelectric properties than the  $[001]_c$  oriented  $\text{BaTiO}_3$  single-domain crystal.

It had been believed that the highest piezoelectric property must be obtained in single-domain crystals, and that it was impossible for the material constants to be beyond the values of single-domain crystal. However, this study reveals that the  $90^\circ$  domain walls in the engineered domain configuration significantly enhance the piezoelectric effects, giving rise to much higher piezoelectric constants than those from single-domain crystals.

In general, under a high E-field drive, the domain walls can move very easily, and this domain wall motion makes no intrinsic contribution to the piezoelectric properties. However, in the engineered domain configuration shown in Fig. 10.3, the  $90^\circ$  domain walls cannot move with or without unipolar dc E-field drive.<sup>20,21</sup> This means that in the engineered domain configuration, the  $90^\circ$  domain walls can exist very stably with or without a unipolar E-field drive. Therefore, the contribution of the domain walls to the piezoelectric properties has been clarified for the first time using the engineered domain configuration. In other words, the engineered domain configuration is considered as domain wall engineering among the domain engineering techniques.<sup>28,29</sup>

*Table 10.1* Domain size dependence of piezoelectric properties for the 31 BaTiO<sub>3</sub> crystal resonators

BaTiO <sub>3</sub> single crystals	$\epsilon_{33}^T$	$s_{11}^E$ (pm <sup>2</sup> /N)	$d_{31}$ (pC/N)	$k_{31}$ (%)
[001] <sup>a</sup> (single domain)	129	7.4	-33.4	-
[111] <sup>b</sup> (single domain)	-	-	-62.0	-
[111], charged (domain size of 80 μm)	1299	10.9	-85.3	24.1
[111], charged (domain size of 50 μm)	2117	7.80	-98.2	25.7
[111], charged (domain size of 40 μm)	2185	7.37	-97.8	25.9
[111], charged + neutral (domain size of 20.0 μm)	2117	8.30	-102.7	26.0
[111], charged + neutral (domain size of 15.0 μm)	2186	8.20	-112.5	28.2
[111], charged + neutral (domain size of 13.3 μm)	2087	7.68	-134.7	35.7
[111], charged + neutral (domain size of 12.0 μm)	1921	8.20	-137.6	36.8
[111], charged + neutral (domain size of 10.0 μm)	2239	9.30	-140.5	32.8
[111], charged + neutral (domain size of 8.0 μm)	2238	9.10	-159.2	37.5
[111], charged + neutral (domain size of 7.0 μm)	2762	9.30	-176.2	36.9
[111], charged + neutral (domain size of 6.5 μm)	2441	8.80	-180.1	41.4
[111], charged + neutral (domain size of 5.5 μm)	2762	9.58	-230.0	47.5
'Soft' PZT ceramics <sup>c</sup> Pb <sub>0.988</sub> (Ti <sub>0.48</sub> Zr <sub>0.52</sub> ) <sub>0.976</sub> Nb <sub>0.024</sub> O <sub>3</sub>	1700	16.4	-171.0	34.4

<sup>a</sup> Measured by Zgonik *et al.* [9].

<sup>b</sup> Calculated using the values measured by Zgonik *et al.* [9].

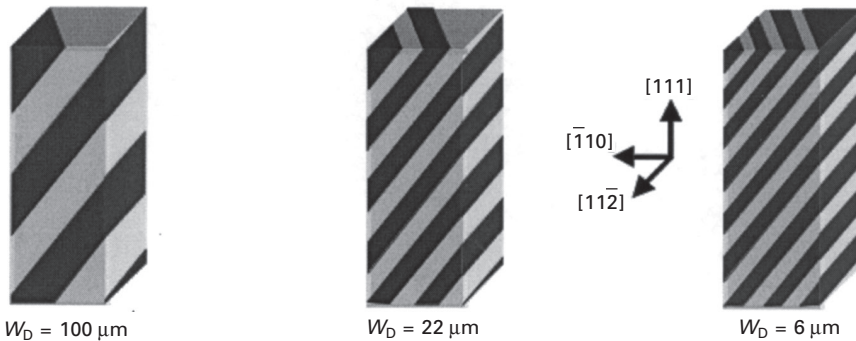
<sup>c</sup> Measured by Jaffe *et al.* [1].

### 10.5.3 Domain size dependence of the piezoelectric property using 33 resonators

By the poling treatment at various electric fields and temperatures,<sup>12,13</sup> the 33 resonators of BaTiO<sub>3</sub> crystals with different domain sizes were prepared. The average domain sizes in the engineered domain configuration (Fig. 10.3) were changed from 100 to 6 μm. The domain configurations for all the 33 resonators prepared in this study were composed of the same 90° domain

walls,<sup>24</sup> and the difference between these domain configurations was just the domain size, as shown in Fig. 10.19.

The piezoelectric properties were measured at 25 °C using a weak ac E-field of 50 mV/mm. Table 10.2 shows the domain size dependence of piezoelectric-related properties using these 33 resonators. As a reference, the calculated  $d_{33}$  piezoelectric constant for the  $[111]_c$  oriented BaTiO<sub>3</sub> single-domain crystal using the material constants reported by Zgonik *et al.*<sup>19</sup> was also listed. All the piezoelectric-related properties increased with decreasing domain size. The most surprising thing is the fact that the piezoelectric



10.19 Schematic of 33 resonators composed of the engineered domain configuration with different domain sizes.

Table 10.2 Domain size dependence of piezoelectric properties for the 33 BaTiO<sub>3</sub> crystal resonators

BaTiO <sub>3</sub> single crystals	$\epsilon_{33}^T$	$s_{33}^E$ (pm <sup>2</sup> /N)	$d_{33}$ (pC/N)	$k_{33}$ (%)
[001] <sup>a</sup> (single domain)	–	–	90	–
[111] <sup>a</sup> (single domain)	–	–	224	–
[111], neutral (domain size of 100 μm)	1984	10.6	235	54.4
[111], neutral (domain size of 60 μm)	1959	10.7	241	55.9
[111], neutral (domain size of 22 μm)	2008	8.8	256	64.7
[111], neutral (domain size of 15 μm)	2853	6.8	274	66.1
[111], neutral (domain size of 14 μm)	1962	10.8	289	66.7
[111], neutral (domain size of 6 μm)	2679	10.9	331	65.2

<sup>a</sup> Measured by Zgonik *et al.* [19].

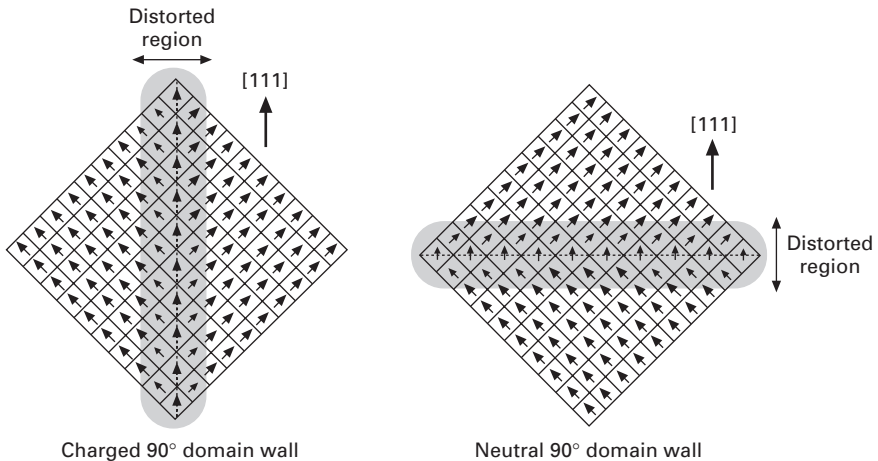
<sup>b</sup> Calculated using the values measured by Zgonik *et al.* [19].



properties significantly depend on the domain size regardless of the 31 or 33 mode. Thus, we must consider the possible effect of non-180° domain walls on the piezoelectric property. Liu *et al.* proposed a model for the role of domain walls in the engineered domain configurations.<sup>30</sup> Here, we consider this useful model to explain the enhanced piezoelectric property with increasing non-180° domain wall density.

## 10.6 Role of non-180° domain wall region on piezoelectric properties

It is well known that a region near the 90° domain walls is gradually distorted to relax the strain between domains with different polar directions, as shown in Fig. 10.20.<sup>31–35</sup> Moreover, for BaTiO<sub>3</sub> crystals, the crystal structure near the 90° domain walls gradually changed from normal tetragonal, with a  $c/a$  ratio of 1.011, to tetragonal, with a  $c/a$  ratio close to 1.0. Thus, it can be expected that the region near the 90° domain walls with pseudo-cubic structure exhibits the material constants of BaTiO<sub>3</sub> single crystals near  $T_C$ , as reported by Budimir *et al.*<sup>35</sup> In this study, the BaTiO<sub>3</sub> crystals with engineered domain configuration were regarded as a composite of (a) normal tetragonal region and (b) distorted 90° domain wall region. On the basis of this two-phase model, a volume fraction of the distorted domain wall region over the normal tetragonal region was estimated as follows. To simplify the calculation, one-dimensional model was applied.<sup>36</sup> First, the thickness of the distorted 90° domain wall region ( $W_{DW}$ ) was assumed using various sizes from 1 to 100 nm.<sup>31–35</sup> Next, using this thickness ( $W_{DW}$ ) and the domain size ( $W_D$ ), the



10.20 Schematic of structure near the 90° domain walls for BaTiO<sub>3</sub> crystals.

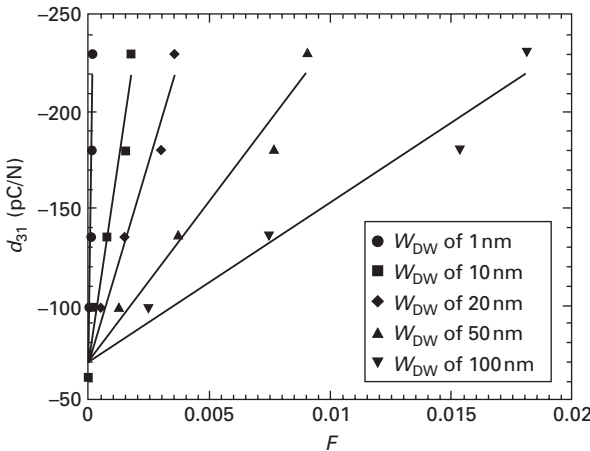
volume fraction of the distorted 90° domain wall region ( $F$ ) was estimated with the following equation:

$$F = \frac{W_{DW}}{W_D} \tag{10.1}$$

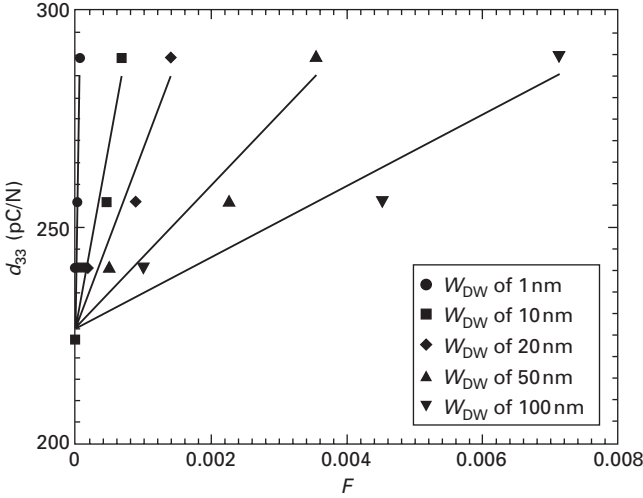
$W_D$  can be measured from the experiment in this study while  $W_{DW}$  is unknown. Thus, we must use valid  $W_{DW}$  values for the above calculation. To date, many researchers tried to estimate the domain wall thickness using Landau–Ginzburg–Devonshire (LGD) theories and transmission electron microscopic (TEM) observation, and their estimated values from 1 to 10 nm.<sup>31–35</sup> Recently, based on the developed measurement equipment and theories, some new methods were proposed to estimate the domain wall thickness.<sup>36–38</sup> In particular, the domain wall thickness was related to point defect, and the defect was responsible for the broadening of the domain wall thickness.<sup>37</sup> This means that it is very difficult to determine the 90° domain wall thickness for BaTiO<sub>3</sub>. Thus, in this study,  $F$  values were calculated using the various domain wall thickness from 1 to 100 nm. Using the  $F$  values, the relationships between  $d_{31}$  and  $F$  and  $d_{33}$  and  $F$  were plotted in Figs 10.21 and 10. 22, respectively, in which the slope of a line indicates the piezoelectric constant expected from the corresponding distorted 90° domain wall region. Using the estimated 90° domain wall thickness of 10 nm,  $d_{31}$  and  $d_{33}$  can be expressed using the following equations:

$$d_{31} = -82\,676F - 69 \tag{10.2}$$

$$d_{33} = 81\,744F + 227 \tag{10.3}$$



10.21 Relationship between  $d_{31}$  and  $F$  calculated using various  $W_{DW}$  values from 1 to 100 nm.



10.22 Relationship between  $d_{33}$  and  $F$  calculated using various  $W_{DW}$  values from 1 to 100 nm.

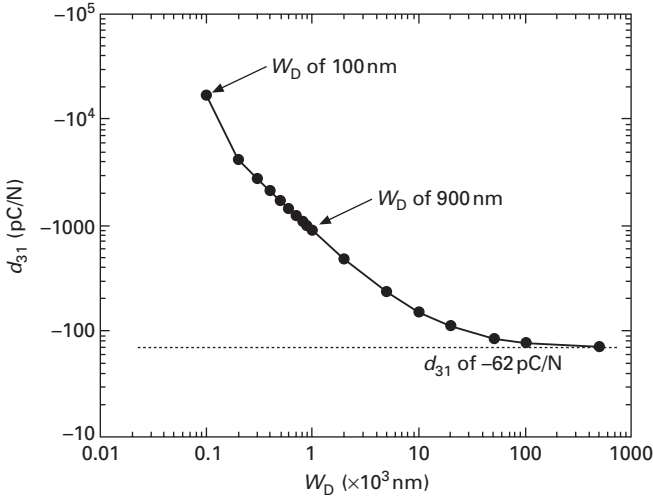
i.e.  $d_{31}$  and  $d_{33}$  from the distorted  $90^\circ$  domain wall region are calculated to be 82 676 and 81 744 pC/N, respectively. Similarly, if the  $90^\circ$  domain wall thickness is 3 nm,  $d_{31}$  and  $d_{33}$  from the distorted  $90^\circ$  domain wall region are estimated to be 275 590 and 272 480 pC/N, respectively. If the  $90^\circ$  domain wall thickness is 1 nm,  $d_{31}$  of 826 760 and  $d_{33}$  of 817 440 can be expected from the distorted  $90^\circ$  domain wall region. The above values reveal that the piezoelectric constants resulting from the distorted  $90^\circ$  domain wall region are significantly high. Based on a recent theoretical calculation, the domain wall width is estimated to be around 3 nm,<sup>32</sup> while the maximum domain wall width is found from recent experiments to be 10 nm.<sup>39</sup> Therefore, the  $d$  constants arising from domain wall region should be higher than 80 000 pC/N.

This study shows that the distorted  $90^\circ$  domain walls can contribute significantly to the piezoelectric properties. When the domain wall density continues to increase, how will the piezoelectric constants increase? The domain size dependences of  $d_{31}$  and  $d_{33}$  can also be expressed as follows:

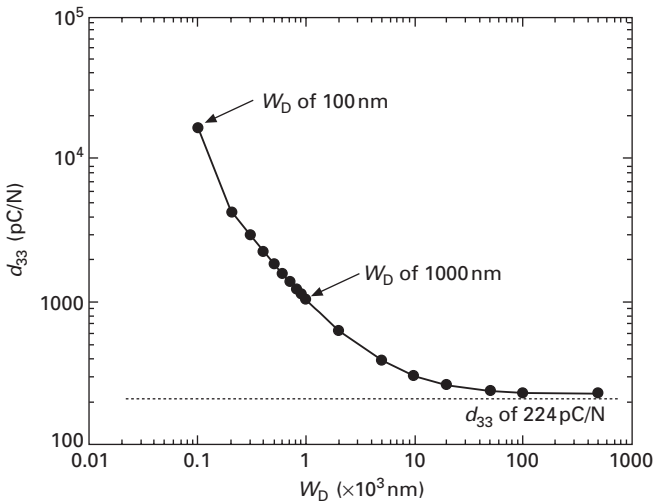
$$d_{31} = \frac{-826\,760}{W_D} - 69 \tag{10.4}$$

$$d_{33} = \frac{817\,440}{W_D} + 227 \tag{10.5}$$

It should be noted that equations (10.4) and (10.5) are independent of  $W_{DW}$ . Thus, using the various  $W_D$  values, the relationships between  $d_{31}$  and  $W_D$  and between  $d_{33}$  and  $W_D$  are plotted in Figs 10.23 and 10.24, respectively. It can



10.23 Relationship between  $d_{31}$  and  $W_D$  calculated using Equation (10.4).



10.24 Relationship between  $d_{33}$  and  $W_D$  calculated using Equation (10.5).

be seen that above the  $W_D$  of  $20 \mu\text{m}$ , the piezoelectric coefficients were almost constant at the calculated single-domain values, while below the  $W_D$  of  $10 \mu\text{m}$ , piezoelectric constants drastically increased with decreasing domain sizes. Moreover, when the domain size decreased down to  $1 \mu\text{m}$ , both  $d_{31}$  and  $d_{33}$  reached around  $1000 \text{ pC/N}$ .

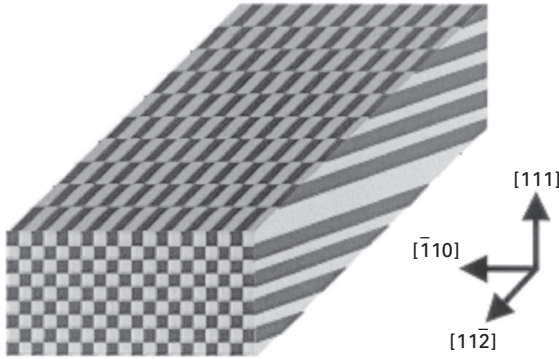
Park and Shrout reported that  $[001]_c$  poled PZN single crystal exhibited

the ultra-high  $d_{33}$  of 1100 pC/N,<sup>40</sup> and the domain size in this PZN crystal was found to be around 1  $\mu\text{m}$ .<sup>10</sup> They also reported that for  $[111]_c$  poled PZN single-domain crystal had a  $d_{33}$  of just 83 pC/N,<sup>40</sup> similar to that of BaTiO<sub>3</sub>. Therefore, it can be expected that when a domain size of around 1  $\mu\text{m}$  is induced in the  $[111]_c$  poled BaTiO<sub>3</sub> crystals, high-performance lead-free piezoelectrics with ultra-high piezoelectric constants over 1000 pC/N can be created.

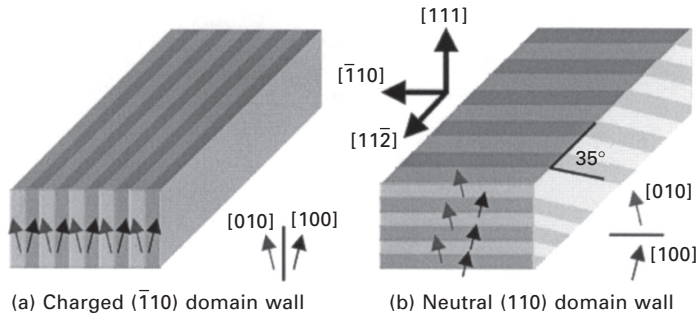
## 10.7 New challenge of domain wall engineering using patterning electrode

In the previous section, it was clarified that in BaTiO<sub>3</sub> crystals with engineered domain configuration the piezoelectric constants significantly increased with increasing domain wall densities, i.e. decreasing domain sizes.<sup>12,13</sup> In the poling treatments, the whole plane electrode was always used, and the minimum domain size was limited to greater than 5  $\mu\text{m}$ . Therefore, it is important to establish a new poling method to induce much smaller domain sizes (below 5  $\mu\text{m}$ ) in the BaTiO<sub>3</sub> crystals. Urenski *et al.* reported that for the KTiOPO<sub>4</sub> single crystals, the periodic domain structure was successfully induced using patterned electrodes.<sup>41</sup> The objective in this section is to prepare the 31 resonators of BaTiO<sub>3</sub> crystals with a high piezoelectric constant ( $d_{31}$ ) by introducing finer engineered domain configurations. For this purpose, a new poling method using a patterning electrode was proposed to induce the engineered domain configuration with smaller domain sizes below 5  $\mu\text{m}$ , and the piezoelectric properties were investigated as a function of domain size.

The patterning electrode with a gold strip line of 3  $\mu\text{m}$  width per 6  $\mu\text{m}$  spacing parallel to the  $[1-10]_c$  direction was prepared on the top surface using a photolithography technique while the whole electrode was prepared on the bottom surface. First, on the top surface of the resonator, a photoresist (Kayaku Microchem, SU-8 3000) layer with 2  $\mu\text{m}$  in thickness was coated. Then, mask alignment, UV radiation and development were performed. After this process, gold electrodes were sputtered on both surfaces with an area of  $1.2 \times 4.0 \text{ mm}^2$ . The fine engineered domain configuration was induced by using the patterning electrodes at various electric fields (0–10 kV/cm) and temperatures (20–140 °C). Figure 10.25 shows the desirable engineered domain configuration for the tetragonal BaTiO<sub>3</sub> single crystals. This domain configuration is composed of just two kinds of polarization along the  $[010]_c$  and  $[100]_c$  directions, as shown in Fig. 10.26. Moreover, a previous study revealed that in the engineered domain configuration, if the engineered domain configuration with average domain size of 3  $\mu\text{m}$  was induced in BaTiO<sub>3</sub> crystals, the  $d_{31}$  is expected to be  $-337.7 \text{ pC/N}$  using equation (10.4). In general, it is known that the  $d_{33}$  value can be expressed as  $|2*d_{31}|$ . Thus, for



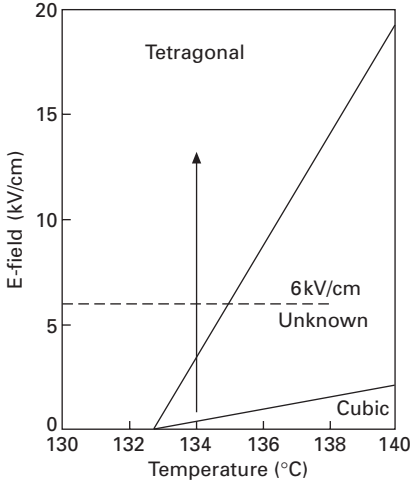
10.25 Schematic of desirable finer domain configuration.



10.26 Domain configuration with (a) 90° charged and (b) 90° neutral domain walls.

a  $d_{31}$  of  $-337.7$  pC/N, the  $d_{33}$  is expected to be  $675.4$  pC/N. Thus, a poling treatment was performed to induce the engineered domain configuration with a domain size of  $3\ \mu\text{m}$ .

Figure 10.27 shows the temperature–electric field phase diagram used for the new poling method using a patterning electrode. The phase transition temperature from tetragonal to cubic was  $132.2\ ^\circ\text{C}$  for  $\text{BaTiO}_3$  crystals. Thus, first, the temperature increased to  $140.0\ ^\circ\text{C}$  without an E-field, and the appearance of the optical isotropic state was confirmed. Then, the temperature decreased slowly to  $134.0\ ^\circ\text{C}$ , and an E-field was applied along the  $[111]_c$  direction at  $134.0\ ^\circ\text{C}$ . The patterning electrode prepared in this study was composed of (1) a photoresist strip line of  $3\ \mu\text{m}$  width per  $6\ \mu\text{m}$  spacing and (2) a gold electrode deposited on both the patterned photoresist and the crystal surface. Thus, it should be noted that in the patterning electrode, photoresist still remained between crystal surface and gold electrode. This is because this photoresist is stable up to  $250\ ^\circ\text{C}$ . However, when an electric field over  $6\ \text{kV/cm}$  was applied at  $134.0\ ^\circ\text{C}$ , photoresist was burned out with

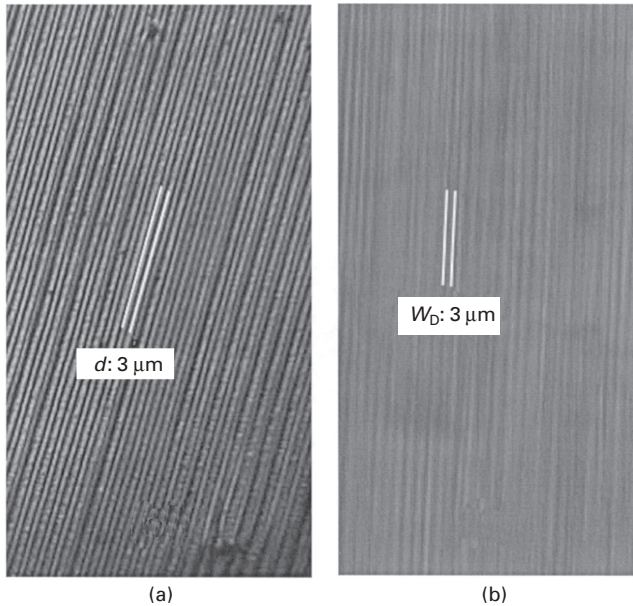


10.27 Phase transition diagram as functions of temperature and E-field for  $[111]_c$  oriented  $\text{BaTiO}_3$  crystals.

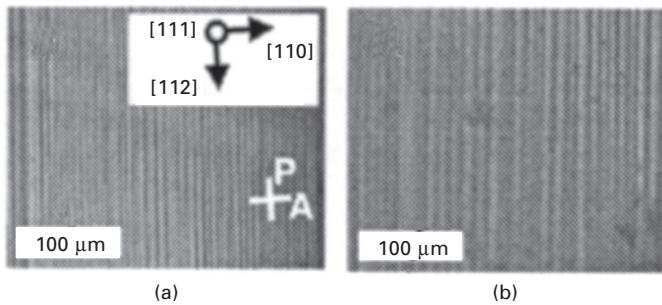
a large leakage current over  $300 \mu\text{A}$ . Thus, in this study, the electric field applied at  $134.0^\circ\text{C}$  was limited below  $6 \text{ kV/cm}$ .

To induce the engineered domain configuration in  $\text{BaTiO}_3$  crystals, the E-field induced phase transition from cubic to tetragonal phases above  $T_C$  of  $132.2^\circ\text{C}$  was required. Thus, the following poling method was applied. At  $134.0^\circ\text{C}$ , an electric field was slowly applied to  $2 \text{ kV/cm}$ , and then rapidly increased to  $5.6 \text{ kV/cm}$ . Without soaking at  $5.6 \text{ kV/cm}$ , the temperature decreased to  $50^\circ\text{C}$  at a cooling rate of  $-10^\circ\text{C/min}$  under the electric field of  $5.6 \text{ kV/cm}$ . Figure 10.28 shows the optical microscope photographs of patterning electrode with a pattern width of  $3 \mu\text{m}$  and the consequently induced engineered domain configuration. In Fig. 10.28(b), the average domain size was estimated to be around  $3 \mu\text{m}$ . When the whole plane electrode was used to induce the finer engineered domain configuration, the minimum domain size was always limited to be above  $5 \mu\text{m}$ . Therefore, using the patterning electrode with a gold strip width of  $3 \mu\text{m}$ , the engineered domain configuration with a domain size of  $3 \mu\text{m}$  was successfully induced in  $\text{BaTiO}_3$  crystals. This reveals that in the poling treatment of  $\text{BaTiO}_3$  crystals, the patterning electrode is a very useful technique.

Finally, for this 31 resonator with  $3 \mu\text{m}$  domain width, the piezoelectric properties were measured using the resonance–antiresonance technique. As mentioned before, a  $d_{31}$  of  $-337.7 \text{ pC/N}$  was expected for the 31 resonator of the engineered domain configuration with a domain width of  $3 \mu\text{m}$ .<sup>15</sup> The measured  $d_{31}$  was  $-243.2 \text{ pC/N}$ , and if assuming  $d_{33}$  as  $|2 \cdot d_{31}|$ , the  $d_{33}$  was estimated to be  $486.4 \text{ pC/N}$ . This measured value of  $d_{31}$  was only 70% of the expected value of  $-337.7 \text{ pC/N}$ . Thus, the origin of this lower than expected



10.28 Photograph of (a) the patterning electrode with a gold electrode width of  $3\mu\text{m}$  and (b) the poled domain structure with an average domain size of  $3\mu\text{m}$ .



10.29 Domain structure of the 31  $\text{BaTiO}_3$  resonator near (a) the top surface (high-voltage side) and (b) the bottom surface (ground side).

value of  $d_{31}$  was investigated. Figure 10.29 shows the domain structures near the top and bottom electrodes of the 31 resonator. The domain size near the top patterning electrode (high-voltage side) was estimated to be  $3\mu\text{m}$  while that near the bottom electrode (ground side) was  $8\text{--}9\mu\text{m}$ . The gradient domain sizes from  $3$  to  $8\text{--}9\mu\text{m}$  along thickness direction ( $[111]_c$ ) were first observed. As mentioned previously, when the whole plane electrode was used for the poling treatment, the minimum domain size was limited to  $5\mu\text{m}$ , but there was no gradient domain size.<sup>12,13</sup> This difference might originate from different



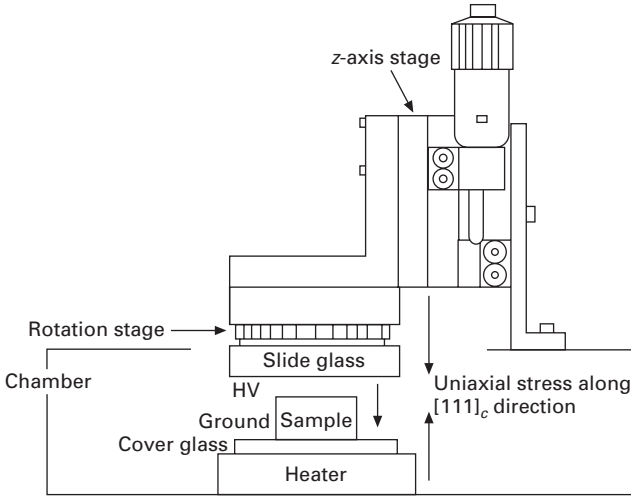
E-fields. For the homogeneous domain size of  $5.5\ \mu\text{m}$  using the whole plane electrode, the applied E-field was  $10.1\ \text{kV/cm}$ . This E-field was almost twice as high as that of  $5.6\ \text{kV/cm}$  used in this study. Urenski *et al.* reported that for the introduction of the expected periodic domain structure similar to the patterning electrode, a much higher E-field than the coercive E-field ( $E_c$ ) was required.<sup>41</sup> Therefore, if the high E-field over  $10.1\ \text{kV/cm}$  is applied to the 31 resonator using the patterning electrode with  $3\ \mu\text{m}$  width, it is expected that a homogeneous domain size of  $3\ \mu\text{m}$  can be induced in the resonator. At present, the patterning electrode without photoresist is designed for this purpose. In the near future, we shall be able to induce much finer homogeneous domain sizes in the resonator to prepare lead-free piezoelectrics with a higher  $d_{31}$  (over  $-500\ \text{pC/N}$ ). Moreover, applying a uniaxial stress field can help reduce the E-field using the above patterned electrodes in the poling method. This new approach will be discussed in the next section.

## 10.8 New challenge of domain wall engineering using uniaxial stress field

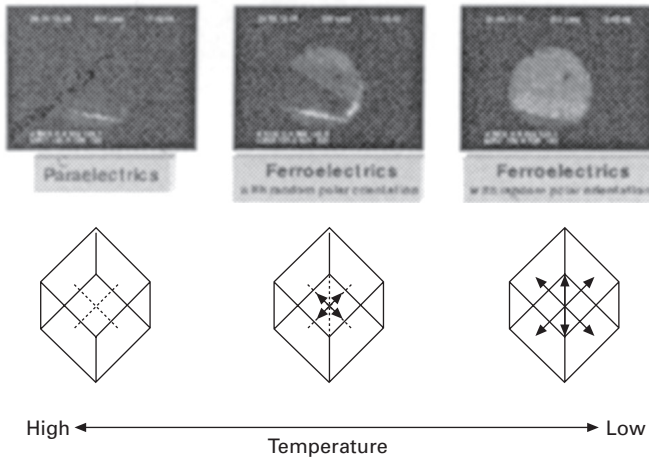
It is well known that the ferroelectric phase transition is affected by temperature, E-field and stress field. Thus, application of a uniaxial stress field to the poling treatment in addition to temperature and E-field may reduce the value of the E-field below  $10\ \text{kV/cm}$  over  $T_c$ . In this section, the phase transition behavior of the  $[111]_c$  oriented  $\text{BaTiO}_3$  crystals was investigated as functions of temperature, uniaxial stress and E-fields. Moreover, on the basis of the results, a new poling method for the  $\text{BaTiO}_3$  crystals will be proposed using control of temperature, uniaxial stress and E-fields.

In the new poling system, temperature, E-field and uniaxial stress-field must be controlled independently. A new poling attachment was designed as shown in Fig. 10.30. The temperature can be changed from  $-190$  to  $600\ ^\circ\text{C}$  while the E-field and uniaxial stress field are applied along the  $[111]_c$  directions, independently. Since the uniaxial stress field was applied using an  $z$ -axis stage and a precise uniaxial pressure value cannot be measured, the moving length ( $\mu\text{m}$ ) of the  $z$ -axis stage from a position at contact with sample without pressure was defined as apparent uniaxial stress field through this chapter. First, the phase transition behavior of the  $\text{BaTiO}_3$  crystals by temperature only was investigated without E-field and uniaxial stress field by domain observation under crossed-polarizers. It was clearly observed that from a temperature above  $T_c$ , with decreasing temperature, the paraelectric phase changed to an intermediate phase with super-paraelectric state, and finally changed to the ferroelectric phase with randomly oriented spontaneous polarization, as shown in Fig. 10.31.

The crystal structure of the intermediate phase with super-paraelectric state is still unknown, but under crossed-polarizers, the crystal remained



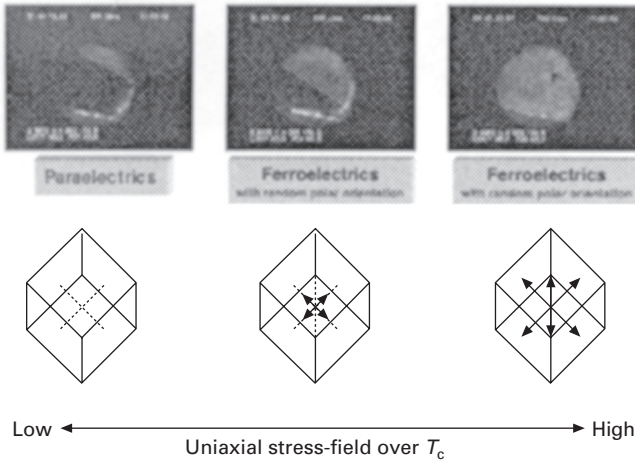
10.30 Schematic new poling attachment with controlled temperature, uniaxial stress field and E-field.



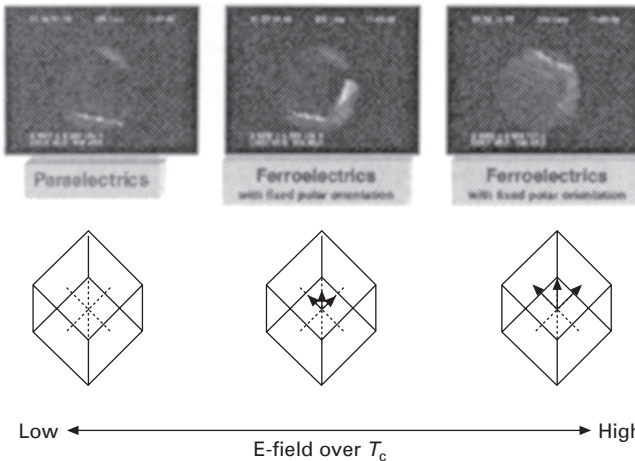
10.31 Phase transition behavior of the  $\text{BaTiO}_3$  crystals by temperature without E-field and uniaxial stress field.

birefringent while being rotated, which suggested that this phase is not the paraelectric cubic phase. Next, above  $T_C$ , the phase transition behavior of the  $\text{BaTiO}_3$  crystals induced only by E-field applied along the  $[111]_c$  direction was investigated without uniaxial stress field by domain observation under crossed polarizers. With increasing E-field, the paraelectric phase changed to the intermediate phase with super-paraelectric state, and finally to the ferroelectric tetragonal phase with three oriented polar directions along  $[100]_c$ .

$[010]_c$  and  $[001]_c$ , as shown in Fig. 10.32. It should be noted that at the temperature of  $(T_c + 1.5)^\circ\text{C}$ , the electric field over  $10\text{ kV/cm}$  is required to induce the tetragonal phase. Finally, above  $T_c$ , the phase transition behavior of the  $\text{BaTiO}_3$  crystals induced only by uniaxial stress field applied along the  $[111]_c$  direction was investigated without an E-field. With increasing uniaxial stress field, the paraelectric phase changed to the intermediate phase with super-paraelectric state, and finally to the ferroelectric phase with randomly oriented spontaneous polarization, as shown in Fig. 10.33. When a poling



10.32 Phase transition behavior of the  $\text{BaTiO}_3$  crystals by uniaxial stress field without E-field at  $(T_c + 1.5)^\circ\text{C}$ .

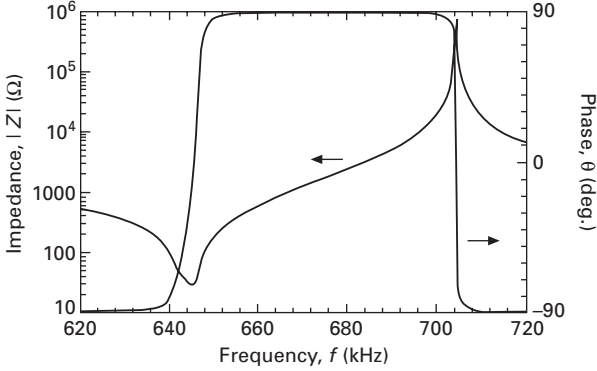


10.33 Phase transition behavior of the  $\text{BaTiO}_3$  crystals by E-field without uniaxial stress-field at  $(T_c + 1.5)^\circ\text{C}$ .

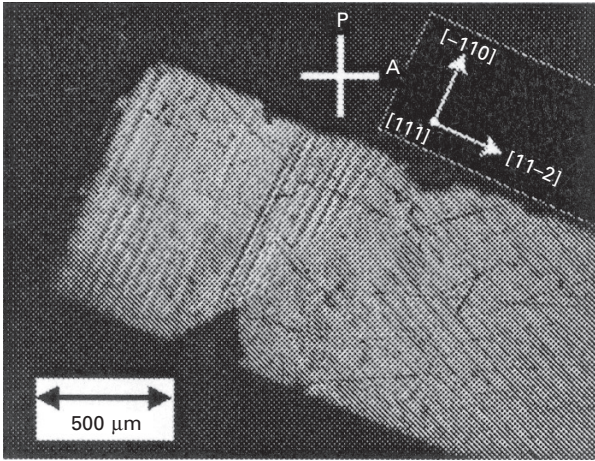
treatment was performed using an E-field, a higher E-field was required with increasing temperature above  $T_C$ . On the other hand, when a poling treatment was performed using a uniaxial stress field, a smaller uniaxial stress field was enough for obtaining as fully poled state with increasing temperature above  $T_C$ . This is because the BaTiO<sub>3</sub> crystal is ferroelectric and ferroelastic, which suggested that uniaxial stress field is quite effective for poling treatment.

The above discussion revealed that the phase transition behavior from cubic to tetragonal by temperature and uniaxial stress field was quite similar because of the formation of the ferroelectric phase with randomly oriented spontaneous polarization. On the other hand, the phase transition behavior by E-field leads to the ferroelectric tetragonal phase with three oriented polar directions. However, the phase transition from the cubic to the intermediate phase with super-paraelectric state induced by temperature, uniaxial stress field and E-field shows completely the same behavior. These results suggested that above  $T_C$ , the combination of uniaxial stress and E-fields might be more effective for the poling of ferroelectric crystals. Thus, the E-field for a poling treatment above  $T_C$  can be reduced by the combination of uniaxial stress-field and E-field drives.

In this poling process,  $(T_C + 3.5)^\circ\text{C}$  was chosen as the poling temperature. This is because at this temperature, it is impossible to pole the BaTiO<sub>3</sub> crystals using only an E-field owing to electric breakdown. Thus, two kinds of poling treatments at  $(T_C + 3.5)^\circ\text{C}$  were performed as follows, i.e. (a) a lower uniaxial stress field below  $10\ \mu\text{m}$  and then a higher electric field above  $10\ \text{kV/cm}$ , and (b) a higher uniaxial stress field above  $10\ \mu\text{m}$  and then a lower electric field below  $10\ \text{kV/cm}$ . Poling treatment (a) was performed first, i.e. an apparent uniaxial stress field of  $9\ \mu\text{m}$  was applied to induce the intermediate phase only, and after that, an electric field of  $14\ \text{kV/cm}$  was applied to induce the ferroelectric phase with the oriented polar direction. As a result, an almost fully poled state was achieved in the  $[111]_c$  poled BaTiO<sub>3</sub> crystals, as shown in Fig. 10.34. The piezoelectric properties were measured from Fig. 10.34. Figure 10.35 shows the domain configuration of the  $[111]_c$  poled BaTiO<sub>3</sub> crystals. An average domain size in Fig. 10.35 was over  $50\ \mu\text{m}$ , and two kinds of  $90^\circ$  domain configuration were clearly observed. Poling treatment (b) was performed next, i.e. an apparent uniaxial stress field of  $17\ \mu\text{m}$  was applied to induce the coexistence of the intermediate and the ferroelectric tetragonal phases, and after that, an electric field of  $9.5\ \text{kV/cm}$  was applied to induce the ferroelectric phase. As a result, an almost fully poled state was achieved for the  $[111]_c$  poled BaTiO<sub>3</sub> crystals as shown in Fig. 10.36. The piezoelectric properties were measured from Fig. 10.36. The domain configuration by the poling treatment (b) was completely the same as shown in Fig. 10.35. On the basis of the two impedance curves, the piezoelectric constants for the  $[111]_c$  poled BaTiO<sub>3</sub> crystals were determined as shown in Table 10.3, when the  $d_{33}$  value was measured using a  $d_{33}$  meter.



10.34 Frequency dependence of the impedance and the phase for the  $[111]_c$  oriented  $\text{BaTiO}_3$  single crystals poled using the poling treatment (a).

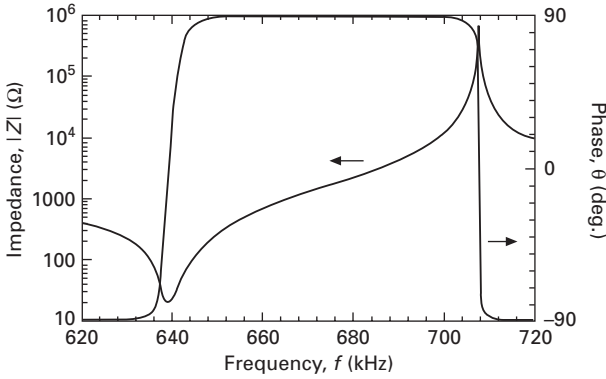


10.35 Domain configuration after the poling treatment of (a).

The  $d_{33}$  along the  $[111]_c$  direction was calculated to be  $224 \text{ pC/N}$  for  $\text{BaTiO}_3$  single-domain crystal.<sup>42</sup> In this study, the  $d_{33}$  was measured to be  $230 \text{ pC/N}$ , which is consistent with the previously calculated value. This revealed that the uniaxial stress field is very effective for the poling treatment above  $T_C$  to reduce the E-field below  $10 \text{ kV/cm}$ . This poling treatment can be universal for all ferroelectric materials including PZT ceramics.

### 10.9 What is domain wall engineering?

To enhance piezoelectric property, we must consider two contributions, i.e. intrinsic and extrinsic effects. The intrinsic effect is dependent on the unit



10.36 Frequency dependence of the impedance and the phase for the [111]<sub>c</sub> oriented BaTiO<sub>3</sub> single crystals poled using the poling treatment (b).

Table 10.3 Piezoelectric properties for the [111]<sub>c</sub> poled BaTiO<sub>3</sub> crystal using the poling treatment of (a) and (b)

Poling treatment	$\epsilon_{33}^T$	$s_{11}^E$ (pN/m <sup>2</sup> )	$d_{31}$ (pC/N)	$k_{31}$ (%)	$d_{33}^*$ (pC/N)
(a)	2114	8.7	-136	34	230
(b)	1983	8.6	-144	37	230

$d_{33}^*$ : measured by  $d_{33}$  meter.

cell with symmetry and chemical composition. In the earlier sections, we discussed the optimum crystal structure and crystallographic direction for the best engineered domain configurations. This discussion should be related to the intrinsic contribution to piezoelectric property. On the other hand, in the later sections, it was revealed that 90° domain wall regions with distorted and structure graduation had ultra-high piezoelectric constants above 80 000 pC/N. This contribution is an extrinsic effect, and this technique is called domain wall engineering. In this technique, we must prepare a domain wall region fixed in the crystals, and an engineered domain configuration is a technique to fix domain wall in the crystals. As a result, we can obtain a composite of domain wall regions and normal domain region.

Thus, to obtain highly piezoelectric crystals, a combination of intrinsic and extrinsic effects is required. To maximize the intrinsic contribution, we should use the [001]<sub>c</sub> oriented orthorhombic crystals, and if this crystal has phase transition from orthorhombic to tetragonal at around -10 to 0 °C, we can expect enhancement of piezoelectric properties. In addition, to maximize the extrinsic contribution, we should induce a domain size of around 150 nm in the [001]<sub>c</sub> oriented orthorhombic crystals. Arlt *et al.* reported that in

BaTiO<sub>3</sub> ceramics, the dielectric constant increased with decreasing grain size and at a grain size of 800 nm, the dielectric constant reached a maximum value of 5000.<sup>43</sup> They also depicted the relationship between the grain size and domain size, and the domain size of BaTiO<sub>3</sub> ceramics with a grain size of 800 nm was 150 nm. This result suggested that for domain sizes above 150 nm, the dielectric and piezoelectric properties can increase with decreasing domain sizes, while for the domain size below 150 nm, the both properties can decrease with decreasing domain sizes.

To induce the fine domain size around 150 nm, a combination of patterned electrode and uniaxial stress-field can be used in the new poling system above  $T_c$ . We consider that domain wall engineering includes a universal concept of ultra-high domain wall contribution to piezoelectricity and any techniques to induce fine domain size of about 150 nm in the [001]<sub>c</sub> oriented orthorhombic crystals. It is expected that the development of the domain wall engineering will allow us to create new lead-free piezoelectrics with ultra-high piezoelectric properties.

## 10.10 Conclusions and future trends

Various engineered domain configurations were induced in BaTiO<sub>3</sub> single crystals, and their piezoelectric properties were investigated as a function of the crystal structure, crystallographic orientation and domain size (domain wall density). As a result, BaTiO<sub>3</sub> crystals with the orthorhombic *mm2* phase showed the highest piezoelectric properties among three kinds of BaTiO<sub>3</sub> crystals of the tetragonal *4mm*, orthorhombic *mm2* and rhombohedral *3m* phases. On the other hand, BaTiO<sub>3</sub> crystals oriented along the [001]<sub>c</sub> direction always exhibited larger piezoelectric properties than those oriented along the [111]<sub>c</sub> direction. The highest piezoelectric properties ( $d_{33}$  of 500 pC/N and  $k_{33}$  of 85%) were obtained for the [001]<sub>c</sub> poled orthorhombic BaTiO<sub>3</sub> crystals, and these values were much larger than those of the conventional PZT ceramics. The domain size dependence of the piezoelectric properties was also discussed, and the result revealed that the piezoelectric properties were strongly dependent on the domain sizes (domain wall density), i.e. the piezoelectric properties significantly increased with decreasing domain size. The calculated  $d_{31}$  of the [111]<sub>c</sub> oriented tetragonal BaTiO<sub>3</sub> single-domain crystal was -62 pC/N, while the measured value of the [111]<sub>c</sub> poled tetragonal BaTiO<sub>3</sub> crystal with a domain size of 3 μm was -243.2 pC/N, i.e. a four-fold increase. When the much finer domain size (below 1 μm) can be induced in the [001]<sub>c</sub> poled orthorhombic BaTiO<sub>3</sub> crystals, the significantly enhanced piezoelectric properties can be expected. However, BaTiO<sub>3</sub> crystals have tetragonal *4mm* symmetry at room temperature and the desirable orthorhombic *mm2* phase is stable below 5 °C. Therefore, ferroelectric single crystals with an orthorhombic *mm2* phase at room temperature are highly desirable, and [001]<sub>c</sub> poled

orthorhombic  $\text{KNbO}_3$  single crystals with domain sizes below  $1\ \mu\text{m}$  will be one of the promising candidates for much enhanced piezoelectric properties.

When application of the domain wall engineering is being considered in the future, single crystals have three disadvantages over other piezoelectric materials. One is very high cost, and this cost can limit applications. Second is very weak mechanical strength, and this weakness also reduces application. Third is an intrinsic difficulty to induce very fine domain sizes below  $3\ \mu\text{m}$ . On the other hand, normal piezoelectric ceramics is completely opposite to the single crystals, and the disadvantage of normal ceramics is lack of crystallographic orientation. Therefore, we must combine the advantages of single crystals and ceramics. I believe that this dream material is grain-oriented ceramics along the engineered domain configuration. This has several advantages, especially for very fine domain sizes. It is well known that it is easy to induce fine domain sizes below  $100\ \text{nm}$  in piezoelectric ceramics. The application of domain wall engineering for grain-oriented ceramics along engineered domain direction can lead to super-piezoelectrics with ultra-high piezoelectric properties over  $d_{33}$  of  $1000\ \text{pC/N}$  and  $k_{33}$  of  $90\%$ .

## 10.11 Acknowledgements

I would like to thank Mr O. Nakao of Fujikura Ltd for preparing the TSSG-grown  $\text{BaTiO}_3$  single crystals with excellent chemical quality. I also would like to thank Dr S.-E. 'Eagle' Park, Dr T. R. Shrout and Dr L. E. Cross of MRL, Pennsylvania State University, for their helpful suggestion and many discussions about the engineered domain configurations. Moreover, I would like to thank Dr Y. Ishibashi of Aichi-shukutoku University, Dr D. Damjanovic of EPFL, Dr A. J. Bell of University of Leeds and Dr L. E. Cross of Pennsylvania State University for their helpful discussions about the domain wall contribution to the piezoelectric properties. I would like to thank Dr J. Erhart and Dr J. Fousek of ICPR, Technical University of Liberec, for their helpful discussions about the analysis of the domain configuration and calculation of the  $d_{31}$  surface. This study was partially supported by (1) a Grant-in-Aid for Scientific Research (11555164 and 16656201) from the Ministry of Education, Culture, Sports, Science, and Technology, Japan, (2) TEPCO Research Foundation, (3) the Japan Securities Scholarship Foundation, (4) Toray Science and Technology Grant, (5) the Kurata Memorial Hitachi Science and Technology Foundation, (6) the Electro-Mechanic Technology Advanced Foundation, (7) the Tokuyama Science Foundation and (8) the Yazaki Memorial Foundation for Science and Technology.

## 10.12 References

1. Jaffe B, Cook, Jr. W R, Jaffe H (1971), *Piezoelectric Ceramics*, New York, Academic Press.



2. Nakamura K, Shimizu H (1983), 'Poling of ferroelectric crystals by using interdigital electrodes and its application to bulk-wave transformer', *Proc. 1983 IEEE Ultrasonic Symp.* 527–530.
3. Nakamura K, Ando H, Shimizu H (1986), 'Partial domain inversion in LiNbO<sub>3</sub> plates and its applications to piezoelectric devices', *Proc. 1986 IEEE Ultrasonic Symp.* 719–722.
4. Lim E J, Fejer M M, Byer R L, Kozlovsky W J (1989), 'Blue light generation by frequency doubling in periodically poled lithium niobate channel waveguide', *Electron Lett.* **25**, 731–732.
5. Webjorn J, Laurell F, Arvidsson G (1989), 'Blue light generated by frequency doubling of laser diode light in a lithium niobate channel waveguide', *IEEE Photonics Technol. Lett.* **1**, 316–318.
6. Hiranaga Y, Fujimoto K, Cho Y, Wagatsuma Y, Onoe A, Terabe K, Kitamura K (2002), 'Nano-sized inverted domain formation in stoichiometric LiTaO<sub>3</sub> single crystal using scanning nonlinear dielectric microscopy', *Integrated Ferro.* **49**, 203–209.
7. Cho Y, Hiranaga Y, Fujimoto K, Wagatsuma Y, Ones A, Terabe K, Kitamura K (2003), 'Tbit/inch<sup>2</sup> ferroelectric data storage based on scanning nonlinear dielectric microscopy', *Trans. Mater. Res. Soc. Jpn.* **28**, 109–112.
8. Terabe K, Higuchi S, Takekawa S, Nakamura M, Goto Y, Kitamura K (2003), 'Nanoscale domain engineering of a Sr<sub>0.61</sub>Ba<sub>0.39</sub>Nb<sub>2</sub>O<sub>6</sub> single crystal using a scanning force microscope', *Ferroelectrics* **292**, 83–89.
9. Park S-E, Mulvihill K L, Lopath P D, Zipparo M, Shrout T R (1996), 'Crystal growth and ferroelectric related properties of (1 - x)Pb(A<sub>1/3</sub>Nb<sub>2/3</sub>)O<sub>3</sub>-xPbTiO<sub>3</sub> (A = Zn<sup>2+</sup>, Mg<sup>2+</sup>)', *Proc. 10th IEEE Int. Symp. Applications of Ferroelectrics* Vol. 1, 79–82.
10. Wada S, Park S-E, Cross L E, Shrout T R (1998), 'Domain configuration and ferroelectric related properties of relaxor based single crystals', *J. Korean Phys. Soc.* **32**, S1290–S1293.
11. Wada S, Park S-E, Cross L E, Shrout T R (1999), 'Engineered domain configuration in rhombohedral PZN-PT single crystals and their ferroelectric related properties', *Ferroelectrics* **221**, 147–155.
12. Wada S, Tsurumi T (2004), 'Enhanced piezoelectric property of barium titanate single crystals with engineered domain configurations', *Br. Ceram. Trans.* **103**, 93–96.
13. Wada S, Yako K, Kakemoto H, Tsurumi T, Erhart J (2004), 'Enhanced piezoelectric property of barium titanate single crystals with the different domain sizes', *Key Eng. Mater.* **269**, 19–22.
14. Park S E, Shrout T R (1997), 'Relaxor based ferroelectric single crystals for electro-mechanical actuators', *Mater. Res. Innovat.* **1**, 20–25.
15. Park S-E, Shrout T R (1997), 'Ultrahigh strain and piezoelectric behavior in relaxor based ferroelectric single crystals', *J. Appl. Phys.* **82**, 1804–1811.
16. Kuwata J, Uchino K, Nomura S (1981), 'Phase transition in the Pb(Zn<sub>1/3</sub>Nb<sub>2/3</sub>)O<sub>3</sub>-PbTiO<sub>3</sub> system', *Ferroelectrics* **37**, 579–582.
17. Kuwata J, Uchino K, Nomura S (1982), 'Dielectric and piezoelectric properties of 0.91Pb(Zn<sub>1/3</sub>Nb<sub>2/3</sub>)O<sub>3</sub>-0.09PbTiO<sub>3</sub> single crystals', *Jpn. J. Appl. Phys.* **21**, 1298–1302.
18. Wada S, Kakemoto H, Tsurumi T, Park S-E, Cross L E, Shrout T R (2002), 'Enhanced ferroelectric related behaviors of ferroelectric single crystals using the domain engineering', *Trans. Mater. Res. Soc. Jpn.* **27**, 281–286.
19. Zgonik M, Bernasconi P, Duelli M, Schlessler R, Gunter P, Garrett M H, Rytz D, Zhu Y, Wu X (1994), 'Dielectric, elastic, piezoelectric, electro-optic, and elasto-optic tensors of BaTiO<sub>3</sub> crystals', *Phys. Rev. B* **50**, 5941–5949.

20. Wada S, Suzuki S, Noma T, Suzuki T, Osada M, Kakihana M, Park E-E, Cross L E, Shrout T R (1999), 'Enhanced piezoelectric property of barium titanate single crystals with engineered domain configurations', *Jpn. J. Appl. Phys.* **38**, 5505–5511.
21. Park S-E, Wada S, Cross L E, Shrout T R (1999), 'Crystallographically engineered BaTiO<sub>3</sub> single crystals for high-performance piezoelectrics', *J. Appl. Phys.* **86**, 2746–2750.
22. Wada S, Tsurumi T (2001), 'Domain configurations of ferroelectric single crystals and their piezoelectric properties', *Trans. Mater. Res. Soc. Jpn.* **26**, 11–14.
23. Matthias B T (1949), 'New ferroelectric crystals', *Phys. Rev.* **75**, 1771.
24. Fousek J (1971), 'Permissible domain walls in ferroelectric species', *Czech. J. Phys.* **B21**, 955–968.
25. Wahlstrom E E (1979), *Optical Crystallography*, New York, John Wiley and Sons.
26. Wada S, Yako K, Kiguchi T, Kakemoto H, Tsurumi T (2005), 'Enhanced piezoelectric properties of barium titanate single crystals with the different engineered domain sizes', *J. Appl. Phys.* **98**, 014109.
27. *IEEE Standard on Piezoelectricity*, American National Standard Institute (1976).
28. Fousek J, Litvin D B, Cross L E (2003), 'Domain geometry engineering and domain average engineering of ferroics', *J. Phys.: Condens. Matter.* **13**, L33–L38.
29. Fousek J, Cross L E (2003), 'Open issues in application aspects of domains in ferroic materials', *Ferroelectrics* **293**, 43–60.
30. Liu S-F, Park S-E, Cross L E, Shrout T R (1999), 'E-field dependence of piezoelectric properties of rhombohedral PZN–PT single crystal', *Ferroelectrics* **221**, 169–174.
31. Damjanovic D (1998), 'Ferroelectric, dielectric and piezoelectric properties of ferroelectric thin films and ceramics', *Rep. Prog. Phys.* **61**, 1267.
32. Ishibashi Y, Salje E (2002), 'A theory of ferroelectric 90 degree domain wall', *J. Phys. Soc. Jpn.* **71**, 2800–2803.
33. Setter N (2002), *Piezoelectric Materials in Devices*, Lausanne, ed. N. Setter, p. 1.
34. Meyer B, Vanderbilt D (2002), 'Ab Initio study of ferroelectric domain walls in PbTiO<sub>3</sub>', *Phys. Rev. B* **65**, 104111.
35. Budimir M, Damjanovic D, Setter N (2003), 'Piezoelectric anisotropy-phase transition relations in perovskite single crystals', *J. Appl. Phys.* **94**, 6753–6761.
36. Chaib H, Schlaphof F, Otto T, Eng L M (2003), 'Electric and optical properties of the 90° ferroelectric domain wall in tetragonal barium titanate', *J. Phys.: Condens. Matter.* **15**, 1–14.
37. Shilo D, Ravichandran G, Bhattacharya K (2004), 'Investigation of twin-wall structure at the nanometer scale using atomic force microscopy', *Nature Mater.* **3**, 453–457.
38. Tsuji T, Ogiso H, Akedo J, Saito S, Fukuda K, Yamanaka K (2004), 'Evaluation of domain boundary of piezo/ferroelectric material by ultrasonic atomic force microscopy', *Jpn. J. Appl. Phys.* **43**, 2907–2913.
39. Ishibashi Y (2004), private communication.
40. Park S-E, Shrout T R (1997), 'Characteristics of relaxor-based piezoelectric single crystals for ultrasonic transducers', *IEEE Trans. Ultrason., Ferroelectr. & Freq. Control.* **44**, 1140.
41. Urenski P, Lesnykh M, Rosenwaks Y, Rosenman G, Molotskii M (2003), *J. Appl. Phys.* **90**, 1950.
42. Wada S, Yako K, Yokoo K, Kakemoto H, Tsurumi T (2006), 'Domain wall engineering in barium titanate single crystals for enhanced piezoelectric properties', *Ferroelectrics* **334**, 1, 17–27.
43. Arlt G, Hennings D, de With G (1985), 'Dielectric properties of fine-grained barium titanate ceramics', *J. Appl. Phys.* **58**, 1619–1625.

# Enhancement of piezoelectric properties in perovskite crystals by thermally, compositionally, electric field and stress-induced instabilities

---

D DAMJANOVIC, M DAVIS and M BUDIMIR,  
Swiss Federal Institute of Technology – EPFL, Switzerland

## 11.1 Introduction

Enhancement of the piezoelectric response and its anisotropy in perovskite crystals has been a central point of the research in ferroelectrics since the rediscovery of the large electromechanical activity in relaxor ferroelectric single crystals in 1997 (Kuwata *et al.*, 1982; Park and Shrout, 1997). Facilitated polarization rotation, specifically in the presence of spontaneously formed or field-induced monoclinic phases, has been proposed in the literature as the origin of the high electromechanical response (Park and Shrout, 1997; Noheda *et al.*, 1999; Fu and Cohen, 2000; Guo *et al.*, 2000). The high dielectric, piezoelectric and elastic properties in the morphotropic phase boundary region of solid solutions have been interpreted in terms of an isotropic free energy profile by Ishibashi and co-workers. They associated the isotropic free energy profile with the large permittivity in directions perpendicular to the polar axis, the latter being equivalent to the propensity of the material for strong polarization rotation (Ishibashi and Iwata, 1998, 1999a,b; Ishibashi, 2002; Carl and Häerdtl, 1971). Results of *ab-initio* calculations by Fu and Cohen (2000) have indicated that in barium titanate ( $\text{BaTiO}_3$ ) crystals the field-induced polarization rotation is accompanied by flattening of a free energy profile in the field region where piezoelectric response is maximized. Subsequent studies have demonstrated that a free energy instability is indeed the thermodynamic origin of the enhanced piezoelectric response in simple perovskites, regardless of whether it is induced by external pressure, electric field, composition or temperature (Wu and Cohen, 2005; Budimir *et al.*, 2006) and whether it is accompanied by polarization rotation or polarization elongation (Budimir *et al.*, 2006). The recently discovered enhancement of the piezoelectric response in some relaxor ferroelectrics near an electric field-induced critical point (Kutnjak *et al.*, 2006) falls in the same category of thermodynamic phenomena. The same is probably the case for the adaptive phase mechanism discussed in Jin *et al.*, (2003) and piezoelectric enhancement by domain density engineering discovered by Wada and co-workers (2004, 2005).

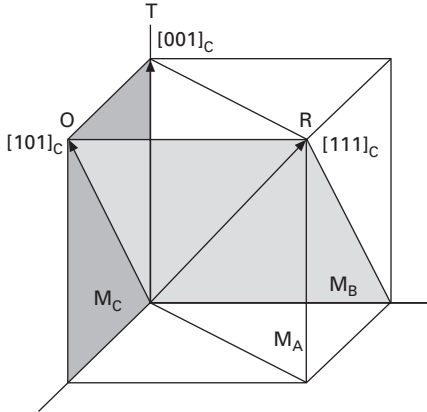
In this chapter we discuss the piezoelectric response and its anisotropy in monodomain single crystal perovskites as a function of temperature, composition variation (morphotropic phase boundary), and external electric field and mechanical stress biases. Using Landau–Ginzburg–Devonshire (LGD) thermodynamic theory it is possible to show that the common feature for different enhancements of the piezoelectric effect is anisotropic flattening of a free energy profile; the enhancement is largest near phase transition points where the system is in metastable states. The second section reviews the deformation of crystals under electric and mechanical fields. Monoclinic deformations obtained from parent tetragonal, orthorhombic and rhombohedral phases are discussed and polarization rotation is contrasted to polarization elongation. The treatment of the piezoelectric enhancement and its anisotropy within the LGD formalism is discussed in the third section. This section also discusses the instabilities in a free energy induced by temperature, composition, electric fields and mechanical stresses and their effect on piezoelectric properties. Some general conclusion and perspectives are given in the fourth section.

## 11.2 Deformation of perovskite crystals under external fields

### 11.2.1 Polarization rotation and monoclinic phases

In this section the deformation of tetragonal, orthorhombic and rhombohedral crystals by external fields is considered in terms of polarization rotation and polarization extension (or contraction). Polarization rotation (Fu and Cohen, 2000) in the presence of monoclinic phases (Noheda, 2002; Noheda and Cox, 2006), particularly in the morphotropic phase boundary region of solid solutions, has been widely considered as the main mechanism of the large piezoelectric response along non-polar axes in complex solid solutions, such as  $(1-x)\text{Pb}(\text{Zn}_{1/3}\text{Nb}_{2/3})\text{O}_3-x\text{PbTiO}_3$  (PZN- $x$ PT),  $(1-x)\text{Pb}(\text{Mg}_{1/3}\text{Nb}_{2/3})\text{O}_3-x\text{PbTiO}_3$  (PMN- $x$ PT) and  $\text{Pb}(\text{Zr}, \text{Ti})\text{O}_3$  (PZT). In the monoclinic phases, the polarization is not fixed along a crystallographic axis but is allowed by symmetry to lie anywhere within a single mirror plane. Thus, the  $M_A$  ( $M_B$ ) and  $M_C$  monoclinic states (see Fig. 11.1), with  $[101]_C$  and  $[010]_C$  mirror planes, respectively, form ‘structural bridges’ (Noheda and Cox, 2006) between the  $\langle 111 \rangle_C$ ,  $\langle 101 \rangle_C$  and  $\langle 001 \rangle_C$  polar directions of the  $3m$  rhombohedral (R),  $mm2$  orthorhombic (O) and  $4mm$  tetragonal ( $T$ ) phases typically observed in perovskite ferroelectrics; the subscript ‘C’ means the direction is defined with respect to the cubic axes of the high-temperature, parent phase.

As it appears that there is some confusion in the literature with respect to the role of a monoclinic phase and polarization rotation in enhanced electromechanical properties, it is perhaps useful to emphasize at this stage



11.1 Mirror planes of the monoclinic phases recently suggested at the morphotropic phase boundaries of PZT, PMN-xPT and PZN-xPT. The polar axes of the monoclinic phases are not fixed but can lie anywhere within their mirror plane between the limiting directions of the rhombohedral ( $R$ ), orthorhombic ( $O$ ) and tetragonal ( $T$ ) phases. The notation is that after Vanderbilt and Cohen (2001). Note that  $M_A$  and  $M_B$  planes are equivalent in the pseudocubic presentation.

the following points which will be elaborated further in the text. Firstly, the fact that the polar vector can lie anywhere within the mirror plane of a monoclinic phase does not necessarily imply facility of the polarization rotation within this plane or enhanced electromechanical response. Secondly, the propensity for polarization rotation under external field, as will be discussed below, can be described in terms of the dielectric susceptibility perpendicular to the polar axis and piezoelectric shear coefficients; large electromechanical response along off-polar directions is equivalent to propensity for large polarization rotation. Both have the same microscopic origin and can be phenomenologically described by a thermodynamic instability. Thirdly, it has been shown by Bell (2006) that extension of the usual sixth order LGD function in PZT to include monoclinic phase by adding eighth order terms reveals additional minima in the free energy profile that decrease the barrier between rhombohedral and tetragonal phases. The resulting flatness of the free energy profile is accompanied by a large dielectric susceptibility and an enhanced piezoelectric response (and thus facilitated polarization rotation), regardless of whether the associated monoclinic phase exists spontaneously or is induced by external fields. Fourthly, the large piezoelectric effect in relaxor ferroelectrics and enhanced electromechanical response of simple perovskites along non-polar axes are essentially weak field effects. This means that the polarization does not have to rotate by a large angle for a crystal to exhibit a large piezoelectric effect. However, the crystal must show *propensity* for the large polarization rotation; this propensity is determined

by the large dielectric susceptibility perpendicular to the polar axis and large shear piezoelectric coefficient. By modifying the crystal's free energy, certain configurations of strong external fields may, however, be helpful in making these coefficients particularly large.

We first consider the resultant rotation of the polar vector in a  $4mm$  tetragonal,  $mm2$  orthorhombic or  $3m$  rhombohedral crystal when an electric field  $E$  is applied in a non-polar  $\langle 001 \rangle_C$ ,  $\langle 101 \rangle_C$  or  $\langle 111 \rangle_C$  type direction. Importantly, these are the directions relevant to actuation of domain engineered crystals (Bell, 2001). In order to do this, it is useful to define the direction of the applied field with respect to the principal axes of the crystal ( $x_1, x_2, x_3$ ) for which the dielectric susceptibility matrix is diagonal. In all cases,  $x_3$  is the polar axis, or the direction of spontaneous polarization  $P$ . For a  $4mm$  tetragonal ( $T$ ) crystal, the principal axes are parallel to the crystallographic axes of the high-temperature cubic phase. Thus, the principal axes ( $x_1, x_2, x_3$ ) of the tetragonal phase are  $[100]_T \equiv [100]_C$ ,  $[010]_T \equiv [010]_C$  and  $[001]_T \equiv [001]_C$ , respectively; with respect to these axes, the crystal has non-zero dielectric susceptibilities  $\chi_{11} = \chi_{22}$  and  $\chi_{33}$ . The subscript ' $T$ ' means a direction defined with respect to the principal axes of the tetragonal phase; likewise ' $O$ ' and ' $R$ ' will mean the same for the orthorhombic and rhombohedral phases, respectively. Furthermore, when applying electric field we shall assume a stress-free crystal.

For an  $mm2$  orthorhombic ( $O$ ) crystal, the principal axes ( $x_1, x_2, x_3$ ) are rotated with respect to the cubic axes by  $45^\circ$ ; respectively, they lie along  $[100]_O \equiv [10\bar{1}]_C$ ,  $[010]_O \equiv [010]_C$  and  $[001]_O \equiv [101]_C$ , directions. With respect to these rotated axes, the crystal has three non-zero dielectric susceptibilities,  $\chi_{11}$ ,  $\chi_{22}$  and  $\chi_{33}$ .

Finally, for a  $3m$  rhombohedral ( $R$ ) crystal, the principal axes are chosen such that  $x_1$  is perpendicular to a mirror plane (Nye, 1985). Thus, the axes are commonly chosen to lie along  $[100]_R \equiv [1\bar{1}0]_C$ ,  $[010]_R \equiv [11\bar{2}]_C$  and  $[001]_R \equiv [111]_C$ , the latter being the polar axis (Zhang *et al.*, 2003a; Zhang and Cao, 2004). Note that the first two of these identities are exact only in the pseudocubic approximation. As will be discussed later, the principal axes might also be chosen to be rotated by  $180^\circ$  about the polar axis.

In the general case the polarization change,  $\Delta P_i$ , and mechanical deformation of the crystal,  $\Delta S_j$ , induced by the field component  $E_j$  are described by the usual piezoelectric and dielectric relations (Nye, 1985):

$$\Delta S_i = d_{ji} E_j \quad 11.1$$

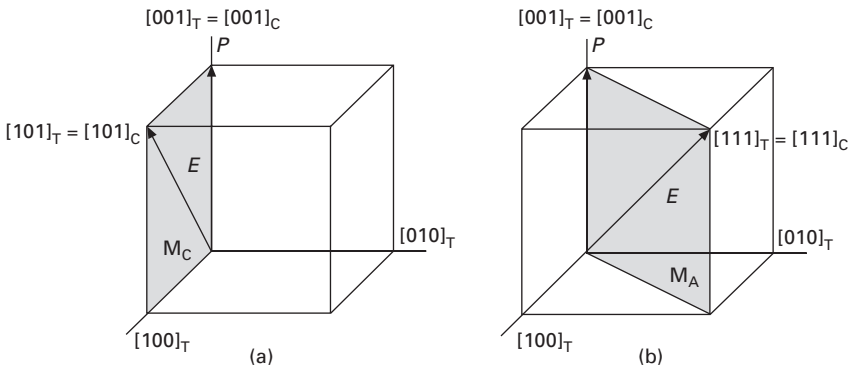
$$\Delta P_i = \epsilon_0 \chi_{ij} E_j \quad 11.2$$

With the polarization vector at zero field and in the crystallographic coordinate system defined as  $(0,0,P_3)$ , the polarization rotation angle  $\theta$  under electric field applied in an arbitrary direction is given by:

$$\tan\theta = \frac{\sqrt{\Delta P_1^2 + \Delta P_2^2}}{P_3 + \Delta P_3} = \frac{\sqrt{(\epsilon_0\chi_{11}E_1)^2 + (\epsilon_0\chi_{22}E_2)^2}}{P_3 + \epsilon_0\chi_{33}E_3} \quad 11.3$$

The field is applied on a free crystal so that the dielectric susceptibilities are taken at zero (constant) stress, i.e.  $\chi_{ij}^\sigma$ . For simplicity, the stress subscript  $\sigma$  is omitted. In crystals of high symmetries such as  $4mm$ ,  $mm2$  and  $3m$ , the deformation described by Eq. [11.1] corresponds to extension (contraction) when the field is applied along the polar direction, e.g.  $\Delta S_3 = d_{33}E_3$ . When the field is applied perpendicular to polarization, for example  $E_1$  in a tetragonal  $4mm$  crystal, the deformation is of shear type, e.g.  $\Delta S_5 = d_{15}E_1$ . Voigt notation is used throughout the text (Nye, 1985).

We first consider application of an electric field  $E$  to a  $4mm$  tetragonal crystal along a  $\langle 110 \rangle_C$  type direction. Without loss of generality, we let the polar vector  $P$  lie along  $[001]_T \equiv [001]_C$  and apply a field along  $[101]_C (\equiv [101]_T)$  in the pseudocubic approximation); this geometry is shown in Fig. 11.2(a). The applied field can be resolved into components  $E_3$  and  $E_1$ , along the  $x_3$  and  $x_1$  principal axes, respectively. Importantly, since there is no component of field along the third principal axis,  $x_2$ , and because the dielectric susceptibility matrix is diagonal, the polar vector will rotate towards the applied field *within* the  $(010)_C$  plane. When this happens, even at infinitesimally small fields, the zero-field  $4mm$  symmetry will be broken. By consideration of all the symmetry elements of the  $4mm$  point group (Nye, 1985), and from Fig. 11.2(a) it can easily be shown that the only remaining symmetry element will be the mirror plane parallel to  $(010)_C$ . In the notation of Vanderbilt and Cohen (2001), this is the  $M_C$  monoclinic plane (see Fig. 11.1). The resultant, field-induced symmetry is monoclinic  $M_C$ .



11.2 Application of an electric field to a  $4mm$  tetragonal ferroelectric along the (a)  $[101]_C$  and (b)  $[111]_C$  directions. Under zero field, the polar vector lies along  $[001]_C$ . Under field, the resultant symmetry will be  $M_C$  and  $M_A$  in (a) and (b), respectively.

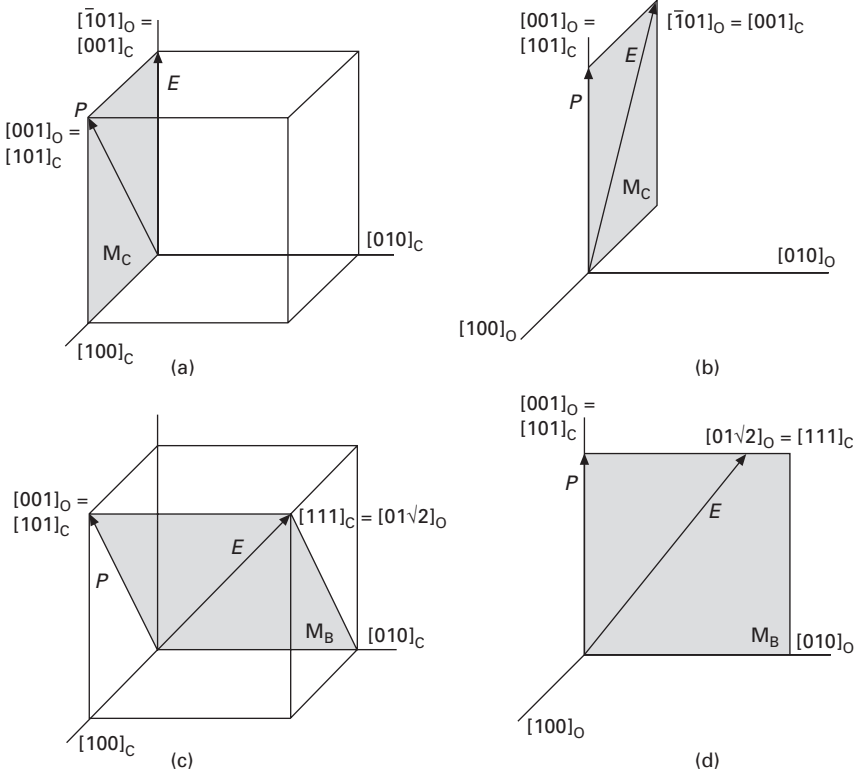
Next, we consider application of an electric field  $E$  to the same crystal, this time along  $\langle 111 \rangle_C$  ( $\equiv [111]_T$  in the pseudocubic approximation) (see Fig. 11.2b). In this case, there are three components of electric field along the three principal axes. Again, the component  $E_3$  will lead to extension of the polar vector. In contrast, the other two components,  $E_1$  and  $E_2$ , will lead to rotations of the polar vector towards the  $x_1$  and  $x_2$  axes. However, since the two transverse dielectric susceptibilities are equal for  $4mm$  symmetry ( $\chi_{11} = \chi_{22}$ ), the polar vector will be constrained to rotate within a plane that bisects the  $x_1$  and  $x_2$  principal axes. That is, it will rotate within a  $M_A$  monoclinic plane (see Fig. 11.2b). The zero-field tetragonal symmetry will be broken under field, with only one mirror plane remaining; the resultant, field-distorted symmetry is monoclinic  $M_A$ .

For an  $mm2$  orthorhombic crystal, we consider application of an electric field along the non-polar  $\langle 011 \rangle_C$  and  $\langle 111 \rangle_C$  directions. Without loss of generality, we first apply an electric field  $E$  along the  $[001]_C \equiv [\bar{1}01]_O$  direction of a crystal whose polar vector  $P$  lies along  $[101]_C \equiv [001]_O$ . This geometry is shown with respect to the cubic axes of the high-temperature phase in Fig. 11.3(a) and with respect to the principal axes of the orthorhombic phase in Fig. 11.3(b). As shown in Fig. 11.3(b), there will be two non-zero components of electric field with respect to the principal axes. Because there is no component of field parallel to the second principal axis, and because the susceptibility matrix is diagonal, the polar vector will rotate towards the applied field in a plane perpendicular to  $x_2$ : that is, a  $M_C$  monoclinic plane. The  $mm2$  orthorhombic symmetry will be broken under field, with the only remaining symmetry element being a  $(010)_C$  mirror plane; the resultant symmetry is monoclinic  $M_C$ . Note that the expression  $[001]_C = [\bar{1}01]_O$  is correct only in the pseudocubic approximation, although this will not affect the general conclusion.

Next we consider application of an electric field to the same orthorhombic crystal along the  $[111]_C \equiv [01\sqrt{2}]_O$  direction; again, this equivalence holds in the pseudocubic approximation. This geometry is shown with respect to the cubic axes in Fig. 11.3(c) and with respect to the principal axes of the orthorhombic phase in Fig. 11.3(d). This time, as shown in Fig. 11.3(d), there is no component of field along the  $x_1$  principal axis. As a result, the polar vector will rotate away from its zero field  $[101]_C \equiv [001]_O$  position, towards the applied field, within a  $M_B$  monoclinic plane. The resultant field-induced symmetry will be monoclinic  $M_B$ .

Lastly, for a  $3m$  rhombohedral crystal we can consider application of an electric field along a non-polar  $\langle 001 \rangle_C$  or  $\langle 101 \rangle_C$  direction. Without loss of generality, we take a crystal with polar vector  $P$  along the  $[111]_C \equiv [001]_R$  direction and first apply an electric field along  $[001]_C \equiv [0\sqrt{2}1]_R$ . This is shown with respect to the cubic axes in Fig. 11.4(a). To complicate matters, with a rhombohedral crystal we have some freedom in how the principal

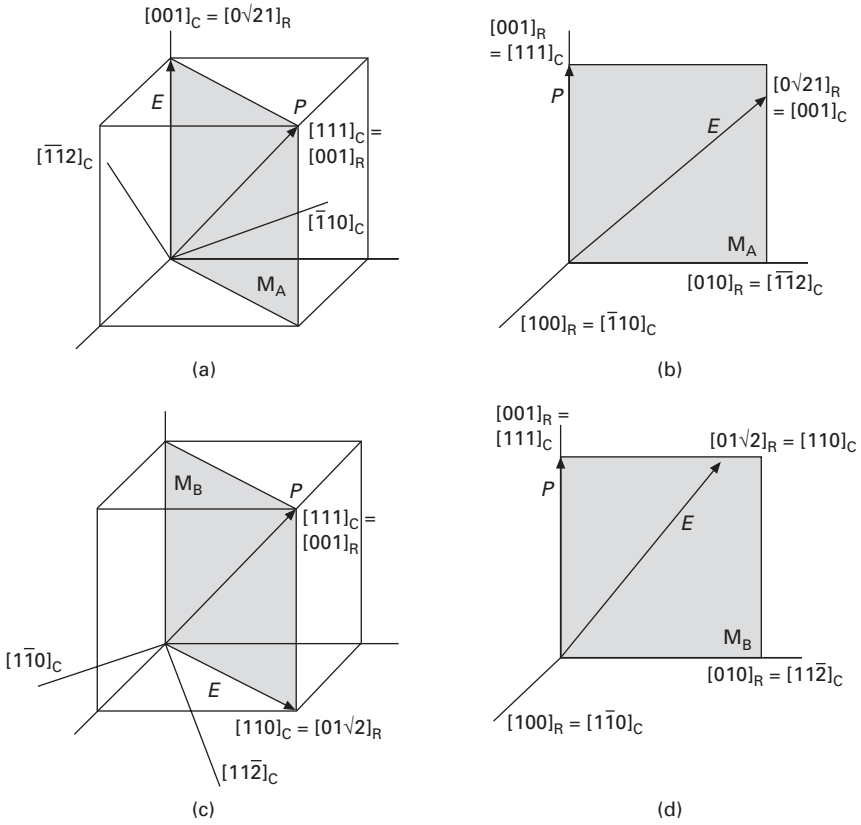




**11.3** Application of an electric field to an  $mm2$  orthorhombic ferroelectric with spontaneous polarization along the  $[101]_C$  direction. In (a), the electric field is applied along the  $[001]_C$  direction; the same situation is shown with respect to the principal axes of the orthorhombic crystal in (b). In (c), the electric field is applied along the  $[111]_C$  direction; the same situation is shown with respect to the principal axes of the orthorhombic crystal in (d). Under field, the resultant symmetry will be  $M_C$  and  $M_B$  in (a) and (c), respectively.

axes are chosen; this has led to a certain amount of confusion in calculations of the piezoelectric coefficient along general non-polar directions in rhombohedral PMN-xPT (Damjanovic *et al.*, 2003ab; Zhang *et al.*, 2003b; Zhang and Cao, 2004). However, as has been discussed elsewhere (Davis, 2006), the second principal axis  $x_2$  can be seen to constitute a secondary polar axis like that found in 32 rhombohedral quartz (Newnham, 2005). For the present purposes, we assume (as justified elsewhere; Davis, 2006) that the secondary polar axis will align itself as close as possible to the applied field. Thus, as shown in Fig. 11.4(a), we choose  $x_2$  to lie along  $[\bar{1}\bar{1}2]_C$ .

The same geometry is shown with respect to the principal axes, within the pseudocubic approximation, in Fig. 11.4(b). As shown, there is no component of electric field along the  $x_1$  axis. Therefore, the polar vector will rotate



**11.4 Application of an electric field to a  $3m$  rhombohedral ferroelectric with spontaneous polarization along the  $[111]_C$  direction.** In (a), the electric field is applied along the  $[001]_C$  direction; the same situation is shown with respect to the principal axes of the rhombohedral crystal in (b). In (c), the electric field is applied along the  $[110]_C$  direction; the same situation is shown with respect to the principal axes of the rhombohedral crystal in (d). Under field, the resultant symmetry will be  $M_A$  and  $M_B$  in (a) and (c), respectively.

within the  $(\bar{1}10)_C$   $M_A$  monoclinic plane towards the direction of applied field. The zero-field rhombohedral symmetry is broken and  $M_A$  monoclinic symmetry results.

Finally, we consider application of an electric field to the same crystal, this time, along the  $[110]_C \equiv [01\sqrt{2}]_R$  direction. Again we assume that the secondary polar axis will align itself as close as possible to the field such that, as shown in Fig. 11.4(c),  $x_2$  is now along  $[11\bar{2}]_C$ . The same geometry is shown with respect to the new principal axes in Fig. 11.4(d). Again, there is no component of field along the  $x_1$  principal axis and the polar vector will rotate within the  $M_B$  monoclinic plane shown. The zero-field rhombohedral

symmetry is broken, even upon application of an infinitesimally small field, and monoclinic  $M_B$  symmetry results.

In summary,  $M_A$ ,  $M_B$  or  $M_C$  monoclinic symmetry can be expected whenever a field (even infinitesimally small) is applied to a rhombohedral, orthorhombic or tetragonal crystal in a non-polar  $\langle 001 \rangle_C$ ,  $\langle 101 \rangle_C$  or  $\langle 111 \rangle_C$  type direction. As soon as the electric field is applied, polarization rotation occurs which breaks the higher-order, zero-field symmetry. The remaining symmetry element is a single mirror plane such that the resultant symmetry is monoclinic  $M_A$ ,  $M_B$  or  $M_C$ . Therefore, field-induced monoclinic symmetries can be expected in truly zero-field rhombohedral, orthorhombic or tetragonal crystals; this is a simple consequence of external field configuration and the intrinsic symmetry of the R, O and T phases. As mentioned above, monoclinic phases can also occur spontaneously (without field assistance) especially in the morphotropic phase boundary region of the solid solutions (Noheda and Cox, 2006). More on field-induced monoclinic distortion and field-induced phases can be found in Davis *et al.* (2006) and Davis (2007). Most often, the field-induced polarization path is more complex than suggested by the simplified pictures given above. Polarization rotation between two end members (e.g. R  $\rightarrow$  T via  $M_A$  plane), for example, may be continuous at weak fields only with polarization jumping discontinuously at a critical field through a first order-like phase transition to the other end member (Davis *et al.*, 2006). Even more complex behavior with polarization moving, e.g. via R- $M_A$ - $M_C$ -T path with multiple first order-like phase transitions has been observed experimentally (Noheda *et al.*, 2001; Davis *et al.*, 2006) and predicted by first principles calculations (Bellaiche *et al.*, 2001).

In their ferroelectric phase, the crystals' polarization can be modified by stress, the main effect being through the piezoelectric coupling. In the simplest case of  $4mm$  tetragonal material, the tensile or compressive stresses applied along or perpendicular to the polar axis have the same role as electric field bias along the polarization direction, resulting in extension or contraction of polarization. Shear stresses have a similar role as electric fields applied perpendicular to polarization and will result in polarization rotation. We take as an example a tetragonal crystal in short circuit condition with polarization  $P_3$  along the  $x_3$  axis. Shear stress  $\sigma_5 \equiv \sigma_{13}$ ,  $\sigma_{31}$  creates charge  $\Delta P_1$  on  $(100)_C$  plane through piezoelectric effect  $\Delta P_1 = d_{15}\sigma_5$ , where  $d_{15}$  is the shear piezoelectric coefficient (Nye, 1985). This effectively rotates the polarization vector from  $(0,0,P_3)$  to  $(\Delta P_1, 0, P_3)$ , that is from  $[001]_C$  toward  $[101]_C$  within  $M_C$  plane; the resulting symmetry is monoclinic. Clearly, the larger the shear piezoelectric coefficient the larger the polarization rotation. Similar structure-polarization rotation relations can be derived for other symmetries and stress configurations. It is implied in the above discussion that the crystal also deforms elastically, the deformation being described by:  $S_i = s_{ij}^E \sigma_j$ , where  $s_{ij}^E$  is elastic compliance at short circuit condition.

### 11.2.2 Polarization rotation vs. polarization extension: 'rotator' and 'extender' ferroelectrics and domain engineering

We have seen in the previous section that the extent of polarization rotation under an applied electric field or mechanical stress is related to the shear deformation of the crystal lattice, as determined by the piezoelectric shear coefficients such as  $d_{15}$  and  $d_{24}$ . In contrast, the relative extension (contraction) of the polar vector under an applied field is related to the collinear piezoelectric effect, as quantified by the longitudinal piezoelectric coefficient such as  $d_{33}$ . The piezoelectric coefficients are in turn related to the dielectric susceptibilities through thermodynamic phenomenological relations  $d \propto \chi Q P^2$  (Haun *et al.*, 1989a,b) where  $Q$  are electrostrictive coefficients. These relations are consequence of the coupling of spontaneous strain,  $S_s$ , and spontaneous polarization  $P_s$ :  $S_s = Q P_s^2$  (Haun *et al.*, 1989a,b). As may be expected from the discussion above, the piezoelectric shear coefficients are related to dielectric susceptibilities perpendicular to polarization axis,  $\chi_{11}$  and  $\chi_{22}$ , while the piezoelectric longitudinal and transverse coefficients are related to the longitudinal dielectric susceptibility  $\chi_{33}$ . In tetragonal  $4mm$  crystals for example,  $d_{33} = 2\varepsilon_0\chi_{33}Q_{11}P_3$  and  $d_{15} = \varepsilon_0\chi_{11}Q_{44}P_3$ .

In a crystal with  $4mm$ ,  $mm2$  or  $3m$  symmetries and with polarization expressed in the crystallographic coordinate system,  $P = (0,0,P_3)$ , an application of electric field  $E_3$  or stress  $\sigma_3$  along the polar direction will lead to a lengthening (or contraction) of the polar vector by an amount  $\Delta P = (0,0,\Delta P_3)$  where  $\Delta P_3 = \varepsilon_0\chi_{33}E_3$  or  $\Delta P_3 = d_{33}\sigma_3$ . Because the dielectric susceptibility matrix is diagonal, there is no change in the perpendicular components of the polar vector (no polarization rotation). To avoid confusion between expressions given in the cubic crystallographic system, as is often made in the LGD approach, and the crystallographic coordinate system, we shall in the remaining text discuss the tetragonal  $4mm$  phase only, where these expressions are identical. For a more general case, the reader can consult Davis *et al.* (2007). Using the phenomenological relation  $d_{33} = 2\varepsilon_0\chi_{33}Q_{11}P_3$  (Haun *et al.*, 1989a,b; Budimir *et al.*, 2003), the relative extension of the polar vector expressed in terms of the electric field and stress is:

$$\frac{\Delta P_3}{P_3} = \frac{\varepsilon_0\chi_{33}E_3}{P_3} = \frac{d_{33}E_3}{2P_3^2Q_{11}} \quad 11.4$$

$$\frac{\Delta P_3}{P_3} = \frac{d_{33}\sigma_3}{P_3} \quad 11.5$$

that is, it is proportional to  $d_{33}$  and  $\chi_{33}$ . The polarization rotation angle  $\theta$  is zero.

In contrast, if an electric field is applied perpendicular to the polar vector,

the polar vector will rotate away from its original position by some angle  $\theta$ . For the special case of an electric field applied along the principal  $x_1$  axis or a shear stress  $\sigma_5$ , there will be a change in polarization given by  $\Delta P = (\Delta P_1, 0, 0)$  where  $\Delta P_1 = \epsilon_0 \chi_{11} E_1$  or  $\Delta P_1 = d_{15} \sigma_5$ .

The change of the polarization in terms of the electric field is given by:

$$\Delta P_1 = \epsilon_0 \chi_{11} E_1 = \frac{d_{15} E_1}{P_3 Q_{44}} \quad 11.6$$

while the relative change also defines the angle of polarization rotation:

$$\tan \theta = \frac{\Delta P_1}{P_3} = \frac{d_{15} E_1}{P_3^2 Q_{44}} = \frac{\epsilon_0 \chi_{11} E_1}{P_3} \quad 11.7$$

$$\tan \theta = \frac{\Delta P_1}{P_3} = \frac{d_{15} \sigma_5}{P_3} \quad 11.8$$

That is, rotation of the polar vector is directly proportional to the piezoelectric shear coefficient  $d_{15}$  and dielectric susceptibility perpendicular to polarization  $\chi_{11}$ . Similar relations are valid for  $mm2$  and  $3m$  point groups (Budimir *et al.*, 2003; Davis *et al.*, 2007).

In summary, polarization extension is strongest in materials with a large longitudinal coefficient  $d_{33}$ , which in turn is due to a large  $\chi_{33}$ . Polarization rotation is strongest in materials with a large shear coefficient  $d_{15}$  (or  $d_{24}$ ) due to a large transverse susceptibility  $\chi_{11}$ . Therefore, when an electric field is applied in some arbitrary direction, the relative contributions to the piezoelectric response from polarization extension (due to any component of field along the polar axis) and polarization rotation (due to any perpendicular component) will be described by the ratios  $d_{15}/d_{33}$  and  $\chi_{11}/\chi_{33}$ , the *piezoelectric* and *dielectric anisotropy factors*, respectively. The two are related via thermodynamic phenomenological equations  $d \propto \chi QP$ .

Let us consider as examples  $\text{BaTiO}_3$  and  $\text{PbTiO}_3$  monodomain single crystals and estimate numerically polarization rotation and anisotropy factors. Numerical values are taken from phenomenological calculations (Budimir *et al.*, 2003). In  $\text{PbTiO}_3$ , at 298 K, with  $d_{33} = 79$  pC/N,  $d_{15} = 56$  pC/N,  $\chi_{33} = 66$ ,  $\chi_{11} = 124$ ,  $P_3 = 0.75$  C/m<sup>2</sup> and the simplest stress (or electric field) configuration with only  $\sigma_1$  (or  $E_1$ ) or  $\sigma_3$  (or  $E_1$ ) applied, the relative polarization extension, Eqs [11.4 and 11.5], is  $\Delta P_3/P_3 = 1.05 \times 10^{-10} \sigma_3$  and  $88 \epsilon_0 E_3$ , while the relative polarization rotation, Eqs [11.6 and 11.7], is  $\Delta P_1/P_3 = 0.74 \times 10^{-10} \sigma_1$  and  $165 \epsilon_0 E_3$ . In  $\text{BaTiO}_3$ , at the same conditions and with  $d_{33} = 99$  pC/N,  $d_{15} = 457$  pC/N,  $\chi_{33} = 192$ ,  $\chi_{11} = 3300$  and  $P_3 = 0.265$  C/m<sup>2</sup>, the relative polarization extension is  $\Delta P_3/P_3 = 3.7 \times 10^{-10} \sigma_3$  and  $724 \epsilon_0 E_3$  while the relative polarization rotation is  $\Delta P_1/P_3 = 17.2 \times 10^{-10} \sigma_1$  and  $12452 \epsilon_0 E_3$ .

Two conclusions can be drawn from these values. First, at 298 K,  $\text{BaTiO}_3$  is in all directions dielectrically and thus piezoelectrically much softer than

PbTiO<sub>3</sub>. Second, propensity of BaTiO<sub>3</sub> to polarization rotation is much higher than for polarization extension (contraction). This can be clearly seen when comparing the dielectric and piezoelectric anisotropy factors  $d_{15}/d_{33} = 0.71$  and  $\chi_{11}/\chi_{33} = 1.87$  for PbTiO<sub>3</sub> and  $d_{15}/d_{33} = 4.59$  and  $\chi_{11}/\chi_{33} = 17.1$  for BaTiO<sub>3</sub>. Numerical examples for a large number of other crystals are given in Davis *et al.* (2007). Before discussing origins of this large difference in BaTiO<sub>3</sub> and PbTiO<sub>3</sub>, we shall first show how these results are related to high or enhanced electromechanical activity along the non-polar axis and to the concept of domain engineering.

Consider for example orientation dependence of the longitudinal  $d_{33}$  piezoelectric coefficient. For crystals with symmetry  $4mm$  this dependence is given by:

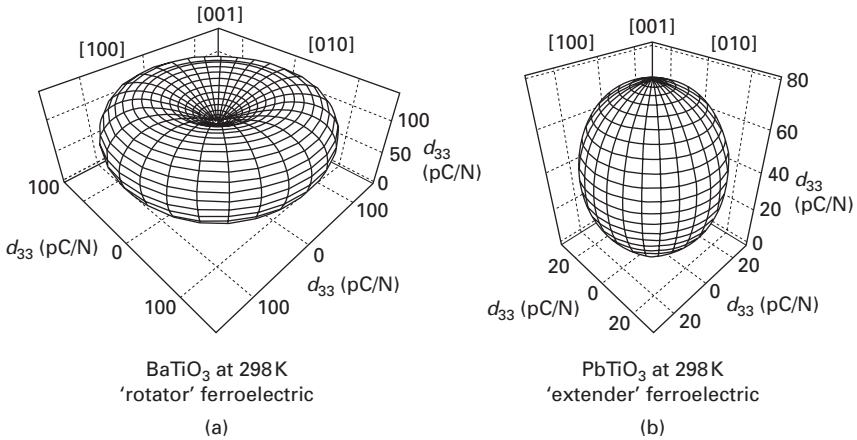
$$d_{33}^*(\theta) = \cos\theta[(d_{15} + d_{31}) \sin^2\theta + d_{33} \cos\theta] \quad 11.9$$

where the asterisk denotes coefficient measured along a direction defined by the Euler angle  $\theta$  ( $\theta$  defines the angle away from the polar axis) and  $d_{ij}$  are coefficients in the crystallographic coordinate system. Equations for  $mm2$  and  $3m$  symmetries as well as definition of Euler angles used can be found in Damjanovic *et al.* (2006). It can be easily shown (Damjanovic *et al.*, 2002) that in crystals with  $4mm$  symmetry the maximal  $d_{33}^*(\theta)$  can appear along a non-polar axis (i.e.  $\theta \neq 0^\circ$ ) only if:

$$\frac{d_{15}}{d_{33}} > \frac{3}{2} - \frac{Q_{12}}{Q_{11}} \quad 11.10$$

The number  $3/2 - Q_{12}/Q_{11}$  is slightly less than 2 for most compounds (1.9 in BaTiO<sub>3</sub> and 1.8 in PbTiO<sub>3</sub>) and is assumed to be temperature independent. Similar relations can be derived for other point groups (Davis *et al.*, 2007). The condition Eq. [11.10] is clearly related to polarization rotation and extension Eqs [11.4 and 11.8] and piezoelectric anisotropy factors introduced above. If  $d_{33}^*(\theta)$  is plotted for BaTiO<sub>3</sub> and PbTiO<sub>3</sub> (Figure 11.5), one finds that for lead titanate with a small  $d_{15}$  and small anisotropy factors ( $d_{15}/d_{33} = 0.71$  and  $\chi_{11}/\chi_{33} = 1.87$ )  $d_{33}^*(\theta)$  exhibits a maximum along the polar axis; BaTiO<sub>3</sub> with a large  $d_{15}$  and large anisotropy factors ( $d_{15}/d_{33} = 4.59$  and  $\chi_{11}/\chi_{33} = 17.1$ ) exhibits a maximum  $d_{33}^*(\theta)$  along a non-polar axis.

Crystals for which  $d_{33}^*(\theta)$  has a maximal value along the polar axis, the polarization extension (contraction) is stronger than polarization rotation and are called ‘extender’ ferroelectrics; crystals in which polarization rotation is stronger are called ‘rotator’ ferroelectrics (Davis *et al.*, 2007). Whether a crystal is a ‘rotator’ or ‘extender’ may depend on temperature, the presence of ferroelectric–ferroelectric phase transitions, and external fields. It turns out that most crystals with rhombohedral and orthorhombic structure are ‘rotators’ while those with tetragonal structure tend to be ‘extenders’. This general behavior appears to be related to anisotropy and electrostrictive



11.5 Orientation dependence of  $d_{33}^*(\theta)$  for (a) BaTiO<sub>3</sub> and (b) PbTiO<sub>3</sub> at 298 K. The maximum  $d_{33}^*(\theta)$  for BaTiO<sub>3</sub> is along a non-polar axis, and it is along polar axis [001] for PbTiO<sub>3</sub>.

properties of oxygen octahedra, the main building block of many oxide ferroelectrics (Yamada, 1972; Davis *et al.*, 2007). Giant piezoelectric response off-polar axis in relaxor-ferroelectrics, PMN- $x$ PT and PZN- $x$ PT, is due to exceptionally strong 'rotator' characteristics and, in particular, a large piezoelectric shear coefficients. In PMN-30PT, for example, the piezoelectric and dielectric anisotropy factors are  $d_{15}/d_{33} \approx 21$  and  $\chi_{11}/\chi_{33} \approx 6.2$ , with  $d_{15} \approx 4100$  pC/N,  $d_{33} \approx 190$  pC/N,  $\chi_{11} \approx 3950$  and  $\chi_{33} \approx 640$  (Zhang *et al.*, 2003b).

In compounds that change symmetry with temperature, such as BaTiO<sub>3</sub>, the 'rotator/extender' character is a function of temperature. Interestingly, BaTiO<sub>3</sub> changes its character within its tetragonal phase: it is an 'extender' close to the ferroelectric-paraelectric phase transition temperature and is a 'rotator' close to tetragonal-orthorhombic phase transition temperature, see Fig. 11.5 and Budimir *et al.* (2003). Lead titanate, which is tetragonal throughout the temperature range of its ferroelectric phase, is a strong 'extender'. However, as shall be shown later, its 'extender' character can be broken by suitably applied external fields. On the other hand, external fields or temperature can increase 'extender' character of certain crystals and thus strongly enhance their piezoelectric response along the polar axis. This is also the case for PbTiO<sub>3</sub> and will be discussed in the following sections. This result hints that the polarization rotation is not the only way the piezoelectric response may be increased. This leads us to the next section in which we shall use the LGD thermodynamic approach to look for a deeper, common origin of the enhanced piezoelectric response of ferroelectric crystals. It will be shown that the thermodynamic origin of the enhancement lies in the instability of a free energy function, regardless whether this instability is

caused by composition variation at a morphotropic phase boundary, temperature-induced phase transitions, or electric field and stress-induced metastable states. It will be further shown that whether the enhancement happens by polarization rotation or by polarization extension (contraction) is determined by the anisotropy of the free energy profile.

Polarization rotation is used for increasing the piezoelectric response of some crystals by so-called domain engineering (see Chapter 10). According to the definition of Bell (2001), a domain engineered crystal is one which has been poled by the application of a sufficiently high field along one of the possible polar axes of the crystal other than the zero-field polar axis, creating a set of domains in which the polarizations are oriented such that their angles to the poling direction are minimized. In a perovskite material there are therefore three possible sets of poling directions  $\langle 111 \rangle_C$ ,  $\langle 101 \rangle_C$  and  $\langle 001 \rangle_C$ , if monoclinic phases are ignored (Wada *et al.*, 1998, 1999, 2004, 2005 Park *et al.*, 1999; Park and Shrout, 1997; Erhart and Cao, 2003, Erhart, 2004; Davis *et al.*, 2005). Obviously, domain engineering can be used to enhance (increase) piezoelectric properties only in ‘rotator’ ferroelectrics; indeed, the domain engineered crystals with the largest enhancement of the piezoelectric properties are strong ‘rotators’ such as PMN- $x$ PT and PZN- $x$ PT (Park and Shrout, 1997). In contrast, ‘extender’ ferroelectrics such as PbTiO<sub>3</sub>, where the zero-field piezoelectric coefficient is highest along the polar axis, will not profit from domain engineering. Thus,  $d_{33}^*$  for example, can be enhanced only by domain-engineering in ‘rotator’ ferroelectrics. As already mentioned, this can be changed under external bias fields (electric or mechanical).

Since poling along the zero-field non-polar direction creates domain walls in the crystals, the question is posed whether enhanced piezoelectric response is due to the presence of domain walls or is related to piezoelectric anisotropy (that is, their intrinsic ‘rotator’ character). It can be shown that in some domain engineered crystals the enhancement is largely accomplished by their ‘rotator’ character (Damjanovic *et al.*, 2003b; Zhang *et al.*, 2003b). However, there is strong evidence that increased density of domain walls in domain engineered crystals can further enhance this intrinsic effect (Wada *et al.*, 2004, 2005). The effect seems to be related to the broadening of the domain walls by the driving field (Rao and Wang, 2007).

### 11.3 Anisotropy of a free energy and piezoelectric enhancement

In this section we discuss enhancement of the piezoelectric effect in terms of the crystal’s free energy. It will be shown that the enhancement may be induced by proximity of thermally induced phase transitions, by presence of a morphotropic phase boundary, and by special configurations of external electric field and stresses. In each case, the origin of the piezoelectric (and



dielectric) enhancement can be traced to instabilities or metastable states of the free energy; term ‘flattening of a free energy profile’ is used to describe associated reduction of the energy barrier between states. A dominant ‘rotator’ or ‘extender’ characteristic of a crystal is a consequence of the anisotropic flattening of the free energy.

### 11.3.1 Gibbs free energy

In the framework of the Landau–Ginzburg–Devonshire phenomenological model (Devonshire, 1949, 1951), the Gibbs free energy  $\Delta G$  of a ferroelectric crystal with symmetry  $4mm$ ,  $mm2$  or  $3m$  can be expressed in the coordinate system of the parent  $m3m$  cubic paraelectric phase as (Haun *et al.*, 1989a; Bell, 2001):

$$\begin{aligned}
 \Delta G = & \alpha_1(P_1^2 + P_2^2 + P_3^2) + \alpha_{11}(P_1^4 + P_2^4 + P_3^4) \\
 & + \alpha_{12}(P_1^2 P_2^2 + P_2^2 P_3^2 + P_1^2 P_3^2) + \alpha_{111}(P_1^6 + P_2^6 + P_3^6) \\
 & + \alpha_{112}[P_1^4(P_2^2 + P_3^2) + P_2^4(P_1^2 + P_3^2) + P_3^4(P_1^2 + P_2^2)] \\
 & + \alpha_{123}(P_1^2 P_2^2 P_3^2) - \frac{1}{2} s_{11}^D(\sigma_1^2 + \sigma_2^2 + \sigma_3^2) \\
 & - s_{12}^D(\sigma_1 \sigma_2 + \sigma_2 \sigma_3 + \sigma_1 \sigma_3) - \frac{1}{2} s_{44}^D(\sigma_4^2 + \sigma_5^2 + \sigma_6^2) \\
 & - Q_{11}(\sigma_1 P_1^2 + \sigma_2 P_2^2 + \sigma_3 P_3^2) - Q_{12}[\sigma_1(P_2^2 + P_3^2) \\
 & + \sigma_2(P_1^2 + P_3^2) + \sigma_3(P_1^2 + P_2^2)] \\
 & - Q_{44}(\sigma_4 P_2 P_3 + \sigma_5 P_1 P_3 + \sigma_6 P_1 P_2) \\
 & - E_1 P_1 - E_2 P_2 - E_3 P_3
 \end{aligned} \tag{11.11}$$

where  $\alpha$ s are dielectric stiffnesses,  $P_i$  the polarization,  $E_i$  the electric field,  $\sigma_i$  stress components in Voight notation,  $s_{ij}^D$  elastic compliances at constant polarization, and  $Q_{ij}$  electrostrictive constants. Under zero field conditions, in the tetragonal phase  $P_1 = P_2 = 0$ ,  $P_3 \neq 0$ , in the orthorhombic  $P_1^2 = P_3^2 \neq 0$ ;  $P_2 = 0$  and in the rhombohedral phase  $P_1^2 = P_2^2 = P_3^2 \neq 0$ . The spontaneous polarization is calculated from the stability condition  $\partial G / \partial P_i = 0$ . The absolute dielectric susceptibilities  $\chi_{ij}$  are defined as  $\chi_{ij} = [\partial^2 G / \partial P_i \partial P_j]^{-1}$ . The piezoelectric coefficients  $g$  are determined from  $g_{im} = \partial^2 G / \partial P_i \partial \sigma_m$  and the  $d$  coefficients, which are the only ones considered here, as  $d_{im} = \chi_{ik} g_{km}$  (Haun *et al.*, 1989a). Coefficients  $\alpha$  may be temperature dependent (Wang *et al.*, 2006). For the present purposes they are taken from Bell (2001) for BaTiO<sub>3</sub>, from Haun *et al.* (1987) for PbTiO<sub>3</sub>, and from Haun *et al.* (1989b) for Pb(Zr,Ti)O<sub>3</sub>. By definition, negative  $\sigma_i$  and  $E_i$  values have the meaning of compressive stress and electric field applied antiparallel to crystal axes (Amin *et al.*, 1989). Note that all coefficients in [11.11] are assumed to be independent on external fields.

In the description of ferroelectric perovskites it is common to terminate function [11.11] with the sixth order terms (Mitsui *et al.*, 1976; Lines and

Glass, 1979). The need for the theory with higher-order terms has emerged with the discovery of the monoclinic phase in PZT (Vanderbilt and Cohen, 2001; Bell, 2006) and recent attempts to describe some details of the BaTiO<sub>3</sub> behavior under pressure (Li *et al.*, 2005; Wang *et al.*, 2006). Atomistic origins of the strong anharmonicity indicated by the presence of eighth order terms are probably related to the mixed order–disorder and displacive character of the paraelectric–ferroelectric phase transition in BaTiO<sub>3</sub> (Zalar *et al.*, 2003) and by chemical disorder in PZT (Vanderbilt and Cohen, 2001). For the present purposes, the sixth order series [11.11] is considered to be sufficient. For further discussion, the reader is advised to consult articles by Vanderbilt and Cohen (2001) and Bell (2006).

### 11.3.2 Thermally induced phase transitions and ‘rotator’ character

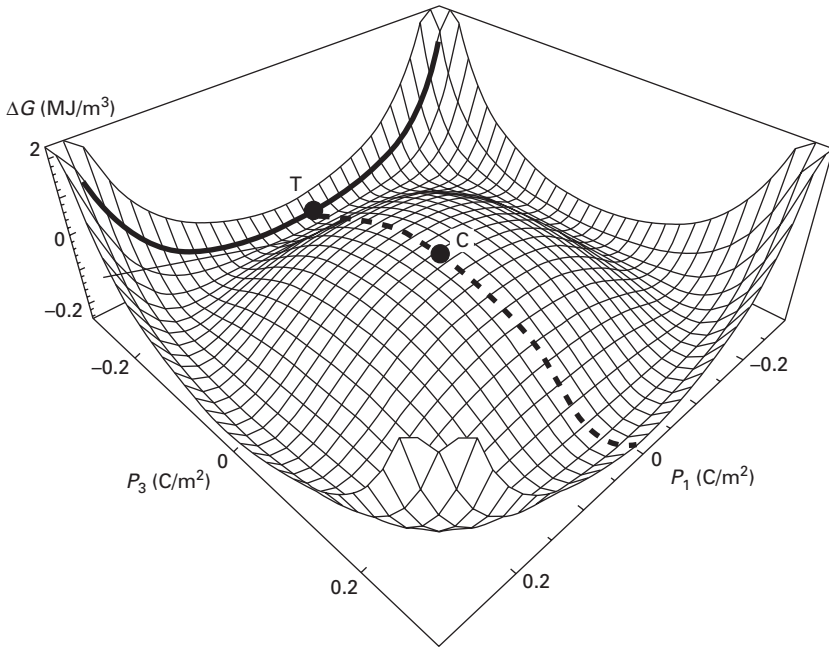
Consider now Eq. [11.11] for a tetragonal crystal, such as BaTiO<sub>3</sub>, and the influence of incipient orthorhombic phase on its anisotropy. BaTiO<sub>3</sub> is a well-known ferroelectric material which on cooling transforms from cubic *m3m* phase to tetragonal *4mm* phase at  $\approx 400$  K, to orthorhombic *mm2* phase at  $\approx 280$  K and to rhombohedral *3m* phase at  $\approx 210$  K (Ishidate *et al.*, 1997) With  $E_i = 0$ ,  $\sigma_i = 0$ , Eq. [11.11] becomes (Budimir *et al.*, 2005):

$$\begin{aligned} \Delta G = & \alpha_1 (P_1^2 + P_3^2) + \alpha_{11} (P_1^4 + P_3^4) + \alpha_{12} (P_1^2 P_3^2) \\ & + \alpha_{111} (P_1^6 + P_3^6) + \alpha_{112} [P_1^4 P_3^2 + P_3^4 P_1^2] \end{aligned} \quad 11.12$$

which is graphically shown in Fig. 11.6 at 298 K.

Two profiles of  $\Delta G(P_1, P_3)$  are marked in Fig. 11.6: the solid line represents  $\Delta G(P_1, P_3 = 0.26)$  and the dashed line  $\Delta G(P_1 = 0, P_3)$ . The flatness of the former indicates propensity of the crystal for polarization rotation from polar axis [001]<sub>C</sub> toward [101]<sub>C</sub>, i.e. within M<sub>C</sub> plane (see Fig. 11.2a) while the flatness of the latter indicates propensity for polarization elongation (contraction) along the polar axis [001]<sub>C</sub>. The profiles are extracted for two temperatures, 298 K and 378 K, and shown in Fig. 11.7 together with orientation dependence of  $d_{33}^*(\theta)$  at each temperature.

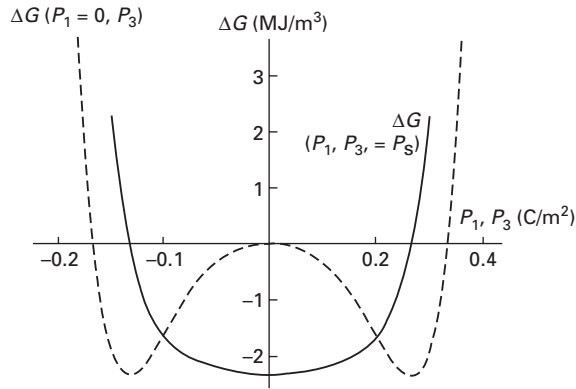
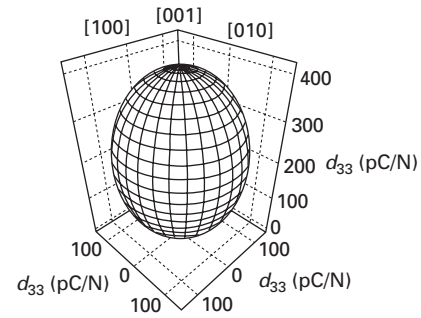
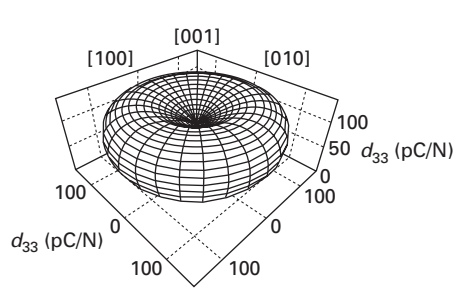
At 298 K (Fig. 11.7a) close to the tetragonal–orthorhombic phase transition temperature ( $\approx 278$  K), the free energy profile corresponding to polarization rotation within the M<sub>C</sub> plane (solid line) is flatter than along the [001]<sub>C</sub> direction (dashed line), indicating large anisotropy factors ( $d_{15}/d_{33} = 4.6$ ,  $\chi_{11}/\chi_{33} = 17.1$ ) (Budimir *et al.*, 2003). The crystal behaves as a rotator and  $d_{33}^*(\theta)$  exhibits maximum along a non-polar direction. At 378 K (Fig. 11.7b) closer to the ferroelectric–paraelectric phase transition temperature ( $\approx 400$  K), the free energy profile is flatter along the polar axis. The anisotropy factors are small ( $d_{15}/d_{33} = 0.6$ ,  $\chi_{11}/\chi_{33} = 2.2$ ), indicating the ‘extender’



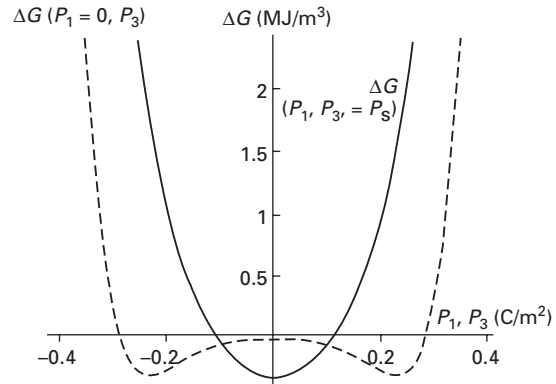
11.6 The Gibbs free energy  $\Delta G$  for BaTiO<sub>3</sub> at 298K calculated from Eq. [11.11]. The solid line shows  $\Delta G$  for variable  $P_1$  and for  $P_3 = 0.26 \text{ C/m}^2$ , i.e. at the zero-field value of the spontaneous polarization at this temperature. This energy profile indicates propensity of the crystal for polarization rotation within  $M_C$  plane. The dashed line shows  $\Delta G$  for variable  $P_3$  and for  $P_1 = 0$ . This energy profile indicates propensity of the crystal for polarization extension. C indicates point of the cubic phase ( $P_1 = 0$ ,  $P_3 = 0$ ), which is not stable at this temperature. See also Budimir *et al.* (2005) and Damjanovic (2005).

character that is reflected in the maximum of  $d_{33}^*(\theta)$  along the polar axis (Budimir *et al.*, 2003).

It is easy to understand why the proximity of a phase transition qualitatively changes the behavior of BaTiO<sub>3</sub> from ‘extender’ to ‘rotator’ and leads to anisotropic flattening of the free energy. The polarization of BaTiO<sub>3</sub> in orthorhombic phase lies along  $[101]_C$ . When the crystal in its tetragonal phase approaches the tetragonal–orthorhombic phase transition temperature it softens along the direction perpendicular to the polar axis ( $\chi_{11}$  and  $d_{15}$  become high) anticipating the new direction of polarization. Close to the tetragonal–paraelectric phase transition temperature the crystal behaves as ‘extender’, softening along the polar axis ( $\chi_{33}$  and  $d_{33}$  become high) anticipating disappearance of the polarization in the cubic phase. These behaviors are analogous to the Curie law in the permittivity above ferroelectric–paraelectric phase transition temperature where crystal becomes soft along the future



(a) BaTiO<sub>3</sub> – ‘rotator’ at 298 K



(b) BaTiO<sub>3</sub> – ‘extender’ at 378 K

11.7 Profiles of  $\Delta G(P_1, P_3)$  corresponding to profiles marked in Fig. 11.6 and orientation dependence of  $d_{33}^*(\theta)$  for BaTiO<sub>3</sub> at 298 K and 378 K: (a) at 298 K, close to the tetragonal–orthorhombic phase transition temperature; (b) at 378 K, closer to the ferroelectric–paraelectric phase transition temperature. See text and caption of Fig. 11.6 for details.

polar direction (Budimir *et al.*, 2003) tens of degrees before the actual phase transition takes place.

### 11.3.3 Compositionally induced phase transitions: morphotropic phase boundary

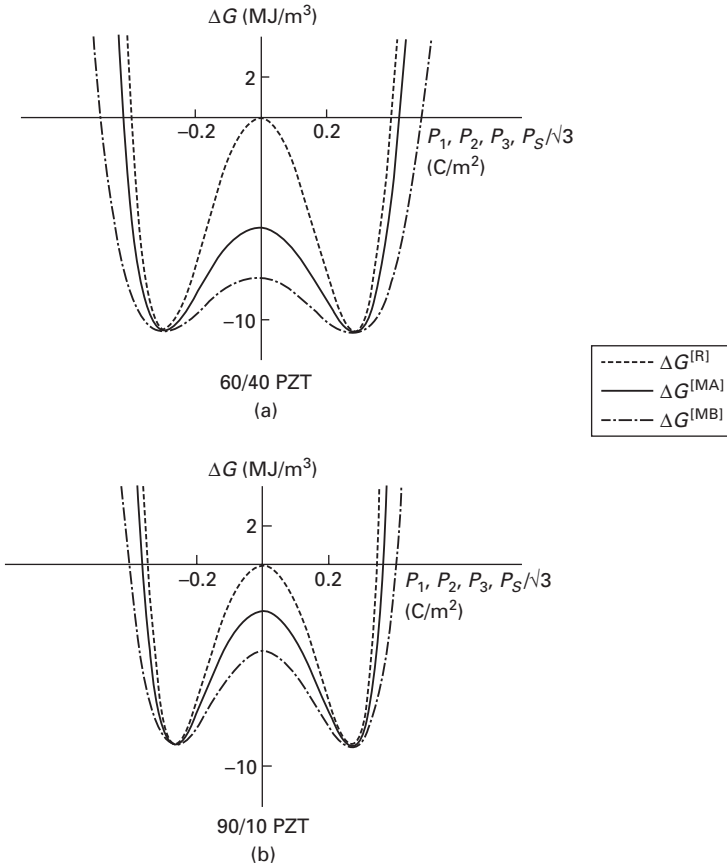
A detailed discussion of the behavior of tetragonal and rhombohedral PZT at each side of the morphotropic phase boundary (MPB) is given in Damjanovic (2005). The phenomenological equation [11.11] cannot describe the monoclinic phase (Noheda *et al.*, 1999) and the discussion is limited to compositions some 10% away from the MPB at Zr/Ti ratio 52/48. For description of the monoclinic phase, see Bell (2006) and Vanderbilt and Cohen (2001).

Thermodynamically, the MPB behaves just like thermally induced phase transitions discussed in the previous section. At the MPB the polarization changes orientation from  $[111]_C$  on the rhombohedral side to  $[001]_C$  on the tetragonal side. In agreement with general behavior of oxygen octahedral perovskites (Section 11.2.2 and Davis *et al.*, 2007) the material changes character from 'extender' on the tetragonal side to 'rotator' on the rhombohedral side of the MPB.

This behavior is accompanied with the anisotropic flattening of the Gibbs free energy as compositions approach the MPB from either side, as shown in Fig. 11.8 for two rhombohedral compositions. On the rhombohedral side, i.e. in 'rotator' compositions, the free energy is flattest along non-polar directions, with propensity for polarization rotation under weak fields being stronger within  $M_B$  than within  $M_A$  plane ( $M_C$  plane not examined) and propensity for polarization extension (i.e. change along polar axis) being the weakest. On the tetragonal side (not shown) the material is softest along polar axis in all compositions. As expected, and clearly seen from Fig. 11.8, the anisotropy increases on approaching the MPB. The above discussion is valid for mono domain single crystals. In ceramics, the complex electro-elastic boundary condition at each grain must be taken into account. The present behaviour may be qualitatively different in ceramics having the same nominal composition as crystals.

### 11.3.4 Electric field and stress-induced enhancement of the piezoelectric properties

Discussions in Sections 11.3.2 and 11.3.3 show that thermally and compositionally induced enhancements of the piezoelectric properties are correlated with increase in free energy instability as phase transitions are approached. Phase transitions can be induced by electric fields and stresses (Davis *et al.*, 2006) and, thermodynamically, the same qualitative effect on



11.8 The Gibbs free energy as a function of polarization for two rhombohedral PZT compositions: (a)  $\text{Pb}(\text{Zr}_{0.6}\text{Ti}_{0.4})\text{O}_3$  (PZT 60/40) and (b)  $\text{Pb}(\text{Zr}_{0.9}\text{Ti}_{0.1})\text{O}_3$  (PZT 90/10). The composition PZT 60/40, which is closer to the morphotropic phase boundary (at Zr/Ti ratio 52/48), has flatter profiles and higher permittivities and piezoelectric properties than PZT 90/10. In both compositions profiles  $\Delta G^{[MA]}$  and  $\Delta G^{[MB]}$  are flatter and energy barrier lower along the directions away from the polar axis than the profile along the polar axis (represented by  $\Delta G^{[R]}$ ), indicating ‘rotator’ character. For details, see Damjanovic, 2005).

piezoelectric anisotropy is obtained as with thermally and compositionally induced instabilities.

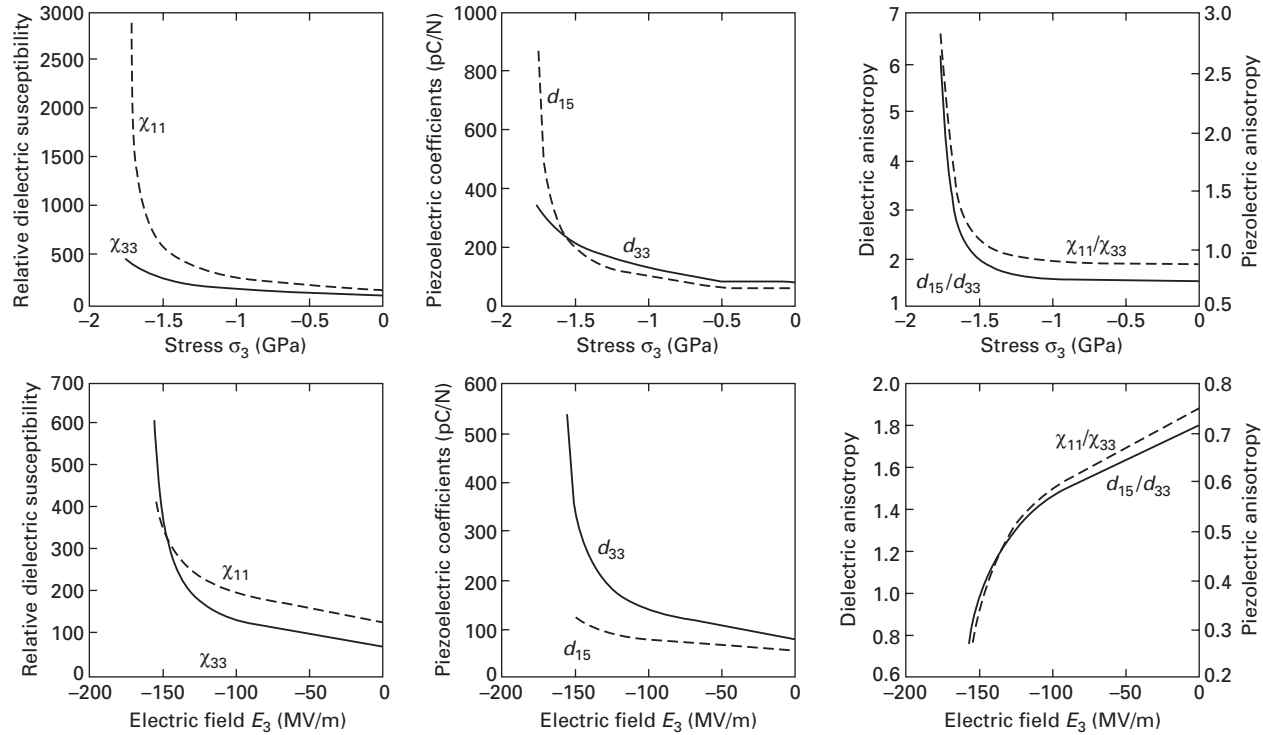
In this section we discuss a special type of instability, which does not include change of the crystal structure. In ferroelectric materials the direction/orientation of the spontaneous polarization can be switched by electric field and/or stress; this is a defining property of ferroelectric crystals (Lines and Glass, 1979). It is easily shown using Eq. [11.11] that near and just below the

switching field the crystal softens and that its properties may reach high values (Budimir *et al.*, 2004, 2005). The thermodynamic description for electric field or stress-induced switching is similar to that for thermally induced phase transitions. The most important issue with thermodynamically treated switching of ferroelectric crystals is that the thermodynamic switching fields are one or more orders of magnitude higher than experimental switching fields. The main reason for this is that the LGD thermodynamics (e.g. Eq. [11.11]) treats perfect crystals while a real crystal contains defects that can serve as nucleation centers for domain reversal (Gerra *et al.*, 2005). In addition, as mentioned earlier, the field dependence of thermodynamic and material coefficients in [11.11] is ignored. Nevertheless, the treatment used in this section gives a qualitative picture how external fields may enhance electromechanical response of ferroelectric crystals.

Different field and stress configurations can be used for such a study, as indicated in the first sections of this chapter. For the sake of simplicity, it is convenient to choose an electric field applied antiparallel to spontaneous polarization direction ( $E_3$ ), and compressive stress applied along polar axis ( $\sigma_3$ ). In a ferroelectric with  $4mm$  structure a sufficiently high antiparallel electric field will cause polarization switching by  $180^\circ$  while a high compressive stress will switch polarization by  $90^\circ$ . As a model material we choose  $\text{PbTiO}_3$  because it does not undergo multiple phase transitions like  $\text{BaTiO}_3$ . This simplifies the analysis by avoiding interference between effects of thermally induced phase transitions and those induced by external fields. The analysis also holds for the tetragonal PZT compositions that are sufficiently far from the MPB (Zr/Ti ratio  $< 40/60$ ).

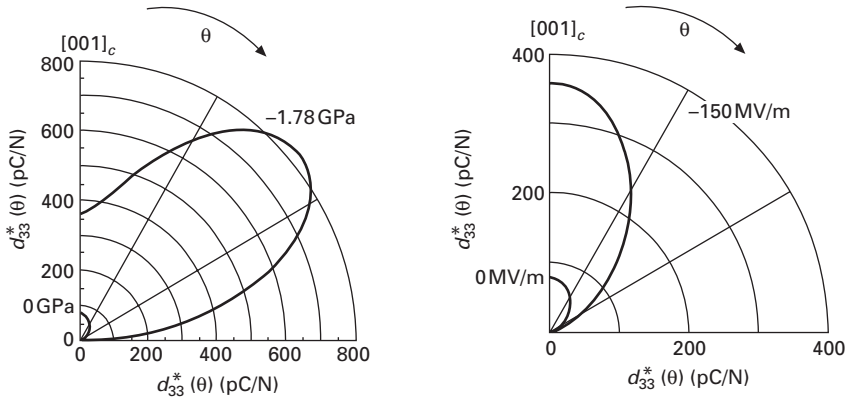
At zero external field  $\text{PbTiO}_3$  is a strong ‘extender’ ferroelectric. Thermodynamic switching fields are high: the absolute value of coercive compressive stress is about  $-1.95$  GPa while the coercive electric field is about  $-160$  MV. Application of the compressive stress and antiparallel electric field decreases polarization and increases permittivity of the monodomain single crystal (Budimir *et al.*, 2004, 2005). Consequently, the piezoelectric response increases. It is assumed that electrostrictive coefficients are independent of stresses and electric fields below coercive values. The results for  $\chi_{11}$ ,  $\chi_{33}$ ,  $d_{15}$  and  $d_{33}$  are shown together with anisotropy ratios in Fig. 11.9. There is a striking difference in the behavior of the crystal subjected to compressive stress and antiparallel field: while stress increases the anisotropy ratios, changing the character of the crystal from ‘extender’ to ‘rotator’ (see Fig. 11.10), the electric field reinforces the ‘extender’ nature of  $\text{PbTiO}_3$ . Importantly, in both cases fields and stresses close to the threshold values for switching lead to a huge enhancement of the piezoelectric effect. Thus, the piezoelectric effect may be enhanced by both colinear effects (polarization contraction) and by polarization rotation.

Despite this qualitative difference, the thermodynamic origin of the



11.9 Dielectric susceptibilities and piezoelectric coefficients in  $\text{PbTiO}_3$  at 298K as a function of compressive stress (upper row) and antiparallel electric field (lower row) applied along the polar axis. Both the stress and electric field enhance the properties. However, the enhancement is anisotropic and the anisotropy ratios increase with stress but decrease with electric field. Thus, under extreme compressive stresses close to coercive stress  $\text{PbTiO}_3$  behaves as a ‘rotator’ while close to switching electric fields it behaves as an ‘extender’. See Figs 11.10 and 11.11.

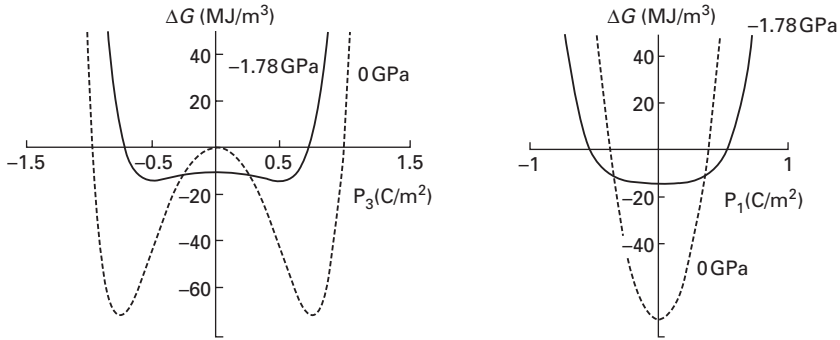




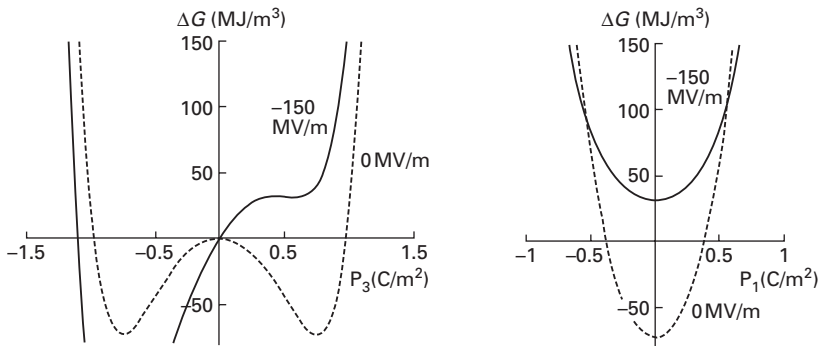
11.10 Orientation dependence of  $d_{33}^*(\theta)$  in  $\text{PbTiO}_3$  at 298K at (a) zero and compressive stress and (b) zero and antiparallel electric field close to switching values. The crystal behaves as a 'rotator' under compressive stress and as an 'extender' under antiparallel field. See Fig. 11.9 and 11.11.

enhancement is the same in the two cases. Figure 11.11 shows that for both enhancement types the free energy becomes less stable (its profile flatter) as the coercive fields are approached: this results in the enhancement of the piezoelectric effect and dielectric susceptibility. The instability in the free energy is, however, anisotropic: at compressive stress  $\sigma_3$ , the instability is higher along the directions perpendicular to the polarization axis; at antiparallel electric field  $E_3$ , the instability is higher along the polar axis. This anisotropy in the free energy instability is responsible for the different character of the enhancement. In the stress case, the sample becomes 'rotator' and the enhancement is by polarization rotation. In contrast, the electric field reinforces the 'extender' character and the enhancement mechanism is by polarization contraction (collinear effect).

One can intuitively understand this qualitative difference by considering polarization switching as a phase transition. In the case of switching by stress, polarization changes direction by  $90^\circ$ . This is analogous to a phase transition between two crystal phases in which polarization changes orientation. Examples are thermally induced tetragonal–orthorhombic phase transition in  $\text{BaTiO}_3$  and compositionally induced tetragonal–orthorhombic phase transition at MPB in PZT. In both cases, the character of the crystal changes from 'extender' to 'rotator' as polarization changes orientation (or even while approaching the phase transition point), and the main enhancement of the piezoelectric effect is by polarization rotation. In the case of the electric field, the switching is by  $180^\circ$ . The polarization changes direction (by going through zero value) but not orientation. This case is analogous to ferroelectric–paraelectric phase transitions, where polarization diminishes and eventually



(a)



(b)

11.11 The Gibbs free energy for PbTiO<sub>3</sub> at 298K, for free crystal and at compressive stress and electric field close to the switching values: (a) as a function of  $P_3$  at zero and near-switching compressive stress; (b) as a function of  $P_1$  and  $P_3 = P_S$  at zero and near-switching compressive stress; (c) as a function of  $P_3$  at zero and near-switching antiparallel electric field and (d) as a function of  $P_1$  and  $P_3 = P_S$  at zero and near-switching antiparallel electric field. See Figs 11.9 and 11.10. Note metastable state at antiparallel field.

becomes zero. In both BaTiO<sub>3</sub> and PbTiO<sub>3</sub>, for example, their ‘extender’ character becomes stronger as it is heated toward the Curie temperature.

### 11.4 Final remarks

By analyzing the free energy of simple perovskite ferroelectrics it is possible to qualitatively understand the origins of the piezoelectric effect enhancement. The enhancement is associated with free energy instabilities (reduction of the energy barrier between states) in a vicinity of phase transitions and critical points; the nature of the phase transition (thermally induced, a morphotropic phase boundary, polarization switching) is not important. The

anisotropy of the enhancement is closely related to the anisotropy of the free energy instability. When the instability is stronger along non-polar directions, the enhancement is due to polarization rotation and crystal can be classified as a 'rotator'. When the instability is stronger along the polar axis, the enhancement is due to collinear effects (polarization extension/contraction) and the crystal can be classified as an 'extender'.

The present analysis (as well as other approaches discussed in the literature (Fu and Cohen, 2000; Kutnjak *et al.*, 2006) does not say anything about the origin of the large, zero-field piezoelectric effect in relaxor-ferroelectrics; it only suggests a possible mechanism for its enhancement. The large piezoelectric response of relaxor ferroelectric single crystals could be related to intrinsic disorder in these materials (chemical disorder, polarization fluctuations on nanoscopic scale) that could lead to a flat energy profile. However, *ab-initio* studies (Wu and Cohen, 2005) and this work (the case of the huge field-induced piezoelectric effect in  $\text{PbTiO}_3$ ) have shown that disorder is not essential for a high piezoelectric effect.

The present analysis could be, in principle, useful in explaining the gradual enhancement of piezoelectric effect in crystals with increasingly denser domain structure (Wada *et al.*, 2005). In domain engineered crystals, the polarization on each side of some domain walls appear to be oriented head-to-head or tail-to-tail. Whether these domain walls are charged or neutralized by the free carriers needs to be verified experimentally. Thermodynamic theory suggests that charged walls should not be stable (Ishibashi and Salje, 2004), however, it is not clear whether a small fraction of the depolarizing field can still be tolerated. If so, then a residual depolarizing field could have the same effect on the polarization within a domain as an antiparallel field discussed here: it would enhance the piezoelectric effect. The enhancing effect would be stronger in crystals with denser domains. Very rough calculations show that the presence of a small amount of charge on a domain wall (a few percent of the total, uncompensated charge of a head-to-head/tail-to-tail domain wall) could be sufficient to account for the enhancement of the piezoelectric effect in domain engineered  $\text{BaTiO}_3$  crystals. The same can be argued about the stress in the domain wall region. Clearly, a rigorous, quantitative model needs to be developed to verify this conjecture. An alternative model in which domain walls broaden by the small driving fields is proposed by Rao and Wang (2007).

Finally, a different approach is needed to uncover atomistic mechanisms leading to a large electromechanical response. The formidable difficulties in understanding ferroelectric materials are well illustrated on the example of  $\text{BaTiO}_3$ , where atomistic details of the phase transition behavior have only recently been elucidated (Zalar *et al.*, 2003). The theoretical *ab-initio* studies are perhaps the most promising approach and have led in the past decade to an enormous progress in understanding microscopic mechanisms operating

in ferroelectric materials (Cohen, 1992; Bellaiche and Vanderbilt, 1999; Bellaiche *et al.*, 2000; Fu and Cohen, 2000; Vanderbilt, 2004) With exception of BaTiO<sub>3</sub> and KNbO<sub>3</sub>, most of the work on understanding enhanced piezoelectric response in ferroelectrics has so far been carried out on lead-based materials. The challenge is to extend the present efforts to lead-free materials and find practical materials with piezoelectric properties comparable to those in PZT and relaxor-ferroelectrics. The current work on lead-free materials based on modified (K,Na)NbO<sub>3</sub> is hopefully only a beginning of broader, more concentrated and systematic investigations.

## 11.5 References

- Amin, A., Cross, L. E. & Newnham, R. E. (1989) Sign notation in ferroelectric free energy function. *Ferroelectrics*, **99**, 145–148.
- Bell, A. J. (2001) Phenomenologically derived electric field–temperature phase diagrams and piezoelectric coefficients for single crystal barium titanate under fields along different axis. *J. Appl. Phys.*, **89**, 3907–3914.
- Bell, A. J. (2006) Factors influencing the piezoelectric behaviour of PZT and other ‘morphotropic phase boundary’ ferroelectrics. *J. Mat. Sci.*, **41**, 13–25.
- Bellaiche, L. & Vanderbilt, D. (1999) Intrinsic piezoelectric response in perovskite alloys: PMN vs PT. *Phys. Rev. Lett.*, **83**, 1347–1350.
- Bellaiche, L., Garcia, A. & Vanderbilt, D. (2000) Finite-temperature properties of Pb(Zr<sub>1-x</sub>Ti<sub>x</sub>)O<sub>3</sub> alloys from first principles. *Phys. Rev. Lett.*, **84**, 5427–5430.
- Bellaiche, L., Garcia, A. & Vanderbilt, D. (2001) Electric-field induced polarization paths in Pb(Zr<sub>1-x</sub>Ti<sub>x</sub>)O<sub>3</sub> alloys. *Phys. Rev. B*, **64**, 060103.
- Budimir, M., Damjanovic, D. & Setter, N. (2003) Piezoelectric anisotropy-phase transition relations in perovskite single crystals. *J. Appl. Phys.*, **94**, 6753–6761.
- Budimir, M., Damjanovic, D. & Setter, N. (2004) Large enhancement of the piezoelectric response in perovskite crystals by electric bias field antiparallel to polarization. *Appl. Phys. Lett.*, **85**, 2890–2892.
- Budimir, M., Damjanovic, D. & Setter, N. (2005) Enhancement of the piezoelectric response of tetragonal perovskite single crystals by uniaxial stress applied along the polar axis: a free energy approach. *Phys. Rev. B*, **72**, 064107.
- Budimir, M., Damjanovic, D. & Setter, N. (2006) Piezoelectric response and free-energy instability in the perovskite crystals BaTiO<sub>3</sub>, PbTiO<sub>3</sub>, and Pb(Zr,Ti)O<sub>3</sub>. *Phys. Rev. B*, **73**, 174106
- Cohen, R. E. (1992) Origin of ferroelectricity in perovskite oxides. *Nature*, **358**, 136–138.
- Damjanovic, D. (2005) Contributions to the piezoelectric effect in ferroelectric single crystals and ceramics. *J. Am. Ceram. Soc.*, **88**, 2663–2676.
- Damjanovic, D., Brem, F. & Setter, N. (2002) Crystal orientation dependence of the piezoelectric  $d_{33}$  coefficient in tetragonal BaTiO<sub>3</sub> as a function of temperature. *Appl. Phys. Lett.*, **80**, 652–654.
- Damjanovic, D., Budimir, M., Davis, M. & Setter, N. (2003a) Erratum: ‘Monodomain versus polydomain piezoelectric response of 0.67 Pb(Mg<sub>1/3</sub>Nb<sub>2/3</sub>)O<sub>3</sub>–0.33PbTiO<sub>3</sub> single crystals along nonpolar directions’ [*Appl. Phys. Lett.* 83, 527 (2003)]. *Appl. Phys. Lett.*, **83**, 2490.

- Damjanovic, D., Budimir, M., Davis, M. & Setter, N. (2003b) Monodomain versus polydomain piezoelectric response of  $0.67\text{Pb}(\text{Mg}_{1/3}\text{Nb}_{2/3})\text{O}_3-0.33\text{PbTiO}_3$  single crystals along nonpolar directions. *Appl. Phys. Lett.*, **83**, 527–529.
- Damjanovic, D., Budimir, M., Davis, M. & Setter, N. (2006) Piezoelectric anisotropy: enhanced piezoelectric response along nonpolar directions in perovskite crystals. *J. Mat. Sci.*, **41**, 65–76.
- Davis, M. (2006) Phase transitions, anisotropy and domain engineering : the piezoelectric properties of relaxor-ferroelectric single crystals. *Ceramics Laboratory*. Lausanne, Swiss Federal Institute of Technology – EPFL.
- Davis, M. (2007) Picturing the elephant: Giant piezoelectric activity and the monoclinic phases of relaxor-ferroelectric single crystals. *J. Electroceramics*, **19**, 25–47.
- Davis, M., Damjanovic, D., Hayem, D. & Setter, N. (2005) Domain engineering of the  $d_{31}$  piezoelectric coefficient in perovskite crystals. *J. Appl. Phys.*, **98**, 014102.
- Davis, M., Damjanovic, D. & Setter, N. (2006) Electric field-, temperature-, and stress-induced phase transitions in relaxor ferroelectric single crystals. *Phys. Rev. B*, **73**, 014115.
- Davis, M., Budimir, M., Damjanovic, D. & Setter, N. (2007) Rotator and extender ferroelectrics: importance of the shear coefficient to the piezoelectric properties of domain-engineered crystals and ceramics. *J. Appl. Phys.*, **101**, 054112.
- Devonshire, A. F. (1949) Theory of barium titanate – Part I. *Phil. Mag.*, **40**, 1040–1063.
- Devonshire, A. F. (1951) Theory of barium titanate – Part II. *Phil. Mag.*, **42**, 1065–1079.
- Erhart, J. (2004) Domain wall orientations in ferroelastics and ferroelectrics. *Phase Transitions*, **77**, 989–1074.
- Erhart, J. & Cao, W. W. (2003) Permissible symmetries of multi-domain configurations in perovskite ferroelectric crystals. *J. Appl. Phys.*, **94**, 3436–3445.
- Fu, H. & Cohen, R. E. (2000) Polarization rotation mechanism for ultrahigh electromechanical response in single-crystal piezoelectrics. *Nature*, **403**, 281–283.
- Gerra, G., Tagantsev, A. K. & Setter, N. (2005) Surface-stimulated nucleation of reverse domains in ferroelectrics. *Phys. Rev. Lett.*, article number: E107602 **94**.
- Guo, R., Cross, L. E., Park, S.-E., Noheda, B., Cox, D. E. & Shirane, G. (2000) Origin of the high piezoelectric response in  $\text{PbZr}_{1-x}\text{Ti}_x\text{O}_3$ . *Phys. Rev. Lett.*, **84**, 5423–5426.
- Haun, M. J., Furman, E., Jang, S. J., Mckinstry, H. A. & Cross, L. E. (1987) Thermodynamic theory of  $\text{PbTiO}_3$ . *J. Appl. Phys.*, **62**, 3331–3338.
- Haun, M. J., Furman, E., Jang, S. J. & Cross, L. E. (1989a) Thermodynamic theory of the lead zirconate–titanate solid solution system, Part I: Phenomenology. *Ferroelectrics*, **99**, 13–25.
- Haun, M. J., Furman, E., Jang, S. J. & Cross, L. E. (1989b) Thermodynamic theory of the lead zirconate–titanate solid solution system, Part V: Theoretical calculations. *Ferroelectrics*, **99**, 63–86.
- Ishibashi, Y. (2002) Theory of the morphotropic phase boundary. *Ferroelectrics*, **267**, 191.
- Ishibashi, Y. & Iwata, M. (1998) Morphotropic phase boundary in solid solution systems of perovskite-type oxide ferroelectrics. *Jpn. J. Appl. Phys.*, **37**, L985–L987.
- Ishibashi, Y. & Iwata, M. (1999a) A theory of morphotropic phase boundary in solid-solution systems of perovskite-type oxide ferroelectrics. *Jpn. J. Appl. Phys. Part 1*, **38**, 800–804.
- Ishibashi, Y. & Iwata, M. (1999b) Theory of morphotropic phase boundary in solid-solution systems of perovskite-type oxide ferroelectrics: elastic properties. *Jpn. J. Appl. Phys. Part 1*, **38**, 1454–1458.

- Ishibashi, Y. & Salje, E. (2004) Theoretical consideration on the 90 degrees domain walls in tetragonal ferroelectrics. *Ferroelectrics*, **303**, 607–611.
- Ishidate, T., Abe, S., Takahashi, M. & Mori, N. (1997) Phase diagram of BaTiO<sub>3</sub>. *Phys. Rev. Lett.*, **78**, 2397.
- Jin, Y. M., Wang, Y. U., Khachaturyan, A. G., Li, J. F. & Viehland, D. (2003) Adaptive ferroelectric states in systems with low domain wall energy: Tetragonal microdomains. *J. Appl. Phys.*, **94**, 3629–3640.
- Kutnjak, Z., Petzelt, J. & Blinc, R. (2006) The giant electromechanical response in ferroelectric relaxors as a critical phenomenon. *Nature*, **441**, 956–959.
- Kuwata, J., Uchino, K. & Nomura, S. (1982) Dielectric and piezoelectric properties of 0.91Pb(Zn<sub>1/3</sub>Nb<sub>2/3</sub>)O<sub>3</sub>-0.09PbTiO<sub>3</sub> single crystals. *Jpn. J. Appl. Phys.*, **21**, 1298–1302.
- Li, Y. L., Cross, L. E. & Chen, L. Q. (2005) A phenomenological thermodynamic potential for BaTiO<sub>3</sub> single crystals. *J. Appl. Phys.*, article number: E064101. **98**.
- Lines, M. E. & Glass, A. M. (1979) *Principles and Applications of Ferroelectrics and Related Materials*, Oxford, Clarendon.
- Mitsui, T., Tatsuzaki, I. & Nakamura, E. (1976) *An Introduction to the Physics of Ferroelectrics*, London, Gordon and Breach.
- Newnham, R. E. (2005) *Properties of Materials: Anisotropy, Symmetry, Structure*, Oxford, Oxford University Press.
- Noheda, B. (2002) Structure and high-piezoelectricity in lead oxide solid solutions. *Curr. Opinion Solid State Mat. Sci.*, **6**, 27–34.
- Noheda, B. & Cox, D. E. (2006) Bridging phases at the morphotropic boundaries of lead oxide solid solutions. *Phase Transitions*, **79**, 5–20.
- Noheda, B., Cox, D. E., Shirane, G., Gonzalo, J. A., Cross, L. E. & Park, S.-E. (1999) A monoclinic ferroelectric phase in the Pb(Zr<sub>1-x</sub>Ti<sub>x</sub>)O<sub>3</sub> solid solution. *Appl. Phys. Lett.*, **74**, 2059–2061.
- Noheda, B., Cox, D. E., Shirane, G., Park, S. E., Cross, L. E. & Zhong, Z. (2001) Polarization rotation via a monoclinic phase in the piezoelectric 92% PbZn<sub>1/3</sub>Nb<sub>2/3</sub>O<sub>3</sub>-8% PbTiO<sub>3</sub>. *Phys. Rev. Lett.*, **86**, 3891–3894.
- Nye, J. F. (1985) *Physical Properties of Crystals*, Oxford, Oxford University Press.
- Park, S.-E., Wada, S., Cross, L. E. & Shrout, T. R. (1999) Crystallographically engineered BaTiO<sub>3</sub> single crystals for high-performance piezoelectrics. *J. Appl. Phys.*, **86**, 2746–2750.
- Park, S. E. & Shrout, T. R. (1997) Ultrahigh strain and piezoelectric behavior in relaxor based ferroelectric single crystals. *J. Appl. Phys.*, **82**, 1804–1811.
- Rao, W.-F. & Wang, Y.-U. (2007) Domain wall broadening mechanism for domain size effect of enhanced piezoelectricity in crystallographically engineered ferroelectric single crystals. *Appl. Phys. Lett.*, **90**, 041915.
- Vanderbilt, D. (2004) First-principles theory of polarization and electric fields in ferroelectrics. *Ferroelectrics*, **301**, 9–14.
- Vanderbilt, D. & Cohen, M. H. (2001) Monoclinic and triclinic phases in higher-order Devonshire theory. *Phys. Rev. B*, **63**, 094108.
- Wada, S., Park, S.-E., Cross, L. E. & Shrout, T. R. (1998) Domain configuration and ferroelectric related properties of relaxor based single crystals. *J. Korean Phys. Soc.*, **32**, S1290–S1293.
- Wada, S., Suzuki, S., Noma, T., Suzuki, T., Osada, M., Kakihana, M., Park, S.-E., Cross, L. E. & Shrout, T. R. (1999) Enhanced piezoelectric property of barium titanate single crystals with engineered domain configuration. *Jpn. J. Appl. Phys.*, **38**, 5505–5511.
- Wada, S., Kakemoto, H. & Tsurumi, T. (2004) Enhanced piezoelectric properties of

- piezoelectric single crystals by domain engineering. *Materials Transactions*, **45**, 178–187.
- Wada, S., Yako, K., Kakemoto, H., Tsurumi, T. & Kiguchi, T. (2005) Enhanced piezoelectric properties of barium titanate single crystals with different engineered-domain sizes. *J. Appl. Phys.*, **98**, 014109.
- Wang, Y. L., Tagantsev, A. K., Damjanovic, D., Setter, N., Yarmarkin, V. K. & Sokolov, A. I. (2006) Anharmonicity of BaTiO<sub>3</sub> single crystals. *Phys. Rev. B*, **73**, 132103.
- Wu, Z. G. & Cohen, R. E. (2005) Pressure-induced anomalous phase transitions and colossal enhancement of piezoelectricity in PbTiO<sub>3</sub>. *Phys. Rev. Lett.*, **95**, 037601.
- Yamada, T. (1972) Electromechanical properties of oxygen-octahedra ferroelectric crystals. *J. Appl. Phys.*, **43**, 328.
- Zalar, B., Laguta, V. V. & Blinc, R. (2003) NMR evidence for the coexistence of order-disorder and displacive components in barium titanate. *Phys. Rev. Lett.*, **90**, 037601.
- Zhang, R. & Cao, W. (2004) Transformed material coefficients for single-domain 0.67Pb(Mg<sub>1/3</sub>Nb<sub>2/3</sub>)O<sub>3</sub>–0.33PbTiO<sub>3</sub> single crystals under differently defined coordinate systems. *Appl. Phys. Lett.*, **85**, 6380–6382.
- Zhang, R., Jiang, B. & Cao, W. (2003a) Orientation dependence of piezoelectric properties of single domain 0.67(Mg<sub>1/3</sub>Nb<sub>2/3</sub>)O<sub>3</sub>–0.33PbTiO<sub>3</sub> crystals. *Appl. Phys. Lett.*, **82**, 3737–3739.
- Zhang, R., Jiang, B. & Cao, W. (2003b) Single-domain properties of 0.67Pb(Mg<sub>1/3</sub>Nb<sub>2/3</sub>)O<sub>3</sub>–0.33PbTiO<sub>3</sub> single crystals under electric field bias. *Appl. Phys. Lett.*, **82**, 787–789.

## Electric field-induced domain structures and phase transitions in PMN–PT single crystals

V H SCHMIDT and R R CHIEN, Montana State University, Bozeman, USA and C - S TU, Fu Jen Catholic University, Taiwan

### 12.1 Introduction

Relaxor ferroelectrics include as their best-known type perovskites with  $ABO_3$ -type unit cell which are crystals in which unlike-valence cations belonging to a given site (A or B) are present in the correct ratio for charge balance, but are situated randomly on these cation sites (Cross, 1987). These randomly different cation charges give rise to random fields, which tend to make the phase transitions ‘diffuse’ instead of sharp as in normal ferroelectrics (Westphal *et al.*, 1993; Ye, 1998). Lead magnesium niobate,  $Pb(Mg_{1/3}Nb_{2/3})O_3$  (PMN), is one of the most interesting relaxor ferroelectric (FE) materials. PMN has a disordered complex structure in which the  $Mg^{2+}$  and  $Nb^{5+}$  cations exhibit only some short range order on the B-site. PMN has cubic symmetry at room temperature with space group  $Pm3m$ , whereas below 200 K a small rhombohedral distortion (pseudocubic) was observed (Cross, 1987; Shebanov *et al.*, 1984). Near 280 K the PMN crystal undergoes a diffuse transition characterized by a broad frequency-dependent dielectric maximum. An extra dielectric peak was observed at  $T_C \sim 212$  K in the field-heating result, and was attributed to the percolating clusters due to the suppression of the random fields (Westphal *et al.*, 1993). The normal FE crystal  $PbTiO_3$  (PT) has a tetragonal symmetry with space group  $P4mm$  at room temperature and has a normal FE phase transition taking place at  $T_C = 760$  K with a long-range FE order occurring below  $T_C$  (Jona, 1962).

The relaxor-based FE crystals  $Pb(Mg_{1/3}Nb_{2/3})_{1-x}Ti_xO_3$  (PMN–PT) are expected to show properties of both relaxor ferroelectric PMN and normal ferroelectric PT. PMN–PT has a morphotropic phase boundary (MPB) in the range of  $\sim 28$  to  $\sim 36$  mol% of PT (Shrout *et al.*, 1990). As temperature decreases, the solid solution crystals PMN– $x$ PT ( $0.28 \leq x \leq 0.36$ ) have successive phase transitions: cubic paraelectric (PE) phase  $\rightarrow$  tetragonal FE phase  $\rightarrow$  rhombohedral FE phase. However, the phase diagram is not unique and depends on many physical parameters, such as poling strength and



crystallographic orientation. Dielectric and piezoelectric properties of PMN–PT are sensitive to Ti content,  $E$ -field strength, crystallographic orientation, mechanical stress (from slicing or external pressure), thermal treatment, sample thickness, and acquisition process (Tu *et al.*, 2004; Davis *et al.*, 2006). The ultra-high piezoelectricity has been theoretically attributed to polarization rotations between tetragonal (T) and rhombohedral (R) phases through monoclinic (M) or orthorhombic (O) symmetry (Fu and Cohen, 2000).

Morphotropic domain structures and phase transitions in PMN–PT crystals have been systematically studied by using polarizing microscopy (Ye and Dong, 2000; Bokov and Ye, 2004; Chien *et al.*, 2005b, 2006). From domain observations,  $R \rightarrow M_A \rightarrow T_{001}$  and  $R \rightarrow M_A \rightarrow T \rightarrow M_A \rightarrow R_{111}$  transition sequences were evidenced respectively at room temperature in (001)-cut PMN–24%PT and (111)-cut PMN–33%PT crystals as the  $E$  field increases (Tu *et al.*, 2003b; Chien *et al.*, 2004). A field-induced  $R \rightarrow O$  transition through an  $M_B$ -type M phase was suggested for a (110)-cut PMN–30%PT crystal (Viehland and Li, 2002). The synchrotron X-ray diffraction of (001)-cut PMN–35%PT crystal after poling ( $E = 43$  kV/cm) shows an  $M_A$ -type M phase, but the weakly poled sample exhibits an average R symmetry (Ye *et al.*, 2001). A coexistence of R and M phases was observed in (001)-cut PMN–33%PT crystals at room temperature (Xu *et al.*, 2002).

For piezoelectric performance, an  $E$ -field poling has usually been performed before application. However, how  $E$ -field poling affects thermal instability (variation with temperature) of physical properties is still a critical issue for long-term operation. It has been a goal to find crystals with high  $T_C$  (Curie temperature) or  $T_d$  (depolarization temperature). ' $T_d$ ' represents the temperature where local polarization exhibits significant and sudden reduction by thermal energy. Among high- $T_C$  piezoelectric crystals,  $Pb(In_{1/2}Nb_{1/2})_{1-x}Ti_xO_3$  (PIN–PT),  $Pb(Yb_{1/2}Nb_{1/2})_{1-x}Ti_xO_3$  (PYN–PT) and  $Pb(Sc_{1/2}Nb_{1/2})_{1-x}Ti_xO_3$  (PSN–PT) have drawn attention in recent years. The (001)-cut PIN–34%PT single crystal (starting composition) grown by the modified Bridgman method with a PMN–29%PT seed crystal, exhibits  $d_{33} > 2000$  pC/N and  $k_{33} \cong 94\%$  (Guo *et al.*, 2003). Domain and dielectric properties of (001)-cut PIN– $x$ PT ( $x = 0.28, 0.30, 0.40$ ) were also studied as functions of temperature and  $E$  field (Yasuda *et al.*, 2003; Tu *et al.*, 2006d). PYN–50%PT, PIN–37%PT, and PSN–42%PT ceramics have  $T_C = 633, 593,$  and  $533$  K, respectively (Yamashita *et al.*, 2002).

Polar nanoclusters or nanoregions (PNR) are believed to be responsible for many physical properties in relaxor ferroelectrics. Field-cooled (FC) and zero-field-cooled (ZFC)  $^{207}Pb$  nuclear magnetic resonance (NMR) spectra of the PMN crystal show the existence of two components – spherical glassy matrix and ferroelectric nanoclusters (Blinic *et al.*, 2003). About 50% of the Pb nuclei reside in the spherical glass matrix which does not respond to the external field, and 50% in the ferroelectric nanoclusters which can respond to  $E$  field ( $>$  threshold field  $E_t$ ). Blinic *et al.* (2003) found a sudden intensity

increase in the ZFC spectra of the anisotropic NMR line corresponding to nanoclusters below  $T_C \cong 210\text{ K}$ , but the magnitude is two times smaller than in the FC spectra ( $E > E_t \cong 1.8\text{ kV/cm}$ ). These evidences indicate that PMN is incipient ferroelectric. The time dependence of permittivity and polarization/depolarization currents after switching on a dc field and also for zero-field warming after different applied-field histories (Colla and Weissman, 2005) were measured in PMN, and in PMN–PT with PT up to 12%, well below the MPB concentration range. They suggested that coupled ferroelectric and glassy order are required to explain their data.

Owing to low domain switching  $E$  field, high-strain piezoelectric crystals have potential for non-linear optical applications. Refractive indices of (001)-cut PMN– $x$ PT ( $x = 0.35$  and  $0.38$ ) crystals showed an obvious birefringence after an  $E$ -field poling, but the phase-matched condition was not found yet in PMN–PT crystals (Wan *et al.*, 2003; Tu *et al.*, 2005). Optical transmission was significantly enhanced by a prior  $E$ -field poling.

In the remainder of this chapter, we present our results concerning phase transitions of variously oriented PMN–PT crystals as functions of temperature, frequency, and  $E$  field by means of dielectric permittivity, polarizing microscopy, hysteresis loop, and X-ray diffraction measurements. Optical transmission and refractive indices before and after poling are also included. The chapter ends with an introduction to Landau free energy analysis of stability of the various crystal phases, followed by conclusions.

## 12.2 Experimental methods

The PMN–PT crystals were grown using a modified Bridgman method at H.C. Materials Corporation, Illinois, and Shanghai Institute of Ceramics, China. Samples were cut perpendicular to the  $\langle 001 \rangle$ ,  $\langle 011 \rangle$ , or  $\langle 111 \rangle$  direction. The Ti concentration ( $x\%$ ) was determined by using the dielectric maximum temperature  $T_m$  upon heating (without poling), i.e.  $x = [T_m(\text{°C}) + 10]/5$  (Feng *et al.*, 2003). For dielectric measurements, a Wayne-Kerr Precision Analyzer PMA3260A was used to obtain capacitance and resistance. A Janis CCS-450 cold-head was used with a Lakeshore 340 controller and the ramping rate was  $1.5\text{ K/min}$ . Before any measurement, the sample was annealed in the cubic (C) phase above  $T_m$ . Three processes were used in this study. The first is called ‘zero-field-heated’ (ZFH) or ‘zero-field-cooled’ (ZFC), in which the data were taken upon heating or cooling respectively without any  $E$ -field poling. The second process is called ‘field-cooled-zero-field-heated’ (FC-ZFH), in which the sample was first cooled from the C phase down to room temperature with an  $E$  field, then cooled to 100 or 150 K without field before ZFH was performed. In the third process, the sample was directly poled at room temperature before ZFH was performed starting below room temperature, i.e. FR-ZFH. During the FC or FR, a dc  $E$  field was applied along the

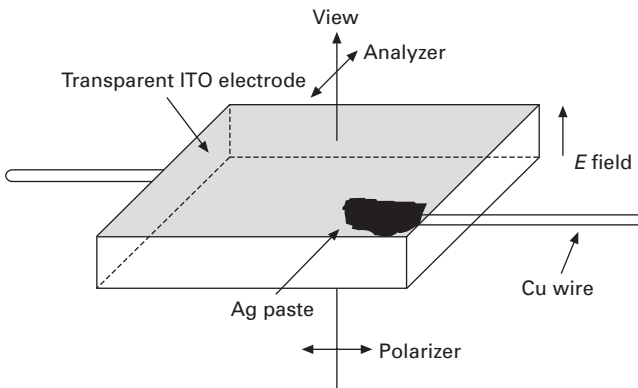
oriented direction. The hysteresis loops were measured by using a Sawyer–Tower circuit at  $f = 46$  Hz.

Domain structures were observed by using a Nikon E600POL polarizing microscope with a crossed polarizer/analyzer (P/A) pair. To avoid domain overlapping, the samples were polished to a thickness of approximately 40–70  $\mu\text{m}$  or less. The edge orientations of the samples were determined by X-ray diffraction. One of the sample edges was aligned with one of the crossed P/A: $0^\circ$  axes so that the extinction angles shown in all domain micrographs were measured from that sample edge as indicated in domain figures. For  $E$ -field-dependent domain observation, transparent conductive films of indium tin oxide (ITO) were deposited on sample surfaces by sputtering. The experimental configuration is shown in Fig. 12.1. The details for using optical extinction to distinguish various phases are discussed in Section 12.3.

For optical transmission measurements, a Varian Model Cary 5E ultraviolet–visible–near infrared spectrophotometer (0.2–3.3  $\mu\text{m}$ ) and a Perkin-Elmer 2000 Model Fourier transform infrared (FTIR) (3.0–27  $\mu\text{m}$ ) were used. Refractive indices were measured by using a Metricon Model 2010 Prism Coupler equipped with three lasers (0.473, 0.790, and 1.323  $\mu\text{m}$ ). The beam diameters are about 1.2, 0.74, and 1.4 mm for wavelengths 0.473, 0.790, and 1.323  $\mu\text{m}$ , respectively. The refractive index was determined by finding the critical angle of total internal reflection.

### 12.3 Polarizing microscopy as applied to perovskite-structure crystals

Various orientations of the polarizations and their corresponding crystallographic symmetries (or phases) can be determined for most cases by

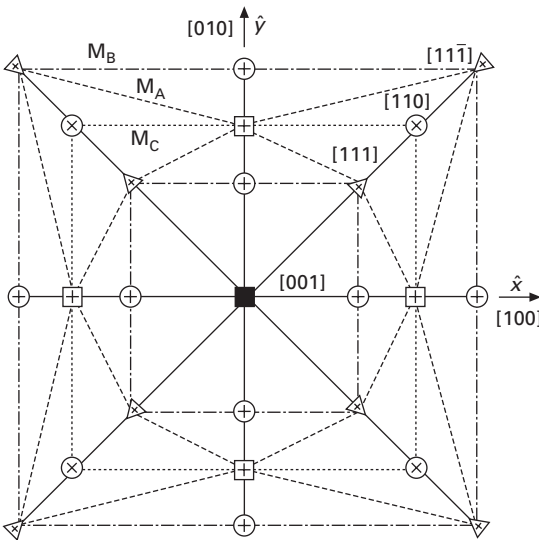


12.1 Experimental configuration for observing domain structures under the polarizing microscope. A dc  $E$  field was applied across the sample.

measuring optical extinction angles from polarizing microscopy. Principles of the optical extinction in polarizing microscopy applied to perovskite-structure crystals are discussed below.

In polarizing microscopy the crystal can be rotated between two crossed linear polarizers. There are two key directions, the light propagation vector  $k$  (perpendicular to the crystal cut plane) and the optical electric field axis  $E$  of the incident light. The relation of  $E$  to the projection of the ferroelectric polarization vector  $P$  onto the plane perpendicular to  $k$  is important for interpreting the results. We display this relation by means of figures that aid in visualizing the possible  $P$  vectors and their projections onto this plane. Each figure consists of the projection along  $k$  of a cube aligned with the parent-phase cubic cell axes, with symbols representing where  $P$  crosses the visible faces of the cube. The origin of  $P$  is at the center of the cube. Some faces with sides parallel to  $k$  are shown folded out somewhat.

Simplest, and thus shown first, is the (001)-cut projection as shown in Fig. 12.2, with all four sides folded out. The inner square outlines the front face of the cube. The triangles at its corners represent four R-phase  $P$  directions, and the circles at its edge midpoints represent four O-phase  $P$  directions. The square symbol at its center represents a T-phase domain whose  $P$  is parallel to  $k$ . This symbol is shown in solid black to indicate that extinction occurs



12.2 Relation between the optical extinction orientations corresponding to the ferroelectric polarization directions for various phases and domains projected on the (001) plane. Dashed, dash-dotted, and dotted lines represent polarization directions for  $M_A^-$ ,  $M_B^-$ , and  $M_C^-$ -type monoclinic phase domains, respectively (adapted from Chien *et al.*, 2006).

for all  $E$  directions because  $E$  is perpendicular to the optic axis for this optically uniaxial domain.

The solid crosses in the other 24 symbols indicate the  $E$  axes for which extinction will occur for the corresponding domains. Extinction occurs if  $E$  is along a principal axis of the ellipse formed by the intersection of the plane perpendicular to  $k$  with the index ellipsoid. The index ellipsoid is a surface whose distance from the origin in a given direction is proportional to the index of refraction  $n$  for light polarized with  $E$  in that direction. The R and T domains are optically uniaxial, so the index ellipsoid is an ellipsoid of revolution.

For the R and T domains, the optic axis is along  $P$ . For such domains in the (001)-cut crystal, the intersection of the (001) plane with the index ellipsoid forms an ellipse that has principal axes parallel and perpendicular to the projection of  $P$  onto the (001) plane. Extinction for these R and T domains occurs for  $E$  along the principal axis directions of these ellipses, as indicated by the directions of the lines forming the crosses inside the triangle and square symbols in Fig. 12.2. A concise and clear mathematical analysis for the general extinction problem appears in Sommerfeld (1964). A detailed treatment was published by Hartshorne and Stuart (1970).

The O domains are optically biaxial. The optic axis directions are arbitrary in a certain plane and are of no practical use in polarizing microscopy for these crystals. Of importance are the principal axes of the index ellipsoid, which for O domains align with the axes of the double-size ( $Z = 2$ ) O unit cell. One of these axes aligns with  $P$  and makes a  $45^\circ$  angle with two cubic axes, another axis is the third cubic axis, and the third is perpendicular to the other two. For instance, for any of the four O domains shown in Fig. 12.2 having  $P$  represented by circles near the four corners, the unit cell projection is a rectangle (almost a square) with edges canted  $45^\circ$  relative to the page edges. In the third direction, the cell edges are perpendicular to the page and are about  $\sqrt{2}$  shorter, that is, they coincide closely with the length of the original primitive cubic unit cell.

For such biaxial domains, under what conditions will the index ellipsoid intersection with the plane perpendicular to  $k$  be an ellipse with a principal axis along the projection of  $P$ , so that extinction will occur with  $E$  along this projection of  $P$ ? There are two independent sufficient conditions. Case 1 is if  $P$  lies in this plane. Case 2 is if an index ellipsoid principal axis is perpendicular to  $E$  when  $E$  is aligned with the projection of  $P$ . For the (001) cut crystal represented by Fig. 12.2, all 12 O symbols satisfy Case 2. The 4 in the central plane (circles near the corners) satisfy Case 1 also, so the extinction directions for all 12 O domains are known to be along the axes shown in the O symbols.

For the (001) cut we see that T domains will give extinctions at  $0^\circ + m90^\circ$ , where  $m$  is any integer. All angles are measured from the vertical direction,

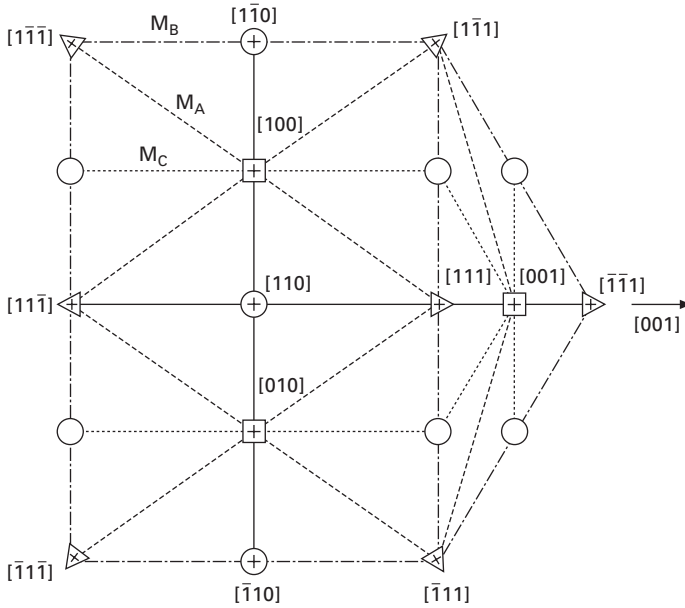
and we will henceforth omit  $m90^\circ$  terms and only consider angles in the  $0^\circ \leq \phi < 90^\circ$  range. We see that R domains only give extinctions at  $45^\circ$ , whereas O domains give extinctions at  $0^\circ$  and  $45^\circ$ . We also see the importance of knowing which direction is which in the plane perpendicular to  $k$ . Thus the (001) cut is particularly useful for distinguishing situations for which only R or only T domains exist. A mixture of R and T domains could give the same extinction angles as a crystal with only O domains. For coexisting R and T domains, T domains can be evidenced by  $90^\circ$  domain walls, i.e. stripes along  $\langle 110 \rangle$ , and T domains have the extinction angle along  $\langle 100 \rangle$ , whereas R domains have extinction along  $\langle 110 \rangle$  (Ye and Dong, 2000).

All monoclinic phases for M domains that may exist in perovskite crystals belong to the  $m$  point group, but only the  $M_C$  phase has a  $Z = 1$  unit cell based on the primitive cubic unit cell. Any  $M_C$  cell  $P$  lies between two adjacent T and O  $P$  vectors (dotted lines in Fig. 12.2). The  $M_A$  and  $M_B$  'phases' in our opinion should be called a single phase whose cell is based on the  $Z = 2$  O cell. The important distinction is that the  $M_A$  cell has  $P$  between two adjacent T and R  $P$  vectors (dashed lines), whereas the  $M_B$  cell has  $P$  between two adjacent R and O  $P$  vectors (dash-dot lines). If the plane of any set of three adjacent  $P$  vectors described above includes  $k$ , extinction occurs for the M phase for  $E$  in the same directions as for the adjacent T, R, or O phases, and the lines representing these monoclinic  $P$  directions are shown solid to indicate that the extinction directions are known. Otherwise, the extinction directions are not known, and complete extinction does not occur for any  $E$  direction because two of the three index ellipsoid principal axes change direction with wavelength. This situation occurs for the O domains shown as open circles in Fig. 12.3 for a (110) crystal cut. Any extinctions at angles other than  $0^\circ$  ( $= 90^\circ$ ),  $35^\circ$ , and  $55^\circ$  must be from these open-circle O domains, M domains, or triclinic (Tri) domains.

Another origin of incomplete extinction in the  $m$  monoclinic and  $mm2$  orthorhombic point groups is the optical activity that occurs unless  $k$  lies in a mirror plane. O domains that have incomplete extinction only because of optical activity are shown by circles with open crosses in Fig. 12.4 for a (111) crystal cut. These satisfy Case 1 above, whereas the O domains represented by the other three circles satisfy Case 2.

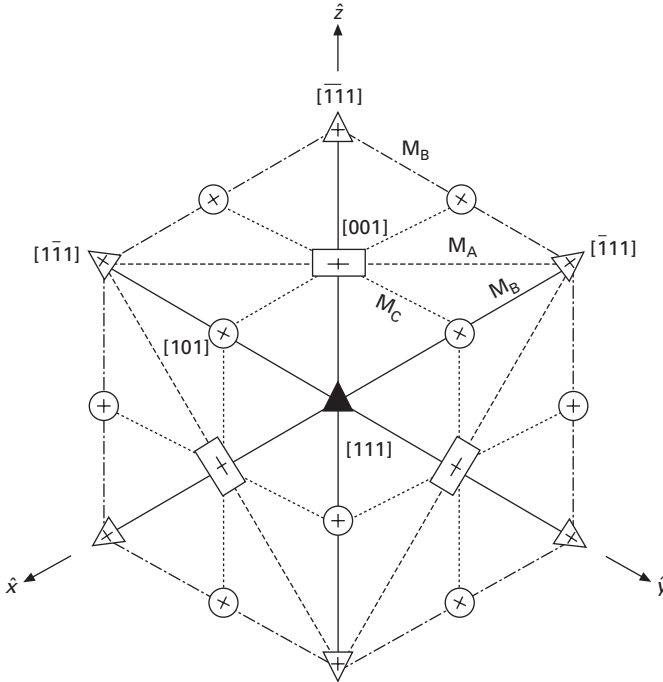
From Figs 12.2–12.4 we see advantages for each of these crystal cuts. The (001) cut of Fig. 12.2 clearly distinguishes R from T phases by the  $45^\circ$  extinction angle difference. The (110) cut of Fig. 12.3 unambiguously distinguishes certain R domains by a special  $35.3^\circ$  extinction angle relative to T, some O, and other R domains. The (111) cut of Fig. 12.4 has the special feature that any extinctions at angles other than  $0^\circ$ ,  $30^\circ$ ,  $60^\circ$ , etc. must be from M or Tri domains.

Here, we describe the experimental procedure for determining the crystal phase (symmetry) of a (001)-cut crystal from measuring the extinction angles



12.3 Relation between the optical extinction orientations corresponding to the ferroelectric polarization directions for various phases and domains projected on the (110) plane (adapted from Chien *et al.*, 2005b).

using the extinction pattern of Fig. 12.2. First, one of the crossed P/A pair axes at reading  $0^\circ$  was aligned with one sample edge, such as  $[110]$  or  $[100]$ . The extinction angles therefore were measured with respect to the  $[110]$  or the  $[100]$  directions. The solid crosses within the symbols in Fig. 12.2 represent the orientation of the extinction. For instance, if the (001)-cut sample's  $[110]$  edge is aligned with P/A:  $0^\circ$ , R phase domains represented by triangles with solid crosses thus have extinction at  $0^\circ$  (or  $90^\circ$ ). T phase domains represented by squares with solid crosses have extinction at  $45^\circ$ . T phase domains with polarization  $P$  along the  $[001]$  axis represented by the solid black square in the center have extinction at every orientation of the crossed P/A pair and are written as 'T<sub>001</sub>' in the following discussion. The O phase domains represented by circles with solid crosses have extinctions at  $0^\circ$  (or  $90^\circ$ ) or  $45^\circ$ , whereas R domains only give extinctions at  $0^\circ$ . Any extinctions at angles other than  $0^\circ$  (or  $90^\circ$ ) and  $45^\circ$  must be from the M or Tri phase domains. Note that all the phases except Tri phase have been reported in various PMN–PT crystals. The large observed variation in extinction angle with  $E$  field or temperature in some of our experiments indicates M domains whose polarization  $P$  can vary with  $E$  field or temperature through a large angle, whereas the polarization directions are nearly fixed for R, T, or O domains as  $E$  field or temperature varies.



12.4 Relation between the optical extinction orientations corresponding to the ferroelectric polarization directions for various phases and domains projected on the (111) plane (adapted from Tu *et al.*, 2003b).

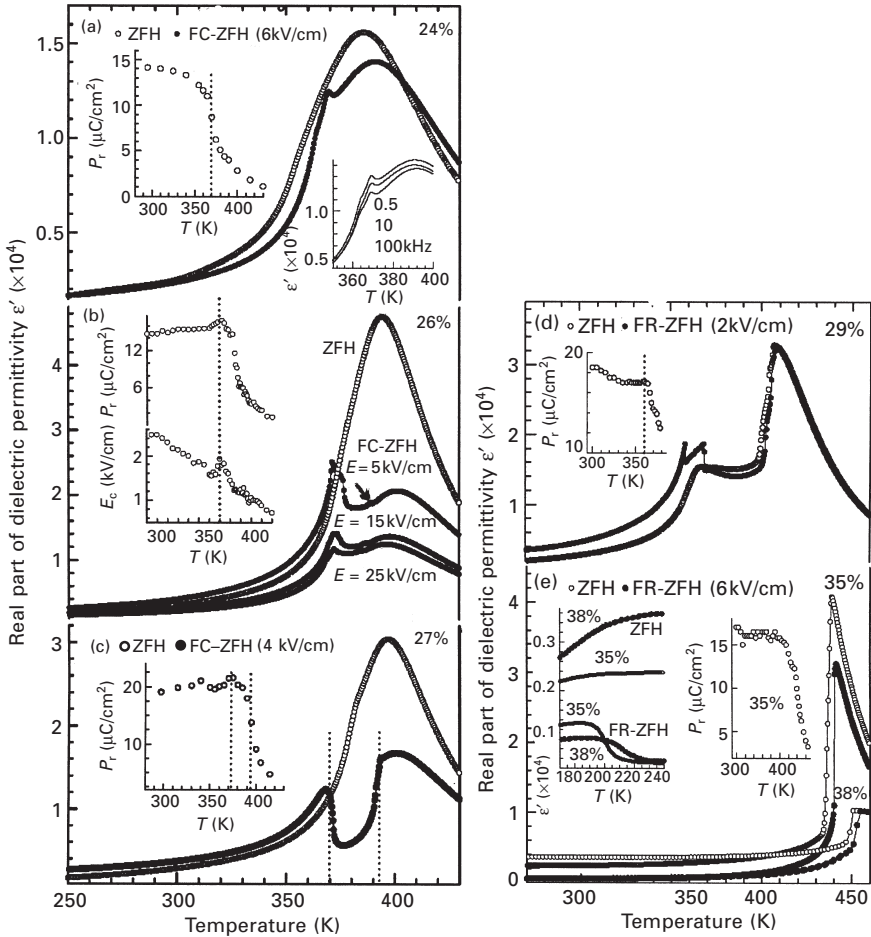
## 12.4 Thermal stability for various PMN-PT compositions

### 12.4.1 (001)-cut PMN-*x*PT crystals (*x* = 0.24, 0.26, 0.27, 0.29, 0.35, 0.38)

To enhance piezoelectric performance, a prior *E*-field poling process has usually been done before employing these materials in applications. However, how prior *E*-field poling affects phase thermal stability still remains unclear. In this section, dielectric permittivity, electric polarization, domain structure, and X-ray spectrum were measured as functions of Ti content, temperature, and poling strength for (001)-cut crystals before and after a dc *E*-field poling.

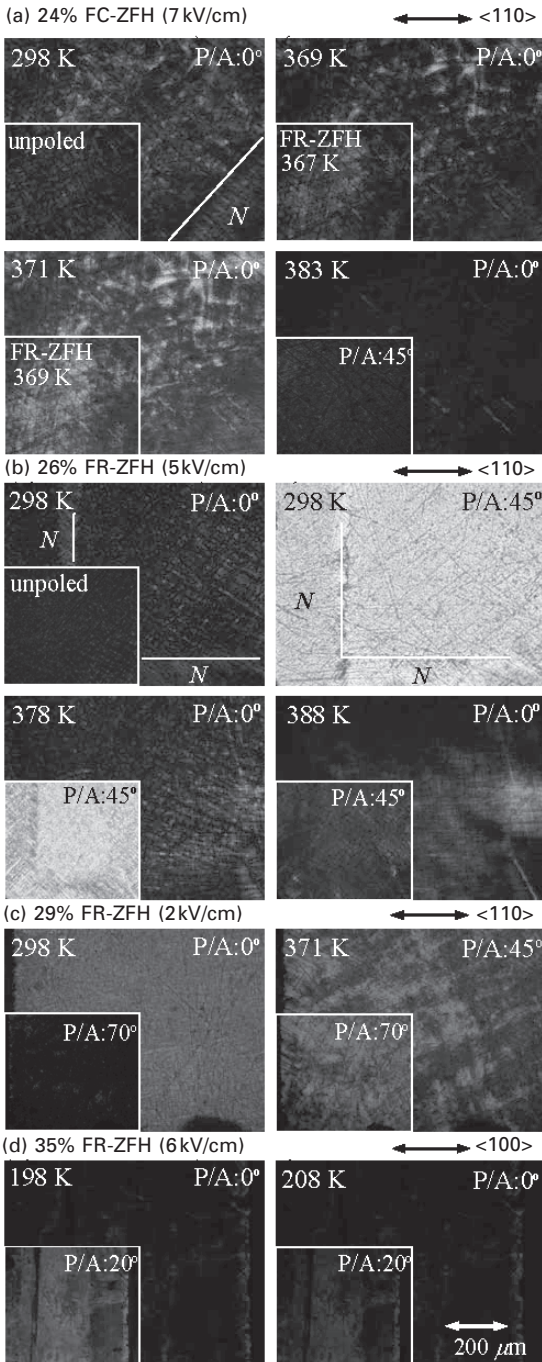
Figure 12.5(a) shows dielectric results of ZFH and FC-ZFH for PMN-24%PT. The maximum temperature  $T_m$  was shifted a few degrees higher in the FC-ZFH. Besides a broad maximum near 390 K an extra peak appears near 370 K in the FC-ZFH, whose position (but not the amplitude) is independent of frequency as seen in the inset. The  $P_r$  also exhibits an abrupt decline near 370 K. The coercive field  $E_C$  is  $\sim 3.8$  kV/cm at room temperature.



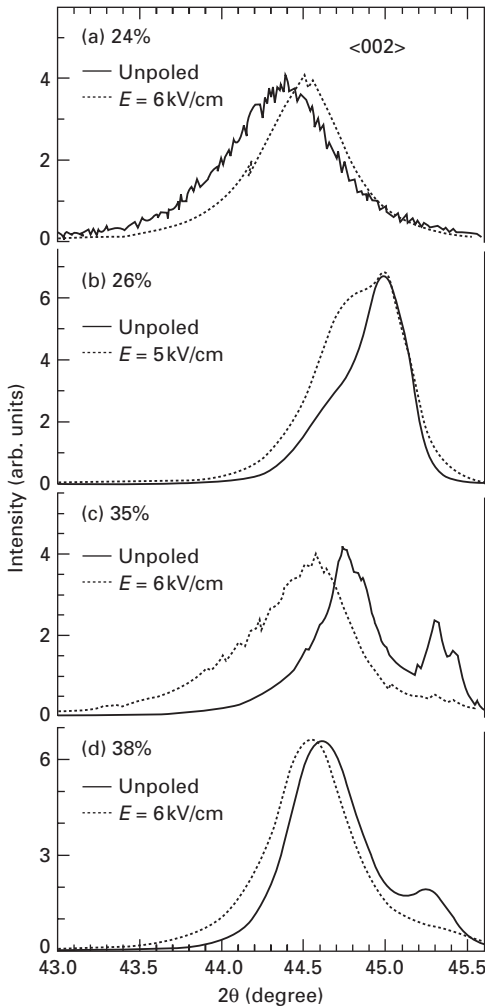


12.5 Dielectric permittivity and remanent polarization for (001)-cut PMN-xPT crystals,  $x =$  (a) 24%, (b) 26%, (c) 27%, (d) 29%, and (e) 35% (adapted from Tu *et al.*, 2004).

ZFH domain structures after FC are shown in Fig. 12.6(a). ‘N’ indicates the area without ITO films. When observing the (001)-cut sample along [001] between a crossed P/A pair with the  $\langle 110 \rangle$  sample edge aligned with P/A:  $0^\circ$ , the optical extinction angle of the R phase is  $0^\circ$ . As seen in the inset which shows extinction at  $0^\circ$ , the symmetry of unpoled PMN-24%PT is mostly R at 298 K. After the FC, besides the R domains at 298 K a small fraction of the domain matrix exhibits extinction in the range of  $\sim 20\text{--}70^\circ$ , indicating M domains (perhaps mixed with T domains whose extinction angle is  $45^\circ$ ). As shown in Fig. 12.7(a), the unpoled  $\langle 002 \rangle$  X-ray diffraction taken at room temperature shows a single peak, indicating the R phase even after poling at  $E = 6$  kV/cm. Near 371 K M domains associated with extinction



12.6 Domain structures. Angles of the P/A pair are with regard to the [110] for PMN–24%PT, 26%PT, and 29%PT and [100] for 35%PT crystals (adapted from Tu *et al.*, 2004). A color version of the figure can be found in Tu *et al.*, 2004.



12.7  $\langle 002 \rangle$  X-ray diffraction spectra taken at room temperature for unpoled and poled (001)-cut PMN- $x$ PT crystals,  $x =$  (a) 24%, (b) 26%, (c) 35%, and (d) 38%.

angles at  $\sim 20\text{--}70^\circ$  expand widely in the domain matrix. This anomaly was also seen in the FR-ZFH (Fig. 12.6a), suggesting that FR and FC have the same poling effect. The crystal becomes cubic phase near 383 K. Thus, after poling the PMN-24%PT undergoes a R(M) $\rightarrow$ M(R) $\rightarrow$ C transition sequence near 370 and 383 K upon heating. 'R(M)' represents that dominant R domains coexist with a smaller fraction of M domains.

More complicated dielectric anomalies were seen in PMN-26%PT. Compared with the ZFH, in the FR-ZFH two other anomalies, as shown in Fig. 12.5(b), were observed near 370–376 K and  $\sim 385$  K (as indicated by an

arrow) which were shifted to lower temperatures with increasing  $E$  field. The minimum  $E$  field to induce this behavior is  $\sim 1.0$  kV/cm which is smaller than room temperature  $E_C \sim 2.5$  kV/cm. As  $E$  field increases, the anomaly seen near 370–376 K becomes a single peak and rather weaker. As shown in Fig. 12.5(b),  $P_r$  and  $E_C$  also exhibit a peak near 370 K. Similar dielectric anomalies were observed in the FC–ZFH. ZFH domain structures after poling are shown in Fig. 12.6(b). The unpoled sample shows optical extinction at  $0^\circ$  at 298 K, indicating R domains. In the FR-ZFH, besides the dominant R domains, a very small fraction of M domain (with extinction angles of  $\sim 0$ – $10^\circ$ ) was observed at 298 K. Near 378 K the M domains dramatically expand with extinction angles of  $\sim 0$ – $15^\circ$ . Near 388 K some domains show extinction at  $45^\circ$ , indicating T domains. The crystal becomes cubic near 393 K. Similar domain anomalies were seen in the FR-ZFH (10 kV/cm). It is important to note that the ‘370 K’ anomaly was also observed in the pure ZFH domain observation, but not as apparent as the FR-ZFH. It implies that a prior poling can reveal a ‘hidden’ transition which is not obvious in an unpoled sample. The unpoled  $\langle 002 \rangle$  X-ray data (Fig. 12.7b) show a broad peak and a weak shoulder, which are similar with the  $\langle 002 \rangle$  synchrotron X-ray profile (Noheda *et al.*, 2002) and probably correspond to R and M phases respectively. The M phase becomes more pronounced after poling at  $E = 5$  kV/cm. Thus, after poling a R(M)  $\rightarrow$  M(R)  $\rightarrow$  M(T)  $\rightarrow$  C transition sequence occurs in PMN–26%PT near 370–376, 388, and 393 K upon heating.

Similar dielectric anomalies were observed in PMN–27%PT as given in Fig. 12.5(c). In the FC-ZFH two clear frequency-independent anomalies (as marked by dashed lines) occurred near 370 and 392 K. The  $P_r$  also shows a maximum peak and a rapid decline near 370 and 392 K. After poling the PMN–27%PT probably goes through a R(M)  $\rightarrow$  M(R)  $\rightarrow$  M(T)  $\rightarrow$  C transition sequence near 370, 392, and 400 K respectively upon heating.

Figure 12.5(d) shows ZFH and FR-ZFH dielectric results for PMN–29%PT. Besides a broad maximum near 407 K, two extra peaks appear near 358 and 368 K after poling. The minimum  $E$  field to induce this anomaly is  $\sim 2.0$  kV/cm which is smaller than room temperature  $E_C \sim 3.3$  kV/cm. The  $P_r$  exhibits an abrupt decline near 365 K. As given in Fig. 12.6(c), at 298 K domains show extinction in the range of  $\sim 40^\circ$ – $80^\circ$ , indicating mostly M domains. At 371 K, besides a small fraction of M domains associated with extinction at  $\sim 60$ – $80^\circ$ , most domains exhibit extinction at  $45^\circ$ , which indicates T phase domains. In other words, an M(T)  $\rightarrow$  T(M) transition occurs near 370 K. A similar anomaly was seen in the pure ZFH domain observation. An extra peak that occurred near 358 K and weak shoulders that appeared in the region of 400–407 K, as seen in Fig. 12.5(d), are probably due to phase segregation.

Instead of a gradual climb up in the ZFH, the FR-ZFH of PMN–35%PT in Fig. 12.5(e) exhibits a step-like decline near 200–210 K. ZFH domain

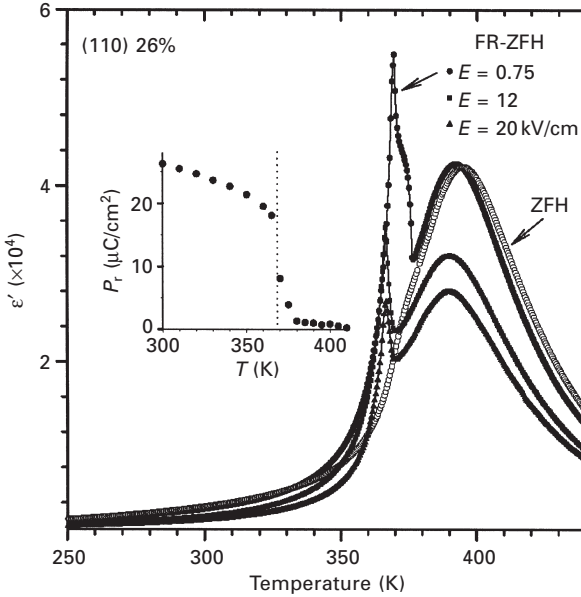
structures observed after poling are shown in Fig. 12.5(d) for 198 and 208 K. Below 198 K domains exhibit extinction from 0 to 10°, but near 208 K the extinction range becomes twice as wide, i.e. 0–20°. A similar anomaly was seen in the pure ZFH domain observation. The 90° domain walls between two domains with their T-phase polar axes along [100] and [010] were seen before the FR process but disappeared after poling. T and M<sub>C</sub>-type M domains have extinction at 0° with regard to [100]. The broad extinction angles (0–20°) imply that polarization directions of M domains are close to [001] T polarization. The crystal reaches mostly total extinction at  $E = 9 \text{ kV/cm}$ .

The unpoled <002> X-ray diffraction [Fig. 12.7c] for PMN–35%PT exhibits at least four peaks. A dominant T phase mixed with M phase was found in the unpoled PMN–35%PT ceramics (Noheda *et al.*, 2002). Thus, these peaks probably are associated with T and M phase domains. After poling, a strong broad peak and a weak shoulder were observed, perhaps indicating two main T and M phase domains. Based on the above evidence, a long-range M(T)→T(M) transition probably takes place in the region of 200–210 K after poling. The crystal becomes cubic near 440 K, where the  $P_r$  exhibits a rapid decline.

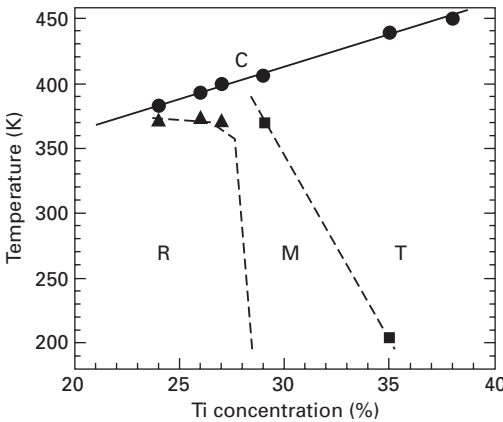
A step-like decline was seen near 210 K in the FR–ZFH of PMN–38%PT as shown in Fig. 12.5(e). This anomaly was not observed for  $E \leq 5 \text{ kV/cm}$  and  $E_C$  is ~6 kV/cm at room temperature. From the ZFH domain observation, a coexistence of T and M domains was seen in a PMN–38%PT crystal in which T domains increase rapidly from 200 to 300 K. Two peaks were seen in the unpoled <002> X-ray diffraction of Fig. 12.7(d), perhaps indicating a coexistence of T and M domains. After poling, only a broad peak was observed. Note that the  $E$  field was along the [001] T polar direction. Thus, the dielectric anomaly seen near 210 K in the FR–ZFH most likely indicates a long-range T(M)→T transition.

Briefly, phase thermal stability of (001)-cut PMN–PT crystals after a prior  $E$ -field poling strongly depends on Ti content and field strength. The ‘370 K’ dielectric anomaly was seen in PMN–24%PT, PMN–26%PT, and PMN–27%PT, and correlates to a R(M)→M(R) transition. FC and FR have the same effect on phase transitions as seen upon subsequent ZFH. For a differently oriented compound, similar dielectric anomalies after a prior field poling were also seen in (110)-cut PMN–26%PT as shown in Fig. 12.8. An extra dielectric anomaly ‘triggered’ by a prior field poling seems to be a common phenomenon in PMN–PT (Chien *et al.*, 2005b) and PZN–PT crystals. However, this extra dielectric anomaly can be easily erased by thermal annealing in the C phase.

Figure 12.9 shows a phase diagram based on the above evidence, in which the phase boundaries may be changed with stronger  $E$  field or different crystallographic orientation. It is very different from the phase diagram for unpoled PMN–PT crystals, in which the M phase was not found. An M<sub>C</sub>



12.8 Dielectric permittivity and remanent polarization for (110)-cut PMN-26%PT crystal (adapted from Chien *et al.*, 2005b).



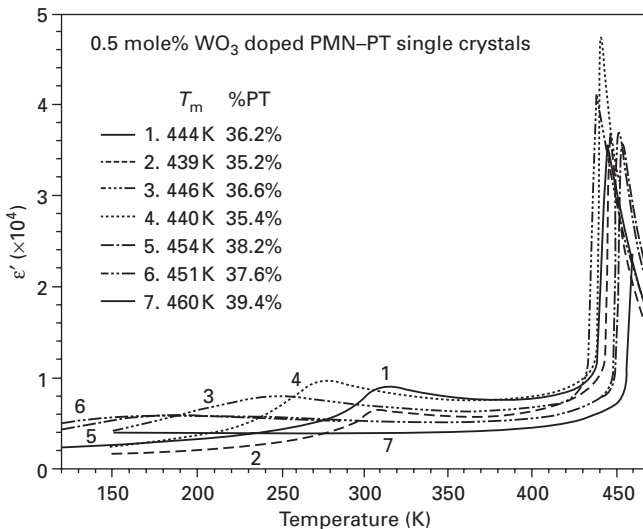
12.9 Phase diagram of (001)-cut PMN-PT crystals after poling. Triangle and square symbols represent R(M) $\rightarrow$ M(R) and M(T) $\rightarrow$ T(M) transitions respectively. Lines are estimated boundaries for various dominant phases (adapted from Tu *et al.*, 2004).

phase was found to coexist with R, T, or O phases in unpoled PMN- $x$ PT ceramics for  $31 \leq x \leq 37$  (Noheda *et al.*, 2002).  $M_B$  and  $M_C$  phases were also found in unpoled PMN- $x$ PT ceramics for  $27 \leq x \leq 30$  and  $31 \leq x \leq 34$  respectively. Regarding the prior poling effect in PMN-PT crystals, more details and references can be found in Tu *et al.* (2004).

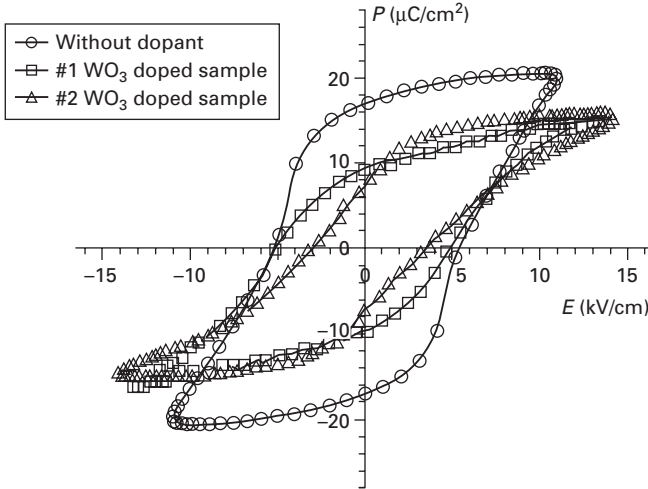
### 12.4.2 WO<sub>3</sub> doped PMN–PT crystals

Recently, an unpoled PMN–PT single crystal with 0.5 mole% WO<sub>3</sub> in the growth solution exhibited an interesting wavelength-dependent photovoltaic response after a prior *E*-field poling (Tu *et al.*, 2006a). In addition, WO<sub>3</sub>-doped PMN–PT crystals show higher dielectric permittivities compared with the pure PMN–PT crystals (without tungsten dopant). Figure 12.10 illustrates temperature-dependent dielectric permittivities from different layers of the same WO<sub>3</sub>-doped unpoled crystals. It shows obvious PT segregation with different dielectric maximum temperature  $T_m$ . Dielectric permittivity exhibits a wide range of thermal stability (below the cubic phase) and can reach  $\sim 10^4$  at room temperature for some compounds, which are promising for piezoelectric applications.

Figure 12.11 shows hysteresis loops (polarization vs. *E* field) from WO<sub>3</sub>-doped PMN–PT crystals (#1 and #2) and an undoped PMN–PT compound. The spontaneous and remanent polarizations and the coercive field ( $E_C$ ) are smaller compared with the undoped crystal. Such significant reduction of electric polarization may be due to a tendency toward a different structure near tungsten ions. Pure WO<sub>3</sub> has a monoclinic ferroelectric phase (Jona and Shirane, 1962).



12.10 Dielectric permittivities of 0.5 mole% WO<sub>3</sub> doped PMN–PT crystals taken at  $f = 10$  kHz upon heating without any *E*-field poling. Crystals #1–6 are from different layers of the same crystal. Crystal #7 is without WO<sub>3</sub> dopant.



12.11 Hysteresis loops of  $\text{WO}_3$ -doped PMN-PT crystals (#1 and #2), and the pure PMN-PT crystal taken at room temperature.

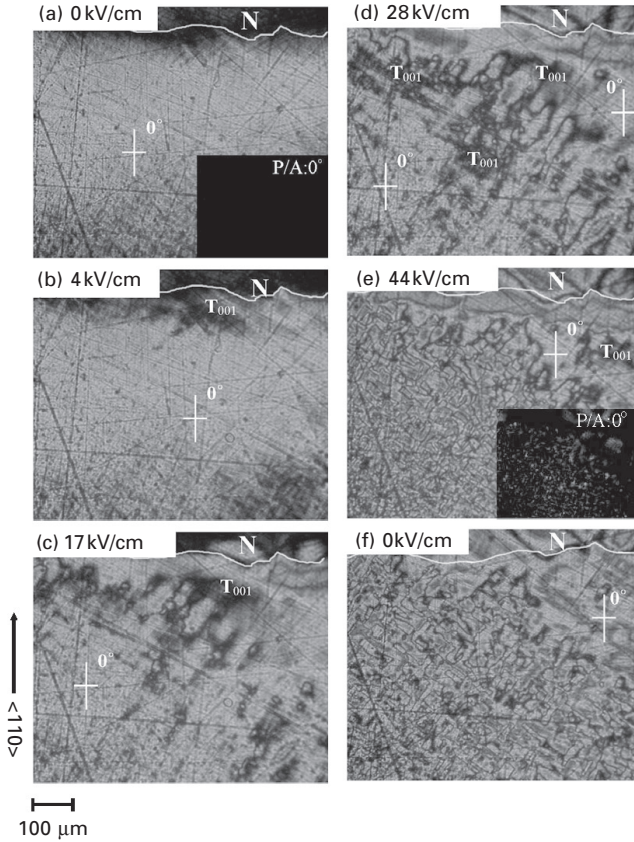
## 12.5 Field-dependent domain structures of various PMN-PT compositions

### 12.5.1 (001)-cut PMN-24% PT crystal

Figure 12.12 shows the  $E$ -field-dependent domain structures taken at  $P/A: 45^\circ$  in a PMN-24%PT crystal as a dc  $E$  field is applied along  $[001]$ . Without  $E$ -field poling, the whole domain matrix exhibits extinction at  $P/A: 0^\circ$  with respect to the  $[110]$  direction as shown in the inset of Fig. 12.12(a). When observing the (001)-cut sample along the  $[001]$  direction between a crossed  $P/A$  pair, as shown in Fig. 12.2, the extinction angle is  $0^\circ$  (or  $90^\circ$ ) for all R domains. Thus, domains in the PMN-24%PT crystal are certainly R phase at  $E = 0\text{ kV/cm}$ . In addition, there is no evidence for the O phase in the PMN-24%PT at zero  $E$  field.

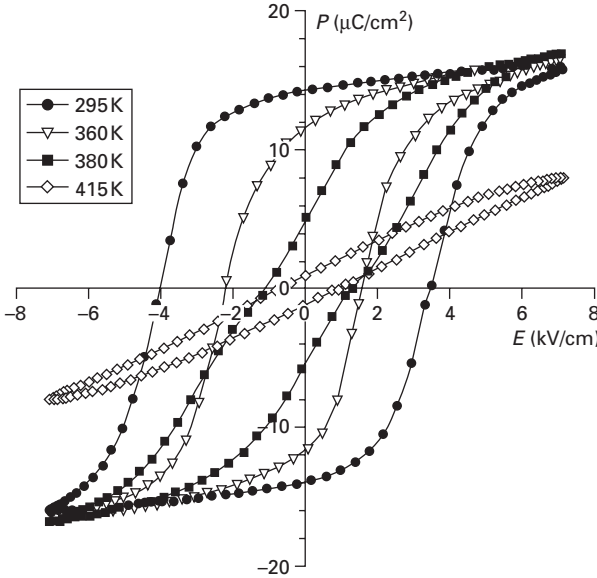
Near  $E = 4\text{ kV/cm}$  (Fig. 12.12b), the domain matrix begins to exhibit change and some domains show extinction at all  $P/A$  angles, indicating a T phase with polarization along the  $[001]$  direction labeled as  $T_{001}$  in the micrograph. This is consistent with the coercive field  $E_C \sim 3.8\text{ kV/cm}$  as shown in Fig. 12.13. The  $T_{001}$  domain corresponds to the black square in Fig. 12.2. The rest of the domain matrix exhibits R phase with extinction at  $0^\circ$ . As the field increases, the  $T_{001}$  phases gradually expand in the domain matrix as shown in Fig. 12.12(c) and (d). Above  $E \sim 30\text{ kV/cm}$  (Fig. 12.12e), the  $T_{001}$  phase rapidly spreads into the domain matrix and forms network-like  $[001]$  T domain chains, indicating a long-range order of the  $[001]$  T phase. Most domains still maintain extinction angle at  $0^\circ$  except for the network-like  $T_{001}$





12.12 E-field-dependent domain micrographs taken with P/A:  $45^\circ$  (except for insets) at room temperature for dc  $E$  field applied perpendicular to the (001)-cut plane of the PMN-24%PT crystal. P/A:  $0^\circ$  was aligned with the  $\langle 110 \rangle$  sample edge. 'N' indicates the area without ITO films (adapted from Chien *et al.*, 2004). A color version of the figure can be found in Chien *et al.* (2004).

domains. However, for  $E \geq 30 \text{ kV/cm}$  spot-like domains that do not exhibit extinction at  $0^\circ$  appear in the domain matrix as shown in the inset of Fig. 12.12(e). These spot-like domains exhibit extinction at angles within a few degrees of  $20^\circ$ , indicating M phase. After the  $E$  field was removed (Fig. 12.12f), domains exhibit very different structures compared with the domains in the beginning at  $E = 0 \text{ kV/cm}$ , showing a hysteretic poling process, in agreement with the hysteresis loop shown in Fig. 12.13. Note that the polarizing microscope results also aid in interpreting the hysteresis loop in Fig. 12.13. The loop appears saturated, so one might think that as the field along [001] is reversed, a single [001] domain is switched into a single  $[00\bar{1}]$  domain. Alternatively, one might think that the crystal converts from the four R

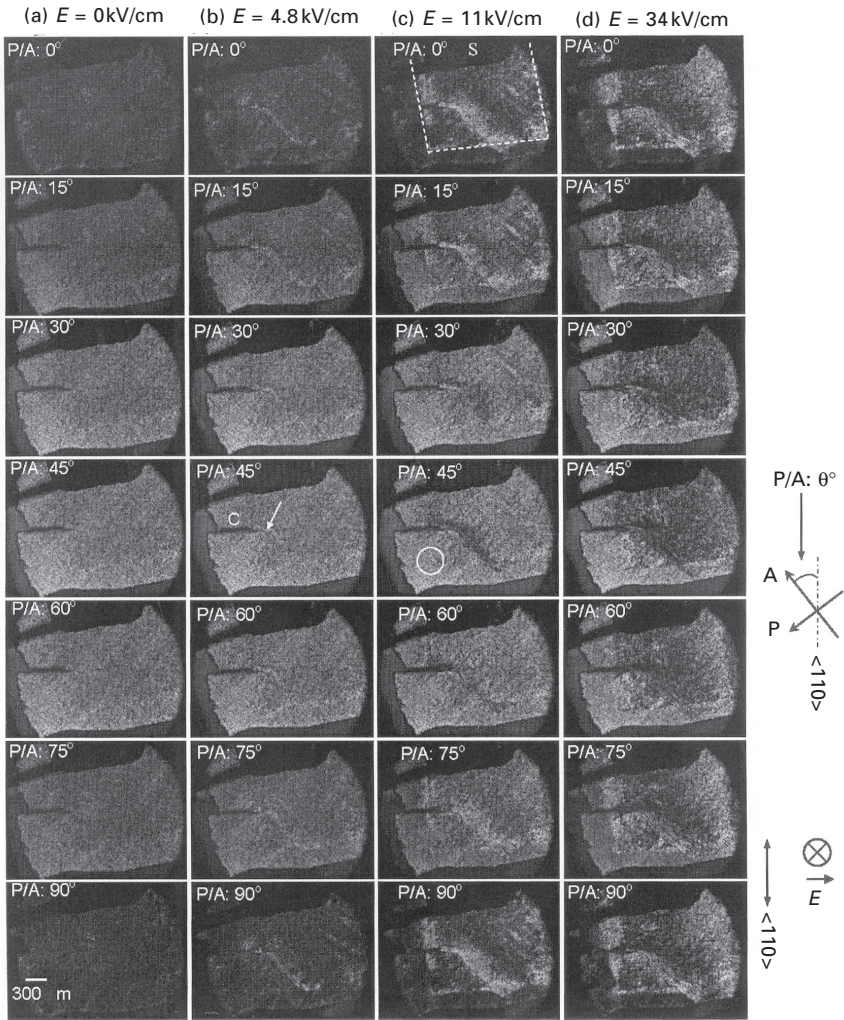


12.13 The hysteresis loops of polarization vs.  $E$  field for various temperatures in the (001)-cut PMN–24%PT crystal.

domains with a positive polarization component along [001] to the four domains with a negative component along [001]. From the domain pictures in Fig. 12.12 it is apparent that the hysteresis loop represents only incomplete switching.

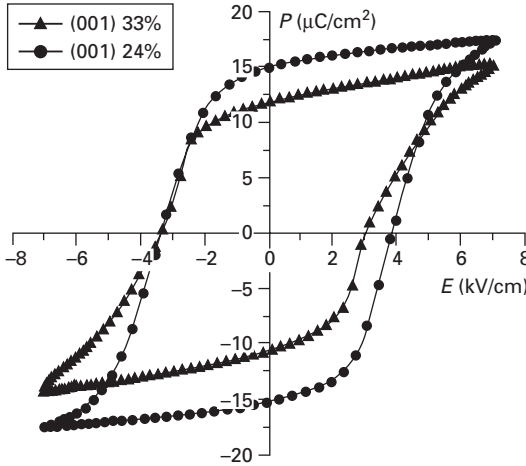
### 12.5.2 (001)-cut PMN–33%PT crystal

Figure 12.14 shows the domain micrographs taken with various  $P/A$  angles at room temperature for various  $E$ -field strengths while a dc  $E$  field was applied along [001] in a (001)-cut PMN–33%PT single crystal. The domain micrograph taken at  $P/A: 0^\circ$  appears the same as that taken at  $P/A: 90^\circ$ . At  $E = 0$  kV/cm (Fig. 12.14a), the domain matrix mostly exhibits extinction at  $P/A = 0^\circ$  with respect to the  $\langle 110 \rangle$  direction, indicating an R phase according to the optical extinction pattern discussed in Section 12.3. If O or T phase domains exist, there will also be extinction at  $P/A: 45^\circ$ . However, no extinction was observed at  $P/A: 45^\circ$ . The domain matrix has no obvious changes until 4.1–4.8 kV/cm as shown in Fig. 12.14(b). The domain matrix mostly still retains R phase, but  $T_{001}$  and M/T phases are induced near the cracking area, as indicated by the arrow in Fig. 12.14(b). The  $T_{001}$  phase domain exhibits extinction at every  $P/A$  angle (i.e. total optical extinction), whereas the M/T phase domain exhibits extinction angles at  $\sim 15\text{--}65^\circ$ . M/T represents the coexistence of M and T phases with more M phase than T phase domains.



**12.14** Domain micrographs taken with P/A angle from  $0^\circ$  to  $90^\circ$  in (001)-cut PMN-33%PT crystal at room temperature (a) under no field, and under the E-field strengths of (b) 4.8 kV/cm, (c) 11 kV/cm, and (d) 34 kV/cm applied perpendicular to the paper. The boundaries of ITO electrodes are indicated by the dashed lines. 'S' indicates silver paste.

Note that the coercive field  $E_C$  for the PMN-33%PT crystal is about 3 kV/cm as given in Fig. 12.15. As the field increases to 11 kV/cm (Fig. 12.14c), the  $T_{001}$  phase domain significantly expands as crossed stripes along [100] and [010] from the cracking area. Some of the R phase domains have also transformed to M and T phase with various non-zero-degree extinction angles, such as 5–15°, 20–50°, and 50–75°. However, a small portion of the domain

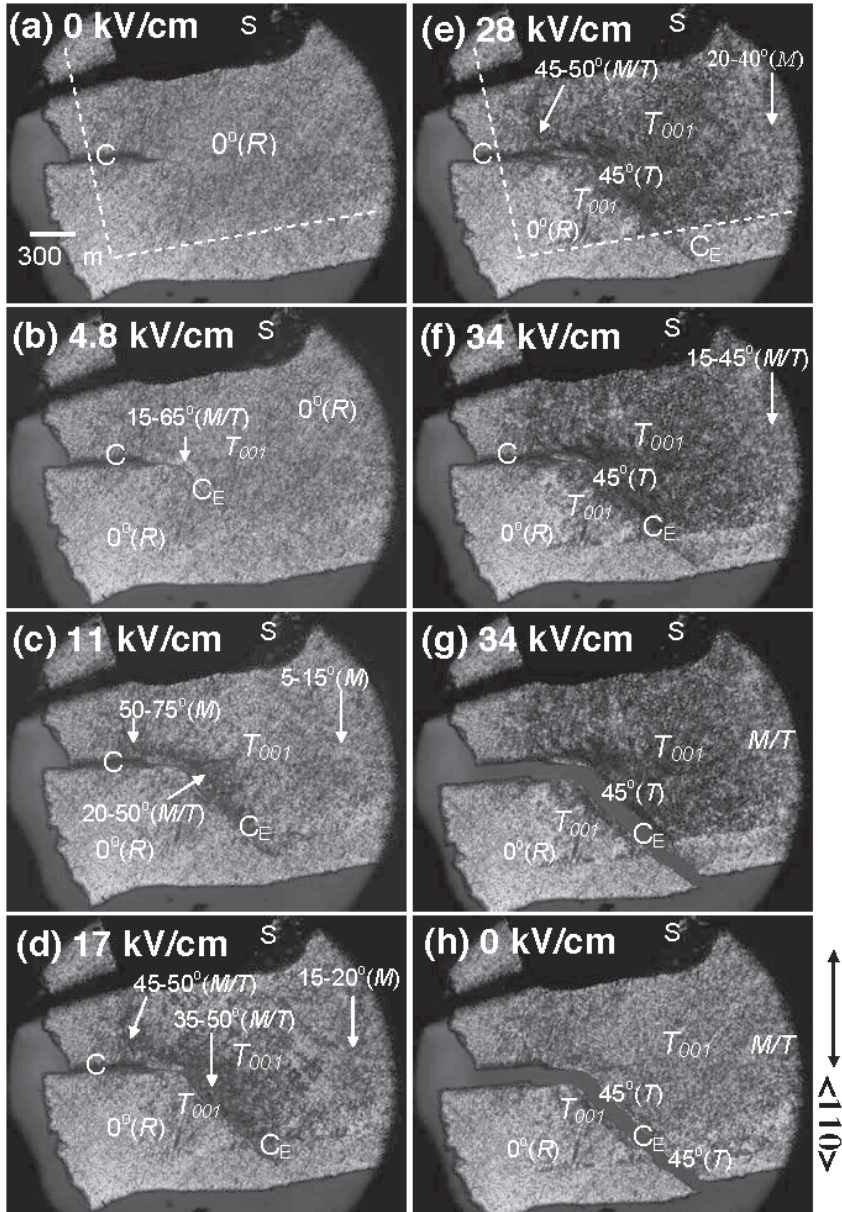


12.15 Hysteresis loops of polarization vs.  $E$  field for (001)-cut PMN-24%PT and PMN-33%PT crystals.

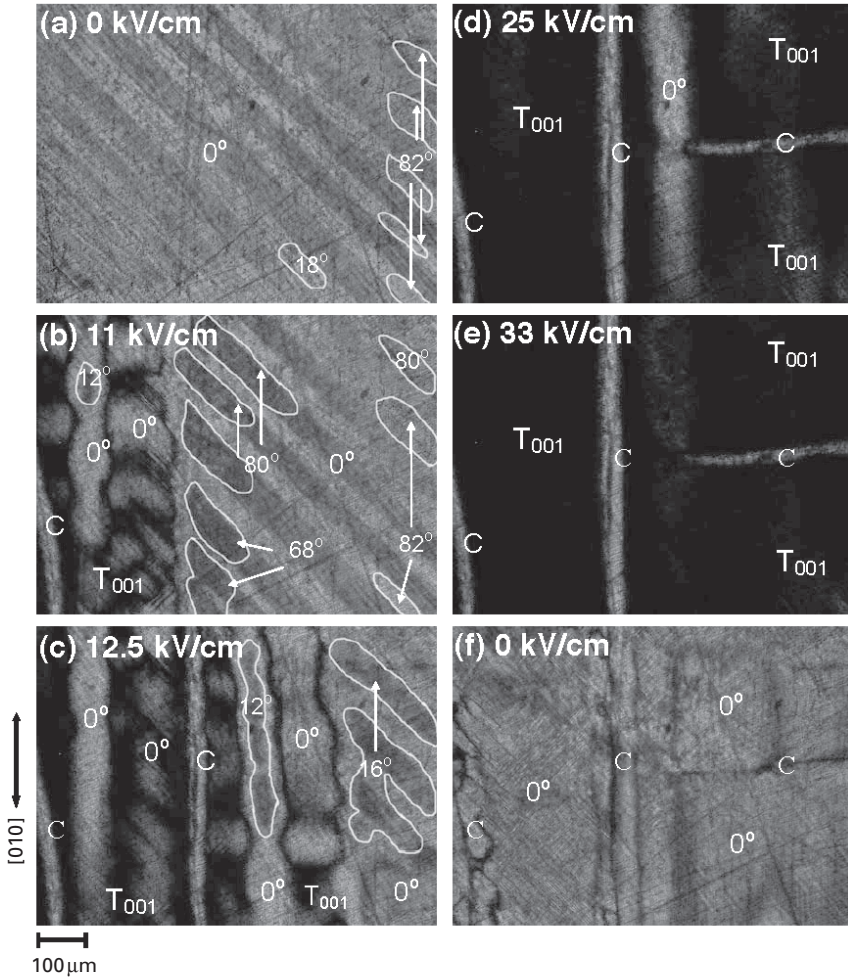
matrix circled in Fig. 12.14(c) still remains in the R phase. With increasing  $E$  field, this  $E$ -field-induced transition is continuously evidenced by the expansion of the  $T_{001}$  phase domain shown as a black area of the domain matrix. At  $E = 34$  kV/cm, most of the domain matrix becomes macroscopic  $T_{001}$  phase domain except for some small R, T, and M phase domains with extinction angles of  $0^\circ$ ,  $45^\circ$ , and  $\sim 15$ – $45^\circ$  as shown in Fig. 12.14(d). In addition, a few domains exhibiting no extinction at any  $P/A$  angle are embedded in the  $T_{001}$  domain matrix, perhaps due to crystal defects and local strain caused by underlying M phase distortions with various different orientations. In brief, the  $E$ -field-dependent phase transition sequences at room temperature in the (001)-cut PMN-33%PT include  $R \rightarrow T_{001}$ ,  $R \rightarrow M \rightarrow T_{001}$ ,  $R \rightarrow T \rightarrow T_{001}$ , and  $R \rightarrow M \rightarrow T \rightarrow T_{001}$ . With a fixed  $P/A$  angle (Fig. 12.16), the  $E$ -field-induced transition is continuously evidenced by the expansion of the  $T_{001}$  phase domain as the  $E$  field increases. The (001)-cut PMN-33%PT and PMN-24%PT crystals show similar behavior in the hysteresis loop of polarization vs.  $E$  field (Fig. 12.15). However, the polarizing light micrographs in Fig. 12.12 and 12.16 exhibit some visual difference between the two crystals in the formation of the  $E$ -field-induced  $T_{100}$  phase domains.

### 12.5.3 (001)-cut PMN-40%PT crystal

Figure 12.17 shows the  $E$ -field-dependent domain structures taken with  $P/A$ :  $45^\circ$  for the PMN-40%PT crystal while a dc  $E$  field was applied along [001] at room temperature. As the  $P/A$  reading  $0^\circ$  was aligned with the [010] sample edge, every optical extinction angle expressed in the picture is the



12.16 E-field-dependent domain micrographs taken with P/A: 45° at room temperature for dc E field applied perpendicular to the (001)-cut plane of the PMN-33%PT crystal. 'S' indicates silver paste. 'C' and 'C<sub>E</sub>' indicate cracks caused by polishing and E field poling, respectively (adapted from Chien *et al.*, 2006). A color version of the figure can be found in Chien *et al.* (2006).



12.17 E-field-dependent domain micrographs taken with P/A:  $45^\circ$  at room temperature for dc  $E$  field applied perpendicular to the (001)-cut plane of the PMN-40%PT crystal. P/A:  $0^\circ$  was aligned with [010] sample edge. 'C' indicates microcracking (adapted from Chien *et al.*, 2005a). A color version of the figure can be found in Chien *et al.* (2005a).

angle between one of the P/A pair axes and [010]. 'C' indicates a crack caused by the polishing and  $E$ -field poling process. At  $E = 0$  kV/cm (Figure 12.17a), the domain matrix mostly exhibits an extinction at  $0^\circ$  and some at non-zero degrees such as  $18^\circ$  and  $82^\circ$  with respect to the [010] direction, indicating the coexistence of a dominant T phase with polarizations  $P$  along the [100] and [010] axes and some minor M phase. As the  $E$  field increases, the domain matrix does not evidently change until 11 kV/cm as seen in Fig.

12.17(b). At  $E = 11$  kV/cm, the domain structure displays the  $T_{001}$  domain with polarization  $P$  along the [001] axis, which is associated with optical extinction at every orientation of the crossed P/A pair (i.e. total optical extinction), and some M domains with various non-zero-degree extinction angles, such as  $12^\circ$ ,  $68^\circ$ ,  $80^\circ$ , and  $82^\circ$  at the expense of the T phase domains. This indicates that some domains have transformed to  $T_{001}$  and M phase. With increasing  $E$  field, more of the M phase domains have been poled to the  $T_{001}$  domain as shown in the dark area in Fig. 12.17(c), and the other M domains have changed their polarization orientations with various non-zero-degree extinction angles, such as  $12^\circ$  and  $16^\circ$ . Most of the domain matrix exhibits total optical extinction (i.e. the  $T_{001}$  phase domains) except a stripe oriented along [010] as the  $E$  field reaches 25 kV/cm (Fig. 12.17d). The entire crystal becomes  $T_{001}$  monodomain near  $E = 33$  kV/cm as seen in Fig. 12.17(e). After the  $E$  field was removed (Fig. 12.17f), the domain structure did not return to the broad  $T_{100}$  and  $T_{010}$  domains separated by the  $90^\circ$  domain walls as shown in Fig. 12.17(a). However, the extinction pattern is in agreement with T microdomains with polarizations  $P$  along the [100] or [010] axes.

#### 12.5.4 Summary for various crystal cuts and compositions

In the (001)-cut PMN–24%PT crystal, an  $R \rightarrow T_{001}$  phase transition is induced near  $E = 4$  kV/cm through  $M_A$  phase domains as  $E$  field increases along [001] at room temperature, i.e.  $R \rightarrow M_A \rightarrow T_{001}$ . In the (001) PMN–40%PT crystal, the  $T_{001}$  phase domains are induced near  $E = 11$  kV/cm at room temperature by the process of polarization rotation of  $T \rightarrow M \rightarrow T_{001}$ , and this  $T_{001}$  phase expands through the whole crystal as the  $E$  field increases further. Similarly, in the (001)-cut PMN–33%PT crystal the  $T_{001}$  phase domains are induced near  $E = 4.1$  kV/cm at room temperature and expand significantly at  $E = 11$  kV/cm by various phase transition sequences  $R \rightarrow T_{001}$ ,  $R \rightarrow M \rightarrow T_{001}$ ,  $R \rightarrow T \rightarrow T_{001}$ , and  $R \rightarrow M \rightarrow T \rightarrow T_{001}$ . Therefore, the intermediate M phases play an essential role in bridging higher symmetries while the  $E$ -field induced transitions are taking place in the PMN–PT crystals.

The  $E$ -field-induced phase results at room temperature differ for the three crystals with various Ti content, while a high dc  $E$  field is applied across the crystal cut plane (001). The (001)-cut PMN–40%PT crystal becomes  $T_{001}$  monodomain near  $E = 33$  kV/cm. On the other hand, the (001)-cut PMN–24%PT and (001)-cut PMN–33%PT crystals cannot reach a  $T_{001}$  monodomain under the maximum  $E$  field of 44 and 34 kV/cm, respectively. However, the (111)-cut PMN–33%PT crystal gradually reaches an  $R_{111}$  monodomain at  $E = 12$  kV/cm applied along [111] at room temperature (Tu *et al.*, 2003b). Therefore, a monodomain with the orientation along the poling field was not

always obtained under the maximum  $E$ -field strength in every crystal at room temperature as expected. The  $E$ -field-induced monodomain can be achieved in the PMNT crystals if the dc poling field is along the polar axes of the phase favored by the temperature, such as the (111)-cut PMN–33%PT and (001)-cut PMN–40%PT crystals. For instance, T polar directions are favored at room temperature in the (001)-cut PMN–40%PT so that less  $E$ -field poling strength is needed to induce the T phase domains with the field applied along [001]. On the other hand, the T phase is not favored at room temperature in the (001)-cut PMN–24%PT so that it takes higher  $E$ -field poling strength to induce the T phase domains. By comparison with the results for (001)-cut PMN– $x$ %PT ( $x = 24, 33,$  and  $40$ ) and (111)-cut PMN–33%PT crystals, it was found that whether or not a monodomain can be induced by a dc electric field strongly depends on crystallographic orientation, PT content, and temperature. More details of the results and discussion were reported for a (001)-cut PMN–24%PT crystal (Chien *et al.*, 2004), (111)-cut PMN–33%PT crystals (Tu *et al.*, 2003a,b), a (001)-cut PMN–33%PT crystal (Chien *et al.*, 2006), and a (001)-cut PMN–40%PT crystal (Chien *et al.*, 2005a).

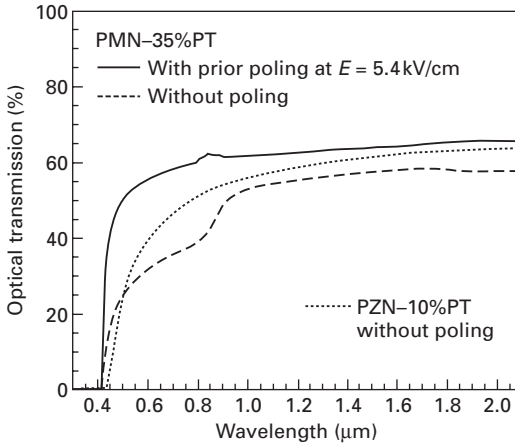
### 12.5.5 Microcracking in PMN–PT single crystals

Microcracking caused by a dc  $E$ -field poling process was observed in the PMN–33%PT and PMN–40%PT crystals with a dc  $E$  field applied along [001] at room temperature. However, no microcracking was found in the PMN–24%PT crystal (Fig. 12.12) under  $E = 44$  kV/cm applied along [001] and the PMN–33%PT with  $E$  field applied along [111] (Tu *et al.*, 2003b). In the PMN–33%PT crystal with a dc  $E$  field applied along [001] as shown in Fig. 12.16, the microcracking indicated by ‘ $C_E$ ’ starts to develop at  $E \sim 4.8$  kV/cm along [100] (or [010]) from the pre-existing crack ‘C’. The crack is enlarged by increasing field strength. At  $E = 34$  kV/cm, the crack reaches the sample edge and the crystal breaks into two pieces. The crystal still maintains the same R, T,  $T_{001}$ , and M phase domains as before it breaks (Fig. 12.16f). In the PMN–40%PT crystal (Fig. 12.17) with a dc  $E$  field applied along [001], the microcracking starts to develop at  $\sim 12.5$  kV/cm along [010] and the cracks tend to develop along [100] (or [010]), which is the growth direction of the  $T_{001}$  phase domain that is being induced by a dc  $E$  field applied along [001]. The crack is also enlarged by increasing field strength.

## 12.6 Field-poling effect on optical properties

Wavelength-dependent optical transmission from 0.3 to 2.1  $\mu\text{m}$  given in Fig. 12.18 for a (001)-cut PMN–35%PT single crystal exhibits little absorption before reaching the cut-off wavelength  $\lambda \cong 0.4 \mu\text{m}$ , which is the same with and without a prior  $E$ -field poling. The same cut-off wavelength  $\lambda \cong 0.4 \mu\text{m}$



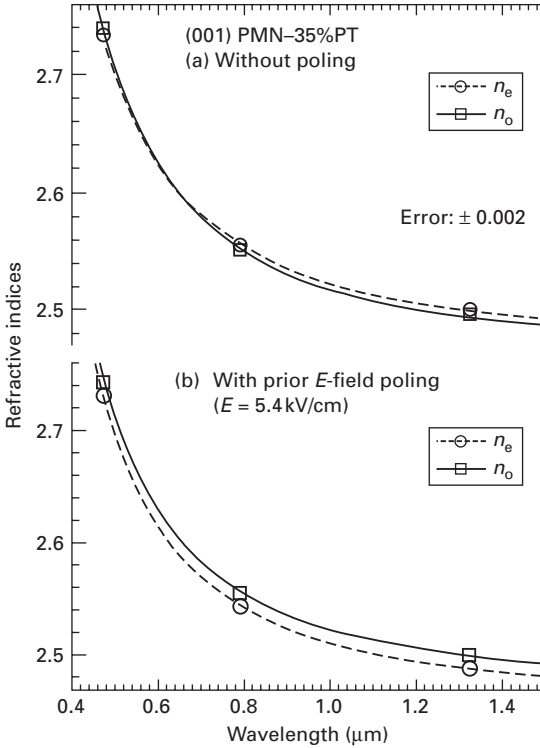


12.18 Optical transmission without poling and with prior poling at  $E = 5.4$  kV/cm for a (001)-cut PMN-35%PT crystal, and without poling for a (001)-cut PZN-10%PT crystal.

was also observed in different PMN-PT crystals with different orientations and Ti contents. Figure 12.18 is shows that a prior poling process can enhance the optical transmission by about 20%, probably because of reduction of internal reflection by domain walls and strains. The cut-off at  $\lambda \cong 0.4 \mu\text{m}$  implies an average electronic energy gap of about 3.0 eV.

Figure 12.19 shows ordinary  $n_o$  and extraordinary  $n_e$  refractive indices measured at room temperature without poling and with a prior poling ( $E = 5.4$  kV/cm). In the prior poling process, the crystal was poled at room temperature along a  $\langle 010 \rangle$  direction which is the optical axis of the uniaxial T symmetry. After a prior poling at  $E = 5.4$  kV/cm, the crystal shows a noticeable 'negative' uniaxial birefringence and  $n_e - n_o$  is about  $-0.0129$  at  $\lambda = 0.790 \mu\text{m}$ . The birefringence does not increase noticeably even with a higher poling field ( $E > 5.4$  kV/cm). For instance, after poling at  $E = 12$  kV/cm, the refractive indices are  $n_o = 2.5025$  and  $n_e = 2.4908$  at  $\lambda = 1.323 \mu\text{m}$ , and  $n_o = 2.5583$  and  $n_e = 2.5466$  at  $\lambda = 0.790 \mu\text{m}$ . The Cauchy equations obtained from fitting data for the sample poled at 5.4 kV/cm are  $n_o(\lambda) = 2.4716 + 0.0483/\lambda^2 + 0.0029/\lambda^4$  and  $n_e(\lambda) = 2.4606 + 0.0467/\lambda^2 + 0.0032/\lambda^4$ , where  $\lambda$  is in  $\mu\text{m}$ .

Without poling, the crystal shows very small birefringence  $|n_o - n_e|$  which is less than 0.004 at  $\lambda = 0.790 \mu\text{m}$ . The birefringence is non-zero because the light goes through a few domains of different size, so the various domains do not completely cancel the birefringence. Different unpoled crystals of the same composition can be expected to show different residual birefringence values. The Cauchy equations obtained from fitting measured data for this particular unpoled sample are  $n_o(\lambda) = 2.4649 + 0.0512/\lambda^2 + 0.0023/\lambda^4$  and  $n_e(\lambda) = 2.4720 + 0.0488/\lambda^2 + 0.0022/\lambda^4$ .



12.19 Refractive indices measured at room temperature for a (001)-cut PMN-35%PT crystal (adapted from Tu *et al.*, 2005).

The calculation of phase-matching angle for second harmonic generation shows that the phase-matching condition does not exist for poling  $E$  field  $< 12 \text{ kV/cm}$ . More optical properties of transmission and refractive indices were studied in PMN-PT (Tu *et al.*, 2005), PZN-PT (Tu *et al.*, 2006c) and PIN-PT (Tu *et al.*, 2006b,d) crystals.

### 12.7 Relation of results to Landau free energy

From the foregoing results, it is evident that PMN-PT crystals near the morphotropic phase boundary composition are delicately balanced among several possible phases. In fact, small distortions from the cubic parent phase can result in the crystal structure being in six of the seven crystal systems. Of these seven, only the hexagonal system is ruled out, and the triclinic system is yet to be seen.

As seen from Figs 12.2-12.4, the spontaneous polarization vector  $P$  can point in a variety of directions for these phases. There are six directions for the T domains, eight for the R domains, and 12 for the O domains, totaling

26 discrete directions. This was probably enough to embolden Pirc and Blinc (1999) to propose the spherical model, within which polar clusters can have  $P$  pointing in all possible directions. Yet besides these 26 discrete directions,  $P$  for the monoclinic  $C$  ( $M_C$ ) can point in any direction in each of the three  $\langle 100 \rangle$ -type planes. For the  $M_A$  and  $M_B$  monoclinic phases,  $P$  can point in any direction in the six  $\langle 110 \rangle$ -type planes, and in fact the phase designation ( $M_A$  or  $M_B$ ) switches as  $P$  rotates in one of these planes past a  $\{111\}$ -type direction. These nine planes (which include the 26 points for the T, R, and O domain polarizations) divide the solid angle sphere into 48 regions. Only for Tri domains can  $P$  point in the interior of such a region. Such domains have not yet been reported, and indeed it would require a careful measurement to distinguish such a polarization direction from a nearby T, R, O, or M domain polarization direction.

How can such a multiplicity of observed phases be explained? Vanderbilt and Cohen (2001) shed much light on this question with a Landau-type free energy analysis. This analysis involves expansion of the free energy  $F$  in terms of even powers of  $P_x$ ,  $P_y$ , and  $P_z$  and products of such factors. The coefficients of the various terms must be consistent with the symmetry of the parent C phase. To fourth order we have

$$F = A_2 P^2 + B_4 (P_x^4 + P_y^4 + P_z^4) + B_{22} (P_x^2 + P_y^2 + P_y^2 P_z^2 + P_z^2 + P_x^2) \quad 12.1$$

The coefficients such as  $A_2$  may be functions of temperature  $T$  and hydrostatic pressure  $p$ , but not of variables such as uniaxial pressure or electric field that break the cubic symmetry. Then, examining Eq. (12.1), we see that if we truncate the expansion at second order, we could have a  $T$ - or  $p$ -induced ferroelectric transition. However, it would have the unphysical property of going from zero polarization to infinite polarization in arbitrary direction as  $A_2$  changes sign to negative. Obviously, we must go to fourth order to begin obtaining physically meaningful results.

Going to fourth order by using all terms in Eq. (12.1), we find that (as also for uniaxial ferroelectrics) there can only be a second-order ferroelectric transition, which again occurs when  $A_2$  becomes negative. The requirements that ensure that  $P$  remains finite are that  $B_4 > 0$  and that  $B_{22} > -B_4$ . The first requirement ensures that  $P$  remains finite in any  $\{100\}$  direction, while the second ensures that  $P$  remains finite also in any  $\{111\}$  direction.

To find the  $P$  values, we first differentiate Eq. (12.1) to obtain

$$\partial F / \partial P_x = 2A_2 P_x + 4B_4 P_x^3 + 3B_{22} P_x (P_y^2 + P_z^2) = 0 \quad 12.2$$

and two analogous equations for the  $P_y$  and  $P_z$  derivatives. The three equations together determine where maxima, minima, and saddle points occur. The  $P = 0$  solution of the three Eq. (12.2) expressions gives minimum  $F$  only for  $A$

$> 0$ , corresponding to the paraelectric C phase. This solution gives a maximum  $F$  for the ferroelectric phases that occur for  $A < 0$ .

Another class of solutions, for the six T domains, exemplified by polarization along the  $+P_x$  axis, is  $P_{100} = [(-A_2/2B_4)^{1/2}, 0, 0]$ , and plugging this result into Eq. (12.1) gives

$$F_T = -A_2^2/4B_4 \quad 12.3$$

This solution indeed gives a minimum  $F$  only if all three second derivatives obey three relations, typified by

$$\partial^2 F / \partial P_x^2 = 2A_2 + 12B_4 P_x^2 + 2B_{22}(P_y^2 + P_z^2) = 0 \quad 12.4$$

The second  $P_x$  derivative, found by plugging in  $P_{100}$ , is  $-4A_2$  which is positive. The second  $P_y$  and  $P_z$  derivatives are  $2A_2 - A_2 B_{22}/B_4$  which is positive only if  $B_{22} > 2B_4$ . Accordingly, we have a stable or metastable T phase only in the wedge-shaped volume in  $A_2, B_4, B_{22}$  parameter space for which  $A_2 < 0, B_4 > 0, B_{22} > 2B_4$ . Note that for  $B_{22} = 2B_4$  the 2nd and 3rd terms in  $F$  in Eq. (12.1) just add to  $B_4 P^4$  so that all polarization directions have the same  $F$  in this case.

Still another class of solutions, for the eight R domains, exemplified by polarization in the  $[1, 1, 1]$  direction, is  $P_{111} = [-A_2/2(B_4 + B_{22})]^{1/2}[1, 1, 1]$ , for which (noting that  $[1, 1, 1]$  has magnitude  $\sqrt{3}$ )

$$F_R = -3A_2^2/4(B_4 + B_{22}) \quad 12.5$$

The second derivative of  $F_R$  with respect to  $P_x$  (or  $P_y$  or  $P_z$ ), evaluated where the first derivative vanishes, is  $-4A_2/(1 + B_{22}/B_4)$  which is positive if  $B_{22} > -B_4$ , the condition already required to keep  $P$  finite. Accordingly, we have a stable or metastable R phase in the wedge-shaped parameter space volume for which  $A_2 < 0, B_4 > 0, B_{22} > -B_4$ . This volume is greater than that for the T phase and includes all of the T phase volume.

Now we investigate which phases are stable, and which metastable, over this parameter space, by comparing the free energies in Eqs. (12.3) and (12.5). We already found that  $F_R = F_T$  for  $B_{22} = 2B_4$  because all  $P$  directions give equal  $F$ , namely  $F = F_T$  from Eq. (12.3), for this condition. This  $B_{22} = 2B_4$  condition was also shown above to be the limit for a stable T phase, so the T phase is stable and not metastable over the whole parameter space for which T-phase minima exist. The R phase, on the other hand, is metastable over the portion of parameter space for which both T-phase and R-phase minima exist, and is stable over the portion of the space for which only R-phase minima exist.

Vanderbilt and Cohen (2001) are correct in saying that the  $T \leftrightarrow R$  transition at  $B_{22} = 2B_4$  is unphysical because all polarization directions have equal free energy there, and thus are equally likely. However, this free energy isotropy can be considered as the first clue (as we go to higher and higher powers of

polarization in the Landau expansion) that it is easy for other phases, such as O, M, and possibly Tri, to exist near this ( $A_2 < 0$ ,  $B_4 > 0$ ,  $B_{22} = 2B_4$ ) quarter-plane, which could be called the morphotropic phase boundary (MPB) plane in this parameter space. To summarize, going only to fourth order in the Landau free energy expansion has already shown us why the T and R phases are the most prevalent in ferroelectric perovskites, and why O and M phases are often found near the MPB.

To obtain results more applicable to PMN–PT, we need to go to higher order. The sixth order will allow first-order FE transitions (as for uniaxial ferroelectrics), and going successively to higher orders allows more phases to become metastable or stable, as was shown by Vanderbilt and Cohen (2001). Specifically, they found that the sixth-order polarization expansion evidences the O phase along with the T and R phases, whereas going to eighth order brings in the various M phases. They proved that expansion to twelfth order is required to bring in the Tri phase. No one has yet had the courage to tackle the details of the twelfth-order expansion.

## 12.8 Conclusions

PMN–PT crystals are well recognized for their superior piezoelectric properties for actuator and sensor applications, and their optical properties are attracting increasing interest. For basic science their multiplicity of phases and their combination of relaxor and ordinary ferroelectric behavior offer challenges for experimentalists and theorists to understand better both their static and dynamic behavior.

For experimentalists, it is vital to use as many techniques as possible, particularly in view of the complicated behavior. Measurements over an extremely wide frequency range are needed because of the combination of glassy behavior, nanoscale clusters, and ordinary domains. The closely balanced tendencies for nanoclustering *vs.* domain formation, and for appearance of one crystal phase *vs.* another, make it especially important to observe hysteretic effects of both temperature cycling and electric field history. We have particularly emphasized in this chapter the usefulness of the polarizing microscopy technique.

Much attention has been paid to the various types of phases that can appear, but more work is needed in developing phase diagrams that systematically take electric field (both magnitude and direction) into account. Not much is known about the nature of pseudo-spin glass, nanocluster, and ordinary domain coexistence, and the nature and rate of transition of material among these three ordering forms. The field-induced cracking phenomena observed by many workers remain an obstacle for applications, and show the importance of mechanical stress in governing which phases will appear, but little is understood about the mechanisms for such behavior. For instance,

when one observes by polarizing microscopy what appear to be monoclinic regions with varying extinction angles, is this evidence that an unstressed crystal at zero field would favor a monoclinic phase, or are the monoclinic-type extinction angles merely evidence that a higher-symmetry phase has been distorted by mechanical stress or applied electric field?

Close collaboration between theorists and experimentalists, and among various research groups and crystal growers around the world, is needed to speed progress on these challenging and technologically vital questions.

## 12.9 References and further reading

- Blinic R, Laguta V V and Zalar B (2003), 'Field cooled and zero field cooled  $^{207}\text{Pb}$  NMR and the local structure of relaxor  $\text{PbMg}_{1/3}\text{Nb}_{2/3}\text{O}_3$ ', *Physical Review Letters*, **91**, 247601/1–4.
- Bokov A A and Ye Z G (2004), 'Domain structure in the monoclinic  $Pm$  phase of  $\text{Pb}(\text{Mg}_{1/3}\text{Nb}_{2/3})\text{O}_3$ – $\text{PbTiO}_3$  single crystals', *Journal of Applied Physics*, **87**, 6347–6359.
- Chien R R, Schmidt V H, Tu C-S, Hung L-W and Luo H (2004), 'Field-induced polarization rotation in (001)-cut  $\text{Pb}(\text{Mg}_{1/3}\text{Nb}_{2/3})_{0.76}\text{Ti}_{0.24}\text{O}_3$ ', *Physical Review B*, **69**, 172101/1–4.
- Chien R R, Schmidt V H, Hung L-W and Tu C-S (2005a), 'Temperature- and electric-field-dependent domain structures and phase transformations in (001)-cut tetragonal  $\text{Pb}(\text{Mg}_{1/3}\text{Nb}_{2/3})_{1-x}\text{Ti}_x\text{O}_3$  ( $x = 0.40$ ) single crystal', *Journal of Applied Physics*, **97**, 114112/1–4.
- Chien R R, Schmidt V H, Tu C-S and Wang F-T (2005b), 'Prior poling effect on thermal phase stability in (110)-cut  $\text{Pb}(\text{Mg}_{1/3}\text{Nb}_{2/3})_{0.74}\text{Ti}_{0.26}\text{O}_3$  single crystal', *Journal of Applied Physics*, **98**, 114106/1–5.
- Chien R R, Tu C-S, Schmidt V H and Wang F-T (2006), 'Electric-field- and temperature-induced phase transitions in high-strain ferroelectric  $\text{Pb}(\text{Mg}_{1/3}\text{Nb}_{2/3})_{0.67}\text{Ti}_{0.33}\text{O}_3$  single crystal', *Journal of Physics: Condensed Matter*, **18**, 8337–8344.
- Colla E V and Weissman M B (2005), 'Two-step phase changes in cubic relaxor ferroelectrics', *Physical Review B*, **72**, 104106/1–7.
- Cross L E (1987), 'Relaxor ferroelectrics', *Ferroelectrics*, **76**, 241–267.
- Davis M, Damjanovic D and Setter N (2006), 'Electric-field-, temperature-, and stress-induced phase transition in relaxor ferroelectric single crystals', *Physical Review B*, **73**, 014115/1–16.
- Feng Z, Luo H, Guo Y, He T and Xu H (2003), 'Dependence of high electric-field-induced strain on the composition and orientation of  $\text{Pb}(\text{Mg}_{1/3}\text{Nb}_{2/3})\text{O}_3$ – $\text{PbTiO}_3$  crystals', *Solid State Communications*, **126**, 347–351.
- Feng Z, Zhao X and Luo H (2006), 'Composition and orientation dependence of dielectric and piezoelectric properties in poled  $\text{Pb}(\text{Mg}_{1/3}\text{Nb}_{2/3})\text{O}_3$ – $\text{PbTiO}_3$  crystals', *Journal of Applied Physics*, **100**, 024104/1–5.
- Fu H and Cohen R E (2000), 'Polarization rotation mechanism for ultrahigh electromechanical response in single-crystal piezoelectrics', *Nature*, **403**, 281–283.
- Guo Y, Luo H, He T, Pan X and Yin Z (2003), 'Electric-field-induced strain and piezoelectric properties of a high Curie temperature  $\text{Pb}(\text{In}_{1/2}\text{Nb}_{1/2})\text{O}_3$ – $\text{PbTiO}_3$  single crystal', *Materials Research Bulletin*, **38**, 857–864.
- Han J and Cao W (2003), 'Electric field effects on the phase transitions in [001] oriented  $(1-x)\text{Pb}(\text{Mg}_{1/3}\text{Nb}_{2/3})\text{O}_3$ – $x\text{PbTiO}_3$  single crystals with compositions near the morphotropic phase boundary', *Physical Review B*, **68**, 134102/1–6.

- Hartshorne N H and Stuart A (1970), *Crystals and the Polarizing Microscope*, London, E. Arnold Ltd.
- Jona F and Shirane G (1962), *Ferroelectric Crystals*, New York, Pergamon Press, 254–255.
- Noheda B, Cox D E, Shirane G, Gao J and Ye Z-G (2002), ‘Phase diagram of the ferroelectric relaxor  $(1-x)\text{Pb}(\text{Mg}_{1/3}\text{Nb}_{2/3})\text{O}_3-x\text{PbTiO}_3$ ’, *Physical Review B*, **66**, 054104/1–10.
- Pirc R and Blinc R (1999), ‘Spherical random-bond-random-field model of relaxor ferroelectrics’, *Physical Review B*, **60**, 13470–13478.
- Shebanov L A, Kaspostins P and Zvirgzds J (1984), ‘The structure change of PMN in the diffuse phase transition region’, *Ferroelectrics*, **56**, 53–56.
- Shrout T R, Chang Z P, Kim N and Markgraf S (1990), ‘Dielectric behavior of single crystals near the  $(1-x)\text{Pb}(\text{Mg}_{1/3}\text{Nb}_{2/3})\text{O}_3-(x)\text{PbTiO}_3$  morphotropic phase boundary’, *Ferroelectrics Letters Section*, **12**, 63–69.
- Sommerfeld A (1964), *Optics*, New York, Academic Press, 129–139.
- Tu C-S, Schmidt V H, Shih I-C and Chien R (2003a), ‘Phase transformation via a monoclinic phase in relaxor-based ferroelectric crystal  $(\text{PbMg}_{1/3}\text{Nb}_{2/3}\text{O}_3)_{1-x}(\text{PbTiO}_3)_x$ ’, *Physical Review B(R)*, **67**, 020102/1–4.
- Tu C-S, Shih I-C, Schmidt V H and Chien R (2003b), ‘E-field-induced polarization rotation in  $(\text{PbMg}_{1/3}\text{Nb}_{2/3}\text{O}_3)_{1-x}(\text{PbTiO}_3)_x$  crystal’, *Applied Physics Letters*, **83**, 1833–1835.
- Tu C-S, Chien R R, Wang F-T, Schmidt V H and Han P (2004), ‘Phase stability after an electric-field poling in  $\text{Pb}(\text{Mg}_{1/3}\text{Nb}_{2/3})_{1-x}\text{Ti}_x\text{O}_3$  crystals’, *Physical Review B(R)*, **70**, 220103/1–4.
- Tu C-S, Wang F-T, Chien R R, Schmidt V H and Tuthill G F (2005), ‘Electric-field effects of dielectric and optical properties in  $\text{Pb}(\text{Mg}_{1/3}\text{Nb}_{2/3})_{0.65}\text{Ti}_{0.35}\text{O}_3$  crystal’, *Journal of Applied Physics*, **97**, 064112/1–5.
- Tu C-S, Wang F-T, Chien R R, Schmidt V H, Hung T-M and Tseng C-T (2006a), ‘Dielectric and photo-voltaic phenomena in tungsten doped  $\text{Pb}(\text{Mg}_{1/3}\text{Nb}_{2/3})_{1-x}\text{Ti}_x\text{O}_3$  crystal’, *Applied Physics Letters*, **88**, 032902/1–3.
- Tu C-S, Hung C-M, Wang F-T, Chien R R and Yang S-W (2006b), ‘Dielectric and optical behaviors in relaxor ferroelectric  $\text{Pb}(\text{In}_{1/2}\text{Nb}_{1/2})_{1-x}\text{Ti}_x\text{O}_3$  crystal’, *Solid State Communications*, **138** (4), 190–193.
- Tu C-S, Chien R R, Schmidt V H, Wang F-T and Lim L C (2006c), ‘Electric-induced dielectric anomalies and optical birefringence in  $\text{Pb}(\text{Zn}_{1/3}\text{Nb}_{2/3})_{1-x}\text{Ti}_x\text{O}_3$ ’, *Journal of Applied Physics*, **100**, 074105/1–6.
- Tu C-S, Wang F-T, Hung C-M, Chien R.R and Luo H (2006d), ‘Dielectric, domain, and optical studies in high-Curie-temperature  $\text{Pb}(\text{In}_{1/2}\text{Nb}_{1/2})_{1-x}\text{Ti}_x\text{O}_3$  ( $x=0.40$ ) single crystal’, *Journal of Applied Physics*, **100**, 104104/1–5.
- Vanderbilt D and Cohen M H (2001), ‘Monoclinic and triclinic phases in higher-order Devonshire theory’, *Physical Review B*, **63**, 09418/1–9.
- Viehland D and Li J F (2002), ‘A hysteretic field-induced rhombohedral to orthorhombic transformation in  $\langle 110 \rangle$ -oriented  $0.7\text{Pb}(\text{Mg}_{1/3}\text{Nb}_{2/3})\text{O}_3-0.3\text{PbTiO}_3$  crystals’, *Journal of Applied Physics*, **92**, 7690–7692.
- Viehland D, Wuttig M and Cross L E (1991), ‘The glassy behavior of relaxor ferroelectrics’, *Ferroelectrics*, **120**, 71–77.
- Wan X, Xu H, He T, Lin D and Luo H (2003), ‘Optical properties of tetragonal  $\text{Pb}(\text{Mg}_{1/3}\text{Nb}_{2/3})_{0.62}\text{Ti}_{0.38}\text{O}_3$  single crystal’, *Journal of Applied Physics*, **93**, 4766–4768.
- Westphal V, Kleemann W and Glinchuk M D (1993), ‘Diffuse phase transitions and

random-field-induced domain states of the “relaxor” ferroelectric  $\text{PbMg}_{1/3}\text{Nb}_{2/3}\text{O}_3$ , *Physical Review Letters*, **68**, 847–850.

- Xu G, Luo H, Xu H and Yin Z (2002), ‘Third ferroelectric phase in PMNT single crystals near the morphotropic phase boundary composition’, *Physical Review B*, **64**, 020102/1–3.
- Yamashita Y, Hosono Y, Harada K and Yasuda N (2002), ‘Present and future of piezoelectric single crystals and the importance of B-site cations for high piezoelectric response’, *IEEE on Transactions on Ultrasonics, Ferroelectrics, and Frequency Control*, **49**, 184–192.
- Yasuda N, Sakaguchi M, Itoh Y, Ohwa H and Yamashita Y (2003), ‘Effect of electric fields on domain structure and dielectric properties of  $\text{Pb}(\text{In}_{1/2}\text{Nb}_{1/2})\text{O}_3$ – $\text{PbTiO}_3$  near morphotropic phase boundary’, *Japanese Journal of Applied Physics*, 42 part 1 (9B), 6205–6208.
- Ye Z-G (1998), ‘Relaxor ferroelectric complex perovskites: structure, properties and phase transitions’, *Key Engineering Materials*, **155–156**, 81–122.
- Ye Z-G and Dong M (2000), ‘Morphotropic domain structures and phase transitions in relaxor-based piezo-/ferroelectric  $(1-x)\text{Pb}(\text{Mg}_{1/3}\text{Nb}_{2/3})\text{O}_3$ – $x\text{PbTiO}_3$  single crystals’, *Journal of Applied Physics*, **87**, 2312–2319.
- Ye Z-G, Noheda B, Dong M, Cox D and Shirane G (2001), ‘Monoclinic phase in the relaxor-based piezoelectric/ferroelectric  $\text{Pb}(\text{Mg}_{1/3}\text{Nb}_{2/3})\text{O}_3$ – $\text{PbTiO}_3$ ’, *Physical Review B*, **64**, 184114/1–5.



# Energy analysis of field-induced phase transitions in relaxor-based piezo- and ferroelectric crystals

---

T LIU and C S LYNCH, The Georgia Institute of Technology, USA

## 13.1 Introduction

Relaxor ferroelectric single crystals, when cut and poled in certain orientations, display extraordinary properties that include very large piezoelectric coefficients, high electromechanical coupling coefficients, and very low loss tangents. These properties are found within a limited range of temperature, electric field, and stress. The limitations on loading range are associated with temperature and field-induced phase transitions (Zhao *et al.*, 2002; Han and Cao, 2003; Liu and Lynch, 2003), composition-temperature behavior (Noheda *et al.*, 2002), electric field-temperature behavior (Ren *et al.*, 2002), and the coexistence of multiple phases (Ye and Dong, 2000; Bertram *et al.* 2003). The stability of phases and field-induced phase transformations show composition dependence. Recent studies include the effect of stress on phase transformations (Samara, *et al.*, 2000; Viehland and Powers, 2001a; Viehland *et al.*, 2003).

Phase transformations can be classified into two types, namely, discontinuous and continuous. Discontinuous phase transformations, also called first-order transformations, involve a discontinuous change in the entropy; continuous phase transformations, also called second-order transformation, occur with continuous changes of entropy. These two types of transformation have been observed in relaxor ferroelectric single crystals (Liu and Lynch, 2003; McLaughlin *et al.*, 2004). Discontinuous phase transformations with large hysteresis result in rapid degradation of the material due to cracking.

Phase transformations can be described within a thermodynamics framework. Thermodynamics-based approaches have been used extensively to elucidate the complex behavior of multi-physics coupled materials (Fiebig *et al.*, 2002). In this chapter domain engineering and multi-field-driven phase transitions are reviewed and a thermodynamics-based analysis of measured material behavior under combined stress, electric field, and temperature loading is discussed (Liu, *et al.*, 2006). This leads to a technique for the direct measurement of internal energy and Gibbs free energy based on combined

electromechanical loading. The approach is applied to an electric field-driven transition from rhombohedral to orthorhombic with associated hysteresis in  $\langle 110 \rangle$  loaded PZN–4.5%PT (Liu and Lynch, 2003), and to an electric field-driven transition from rhombohedral to orthorhombic with rotation through an intermediate monoclinic phase in  $\langle 110 \rangle$  PMN–32%PT driven by both electric field and stress (McLaughlin *et al.*, 2004).

## 13.2 Background

### 13.2.1 Anisotropy and domain engineering

Ferroelectric single crystals exhibit anisotropic elastic, dielectric, and piezoelectric properties. The macroscopic behavior of the crystals can be described in terms of a volume average of the behavior at smaller length scales within the crystals. This includes domain wall motion, nucleation and growth of phases, phase boundary motion, diffusion of defects, and unit cell behavior (intrinsic piezoelectricity). Actuators fabricated from ferroelectric materials are generally pre-loaded under uniaxial stress (one non-zero stress component) and under uniaxial electric field. The actuators are designed such that the stress and electric field within the active material are uniform. If the electric field is bipolar and exceeds the coercive field, polarization reversal will occur and the typical electric displacement/electric field (D-E) and the butterfly-shaped strain/electric field (S-E) hysteresis loops will be observed. If the ferroelectric material is subjected to a unipolar field, minor hysteresis loops can be observed. The area within the D-E loop is associated with material loss and results in the generation of heat. If the stress is varying during the cycle, the area within the stress/strain (T-S) hysteresis loop represents additional loss. If the stress and electric field at a given temperature exceed critical values, a phase transformation occurs and additional hysteresis takes place with the associated generation of heat.

Rhombohedral phase relaxor ferroelectric single crystals with compositions close to the morphotropic phase boundary (MPB) display large piezoelectric coefficients and low loss when poled in a  $\langle 001 \rangle$  or a  $\langle 110 \rangle$  direction (Park and Shrout, 1997; Liu *et al.*, 1999; Liu and Lynch, 2003). When single crystals are cut and poled in the  $\langle 001 \rangle$  or  $\langle 011 \rangle$  orientations, there is optimal domain compatibility and minimized domain wall motion. This greatly reduces the minor hysteresis loops and the corresponding heat generation. The electromechanical properties of these crystals are directly related to their engineered domain structures: an effective four-domain state for the  $\langle 001 \rangle$  poled crystals and a two-domain state for the  $\langle 110 \rangle$  poled crystals. Such engineered multi-domain states enable the calculation of piezoelectric coefficients from that of a single domain (crystal variant). The technique is called crystal variant-based modeling. Various calculations of piezoelectric

coefficients have been conducted for engineered multi-domain ferroelectrics (Yin *et al.*, 1999, 2000b; Damjanovic *et al.*, 2003; Dammak *et al.*, 2003; Liu and Lynch, 2003; Zhang *et al.*, 2003; Topolov, 2004; Davis *et al.*, 2005). The crystal variant model can be extended to describe the evolution of polarization switching and phase changes by including the appropriate variant evolution criteria.

### 13.2.2 Phase stability

The phases present in relaxor PZN-*x*PT and PMN-*x*PT single crystals depend on their composition and temperature (Lu *et al.*, 2001; La Orattapong *et al.*, 2002; Ye, 2002). The most widely used compositions (PMN-28~32%PT) are very near the MPB. High-resolution diffraction studies have revealed that the morphotropic phase boundary compositions comprise the rhombohedral (R), tetragonal (T), orthorhombic (O) and monoclinic (M) phases (Fujishiro *et al.*, 1998; Uesu *et al.*, 1998; Ye *et al.*, 1999, 2001; Zhang *et al.*, 2000; Cox *et al.*, 2001; Lu *et al.* 2001; Noheda *et al.*, 2001a,b). The coexistence of rhombohedral and tetragonal domains in PZN-*x*PT and PMN-*x*PT crystals have been observed at room temperature (Fujishiro *et al.* 1998; Uesu *et al.* 1998; Belegundu *et al.*, 1999; Ye *et al.* 1999; Ye and Dong 2000). Recently the extent of different phases (R, M/O, T) in PZN-*x*PT and the dependency of their volume fractions on the PT content were characterized (Bertram *et al.* 2003).

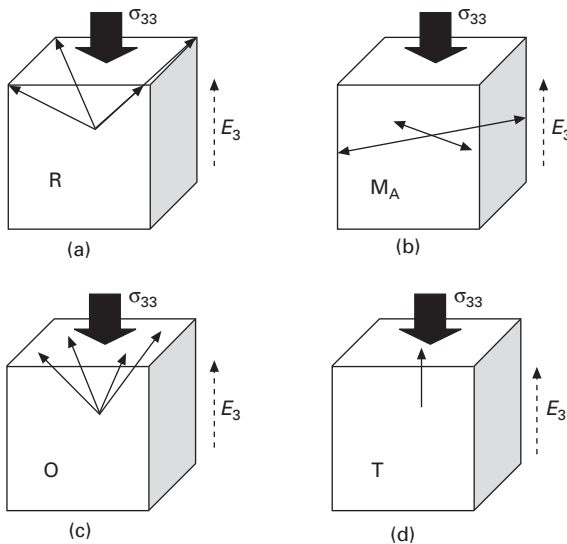
Multi-domain structures and multi-phase coexistence around the MPB contribute to the enhanced electromechanical properties of relaxor single crystals (Yin *et al.*, 2000a; Zhang *et al.*, 2001). At the same time the coexistence of various phases leads to complex microscale behavior (Noheda *et al.*, 2002; Ye, 2002; Singh and Pandey, 2003). The stability of the phases depends on composition, orientation, and temperature as well as the electrical and mechanical boundary conditions (Viehland *et al.*, 2001; Zhao *et al.*, 2002). Application of temperature, electric field, and stress leads to polarization switching and phase transitions that dramatically alter the electromechanical properties of these crystals and may induce cracking and fatigue that lead to premature failure in applications.

## 13.3 Multi-field-induced phase transitions

Phase transformations can be driven by combinations of stress and electric field in PZN-*x*PT and PMN-*x*PT single crystals (Samara *et al.* 2000; Shang and Tan, 2001; Viehland and Powers, 2001a,b; Fang and Yang, 2002; Viehland *et al.* 2003). This effect is most easily described in terms of the <001> and <011> cut and poled crystals.

13.3.1  $\langle 001 \rangle$  poled single crystals

Transformation between the rhombohedral phase and tetragonal phase can be induced by stress and electric field in  $\langle 001 \rangle$  oriented relaxor single crystals (Meeks and Timme, 1975; Liu *et al.* 1999; Viehland, 2000; Noheda *et al.* 2001a; Chen *et al.*, 2002; Park and Hackenberger, 2002; Ren *et al.* 2002). The  $\langle 001 \rangle$  electric field provides a driving force to align the polarization vector with the electric field vector. When the driving force is large enough, the transformation takes place. Han and Cao (2003) found that application of an electric field bias along  $\langle 001 \rangle$  decreases the R-T phase transition temperature. Ren *et al.* (2002) measured the R-T phase transition fields of PZN-4.5%PT and PZN-8%PT crystals as a function of temperature and found linearly decreasing field values relative to increase of temperature. Schmidt *et al.* (2003) and Tu *et al.* (2003) suggested that the R-T phase transition in PMN-PT single crystals progresses through a rotation of polarizations of monoclinic (M) phases. Multiple phase transitions have been observed in the  $\langle 001 \rangle$  PMN-32%PT single crystal under combined electric field and stress loading (both along  $\langle 001 \rangle$ ) at different temperatures (McLaughlin *et al.*, 2005). These field-induced phase transitions are depicted in Fig. 13.1.



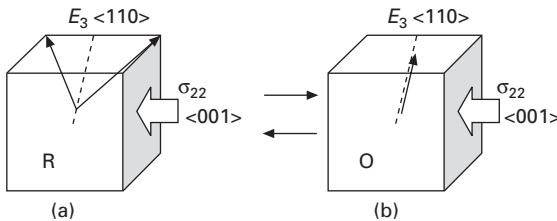
13.1 Crystal variants of a  $\langle 001 \rangle$  poled single crystal and the possible phase changes under electric field and stress loadings: (a) rhombohedral phase polarized into a four-variant state; (b) orthorhombic phase depolarized under large compressive stress; (c) monoclinic (MA) phase under large electric field; (d) tetragonal phase under further increased electric field.

### 13.3.2 <110> Poled single crystals

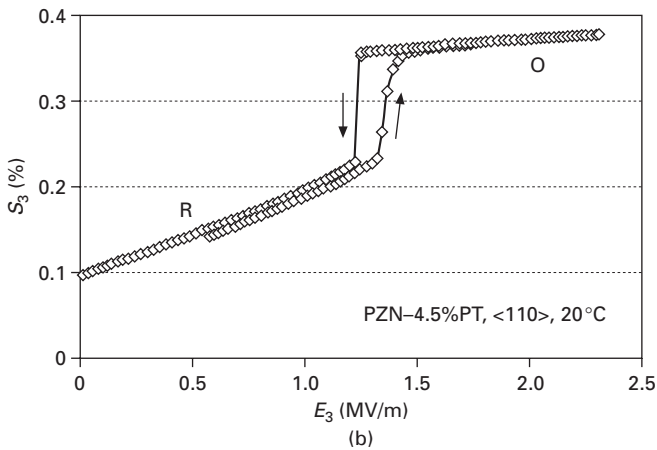
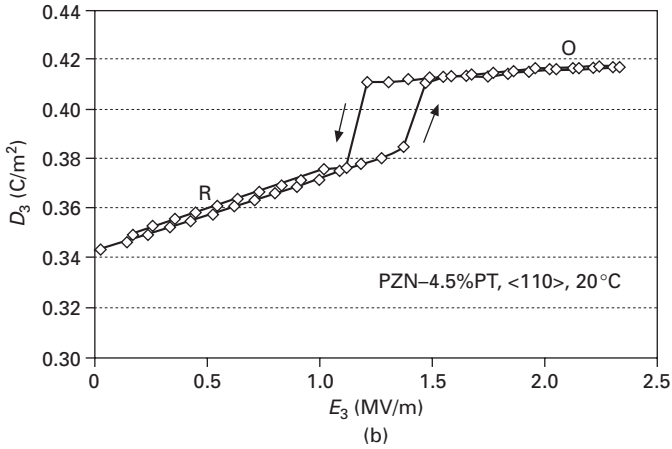
A rhombohedral to orthorhombic (R-O) phase transformation can occur in either <001> or <110> PZN- $x$ PT and PMN- $x$ PT single crystals under stress and electric field loading (Lu *et al.* 2001, 2002; Viehland and Li, 2002; Feng *et al.*, 2003; Liu and Lynch 2003; McLaughlin *et al.* 2004, 2005). Crystal variants present in a <110> poled single crystal and the rhombohedral-orthorhombic (R-O) phase transition under electric field  $E_3$  and stress  $\sigma_{22}$  are illustrated in Fig. 13.2. This phase change is effectively a <111> to <110> polarization rotation. Both the positive <110> electric field and the <001> compressive stress drive the R-O phase transition and stabilize the O phase.

Figure 13.3 shows the electric displacement and strain curves for single crystal PZN-4.5%PT (Liu and Lynch, 2003) during an electric field-driven R-O phase transformation at room temperature and zero stress. There is a jump in electric displacement as well as strain during the phase transformation. This is a discontinuous (first-order) phase transformation with hysteresis.

This phase transformation induced by combined stress and electric field was mapped out in a series of experiments performed on relaxor PMN-32%PT single crystals (McLaughlin *et al.*, 2004), the electric field-induced strain for a series of pre-stress levels and the stress-induced strain for a series of bias electric field levels on <110> oriented PMN-32%PT single crystals were measured at three different temperatures. These data were used to generate plots of the electric displacement and strain versus the applied electric field and stress. The plots at 40°C are shown in Fig. 13.4. There are two distinct planar regions in these three-dimensional surfaces. These correspond to the rhombohedral (R) region at low field level and the orthorhombic (O) region at high field level. Between them is an R-O phase transition region showing sharp changes of strain and electric displacement. The phase transition is associated with a change of internal energy. The question arises as to whether the onset and completion of the phase transition can be identified by a scalar internal energy density level and whether the



13.2 Crystal variants of a <110> poled single crystal and the rhombohedral-orthorhombic phase change under electric field and stress loadings: (a) rhombohedral phase polarized into a two-variant state; (b) orthorhombic phase polarized into a single-variant state.

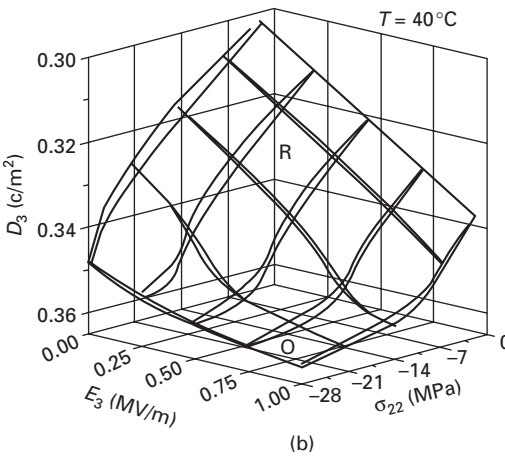
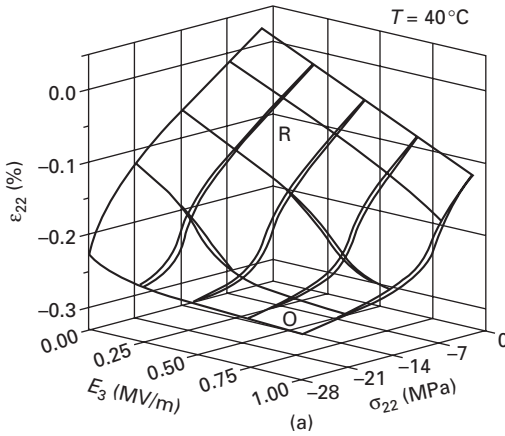


13.3 Electric field driven R-O phase transition in a  $\langle 110 \rangle$  oriented relaxor PZN-4.5%PT single crystal at room temperature (Liu and Lynch, 2003): (a) electric displacement vs. electric field; (b) strain vs. electric field.

progression of the transition can be indicated by the scalar Gibbs free energy. This is explored through numerical integration of the three-dimensional coupled surfaces along various paths.

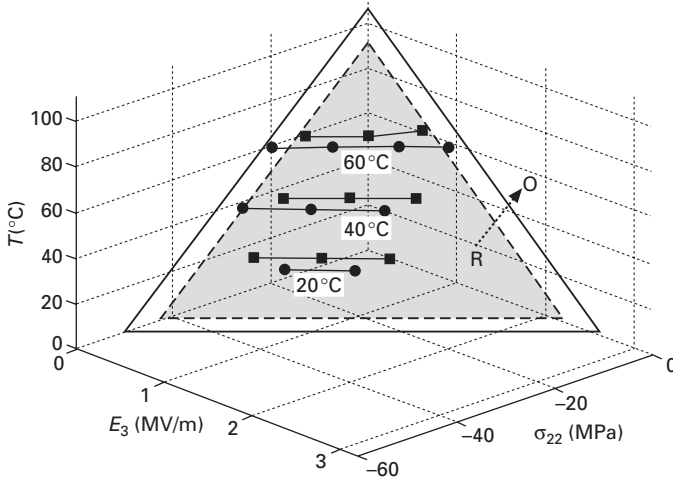
Compared with the phase change of PZN-4.5%PT in Fig. 13.3, the PMN-32%PT single crystal shows a gradual transformation with little hysteresis. The transformation takes place over a range of field levels and there is no distinct phase transition point. (Note that the apparent hysteresis in the D-E curves in Fig. 13.4b was attributed to difficulties with the polarization measurements.)

The  $\langle 110 \rangle$  electric field  $E_3$  and the  $\langle 001 \rangle$  compressive stress  $\sigma_{22}$  each provide a positive driving force for the R-O phase transition in the  $\langle 110 \rangle$  cut



13.4 Strain ( $\epsilon_{22}$ ) and electric displacement ( $D_3$ ) response of PMN–32%PT single crystals under combined electric field ( $E_3$ ) and stress ( $\sigma_{22}$ ) loadings at 40 °C (McLaughlin *et al.* 2004): (a) strain; (b) electric displacement.

and poled crystals. This is apparent when considering the change in polarization and strain that take place during the transformation. The strain change is in the direction of the applied stress and the polarization change is in the direction of the applied field. The driving force for this transformation decreases with increasing temperature. As shown in Fig. 13.5, when plotted in the electric field–stress–temperature ( $E_3$ – $\sigma_{22}$ – $T$ ) coordinate system, the starting points ( $E_3$ ,  $\sigma_{22}$ ,  $T$ ) for the phase transformation lie in one plane and the finishing points in another (McLaughlin *et al.* 2004). By least square fitting of the data, the equation for the start plane is  $T = 91.1 - 41.3E_3 + 2.12\sigma_{22}$  and the equation for the finish plane is  $T = 105 - 40.6E_3 + 2.12\sigma_{22}$ . These two



13.5 R-O phase change plane for PMN-32%PT single crystal plotted in electric field-stress-temperature ( $E_3$ - $\sigma_{22}$ - $T$ ) coordinate system (McLaughlin *et al.*, 2004). Electric field  $E_3$  is in  $\langle 110 \rangle$  direction, and stress  $\sigma_{22}$  is in  $\langle 001 \rangle$  direction. The bottom (small) triangle refers to the onset plane of the transition, and the top (big) triangle is in the plane for the end of the transition.

planes are nearly parallel, giving an estimate of the R-O phase change temperature range  $T_c = 90 \sim 105^\circ\text{C}$  at zero electric field and stress.

It is of interest to compare the R-O phase transitions in  $\langle 110 \rangle$  and  $\langle 001 \rangle$  cuts. In the  $\langle 110 \rangle$  oriented crystals, with the electric field in  $\langle 110 \rangle$ , one of the spontaneous polarization directions of the orthorhombic phase, the transformed orthorhombic crystals are poled into a single-domain state (Fig. 13.2b); in the  $\langle 001 \rangle$  oriented crystals, under  $\langle 001 \rangle$  compressive stress, the transformed orthorhombic phase is in a multi-domain depolarized state with spontaneous polarizations perpendicular to the poling direction (Fig. 13.1b).

## 13.4 Energy analysis of phase transitions

### 13.4.1 Energy-based modeling

A number of analytical and computational approaches have been used to describe and predict phase transformation behavior in relaxor single crystals. Theoretical investigations have been carried out to study structure-property relations from the atomic level (Allen, 1976; Cohen, 1992; Rabe and Waghmare, 1996; Fu and Cohen, 2000; George *et al.*, 2001; Tadmor *et al.*, 2002) to the continuum level (Chen and Lynch, 1998a,b; Lynch, 1998; Kamlah and Tsakmakis, 1999; Mauck, 2002; McMeeking and Landis, 2002; Landis *et al.*, 2003; Glinchuk, 2004). Landau-Devonshire phenomenological theory



has been widely used to explain observed phases and phase transition phenomena (Su, *et al.*, 2001; Vanderbilt and Cohen, 2001; Li *et al.*, 2003; Wang *et al.*, 2004). An energy-based approach is particularly useful for multi-physics coupled materials such as ferroelectrics, ferromagnetics (Asamitsu *et al.*, 1995), and ferroelectromagnets (Fiebig *et al.*, 2002) because it provides a scalar phase transformation criterion that can be measured. Such an energy criterion can be applied to multi-axial multi-field loading.

Energy minimization has been used to analyze the engineered domain configurations of ferroelectric single crystals (Shu and Bhattacharya, 2001; Jiang and Dan, 2004). By considering the contributions to the free energy, numerical simulations of the formation of domain structures can be performed (Yang and Chen, 1995; Hu and Chen, 1997; Hu and Chen, 1998; Khachatryan, 2000; Li *et al.*, 2001). Energy-based polarization switching and phase transition criteria have also been used to simulate the behavior of ferroelectric ceramic PZT (Hwang *et al.*, 1995; McMeeking and Hwang, 1997; Chen and Lynch, 1998a; Huber *et al.*, 1999), electrostrictive PMN-*x*PT (Hom and Shankar, 1996), and antiferroelectric PLSnZT (Chen and Lynch 1998b; Essig *et al.*, 1999).

The R-O phase transitions observed in the <110> oriented PZN-4.5%PT (Liu and Lynch, 2003) and PMN-32%PT crystals (McLaughlin *et al.*, 2004) is the subject of much of the following discussion. Work done by the electric field and stress is computed by path integration of recorded data and the energy balance during the phase transitions is analyzed. The path integrals needed to analyze the data are obtained through a continuum mechanics derivation that follows the details presented by Malvern (1969) plus an expression for the work done by electrical loading.

### 13.4.2 Equations of energy equilibrium

Energy balance of a system can be expressed in rate form as

$$\dot{K} + \dot{E} = \dot{W}^m + \dot{W}^e + \dot{Q} \quad 13.1$$

where the terms are rate of change of kinetic energy  $\dot{K}$  and rate of change of internal energy  $\dot{E}$ , mechanical work rate  $\dot{W}^m$ , and electrical work rate  $\dot{W}^e$  (superscripts *m* and *e* refer to mechanical and electrical components), and rate of heat addition  $\dot{Q}$ .

With the restriction to stationary bodies and an absence of body forces and body charges, a local expression for the rate of change of internal energy is

$$\dot{u} = \rho \dot{e} = \sigma_{ij} \dot{\epsilon}_{ij} + E_j \dot{D}_j + \dot{q} \quad 13.2$$

where  $\dot{q}$  is the rate of heat added per unit volume from external sources,  $\rho$  is the mass density, and  $\dot{e}$  is the rate of change of internal energy per unit mass.

For a single crystal ferroelectric with rate-independent dissipation, the internal energy can be written in incremental form

$$du = \sigma_{ij}d\varepsilon_{ij} + E_j dD_j + dq \quad 13.3$$

where  $dq$  is the thermal energy per unit volume added from external sources.

Integrating each term of Equation (13.3) along a loading path gives

$$\Delta u = \int_A^B du \quad 13.4$$

$$w^m = \int_A^B \sigma_{ij} d\varepsilon_{ij} \quad 13.5$$

$$w^e = \int_A^B E_j dD_j \quad 13.6$$

$$\Delta q = \int_A^B dq \quad 13.7$$

Combining equations (13.4–13.7) gives the following form of (13.3):

$$\Delta u = w^m + w^e + \Delta q \quad 13.8$$

Equations (13.5) and (13.6) can be applied directly to measured stress–strain and electric field–electric displacement data. Under adiabatic loading ( $\Delta q = 0$ ) the temperature will increase after a cycle due to internal dissipation. Under isothermal loading through a closed cycle ( $\Delta u = 0$ ), Equation (13.7) represents the amount of heat leaving the body that is equal to the heat generated by the dissipative terms.

Assume the final state is the same as the initial state after a loading cycle, i.e.  $\Delta u = 0$

$$\oint (w^m + w^e) = \oint (-\Delta q) \quad 13.9$$

This states that the irreversible work done by the stress and the electric field will be converted into heat and dissipate into the environment to maintain a constant temperature. Equation (13.9) can be used to obtain the relative internal energy density levels before and after a phase transition.

The Gibbs free energy gives a measure of the driving force for the transformations. This can also be determined by direct integration of the experimental data. Performing a Legendre transformation on the expressions for electrical and mechanical work leads to the equation for Gibbs free energy

$$\Delta g = \Delta u - \sigma_{ij}\varepsilon_{ij} - E_j D_j = \int_A^B -\varepsilon_{ij} d\sigma_{ij} + \int_A^B -D_j dE_j + \Delta q \quad 13.10$$

### 13.4.3 Work–energy analysis

Details of the work in this section can be found in Liu *et al.* (2006). Path integrals were conducted to compute the work done by the electric field and stress. The external work for the loading scheme shown in Fig. 13.2 includes mechanical work done by the stress  $\sigma_{22}$  and electrical work done by the electric field  $E_3$ . For the PZN–4.5%PT single crystal, only electrical work is done during the phase transition due to the stress-free condition. Equation 13.6 is applied to compute the electrical work and Fig. 13.6(a) shows the result of the numerical integration of the PZN–4.5%PT data. Note that there is an offset (non-zero external work) over a loading cycle. This is the irreversible work converted into heat in a cycle. Assuming that half of the heat is generated during the forward transformation and half during the reverse transformation, the results after subtracting the heat are shown in Fig. 13.6(b). This is the internal energy before and after the phase transition.

With the assumption that the material is linear piezoelectric both before and after the transformation, the energy functions can be written in quadratic form. The general ferroelectric constitutive relations can be expressed in incremental form as:

$$\Delta(\varepsilon_{ij} - \varepsilon_{ij}^r) = s_{ijkl}^E \Delta\sigma_{kl} + d_{nij} \Delta E_n \quad 13.11$$

$$\Delta(D_m - D_m^r) = d_{mkl} \Delta\sigma_{kl} + k_{mn}^\sigma \Delta E_n \quad 13.12$$

The remnant strain  $\varepsilon_{ij}^r$  and remnant electric displacement  $D_m^r$  are associated with the non-linearity and the irreversibility. In a linear region under the prescribed loads  $\sigma_{22}$ ,  $E_3$  (either in the R phase or O phase), the constitutive equations reduce to:

$$\varepsilon_{22} - \varepsilon_{22}^r = s_{2222}^E \sigma_{22} + d_{322} E_3 \quad 13.13$$

$$D_3 - D_3^r = d_{322} \sigma_{22} + k_{33}^\sigma E_3 \quad 13.14$$

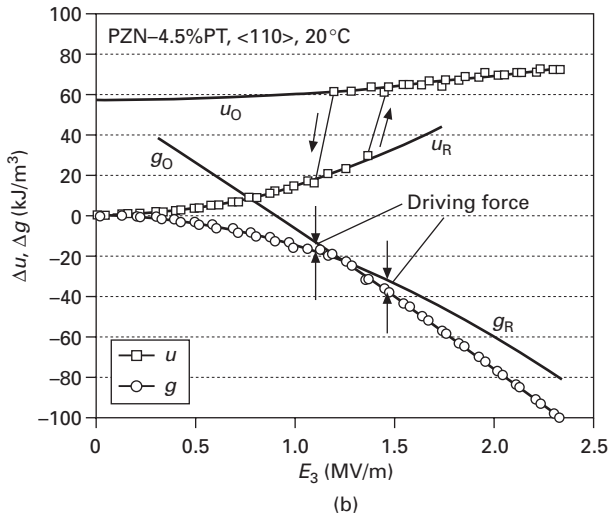
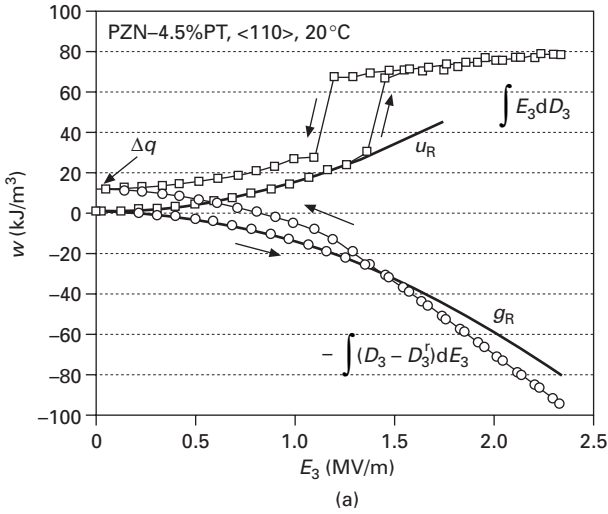
For the linear behavior of a single phase at constant temperature, the quadratic form of the internal energy function for the single crystal is then given by

$$u = u^0 + \frac{1}{2} s_{2222}^E \sigma_{22}^2 + d_{322} \sigma_{22} E_3 + \frac{1}{2} k_{33}^\sigma E_3^2 \quad 13.15$$

The quadratic form of the Gibbs free energy is given by

$$g = g^0 - \left( \frac{1}{2} s_{2222}^E \sigma_{22}^2 + d_{322} \sigma_{22} E_3 + \frac{1}{2} k_{33}^\sigma E_3^2 \right) \quad 13.16$$

Where  $u^0$  and  $g^0$  are the reference internal energy and Gibbs free energy at zero electric field and stress. The experimental data give direct measures of the  $s_{2222}^E$ ,  $d_{322}$  and  $k_{33}^\sigma$  coefficients for both the R phase and the O phase



13.6 Work-energy analysis of the PZN-4.5%PT single crystal under electric field loading (Liu *et al.*, 2006). Internal energy and Gibbs free energy values for the R phase and O phase based on linear electromechanical response are superimposed: (a) work done by the electric field; (b) change of internal energy and Gibbs free energy density.

(McLaughlin *et al.*, 2004). With these coefficients, quadratics given by equations (13.15) and (13.16) are obtained and overlain on the data in Fig. 13.6.

Shown in Fig. 13.6, both  $u^0$  and  $g^0$  are higher for the O phase. At the phase transition field level, the Gibbs free energies for the two phases become

equal. The difference of the Gibbs free energy between the two phases gives the driving force for the phase transformation as the electric field increases. The crystal will stay in the phase with lower Gibbs free energy at given stress and electric field. There is a jump in the internal energy during the phase transition corresponding to the differences in phase energies.

Two phases may coexist when they have the same Gibbs free energy. In addition, considering inhomogeneous microscopic stress and electric field present in the crystals, coexistence of two or more ferroelectric phases can be expected when the phase energies are not too different in value.

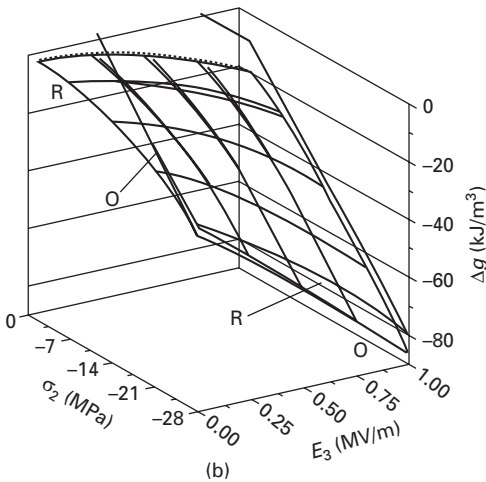
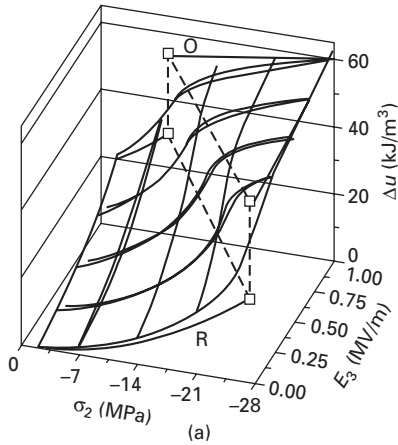
Internal energy density and the Gibbs free energy surfaces for the <110> PMN–32%PT single crystals were computed from experimental data (Fig. 13.4) through path integrals and plotted in Fig. 13.7. The quadratic energy functions for the linear R and O phases are superimposed on these plots. Figure 13.7(b) shows the Gibbs free energy of the crystal as a function of applied stress and electric field at fixed temperature (40 °C). At low stress and electric field, the R phase has a lower Gibbs free energy compared with the O phase, therefore it is the stable phase; as the applied stress and electric field increase, the Gibbs free energy decreases, but the Gibbs free energy of the O phase decreases faster than that of the R phase. When the Gibbs free energies of the two phases are equal, the crystal reaches a critical point. A further increase of stress and/or electric field leads to a lower Gibbs free energy of the O phase and R-O phase transition occurs. The observed gradual phase transition behavior with small hysteresis is believed to be the result of multi-phase coexistence with intermediate monoclinic phases (Bai *et al.*, 2004).

A similar analysis was performed on the data for each of the three temperatures. The relative internal energy density at the onset of non-linearity on the rhombohedral and the orthorhombic sides of the transition are plotted as a function of temperature in Fig. 13.8. Note that the relative energies converge very near the rhombohedral to cubic transition temperature seen in the zero load phase diagram and that the energies of the phases are linear with temperature in the range measured.

#### 13.4.4 Irreversible work and hysteresis loss

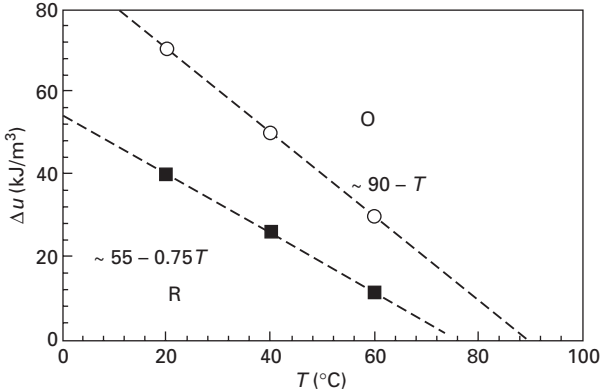
Ferroelectric materials exhibit major hysteresis loops during field-induced polarization switching. Hysteresis also occurs during a phase transition, which is dependent on the material composition, temperature and other factors. Minor hysteresis loops are displayed under unipolar loading, even though the electric field and stress cycles do not induce apparent polarization switching and phase transitions.

Domain and phase activities in ferroelectric materials contribute to non-linear and hysteretic electromechanical response and other reliability issues (Lines and Glass, 1977; Lynch, 1996; Damjanovic, 2001). Hysteresis below



13.7 Internal energy and Gibbs free energy of PMN–32%PT single crystal as functions of stress and electric field (Liu *et al.*, 2006). Values for the R phase and O phase based on linear electromechanical response were overlain for comparison: (a) change of internal energy; (b) change of Gibbs free energy.

the Curie temperature is mainly caused by domain wall movements (Hardtl, 1982). Hysteresis is associated with energy loss and heat generation in the materials. Heat generation is a serious issue in piezoelectric devices working at high frequencies such as ultrasonic motors. It is important to be able to accurately model the hysteretic loss in piezoelectric actuators under dynamic loading (Hall, 2001). The minor hysteresis loops under small variations of stress and electric field may be expressed by a Rayleigh relationship in which the coefficients are taken to be quadratic functions of applied stress and electric field, with a different function for loading and unloading



13.8 Critical energy-temperature phase diagram for <110> poled PMN-32%PT (Liu *et al.*, 2006). Symbols are from measurements of electric field and stress-induced phase transition at three temperatures (20, 40, and 60 °C).

(Damjanovic and Demartin, 1996; Damjanovic, 1997; Eitel *et al.*, 2006). This can be used for the computation of hysteresis loss energy and an effective loss tangent (Eitel *et al.* 2006; Zhou *et al.*, 2006). When the hysteresis is small, the ferroelectric constitutive relations can be expressed using complex variables in time harmonic form using the concepts of dielectric, elastic, and piezoelectric loss tangents (Holland, 1967). The dielectric, mechanical, and piezoelectric loss tangents are field and frequency-dependent along with complex correlation, which depends on the mechanism behind them (Gerthsen *et al.*, 1980; Hardtl, 1982; Herbiet *et al.*, 1989; Robels *et al.*, 1989; Uchino and Hirose, 2001; Eitel *et al.* 2006). The complex variable approach introduces a phase lag between the applied loads and the response variables as an approximation to the observed hysteresis. It is well known and discussed in detail in the references cited above.

There are both dielectric and mechanical hysteretic losses in ferroelectric materials. They are due to irreversible work done by the electric field and stress respectively, which are directly related to the remnant electric displacement and remnant strain changes. In ferroelectric materials, changes of strain and electric displacement include reversible (superscript *rev*) and irreversible (remnant, superscript *r*) components:

$$d\epsilon_{ij} = d\epsilon_{ij}^{rev} + d\epsilon_{ij}^r \tag{13.17}$$

$$dD_i = dD_i^{rev} + dD_i^r \tag{13.18}$$

A change of internal energy can then be expressed as

$$du = \sigma_{ij}d\epsilon_{ij}^{rev} + E_jdD_j^{rev} + \rho TdS \tag{13.19}$$

with

$$\rho T dS = \sigma_{ij} d\epsilon_{ij}^r + E_j dD_j^r + dq \quad 13.20$$

Here  $T$  is the temperature and,  $dS$  is change of entropy per unit mass. This expression relates the dissipative increments of the strain and electric displacement to the generation of thermal energy.  $\sigma_{ij} d\epsilon_{ij}^r$  is the irreversible work increment done by stress and  $E_j dD_j^r$  is the irreversible work increment done by the electric field. Models that describe the evolution of remnant strain and remnant electric displacement may be developed and used to compute the dissipative terms (loss) and heat generation. The second law states that the dissipation will be non-negative:  $\sigma_{ij} d\epsilon_{ij}^r + E_j dD_j^r \geq 0$ .

### 13.5 Discussion

The phase transformation behavior under combined stress, electric field, and thermal loading is a coupled multi-field phenomenon. The work–energy analysis shows that at a given temperature the phase transformation begins at a critical level of internal energy density and ends at a second critical level. A second criterion, minimization of the Gibbs free energy, determines whether the transformation will take place. The critical energy levels were found to be independent of the combinations of stress and electric field that induced them.

This leads back to the analysis of the electric displacement – electric field data, discussed initially. Collection of D-E data is straightforward and can be readily performed at a series of temperatures. The data can be used to identify the relative energy levels of the phases. To generate plots like Fig. 13.7 from a limited number of measurements, a set of the elastic, piezoelectric, and dielectric coefficients of each phase is needed. This provides sufficient information to characterize the multi-field-driven transformation. These results are expected to reduce the amount of experimental work required to fully characterize multi-field-driven phase transformations.

The ‘engineered domain state’ is critical to the utilization of this approach. In the  $\langle 001 \rangle$  and  $\langle 011 \rangle$  crystal cuts the domain walls are stable. This means there is little or no ferroelectric or ferroelastic polarization reorientation. In other crystal cuts there is domain wall motion under applied stress and electric fields. This gives rise to hysteresis associated with domain wall motion and energy dissipation under applied fields. In this case it would be difficult to distinguish between energy barriers to transformation and the highly rate dependent and dissipative process of domain wall motion.

Domain structures and domain wall motion introduce energy terms to the total energy. Incompatible spontaneous strain and spontaneous polarization at grain and domain boundaries give rise to local stress and local electric field at the microstructural level. Although the volume averages of these



local fields are zero, the stored energy associated with these quantities is non-zero. These must be included in the expression for the total energy.

The microstructural stress and electric fields contribute to the driving forces for domain wall motion (evolution of the remnant strain and remnant polarization). The microstructural stress would drive the nucleation and motion of domain walls such that the new domain configuration would reduce the microstructural energy. The application of an external field can thus move domain walls in one direction and on removal of the field the microstructural stress can move them back. The dissipation associated with this process gives rise to minor hysteresis loops. The same arguments apply to local electric field, domain walls with charge compatibility will form to reduce the electrical energy.

Domain wall dynamics and phase field theory have been used to model domain wall structures and their evolution (Bhattacharya and Ravichandran, 2003; Huber, 2005). Domain wall dynamics analyzes domain wall motion under external loads that alter the domain wall energy balance. The phase field modeling uses the framework of the time-dependent Ginzburg–Landau equations. Changes of the remnant electric displacement and remnant strain reflect domain reorientations and domain wall movements. Microscopic or phenomenological models may be developed to describe the evolutions of these irreversible variables (Kamlah, 2001; Landis, 2004).

## 13.6 Concluding remarks and future trends

Thermodynamics analysis leads to the utilization of changes of internal energy and the Gibbs free energy as criteria that determine whether the phase transformation will take place under combined external field loading. The critical energy levels were found to be independent of the combinations of applied stress and electric field. The energy criteria based on experimental measurements provide important parameters for theoretical modelling. Development of constitutive models for ferroelectric materials and their implementation allow the solution of problems encountered in applications of these materials.

Models at different length scales have their merits. From atomistic modeling to domain wall dynamics and phase-field approaches, from microscopic models to macroscopic (structural) computation, material parameters are needed as inputs. Energy criteria and parameters based on measurements seem to be the bridges connecting models at different length scales and achieving reliable multi-scale models.

Field-induced phase transformations in ferroelectric  $ABO_3$  perovskite type oxides are critical to a number of applications, yet characterization and modeling of this behavior has been rather limited. These transformations occur in thin films due to large in-plane stress, in shock-driven ferroelectric

generators, and in large field single crystal actuators. The design of devices that take advantage of these properties requires a finite element code with accurate constitutive models governing this behavior. Multi-axial phenomenological models developed within a thermodynamics framework using internal state variables are less computationally intensive than micromechanics-based constitutive models and are thus the most efficient when implemented in finite element codes. Micromechanics models explicitly link the physical behavior at smaller length scales to the observed macroscale behavior. They are more computationally intensive, but provide the capability of accurately simulating multi-axial loads that cannot be readily achieved experimentally. To date, little work has been done on the development of rate-dependent constitutive models governing ferroelectric phase transformations. A finite element code implemented with these constitutive models will enable exploration of the effects of geometry on the behavior of phase transforming materials and devices.

### 13.7 Acknowledgement

The authors gratefully acknowledge the support of the United States Office of Naval Research for their support of this work under grant N00014-03-1-0987.

### 13.8 References

- Allen, R.E. 1976. 'Structural phase transitions in solids with applied stresses and fields, and effect of isotopic impurities on the free energy,' *J. Chem. Phys.*, **64**(2): 552–553.
- Asamitsu, A., Moritomo, Y., Tomioka, Y., Arima, T., and Tokura, Y. 1995. 'A structural phase transition induced by an external magnetic field,' *Nature*, **373**(6513): 407–409.
- Bai, F., Wang, N., Li, J., Viehland, D., Gehring, P.M., Xu, G., and Shirane, G. 2004. 'X-ray and neutron diffraction investigation of the structural phase transformation sequence under electric field in  $0.7\text{Pb}(\text{Mg}_{1/3}\text{Nb}_{2/3})\text{O}_3$ - $0.3\text{PbTiO}_3$  crystals,' *J. Appl. Phys. Cond. Mater.*, **96**: 1620–1627.
- Belegundu, U., Du, X.H., Cross, L.E., and Uchino, K. 1999. 'In situ observation of domains in  $0.9\text{Pb}(\text{Zn}_{1/3}\text{Nb}_{2/3})\text{O}_3$ - $0.1\text{PbTiO}_3$  single crystals,' *Ferroelectrics*, **221**(1–4): 67–71.
- Bertram, R., Reck, G., and Uecker, R. 2003. 'Growth and correlation between composition and structure of  $(1-x)\text{Pb}(\text{Zn}_{1/3}\text{Nb}_{2/3})\text{O}_3$ - $x\text{PbTiO}_3$  crystals near the morphotropic phase boundary,' *J. Cryst. Growth*, **253**(1–4): 212–220.
- Bhattacharya, K., and Ravichandran, G. 2003. 'Ferroelectric perovskites for electromechanical actuation,' *Acta Mater.*, **51**(19): 5941–5960.
- Chen, K.-P., Zhang, X.-W., and Luo, H.-S. 2002. 'Electric-field-induced phase transition of  $\langle 001 \rangle$  oriented  $\text{Pb}(\text{Mg}_{1/3}\text{Nb}_{2/3})\text{O}_3$ - $\text{PbTiO}_3$  single crystals,' *J. Phys.: Condens. Matter*, **14**: 571–576.
- Chen, W., and Lynch, C.S. 1998a. 'A micro-electro-mechanical model for polarization switching of ferroelectric materials,' *Acta Mater.*, **46**(15): 5303–5311.
- Chen, W., and Lynch, C.S. 1998b. 'Model for simulating polarization switching and AF-

- F phase changes in ferroelectric ceramics,' *J. Intell. Mater. Syst. Struct.*, **9**(6): 427–431.
- Cohen, R.E. 1992. 'Origin of ferroelectricity in perovskite oxides,' *Nature*, **358**(6382): 136–138.
- Cox, D.E., Noheda, B., Shirane, G., Uesu, Y., Fujishiro, K., and Yamada, Y. 2001. 'Universal phase diagram for high-piezoelectric perovskite systems,' *Appl. Phys. Lett.*, **79**(3): 400–402.
- Damjanovic, D. 1997. 'Stress and frequency dependence of the direct piezoelectric effect in ferroelectric ceramics,' *J. Appl. Phys.*, **82**(4): 1788–1797.
- Damjanovic, D. 2001. 'Piezoelectric properties of perovskite ferroelectrics: unsolved problems and future research,' *Annales de Chimie Science des Materiaux*, **26**(1): 99–106.
- Damjanovic, D., and Demartin, M. 1996. 'Rayleigh law in piezoelectric ceramics,' *J. Phys. D: Appl. Phys.*, **29**(7): 2057–2060.
- Damjanovic, D., Budimir, M., Davis, M., and Setter, N. 2003. 'Monodomain versus polydomain piezoelectric response of 0.67Pb(Mg<sub>1/3</sub>Nb<sub>2/3</sub>)O<sub>3</sub>–0.33PbTiO<sub>3</sub> single crystals along nonpolar directions,' *Appl. Phys. Lett.*, **83**(3): 527–529.
- Dammak, H., Renault, A.E., Gaucher, P., Thi, M.P., and Calvarin, G. 2003. 'Origin of the giant piezoelectric properties in the [001] domain engineered relaxor single crystals,' *Jpn. J. Appl. Phys. Part 1*, **42**(10): 6477–6482.
- Davis, M., Damjanovic, D., Hayem, D., and Setter, N. 2005. 'Domain engineering of the transverse piezoelectric coefficient in perovskite ferroelectrics,' *J. Appl. Phys.*, **98**(1): 014102.
- Eitel, R.E., Shrout, T.R., and Randall, C.A. 2006. 'Nonlinear contributions to the dielectric permittivity and converse piezoelectric coefficient in piezoelectric ceramics,' *J. Appl. Phys.*, **99**(12): 124110–124111.
- Essig, O., Wang, P., Hartweg, M., Janker, P., Nafe, H., and Aldinger, F. 1999. 'Uniaxial stress and temperature dependence of field induced strains in antiferroelectric lead zirconate titanate stannate ceramics,' *J. Eur. Ceram. Soc.*, **19**(6–7): 1223–1228.
- Fang, F., and Yang, W. 2002. 'Indentation-induced cracking and 90 degrees domain switching pattern in barium titanate ferroelectric single crystals under different poling,' *Mater. Lett.*, **57**(1): 198–202.
- Feng, Z., Luo, H., Guo, Y., He, T., and Xu, H. 2003. 'Dependence of high electric-field-induced strain on the composition and orientation of Pb(Mg<sub>1/3</sub>Nb<sub>2/3</sub>)O<sub>3</sub>–PbTiO<sub>3</sub> crystals,' *Solid State Commun.*, **126**(6): 347–351.
- Fiebig, M., Lottermoser, T., Frohlich, D., Goltsev, A.V., and Pisarev, R.V. 2002. 'Observation of coupled magnetic and electric domains,' *Nature*, **419**(6909): 818–820.
- Fu, H., and Cohen, R.E. 2000. 'Polarization rotation mechanism for ultrahigh electromechanical response in single-crystal piezoelectrics,' *Nature*, **403**(6767): 281–283.
- Fujishiro, K., Vlokh, R., Uesu, Y., Yamada, Y., Kiat, M., Dkhil, B., and Yamashita, Y. 1998. 'Optical observation of heterophase and domain structures in relaxor ferroelectrics Pb(Zn<sub>1/3</sub>Nb<sub>2/3</sub>)O<sub>3</sub>–9%PbTiO<sub>3</sub>,' *Jpn. J. Appl. Phys., Part 1*, **37**: 5246–5248.
- George, A.M., Iniguez, J., and Bellaiche, L. 2001. 'Anomalous properties in ferroelectrics induced by atomic ordering,' *Nature*, **413**(6851): 54–57.
- Gerthsen, P., Hardtl, K.H., and Schmidt, N.A. 1980. 'Correlation of mechanical and electrical losses in ferroelectric ceramics,' *J. Appl. Phys.*, **51**(2): 1131–1134.
- Glinchuk, M.D. 2004. 'Relaxor ferroelectrics: from cross superparaelectric model to random field theory,' *Br. Ceram. Trans.*, **103**(2): 76–82.

- Hall, D.A. 2001. 'Nonlinearity in piezoelectric ceramics,' *J. Mater. Sci.*, **36**(19): 4575–4601.
- Han, J., and Cao, W. 2003. 'Electric field effects on the phase transitions in [001]-oriented  $(1-x)\text{Pb}(\text{Mg}_{1/3}\text{Nb}_{2/3})\text{O}_3-x\text{PbTiO}_3$  single crystals with compositions near the morphotropic phase boundary,' *Phys. Rev. B*, **68**(13): 134102–134106.
- Hardtl, K.H. 1982. 'Electrical and mechanical losses in ferroelectric ceramics,' *Ceram. Int.*, **8**(4): 121–127.
- Herbiet, R., Robels, U., Dederichs, H., and Arlt, G. 1989. 'Domain wall and volume contributions to material properties of PZT ceramics,' *Ferroelectrics*, **98**: 107–121.
- Holland, R. 1967. 'Representation of dielectric, elastic and piezoelectric losses by complex coefficients,' *IEEE Transactions on Sonics and Ultrasonics*, SU-**14**(1): 18–20.
- Hom, C.L., and Shankar, N. 1996. 'A finite element method for electrostrictive ceramic devices,' *Int. J. Solids Struct.*, **33**(12): 1757–1779.
- Hu, H.L., and Chen, L.Q. 1997. 'Computer simulation of  $90^\circ$  ferroelectric domain formation in two-dimensions,' *Mater. Sci. Eng. A*, **A238**(1): 182–191.
- Hu, H.L., and Chen, L.Q. 1998. 'Three-dimensional computer simulation of ferroelectric domain formation,' *J. Am. Ceram. Soc.*, **81**(3): 492–500.
- Huber, J.E. 2005. 'Micromechanical modelling of ferroelectrics,' *Curr. Opin. Solid State Mater. Sci.*, **9**(3): 100–106.
- Huber, J.E., Fleck, N.A., Landis, C.M., and McMeeking, R.M. 1999. 'Constitutive model for ferroelectric polycrystals,' *J. Mech. Phys. Solids*, **47**(8): 1663–1697.
- Hwang, S.C., Lynch, C.S., and McMeeking, R.M. 1995. 'Ferroelectric/ferroelastic interactions and a polarization switching model,' *Acta Metall. Mater.*, **43**(5): 2073–2084.
- Jiang, Y.L., and Dan, L. 2004. 'On ferroelectric crystals with engineered domain configurations,' *J. Mech. Phys. Solids*, **52**(8): 1719–1742.
- Kamlah, M. 2001. 'Ferroelectric and ferroelastic piezoceramics modeling of electromechanical hysteresis phenomena,' *Continuum Mech. Thermodynam.*, **13**(4): 219–268.
- Kamlah, M., and Tsakmakis, C. 1999. 'Phenomenological modeling of the non-linear electro-mechanical coupling in ferroelectrics,' *Int. J. Solids Struct.*, **36**(5): 669–695.
- Khachaturyan, A.G. 2000. 'Prospects of 3-dimensional nanoscale modeling of engineering materials,' *Proceedings of the TMS Fall Meeting*, 293–308.
- La Ouantapong, D., Noheda, B., Ye, G., Gehring, P.M., Toulouse, J., Cox, D.E., and Shirane, G. 2002. 'Phase diagram of the relaxor ferroelectric  $(1-x)\text{Pb}(\text{Zn}_{1/3}\text{Nb}_{2/3})\text{O}_3-x\text{PbTiO}_3$ ,' *Phys. Rev. B*, **65**(14): 144101.
- Landis, C.M. 2004. 'Non-linear constitutive modeling of ferroelectrics,' *Curr. Opin. Solid State Mater. Sci.*, **8**(1): 59–69.
- Landis, C.M., Wang, J., and Sheng, J. 2003. 'Micro-electromechanically informed phenomenological constitutive models for ferroelectrics,' *Proceedings of SPIE – The International Society for Optical Engineering*, **5053**, 335–346.
- Li, W., Guo, S., Tang, Y., and Zhao, X. 2003. 'Phase transition induced by thermal and electric fields in electron-irradiated poly(vinylidene fluoride-trifluoroethylene) copolymers,' *J. Phys. D: Appl. Phys.*, **36**(19): 2382–2385.
- Li, Y.L., Hu, S.Y., Liu, Z.K., and Chen, L.Q. 2001. 'Phase-field simulation of domain structure evolution in ferroelectric thin films,' *Materials Research Society Symposium – Proceedings*, **652**, Y4.2.1–Y4.2.10.
- Lines, M.E., and Glass, A.M. 1977. *Principles and Applications of Ferroelectrics and Related Materials*, Clarendon Press, Oxford.

- Liu, S.F., Park, S.E., Shrout, T.R., and Cross, L.E. 1999. 'Electric field dependence of piezoelectric properties for rhombohedral  $0.955\text{Pb}(\text{Zn}_{1/3}\text{Nb}_{2/3})\text{O}_3\text{-}0.045\text{PbTiO}_3$  single crystals,' *J. Appl. Phys.*, **85**(5): 2810.
- Liu, T., and Lynch, C.S. 2003. 'Ferroelectric properties of [110], [001] and [111] poled relaxor single crystals: measurements and modeling,' *Acta Mater.*, **51**(2): 407–416.
- Liu, T., Lynch, C.S., and McLaughlin, E.A. 2006. 'Thermodynamics of stress and electric field induced phase transition in relaxor ferroelectric crystals,' *J. Intell. Mater. Syst. Struct.*, **18**: 409–415.
- Lu, Y., Jeong, D.Y., Cheng, Z.Y., Zhang, Q.M., Luo, H.S., Yin, Z.-W., and Viehland, D. 2001. 'Phase transitional behavior and piezoelectric properties of the orthorhombic phase of  $\text{Pb}(\text{Mg}_{1/3}\text{Nb}_{2/3})\text{O}_3\text{-PbTiO}_3$  single crystals,' *Appl. Phys. Lett.*, **78**(20): 3109–3111.
- Lu, Y., Jeong, D.Y., Cheng, Z.Y., Shrout, T., and Zhang, Q.M. 2002. 'Phase stabilities of "morphotropic" phases in  $\text{Pb}(\text{Zn}_{1/3}\text{Nb}_{2/3})\text{O}_3\text{-PbTiO}_3$  single crystals,' *Appl. Phys. Lett.*, **80**(11): 1918.
- Lynch, C.S. 1996. 'The effect of uniaxial stress on the electro-mechanical response of 8/65/35 PLZT,' *Acta Mater.*, **44**(10): 4137–4148.
- Lynch, C.S. 1998. 'On the development of multi-axial phenomenological constitutive laws for ferroelectric ceramics,' *J. Intell. Mater. Syst. Struct.*, **9**(7): 555–563.
- Malvern, L.E. (1969). *Introduction to the Mechanics of a Continuous Medium*, Prentice-Hall, Inc., Englewood Cliffs, NJ.
- Mauck, L.D. 2002. 'The role of rate dependence and dissipation in the constitutive behavior of ferroelectric ceramics for high power applications,' Ph.D. Dissertation. The Georgia Institute of Technology.
- McLaughlin, E.A., Liu, T., and Lynch, C.S. 2004. 'Relaxor ferroelectric PMN–32%PT crystals under stress and electric field loading: I–32 mode measurements,' *Acta Mater.*, **52**(13): 3849–3857.
- McLaughlin, E.A., Liu, T., and Lynch, C.S. 2005. 'Relaxor ferroelectric PMN–32%PT crystals under stress, electric field and temperature loading: II–33–mode measurements,' *Acta Mater.*, **53**(14): 4001–4008.
- McMeeking, R.M., and Hwang, S.C. 1997. 'On the potential energy of a piezoelectric inclusion and the criterion for ferroelectric switching,' *Ferroelectrics*, **200**(1–4): 151–173.
- McMeeking, R.M., and Landis, C.M. 2002. 'A phenomenological multi-axial constitutive law for switching in polycrystalline ferroelectric ceramics,' *Int. J. Eng. Sci.*, **40**(14): 1553–1577.
- Meeks, S.W., and Timme, R.W. 1975. 'Effects of one-dimensional stress on piezoelectric ceramics,' *J. Appl. Phys.*, **46**(10): 4334–4338.
- Noheda, B., Cox, D.E., Shirane, G., Guo, R., Jones, B., and Cross, L.E. 2001a. 'Stability of the monoclinic phase in the ferroelectric perovskite  $\text{PbZr}_{1-x}\text{Ti}_x\text{O}_3$ ,' *Phys. Rev. B*, **63**: 1–6.
- Noheda, B., Cox, D.E., Shirane, G., Park, S.E., Cross, L.E., and Zhong, Z. 2001b. 'Polarization rotation via a monoclinic phase in the piezoelectric 92% $\text{Pb}(\text{Zn}_{1/3}\text{Nb}_{2/3})\text{O}_3\text{-}8\%\text{PbTiO}_3$ ,' *Phys. Rev. Lett.*, **86**(17): 3891–3894.
- Noheda, B., Cox, D.E., Shirane, G., Gao, J., and Ye, G. 2002. 'Phase diagram of the ferroelectric relaxor  $(1-x)\text{Pb}(\text{Mg}_{1/3}\text{Nb}_{2/3})\text{O}_3\text{-}x\text{PbTiO}_3$  crystals,' *Phys. Rev. B*, **66**(5e): 054104.
- Park, S.E., and Hackenberger, W. 2002. 'High performance single crystal piezoelectrics: applications and issues,' *Curr. Opin. Solid State Mater. Sci.*, **6**(1): 11–18.

- Park, S.E., and Shrout, T.R. 1997. 'Ultrahigh strain and piezoelectric behavior in relaxor based ferroelectric single crystals,' *J. Appl. Phys.*, **82**(4): 1804–1811.
- Rabe, K.M., and Waghmare, U.V. 1996. 'Ferroelectric phase transitions from first principles,' *J. Phys. Chem. Solids*, **57**(10): 1397–1403.
- Ren, W., Liu, S.F., and Mukherjee, B.K. 2002. 'Piezoelectric properties and phase transitions of <001>-oriented  $\text{Pb}(\text{Zn}_{1/3}\text{Nb}_{2/3})\text{O}_3$ - $\text{PbTiO}_3$  single crystals,' *Appl. Phys. Lett.*, **80**(17): 3174.
- Robels, U., Herbiet, R., and Arlt, G. 1989. 'Coupled losses in PZT near the morphotropic phase boundary,' *Ferroelectrics (UK)*, **93**, 95–103.
- Samara, G.A., Venturini, E.L., and Schmidt, V.H. 2000. 'Pressure-induced crossover from long-to-short-range order in  $[\text{Pb}(\text{Zn}_{1/3}\text{Nb}_{2/3})\text{O}_3]_{0.905}$ - $(\text{PbTiO}_3)_{0.095}$  single crystal,' *Appl. Phys. Lett.*, **76**(10): 1327–1329.
- Schmidt, V.H., Chien, R., Shih, I.C., and Tu, C.-S. 2003. 'Polarization rotation and monoclinic phase in relaxor ferroelectric PMN-PT crystal,' *AIP Conf. Proc.*, **677**(1): 160–167.
- Shang, J.K., and Tan, X. 2001. 'Indentation-induced domain switching in  $\text{Pb}(\text{Mg}_{1/3}\text{Nb}_{2/3})\text{O}_3$ - $\text{PbTiO}_3$  crystal,' *Acta Mater.*, **49**(15): 2993–2999.
- Shu, Y.C., and Bhattacharya, K. 2001. 'Domain patterns and macroscopic behaviour of ferroelectric materials,' *Philos. Mag. B*, **81**(12): 2021–2054.
- Singh, A.K., and Pandey, D. 2003. 'Evidence for  $M_B$  and  $M_C$  phases in the morphotropic phase boundary region of  $(1-x)[\text{Pb}(\text{Mg}_{1/3}\text{Nb}_{2/3})\text{O}_3]$ - $x\text{PbTiO}_3$ : a Rietveld study,' *Phys. Rev. B*, **67**(6): 064102.
- Su, C., Vugmeister, B., and Khachaturyan, A.G. 2001. 'Dielectric properties of material with random off-center defects: Monte Carlo simulation of relaxor ferroelectrics,' *J. Appl. Phys.*, **90**(12): 6345–6356.
- Tadmor, E.B., Waghmare, U.V., Smith, G.S., and Kaxiras, E. 2002. 'Polarization switching in  $\text{PbTiO}_3$ : an *ab initio* finite element simulation,' *Acta Mater.*, **50**(11): 2989–3002.
- Topolov, V.Y. 2004. 'The remarkable orientation and concentration dependences of the electromechanical properties of  $0.67\text{Pb}(\text{Mn}_{1/3}\text{Nb}_{2/3})\text{O}_3$ - $0.33\text{PbTiO}_3$  single crystals,' *J. Phys.: Condens. Matter*. **12**: 2115–2128.
- Tu, C.-S., Huang, L.W., Chien, R., and Schmidt, V.H. 2003. 'E-field and temperature dependent transformation in <102>-cut PMN-PT crystal,' *AIP Conf. Proc.*, **677**(1): 152–159.
- Uchino, K., and Hirose, S. 2001. 'Loss mechanisms in piezoelectrics: How to measure different losses separately,' *IEEE T. Ultrason. Ferr.*, **48**(1): 307–321.
- Uesu, Y., Yamada, Y., Fujishiro, K., Tazawa, H., Enokido, S., Kiat, J.M., and Dkhil, B. 1998. 'Structural and optical studies of development of the long-range order in ferroelectric relaxor  $\text{Pb}(\text{Zn}_{1/3}\text{Nb}_{2/3})\text{O}_3$ -9% $\text{PbTiO}_3$ ,' *Ferroelectrics*, **217**(1): 319–325.
- Vanderbilt, D. and Cohen, M.H. 2001. 'Monoclinic and triclinic phases in higher-order Devonshire theory,' *Phys. Rev. B*, **63**(9): 094108.
- Viehland, D. 2000. 'Symmetry-adaptive ferroelectric mesostates in oriented  $\text{Pb}(\text{Bi}_{1/3}\text{II}_{2/3})\text{O}_3$ - $\text{PbTiO}_3$  crystals,' *J. Appl. Phys.*, **88**(8): 4794–4806.
- Viehland, D. and Li, J.F. 2002. 'Anhydretic field-induced rhombohedral to orthorhombic transformation in <110>-oriented  $0.7\text{Pb}(\text{Mg}_{1/3}\text{Nb}_{2/3})\text{O}_3$ - $0.3\text{PbTiO}_3$  crystals,' *J. Appl. Phys.*, **92**(12): 7690–7692.
- Viehland, D., and Powers, J. 2001a. 'Effect of uniaxial stress on the electromechanical properties of  $0.7\text{Pb}(\text{Mg}_{1/3}\text{Nb}_{2/3})\text{O}_3$ - $0.3\text{PbTiO}_3$  crystals and ceramics,' *J. Appl. Phys.*, **89**(3): 1820–1825.
- Viehland, D., and Powers, J. 2001b. 'Electromechanical coupling coefficient of <001>-

- oriented  $\text{Pb}(\text{Mg}_{1/3}\text{Nb}_{2/3})\text{O}_3\text{-PbTiO}_3$  crystals: Stress and temperature independence,' *Appl. Phys. Lett.*, **78**(20): 3112–3113.
- Viehland, D., Amin, A., and Li, J.F. 2001. 'Piezoelectric instability in  $\langle 011 \rangle$ -oriented  $\text{Pb}(\text{B}_{1/3}\text{B}_{2/3}^{\text{II}})\text{O}_3\text{-PbTiO}_3$  crystals,' *Appl. Phys. Lett.*, **79**(7): 1006–1008.
- Viehland, D., Li, J.F., Gittings, K., and Amin, A. 2003. 'Electroacoustic properties of  $\langle 110 \rangle$ -oriented  $\text{Pb}(\text{Mg}_{1/3}\text{Nb}_{2/3})\text{O}_3\text{-PbTiO}_3$  crystals under uniaxial stress,' *Appl. Phys. Lett.*, **83**(1): 132–134.
- Wang, X., Liu, M., Chan, L.W., and Choy, C.L. 2004. 'Monte Carlo simulation on dielectric and ferroelectric behaviors of relaxor ferroelectrics,' *J. Appl. Phys.*, **95**(8): 4282–4290.
- Yang, W., and Chen, L.Q. 1995. 'Computer simulation of the dynamics of  $180^\circ$  ferroelectric domains,' *J. Am. Ceram. Soc.*, **78**(9): 2554–2556.
- Ye, G., Noheda, B., Dong, M., Cox, D., and Shirane, G. 2001. 'Monoclinic phase in the relaxor-based piezoelectric/ferroelectric  $\text{Pb}(\text{Mg}_{1/3}\text{Nb}_{2/3})\text{O}_3\text{-PbTiO}_3$  system,' *Phys. Rev. B*, **64**(18): 184114.
- Ye, Z.-G. 2002. 'Crystal chemistry and domain structure of relaxor piezocrystals,' *Curr. Opin. Solid State Mater. Sci.*, **6**(1): 35–44.
- Ye, Z.-G. and Dong, M. 2000. 'Morphotropic domain structures and phase transitions in relaxor-based piezo-/ferroelectric  $(1-x)\text{Pb}(\text{Mg}_{1/3}\text{Nb}_{2/3})\text{O}_3\text{-xPbTiO}_3$  single crystals,' *J. Appl. Phys.*, **87**(5): 2312–2319.
- Ye, Z.-G., Dong, M., and Zhang, L. 1999. 'Domain structure and phase transitions in relaxor-based piezo-/ferroelectric  $(1-x)\text{Pb}(\text{Zn}_{1/3}\text{Nb}_{2/3})\text{O}_3\text{-xPbTiO}_3$  single crystals,' *Ferroelectrics*, **229**: 223–232.
- Yin, J., Jiang, B., and Cao, W. 1999. 'Determination of elastic, piezoelectric and dielectric properties of  $\text{Pb}(\text{Zn}_{1/3}\text{Nb}_{2/3})\text{O}_3\text{-PbTiO}_3$  single crystals,' *Proceedings of SPIE – The International Society for Optical Engineering*, **3664**, 239–246.
- Yin, J., Jiang, B., and Cao, W. 2000a. 'Elastic, piezoelectric, and dielectric properties of  $0.955\text{Pb}(\text{Zn}_{1/3}\text{Nb}_{2/3})\text{O}_3\text{-0.045PbTiO}_3$  single crystal with designed multidomains,' *IEEE T. Ultrason. Ferr.*, **47**(1): 285–291.
- Yin, J., Jiang, B., and Cao, W. 2000b. 'Elastic, piezoelectric, and dielectric properties of  $0.955\text{Pb}(\text{Zn}_{1/3}\text{Nb}_{2/3})\text{O}_3\text{-0.045PbTiO}_3$  single crystal with designed multidomains,' *IEEE T. Ultrason. Ferr.*, **47**(1): 285–291.
- Zhang, L., Dong, M., and Ye, Z.-G. 2000. 'Flux growth and characterization of the relaxor-based  $\text{Pb}[(\text{Zn}_{1/3}\text{Nb}_{2/3})_{1-x}\text{Ti}_x]\text{O}_3$  [PZNT] piezocrystals,' *Mat. Sci. Eng. B*, **78**(2–3): 96–104.
- Zhang, R., Jiang, B., and Cao, W. 2001. 'Elastic, piezoelectric, and dielectric properties of multidomain  $0.67\text{Pb}(\text{Mg}_{1/3}\text{Nb}_{2/3})\text{O}_3\text{-0.33PbTiO}_3$  single crystals,' *J. Appl. Phys.*, **90**(7): 3471–3475.
- Zhang, R., Jiang, B., and Cao, W. 2003. 'Orientation dependence of piezoelectric properties of single domain  $0.67\text{Pb}(\text{Mn}_{1/3}\text{Nb}_{2/3})\text{O}_3\text{-0.33PbTiO}_3$  crystals,' *Appl. Phys. Lett.*, **82**(21): 3737–3739.
- Zhao, X., Fang, B., Cao, H., Guo, Y., and Luo, H. 2002. 'Dielectric and piezoelectric performance of PMN-PT single crystals with compositions around the MPB: influence of composition, poling field and crystal orientation,' *Mat. Sci. Eng. B*, **96**(3): 254–262.
- Zhou, X., Chu, B., and Zhang, Q.M. 2006. 'Complex notation for the dielectric response of ferroelectric materials beyond the small sinusoidal fields,' *IEEE Transactions on Ultrasonics, Ferroelectrics, and Frequency Control*, **53**(8): 1540–1543.

## From the structure of relaxors to the structure of MPB systems

---

J - M KIAT and B DKHIL, Ecole Centrale Paris, France

### 14.1 Introduction

Very good reviews have already addressed relaxors (Bokov and Ye, 2006) and the structural aspects of morphotropic phase boundary (MPB) systems (Noheda, 2002; Noheda and Cox, 2006) and therefore it is not the intent of this chapter to repeat this difficult work. Instead here we would like to focus on the connection between two features of this issue which are usually treated in a separate manner but which are, in our opinion, connected: relaxor compounds and MPB systems.

For a long time, numerous studies have pointed out the need of a structural knowledge at the nanoscale for understanding the physical properties of these fascinating materials. Recently it has been shown that the local *chemical* composition deeply determines the *polar* ordering. Keeping this fact in mind will make it easy for the reader, with the help of some simplistic pictures, to understand the basic ideas about the structure of a relaxor, why it is already a ‘potential’ or ‘virtual’ MPB and what changes are needed to make it behave like a ‘true’ MPB compound.

Several groups around the world have contributed to and continue to work on these topics; in particular the contribution of researchers doing modelling has grown impressively recently. It is obviously impossible to make an extensive bibliography and we will not pretend to have read everything. In the following we will restrict ourselves to experimental results mainly from diffraction and diffuse scattering by X-ray, neutron and Raman techniques.

This chapter is mainly an informal discussion, suitable for a wide readership with many ideas and basic sketches showing the crossover from relaxor towards MPB through their structure on a nanoscale. Moreover, for the sake of clarity we have focused our description on perovskite-like structure and especially lead-based complex perovskite as it is the most widely studied family.

Therefore this chapter is organised as follows: On Section 14.2 we will make a brief historical introduction, through two simple sets of experimental



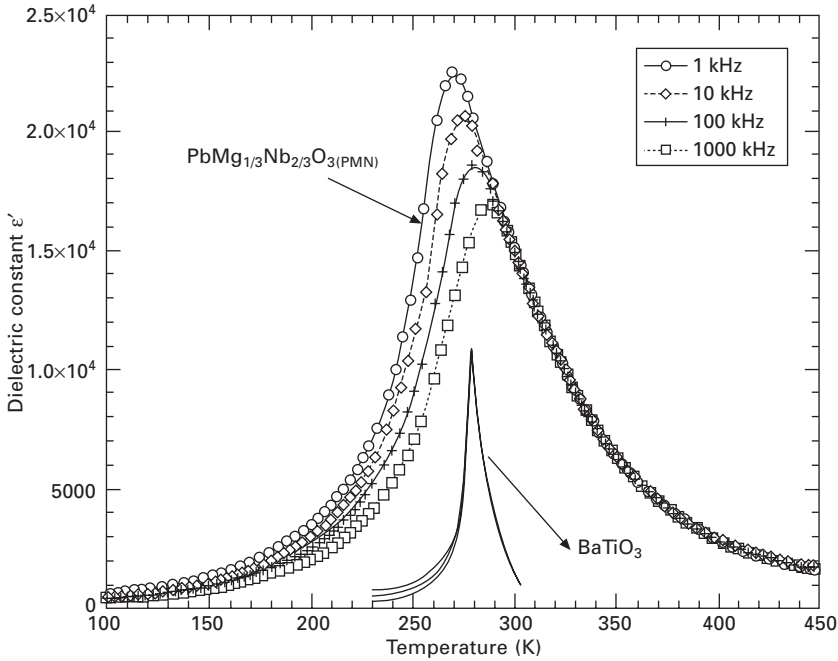
observations stressing the two basic ingredients we shall use throughout this chapter, namely the polar nano-regions (PNRs) and chemically ordered regions (CORs). In Section 14.3 we will discuss the question of order and disorder as it has been studied from structural measurements in archetypal relaxors  $\text{PbMg}_{1/3}\text{Nb}_{2/3}\text{O}_3$  (PMN) and  $\text{PbSc}_{1/2}\text{Nb}_{1/2}\text{O}_3$  (PSN). Section 14.3.1 deals with the question of long-range and short-range polar order; the concept of PNRs will be addressed; in Section 14.3.2 we will discuss the question of chemical order and in Section 14.3.3 we will focus on the interaction between both entities. At this point the reader will have, we hope, a simplistic but adequate physical picture of the structure of a relaxor.

In Section 14.4 we will move towards the MPB compounds by studying the influence of titanium substitution, using the same basic ingredients of chemical and polar orders. The rotation of polarisation is discussed in different systems in Section 14.4.1; in Section 14.4.2 the progressive crossover from short (local) range to long-range (macroscopic phase) monoclinic order is discussed. Those experimental results are also connected to the results from *ab-initio* modelling in Section 14.4.3. In Section 14.4.4 the concept of local chemical composition is discussed more deeply in relation to cationic ordering. At the end of this section the relationship between the structure of a relaxor and the structure of the morphotropic phases will be displayed through simplistic sketches to make it, we again hope, clear for the reader.

In this framework, Section 14.5 will present some selected experimental results on the effects of electric field (14.5.1), pressure (14.5.2), grain size reduction (14.5.3) and in thin films (14.5.4) in connection with the ideas developed before. Finally Section 14.6 will conclude by summarizing in a table and schematic figures all the ideas discussed in this text.

## 14.2 Historical context

Smolenskii (1984) and his group make the pioneering studies of ‘textbook’ relaxor compound  $\text{PbMg}_{1/3}\text{Nb}_{2/3}\text{O}_3$  (PMN) using dielectric measurements. In order to explain the huge spread (compared with conventional ferroelectric, see Fig. 14.1) in the temperature dependence of the dielectric permittivity, they proposed the first structural model of PMN, introducing the concept of ‘diffuse phase transition’. Indeed up to that time, maximum of the temperature dependence of dielectric permittivity  $\epsilon(T)$  was associated with critical behaviour at ferroelectric phase transitions with Curie–Weiss law close to critical temperature  $T_c$ . They considered the relaxation of isolated polar regions and relaxation or resonance of the boundaries of these regions to be at the origin of the anomalous dielectric permittivity, which is still recognized by most modern researchers. Other authors suggested that owing to chemical inhomogeneities, different local concentrations of cations induce ferroelectric phase transition with concentration-dependent critical temperature  $T_c$ :



14.1 Real part of dielectric permittivity of PMN compared with BaTiO<sub>3</sub> ( $T_c$  of which is 393K, the temperature scale has been shifted).

observation of the diffuseness should therefore be due to convolution of multiple  $\epsilon(T)$ -curves.

It is noteworthy that, nevertheless, these chemical inhomogeneities alone, even if they explain the broad dielectric anomaly, are not enough to understand the so-called ‘relaxor’ behaviour described by the frequency-dependence of the maximum value of dielectric permittivity  $\epsilon_{\max}(T_{\max})$  with a non-Debye evolution.

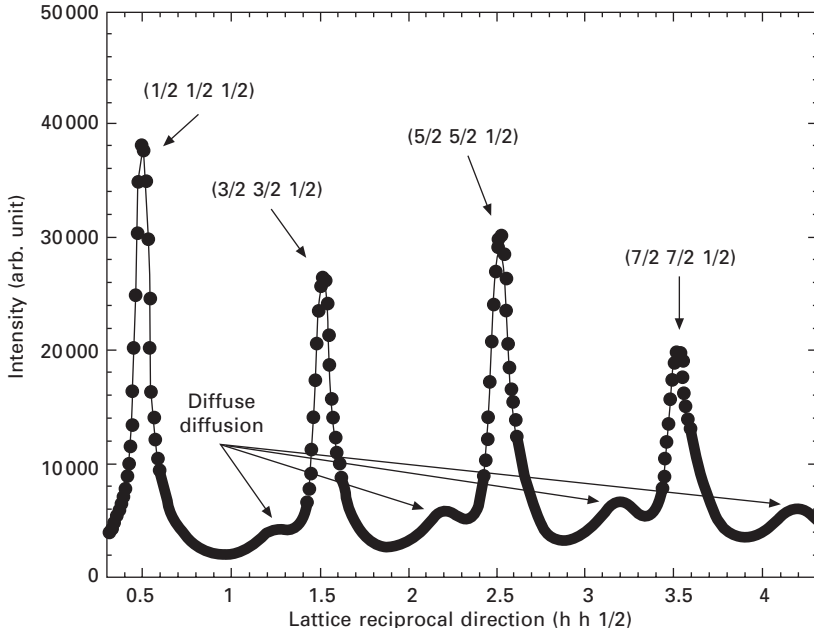
Much later, our group was the first to make a structural investigation of PMN at different temperature by combined X-ray and neutron diffraction (Bonneau *et al.*, 1989, 1991; Mathan *et al.*, 1990, 1991). The first surprise was the observation down to 5 K of very high thermal parameters, indicating some kind of disorder from the ideal perovskite structure, whereas no long-range deviation from a cubic, i.e. non-ferroelectric phase, is observed, consistent with previous observations (Cross, 1987). Statistic displacements of atoms out of cubic special positions allowed us to improve the quality of the structure refinement and the thermal parameters recovered more standard values. The second surprise during the same set of experiments was the observation in the powder patterns of very strong diffuse scattering on the basis of the line profile of Bragg peaks which progressively grows from high temperature.

These sets of results were explained by introducing the concept of *polar*

*nano-regions* (PNRs), at high temperature and in the vicinity of the  $T_{\max}$  temperature (the exact range of temperature is given below). At low temperature when the situation appears to be frozen, a structural model for the local polar order with rhombohedral symmetry was proposed by de Mathan *et al.* (1991) to take into account the additional diffuse scattering.

Let us now turn back to the chemical inhomogeneities introduced by Smolenskii. Indeed besides the polar feature of relaxors, another common local characteristic concerns the intrinsic compositional disorder of non-isovalent ions (on the B-site of the perovskite). This random distribution of heterovalent ions is expected to give rise to *random fields* (RFs) which in turn may influence the polar properties (Westphal *et al.*, 1992; Kleemann, 1993). Besides this random arrangement and following Smolenskii's ideas, Krause *et al.* (1979) observed cations ordering in PMN in the form of *chemically ordered regions* (CORs). Indeed, in addition to Bragg peaks and diffuse scattering, superstructure peaks indicating local change in the average composition are easily observed in diffraction experiments ( Fig. 14.2). This peculiar chemical arrangement through CORs is of huge interest in the understanding of relaxors, as we shall see later.

At this time the two basic concepts for the understanding of relaxors – as well as MPB compounds – were introduced. Numerous studies followed and



14.2 X-ray diffraction Q-scan showing both superstructure peaks and diffuse scattering in a single crystal of PMN at 10K.

progressively the idea emerged that the connection between these two sets of basic experimental observations, i.e. atomic shift disorder and PNRs on one side and chemical disorder and CORs or RFs on the other, was the key to understanding relaxor behaviour.

### 14.3 Structure of archetypal relaxors $\text{PbMg}_{1/3}\text{Nb}_{2/3}\text{O}_3$ (PMN) and $\text{PbSc}_{1/2}\text{Nb}_{1/2}\text{O}_3$ (PSN)

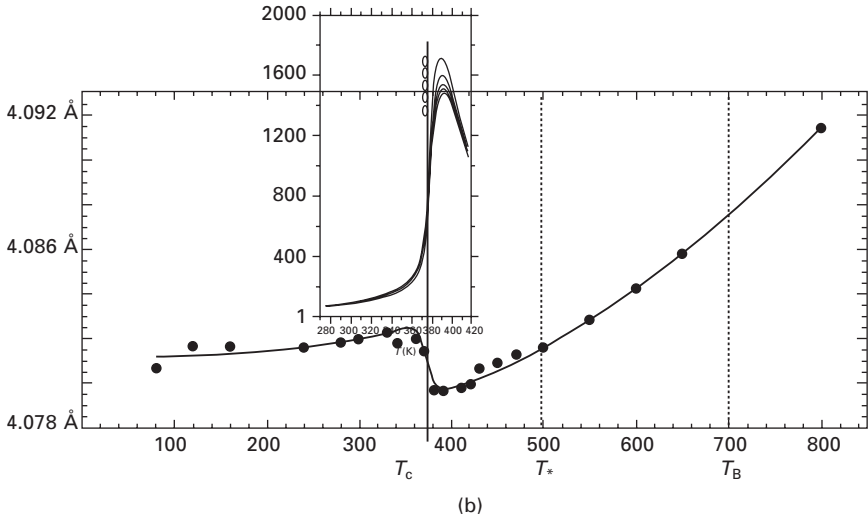
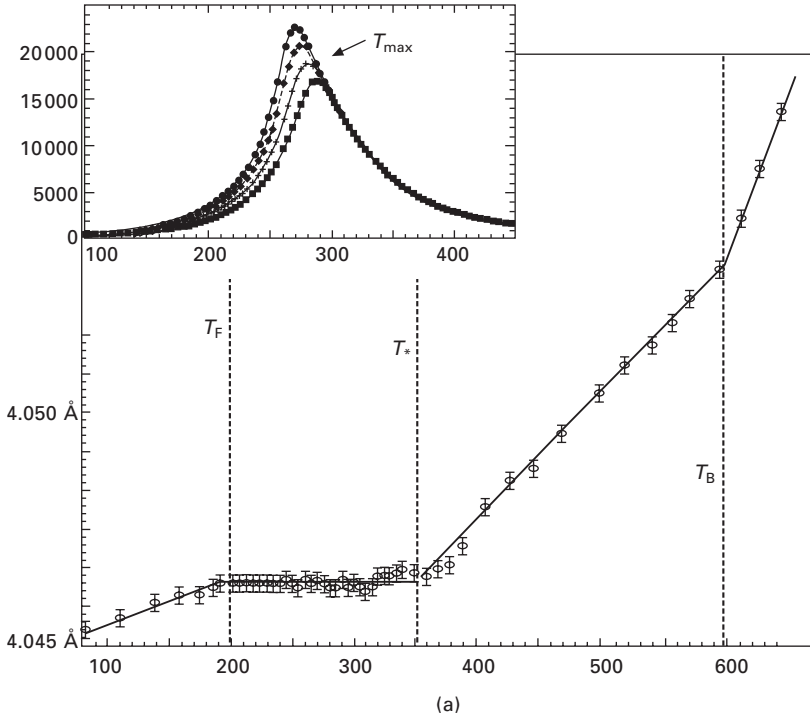
The two main features for the understanding of relaxor structures, i.e. PNR and COR, were introduced in the last section; this section is devoted to a deeper experimental investigation of these basic ideas. To this purpose we focus our description on both relaxors  $\text{PbMg}_{1/3}\text{Nb}_{2/3}\text{O}_3$  (PMN) and  $\text{PbSc}_{1/2}\text{Nb}_{1/2}\text{O}_3$  (PSN) which are representative of the two main families of lead-based relaxors, namely the 1/3:2/3 and 1/2:1/2 compounds. (1/3:2/3 and 1/2:1/2 refer to the ion distribution on the B-site of the perovskite.) Their common characteristics and differences will be discussed in the following sections.

#### 14.3.1 Polar order

Whereas the dielectric properties of PMN and PSN are quite similar, their low temperature structures differ significantly. Indeed whereas PMN does not exhibit any ‘true’, i.e. long-ranged, ferroelectric transition but short-range polar order, PSN (as well as PMN–PT with concentration close and above ~5% of PT (Ye *et al.*, 2003) displays a rhombohedral  $R3m$ , i.e. ferroelectric, phase with clear and weakly first-order anomalies whereas the behaviour of PMN appears to be more complex (Fig. 14.3), with several characteristic temperatures that are explained below. The situation of  $\text{PbZn}_{1/3}\text{Nb}_{2/3}\text{O}_3$  (PZN), which is also considered as a model relaxor, displays similar changes to that of PSN, although it is a 1/3:2/3-type compound (it will be briefly analysed in Section 14.4.1).

It is well known that inside the high-temperature cubic phase not all atoms of lead-based relaxor compound are sited at their cubic special positions: the first observation in PMN was reported by Bonneau *et al.* (1991). Several attempts have been made to model such behaviour in different lead-based compounds: in particular split-ion (Malibert *et al.*, 1997), rotator (spherical layer) (Vakhrushev *et al.*, 1994), and anharmonic Graham–Charlier expansion (Kiat *et al.*, 2000); interesting results have also been obtained via pair distribution function analysis but will not be discussed here; we refer the reader to the book by Egami and Billinge (2003).

In all cases the parameters describing the displacement of ions from their undistorted positions were found to be temperature dependent. The Graham–Charlier expansion which is based on a high-order (i.e. anharmonic)



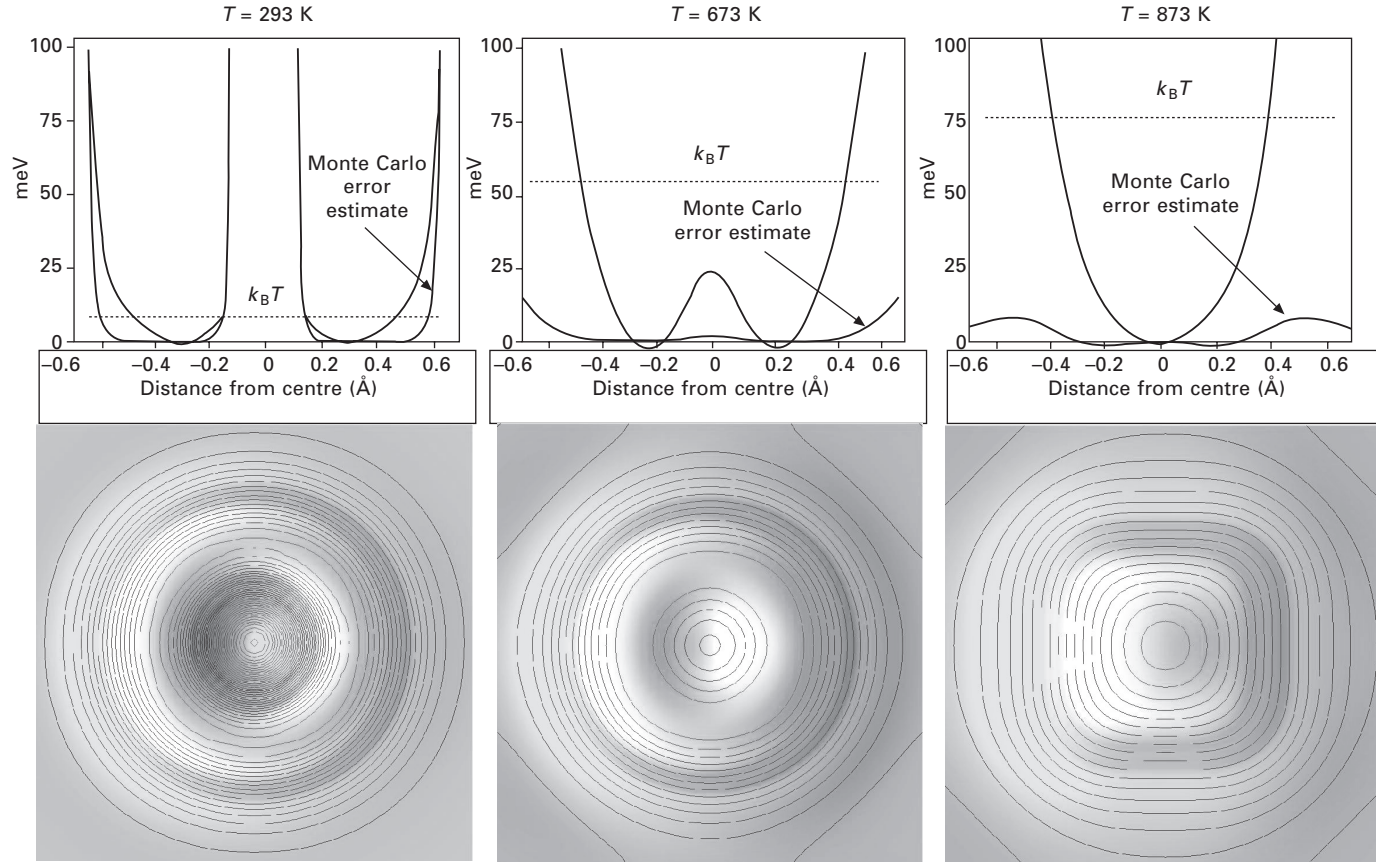
14.3 Comparison of temperature dependence of the lattice parameter with temperature dependence of real part of dielectric permittivity in (a) PMN and (b) PSN.

development of thermal parameters, seems to be the more versatile way to model the disorder of the cubic phase.

The lead atoms appears to play a more significant role in the local non-cubic behaviour. For instance in PMN at 673 K (Fig. 14.4) lead atoms stand on a highly anharmonic potential and are never at their special position but on a spherical shell. This situation is strongly different for instance from that in for  $\text{PbTiO}_3$  where this situation is observed only in the very close vicinity of  $T_C$  (Malibert *et al.*, 1997; Kiat *et al.*, 2000); in the case of lead-free perovskites such as  $\text{BaTiO}_3$  and  $\text{KNbO}_3$ , this situation for barium and potassium atoms respectively is never observed (Kiat *et al.*, 2000). In PMN in cooling, the potential deep increases and anharmonicity is stronger; in fact at room temperature (Fig. 14.4) it is so strong that Graham–Charlier approximations is no more valid and one is faced with more simplistic treatments. For instance disordered displacements are introduced via split-atoms in the structural refinements and possible decrease of agreement factor between the calculated–experimental difference are researched. At high-temperature (for instance 523 K) in PMN–PT10% (Fig. 14.5), shifting the lead atoms, along any directions, induces better agreement factor and diminishes the abnormal high-temperature factor (harmonic) (Dkhil *et al.*, 2002). This situation corresponds to the spherical shell disorder; at lower temperature (300 K) but still in the cubic phase, i.e. above the critical temperature  $T_C$ , the shifts are no more isotropic but rather along the  $\langle 001 \rangle$  direction (Fig. 14.5). This situation persists down to the lowest temperature in the case of the (on average) paraelectric PMN.

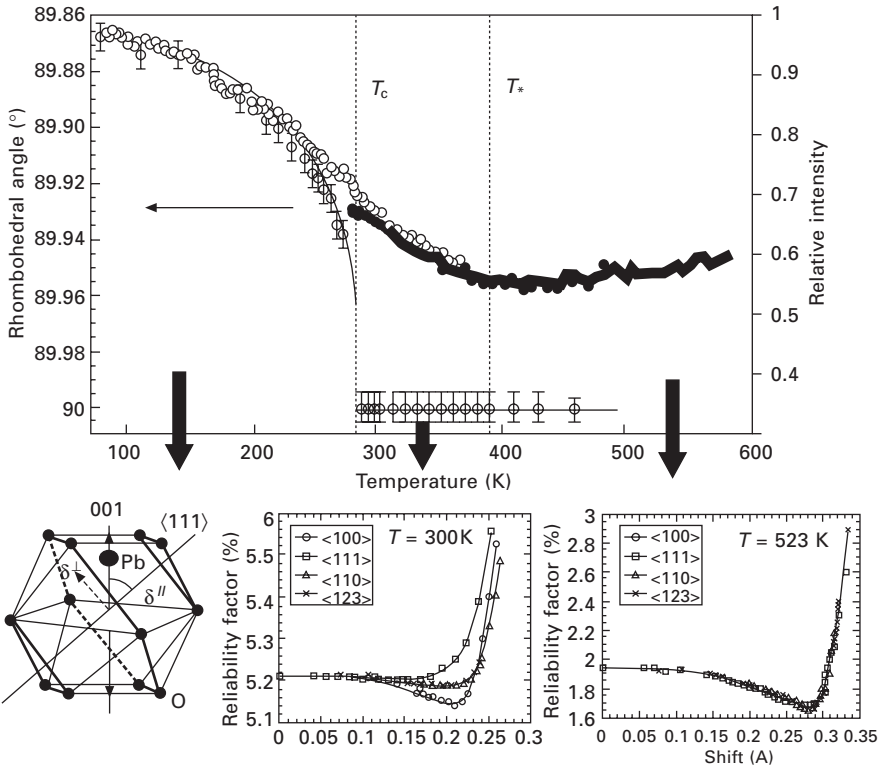
These results indicate that relaxor compounds (PSN, PMN–10%, PT etc.) that show, below a critical temperature, a long-ranged rhombohedral [111] polarisation, display in their ferroelectric phase an additional perpendicular disordered (in the sense of short-range) component. This additional component composes (see the lead cuboctahedron in Fig. 14.5) with the ordered/long-range polarisation and induces atomic displacements of lead in a direction close to [100].

The chemical explanation of such displacement is quite obvious: looking at the oxygen cuboctahedra around lead atoms, shifting the lead atom in the [100] direction creates 4 shorter bonding lengths, 4 medium and 4 longer, instead of 12 identical medium, bonds. This situation is known to be more favourable for the stability of the structure than the situation in which the lead stands on the barycentre of the polyhedron and is observed in simpler lead oxides such as  $\text{PbTiO}_3$ ,  $\text{PbO}$ , etc. The physical origin of this effect is related to the existence of the electronic lone pair (Le Bellac *et al.*, 1995b). This lone pair can occupy a steric volume equivalent to an oxygen atoms: for instance the volumes of  $\text{PbO}_\alpha$  (anathase) and  $\text{PbO}_2$  are the same. Calculations of the lone pair extension and possible interaction have been performed in the simplistic approximation of ionic model (Malibert, 1998). The result



Lead atoms are randomly on a sphere at high temperature

14.4 Temperature evolution of anharmonic potential of lead atom from Graham–Charlier expansion [courtesy of G. Baldinozzi].



14.5 Temperature evolution of (210) Bragg peak neutron intensity and of the rhombohedral angle of PMN. Above a  $T^*$  temperature (see text) indicated here by a change of slope in the (210) intensity,  $R_{\text{Bragg}}$  agreement factor versus shift of lead has an isotropic minimum whereas at lowest temperature but above the critical temperature  $T_c$  indicated by the rhombohedral distortion the shifts are along (100). Below  $T_c$  the lead inside its oxygen cuboctahedron is shown with the long-ranged  $\langle 111 \rangle$  displacements and the perpendicular short-ranged (disordered) component which compose into  $\langle 001 \rangle$  displacements.

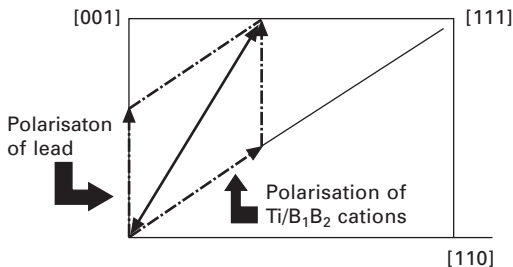
confirms the extension in both cubic and rhombohedral phases of the lone pair in the steric volume of the oxygen cuboctahedron, but with a value lower than in another structure such as  $\text{PbO}$ ,  $\text{Pb}_3\text{O}_4$ . Moreover the interaction between neighbouring lone pairs of lead atoms is shown to play a negligible part in the interaction leading to the phase transition, whereas it has been proved to be essential for other compounds (Le Bellac *et al.*, 1995a).

Thus the Pb atom in lead-based relaxor is considered to be the key cation involved in the relaxor-like behaviour. Nevertheless, in general, ferroelectricity is known to be driven by the B cation in  $\text{ABO}_3$  ferroelectric perovskite (Cohen, 1992). Indeed, the strong difference between  $T_{\text{max}}$  of dielectric constant



( $\approx 80$  K) of  $\text{Pb}(\text{Mg}_{1/3}\text{Ta}_{2/3})\text{O}_3$  and of PMN is indicative of the strong influence of the Nb(Ta)–O chemical bonds. However, only one of the B cation is a ferroactive atom, and it was admitted that Mg in PMN, Sc in PSN or Zr in PZT are less involved in the ferroelectricity (Chen *et al.*, 1995, and references therein) and that the associated oxygen octahedra are only weakly distorted (if any). Besides, Nb cations are known to be displaced along the  $\langle 111 \rangle$  directions with respect to their oxygen octahedra (about  $0.1 \text{ \AA}$ ) from extended X-ray absorption fine structure (EXAFS) (Prouzet *et al.*, 1993). However results from nuclear magnetic resonance (NMR) measurements (Laguta *et al.*, 2003) seem to be contradictory as they indicate that Sc is the ferroactive ions. Ti cations are also considered to be displaced but there are more ‘versatile’ in their direction than Nb cation. Indeed it was shown in  $\text{Pb}(\text{ZrTi})\text{O}_3$  (PZT) (Grinberg *et al.*, 2002) and  $\text{PbSc}_{1/2}\text{Ta}_{1/2}\text{O}_3$ –PT (PST–PT) (Frenkel *et al.*, 2004) that the direction of Ti cations gradually changes from  $[111]$ , as in  $\text{BaTiO}_3$ , to  $[001]$  direction, as in  $\text{PbTiO}_3$ , with increase of Ti. In a way Ti plays the same role as the polarisations in MPB systems by rotating from a rhombohedral-like direction to a tetragonal-like one (see below). Actually the displacement of Pb cations, which are considered as the most active ions, are somewhat governed by the B cation distribution via coupling through the oxygen cages. A Pb cation inside an ordered distribution of B cation should be displaced differently from when these B cations are randomly distributed (Grinberg *et al.*, 2002). The role of B cation is thus also very important.

It is interesting to observe that inside the ferroelectric rhombohedral phase of PSN and PMN–PT, the  $[100]$ , i.e. tetragonal-like displacement of lead atoms, together with the  $[111]$ , i.e. rhombohedral-like displacement of B cation (Fig. 6), composes a global polarisation which stands evidently out of the  $[111]$  and  $[100]$  directions and inside a plane of symmetry corresponding to a monoclinic  $C_m$  phase: the local polar order of the ferroelectric phase results from a competition between both types of displacements associated



14.6 Schematic decomposition of local polarisation in PSN and PMN–PT: the polarisation due to  $[100]$  displacements of lead atoms and the polarisation of B cations along  $[111]$  rhombohedral direction compose into a resulting polarisation inside a  $C_m$  monoclinic plane.

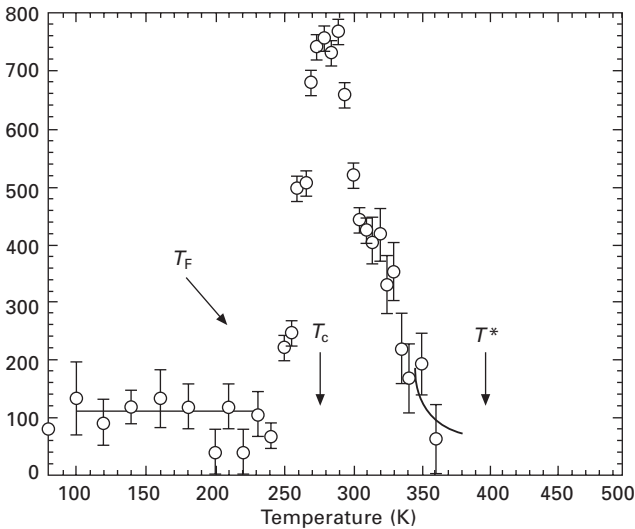
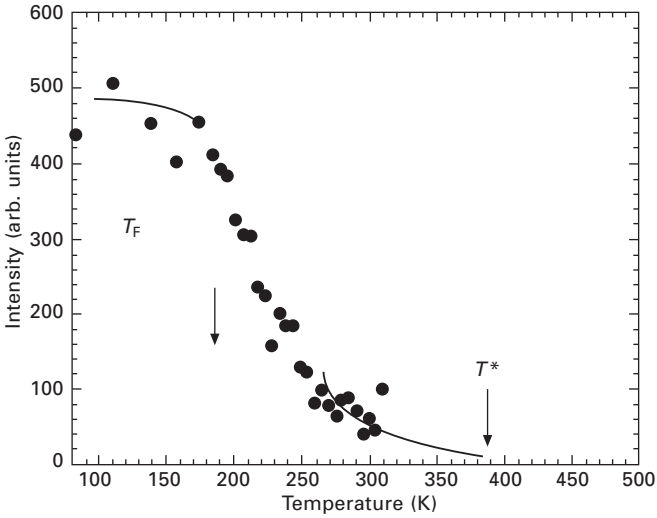
to the cations and prefigures the long-range monoclinic polar phase which is observed in the MPB phase, as we discuss below.

From this set of experiments we obtain this preliminary physical picture: at high temperatures isotropic but highly anharmonic dynamical displacements of lead are observed along a spherical shell. Upon cooling, these displacements gradually slow down and begin to correlate below the so-called Burns temperature  $T_B$ : it is tempting to call **PNRs** these ‘regions’ of correlation, forgetting a possible discussion about the pertinence of this notion of well-delimited domains with abrupt boundaries, etc.

Keeping this idea in mind, we have to consider that whereas the PNRs result from the *intra*-correlation of displacements, close to  $T_B$ , the *inter*-correlation between the PNRs is weak. When these correlations get strong enough at lower temperature, dynamical displacements are evidenced which are no more along a spherical shell but get more and more anisotropic along the  $\langle 100 \rangle$  direction and the associated diffuse scattering appears in the diffraction experiments below a  $T^*$  temperature.  $T^*$  may correspond to a local order–disorder phase transition related to Pb atoms (Dkhil *et al.*, 2002), and, by analogy with magnetic systems, may be related to a crossover from a Heisenberg to an Ising-like transformation (Stock *et al.*, 2004).

In the case of PMN these displacements freeze below  $T_F$  ( $\sim 200$  K), the intensity of the associated diffuse scattering becomes constant (Fig. 14.7a), and no long-range polarisation appears. In the case of PSN and PMN with 5% and higher concentration of PT, the temperature evolution of the diffuse scattering intensity gets a critical evolution (Fig. 14.7b): a  $[111]$  long-range polarisation appears below a critical temperature  $T_C$ . The same feature was also evidenced in PZN (Bing *et al.*, 2005). However below  $T_C$  the short-range component of the polarisation (perpendicular to  $(111)$ ) manifests itself by a non-zero intensity of the diffuse scattering at the lowest temperature.

A contradiction emerges from the mere assimilation of the local order which develops below  $T_B$  to the notion of PNRs: this identification should lead to a monoclinic symmetry for the PNRs in opposition with the model of rhombohedral local order proposed by Mathan *et al.* in PMN and the intuitive idea of nucleation from the PNRs of the rhombohedral phase observed in PSN or in PMN–PT. It is noteworthy that when de Mathan *et al.* did their modelling for the diffuse scattering they found that either the rhombohedral or the orthorhombic symmetry may explain the diffuse scattering observed on the diffraction patterns and thus the PNRs, but at this time, as it was known that an electric field induces a rhombohedral phase at low temperature in PMN, it was admitted that the PNRs should be of rhombohedral symmetry and the orthorhombic symmetry was discarded. Another observation related to this question is the existence of a (long-range) rhombohedral phase in PMN at low temperature when an electric field is applied above a critical value (see Section 14.6). This phase arises from nucleation (Vakhrushev



14.7 (a) Diffuse scattering in PMN: below a (extrapolated) temperature  $T^*$  the diffuse scattering appears; it saturates below a  $T_F$  temperature. (b) Diffuse scattering in PMN-10%PT: below  $T^*$  the diffuse scattering gets a critical behaviour at  $T_c$ ; below  $T_F$  it gets a non-zero saturated value.

*et al.*, 1997) and percolation of nanodomains which could be identical to the PNRs. We will see in Section 14.3.3. that this question is rather complex and in fact not completely understood, but for the moment we ignore these facts and consider the PNRs to be the local polar order evidenced by the experiments described in this section.

Raman experiments by Toulouse and coworkers (Svitelskiy *et al.*, 2003, 2005) as well as neutron inelastic experiments by Shirane and coworkers (see references in text below), Vakhrushev and coworkers (Naberezhnov *et al.*, 1999) and Hlinka *et al.* (2003) showed above  $T_B$  a soft TO mode with increasing (when cooling) couplings to local mode associated to spherical displacement of lead and tunnelling of niobium atoms. This soft mode could condense at  $T \approx T^*$ , but below  $T_B$  a drop of the transverse optic (TO) phonon branch into the transverse acoustic (TA) one at a non-zero wave vector  $q$  and its strong damping below a sufficiently small  $q$  vector were related to the condensation of the PNRs. This condensation inhibits the propagation of the long-wavelength TO polar modes when the phonon wavelength is comparable to the size of the PNRs. This anomaly has been called the ‘waterfall effect’ (Gehring *et al.*, 2000; Wakimoto *et al.*, 2002). A central peak appears (Naberezhnov *et al.*, 1999), associated to the PNRs, i.e. polar correlated atomic fluctuation below  $T_B$ , which progressively couple between each other and slow down, becoming static below  $T_f$ .

The PNRs being polar, they couple to the polar TO phonon mode, which in turn can serve as a microscopic probe of the PNRs. However, based on analogous experimental observations on the classic ferroelectric BaTiO<sub>3</sub> (Shirane *et al.*, 1970) and reinvestigation of neutron experiments, some doubt on the connection of the PNRs and the waterfall effect was expressed (Hlinka *et al.*, 2003). An explanation based on classic interference of line shape anomalies due to the coupled acoustic and optic branches without any *ad hoc* assumption was proposed (Hlinka *et al.*, 2003). This controversy is complicated by the fact that different probes are used to investigate the soft mode: neutron vs. infra red and Raman techniques. Indeed these techniques use phonons with different wave-vectors; therefore, the TO and TA modes, their over- and/or under-damping and their possible coupling in neutron data are not necessary similar to those of IR for instance. In order to reconcile the observations, the ‘phase-shifted model’ (Hirota *et al.*, 2002) was introduced. In this model, a PNR consists of two components. The first one corresponds to the polar soft mode and thus gives rise to the spontaneous polarisation within the PNRs. The second one is associated with the acoustic mode and corresponds to a uniform displacement of all atoms inside the PNR; a TO–TA coupling is therefore possible. In Section 14.3.3 we will see that this picture is consistent with the mechanism proposed from diffuse scattering experiments.

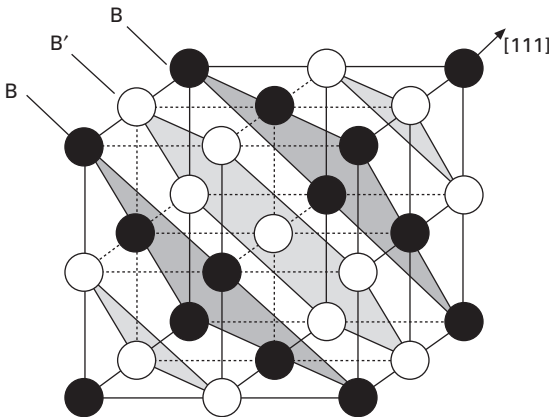
### 14.3.2 Chemical order

As pointed out in the introduction it was recognized very early that ‘textbook’ PMN was not chemically homogeneous and the first model of explanation for diffusivity of dielectric properties was based on a  $T_C$  dependence of the

local chemistry. Later observations by electronic microscopy (Krause *et al.*, 1979; Randall *et al.*, 1986) were reported: the absence of temperature dependence of superstructure intensities assigned a chemical origin and these peaks were interpreted as arising from nanodomains with a non-stoichiometric composition  $\text{Pb}(\text{Mg}_{1/2}\text{Nb}_{1/2})\text{O}_3$ . This local composition results in negative unbalanced charge which have to be compensated by rich Nb zones with positive charge in order to get a global  $\text{Pb}(\text{Mg}_{1/3}\text{Nb}_{2/3})\text{O}_3$  concentration.

The size of these nanoregions should result from equilibrium between elastic and electric energies. The associated static charges induce the creation of random electric fields which are at the origin of modern interpretations for the non-growing of polar order at low temperature in PMN. A simple picture of cationic distribution was straightforward (Fig. 14.8) and was denoted the 1:1 model due to the alternating Nb or Mg [111] planes in the structure. Latter, observation of equivalent superstructure peaks in PSN seemed to confirm this structural model because in this compound it is more 'natural' since the global 1/2:1/2 stoichiometry instead of 1/3:2/3 does not imply an unbalanced charge.

However, an alternative structural model in PMN proposed by Davies and Akbas (2000) and Chen *et al.* (1989) was inspired from the structure of compounds such as  $\text{Ba}(\text{Mg}_{1/3}\text{Nb}_{2/3})\text{O}_3$  and,  $\text{Sr}(\text{Mg}_{1/3}\text{Nb}_{2/3})\text{O}_3$  in which the ordered  $\text{Pb}(\text{B}'_{1/2}\text{B}''_{1/2})\text{O}_3$  regions are electrically neutral due to random occupation of  $\text{B}^{2+}$  and  $\text{B}^{5+}$  on the  $\text{B}'$  site whereas the  $\text{B}''$  site is only occupied by  $\text{B}^{5+}$ , leading to a global formula  $\text{Pb}[(\text{B}^{2+}_{2/3}\text{B}^{5+}_{1/3})_{1/2}\text{B}^{5+}_{1/2}]\text{O}_3$ . With such a model, a global 1:2 stoichiometry of B cation is retained within the sample. The explanation for nanometric size of these ordered domains within this model is based (Viehland and Li, 1993) on the competition of stability between perovskite  $\text{ABO}_3$  and pyrochlore structure  $\text{A}_2\text{B}_2\text{O}_7$ : above a nanometric critical

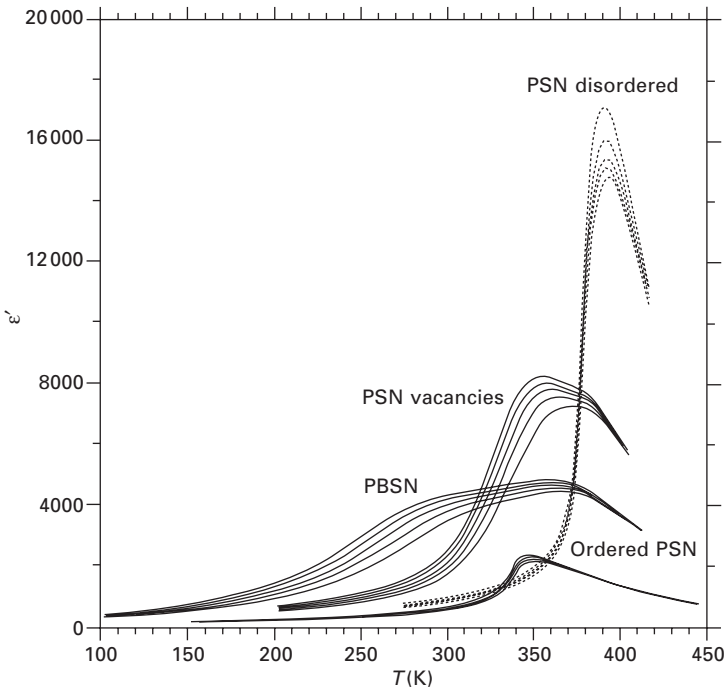


14.8 Ordered structure 1:1, perpendicular to [111] direction, of  $\text{PbB}'\text{B}''\text{O}_3$ ; only B cations are shown.

size the ordered perovskite region transforms into parasitic pyrochlore phase.

In the case of PSN the situation appears to be simpler. Indeed since pioneering work by Setter and coworkers (Chu *et al.*, 1995a,b), it is well known that due to a high-temperature (1510 K) order–disorder phase transition Sc/Nb can diffuse through the structure and arranges in a structural scheme probably identical to that depicted in Fig. 14.8. This is due to cationic radius and valency with close values (0.74 Å, 0.69 Å and III, V for Sc and Nb, respectively), as systematic investigations of cationic order of  $\text{PbBB}'\text{O}_3$  oxide have shown. Ordered PSN displays much lowest value of real permittivity with lowest relaxation than disordered compounds (Fig. 14.9). The lead vacancies as well as the substitution of barium for lead (6% on Fig. 14.9) strongly increase the diffusivity of the dielectric behaviour. Notice, however, that in all cases considered, a well-defined cubic–rhombohedral transition is found.

Persistence of relaxation in an ordered compound is against the intuitive idea on the need of disorder for the dielectric relaxation to appear. TEM and



14.9 Temperature dependence of real permittivity in disordered PSN ( $T_C = 380(\pm 5)$  K), ordered PSN ( $T_C = 350(\pm 5)$  K), lead vacancies PSN ( $T_C = 365(\pm 7)$  K) and PSN with 6% of Ba on Pb site ( $T_C = 375(\pm 6)$  K);  $T_C$  is deduced from X-ray measurements.

X-ray diffraction have shown that the so-called 'ordered' or 'disordered' PSN is only an unrealistic limit case: indeed, measurement of  $\{h + 1/2, k + 1/2, l + 1/2\}$  superstructure peaks intensity allows one to calculate a simplistic coefficient:

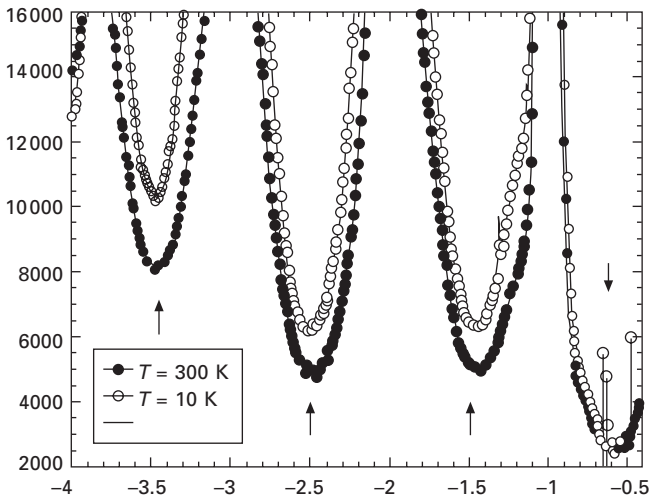
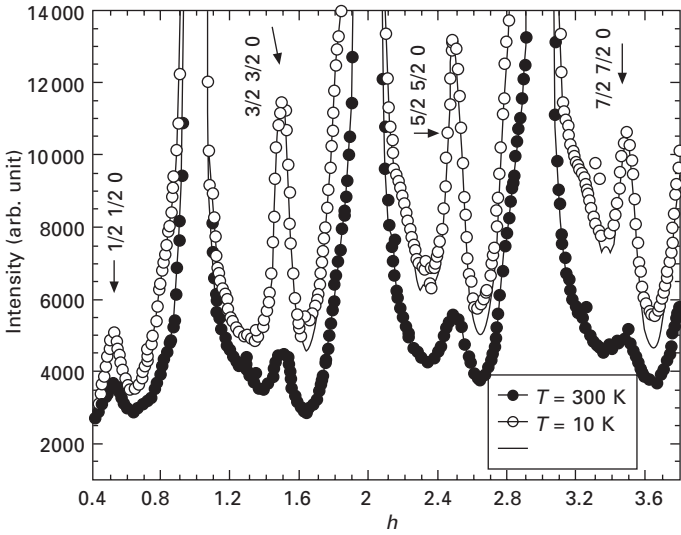
$$S^2 = \frac{\left( \frac{I_{\text{surst}}}{I_{\text{Bragg}}} \right)_{\text{observed}}}{\left( \frac{I_{\text{surst}}}{I_{\text{Bragg}}} \right)_{S=1}}$$

where  $(I_{\text{surst}}/I_{\text{Bragg}})_{S=1}$  is a calculated value with hypothesis of a totally ordered compound, whose value is roughly the same whatever the model of order one considers.  $S$  is therefore a rough measurement of volumic ratio of ordered regions.

In PSN, the experimental value for the ordered compound is never higher than  $\approx 0.92$  instead of 1. On the other hand, although the  $S$  value of disordered PSN which results from quenching is equal to zero, a weak value is always observed (Malibert *et al.*, 1997). One should also take into consideration the coherent length  $\xi$  of the local order which is easily deduced from profile fitting of superstructure peaks and is in a simplistic way a 'typical' size for ordered regions: in a so-called 'ordered' PSN, one gets a typical value of  $\xi = 20$  nm, whereas in the case of PMN (in which cation ordering cannot be modified by thermal annealing), the typical size of ordered regions is about 5 nm and  $S$  is less than 20%.

Weak (less than 5% of Bragg peak in PMN; see Fig. 14.10) supplementary  $\{h + 1/2, k + 1/2, 0\}$  peaks have also been found in PMN and PSN. Moreover, in PMN a temperature dependence of at least between 300 K and 10 K was evidenced, suggesting possible structural origin from displacement correlations. This hypothesis is reinforced by a non-monotonic evolution of intensity with scattering vector. Moreover, a condensation of the  $M_3$  phonon mode due to the contribution of local antiferroelectric order (Takesue *et al.*, 1999; Miao *et al.*, 2001) was proposed to explain these additional superstructures. In PST (a compound that behaves very similarly to PSN, with tantalum instead of niobium) the  $\{h + 1/2, 0, 0\}$  peaks were observed at room temperature by transmission electron microscopy (TEM) (Randall *et al.*, 1986): an interpretation based on the existence of tetragonally distorted ordered zone was proposed (Caranoni *et al.*, 1992); however these peaks are absent in both PSN (Malibert, 1998) and PMN (Dkhil, 1999) (Fig. 14.10).

The associated domain size deduced from full width at half maximum (FWHM) is the same order of magnitude as for the  $\{h + 1/2, k + 1/2, l + 1/2\}$  peaks and is about 5 nm in PMN and disordered PSN. Depero and Sangaletti (1997) have proposed a tetragonal distortion of cubic lattice cell with rotation of octahedral to explain the existence of these superstructure peaks. In fact



14.10 Q-scan along  $[hh0]$  and  $[h00]$  in PMN at  $T = 300\text{ K}$  and  $T = 10\text{ K}$  (beamline ID15A at European Synchrotron Radiation Facility (ESRF) showing the  $\{h + 1/2, k + 1/2, 0\}$  superstructure peaks; no  $\{h + 1/2, 0, 0\}$  peaks are detected.

neutron experiments showed afterwards the absence of such tiltings, but the idea of a tetragonal distortion for the regions of ordered cation appeared to be correct and was demonstrated by careful analysis of the diffuse scattering (see Section 14.3.3).



In summary, many observations demonstrate the existence in PMN and disordered PSN of CORs with typical sizes of 5 nm whose composition does not change with temperature. Some other observations (see below) suggest that, at least at 300 K and below, these regions are tetragonally distorted, and that this distortion probably disappears at higher temperature.

### 14.3.3 Interaction between CORs and PNRs: diffuse scattering experiments

As noted in Section 14.2, the first observation of diffuse scattering in PMN was carried out by X-ray and neutron powder diffraction. Afterwards Vakhrushev *et al.* (1994) were the first to perform comprehensive sets of experiments in single crystals, gaining deep insights of the origin of this phenomenon. Later on, several other teams, in particular those of Shirane and Toulouse, contributed to these types of study.

In particular, diffuse scattering located around  $\langle h00 \rangle$  reflections with extension along  $\langle 110 \rangle$  directions produces the so-called ‘butterfly-shape’ diffuse scattering. Such anisotropic diffuse scattering was observed in many types of relaxors, PMN, PSN, PZN and MPB systems such as PZN–PT. Diffuse scattering arises from local departures from the average structure and even if the correct model for this butterfly-type diffuse scattering is still a matter of debate, it is generally attributed to the formation of polar correlations.

It has been, for instance, suggested that the rather localised rod-type diffuse scattering indicates planar nano-domains which are oriented normal to the  $\langle 110 \rangle$  crystal directions and contain correlated  $\text{Pb}^{2+}$  displacements. However, such ionic displacements cannot be described as ‘pure polarisation’ and there is a large contribution corresponding to the elastic deformation as proposed in the phase-shifted model (Hirota *et al.*, 2002). Taking into account the elastic deformation the appearance of the PNRs should create severe host-lattice elastic distortions. Therefore, the appearance of such elastic defects should produce very strong diffuse scattering which is well known in the case of phase precipitation through the so-called Huang scattering.

In this framework, it has been demonstrated that the observed anisotropic diffuse scattering can be very well reconstructed by a strain field produced by defects of tetragonal symmetry. In other words the source of the anisotropic diffuse scattering comes from tetragonal clusters which are responsible, all around them, of the appearance of static and elastic deformations of the host-matrix.

It is worth noting that in contrast to previous conclusions, in the above approach the anisotropic diffuse scattering, induced by the tetragonal clusters, is not necessarily related to the PNRs. In fact, there is rather a clear correlation between the anisotropic diffuse scattering and the CORs. Indeed, the weakening of the superstructure spots by doping PMN with  $\text{PbTiO}_3$  results in the

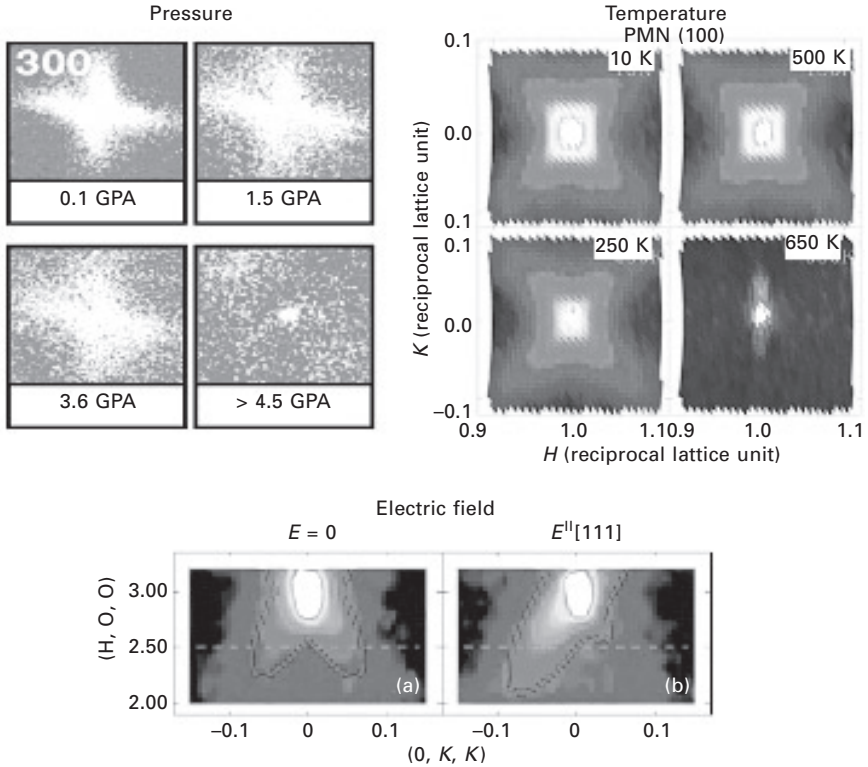
simultaneous decrease of the intensity of the anisotropic diffuse scattering (see Fig. 14.24 of Section 14.4.4). This observation may be understood by considering that the tetragonal clusters are actually the CORs.

Nevertheless, one has to keep in mind that another way to describe the anisotropic diffuse scattering is to consider PNRs through correlated lead displacement in agreement with the structural data shown in Section 14.3.1 and recent calculations on PZN (Welberry *et al.*, 2005). Therefore, a possible scenario which satisfies the above conclusions consists of coupling the CORs to the PNRs, assuming that the PNRs coincide at least to some extent with the CORs. Around such defect regions, strong (strain and electric) fields are expected and as the matrix is highly deformable and polarisable, they can be considered as the ‘embryos’ for the nucleation of PNRs. The PNRs are therefore both pinned and driven by the chemical ordering and coexist with the matrix, which can adopt a different symmetry. However as in the traditional pictures of nucleation, several types of defects can be at the origin of the low-temperature nucleus: for instance Laguta *et al.* (2004) observed PNRs in disordered part of samples, which obviously do not nucleate on CORs.

This picture arises also from the recent simulations by Burton *et al.* (2006) who showed that the polarisation and the polarisation fluctuations in relaxors are strongly enhanced inside the CORs. Particularly in the temperature range where they appear, polar nanoregions have not already grown and they are essentially the same as CORs (Fig. 14.13 below). They also showed that arbitrarily increasing the magnitudes of local electric fields, by increasing the chemical disorder, broadens the dielectric peak, and reduces the ferroelectric transition temperature, while sufficiently strong local fields suppress the transition as in PMN.

Temperature, electric field and pressure effects are coherent with the above scenario. In particular, the appearance on cooling of diffuse scattering at a temperature  $T^*$  well below  $T_B$  (which marks the appearance of the PNRs) shows the importance of the elastic contribution (otherwise,  $T^*$  should be equal to  $T_B$ ). Recent experiments in PMN conducted by our group have associated this  $T^*$  to strain released with the appearance of a static component of the PNRs (Dul’kin *et al.*, 2006). Furthermore Toulouse and coworkers (Svitelskiy *et al.*, 2005) suggested a tetragonal symmetry around  $T^*$  which, as the Raman lines are normally forbidden and arise from CORs, might occur only inside the CORs. A plausible explanation is that the static component of the PNRs is associated to the pinning of the dynamic PNRs by the tetragonal CORs.

Application of pressure (Fig. 14.11) also leads to the disappearance of the anisotropic diffuse scattering in relaxors: this is consistent with the above scenario where the average crystal structure and the PNRs adopt the same crystal structure, which in turn effectively suppresses the deformation between the host-matrix and the PNRs (Chaabane *et al.*, 2003b). In this framework,

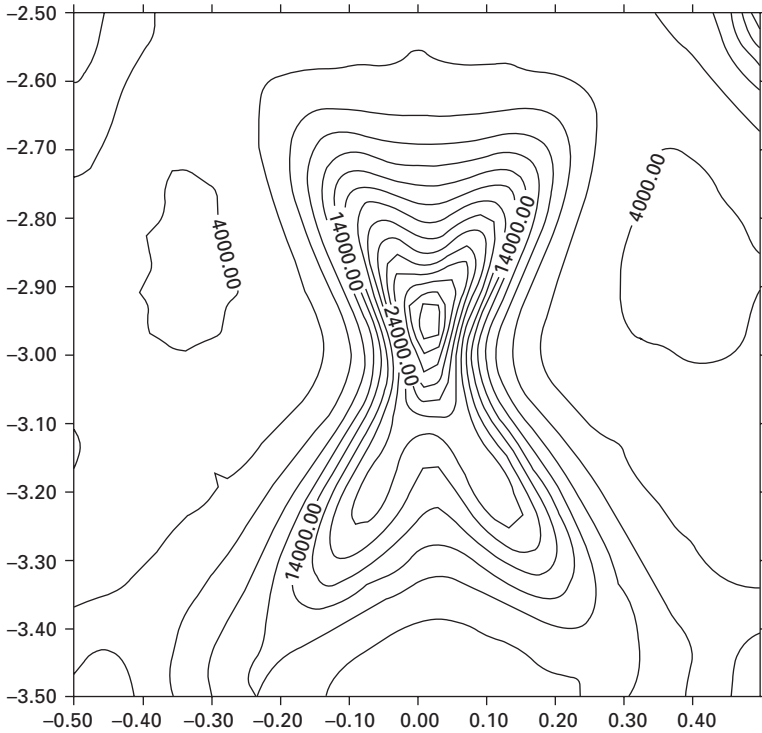


14.11 Diffuse scattering around  $\langle h00 \rangle$ ; evolution with pressure in PMN (Chaabane *et al.*, 2003a), temperature in PMN (Xu *et al.*, 2004) and electric field in PZN (Xu *et al.*, 2005).

Vakhrushev *et al.*, (2007) demonstrated that the observed anisotropic diffuse scattering can be very well reconstructed by strain field produced by defects of tetragonal symmetry (Fig. 14.12).

In contrast, the application of an electric field does not lead to the suppression of the diffuse scattering and even under a high-strength field (40kV/cm), the ‘butterfly-shape’ diffuse scattering is only partially affected (Xu *et al.*, 2006): a redistribution of the intensity occurs via changes in elastic constants. With the assumption that the butterfly-shape diffuse scattering originates only in polar nanoregions, one might expect the diffuse scattering to disappear because the electric field is, in principle, strong enough to align these nanoregions and to achieve a uniform polar state. The fact that this is not observed suggests that the polar defects that are supposed to be responsible for the anisotropic diffuse scattering are coupled to a deformation that inhibits the alignment of the PNRs. It is this idea that has been developed in this section.

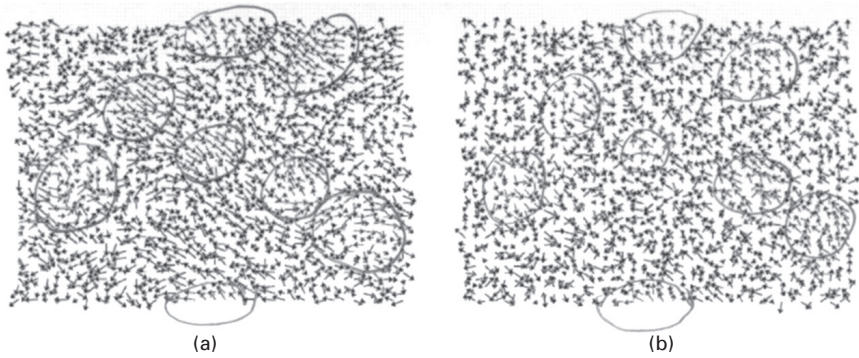
We would like to come back to the question of local symmetry of PNRs (whether it is rhombohedral, tetragonal or monoclinic) and their mere existence



14.12 Calculated 2D plot of the diffuse scattering intensity distribution in PMN near the (003) point.

as a well-delimited zone of polar correlation with an abrupt boundary. This section shows that the reality is obviously much more complex. Indeed, a glance at Fig. 14.13 readily shows that these questions, as well as the question of a clear separation between PNRs and CORs, are due to the need to build simplistic objects which should help us to understand reality: there is no clear separation between PNRs, CORs and the monoclinic adaptive zone (see Section 14.4.2).

To conclude this section a few words have to be added to the connection of the structural pictures of relaxors presented here and the theoretical background. Some years ago, in parallel to phenomenological models, random field models with ideas issued from renormalisation theories were developed in particular to explain the experimental observations of non-mean-field critical exponent. The success of these types of model was important, but still conflicting results with experiments pointed out the important part played by the point or extended defects: there was clearly a need to take into account these defects in the models. The notion of 'random field' is one way, among several, to explain more accurately the experimental observations by taking into account some types of defects. In the field of relaxors, the Imry and Ma



14.13 Snapshot of local mode polarisation in (a) PSN at 600K and (b) PMN at 130K. More highly correlated circled regions are chemically ordered and the more disordered matrix is chemically disordered. From calculations by Burton *et al.* (2006).

argument was used by Kleemann (1993) to explain the diffuseness of PMN by quenched random electric field arising from charged compositional fluctuations and inducing a nanodomain state. However, other approaches, based on random bond interaction and giving rise to glassy behaviour, were also developed: that is why relaxors are sometime also called glassy ferroelectrics. The situation has been clarified by Pirc and Blinc (1999) who developed the random bond–random field model. In this model, the PNRs not only interact between each other as expected in classical glass-like systems (dipolar or quadrupolar) but may also interact with random fields arising from the compositionally chemical disorder. In this model the change with temperature from isotropic (Heisenberg) to discrete value of the order parameter is considered. And this is indeed what is observed from the experimental point of view (see Fig. 14.5 for instance, showing the isotropic to anisotropic positions of lead atoms). However, this model considers pseudospins (as PNRs) interactions with quenched random electric fields and describes in an elegant manner the static behaviour of relaxors but it cannot currently satisfactorily describe the dynamic properties and, especially, the dielectric relaxation.

## 14.4 Towards the MPB: substitution of titanium

### 14.4.1 Rotation of polarisation via monoclinic phase

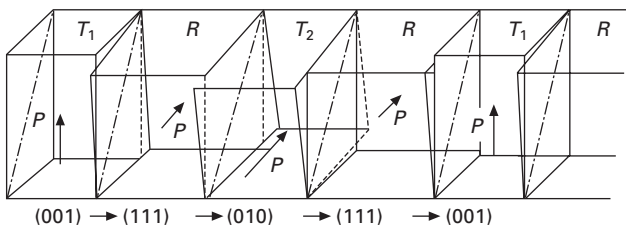
In this section we summarise the current situation in some MPB systems from the standpoint of the long-range polar order. Indeed as is shown in Section 14.4.2 the question of symmetry in these systems is a difficult one as there is a progressive transformation of local to long-range polar order: for instance PMN can be viewed as, ‘on average’, a cubic phase but we have seen that at low temperature frozen PNRs exist. Moreover, a very small

amount of titaniums doping transforms the local polar order into, ‘on average’ a rhombohedral phase in which local monoclinic regions might still manifest themselves. These difficulties are in fact more or less identical to the question of the exact symmetry of the PNRs in non-doped compounds as discussed above: can they be considered as a rhombohedral polar order with a monoclinic zone of adaptation between the tetragonal symmetry imposed by the CORs? Again Fig. 14.13 shows the difficulty of clearly separating or even identifying the different objects under consideration.

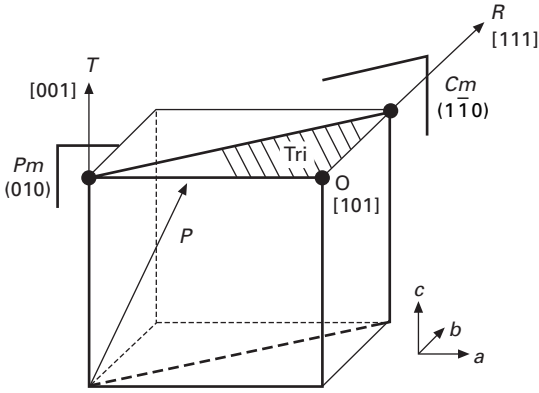
Before the discovery of the monoclinic phase in the MPB of PZT (Noheda *et al.*, 1999) the rotation of polarisation between the rhombohedral and the tetragonal phase was explained by a complex texture of microdomains (Lucuta, 1989) as shown in Fig. 14.14. The joint experimental and theoretical works showed that the key point for explaining the giant piezoelectric properties inside the MPB, i.e. the huge effect of a weak electric field on the direction and magnitude of polarisation, is the fact that in a monoclinic phase the polarisation is no longer restricted along a linear direction ([111] or [100] for instance) but can rotate freely in a plane. In fact, up to now several monoclinic phases have been discussed and evidenced. These phases are easily visualised and related to the other ferroelectric phase via a picture proposed by Fu and Cohen (2000) (Fig. 14.15).

*PZT phase diagram*

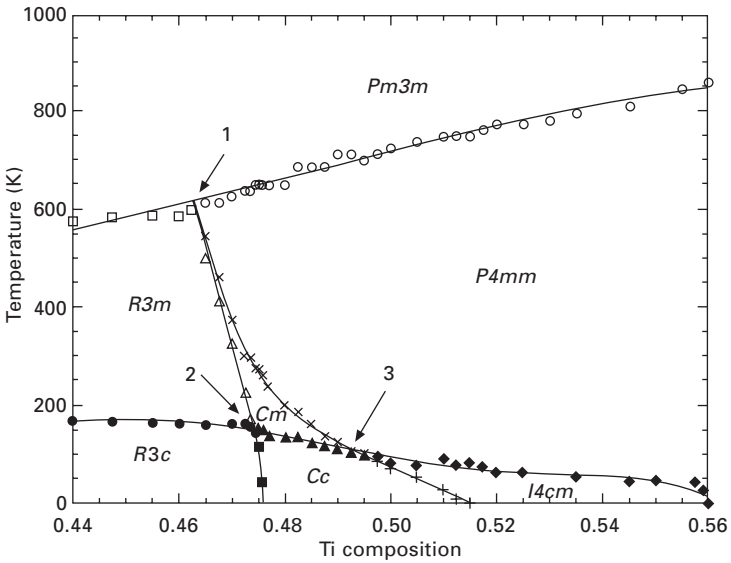
The situation in PZT (Fig. 14.16) has been discussed by several authors, in particular by Noheda (2002). A unique monoclinic phase of the  $M_A$  type was evidenced in addition to the adjacent tetragonal and rhombohedral phases. However a distinction must be made regarding the low-temperature rhombohedral phase in which a rotation of oxygen octahedra occurs along the [111] direction in addition to the ferroelectric shifts of the  $R3m$  phase, inducing an  $R3c$  phase. Persistence of superlattice reflections inside the concentration range of the monoclinic phase raises the question of the exact space group for these concentration: if long ranged, a  $Pc$ , instead of  $Cm$ ,



14.14 Lucuta’s juxtaposition of tetragonal and rhombohedral domains in the morphotropic phase boundary.



14.15 Different phases implied in the study of MPB compounds, described in the pseudo-cubic cell. Monoclinic phase  $Pm$  is also denoted  $M_C$ , while  $Cm$  is also denoted  $M_A$  or  $M_B$  depending on the direction of polarization above or below the diagonal direction  $[111]$ . In between the two monoclinic planes is a triclinic phase. T stands for tetragonal, O for orthorhombic and R for rhombohedral.



14.16 Phase diagram of PZT, from Kornev *et al.* (2006).

space group should be considered from Rietveld analysis (Ranjan *et al.*, 2002). Later, the same group reported that the correct space group for this phase is in fact  $Cc$  (Hatch *et al.*, 2002). Moreover recent models involving mixing with  $Cc$  phase were also considered (Cox *et al.*, 2005; Ranjan *et al.*, 2005). TEM observation by Woodward *et al.* (2005) suggests a  $Cc$  phase and

underlines the ability of such phase to bridge the  $R3c$  and  $Cm$  phases. Recently (Kornev *et al.*, 2006) the  $Cc$  phase existence was confirmed as one of the ground states of PZT but the oxygen octahedra in this  $Cc$  phase rotate neither about the [001] direction nor about the [111] direction, but rather about an axis that is between these two directions. Interestingly, for the largest Ti concentrations, a new tetragonal phase with the  $I4cm$  space was suggested and confirmed experimentally. This phase involves the coexistence of ferroelectricity and rotation of oxygen octahedra, but is associated with the tetragonal symmetry (unlike  $R3c$  and  $Cc$ ). As a result, an increase in Ti concentration from 47% to 52% results not only in the continuous rotation of the spontaneous polarization from [111] to [001], but also in the change of the oxygen octahedra rotation axis from [111] to [001].

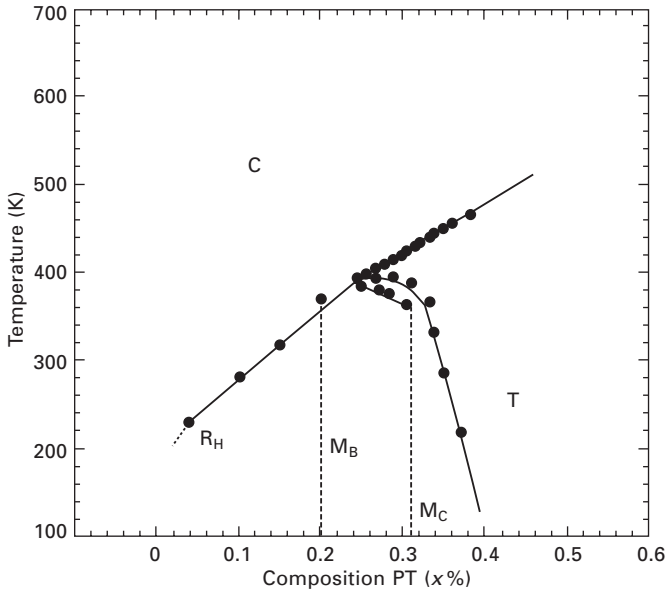
#### *PMN–PT phase diagram*

Shortly after the discovery of the monoclinic phase in PZT, the same situation was reported in PMN–PT with, however, some discussions about the exact symmetry. Ye *et al.* (2001) reported a  $Cm$  ( $M_A$ ) phase whereas we reported (Kiat *et al.*, 2002) a  $Pm$  ( $M_C$ ) phase. In fact it appears that both groups were right (or wrong !) because the three monoclinic phases can appear in addition to rhombohedral and tetragonal phases, depending on the concentration/temperature/electric field/pressure/strain ranges; moreover with, in many cases, the coexistence of phases (Akhilesh Kumar and Dhananjai, 2003; Akhilesh Kumar *et al.*, 2006; Singh *et al.*, 2006). In fact the path of rotation experimentally observed with two monoclinic phases when the concentration is changed, i.e. rhombohedral  $\rightarrow M_A \rightarrow M_C \rightarrow$  tetragonal, was predicted by Fu and Cohen (2000) and shows how to minimise the internal energy of the system. Recent results also show that the extent of the MPB appears to be underestimated (Akhilesh Kumar *et al.*, 2006; Carreaud *et al.*, 2006), as well as for the rhombohedral phase (Ye *et al.*, 2003). We plot on Fig. 14.17 tentative phase diagram which includes these recent results. The question of the average symmetry, in particular, in the low PT concentration range is still a matter of debate: whether it can be more adequately described as an ‘average’ rhombohedral phase or a local monoclinic order is a difficult question, as explained above. The question of an orthorhombic phase has also been raised in this system as well as in PZN–PT: we discuss these questions more deeply in Section 14.4.4 in relation to PSN–PT.

#### *PZN–PT phase diagram*

The observation (Lebon *et al.*, 2002) in PZN by our group of splitting at 385 K of the [111] cubic peaks as well as anomalous widening of [100] peaks and the report of a field-induced monoclinic phase (Lebon *et al.*, 2005)

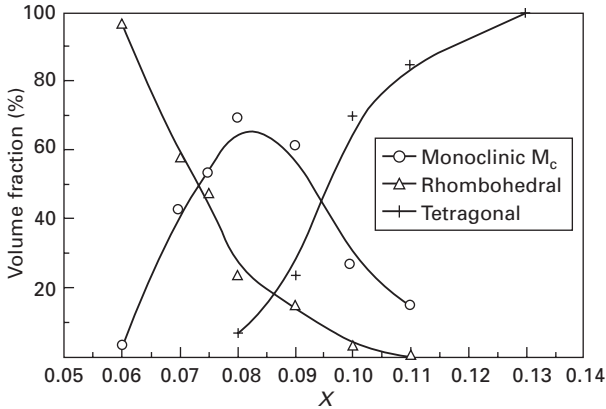




14.17 Phase diagram of PMN-PT resulting from computation of several works (see text).

showed that the structure of this system is at least as complex as other relaxors. Recent results by Jeong and Lee (2006) suggest describing the rhombohedral phase rather as a mixture of meso-scale PNRs in a disordered lattice: their results show that in PZN, these PNRs are simply ‘larger’ at room temperature ( $150 \text{ \AA}$ ) (La-Orauttapong *et al.*, 2001) than those in PMN ( $20 \text{ \AA}$ ) so they are visible in powder diffraction measurements as a split of Bragg peaks. Besides they propose that PZN and PMN have the same ground state, i.e. mixed state of disordered cubic phase and rhombohedral PNRs. Another point of view was also proposed and considers another ground state for PZN as a lower symmetry phase which could be monoclinic rather than rhombohedral (Bing *et al.*, 2005).

In PZN-PT, since the optical observation by Fujishiro *et al.* (1998) of heterophases in PZN-PT9% which showed a lowering of symmetry between the rhombohedral and tetragonal domains, conflicting reports have been published regarding the exact symmetry of the MPB. We reported a  $Pm$  ( $M_C$ ) phase (Kiat *et al.*, 2002) coexisting with the tetragonal phase whereas an orthorhombic phase was reported whose unit cell was afterward described in a monoclinic setting (this confusion was also made in PMN-PT, see pages 419–20). The situation has recently been clarified by Bertram *et al.* (2003), who confirm the  $M_C$  as the unique monoclinic MPB phase and clarify the extent of the MPB as well as the phase coexistence (Fig. 14.18).



14.18 Extent and volume fractions of the different phases in PZN–PT, from Bertram *et al.* (2003).

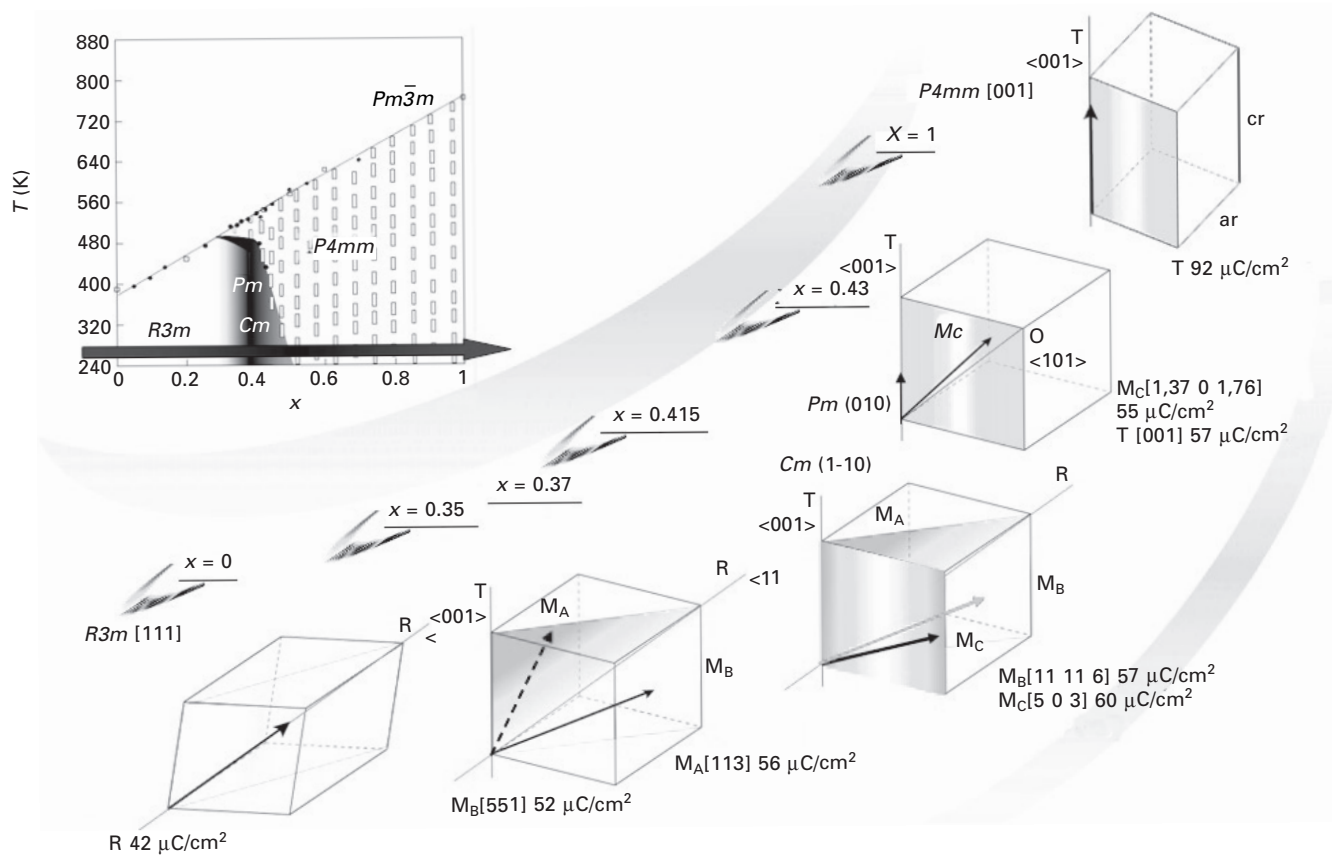
### PSN–PT system

PSN–PT and PMN–PT phase diagrams show great similarities, with an overall path of polarisation rotation via  $M_B$  and  $M_C$  monoclinic phases, and a significant temperature and composition-dependent mixing between these phases.

The complete path of rotation with concentration in PSN–PT has been precisely studied in our group by Haumont *et al.* (2003, 2005, 2006a) (Fig. 14.19). In particular, using apparent charge and the results of Rietveld analysis, they studied the evolution of the polarisation (modulus and angle) inside the Fu and Cohen cube.

At low temperature, five regions of concentration have been found:

- (1)  $Rh$  ( $0 < x \leq 0.26$ ): The addition of titanium in PSN increases the rhombohedral distortion as well as amplitudes of shifts of atoms out of their cubic positions. The polarisation increases from  $P = 42 \mu\text{C}\cdot\text{cm}^2$ .
- (2)  $Rh \rightarrow M_B$  ( $0.26 < x \leq 0.37$ ): The polarisation rotates in the (011) plane. The symmetry becomes  $Cm$  of the  $M_B$  type; the augmentation of the amplitude of polarisation is stronger than in the R region.
- (3)  $M_B \rightarrow M_C$  ( $0.37 < x \leq 0.43$ ): The polarisation goes into the (010) plane, not via intermediate values (which would have led to a triclinic phase) but instead through a jump which occurs with strong phase coexistence: ( $Cm + Pm$ ). When the titanium concentration increases, the  $Pm$  proportion of phase increases, the polarisation in the (011) plane decreases and polarisation in the (010) plane increases.
- (4)  $M_C \rightarrow T$  ( $0.43 < x \leq 0.55$ ): The  $Cm$  phase has disappeared,  $P4mm$  appears inside the  $Pm$  phase and its distortion and proportion increase with Ti. A rotation of polarisation arises via the phase mixing  $Pm-P4mm$ . The modulus of polarisation of the  $P4mm$  increases with Ti. The monoclinic phase completely disappears at  $x$  close to 0.55.



14.19 Phase diagram with corresponding rotation of polarization in PSN-PT. Notice also the phase coexistence.

- (5)  $T$  ( $0.55 < x \leq 1$ ): The system is single phased with a polarisation which increases in a slower way and saturates at  $P = 92 \mu\text{C}/\text{cm}^{-2}$  (PT).

Several interesting points have been noticed:

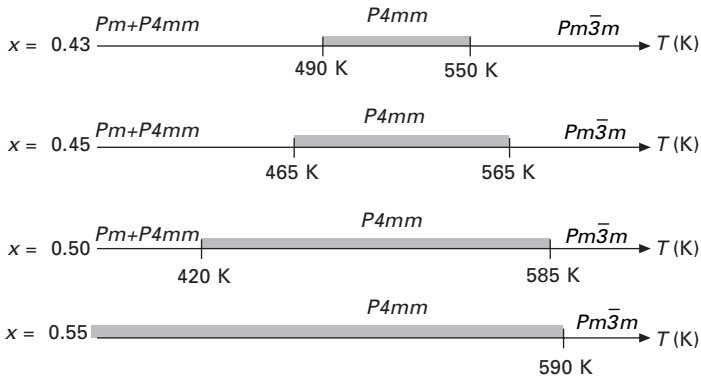
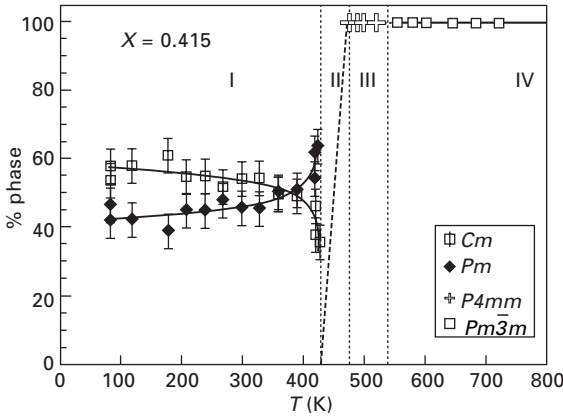
- (1) No phase coexistence is found between the rhombohedral and any other phase. The only report of such coexistence is for  $R3m + Cm$  at the concentration  $x = 0.31$  of PMN–PT by Noheda *et al.* (2002).
- (2) Only 1.5% of titanium separates the two states: ( $Cm + Pm$ ) and ( $Pm + P4mm$ ). An extreme weak change of concentration completely changes the structure. Although not observed, a single  $Pm$  phase may occur at a very specific concentration between  $x = 0.415$  and  $x = 0.43$ . Such single phases have been reported by Singh *et al.* (2003) in PMN–PT for  $x = 0.31$  and for  $x = 0.35$  by our group (Kiat *et al.*, 2002).
- (3) At concentration  $x = 0.43$  the direction of polarisation of the  $Pm$  phase is very close to the orthorhombic direction [101], but this symmetry is definitively out of consideration because atoms clearly adopt non-orthorhombic positions, even though the resulting polarisation stands close to an orthorhombic direction. This orthorhombic  $Amm2$  symmetry has also been proposed in PZN–PT, as well as for PMN–PT but only from a fitting profile of rocking curves, which is in our opinion not sufficient. On the contrary a monoclinic  $M_C$  phase but with a direction of polarisation closes to the orthorhombic direction [101] is evidenced via Rietveld analysis of  $x = 0.09$  in PZN–PT and  $x = 0.35$  in PMN–PT. The real existence of a ‘true’ orthorhombic phase remains questionable in these MPB systems.

The temperature evolution of these systems is also complex: for instance the evolution of PSN–PT  $x = 0.415$  compound’s phase mixing is detailed in Fig. 14.20. Other concentration evolutions (less detailed) are also shown.

In the  $x = 0.415$  compound, the  $Cm$  and  $Pm$  phases coexist from the lowest temperatures up to about 400 K when the progressive destabilisation of the  $Cm$  phase is observed. Close to 435 K, the tetragonal  $P4mm$  phase was found, coexisting with the  $Pm$  phase, while the  $Cm$  phase has vanished. Above 480 K, this tetragonal phase is observed *alone* up to about 545 K, the temperature at which it transforms toward the high-temperature paraelectric  $Pm\text{--}3m$  phase. For highest concentration a coexistence of the  $Pm$  and  $P4mm$  phases is observed at low temperature, and a pure tetragonal phase is recovered above 0.55 concentration of Ti.

Interestingly we have also reported for  $x = 0.35$  in PSN–PT a transition (observed below room temperature) from a  $M_A$  to a  $M_B$  phase when cooling which corresponds to a rotation of polarisation inside the (011) plane from one side to the other side of the rhombohedral [111] direction.

The observation of the phases mentioned shows agreement with predictive theoretical work by Vanderbilt and Cohen (2001). However, not all experimental



14.20 Temperature evolution of the phase coexistence for some PSN-PT compounds.

observations agree, in particular the extensive observation of phase mixing in this system as well as in others is in opposition with prediction of second-order phase transition, also the possibility of triclinic phase was not observed. It should also be mentioned that no direct transitions  $Pm \rightarrow Pm3m$  or  $Cm \rightarrow Pm3m$  have been observed in any system. Also the question of multiple points should be examined more in detail in further studies: for instance to answer the question of how the cubic-tetra-rhombo-monoclinic regions are connected.

#### 14.4.2 From local polar order to long-range order: monoclinic phase as adaptive phase

In Section 14.3.3, it has been proposed from diffuse scattering experiments that the elastic accommodation between the CORs and the PNRs is realised via a monoclinic short-ranged zone, which is also in agreement with the

structural data described in Section 14.3.1. Thus, on the mesoscale (i.e. few nanometres) the monoclinic order may be considered as an adaptive phase and serves as a ‘bridge’ between the CORs and the host-matrix. This local and embedded monoclinic phase previously reported on relaxor-based systems has also been observed by TEM on the non-relaxor PZT system (Glazer *et al.*, 2004) and in PMN–PT35% (Wang *et al.*, 2006).

The progressive ‘growing’ of monoclinic phase when doping by Ti in PMN–PT, PSN–PT or PZN–PT can be easily detected in diffraction experiments through the observation of continuous widening of H00 peaks (which are single in the rhombohedral patterns). In fact as already pointed-out, local monoclinic order is detected even in the pure compounds, except that the correlation length of the associated local polarisation appears to be higher in PZN than in PMN, whereas weak Ti doping is needed in PSN to observe such widening.

The notion of an adaptive phase first developed for martensitic transformation was proposed by Khachaturyan *et al.* (1991) and Jin *et al.* (2003) to explain the transformation pathway through the monoclinic phase and associated features such as the tweed-like domain patterns observed in MPB systems. The adaptive phase is issued from martensitic-like phase transitions and is based on stress-accommodating twinned domains in a similar way to the mesoscale structure proposed through the investigation of the anisotropic diffuse scattering.

Some authors have also proposed that the different monoclinic phases of MPB systems are in fact nothing other than tetragonal or rhombohedral twinned nanodomains. A long time ago, such an idea was successfully used in the field of incommensurate and quasicrystal systems, leading to debates about the real existence of (for instance) five-fold (pentagonal) symmetries or nano-twinning of six-fold twins. It appears in the end that both types of system exist, i.e. ‘true’ incommensurate or quasicrystal systems and ‘ersatz’ nanotwinned commensurate or crystal. Perhaps the same situation will be disclosed in the field of MPB. This is left for further studies.

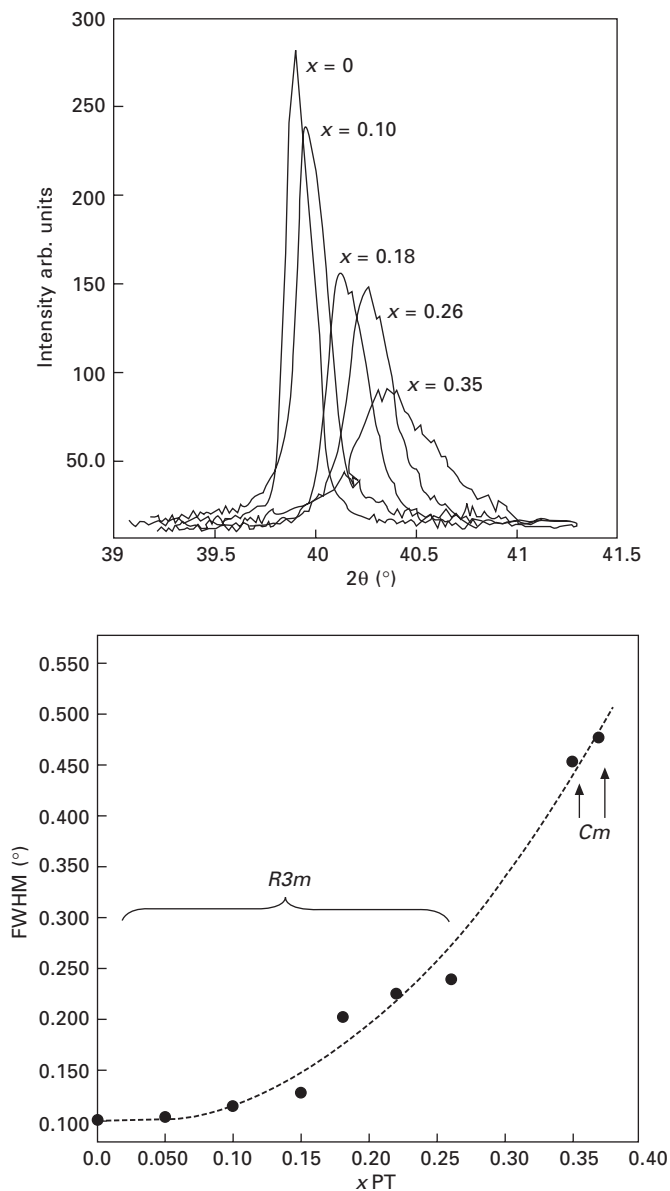
#### 14.4.3 Modelling of MPB phase diagrams

The origin of the term ‘morphotropic phase boundary’ is related to the experimental observation of optimal properties in a restricted range of concentration where two phases, rhombohedral and tetragonal, were supposed to coexist. From this point of view the existence of monoclinic structures appeared as a simpler way to rotate the polarisation; however, the discovery that several monoclinic phases can exist and moreover coexist, also with the rhombohedral or tetragonal phase involved, showed that the reality is in fact rather complex. From a simplistic thermodynamic point of view the coexistence of three phases is possible only at a definite and unique composition at

which an abrupt change of structure is supposed to happen when the composition is changed. As pointed out by Rossetti *et al.* (2006), the diagrams shown on Figs. 14.16 to 14.18 with abrupt boundaries cannot be equilibrium phase diagrams and their geometry, with or without consideration of an adjacent low-temperature monoclinic phase, contradicts thermodynamics: according to the Gibbs phase rule, the single-phase fields on the phase diagram must be separated by two-phase regions rather than by line boundaries. A low-order Landau expansion in the approximation of the theory of regular solutions by these authors showed that the phase coexistences appear to be an equilibration process implicated by the thermodynamic. These questions have been discussed in detail in PSN–PT by Haumont (2004).

The success of the phenomenological theory based on Landau–Devonshire development had proved very successful in the field of magnetic and structural phase transitions, well before the discovery of the MPB phases. The problem of higher complexity, such as incommensurate systems for instance, has been explained within this theoretical framework. Therefore an interpretation of the phase diagram of PZT based on a eighth-order development of free energy by Vanderbilt and Cohen (2001) quickly followed the experimental report by Noheda *et al.* (1999). Local-density approximation (LDA) calculation by Fu and Cohen (2000) was published the same year. The different paths of rotation between the different possible phases have been studied and synthetically condensed in figures such as Fig. 14.15, eventually involving possible triclinic phase if twelfth-order polynomials are taken into account. The main results of these works have been very briefly discussed above.

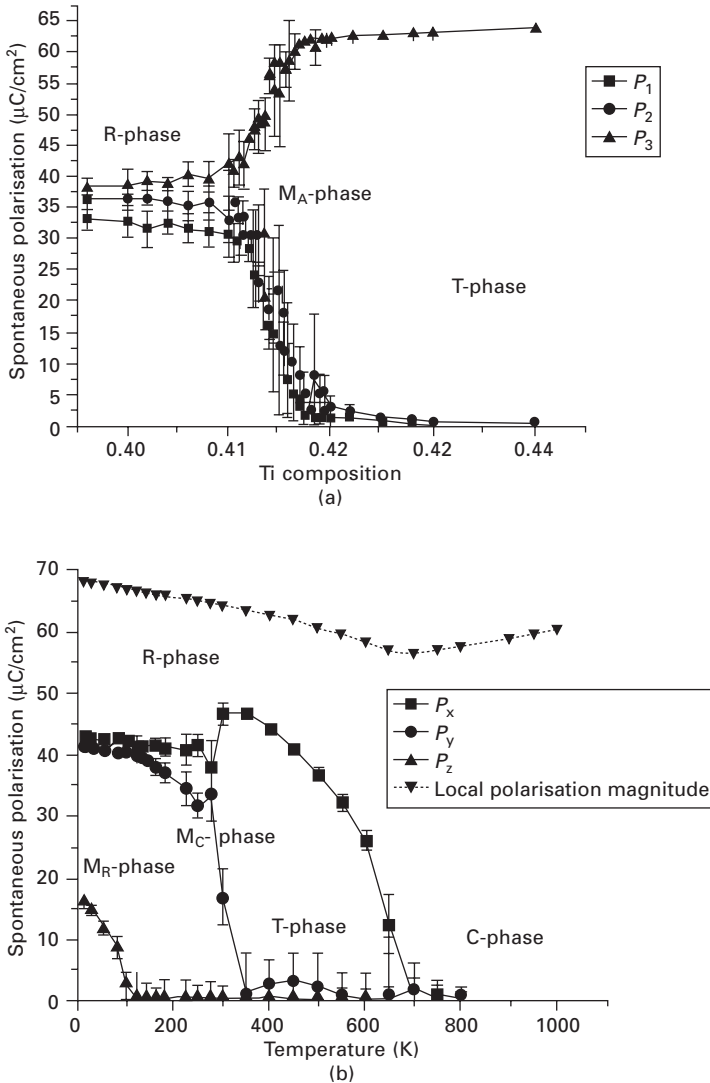
In connection with the experimental studies of the structures of MPB diagrams we would like also to report some works from Bellaiche and coworkers based on effective Hamiltonian calculation which have clarified the problem of chemical versus polar order as discussed in this paper. Initially the first system studied using these techniques was PZT (Bellaiche *et al.*, 2000). The results on PSN–PT (Haumont *et al.*, 2003, 2006a) were published later. The progressive ‘growing’ of monoclinic phase when doping by Ti in PMN–PT, PSNPT or PZN–PT can be easily detected in diffraction experiments through the observation of continuous widening of H00 peaks (which are single in the rhombohedral patterns) (Fig. 14.21). Interestingly the first principles simulations for disordered PSN–PT were unable to mimic the observed path: only the  $M_A$  phase was observed in the simulations among all possible monoclinic phases. Moreover, it happened that the width of the MPB obtained in the simulation was much smaller than that measured. Since the disorder is responsible for the introduction of strong random fields, which modify the ground state, it seems obvious that a deviation from a perfectly homogeneous and disordered state should be realised. Simulations made for different ordered states (some of them unrealistic!) showed other interesting results; in particular the appearance of the  $M_B$  phase (Fig. 14.22).



14.21 X-ray rocking-curve of (200) peak in PSN-PT and associated FWHM.

Another result from these simulations is that none of the theoretically investigated ordered alloys has a rhombohedral ground state at compositions with low Ti content: they all rather adopt a monoclinic phase at low temperature. In fact, the simulations showed that the existence of chemically ordered





14.22 Spontaneous polarization as predicted by the Heff approach: (a) versus composition in disordered PSN-PT at  $T = 50\text{K}$ ; (b), versus temperature in PSN-PT41 for ordered structure.

clusters inside the disordered matrix is needed to widen the Ti-poor part of the calculated MPB and thus to mimic the experimental observations. For low Ti content this heterogeneous state leads to the appearance of a rhombohedral phase.

These simulations explain the strong connection between chemical composition at a local scale and polar states. It is probable that the same

scenario exists in other MPB systems as very similar polarisation path is observed.

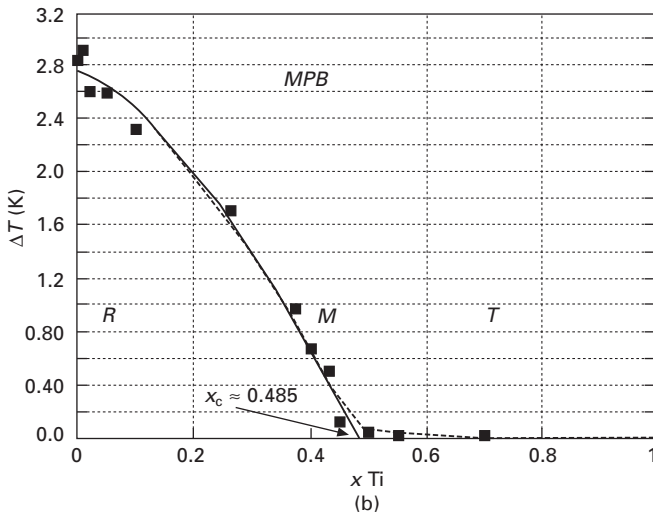
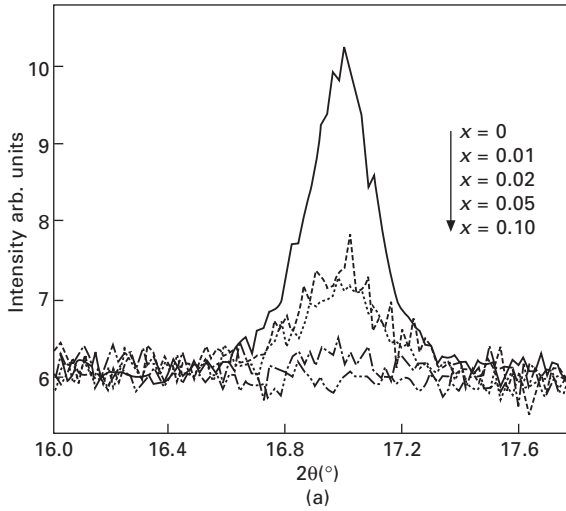
In fact these considerations arising from modelling allows the MPB systems to be divided in two groups. The first group includes homogeneous systems such as PZT in which no chemical order (CORs) has been observed and for which the MPB is confined in a restricted concentration range, in direct agreement with the results from simulations. Others are the relaxor-based morphotropic systems such as PMN–PT characterised by the existence of CORs and huge regions of concentration in which monoclinic order is detected. A further example, among the BiBB'O<sub>3</sub>–PT systems (Suchomel and Davies, 2004) is BiScO<sub>3</sub>–PT (Eitel *et al.*, 2004; Chaigneau *et al.*, 2007) which illustrates the ideas that homogeneous systems exhibit a confined MPB region, with a unique monoclinic phase. However, in this distinction one has to take care about the scale that is considered: indeed in PZT very short chemical order (the first core shell around Zr or Ti) was considered in first-principles calculation which clearly shows that the very local order may also strongly affect the ground state (George *et al.*, 2003).

#### 14.4.4 From CORs to chemical inhomogeneity regions (CIRs) in the MPB phase diagrams

It is known that doping PMN or PSN with PbTiO<sub>3</sub> results in the suppression of the short-range chemical order (CORs) as is evidenced by the continuous decrease of intensity and correlation length of the superstructure (SS) peaks associated with cation chemical ordering. In PSN–PT (Fig. 14.23) with about 10% of titanium concentration, no more chemical ordering could be detected but as SS factor peaks are also intrinsically diminished when Ti content is increased, even in a perfectly ordered situation, Raman scattering experiments are more accurate: indeed we were able to follow the local ordering of Sc/Nb cations up to  $x = 0.16$  concentration, a value above which no more ordering is observed. However, we also observed the vanishing of dielectric relaxation at concentrations far from  $x = 0.16$  i.e.  $x = 0.485$ , just inside the MPB (Fig. 14.23) in contradiction to the mechanism of relaxation based on the interaction of PNRs with CORs.

The same type of contradiction appears if one compares the concentration evolution of the diffuse scattering in PMN–PT, associated with elastic accommodation of PNRs with CORs which disappears between 0.25 and 0.30 (Fig. 14.24) whereas the dielectric relaxation is observed at least up to  $x = 0.40$ , inside the MPB. These sets of observation seem to indicate that the local ordering of Mg/Nb/Ti or Sc/Nb/Ti is not exactly the correct parameter to consider for a global picture of relaxation and MPB in lead-based systems.

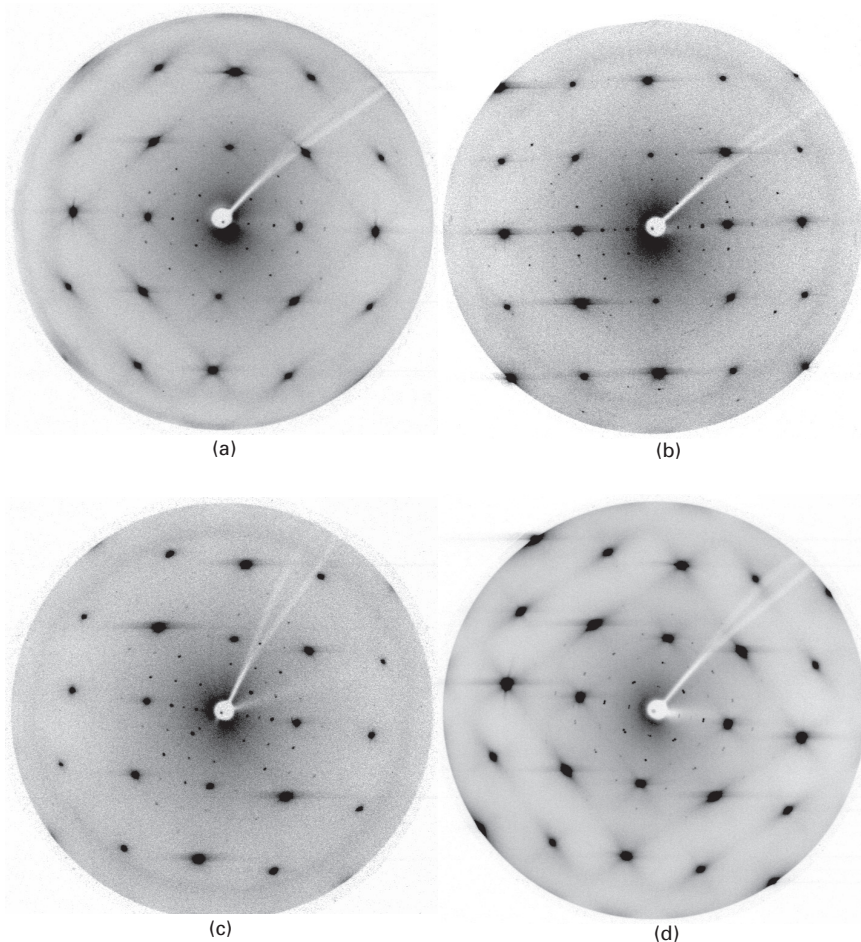
Disappearance of local ordering in PSN–PT well before the MPB composition is reached is corroborated by the measurements of hysteresis



14.23 In PSN–PT, (a) vanishing of superstructure peaks associated to CORs in PSN–PT; (b) concentration evolution of dielectric relaxation.

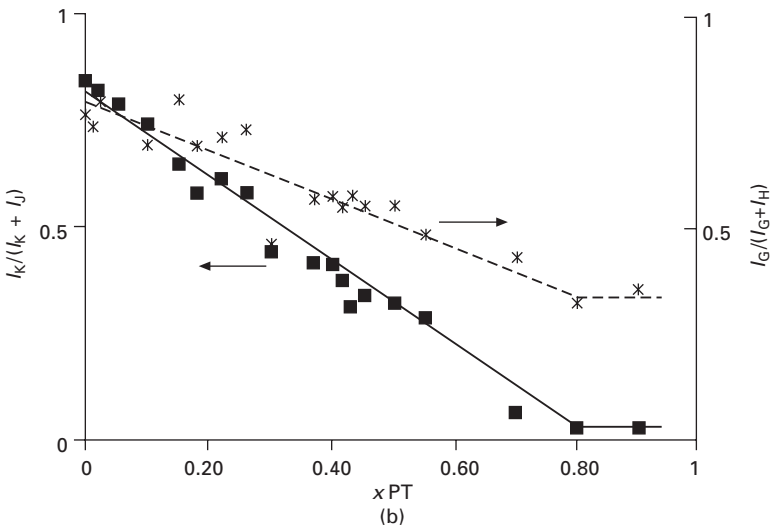
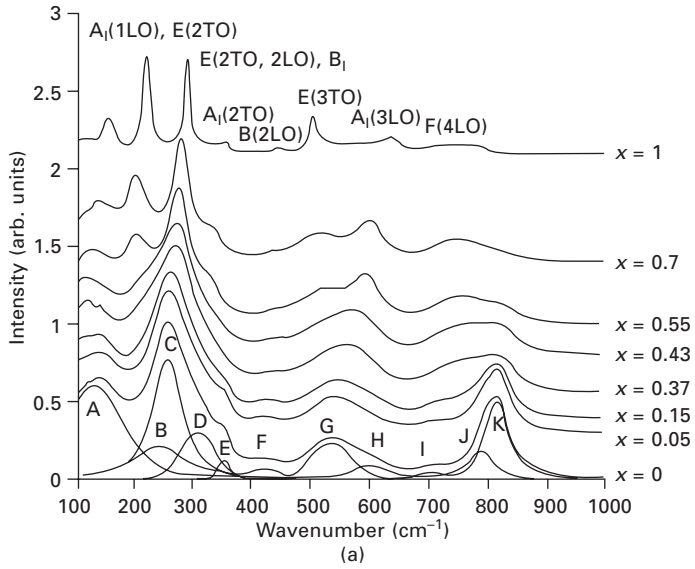
loops of polarization in disordered and long-annealed samples of PSN–PT, whereas for low concentration of titanium, difference in the  $P = F(E)$  evolution between both types of samples is found, and above  $x = 0.16$  no difference exists. The same result is obtained when comparing the temperature evolution of dielectric constant: above  $x = 0.16$  the evolution is identical for the disordered or long-annealed samples.

In fact, micro-Raman spectroscopy, which is very sensitive to the local Sc/Nb/Ti arrangement of samples, shows a great variation of signal with the



14.24  $(hk0)$  sections of the room-temperature X-ray precession patterns of the PMN-PT solid solutions with different lead titanate content.

location of the beam on the surface of the ceramics, indicating a great inhomogeneity of the Ti/Sc/Nb occupancy on the B-site of the perovskite. A comprehensive Raman study of PSN-PT as a function of Ti content shows that, on a local scale, heterogeneities exist up to 80% of PT (Haumont *et al.*, 2006a). The most striking feature in the Raman spectra (Fig. 14.25) arises from the evolution of the relative intensity defined as  $I_1/(I_1 + I_2)$ , where  $I_1$  and  $I_2$  are intensities of band K (or G) and band J (or H), respectively. The value of this ratio, continuously decreases and changes close to  $x = 0.80$ . In the PMN-PT system, the similar band K disappears at about the same  $\text{Ti}^{4+}$  content (Ohwa *et al.*, 2001) and is a signature that a true tetragonal symmetry is recovered above this concentration.



14.25 (a) Room-temperature Raman spectra of PSN-PT powder samples with various titanium concentration with a representative deconvolution for pure PSN in insert. (b) Ti-dependence of the relative intensity of band K (or G) and band J (or H).

Below  $x = 0.80$  the Raman spectral evolution presented on Fig. 14.25 can be described on the basis of the so-called two-mode behaviour which was also proposed for the PMN-PT system (Chaabane *et al.*, 2004). In this two-mode scenario the vibration modes associated with band J and band K do not

couple, that involves the existence of local phase segregation. The origin of those bands should be due to alternation of zones richer in one constituent than the other, with band J being associated with a very local segregation of Ti-rich regions whereas band K corresponding to Mg/Nb-rich ones. These local chemical orders would occur on the scale of a couple of unit cells making them difficult to be detected by diffraction probes. In the PSN–PT system, the same situation was also considered. Further complexity arises from the fact that band J is detected also in pure PSN, meaning that this band cannot be explained only on the basis of Ti-rich regions but should also be associated with the CORs.

These sets of experiments show that the structure of the CORs transforms with PT doping, even if they are not more detectable above  $x \approx 0.16$  by diffraction technique. Above this concentration it is better to call them *chemical inhomogeneity regions (CIRs)* which continue to act as a nucleation centre for PNRs.

Additional proofs were obtained by the comparison of the diffraction pattern of a MPB sample of PSN–PT ( $x = 0.43$ ) which revealed definite changes, before and after long-term annealing, in particular in the phase mixing ratio of monoclinic phase *Pm* and tetragonal *P4mm* phase (85% of *Pm* phase in annealed sample, instead of 79%). A comparative Rietveld analysis shows in addition changes in the monoclinic angle ( $90.20^\circ$  after annealing instead of  $90.09^\circ$ ), and also in the magnitude of polarisation for both phases ( $62$  and  $67 \mu\text{C}/\text{cm}^2$  after annealing instead of  $55$  and  $57 \mu\text{C}/\text{cm}^2$ ). These experiments clearly indicate the strong effect of a chemical rearrangement onto the ground state in the MPB region.

## 14.5 Stability of the MPB phases under external and internal fields

Up to now we have mainly discussed the concentration and temperature structural evolution of relaxors and MPB compounds. However, many potential applications of these materials arise from the strong effect of electric field on properties. Moreover these applications often require the use of materials in the form of ceramics or thin films. That is why the effects of size reduction, external pressure, substrate-induced misfit, etc., have been recently considered. The electric field and pressure evolution of diffuse scattering have been briefly discussed in Section 14.3.3. The object of this section is to point out some results related to the question of phase stability.

### 14.5.1 Electric field effects

Pioneering works reported investigations of the non-ergodic state of PMN under an electric field. Indeed, when the electric field is applied along the

[111] direction above a threshold value (1.7 kV/cm), PMN transforms into a rhombohedral phase at around 230 K upon field cooling (Calvarin *et al.*, 1995). Interestingly, when the electric field is applied below the freezing temperature, a time-dependent phase transition occurs (Vakhrushev *et al.*, 1997) with nucleation of polar rhombohedral nanodomains without growth and after an incubation time, a percolation of these domains giving rise to a microdomain state. Since these works and the discovery of monoclinic phases in the MPB,  $E$ - $T$  phase diagrams have been constructed in several studies for [111]-oriented PMN (Sommer *et al.*, 1993; Colla *et al.*, 1996; Ye, 1998) and PMN-PT (Emelyanov *et al.*, 1993; Raevski *et al.*, 2005) crystals. It is interesting to notice that recent NMR investigations have also demonstrated the percolation character of the induced phase transition in PMN (Blinic *et al.*, 2003). Furthermore, these NMR measurements have also revealed that although the ferroelectric phase occurs, about 50% of the crystal remains in the glassy matrix state, suggesting the polar inhomogeneities existing in these systems. The same situation was also reported on PSN (Laguta *et al.*, 2004).

Other relaxors and/or other crystal orientations have also been studied. For instance a recent investigation on PZN showed that a monoclinic phase can be induced when the electric field is applied along the [001] direction (Lebon *et al.*, 2005). However, some experimental results show that this monoclinic phase could already exist without an electric field (see pages 416–22). PSN has also been recently studied by Samara and Venturini (2006) and Venturini *et al.* (2006) who showed that a biasing electric field favours the ferroelectric phase over the relaxor state, and that above 5 kV/cm the relaxor state vanishes.

Owing to the discovery of very high piezoelectric responses, the effort has recently been concentrated on the MPB concentrations. For instance, application of an electric field along the [001] direction on PZN-8%PT induces the following phase sequence: rhombohedral  $\rightarrow M_A \rightarrow M_C \rightarrow$  tetragonal. Interestingly, when the field is removed, the reverse sequence is  $T \rightarrow M_C \rightarrow O$ . In PMN-35%PT a phase transformation sequence of cubic  $\rightarrow$  tetragonal  $\rightarrow$  orthorhombic was found for  $E//110$ , whereas a sequence of cubic  $\rightarrow$  tetragonal  $\rightarrow M_C$  for  $E//001$  was evidenced (Cao *et al.*, 2006).

Recently Kutnjak *et al.* (2006) have shown that the giant electromechanical response in PMN-29.5%PT and potentially in other ferroelectric relaxors is the manifestation of a critical point inside the electrical field-temperature phase diagram. They describe how, close to the critical point, both the energy cost and the electric field necessary to induce ferroelectric polarization rotations decrease significantly, thus explaining the giant electromechanical response of these relaxors. This points out the extreme importance of these studies for the understanding of the electromechanical properties of these materials for technological applications.

### 14.5.2 External pressure effect

A very good review paper by Samara and Venturini (2006) on this subject has already been published. Among the results it is pointed out that at moderate value (15 kbar), the hydrostatic pressure is known to amplify the relaxor behaviour of PMN by decreasing the correlation length associated with the PNRs. In PZN–9.5%PT, up to 3 kbar the main influence of pressure is a decrease of  $T_c$  but above 3 kbar a ferroelectric to relaxor crossover is induced. At higher pressure the structure is strongly changed in both systems with, at a first stage, the disappearance of the polar behaviour as expected by the continuous decrease of the correlation length of the polar regions. In the case of the relaxor PZN (Janolin *et al.*, 2006), which is characterised by a disordered rhombohedral polar  $R3m$  phase, a homogeneous state is achieved at a pressure of  $p_{c1} \approx 5$  GPa. The new high pressure phase is consistent with a non-polar  $R-3c$  space group associated with antiphase tilting of the oxygen octahedra, similarly to PMN (Kreisel *et al.*, 2002; Chaabane *et al.*, 2003b) or PZN–4.5%PT (Ahart *et al.*, 2005), and is related to the appearance of new superstructures on the diffraction patterns and a narrow peak at around  $350 \text{ cm}^{-1}$  in the Raman spectra (Chaabane *et al.*, 2004). It is noticeable that the oxygen tilting appears only when the system becomes homogeneous. With further increasing pressure, the octahedral tilt angle increases and the  $R-3c$  structure is destabilised above  $p_{c2} \approx 10$  GPa towards a monoclinic non-polar  $C2/c$  structure, the tilt system being essentially conserved. Above  $p_{c3} \approx 23$  GPa, a polar state reappears and is described by a monoclinic structure with  $Cc$  space group which combines both ferroelectric and antiferrodistortive instabilities (Janolin *et al.*, 2006). The re-entrance of the polar state is similar to recent observations for  $\text{PbTiO}_3$  and is due to a new kind of ferroelectricity (Kornev *et al.*, 2005), that is driven by an original electronic effect, and can be considered as a general feature of perovskites and related materials. The monoclinic  $Cc$  phase has also been reported in such MPB systems as PZT (Rouquette *et al.*, 2005), with lower symmetries as triclinic  $P1$  and  $P\bar{1}$ . The fact that the monoclinic phase is obtained in these systems at high pressure suggests that this monoclinic phase may store an important strain (energy), a key point for the understanding of the giant piezoelectric properties.

### 14.5.3 Grain size reduction effect

The question of ferroelectricity when size is reduced is an old problem which has recently been revived owing to the experimental observation of polarisation in nanocrystal of  $\text{BaTiO}_3$  with a size as small as 70 nm (Scott, 2006), in contradiction with previous experimental and theoretical reports. Regarding relaxors, we have recently addressed the question of reduction of size grains in the ceramics (Carreaud *et al.*, 2005) of PMN in which the dielectric relaxation at size below around 30 nm was found to disappear (Fig. 14.26).



The compounds of PMN–20%PT, which is just at the border of the MPB region, and PMN–35%PT have also been studied. In the former, a path of rotation from  $M_B$  to  $M_A$  is observed and below a critical value of  $\sim 200$  nm a rhombohedral structure is stabilised (Carreaud *et al.*, 2006), whereas the latter displays a destruction of ferroelectric domain states toward PNRs with typical sizes equal to the size of the grains below 200 nm (Fig. 14.26b). These effects are also discussed in connection with pressure experiments and strain/field effects.

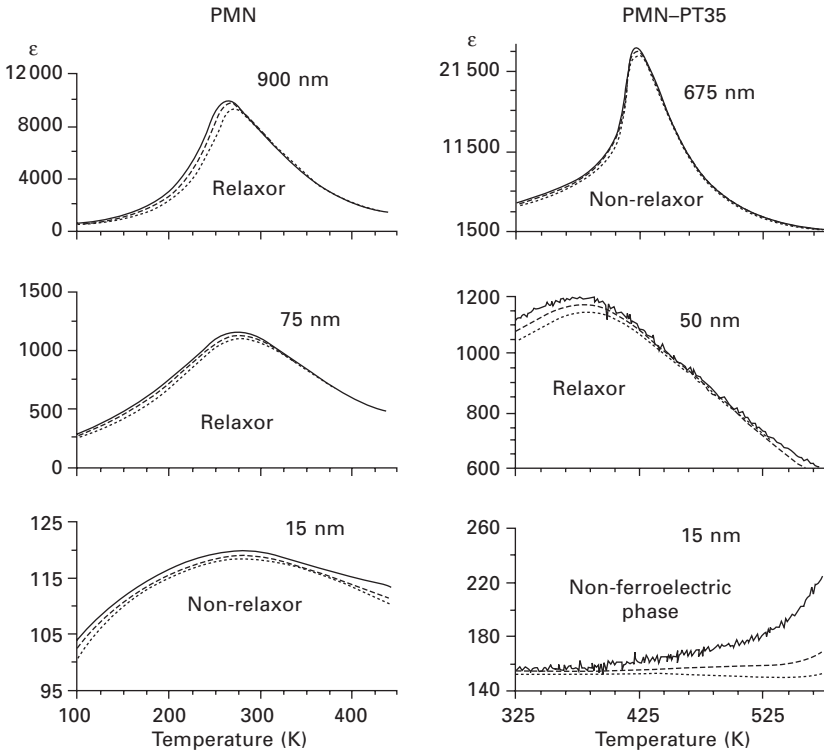
The sensibility to the reduction of size appears to be extreme. Although not discussed in this chapter, it probably explains the so-called ‘X phase’ related to a probable skin effect, which has been well documented in BaTiO<sub>3</sub> for a long time. For further information the reader may consult the chapter in this book on the grain size effect by Alguero *et al.*, Chapter 15.

#### 14.5.4 Rotation of polarisation in thin films

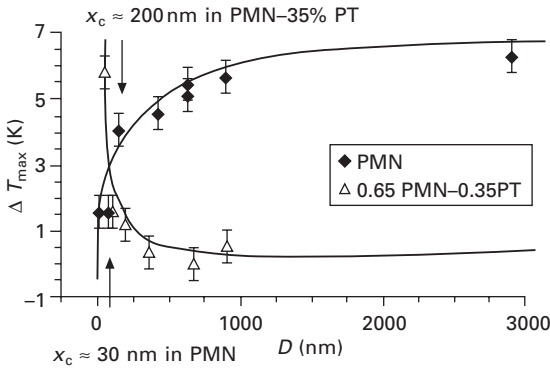
Evidently the study of thin films is going to take increasing interest in the field of relaxor/MPB compounds. Several authors have studied temperature dependence of dielectric properties in the thin films of PMN, PMN–PT, PSN and PZT but up to now the question of structural evolution has only mainly addressed in simple perovskites such PbTiO<sub>3</sub> and BaTiO<sub>3</sub>. We have recently studied (Haumont *et al.*, 2006b; Janolin, 2007) the thin films of PSN and PSN–PT43% (i.e. inside the MPB) of various thickness, deposited on STO and MgO substrates. In the former compound we have evidenced at room temperature a polar tetragonal phase instead of the rhombohedral phase; this raises the question of the existence of monoclinic phases for MPB PSN–PT films, as in this case both PSN and PT have a polar tetragonal phase. However, in the latter compound a single monoclinic  $Pm$  ( $M_C$ ) phase is nevertheless observed whereas in bulk material this phase is mixed with a tetragonal phase; this indicates that the origin of the monoclinic phase in films of PSN–PT with morphotropic concentration is different from that of bulk materials and is directly associated to the strains induced by the changing on substrate. Depending on the substrate and the thickness, different domains configuration are obtained (Fig. 14.27). Nevertheless, even in the polydomain configurations observed in the thicker films, the stress is never completely relaxed and induces complex structural evolution with temperature completely different from that of bulk compound: in case of the MPB compound, at high temperature, a succession of transformations toward a tetragonal non-polar phase is observed and the cubic phase never reaches 95 K.

### 14.6 Conclusions and future trends

In conclusion, we propose some simplistic pictures which summarise the main ideas developed in this chapter.

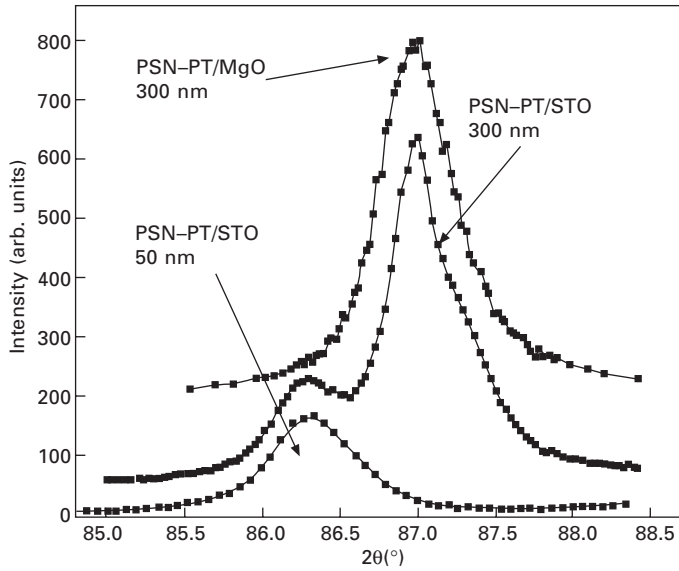


(a)

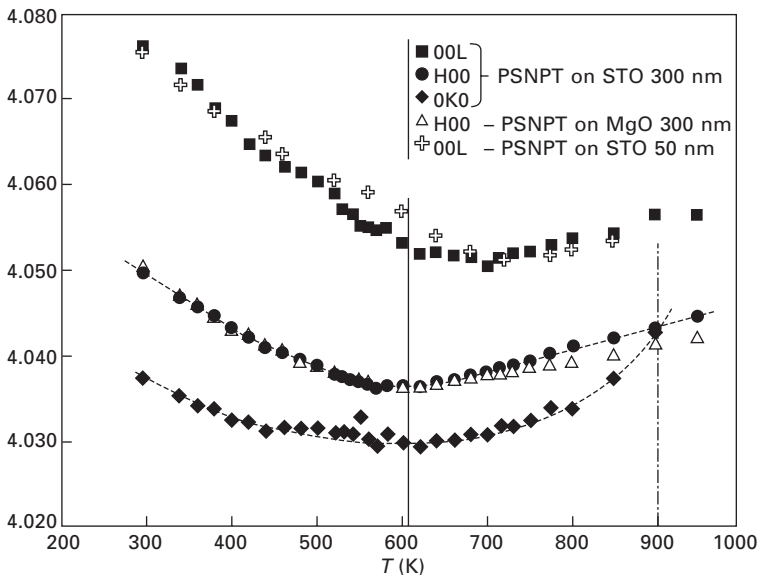


(b)

14.26 (a) Temperature and grain size dependence of dielectric constant in PMN (left) and in PMN-35%PT (right). Plain, dotted and dashed lines correspond to frequency ranges between 1 and 100 kHz (b) Grain size dependence of dielectric relaxation, defined by  $\Delta T_{\epsilon_{\max}}(f) = T(\epsilon_{\max}(f=100 \text{ kHz})) - T(\epsilon_{\max}(f=10 \text{ kHz}))$  for PMN and PMN-35%PT.



(a)



(b)

14.27 (a)  $\theta/2\theta$  scans of (004) peak for PSN-PT film on MgO substrate (300 nm) and for two films of PSN-PT on STO with a 50 nm and 300 nm thickness. (b) Temperature dependence of inter-reticular distance of the  $Pm$  phase for different films.

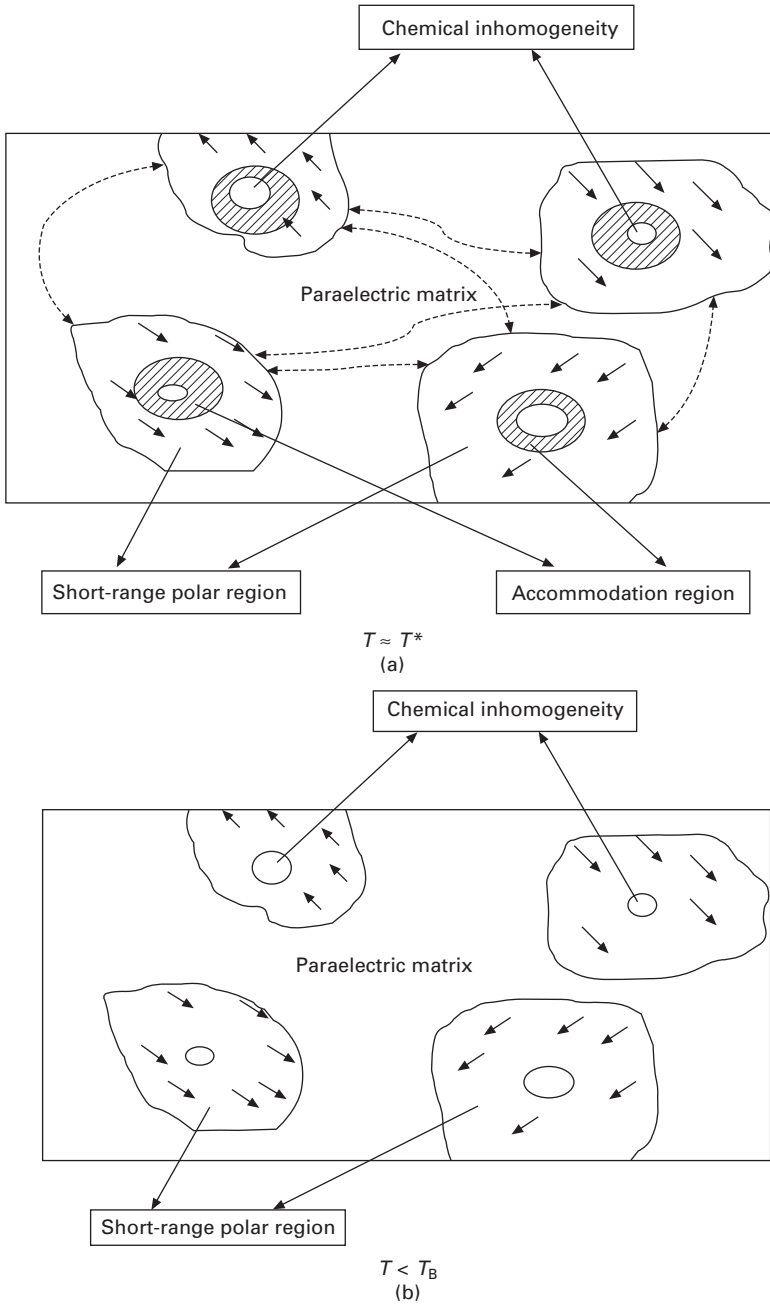
### 14.6.1 Temperature evolution of the structure of relaxors

The physical situation can be roughly summarized by Table 14.1 and the captions to Figs 14.28–14.31. We have reviewed some main experimental results, even though many others, not described in this paper have been reported. A ‘snap-shot’ close to and below the Burns temperature could therefore give the schematic pictures, as shown in Fig. 14.28. Figure 14.29

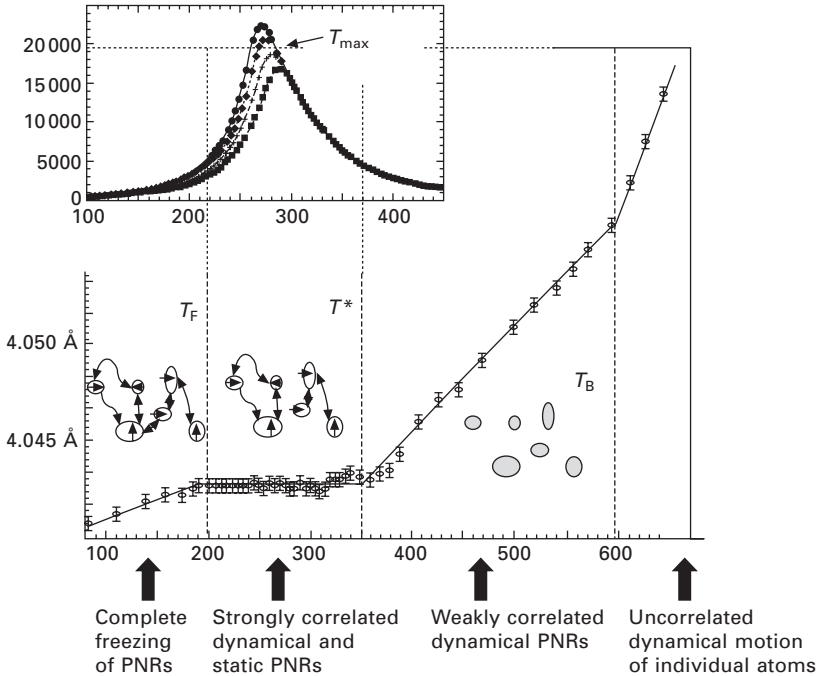
*Table 14.1* Brief and simplistic summary of the temperature evolution of the structure of a relaxor.

	$T \leq T_f$	$T_f < T \leq T^*$	$T^* < T = T_B$	$T_B \ll T$
Physical pictures	<ul style="list-style-type: none"> <li>Complete freezing of PNRs in the form of local polar order, coexisting with eventual long-range polar order</li> </ul>	<ul style="list-style-type: none"> <li>PNRs strongly correlated, some become static</li> <li>Lattice accommodation (monoclinic) between CORs (tetragonal) and PNRs (rhombohedral)</li> <li>Eventually at <math>T_c</math> with <math>T_c &lt; T^*</math>: appearance of long-range polar order (PSN, PMN-PT and other related systems)</li> </ul>	<ul style="list-style-type: none"> <li>At <math>T_B</math> displacements gradually have slow down and correlate, forming dynamic PNRs weakly correlated</li> <li>CORs/CIRs may act as nucleation centre for the PNRs</li> </ul>	<ul style="list-style-type: none"> <li>Isotropic but highly anharmonic dynamical displacements of the lead along a spherical shell</li> <li>Chemical ordered regions (CORs/CIRs) with local composition different from the bulk exist in the samples (whatever <math>T</math> is)</li> </ul>
Main experimental evidences described in this text	<ul style="list-style-type: none"> <li>Lattice parameter anomaly</li> <li>Anisotropic minimum in agreement factor versus shifts</li> <li>Diffuse scattering</li> <li>Vanishing of dielectric peak</li> </ul>	<ul style="list-style-type: none"> <li>Lattice parameter anomaly</li> <li>Raman anomalies</li> <li>Anisotropic minimum in agreement factor versus shifts</li> <li>Diffuse scattering with eventual critical component</li> <li>Dielectric maximum, relaxation with <math>T_{\max}(\omega)</math></li> </ul>	<ul style="list-style-type: none"> <li>Lattice parameter anomaly</li> <li>Raman anomalies</li> <li>Anharmonic thermal parameter, isotopic minimum in agreement factor versus shifts</li> </ul>	<ul style="list-style-type: none"> <li>Anharmonic thermal parameter, isotropic minimum in agreement factor versus shifts</li> <li>Superstructure peaks (CORs) whatever <math>T</math> is</li> <li>Raman scattering (CORs/CIRs) (whatever <math>T</math> is)</li> </ul>

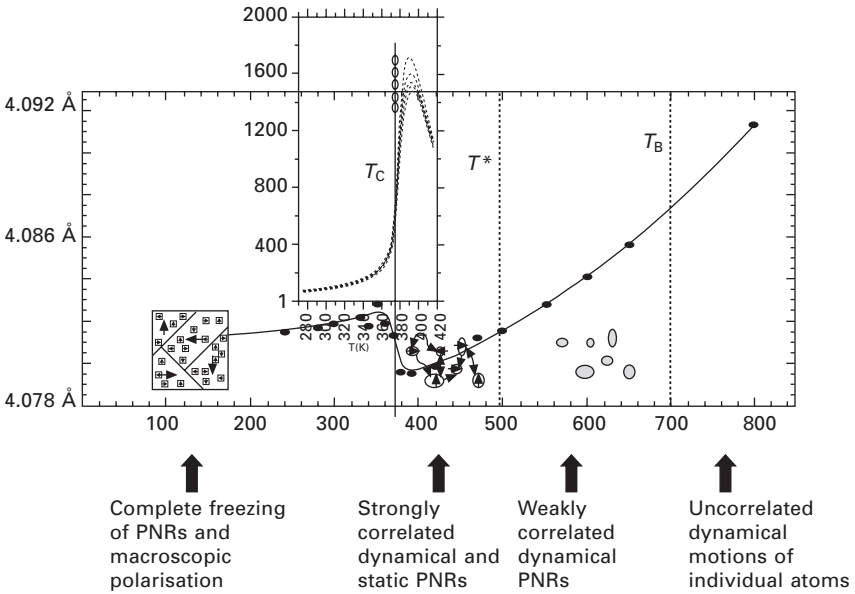
$T_f$  = freezing temperature;  $T^*$  = temperature when diffuse scattering appears on cooling;  $T_c$  = critical temperature (for compounds with phase transition);  $T_B$  = Burns temperature when PNRs are created.



14.28 Schematic picture of the 'structure' of a relaxor close to  $T_B$  and close to  $T^*$ . The arrows symbolise the correlations. Note that many details are not addressed in this picture, in particular the questions of dynamic versus static displacements.



(a)



(b)

14.29 Schematic picture of temperature-dependence of the 'structure' of a PMN-like relaxor (a) and a PSN-like ferroelectric relaxor (b).

shows the comparative evolution of PMN and PSN (and other relaxors with ferroelectric phase).

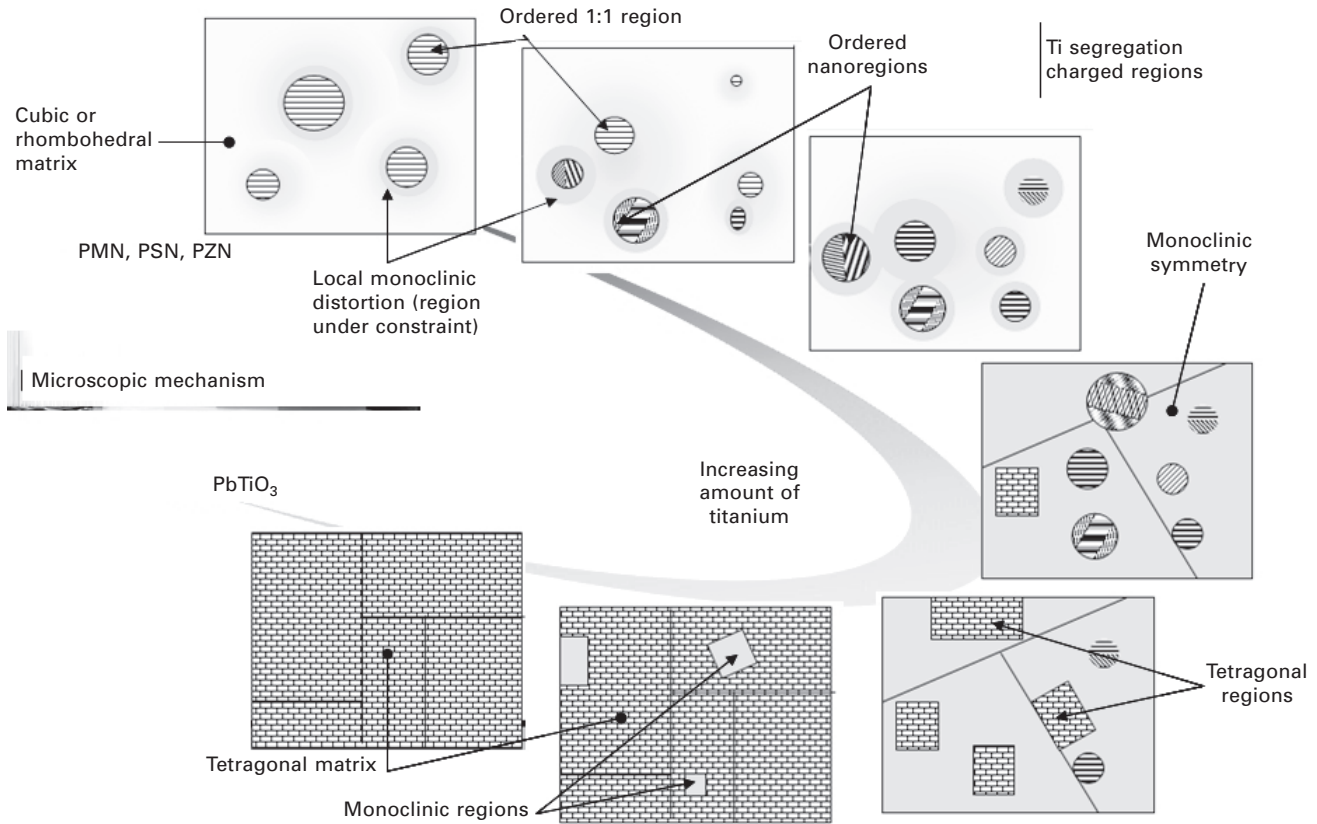
Of course these pictures should not be taken as being exact and definitive, in particular, regarding the accuracy of the different temperatures as well as the notion of PNRs or CORs with well defined ‘domains’ and sharp boundaries. Indeed, at a ‘zero’ level diffraction/diffuse scattering experiments do not allow us to differentiate a ‘cake with grapefruit’ model (as depicted in Figs 14.30 and Fig. 14.31), implying nanodomains with sharp boundaries inside a matrix) from a ‘cake with grape flavour’ model, i.e. a situation in which the polar order does not form a boundary but is characterised by a correlation length exponentially decaying and penetrating the whole sample. In fact, the situation appears to be probably much more complex than these two extreme (limiting) cases. Indeed by the careful fittings of diffuse scattering profiles, ‘fractal’ or ‘hierarchical’ organisation of the PNRs is possible. Clarification of the situation is left for the future.

Many other questions are still unsolved, among them the coexistence and the structure of the ‘frozen’ PNRs inside the ferroelectric domain states which is probably much more complicated than a simple rhombohedral or monoclinic local symmetry. One proposal is to use below the freezing temperature  $T_f$ , the term SPNRs (static polar nanoregions) instead of PNRs.

#### 14.6.2 The concentration evolution of MPB systems: MPB or morphotropic phase region?

We have discussed in the above sections that the monoclinic polar order already exists in ‘pure’ relaxors in the form of PNRs or in connection with PNRs (SPNRs). When doping with PT this polar order progressively develops in the form of long-range ferroelectric phases. We have seen that the CORs which act as nucleation centres for the PNRs also transforms into chemical inhomogeneous regions (CIRs) characterised by very local fluctuation or segregation of titanium which may act as nucleation centres for the monoclinic MPB phases. How the CORs transform into the CIRs when doping with titanium is a question that is not yet clearly understood. So, although further experiments are clearly needed to understand the nanoscale cation distribution, a possible global simplistic picture of polar and chemical distributions with increasing content of PT can be drawn to summarise what has been discussed (Fig. 14.30).

This picture points out the important fact that the relaxors and the MPB systems are highly inhomogeneous and may be viewed as some kind of composite materials (Fig. 14.31) in which nanoregions of local compositions and of ferroelectric displacements coexist, forming self-organised nanostructured systems. The notion of a matrix of average composition and average symmetry that embeds these nanoregions is probably not correct as discussed above, but it remains important at least for getting a rough picture of these systems.



14.30 Low-temperature structure versus the concentration of the titanium of MPB relaxors/compounds.





14.31 Relaxor/MPB compound as a typical composite material (dedicated to the reader).

The final conclusion of this overview is that the notion of MPB in the sense of a confined concentration region where the polarisation rotates from the rhombohedral [111] direction to the tetragonal [001] direction in a definite region of the phase diagram should probably be replaced by the notion of morphotropic phase region (MPR).

## 14.7 Acknowledgements

Our group has worked on the understanding of the relaxor and related material for almost 20 years and many researchers and students have contributed to these studies, as can be seen from the references. We would like also to thank Serguey Vakhrushev from Ioffe Institute for many illuminating discussions. Many figures in this chapter are from or adapted from Raphael Haumont's thesis.

## 14.8 References

- Ahart M., Cohen, R. E., Struzhkin V., Gregoryanz E., Rytz D., Prosandeev S. A., Mao H.-K. and Hemley R. J. (2005) High-pressure Raman scattering and X-ray diffraction of the relaxor ferroelectric  $0.96\text{Pb}(\text{Zn}_{1/3}\text{Nb}_{2/3}\text{O}_3-0.04\text{PbTiO}_3)$ . *Phys. Rev. B*, **71**, 144102.
- Akhilesh Kumar S. and Dhananjai P. (2003) Evidence for  $M_B$  and  $M_C$  phases in the morphotropic phase boundary region of  $(1-x)[\text{PbMg}_{1/3}\text{Nb}_{2/3}\text{O}_3]-x\text{PbTiO}_3$ : A Rietveld study. *Phys. Rev. B* **67**, 064102.
- Akhilesh Kumar S., Dhananjai P. and Oksana Z. (2006) Evolution of short-range to long-range monoclinic order of MB type with decreasing temperature in  $0.75[\text{PbMg}_{1/3}\text{Nb}_{2/3}\text{O}_3]-0.25\text{PbTiO}_3$ . *J. Appl. Phys.*, **99**, 076105.

- Bellaiche L., Garcia A. and Vanderbilt D. (2000) Finite-temperature properties of  $\text{pb}(\text{Zr}_{1-x}\text{Ti}_x)\text{O}_3$  alloys from first principles. *Phys. Rev. Lett.*, **84**, 5427.
- Bertram R., Reck G. and Uecker R. (2003) Growth and correlation between composition and structure of  $(1-x)\text{Pb}(\text{Zn}_{1/3}\text{Nb}_{2/3})\text{O}_3-x\text{PbTiO}_3$  crystals near the morphotropic phase boundary. *J. Crystal Growth*, **253**, 212.
- Bing Y.-H., Bokov A. A., Ye Z.-G., Noheda B. and Shirane G. (2005) Structural phase transition and dielectric relaxation in  $\text{Pb}(\text{Zn}_{1/3}\text{Nb}_{2/3})\text{O}_3$  single crystals. *J. Phys.: Condens. Matter*, **17**, 2493.
- Blinic R., Laguta V. and Zalar B. T. (2003) Field cooled and zero field cooled  $\{207\}\text{Pb}$  NMR and the local structure of relaxor  $\text{PbMg}_{1/3}\text{Nb}_{2/3}\text{O}_3$ . *Phys. Rev. Lett.*, **91**, 247601.
- Bokov A. A. and Ye Z. G. (2006) Recent progress in relaxor ferroelectrics with perovskite structure. *J. Mater. Sci.*, **41**, 31.
- Bonneau P., Garnier P., Husson E. and Morell, A. (1989) Structural study of PMN ceramics by X-ray diffraction between 297 and 1023 K. *Mater. Res. Bull.*, **24**, 201.
- Bonneau P., Garnier P., Calvarin G., Husson E., Gavarrin J. R., Hewat A. W. and Morell A. (1991) X-ray and neutron diffraction studies of the diffuse phase transition in  $\text{PbMg}_{1/3}\text{Nb}_{2/3}\text{O}_3$  ceramics. *J. Solid State Chem.*, **91**, 350.
- Burton B. P., Cockayne E., Tinte S. and Waghmare U. V. (2006) First-principles-based simulations of relaxor ferroelectrics. *Phase Transitions*, **79**, 91.
- Calvarin G., Husson E. and Ye Z. G. (1995) X-ray study of the electric field-induced phase transition in single crystal  $\text{Pb}(\text{Mg}_{1/3}\text{Nb}_{2/3})\text{O}_3$ . *Ferroelectrics*, **165**, 349.
- Cao H., Li J., Viehland D., Xu G. and Shirane G. (2006) Monoclinic  $M_C$  vs orthorhombic in  $[001]$  and  $[110]$  electric-field-cooled  $\text{Pb}(\text{Mg}_{1/3}\text{Nb}_{2/3}\text{O}_3)$ -35% $\text{PbTiO}_3$  crystals. *Appl. Phys. Lett.*, **88**, 72915.
- Caranoni C., Lampini P. and Siny I. *et al.*, (1992) Comparative Study of the ordering of B-site cations in PST and PSN perovskites, *Physica Status Solid A-Applied Research*, **130**(1): 25–37.
- Carreard J., Gemeiner P., Kiat J. M., Dkhil B., Bogicevic C., Rojac T. and Malic B. (2005) Size-driven relaxation and polar states in  $\text{PbMg}_{1/3}\text{Nb}_{2/3}\text{O}_3$ -based system. *Phys. Rev. B*, **72**, 174115.
- Carreard J., Kiat J. M., Dkhil B., Algueró M., Jiménez R., Jiménez B., Holc J. and Kosec M. (2006) Monoclinic morphotropic phase and rotation of polarisation induced by reduction of grain size in PMN-PT. *Appl. Phys. Lett.*, **89**, 252906.
- Chaabane B., Kreisel J., Dkhil B., Bouvier P. and Mezouar M. (2003a) Pressure-Induced Suppression of the Diffuse Scattering in the Model Relaxor Ferroelectric  $\text{PbMg}_{1/3}\text{Nb}_{2/3}\text{O}_3$ . *Phys. Rev. Lett.*, **90**, 257601.
- Chaabane B., Kreisel J., Dkhil B., Bouvier P. and Mezouar M. (2003b) Pressure-induced suppression of the diffuse scattering in the model relaxor ferroelectric PMN. *Phys. Rev. Lett.*, **90**, 257601.
- Chaabane B., Kreisel J., Bouvier P., Lucazeau G. and Dkhil B. (2004) Effect of high pressure on the PMN-PT solid solution: a Raman scattering investigation. *Phys. Rev. B*, **70**, 134114.
- Chaigneau J., Kiat J. M. and Malibert C. (2007) Chemical and polar order and morphotropic phase boundaries in  $\text{BiScO}_3$ - $\text{PbTiO}_3$  system., *Phys. Rev. B* accepted.
- Chen I.W., Li P. and Wang Y. (1995) Structural origin of relaxor perovskites. *J. Phys. Chem. Solids*, **57**, 1525.
- Chen J., Chan H. M. and Harmeer M. H. (1989) Ordering structure and dielectric properties of undoped and La/Na-doped  $\text{Pb}(\text{Mg}_{1/3}\text{Nb}_{2/3})\text{O}_3$ . *J. Am. Ceram. Soc.*, **72**, 593.

- Chu F., Reaney I. M. and Setter N. (1995a) Spontaneous (zero-field) relaxor-to-ferroelectric-phase transition in disordered  $\text{Pb}(\text{Sc}_{1/2}\text{Nb}_{1/2})\text{O}_3$ . *J. Appl. Phys.*, **77**, 1671.
- Chu F., Reaney I. M. and Setter N. (1995b) Role of defects in the ferroelectric relaxor lead scandium tantalate. *J. Am. Ceram. Soc.*, **78**, 1947.
- Cohen R. E. (1992) Origin of ferroelectricity in perovskite oxides. *Nature*, **358**, 136.
- Colla E. V., Vakhrushev S. B., Koroleva E. Y. and Okuneva N. M. (1996) Properties of field induced ferroelectric phase transition in single-crystal lead magnoniobate. *Phys. Solid State*, **38**, 1202.
- Cox D. E., Noheda B. and Shirane G. (2005) Low-temperature phases in  $\text{PbZr}_{0.52}\text{Ti}_{0.48}\text{O}_3$ : a neutron powder diffraction study. *Phys. Rev. B*, **71**, 134110.
- Cross L. E. (1987) Relaxor ferroelectrics. *Ferroelectrics*, **76**, 241.
- Davies P. K. and Akbas M. A. (2000) Chemical order in PMN-related relaxors: structure, stability, modification, and impact on properties. *J. Phys. Chem. Solids*, **61**, 159.
- Depero L. E. and Sangaletti L. (1997) Structural models for lead magnesium niobate. *Solid State Comm.*, **102**, 615.
- Dkhil B. (1999) Rôle des nanostructures chimique et polaire sur la transition de phase relaxeur-ferroélectrique dans les composés  $\text{PbMg}_{1/3}\text{Nb}_{2/3}\text{O}_3$  et  $\text{PbMg}_{0.3}\text{Nb}_{0.6}\text{Ti}_{0.1}\text{O}_3$ , Université Paris XI Orsay.
- Dkhil B., Kiat J. M., Calvarin G., Baldinozzi G., Vakhrushev S. B. and Suard E. (2002) Local and long range polar order in the relaxor-ferroelectric compounds PMN-PT. *Phys. Rev. B*, **65**, 0241041.
- Dul'kin E., Roth M., Janolin P. E. and Dkhil B. (2006) Acoustic emission study of phase transitions and polar nanoregions in relaxor-based systems: application to the  $\text{PbZn}_{1/3}\text{Nb}_{2/3}\text{O}_3$  family of single crystals. *Phys. Rev. B*, **73**, 012102.
- Egami T. & Billinge S. J. L. (2003) *Underneath the Bragg Peaks: Structural Analysis of Complex Materials*. Pergamon Press, Oxford, UK.
- Eitel R. E., Zhang S. J., Shrout T. R., Randall C. A. and Levin I. (2004) Phase diagram of the perovskite system  $(1-x)\text{BiScO}_3-x\text{PbTiO}_3$ . *J. Appl. Phys.*, **96**, 2828.
- Emelyanov S. M., Savenko F. I., Trusov Y. A., Torgashev V. I. and Timonin P. N. (1993) Dilute ferroelectric in random electric field: phase transitions in  $\text{Pb}(\text{Mg}_{1/3}\text{Nb}_{2/3})_{1-x}\text{Ti}_x\text{O}_3$  crystals. *Phase Transitions*, **45**, 251.
- Frenkel A. I., Pease D. M., Giniewicz J., Stern E. A., Brewe D. L., Daniel M. and Budnick J. (2004) Concentration-dependent short-range order in the relaxor ferroelectric  $(1-x)\text{Pb}(\text{Sc,Ta})\text{O}_3-x\text{PbTiO}_3$ . *Physical Rev. B*, **70**, 014106.
- Fu H. and Cohen R. E. (2000) Polarization rotation mechanism for ultrahigh electromechanical response in single-crystal piezoelectrics. *Nature*, **403**, 281.
- Fujishiro K., Vlokh R., Uesu Y., Yamada Y., Kiat J.-M., Dkhil B. and Yamashita Y. (1998) Optical observation of heterophase and domain structures in relaxor ferroelectrics PZN/PT. *Jpn. J. Appl. Phys.*, **37**, 5246.
- Gehring P. M., Park S. E. and Shirane G. (2000) Soft phonon anomalies in the relaxor ferroelectric  $\text{Pb}(\text{Zn}_{1/3}\text{Nb}_{2/3})_{0.92}\text{Ti}_{0.08}\text{O}_3$ . *Phys. Rev. Lett.*, **84**, 5216.
- George A. M., Iniguez J. and Bellaiche L. (2003) Effects of atomic short-range order on the properties of perovskite alloys in their morphotropic phase boundary. *Phys. Rev. Lett.*, **91**, 045504.
- Glazer A. M., Thomas P. A., Baba-Kishi K. Z., Pang G. K. H. and Tai C. W. (2004) Influence of short-range and long-range order on the evolution of the morphotropic phase boundary in PZT. *Phys. Rev. B*, **70**, 184123.
- Grinberg I., Cooper V. R. and Rappe A. M. (2002) Relationship between local structure and phase transitions of a disordered solid solution. *Nature*, **419**, 909.

- Hatch D. M., Stokes H. T., Ranjan R., Ragini S. K., Mishra, S. K., Pandey, D. and Kennedy, B. J. (2002) Antiferrodistortive phase transition in  $\text{Pb}(\text{Ti}_{0.48}\text{Zr}_{0.52}\text{O}_3$ : Space group of the lowest temperature monoclinic phase. *Phys. Rev. B*, **65**, 212101.
- Haumont R. (2004) Rotation de la Polarisation Dans Les System Morphotropiques: Cas De  $\text{Pb}(\text{Sc}_{1/2}\text{Nb}_{1/2}\text{O}_3\text{-PbTiO}_3$ , École Centrale des Arts et Manufactures.
- Haumont R., Dkhil B., Kiat J. M., Al-Barakaty A., Dammak H. & Bellaïche L. (2003) Cationic-competition-induced monoclinic phase in high piezoelectric PSN–PT compounds. *Phys. Rev. B*, **68**, 014114.
- Haumont R., Al-Barakaty A., Dkhil B., Kiat J. M. and Bellaïche L. (2005) Morphotropic phase boundary of heterovalent perovskite solid solutions: experimental and theoretical investigation of PSN–PT. *Phys. Rev. B*, **71**, 104106.
- Haumont R., Gemeiner P., Dkhil B., Kiat J. M. and Bulou A. (2006a) Polar and chemical states at a nanometer scale in a PSN–PT system investigated by Raman spectroscopy. *Phys. Rev. B*, **73**, 104106.
- Haumont R., Malibert C., Dkhil B., Kiat J. M., Lemarrec F., Asanuma S. and Uesu Y. (2006b) Observation of rotation of polarization in thin films of PSN–PT via a monoclinic phase. *Jpn. J. Appl. Phys.*, **45**, L42.
- Hirota K., Ye Z. G., Wakimoto S., Gehring P. M. and Shirane G. (2002) Neutron diffuse scattering from polar nanoregions in the relaxor  $\text{PbMg}_{1/3}\text{Nb}_{2/3}\text{O}_3$ . *Phys. Rev. B*, **65**, 104105.
- Hlinka J., Kamba S., Petzelt J., Kulda J., Randall C. A. and Zhang S. J. (2003) Origin of the ‘waterfall’ effect in phonon dispersion of relaxor perovskites. *Phys. Rev. Lett.*, **91**, 107602.
- Janolin P. E., Dkhil B., Bouvier P., Kreisel J. and Thomas P. A. (2006) Pressure instabilities up to 46 GPa in the relaxor ferroelectric  $\text{PbZn}_{1/3}\text{Nb}_{2/3}\text{O}_3$ . *Phys. Rev. B*, **73**, 094128.
- Janolin P. E., Kiat J. M., Malibert C., Asanuma S. and Uesu Y. (2007) Origin of temperature evolutions of lattice strains in relaxor  $\text{PbSc}_{1/3}\text{Nb}_{1/2}\text{O}_3$  thin films *Appl. Phys. Lett.* (in press).
- Jeong I.-K. & Lee J. K. (2006) Local structure and medium-range ordering in relaxor ferroelectric  $\text{Pb}(\text{Zn}_{1/3}\text{Nb}_{2/3})\text{O}_3$  studied using neutron pair distribution function analysis. *Appl. Phys. Lett.*, **88**, 262905.
- Jin Y. M., Wang Y. U., Khachatryan A. G., Li J. F. and Viehland D. (2003) Conformal miniaturization of domains with low domain-wall energy: monoclinic ferroelectric states near the morphotropic phase boundaries. *Phys. Rev. Lett.*, **91**, 197601.
- Khachatryan A. G., Shapiro S. M. and Semenovskaya S. (1991) Adaptive phase formation in martensitic transformation. *Phys. Rev. B*, **43**, 10832.
- Kiat J.-M., Baldinozzi G., Dunlop M., Malibert C., Dkhil B., Menoret C., Masson O. and Fernandez-Diaz M.-T. (2000) Anharmonicity and disorder in simple and complex provskites: a high energy synchrotron and hot neutron diffraction study. *J. Phys.: Condens. Matter.*, **12**, 8411.
- Kiat J.-M., Uesu Y., Dkhil B., Matsuda M., Malibert C. and Calvarin G. (2002) Monoclinic structure of unpoled morphotropic high piezoelectric PMN–PT and PZN–PT compounds. *Phys. Rev. B*, **65**, 064106.
- Kleemann W. (1993) Random-field induced antiferromagnetic, ferroelectric and structural domain states. *Int. J. Modern Phys.*, **7**, 2469.
- Kornev I. A., Bellaïche L., Bouvier P., Janolin P. E., Dkhil B. and Kreisel J. (2005) Ferroelectricity of perovskites under pressure. *Phys. Rev. Lett.*, **95**, 196804.
- Kornev I. A., Bellaïche L., Janolin P. E., Dkhil B. and Suard E. (2006) Phase diagram of  $\text{Pb}(\text{Zr}, \text{Ti})\text{O}_3$  solid solutions from first principles. *Phys. Rev. Lett.*, **97**, 157601.

- Krause H. B., Cowley J. M. and Wheatley J. (1979) Short-range ordering in  $\text{PbMg}_{1/3}\text{Nb}_{2/3}\text{O}_3$ . *Acta Cryst. A*, **35**, 1015.
- Kreisel J., Dkhil B., Bouvier P. and Kiat J. M. (2002) Effect of high pressure on relaxor ferroelectrics. *Phys. Rev. B*, **65**, 172101.
- Kutnjak Z., Petzelt J. and Blinc R. (2006) The giant electromechanical response in ferroelectric relaxors as a critical phenomenon. *Nature*, **441**, 956.
- La-Orautapong D., Toulouse J., Robertson J. L. and Ye Z.-G. (2001) Diffuse neutron scattering study of a disordered complex perovskite  $\text{Pb}(\text{Zn}_{1/3}\text{Nb}_{2/3})\text{O}_3$  crystal. *Phys. Rev. B*, **64**, 212101.
- Laguta V. V., Glinchuk M. D., Nokhrin S. N., Bykov I. P., Blinc R., Gregorovič A. and Zalar B. (2003) NMR study of local structure and chemical ordering in PMN and PbSN relaxor ferroelectrics. *Phys. Rev. B*, **67**, 104106.
- Laguta V. V., Glinchuk M. D., Bykov I. P., Blinc R. and Zalar B. (2004) NMR study of ionic shifts and polar ordering in the relaxor ferroelectric PSN. *Phys. Rev. B*, **69**, 054103.
- Le Bellac D., Kiat J. M., Garnier P., Moudden H., Sciau P., Buffat P. A. and André G. (1995) Mechanism of the incommensurate phase in lead oxide  $\alpha\text{-PbO}$ . *Phys. Rev. B*, **52**, 13184.
- Lebellac D., Kiat J. M. and Garnier P. (1995b) Electronic lone pair localization and electrostatic energy calculation: application to  $\text{PbO}$ ,  $\text{SnO}$ ,  $\text{Pb}_{1-x}(\text{TiO})_x\text{O}$ ,  $\text{Pb}_3\text{O}_4$ ,  $\text{Pb}_3(\text{V,P})_2\text{O}_8$  and a  $\text{BiSrCaCuO}$ -type superconductor. *J. Solid State Chem.*, **114**, 459.
- Lebon A., Dammak H., Calvarin G. and Ahmedou I. O. (2002) The cubic-to-rhombohedral phase transition of  $\text{Pb}(\text{Zn}_{1/3}\text{Nb}_{2/3})\text{O}_3$ : a high-resolution X-ray diffraction study on single crystals. *J. Phys.: Condens. Matter*, **14**, 7035.
- Lebon A., Dammak H. and Calvarin G. (2005) Easy induction of a ferroelectric fourfold monoclinic domain state from a tetragonal ferroelectric monodomain state in  $\text{PbZn}_{1/3}\text{Nb}_{2/3}\text{O}_3$ . *J. Phys.: Condens. Matter*, **17**, 6385.
- Lucuta P. G. (1989) Ferroelectric-domain structure in piezoelectric ceramics. *J. Am. Ceram. Soc.*, **72**, 933.
- Malibert C. (1998) Ordre et désordre dans la pérovskite ferroélectrique relaxeur  $\text{PbSc}_{1/2}\text{Nb}_{1/2}\text{O}_3$  Comparaison avec quelques pérovskites simples et complexes, université Paris 6.
- Malibert C., Dkhil B., Kiat J. M., Durand D., Berar J. F. and Spasojevic A. (1997) Order and disorder in the relaxor ferroelectric perovskites PSN, comparison with  $\text{BaTiO}_3$  and  $\text{PbTiO}_3$ . *J. Phys.: Condens. Matter*, **9**, 7485.
- Mathan N. D., Husson E., Gaucher P. and Morell A. (1990) Modification of the B-site order of  $\text{PbMg}_{1/3}\text{Nb}_{2/3}\text{O}_3$  ceramics by thermal annealing or by La-doping. *Mater. Res. Bull.*, **25**, 427.
- Mathan N. D., Husson E., Calvarin G. and Morell A. (1991) Structural study of a poled  $\text{PbMg}_{1/3}\text{Nb}_{2/3}\text{O}_3$  ceramic at low temperature. *Mater. Res. Bull.*, **26**, 1167.
- Miao S., Zhu J., Zhang X. and Cheng Z. Y. (2001) Electron diffraction and HREM study of a short-range ordered structure in the relaxor ferroelectric  $\text{PbMg}_{1/3}\text{Nb}_{2/3}\text{O}_3$ . *Phys. Rev. B*, **65**, 052101.
- Naberezhnov A., Vakhrushev S., Dorner B., Strauch D. and Moudden H. (1999) Inelastic neutron scattering study of the relaxor ferroelectric  $\text{PbMg}_{1/3}\text{Nb}_{2/3}\text{O}_3$  at high temperatures. *Eur. Phys. J. B*, **11**, 13.
- Noheda B. (2002) Structure and high-piezoelectricity in lead oxide solid solutions. *Curr. Opin. Solid State Mater. Sci.*, **6**, 27.
- Noheda B. and Cox, D. E. (2006) Bridging phases at the morphotropic boundaries of lead oxide solid solutions. *Phase Transitions*, **79**, 5.

- Noheda B., Cox D. E., Shirane G., Gonzalo J. A., Cross L. E. and Park S.-E. (1999) A monoclinic ferroelectric phase in the  $\text{Pb}(\text{Zr}_{1-x}\text{Ti}_x)\text{O}_3$  solid solution. *Appl. Phys. Lett.*, **74**, 2059.
- Noheda B., Cox D. E., Shirane G., Gao J., and Ye Z.-G. Ye (2002) Phase diagram of the ferroelectric relaxor  $(1-x)\text{PbMg}_{1/3}\text{Nb}_{2/3}\text{O}_3-x\text{PbTiO}_3$ . *Phys. Rev. B*, **66**, 54104.
- Ohwa H., Iwata M., Orihara H., Yasuda N. and Ishibashi Y. (2001) Raman Scattering in  $(1-x)\text{Pb}(\text{Mg}_{1/3}\text{Nb}_{2/3})\text{O}_3-x\text{PbTiO}_3$ . *J. Phys. Soc. Jpn.*, **70**, 3149.
- Pirc R. and Blinc R. (1999) Spherical random-bond-random-field model of relaxor ferroelectrics. *Phys. Rev. B*, **60**, 13470.
- Prouzet E., Husson E., Mathan N. D. and Morell A. (1993) A low-temperature extended X-ray absorption study of the local order in simple and complex perovskites: II. PMN ( $\text{PbMg}_{1/3}\text{Nb}_{2/3}\text{O}_3$ ). *J. Phys.: Condens. Matter*, **5**, 4889.
- Raevskii I. P., Prosandeev S. A., Emelyanov A. S., Raevskaya S. I., Colla E. V., Viehland D., Kleemann W., Vakhrushev S. B., Dellis J. L., El Marssi M. and Jastrabik L. (2005) Bias-field effect on the temperature anomalies of dielectric permittivity in PMN-PT single crystals. *Phys. Rev. B*, **72**, 184104.
- Randall C. A., Barber D. J., Whatmore R. W. and Groves P. (1986) A TEM study of ordering in the perovskite,  $\text{Pb}(\text{Sc}_{1/2}\text{Ta}_{1/2})\text{O}_3$ . *J. Mater. Sci.*, **21**, 4456.
- Ranjan R., Ragini, Mishra S. K., Pandey D. and Kennedy B. J. (2002) Antiferrodistortive phase transition in  $\text{Pb}(\text{Ti}_{0.48}\text{Zr}_{0.52})\text{O}_3$ : A powder neutron diffraction study. *Phys. Rev. B*, **65**, 060102.
- Ranjan R., Singh A. K., Ragini and Pandey D. (2005) Comparison of the  $Cc$  and  $R3c$  space groups for the superlattice phase of  $\text{PbZr}_{0.52}\text{Ti}_{0.48}\text{O}_3$ . *Phys. Rev. B*, **71**, 092101.
- Rossetti G. A., J., Zhang W. and Khachatryan A. G. (2006) Phase coexistence near the morphotropic phase boundary in lead zirconate titanate ( $\text{PbZrO}_3\text{-PbTiO}_3$ ) solid solutions. *Appl. Phys. Lett.*, **88**, 72912.
- Rouquette J., Haines J., Bornand V., Pintard M., Papet P., Marshall W. G. and Hull S. (2005) Pressure-induced rotation of spontaneous polarization in monoclinic and triclinic  $\text{PbZr}_{0.52}\text{Ti}_{0.48}\text{O}_3$ . *Phys. Rev. B*, **71**, 024112.
- Samara G. A. and Venturini E. L. (2006) Ferroelectric/relaxor crossover in compositionally disordered perovskites. *Phase Transitions*, **79**, 21.
- Scott J. F. (2006) Nanoferroelectrics: statics and dynamics. *J. Phys.: Condens. Matter*, **18**, R361.
- Shirane G., Axe J. D., Harada J. and Linz A. (1970) Inelastic neutron scattering from single-domain  $\text{BaTiO}_3$ . *Phys. Rev. B*, **2**, 3651.
- Singh A. K. and Pandey D. (2003) Evidence for  $M_B$  and  $M_C$  phases in the morphotropic phase boundary region of  $(1-x)[\text{Pb}(\text{Mg}_{1/3}\text{Nb}_{2/3})\text{O}_3]-x\text{PbTiO}_3$ . A Rietveld study, *Phys. Rev. B* **67**, 64102.
- Singh A. K., Pandey D. and Zaharko O. (2006) Powder neutron diffraction study of phase transitions in and a phase diagram of PMN-PT. *Phys. Rev. B*, **74**, 024101.
- Smolenskii G. A., Bokor V.A., Isupov N. N., Krainik V.A., Pasynkov R. E. and Sokolov A. I. (1984) In: *Ferroelectrics and Related Phenomena*. G.A. Smolenski (ed.), Gordon and Breach Science, Amsterdam.
- Sommer R., Yushin N. K. and Van Der Klink J. J. (1993) Polar metastability and an electric-field-induced phase transition in the disordered perovskite  $\text{Pb}(\text{Mg}_{1/3}\text{Nb}_{2/3})\text{O}_3$ . *Phys. Rev. B*, **48**, 13230.
- Stock C., Birgeneau R. J., Wakimoto S., Gardner J. S., Chen W., Ye Z. G. and Shirane G. (2004) Universal static and dynamic properties of the structural transition in  $\text{PbZn}_{1/3}\text{Nb}_{2/3}\text{O}_3$ . *Phys. Rev. B*, **69**, 094104.

- Suchomel M. R. and Davies P. K. (2004) Predicting the position of the morphotropic phase boundary in high temperature  $\text{PbTiO}_3$ - $\text{Bi}(\text{BB})\text{O}_3$  based dielectric ceramics. *J. Appl. Phys.*, **96**, 4405.
- Svitelskiy O., La-Orauttapong D., Toulouse J., Chen W. and Ye Z. G. (2005)  $\text{PbTiO}_3$  addition and internal dynamics in  $\text{PbZn}_{1/3}\text{Nb}_{2/3}\text{O}_3$  crystal studied by Raman spectroscopy. *Phys. Rev. B*, **72**, 172106.
- Svitelskiy O., Toulouse J., Yong G. and Ye Z. G. (2003) Polarized Raman study of the phonon dynamics in  $\text{PbMg}_{1/3}\text{Nb}_{2/3}\text{O}_3$  crystal. *Phys. Rev. B*, **68**, 104107.
- Takesue N., Fujii Y., Ichihara M. and Chen H. (1999) Self-accommodation of ionic size-effect atomic displacements in antiferroelectric order in relaxor lead scandium niobate. *Phys. Rev. Lett.*, **82**, 3709.
- Vakhrushev S., Zhukov S., Fetisov G. and Chernyshov V. (1994) The high-temperature structure of lead magnoniobate. *J. Phys.: Condens. Matter.*, **6**, 4021.
- Vakhrushev S. B., Kiat J. M. and Dkhil B. (1997) X-ray study of the kinetics of field induced transition from the glass-like to the ferroelectric phase in lead magnoniobate. *Solid State Comm.*, **103**, 477.
- Vakhrushev S., Dkhil B. and Kiat J.M. (2007) unpublished work.
- Vanderbilt D. and Cohen M. H. (2001) Monoclinic and triclinic phases in higher-order Devonshire theory. *Phys. Rev. B*, **63**, 094108.
- Venturini E. L., Grubbs R. K., Samara G. A., Bing Y. and Ye Z. G. (2006) Ferroelectric and relaxor properties of PSN: Influence of pressure and biasing electric field. *Phys. Rev. B*, **74**, 064108.
- Viehland D. and Li J. F. (1993) Compositional instability and the resultant charge variations in mixed B-site cation relaxor ferroelectrics. *J. Appl. Phys.*, **74**, 4121.
- Wakimoto S., Stock C., Ye Z. G., Chen W., Gehring P. M. and Shirane G. (2002) Mode coupling and polar nanoregions in the relaxor ferroelectric  $\text{PbMg}_{1/3}\text{Nb}_{2/3}\text{O}_3$ . *Phys. Rev. B*, **66**, 224102.
- Wang H., Zhu J., Lu N., Bokov A. A., Ye Z.-G. and Zhang X. W. (2006) Hierarchical micro-/nanoscale domain structure in  $M_C$  phase of  $(1-x)\text{Pb}(\text{Mg}_{1/3}\text{Nb}_{2/3}\text{O}_3)_x\text{PbTiO}_3$  single crystal. *Appl. Phys. Lett.*, **89**, 42908.
- Welberry T. R., Gutmann M. J., Woo H., Goossens D. J., Xu G., Stock C., Chen W. and Ye, Z.-G. (2005) Single-crystal neutron diffuse scattering and Monte Carlo study of the relaxor ferroelectric  $\text{PbZn}_{1/3}\text{Nb}_{2/3}\text{O}_3$  (PZN). *J. Appl. Cryst.*, **38**, 639.
- Westphal V., Kleemann W. and Glinchuk M. D. (1992) Diffuse phase transitions and random-field-induced domain states of the 'relaxor' ferroelectric  $\text{PbMg}_{1/3}\text{Nb}_{2/3}\text{O}_3$ . *Phys. Rev. Lett.*, **68**, 847.
- Woodward D. I., Knudsen J. and Reaney I. M. (2005) Review of crystal and domain structures in the PZT solid solution. *Phys. Rev. B*, **72**, 104110.
- Xu G., Shirane G., Copley J. R. D. and Gehring P. M. (2004) Neutron elastic diffuse scattering study of  $\text{PbMg}_{1/3}\text{Nb}_{2/3}\text{O}_3$ . *Phys. Rev. B*, **69**, 064112.
- Xu G., X., Gehring P. M. and Shirane G. (2005) Persistence and memory of polar nanoregions in a ferroelectric relaxor under an electric field. *Phys. Rev. B*, **72**, 214106.
- Xu G., Zhong Z., Bing Y., Ye Z.-G. and Shirane G. (2006) Electric-field-induced redistribution of polar nano-regions in a relaxor ferroelectric. *Nature Mater.*, **5**, 134.
- YE Z.-G. (1998) Relaxor ferroelectric complex perovskites: structures, crystals, properties and phase transaction *Key Eng. Mater.*, **155-156**, 81.
- Ye Z. G., Noheda B., Dong M., Cox D. and Shirane G. (2001) Monoclinic phase in the relaxor-based piezoelectric/ferroelectric PMN-PT system. *Phys. Rev. B*, **64**, 184114.
- Ye Z. G., Bing Y., Gao J., Bokov A. A., Stephens, P., Noheda, B. and Shirane, G. (2003) Development of ferroelectric order in relaxor  $(1-x)\text{PbMg}_{1/3}\text{Nb}_{2/3}\text{O}_3x\text{PbTiO}_3(x)$ . *Phys. Rev. B*, **67**, 104104.

## Size effects on the macroscopic properties of the relaxor ferroelectric $\text{Pb}(\text{Mg}_{1/3}\text{Nb}_{2/3})\text{O}_3\text{-PbTiO}_3$ solid solution

---

M ALGUERÓ, J RICOTE, P RAMOS and  
R JIMÉNEZ, Instituto de Ciencia de Materiales de Madrid,  
CSIC, Spain, J CARREAUD, J-M KIAT and  
B D KHIL, Ecole Centrale Paris, France and J HOLC and  
M KOSEC, Institute Jozef Stefan, Slovenia

### 15.1 Introduction

Ferroelectric perovskite, morphotropic phase boundary (MPB)  $\text{Pb}(\text{Zr,Ti})\text{O}_3$  (PZT)-based ceramics are the basis of a wide range of piezoelectric technologies, such as sensors, actuators, smart systems, ultrasound generation and sensing and underwater acoustics (Setter, 2002). Their high electromechanical activity is associated with the presence of a monoclinic phase in the MPB region, between the rhombohedral and tetragonal phases (Noheda, *et al.* 2000), and the mechanism of polarisation rotation among the phases (Guo *et al.*, 2000). This is the same mechanism responsible for the ultra-high piezoelectricity,  $d_{33}$  coefficient  $> 1500$  pC/N, of the rhombohedral  $\text{Pb}(\text{Zn}_{1/3}\text{Nb}_{2/3})\text{O}_3\text{-PbTiO}_3$  (PZN-PT) and  $\text{Pb}(\text{Mg}_{1/3}\text{Nb}_{2/3})\text{O}_3\text{-PbTiO}_3$  (PMN-PT) single crystals (Park and Shrout, 1997) and textured ceramics (Kwon *et al.*, 2005) near or in their respective MPBs (Noheda *et al.*, 2001). The commercial PZT based ceramics with the highest sensitivity are the so-called soft PZT, for which the  $d_{33}$  piezoelectric coefficient is raised from  $\sim 200$  pC/N up to  $\sim 600$  pC/N by composition engineering of the Curie temperature and domain wall mobility (Takahashi, 1982). Piezoelectric devices are not oblivious to the current miniaturisation trends in ceramic technology for microelectronics. Multilayer ceramic capacitors (MLCC) are being down-scaled (Pithan *et al.*, 2005), and an analogous trend can be anticipated for multilayer ceramic actuators (MLCA) and for other piezoelectric device configurations (Uchino, 1998). This technological trend benefits from the scaling behaviour of piezoelectricity: longitudinal deformation under a given voltage does not depend on size and thus, the down-scaling of a MLCA does not affect the piezoelectric response. Also, the total displacement is proportional to the number of layers and so, there is a general driving force to reduce the thickness. With the ceramic layers in MLCC approaching the thickness of 1  $\mu\text{m}$ , reliability requires five to ten grains per layer and thus, submicrometre grain sizes close to the 100 nm limit are necessary. Similar and even lower sizes are involved in Si integrated thick (Gentil *et al.*, 2004) and thin (Trolier-



McKinstry and Muralt, 2004) film piezoelectric technologies. This raises the issue of how properties are affected by the size reduction. In this chapter, we review our work on the size effects in the PMN–PT solid solution. This MPB system shows distinctive features that point to a better down-scaling behaviour than PZT in terms of the electromechanical properties.

Firstly, current knowledge of size effects in ferroelectrics is briefly reviewed. Emphasis is put on polycrystals and on the macroscopic properties, not only because they are the basis for the functionality of the materials, but also as a means of addressing some fundamental issues, e.g. the size effect on the ferroelectric phase transition. Secondly, background on the PMN–PT relaxor–ferroelectric solid solution is also reviewed. The relevance of this system for its fundamental and applied interests is emphasised. Next, procedures used for the processing of PMN–PT submicro- and nanostructured ceramics are described, and the ceramic materials studied, their density and grain size are introduced. Then, size effects on the macroscopic properties, the electric, mechanical and electromechanical properties of 0.8PMN–0.2PT and 0.65PMN–0.35PT ceramics are successively presented. Based on these results, the size effects on the transition between the relaxor and ferroelectric states, the room temperature phases, the polar domain structure, and the functionality of the materials will be discussed. The chapter ends with a section devoted to final remarks and future trends.

## 15.2      Size effects in ferroelectrics

Most of the studies on size effects in polycrystals have focused on tetragonal BaTiO<sub>3</sub> as the basis of MLCC. The room temperature dielectric permittivity of BaTiO<sub>3</sub> ceramics presents a distinctive variation with grain size that is associated with the evolution of the ferroelectric domain configuration (Arlt and Sasko, 1980; Arlt *et al.* 1985; Arlt 1990a). Above 10 μm, a three-dimensional ferroelectric/ferroelastic 90° domain configuration is formed that fully relaxes stresses caused by ceramic clamping. Between ~0.3 and 10 μm, a banded configuration is formed that is capable of relaxing the stress only in two dimensions. Below 0.3 μm, the decrease in elastic energy by twinning does not compensate the surface energy of the wall, and 90° domains are not formed. The dielectric permittivity, like the piezoelectric and elastic coefficients, comprises a contribution from domain wall mobility, and so it is dependent on the density of walls. This density does not change above 10 μm, and the permittivity does not depend on size in this size range. Below 10 μm, domain size varies with the square root of the grain size, which causes wall density, and thereby the permittivity to increase when the size decreases. However, permittivity does not continuously increase until 0.3 μm, but presents a maximum at 0.8–1 μm. This is the size at which the structural distortion of the perovskite starts decreasing, most probably as a consequence

of the increasing stresses caused by the clamping. These stresses reduce the domain wall mobility (Demartin and Damjanovic, 1996). Therefore, the decrease of permittivity below 0.8–1  $\mu\text{m}$  results from the decrease in wall mobility. The stresses reach their highest levels with the disappearance of the 90° domain walls at  $\sim 0.3 \mu\text{m}$ .

Non-linear thermodynamic theory shows that the clamping modifies the room temperature phase of the single domain crystals, so as to have a coexistence of rhombohedral and orthorhombic phases, instead of the tetragonal phase, at room temperature (Zemilgotov *et al.*, 2005). Polarisation switching is also affected by the changes in the domain configuration with size reduction, and the remnant polarisation of the hysteresis loops decreases when the banded structure is formed (Arlt, 1990b), and is further reduced when the 90° domains disappear, and only 180° switching is possible (Hungria *et al.*, 2005). It is expected that there is a size limit below which ferroelectricity is lost (Li *et al.*, 1997). This would set a lower limit for the down-scaling of piezoelectric ceramic technologies.

Dense BaTiO<sub>3</sub> ceramics with a grain size of 20 nm still present the anomaly associated with the transition between the ferroelectric and paraelectric states in the temperature dependence of the dielectric permittivity (Deng *et al.*, 2006). This anomaly shows significant broadening and flattening for nanostructured materials as compared with coarse-grained ceramics, which has been shown to be a boundary effect (Bratkovsky and Levanyuk, 2005). The actual values of permittivity are very sensitive to the nature of the grain boundary, which acts as a low dielectric permittivity coating that decreases the permittivity (Zhao *et al.*, 2004). Figures as high as 1600 have been reported for ceramics with a size of 30 nm and tailored boundaries (Buscaglia *et al.*, 2006). Ferroelectric switching was not observed for the previous ceramics, which was proposed to be caused by the pinning of transgranular 180° domain walls at the grain boundaries, yet local switching was demonstrated by piezoresponse force microscopy.

Less attention has been paid to MPB materials and their electromechanical properties. The  $d_{33}$  piezoelectric coefficient of soft PZT ceramics continuously decreases with grain size from 550 pC/N for 4  $\mu\text{m}$ , down to 350 pC/N for 0.17  $\mu\text{m}$ , which was associated with the decrease of the ferroelectric/ferroelastic domain wall mobility because of the clamping (Randall *et al.*, 1998). The non-linear thermodynamic theory predicts a wide region of coexistence of rhombohedral and tetragonal phases with the disappearance of the domains (Zemilgotov *et al.*, 2005). In relation to the size limit of ferroelectricity, ferroelectric switching has been observed in thin film compacts of 9 nm size PZT particles (Seol and Takeuchi, 2004). Recently, the size effects were studied in the MPB PMN–PT (Carreaud *et al.*, 2005). Structural characterisation and dielectric properties of bulk compacts indicate that a room temperature relaxor state is present for sizes below 0.2  $\mu\text{m}$ , instead of

the ferroelectric phase, and that a paraelectric cubic phase exists below 30 nm.

### 15.3      **The relaxor ferroelectric Pb(Mg<sub>1/3</sub>Nb<sub>2/3</sub>)O<sub>3</sub>-PbTiO<sub>3</sub> solid solution**

PMN is a prototype of relaxor. Its dielectric permittivity as a function of temperature shows a broad maximum of  $\sim 20\,000\epsilon_0$  at  $-8\text{ }^\circ\text{C}$  and 1 kHz, the position of which,  $T_m$ , shifts towards higher temperatures with increasing frequency within a range of  $20\text{ }^\circ\text{C}$  (the so-called Curie range) in the 100 Hz–1 MHz interval. Below  $T_m$ , the permittivity also shows dispersion; it increases when the frequency is decreased. PMN presents slim ferroelectric hysteresis loops that result in small remnant polarisation. The saturation and remnant polarisation decrease when the temperature is increased, but do not vanish at  $T_m$  and maintain finite values up to significantly higher temperatures (Cross, 1994). No macroscopic phase transition occurs at the Curie range and the overall symmetry remains cubic at low temperatures, even though nanometre size polar regions (PNRs) exist within the cubic phase (Burns and Dacol, 1983; De Mathan *et al.*, 1991; Dkhil *et al.*, 2002). PNRs originate from site disorder and their dynamics is responsible from the relaxor characteristics, yet the actual mechanisms are under debate. Relaxors were proposed to be dipolar glass-like systems (Viehland *et al.*, 1990), for which the (interacting) PNRs present thermally activated polarisation fluctuations above a freezing temperature,  $T_f$ , of  $-56\text{ }^\circ\text{C}$  for PMN (Viehland *et al.*, 1991), and evolve to a non-ergodic glass state below  $T_f$ . Frustration of polar long range order results from competing interactions (random bonds).

This model was questioned, and random fields were proposed to be the origin (Westphal *et al.*, 1992) or to play a significant role (Pirc and Blinc, 1999) in the relaxor state. A large set of experiments, and also recent calculation results, suggest a physical picture (see Chapter 14), in which local chemical inhomogeneities (CIRs, i.e. chemical inhomogeneity regions) act as nucleation sites for PNRs and therefore, eventually, to long-range polar order: a high enough electric field causes a ferroelectric, rhombohedral long range order to develop below a temperature that is field dependent (Arndt *et al.*, 1988); this ferroelectric phase undergoes a first-order phase transition to the relaxor state during subsequent heating without field (Ye and Schmid, 1993; Calvarin *et al.*, 1995). In the case of PMN and other ‘simple’ relaxors such as PZN, Pb(Sc<sub>1/2</sub>Nb<sub>1/2</sub>)O<sub>3</sub>, etc., these CIRs were for a long time mainly associated with charged regions with local B-cations ordering (CORs, i.e. charged ordered regions). However, more recent observations in PMN as well as preservation of relaxor behaviour when doping with titanium (which should destroy B-cation ordering) indicate a more complex (but non-charged) cations distribution. The temperature, composition, electric field, pressure, etc. dependence of

physical and structural properties of relaxors should receive an interpretation in this framework of interacting CORs with the CIRs, in which the local chemistry and the local polarisation are intimately coupled.

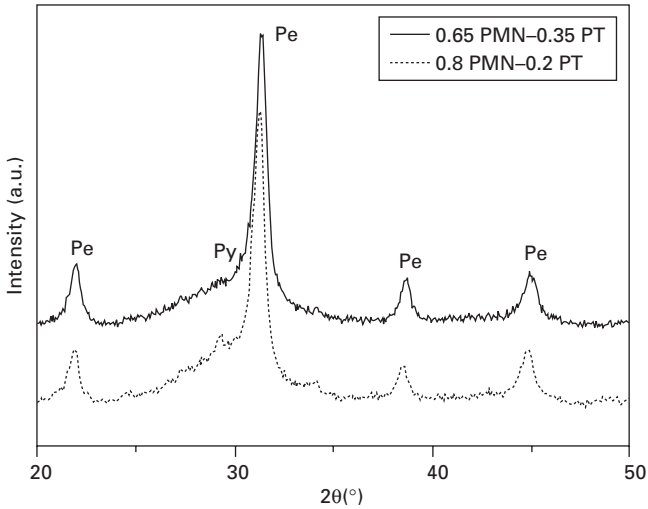
From the standpoint of properties and applications, the addition of small amounts of PT increases the Curie range to  $\sim 40^\circ\text{C}$  for 0.9PMN–0.1PT (Swartz *et al.*, 1984). This composition is the basis of the electrostrictive ceramic multilayer actuators used in applications requiring no hysteresis (Nomura and Uchino, 1982). On cooling, 0.9PMN–0.1PT presents a spontaneous relaxor–ferroelectric transition to the rhombohedral phase ( $R3m$  space group) below room temperature (RT). Further addition of PT causes the shift of the relaxor state towards higher temperatures, and the rhombohedral phase is stabilised at RT for 0.85PMN–0.15PT (Ye *et al.*, 2003). This phase was thought to be the room temperature phase up to  $\sim 0.65\text{PMN–}0.35\text{PT}$  (Noblanc *et al.*, 1996), at which a morphotropic phase boundary (MPB) with a tetragonal phase ( $P4mm$  space group) had been earlier described (Choi *et al.*, 1989). However, after the discovery of the monoclinic phase ( $Cm$  space group) in the MPB PZT, a number of studies on the structure of MPB phases in relaxor–PT systems have reported the presence of monoclinic phases (with space groups  $Cm$  and  $Pm$ ) in the MPB region (Ye *et al.*, 2001; Noheda *et al.*, 2002; Kiat *et al.*, 2002; Singh and Pandey, 2003; Haumont *et al.*, 2003). For the MPB PMN–PT, Rietveld analysis of powder X-ray diffraction (XRD) and neutron diffraction data has shown that two monoclinic phases ( $Cm$  and  $Pm$  space groups, respectively) exist between 0.75PMN–0.25PT and 0.65PMN–0.35PT (Singh and Pandey, 2003; Singh *et al.*, 2006). Very recently, the region of existence of the  $Cm$  monoclinic phase has been shown to extend down to 0.8PMN–0.2PT (Jiménez *et al.*, 2006). The phase transition between the relaxor and ferroelectric states for this composition presents distinctive features that shed light on the development of polar long-range order in the system (Algueró *et al.*, 2005a; Jiménez *et al.*, 2006). The MPB PMN–PT single crystals and textured ceramics are under consideration for the new generation of high sensitivity and high-power piezoelectric devices because of their ultra-high piezoelectric performance under electric field. Also, the MPB PMN–PT ceramics can present  $d_{33}$  piezoelectric coefficients as high as 720 pC/N (Kelly *et al.*, 1997); that is, higher than soft PZT, and significantly lower piezoelectric losses (Algueró *et al.*, 2005b). Furthermore, its mechanical response is linear across a range of stress for which PZT already presents Rayleigh-type behaviour associated with the movement of walls (Algueró *et al.*, 2003). These results strongly suggest that the contribution of ferroelectric/ferroelastic domain wall displacements to the electromechanical and mechanical responses of this material is significantly less important than in soft PZT and, thus, one can expect a smaller effect of the ceramic clamping on the linear coefficients, when the domain configuration changes with the decrease of size.

## 15.4 Processing of submicrometre- and nanostructured $\text{Pb}(\text{Mg}_{1/3}\text{Nb}_{2/3})\text{O}_3$ – $\text{PbTiO}_3$ ceramics

The processing of dense, submicrometre- and nanostructured ceramics requires the combination of techniques for the synthesis of very fine powders and sintering procedures that enhance densification but limit grain growth, basically involving the application of pressure. For instance, 93% density, ~35 nm grain size  $\text{BaTiO}_3$  ceramics have been processed by hot isostatic pressing (860 °C, 200 MPa in  $\text{N}_2$ ) of 10 nm particle size powders obtained by hydrolysis and decomposition (Guo *et al.*, 2005). Also, 97% density, ~30 nm grain size  $\text{BaTiO}_3$  ceramics have been processed by spark plasma sintering (1000 °C, 3 min) from 10–20 nm particle size powders by solution precipitation (Buscaglia *et al.*, 2006).

In our case, mechanosynthesis was used for obtaining  $(1-x)\text{PMN}-x\text{PT}$  nanocrystalline powders. This was done with a high-energy planetary mill and tungsten carbide milling media, by mechanochemical activation of a stoichiometric mixture of the oxides. Details of the procedure and of the mechanisms taking place during the activation can be found elsewhere (Kuscer *et al.*, 2006, 2007). The final powder consists of a major nanocrystalline perovskite phase, a ~30 wt% of amorphous phase fully depleted of  $\text{MgO}$ , and trace amounts of pyrochlore and crystalline  $\text{MgO}$ . Contamination levels were controlled below 50 and 600 ppm for Co and W, respectively. A deagglomeration treatment was finally carried out by attrition milling in isopropanol for 4 h. Particles with such a size distribution that the 10, 50 and 90 wt% were under 0.37, 0.84 and 5.49  $\mu\text{m}$ , respectively, were obtained. Coarse-grained ceramics of different compositions with high chemical homogeneity and crystallographic quality have been processed from these powders by sintering in  $\text{PbO}$  (Algueró *et al.*, 2006), and submicrometre grain size ceramics can be obtained with hot pressing (Algueró *et al.*, 2004).

XRD patterns for the 0.8PMN–0.2PT and 0.65PMN–0.35PT powders synthesised are shown in Fig. 15.1. Dense, coarse-grained 0.8PMN–0.2PT and 0.65PMN–0.35PT ceramics with a grain size of 4  $\mu\text{m}$  were obtained by sintering at 1200 °C in a  $\text{PbO}$  atmosphere, created by burying the pellets in  $\text{PbZrO}_3$  powder inside a closed alumina crucible. XRD patterns for these ceramics are shown in Fig. 15.2. Dense, submicrometre grain size ceramics of the same compositions with decreasing grain size approaching the nanoscale (~100 nm) were obtained by hot pressing at 60 MPa and decreasing temperatures from 1000 °C down to 700 °C. 1000 °C is the upper limit above which  $\text{PbO}$  volatilisation is significant and it is necessary to control the atmosphere. 700 °C is the lower limit, below which the residual pyrochlore in the powder cannot transform into the perovskite. The XRD patterns for the ceramics prepared by hot pressing are also shown in Fig. 15.2. In this

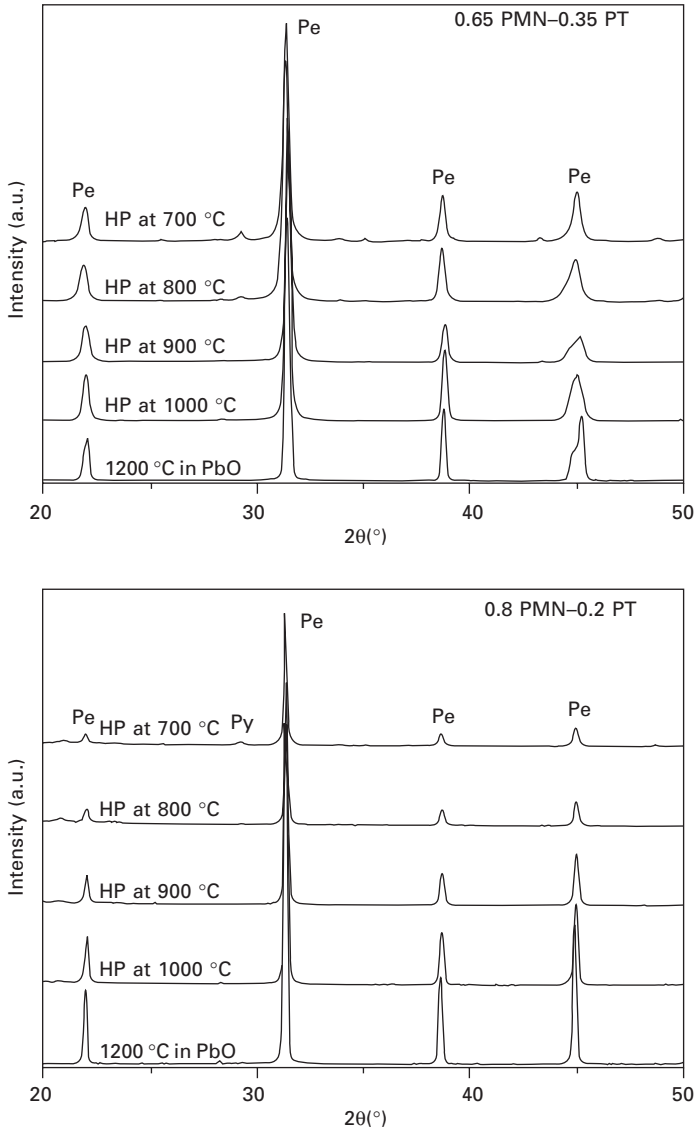


15.1 XRD patterns for the PMN-PT powders synthesised by mechanochemical activation, used for the subsequent processing of the ceramic materials with decreasing grain size (Pe: perovskite, Py: pyrochlore).

temperature interval, mostly single phase, dense ceramics are obtained at all temperatures as illustrated in Fig. 15.2 and 15.3. The density was evaluated from weight and dimension measurements, and from porosity levels obtained by quantitative image analysis of polished surfaces. Note that both techniques provided consistent trends with temperature, yet slightly lower values were obtained from the ceramic dimensions and weight. This is probably a consequence of some systematic error introduced when an ideal disc is assumed. Nevertheless, all ceramics studied here have closed porosity and a density well above 90%. Scanning force microscopy images of the polished and thermally etched surfaces of all the samples are shown in Fig. 15.4. Grain sizes of  $\sim 0.4$ ,  $0.2$ ,  $0.15$  and  $0.1$   $\mu\text{m}$  were obtained by hot pressing the  $0.8\text{PMN}-0.2\text{PT}$  powder at  $1000$ ,  $900$ ,  $800$  and  $700$   $^{\circ}\text{C}$ , respectively, and similar results were obtained for  $0.65\text{PMN}-0.35\text{PT}$ . The size effects on the macroscopic properties of this group of ceramic samples have been studied.

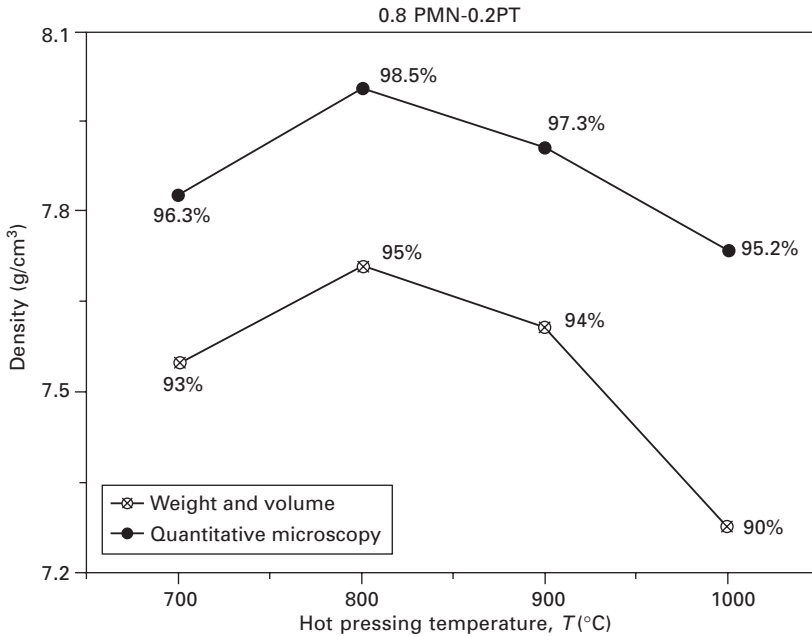
## 15.5 Size effects on the macroscopic properties of $0.8\text{Pb}(\text{Mg}_{1/3}\text{Nb}_{2/3})\text{O}_3-0.2\text{PbTiO}_3$

$0.8\text{PMN}-0.2\text{PT}$  is at the PMN edge of the MPB region. The phase transition between the room temperature ferroelectric phase and the high-temperature relaxor state has been recently described for coarse-grained ceramic samples processed from the powders synthesised by mechanochemical activation



15.2 XRD patterns for the PMN-PT ceramic materials processed from the mechano synthesised powders (Pe: perovskite, Py: pyrochlore). Sintering conditions aimed at obtaining decreasing grain sizes are indicated (HP: hot pressing).

(Algueró *et al.*, 2005a; Jiménez *et al.*, 2006). The material presents a transition between the monoclinic  $Cm$  ferroelectric phase and the non-ergodic relaxor state with well-defined, different transition ( $T_C^h = 71^\circ\text{C}$  and  $T_C^c = 61^\circ\text{C}$  on heating and cooling, respectively) and freezing ( $T_f = 77^\circ\text{C}$ ) temperatures.



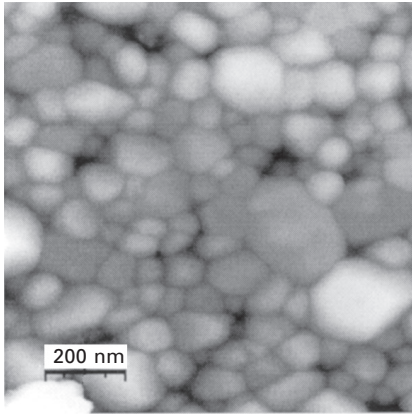
15.3 Density measured by two different techniques for the 0.8PMN-0.2PT ceramic materials processed by hot pressing the mechanosynthesised powders at decreasing temperatures.

The transition also presents thermal hysteresis in the kinetics that is much slower on cooling than on heating. This indicates that quite a sharp slowing down occurs in the temperature interval between the transition temperatures on cooling and heating.

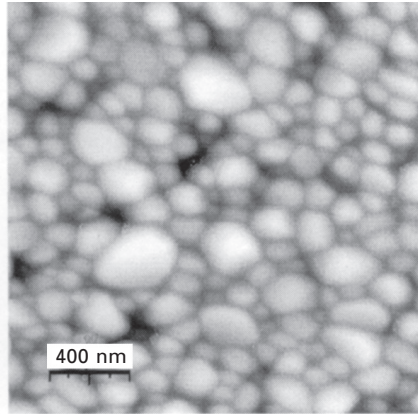
These features were established by studying the temperature dependence of the dielectric permittivity and the Young's modulus across the transition in combination with thermal expansion measurements. The dielectric permittivity measured on heating at five frequencies is shown in Fig. 15.5 for a ceramic with 4  $\mu\text{m}$  grain size. Note the sharp increase between 67 and 77  $^{\circ}\text{C}$ , and the relaxor-type characteristics above the latter temperature. This corresponds to the freezing temperature  $T_f$ , obtained by the fit of the frequency dependence of the temperature of the maximum dielectric permittivity,  $T_m$ , to the Vogel-Fulcher relationship, as shown in Fig. 15.6. The permittivity presents a clear thermal hysteresis, as illustrated in Fig. 15.7 for the same ceramics at 10 kHz. A sharp decrease is not observed on cooling at any temperature. The thermal hysteresis of the Young's modulus is shown in the same figure. The minima are associated with the phase transition, which is much sharper on heating than on cooling, reflecting the slowing down of the phase transition within the temperature interval between the transition on heating and cooling: 71 and 61  $^{\circ}\text{C}$ . The slowing down can be interpreted



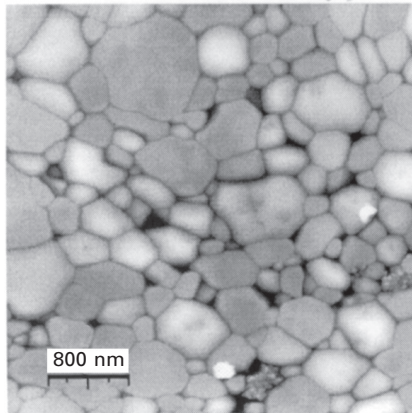
## 0.8 PMN-0.2PT



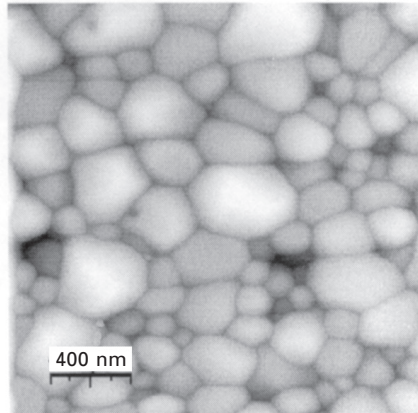
(a) HP at 700 °C



(a) HP at 800 °C



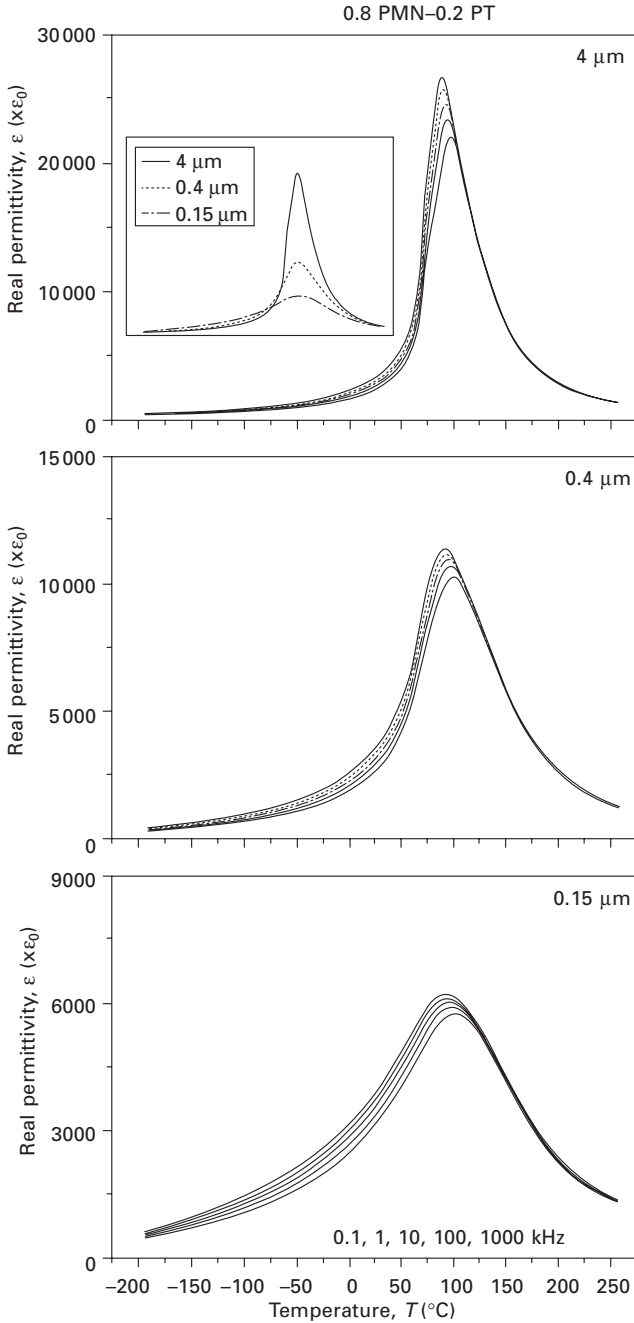
(d) HP at 1000 °C



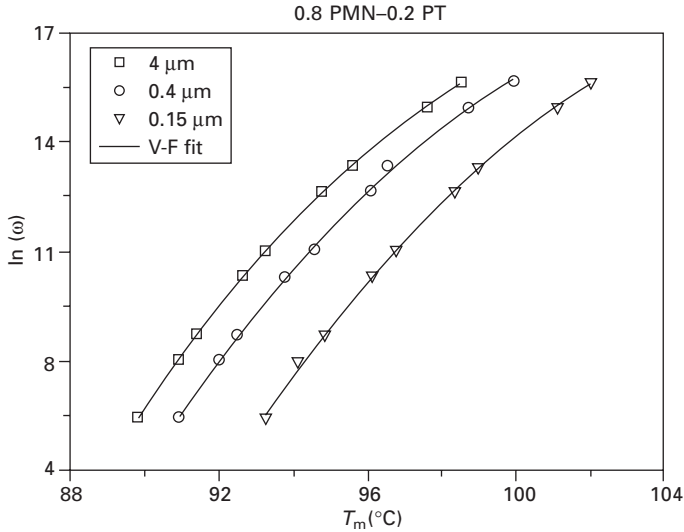
(c) HP at 900 °C

15.4 Atomic force microscopy images of polished and thermally etched surfaces of the 0.8PMN-0.2PT ceramic materials processed by hot pressing (HP) the mechanosynthesised powders at decreasing temperatures.

within the two-stage model for the development of ferroelectric long-range order in relaxor systems, as recently proposed by Ye *et al.* (2003). In the first stage, PNRs start condensing at high temperature. Their number and size increase as the temperature is decreased until the temperature of the phase transition is reached. Then, the second stage begins that is characterised by the onset of ferroelectric fluctuations. The model proposes that the kinetics of the transition is controlled by the number of PNRs at the onset of the ferroelectric fluctuations, which depends on temperature. Therefore, the slower the kinetics, the lower the temperature of the transition. The thermal hysteresis



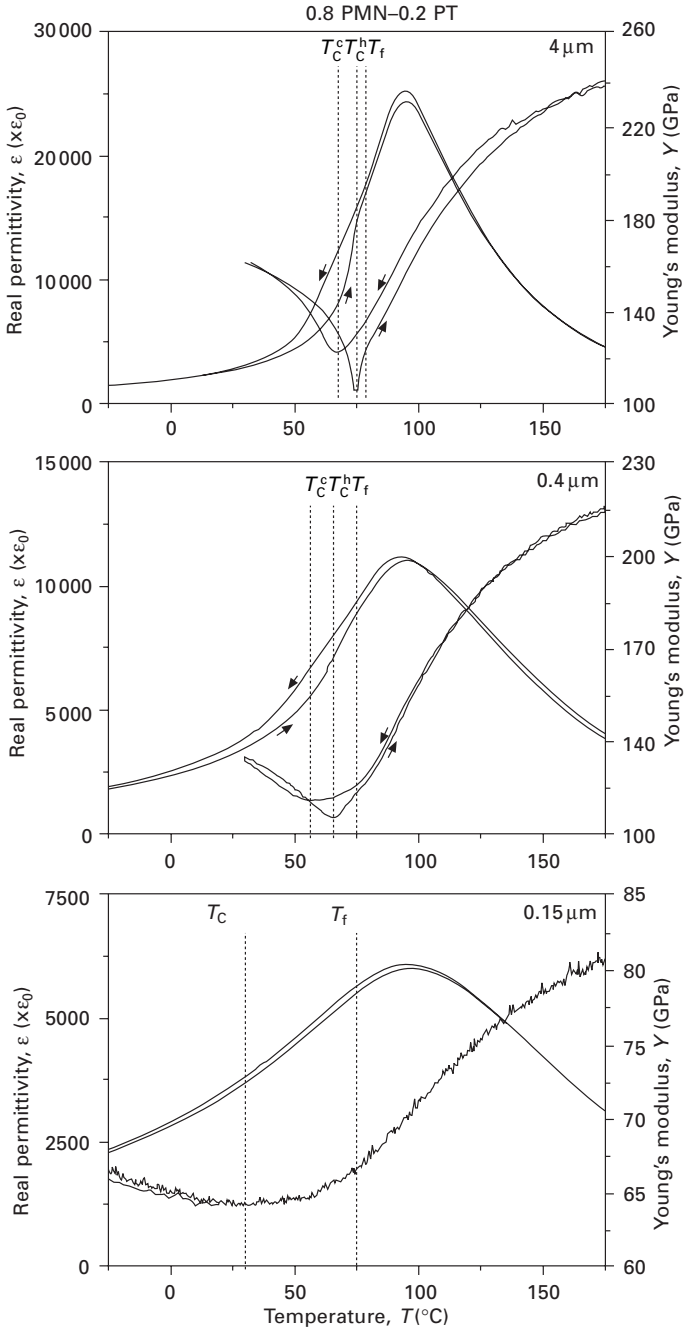
15.5 Dielectric permittivity measured on heating at five frequencies for 0.8PMN-0.2PT ceramics with decreasing grain size. Curves at 10 kHz are directly compared in the inset.



15.6 Temperature of the maximum dielectric permittivity,  $T_m$ , as a function of frequency, and fit to the Vogel–Fulcher relationship for the 0.8PMN–0.2PT ceramics with decreasing grain size.

in the kinetics of the transition for 0.8PMN–0.2PT would then be a consequence of the hysteresis in the temperature of the transition, and of the transition being slowed down in this interval.

The same macroscopic properties for ceramics with 0.4 and 0.15  $\mu\text{m}$  grain size are also shown in Figs 15.5–15.7. Note the absence of dielectric dispersion above  $T_m$  for the submicrometre size ceramics (see Fig. 15.5). This indicates the absence of Maxwell–Wagner type polarisation at the grain boundaries, which is associated with the presence of segregated second phases or defects (Buscaglia *et al.*, 2006). The permittivity still presents a sharp, yet less pronounced, increase on heating for the ceramic with a grain size of 0.4  $\mu\text{m}$ , but not for the sample with a size of 0.15  $\mu\text{m}$ . A direct comparison of the permittivity values of all materials with different grain sizes is given in the inset of Fig. 15.5 at 10 kHz. The broadening and depression of the maximum with the decrease in size is similar to that observed in BaTiO<sub>3</sub> (Zhao *et al.*, 2004) and is thus most probably a boundary effect. Note that ceramics present similar permittivity values at 250 °C in spite of the large difference in the density of boundaries, which further indicates the good quality of the materials processed. The high-temperature relaxor state exists for all sizes. Fits to the Vogel–Fulcher relationship for the submicrometre-structured materials are also given in Fig. 15.6. The parameters of the fits are given in Table 15.1. No size effect was observed on either the freezing temperature or the activation energy. The thermal hysteresis of permittivity and Young’s modulus for the ceramics with submicrometre grain sizes are also shown in Fig. 15.7. The



15.7 Thermal hysteresis of the dielectric permittivity at 10 kHz and Young's modulus across the transition for the 0.8PMN-0.2PT ceramics with decreasing grain size.

Table 15.1 Parameters of the Vogel–Fulcher behaviour for the relaxor state in the PMN–PT system

	Size	$T_f(^{\circ}\text{C})$	$E_a(\text{meV})$
PMN <sup>1</sup>	Single crystal	–56	79
0.9PMN–0.1PT <sup>2</sup>	Ceramic	18	41
0.8PMN–0.2PT <sup>3</sup>	4 $\mu\text{m}$	77	30
	0.4 $\mu\text{m}$	75	37
	0.15 $\mu\text{m}$	75	44
0.65PMN–0.35PT	0.15 $\mu\text{m}$	167	3

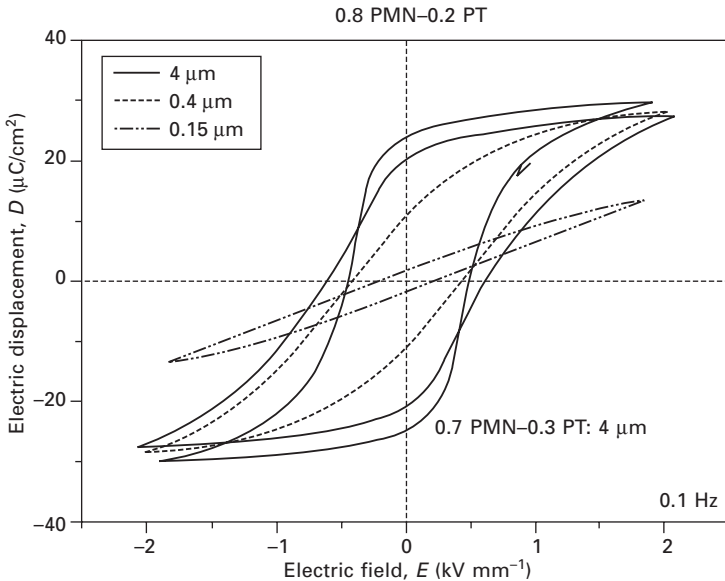
<sup>1</sup>Viehland *et al.* (1991).

<sup>2</sup>Viehland *et al.* (1990).

<sup>3</sup>Jiménez *et al.* (in preparation).

material with 0.4  $\mu\text{m}$  presents the transition at 65 and 56  $^{\circ}\text{C}$  on heating and cooling, respectively. Therefore, a shift towards lower temperatures has occurred. There is still hysteresis in the sharpness of Young's modulus minima and, so, in the kinetics of the transition. This allows one to narrow the temperature interval in which the slowing down takes place, from 71–61 to 65–61  $^{\circ}\text{C}$ . The material with 0.15  $\mu\text{m}$  presents a broad mechanical anomaly at  $\sim 30^{\circ}\text{C}$  with negligible hysteresis, neither in the temperatures nor in its sharpness. This suggests that the transition has further shifted down to lower temperatures, and that its kinetics is always slow. This is consistent with the slowing down occurring in the 65–61  $^{\circ}\text{C}$  interval, which is therefore size independent. The size effect is thus to decrease the transition temperature, and as a consequence, there is a size range between 0.4 and 0.15  $\mu\text{m}$ , for which the transition is shifted below the temperature of its slowing down, between 65 and 61  $^{\circ}\text{C}$ , and the kinetics becomes very slow (Jiménez *et al.*, in preparation).

The room temperature ferroelectric hysteresis loops for ceramics with 4, 0.4 and 0.15  $\mu\text{m}$  grain size are shown in Fig. 15.8. The saturation polarisation for the ceramics with 4 and 0.4  $\mu\text{m}$  is similar, 25–22  $\mu\text{C}/\text{cm}^2$ , though the remnant polarisation is significantly decreased from 21 to 11  $\mu\text{C}/\text{cm}^2$  with size decrease. The material with 0.15  $\mu\text{m}$  only presents incipient switching. The room temperature phases have been studied by Rietveld analysis of XRD data. The agreement factors of the Rietveld analysis along with the cell parameters are given in Table 15.2. Only those for  $Cm$  monoclinic and  $R3m$  rhombohedral phases are included because they always gave the best factors, though monoclinic  $Pm$ , orthorhombic  $Bmm2$ , tetragonal  $P4mm$ , cubic  $Pm3m$ , and phase mixing were also considered. The Rietveld results indicate that ceramics with 4 and 0.4  $\mu\text{m}$  are monoclinic, while that with 0.15  $\mu\text{m}$  is rhombohedral. The spontaneous polarisation was calculated from the Rietveld results (errors between 5 and 29  $\mu\text{C}/\text{cm}^2$ ) and values of 58 with a dispersion of 12  $\mu\text{C}/\text{cm}^2$  were obtained with no size dependence (Carreaud *et al.*, 2006).



15.8 Room temperature ferroelectric hysteresis loops for the 0.8PMN-0.2PT ceramics with decreasing grain size. The loop for a coarse-grained 0.7PMN-0.3PT material is included for comparison.

This indicates that the size effect on the saturation and remnant polarisation is associated with the domain configuration rather than with the spontaneous polarisation. Domain size that must be strongly linked with the kinetics of the relaxor to ferroelectric transition would, thus, strongly influence ferroelectric switching, this being hindered by small sizes (Jiménez *et al.*, in preparation). The increase of the monoclinic domain size has been proposed to be the origin of the higher remnant polarisation for coarse-grained 0.7PMN-0.3PT (also included in Fig. 15.8) as compared with 0.8PMN-0.2PT ceramics, both with  $C_m$  symmetry (Jiménez *et al.*, 2006).

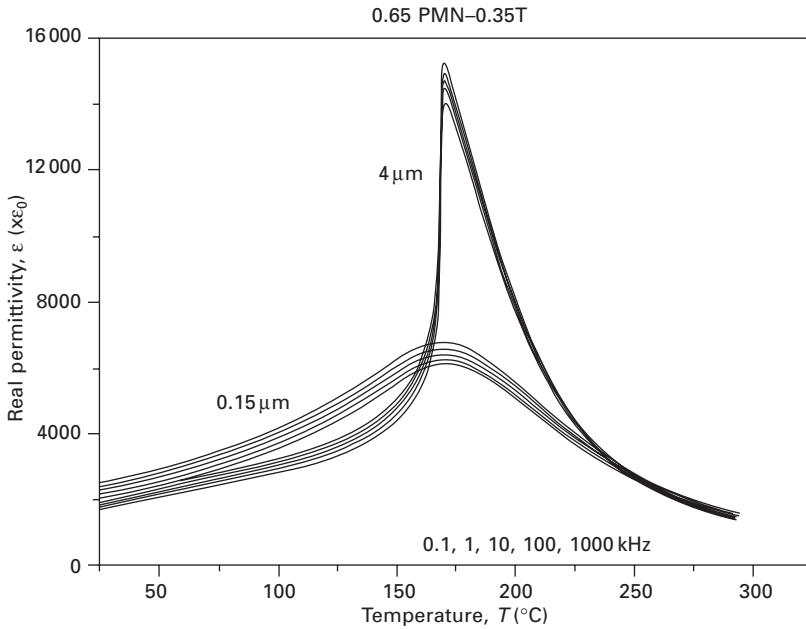
### 15.6 Size effects on the macroscopic properties of $0.65\text{Pb}(\text{Mg}_{1/3}\text{Nb}_{2/3})\text{O}_3-0.35\text{PbTiO}_3$

0.65PMN-0.35PT is located at the core of the MPB region, and it is the composition for which the electromechanical properties are better for bulk ceramics. The temperature dependence of permittivity measured on heating at five frequencies for a coarse-grained ceramic with  $4\ \mu\text{m}$  grain size is shown in Fig. 15.9. A well-defined anomaly typical of a first-order ferroelectric phase transition is observed. Hysteresis is also illustrated for the reciprocal permittivity at 10 kHz. Transition occurs at 169 and 164 °C on heating and

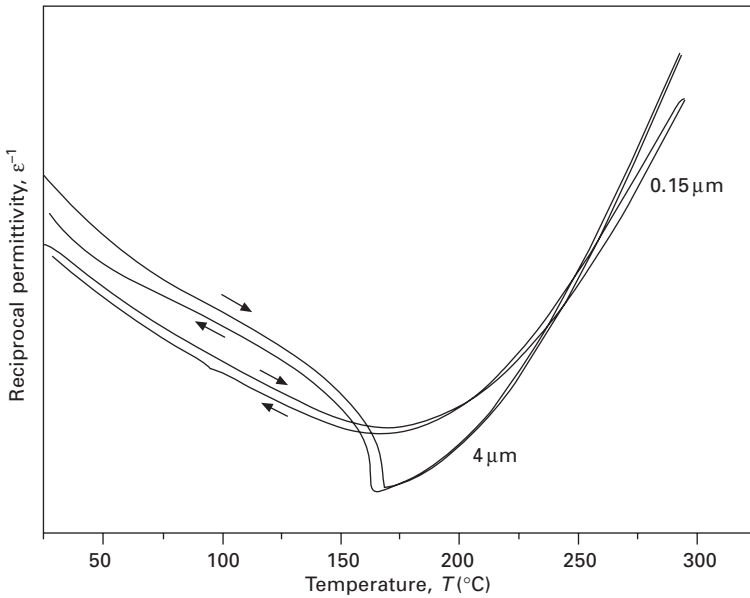
Table 15.2 Agreement factors and cell parameters of the Rietveld analysis of XRD data for PMN–PT ceramics

Composition	Size	Symmetry	$R_{wp}$	Goodness of fit	$R_{Bragg}$	
0.8PMN–0.2PT (Carreaud <i>et al.</i> , 2006)	4 $\mu\text{m}$	<i>R3m</i>	6.97	1.44	5.22	
		<i>a</i> = 4.0291 $\text{\AA}$ , $\beta$ = 89.92°				
		<i>Cm</i>	6.71	1.39	2.73	
	0.4 $\mu\text{m}$	<i>R3m</i>	<i>a</i> = 5.6991 $\text{\AA}$ , <i>b</i> = 5.6928 $\text{\AA}$ , <i>c</i> = 4.0303 $\text{\AA}$ , $\beta$ = 89.88°			
				6.22	1.33	4.26
			<i>a</i> = 4.0284 $\text{\AA}$ , $\beta$ = 89.97°			
		0.15 $\mu\text{m}$	<i>Cm</i>	6.15	1.31	2.70
			<i>a</i> = 5.6982 $\text{\AA}$ , <i>b</i> = 5.6953 $\text{\AA}$ , <i>c</i> = 4.0289 $\text{\AA}$ , $\beta$ = 89.94°			
			<i>R3m</i>	7.07	1.35	2.57
	0.65PMN–0.35PT (Algueró <i>et al.</i> , 2007)	4 $\mu\text{m}$	<i>a</i> = 4.0300 $\text{\AA}$ , $\beta$ = 89.99°			
			<i>Cm</i>	7.15	1.36	2.97
			<i>a</i> =5.6983 $\text{\AA}$ , <i>b</i> =5.6980 $\text{\AA}$ , <i>c</i> =4.0311 $\text{\AA}$ , $\beta$ =89.99°			
0.15 $\mu\text{m}$		<i>Pm + P4mm</i>	5.50	1.19	4.25	
		89/11 %				
		<i>Pm</i> : <i>a</i> = 4.015 $\text{\AA}$ , <i>b</i> = 4.001 $\text{\AA}$ , <i>c</i> = 4.031 $\text{\AA}$ , $\beta$ = 89.85°				
		<i>P4mm</i> : <i>a</i> = 4.001 $\text{\AA}$ , <i>c</i> = 4.046 $\text{\AA}$				
		<i>Pm + P4mm</i>	5.42	1.23	3.23	
		95/5 %				
0.15 $\mu\text{m}$		<i>Pm</i> : <i>a</i> = 4.016 $\text{\AA}$ , <i>b</i> = 4.012 $\text{\AA}$ , <i>c</i> = 4.019 $\text{\AA}$ , $\beta$ = 89.92°				
		<i>P4mm</i> : <i>a</i> = 4.005 $\text{\AA}$ , <i>c</i> = 4.024 $\text{\AA}$				

cooling, respectively. Note the deviation from the Curie–Weiss law above the transition temperature that indicates the presence of a high-temperature relaxor state. Relaxor behaviour has been observed up to 0.5PMN–0.5PT (Bokov *et al.*, 2005). The same results for a ceramic with a grain size of 0.15  $\mu\text{m}$  are also shown in the figure. The first-order type anomaly has vanished and, instead, the relaxor type behaviour is observed in agreement with previous results (Carreaud *et al.*, 2005). The parameters of the fit to the Vogel–Fulcher relationship are included in Table 15.1. A freezing temperature of 167 °C is obtained. These results are analogous to those obtained for 0.8PMN–0.2PT, which were associated with the decrease of the transition temperature below that at which the kinetics of the transition slows down. This suggests that the temperature at which the transition slows down is higher for 0.65PMN–0.35PT and is, thus, composition dependent. According to Ye’s model, this is the temperature at which the volume (number and size) of PNRs reaches a certain threshold that hinders ferroelectric fluctuations triggered by the phase transition, and slows down its kinetics. The PNRs in PMN have been observed to coarsen with the addition of PT (Hilton *et al.*, 1989). This is consistent with the threshold volume to occur at a higher temperature for 0.65PMN–0.35PT than for 0.8PMN–0.2PT, as suggested by the results (Algueró *et al.*, 2007).



(a)

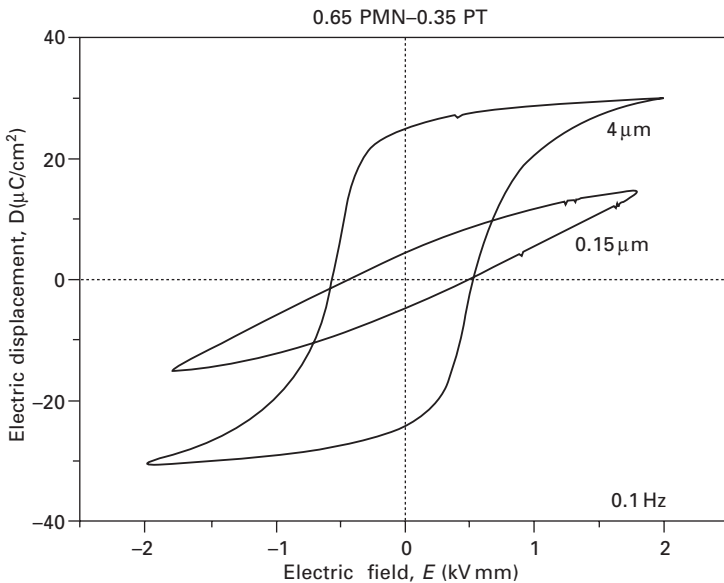


(b)

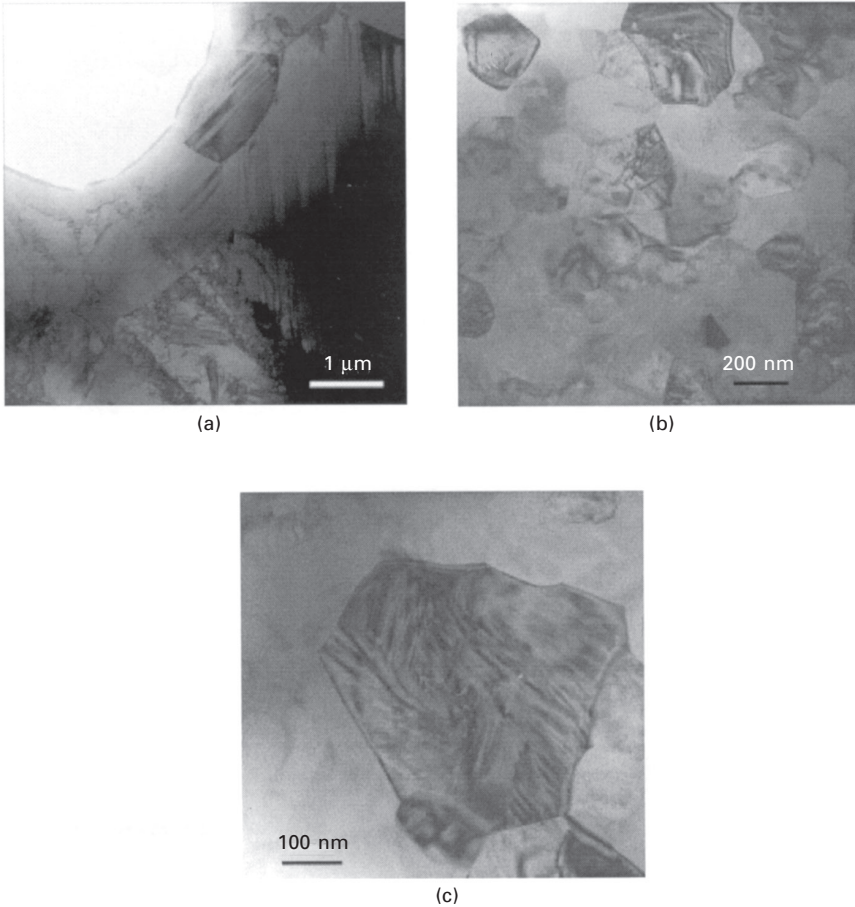
15.9 (a) Dielectric permittivity measured on heating at five frequencies for 0.65PMN-0.35PT ceramics with decreasing grain size. (b) Thermal hysteresis of the reciprocal permittivity at 10 kHz for the same ceramics.



Ferroelectric hysteresis loops for the MPB PMN–PT ceramics with 4 and 0.15  $\mu\text{m}$  grain size are shown in Fig. 15.10. High values of saturation and remnant polarisation – 28 and 25  $\mu\text{C}/\text{cm}^2$ , respectively – were obtained for the coarse-grained ceramic, while only incipient switching is observed for the 0.15  $\mu\text{m}$  material. The room temperature phases were also studied by Rietveld analysis of XRD data. Best agreement factors were obtained for a mixture of  $Pm$  monoclinic and  $P4mm$  phases, and are given in Table 15.2 along with the cell parameters. Rietveld results indicate that both ceramics with 4 and 0.15  $\mu\text{m}$  present coexistence of monoclinic and tetragonal phases, with the amount of tetragonal phase decreasing from 11 to 5% with the size decrease. Domain configuration as a function of size was studied by transmission electron microscopy (TEM). Images for the two ceramics are shown in Fig. 15.11. Three types of domains – micrometre-sized simple lamellar domains, wedge-type domains with the same size, and submicrometre/nanometre sized crosshatched domains – exist in the coarse-grained material, while only crosshatched domains are present in the submicrometre material. The latter domains, also referred to as tweedlike, have been proposed to be precursors of polar long-range order (Viehland *et al.*, 1995), which has thus partially developed for the 4  $\mu\text{m}$  ceramic but not for the 0.15  $\mu\text{m}$  material. This is consistent with the size effect on ferroelectric switching being associated with the decrease of the monoclinic domain size. The decrease would again



15.10 Room temperature ferroelectric hysteresis loops for the 0.65PMN–0.35PT ceramics with decreasing grain size.



15.11 TEM images for the 0.65PMN-0.35PT ceramics with (a) 4 μm and (b, c) 0.15 μm grain size. (c) Illustration of typical crosshatched domains.

be a consequence of the decrease of the transition temperature below that of the slowing down of its kinetics (Algueró *et al.*, 2007).

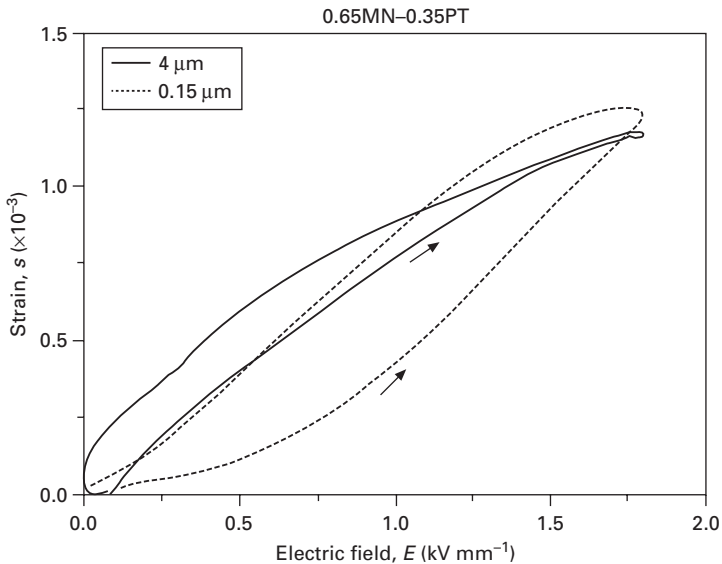
Poling was carried out at 3 kV mm<sup>-1</sup> and 150 °C for 15 min. Ceramics were then cooled to 50 °C with the field kept on. A  $d_{33}$  of  $525 \pm 15$  and  $290 \pm 15$  pC/N was achieved for the materials with a size of 4 and 0.15 μm, respectively, which was measured with a Berlincourt meter. It is remarkable that the 0.15 μm ceramic presents a piezoelectric coefficient as high as ~300 pC/N, in spite of the limited ferroelectric switching observed at room temperature. This could be a consequence of the high field under which the material undergoes the relaxor to ferroelectric transition during the poling, which might speed up the kinetics of the transition and result in a larger domain size. The room temperature strain under unipolar field is shown in

Fig. 15.12. The electromechanical behaviour for the coarse-grained material is typical of a PZT-based ceramic, with an initial high slope of  $\sim 1100$  pC/N associated with extensive domain wall movement and hysteresis. The slope continuously decreases when the field increases down to a saturation value of  $\sim 350$  pC/N at high field, when hysteresis vanishes. Strain under field for the submicrometre-structured material is quite different. Though the initial slope is low, strain readily increases, so that values at high field that are comparable to those of the coarse-grained material;  $\sim 1.2 \times 10^{-3}$  (average  $d_{33}$  of  $\sim 700$  pC/N) are obtained. Saturation is not observed and large hysteresis exists. These characteristics that somehow resemble those of electrostrictive materials, yet hysteretic, are most probably linked to the growth of the monoclinic domains under the field and the change in their configuration from crosshatched to micrometre-sized bands.

These results show that the MPB PMN–PT ceramics with  $0.15 \mu\text{m}$  grain size are highly sensitive materials with low field piezoelectric coefficients of  $\sim 300$  pC/N, and high field-effective coefficients of  $\sim 700$  pC/N. Thus, this MPB material presents promising down scaling properties.

## 15.7 Final remarks and future trends

The study of the macroscopic properties in combination with advanced structural analysis and polar domain characterisation has allowed us to



15.12 Room temperature strain under high unipolar field for the 0.65PMN–0.35PT ceramics with decreasing grain size.

characterise and discuss the size effects in the PMN–PT system. In the range investigated, which spanned the submicrometre range approaching the nanoscale (~100 nm), the size effects seem to be strongly linked to the mechanisms of development of polar long-range order and kinetic aspects. The primary size effect is the shift of the ferroelectric-relaxor transition towards lower temperatures, and large effects on the properties turn up when it is shifted below the temperature at which the transition slows down. Once this occurs, the kinetics becomes slow and as a result, the size of the monoclinic domains decreases and the ferroelectric switching is hindered. This is very different from the case of PZT, for which size effects mainly originate from the clamping of the ferroelectric/ferroelastic domain walls. Despite these effects, high-sensitivity PMN–PT materials with a grain size of 0.15  $\mu\text{m}$  can be obtained by the application of a high electric field during the transition from the relaxor to the ferroelectric state.

These results are not only relevant for bulk ceramic technology, but also for thick and thin films in Si-integrated technologies. As a matter of fact, the PMN–PT films prepared on Si-based substrates by chemical solution deposition show very low retention of polarisation, i.e. saturation polarisation much higher than remnant polarisation, as compared with bulk ceramics of the same compositions (Park *et al.*, 2001, Calzada, 2007).

Interest in alternative (to PZT) MPB materials is high. Lead-free, niobate-based MPB ceramic materials have recently been developed as an environmentally friendly alternative to PZT (Saito *et al.*, 2004), and novel, high Curie temperature MPB systems based on Bi perovskites are under intense research for high-temperature applications (Zhang *et al.*, 2003). The behaviour of the properties on down-scaling, not only the properties themselves, needs to be considered when novel materials are devised and assessed. This involves understanding the size effects.

## 15.8 References

- Algueró M, Jiménez B, Pardo L (2003), 'Rayleigh type behaviour of the Young's modulus of unpoled ferroelectric ceramics and its dependence on temperature', *Appl. Phys. Lett.*, **83**(13), 2641–3.
- Algueró M, Alemany C, Jiménez B, Holc J, Kosec M, Pardo L (2004), 'Piezoelectric PMN–PT ceramics from mechanochemically activated precursors', *J. Eur. Ceram. Soc.*, **24**, 937–40.
- Algueró M, Jiménez B, Pardo L (2005a), 'Transition between the relaxor and ferroelectric states for  $(1-x)\text{Pb}(\text{Mg}_{1/3}\text{Nb}_{2/3})\text{O}_3-x\text{PbTiO}_3$  with  $x = 0.2$  and  $0.3$  polycrystalline aggregates', *Appl. Phys. Lett.*, **87**, 082910, 1–3.
- Algueró M, Alemany C, Pardo L, Pham-Thi M (2005b), 'Piezoelectric resonances, linear coefficients and losses of morphotropic phase boundary  $\text{Pb}(\text{Mg}_{1/3}\text{Nb}_{2/3})\text{O}_3\text{--PbTiO}_3$  ceramics', *J. Am. Ceram. Soc.*, **88**(10), 222780–7.
- Algueró M, Moure A, Pardo L, Holc J, Kosec M (2006), 'Processing by mechanosynthesis

- and properties of piezoelectric  $\text{Pb}(\text{Mg}_{1/3}\text{Nb}_{2/3})\text{O}_3\text{-PbTiO}_3$  with different compositions', *Acta Mater.*, **54**, 501–11.
- Algueró M, Jiménez R, Ricote J, Ramos P, Carreaud J, Dkhil B, Kiat J M, Holc J, Kosec M. (2007), 'Size effect in morphotropic phase boundary  $\text{Pb}(\text{Mg}_{1/3}\text{Nb}_{2/3})\text{O}_3\text{-PbTiO}_3$  ceramics'. *Appl. Phys. Lett.*, **91**, 112905, 1–3.
- Arlt G (1990a) 'Twinning in ferroelectric and ferroelastic ceramics: stress relief', *J. Mater. Sci.*, **25**(6), 2655–66.
- Arlt G (1990b), 'The influence of microstructure on the properties of ferroelectric ceramics', *Ferroelectrics*, **104**, 217–27.
- Arlt G, Sasko P (1980), 'Domain configuration and equilibrium size of domains in  $\text{BaTiO}_3$  ceramics', *J. Appl. Phys.*, **51**(9), 4956–60.
- Arlt G, Hennings D, Dewith G (1985), Dielectric properties of fine grained barium titanate ceramics', *J. Appl. Phys.*, **58**(4), 1619–25.
- Arndt H, Sauerbier F, Schmidt G, Shebanov L A (1988), 'Field induced phase transition in  $\text{PbMg}_{1/3}\text{Nb}_{2/3}\text{O}_3$  single crystals', *Ferroelectrics*, **79**, 439–42.
- Bokov A A, Luo H, Ye Z G (2005), 'Polar nanodomains and relaxor behaviour in  $(1-x)\text{Pb}(\text{Mg}_{1/3}\text{Nb}_{2/3})\text{O}_3\text{-xPbTiO}_3$  crystals with  $x = 0.3\text{--}0.5$ ', *Mater. Sci. Eng. B*, **120**, 206–9.
- Bratkovsky A M, Levanyuk A P (2005), 'Smearing of phase transition due to a surface effect or a bulk inhomogeneity in ferroelectric nanostructures', *Phys. Rev. Lett.*, **94**, 107601, 1–4.
- Burns G, Dacol F H (1983), 'Crystalline ferroelectrics with glassy polarisation behaviour', *Phys. Rev. B*, **28**(5), 2527–30.
- Buscaglia M T, Viviani M, Buscaglia V, Mitoseriu L, Testino A, Nanni P, Zhao Z, Nygren M, Harneaga C, Piazza D, Galassi (2006), 'High dielectric constant and frozen macroscopic polarisation in dense nanocrystalline  $\text{BaTiO}_3$  ceramics', *Phys. Rev. B*, **73**, 064114, 1–10.
- Calvarin G, Husson E, Ye Z G (1995), 'X-ray study of the electric field induced phase transition in single crystal  $\text{PbMg}_{1/3}\text{Nb}_{2/3}\text{O}_3$ ', *Ferroelectrics*, **165**(3–4), 349–58.
- Calzada M L, Algueró M, Ricote J, Santos A, Pardo L (2007), 'Preliminary results on sol-gel processing of <100> oriented  $\text{Pb}(\text{Mg}_{1/3}\text{Nb}_{2/3})\text{O}_3\text{-PbTiO}_3$  thin films using diol-based solutions', *J. Sol-Gel Sci. Technol.* **42**, 331, 6.
- Carreaud J, Gemeiner P, Kiat J M, Dkhil B, Bogicevic C, Rojac T, Malic B (2005), 'Size driven relaxation and polar states in  $\text{PbMg}_{1/3}\text{Nb}_{2/3}\text{O}_3$  based systems'. *Phys. Rev. B*, **72**, 174115, 1–6.
- Carreaud J, Kiat J M, Dkhil B, Algueró M, Ricote J, Jiménez R, Holc J, Kosec M (2006), 'Monoclinic morphotropic phase and grain size induced polarisation rotation in  $\text{Pb}(\text{Mg}_{1/3}\text{Nb}_{2/3})\text{O}_3\text{-PbTiO}_3$ ', *Appl. Phys. Lett.*, **89**, 252906, 1–3.
- Choi S W, Shrout T R, Jang S J, Bhalla A S (1989), 'Dielectric and pyroelectric properties in the  $\text{Pb}(\text{Mg}_{1/3}\text{Nb}_{2/3})\text{O}_3\text{-PbTiO}_3$  system', *Ferroelectrics*, **100**, 29–38.
- Cross L E (1994), 'Relaxor ferroelectrics: an overview', *Ferroelectrics*, **15**, 305–20.
- De Mathan N, Husson E, Calvarin G, Gavarrí J R, Hewat A W, Morrel A (1991), 'A structural model for the relaxor  $\text{PbMg}_{1/3}\text{Nb}_{2/3}\text{O}_3$ ', *J. Phys.: Condens. Matter*, **3**, 8159–71.
- Demartin M, Damjanovic D (1996), 'Dependence of the direct piezoelectric effect in coarse and fine grain barium titanate ceramics on dynamic and static pressure'. *Appl. Phys. Lett.*, **68**, 3046–8.
- Deng X, Wang X, Wen H, Chen L, Chen L, Li L (2006), 'Ferroelectric properties of nanocrystalline barium titanate ceramics', *Appl. Phys. Lett.*, **88**, 252905–13.

- Dkhil B, Kiat J M, Calvarin G, Baldinozzi G, Vakhrushev S B, Suard E (2002), 'Local and long range order in the relaxor-ferroelectric compounds  $\text{Pb}(\text{Mg}_{1/3}\text{Nb}_{2/3})\text{O}_3$  and  $\text{PbMg}_{0.3}\text{Nb}_{0.6}\text{Ti}_{0.1}\text{O}_3$ ', *Phys. Rev. B*, **65**, 024104, 1–8.
- Gentil S, Damjanovic D, Setter N (2004), ' $\text{Pb}(\text{Mg}_{1/3}\text{Nb}_{2/3})\text{O}_3$  and  $(1-x)\text{Pb}(\text{Mg}_{1/3}\text{Nb}_{2/3})\text{O}_3-x\text{PbTiO}_3$  relaxor ferroelectric thick films: processing and electrical characterization', *J. Electroceram.*, **12**(3), 151–61.
- Guo R, Cross L E, Park S E, Noheda B, Cox D E, Shirane G (2000), 'Origin of the high piezoelectric response in  $\text{PbZr}_{1-x}\text{Ti}_x\text{O}_3$ ', *Phys. Rev. Lett.*, **84**(23), 5423–6.
- Guo X, Pithan C, Ohly C, Jia C L, Dornseiffer J, Haegel F H (2005), 'Enhancement of p-type conductivity in nanocrystalline  $\text{BaTiO}_3$  ceramics', *Appl. Phys. Lett.*, **86**, 082110, 1–3.
- Haumont R, Dkhil B, Kiat J M, Al-Barakaty H, Dammak H, Bellaiche L (2003), 'Morphotropic phase boundary of heterovalent perovskite solid solutions: experimental and theoretical investigation of  $\text{PbSc}_{1/2}\text{Nb}_{1/2}\text{O}_3-\text{PbTiO}_3$ ', *Phys. Rev. B* **68** 014114, 1–10.
- Hilton A D, Randall C A, Barber D J, Shrout T R (1989), 'TEM studies of  $\text{Pb}(\text{Mg}_{1/3}\text{Nb}_{2/3})\text{O}_3-\text{PbTiO}_3$  ferroelectric relaxors', *Ferroelectrics*, **93**, 379–86.
- Hungría T, Algueró M, Hungría A B, Castro A (2005), 'Dense fine grained  $\text{Ba}_{1-x}\text{Sr}_x\text{TiO}_3$  ceramics prepared by the combination of mechanosynthesized powders and spark plasma sintering'. *Chem. Mater.*, **17**, 6205–12.
- Jiménez R, Jiménez B, Carreaud J, Kiat J M, Dkhil B, Holc J, Kosec M, Algueró M (2006), 'The transition between the ferroelectric and relaxor states for  $0.8\text{Pb}(\text{Mg}_{1/3}\text{Nb}_{2/3})\text{O}_3-0.2\text{PbTiO}_3$  ceramics', *Phys. Rev. B*, **74** 184106, 1–8.
- Jiménez R, Ricote J, Amorín H, Carreaud J, Kiat J M, Dkhil B, Holc J, Kosec M, Algueró M (in preparation), 'Size effect in the transition between the ferroelectric and relaxor states for  $0.8\text{Pb}(\text{Mg}_{1/3}\text{Nb}_{2/3})\text{O}_3-0.2\text{PbTiO}_3$  ceramics' (provisional title).
- Kelly J, Leonard M, Tantigate C, Safari A (1997), 'Effect of composition on the electromechanical properties of  $(1-x)\text{Pb}(\text{Mg}_{1/3}\text{Nb}_{2/3})\text{O}_3-x\text{PbTiO}_3$  ceramics', *J. Am. Ceram. Soc.*, **80**(4) 957–64.
- Kiat J M, Uesu Y, Dkhil B, Matsuda M, Malibert C, Calvarin G (2002), 'Monoclinic structure of unpoled morphotropic high piezoelectric PMN–PT and PZN–PT compounds', *Phys. Rev. B*, **65**, 064106, 1–4.
- Kuscer D, Holc J, Kosec M (2006), 'Mechanosynthesis of lead magnesium niobate ceramics', *J. Am. Ceram. Soc.*, **89**(10) 3081–88.
- Kuscer D, Holc J, Kosec M (2007), 'The formation of  $0.65\text{Pb}(\text{Mg}_{1/3}\text{Nb}_{2/3})\text{O}_3-0.35\text{PbTiO}_3$  using a high energy milling process', *J. Am. Ceram. Soc.*, **90**(1) 29–35.
- Kwon S, Sabolsky E M, Messing G L, Trolrier-McKinstry S (2005), 'High strain,  $\langle 001 \rangle$  textured  $0.675\text{Pb}(\text{Mg}_{1/3}\text{Nb}_{2/3})\text{O}_3-0.325\text{PbTiO}_3$  ceramics: templated grain growth and piezoelectric properties', *J. Am. Ceram. Soc.*, **88**(2), 312–17.
- Li S, Eastman J A, Vetrone J M, Foster C M, Newham R E, Cross L E (1997), 'Dimension and size effects in ferroelectrics', *Jpn. J. Appl. Phys.*, **36**, 5169–74.
- Noblanc O, Gaucher P, Calvarin G (1996), 'Structural and dielectric studies of  $\text{Pb}(\text{Mg}_{1/3}\text{Nb}_{2/3})\text{O}_3-\text{PbTiO}_3$  ferroelectric solid solutions around the morphotropic phase boundary', *J. Appl. Phys.*, **79**, 4291–7.
- Noheda B, Gonzalo J A, Cross L E, Guo R, Park S E, Cox D E, Shirane G (2000), 'Tetragonal to monoclinic phase transition in a ferroelectric perovskite: the structure of  $\text{PbZr}_{0.52}\text{Ti}_{0.48}\text{O}_3$ ', *Phys. Rev. B*, **61**(13), 8687–95.
- Noheda B, Cox D E, Shirane G, Park S E, Cross L E, Zhong Z (2001), 'Polarisation rotation via a monoclinic phase in the piezoelectric  $92\%\text{Pb}(\text{Zn}_{1/3}\text{Nb}_{2/3})\text{O}_3-8\%\text{PbTiO}_3$ ', *Phys. Rev. Lett.*, **86**(17), 3891–4.

- Noheda B, Cox D E, Shirane G, Gao J, Ye Z G (2002), 'Phase diagram of the ferroelectric-relaxor  $(1-x)\text{Pb}(\text{Mg}_{1/3}\text{Nb}_{2/3})\text{O}_3-x\text{PbTiO}_3$ ', *Phys. Rev. B*, **66**, 054104, 1–10.
- Nomura S, Uchino K (1982), 'Electrostrictive effect in  $\text{Pb}(\text{Mg}_{1/3}\text{Nb}_{2/3})\text{O}_3$  type materials', *Ferroelectrics*, **41**, 117–32.
- Park J H, Xu F, Trolrier-McKinstry (2001), 'Dielectric and piezoelectric properties of sol-gel derived lead magnesium niobium titanate films with different textures', *J. Appl. Phys.*, **89**(1), 568–74.
- Park S E, Shrout T R (1997), 'Ultrahigh strain and piezoelectric behaviour in relaxor based ferroelectric single crystals', *J. Appl. Phys.*, **82**(4), 1804–11.
- Pirc R, Blinc R (1999), 'Spherical random bond random field model of relaxor ferroelectrics', *Phys. Rev. B*, **60**(19), 13470–78.
- Pithan C, Hennings D, Waser R (2005), 'Progress in the synthesis of nanocrystalline  $\text{BaTiO}_3$  powders for MLCC', *Int. J. Appl. Ceram. Technol.*, **2**(1), 1–14.
- Randall C A, Kim N, Kucera J P, Cao W, Shrout T R (1998), 'Intrinsic and extrinsic size effects in fine grained morphotropic phase boundary lead zirconate titanate ceramics', *J. Am. Ceram. Soc.*, **81**(3), 677–88.
- Saito Y, Takao H, Tani T, Nonoyama T, Takatori K, Homma T, Nagaya T, Nakamura M (2004), 'Lead-free piezoceramics', *Nature*, **432**, 84–7.
- Seol K S, Takeuchi K (2004), 'Ferroelectricity of single-crystalline, monodisperse lead zirconate titanate nanoparticles of 9 nm in diameter', *Appl. Phys. Lett.*, **85** (12), 2325–7.
- Setter N (2002), *Piezoelectric Materials in Devices*, Lausanne, N. Setter, Ceramics Laboratory, EPFL Swiss Institute of Technology.
- Singh A K, Pandey D (2003), 'Evidence for  $M_B$  and  $M_C$  phases in the morphotropic phase boundary region of  $(1-x)\text{Pb}(\text{Mg}_{1/3}\text{Nb}_{2/3})\text{O}_3-x\text{PbTiO}_3$ : a Rietveld study', *Phys. Rev. B*, **67**, 064102, 1–12.
- Singh A K, Pandey D, Zaharko O (2006), 'Evolution of short range to long range monoclinic order of  $M_B$  type with decreasing temperature in  $0.75\text{Pb}(\text{Mg}_{1/3}\text{Nb}_{2/3})\text{O}_3-0.25\text{PbTiO}_3$ ', *J. Appl. Phys.*, **99**, 076105, 1–3.
- Swartz S L, Shrout T R, Schulze W A, Cross L E (1984), 'Dielectric properties of lead magnesium niobate ceramics', *J. Am. Ceram. Soc.*, **67**, 311–15.
- Takahashi T (1982), 'Effects of impurity doping in lead zirconate titanate ceramics', *Ferroelectrics*, **41**, 143–56.
- Trolrier-McKinstry S, Muralt P (2004), 'Thin film piezoelectrics for MEMS', *J. Electroceram.* **12**(1–2), 7–17.
- Uchino K (1998), 'Materials issues in design and performance of piezoelectric actuators: an overview', *Acta Mater.*, **46**(11) 3745–53.
- Viehland D, Jang S J, Cross L E, Wutting M (1990), 'Freezing of the polarisation fluctuations in lead magnesium niobate relaxors', *J. Appl. Phys.*, **68**(6), 2916–21.
- Viehland D, Wutti G M, Cross L E (1991), 'The glassy behaviour of relaxor ferroelectrics', *Ferroelectrics*, **120**, 71–77.
- Viehland D, Kim M C, Xu Z, Li J F (1995), 'Long time present tweedlike precursors and paraelectric clusters in ferroelectrics containing strong quenched randomness', *Appl. Phys. Lett.*, **67**(17) 2471–3.
- Westphal V, Kleemann W, Glinchuk M D (1992), 'Diffuse phase transition and random field induced domain states of the relaxor ferroelectric  $\text{Pb}(\text{Mg}_{1/3}\text{Nb}_{2/3})\text{O}_3$ ', *Phys. Rev. Lett.*, **68**(6), 847–50.
- Ye Z G, Schmid H (1993), 'Optical, dielectric and polarization studies of the electric field-induced phase transition in  $\text{Pb}(\text{Mg}_{1/3}\text{Nb}_{2/3})\text{O}_3$  (PMN)', *Ferroelectrics*, **145**, 83–106.

- Ye Z G, Noheda B, Dong M, Cox D, Shirane G (2001), 'Monoclinic phase in the relaxor-based piezo-/ferroelectric  $\text{Pb}(\text{Mg}_{1/3}\text{Nb}_{2/3})\text{O}_3\text{-PbTiO}_3$  system', *Phys. Rev. B*, **64**, 184114, 1–5.
- Ye Z G, Bing Y, Gao J, Bokov A A, Stephens P, Noheda B, Shirane G (2003), 'Development of ferroelectric order in relaxor  $(1-x)\text{Pb}(\text{Mg}_{1/3}\text{Nb}_{2/3})\text{O}_3\text{-}x\text{PbTiO}_3$  ( $0 \leq x \leq 0.15$ )', *Phys. Rev. B*, **67**, 104104, 1–8.
- Zemilgotov A G, Pertsev N A, Waser R (2005), 'Phase states of nanocrystalline ferroelectric ceramics and their dielectric properties', *J. Appl. Phys.*, **97**, 114315, 1–9.
- Zhang S, Randall C A, Shrout T R (2003), 'High Curie temperature piezocrystals in the  $\text{BiScO}_3\text{-PbTiO}_3$  perovskite system', *Appl. Phys. Lett.*, **83**(15), 3150–52.
- Zhao Z, Buscaglia V, Viviani M, Buscaglia M T, Mitoseriu L, Testino A, Nygren M, Johnson M, Nanni P (2004), 'Grain size effects on the ferroelectric behaviour of dense nanocrystalline  $\text{BaTiO}_3$  ceramics', *Phys. Rev. B*, **70**, 024107, 1–8.



## Loss mechanisms and high-power piezoelectric components

---

K. UCHINO, Pennsylvania State University and  
 Micromechatronics Inc., USA, J H ZHENG, Y GAO,  
 S URAL, S-H PARK and N BHATTACHARYA,  
 Pennsylvania State University, USA and  
 S HIROSE, Yamagata University, Japan

### 16.1 Introduction

Loss or hysteresis in piezoelectrics exhibits both merits and demerits. For positioning actuator applications, hysteresis in the field-induced strain causes a serious problem, and for resonance actuation such as ultrasonic motors, loss generates significant heat in the piezoelectric materials. Further, in consideration of the resonant strain amplified in proportion to a mechanical quality factor, low (intensive) mechanical loss materials are preferred for ultrasonic motors. In contrast, for force sensors and acoustic transducers, a low mechanical quality factor  $Q_m$  (which corresponds to high mechanical loss) is essential to widen a frequency range for receiving signals.

K. H. Haerdtl wrote a review article on electrical and mechanical losses in ferroelectric ceramics [1]. Losses are considered to consist of four portions: (1) domain wall motion, (2) fundamental lattice portion, which should also occur in domain-free monocrystals, (3) microstructure portion, which occurs typically in polycrystalline samples, and (4) conductivity portion in highly ohmic samples. However, in the typical piezoelectric ceramic case, the loss due to the domain wall motion exceeds the other three contributions significantly. Haerdtl reported interesting experimental results on the relationship between electrical and mechanical losses in piezoceramics,  $\text{Pb}_{0.9}\text{La}_{0.1}(\text{Zr}_{0.5}\text{Ti}_{0.5})_{1-x}\text{Me}_x\text{O}_3$ , where Me represents the dopant ions Mn, Fe or Al and  $x$  varies between 0 and 0.09. However, they measured the mechanical losses on poled ceramic samples, while the electrical losses on unpoled samples, i.e. in a different polarization state, which led to big ambiguity in the discussion.

Few systematic studies of the loss mechanisms in piezoelectrics have been reported, particularly in high electric field and high power density ranges. Although some of the formulas in this chapter were described by T. Ikeda in his textbook [2], the piezoelectric losses, which have been found in our investigations to play an important role, were totally neglected. In this chapter, we review the loss mechanisms in piezoelectrics first, followed by

the heat generation processes for various drive conditions. Then, loss anisotropy is discussed, the importance of which is demonstrated in a finite element method simulation of a piezoelectric transformer. Second, practical high-power ‘hard’ PZT materials developed at Penn State are introduced, which exhibit a vibration velocity higher than 1 m/s, leading to a power density capability ten times that of the commercially available ‘hard’ PZTs. We propose an internal bias field model to explain the low loss and high power origin of these materials, which are suitable to actuator (ultrasonic motor) applications. We also describe ‘semi-hard’ materials based on PZT–Pb(Zn,Nb)O<sub>3</sub>–Pb(Ni,Nb)O<sub>3</sub>, with reasonable piezoelectric  $d$  constants, which are suitable for piezoelectric transducers. Third, using a low-temperature sinterable ‘semi-hard’ PZT, we demonstrate high-power multilayer piezoelectric transformers with Cu or Ag internal electrodes.

The terminologies ‘intensive’ and ‘extensive’ losses are introduced in the relation with ‘intensive’ and ‘extensive’ parameters in the phenomenology. These are not directly related with the ‘intrinsic’ and ‘extrinsic’ losses which were introduced to explain the loss contribution from the mono-domain single crystal state and from the others [3]. In this chapter, our discussion is focused on the ‘extrinsic’ losses, in particular, domain-reorientation originated losses.

## 16.2      **General consideration of loss and hysteresis in piezoelectrics**

### 16.2.1    Theoretical formulas

Since the detailed mathematics have been described in a previous paper [4], we only summarize the results in this section. We start from the following two piezoelectric equations:

$$x = s^E X + d E \quad 16.1$$

$$D = d X + \epsilon^X \epsilon_0 E \quad 16.2$$

where  $x$  is strain,  $X$ , stress,  $D$ , electric displacement,  $E$ , electric field. Equations (16.1) and (16.2) are the expression in terms of intensive (i.e. externally controllable) physical parameters  $X$  and  $E$ . The elastic compliance  $s^E$ , the dielectric constant  $\epsilon^X$  and the piezoelectric constant  $d$  are temperature-dependent. Note that, in general, the piezoelectric equations cannot yield a delay-time related loss, without taking into account irreversible thermodynamic equations or dissipation functions. However, the latter considerations are mathematically equivalent to the introduction of complex physical constants into the phenomenological equations, if the loss is small and can be treated as a perturbation.

Therefore, we will introduce complex parameters  $\epsilon^{X*}$ ,  $s^{E*}$  and  $d^*$  in order to consider the hysteresis losses in dielectric, elastic and piezoelectric coupling energy:

$$\epsilon^{X*} = \epsilon^X (1 - j \tan \delta')$$
16.3

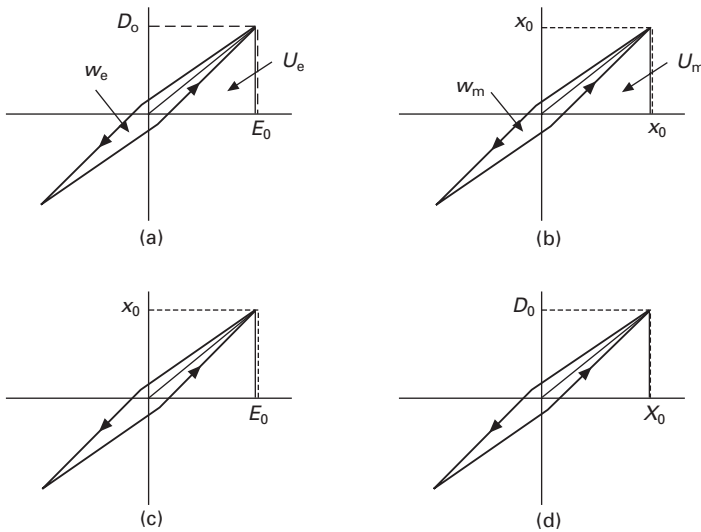
$$s^{E*} = s^E (1 - j \tan \phi')$$
16.4

$$d^* = d (1 - j \tan \theta')$$
16.5

$\theta'$  is the phase delay of the strain under an applied electric field, or the phase delay of the electric displacement under an applied stress. Both delay phases should be exactly the same if we introduce the same complex piezoelectric constant  $d^*$  into Eqs. (16.1) and (16.2).  $\delta'$  is the phase delay of the electric displacement to an applied electric field under a constant stress (e.g. zero stress) condition, and  $\phi'$  is the phase delay of the strain to an applied stress under a constant electric field (e.g. short-circuit) condition. We will consider these phase delays as 'intensive' losses.

Figure 16.1 shows the model hysteresis curves for practical experiments:  $D$  vs.  $E$  curve under a stress-free condition,  $x$  vs.  $X$  under a short-circuit condition,  $x$  vs.  $E$  under a stress-free condition and  $D$  vs.  $X$  under a short-circuit condition for measuring current, respectively. Note that these measurements are easily conducted in practice.

The stored energies and hysteresis losses for pure dielectric and elastic energies can be calculated as:



16.1 (a)  $D$  vs.  $E$  (stress-free), (b)  $x$  vs.  $X$  (short-circuit), (c)  $x$  vs.  $E$  (stress-free) and (d)  $D$  vs.  $X$  (short-circuit) curves with a slight hysteresis in each relation.

$$U_e = (1/2) \epsilon^X \epsilon_0 E_0^2 \quad 16.6$$

$$w_e = \pi \epsilon^X \epsilon_0 E_0^2 \tan \delta' \quad 16.7$$

$$U_m = (1/2) s^E X_0^2 \quad 16.8$$

$$w_m = \pi s^E X_0^2 \tan \phi' \quad 16.9$$

The electromechanical hysteresis losses are more complicated, which can be calculated as follows, depending on the method used for measuring; when measuring the induced strain under an electric field,

$$U_{em} = (1/2) (d^2/s^E) E_0^2 \quad 16.10$$

and

$$w_{em} = \pi (d^2/s^E) E_0^2 (2 \tan \theta' - \tan \phi') \quad 16.11$$

Note that the strain vs. electric field measurement should provide the combination of piezoelectric loss  $\tan \theta'$  and elastic loss  $\tan \phi'$ . When we measure the induced charge under stress, the stored energy  $U_{me}$  and the hysteresis loss  $w_{me}$  during a quarter and a full stress cycle, respectively, are obtained as

$$U_{me} = (1/2) (d^2/\epsilon_0 \epsilon^X) X_0^2 \quad 16.12$$

$$w_{me} = \pi (d^2/\epsilon_0 \epsilon^X) X_0^2 (2 \tan \theta' - \tan \delta') \quad 16.13$$

Hence, from the measurements of  $D$  vs.  $E$  and  $x$  vs.  $X$ , we obtain  $\tan \delta'$  and  $\tan \phi'$ , respectively, and either the piezoelectric ( $D$  vs.  $X$ ) or converse piezoelectric measurement ( $x$  vs.  $E$ ) provides  $\tan \theta'$  through a numerical subtraction.

So far, we have discussed the 'intensive' dielectric, mechanical and piezoelectric losses in terms of 'intensive' parameters  $X$  and  $E$ . In order to consider real physical meanings of the losses in the material, we will introduce the 'extensive' losses [4] in terms of 'extensive' parameters  $x$  and  $D$ . In practice, intensive losses are easily measurable, but extensive losses are not, but obtainable from the intensive losses. When we start from the piezoelectric equations in terms of extensive physical parameters  $x$  and  $D$ ,

$$X = c^D x - h D \quad 16.14$$

$$E = -h x + \kappa^x \kappa_0 D \quad 16.15$$

we introduce the extensive dielectric, elastic and piezoelectric losses as

$$\kappa^{x*} = \kappa^x (1 + j \tan \delta) \quad 16.16$$

$$c^{D*} = c^D (1 + j \tan \phi) \quad 16.17$$

$$h^* = h (1 + j \tan \theta) \tag{16.18}$$

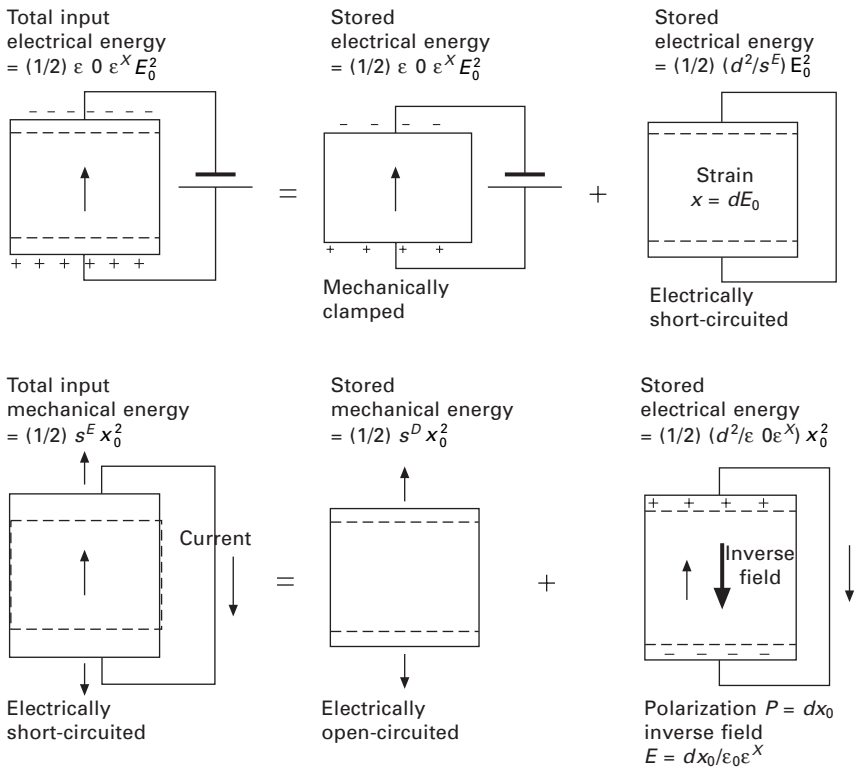
It is notable that the permittivity under a constant strain (e.g., zero strain or completely clamped) condition,  $\epsilon^{x^*}$  and the elastic compliance under a constant electric displacement (e.g. open-circuit) condition,  $s^{D^*}$  can be provided as an inverse value of  $\kappa^{x^*}$  and  $c^{D^*}$ , respectively, in this simplest one-dimensional expression (in the case of a general 3D expression, this part must be translated as ‘inverse matrix components of  $\kappa^{x^*}$  and  $c^{D^*}$  tensors’). Thus, using exactly the same losses in Eqs. (16.16) and (16.17),

$$\epsilon^{x^*} = \epsilon^x (1 - j \tan \delta) \tag{16.19}$$

$$s^{D^*} = s^D (1 - j \tan \phi) \tag{16.20}$$

we will consider these phase delays again as ‘extensive’ losses.

Here, we consider the physical property difference between the boundary conditions:  $E$  constant and  $D$  constant, or  $X$  constant and  $x$  constant in a simple 1D model. When an electric field is applied to a piezoelectric sample as illustrated at the top of Fig. 16.2, this state will be equivalent to the



16.2 Conceptual figure for explaining the relation between  $\epsilon^{x^*}$  and  $\epsilon^x$ ,  $s^E$  and  $s^D$ .

superposition of the following two steps: first, the sample is completely clamped and the field  $E_0$  is applied (pure electrical energy  $(1/2) \epsilon^x \epsilon_0 E_0^2$  is input); second, keeping the field at  $E_0$ , the mechanical constraint is released (additional mechanical energy  $(1/2) (d^2/s^E) E_0^2$  is necessary). The total energy should correspond to the total input electrical energy  $(1/2) \epsilon^X \epsilon_0 E_0^2$ . Similar energy calculation can be obtained from the bottom of Fig. 16.2, leading to the following equations:

$$\epsilon^x/\epsilon^X = (1 - k^2) \quad 16.21$$

$$s^D/s^E = (1 - k^2) \quad 16.22$$

$$\kappa^X/\kappa^x = (1 - k^2) \quad 16.23$$

$$c^E/c^D = (1 - k^2) \quad 16.24$$

where

$$k^2 = \frac{d^2}{s^E \epsilon_0 \epsilon^x} = \frac{h^2}{c^D \kappa^x \kappa_0} \quad 16.25$$

This  $k$  is called the *electromechanical coupling factor*, which is defined as a real number in this chapter.

In order to obtain the relationships between the intensive and extensive losses, the following three equations are essential:

$$\epsilon_0 \epsilon^X = \left[ \kappa^x \kappa_0 \left( \frac{1 - h^2}{c^D \kappa^x \kappa_0} \right) \right]^{-1} \quad 16.26$$

$$s^E = \left[ c^D \left( \frac{1 - h^2}{c^D \kappa^x \kappa_0} \right) \right]^{-1} \quad 16.27$$

$$d = \left[ \frac{h^2}{c^D \kappa^x \kappa_0} \right] \left[ h \left( \frac{1 - h^2}{c^D \kappa^x \kappa_0} \right) \right]^{-1} \quad 16.28$$

Replacing the parameters in Eqs. (16.26) and (16.27) by the complex parameters in Eqs. (16.3) – (16.5), (16.16) – (16.18), we obtain the relationships between the intensive and extensive losses:

$$\tan \delta' = \frac{1}{1 - k^2} [\tan \delta + k^2(\tan \phi - 2 \tan \theta)] \quad 16.29$$

$$\tan \phi' = \frac{1}{1 - k^2} [\tan \phi + k^2(\tan \delta - 2 \tan \theta)] \quad 16.30$$

$$\tan \theta' = \frac{1}{1 - k^2} [\tan \delta + \tan \phi + (1 + k^2) \tan \theta] \quad 16.31$$

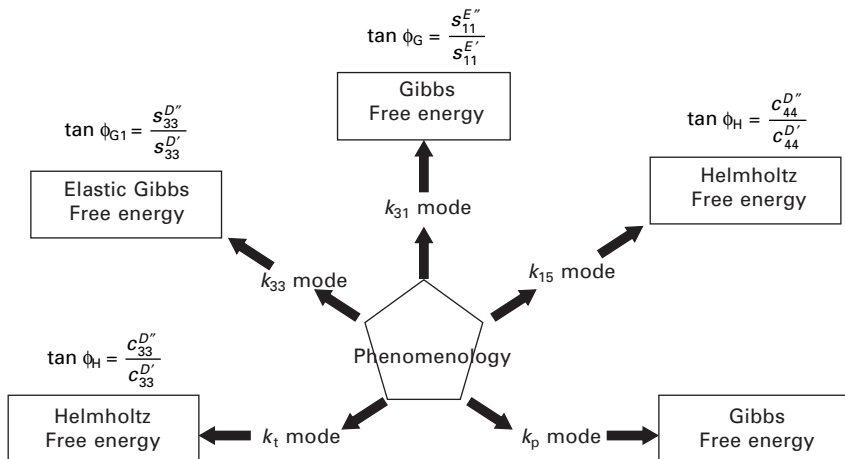
where  $k$  is the electromechanical coupling factor defined by Eq. (16.25), and

here as a real number. It is important that the intensive dielectric and elastic losses are mutually correlated with the extensive dielectric, elastic and piezoelectric losses through the electromechanical coupling  $k^2$ , and that the denominator  $(1 - k^2)$  comes basically from the ratios,  $\epsilon^x / \epsilon^X = (1 - k^2)$  and  $s^D / s^E = (1 - k^2)$ , and this real part reflects to the dissipation factor when the imaginary part is divided by the real part.

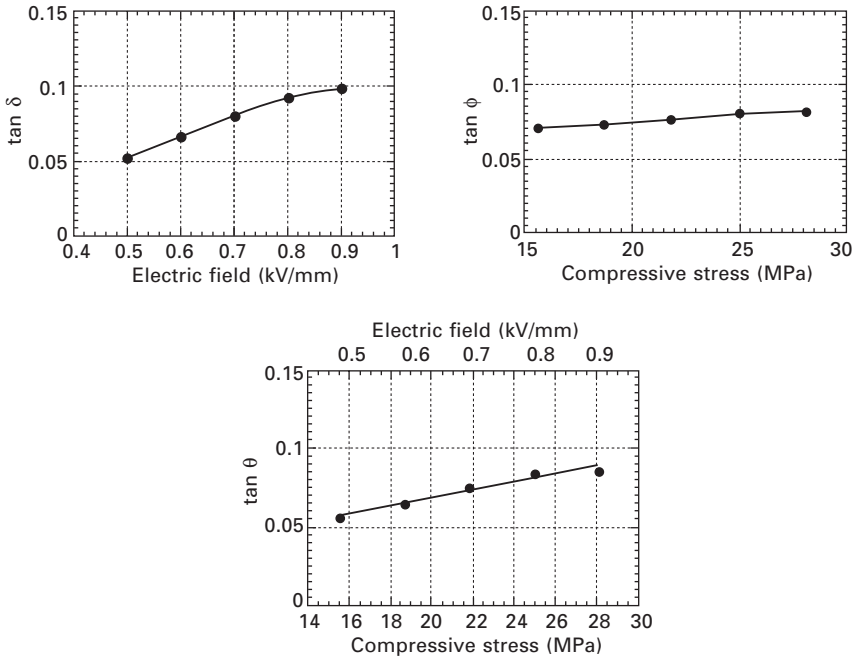
Expanding the discussion above, we introduce various loss formulas, as summarized in Fig. 16.3, where the relationship between the vibration mode and the corresponding elastic loss formula is provided. Refer to Bhattacharya and Uchino [5] for further explanation.

### 16.2.2 Experimental example

We determine ‘intensive’ dissipation factors first from (a)  $D$  vs.  $E$  (stress-free), (b)  $x$  vs.  $X$  (short-circuit), (c)  $x$  vs.  $E$  (stress-free) and (d)  $D$  vs.  $X$  (short-circuit) curves for a soft PZT-based multilayer actuator [6]. Then, we calculate the ‘extensive’ losses as shown in Fig. 16.4. Note that the piezoelectric losses  $\tan\theta'$  and  $\tan\theta$  are not so small as previously believed, but comparable to the dielectric and elastic losses, and increase gradually with the field or stress. Also it is noteworthy that the extensive dielectric loss  $\tan\delta$  increases significantly with an increase of the intensive parameter, i.e. the applied electric field, while the extensive elastic loss  $\tan\phi$  is rather insensitive to the intensive parameter, i.e. the applied compressive stress. With similar measurements to Fig. 16.1(a) and 1(b), but under constrained conditions, i.e.  $D$  vs.  $E$  under a completely clamped state, and  $x$  vs.  $X$  under an open-circuit



16.3 Relationship between the vibration mode and the corresponding elastic loss.



16.4 Extensive loss factors,  $\tan \delta$ ,  $\tan \phi$  and  $\tan \theta$  as a function of electric field or compressive stress, measured for a PZT-based actuator.

state, respectively, we can expect smaller hystereses, that is, extensive losses,  $\tan \delta$  and  $\tan \phi$ . These measurements seem to be alternative methods to determine the three losses separately; however, they are rather difficult in practice.

### 16.2.3 Physical meaning of extensive losses

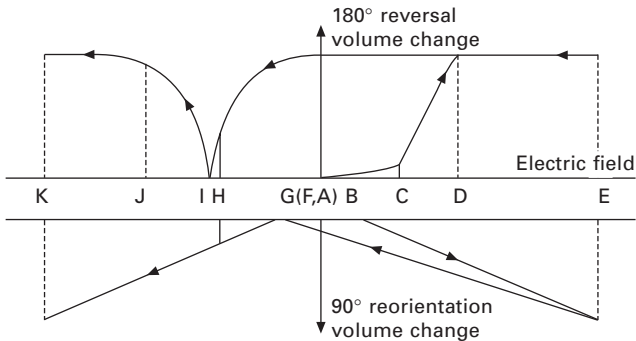
To make the situation simplest, we consider here only the domain wall motion-related losses. Taking into account the fact that the polarization change is primarily attributed to  $180^\circ$  domain wall motion, while the strain is attributed to  $90^\circ$  (or non- $180^\circ$ ) domain wall motion, we suppose that the extensive dielectric and mechanical losses are originated from  $180^\circ$  and  $90^\circ$  domain wall motions, respectively, as illustrated in Fig. 16.5. The dielectric loss comes from the hysteresis during the  $180^\circ$  polarization reversal under  $E$ , while the elastic loss comes from the hysteresis during the  $90^\circ$  polarization reorientation under  $X$ . In this model, the intensive (observable) piezoelectric loss is explained by the  $90^\circ$  polarization reorientation under  $E$ , which can be realized by superimposing the  $90^\circ$  polarization reorientation under  $X$  and the  $180^\circ$  polarization reversal under  $E$ . This is the primary reason why Eq. (16.11) includes a combination term as  $(2 \tan \theta' - \tan \phi')$ .



	Electric field	Stress
Dielectric $\tan \delta$		
Mechanical $\tan \phi$		
Piezoelectric $\tan \theta$		

16.5 Polarization reversal/reorientation model for explaining dielectric, elastic and piezoelectric losses.

If we adopt the Uchida–Ikeda polarization reversal/reorientation model [7], we can explain the loss change with intensive parameter (externally controllable parameter). By finding the polarization  $P$  and the field-induced strain  $x$  as a function of the electric field  $E$ , it is possible to estimate the volume in which a  $180^\circ$  reversal or a  $90^\circ$  rotation occurred. This is because the  $180^\circ$  domain reversal does not contribute to the induced strain, only the  $90^\circ$  rotation does, whereas the  $180^\circ$  domain reversal contributes mainly to the polarization. The volume change of the domains with external electric field is shown schematically in Fig. 16.6. It can be seen that with the application of an electric field the  $180^\circ$  reversal occurs rapidly whereas the  $90^\circ$  rotation occurs slowly. It is notable that at G in the figure, there remains some polarization while the induced strain is zero, at H the polarizations from the



16.6 Polarization reversal/reorientation model for explaining the loss change with electric field.

$180^\circ$  and  $90^\circ$  reorientations cancel each other and become zero, but the strain is not at its minimum. Owing to a sudden change in the  $180^\circ$  reversal above a certain electric field, we can expect a sudden increase in the polarization hysteresis and in the loss (this may reflect to the extensive dielectric loss measurement in Fig. 16.4 top left); while the slope of  $90^\circ$  reorientation is almost constant, we can expect a constant loss or a mechanical quality factor  $Q_m$  with changing the external parameter,  $E$  or  $X$  (extensive elastic loss in Fig. 16.4 top right). This situation will be discussed again in the following section.

### 16.3 Losses at a piezoelectric resonance

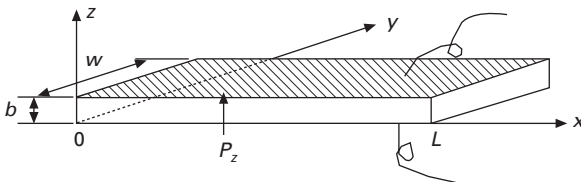
So far, we have considered the losses for a quasi-static or off-resonance state. Problems in ultrasonic motors which are driven at the resonance frequency include significant distortion of the admittance frequency spectrum due to the nonlinear behavior of elastic compliance at a high vibration amplitude, and the heat generation which causes a serious degradation of the motor characteristics through the depoling of the piezoceramic. Therefore, the ultrasonic motor requires a very hard type piezoelectric with a high mechanical quality factor  $Q_m$ , leading to the suppression of heat generation. It is also notable that the actual mechanical vibration amplitude at the resonance frequency is directly proportional to this  $Q_m$  value.

#### 16.3.1 Vibration at a piezoelectric resonance

Let us review the longitudinal mechanical vibration of a piezoceramic plate through the transverse piezoelectric effect ( $d_{31}$ ) as shown in Fig. 16.7 [8]. Assuming that the polarization is in the  $z$ -direction and the  $x$ - $y$  planes are the planes of the electrodes, the extensional vibration in the  $x$  direction is represented by the following dynamic equation:

$$(\partial^2 u / \partial t^2) = F = (\partial X_{11} / \partial x) + (\partial X_{12} / \partial y) + (\partial X_{13} / \partial z) \quad 16.32$$

where  $u$  is the displacement of the small volume element in the ceramic plate in the  $x$ -direction. When the plate is very long and thin,  $X_2$  and  $X_3$  may be set



16.7 Longitudinal vibration through the transverse piezoelectric effect ( $d_{31}$ ) in a rectangular plate.

equal to zero through the plate, and the following solutions can be obtained:

$$\text{(strain)} \quad \frac{\partial u}{\partial x} = x_1 = d_{31} E_Z \frac{[\sin \omega(L-x)/v + \sin(\omega x/v)]}{\sin(\omega L/v)} \quad 16.33$$

$$\text{(total displacement)} \quad \Delta L = \int_0^L x_1 dx = d_{31} E_Z L(2v/\omega L) \tan(\omega L/2v) \quad 16.34$$

Here,  $v$  is the sound velocity in the piezoceramic which is given by

$$v = 1/\sqrt{\rho s_{11}^E} \quad 16.35$$

The admittance for the mechanically free sample is calculated to be:

$$\begin{aligned} Y &= (1/Z) = (i/V) = (i/E_Z t) \\ &= (j\omega w L/t) \epsilon_0 \epsilon_3^{LC} \left[ \frac{1 + (d_{31}^2/\epsilon_0 \epsilon_3^{LC} s_{11}^E)(\tan(\omega L/2v))}{\omega L/2v} \right] \end{aligned} \quad 16.36$$

where  $w$  is the width,  $L$  the length,  $t$  the thickness of the sample, and  $V$  the applied voltage.  $\epsilon_3^{LC}$  is the permittivity in a longitudinally clamped sample, which is given by

$$\epsilon_0 \epsilon_3^{LC} = \epsilon_0 \epsilon_3^x - (d_{31}^2/s_{11}^E) = \epsilon_0 \epsilon_3^x (1 - k_{31}^2) \quad 16.37$$

Now, we will introduce the complex parameters into the admittance curve around the resonance frequency, in a similar way to the previous section:  $\epsilon_3^{x*} = \epsilon_3^x (1 - j \tan \delta')$ ,  $s_{11}^{E*} = s_{11}^E (1 - j \tan \phi')$ , and  $d_{31}^* = d (1 - j \tan \theta')$  into Eq. (16.36):

$$\begin{aligned} Y &= Y_d + Y_m \\ &= j\omega C_d (1 - j \tan \delta) + j\omega C_d K_{31}^2 [(1 - j(2 \tan \theta' - \tan \phi')) \\ &\quad \times \left[ \frac{(\tan(\omega L/2v^*))}{(\omega L/2v^*)} \right] \end{aligned} \quad 16.38$$

where

$$C_0 = (wL/t) \epsilon_0 \epsilon_3^x \quad 16.39$$

$$C_d = (1 - k_{31}^2) C_0 \quad 16.40$$

Note that the loss for the first term (damped conductance) is represented by the 'extensive' dielectric loss  $\tan \delta$ , not by the intensive loss  $\tan \delta'$ . We further calculate  $1/[\tan(\omega L/2v^*)]$  with an expansion-series approximation around  $(\omega L/2v) = \pi/2$ , taking into account that the resonance state is defined in this case for the maximum admittance point.

Using new frequency parameters,

$$\Omega = \omega L/2 \nu, \Delta\Omega = \Omega - \pi/2 \ (\ll 1) \quad 16.41$$

and  $K_{31}^2 = k_{31}^2 / (1 - k_{31}^2)$ , the motional admittance  $Y_m$  is approximated around the first resonance frequency by

$$Y_m = j(8/\pi^2) \omega_0 C_d K_{31}^2 \left[ \frac{(1 + j((3/2)\tan\phi' - 2\tan\theta'))}{-(4/\pi)\Delta\Omega + j\tan\phi'} \right] \quad 16.42$$

The maximum  $Y_m$  is obtained at  $\Delta\Omega = 0$ :

$$Y_m^{\max} = (8/\pi^2) \omega_0 C_d K_{31}^2 (\tan\phi')^{-1} = (8/\pi^2) \omega_0 C_d K_{31}^2 Q_m \quad 16.43$$

where  $Q_m = (\tan\phi')^{-1}$ . Similarly, the maximum displacement  $u_{\max}$  is obtained at  $\Delta\Omega = 0$ :

$$u_{\max} = (8/\pi^2) d_{31} E_z L Q_m \quad 16.44$$

The maximum displacement at the resonance frequency is  $(8/\pi^2)Q_m$  times larger than that at a non-resonance frequency,  $d_{31}E_zL$ .

In a brief summary, when we observe the admittance or displacement spectrum as a function of drive frequency, and obtain the mechanical quality factor  $Q_m$  estimated from  $Q_m = \omega_0/2\Delta\omega$ , where  $2\Delta\omega$  is a full width of the 3 dB down (i.e.  $1/\sqrt{2}$ ) of the maximum value at  $\omega = \omega_0$ , we can obtain the intensive mechanical loss  $\tan\phi'$ .

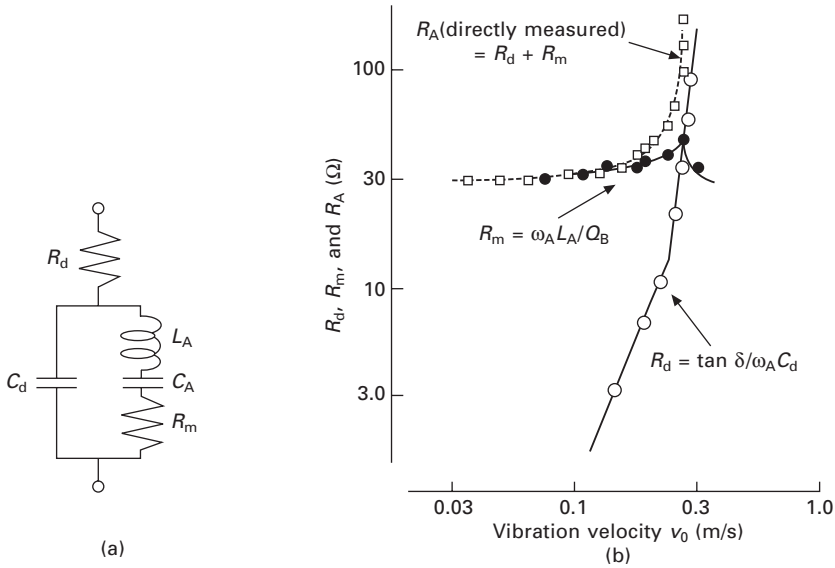
### 16.3.2 Equivalent circuit under high-power drive

The equivalent circuit for the piezoelectric actuator is represented by a combination of  $L$ ,  $C$  and  $R$ . Figure 16.8(a) shows an equivalent circuit for the resonance state, which has very low impedance. Taking into account Eq. (16.42), we can understand that  $C_d$  and  $R_d$  correspond to the electrostatic capacitance (for a longitudinally clamped sample in the previous case, not a free sample) and the clamped (or 'extensive') dielectric loss  $\tan\delta$ , respectively, and the components  $L_A$  and  $C_A$  in a series resonance circuit are related to the piezoelectric motion. For example, in the case of the longitudinal vibration of the above rectangular plate through  $d_{31}$ , these components are represented approximately by

$$L_A = (\rho/8)(Lb/w)[(s_{11}^E)^2/d_{31}^2] \quad 16.45$$

$$C_A = (8/\pi^2)(Lw/b)(d_{31}^2/s_{11}^E) \quad 16.46$$

The total resistance  $R_A (= R_d + R_m)$  should correspond to the loss  $\tan\phi'$ , which is composed of the extensive mechanical loss  $\tan\phi$  and dielectric/piezoelectric coupled loss  $(\tan\delta - 2\tan\theta)$  (see Eq. (16.30)). Thus, intuitively speaking,  $R_d$  and  $R_m$  correspond to the extensive dielectric and mechanical losses, respectively. Note that we have introduced an additional resistance  $R_d$



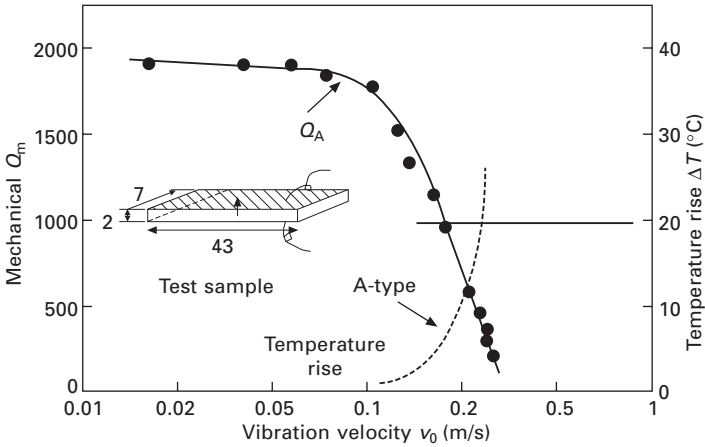
16.8 (a) Equivalent circuit of a piezoelectric device for the resonance under high power drive. (b) Vibration velocity dependence of the resistances  $R_d$  and  $R_m$  in the equivalent electric circuit for a longitudinally vibrating PZT ceramic transducer through the transverse piezoelectric effect  $d_{31}$ . Note a dramatic change in  $R_d$  above a certain threshold vibration velocity.

to explain a large contribution of the dielectric loss when a vibration velocity is relatively large. There are, of course, different ways to introduce  $R_d$  in an equivalent circuit [9].

### 16.3.3 Losses as a function of vibration velocity

Let us consider here the degradation mechanism of the mechanical quality factor  $Q_m$  with increasing electric field and vibration velocity. Figure 16.9 shows the change in mechanical  $Q_m$  with vibration velocity.  $Q_m$  is almost constant for a small electric field/vibration velocity, but above a certain vibration level  $Q_m$  degrades drastically, where temperature rise starts to be observed [10].

Figure 16.8(b) depicts an important notion on heat generation from the piezoelectric material, where the damped and motional resistances,  $R_d$  and  $R_m$ , in the equivalent electrical circuit of a PZT sample (Fig. 16.8a) are separately plotted as a function of vibration velocity. Note that  $R_m$ , mainly related to the extensive mechanical loss ( $90^\circ$  domain wall motion), is insensitive to the vibration velocity, while  $R_d$ , related to the extensive dielectric loss ( $180^\circ$  domain wall motion), increases significantly around a certain critical



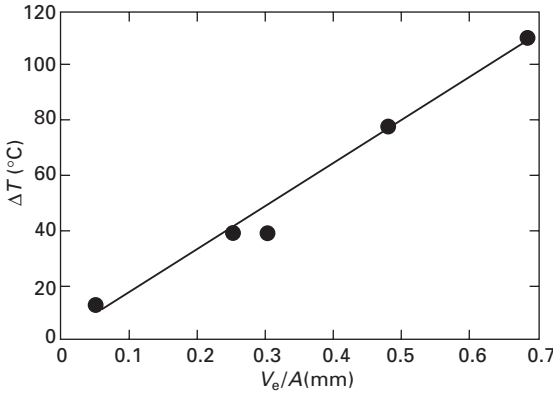
16.9 Vibration velocity dependence of the quality factor  $Q_A$  and temperature rise for A (resonance) type resonance of a longitudinally vibrating PZT ceramic transducer through the transverse piezoelectric effect  $d_{31}$ . The maximum vibration velocity is defined at the velocity where a 20 °C temperature rise from room temperature occurs.

vibration velocity. Thus, the resonance loss at a small vibration velocity is mainly determined by the extensive mechanical loss which provides a high mechanical quality factor  $Q_m$ , and with increasing vibration velocity, the extensive dielectric loss contribution significantly increases. This is consistent with the discussion on Fig. 16.6. After  $R_d$  exceeds  $R_m$ , we started to observe heat generation.

### 16.4 Heat generation in piezoelectrics

Heat generation in various types of PZT-based actuators has been studied under a large electric field applied (1 kV/mm or higher) at an off-resonance frequency and under a relatively small electric field applied (100 V/mm) at a resonance frequency.

Zheng *et al.* reported the heat generation at an off-resonance frequency from various sizes of multilayer-type piezoelectric ceramic actuators [6]. The temperature change with time in the actuators was monitored when driven at 3 kV/mm and 300 Hz, and Fig. 16.10 plots the saturated temperature as a function of  $V_e/A$ , where  $V_e$  is the effective volume (electrode overlapped part) and  $A$  is the surface area. This linear relation is reasonable because the volume  $V_e$  generates the heat and this heat is dissipated through the area  $A$ . Thus, if we need to suppress the temperature rise, a small  $V_e/A$  design is preferred. From these experimental results, we calculated the total loss  $u$  of the piezoelectric, which is summarized in Table 16.I. The experimental data of  $P$ - $E$  hysteresis losses under a stress-free condition is also listed for



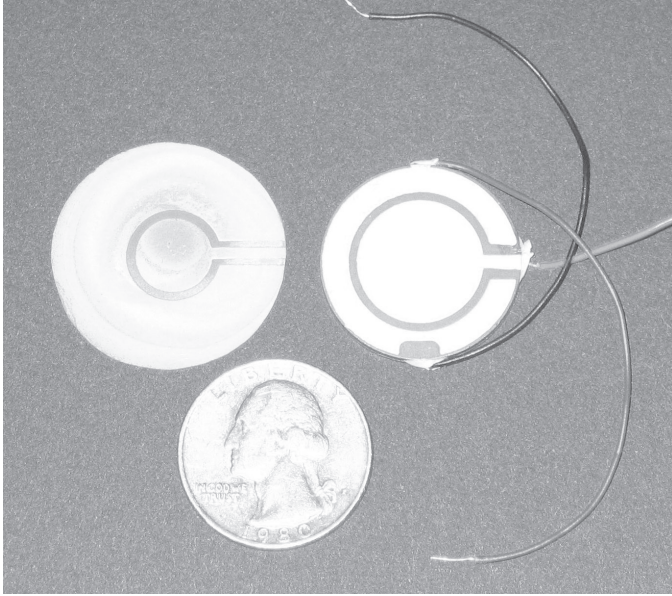
16.10 Temperature rise at off-resonance versus  $V_e/A$  (3 kV/mm, 300 Hz) in various size soft PZT multilayer actuators, where  $V_e$  is the effective volume generating the heat and  $A$  is the surface area dissipating the heat.

Table 16.1 Loss and overall heat transfer coefficient for PZT multilayer samples ( $E = 3$  kV/mm,  $f = 300$  Hz). The effective heat transfer coefficient here is the sum of the rates of heat flow by radiation and by convection, neglecting the conduction effect

Actuator	$4.5 \times 3.5 \times 2 \text{ mm}^3$	$7 \times 7 \times 2 \text{ mm}^3$	$17 \times 3.5 \times 1 \text{ mm}^3$
Total loss ( $\times 10^3 \text{ J/m}^3$ )	19.2	19.9	19.7
$u = \frac{\rho c V}{f V_e} \left( \frac{dT}{dt} \right)_{t \geq 0}$			
$P$ - $E$ hysteresis loss ( $\times 10^3 \text{ J/m}^3$ )	18.5	17.8	17.4
$k(T)$ ( $\text{W/m}^2 \text{ K}$ )	38.4	39.2	34.1

comparison. It is very important that the  $P$ - $E$  hysteresis intensive loss agrees well with the total loss contributing to the heat generation under an off-resonance drive.

Tashiro *et al.* observed the heat generation in a rectangular piezoelectric plate during a resonating drive [11]. Even though the maximum electric field is not very large, heat is generated due to the large induced strain/stress at the resonance. Figure 16.11 depicts an infrared image taken for a resonating rectangular PZT plate in our laboratory. The maximum heat generation was observed at the nodal point of the resonance vibration, where the maximum strain/stress is generated. This observation supports that the heat generation in a resonating sample is attributed to the intensive elastic loss  $\tan \phi'$ . This is not contradictory to the result in the previous paragraph, where a high voltage was applied at an off-resonance frequency. We concluded there that the heat is originated from the intensive dielectric loss  $\tan \delta'$ . In consideration



16.11 An infrared image of a 'hard' PZT rectangular plate driven at the second resonance mode. Note the three hot points which correspond to the nodal points for this vibration mode.

that both the 'intensive' dielectric and mechanical losses are composed of the 'extensive' dielectric and mechanical losses, and that the extensive dielectric loss  $\tan \delta$  changes significantly with the external electric field and stress, the major contribution to the heat generation seems to come from the 'extensive' dielectric loss (i.e.  $180^\circ$  domain wall motion). Since this is just our model, there can be different domain reorientation models, and further investigations are waited for the microscopic observation of this phenomenon.

## 16.5 Loss anisotropy

Typically the specification sheet provided by the manufacturer gives only one mechanical quality factor ( $Q_m$ ) and one dielectric loss tangent, which are applicable only for the  $k_{31}$  length extensional mode (i.e. imaginary parts of  $s_{11}^E$  and  $\epsilon_{33}^X$ , respectively). Losses can be, in general, introduced in the complex material constants, where the real part indicates the usual material constant and the imaginary part indicates the loss. As introduced in the previous section in Fig. 6.3, in order to determine the loss tangent as a tensor, the phenomenology for lateral ( $k_{31}$ ), longitudinal ( $k_{33}$ ), thickness ( $k_t$ ) and shear ( $k_{15}$ ) modes has been repeated with complex material constants. The theoretical thermodynamic analysis has been performed by considering the intensive variables, stress and electric field (relating to generalized forces),



and extensive variables, strain and electric displacement (relating to generalized displacement), and four distinct phase angles, identified by their respective free energies (denoted as Helmholtz loss tangent, Gibbs loss tangent, electric Gibbs loss tangent and elastic Gibbs loss tangent). The data for the Gibbs tangents for typical ‘soft’ and ‘hard’ piezoceramics (APC-850 and 841, American Piezo Ceramics, PA) is presented in Table 16.2. The detailed measuring technique and processes are reported in Ref. [5]. Note that the  $Q_m$  ( $= 222$ ) for the  $k_{33}$  mode (imaginary part of  $s_{33}^E$ ) is only 1/5 of that ( $= 1087$ ) for the  $k_{31}$  mode (imaginary part of  $s_{11}^E$ ).

This significant anisotropy in  $Q_m$  reflects largely in designing the transducers and transformers. Figure 16.12 exhibits an important example simulated for a Rosen-type piezoelectric transformer, which includes both  $k_{33}$  and  $k_{31}$  mode in one device. We adopted ATILA Finite Element Method software (ISEN, distributed by Micromechanics Inc., PA) for simulating a Rosen-type piezoelectric transformer with 40 mm in length (see Fig. 16.12a). Figures 12(b) and 16.12(c) show admittance spectra simulated for an isotropic loss condition ( $Q_m = 1087$ ) and for an anisotropic loss condition ( $Q_m = 1087$  and 222). As shown in the inserted magnified spectra, a half of the admittance value at the peak is significant, as well as a slight resonance peak shift to a lower frequency. Without knowing the peak admittance, it is difficult to design a drive circuit for this transformer.

## 16.6 High-power piezoelectric ceramics

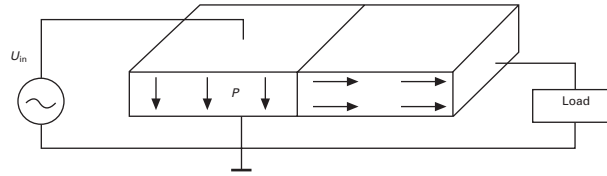
### 16.6.1 Very hard PZT-based ceramics

‘High power’ in this chapter stands for high-power density in mechanical output energy converted from the maximum input electrical energy under the drive condition with 20 °C temperature rise. For an off-resonance drive condition, the figure of merit of piezo-actuators is give by the piezoelectric  $d$  constant ( $\Delta L = dEL$ ). Heat generation can be evaluated by the intensive dielectric loss  $\tan \delta'$  (i.e.  $P$ – $E$  hysteresis).

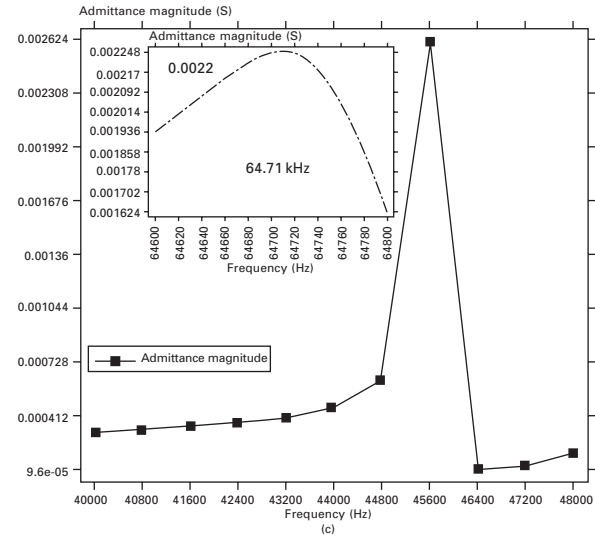
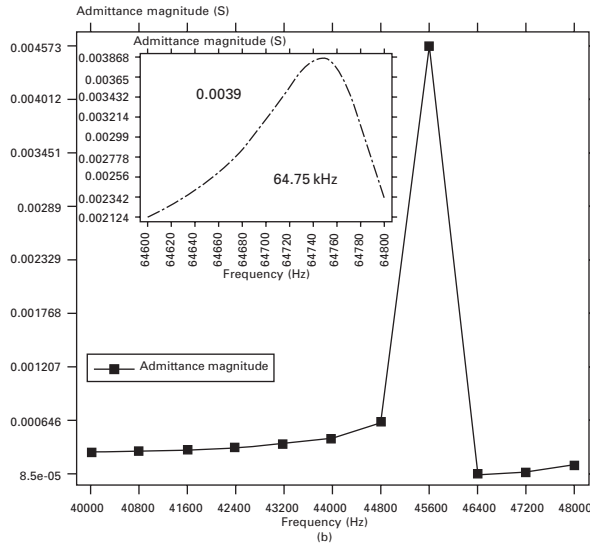
In contrast, for a resonance drive condition, the figure of merit is the vibration velocity  $v_0$ , which is roughly proportional to  $Q_m dEL$ . Heat generation is originated from the intensive elastic loss  $\tan \phi'$  (inverse value of  $Q_m$ ). The mechanical power density can be evaluated by the square of the maximum vibration velocity ( $v_0^2$ ), which is a sort of material constant. Remember that there exists the maximum mechanical energy density, above which level the piezoelectric material becomes a ceramic heater. High-vibration velocity materials are suitable for actuator applications such as ultrasonic motors. Further, when we consider transformers and transducers, where both transmitting and receiving functions are required, the figure of merit will be the product of  $v_0 k$  ( $k$ : electromechanical coupling factor).

Table 16.2 Gibbs loss tangents for typical 'soft' and 'hard' piezoceramics (APC-850 and 841, American Piezo Ceramics, PA)

Complex material constant	APC850 ('Soft Ceramic')			APC841 ('hard ceramic')		
	Real part	Imaginary part	Loss tangent	Real part	Imaginary part	Loss tangent
<b>Elastic compliance (<math>10^{-12} \text{ m}^2/\text{N}</math>)</b>						
$S_{11}^E$	16.9	-0.205	-0.012 2	11.4	-0.010 5	-0.000 92
$S_{12}^E$	-6.4	0.0779	-0.012 1	-3.42	0.003 83	-0.001 12
$S_{13}^E$	-5.6	0.067	-0.011 98	-5.65	-0.032	0.005 66
$S_{33}^E$	17.4	-0.347	-0.02	15.35	-0.069 2	-0.004 51
$S_{44}^E$	52.6	-3.82	-0.072 56	20.8	-0.24	-0.011 5
$S_{66}^E$	46.7	-1.968	-0.042	29.64	-0.028	-0.000 945
<b>Dielectric constant (<math>10^{-9} \text{ F/m}</math>)</b>						
$\epsilon_{11}^T$	10.01	0.346	-0.0346	12	-0.048	-0.004
$\epsilon_{33}^T$	15.8	-0.34	-0.022	18	-0.162	-0.009



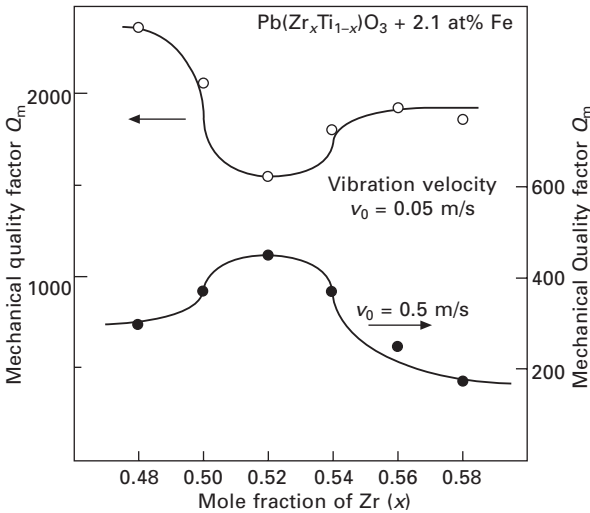
(a)



16.12 (a) Schematic structure of a Rosen-type piezoelectric transformer (40 mm in length); (b) admittance spectrum simulated for an isotropic loss condition ( $Q_m = 1087$ ), and admittance spectrum for an anisotropic loss condition ( $Q_m = 1087$  and 222).

Let us discuss high-vibration velocity materials first. Figure 16.13 shows the mechanical  $Q_m$  versus basic composition  $x$  at two effective vibration velocities  $v_0 = 0.05$  m/s and 0.5 m/s for  $\text{Pb}(\text{Zr}_x\text{Ti}_{1-x})\text{O}_3$  doped with 2.1 at.% of Fe [12]. The decrease in mechanical  $Q_m$  with an increase of vibration level is minimum around the rhombohedral–tetragonal morphotropic phase boundary (52/48). In other words, the smallest  $Q_m$  material under a small vibration level becomes the highest  $Q_m$  material under a large vibration level, and the data obtained by a conventional impedance analyzer with a small voltage/power do not provide any information relevant to high-power characteristics. Thus, we have developed various measuring techniques of high-power piezoelectricity, including ‘constant current’ and ‘pulse drive’ methods [13].

Conventional piezoceramics have a limitation in the maximum vibration velocity ( $v_{\text{max}}$ ), since the additional input electrical energy is converted into heat, rather than into mechanical energy. The typical rms value of  $v_{\text{max}}$  for commercially available materials, defined by the temperature rise of 20 °C from room temperature, is around 0.3 m/s for rectangular samples operating in the  $k_{31}$  mode (like a Rosen-type transformer) [10].  $\text{Pb}(\text{Mn,Sb})\text{O}_3$  (PMS)–lead zirconate titanate (PZT) ceramics with a  $v_{\text{max}}$  of 0.62 m/s are currently used for NEC transformers [12]. By doping the PMS–PZT or  $\text{Pb}(\text{Mn,Nb})\text{O}_3$ –PZT with rare-earth ions such as Yb, Eu and Ce, we recently developed high-power piezoelectrics, which can operate with  $v_{\text{max}}$  up to 1.0 m/s [14, 15]. Compared with commercially available piezoelectrics, 10 times higher-



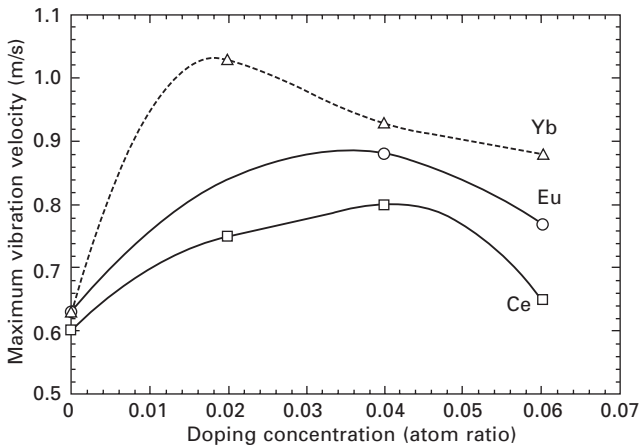
16.13 Mechanical  $Q_m$  versus basic composition  $x$  at two effective vibration velocities  $v_0 = 0.05$  m/s and 0.5 m/s for  $\text{Pb}(\text{Zr}_x\text{Ti}_{1-x})\text{O}_3$  doped with 2.1 at.% of Fe.

input electrical energy and output mechanical energy can be expected from these new materials without generating a significant temperature rise, which corresponds to  $100 \text{ W/cm}^2$ . Figure 16.14 shows the dependence of the maximum vibration velocity  $v_0$  ( $20^\circ\text{C}$  temperature rise) on the atomic % of rare-earth ion, Yb, Eu or Ce in the  $\text{Pb}(\text{Mn},\text{Sb})\text{O}_3$  (PMS)–PZT-based ceramics. Enhancement in the  $v_0$  value is significant by adding a small amount of the rare-earth ion [15].

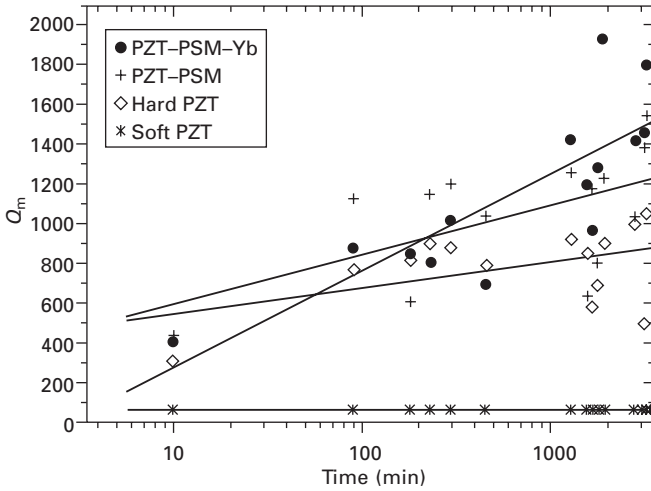
### 16.6.2 Origin of high-power piezoelectrics

‘Hard’ PZT is usually used for high-power piezoelectric applications, because of its high coercive field, in other words, the stability of the domain walls. Acceptor ions, such as  $\text{Fe}^{3+}$ , introduce oxygen deficiencies in the PZT crystal (in the case of donor ions, such as  $\text{Nb}^{5+}$ , Pb deficiency is introduced). Thus, in the conventional model, the acceptor doping causes domain pinning through the easy reorientation of deficiency-related dipoles, leading to ‘hard’ characteristics (domain wall pinning model [16]). In this section, we explore the origin of our high-power piezoelectric ceramics.

High mechanical  $Q_m$  is essential in order to obtain a high-power material with a large maximum vibration velocity. Figure 16.15 exhibits suggestive results in the mechanical  $Q_m$  increase with time lapse (minute) after the electric poling measured for various commercial soft and hard PZTs, PSM–PZT, and PSM–PZT doped with Yb. It is notable that the  $Q_m$  values for commercial hard PZT and our high power piezoelectrics were almost the same, slightly higher than soft PZTs, and around 200–300 immediately after the poling. After a couple of hours, the  $Q_m$  values increased more than



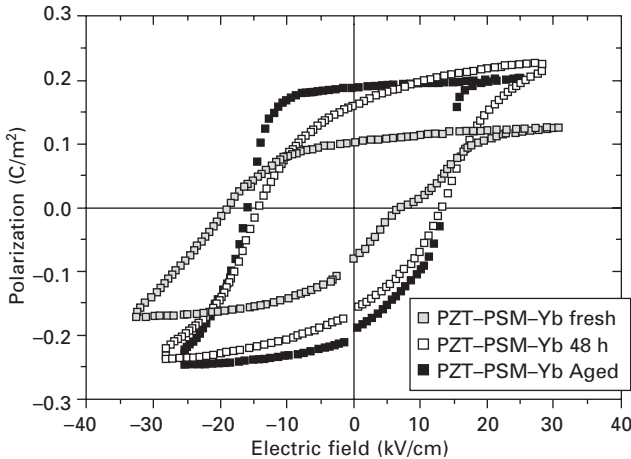
16.14 Dependence of the maximum vibration velocity  $v_0$  ( $20^\circ\text{C}$  temperature rise) on the atomic % of rare-earth ion, Yb, Eu or Ce in the  $\text{Pb}(\text{Mn}, \text{Sb})\text{O}_3$  (PMS)–PZT based ceramics.



16.15 Change in the mechanical  $Q_m$  with time lapse (minute) just after the electric poling measured for various commercial soft and hard PZTs, PSM-PZT, and PSM-PZT doped with Yb.

1000 for the ‘hard’ materials, while no change was observed in the ‘soft’ material. The increasing slope is the maximum for the Yb-doped PSM-PZT. We also found a contradiction that this gradual increase (in a couple of hours) in the  $Q_m$  cannot be explained by the above-mentioned ‘domain wall pinning’ model, but more likely by some ionic diffusion model.

Figure 16.16 shows the polarization vs. electric field hysteresis curves measured for the Yb-doped  $\text{Pb}(\text{Mn,Sb})\text{O}_3\text{-PZT}$  sample immediately after



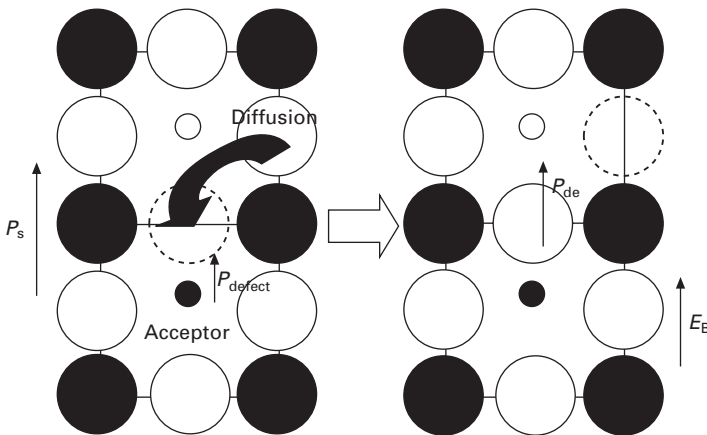
16.16 Polarization vs. electric field hysteresis curves measured for the Yb-doped  $\text{Pb}(\text{Mn,Sb})\text{O}_3\text{-PZT}$  sample just after poling (fresh), 48 hours after, and a week after (aged).

poling (fresh), 48 hours after, and a week after (aged). Remarkable aging effects could be observed: (a) in the decrease in the magnitude of the remnant polarization and (b) in the positive internal bias electric field growth (i.e. the hysteresis curve shift leftwards in terms of the external electric field axis). The phenomenon (a) can be explained by the local domain wall pinning effect, but the large internal bias (more than 1 kV/mm) growth (b) seems to be the origin of the high-power characteristics. Suppose that the vertical axis in Fig. 16.16 shifts rightwards, the inverse electric field required for realizing the 180° polarization reversal is increased, leading to the resistance enhancement against generating the hysteresis or heat.

Finally, let us propose the origin of this internal bias field growth. Based on the presence of the oxygen deficiencies and the relatively slow (a couple of hours) growth rate, we assume here the oxygen deficiency diffusion model, which is illustrated in Fig. 16.17. Under the electric poling process, the defect dipole  $P_{\text{defect}}$  (a pair of acceptor ion and oxygen deficiency) will be arranged parallel to the external electric field. After removing the field, oxygen diffusion occurs, which can be estimated in a scale of hour at room temperature. Taking into account slightly different atomic distances between the A and B ions in the perovskite crystal in a ferroelectric (asymmetric) phase, the oxygen diffusion probability will be slightly higher for the downward, as shown in the figure, leading to the increase in the defect dipole with time. This may be the origin of the internal bias electric field.

### 16.6.3 Semi-hard PZT-based ceramics

Though the rare-earth doped PZT–Pb(Mn,Sb)O<sub>3</sub> system with the highest vibration velocity satisfies actuator applications, due to relatively smaller



16.17 Oxygen deficiency diffusion model for explaining the internal bias electric field growth.

piezoelectric  $d$  constants, it cannot replace transducer or transformer materials, where the direct piezoelectric effect is successively utilized to convert the mechanical energy into final electrical energy. In this sort of electric–mechanical–electric conversion application, since the figure of merit is  $\nu_0 k$ , we modified the composition to improve the high  $Q_m$  by sustaining the high  $d$  and  $k$ , starting from originally soft  $\text{Pb}(\text{Zn}_{1/3}\text{Nb}_{2/3})\text{O}_3\text{–Pb}(\text{Ni}_{1/3}\text{Nb}_{2/3})\text{O}_3\text{–Pb}(\text{Zr}_{0.5}\text{Ti}_{0.5})\text{O}_3$ . Sb, Li and Mn were substituted to the  $0.8\text{Pb}(\text{Zr}_{0.5}\text{Ti}_{0.5})\text{O}_3\text{–}0.16\text{Pb}(\text{Zn}_{1/3}\text{Nb}_{2/3})\text{O}_3\text{–}0.04\text{Pb}(\text{Ni}_{1/3}\text{Nb}_{2/3})\text{O}_3$  ceramics. The composition  $0.8\text{Pb}(\text{Zr}_d\text{Ti}_{1-d})\text{O}_3\text{–}0.2\text{Pb}\{(1-c)\{(1-b)(\text{Zn}_{0.8}\text{Ni}_{0.2})_{1/3}(\text{Nb}_{1-a}\text{Sb}_a)_{2/3}\text{–}b(\text{Li}_{1/4}(\text{Nb}_{1-a}\text{Sb}_a)_{3/4})\}\text{–}c(\text{Mn}_{1/3}(\text{Nb}_{1-a}\text{Sb}_a)_{2/3})\}\text{O}_3$  ( $a = 0.1$ ,  $b = 0.3$ ,  $c = 0.3$  and  $d = 0.5$ ) showed the value of  $k_p = 0.56$ ,  $Q_m = 1951$  (planar mode),  $d_{33} = 239$  pC/N,  $\epsilon_3^T/\epsilon_0 = 739$  and the maximum vibration velocity = 0.6 m/s at 31-mode. By adjusting the Zr/Ti ratio, compromised properties of  $k_p = 0.57$ ,  $Q_m = 1502$  (planar mode),  $d_{33} = 330$  pC/N,  $\epsilon_3^T/\epsilon_0 = 1653$  and the maximum 31-mode vibration velocity = 0.58 m/s were obtained when Zr/Ti = 0.48/0.52 [17]. These compositions are suitable for piezoelectric transformers and transducers.

## 16.7 High-power piezoelectric components

Though we have developed ‘high-power density’ piezoelectric ceramics, the multilayer structure is a key to developing actual ‘high-power’ components from the device-designing viewpoint. However, the present Ag–Pd electrode structure includes two problems: (1) expensive Pd and (2) although Ag migration during sintering and under electric field applied can be suppressed by Pd, the electrode conductance is significantly decreased. The latter is the major problem in designing multilayer transformers, because the electrode loss appears to be large, leading to heat generation and low efficiency. In order to solve the problems, pure Cu electrode will be a key. But, the multilayer samples need to be sintered at a relatively low temperature (90 °C or lower) in a reduced atmosphere, when utilizing Cu embedded electrodes. Thus, it is necessary to develop low-temperature sintering of ‘hard’ type PZTs. Unlike soft PZTs, most of the conventional dopants to decrease the sintering temperature failed to be used, because these dopants also degrade the  $Q_m$  value significantly.

We further modified our high-power piezoelectric ceramics, the Sb, Li and Mn-substituted  $0.8\text{Pb}(\text{Zr}_{0.5}\text{Ti}_{0.5})\text{O}_3\text{–}0.16\text{Pb}(\text{Zn}_{1/3}\text{Nb}_{2/3})\text{O}_3\text{–}0.04\text{Pb}(\text{Ni}_{1/3}\text{Nb}_{2/3})\text{O}_3$ , by adding CuO and  $\text{Bi}_2\text{O}_3$  in order to lower the sintering temperature of the ceramics. Table 16.3 summarizes piezoelectric properties of semi-hard piezoelectric ceramics based on  $\text{Pb}(\text{Zn}_{1/3}\text{Nb}_{2/3})\text{O}_3\text{–Pb}(\text{Ni}_{1/3}\text{Nb}_{2/3})\text{O}_3\text{–Pb}(\text{Zr}_{0.5}\text{Ti}_{0.5})\text{O}_3$ , sinterable at 900 °C. Under a sintering condition of 900 °C for 2 h, the properties were  $k_p = 0.56$ ,  $Q_m$  (31-mode) = 1023,  $d_{33} = 294$  pC/N,  $\epsilon_{33}/\epsilon_0 = 1282$  and  $\tan\delta = 0.59\%$ , when CuO and  $\text{Bi}_2\text{O}_3$  were added 0.5 wt% each. The maximum vibration velocity of this composition was 0.41 m/s.



*Table 16.3* Piezoelectric properties of semi-hard piezoelectric ceramics based on  $\text{Pb}(\text{Zn}_{1/3}\text{Nb}_{2/3})\text{O}_3\text{-Pb}(\text{Ni}_{1/3}\text{Nb}_{2/3})\text{O}_3\text{-Pb}(\text{Zr}_{0.5}\text{Ti}_{0.5})\text{O}_3$ , sinterable at 900 °C.

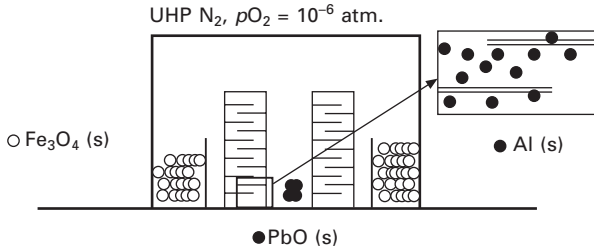
Composition	Sintering condition	$Q_m$ (planar)	$Q_m$ (31-mode)	$\varepsilon_3^T/\varepsilon_0$	$d_{33}$	$k_p$	$k_{31}$	$T_c(^{\circ}\text{C})$	$v_0$ (m/s)
HP-HT-6-2	1200/2 h	1951	1815	739	239	0.56	0.3	285.6	0.6
HP-HT-12-4	1200/2 h	1502	1404	1653	330	0.573	0.33	289.58	0.58
HP-LT-17-3	900/2 h	1282	*	1326	294	0.56	*	*	0.41

\* *On measuring.*

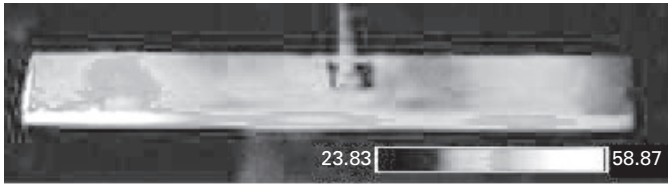
HP-HT-6-2:  $\text{Pb}(\text{Zr,Ti})\text{-Pb}(\text{Zn,Ni})\text{Nb}$  with Sb, Li and Mn substitution.

HP-HT-12-4: Further modification on the HP-HT-6-2.

HP-LT-17-3: Low temperature sintering of the HP-HT-12-4 with  $\text{CuO}$  and  $\text{Bi}_2\text{O}_3$ .



16.18 Experimental setup for sintering Cu-electrode-embedded multilayer transformers in a reducing  $N_2$  atmosphere.



16.19 Multilayer co-fired transformer with hard PZT and Cu (left) or pure Ag (right) electrode, sintered at  $900^\circ C$  (Penn State trial products).

Cu-embedded multilayer transformers are now being developed. Figure 16.18 illustrates an experimental setup for sintering Cu-electrode-embedded multilayer transformers in a reduced  $N_2$  atmosphere. Figure 16.19 shows co-fired multilayer transformers with pure Ag (right) and Cu (left) electrodes sintered at  $900^\circ C$ . The transformer performance will be reported in a successive paper.

## 16.8 Summary and conclusions

- There are three loss origins in piezoelectrics: the dielectric, elastic and piezoelectric losses. The  $180^\circ$  and non- $180^\circ$  domain wall motions contribute primarily to the extensive dielectric and elastic losses, respectively.
- Heat generation occurs in the sample uniformly under an off-resonance mainly due to the intensive dielectric loss, while heat is generated primarily at the vibration nodal points via the intensive elastic loss under a resonance. In both cases, the loss increase originates from the extensive dielectric loss change with electric field and/or stress.
- In a 'hard' piezoelectric PZT, the mechanical quality factor  $Q_m$  for the  $k_{33}$  mode is only 1/5 of that of the  $k_{31}$  mode. We integrated the loss anisotropy with an FEM software code and obtained more accurate simulation results for the piezo-transducer designing.
- Actuator materials: doping rare-earth ions into PZT-Pb(Mn,X)O<sub>3</sub> (X = Sb, Nb) ceramics increases the maximum vibration velocity up to 1 m/s,

which corresponds to one order of magnitude higher energy density than conventionally commercialized piezo-ceramics. To obtain high-power density/high-vibration velocity materials, domain wall immobility/stabilization via the positive internal bias field seems to be essential, rather than the local domain wall pinning effect.

- Transducer materials: the Sb, Li and Mn-substituted  $0.8\text{Pb}(\text{Zr}_{0.48}\text{Ti}_{0.52})\text{O}_3$ – $0.16\text{Pb}(\text{Zn}_{1/3}\text{Nb}_{2/3})\text{O}_3$ – $0.04\text{Pb}(\text{Ni}_{1/3}\text{Nb}_{2/3})\text{O}_3$  ceramics showed the value of  $k_p = 0.57$ ,  $Q_m = 1502$  (planar mode),  $d_{33} = 330$  pC/N,  $\epsilon_3^T/\epsilon_0 = 1653$  and the maximum vibration velocity = 0.58 m/s at 31-mode. Low-temperature sinterable ‘hard’ piezoelectrics were also synthesized based on the Sb, Li and Mn-substituted ceramics of  $0.8\text{Pb}(\text{Zr}_{0.5}\text{Ti}_{0.5})\text{O}_3$ – $0.16\text{Pb}(\text{Zn}_{1/3}\text{Nb}_{2/3})\text{O}_3$ – $0.04\text{Pb}(\text{Ni}_{1/3}\text{Nb}_{2/3})\text{O}_3$ , by adding CuO and  $\text{Bi}_2\text{O}_3$ , giving rise to  $k_p = 0.56$ ,  $Q_m$  (31-mode) = 1023,  $d_{33} = 294$  pC/N,  $\epsilon_{33}/\epsilon_0 = 1282$  and  $\tan\delta = 0.59\%$ , and vibration velocity 0.41 m/s.
- Cu embedded multilayer piezo-transformers were trial-manufactured under a low temperature sintering process (900 °C for 2 hours).

## 16.9 Future trends

Since the above conclusions have been derived only from a limited number of PZT-based soft and hard piezoelectrics, it is too early to generalize these conclusions. Further investigations are highly required, including:

- determination of the three (dielectric, elastic and piezoelectric) losses for various piezoceramics;
- determination of loss anisotropy for piezoceramics;
- loss origin clarification through dynamic domain observations, and the modeling of loss mechanisms in piezoelectrics;
- high-power density piezoelectric actuators and transducer developments.

## 16.10 Acknowledgement

Part of this research was supported by the Office of Naval Research through the grant no. N00014-96-1-1173 and N00014-99-1-0754.

## 16.11 References

1. K. H. Haerdtl, *Ceram. Int* 1, **8**, 121–127 (1982).
2. T. Ikeda, *Fundamentals of Piezoelectric Materials Science* (Ohm Publication Co., Tokyo, 1984), p. 83.
3. N. Setter ed., *Piezoelectric Materials in Devices* (2002).
4. K. Uchino and S. Hirose, *IEEE-UFFC Trans.*, **48**, 307–321 (2001).
5. N. Bhattacharya and K. Uchino, *IEEE-UFFC Trans.* (2006) [on review].
6. J. Zheng, S. Takahashi, S. Yoshikawa, K. Uchino and J. W. C. de Vries, *J. Amer. Ceram. Soc.*, **79**, 3193–3198 (1996).

7. N. Uchida and T. Ikeda, *Jpn. J. Appl. Phys.*, **6**, 1079 (1967).
8. K. Uchino, *Piezoelectric Actuators and Ultrasonic Motors* (Kluwer Academic Publ., Boston, 1997), p. 197.
9. M. Umeda, K. Nakamura and S. Ueha, *Jpn. J. Appl. Phys.*, **38**, 3327–3330 (1999)
10. S. Hirose, M. Aoyagi, Y. Tomikawa, S. Takahashi and K. Uchino, *Proc. Ultrasonics Intl 95*, Edinburgh, pp. 184–187 (1995).
11. S. Tashiro, M. Ikehiro and H. Igarashi, *Jpn. J. Appl. Phys.*, **36**, 3004–3009 (1997).
12. S. Takahashi and S. Hirose, *Jpn. J. Appl. Phys.*, **32**, 2422–2425 (1993).
13. K. Uchino, J. Zheng, A. Joshi, Y. H. Chen, S. Yoshikawa, S. Hirose, S. Takahashi and J. W. C. de Vries, *J. Electroceramics*, **2**, 33–40 (1998).
14. J. Ryu, H. W. Kim, K. Uchino and J. Lee, *Jpn. J. Appl. Phys.*, **42**, No. 3, 1–4 (2003).
15. Y. Gao, K. Uchino and D. Viehland, *J. Appl. Phys.*, **92**, 2094–2099 (2002).
16. K. Uchino, *Ferroelectric Devices* (Marcel Dekker, Inc., New York, 2000), p. 63.
17. Park, S.-H., S. Ural, C.-W. Ahn, S. Nahm and K. Uchino, *Jpn. J. Appl. Phys.*, **45**, 2667–2673 (2006).

## Bismuth-based pyrochlore dielectric ceramics for microwave applications

HONG WANG and X YAO,  
Xi'an Jiaotong University, China

### 17.1 Introduction

$\text{Bi}_2\text{O}_3\text{-ZnO-Nb}_2\text{O}_5$  (BZN)-based pyrochlore ceramics are lead-free dielectrics with high permittivity, low loss and low sintering temperatures. BZN dielectric ceramics were first developed in the 1970s by Chinese researchers for low sintering temperature multilayer ceramic capacitors (MLCC) (ZP Wang *et al.*, 1985; Li *et al.*, 1986). However, the very complex chemical compositions and unknown complicated phase structures frustrated the early attempts to make these promising low-sintering dielectrics in practical applications for MLCC. In the late 1980s, BZN compositions were picked up and studied by Yan and coworkers in Bell Lab (MF Yan *et al.*, 1990; Ling, 1990). Their studies involved much simplified chemical compositions using a two-step powder process technology by mixing together calcined powders of BZN and  $\text{Bi}_2\text{O}_3\text{-NiO-Nb}_2\text{O}_5$  (BNN). The resulting phase structures were still complex and unclear. From the late 1980s up to now, Yao's group has been studying the  $\text{Bi}_2\text{O}_3\text{-ZnO-Nb}_2\text{O}_5$  (BZN) system and related dielectric materials systematically. From their early studies (DH Liu *et al.*, 1993; H Wang *et al.*, 1994a,b, 1995, 1996a,b, 1997; XL Wang *et al.*, 1997; Cai *et al.*, 1994a,b, c;), the cubic pyrochlore structure was first recognized as a main phase in this system in the compositions around  $\text{Bi}_{3x}\text{Zn}_{2-2x}\text{Nb}_{2-x}\text{O}_7$  ( $x = 0.45\text{-}0.55$ ), while another main phase  $\text{Bi}_2(\text{Zn}_{2/3}\text{Nb}_{4/3})\text{O}_7$  with low symmetry in this system was identified as orthorhombic then monoclinic pyrochlore. The PDF file 54-971 for  $(\text{Bi}_{1.5}\text{Zn}_{0.5})(\text{Zn}_{0.5}\text{Nb}_{1.5})\text{O}_7$  cubic pyrochlore and 54-972 for  $\text{Bi}_2(\text{Zn}_{1/3}\text{Nb}_{2/3})_2\text{O}_7$  pyrochlore were added to the International Center of Diffraction Data. The continuous investigation has been focused on the structure-property relations including phase diagram, phase equilibrium and dielectric property optimization. Those fundamental works provide a useful understanding of the BZN material system and accelerate the studies for dielectric properties improvements and potential applications.

With the recent development in low-temperature co-fired ceramic (LTCC) devices, the demands for new materials that can be co-fired with base metal

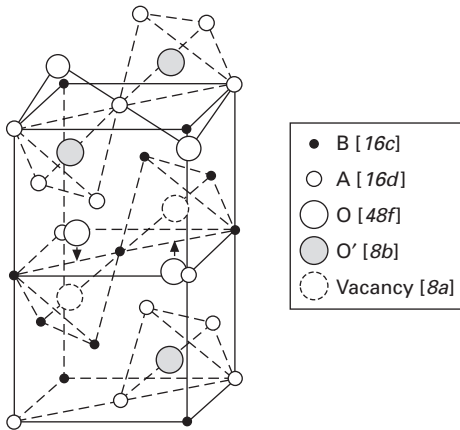
electrodes at lower temperatures (normally less than 1000 °C) have significantly increased in the past decade. Bismuth-based pyrochlore dielectrics thus attracted more and more attention due to their excellent dielectric properties and lower sintering temperatures and have become promising candidates for LTCC and microwave passive components since late 1990s (Cann *et al.*, 1996; Mergen *et al.*, 1996, 1997). High-performance BZN-based temperature stable dielectrics with low sintering temperature below 940 °C were developed for multilayer ceramic capacitors (MLCC) (M Chen *et al.*, 1998; Du *et al.*, 2001). Recent publications reported on the formation, stability, processing windows and crystallographic characterization in this system as well as successful manufacturing of prototype devices including LC filters and LTCC components (H Wang, 1999a, 2004a; Randall, 2003; Zanetti, 2004). The high tunability found in BZN cubic pyrochlore thin films makes this material a new candidate for microwave tunable devices which may replace the conventional  $(\text{Ba}_x\text{Sr}_{1-x})\text{TiO}_3$  thin film (Ren *et al.*, 2001). Potential applications of BZN dielectrics include their use in MLCC, tunable filters, phase shifters, and electrically steerable antennas.

This chapter aims to review the highlights of the bismuth-based pyrochlore dielectrics developed so far and discuss the strategy for tailoring both structure and performance towards applications.

## 17.2      Crystal structures in the BZN system

The general formula of oxide pyrochlores can be written as  $\text{A}_2\text{B}_2\text{O}_6\text{O}'$  with four crystallographically non-equivalent ions which are A (site 16d), B (site 16c), O (site 48f), and O' (site 8b) (Subramanian, 1983). The space group of an ideal pyrochlore structure is  $Fd\bar{3}m - O_h^7$  and there are eight formula units per unit cell ( $Z = 8$ ). Figure 17.1 shows the schematic of 1/4 unit cell of pyrochlore structure. The pyrochlore can be regarded as a derivative structure from a defective fluorite structure with anion vacancies on 8a sites. Table 17.1 gives the atomic coordinate data of an ideal cubic pyrochlore. Owing to the existence of vacancies on 8a site, the 48f anions thus have a balance shift towards the two neighboring B cations. The A cations (usually with  $\sim 1 \text{ \AA}$  ionic radius) are eight coordinated and are located within scalenohedra (distorted cubes) that contains two equally spaced O' anions at a slightly shorter distance from the central cations ( $\text{A}_2\text{O}_6\text{O}'_2$ ). The smaller B cations ( $\sim 0.6 \text{ \AA}$  ionic radius) are six coordinated and are located within trigonal antiprisms (distorted octahedral,  $\text{BO}_6$ ) with all the six anions at equal distances from the central cation. Thus the pyrochlore structure can be described as a 3D network with the corner-sharing  $\text{BO}_6$  octahedra and the eight coordinated A cations ( $\text{A}_2\text{O}_6\text{O}'_2$ ) locating in the interstices of  $\text{BO}_6$  network (see Fig. 17.2).

The main crystal structures in the BZN ternary system were revealed as a cubic pyrochlore ( $\alpha$ )  $Fd\bar{3}m - O_h^7$ ,  $Z = 8$  and a low symmetry pyrochlore ( $\beta$ ),



17.1 Schematic of pyrochlore structure (1/4 unit cell).

Table 17.1 Pyrochlore ( $A_2B_2O_6O'$ ) structural data (origin on the B site)

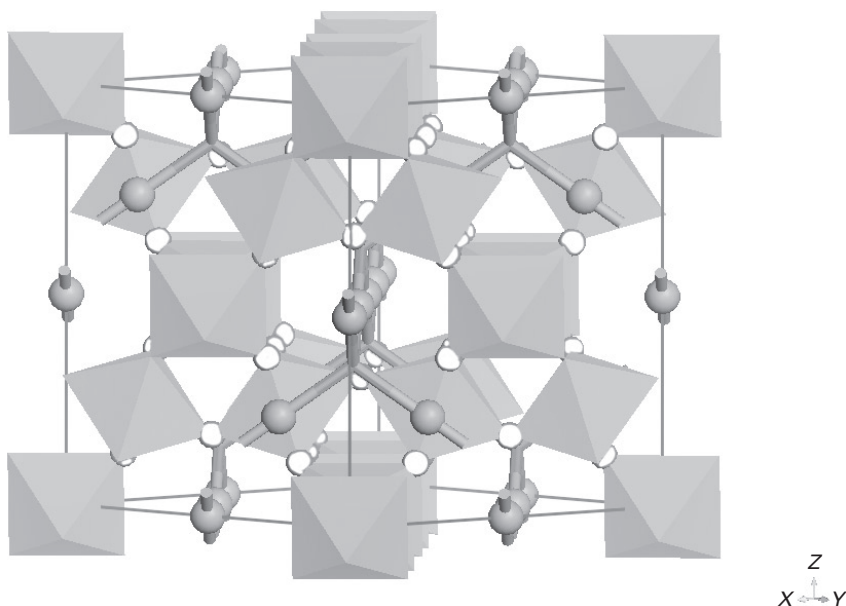
Ion	Location	Site symm.	Coordinates
16A	16d	$D_{3d}$	$(0,0,0; 0,1/2,1/2; 1/2,0,1/2; 1/2,1/2,0) +$ $1/2,1/2,1/2; 1/2,1/4,1/4; 1/4,1/2,1/4; 1/4,1/4,1/2$
16B	16c	$D_{3d}$	$0,0,0; 0,1/4,1/4; 1/4,0,1/4; 1/4,1/4,0$
48O	48f	$C_{2v}$	$x,1/8,1/8; -x,7/8,7/8; 1/4-x,1/8,1/8; 3/4+x,7/8,7/8$ $1/8,x,1/8; 7/8,-x,7/8; 1/8,1/4-x,1/8; 3/4+x,7/8$ $1/8,1/8,x; 7/8,7/8,-x; 1/8,1/8,1/4-x; 7/8,7/8,3/4+x$
8O'	8b	$T_d$	$3/8,3/8,3/8; 5/8,5/8,5/8$ $x$ for regular octahedra: 0.3125 (5/16) $x$ for regular cube: 0.375 (3/8)

which was indexed as orthorhombic first, then determined as monoclinic zirconolite-like pyrochlore ( $C2/c - C_{2h}^6$ ) (H Wang *et al.*, 1994b; XL Wang *et al.*, 1997; Levin *et al.* 2002b).

### 17.2.1 Crystal structure of cubic pyrochlore

The cubic pyrochlores in the BZN ternary system were first observed in the region of  $Bi_xZn_{2/3}Nb_{4/3}O_{4+3x/2}$  ( $1 \leq x \leq 10/6$ ),  $Bi_xZn_{8/3-x}Nb_{4/3}O_{6+x+2}$  ( $1 \leq x \leq 10/6$ ), and  $Bi_xZn_{2-2x/3}Nb_{2-x/3}O_7$  ( $1.5 \leq x \leq 1.8$ ) (DH Liu *et al.*, 1993). It was found to exist in a wide region around the composition of  $Bi_{1.5}ZnNb_{1.5}O_7$  (H Wang *et al.*, 1994b, 1996a; XL Wang *et al.*, 1997), while the ideal pyrochlore composition  $Bi_2(Zn_{1/3}Nb_{2/3})_2O_7$  was identified as a low symmetry pyrochlore (H Wang *et al.*, 1996b, 1997; XL Wang *et al.*, 1997).

The structure of  $Bi_{1.5}ZnNb_{1.5}O_7$  cubic pyrochlore was studied using X-ray diffraction (H Wang *et al.*, 1994b, 1995). By comparing the theoretically



17.2 Crystal structure of the BZN cubic pyrochlore ( $\text{BO}_6$  network, ● A site; octahedral: B site; ○ O atom).

calculated X-ray diffraction patterns with the observed ones, the chemical formula of this material was determined as a stuffed  $(\text{Bi}_{1.5}\text{Zn}_{0.5})(\text{Zn}_{0.5}\text{Nb}_{1.5})\text{O}_7$  pyrochlore with disordered cation distribution (H Wang *et al.*, 1995). The lattice parameter was refined by the Rietveld method as  $a = 10.555 \text{ \AA}$ . Combining with Raman spectroscopy, the site occupation of  $(\text{Bi}_{1.5}\text{Zn}_{0.5})(\text{Zn}_{0.5}\text{Nb}_{1.5})\text{O}_7$  was found to occur in such a way that  $\text{Zn}^{2+}$  is apt to occupy the B site first and then enters the A site after the B site is fully occupied (H Wang *et al.*, 2003).

Levin *et al.* (2002a) have carried out a careful structural investigation on the  $\text{Bi}_{1.5}\text{ZnNb}_{1.5}\text{O}_7$  composition using combined electron, X-ray and neutron powder diffraction techniques. Their results showed small amounts of  $\text{ZnO}$  existing in addition to the main cubic pyrochlore phase of  $\text{Bi}_{1.5}\text{ZnNb}_{1.5}\text{O}_7$ . The single pyrochlore phase forms at the composition  $\text{Bi}_{1.5}\text{Zn}_{0.92}\text{Nb}_{1.5}\text{O}_{6.92}$ . Rietveld refinements using neutron powder diffraction data confirmed an average pyrochlore structure  $\text{A}_2\text{B}_2\text{O}_6\text{O}'$  ( $Fd\bar{3}m - O_h^7$ ;  $a = 10.5616(1) \text{ \AA}$ ) with both Bi and Zn mixed on the A-sites. Refinements also revealed significant local deviations from the ideal pyrochlore arrangement which were caused by apparent displacive disorder on both the A and  $\text{O}'$  sites. The best fit was obtained with a disordered model in which the A-cations were randomly displaced by  $\sim 0.39 \text{ \AA}$  from the ideal eight-fold coordinated positions. The refined structural parameters of  $(\text{Bi}_{1.5}\text{Zn}_{0.5})(\text{Zn}_{0.5}\text{Nb}_{1.5})\text{O}_7$  is presented in Table 17.2.



*Table 17.2* Room temperature structural parameters of  $(\text{Bi}_{1.5}\text{Zn}_{0.5})(\text{Zn}_{0.5}\text{Nb}_{1.5})\text{O}_7$  pyrochlore (Melot *et al.*, 2006)

Atom	Site	Occ.	x	y	z	U
Bi/Zn	96g	0.125/0.035	0.4689(1)	0.5174(2)	0.5174(2)	1.55(3)
Nb/Zn	16c	0.750/0.250	0	0	0	1.32(2)
O'	96g	0.0767	0.3443(2)	0.3443(2)	0.3770(4)	2.2(1)
O	48f	1	0.31996(4)	1/8	1/8	2.20*

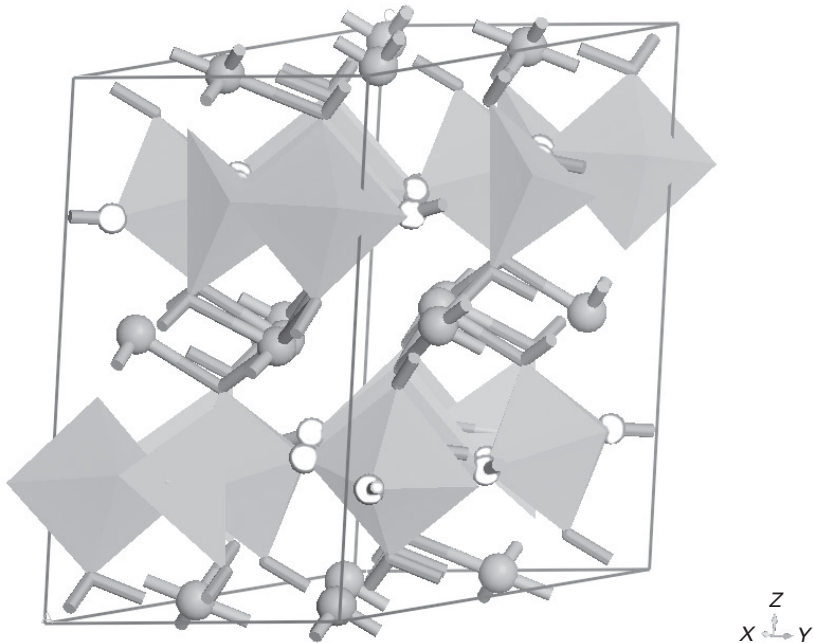
\* $U_{11}$ , 3.30(3);  $U_{22}=U_{33}$  1.64(2);  $U_{23}$ , 0.90(2). SG (space group).  $Fd3m$  (No. 227, origin 2)  $a = 10.5555(5)$  Å,  $\chi^2 = 1.872$ . Anisotropic parameters are presented for O.

### 17.2.2 Crystal structure of monoclinic zirconolite-like structure

The low-symmetry phase in BZN system was identified as orthorhombic first and then as monoclinic pyrochlore by using X-ray diffraction technology on ceramic powder (XL Wang *et al.*, 1997; H Wang *et al.*, 2001a). Attempts to grow the single crystal of this low-symmetry phase were not successful because this  $\beta$  phase is incongruent (H Wang *et al.*, 2001b). Levin *et al.* (2002b) used electron, X-ray and neutron diffraction to investigate the  $\beta$  phase in detail and obtained useful structural information of  $\text{Bi}_2\text{Zn}_{2/3}\text{Nb}_{4/3}\text{O}_7$  composition. The crystal structure of  $\text{Bi}_2\text{Zn}_{2/3}\text{Nb}_{4/3}\text{O}_7$  (see Fig. 17.3) was thus determined as a monoclinic zirconolite-like structure (space group  $C2/c - C_{2h}^6$ ,  $a = 13.1037(9)$  Å,  $b = 7.6735(3)$  Å,  $c = 12.1584(6)$  Å,  $\beta = 101.318(5)^\circ$ ). According to the structural refinement using neutron diffraction data, Nb preferentially occupies the six-fold coordinated sites in octahedral sheets parallel to the (001) planes, while Zn is statically distributed between the two half-occupied (5+1)-fold coordinated sites near the centres of six-membered rings of the  $[\text{Nb}(\text{Zn})\text{O}_6]$  octahedral. The Nb/Zn cation layers alternate along the  $c$ -axis with Bi-layers, in which Bi cations occupy both eight- and seven-fold coordinated sites.

### 16.2.3 Non-stoichiometric pyrochlores and local crystal chemistry

The pyrochlore with the formula  $\text{A}_2\text{B}_2\text{O}_7$  is often written as  $\text{A}_2\text{B}_2\text{O}_6\text{O}'$  to distinguish the oxygen atoms in the two different networks of  $\text{BO}_6$  and  $\text{A}_2\text{O}'$ . The 'defect' pyrochlores form easily since the network of  $\text{A}_2\text{O}'$  can be partially occupied or even completely absent. In the bismuth-based pyrochlores, the composition  $\text{Bi}_{1.5}\text{ZnNb}_{1.5}\text{O}_7$  was shown to be a two-phase mixture of pyrochlore and ZnO. The single-phase cubic pyrochlore structure was obtained at the composition  $\text{Bi}_{1.5}\text{Zn}_{0.92}\text{Nb}_{1.5}\text{O}_{6.92}$  where A sites were assumed to be occupied by a disordered mixture of  $\text{Bi}^{3+}$ ,  $\text{Zn}^{2+}$  and vacancies (Levin *et al.*, 2002a).



17.3 Crystal structure of the monoclinic zirconolite-like phase. ( $\text{BO}_6$  network, ● A site; Octahedral: B site; ○ O atom)

The single phase cubic pyrochlores were found mostly in the non-stoichiometric compositions, such as  $\text{Bi}_{1.50}\text{Zn}_{0.45}(\text{Zn}_{0.46}\text{Nb}_{1.54})\text{O}_7$ ,  $\text{Bi}_{1.50}\text{Zn}_{0.45}(\text{Zn}_{0.48}\text{Nb}_{1.52})\text{O}_7$ ,  $\text{Bi}_{1.55}\text{Zn}_{0.42}(\text{Zn}_{0.49}\text{Nb}_{1.51})\text{O}_7$ ,  $\text{Bi}_{1.60}\text{Zn}_{0.40}(\text{Zn}_{0.53}\text{Nb}_{1.47})\text{O}_7$ , and  $\text{Bi}_{1.63}\text{Zn}_{0.35}(\text{Zn}_{0.53}\text{Nb}_{1.47})\text{O}_7$ , with  $\text{Zn}^{2+}$  being partially absent on A sites while the B sites being fully occupied by  $\text{Nb}^{5+}$  and  $\text{Zn}^{2+}$  (Vanderah *et al.*, 2005). The structural study using Raman spectroscopy revealed that the site occupation of  $\text{Bi}_{1.5-2y}\text{Zn}_{1+2y}\text{Nb}_{1.5}\text{O}_{7-y}$  ( $-0.3 \leq y \leq 0.3$ ) could be explained as  $\text{Bi}_{1.5-2y}\text{Zn}_{0.5+2y}(\text{Zn}_{0.5}\text{Nb}_{1.5})\text{O}_{7-y}$  with  $\text{Zn}^{2+}$  occupying the B site first and then entering the A site after the B site was fully occupied (H Wang *et al.*, 2003; Du *et al.*, 2004a). The ZnO deficiency compared to  $\text{Bi}_{1.5}\text{ZnNb}_{1.5}\text{O}_7$  was also confirmed by stoichiometric study on the compositions  $\text{Bi}_{3+y}\text{Zn}_{2-x}\text{Nb}_{3-y}\text{O}_{14-x-y}$  ( $-0.11 \leq y \leq 0.14$ ,  $-0.03 \leq x \leq 0.31$ ) (Tan *et al.*, 2005). Local crystal chemistry and structure diffused scattering on  $(\text{Bi}_{1.5-\alpha}\text{Zn}_{0.5-\beta})(\text{Zn}_{0.5-\gamma}\text{Nb}_{1.5-\delta})\text{O}_{7-1.5\alpha-\beta-\gamma-2.5\delta}$  and  $(\text{Bi}_{1-x}\text{Y}_x)(\text{M}^{\text{III}}\text{Nb}^{\text{V}})\text{O}_7$  ( $\text{M} = \text{Fe}^{3+}$ ,  $\text{In}^{3+}$ ) were carefully studied by using electron diffraction technique (Withers *et al.*, 2004; Y Liu *et al.*, 2006, 2007; Somphon *et al.*, 2006). The fundamental underlying crystal chemistry of bismuth-based pyrochlore is based on a strong local displacive disorder in the  $\text{A}_2\text{O}'$  network which gives rise to the dielectric relaxation in the cubic bismuth-based pyrochlores (Withers *et al.*, 2004; Vanderah *et al.*, 2005; Y Liu *et al.*, 2007). The displacive disorder in the  $(\text{Bi}_{1.5}\text{Zn}_{0.5})(\text{Zn}_{0.5}\text{Nb}_{1.5})\text{O}_7$ ,

$(\text{Bi}_{1.5}\text{Zn}_{0.5})(\text{Zn}_{0.5}\text{Sb}_{1.5})\text{O}_7$  and  $(\text{Bi}_{1.5}\text{Zn}_{0.5})(\text{Zn}_{0.5}\text{Sb}_{1.5})\text{O}_7$  pyrochlores was studied by time-of-flight neutron powder diffraction (Melot *et al.*, 2006). Although the precise nature of the disorder in the three pyrochlores is quite similar, the reported dielectric constants of the three compounds are related to the extent of local displacement, and  $(\text{Bi}_{1.5}\text{Zn}_{0.5})(\text{Zn}_{0.5}\text{Nb}_{1.5})\text{O}_7$  with the largest extent of local atomic displacement of A and O' is reported to have the highest dielectric constant.

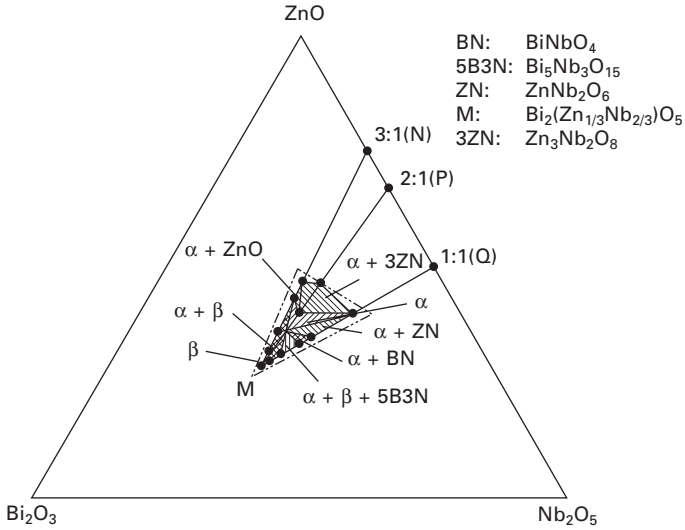
## 17.3 Phase equilibrium and phase relation of BZN pyrochlores

### 17.3.1 Phase equilibrium and phase diagram

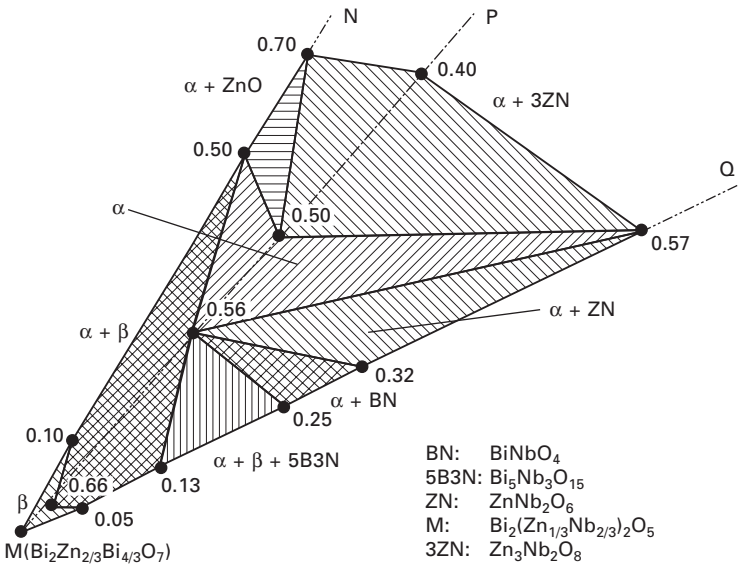
The phase equilibrium, phase formation, and phase relations in the  $\text{Bi}_2\text{O}_3$ – $\text{ZnO}$ – $\text{Nb}_2\text{O}_5$  ternary system were investigated (H Wang *et al.*, 1998; Kim *et al.*, 2002; Tan *et al.*, 2005; Vanderah *et al.*, 2005). The ceramic samples in a triangular area (see Fig. 17.4) around the cubic pyrochlore phase  $\text{Bi}_{1.5}\text{ZnNb}_{1.5}\text{O}_7$  with the compositions of  $(\text{Bi}_{3-x}\text{Zn}_{2-3x})(\text{Zn}_x\text{Nb}_{2-x})\text{O}_7$  ( $0 \leq x \leq 2/3$ ),  $(\text{Bi}_{2-x}\text{Zn}_x)(\text{Zn}_{(5-x)/15}\text{Nb}_{(10+x)/15})_2\text{O}_{7-0.3x}$  ( $0 \leq x \leq 2$ ),  $(\text{Bi}_{2-2x}\text{Zn}_x)(\text{Zn}_{(1-x)/3}\text{Nb}_{(2+x)/3})_2\text{O}_{7-x}$  ( $0 \leq x \leq 1$ ) and some other compositions around the 'ideal' pyrochlore composition  $\text{Bi}_2(\text{Zn}_{1/3}\text{Nb}_{2/3})\text{O}_7$  were selected and prepared by conventional powder processing technique (H Wang *et al.*, 1998). Quenching technology was adopted to keep the high-temperature phase of the samples after they reached the equilibrium. Based on X-ray diffraction analysis and thermal analysis, the phase formation was studied from 550 °C to 1050 °C with a temperature increment of 50 °C. The isothermal phase diagrams have been obtained. The pure  $\alpha$  phase region and  $\beta$  phase region were determined in different temperatures, while the  $\alpha$ – $\beta$  co-existing phase was found to exist between the two single phases region. The phase diagrams of pyrochlores in the  $\text{Bi}_2\text{O}_3$ – $\text{ZnO}$ – $\text{Sb}_2\text{O}_5$  (Miles *et al.*, 2006),  $\text{Bi}_2\text{O}_3$ – $\text{NiO}$ – $\text{Nb}_2\text{O}_5$  (Valant *et al.*, 2005) and  $\text{Bi}_2\text{O}_3$ – $\text{ZnO}$ – $\text{Ta}_2\text{O}_5$  (Khaw *et al.*, 2007) ternary systems have also been elaborated.

### 17.3.2 Phase formation of cubic pyrochlore and monoclinic pyrochlore

The phase formation study was carried out by X-ray diffraction (XRD) technique and thermal analysis (XL Wang *et al.*, 1997; H Wang, 1998). The results show that  $\text{Bi}_2\text{O}_3$ ,  $\text{ZnO}$  and  $\text{Nb}_2\text{O}_5$  do not react at 450 °C in the BZN system. X-ray diffraction lines of the  $24\text{Bi}_2\text{O}_3 \cdot \text{ZnO}$  phase were observed at 500 to 550 °C. The diffraction lines of  $\text{Bi}_2\text{O}_3$  disappeared at 550 °C while those of  $24\text{Bi}_2\text{O}_3 \cdot \text{ZnO}$  increased. This indicates that  $\text{Bi}_2\text{O}_3$  reacts with  $\text{ZnO}$



(a)



(b)

17.4 Isothermal phase diagram of the BZN ternary system at 1000 °C

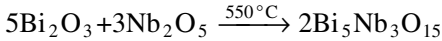
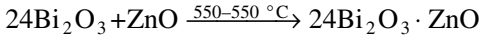
(a) and magnified pyrochlore region (b). (M:  $\text{Bi}_2(\text{Zn}_{1/3}\text{Nb}_{2/3})_2\text{O}_7$ ;

M-P:  $(\text{Bi}_{3-x}\text{Zn}_{2-3x})(\text{Zn}_x\text{Nb}_{2-x})\text{O}_7$  ( $0 \leq x \leq 2/3$ );

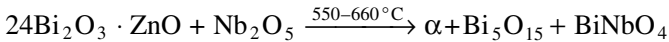
M-N:  $(\text{Bi}_{2-x}\text{Zn}_x)(\text{Zn}_{(5-x)/15}\text{Nb}_{(10+x)/15})_2\text{O}_7-0.3x\text{O}_3$  ( $0 \leq x \leq 2$ );

M-Q:  $(\text{Bi}_{2-2x}\text{Zn}_{x/3})(\text{Zn}_{(1-x)/3}\text{Nb}_{(2+x)/3})_2\text{O}_7-x\text{O}_3$  ( $0 \leq x \leq 1$ ).

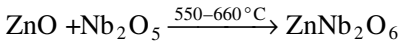
first to form  $24\text{Bi}_2\text{O}_3 \cdot \text{ZnO}$  and  $\text{Bi}_5\text{Nb}_3\text{O}_{15}$  phase appears as well. The reaction is expressed as follows.



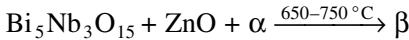
The cubic  $\alpha$  phase forms at  $600^\circ\text{C}$  with the reaction as in the following equation:



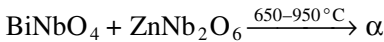
Simultaneously  $\text{ZnO}$  and  $\text{Nb}_2\text{O}_5$  react to form  $\text{ZnNb}_2\text{O}_6$ :



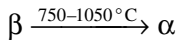
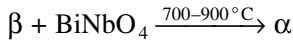
Then the  $\beta$  phase forms at  $650^\circ\text{C}$  with the reaction as in the following equation:



With the disappearance of  $\text{BiNbO}_4$  and  $\text{ZnNb}_2\text{O}_6$ , the  $\alpha$  phase content increases, thus the following reaction takes place:



In the  $\alpha$ - $\beta$  coexisting area, with the calcined temperature increasing,  $\text{BiNbO}_4$  continues to react with the  $\beta$  phase, and as a result, the  $\alpha$  phase content increases while the  $\beta$  phase content decreases:



In summary, the  $\alpha$  phase forms at  $550\text{--}600^\circ\text{C}$  by the reaction of  $24\text{Bi}_2\text{O}_3 \cdot \text{ZnO}$  and  $\text{Nb}_2\text{O}_5$ , while the  $\beta$  phase forms at  $650\text{--}750^\circ\text{C}$  by the reaction of  $\text{Bi}_5\text{Nb}_3\text{O}_{15}$ ,  $\text{ZnO}$  and  $\alpha$  phase. With the calcining temperature increasing, the  $\beta$  phase gradually transforms to the  $\alpha$  phase. Table 17.3 shows the phase formation of compositions  $(\text{Bi}_{3x}\text{Zn}_{2-3x})(\text{Zn}_x\text{Nb}_{2-x})\text{O}_7$ .

### 17.3.3 Melting behavior of BZN pyrochlores

The melting behaviour of pyrochlores in the  $\text{Bi}_2\text{O}_3\text{--ZnO--Nb}_2\text{O}_5$  system was investigated by X-ray diffraction and thermal analysis (H Wang *et al.*, 2001b). The main crystal structures in the  $\text{Bi}_2\text{O}_3\text{--ZnO--Nb}_2\text{O}_5$  system include a cubic pyrochlore ( $\alpha$ ), a monoclinic zirconolite-like phase ( $\beta$ ) and a defect cubic fluorite (F). The  $\alpha$  pyrochlore and F fluorite are congruent melting compounds and the  $\beta$  pyrochlore is an incongruent melting compound. The melting

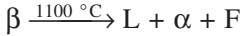
Table 17.3 Phase formation of compositions  $(\text{Bi}_{3-x}\text{Zn}_{2-3x})(\text{Zn}_x\text{Nb}_{2-x})\text{O}_7$ . (H Wang *et al.*, 1997)

Compo- sitions	550 °C	600 °C	650 °C	700 °C	750 °C	800 °C	850 °C	900 °C	950 °C	1000 °C	1050 °C
$x=0.67$ (M)	N,24BZ,5B3N,Z 100,55,33,10	$\alpha$ ,5B3N,BN,ZN,Z 12,100,98,7,9	$\alpha$ ,5B3N,BN,ZN,Z 8,100,49,4,6	$\alpha,\beta$ ,BN 12,100,20	$\beta$ $\beta$	$\beta$ $\beta$	$\beta$ $\beta$	$\beta$ $\beta$	$\beta$ $\beta$	$\beta$ $\beta$	$\beta$ $\beta$
$x=0.64$	N,24BZ,5B3N,Z 100,47,37,10	$\alpha$ ,5B3N,BN,ZN,Z 11,100,73,7,8	$\alpha$ ,5B3N,BN,ZN,Z 13,100,38,6,6	$\alpha,\beta$ ,BN 11,100,7	$\alpha,\beta$ ,BN 9,100,5	$\alpha,\beta$ 8,100	$\alpha,\beta$ 9,100	$\alpha,\beta$ 4,100	$\alpha,\beta$ 2,100	$\alpha,\beta$ 9,100	$\alpha,\beta$ 23,100
$x=0.57$	N,24BZ,5B3N,Z 100,41,42,13	$\alpha$ ,5B3N,BN,ZN,Z 21,100,64,11,10	$\alpha$ ,5B3N,BN,ZN,Z 22,100,51,8,8	$\alpha,\beta$ ,BN 68,100,7	$\alpha,\beta$ ,BN 60,100,14	$\alpha,\beta$ 100,76	$\alpha,\beta$ 100,50	$\alpha,\beta$ 100,47	$\alpha,\beta$ 100,45	$\alpha,\beta$ 100,23	$\alpha,\beta$ 100,12
$x=0.56$	N,24BZ,5B3N,Z 100,43,47,14	$\alpha$ ,5B3N,BN,ZN,Z 21,100,67,12,11	$\alpha$ ,5B3N,BN,ZN,Z 27,100,59,9,9	$\alpha,\beta$ ,BN 85,100,18	$\alpha,\beta$ ,BN 78,100,15	$\alpha,\beta$ 100,56	$\alpha,\beta$ 100,33	$\alpha,\beta$ 100,27	$\alpha,\beta$ 100,26	$\alpha,\beta$ 100,9	$\alpha$
$x=0.55$	N,24BZ,5B3N,Z 100,80,63,19	$\alpha$ ,5B3N,BN,ZN,Z 26,100,73,16,11	$\alpha$ ,5B3N,BN,ZN,Z 44,100,51,11,8	$\alpha$ ,5B3N,BN,ZN,Z 81,100,43,11,8	$\alpha,\beta$ ,BN 83,100,8	$\alpha,\beta$ 100,52	$\alpha,\beta$ 100,25	$\alpha,\beta$ 100,19	$\alpha,\beta$ 100,9	$\alpha$	$\alpha$
$x=0.5$	N,24BZ,5B3N,Z 100,80,65,24	$\alpha$ ,5B3N,BN,ZN,Z 40,100,73,24,14	$\alpha$ ,5B3N,BN,ZN,Z 71,100,55,17,10	$\alpha$ ,5B3N,BN,ZN,Z 100,75,38,10,7	$\alpha,\beta$ ,BN,ZN 100,61,6,2	$\alpha,\beta$ ,ZN 100,16,4	$\alpha$	$\alpha$	$\alpha$	$\alpha$	$\alpha$
$x=0.45$	N,24BZ,5B3N,Z 100,74,68,28	$\alpha$ ,5B3N,BN,ZN,Z 52,100,60,27,16	$\alpha$ ,5B3N,BN,ZN,Z 100,78,43,22,10	$\alpha$ ,5B3N,BN,ZN,Z 100,27,22,15,6	$\alpha, \beta, \text{ZN}$ 100,30,7	$\alpha,\beta$ ,ZN 100,6,5	$\alpha$ ,ZN 100,4	$\alpha$ ,3ZN 100,2	$\alpha$ ,3ZN 100,3	$\alpha$ ,3ZN 100,3	$\alpha$ ,3ZN 100,2
$x=0.4$	N,24BZ,5B3N,Z 100,52,62,28	$\alpha$ ,5B3N,BN,ZN,Z 61,100,66,31,21	$\alpha$ ,5B3N,BN,ZN,Z 82,100,82,36,17	$\alpha$ ,5B3N,BN,ZN,Z 100,16,11,15,4	$\alpha, \beta, \text{ZN}$ 100,15,13	$\alpha, \text{ZN}$ 100,9	$\alpha, \text{ZN}$ 100, 8	$\alpha, 3\text{ZN}$ 100,2	$\alpha, 3\text{ZN}$ 100,5	$\alpha, 3\text{ZN}$ 100,5	$\alpha, 3\text{ZN}$ 100,5

ZN:  $\text{ZnNb}_2\text{O}_6$ ; 3ZN:  $\text{Zn}_3\text{Nb}_2\text{O}_8$ ; BN:  $\text{BiNbO}_4$ ; 5B3N:  $\text{Bi}_5\text{Nb}_3\text{O}_{15}$ ; Z:  $\text{ZnO}$ ; 24BZ:  $24\text{Bi}_2\text{O}_3 \cdot \text{ZnO}$ . The datum under each phase is the relative intensity of the strongest peak of each phase.

temperature of  $\alpha$  pyrochlore is 1187 °C. The  $\beta$  pyrochlore decomposes to the  $\alpha$  pyrochlore, the F fluorite and a liquid phase at 1100 °C. A secondary peritectic reaction in which the liquid phase absorbs  $\alpha$  phase and F phase to precipitate  $\beta$  phase takes place upon cooling.

Thus the  $\beta$  phase of  $\text{Bi}_2(\text{Zn}_{1/3}\text{Nb}_{2/3})_2\text{O}_7$  composition is a incongruent compound. The decomposition reaction of the  $\beta$  phase at 1100 °C is expressed as:



From the thermal analysis and XRD data, when the melted liquid phase is cooling, the  $\alpha$  phase precipitates from the liquid phase at 1170 °C and then the F phase precipitates from the liquid phase at 1130 °C. Finally a precipitation reaction happens at 1100 °C when the liquid phase absorbs the  $\alpha$  phase and the F phase to precipitate the  $\beta$  phase. The secondary peritectic reaction can be expressed as:

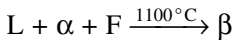


Table 17.4 shows the phase formation at 1000~1100 °C/5h and melting point data of the BZN compositions.

#### 17.3.4 Phase transition and phase relation

The influences of chemical composition, calcining temperature and calcining time on the  $\alpha$ - $\beta$  phase transition were studied (H Wang *et al.*, 1998, 1999a; SY Chen *et al.*, 2003). The single  $\alpha$  phase and single  $\beta$  phase can only form at some specific compositions. There is an  $\alpha$ - $\beta$  co-existing area between the two single pyrochlore phase areas (H Wang *et al.*, 1998). For example, for the compositions  $\text{Bi}_{3x}\text{Zn}_{2-2x}\text{Nb}_{2-x}\text{O}_7$  ( $0.4 \leq x \leq 2/3$ ) calcined at 1000 °C, the  $\alpha$  phase forms in  $0.5 \leq x \leq 0.56$ , the  $\beta$  phase forms in  $0.66 \leq x \leq 2/3$  and  $\alpha$ - $\beta$  co-existing area is in  $0.57 \leq x \leq 0.65$ . The higher calcination temperature and longer calcination time are beneficial to the formation of the  $\alpha$  phase. With the increasing calcination temperature and calcination time, the  $\beta$  phase

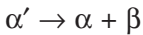
Table 17.4 Phase formation at 1000 ~1100 °C/5h and melting point data of the BZN compositions (H Wang *et al.*, 2001b)

Compositions	Phase formation			
	1000 °C/5h	1050 °C/5h	1100 °C/5h	Melting point (°C)
$\text{Bi}_2(\text{Zn}_{1/3}\text{Nb}_{2/3})_2\text{O}_7$	$\beta$	$\beta$	$\alpha, \text{F}$	1103
$\text{Bi}_{1.5}\text{Zn}_{0.5}(\text{Zn}_{0.5}\text{Nb}_{1.5})\text{O}_7$	$\alpha$	$\alpha$	$\alpha$	1187
$\text{Bi}_{1.7}\text{Nb}_{0.3}\text{O}_{3.3}$	F	F		1067
$\text{Bi}_3\text{NbO}_7$	F	F	F	1132

Table 17.5 Calculated activation energy and reaction order of pyrochlore  $\alpha$  phase formation for the compositions  $(\text{Bi}_{3x}\text{Zn}_{2-3x})(\text{Zn}_x\text{Nb}_{2-x})\text{O}_7$  ( $x = 0.5, 0.55, 0.57$ ). (H Wang *et al.*, 1999a)

Composition	$n$	$E$ (kJ/mol)
$x = 0.5$	0.3	431
$x = 0.55$	0.2	686
$x = 0.57$	0.2	706

gradually transforms to the  $\alpha$  phase. According to the calculated reaction order  $n$  and the activation energy, the  $\alpha$ - $\beta$  phase transition belongs to the diffusion controlled precipitation of solid solution phase transition (H Wang *et al.*, 1999a). A saturated solid solution  $\alpha'$  exists in the  $\alpha$ - $\beta$  co-existing area and the precipitation reaction can be expressed as



This means that the  $\alpha$  phase can tolerate a small amount of the  $\beta$  phase solving in it and maintains its own crystal structure. The  $\alpha$  phase is a cubic pyrochlore with high symmetry, which is more open and stable than the  $\beta$  phase for ionic diffusion. Owing to the differential concentration of the constituted ions in the  $\alpha$  phase and the  $\beta$  phase, the solid solution phase transition happens through continuous ion diffusion between the two phases. Since the ionic diffusion is thermally activated, the solid solubility of the  $\beta$  phase in the  $\alpha$  phase increases with the increasing calcining temperature and with the prolonged calcining time. That is why the  $\alpha$ - $\beta$  phase transition is a continuous process versus chemical composition, calcining temperature and calcining time.

Table 17.5 shows the calculated activation energy and reaction order of pyrochlore  $\alpha$  phase formation for the compositions  $(\text{Bi}_{3x}\text{Zn}_{2-3x})(\text{Zn}_x\text{Nb}_{2-x})\text{O}_7$  ( $x = 0.5, 0.55, 0.57$ ).

## 17.4 Dielectric properties of BZN pyrochlores

### 17.4.1 Basic dielectric properties of BZN ceramics

Previous work revealed that the two main phases in the BZN system have different dielectric properties (Cann *et al.*, 1996; XL Wang *et al.*, 1997; Valant *et al.*, 2000). The cubic pyrochlore phase  $\text{Bi}_{1.5}\text{ZnNb}_{1.5}\text{O}_7$  has a higher dielectric constant  $\sim 150$  and a negative temperature coefficient of permittivity ( $\alpha_\epsilon \sim -470$  ppm/ $^\circ\text{C}$ ), while the monoclinic zirconolite-like pyrochlore phase  $\text{Bi}_2\text{Zn}_{2/3}\text{Nb}_{4/3}\text{O}_7$  has a lower dielectric constant  $\sim 80$  and a positive temperature coefficient of permittivity ( $\alpha_\epsilon \sim +200$  ppm/ $^\circ\text{C}$ ). Thus the dielectric properties of BZN ceramics with co-existing  $\alpha$ - $\beta$  phases can be easily tailored between that of  $\alpha$  and that of  $\beta$ , as shown in Table 17.6. Table 17.7 shows the



**Table 17.6** Structure and dielectric properties (at 1 MHz) of the compositions  $\text{Bi}_{3x}\text{Zn}_{2-2x}\text{Nb}_{2-x}\text{O}_7$  ( $0.5 \leq x \leq 0.67$ )

Composition	$\beta\%^*$	$\alpha\%^*$	$\epsilon(20^\circ\text{C})$	$\alpha_e$ (ppm/ $^\circ\text{C}$ )
$x = 0.67$	100	0	78	+230
$x = 0.65$	100	0	83	+210
$x = 0.63$	85.5	14.5	87	+120
$x = 0.61$	69.5	30.5	96	+27
$x = 0.59$	48.7	51.3	110	-210
$x = 0.56$	10.7	89.3	155	-450
$x = 0.53$	0	100	160	-470
$x = 0.50$	0	100	150	-520

\* Phase relative ratio: calculated from the XRD results.

**Table 17.7** Dielectric properties (at MHz and GHz) of typical compositions in the BZN system (H Wang *et al.*, 2006b)

Compositions	Phase	MHz			GHz		
		$\epsilon_r$	$\tan\delta$	$\alpha_e$ ( ppm/ $^\circ\text{C}$ )	$\epsilon_r$	$Q$	$Qf$
$(\text{Bi}_{1.5}\text{Zn}_{0.5})(\text{Zn}_{0.5}\text{Nb}_{1.5})\text{O}_7$	$\alpha$	150	$<1 \times 10^{-3}$	-520	145	35	160
$(\text{Bi}_{1.8}\text{Zn}_{0.2})(\text{Zn}_{0.6}\text{Nb}_{1.4})\text{O}_7$	$\alpha$ - $\beta$	100	$<6 \times 10^{-4}$	-37	97	80	300
$\text{Bi}_2(\text{Zn}_{2/3}\text{Nb}_{4/3})\text{O}_7$	$\beta$	80	$<6 \times 10^{-4}$	+230	76	1000	3700

dielectric properties in the MHz and GHz range of the typical BZN pyrochlores with  $\alpha$ ,  $\alpha$ - $\beta$  and  $\beta$  phases.

### 17.4.2 Effect of ion substitution

Pyrochlore is known as a highly 'tailorable' structure with very large tolerance for introduction of different ions on the A, B and O sites. The electrical properties of pyrochlore oxides can be changed from insulator to conductor by ion substitution. In bismuth-based pyrochlores, ion substitutions in both A site and B site of BZN pyrochlores were extensively studied. A wide range of ions with large radii were introduced on the A site, such as  $\text{Gd}^{3+}$  (Valant *et al.*, 2000),  $\text{La}^{3+}$  (H Wang *et al.*, 1999b),  $\text{Mg}^{2+}$  (SS Kim *et al.*, 2005),  $\text{Sr}^{2+}$  (Du *et al.*, 2003; H Wang *et al.*, 2006b),  $\text{Ca}^{2+}$  (H Wang *et al.*, 2006b),  $\text{Cd}^{2+}$  (H Wang *et al.*, 2006b),  $\text{Ba}^{2+}$  (H Wang *et al.*, 2006b),  $\text{K}^+$  (Cai *et al.*, 1994b),  $\text{Li}^+$  (Cai *et al.*, 1994b), etc., and small radius ions, such as  $\text{Ta}^{5+}$  (A Chen *et al.*, 2003; Shen *et al.*, 2004; D Peng *et al.*, 2004),  $\text{Sb}^{5+}$  (Mergen *et al.*, 1997; Du *et al.*, 2004b),  $\text{V}^{5+}$  (H Wang *et al.*, 2004c; Yee *et al.*, 1999; GK Choi *et al.*, 2004),  $\text{Ti}^{4+}$  (Valant *et al.*, 1999; Du *et al.*, 2002a, 2006),  $\text{Sn}^{4+}$  (Du *et al.*, 2006),  $\text{Zr}^{4+}$  (Du *et al.*, 2006),  $\text{Ce}^{4+}$  (Du *et al.*, 2006),  $\text{Mn}^{4+}$  (H Wang *et al.*, 2004b),  $\text{W}^{6+}$  (H Wang *et al.*, 2004b), etc., on the B site while  $\text{O}^{2-}$  can be substituted by  $\text{F}^-$  or  $\text{OH}^-$  (Cai *et al.*, 1994b). The results show that the B site

is more 'sensitive' to substitution by other ions and can accommodate only the ions with similar radius and valence.  $\text{Bi}_{1.5}\text{ZnM}_{1.5}\text{O}_7$  ( $M = \text{Ta}, \text{Sb}$ ) are kept to be the pure cubic pyrochlores with lattice parameters of  $10.5407(5) \text{ \AA}$  for Ta and  $10.452(1) \text{ \AA}$  for Sb (Melot *et al.*, 2006).  $\text{Bi}_{1.5}\text{ZnNb}_{1.5}\text{O}_7$  cubic pyrochlore with Cu, Mg, Mn, Ni substituting Zn still keeps its pure cubic pyrochlore and the lattice parameters are in the range  $a = 10.495\text{--}10.570 \text{ \AA}$  (Sirotinkin *et al.*, 2003). Through ion substitution on the A site and B site, the dielectric properties of the bismuth-based pyrochlores can be adjusted to have permittivity from 30 to 200 and temperature coefficient of capacitance from  $+800$  to  $-1300 \text{ ppm/}^\circ\text{C}$  as shown in Table 17.8.

### 17.4.3 Microwave and infrared dielectric response

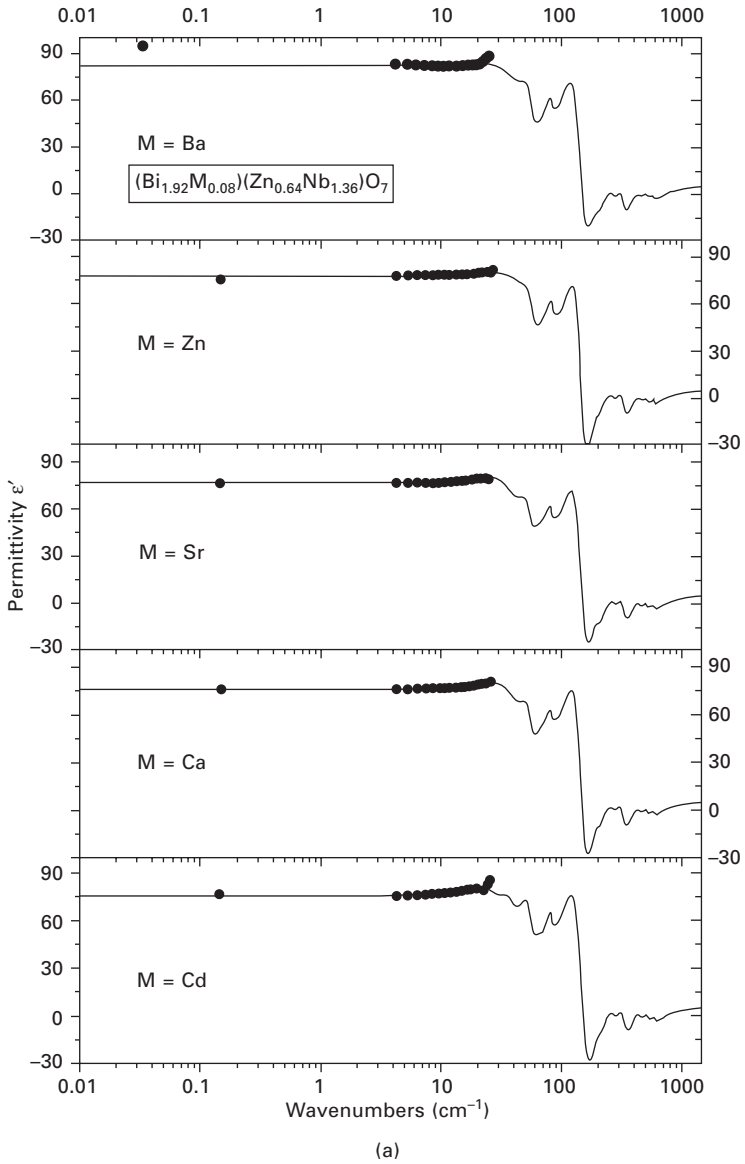
The microwave and infrared dielectric response of bismuth-based pyrochlores was investigated using microwave, infrared and terahertz (THz) spectrum measurements (H Wang *et al.*, 2006b; MH Chen *et al.*, 2005; Cheng *et al.*, 2000, 2003; Nino *et al.*, 2001a, 2002; Kamba *et al.*, 2002). The cubic pyrochlore  $\text{Bi}_{1.5}\text{ZnNb}_{1.5}\text{O}_7$  exhibits higher permittivity and dielectric loss than the monoclinic  $\text{Bi}_2\text{Zn}_{2/3}\text{Nb}_{4/3}\text{O}_7$ , due to structural disorder on the A sites of  $\text{Bi}_{1.5}\text{ZnNb}_{1.5}\text{O}_7$ .

The temperature dependence of the reflectance of the cubic bismuth pyrochlores  $\text{Bi}_{3/2}\text{ZnTa}_{3/2}\text{O}_7$ ,  $\text{Bi}_{3/2}\text{MgNb}_{3/2}\text{O}_7$ ,  $\text{Bi}_{3/2}\text{MgTa}_{3/2}\text{O}_7$  and  $\text{Bi}_{3/2}\text{Zn}_{0.92}\text{Nb}_{1.5}\text{O}_{6.92}$  were investigated by infrared spectroscopy and the behaviour of the phonon modes confirms the A-site-cation and O'-anion displacement which is influenced by the mixing of  $\text{Bi}^{3+}$  6s electron with  $d$  orbital in B-site ions (MH Chen *et al.*, 2005). A splitting of B-O stretching phonon modes and O-B-O bending modes is assigned to mixed-cation occupancy. The temperature dependence of resonant frequencies and damping coefficients confirms both the decreasing of the lattice constant and the orientational dipolar disorder in the bismuth pyrochlore at low temperature.

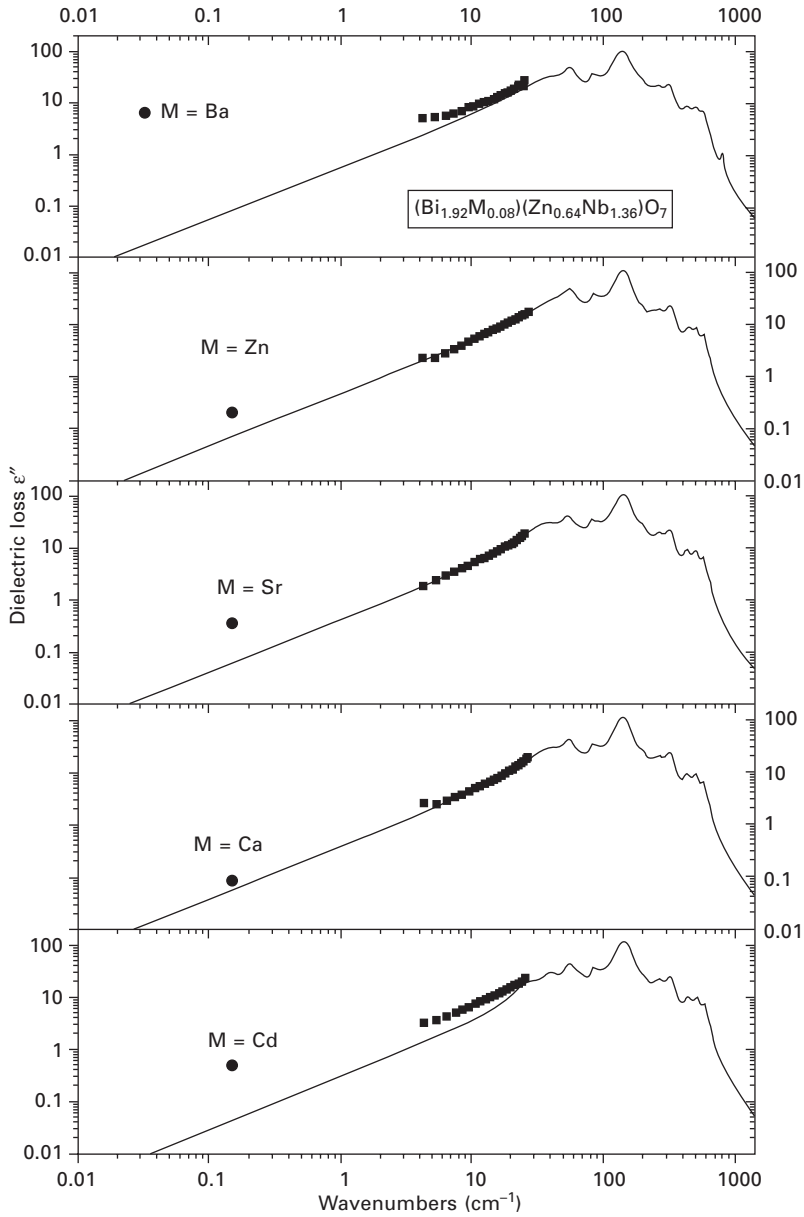
The impact of the ion substitution on the A site of the monoclinic  $\text{Bi}_2\text{Zn}_{2/3}\text{Nb}_{4/3}\text{O}_7$  on the structure and microwave dielectric properties was studied (H Wang *et al.*, 2006b). It was shown that the structure and permittivity of  $(\text{Bi}_{1.92}\text{M}_{0.08})(\text{Zn}_{0.64}\text{Nb}_{1.36})\text{O}_7$  ( $M = \text{Zn}, \text{Ca}, \text{Cd}, \text{Sr}, \text{Ba}$ ) ceramics remain almost the same as in monoclinic  $\text{Bi}_2\text{Zn}_{2/3}\text{Nb}_{4/3}\text{O}_7$ , only the Ba-substituted ceramic has a higher permittivity due to a multiphase structure. Microwave dielectric properties were compared with complex dielectric response in THz and infrared frequency range between 0.1 and 100 THz, which allows us to estimate the intrinsic and extrinsic contributions to microwave dielectric losses. Figure 17.5 shows calculated permittivity  $\epsilon'(\omega)$  and loss  $\epsilon''(\omega)$  spectra obtained from the fits to experimental results based on the IR reflectivity, terahertz transmittance, and MW disagreement between the extrapolated and experimental MW losses in all ceramics due to the high extrinsic dielectric

Table 17.8 Reported dielectric properties of primary A site- and B site-doped bismuth-based pyrochlores

Composition	$\epsilon$	$\tan\delta$	TCC (ppm/°C)	References
$(\text{Bi}_{1.5}\text{Zn}_{0.5})(\text{Zn}_{0.5}\text{Nb}_{1.5})\text{O}_7$	~150@1 MHz	0.0003	~-500	Mergen <i>et al.</i> , 1996, Du <i>et al.</i> , 2004, Valant <i>et al.</i> , 2000
$(\text{Bi}_{1.3}\text{Gd}_{0.2}\text{Zn}_{0.5})(\text{Zn}_{0.5}\text{Nb}_{1.5})\text{O}_7$	116@1 MHz	0.0004	-350	Valant <i>et al.</i> , 2000
$(\text{Bi}_{1.0}\text{La}_{0.5}\text{Zn}_{0.5})(\text{Zn}_{0.5}\text{Nb}_{1.5})\text{O}_7$	116@1 MHz	0.0009	-305	H Wang <i>et al.</i> , 1999a, b
$(\text{Bi}_{0.5}\text{La}_{1.0}\text{Zn}_{0.5})(\text{Zn}_{0.5}\text{Nb}_{1.5})\text{O}_7$	89@1 MHz	0.0094	-266	H Wang <i>et al.</i> , 1999a, b
$(\text{La}_{1.5}\text{Zn}_{0.5})(\text{Zn}_{0.5}\text{Nb}_{1.5})\text{O}_7$	30@1 MHz	0.056	+93	H Wang <i>et al.</i> , 1999a, b
$(\text{Bi}_{1.5}\text{Sr}_{0.2}\text{Zn}_{0.3})(\text{Zn}_{0.5}\text{Nb}_{1.5})\text{O}_7$	172.5@1 MHz	0.0001	-215	Du <i>et al.</i> , 2003
$(\text{Bi}_{1.5}\text{Sr}_{0.5})(\text{Zn}_{0.5}\text{Nb}_{1.5})\text{O}_7$	148.3@1 MHz	0.007	+515	Du <i>et al.</i> , 2003
$(\text{Bi}_{1.5}\text{Zn}_{0.5})(\text{Zn}_{0.5}\text{Nb}_{1.45}\text{V}_{0.05})\text{O}_7$	142@1 MHz	0.0011	-349	H Wang <i>et al.</i> , 2004
$(\text{Bi}_{1.5}\text{Zn}_{0.5})(\text{Zn}_{0.5}\text{Ta}_{1.5})\text{O}_7$	76@1 MHz	0.0001	-146	Du <i>et al.</i> , 2004b
$(\text{Bi}_{1.5}\text{Zn}_{0.5})(\text{Zn}_{0.5}\text{Sb}_{1.5})\text{O}_7$	32@1 MHz	0.0001	-98	Du <i>et al.</i> , 2004b
$(\text{Bi}_{1.5}\text{Zn}_{0.4}\text{Cd}_{0.1})(\text{Zn}_{0.5}\text{Sb}_{1.5})\text{O}_7$	33.4@100 kHz	0.002	-	Mergen <i>et al.</i> , 1997
$(\text{Bi}_{1.5}\text{Zn}_{0.3}\text{Cd}_{0.2})(\text{Zn}_{0.5}\text{Sb}_{1.5})\text{O}_7$	34.8@100 kHz	0.0025	-	Mergen <i>et al.</i> , 1997
$(\text{Bi}_{1.5}\text{Zn}_{0.4}\text{Sr}_{0.1})(\text{Zn}_{0.5}\text{Sb}_{1.5})\text{O}_7$	33.9@100 kHz	0.001	-	Mergen <i>et al.</i> , 1997
$(\text{Bi}_{1.5}\text{Zn}_{0.4}\text{Ca}_{0.1})(\text{Zn}_{0.5}\text{Sb}_{1.5})\text{O}_7$	31.9@100 kHz	0.0046	-	Mergen <i>et al.</i> , 1997
$(\text{Bi}_{1.5}\text{Zn}_{0.5})(\text{Zn}_{0.5}\text{Ti}_{1.5})\text{O}_7$	200@1 MHz	0.0001	-1300	Valant <i>et al.</i> , 2000, Valant <i>et al.</i> , 1999, Du <i>et al.</i> , 2002,
$(\text{Bi}_{1.3}\text{Gd}_{0.2}\text{Zn}_{0.5})(\text{Zn}_{0.5}\text{Ta}_{1.5})\text{O}_7$	143@1 MHz	0.0006	-560	Valant <i>et al.</i> , 2000
$(\text{Bi}_{1.5}\text{Zn}_{0.5})(\text{Zn}_{0.5}\text{Sn}_{1.5})\text{O}_7$	68@1 MHz	0.0001	-120	Du <i>et al.</i> , 2006
$(\text{Bi}_{1.5}\text{Zn}_{0.5})(\text{Zn}_{0.5}\text{Zr}_{1.5})\text{O}_7$	95@1 MHz	0.0001	+146	Du <i>et al.</i> , 2006
$(\text{Bi}_{1.5}\text{Zn}_{0.5})(\text{Zn}_{0.5}\text{Ce}_{1.5})\text{O}_7$	61@1 MHz	0.0001	-13	Du <i>et al.</i> , 2006
$\text{Bi}_2(\text{Zn}_{2/3}\text{Nb}_{4/3})\text{O}_7$	90@1 MHz	0.0004	+150	XL Wang <i>et al.</i> , 1997, Valant <i>et al.</i> , 2000
$(\text{Bi}_{1.8}\text{Gd}_{0.2})(\text{Zn}_{2/3}\text{Nb}_{4/3})\text{O}_7$	80@1 MHz	0.0005	+240	Valant <i>et al.</i> , 2000
$\text{Bi}_2(\text{Zn}_{2/3}\text{Nb}_{4/3-0.08}\text{V}_{0.08})\text{O}_7$	67.8@1 MHz	0.002	-	GK Choi <i>et al.</i> , 2004b
$(\text{Bi}_{1.92}\text{Cd}0.08)(\text{Zn}_{0.64}\text{Nb}_{1.36})\text{O}_7$	88@1 MHz	0.0044	+336	H Wang <i>et al.</i> , 2006b
$(\text{Bi}_{1.92}\text{Ca}0.08)(\text{Zn}_{0.64}\text{Nb}_{1.36})\text{O}_7$	80@1 MHz	0.0005	+214	H Wang <i>et al.</i> , 2006b
$(\text{Bi}_{1.92}\text{Sr}0.08)(\text{Zn}_{0.64}\text{Nb}_{1.36})\text{O}_7$	93@1 MHz	0.0013	+272	H Wang <i>et al.</i> , 2006b
$(\text{Bi}_{1.92}\text{Ba}0.08)(\text{Zn}_{0.64}\text{Nb}_{1.36})\text{O}_7$	99@1 MHz	0.013	+819	H Wang <i>et al.</i> , 2006b



17.5 Real (a) and imaginary (b) part of the complex dielectric spectra of  $(\text{Bi}_{1.92}\text{M}_{0.08})(\text{Zn}_{0.64}\text{Nb}_{1.36})\text{O}_7$  ( $\text{M} = \text{Zn}, \text{Ca}, \text{Cd}, \text{Sr}, \text{Ba}$ ) ceramics. Full symbols are experimental MW and THz data; solid line are the results of the fits to IR and THz spectra (H Wang *et al.*, 2006b).



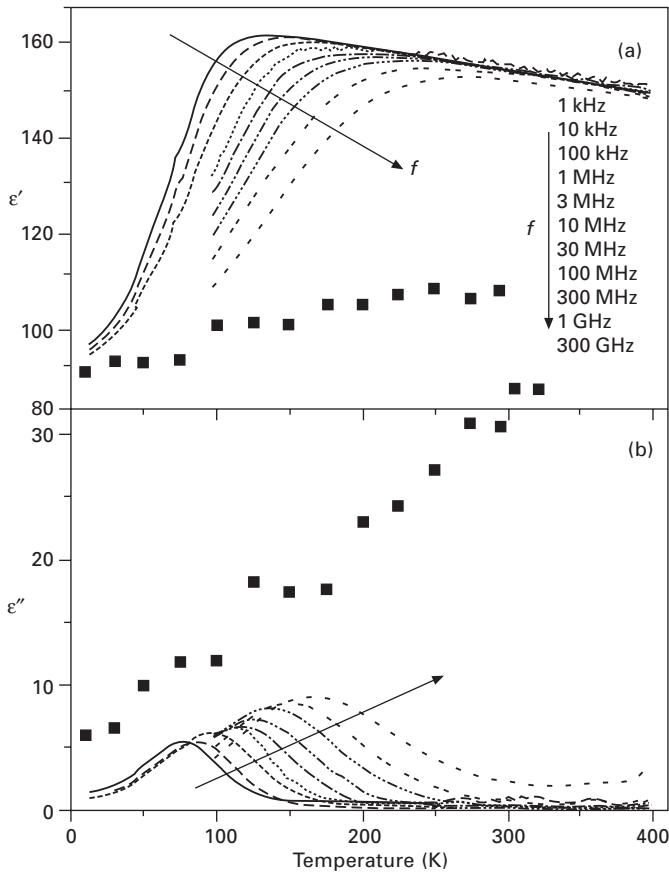
(b)

17.5 (Continued)

losses. The dielectric spectra obtained in a broad spectral range show that the best MW properties, i.e. the lowest dielectric losses, were observed in the Ca-substituted monoclinic BZN ( $\epsilon \sim 75$ ,  $Qf \geq 5000$  GHz), apparently due to the reduced extrinsic contributions to dielectric losses.

#### 17.4.4 Dielectric relaxation

A low-temperature dielectric anomaly in bismuth-based cubic pyrochlores was first observed by Cai *et al.* (1994) and then studied by Cann *et al.* (1996) and Nino *et al.* (2001a) who stated that the anomaly appears similar to the dispersion that occurs near the freezing temperature of dipolar glass systems. A wide-range dielectric response of the cubic pyrochlore  $\text{Bi}_{1.5}\text{ZnNb}_{1.5}\text{O}_7$  and



17.6 Temperature dependence of the real (a) and imaginary (b) part of dielectric permittivity at selected frequencies between 1 kHz and 300 GHz (full squares) (Kamba *et al.*, 2002).

zirconolite-like pyrochlore phase  $\text{Bi}_2\text{Zn}_{2/3}\text{Nb}_{4/3}\text{O}_7$  was studied in detail by Kamba *et al.* (2002) and Nino *et al.*, (2002) (see Fig. 17.6) The results showed that no dielectric relaxation exists in  $\text{Bi}_2\text{Zn}_{2/3}\text{Nb}_{4/3}\text{O}_7$  below the phonon frequencies because of the ordered crystal structure, while in the case of  $\text{Bi}_{1.5}\text{ZnNb}_{1.5}\text{O}_7$  a strong relaxation arises as a consequence of the local hopping of atoms in the A and O' positions of the pyrochlore structure among several local potential minima. The broad distribution of relaxation frequencies is a consequence of distribution of the barrier heights for the hopping of disordered atoms, due to random fields from inhomogeneous distribution of  $\text{Zn}^{2+}$  atoms and vacancies on the  $\text{Bi}^{3+}$  sites.

Cubic pyrochlore  $(\text{Bi}_{1.5}\text{Zn}_{0.5})(\text{Zn}_{0.5-x/3}\text{Ti}_x\text{Nb}_{1.5-2x/3})\text{O}_7$  ceramics with  $0 \leq x \leq 1.5$  were synthesized and investigated between 100 Hz and 100 THz by means of broad-band dielectric spectroscopy, time-domain THz transmission spectroscopy, Fourier transform infrared reflectivity spectroscopy and Raman scattering (Du *et al.*, 2002b; H Wang *et al.*, 2006a). Substitution of Ti atoms on the B-sites, i.e. increasing  $x$ , results in an increase of the microwave permittivity from 150 to 200, of the relaxation frequency and also of the microwave quality factor  $Q$ . Low-temperature Raman scattering experiments did not reveal any phase transition in the samples under study. As for the origin of the relaxation, it might stem from the hopping of dynamically disordered A and O' atoms among the possible sites. Disorder of these atoms is only slightly influenced by Ti substitution in the B sites while the activation energy for the hopping of disordered atoms decreases and MW permittivity increases with Ti substitution due to enhanced polar phonon and dielectric relaxation contributions (H Wang *et al.*, 2006a). It is clear that the inhomogeneous distribution of Zn atoms and vacancies on the Bi sites gives rise to additional random fields. This could yield multi-well potentials for the Zn and Bi cations on the A sites that have a wide distribution of potential heights and therefore of transition rates for anharmonic hopping.

An atomic disorder on A sites together with the associated structural relaxation of O'A<sub>2</sub> substructure was first proposed by Levin *et al.* (2002a) and recently it has been confirmed by direct TEM observations (Withers *et al.*, 2004; Y Liu *et al.*, 2007). It was also shown that such structural disorder is not affected by the B site substitution of the Ti or Sn ions for Nb ions (Y Liu *et al.*, 2007). The broad distribution of relaxation frequencies is caused by a distribution of activation energies for the hopping of A and O' atoms from zero to about  $E_a = 0.2$  eV in pure  $(\text{Bi}_{1.5}\text{Zn}_{0.5})(\text{Zn}_{0.5}\text{Nb}_{1.5})\text{O}_7$  (Kamba *et al.*, 2002). In the case of Ti containing samples, a similar broad relaxation was also observed and the upper limit for activation energies  $E_a$  decreases with Ti concentration.

Similar dielectric relaxation was observed and studied in the  $\text{Bi}_2\text{O}_3$ -ZnO-Ta<sub>2</sub>O<sub>5</sub> system as well (Youn *et al.*, 2002; A Chen *et al.*, 2003; Shen *et al.*, 2005).

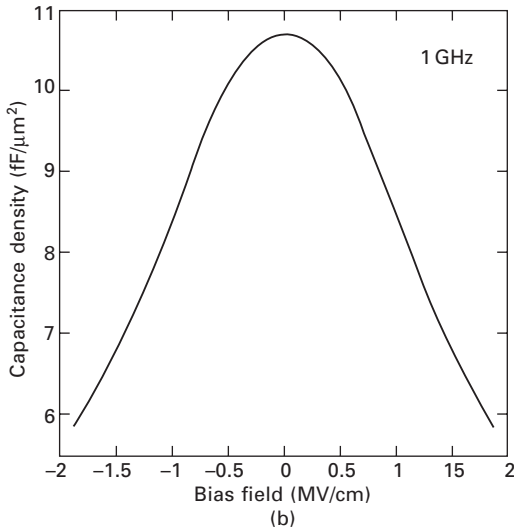
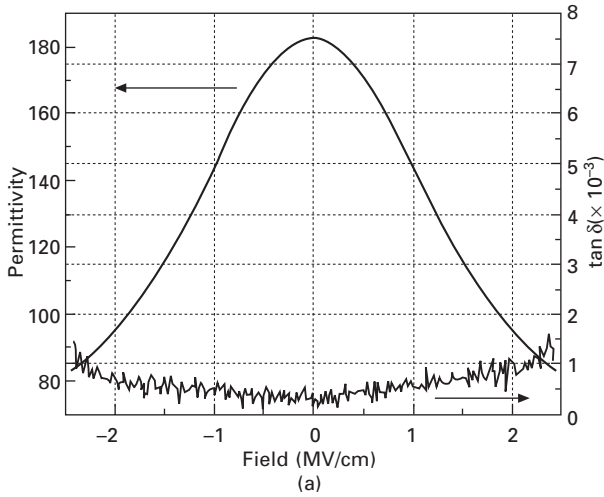
*Table 17.9* Dielectric data of  $(\text{Bi}_{1.92}\text{M}_{0.08})(\text{Zn}_{0.64}\text{Nb}_{1.36})\text{O}_7$  (M = Zn, Ca, Cd, Sr, Ba) ceramics in MHz, MW and THz range (H Wang *et al.*, 2006b)

M=	ST (°C)	Radius of M ions (Å)	Polarizabilities of M ions	$\rho$ ( $\Omega\text{cm}$ )	Density ( $\text{g}/\text{cm}^3$ )	$\epsilon_r$ (MHz)	$\epsilon_r$ (GHz)	$\epsilon_r$ (THz)	$\tan\delta$ (MHz)	$Qf$ (GHz)	$Qf$ (THz)	$\alpha_\epsilon$ (ppm/°C)
Zn	1000	0.75	2.09	$\geq 10^{12}$	7.516	82	75	77	0.0014	1755	3090	248
Cd	980	1.07	3.40	$\geq 10^{12}$	7.590	88	76	76	0.0044	660	3130	336
Ca	960	1.12	3.05	$\geq 10^{12}$	7.440	80	76	76	0.0005	3989	3050	214
Sr	940	1.25	4.25	$\geq 10^{12}$	7.536	93	76	76	0.0013	1100	3310	272
Ba	1000	1.42	6.40	$\geq 10^{12}$	7.631	99	90	83	0.013	20	3660	819



### 17.4.5 Dielectric tunability in BZN thin films

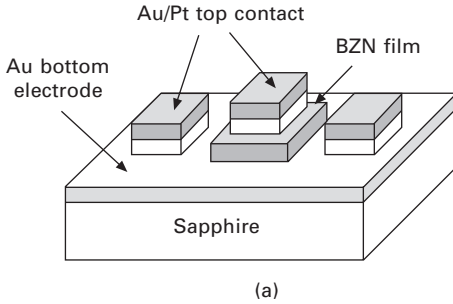
High-permittivity thin films are being investigated for high frequency (HF) and microwave applications in integrated high-density storage devices, decoupling capacitors and electric-field tunable devices. For these applications, both high permittivity and low dielectric loss are needed. (Ba,Sr)TiO<sub>3</sub> thin films, currently a main candidate for these applications, have some shortcomings such as over-high permittivity to make the impedance matching difficult and higher dielectric loss. The family of BZN thin films having medium permittivity (170), low loss (0.0005) and a modest temperature coefficient (−470~+200 ppm/°C) is a good candidate for integration applications (Ren *et al.*, 2001; Lu *et al.*, 2003a). Especially the observed tunability of the BZN cubic pyrochlore thin film caused great interests and attentions for tunable device applications (Ren *et al.*, 2001). The BZN thin films were thus extensively studied and successfully prepared by several chemical or physical routes, such as radio frequency (RF) magnetron sputtering (Lu *et al.*, 2003b, 2004; Ha *et al.*, 2005; Hong *et al.*, 2002), metal organic decomposition (MOD) (Ren *et al.*, 2001; Thayer *et al.*, 2003; JG Chen *et al.*, 2005; JY Kim *et al.*, 2005), metal organic chemical vapor deposition (MOCVD) (Okaura *et al.*, 2005) and pulsed laser deposition (PLD) (Cheng *et al.*, 2000, 2004; Jiang *et al.*, 2006; Ko *et al.*, 2005). The tunability was observed in cubic Bi<sub>1.5</sub>ZnNb<sub>1.5</sub>O<sub>7</sub> thin film but not in monoclinic zirconolite-like Bi<sub>2</sub>(Zn<sub>1/3</sub>Nb<sub>2/3</sub>)<sub>2</sub>O<sub>7</sub> thin film. The tunability of Bi<sub>1.5</sub>ZnNb<sub>1.5</sub>O<sub>7</sub> thin film made by RF magnetron sputtering was reported to be the highest, up to 55% (see Fig. 17.7a), with low dielectric loss of 0.0005 on sapphire substrates at 1 MHz under a bias of 2.4 MV/cm (Lu, 2003a). It is interesting that the high tunability of the Bi<sub>1.5</sub>ZnNb<sub>1.5</sub>O<sub>7</sub> thin film is still observed at 1 GHz as shown in Fig. 17.7(b) and seems frequency independent compared with that at 1 MHz. Attempts to lower the conductor loss from the bottom electrodes of BZN thin film were made on using Au bottom electrodes on sapphire substrates (see Fig. 17.8a), which achieved a low-loss BZN metal–insulator–metal capacitors with tunabilities of ~50% and the dielectric loss tangents of 0.0005 (see Fig. 17.8b) at 1 MHz (Lu *et al.*, 2006). The electric field tunability of the permittivity was weakly temperature dependent and increased with decreasing temperature up to the onset of dielectric relaxation (Tagantsev *et al.*, 2005). At temperatures below the onset of the dielectric relaxation (~150 K at 1 MHz), larger electric fields were required to achieve the highest tunabilities. However, the weak temperature dependence at temperatures after the onset of dielectric relaxation of BZN thin films gives them a practical advantage over ferroelectric materials in making the temperature-stable tunable devices. In a first approximation, at temperatures above the dielectric relaxation, the temperature dependence of the BZN film tunability can be described by a simple model of hopping dipoles under the influence of random fields. This is consistent with the chemical and displacive randomness of the BZN structure that



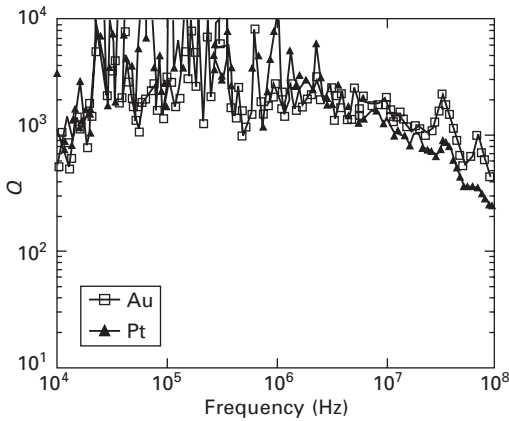
17.7 Bias dependence of permittivity of BZN thin film at 1 MHz (a) (Lu *et al.*, 2003a) and at 1 GHz (b) (Tagantsev *et al.*, 2005).

controls the dielectric behaviour (Kamba *et al.*, 2002; Levin *et al.*, 2002a; Withers *et al.*, 2004). It is deduced (H Wang *et al.*, 2006b) and evidenced (JY Kim *et al.*, 2005) that the Ti-doped BZN cubic pyrochlore thin films with decreased activation energies  $E_a$  for hopping have higher tunabilities than those of pure BZN thin films.

To combine the advantages of both the BST thin film (higher tunability) and the BZN thin film (low dielectric loss), composite BST–BZN thin film and hetero-layered BST/BZN were proposed and prepared. The BST/BZN composite thin films were found to have tunability around 6.2% under the



(a)



(b)

17.8 Schematic of the parallel plate BZN capacitor devices (a) and the  $Q$  factors of an  $\sim 200$  nm thick BZN thin film on 200 nm thick Au bottom electrode and 100 nm thick Pt bottom electrode (b) (Lu *et al.*, 2006).

bias of 8.1 kV/cm (L Yan *et al.*, 2004) and an abnormal  $C$ - $V$  characteristic (Tian *et al.*, 2006), while the heterolayered BST/BZN thin film was found to have a higher tunability up to 25% and very low loss of 0.0025 at 1 MHz, which leads the way for further developing new tunable dielectric thin films by controlling the layer ratio of BST and BZN layers (Fu *et al.*, 2006).

To make the integration with polymeric substrates possible, further lowering the processing temperature is needed. The crystallization temperature of  $\text{Bi}_{1.5}\text{Zn}_{0.5}\text{Nb}_{1.5}\text{O}_{6.5}$  (BZN) films was reduced by combining the conventional heating and irradiation with a pulsed KrF excimer laser to MOD-derived BZN thin films at substrate temperatures  $\leq 400$  °C (JG Chen *et al.*, 2005).

## 17.5 Potential RF and microwave applications

The high dielectric constants, relatively low dielectric losses (high-quality factor), controllable TCC with the low sintering temperatures (below 1000 °C)

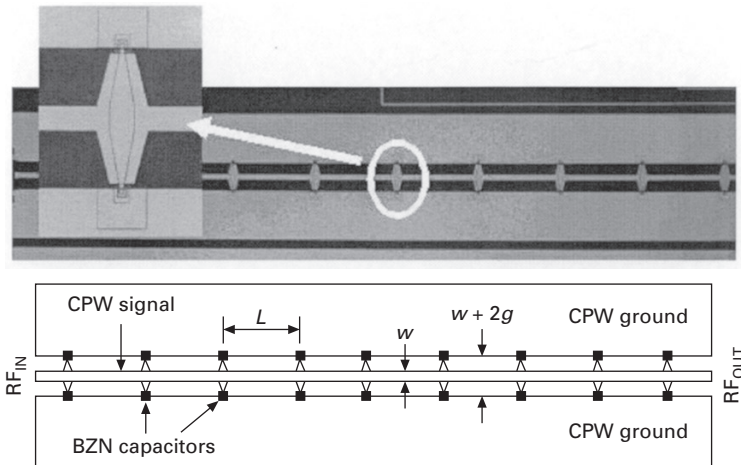
and high electrical tunability make the BZN system a very appealing candidate for applications in low-fire multilayer devices and tunable devices from high-frequency to microwave range.

### 17.5.1 Voltage tunable devices

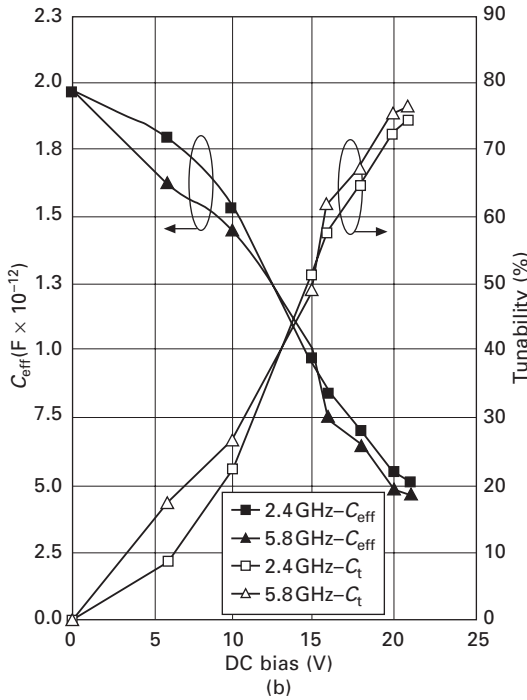
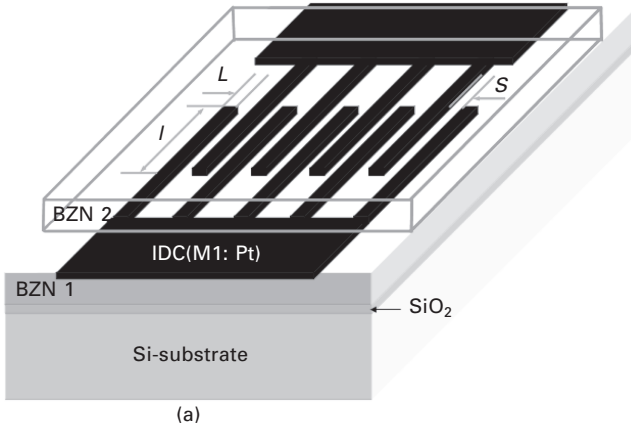
As mentioned above, BZN cubic pyrochlores have high dielectric tunability ( $\sim 55\%$ ) and very low dielectric loss tangent ( $< 0.0005$ ) which make them the new candidates for voltage-tunable devices, such as tunable filter, tunable antenna and phase shifter, etc. Lu *et al.* (2006) reported a low-loss tunable capacitors fabricated directly on gold bottom electrodes by using BZN cubic pyrochlore thin film (J Park *et al.*, 2005). The total device loss was reduced compared with that with Pt bottom electrodes. Figure 17.8 (a) shows the schematic of the parallel plate capacitor devices and the Q factors of the Au/BZN capacitors. This result is of interest for other microwave-tunable devices applications which require a low thermal budget and high-quality, high-permittivity dielectric films.

J Park *et al.* (2006) reported a monoclinic Ku-band phase shifter employing voltage tunable  $\text{Bi}_{1.5}\text{ZnNb}_{1.5}\text{O}_7$  thin film parallel plate capacitors. The BZN films were deposited by RF magnetron sputtering on single-crystal sapphire substrates. By using a nine-section distributed coplanar waveguide loaded-line phase-shifter structure (see Fig. 17.9), a phase shifter with a differential phase shift of  $175^\circ$  and a maximum insertion loss of 3.5 dB at 15 GHz was achieved.

Very recently Lee *et al.* (2006) reported a very high-tunable inter-digital capacitor (IDC) using BZN pyrochlore thin film dielectrics for microwave



17.9 Photograph and schematic of the BZN phase shifter ( $L$ :  $340\ \mu\text{m}$ ,  $w$ :  $30\ \mu\text{m}$ ,  $g$ :  $70\ \mu\text{m}$ ) (J Park *et al.*, 2006).



17.10 Inter-digital capacitor with electrodes fully embedded into BZN dielectrics ( $L=1.5 \mu\text{m}$ ,  $S = \mu\text{m}$ ,  $l = 47 \mu\text{m}$ ) (a) and its measured effective capacitance and tunability (b) (Lee *et al.*, 2006).

applications. They used a structure with the electrodes fully embedded into tunable BZN dielectrics as show in Figure 17.10 to increase the tunability of the IDC and reduce dc bias voltage. The results show that at 20 V dc the IDC yields a tunability up to 72 and 75% at 2.4 and 5.8 GHz respectively. That is the highest tunability of BZN dielectrics reported so far.

### 17.5.2 Antenna applications

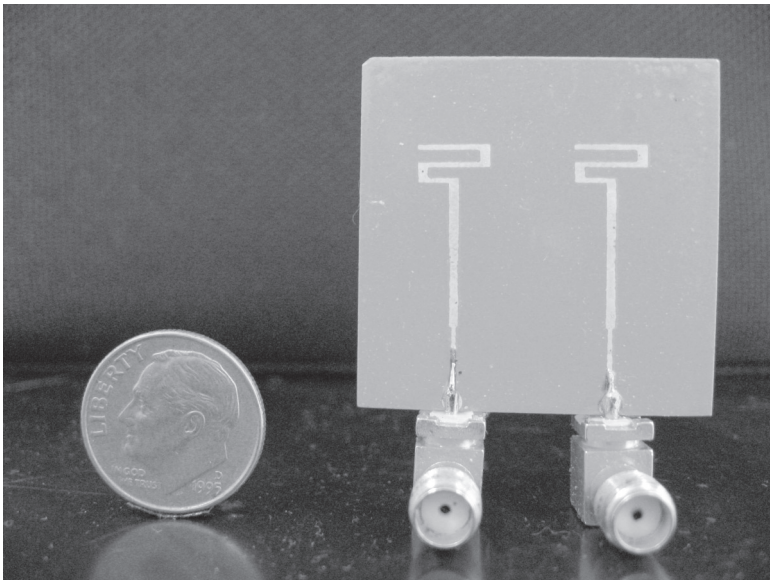
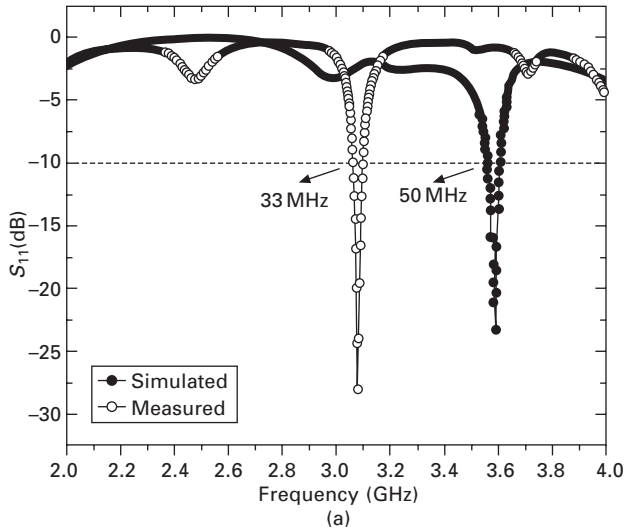
Among various possible internal antennas in wireless hand-held devices, the ceramic antenna is a good candidate because it has the advantages of compact size and easier fabrication. Ceramic antennas can be mounted on the circuit board by Surface Mount Technology (SMT) which can reduce the cost of the installation. Bismuth-based ceramics are suited for the antenna application due to their relatively high dielectric constant and low dielectric loss in RF and microwave range. A prototype resonator antenna was simulated and fabricated (Z Peng *et al.*, 2004). Then a two-element antenna array has been designed and fabricated as shown in Fig. 17.11. It shows the simulated and measured  $S_{11}$  parameters of the model. The simulated resonant frequency is 3.59 GHz and the simulated bandwidth is 50 MHz (based on  $S_{11} < -10$  dB). The measured result shows that the element antenna resonates at 3.08 GHz and has a bandwidth of 33 MHz (Zhou *et al.*, 2007).

### 17.5.3 LTCC applications

A low-temperature co-fired ceramic (LTCC) device is one of the most rapidly developed integral passive devices which provides a solution to the integration of passive components, such as capacitor, resistor, inductor, resonator and filter, etc. into a multilayered ceramic module by interconnecting each component in layers. Recently most of the commercial LTCC systems have a relative dielectric constant ( $K$ ) between 5 and 10 with only a few between 10 and 20. However, mid- $K$  or high- $K$  LTCC dielectrics with a dielectric constant  $>20$  are necessary for miniaturized LC filters and for increasing the capacitive volumetric efficiency of embedded components. Bismuth-based pyrochlore dielectrics BZS ( $K = 35$ ), BZT ( $K = 60$ ) and BZN ( $K = 75-100$ ) with dielectric constants in series are highly suitable for capacitor integration in LTCC. The BZN dielectrics also show the advantages of their compatibility with Ag electrodes without chemical reaction for LTCC applications (Nino *et al.*, 2001b; Su *et al.*, 2003). A multilayered prototype resonator and filter were fabricated (Randall *et al.*, 2003). A high- $K$  bismuth-based pyrochlore was successfully embedded in Dupont 951 LTCC as shown in Fig. 17.12, which reveals that the shrinkage rates of all the layers were well matched and no chemical reaction took place between the LTCC dielectrics and Ag electrodes.

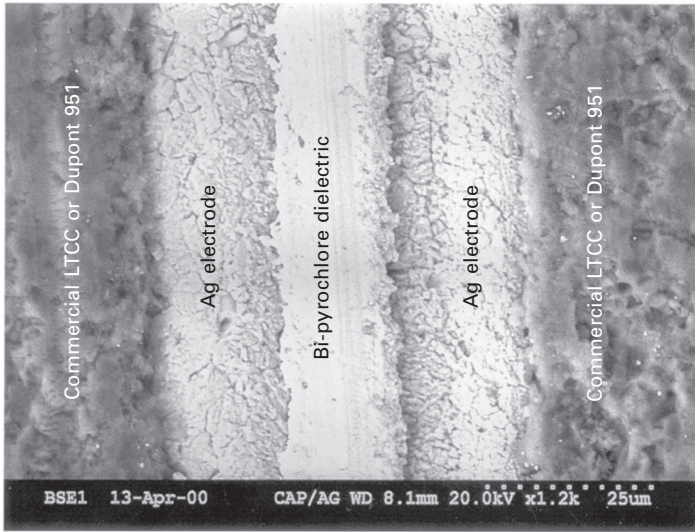
### 17.5.4 EBG structure and new devices

Novel two-dimensional electromagnetic bandgap structures (2D EBGs) (Fig. 17.13) were fabricated by the moulding/demoulding technology based on the simulations, with high permittivity BZN dielectrics. The impacts of



17.11 Measured and simulated resonate frequencies (a) of a two-element antenna by using BZN dielectric as substrates (b).

high permittivity on the 2D EBGs' properties showed very interesting multi-bandgap phenomenon (Shi *et al.*, 2007), which is different from that of the photonic crystals by using low permittivity dielectrics. The experiments (see Fig. 17.13) showed that the wider electromagnetic band gaps are found in the frequency ranges from 5.6 to 10.6 GHz, and 12.6 to 16.6 GHz. The first



17.12 Embedded capacitor in an LTCC structure (Randall *et al.*, 2003).

gap is greater than 60% of the gap center frequency, while the second gap is 25% of the center frequency (see Fig. 17.13). The interval between the two gaps is larger than 2 GHz. The return loss of both gaps is as large as  $-40$  dB. This interesting multi-bandgap characteristic is very useful for diplexers, multi-mode tunable dielectric antennas and resonators.

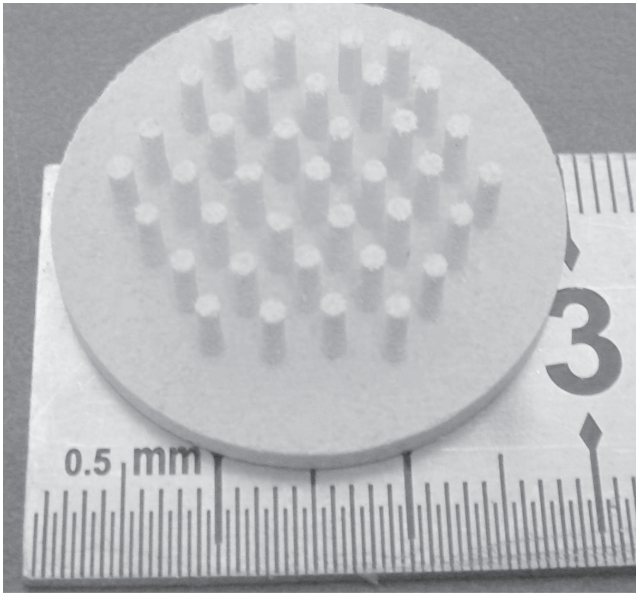
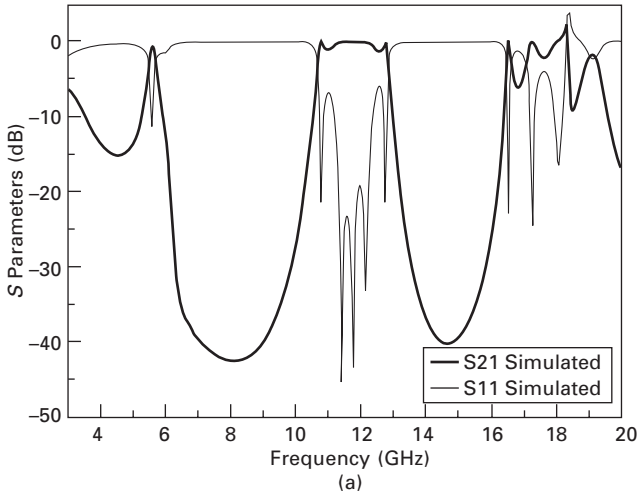
### 17.5.5 Applications as high- $K$ dielectrics for integrated circuit

With the trend of electronic devices development towards miniaturization, the demand for high- $K$  dielectrics in integrated circuits (IC) becomes more and more imminent. The BZN dielectrics are very promising candidates for being used as integrated dielectrics in IC, such as integrated capacitor, embedded capacitors and gate insulator in thin film transistors, because of their high dielectric constant and low dielectric loss.

Recently, J H Park *et al.* (2006) fabricated metal–insulator–metal (MIM) thin film capacitors with  $\text{Bi}_{1.5}\text{ZnNb}_{1.5}\text{O}_7$  (BZN) dielectric films. The BZN thin films were deposited at room temperature by pulsed laser deposition and annealed below  $200^\circ\text{C}$ , which is compatible with the polymer-based substrates. The BZN thin films although being amorphous still exhibit a high capacitance density of  $150\text{ nF/cm}^2$  and a low leakage current less than  $1\ \mu\text{A/cm}^2$  at 5 V. These results show that the MIM structures using amorphous BZN thin films will be a promising candidate for the PCB-embedded capacitors.

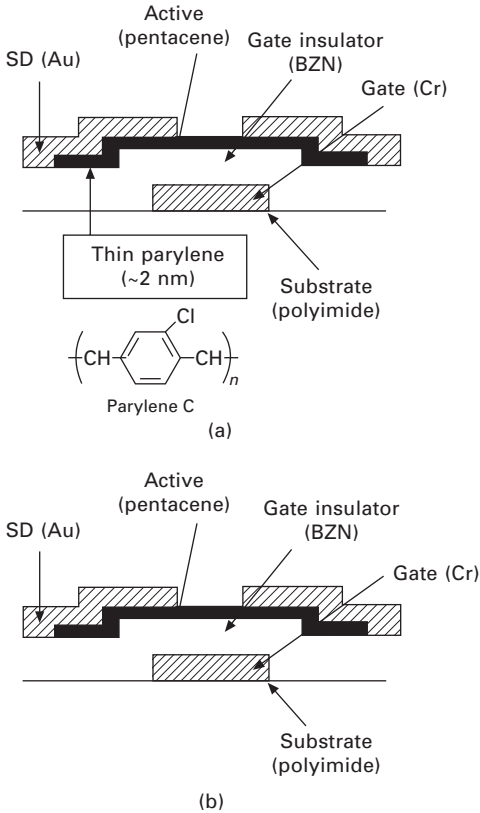
$\text{Bi}_{1.5}\text{ZnNb}_{1.5}\text{O}_7$  (BZN) dielectric films were also successfully prepared via a room temperature process by PLD on polyimide substrates by Kim *et*





17.13 Transmission and reflection coefficients (a) of a honeycomb sample and (b) of 2D EBGs made of BZN dielectrics.

*al.* for the use as gate insulators in pentacene organic thin-film transistor (OTFT) and ZnO thin film transistor (YW Choi *et al.*, 2005; ID Kim *et al.*, 2005). Figure 17.14 shows the schematic cross-section of the OTFTs. The OTFT and ZnO TFT devices exhibited very low operating voltages (<2 V and <4 V, respectively) due to the high capacitance of the BZN dielectric (Fig. 17.15). The high optical transparency (>80% for wavelength >400

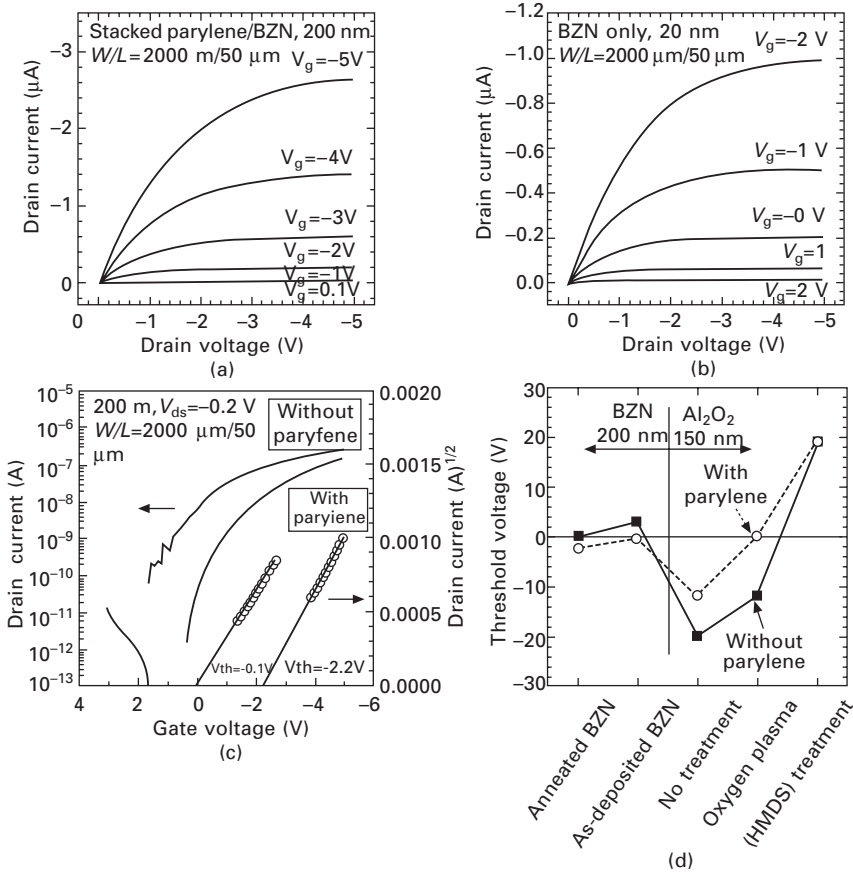


17.14 Schematic cross-section of the OTFTs with the stacked parylene/BZN, threshold voltage  $-2.2$  V, (a), and BZN only, threshold voltage  $0.1$  V (b), gate dielectric (YW Choi *et al.*, 2005).

nm), low-temperature processing and low operating voltage of the TFT devices with integrated BZN dielectric offer a promising route for the development of transparent and flexible electronics.

## 17.6 Summary and future trends

With the rapid development of wireless hand-held devices, the needs for passive component devices working in the high-frequency to microwave range with enhanced reliability, miniaturization and electrical performance are increasing fast. The motivation for the technological innovation is clearly reflected in the ratio of passive components count to active integrated circuits, 40:1 in some wireless devices (Randall *et al.*, 2003). This component count ratio was predicted to increase as functionality of hand-held devices increases. LTCC technology provides a good solution for integrating the passive components as a functional module for microwave applications. The electrically



17.15 Drain current versus drain-to-source voltage curves at various gate-to-source voltages for OTFT with parylene/BZN stacked gate dielectric (a) and BZN only gate dielectric (b). Drain current and root drain current versus gate-to-source voltage curve of OTFTs with BZN only and parylene/BZN stacked gate dielectrics (c). Threshold voltages of OTFTs with surface treatment of BZN and  $\text{Al}_2\text{O}_3$  gate dielectrics before and after deposition of parylene film (d) (YW Choi *et al.*, 2005).

steerable devices demand new dielectrics with high tunability and low dielectric loss. The BZN cubic pyrochlore thin films exhibit high tunability, up to 55%, with low dielectric loss, making them promising candidates for microwave tunable devices. However, the electric bias field required for tuning in the BZN thin films are still very high (2.4 MV/cm for a tunability of 55%) that obstructs further practical application. The future R&D on bismuth-based pyrochlores thus would be driven to further satisfy the potential application demands. More efforts could be made to improve the fundamental understanding of the structure and properties relation specifically to the

optical response (Zanetti *et al.*, 2006), to explore new process routes (H Wang *et al.*, 2004a; Zanetti *et al.*, 2004; Silva *et al.*, 2005) to lower the cost and improve the microwave dielectric properties, to investigate the co-firing technology of bismuth-based dielectrics with Ag or Cu electrodes for LTCC application, lowering the crystallization temperature of thin films (JG Chen *et al.*, 2005) and thick films to approach the semiconductor technology, and to lower the bias field applied for tuning, so as to accelerate the applications in microwave tunable devices.

## 17.7 Acknowledgements

The authors acknowledge the financial support by the National 973-project of China under grant 2002CB613302, NSFC project of China under grant 50572085 and National 863-project of China under grant 2006AA03Z0429.

## 17.8 References

- Cai X K *et al.* (1994a), 'Formation mechanism of bismuth-zinc-niobium oxide pyrochlores', in Waser R, *Proceedings of 4th International Conference on Electronic Ceramics & Applications*, Aachen, Germany, 147–151.
- Cai X K *et al.* (1994b), 'The preparation and structures of bismuth-based oxide and oxyfluoride pyrochlores', in Waser R, *Proceedings of 4th International Conference on Electronic Ceramics & Applications*, Aachen, Germany, 152–154.
- Cai X K *et al.* (1994c), 'Synthesis and dielectric properties of new compounds with pyrochlore type structure', *Ferroelectrics*, **154**, 319–324.
- Cann D P *et al.* (1996), 'Investigation of the dielectric properties of bismuth pyrochlores', *Solid State Comm*, **1100**(7), 529–534.
- Chen A *et al.* (2003), 'Dielectric properties of Bi<sub>2</sub>O<sub>3</sub>-ZnO-Ta<sub>2</sub>O<sub>5</sub> pyrochlore and zirconolite structure ceramics', *Appl Phys Lett*, **82**, 3734–3736.
- Chen J G *et al.* (2005), 'Low-temperature crystallized pyrochlore bismuth zinc niobate thin films by excimer laser annealing', *Appl Phys Lett*, **87**, 232905.
- Chen M *et al.* (1998), 'High performance multilayer ceramic capacitor with low sintering temperatures', *J Korean Phys Soc*, **32S**, 1210–1213.
- Chen M H *et al.* (2005), 'Infrared study of the phonon modes in bismuth pyrochlore', *Phys. Rev. B*, **72**, 054303.
- Chen S Y *et al.* (2003), 'Phase transformation, reaction kinetics and microwave characteristics of Bi<sub>2</sub>O<sub>3</sub>-ZnO-Nb<sub>2</sub>O<sub>5</sub> ceramics', *J Euro Ceram Soc*, **23**, 873–881.
- Cheng H-F *et al.* (2000), 'Frequency response of microwave dielectric Bi<sub>2</sub>(Zn<sub>1/3</sub>Nb<sub>2/3</sub>)O<sub>7</sub> thin films laser deposited on indium-tin oxide coated glass', *J Appl Phys*, **87** 479–483.
- Cheng H-F *et al.* (2003), 'Full spectrum dielectric response of Bi<sub>2</sub>(Zn<sub>1/3</sub>Nb<sub>2/3</sub>)O<sub>7</sub> thin films in terahertz, infrared and optical frequency regions', *Mater Chem Phys*, **79**, 161–163.
- Cheng H-F *et al.* (2004), 'Correlation of microwave dielectric properties and crystallinity for pulsed laser deposited Bi<sub>2</sub>(Zn<sub>1/3</sub>Nb<sub>2/3</sub>)<sub>2</sub>O<sub>7</sub> thin films', *J Euro Ceram Soc*, **24**, 1791–1794.
- Choi G-K *et al.* (2004), 'Influence of V<sub>2</sub>O<sub>5</sub> substitutions to Bi<sub>2</sub>(Zn<sub>1/3</sub>Nb<sub>2/3</sub>)O<sub>7</sub> pyrochlore on sintering temperature and dielectric properties', *Ceram Int*, **30**, 1187–1190.

- Choi Y W *et al.* (2005), 'Low-voltage organic transistors and depletion-load inverters with high-*k* pyrochlore BZN gate dielectric on polymer substrate', *IEEE Trans. Electron Devices*, **52**(12), 2819–2823.
- Du H *et al.* (2001), 'Electro-plating technology of high performance low sintering BZN based MLC', *Ferroelectrics Lett*, **28**, 1–2.
- Du H *et al.* (2002a), 'Evolution of structure and dielectric properties on bismuth-based pyrochlore with TiO<sub>2</sub> incorporation', *J Electroceramics*, **9**, 117–124.
- Du H *et al.* (2002b), 'Dielectric relaxation characteristics of bismuth zinc niobate pyrochlores containing titanium', *Physica B*, **324**, 121–126.
- Du H *et al.* (2003), 'Effect of Sr substitution on dielectric characteristics in Bi<sub>1.5</sub>ZnNb<sub>1.5</sub>O<sub>7</sub> ceramics', *Mater Sci Eng B*, **99**, 437–440.
- Du H *et al.* (2004a), 'Observations on structural evolution and dielectric properties of oxygen-deficient pyrochlores', *Ceramics International*, **30**, 1383–1287.
- Du H *et al.* (2004b), 'Structural trends and dielectric properties of Bi-based pyrochlores', *J Mater Sci*, **15**, 613–616.
- Du H *et al.* (2006), 'Dielectric properties of pyrochlore (Bi<sub>1.5</sub>Zn<sub>0.5</sub>)(Nb<sub>0.5</sub>M<sub>1.5</sub>)O<sub>7</sub> (M= Ti, Sn, Zr and Ce) dielectrics', *Appl Phys Lett*, **88**(21), 212901.
- Fu W Y *et al.* (2006), 'Dielectric properties of Bi<sub>1.5</sub>Zn<sub>1.0</sub>Nb<sub>1.5</sub>O<sub>7</sub>/Mn-doped Ba<sub>0.6</sub>Sr<sub>0.4</sub>TiO<sub>3</sub> heterolayered films grown by pulsed laser deposition', *Appl Phys Lett*, **89**, 132908.
- Ha S *et al.* (2005), 'The effect of substrate heating on the tunability of rf-sputtered Bi<sub>2</sub>O<sub>3</sub>–ZnO–Nb<sub>2</sub>O<sub>5</sub> thin films', *Appl Phys A*, **80**, 585–590.
- Hong Y P *et al.* (2002), 'Voltage tunable dielectric properties of rf sputtered Bi<sub>2</sub>O<sub>3</sub>–ZnO–Nb<sub>2</sub>O<sub>5</sub> pyrochlore thin films', *Thin Solid Films*, **419**, 83–188.
- Jiang S W *et al.* (2006), 'Laser deposition and dielectric properties of cubic pyrochlore bismuth zinc niobate thin films', *J Vac Sci Technol A*, **24**(2), 261–263.
- Kamba S *et al.* (2002), 'Anomalous broad dielectric relaxation in Bi<sub>1.5</sub>Zn<sub>1.0</sub>Nb<sub>1.5</sub>O<sub>7</sub> pyrochlore', *Phys Rev B*, **66**, 054106.
- Khaw C C *et al.* (2007), 'Pyrochlore phase formation in the system Bi<sub>2</sub>O<sub>3</sub>–ZnO–Ta<sub>2</sub>O<sub>5</sub>', *J Am Ceram Soc*, **90** (9), 2900–2904.
- Kim I D *et al.* (2005), 'Low-voltage ZnO thin-film transistors with high-*K* Bi<sub>1.5</sub>Zn<sub>1.0</sub>Nb<sub>1.5</sub>O<sub>7</sub> gate insulator for transparent and flexible electronics', *Appl Phys Lett*, **87**, 043509.
- Kim J S *et al.* (2002), 'Phase relation and dielectric properties of Bi<sub>2</sub>O<sub>3</sub>–ZnO–Nb<sub>2</sub>O<sub>5</sub>–based ceramics', *Ferroelectrics*, **272**, 273–278.
- Kim J Y *et al.* (2005), 'Voltage-tunable dielectric properties of pyrochlore Bi–Zn–Nb–Ti–O solid solution thin films', *Jpn J Appl Phys*, **44**, 6648–6653.
- Kim S S *et al.* (2005), 'Electrical properties of sol–gel derived pyrochlore-type bismuth magnesium niobate Bi<sub>2</sub>(Mg<sub>1/3</sub>Nb<sub>2/3</sub>)<sub>2</sub>O<sub>7</sub> thin films', *J Cryst Growth*, **281**, 432–439.
- Ko K H *et al.* (2005), 'Phase decomposition and dielectric properties of reactively sputtered bismuth zinc niobate pyrochlore thin films deposited from monoclinic zirconolite target', *J Electroceramics*, **14**, 171–175.
- Lee Y C *et al.* (2006), 'Very high tunable inter-digital capacitor using bismuth zinc niobate thin-film dielectrics for microwave applications', *Electronics Lett.*, **42**(15), 851–853.
- Levin I *et al.* (2002a), 'Structural study of an unusual cubic pyrochlore Bi<sub>1.5</sub>Zn<sub>0.92</sub>Nb<sub>1.5</sub>O<sub>6.92</sub>', *J Solid State Chem*, **168**, 69–75.
- Levin I *et al.* (2002b), 'Crystal structure of the compound Bi<sub>2</sub>Zn<sub>2/3</sub>Nb<sub>4/3</sub>O<sub>7</sub>', *J Mater Res*, **17**(6), 1406–1411.
- Li B Y *et al.* (1986), *Inorganic Dielectric Materials* (in Chinese), Shanghai, Shanghai Science and Technology Press, 1986.

- Ling H C *et al.* (1990), 'High dielectric constant and small temperature coefficient bismuth-based dielectric compositions', *J Mater Res*, **5**(8), 1752–1762.
- Liu D H *et al.* (1993), 'Phase structure and dielectric properties of  $\text{Bi}_2\text{O}_3\text{-ZnO-Nb}_2\text{O}_5$ -based dielectric ceramics', *J Am Ceram Soc*, **76**(8), 2129–2132.
- Liu Y *et al.* (2006), 'Crystal chemistry on a lattice: the case of BZN and BZN-related pyrochlores', *J Solid State Chem*, **179**, 2141–2149.
- Liu Y *et al.* (2007), 'Direct observation of structural disordering of BZN-based pyrochlores', *J Electroceramics*, published online.
- Lu J *et al.* (2003a), 'Low-loss, tunable bismuth zinc niobate films deposited by rf magnetron sputtering', *Appl Phys Lett*, **83**, 2411–2413.
- Lu J *et al.* (2003b), 'Composition control and dielectric properties of bismuth zinc niobate thin films synthesized by radio-frequency magnetron sputtering', *J Vac Sci Technol*, **21**(5) 2855–2862.
- Lu J *et al.* (2004), 'Influence of strain on the dielectric relaxation of pyrochlore bismuth zinc niobate thin films', *Appl Phys Lett*, **84**, 957–959.
- Lu J *et al.* (2006), 'Low-loss tunable capacitors fabricated directly on gold bottom electrodes', *Appl Phys Lett*, **88**, 112905.
- Melot B *et al.* (2006), 'Displacive disorder in three high-*k* bismuth oxide pyrochlores', *Mater Res Bull*, **41**, 961–966.
- Mergen A *et al.* (1996), 'Fabrication and crystal chemistry of  $\text{Bi}_{3/2}\text{ZnSb}_{3/2}\text{O}_7$  pyrochlore', *J Euro Ceram Soc*, **16**, 1041–1050.
- Mergen A *et al.* (1997), 'Crystal chemistry, thermal expansion and dielectric properties of  $(\text{Bi}_{1.5}\text{Zn}_{0.5})(\text{Sb}_{1.5}\text{Zn}_{0.5})\text{O}_7$  pyrochlore', *Mater Res Bull*, **32**(2), 175–189.
- Miles G C *et al.* (2006), West A R, 'Pyrochlore phases in the system  $\text{ZnO-Bi}_2\text{O}_3\text{-Sb}_2\text{O}_5$ : I. Stoichiometries and phase equilibria', *J Am Ceram Soc*, **89**(3), 1042–1046.
- Nino J C *et al.* (2001a), 'Dielectric relaxation in  $\text{Bi}_2\text{O}_3\text{-ZnO-Nb}_2\text{O}_5$  cubic pyrochlore', *J Appl Phys*, **89**, 4512–4516.
- Nino J C *et al.* (2001b), 'Phase formation and reactions in the  $\text{Bi}_2\text{O}_3\text{-ZnO-Nb}_2\text{O}_5\text{-Ag}$  pyrochlore system', *J Mater Res*, **16**(5), 1460–1464.
- Nino J C *et al.* (2002), 'Correlation between infrared modes and dielectric relaxation in  $\text{Bi}_2\text{O}_3\text{-ZnO-Nb}_2\text{O}_5$  cubic pyrochlore', *Appl Phys Lett*, **23**, 4404–4406.
- Okaura S *et al.* (2005), 'MOCVD growth of  $\text{Bi}_{1.5}\text{Zn}_{1.0}\text{Nb}_{1.5}\text{O}_7$  (BZN) epitaxial thin films and their electrical properties', *Jpn J Appl Phys*, **44**, 6957–6959.
- Park J *et al.* (2005), 'Microwave dielectric properties of tunable capacitors employing bismuth zinc niobate thin films', *J Appl Phys*, **97**, 084110.
- Park J *et al.* (2006), 'Distributed phase shifter with pyrochlore bismuth zinc niobate thin films', *IEEE Microwave and Wireless Components Letters*, **5**, 264–266.
- Park J-H *et al.* (2006), 'Bismuth-zinc-niobate embedded capacitors grown at room temperature for printed circuit board applications', *Appl. Phys. Lett.*, **88**, 192902.
- Peng D *et al.* (2004), 'Study on relationship between sintering atmosphere and dielectric properties for  $\text{Bi}_2\text{O}_3\text{-ZnO-Ta}_2\text{O}_5$  system', *Ceram Int*, **30**, 1199–1202.
- Peng Z *et al.* (2004), 'Dielectric resonator antennas using high permittivity ceramics', *Ceram. Int.*, **30**, 1211–1214.
- Randall C A *et al.* (2003), 'Bi-pyrochlore and zirconolite dielectrics for integrated passive component applications', *Am Ceram Soc Bull*, **11**, 9103–9108.
- Ren W *et al.* (2001), 'Bismuth zinc niobate pyrochlore dielectric thin films for capacitive applications', *J Appl Phys*, **89**, 767–774.
- Shen B *et al.* (2004), 'Structure and dielectric properties of  $\text{Bi}_2\text{O}_3\text{-ZnO-CaO-Ta}_2\text{O}_5$  ceramics', *Ceram Int*, **30**, 1207–1210.

- Shen B *et al.* (2005), 'Dielectric relaxation and tunability of  $\text{Bi}_2\text{O}_3\text{-ZnO-CaO-Ta}_2\text{O}_5$  ceramics', *Appl Phys Lett*, **86**, 072902.
- Shi J Z *et al.* (2007), 'Fabrication of 2-D EBGs by moulding/demoulding with high dielectric constant ceramic and their properties', *J. Electroceramics*, published online.
- Silva S A *et al.* (2005), 'Bismuth zinc niobate pyrochlore  $\text{Bi}_{1.5}\text{ZnNb}_{1.5}\text{O}_7$  from a polymeric urea-containing precursor', *Mater Chem Phys*, **93**, 521–525.
- Sirotninkin V P *et al.* (2003), 'Preparation and dielectric properties of  $\text{Bi}_{1.5}\text{MNb}_{1.5}\text{O}_7$  (M = Cu, Mg, Mn, Ni, Zn) pyrochlore oxides', *Inorg Mater*, **39**(9), 054303.
- Somphon W *et al.* (2006), 'Local crystal chemistry, structured diffuse scattering and dielectric properties of  $(\text{Bi}_{1-x}\text{Y}_x)(\text{M}^{\text{III}}\text{Nb}^{\text{V}})\text{O}_7$  (M=Fe<sup>3+</sup>, In<sup>3+</sup>) Bi-pyrochlores', *J Solid State Chem*, **179**, 2495–2505.
- Su W-F *et al.* (2003), 'Interfacial behaviour between  $\text{Bi}_{1.5}\text{ZnNb}_{1.5}\text{O}_7 \bullet 0.02\text{V}_2\text{O}_5$  and Ag', *J Euro Ceram Soc*, **23**, 2593–2596.
- Subramanian M A (1983), 'Oxide pyrochlore – a review', *Prog Solid State Chem*, **15**, 55–143.
- Tagantsev A K *et al.* (2005), 'Temperature dependence of the dielectric tunability of pyrochlore bismuth zinc niobate thin films', *Appl Phys Lett*, **86**, 032901.
- Tan K B *et al.* (2005), 'Stoichiometry and doping mechanism of the cubic pyrochlore phase in the system  $\text{Bi}_2\text{O}_3\text{-ZnO-Nb}_2\text{O}_5$ ', *J Mater Chem*, **15**, 3501–3506.
- Thayer R L *et al.* (2003), 'Medium permittivity bismuth zinc niobate thin film capacitors', *J Appl Phys*, **94**, 1941–1946.
- Tian H Y *et al.* (2006), 'Dielectric properties and abnormal C–V characteristics of  $\text{Ba}_{0.5}\text{Sr}_{0.5}\text{TiO}_3\text{-Bi}_{1.5}\text{ZnNb}_{1.5}\text{O}_7$  composite thin films grown on MgO (001) substrates by pulsed laser deposition', *Appl Phys Lett*, **89**(14), 142905.
- Valant M *et al.* (1999), 'Synthesis and dielectric properties of pyrochlore solid solutions in the  $\text{Bi}_2\text{O}_3\text{-ZnO-Nb}_2\text{O}_5\text{-TiO}_2$  system', *J Mater Sci*, **34**, 5437–5442.
- Valant M *et al.* (2000), 'Crystal chemistry and dielectric properties of chemically substituted  $(\text{Bi}_{1.5}\text{Zn}_{1.0}\text{Nb}_{1.5})\text{O}_7$  and  $\text{Bi}_2(\text{Zn}_{2/3}\text{Nb}_{4/3})\text{O}_7$  pyrochlores', *J Am Ceram Soc*, **83**(1), 147–153.
- Valant M *et al.* (2005), 'The  $\text{Bi}_2\text{O}_3\text{-Nb}_2\text{O}_5\text{-NiO}$  phase diagram', *J Am Ceram Soc*, **88**(9), 2540–2543.
- Vanderah T A *et al.* (2005), 'An unexpected crystal-chemical principle for the pyrochlore structure', *Eur J Inorg Chem*, 2895–2901.
- Wang H *et al.* (1994a), 'Effect of  $\text{Bi}_2\text{O}_3$  and sintering temperature on pyrochlore structure in the  $\text{Bi}_2\text{O}_3\text{-ZnO-Nb}_2\text{O}_5$  system', in Waser R, *Proceedings of 4th International Conference on Electronic Ceramics & Applications*, Aachen, Germany, 139–142.
- Wang H *et al.* (1994b), 'Structural study of cubic pyrochlore in the  $\text{Bi}_2\text{O}_3\text{-ZnO-Nb}_2\text{O}_5$  system', in Waser R, *Proceedings of 4th International Conference on Electronic Ceramics & Applications*, Aachen, Germany, 143–146.
- Wang H *et al.* (1995), 'Cubic pyrochlore structure in the  $\text{Bi}_2\text{O}_3\text{-ZnO-Nb}_2\text{O}_5$  system', *J Chin Ceram Soc (in Chinese)*, **23**(3) 241–247.
- Wang H *et al.* (1996a), 'Phase transformation and phase distribution of pyrochlore structure in  $\text{Bi}_2\text{O}_3\text{-ZnO-Nb}_2\text{O}_5$  system', *Proceedings of 10th IEEE International Symposium on Applications of Ferroelectrics*, East Brunswick, USA, 787–790.
- Wang H *et al.* (1996), 'Preparation, structure and dielectric properties of bismuth-based ceramic dielectrics', *Proceedings of 9th IEEE International Symposium on Electrets*, Shanghai, China, 1024–1029.
- Wang H *et al.* (1997), 'Phase equilibrium in  $\text{Bi}_2\text{O}_3\text{-ZnO-Nb}_2\text{O}_5$  system', *Ferroelectrics*, **195**, 19–22.

- Wang H (1998), 'Structure, phase relations and dielectric properties of  $\text{Bi}_2\text{O}_3\text{-ZnO-Nb}_2\text{O}_5$  based ceramics', *PhD Thesis*, Xi'an Jiaotong University.
- Wang H *et al.* (1999a), 'Phase transition of pyrochlore structure in  $\text{Bi}_2\text{O}_3\text{-ZnO-Nb}_2\text{O}_5$  system', *Ferroelectrics*, **229**, 95–101.
- Wang H *et al.* (1999b), 'Effect of  $\text{La}_2\text{O}_3$  substitution on structure and properties of  $\text{Bi}_2\text{O}_3\text{-ZnO-Nb}_2\text{O}_5$  based pyrochlore ceramics', *J Mater Res*, **14**(2), 546–548.
- Wang H *et al.* (2001a), 'Structure study of a new distorted pyrochlore in  $\text{Bi}_2\text{O}_3\text{-ZnO-Nb}_2\text{O}_5$  system', *Ferroelectrics*, **262**, 71–76.
- Wang H *et al.* (2001b), 'Melting behaviors of pyrochlores in  $\text{Bi}_2\text{O}_3\text{-ZnO-Nb}_2\text{O}_5$  system', *Ferroelectrics*, **261**, 225–231.
- Wang H *et al.* (2003), 'Structural study of  $\text{Bi}_2\text{O}_3\text{-ZnO-Nb}_2\text{O}_5$  based pyrochlores', *Mater Sci & Eng B*, **99**, 20–24.
- Wang H *et al.* (2004a), 'Bismuth zinc niobate ( $\text{Bi}_{1.5}\text{ZnNb}_{1.5}\text{O}_7$ ) ceramics derived from metallo-organic decomposition precursor solution', *Solid State Comm*, **132**, 481–486.
- Wang H *et al.* (2004b), ' $\text{Mn}^{4+}$  and  $\text{W}^{6+}$  substitution on  $\text{Bi}_2\text{O}_3\text{-ZnO-Nb}_2\text{O}_5$ -based low firing ceramics', *Ceram Int*, **30**, 1219–1223.
- Wang H *et al.* (2004c), 'Improvements of sintering and dielectric properties on  $\text{Bi}_2\text{O}_3\text{-ZnO-Nb}_2\text{O}_5$  pyrochlore ceramics by  $\text{V}_2\text{O}_5$  substitution', *Ceram Int*, **30**, 1225–1229.
- Wang H *et al.* (2006a), 'Microwave dielectric relaxation in cubic bismuth-based pyrochlores containing Titanium', *J Appl Phys*, **100**, 014105.
- Wang H *et al.* (2006b), 'Microwave and infrared dielectric response of monoclinic Bismuth Zinc Niobate based pyrochlore ceramics with ion substitution in A site', *J Appl Phys*, **100**, 034109.
- Wang X L *et al.* (1997), 'Structure, phase transformation and dielectric properties of pyrochlores containing bismuth', *J Am Ceram Soc*, **80**(10), 2745–2748.
- Wang Z P *et al.* (1985), 'Lead free low firing MLCC dielectric materials', *Electronic Components & Materials (in Chinese)*, **1**, 383–389.
- Withers R L *et al.* (2004), 'Local crystal chemistry, induced strain and short range order in the cubic pyrochlore ( $\text{Bi}_{1.5-\alpha}\text{Zn}_{0.5-\beta}$ )( $\text{Zn}_{0.5-\gamma}\text{Nb}_{1.5-\delta}$ ) $\text{O}_{7-1.5\alpha-\beta-\gamma-2.5\delta}$  (BZN)', *J Solid State Chem*, **177**, 231–244.
- Yan L *et al.* (2004), ' $\text{Ba}_{0.5}\text{Sr}_{0.5}\text{TiO}_3\text{-Bi}_{1.5}\text{Zn}_{1.0}\text{Nb}_{1.5}\text{O}_7$  composite thin films with promising microwave dielectric properties for microwave devices applications', *Appl Phys Lett*, **85**, 3522–3524.
- Yan M F *et al.* (1990), 'Low-firing, temperature-stable dielectric compositions based on bismuth nickel zinc niobates', *J Am Ceram Soc*, **72**(4), 1106–1107.
- Yee K A *et al.* (1999), 'The effect of  $\text{V}_2\text{O}_5$  on the sinterability and physical properties of  $\text{Bi}_2\text{O}_3\text{-NiO-Nb}_2\text{O}_5$  and  $\text{Bi}_2\text{O}_3\text{-ZnO-Nb}_2\text{O}_5$  temperature-stable dielectrics', *J Mater Sci*, **34**, 4699–4704.
- Youn H-J *et al.* (2002), 'Dielectric relaxation and microwave dielectric properties of  $\text{Bi}_2\text{O}_3\text{-ZnO-Ta}_2\text{O}_5$  ceramics', *J Mater Res*, **17**(6), 1502–1506.
- Zhou D *et al.* (2007), 'The two element antennas using high permittivity bismuth-based ceramics', submitted to *Mater & Sci Eng A*. published online.
- Zanetti S M *et al.* (2004), 'A chemical route for the synthesis of cubic bismuth zinc niobate pyrochlore nanopowders', *J Solid State Chem*, **177**, 4564–4551.
- Zanetti S M *et al.* (2006), 'Structural and optical properties of  $\text{Bi}_{1.5}\text{ZnNb}_{1.5}\text{O}_7$  pyrochlore thin films prepared by chemical method', *Thin Solid Films*, **497**, 72–76.



## 18.1 Introduction

The principal thrust of ferroelectric thin-film research and development has been to the production of non-volatile random access memories (FRAMs); in contrast to ‘volatile’ dynamic RAMs (DRAMs), such non-volatile devices retain stored memory in the event of a power failure. Although DRAMs are volatile, they are unlikely to disappear in the foreseeable future, because they combine high density (Gbits), high speed and low cost. Nevertheless, in applications where volatility would require heavy, power-consuming and cumbersome hard-disk back-up memory (banking, aerospace, or mobile telephones and digital cameras), the new ferroelectric FRAMs compete primarily with ‘Flash’/EEPROM devices (electrically erasable read-only memories). The long-term advantages of FRAMs over EEPROMs are in part due to the lowering of standard silicon logic levels from the present 5.0 volt standard to 3.3 V, 1.1 V and eventually 0.5 V. FRAMs can already meet these lower voltage requirements, whereas it will be physically difficult for Flash devices to do so, perhaps necessitating cumbersome and unreliable ‘charge pumps’ to provide 5 V internally from a 1.0V external source. The next application of FRAMs is likely to be memories in digital cameras, and the size (see below) is now nearly sufficient for use as the audio memory in stereo devices such as the Sony Walkman. FRAMs are already in use for ‘smart’ credit cards and for video games (a 32 kb FRAM from Fujitsu is already in every Sony Playstation 2).

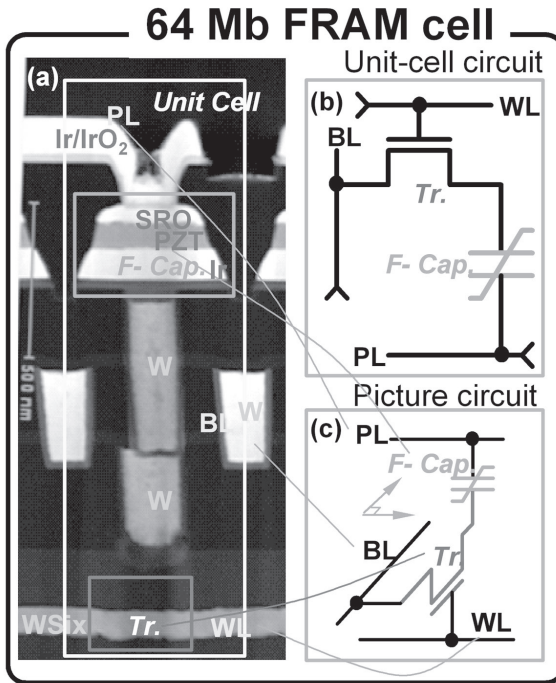
Despite the attention focused on FRAMs, memories are not the only trendy development in ferroelectric thin-film devices (Clark and Lagerwall 1980; Lagerwall 2004), and below I review a dozen other major trends and areas of R&D, based in part upon my recent reviews of the field in *Science* and the *Journal of Physics Condensed Matter* (Scott, 2006ab).

Recent prototype applications and milestones include ultra-fast (280 ps) switching (Li *et al.*, 2004), cheap room-temperature magnetic field detectors to replace SQUIDS (superconducting quantum interference devices),

piezoelectric nanotubes for microfluidic systems, electrocaloric coolers for computers, phased-array radar and three-dimensional trenched capacitors for DRAMs. Tera-bit/square-inch ferroelectric arrays of lead zirconate–titanate have been reported on Pt nanowire interconnects, and nano-rings with 5–10 nm diameters. Finally, electron emission from ferroelectrics is a relatively unexploited phenomenon that already yields prototypes of cheap, very small, high-power microwave devices, as well as miniature X-ray and neutron sources ('cold fusion').

## 18.2 Ferroelectric nanostructures

The prefix 'nano-' is generally defined as <0.1 micrometres, and although ferroelectric capacitors and related devices are now submicrometre, they are 400–500 nm on a side, not 100, with thickness ca. 50–150 nm (Fig. 18.1). As the sizes of ferroelectric cells continue to shrink to true nano-scale, two



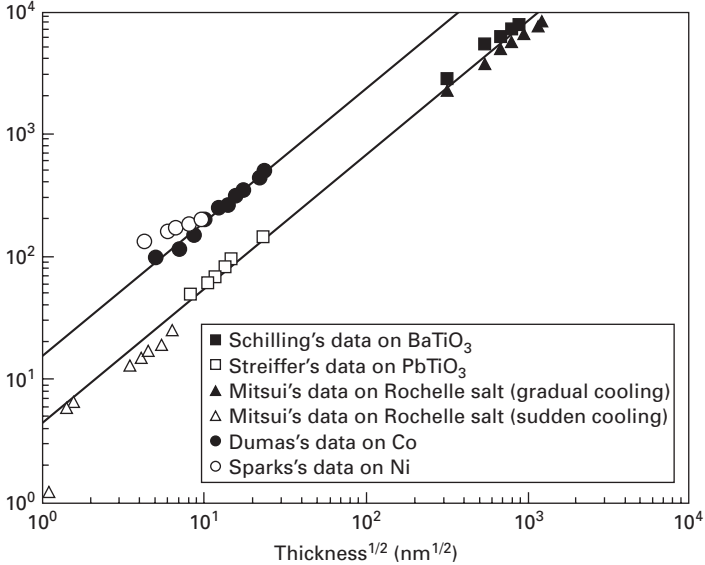
18.1 (a) TEM cross-section for state-of-the-art FRAM: a 64 Mb PZT device with cell size approximately  $400 \times 450 \times 144 \text{ nm}^3$ . (b) and (c) illustrate the relationship of each component in the TEM micrograph to the equivalent circuit diagram. The symbols on the left side are: Ir – iridium; SR – SrRuO<sub>3</sub>; W – tungsten; and Tr. – transistor. On the right side: WL – word-line; BL – bit-line; PL – plate; Tr. – transistor; and F – ferroelectric thin film." (Samsung; used by permission).

physics questions are important for nano-ferroelectrics: first, are there physical phenomena such as crystallographic phases or domain structures that are stable at these sizes that are not present in bulk? And second, are the device properties qualitatively different on the nano-scale? Phenomena one might examine include ferroelectric quantum dots and confinement energies, direct electron tunnelling, unusual phases due to substrate interface strain, and the general properties of semiconducting ferroelectrics. Most textbooks make the assumption that ferroelectrics are insulators. Although this is a good approximation for bulk samples (Pulvari and Kuebler, 1958a,b), in thin film ferroelectric oxides are generally rather good p-type semiconductors, with a variety of conduction mechanisms, including Poole-Frenkel and Schottky (Dawber *et al.*, 2003a; Liu and Li 2004; Pintilie and Alem 2005; Pintilie *et al.*, 2005). Typical oxide ferroelectrics are wide-gap semiconductors with band gaps  $E_g = 3.5\text{--}4.1\text{ eV}$  and both electronic and ionic conduction. Most are p-type as grown (due to unintentional impurities of low valence, e.g. Na or K for Ba; Fe for Ti or Nb, and oxygen vacancies). Electron and hole mobilities are low, ca.  $0.1\text{--}3.0\text{ cm}^2/\text{Vs}$ ; ionic mobilities (e.g. oxygen vacancies), ca.  $10^{-12}\text{ cm}^2/\text{Vs}$ ; effective masses are very high, typically  $m^* = 5.0\text{--}6.7m_e$ . Note that the band mass and the tunnelling effective mass need not be identical in general, but in most cases they are quite close. If the tunnelling is across  $> 2\text{ nm}$ , the masses should be equal (Conley and Mahan, 1967; Schnupp, 1967). This means that tunnelling processes at ferroelectric thin film junctions are quite unlikely, contrary to some hypotheses (Kohlstedt *et al.*, 2002; Contreras *et al.*, 2003a,b,c) and the conclusions by Tagantsev *et al.* (2002) or Baniecki *et al.* (2003) about Fowler–Nordheim tunnelling with  $m^* = \text{ca. } 1.0m_e$  are very unlikely. The large effective mass in these materials, ignored by Tagantsev, Baniecki *et al.*, should make us sceptical about some physical hypotheses. Lead zirconate–titanate (PZT), strontium bismuth tantalate (SBT) and bismuth titanate (BiT) remain the device favourites (Scott and Araujo, 1989; Paz de Araujo *et al.*, 1995).

For any switching ferroelectric device we must understand how the domains and domain kinetics differ from bulk. Kittel’s law was the first breakthrough in understanding how domain widths scale with thickness. Some 60 years ago Kittel published a paper (Kittel, 1946) that showed magnetic domains exhibit 180-degree stripe widths  $w$  that are proportional to the square root of the crystal thickness  $d$ :

$$w^2 = a'd \quad 18.1$$

This expresses a balance between domain wall energy and surface energy and was extended to ferroelectrics (Mitusui and Furuichi, 1953) and to ferroelastics by Roitburd, (1976). It is verified in Fig. 18.2. More recently Scott (2006a) has shown that this law can be made dimensionless by dividing by the wall thickness:



18.2 Stripe width  $w$  vs. thickness  $d$  in  $\text{PbTiO}_3$ ,  $\text{BaTiO}_3$  and Rochelle Salt (Schilling *et al.* 2006).

$$w^2 = ad\delta \tag{18.2}$$

where  $\delta$  is the domain wall width. In this case, rather remarkably, the equation applies to all ferroics (ferromagnets, ferroelectrics and ferroelastics) with the same coefficient (Catalan and Scott 2006):

$$a = [2\pi^3/21\zeta(3)] [\chi(a)/\chi(c)]^{1/2} = 2.455 [\chi(a)/\chi(c)]^{1/2} \tag{18.3}$$

where  $\chi(x)$  are the susceptibilities and  $\zeta(3)$  the Riemann zeta function of power 3.

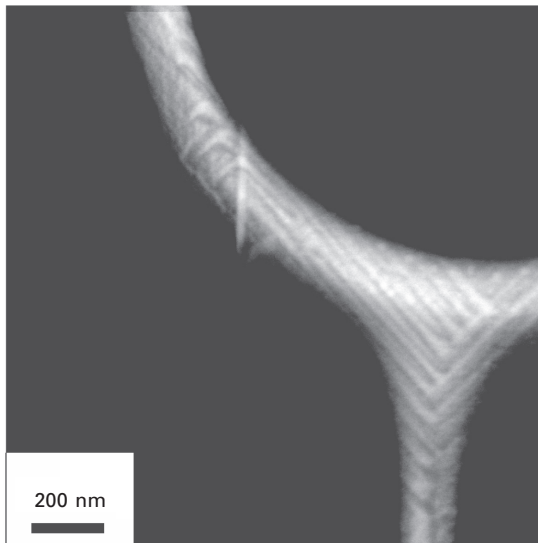
In addition to understanding the static configurations of nano-domains, we need to understand how their switching depends upon size. That brings us to the 1962 Kay–Dunn law, which consists of an equally simple law for the coercive field (minimum switching field  $E$ ):  $E_c = bd^{-2/3}$  and coercive voltage  $V_c = bd^{1/3}$ .

Both of these laws hold from macroscopic millimetre thickness  $d$  down to ca. 2nm. Thus, surprisingly, much of the behaviour of nano-ferroelectric domains can be derived from bulk classical physics. However, the smallest domains found in  $\text{BaTiO}_3$  – 1.0nm – as well as three-dimensional nano-domains – both violate the Kittel law, and recently Catalan has provided a multi-dimensional extension of Kittel’s one-dimensional law that clarifies this. Domains are usually studied in flat planes, but some [3D] nanodomains are shown in Fig. 18.3. Another qualitative difference is that domain switching in ferroelectrics of submicrometre lateral widths is much more determined

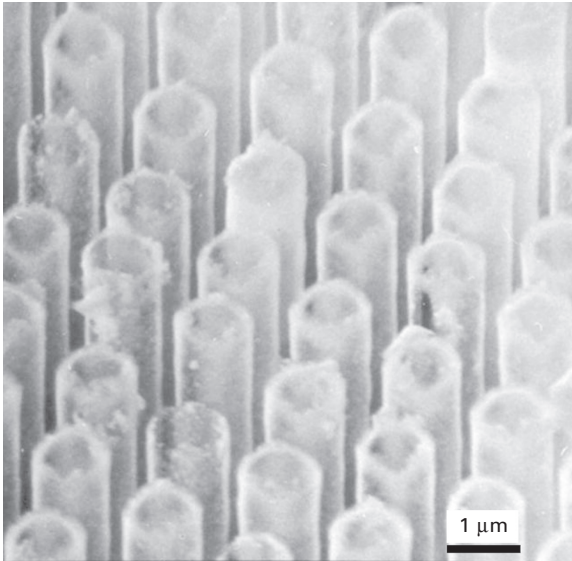
(rate-limited) by nucleation than by domain wall velocities, so that the early theory of Pulvari and Kuebler (1958a,b), which included nucleation, works better than does that of Landauer *et al.* (1956), as shown recently for Samsung  $0.18\mu\text{m}^2$  area PZT cells (Jung *et al.*, 2005). Landauer *et al.* did not ignore nucleation; actually they considered it and rejected it, because it would imply an inductive (phase-lag) part of the switching response, and they found none in their early experiments. Switching as fast as 280ps has been demonstrated recently in thin PZT films (Li *et al.*, 2004); however, this is for small-area capacitors with very small load resistance and a very large driving source – for real devices with 5 V sources and a 10–100 ohm load, 60 ns is a more realistic design access time (RC-limited).

Figures 18.4 and 18.5 illustrate nanostructures in thin ceramic films: Fig. 18.4 shows nanotubes; Fig. 18.5,  $0.3\text{ Tbit/in}^2$  nano-array of Pt-nanowires/PZT. A rather interesting development in 2005-6 has been the attachment of nano-capacitors onto the ends of a registered array of carbon nanotubes. This was first done by Jang *et al.* (2005), using  $\text{Si}_3\text{N}_4$  as the dielectric for the capacitor; more recently Kawasaki *et al.* (2007) in our Cambridge lab have achieved this with a ferroelectric PZT capacitor rather than the non-switching silicon nitride. In Figs 18.6 and 18.7 other non-planar complex nano-device structures are shown: Fig. 18.6 is an SEM cross-section of a PZT/CFO (cobaltous ferrite) magneto-electric composite (Ramesh, Berkeley); Fig. 18.7 shows atomic force microscopy (AFM) nano-writing (Paruch *et al.*, 2006).

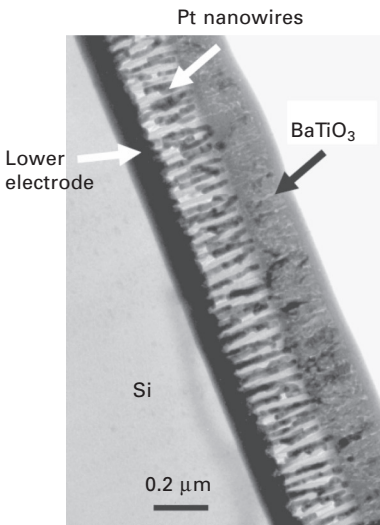
Tera-bit ferroelectric memories are not yet a reality: The state of the art for hard-wired devices is a  $0.3\text{ Tbit/in}^2$  PZT array on Pt-nanowires encased



18.3 [3D] nano-domains in  $\text{BaTiO}_3$  (Saad *et al.*, 2006).

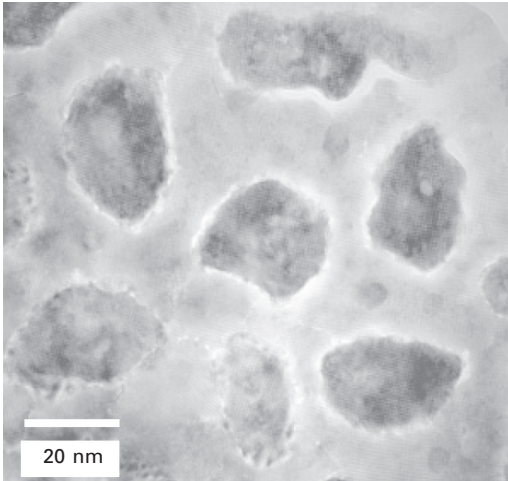


18.4 SrBi<sub>2</sub>Ta<sub>2</sub>O<sub>9</sub> nanotubes (Morrison *et al*)2003).

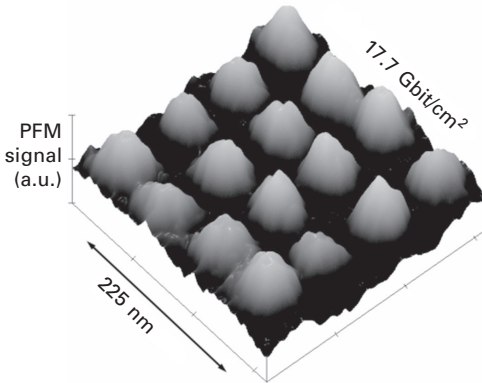


18.5 0.5 Tbit/in<sup>2</sup> nano-array of Pt-nanowires/PZT (Evans *et al.*, 2007).

in meso-porous Al<sub>2</sub>O<sub>3</sub> (Evans *et al.*, 2007). (An AFM-system 1 Tbit/in<sup>2</sup> single-crystal device was shown earlier by Cho *et al.*, 2002). Such a 30 nm diameter capacitor still switches 1000–2000 electrons per bit, which is readable at room temperature (and a good rule of thumb for minimum charge for sense amplifier error-free detection – single-electron devices are definitely *not* realistic in this context), but the registration shown in Fig. 18.4 is not sufficiently

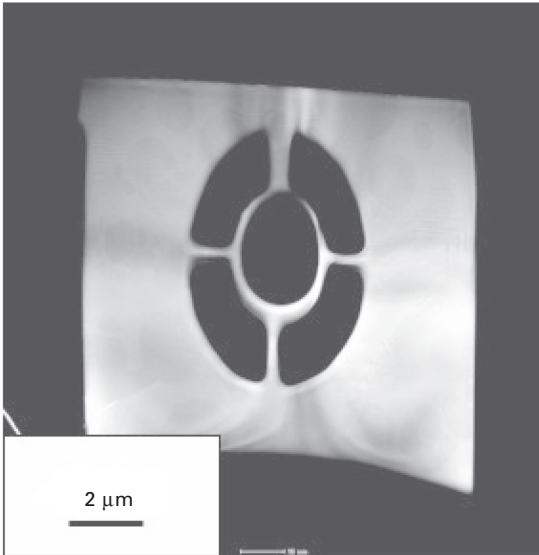


18.6 Magneto-electric composite of  $\text{CoFe}_2\text{O}_4$  pillars in a  $\text{BaTiO}_3$  matrix (Zheng *et al.*, 2006).

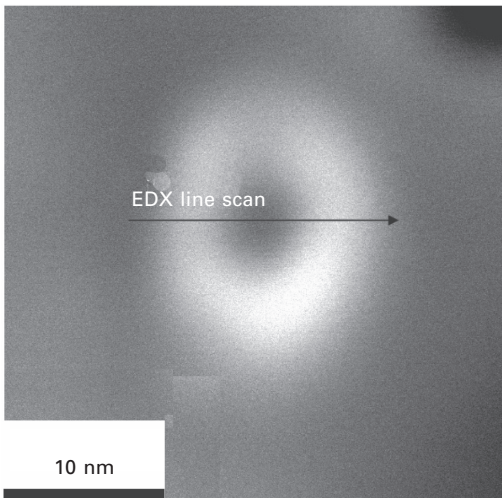


18.7 AFM nano-writing on PZT (Paroch *et al.*, 2001).

long range to make a commercial device, and the prototype wiring has no individual bit-line interconnects. The problem of registration in mesoporous alumina has been partially solved by Masuda and Fukuda (1995), who obtained perfect registration over lengths  $\gg 1 \mu\text{m}$ . Figures 18.5–18.8 illustrate nano-ferroelectrics fabricated as composites (Fig. 18.5) and from AFM writing (Fig. 18.6), and via a focused ion beam (FIB) (Figs 18.7, 18.8). The Belfast group has fabricated complicated [3D] nano-structures, including free-standing micro-rings from FIB (Fig. 18.8), and a 5 nm inside-diameter PZT nano-ring (Fig. 18.9) within a pore of mesoporous Si done by chemical solution deposition. It is important that on the nano-scale these devices can still be



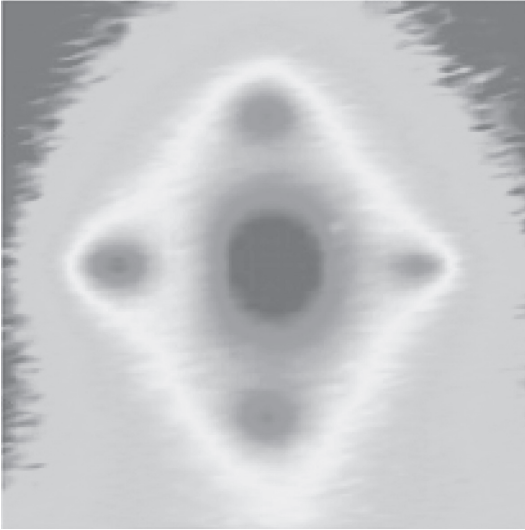
18.8 Nano-toroid of single-crystal BaTiO<sub>3</sub> (Saad *et al.*, 2006).



18.9 Ultra-nano-toroid of PZT inside a meso-porous Al<sub>2</sub>O<sub>3</sub> pore (Zhu *et al.*, 2006 (EDX = energy dispersive X-ray analysis).).

switched electrically or used for optical storage (Cho *et al.*, 2002). Using synchrotron sources (Fig. 18.10) one can study the structure of such very thin films as functions of temperature and thickness. The 2004 32-Mb FRAM from Samsung (PZT) or Matsushita (SBT) are still ahead of the commercial MRAM development (4Mb MRAM from Freescale Co., July 2006), and



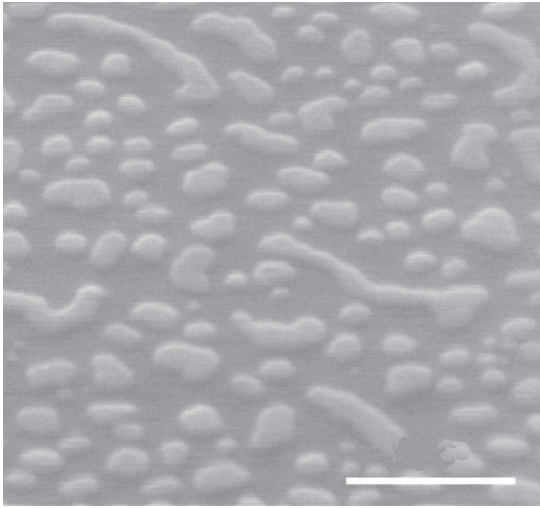


18.10 In-plane diffuse X-ray scattering profiles around the  $\text{PbTiO}_3$   $\langle 303 \rangle$  Bragg peak at 549 K (Auciello, 2006).

Samsung has now (July 2006) a 64 Mb FRAM. The ferroelectric-gate field effect transistor (FET) offers non-destructive read operation, but short retention times (maximum of a few days – Ishiwara *et al.*, 2004) have thus far precluded commercial products. A detailed comparison of MRAMs and FRAMs is given by the author (Scott, 2007), including complex 4T-6C circuits in which four transistors and six capacitors store each bit. Although the latter circuitry prevents high-density RAMs, it permits non-destructive read-out.

### 18.3 Self-patterning

The two basic ways of fabricating nano-ferroelectric devices are, to use industry jargon, ‘top-down’ – meaning submicrometre lithography – and ‘bottom-up’ – meaning self-assembly. The development of meso-porous silicon and alumina (and GaN and GaAs) has presented experimentalists with templates for the latter, and other techniques for coating nano-wires (Sebald *et al.*, 2005; Fan *et al.*, 2006) have developed independently. Self-assembly of nano-electrodes on ferroelectric films was first reported by Alexe *et al.* (1998) and in PZT nano-arrays, data and a model were published by Dawber, *et al.* (2003b) (Fig. 18.11) based upon the original theory (Andreev, 1981) that such islands would repel each other through their mutual strain interactions with the substrate. Although self-assembly often results in arrays that have only short-range order, complete registration satisfactory for commercial RAM memory devices was achieved by Ma and Hesse (2004) via deposition with inert spacers, such as mono-disperse submicrometre or micrometre-



18.11 PZT self assembly – AFM scan of PZT on SrTiO<sub>3</sub> (Dawber *et al.*, 2003b).

sized silicon or latex spheres. See also Chu *et al.* (2004) and Alexe and Hesse (2006). Self-assembly can be used to make nano-particles, nano-tubes or nano-wires. In each case theoretical physicists have pursued the idea that true finite-size effects might occur at dimensions slightly less than 100 nm, but this does not seem to be the case. In nano-spheres of BaTiO<sub>3</sub> the outside shell is cubic (paraelectric) and the interior is (Tanaka and Makino, 1998) tetragonal and ferroelectric (this shell–core structure resembles that in an M&M candy). As diameter is reduced the nano-sphere is all cubic and not ferroelectric. But this is just a surface chemistry effect and not a finite size physics effect. Real finite size effects may occur for diameters < 3 nm.

Most readers are familiar with carbon nanotubes. These are generally good conductors, metallic or semiconducting. By comparison, ferroelectric nanotubes are fairly good insulators. When a voltage is applied to them, they expand, contract, or bend (piezoelectric). First fabricated by Hernandez *et al.* (2002) in Colorado, Mishina *et al.* (2002, 2003) and Mishina (2005) in Moscow, such oxide nanotubes have been most recently characterized by Tenne (2004) and Mao *et al.* (2005). A brief review is given by Morrison *et al.* (2003).

Note that the size distribution graph for the self-assembled nano-islands of PZT in Fig. 18.11 is not a phase diagram (it is not a system in thermal equilibrium). The distribution function for fractional percentage  $w$  of islands of a certain volume  $V$  has

$$\log(w) = a_0V + b_0V^{1/3} + c_0V^{2/3} \quad 18.4$$

assumed, with coefficients  $a_0$ ,  $b_0$ ,  $c_0$  as fitted parameters. This gave very

good agreement with experiment. Physically this means that energy terms proportional to nano-island volume, surface area, and edge lengths are included. One could also add a term proportional to the number of vertices (as has been done by J. Maier (Jamnik *et al.*, 1995) in a different context for ionic conductors), but that was not included.

The most interesting new developments expected in the coming year are hybrid devices combining piezoelectric nanotubes with carbon nano-wires. See Jang *et al.*, (2005) for a preview of such designs.

## 18.4 Magnetolectrics and magnetoelectric devices

The original idea that crystals could be simultaneously electrically and magnetically ordered probably arose with Pierre Curie at the turn of the twentieth century. However, crystals whose Hamiltonians or free energies contained linear coupling between electric polarization  $P$  and magnetization  $M$  were thought to be impossible after an era in the 1920s of their spurious discovery in France by A. Perrier *et al.* in materials such as Ni in which the effect is actually forbidden. This caused a black cloud to settle over the field similar to the more recent case of ‘cold fusion’, and resulted in a hiatus in ‘magnetoelectricity’ R&D until the 1950s, when the Moscow groups, stimulated by Shubnikov and understanding magnetic symmetry better than the rest of the world, resurrected the problem. Dzyaloshinskii (1959) predicted such an effect in antiferromagnetic  $\text{Cr}_2\text{O}_3$ , rapidly confirmed by Astrov (1960), and also piezomagnetism, quickly found by Borovik-Romanov (1960). In contrast to magnetostriction, which is a quadratic effect, piezomagnetism, like piezoelectricity, is a linear vector response. Most physicists had thought that the linear magnetoelectric effect and piezomagnetism were forbidden, because the Hamiltonians that include them do not obey time-reversal symmetry (in general, magnetism does not!). During the 1970s a successful search for other linear magnetoelectrics (‘multiferroics’) was led by Hans Schmid in Geneva. The primary device interest was multi-state logic elements for computer bit storage that could be greater than binary. As such, it was imperative to show switching of magnetic states with electric fields and/or of ferroelectric states with magnetic fields. Hence the independence of, or coupling between, magnetic and electric domain walls was of great importance. This work has had a renaissance since 2000, with new work emphasizing Mn and Tb compounds (Kimura *et al.*, 2003; Hur *et al.*, 2004). The study of magnetoelectricity emphasizes two terms, given in Eq. [18.5]:

$$H = \alpha_{ij} \langle P_i \rangle \langle M_j \rangle + \beta_{ijk} \langle P_i \rangle \langle M_j M_k \rangle \quad 18.5$$

Note that due to the first term this Hamiltonian is not time-reversal invariant. Here the linear magnetoelectric effect due to  $\alpha_{ij}$  vanishes above  $T_N$ , the Neel temperature) or  $T_C$  (the Curie temperature), since  $\langle M \rangle = 0$ ; however, the

quadratic term due to  $\beta_{ijk}$  is proportional to  $\langle M^2 \rangle$  – the rms value of magnetization – and remains finite well above  $T_N$  (until  $T \sim 3T_N$  in magnets such as  $\text{BaMnF}_4$  with [2D] planar spin ordering). Such quadratic magnetoelectric effects in paramagnets were first discovered by Hou and Bloembergen (1965).

If we wish to switch a magnetic domain with an electric field, we need to know how much the magnetization  $M$  depends upon the polarization  $P$ . Does reversing  $P$  influence  $M$  by 1%, 10% or 100%? The idea that ferroelectricity could actually *cause* ferromagnetism (a 100% effect) was explained by Fox and Scott (1977) and later by Privratska and Janovec (1997) and exemplified with the  $\text{BaMF}_4$  family ( $M = \text{Mn, Ni, Co, Fe}$  and mixed compounds  $\text{BaM}_{1-x}\text{M}'_x\text{F}_4$ ). Fox and Scott made a semi-empirical quantitative estimate of the effect by using known values of  $\alpha$  in other Mn-compounds; Privratska and Janovec used a group theory calculation which could not predict magnitudes (or even whether the effect is large enough to measure), but they showed which domain walls in which point group symmetries would permit it. By producing a weak ferromagnetic moment (canting of antiferromagnetic spin sublattices)  $M_i = \alpha_{ij} P_j$  through the Dzyaloshinskii-Moriya anisotropic exchange, the ferroelectric polarization can produce this effect in some symmetry groups (e.g.  $2'$  in  $\text{BaMnF}_4$ ) but not others (e.g.  $2$  in  $\text{BaCoF}_4$ ). The angle of spin canting (3 mrad = 0.17 degrees in  $\text{BaMnF}_4$ ) implies a plausible value for the anisotropic exchange in comparison with off-diagonal  $\alpha_{ij}$  in other  $\text{Mn}^{+2}$  compounds.

This Fox–Scott mechanism has recently been rediscovered in  $\text{BaNiF}_4$  and developed in the context of *ab initio* models by Ederer and Spaldin (2006a,b); it can also produce ferromagnetism within domain walls in antiferromagnets (Privratska and Janovec, 1997). This mechanism is too weak to reconcile conflicting  $\text{BiFeO}_3$  magnetization data of Wang *et al.* (2003, 2005) with the near-zero values reported by Eerenstein *et al.* (2005), and it is symmetry-forbidden in the  $R3c$  structure of bismuth ferrite; however, a more general model for ferromagnetism in antiferromagnetic domain walls which might be stronger has been detailed by Privratska and Janovec (1997) which is allowed for  $R3c$ . (Although the strong ferromagnetism initially reported in *Science* by Wang *et al.* is not intrinsic to pure  $\text{BiFeO}_3$ , it would appear that not all of the discrepancy can be attributed to oxygen vacancies and resultant mixed valence states for the Fe ions; perhaps some of the ferromagnetism is due to net ferromagnetic moments in the antiferromagnetic domain walls.) The Fox–Scott model is a bulk effect; weaker coupling between magnetic and ferroelectric domain walls has been demonstrated by Cheong's group at Rutgers and is also of great theoretical interest.

Brown *et al.* (1968) showed that for direct magnetoelectric coupling, explicit in the first term of Eq. [18.5], the square of the magnetoelectric susceptibility cannot exceed the product of the electric susceptibility and the

magnetic susceptibility,  $\chi_{me}^2 \leq \chi_m \chi_e$ , making it uselessly weak for devices (see also Ascher *et al.*, 1966). However, that ignores indirect coupling through strain. The latter can be important in a single material (i.e. piezoelectric terms and electrostrictive terms such as  $sP$  and  $sP^2$  plus piezomagnetic terms such as  $sM$  and magnetostrictive terms  $sM^2$ ); and they permit binary structures in which one substance has large piezoelectricity (or electrostriction) and the other has large piezomagnetism or magnetostriction. By choosing two materials in a laminated or nano-structured bimorph, one can cause large magnetostriction in, say, terphenyl-d, and large piezoelectricity in, say, PZT. The result is a prototype room temperature detector of weak magnetic fields, which might be a very low-cost (uncooled) replacement for SQUID detectors. The best result to date is a laminar bimorph of a ferromagnet (LSMO) and barium titanate (Eerenstein *et al.*, 2007). Unfortunately, the ‘Holy Grail’ of multiferroics – a strong (uncanted) ferromagnet that is also ferroelectric at room temperature – is still sought for. But it is unlikely to have device parameters superior to PZT/terphenyl anyway. As a memory element, however, it would permit electric WRITE operation and magnetic READ; this would eliminate the need for a destructive read (and reset) for present-day FRAMs and make possible fatigue-free memories. Its READ operation could be extremely fast and low power. This very attractive possibility requires a ferroelectric ( $P > 1 \mu\text{C}/\text{cm}^2$ ) that is also a strong ferromagnet ( $M \geq 1$  Bohr magneton/unit cell) and has low electrical conductivity ( $\ll 10^{-6} \text{ohm}^{-1} \text{cm}^{-1}$ ) at ambient temperatures. Although  $\text{BiFeO}_3$  doped to increase resistivity remains a possible candidate, ferroelectric-ferromagnetic fluorides such as  $\text{Sr}_3(\text{FeF}_6)_2$  or  $\text{K}_3\text{Fe}_5\text{F}_{15}$  with respectively  $T_c \approx 700 \text{K}$  and  $495 \text{K}$  merit much more study (Abrahams, 1996, 1999; Abrahams *et al.*, 1996; Ederer and Spaldin, 2006a,b).

From a device point of view, the advantage of a magnetoelectric RAM is that it could be electrically written (fast, low power) but magnetically read (non-destructive read-out, no re-set and little fatigue). Unfortunately, several recent papers report magnetic effects on dielectric constants and interpret them as evidence for magnetoelectricity (Hemberger *et al.*, 2005); Catalan and Scott (2007) have shown that this is usually not true and can arise from magnetoresistance plus Maxwell–Wagner space charge in non-ferroelectrics, including cubic spinels.

## 18.5 Toroidal and circular ordering of ferroelectric domains in ferroics

Ferroic domains are usually rectilinear, although needle-like domain structures are also common. However, circular or toroidal patterns can occur, and most ferroelectrics (or antiferroelectrics) order with polarizations parallel or antiparallel. As Kittel (1946) first pointed out, ferromagnets in nano-size diameters will order with four  $90^\circ$  domains forming a circle or square. This

kind of topological spin defect (vortex) was treated theoretically by Mermin (1979) in terms of winding numbers, and is commonly found in nano-magnets, in both naturally occurring minerals (such as titanium-ilmenite) and synthetics (Harrison *et al.*, 2002). The latter authors achieved superb micrographs of such vortex domains via electron holography. Typical size (diameter) of these vortex domains is 100 nm.

A completely different origin for circular or toroidal domains occurs in magnetoelectrics, even in bulk. First analysed in detail by Ginzburg and by Sannikov, this has been reviewed by several authors (Dubovik and Tugushev, 1990; Schmid, 1994; Fiebig, 2005; Eerenstein *et al.*, 2006); and subject to a flurry of recent papers (Naumov *et al.*, 2004; Scott, 2005; Ponomareva *et al.*, 2005a,b; Prosandeev *et al.*, 2006) but not yet unambiguously observed (a newly recognized complication is that domain walls in antiferromagnets can themselves be ferromagnetic). Such a system offers the possibility of very high-density (Tbit/in<sup>2</sup>) memory and electrical WRITE with magnetic READ operations. The read operations are facilitated by simultaneous application of a large dc electric field, as recently shown by Prosandeev, *et al.* (2006). Although permitted in bulk, the occurrence of such toroidal ordering in ferroelectrics is favoured in nano-tubes and nano-disks (Naumov *et al.*, 2004), and recently Zhu *et al.* (2006) have fabricated such ferroelectric 'doughnuts' as small as 5 nm inside diameter.

## 18.6      Electron emission from ferroelectrics

The fact that ferroelectrics emit copious electrons from their surfaces during switching was discovered in Michigan (Rosenblum *et al.*, 1974) and later studied extensively in Sverdlovsk. Its use as synchronized electron sources for accelerators was investigated by Gundel (1995; 1996) in CERN (now Nantes), Le Bihan and others in France (Sviridov *et al.*, 1998), Biedrzycki in Poland, and several Russian/Israeli (Rosenman *et al.*, 2000) and American groups (Auciello *et al.*, 1995). The prototype use as a synchronized, pulsed electron source for accelerators was developed, but no commercial devices were ever manufactured, primarily because of fatigue.

The extension to flat channel-plate structures with ferroelectric thin films was studied in Nantes, but films gave inferior performance compared with bulk ceramics. A good summary (yet unpublished) of the present situation has been given by Kafadaryan (2006). Currents of tens of amps have been obtained with synchronized, rather mono-energetic pulse lengths of 100 ns to 1  $\mu$ s. These are superior to thermionic cathodes in that they have higher current densities and lifetimes and also have instant turn-on (thermionic cathodes require a warm-up). The ferroelectric electron emitters can be operated in poor vacuum and require no separate activation process. The commercial drawbacks are that the intense electric fields cause micro-cracking and device

failure and that the effect is poorer in thin films than in bulk. Moreover, no unambiguous theoretical model has been accepted for the basic emission process. One published mechanism invokes a surface plasma layer creation during switching that I regard as very unlikely (its supposed experimental detection was actually to interference patterns similar to Newton's rings and not to plasmon reflectivity). Although fields of  $E = 10^7$  V/cm are required for good performance, this value has recently been achieved in FIB-cut single crystals as well as PZT ceramics; note that  $10^7$  V/cm is a huge field (1 GV/m) but is only 50 V across 50 nm.

In my opinion this is an unexploited device area for which commercial development of, for example, miniature high-power microwave devices that could be made within a few years. Samsung explored in the 1990s the use of this phenomenon for nano-lithography, and a comprehensive review was published in 2000. Most recently this effect was used by Putterman's group for a kind of cold fusion (Naranjo *et al.*, 2005) as a miniaturized source of X-rays and neutrons.

## 18.7 Base–metal–electrode capacitors

The majority of all condensers used in electronics (billions/year) are barium–titanate-based ceramic capacitors based on the original discovery by von Hippel (1944). Leading producers include Kyocera in Kyoto and AVX Corp. near Belfast. These are multi-layer capacitors (MLCs) with Ag/Pd electrode stacks. Some of the electrodes are internal in an MLC and are 'floating' (no contact to the external circuitry). Present efforts are to increase high-voltage performance to higher breakdown voltages and to further reduce costs by replacing silver-palladium with base metals, especially nickel. Electrode separations  $d$  vary from submicrometre to ca. 20  $\mu\text{m}$ . Recently Milliken *et al.* (2006b) and Scott (2006) have shown that the breakdown field varies as the dc thermal model predicts (ignoring transient effects of applied field ramp rate):  $E_B = c_1 d^{-1/2}$  for thicknesses above 1  $\mu\text{m}$ , but no theory exists for the submicrometre-spaced devices, where electrode surface roughness may be the limiting parameter. Progress would be expected in this high-volume commercial area in the next five years: Ni replacement; higher breakdown devices; and a reliable theory for both Ni–BaTiO<sub>3</sub> interfaces and the non-monotonic dependence of breakdown voltage on the electrode separation  $d$ . This has not been a fashionable research area in universities, but the financial pay-off is potentially huge.

## 18.8 Electrocaloric cooling for mainframes and MEMs

The fact that ferroelectrics can be cooled by applying an electric field to them under certain conditions has been known for 50 years. Termed the

'electrocaloric effect' after analogous magnetocaloric effects in magnets, the mechanism was poorly analyzed for some years, with the three standard texts on ferroelectricity by Jona and Shirane (1962), by Fatuzzo and Merz (1962), and by Mitsui *et al.* (1969) giving three different predictions for behaviour above and below  $T_C$ . From Maxwell's relations

$$(\partial T/\partial D)_S = (\partial E/\partial S)_D = (T/c^D) (\partial E/\partial T)_D \quad 18.6$$

where  $T$  is temperature;  $E$ , electric field;  $S$ , entropy;  $D$ , displacement vector; and  $c$ , specific heat at constant displacement  $D$ . This gives in terms of the Devonshire coefficient  $\beta$  from a Landau expansion of the free energy

$$(\partial T/\partial D)_S = \beta DT/c^D \quad 18.7$$

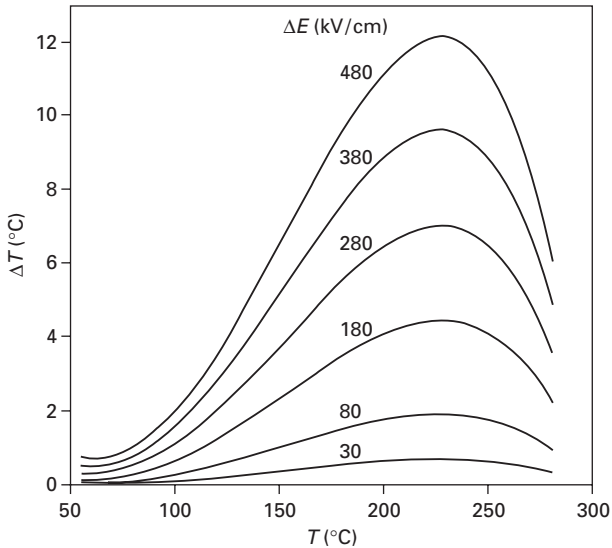
and, integrating over  $T$ , assuming  $T_1 - T_2$  is small,

$$\Delta T = T_1 - T_2 = \frac{\beta T}{2c^D} (D_1^2 - D_2^2) \approx [(\beta T/(2c^D))][P_1^2(E) - P_2^2(0)] \quad 18.8$$

The derivation above is misleading in popular textbooks (e.g. Lines and Glass (1967)), because the field dependence  $P(E)$  is usually neglected at  $T_2$ ; indeed  $T_2$  is not shown in any diagram, and it is unclear whether the heat cycle has three legs or four. The error lies in the fact that  $(\partial P/\partial E)_T \gg (\partial P/\partial T)_E$ . Thus significant effects also occur for  $T_1$  and  $T_2$  both above, or one above and one below; and in fact the peak electrocaloric effect can be 5–10 K above  $T_C$ . It is complicated for first-order transitions, where a modest applied field  $E$  can drive the crystal ferroelectric at temperatures well above  $T_C$  (e.g. up to  $T = T_C + 8.0$  K in barium titanate).

The different conclusions about the electrocaloric effect in textbooks has been reviewed by Scott (1993) and studied in careful detail by Tuttle and Payne (1981), Strukov (1967) and Shebanov and Borman (1992), but because the effect was small in bulk (measured in millidegrees/volt), it remained a laboratory curiosity. However, Mischenko *et al.* (2006) inferred  $\Delta T = 12$  K at 25 V across 350 nm for cooling (Fig. 18.12) in ferroelectric thin films, sufficient to design a prototype cooler for MEMs or even computer mainframes, which has stimulated a burst of R&D on the subject. There are two subtleties: first, the thermal cycle has only three legs and not four as is sometimes shown for magnetoelectric cooling. The first step is to turn on the field at  $T = T_1$  and isothermally reduce the entropy  $S$  by increasing polarization  $P$  from zero to  $P_1$ . The second step is to turn the field off. Although this lowers  $E$  to zero almost instantly, it certainly does not drop  $P$  to zero as quickly; instead,  $P$  relaxes slowly (and approximately adiabatically). This adiabatic cooling lowers  $T$  to  $T_2$  and  $P$  to zero. The third leg of the heat cycle is to warm up from  $T_2$  to  $T_1$  by extracting heat from the surrounding system; this is at constant (zero) polarization and is hence 'isochoric'. Secondly, this heat cycle is more complicated for a first-order phase transition slightly above the transition





18.12 Electrocaloric effect in lead scandium tantalate PST (Mischenko *et al*, 2006).

temperature  $T_0$ . In  $\text{BaTiO}_3$  up to  $T = T_0 + 8.0\text{K}$  ferroelectricity can be induced by the applied field. Hence switching the field on at  $T_0 < T < T_0 + 8\text{K}$  can produce extremely large changes in entropy due to domain formation and consequently large changes in temperature. In such cases the maximum electrocaloric effect can occur above  $T_0$ , contrary to the conclusion in some textbooks or in Strukov's papers on triglycine sulphate (which is second-order).

## 18.9 Interfacial phenomena

Ferroelectrics in some ways are more complicated than ferromagnets, simply because magnets can be measured in air with no electrical contact, whereas ferroelectric electrical measurements generally must be made on a sandwich consisting of two electrodes around a dielectric (Valasek, 1921). The interface between the metal electrodes and the semiconducting ferroelectric is very complex, involving screening in the metal (Dawber *et al.*, 2003a, 2005a) and instabilities at ca. 3 nm dielectric thickness (Junquera and Ghosez, 2003), reduced perhaps to 1 nm by electrode-ferroelectric ionic interactions more complex than simple Fermi–Thomas screening (Gerra *et al.*, 2006). There are rather subtle differences in the behaviour of ferroelectric thin films with elemental metal electrodes (Pt, Au, Ni) and oxide metal electrodes, such as  $\text{SrRuO}_3$ ,  $\text{IrO}_2$  or  $\text{RuO}_2$ . The primary criterion for good electrodes is a large

work function (ca. 5.0–5.5 eV), to prevent ohmic or near-ohmic contacts on the dielectrics (which typically have electron affinities of 3.5 eV and bandgaps of 3–4 eV, so that the Pt 5.3 eV work function nicely puts the Pt Fermi level at mid-gap in the dielectric). Full oxidation of most oxide electrodes is therefore important, because, for example, the work function of RuO<sub>2</sub> is at 4.95 eV, but unoxidized elemental Ru nano-islands in the electrode deposited below ca. 840 K are at 4.65 eV, causing ‘hot spots’ and leakage (Hartmann *et al.*, 2000).

Both leakage currents and charge injection are serious problems and can produce artefacts in switching data. The resulting leakage current in PZT films can be Schottky-limited in a partially depleted film (Pintilie and Alexe, 2005; Pintilie *et al.*, 2005) for somewhat conducting lead zirconate titanate (PZT) but Poole–Frenkel limited in a fully depleted PZT film from the Samsung 32 Mbit production line (Zubko *et al.*, 2006a,b). These differences in conduction mechanisms were very well illustrated in an early paper by Li and Lu (1991). Understanding and optimizing interfacial phenomena are paramount to the commercialization of thin film memories and ferroelectric DRAM capacitors, and have been reviewed by Auciello (2006). Early problems with fatigue, primarily due to perovskite-pyrochlore conversion (Lou *et al.*, 2006) in FRAMs have now been overcome via oxide electrodes.

## 18.10 Phased-array radar

Phased-array radar devices produce an angular scanning of the horizon without mechanical rotation of the antenna. This can be achieved by a voltage-dependent phase shift in the antenna elements. Such shifts can be generated in bulk ferroelectrics, but only at very high voltages (kV), which entails large sizes and weights. It would be desirable to produce phased array radar devices with ferroelectric thin films, since this could entail very low voltages (5 V) compatible with silicon chip technology, and hence embodiments with small size and weight. Thin-film ferroelectrics exhibit a large decrease in dielectric constant with application of modest voltages, typically 25–60% at 5 V. This suggested that they could be used as the active phase-shift element in phased-array radar, a project studied carefully in the 1990s by researchers at Grumman and TRW in the USA and by Vendik’s group in Leningrad. Unfortunately the dielectric loss tangent in these films remains too large for acceptable insertion losses in such devices, so nothing has been made commercially. There is hope that this loss is not intrinsic, since it is orders of magnitude smaller in bulk. Therefore significant efforts to improve the quality of thin films have been underway, with perhaps the best results obtained at Penn State University. A status report was published recently by Miranda *et al.* (2002).

### 18.11 Focal-plane arrays

All ferroelectrics are pyroelectric and hence application of thin-film ferroelectric technology to pyroelectric detectors, including focal-plane arrays, is of interest. This may be enhanced by the fact that high-quality films can be deposited on curved substrates via chemical vapor deposition or misted CSD (chemical solution deposition). This was shown both at Symetrix and at SONY in 1997 (Isobe *et al.*, 1997; Solayappan *et al.*, 1997). No breakthroughs have been reported in the open literature, although LG Electronics has reported using the mist system for DRAM capacitors (Kim *et al.*, 1997).

### 18.12 Ferroelectric superlattices

The study of artificially layered ferroelectric superlattices, such as BaTiO<sub>3</sub>/SrTiO<sub>3</sub> is of great current interest (Tenne *et al.*, 2006). Such superlattices can produce enhanced polarization  $P$  and dielectric constant  $\epsilon$ . Their physics is generally very well understood but remains somewhat enigmatic at very small repeat distances of one to three unit cells (Dawber *et al.*, 2005b). PbTiO<sub>3</sub>/SrTiO<sub>3</sub> is particularly interesting because it has a near-perfect lattice constant match. A surprising phenomenon is that in BaTiO<sub>3</sub>/SrTiO<sub>3</sub> the polarization flops from along [001] to [110] in the relaxed superlattice (Jiang *et al.*, 2003; Rios *et al.*, 2003; Johnston *et al.*, 2005). Jiang *et al.* (2002) also showed that PbZr <sub>$x$</sub> Ti <sub>$1-x$</sub> O<sub>3</sub>/PbZr <sub>$y$</sub> Ti <sub>$1-y$</sub> O<sub>3</sub> (all-PZT) superlattices with  $x \gg y$  had significant Maxwell–Wagner space charge at the layer interfaces that influenced fatigue. ‘Tri-color’ superlattices are particularly interesting; these materials have a stacking sequence of ABCABCABC... that lacks inversion symmetry.

A related topic is periodically poled crystals of LiNbO<sub>3</sub> and other non-linear optical materials (Walker *et al.*, 2005; Glickman *et al.*, 2006). Here the superlattice consists not of different chemical compositions such as BaTiO<sub>3</sub>/SrTiO<sub>3</sub>, but of + $P$  and – $P$  domains. Such materials provide highly efficient phase-matching for non-linear optics. The quest at present is to produce shorter wavelengths ( $< 1 \mu\text{m}$ ) and to understand domain widths and stability (the positive + $P$  domains are not always the same width as the negative – $P$  domains, and the widths can vary with time).

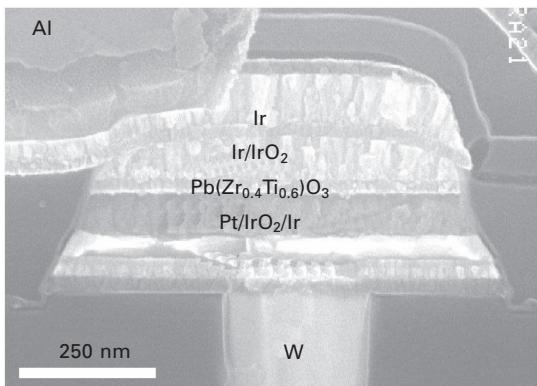
### 18.13 Ultra-thin single crystals

Until very recently the conventional wisdom with regard to ferroelectric thin films was that for thicknesses much below  $1.0 \mu\text{m}$ , the dielectric peak versus temperature  $\chi(T)$  was greatly broadened and shifted to much lower (hundreds of degrees) temperatures. Most scientists assumed that this was due to intrinsic size effects, theoretically predicted. However, we now know that for thicknesses

$\gg 3$  nm such effects are extrinsic, usually caused by oxygen vacancy gradients or strain gradients near the electrode interfaces (Bratkovsky and Levanyuk, 2005). This conclusion is based on recent Belfast–Cambridge studies on very thin (50–100 nm) single crystals, prepared via FIB. The use of FIBs to cut nano-ferroelectrics was pioneered by Ramesh’s group in Maryland (Ganpule *et al.*, 1999) for ceramic films but recently extended by Gregg’s group in Belfast to preparing single crystals of  $\text{BaTiO}_3$  (Saad *et al.*, 2004). The results of the latter team have been to characterize single-crystal capacitors of thickness down to ca. 65 nm. This has shown unambiguously that effects of Curie temperature shift or dielectric peak broadening are extrinsic (Bratkovsky and Levanyuk, 2005), contrary to the previous conventional wisdom. The availability of single crystals with thickness  $d < 50$  nm should permit clear tests of finite-thickness theory. Cho *et al.* (2002) have shown that they permit some elegant optical devices for the future, despite the high cost of such single-crystal devices.

### 18.14 Summary

It has now been over 80 years since ferroelectricity was discovered (Valasek, 1921) and 62 years since oxide ferroelectrics without hydrogen bonds (originally thought to be requisite) were found in several countries during World War II (von Hippel, 1944). The progress in the past few years has been quite rapid, emphasizing thin films and nano-devices. A brief review has been given in this chapter of a dozen subtopics of current experimental interest in modern ferroelectricity. Most relate to nano-structures, and many suggest device development of great commercial potential. Present commercial ferroelectric cells in 64 Mb or 32 Mb FRAMs (Figs 18.1 and 18.13) are as small as  $450 \times 400 \times 120 \text{ nm}^3$  in ceramic form; single crystals as thin as

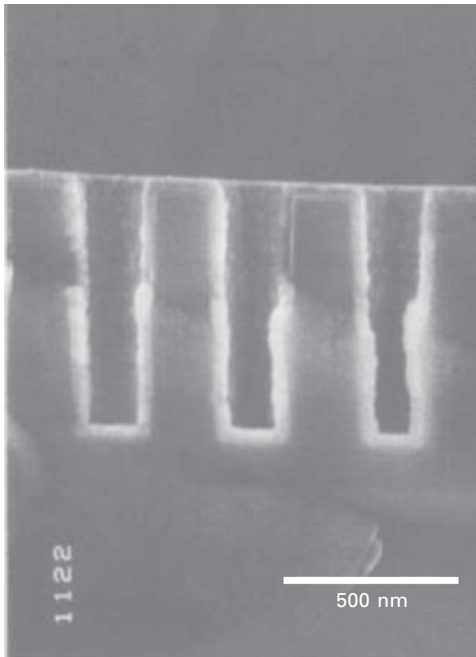


18.13 32 Mbit PZT FRAM (Samsung).

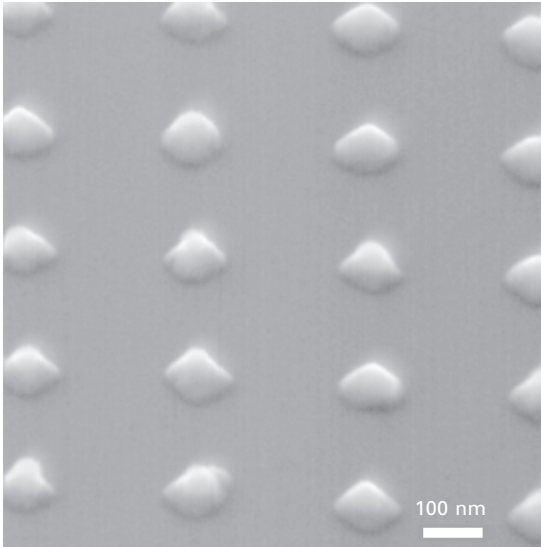
50–70 nm and films as thin as 2 nm are under study at universities, as are high-aspect DRAM trenches (Fig. 18.14) and [3D] nanotubes for microfluidics as well as 5 nm diameter rings and 1 nm domain widths, with PZT/Pt-nanowire arrays giving nearly 1 Tb/in<sup>2</sup> nonvolatile memory arrays. Read–write speeds are as fast as 280 ps for laboratory devices and e-beam lithography (Fig. 18.15) still leads self-assembly techniques for the registration required for commercial random access memories.

### 18.15 Future trends

The near-term predictions for ferroelectrics are that they will emphasize submicrometre thin films. These are already at 140 nm for commercial FRAM memories and could go down to ca. 20 nm without incurring very detrimental leakage currents. Lateral sizes are ca. 400 nm in 64 Mb FRAMs, and could decrease further to real nano-scale (<100 nm) and still produce enough switched charge for the sense amplifiers (>1000 *e* is a good rule of thumb). In the next five years the competition between MRAMs and FRAMs to replace ‘flash’ EEPROMs should be a stimulus for researchers. In other non-memory areas, the application to microfluidic transport seems appealing. Pfizer has a new insulin inhaler on the market (‘Exubera’), and the need for this and similar medical devices for monodisperse small droplets is paramount. There are



18.14 Ruthenium nano-trenches in Si (Funakubo).



18.15 e-beam lithography: PZT capacitor array (Alexe) lithography: PZT capacitor array (Alexe *et al.*, 2001).

190 million people with diabetes in the world, and the US market for diabetes is \$25 million/year and growing at more than 10% per year as the population ages and obesity becomes more common. Similar inroads may occur with inkjet printers, where nano-tube piezoelectric print heads could give improved grey scale control. Finally, the combination of carbon nanotubes with piezoelectric/pyroelectric PZT tips seems intriguing (Jang *et al.*, 2005; Kawasaki *et al.*, 2007), for both pyroelectric detectors and piezoelectric arrays. Both nano-scale lithography ('top-down') and self-assembly ('bottom-up') techniques will continue to share importance, with lithography continuing to dominate industry products for another decade but self-assembly becoming dominant thereafter. It is likely that the optoelectronic aspects of such devices will be useful. Photonic arrays utilizing registered self-patterned ferroelectrics are already in prototype form (Gregg and Scott, 2007). It should be noted that GaAs and GaN are available in mesoporous form, so ferroelectric nanotubes and nanorods need not be limited to Si or Al<sub>2</sub>O<sub>3</sub>. Although non-oxide ferroelectrics, especially fluorides, will receive increased attention, commercial devices are likely to emphasize oxide films for the foreseeable future, with some increase in the use of polymeric ferroelectrics, such as polyvinylidene fluoride (PVDF). The replacement of SQUIDs by much cheaper magnetoelectric (ferroelectric) sensors for weak magnetic fields may occur within the decade, on the basis of room temperature operation. This could permit portable devices for geologists and oil exploration, along with solid-state research devices.

## 18.16 Further reading

The attention of readers is called to the Proceedings of the Rank Prize Conference on Electrooptics, Grasmere, UK (September 11–14, 2006), which will be published as a special issue in *Ferroelectrics* (2007), edited by J. M. Gregg and J. F. Scott. This issue deals primarily with applications of ferroelectric nanostructures to electrooptics. Other recent topical reviews on the subjects discussed here are to be found by Miranda *et al.*, (2002) – agile microwave devices, Scott (2006a) – nano-ferroelectrics, Fiebig (2005), Catalan (2006), Catalan and Scott (2007), Hill (2000) Hemberger *et al.*, (2005), Schmid (2001) – magnetoelectrics, Auciello *et al.* (1998), Auciello (2006) – electroding and interface physics, Dawber *et al.* (2005a) theory and experiment of oxide films and Eerenstein *et al.* (2006) – multiferroics. The Springer series ‘Topics in Applied Physics’ provides very good texts on ferroelectric memories (FRAMs), especially that of Ishiwara *et al.* (2004) and the earlier text by the present author (Scott, 2000) [available also in Japanese (Springer Japan, translated by M. Tanaka *et al.*, Tokyo 2003) and in Chinese (Tsinghua Press, translated by J. Zhu, Beijing, 2004)]. The rapid increase in ferroelectric memory R&D in China is noticeable, and the author hopes this very inexpensive Chinese text will help. Another book in this series, emphasizing nano-ferroelectric memory devices and the Samsung FRAM design strategy, is expected in 2007 by the author’s group (Jung *et al.*, 2007).

## 18.17 References

- Abrahams S C (1996), ‘New ferroelectric inorganic materials predicted in point group  $4mm$ ’, *Acta Cryst.* **B52**, 790–805.
- Abrahams S C (1999), ‘Systematic prediction of new inorganic ferroelectrics in point group  $4$ ’, *Acta Cryst.* **B55**, 494–506.
- Abrahams S C, Mirsky K, and Nielson R M (1996), ‘Prediction of ferroelectricity in recent inorganic crystal structure database entries under space group  $Pba2$ ’, *Acta Cryst.* **B52**, 806–809.
- Alexe M and Hesse D (2006), ‘Self-assembled nanoscale ferroelectrics’, *J. Mater. Sci.* **41**, 1–11.
- Alexe M, Scott J F, Curran C, Zakharov N D, Hesse D, and Pignolet A (1998), ‘Self-patterning nano-electrodes on ferroelectric thin films for gigabit memory applications’, *Appl. Phys. Lett.* **73**, 1592–1594.
- Alexe M, Harnagea C, Hesse D, and Goesele U (2001), ‘Polarization imprint and size effects in mesoscopic ferroelectric structures’, *Appl. Phys. Lett.* **79**, 242–244.
- Andreev A F (1981), ‘Faceting transactions in crystal’, *2h. Eksp. Teor. Fiz.* **80**, 2042–2052.
- Ascher E, Rieder H, Schmid H, and Stoessel H (1966), ‘Some properties of ferromagnetoelectric nickel iodine boracite’, *J. Appl. Phys.* **37**, 1404–1405.
- Astrov D N (1960), ‘The magnetoelectric effect in antiferromagnets’, *Sov Phys JETP* **11**, 708–709.
- Auciello O (2006), ‘Science and technology of thin films and interfacial layers in ferroelectric

- and high-dielectric constant heterostructures and application to devices', *J. Appl. Phys.* **100**, 051614 (2006).
- Auciello O, Scott J F, and Ramesh R (1998), 'The physics of ferroelectric memories', *Physics Today* **51**, 22–27.
- Auciello O, Ray M A, Palmer D, Duarte J, McGuire G E, and Temole D (1995), 'Low voltage electron emission from  $\text{Pb}(\text{Zr}_x\text{Ti}_{1-x})\text{O}_3$ -based thin film cathodes', *Appl. Phys. Lett.* **66**, 2183–2185.
- Baniecki J D *et al.* (2003), 'Barium strontium titanate thin-film capacitors for low inductance decoupling devices', *MRS Proc* **748**, 441–450.
- Borovik-Romanov S (1960), 'Piezomagnetism in the antiferromagnetic fluorides of cobalt and manganese, *Sov. Phys. JETP* **11**, 786–790.
- Bratkovsky A M and A. P. Levanyuk A P (2005), 'Smearing of phase transition due to a surface effect or a bulk inhomogeneity in ferroelectric nanostructures', *Phys. Rev. Lett.* **94**, 107601.
- Brown W F Jr., Hornreich R M, and Shtrikman S (1968), 'Upper bound on the magnetoelectric susceptibility', *Phys. Rev.* **168**, 574–577.
- Catalan G (2006), 'Magnetocapacitance without magnetoelectric coupling', *Appl. Phys. Lett.* **88**, 102902.
- Catalan G and Scott J F (2006), 'Comments on "Giant dielectric response in the one-dimensional charge-ordered semiconductor  $(\text{NbSe}_4)_3\text{I}$ " and "Colossal magnetocapacitance and colossal magnetoresistance in  $\text{HgCr}_2\text{S}_7$ "', *Phys. Rev. Lett.* (submitted).
- Catalan G and Scott J F (2007), 'Is  $\text{CdCr}_2\text{S}_4$  a multiferroic relaxor?' *Nature* **448**, E4–E5.
- Cho Y, Fujimoto K, Hiranaga Y, Wagatsuma, Onoe A, Terabe K and Kitamura K, (2002), 'Tbit/inch<sup>2</sup> ferroelectric data storage based on scanning nonlinear dielectric microscopy', *Appl. Phys. Lett.* **81**, 4401–4403.
- Chu M W, Szafraniak I, Scholz R, Harnagea C, Hesse D, Alexe M and Gosele U (2004), 'Impact of misfit dislocations on the polarization instability of epitaxial nanostructured ferroelectric perovskites', *Nature Mat.* **3**, 87–90.
- Clark N A and Lagerwall S T (1980), 'Submicrosecond bistable electrooptic switching in liquid crystals', *Appl. Phys. Lett.* **36**, 899–901.
- Conley J W and Mahan G D (1967), 'Tunneling spectroscopy in GaAs', *Phys. Rev.* **161**, 681–695.
- Contreras J R *et al.* (2003a), 'Surface treatment effects on the thickness dependence of the remanent polarization of 5  $\text{PbZr}_{0.52}\text{Ti}_{0.48}\text{O}_3$  capacitors', *Appl. Phys. Lett.* **83**, 126–128.
- Contreras J R *et al.* (2003b), 'Resistive switching in metal-ferroelectric-metal junctions', *Appl. Phys. Lett.* **83**, 4595–4597.
- Contreras J R *et al.* (2003c), 'Structure and ferroelectric properties of epitaxial  $\text{PbZr}_{0.52}\text{Ti}_{0.48}\text{O}_3$  and  $\text{BaTiO}_3$  thin films prepared on  $\text{SrRuO}_3/\text{SrTiO}_3$  (100) substrates', *MRS Proc.* **688**, C8.10.
- Dawber M, Chandra P, Littlewood P B, and Scott J F (2003a), 'Depolarization corrections to the coercive field in thin-film ferroelectrics', *J. Phys. Condens. Mat.* **15**, L393–398.
- Dawber M, Szafraniak I, Alexe M, and Scott J F (2003b), 'Self-patterning of arrays of ferroelectric capacitors: description by theory of substrate mediated strain interactions', *J. Phys. Condens. Mat.* **15**, L667–671.
- Dawber M, Rabe K M, and Scott J F (2005a), 'Physics of thin-film ferroelectric oxides', *Rev. Mod. Phys.* **77**, 1083–1131.
- Dawber M *et al.* (2005b) 'Unusual behavior of the ferroelectric polarization in  $\text{PbTiO}_3/\text{SrTiO}_3$  superlattices', *Phys. Rev. Lett.* **95**, 177601.



- Dubovik V M and Tugushev V V (1990), 'Toroid moments in electrodynamics and solid-state physics', *Physics Reports* **187**, 145–202.
- Dzyaloshinskii I E (1959), 'On the magnetoelectrical effects in antiferromagnets', *Sov Phys JETP* **10**, 628–629.
- Ederer C and Spaldin N A (2006a), 'Origin of ferroelectricity in the multiferroic barium fluorides BaMF<sub>4</sub>: a first principles study', *Phys. Rev. B* **74**, 024102.
- Ederer C and Spaldin N A (2006b), 'Electric-field-switchable magnets: the case of BaNiF<sub>4</sub>', *Phys. Rev. B* **74**, 020401.
- Eerenstein W *et al.* (2005), 'Comment on epitaxial BiFeO<sub>3</sub> multiferroic thin-film heterostructures', *Science* **419**, 1203a.
- Eerenstein W, Mathur N D, and Scott J F (2007), 'Multiferroic and magnetoelectric materials', *Nature* **442**, 759–765.
- Eerenstein W, Wiora M, Prieto J L, Scott J F and Mathur N D (2007), 'Giant, sharp and persistent converse magnetoelectric effects in multiferroic epitaxial heterostructures', *Nature Mater* **6**, 348–351.
- Evans P R, Zhu X H, Baxter P, *et al.* (2007), 'Toward self-assembled ferroelectric random access memories. Hard-wired switching capacitor arrays with almost tb/in (2) densitier. *Nano. Letters* **7**, 1134–1137.
- Fan H-J *et al.* (2006), 'Monocrystalline spinel nanotube fabrication based on the Kirkendall effect', *Nature Mat.* **5**, 627–631.
- Fatuzzo E and Merz W (1967), 'Ferroelectricity,' North-Holland, Amsterdam, Ertson, *Phys. Rev. B* **67**, 134110.
- Fiebig M (2005), 'Revival of the magnetoelectric effect', *J. Phys. D* **38**, R123–152.
- Fox D L and Scott J F (1977), 'Ferroelectrically induced ferromagnetism', *J. Phys. C* **10**, L329–331.
- Ganpule C S *et al.* (1999), 'Scaling of ferroelectric properties in thin films', *Appl. Phys. Lett.* **75**, 409–411.
- Gerra G, Tagantsev A K, Setter N, and Parlinski K (2006), 'Ionic polarizability of conductive metal oxides and critical thickness for ferroelectricity in BaTiO<sub>3</sub>', *Phys. Rev. Lett.* **96**, 107603.
- Glickman Y, Winebrand E, Arie A, and Rosenman G (2006), 'Electron-beam-induced domain poling in LiNbO<sub>3</sub> for two-dimensional nonlinear frequency conversion', *Appl. Phys. Lett.* **88**, 011103.
- Gundel H W (1995), 'Nature and application of ferroelectric electron-beam sources (FEBS)', *Integ. Ferroelec.* **9**, 115–116.
- Gregg J M and Scott J F (eds) (2007), Proc. Rank Prize Conference (Grasmere, September 2006); Integrated Ferroelectrics.
- Gundel H W (1996), 'High-intense pulsed electron emission by fast polarization changes in ferroelectrics', *Ferroelectrics* **184**, 89–98.
- Harrison R J, Dunin-Borkowski R E, and Putnis A (2002), 'Direct imaging of nanoscale magnetic interactions in minerals', *Proc. US Nat. Acad. Sci.* **99**, 16556–16561.
- Hartmann A J, Nielson M, Lamb R N, Watanabe K, and Scott J F (2000), 'Ruthenium oxide and strontium ruthenate electrodes for ferroelectric thin-film capacitors', *Appl. Phys.* **A70**, 239–242.
- Hemberger J, Lunkenheimer P, Fishtl R and Loidi A (2005), 'Relaxor ferroelectricity and colossal magnetocapacitive coupling in ferromagnetic CdCr<sub>2</sub>S<sub>4</sub>', *Nature* **434**, 364–367.
- Hernandez B A *et al.* (2002), 'Sol–gel template synthesis and characterization of BaTiO<sub>3</sub> and PbTiO<sub>3</sub> nanotubes', *Chem. Mater.* **14**, 481–482.

- Hill N A (2000), 'Why are there so few magnetic ferroelectrics?', *J. Phys. Chem.* **B104**, 6694–6709.
- Hou S L and Bloembergen N (1965), 'Paramagnetolectric effects in  $\text{NiSO}_4 \cdot 6\text{H}_2\text{O}$ ', *Phys. Rev.* **138**, A1218–1226.
- Hur N *et al.* (2004), 'Electric polarization reversal and memory in a multiferroic material induced by magnetic fields', *Nature* **429**, 392–395.
- Ishiwara H, Okuyama M, and Arimoto Y (2004), *Ferroelectric Random Access Memories*, Springer, Heidelberg.
- Isobe C, Ami T *et al.* (1997), 'Characteristics of ferroelectric strontium bismuth tantalite thin films grown by "flash" MOCVD', *Integ. Ferroelec.* **14**, 95–103.
- Jamnik J, Maier J and Pejovnik S (1995), 'Interfaces in solid ionic conductors', *Solid St. Ionics* **75**, 51–58.
- Jana F and Shirane G (1962), *Ferroelectric Crystals*, Macmillan, New York.
- Jang J E *et al.* (2005), 'Nanoscale capacitors based on metal–insulator–carbon nanotube–metal structures', *Appl. Phys. Lett.* **87**, 263103.
- Jiang A Q, Scott J F, Dawber M, and Wang C (2002), 'Fatigue in artificially layered  $\text{Pb}(\text{Zr}, \text{Ti})\text{O}_3$  ferroelectric films', *J. Appl. Phys.* **92**, 6756–6761.
- Jiang A Q, Scott J F, Lu H, and Chen Z (2003), 'Phase transitions and polarizations in epitaxial  $\text{BaTiO}_3/\text{SrTiO}_3$  superlattices studied by second-harmonic generation', *J. Appl. Phys.* **93**, 1180–1185.
- Johnston K, Huang X, Neaton J B, and Rabe K M (2005), 'First-principles study of symmetry lowering and polarization in  $\text{BaTiO}_3/\text{SrTiO}_3$  superlattices with in-plane expansion', *Phys. Rev.* **B71**, 100103.
- Jung D J, Kim K, and Scott J F (2005), 'Switching kinetics in nanoferroelectrics', *J. Phys. Condens. Mat.* **17**, 4843–4852.
- Jung D J, Morrison F D, and Scott J F (2007), *Nano-ferroelectric Memories*, Springer, Heidelberg (to be published).
- Junquera J and Ghosez P (2003), 'Critical thickness for ferroelectricity in perovskite ultrathin films', *Nature* **422**, 506–509.
- Kafadaryan E A (2006), Ashtarak-2, Armenia (unpublished).
- Kawasaki S, Scott J F, Angel M, Fan H, Catalan G, Gregg J, Morrison F D, Tsutsui T and Tsuji O (2007) 'Recent progress of liquid source misted chemical deposition process for related three-dimensional nano-ferroelectrics,' paper 7A-110, ISIF-19, Bordeaux, France.
- Kim D C, Jo W, Lee H M, and Kim K Y (1997), 'Properties of  $(\text{Ba}, \text{Sr})\text{TiO}_3$  thin films prepared by liquid source delivery chemical vapor deposition', *Integ. Ferroelec.* **18**, 137–144.
- Kimura T, Goto T, Shintani H, Ishizaka K, Arima T and Tokura Y. (2003), 'Magnetic control of ferroelectric polarization', *Nature* **426**, 55–58.
- Kittel C (1946), 'Theory of the structure of ferromagnetic domains in films and small particles', *Phys. Rev.* **70**, 965–971.
- Kohlsdtedt H, Pertsev N A, and Waser R (2002), 'Size effects of polarization in epitaxial ferroelectric films and the concept of ferroelectric tunnel junctions including first results', *MRS Proc.* **688**, C6.5.
- Lagerwall S T (2004), 'Ferroelectric and antiferroelectric liquid crystals', *Ferroelectrics* **301**, 15–45.
- Landauer R, Young D R, and Drougard M E (1956), 'Polarization reversal in the barium titanate hysteresis loop', *J. Appl. Phys.* **27**, 752–758.
- Li J, Nagaraj B, Liang H, *et al.* (2004), 'Ultrafast polarization switching in thin-film ferroelectrics', *Appl. Phys. Lett.* **84**, 1174–1176.

- Li P and Lu T-M (1991), 'Conduction mechanisms in BaTiO<sub>3</sub> thin films', *Phys. Rev. B* **43**, 14261–14264.
- Lines M and Glass A M (1967), *Principles and Applications of Ferroelectrics and Related Materials*, Clarendon, Oxford.
- Liu S and Li Y (2004), 'Research on the electrocaloric effect of PMN/PT solid solution for ferroelectrics MEMS microcooler', *Mat. Sci. & Eng.* **B113**, 46–49.
- Lou X, Zhang M, Redfern S A T, and Scott J F (2006), 'Local phase decomposition as a cause of polarization fatigue in ferroelectric thin films', *Phys. Rev. Lett.* **97**, 177601 (2006).
- Ma W H and Hesse D (2004), 'Microstructure and piezoelectric properties of sub-80 nm high polycrystalline SrBi<sub>2</sub>Ta<sub>2</sub>O<sub>9</sub> nanostructures within well-ordered arrays', *Appl. Phys. Lett.* **85**, 3214–3216.
- Mao Y, Park T-J and Wong S S (2005), 'Synthesis of classes of ternary metal oxide nanostructures', *Chem. Commun.* **2005**, 5721–5735.
- Masuda H and Fukuda K (1995), 'Ordered metal nanohole arrays made by a two-step replication of honeycomb structures of anodic alumina', *Science* **268**, 1466–1468.
- Mermin N D (1979), 'The topological theory of defects in ordered media', *Rev. Mod. Phys.* **51**, 591–648.
- Milliken A D, Bell A J, and Scott J F (2006), 'Dependence of breakdown field on dielectric (inter-electrode) thickness in base-metal electroded multilayer capacitors', *Appl. Phys. Lett.* **90**, 112910.
- Miranda F A *et al.* (2002), 'Ferroelectric thin films-based technology for frequency- and phase-agile microwave communications applications', *Integ. Ferroelectrics* **42**, 131.
- Mischenko A, Zhang Q, Scott J F, Whatmore R W, and Mathur N D (2006), 'Giant electrocaloric effect in thin-film PZT', *Science* **311**, 1270–1271.
- Mishina E D, Vorotilov K A, Vasil'ev V A, *et al.* (2002), 'Porous silicon-based ferroelectric nanostructures', *J. Exp. Theor. Phys.* **95**, 502–504.
- Mishina E D, Sherstyuk N E, Stadnuchyuk V, *et al.* (2003), 'Ferroelectrics templated in nanoporous silicon membranes', *Ferroelectrics* **286**, 927–933.
- Mishina E D (2005), 'Nonlinear optics of ferroelectrics: towards nanometers and picoseconds', *Ferroelectrics* **314**, 57–72.
- Mitsui T and Furuichi J (1953), 'Domain structure of rochelle salt and KH<sub>2</sub>P0<sub>4</sub>,' *Phys. Rev.* **90**, 193–202.
- Mitsui T, Tatsuzaki, I and Nakamura E (1969), 'An introduction to the physics of ferroelectrics,' *Maki-Shoten, Tokyo*, (translation: Gordon and Breach, London, 1976).
- Morrison F D, Ramsay L and Scott J F (2003), 'High aspect ratio piezoelectric strontium-bismuth-tantalate nanotubes', *J. Phys. Condens. Mat.* **15**, L527–532.
- Naranjo B, Gimzewski J K, and Putterman S (2005), 'Observation of nuclear fusion driven by a pyroelectric crystal', *Nature* **434**, 1115–1117.
- Naumov I, Bellaiche L and Fu H (2004), 'Unusual phase transitions in ferroelectric nanodisks and nanorods', *Nature* **432**, 737–740.
- Paruch P, Giamarchi T, Tybell T and Triscone J-M (2006), 'Nanoscale studies of domain wall motion in epitaxial ferroelectric thin films', *J. Appl. Phys.* **100**, 051608.
- Parsuch P, Tybell T and Triscone J M (2001), 'Nanoscale control of ferroelectric polarization and domain size in epitaxial Pb(ZrO.2TiO.8)0-3 thin films. *Applied Physics Letters*, **79**: 530–532.
- Paz de Araujo C A, Cuchiaro J D, McMillan L D, Scott M C, and Scott J F (1995), 'Fatigue-free ferroelectric capacitors with platinum electrodes', *Nature* **374**, 627–629.
- Pintilie L and Alexe M (2005), 'Metal-ferroelectric-metal heterostructures with Schottky contacts. I. Influence of the ferroelectric properties', *J. Appl. Phys.* **98**, 124103.

- Pintilie L *et al.* (2005), 'Metal–ferroelectric–metal structures with Schottky contacts. II. Analysis of the experimental current–voltage and capacitance–voltage characteristics of Pb(Zr,Ti)O<sub>3</sub> thin films', *J. Appl. Phys.* **98**, 124104.
- Ponomareva I, Naumov I, and Bellaiche L (2005a), 'Low-dimensional ferroelectrics under different electrical and mechanical boundary conditions: atomistic simulations', *Phys. Rev.* **B72**, 214118.
- Ponomareva I, Naumov I, Kornev I, Fu H, and Bellaiche L (2005b), 'Atomistic treatment of depolarizing energy and field in ferroelectric nanostructures', *Phys. Rev.* **B72**, 140102.
- Privratska J and Janovec V (1997), 'Pyromagnetic domain walls connecting antiferromagnetic non-ferroelastic magnetoelectric domains', *Ferroelectrics* **204**, 321–331.
- Prosandeev S, Ponomareva I, Kornev I, Naumov I, and Bellaiche L (2006), 'Controlling toroidal moment by means of an inhomogeneous static field: an *ab initio* study', *Phys. Rev. Lett.* **96**, 237601.
- Pulvari C F and Kuebler W (1958a), 'Phenomenological theory of polarization reversal in BaTiO<sub>3</sub> single crystals', *J. Appl. Phys.* **29**, 1315–1321.
- Pulvari C F and Kuebler W (1958b), 'Polarization reversal in tri-glycine fluoberyllate and tri-glycine sulfate single crystals', *J. Appl. Phys.* **29**, 1742–1746.
- Ríos S, Ruediger A, Jiang A Q, Scott J F, Lu H and Chen Z (2003), 'Orthorhombic strontium titanate in BaTiO<sub>3</sub>–SrTiO<sub>3</sub> superlattices', *J. Phys. Condens. Mat.* **15**, L305–310.
- Roitbord A L (1976) 'Equilibrium structure of epitaxial layers', *Phys. Status Solid A* **37**, 329–339.
- Rosenblum B, Bräunlich P, and Carrico J P (1974), 'Thermally stimulated field emission from pyroelectric LiNbO<sub>3</sub>', *J. Appl. Phys.* **25**, 17–19.
- Rosenman G, Shur D, Krasik Y E, and Dunaevsky D (2000), 'Electron emission from ferroelectrics', *J. Appl. Phys.* **88**, 6109–6161.
- Saad M M, Baxter P, Bowman R M, Gregg J M, Morrison F D, and Scott J F (2004), 'Intrinsic dielectric response in ferroelectric nano-capacitors', *J. Phys. Condens. Mat.* **16**, L451–456.
- Saad M M, Baxter P, McAnaney J, Gregg J M, Catalan G and Scott J F (2006), 'Investigating the effects of reduced size on the properties of ferroelectrics,' *IEEE Transactions on Ultrasonics Ferroelectrics and Frequency Control*, **55**, 2208–2225.
- Schilling A, Adams T B, Bowman R M, Gregg J M, Catalan A and Scott J F (2006), 'Scaling of domain periodicity with thickness measured in BaTiO<sub>3</sub> single crystal lamellae and comparison with other ferroics', *Phys. Rev. B* **74**, 024115.
- Schmid H (1994), 'Introductions to the Proceedings of the Second International Conference on Magnetoelectrics', *Ferroelectrics* **161**, 1–28.
- Schmid H (2001), 'On ferrotoroidics and electrotoroidic, magnetotoroidic and piezotoroidic effects', *Ferroelectrics* **252**, 41–50.
- Schnupp H (1967), 'Model for tunnelling through a non-crystalline thin dielectric film', *Phys. Stat. Sol.* **21**, 567.
- Scott J F (1993), 'Dielectric properties of insulators', *Encyclopedia of Applied Physics* (ed. George Trigg, VCH Pub. Co., Berlin); Vol. **5**, pp. 25–45.
- Scott J F (2000), *Ferroelectric Memories*, Springer, Heidelberg.
- Scott J F (2005), 'Novel geometric ordering of ferroelectricity', *Nature Materials* **4**, 13–14.
- Scott J F (2006a), 'Nanoferroelectrics: statics and dynamics', *J. Phys. Condens. Mat.* **18**, R361–386.

- Scott J F (2006b), 'Applications of modern ferroelectrics', *Science* (in press).
- Scott J F (2007), 'A comparison of FRAMs and MRAMs', in *Ferro- and Antiferroelectricity* (eds. Dalal N S and Bussmann-Holder A; Springer, Berlin), pp. 199–208).
- Scott J F and C A Araujo (1989), 'Ferroelectric memories', *Science* **246**, 1400–1406.
- Sebald G, Qiu J and Guyomar D (2005), 'Modelling the lateral resonance mode of piezoelectric fibers with metal core', *J. Phys. D* **38**, 3733–3740.
- Shebanov L and Borman K (1992), 'On lead-scandium tantalite solid solutions with high electrocaloric effect', *Ferroelectrics* **127**, 143–148.
- Solayappan N, McMillan L D, Paz de Araujo C A, and Grant B (1997), *Integ. Ferroelec.* **18**, 127–134.
- Strukov B A (1967), 'Electrocaloric effect in triglycine sulfate', *Sov. Phys. Crystallog.* **11**, 757–762.
- Sviridov E, Le Bihan R, Liateni S F, and Descures A (1998), 'Electron emission spectra from lead zirconate titanate ferroelectric films on stainless-steel substrates', *Appl. Phys. Lett.* **73**, 3953–3955.
- Tagantsev A K, Stolichnov I, Setter N, Cross J S, and Tsukada M (2002), *Phys. Rev.* **B66**, 214109.
- Tanaka M and Makino Y (1998), 'Ferroelectricity in barium titanate nano-particles', *Ferroelec. Lett.* **24**, 13–18.
- Tenne R (2004), 'Materials physics – doping control for nanotubes', *Nature* **431**, 640–641.
- Tenne D A *et al.* (2006), 'Probing nanoscale ferroelectricity by ultraviolet Raman spectroscopy', *Science* **313**, 1614–16.
- Tuttle B A and Payne D A (1981), 'The effects of microstructure on the electrocaloric properties of Pb(Zr,Sn,Ti)O<sub>3</sub> ceramics', *Ferroelectrics* **37**, 603–606.
- Valasek J (1921), 'Piezo-electric and allied phenomena in Rochelle salt', *Phys. Rev.* **17**, 475–482 (1921).
- von Hippel A (1944), US National Defense Research Committee report 300.
- Walker D, Thomas P A, Jiang Q, Pernot-Rejmánková P, Baruchel J and Agyavives T (2005), 'X-ray imaging investigation of periodically electroded rubidium titanyl arsenate, RbTiOAsO<sub>4</sub>, under an applied electric field', *J. Phys. D: Appl. Phys.* **38**, A55–60.
- Wang J *et al.* (2003), 'Epitaxial BiFeO<sub>3</sub> multiferroic thin-film heterostructures', *Science* **299**, 1719–1725.
- Wang J *et al.* (2005), 'Response to comment on epitaxial BiFeO<sub>3</sub> multiferroic heterostructures', *Science* **419**, 1203b.
- Zheng H M, Straub F, Zhou Q *et al.* (2006), 'Self-assembled growth of BiFeO<sub>3</sub>-CoFe<sub>2</sub>O<sub>4</sub> nanostructures', *Advanced Materials*, **18**, 2747–2751.
- Zhu X H *et al.* (2006), 'Perovskite lead zirconium titanate nanorings: towards nanoscale ferroelectric "solenoids"?'', *Appl. Phys. Lett.* **89**, 129913.
- Zubko P, Jung D J, and Scott J F (2006a), 'Space charge effects in ferroelectric thin films,' *J. Appl. Phys.* **100**, 114112.
- Zubko P, Jung D J, and Scott J F (2006b), 'Electrical characterization of PbZr<sub>0.4</sub>Ti<sub>0.6</sub>O<sub>3</sub> capacitors', *J. Appl. Phys.* **100**, 114113.

## Domains in ferroelectric nanostructures from first principles

---

I A KORNEV, University of Arkansas, USA and  
Madas Clausen Institute, University of Southern Denmark,  
Denmark and B - K LAI, I NAUMOV,  
I PONOMAREVA, H FU and L BELLAICHE,  
University of Arkansas, USA

### 19.1 Introduction

Understanding the physical properties in ferroelectric nanostructures (FEN), which is a major requirement for the future progress in ferroelectric-based technologies (Auciello *et al.*, 1998; Scott, 1998, 2000; Ramesh *et al.*, 2001; Setter *et al.*, 2006), has become an issue of interest over the past decade (see, e.g., Dawber *et al.*, 2005; Kornev *et al.*, 2006; Ponomareva *et al.*, 2005a; Rabe, 2005; Yacoby *et al.*, 2006). An intriguing problem in FEN concerns their domain structures which are often non-equilibrium dipole patterns that depend on sample history, temperature, boundary conditions, and other factors. For instance, the various following patterns have recently been predicted or observed in thin films: out-of-plane *monodomains* (Tybell *et al.*, 1999; Ghosez and Rabe, 2000; Junquera and Ghosez, 2003; Streiffer *et al.*, 2002), 180° out-of-plane *stripe domains* (Kopal *et al.*, 1997; Tinte and Stachiotti, 2001; Streiffer *et al.*, 2002), 90° multidomains that are oriented *parallel* to the film (Li *et al.*, 2002), and *microscopically paraelectric* phases (Junquera and Ghosez, 2003). The fact that different patterns have been reported for similar *mechanical* boundary conditions supports a concept discussed in (Junquera *et al.* (2004), Mehta *et al.* (1973) and Junquera and Ghosez (2003), namely that they arise from different *electrical* boundary conditions. A reactive atmosphere can indeed lead to a partial compensation of surface charges in films with nominal ideal open-circuit conditions (Streiffer *et al.*, 2002), while metallic or semiconductor electrodes ‘sandwiching’ films do not always provide *ideal* short-circuit conditions – resulting in a non-zero internal field (Junquera and Ghosez, 2003). The *degree* of surface charges’ screening in thin films can thus vary from one experimental set-up to another, possibly generating *different* dipole patterns (Streiffer *et al.*, 2002; Junquera and Ghosez, 2003).

The main theoretical methods used/developed so far in the study of dipole patterns in low-dimensional ferroelectrics fall into two categories, namely: (1) approaches based on the Ginzburg–Landau theory (Landau and Lifshitz,

1935, 1984) versus (2) first-principles-based schemes (Meyer and Vanderbilt, 2002; Ponomareva *et al.*, 2005a; Rabe, 2005; Kornev *et al.*, 2006).

The simplest description of the domain structure and a domain wall which is an interface between uniformly polarized regions (domains) with different polarization directions can be given within the Ginzburg–Landau theory for a *uniaxial* ferroelectric. Within this oversimplified theory, below  $T_c$ , two uniform solutions exist, which correspond to two different orientations of the spontaneous polarization. Under appropriate *boundary conditions* such that the polarization points ‘up’ on the left, but ‘down’ on the right, the  $180^\circ$  domain wall (phase boundary) will form separating regions corresponding to the two different phases (Hubert and Schafer, 1998). Therefore, the domains of alternating spontaneous polarization can be viewed as the regions of different phases in local thermodynamic equilibrium separated by phase boundaries. Generally, the phase boundaries will have a higher free energy than in either phase and, naturally, cost energy. Although introduction of  $180^\circ$  domain walls raises the wall energy, at the same time it reduces high stray field (or dipolar) energy (Hubert and Schafer, 1998). In order to minimize the large depolarizing energy costs further, closure domains oriented at  $90^\circ$  to the main domains may form if the wall energy advantage overwhelms the anisotropy energy cost. The  $90^\circ$  closure domains eliminate electrostatic energy but increase anisotropy energy in uniaxial material. Since  $90^\circ$  domain walls are usually ferroelastic and since domains are constrained by their neighbors, an additional complication appears due to a *coupling* between polarization and strain (Roitburd, 1976) which is known to be strong in the technologically and fundamentally important perovskite class of materials. All in all, the domain structure in zero field results from a subtle competition between different interactions, and depends considerably on the size, shape, and type of ferroelectric material. Within the framework of the Ginzburg–Landau theory, many of the characteristics of nanoscale ferroelectrics can be faithfully reproduced (see, e.g., Tinte and Stachiotti, 2001; Li *et al.*, 2002; Glinchuk *et al.*, 2003; Pertsev *et al.*, 2003, and references therein). However, microscopic foundations of phenomenological approaches are somewhat arbitrary and atomic-scale mechanisms are difficult to assess.

An alternative approach to continuum models is first-principles-based calculations that require no experimental input. Some phenomena in low-dimensional ferroelectrics can be understood by using *direct* first-principles methods. However, their large computational cost currently prevents them from being used to study some other rather complex phenomena and/or systems with large number of atoms. On the other hand, first-principles-*derived* computational approaches have proved to be powerful methods in recent years for understanding complex materials. Moreover, a precise correlation between the amount of screening of surface charges and the morphology of the dipole pattern, and how this correlation depends on

*mechanical* boundary conditions, starts to emerge thanks to these latter approaches (Ghosez and Rabe, 2000; Almahmoud *et al.*, 2004; Kornev *et al.*, 2004; Wu *et al.*, 2004; Ponomareva and Bellaiche, 2006).

In this chapter we review progress in *first-principles-based* calculations that have addressed the morphology of the dipole patterns in FEN. Section 19.2 describes the theoretical method that was developed and used to tackle domains in FEN. Section 19.3 discusses the morphology of domains in ferroelectric thin films, and how this morphology (i) depends on the considered material, film thickness, boundary conditions or film orientation and (ii) evolves under an applied electric field. Section 19.4 discusses domain structures never observed before in ferroelectrics, and that are predicted to occur in ferroelectric nanodots and nanowires. Finally, Section 19.5 provides a summary.

## 19.2 Methods

In this section, we briefly describe a first-principles-derived approach allowing predictions of finite-temperature properties of ferroelectric nanostructures – under any possible electrical and mechanical boundary condition. More precisely, the total energy for such low-dimensional systems is written as:

$$\begin{aligned} \varepsilon_{\text{tot}}(\{\mathbf{u}_i\}, \{\sigma_i\}, \{\mathbf{v}_i\}, \eta) = & \varepsilon_{\text{Heff}}(\{\mathbf{u}_i\}, \{\sigma_i\}, \{\mathbf{v}_i\}, \eta) \\ & + \beta \sum_i \langle \mathbf{E}_{\text{dep}} \rangle \cdot Z^* \mathbf{u}_i - \sum_i \mathbf{E} \cdot Z^* \mathbf{u}_i \end{aligned} \quad 19.1$$

where  $\mathbf{u}_i$  is the local soft mode in the unit cell  $i$  of the film – whose product with the effective charge  $Z^*$  yields the local electrical dipole in this cell; while  $\eta$  and  $\{\mathbf{v}_i\}$  are the homogeneous strain tensor and inhomogeneous strain-related variables in unit cell  $i$ , respectively (Zhong *et al.*, 1994, 1995). The  $\{\sigma_i\}$  arrangement characterizes the atomic configuration of the alloy.  $\varepsilon_{\text{Heff}}$  represents the intrinsic (effective Hamiltonian) energy of the ferroelectric nanostructure. Its analytical expression is the one from Zhong *et al.*, (1994, 1995) for bulks made of simple perovskites (such as  $\text{BaTiO}_3$  bulk) and from Bellaiche *et al.* (2000, 2002) for bulks made of solid solutions (such as  $\text{Pb}(\text{Zr}, \text{Ti})\text{O}_3$ ), except for two modifications. The first modification applies when the nanostructure is surrounded by vacuum, and consists of adding energetic terms associated with the direct interaction between the vacuum surrounding the dot and both the surface dipoles and inhomogeneous strain near the surface (Almahmoud *et al.*, 2004). The second modification consists of replacing the (3D reciprocal-space-based) matrix associated with long-range dipole–dipole interactions in the bulk (Zhong *et al.*, 1994, 1995) by the corresponding matrix characterizing dipole–dipole interactions in the investigated ferroelectric nanostructure. Such a matrix is given in Ponomareva *et al.* (2005c) for thin films, wires, and dots, and corresponds to ideal open-circuit (OC) conditions. Such electrical boundary conditions naturally lead to the possible existence of a maximum depolarizing field (denoted by  $\langle \mathbf{E}_{\text{dep}} \rangle$ )



inside the nanostructure. The second term of Eq. (19.1) mimics a screening of  $\langle \mathbf{E}_{\text{dep}} \rangle$  via the  $\beta$  parameter. More precisely, the residual depolarizing field resulting from the combination of the first and second term of Eq. (19.1) has a magnitude equal to  $(1 - \beta)|\langle \mathbf{E}_{\text{dep}} \rangle|$ .  $\beta = 0$  thus corresponds to ideal OC conditions, while an increase in  $\beta$  lowers the magnitude of the resulting depolarizing field, and  $\beta = 1$  corresponds to ideal short-circuit (SC) conditions for which the depolarizing field has vanished. Technically,  $\langle \mathbf{E}_{\text{dep}} \rangle$  is calculated at an atomistic level via the proposed approach of Ponomareva *et al.* (2005c), and depends on the dimensionality, size, and dipole pattern of the investigated nanostructure. Note that real thin films are likely neither in ideal open-circuit conditions – for which unscreened polarization-induced surface charges can generate a large depolarizing electric field along the film orientation (Meyer and Vanderbilt, 2001) – nor in ideal short-circuit conditions – that are associated with a vanishing internal field resulting from the full screening of surface charges – but rather experience a situation in-between.

Different *mechanical* boundary conditions can also be simulated thanks to the homogeneous strain  $\eta$  (Li *et al.*, 2002; Pertsev *et al.*, 2003). For example during the simulation associated with a *substrate-induced* epitaxial strain in the  $(x, y)$ -plane, three components of  $\eta$  – in Voigt notation – are kept fixed (namely,  $\eta_6 = 0$ , and  $\eta_1 = \eta_2 = \delta$ , with  $\delta$  characterizing the lattice mismatch between the material forming the nanostructure and the chosen substrate) while the other three components relax.<sup>1</sup> On the other hand, *all* the components of strain tensor are allowed to relax during the simulation of freestanding (i.e. stress-free) phase. The third term of Eq. (19.1) mimics the effect of an applied electric field on properties of ferroelectric nanostructures.

The parameters of Eq. (19.1) are determined from first-principles calculations performed on relatively small supercells (typically, up to 40 atom-per-cell). Once the effective Hamiltonian is fully specified, its total energy is used in Monte-Carlo (MC) simulations on supercells mimicking the FEN structure under investigation. Typical outputs of the MC procedure are the local mode vectors – whose supercell average is directly proportional to the macroscopic spontaneous polarization – and the homogeneous strain tensor – which provides information about the crystallographic system.

## 19.3 Domains in ferroelectric thin films

### 19.3.1 Domains in $\text{Pb}(\text{Zr},\text{Ti})\text{O}_3$ ultra-thin films

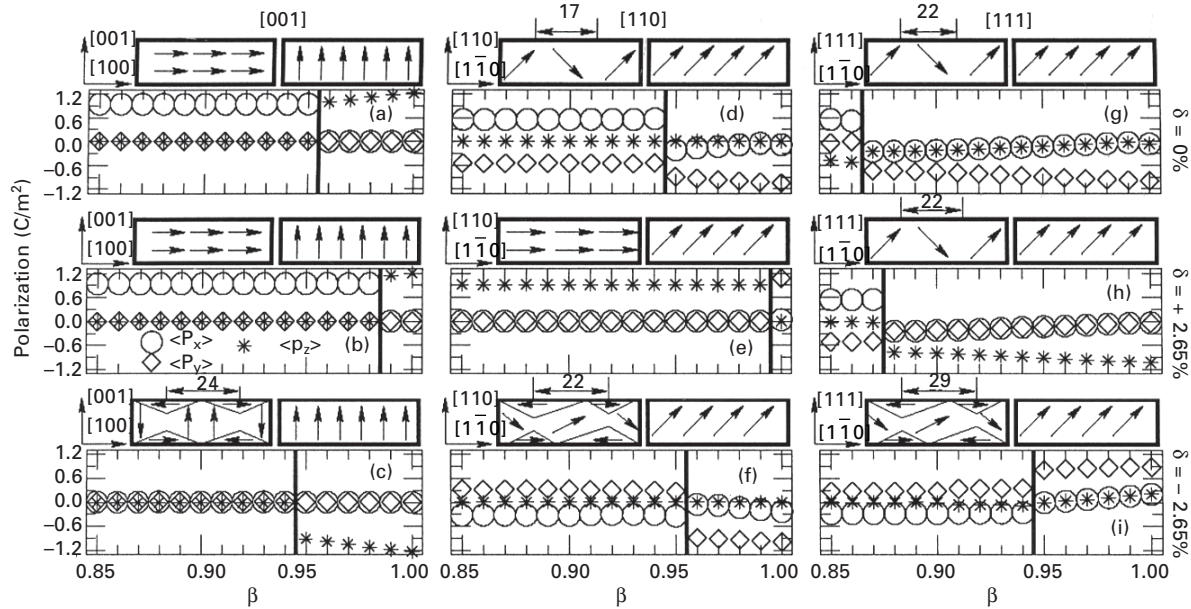
Let's first focus on the results of Ponomareva and Bellaiche, (2006) for thin films made of  $\text{Pb}(\text{Zr}_{0.4}\text{Ti}_{0.6})\text{O}_3$  (PZT), as predicted by the use of the effective

<sup>1</sup>Here, we assumed homogeneously strained nanostructures, which should be realistic for the ultra-small nanostructures we considered here. On the other hand, the strain may become inhomogeneous and significantly relax in thicker systems.

Hamiltonian technique described above. The corresponding *bulk* (i.e., having the same composition) possesses a polarization pointing along  $\langle 001 \rangle$  and lies *outside* the morphotropic phase boundary (Bellaiche *et al.*, 2000; Noheda *et al.*, 2001) (and thus does not have dipoles that easily rotate). As a result, the qualitative predictions for  $\text{Pb}(\text{Zr}_{0.4}\text{Ti}_{0.6})\text{O}_3$  films should also apply to  $\text{PbTiO}_3$  films. Three common growth orientations (Maruyama *et al.*, 1998; Zybilla *et al.*, 2000; Kelman *et al.*, 2001; Kanno *et al.*, 2003; Fong *et al.*, 2004; Liang and Wu, 2005) are investigated, namely [001], [110], and [111]. The films all have Pb-O terminated surfaces, and are represented by supercells that are *finite* along the film orientation, to be denoted as the  $z'$ -direction, and repeated periodically along two in-plane  $x'$ - and  $y'$ -directions. The investigated thin films are either stress-free or experience an epitaxial strain in the  $(x', y')$ -planes. The atomic sites' coordinates, the matrices appearing in the dipole-dipole interactions (Ponomareva *et al.*, 2005c) and the strain tensor are all first expressed in the  $x'y'z'$  coordinate system and then transformed into the  $xyz$  system (in which the  $x$ -,  $y$ - and  $z$ -axes are along the [100], [010], and [001] directions, respectively) before using the total energy in Monte-Carlo simulation.

Figure 19.1 show the  $x$ -,  $y$ -, and  $z$ -components of the spontaneous polarization (and the resulting dipole patterns) for the PZT thin films at 10 K as a function of the  $\beta$  screening coefficient. Parts (a), (b) and (c) correspond to [001] films under stress-free conditions, a tensile strain of 2.65% in the  $(x', y')$ -planes, and under a compressive strain of  $-2.65\%$  in the  $(x', y')$ -planes, respectively. Parts (d)–(f) and (g)–(i) show similar data but for a film orientation along [110] and [111], respectively. The thicknesses of the [001], [110], and [111] films are equal to 48.0, 48.1, and 46.2 Å, respectively. A broad variety of dipole pattern is clearly seen. In particular, one can enunciate the following *general rule*: the films adopt patterns for which the out-of-plane component of the spontaneous polarization vanishes *for OC-like* conditions (i.e. below a critical value of  $\beta$ ). Such vanishing occurs to ‘kill’ the large depolarizing field (associated with such boundary conditions) that would occur if the polarization would have a non-zero component along the out-of-plane direction. For instance, and as indicated by Fig. 19.1(a), the stress-free [001]  $\text{Pb}(\text{Zr}_{0.4}\text{Ti}_{0.6})\text{O}_3$  film exhibits dipoles that all point along [100] for small  $\beta$ . In order to satisfy the general rule, this film thus adopts a polarization lying along a direction that is a possible minimum-energy direction of the polarization in the bulk and that is *perpendicular* to the film orientation.

There is a second way to satisfy the general rule, as followed by the stress-free  $\text{Pb}(\text{Zr}_{0.4}\text{Ti}_{0.6})\text{O}_3$  films grown along [110] and [111] for small  $\beta$ : the supercell average of the out-of-plane polarization component in these two cases is still equal to zero as in [001]  $\text{Pb}(\text{Zr}_{0.4}\text{Ti}_{0.6})\text{O}_3$ , but (as indicated in the left schematizations above Figs 19.1d and e) this annihilation occurs by developing  $\approx 90^\circ$  periodic nanostripe domains [note that the average angle



19.1 Cartesian components of the ground-state spontaneous polarization in  $\text{Pb}(\text{Zr}_{0.4}\text{Ti}_{0.6})\text{O}_3$  ( $\approx 46\text{--}48\text{\AA}$ -thick) films as a function of the screening coefficient  $\beta$  and expressed in the  $xyz$  coordinate system, when choosing 16 and 24 unit cells for the periodicity of the (in-plane)  $x'$ - and  $y'$ -directions for [110] and [111] films under compressive strain and 12 unit cells for the periodicity of the  $x'$ - and  $y'$ -directions for all other films (see text for the definition of the  $xyz$  and  $x'y'z'$  coordinate systems). (a), (b) and (c): [001] films under stress free, 2.65% tensile strain and  $-2.65\%$  compressive strain, respectively; (d)–(f): same as (a)–(c) but for a [110] film; (g) and same as (a)–(c) but for a [111] film. The vertical lines characterize the transition of the dipoles pattern from SC-like conditions to OC-like conditions. The schematization of these two different patterns is given above each part. The width of the stripe domains is given in  $\text{\AA}$ . Open circles, diamonds and stars display  $P_x$ ,  $P_y$  and  $P_z$ , respectively. (Reprinted with permission from Ponomareva and Bellaiche, 2006).

made by the dipoles belonging to different stripes is in fact close to  $70^\circ$ ]. The dipoles inside each domain are aligned along directions that are close to [100] or [010] (that are possible minimum-energy directions for the bulk polarization). The reason behind the dramatic difference in homogeneity of dipole patterns between the [111] and [001] films is that all the possible  $\langle 001 \rangle$  minimum-energy directions of the bulk polarization are far away from the planes perpendicular to the film orientation in the case of the [111] film. An homogeneously in-plane polarized [111] film would thus require a significant deviation of the direction of the dipoles with respect to the minimum-energy directions of the bulk polarization. Such significant deviation does not occur in stress-free [111]  $\text{Pb}(\text{Zr}_{0.4}\text{Ti}_{0.6})\text{O}_3$  because of its large anisotropy. On the other hand, the dipoles in the [110] film do have the possibility to all lie along an *in-plane* direction that is also a minimum-energy direction for the bulk, namely [001]. However, the analysis of our computations reveals that the stress-free [110] film prefers to rather form  $\approx 90^\circ$  nanostripe domains because of a gain in short-range interactions. Interestingly,  $90^\circ$  periodic stripe domains were previously observed in [111] PZT films (Zybill *et al.*, 2000), but *not yet* in [110] ferroelectric films – to the best of our knowledge.

A tensile strain and OC-like conditions both disfavor out-of-plane components of dipoles, because of the strain–dipole coupling and the existence of a large depolarizing field along the film orientation, respectively. As a result, most of the films under tensile strain develop *homogeneous* in-plane polarization pattern for small  $\beta$  (see, left schematizations above Fig. 19.1b and e). The only exception from this trend is the [111]  $\text{Pb}(\text{Zr}_{0.4}\text{Ti}_{0.6})\text{O}_3$  film, as seen in Fig. 19.1(h). Such exception is once again caused by the material desire to have dipoles close to the possible minimum-energy polarization directions of the bulk.

As indicated by the left schematizations above Figs 19.1(c)–(i), the thin films all adopt flux-closure *periodic nanostripe domains* (which bear resemblance with those observed in magnetic films; Patel *et al.*, 1968; Aitlamine *et al.*, 1991; Hubert and Schafer, 1998) for compressive strains and large residual depolarizing fields – because of the competition between the compressive strain that favors out-of-plane components of the dipoles and the large depolarizing field that desires to kill the out-of-plane component of the polarization (Fong *et al.*, 2004; Kornev *et al.*, 2004). Interestingly, the morphology of the stripe domains depends on the film orientation: [001]  $\text{Pb}(\text{Zr}_{0.4}\text{Ti}_{0.6})\text{O}_3$  exhibits the out-of-plane  $180^\circ$  nanostripes that were observed (Fong *et al.*, 2004) in [001]  $\text{PbTiO}_3$  ultra-thin films under similar boundary conditions. On the other hand, [110] and [111]  $\text{Pb}(\text{Zr}_{0.4}\text{Ti}_{0.6})\text{O}_3$  films are more reluctant to have dipoles along the film orientation and prefer to adopt  $\approx 90^\circ$  nanodomains (note that the average angle made by the dipoles belonging to different stripes is in fact close to  $105^\circ$ ). The existence of these latter domains for compressive strain can be traced back to the difficulty of rotating

the polarization away from a  $\langle 100 \rangle$  direction in the  $\text{Pb}(\text{Zr}_{0.4}\text{Ti}_{0.6})\text{O}_3$  bulk – as demonstrated by the fact that it is possible to transform these  $\approx 90^\circ$  domains into  $180^\circ$  out-of-plane nanostripe domains in thin films grown along  $[110]$  or  $[111]$  and having compositions associated with a tetragonal phase in the bulk via two different processes: (1) increase the magnitude of the compressive strain – as we numerically found out in  $\text{Pb}(\text{Zr}_{0.4}\text{Ti}_{0.6})\text{O}_3$ ; or (2) decrease the composition towards the morphotropic phase boundary of PZT bulk – i.e. making the polarization easier to rotate – as we numerically checked when going from  $\text{Pb}(\text{Zr}_{0.4}\text{Ti}_{0.6})\text{O}_3$  to  $\text{Pb}(\text{Zr}_{0.5}\text{Ti}_{0.5})\text{O}_3$ .

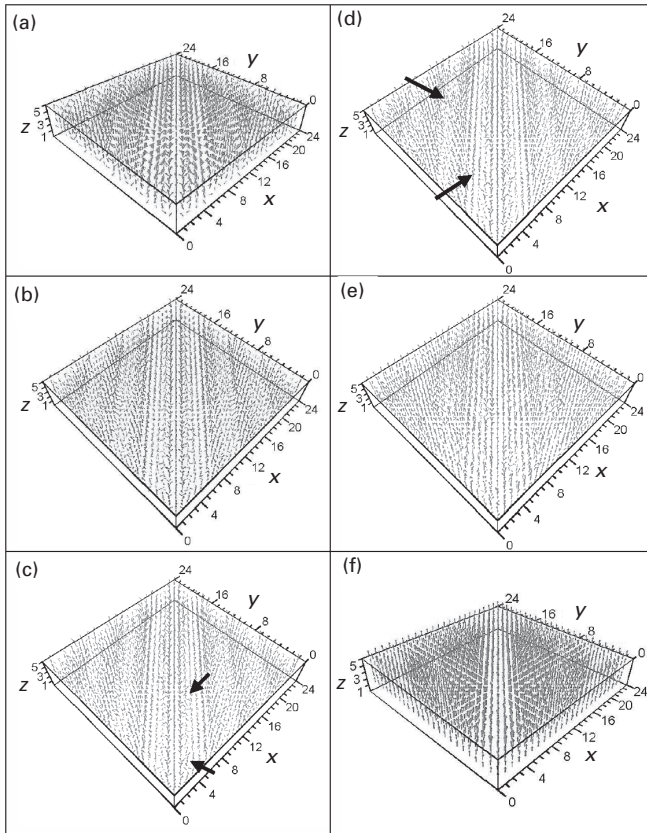
The equilibrium width (which is half the period) of the periodic stripe domains is found by varying the in-plane supercell sizes, and is given in Å in Fig. 19.1. The predicted equilibrium domain width is  $\approx 24 \text{Å}$  for the compressed  $[001]$  film (having a thickness of  $48 \text{Å}$ ). This is in excellent agreement with the experimental data of Fong *et al.* (2004) and Streiffer *et al.* (2002) for  $\text{PbTiO}_3$  ultra-thin films having similar thickness and growth orientation. Such width is unusually small with respect to the domain width of around  $1000\text{--}10\,000 \text{Å}$  observed in bulks (Merz, 1954; Arlt and Sasko, 1980). Interestingly, Kornev *et al.* (2004) predicted that  $[001]$  PZT thin films having a thickness of  $\approx 20 \text{Å}$  exhibit an equilibrium width of  $\approx 16 \text{Å}$  (i.e. four lattice constants) for the laminar domains, which implies that the equilibrium width of domains in ultra-thin films has a square root dependency on the film thickness – as consistent with the prediction of Landau and Lifshitz (1935), Kittel (1946), Kopal *et al.* (1997) and Catalan *et al.* (2006).

The stripe domain sizes can thus be intriguingly close to the ultimate limit of a single-molecule ferroelectric memory element. The domain width of  $\approx 22 \text{Å}$  we found for the stress-free and tensile  $[111]$   $46.2 \text{Å}$ -thick films agrees also very well with the interpolation, via this square root dependency on the film thickness (Landau and Lifshitz, 1935; Kittel, 1946; Kopal *et al.*, 1997), of the experimental data of Zybilla *et al.* (2000) down to the thickness of  $\approx 46 \text{Å}$ . Specifically, such interpolation results in a domain width of  $\approx 21 \text{Å}$ . We are not aware of any measurements done in stress-free  $[110]$ , compressed  $[110]$ , or compressed  $[111]$  ultra-thin films, for which we predict a domain width of  $\approx 17 \text{Å}$ ,  $22 \text{Å}$ , and  $29 \text{Å}$ , respectively, when these films have a thickness around  $\approx 46\text{--}48 \text{Å}$ .

### 19.3.2 Domains in $\text{BaTiO}_3$ ultra-thin films

We now want to determine the morphology of stripe nanodomains in  $[001]$   $\text{BaTiO}_3$  (BTO) ultra-thin films, and compare it with those in  $[001]$   $\text{Pb}(\text{Zr},\text{Ti})\text{O}_3$  ultra-thin films. We focus here on a  $20 \text{Å}$ -thick BTO film, as mimicked by a  $24 \times 24 \times 5$  supercell, under a compressive strain of  $-2.2\%$  and having a realistic electrical boundary condition corresponding to  $\beta = 0.8$  (Lai *et al.*, 2005). As consistent with Streiffer *et al.* (2002), Kornev *et al.* (2004) and Lai

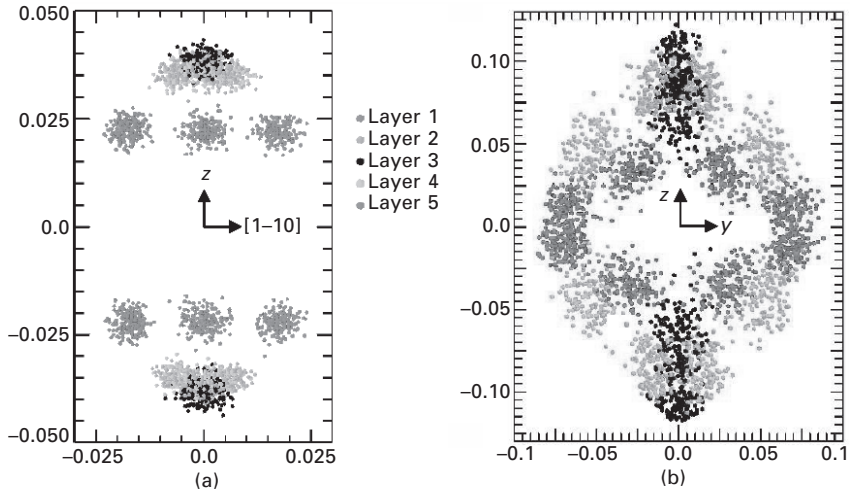
*et al.* (2006), the combination of a significant compressive epitaxial strain (which favors dipoles along the  $z$  direction) with such electrical boundary condition (that will lead to a large enough residual depolarizing field if all the dipoles would point in parallel along the  $z$ -axis) generates stripe domains at low temperature. Figure 19.2(a) displays such domains at 10 K (which were obtained by slowly cooling down the system) and indicates that the stripe domains in the BTO thin films consist of periodically alternating ‘up’ and ‘down’ domains (here, the up (down) domains refer to the domains with the  $z$ -component of the local dipoles along the  $+z$  ( $-z$ ) direction), as in compressively strained [001] PZT and  $\text{PbTiO}_3$  thin films (Streiffer *et al.*,



**19.2**  $T=10\text{K}$  three-dimensional polarization patterns in  $20\text{\AA}$ -thick BTO (001) films under a compressive strain of  $-2.2\%$  and a 80% screening of the maximum depolarizing field, for different  $E_z$ : stripe domains under (a)  $E_z = 0$ , (b)  $E_z = 30 \times 10^7$  and (c)  $E_z = 41 \times 10^7 \text{V/m}$ ; bubble domains under (d)  $E_z = 51 \times 10^7$  and (e)  $E_z = 71 \times 10^7 \text{V/m}$ ; and monodomain under (f)  $E_z = 104 \times 10^7 \text{V/m}$ . Light (dark) arrows characterize local dipoles having a positive (negative) component along the  $z$ -axis. (Reprinted with permission from Lai *et al.*, 2007).

2002; Kornev *et al.*, 2004; Wu *et al.*, 2004; Fong *et al.*, 2005; Lai *et al.*, 2006; Ponomareva and Bellaiche, 2006). However, the stripe domains in the BTO film run along  $[110]$  and alternate along  $[1\bar{1}0]$  – as also previously found in Tinte and Stachiotti (2001) – while the stripe domains in PZT and  $\text{PbTiO}_3$  thin films run along  $[100]$  and alternate along  $[010]$  (Streiffner *et al.*, 2002; Kornev *et al.*, 2004; Wu *et al.*, 2004; Fong *et al.*, 2005; Lai *et al.*, 2006; Ponomareva and Bellaiche, 2006). Moreover, the periodicity of these ‘diagonal’ stripes in the 20 Å-thick BTO film is of  $\approx 4.3$  lattice constants along  $[1\bar{1}0]$  (which is consistent with Tinte and Stachiotti (2001) since Fig. 19.2(a) indicates an alternation of the stripe of six lattice constants along the  $[100]$  and  $[010]$  directions. (In the following, we will refer to this ground-state of BTO films as BTO-110-4.3.) On the other hand, as indicated above, the periodicity of the laminar domains in a PZT film with the same thickness (namely, 20 Å) is equal to eight lattice constants along the  $[010]$  direction. We numerically found that the  $\langle 110 \rangle$ -oriented stripes are energetically preferred over the  $\langle 010 \rangle$ -alternating stripes in BTO films mainly because of long-range dipole–dipole interaction energy,  $E^{\text{dpl}}$ , albeit at the cost of short-range energy,  $E^{\text{short}}$ . Interestingly, the lower  $E^{\text{dpl}}$  in BTO-110-4.3 stripes can be understood by solely focusing on the dipoles close to the domain walls: any of such dipoles, say located at site  $i$ , will interact with the two (respectively, one) antiparallel dipoles and with the two (respectively, three) parallel dipoles located at the four sites that are nearest neighbor (in the  $(001)$  plane) of site  $i$ , when the stripes alternate along  $[1\bar{1}0]$  (respectively,  $[010]$ ). This gain in number of nearest-neighbor antiparallel dipoles when going from stripes alternating along  $[010]$  to stripes alternating along  $[1\bar{1}0]$  effectively lowers  $E^{\text{dpl}}$  – while raising  $E^{\text{short}}$  at the same time. In the case of BTO,  $E^{\text{dpl}}$  is lowered more than  $E^{\text{short}}$  is raised, while we numerically found that the opposite occurs for PZT films because of the different parameters inherent to that latter material – which explains the difference in morphology of stripe domains in these two films.

Furthermore, and as can be seen in Fig. 19.3, which shows the real-space distribution of the local dipoles in the ground-states, two other main differences exist between the morphology of the stripe domains in BTO versus PZT films. They are: (1) the dipoles of a given stripe domain are nearly constant in direction (i.e. parallel or antiparallel to the  $z$ -axis) and magnitude inside the BTO films, while such dipoles continuously rotate across the stripe inside the PZT films; (2) the dipoles at the surfaces can ‘only’ deviate from the  $z$ -axis by up to  $45^\circ$  in the BTO film, while in-plane surface dipoles occurs in PZT films in order to close the flux (Kornev *et al.*, 2004; Wu *et al.*, 2004; Lai *et al.*, 2006). To better understand such differences, we decided to construct another domain pattern in a 20 Å-thick BTO film (keeping the same boundary conditions as above), to be denoted by BTO<sub>PZT</sub>-010-8. Such latter state exhibits the same dipole configuration as the equilibrium domain pattern of a 20 Å-



19.3 Real-space distribution of the local modes in (a) BTO-110-4.3 and (b) PZT-010-8 films. These films possess five (001) B-layers, or equivalently, have a thickness of around 20 Å. The X and  $\diamond$  symbols correspond to the surface B-layers, while the  $\bullet$  symbol characterizes the dipoles at the most inner layer. The  $\square$  and  $\circ$  symbols refer to the other two (001) planes (located between the surface and most-inner layers). Vertical and horizontal axes (in both (a) and (b) parts) represent the projection of the local modes (given in atomic units) along the z-axis and stripe alternating direction, respectively. (Reprinted with permission from Lai *et al.*, 2007).

thick PZT film, but with the average magnitude of the dipoles having been rescaled (with respect to that of the PZT film) in order to be identical to that of fully relaxed BTO films. As a result, BTO<sub>PZT</sub>-010-8 exhibits continuously rotating dipoles across a given stripe and in-plane surface dipoles, as in the equilibrium domain pattern of PZT but unlike in BTO-110-4.3. Interestingly, BTO<sub>PZT</sub>-010-8 is found to be thermodynamically unstable because it directly transforms into another domain structure, having no significantly rotating or in-plane dipoles, after a couple of MC sweeps. BTO films thus profoundly dislike significantly rotating and in-plane dipoles. Such disliking takes a major part of its origin in the strain-soft mode interaction energy,  $E^{\text{int}}$ . In other words, the local soft modes in BTO prefer to follow the easy polarization z-axis introduced by the elastic compressive strain. (In contrast, we numerically found that  $E^{\text{short}}$  becomes the predominant contributing factor for the PZT domain patterns to exhibit rotating dipoles across stripes.)

### 19.3.3 Domain evolution under electric field

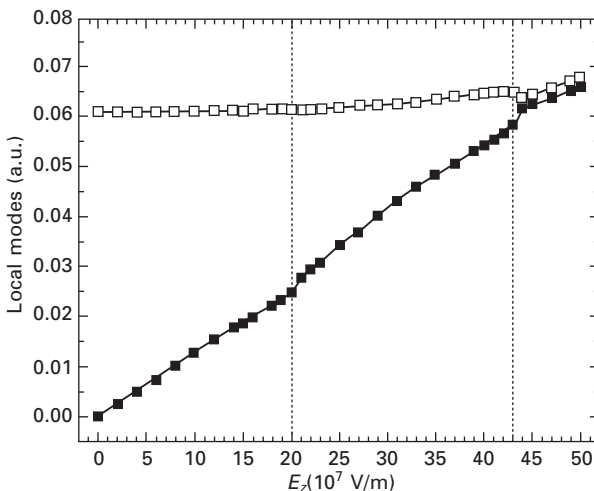
The aim of this subsection is to summarize recent first-principles-based works (Lai *et al.*, 2006, 2007) that revealed, as well as provided detailed



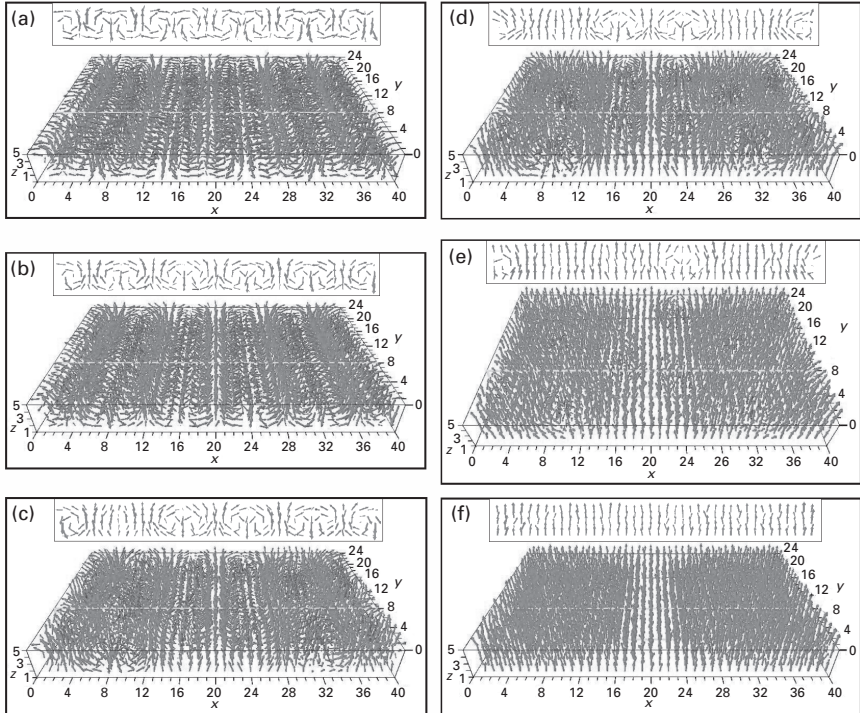
atomistic features of, the stripe domains' evolution in [001]  $\text{PbZr}_{0.5}\text{Ti}_{0.5}\text{O}_3$  and [001]  $\text{BaTiO}_3$  ultra-thin films under an external electric field applied along the [001] direction (chosen to be the  $z$ -axis). In the following, the magnitude of this field is denoted as  $E_z$ .

#### Domain evolution in $\text{PbZr}_{0.5}\text{Ti}_{0.5}\text{O}_3$ films

Figure 19.4 shows the supercell average of the  $z$ -Cartesian component of the local modes  $\langle u_z \rangle$  and of the magnitude of the local modes  $\langle u_M \rangle$  as a function of  $E_z$  in 20 Å-thick  $\text{PbZr}_{0.5}\text{Ti}_{0.5}\text{O}_3$  ultrathin films (as mimicked by a  $40 \times 20 \times 5$  supercell), as predicted by the effective Hamiltonian technique (Lai *et al.*, 2006). The temperature is 10 K and the misfit (compressive) strain is 2.65%. We chose here a realistic electrical boundary condition (Streiffer *et al.*, 2002; Junquera and Ghosez, 2003), which corresponds to an 81% screening of the maximum depolarizing field. As consistent with Streiffer *et al.* (2002) and Kornev *et al.*, 2004) and as discussed above, the combination of a compressive epitaxial strain with a large enough residual depolarizing field leads to the formation of  $180^\circ$  stripe domains, when no external electric field is applied. Figure 19.5(a) displays such domains that adopt a periodicity of eight unit cells (32 Å) for the considered 20 Å-thick ultra-thin film. Inside



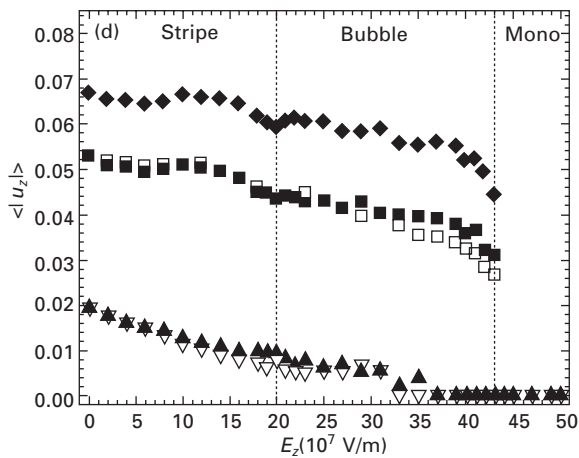
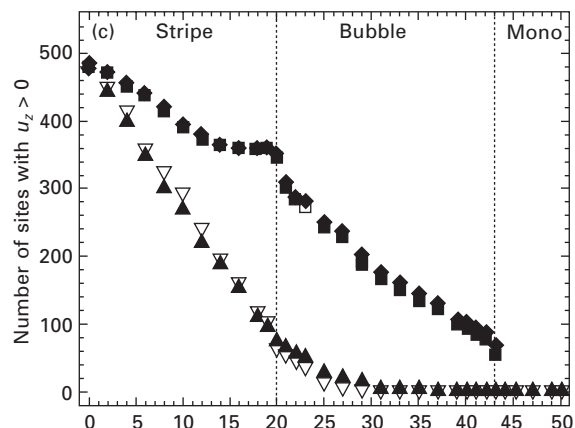
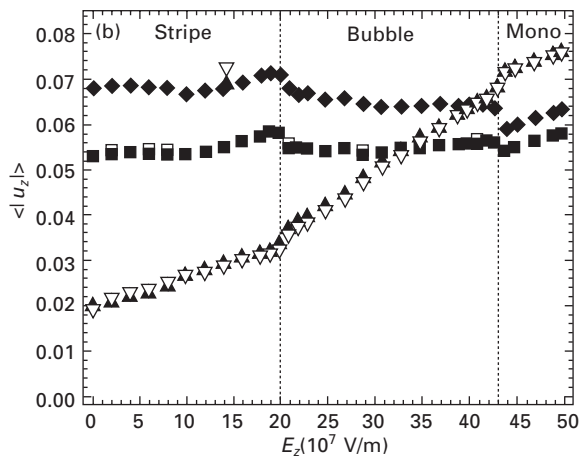
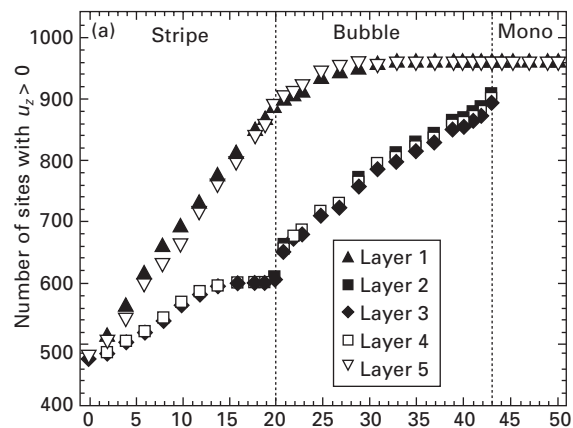
19.4 Supercell average of the  $z$ -Cartesian component of the local modes,  $\langle u_z \rangle$ , and supercell average of the magnitude of the local modes,  $\langle u_M \rangle$ , as a function of the  $E_z$ , applied electric field along the  $z$ -axis for 20 Å-thick  $\text{Pb}(\text{Zr}_{0.5}\text{Ti}_{0.5})\text{O}_3$  films under a compressive strain of  $-2.65\%$ , a 81% screening of the maximum depolarizing field, and at  $T = 10$  K. Kinks in the curves reflect changes in the dipole pattern. Open and solid symbols display  $\langle u_M \rangle$  and  $\langle u_z \rangle$ , respectively. (Reprinted with permission from Lai *et al.*, 2006).



**19.5**  $T=10$  K three-dimensional polarization patterns in (001)  $\text{Pb}(\text{Zr}_{0.5}\text{Ti}_{0.5})\text{O}_3$  films under different  $E_z$  fields: stripe domains under (a)  $E_z = 0$  and (b)  $E_z = 18 \times 10^7$  V/m; bubble domains under (c)  $E_z = 25 \times 10^7$ , (d)  $E_z = 31 \times 10^7$  and (e)  $E_z = 43 \times 10^7$  V/m; and monodomain under (f)  $E_z = 47 \times 10^7$  V/m. The insets show the cross-sections of a specific  $(x, z)$  plane. Light (dark) arrows characterize local dipoles having a positive (negative) component along the  $z$ -axis. (Reprinted with permission from Lai *et al.*, 2006).

each period, two stripe domains with (mostly) opposite out-of-plane dipoles which we will refer to as ‘up’ and ‘down’ domains alternate along the  $x$  axis. (Note that, as discussed above, dipoles lying in plane can also be found at the top and bottom surfaces to further minimize the residual depolarizing field.) The up and down domains can be considered as each having an equal width of four unit cells for  $E_z = 0$ , explaining why  $\langle u_z \rangle$  vanishes while  $\langle u_M \rangle$  is significantly larger than zero (see Fig. 19.4). Furthermore, Figs 19.5(b)–(f) provide atomistic detail on the evolution of the dipole patterns of the film, as given by the last snapshot of our MC simulations, when activating and increasing an applied electric field.

Figure 19.6 provides complementary information on the number of supercell sites having a positive or negative  $z$  component of their dipoles, as well as on the average magnitude of such dipoles in the different (001) planes, as a



19.6 (a) Number of sites with a positive  $z$ -Cartesian component of the local modes and (b) the corresponding  $\langle |u_z| \rangle$  average magnitude of their  $z$ -Cartesian component of the local modes, as a function of  $E_z$ , in the different (001) layers of the  $\text{Pb}(\text{Zr}_{0.5}\text{Ti}_{0.5})\text{O}_3$  film at  $T=10$  K. (c) and (d) are the same as (a) and (b), respectively, but for a negative  $z$ -Cartesian component of the local modes. The layer index of thin films from the first layer (layer 1, which is a surface layer) to the last layers (layer 5, which is the other surface layer) are indicated via solid triangle, solid square, solid diamond, open square and reversed open triangle, respectively. (Reprinted with permission from Lai *et al.*, 2006).

function of  $E_z$ . Figures 19.4 and 19.6 indicate that, when  $E_z$  increases from zero to  $20 \times 10^7$  V/m,  $\langle u_z \rangle$  linearly increases while  $\langle u_M \rangle$  barely increases, because some sites rotate and flip their local dipoles towards  $E$  while very slightly increasing their magnitude. Comparing Figs 19.5(a) and (b) reveals that such rotation and flip occur near the domain walls separating the up and down nanodomains. The up domains (i.e. for which the dipoles have a  $z$  component aligned along  $E$ ) thus grow laterally at the cost of the adjacent down (antiparallel) domains. Interestingly, the studied thin films still adopt a periodic stripe domain structure, with the overall periodicity remaining unchanged, during that lateral growth process. Figures 19.5(b), 19.6(a) and 19.6(c) also indicate that, at the surfaces, the number of dipoles with in-plane components is reduced with respect to the  $E_z = 0$  case in favor of dipoles having a positive  $z$  component. At the critical value  $E_z = 20 \times 10^7$  V/m, the average width of the up and down domains is numerically found to be five and three lattice constants, respectively. As  $E_z$  keeps increasing above  $20 \times 10^7$  V/m, a slight change in the slope of the  $\langle u_z \rangle$  versus  $E_z$  curve occurs (see Fig. 19.4), which is associated with the occurrence of the structural modification seen in Fig. 19.5(c): the smaller down domains become pinched along the  $y$  direction (which is parallel to the [010] direction) and three-dimensional nanobubbles (having dipoles still being antiparallel to the applied field) now emerge from this pinching. Such bubbles are elongated along the  $y$  direction and have a width of three lattice constants along the  $x$ -axis (which is parallel to the [100] direction), as direct consequences of the breaking of the previous down stripe domains along the  $y$  direction.

As revealed by Figs 19.6(a) and (c), the transition from stripe-to-bubble domains is accompanied by a sudden and discontinuous increase (respectively, decrease) of the number of sites belonging to the inner layers with positive (respectively, negative)  $z$  components for their dipoles. A minimal lateral ( $x$ ) size of down domains of three lattice constants ( $12 \text{ \AA}$ ), below which a periodic stripe domains structure cannot be stable anymore, thus exists in our  $20 \text{ \AA}$ -thick films (see Figs 19.5b and c). Interestingly, when the down stripe domains reach such a minimal size, the dipole pattern first tends to rearrange itself while maintaining a periodic stripe domains structure before forming bubbles. Such rearrangement occurs when increasing the applied field from  $15 \times 10^7$  to  $20 \times 10^7$  V/m in the present case and essentially concerns the surface layers, where more dipoles acquire a positive and larger-in-magnitude  $z$  component, while inner layers do not flip or rotate their dipoles (see Fig. 19.6). As a result, bubbles do not (predominantly) ‘touch the surface,’ once the transition from periodic up and down stripes to bubble domains occurs. Moreover, dipoles with (small) in-plane components exist around the bubbles in order to minimize the short-range energy costs associated with dipoles being antiparallel to the polarization. Increasing even more  $E_z$  first leads to a shrinking of the bubbles along the  $y$ -axis, and then to a decrease of the

number of such bubbles once they reach a critical size of around three lattice constants along this  $y$  axis; see Fig. 19.5(c)–(e). The lateral size of the bubbles along the  $x$ -axis remains equal to three lattice constants during these processes. When the applied electric field becomes as large as  $43 \times 10^7$  V/m, the bubbles disappear in favor of a monodomain state (see Fig. 19.5f). Increasing  $E_z$  further results in the elongation of the dipoles along  $z$  within the monodomain, as indicated by the increase of both  $\langle u_z \rangle$  and  $\langle u_M \rangle$  seen in Fig. 19.4. Moreover, we also decreased  $E_z$  from  $50 \times 10^7$  V/m to zero, and found that the resulting domain evolution sequence is simply the reversal process of the one just described when increasing the applied electric field.

We also investigated the effects of the residual depolarizing field's magnitude, misfit strain, and film thickness on the domain evolution. For instance, solely decreasing the screening coefficient  $\beta$  from 81% to 41% does not qualitatively affect the domain evolution described above but rather increases 'only' the critical applied fields (which are now equal to  $120 \times 10^7$  and  $320 \times 10^7$  V/m at the stripe-to-bubble and bubble-to-monodomain transitions, respectively, versus  $20 \times 10^7$  and  $43 \times 10^7$  V/m before). This increase occurs because a smaller  $\beta$  yields a larger depolarizing field, and that larger depolarizing field favors the formation of up and down domains (to fight against it) over bubbles and even more over monodomains. Similarly, an increase of the film thickness from 20 to 36 Å, while maintaining  $\beta = 0.81$  and a misfit strain of 2.65%, leads to an increase of these critical fields (now around  $74 \times 10^7$  and  $90 \times 10^7$  V/m at the stripe-to-bubble and bubble-to-monodomain transitions, respectively). This is probably because thicker films under a residual depolarizing field and a compressive strain have a larger initial (i.e. corresponding to  $E_z = 0$ ) stripe domains period (Streiffer *et al.*, 2002; Wu *et al.*, 2004). It thus takes larger applied fields to move the domain walls until reaching the minimal lateral  $x$  width of the down domains, which we found to be around 8–12 Å, independently of the film thickness. Note also that the range of electric field associated with nanobubbles becomes smaller when increasing the thickness. This is caused by the fact that the bubbles are laterally (i.e. along the  $x$ -axis) farther away from each other, because of the initially larger stripe period. We also found that increasing the magnitude of the compressive strain slightly decreases the critical fields; e.g. a misfit strain of 3.0% yields stripe-to-bubble and bubble-to-monodomain transitions at  $18 \times 10^7$  and  $40 \times 10^7$  V/m, respectively (to be compared with  $20 \times 10^7$  and  $43 \times 10^7$  V/m for the misfit strain of 2.65%), because higher compressive strain favors elastic-related energies (which prefer monodomains and then bubbles in this order (Hubert and Schafer, 1998) rather than stripe domains) over the depolarizing energy (that is, the lowest in stripes and the highest in monodomains and in between for bubbles).

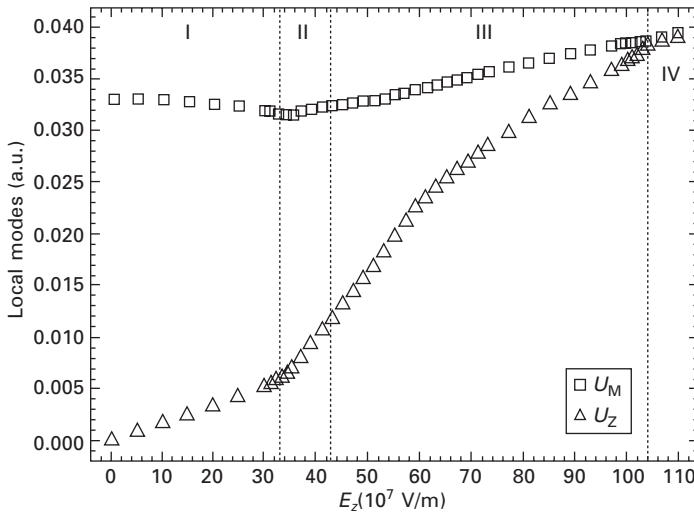
Let us now draw parallels and differences between these predictions for ferroelectric films under an applied electric field (displayed in Figs 19.4–

19.6) and known features of ferromagnetic thin films subject to an external magnetic field. For that, it is important to realize that modification of periodic stripes, and transitions from stripes-to-bubbles domains and bubbles-to-monodomains are also known to occur in ferromagnetic films under magnetic fields (Hubert and Schafer, 1998). However, it is commonly believed that the lateral growth of up domains at the expense of down domains is accompanied by a modification of the stripes' periodicity in magnetic films under magnetic fields (Hubert and Schafer, 1998), while our results on ferroelectric films under electric field show otherwise. This may be due to the fact that the stripe periods are an order of magnitude smaller in ferroelectric films with respect to ferromagnetic films (Liebmann *et al.*, 2005). Moreover, the shape of ferroelectric bubbles is elliptical rather than spherical, as commonly assumed in magnetic bubbles (Hubert and Schafer, 1998). Furthermore, the ferroelectric bubbles avoid the surfaces, which is in contrast with a common belief (Shur and Rumyantsev, 1997) (based on the presence of defects at the surfaces) and which can be due to the fact that the studied thin films are defect free. Finally, the ferroelectric bubbles (which have a lateral width of  $12 \text{ \AA}$ ) are far smaller than the ferromagnetic bubbles (which are at least  $500 \text{ \AA}$  in diameter) (O'Dell, 1986). The ferroelectric bubbles domains could thus deliver the promises that the magnetic bubbles have never fulfilled for memory or logic devices applications, because of their relatively large diameter and low operation speed (O'Dell, 1986).

#### *Domain evolution in BaTiO<sub>3</sub> films*

We now consider the electric-field-induced evolution of stripe nanodomains in [001] BaTiO<sub>3</sub> (BTO) ultra-thin films, and compare it with that of [001] Pb(Zr,Ti)O<sub>3</sub> ultra-thin films.

As in Section 19.3.2, we study a  $20 \text{ \AA}$ -thick [001] BTO film, as mimicked by a  $24 \times 24 \times 5$  supercell, under a compressive strain of  $-2.2\%$  and having a realistic electrical boundary condition corresponding to  $\beta = 0.8$  (Lai *et al.*, 2007). The resulting ground-state (which exhibits periodic stripe domains) was denoted as BTO-110-4.3 in Section 19.3.2. Figure 19.7 shows the supercell average of the  $z$ -Cartesian component of the local modes  $\langle u_z \rangle$  and of the magnitude of the local modes  $\langle u_M \rangle$  as a function of  $E_z$  in this  $20 \text{ \AA}$ -thick BTO ultra-thin film. (For instance, Fig. 19.7 indicates that, when no electric field is applied ( $E_z = 0$ ),  $\langle u_z \rangle$  vanishes while  $\langle u_M \rangle$  exhibits a non-zero value, which is consistent with the BTO-110-4.3 domain pattern shown in Fig. 19.2a). Atomistic detail on the evolution of the local dipoles under the applied electric field – as given by the last snapshot of our MC simulations – is given in Figs 19.2 (a)–(f). Moreover, Fig. 19.8 displays complementary statistical information on the number of supercell sites having positive or negative  $z$ -component of their dipoles, as well as, on the average magnitude of such



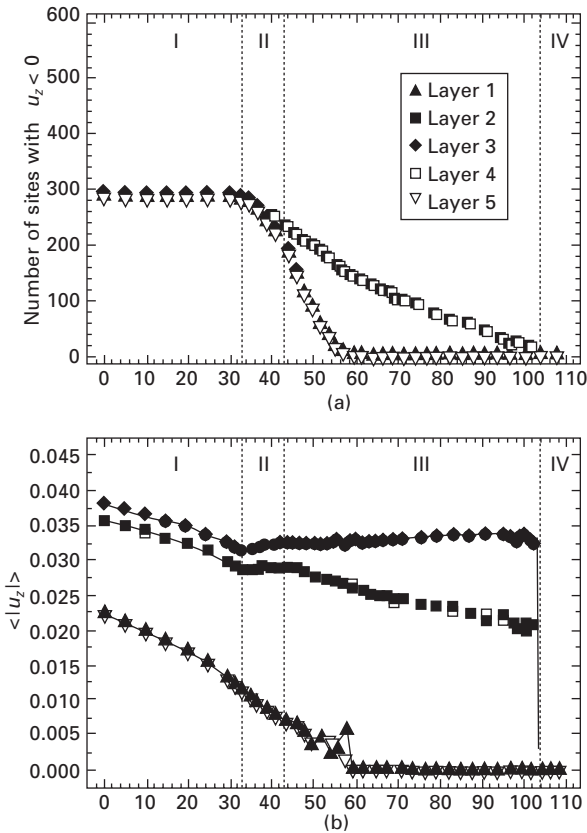
19.7 Supercell average of the z-Cartesian component of the local modes,  $\langle u_z \rangle$ , and supercell average of the magnitude of the local modes,  $\langle u_M \rangle$ , as a function of  $E_z$  for 20 Å-thick BTO films under a compressive strain of  $-2.2\%$ , a 80% screening of the maximum depolarizing field, and at  $T=10$  K. Square and triangle symbols display  $\langle u_M \rangle$  and  $\langle u_z \rangle$ , respectively. The supercell averages of the x- and y-Cartesian components of the local modes are essentially null and are not shown for clarity. (Reprinted with permission from Lai *et al.*, 2007).

dipoles in the different (001) planes, as a function of  $E_z$ . As we will see, four regions can be distinguished, with their electric-field range being indicated in Figs 19.7 and 19.8 for our film of interest (note that such a range depends on the film's thickness and boundary conditions; Lai *et al.*, 2006).

Region I: Fig. 19.8 tells us that, when the electric field is applied from zero to  $33 \times 10^7$  V/m (Region I), the local dipoles in the 'down' domains do not switch their direction to point along the  $+z$  direction (i.e. parallel to the electrical field) but rather 'simply' significantly decrease their magnitude – while the dipoles in the 'up' domains more modestly increase in magnitude. Such behaviors lead to  $\langle u_z \rangle$  and  $\langle u_M \rangle$  increasing and slightly decreasing with  $E_z$ , respectively (see Fig. 19.7), and to domain walls not moving with respect to the  $E_z = 0$  case (as shown in Fig 19.2b). Interestingly, Region I (unlike Regions II, III, and IV, be discussed below) was not found in PZT films subject to an electric field (Lai *et al.*, 2006), because of the easiness in rotating dipoles in these latter systems.

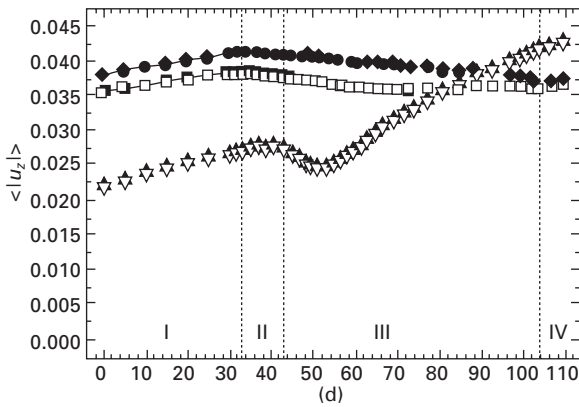
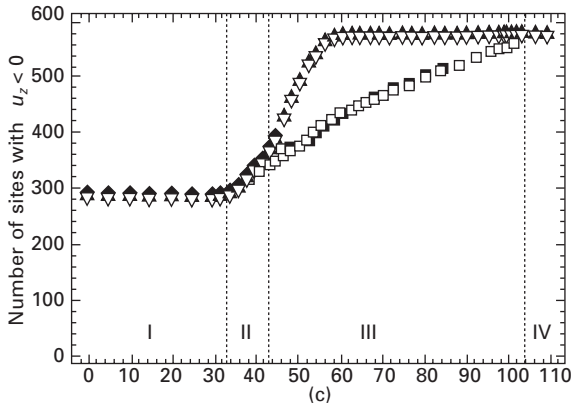
Region II: A further increase of  $E_z$  from  $33 \times 10^7$  to  $43 \times 10^7$  V/m (Region II) induces a switch, from the  $-z$  to  $+z$  direction, of some dipoles in the down domains – as indicated by Fig. 19.8 (a) and (c). Such a switch thus results in

an increase of  $\langle u_z \rangle$  when increasing  $E_z$  (see Fig. 19.7) and in an expansion of the majority domains at the expense of minority domains while maintaining the same overall stripe periodicity – as in the corresponding region for PZT films (Lai *et al.*, 2006). However, unlike in PZT (Lai *et al.*, 2006) and as seen in Fig. 19.2(c), this expansion of majority domains is not synchronous throughout the domain walls. Rather, scattered regions of switched dipoles (with five lattice constants along the  $z$ -axis and one lattice constant along



19.8 (a) Number of sites with a negative  $z$ -Cartesian component of the local modes and (b) the corresponding  $\langle |u_z| \rangle$  average magnitude of their  $z$ -Cartesian component of the local modes, as a function of  $E_z$ , in the different (001) layers at  $T=10$  K for 20 Å-thick BTO films under a compressive strain of  $-2.2$  and a 80% screening of the maximum depolarizing field. (c) and (d) are the same as (a) and (b), respectively, but for a positive  $z$ -Cartesian component of the local modes. The layer index of thin films from the first layer (layer 1, which is a surface layer) to the last layer (layer 5, which is the other surface layer) are indicated via solid triangle, solid square, solid diamond, open square and reversed open triangle, respectively. (Reprinted with permission from Lai *et al.*, 2007).





19.8 (Continued)

both the  $x$ - and  $y$ -axes) that are bounded by (100) and (010) side surfaces ‘pop out’ adjacent to the original domain walls. Therefore, the domain walls expand along [100] and [010] by one lattice constant at a time, and now exhibit a zigzag pattern (while these domain walls are straight in PZT films (Lai *et al.*, 2006)). Moreover, the switching behaviors of the dipoles at the surfaces and inside the films are documented in Fig. 19.8. In particular, one can see that the dipoles on surfaces are slightly easier to switch than the dipoles inside the films because they have a smaller magnitude just before the switching. The real-space distribution of dipoles (data not shown) in Region II further indicates that the switching of the surface dipoles occurs through both rotation and flipping mechanisms. The former mainly involves the dipoles that initially deviate from the  $z$ -axis (see Fig. 19.3) and is accomplished by local dipoles rotating away from the  $z$ -axis while decreasing their magnitude at the same time. The latter applies to the dipoles that were initially aligned along the  $z$ -direction (see Fig. 19.3), is preceded by a decreasing

of the dipoles' magnitude and leads to a significant change of this magnitude after the flipping (see Fig. 19.8b and d). In contrast, the dipoles inside the films switch predominantly through flipping (see Fig. 19.2a–c), with the direction being reversed and the magnitude of dipoles being only very slightly increased after such flipping (see Fig. 19.8b and d). In other words, the slight increase of  $\langle u_M \rangle$  when increasing  $E_z$  in Region II (see Fig. 19.7) mostly originates from the surface dipoles.

Region III: As  $E_z$  keeps increasing, the minority (down) stripe domains become pinched along [110]. Nanobubbles now form (see Fig. 19.2d), as in PZT thin films under electric field. Note that the stripe to bubble domain transition is numerically found for  $E_z$  in between  $41 \times 10^7$  and  $45 \times 10^7$  V/m (because of the zigzagged domain walls, it is difficult to exactly pinpoint the onset of stripe to bubble domain transition, unlike in PZT thin films (Lai *et al.*, 2006). Once the nanobubbles are formed, they dramatically contract along [110] while keeping their width along  $[1\bar{1}0]$  more or less the same under further applied field – as seen in Fig. 19.2(d) and (e). In other words, as in PZT films (Lai *et al.*, 2006), the bubbles contract parallel to the direction along which the initial stripe domains were running (i.e. [110] in BTO versus [100] in PZT films) while keeping their width fixed parallel to the direction along which the initial stripe domains were alternating (i.e.  $[1\bar{1}0]$  in BTO versus [010] in PZT ultra-thin films). Interestingly, Fig. 19.8(d) reveals that, between  $43 \times 10^7$  and  $51 \times 10^7$  V/m, the average magnitude of the surface dipoles having a positive component along the direction of the field (i.e. with  $u_z > 0$ ) decreases with  $E_z$ . This is because the number of switched surface dipoles (i.e. having now  $u_z > 0$  while initially exhibiting  $u_z < 0$ ) increases rather rapidly with  $E_z$  (see Fig. 19.8c) while such dipoles had a rather small magnitude before this switching (see Fig. 19.8b). Figure 19.8(a) further indicates that the critical field for which all the surface dipoles belonging to the initial down stripes have completely switched is around  $E_z = 61 \times 10^7$  V/m (note that half of the dipoles inside the film that belonged to the initial down domains are still not flipped under such field, according to Fig. 19.8a). In other words, the part of Region III located above  $E_z = 61 \times 10^7$  V/m possesses nanobubbles that are encapsulated (i.e. that do not touch the surfaces, as in PZT films). With a further increase of  $E_z$  (see Fig. 19.2e), the bubbles still continue to contract along [110]. Once they reach a critical size of two lattice constants along both  $x$ - and  $y$ -axes and of three lattice constants along the  $z$ -axis, some bubbles pop out and thus the number of nanobubbles decreases with  $E_z$ . Note that the collapse of BTO bubbles is via flipping dipoles inside the films, while the collapse of PZT bubbles is via dipole rotation.

Region IV: At  $E_z = 104 \times 10^7$  V/m, all the nanobubbles have disappeared and a single monodomain, with all the dipoles pointing along the  $+z$  direction, is thus formed – as seen in Fig. 19.2(f) and as consistent with the fact that Fig. 19.7 indicates that  $\langle u_z \rangle$  and  $\langle u_M \rangle$  are now identical. In this monodomain

state, all the dipoles increase in magnitude with  $E_z$ , with the surface dipoles being larger in size.

## 19.4 Domains in one-dimensional and zero-dimensional ferroelectrics

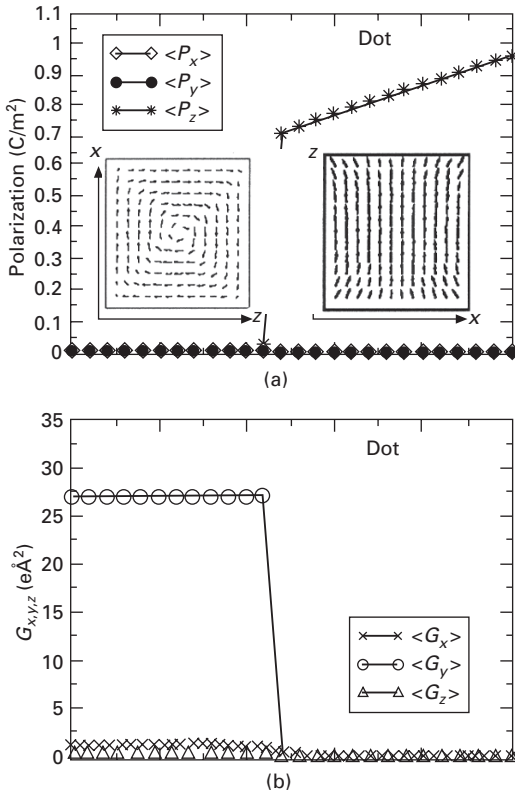
In this section, we will discuss the results of Ponomareva *et al.* (2005b), in general, and will focus on the predicted domains in ferroelectric nanodots and nanowires of  $\text{Pb}(\text{Zr}_{0.4}\text{Ti}_{0.6})\text{O}_3$ , in particular. Technically, the investigated nanodot is cubic in shape with a  $48 \text{ \AA}$  lateral size, while the nanowire is periodic along the  $z$ -direction (chosen along the pseudo-cubic  $[001]$  direction) and has a cubic cross-section of  $48 \times 48 \text{ \AA}^2$ .

The results of the simulation for the spontaneous polarization are shown in Figs 19.9(a) and (c) for the *stress-free* dot and wire, respectively. The left and right insets of Figs 19.9(a) and (c) further display a cross-section of a snapshot of the dipole pattern for ideal OC and SC conditions, respectively, in these two systems. Under SC-like conditions (i.e.  $\beta$  larger than 88%), the dot and nanowire exhibit a spontaneous polarization.

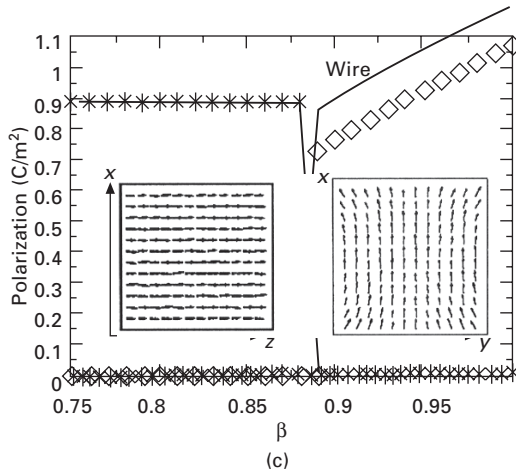
Below the critical values of  $\beta \approx 88\%$ , the magnitude of the residual depolarization field inside the ferroelectric nanostructure becomes so large that the dipoles have to rearrange themselves to efficiently suppress it. A structural phase transition thus occurs. In the case of the dot, such transition is characterized by the vanishing of the spontaneous polarization – as also found in Stachiotti (2004) for some  $\text{BaTiO}_3$  nanodots under OC conditions – and the formation of a vortex dipole structure (see left inset of Fig. 19.9a) that results in the appearance of a spontaneous toroid moment of polarization (which involves the cross-product between local dipoles at the sites  $i$  and the vectors locating these sites  $i$ ) (Naumov *et al.*, 2004) – as indicated by Fig. 19.9(b). Such vortex can also be thought as an original pattern made by four  $90^\circ$  domains. On the other hand, the wire energetically chooses a different dipole pattern (see left inset of Fig. 19.9c) to annihilate the macroscopic depolarization field, namely the dipoles now align along the infinite direction of this wire (rather than perpendicular to it as for SC conditions). This difference between the dipole pattern in the dot versus the wire can be simply understood by realizing that, unlike the wire, the dot is confined along *any* direction. As a result, any non-zero macroscopic polarization pointing along any direction would lead to the activation of a depolarizing field in the dot. Moreover, the infinite wire prefers to have a macroscopic polarization rather than adopting a vortex-like dipole pattern below a critical value of  $\beta$  because the formation of the latter pattern is more costly in terms of short-range and elastic energies.

Similarly, stress-free thin films under OC-like conditions have also been found to have a macroscopic polarization pointing along a periodic direction

(Kornev *et al.*, 2004). Interestingly, Fig. 19.9(b) and (c) and Kornev *et al.* (2004) tell us that the magnitude of the order parameter – that is the spontaneous polarization in wires and films versus spontaneous toroid moment of polarization in the dot – in stress-free ferroelectric nanostructures is independent of  $\beta$  below the critical values. In other words, a given ferroelectric nanostructure adopts a *specific* dipole pattern, once the depolarizing field is large enough.



**19.9** Ground-state spontaneous polarization in free-standing dot (part (a)) and wire (part (c)) as a function of the screening coefficient  $\beta$ . The  $\beta$ -dependency of the toroid moment of polarization in the freestanding nanodot is shown in part (b). Right and left insets to both parts (a) and (c) show the projection of the dipole patterns on a chosen plane for perfect SC and OC conditions, respectively, in the corresponding nanostructure. (Note that these dipoles nearly lie in the plane shown in the insets, that is there is only a slight difference between the dipole vectors and their displayed projections.) The infinite direction of the wire is along the z-axis. The x-, y- and z-axis are chosen along the pseudo-cubic [100], [010] and [001] directions, respectively. (Reprinted with permission from Ponomareva *et al.*, 2005b). The toroidal moment,  $G$  is given in  $e\text{\AA}^2$  units, where  $e$  is minus the electron charge and  $1 e\text{\AA}^2 = 1.60217653 \times 10^{(-39)} C/m^2$  in SI units.

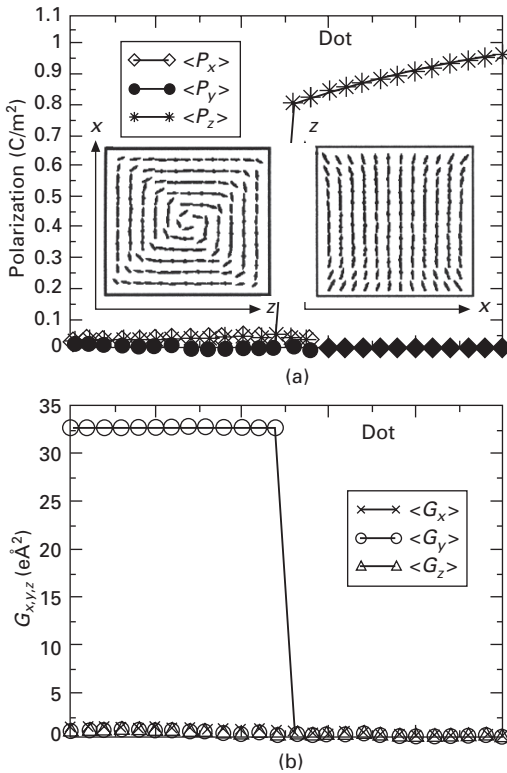


19.9 (Continued)

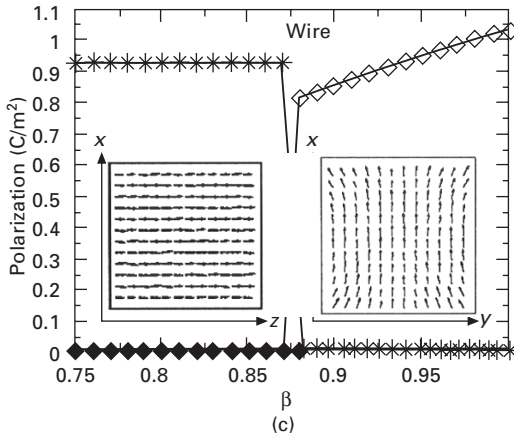
We next turn our attention to the same dot and wire, but under different mechanical boundary conditions, namely those mimicking an epitaxial growth in the  $(x, z)$ -planes. The infinite  $z$ -direction of the wire is thus chosen to lie in such planes. The results for a *tensile* strain  $\delta$  of +2.65% are shown in Fig. 19.10, and are in overall qualitatively close to the corresponding ones in the freestanding systems. There are, however, three differences worth attention. First of all, dipoles aligned along the  $z$ - or  $x$ -axis are now preferred over dipoles parallel to the  $y$ -axis because of our chosen tensile strains. This implies that the toroid moment of the dot under OC-like conditions can only be along the  $y$ -axis as opposed to the case of stress-free dots for which this moment has an equal probability of being along any of the three Cartesian directions. Secondly, the magnitudes of the spontaneous polarization and toroid moment are larger than those of the freestanding systems for small  $\beta$ . Such a feature is due to the fact that the  $x$  and  $z$ -components of the dipoles expand as a result of their coupling with the tensile strains (Cohen, 1992; Zhong *et al.*, 1994, 1995). Thirdly, we numerically found another configuration (Fig. 19.11) for a nanowire under tensile strain, and with  $\beta$  smaller than 86%, that is slightly larger in energy than the configuration shown in the left part of the inset of Fig. 19.10(c). It consists of an infinite number of vortices assembled along the  $z$ -direction of the wire, with neighboring vortices rotating in opposite directions. The formation of this configuration is driven by the desire of the wire to have non-zero components of the dipole in *both*  $x$ - and  $z$ -directions, as dictated by the tensile strain, while minimizing the depolarizing field inside the wire.

We now study the effect of a *compressive* strain  $\delta$  of -2.65% – still applied in the  $(x, z)$ -plane – on the dipole pattern in the nanodot and wire.

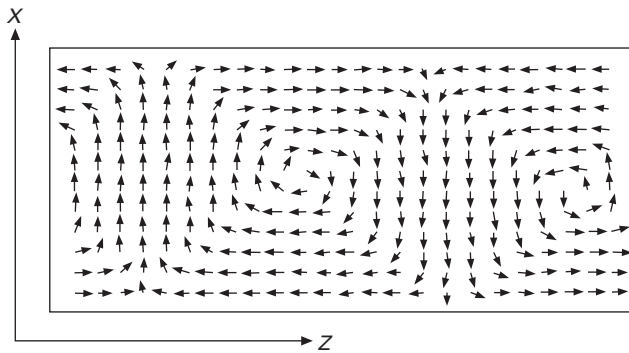
The results of our simulation are shown in Fig. 19.12. Such compressive strain favors dipoles aligned along the  $y$ -axis via the strain–dipole coupling (Cohen, 1992; Zhong *et al.*, 1994, 1995), which explains why the spontaneous polarization of the dot and wire lies along such direction for electrical boundary conditions close to SC (see Figs 19.12a and b and their right insets). However, for the smallest  $\beta$  values, any macroscopic polarization aligned along the  $y$ -axis would generate a relatively large depolarizing field that should strongly



19.10 Ground-state spontaneous polarization in dot (a) and wire (c), under a tensile strain +2.65% applied in the  $(x, z)$  plane, as a function of the screening coefficient  $\beta$ . The  $\beta$ -dependency of the toroidal moment of polarization in the nanodot is shown in (b). Right and left insets to both (a) and (c) show the projection of the dipole patterns on a chosen plane for perfect SC and OC conditions, respectively, in the corresponding nanostructure. (Note that these dipoles nearly lie in the plane shown in the insets, that is there is only a slight difference between the dipole vectors and their displayed projections.) The infinite direction of the wire is along the  $z$ -axis. The  $x$ -,  $y$ - and  $z$ -axes are chosen along the pseudo-cubic [100], [010] and [001] directions, respectively. (Reprinted with permission from Ponomareva *et al.*, 2005b). The toroidal moment,  $G$  is given in  $\text{e}\text{\AA}^2$  units, where  $e$  is minus the electron charge and  $1 \text{ e}\text{\AA}^2 = 1.60217653 \times 10^{(-39)} \text{C/m}^2$  in SI units.

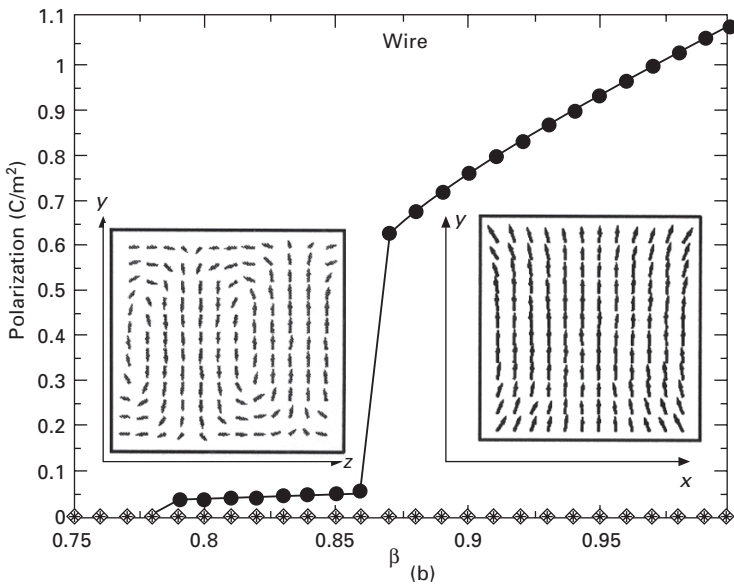
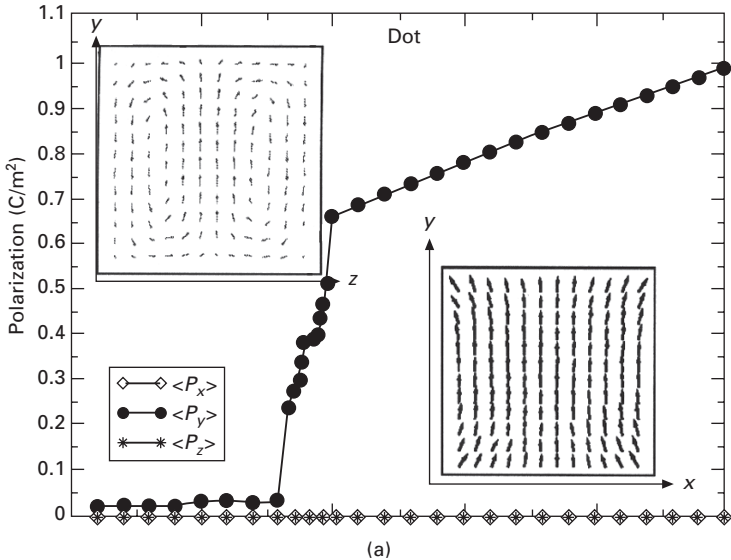


19.10 (Continued)



19.11 A cross-section of another possible dipole pattern for a nanowire periodic along the z-direction, and under OC-like electrical boundary conditions and a tensile strain applied in the (x, z)-plane. The arrows show the projection of the dipole patterns on a chosen plane. (Note that these dipoles nearly lie in the plane shown in the insets, that is there is only a slight difference between the dipole vectors and their displayed projections.) The x-, y- and z-axis are chosen along the pseudo-cubic [100], [010] and [001] directions, respectively. (Reprinted with permission from Ponomareva *et al.*, 2005b.)

oppose such polarization. The resulting ground-state configurations must thus arise from a compromise between these strain *versus* depolarizing field factors. As a result, both nanosystems form 180° stripe domains with the dipoles being mostly ‘up’ or ‘down’ along the y-direction, with two neighboring and opposite stripes having a very small overall width (namely, 24 Å in the present case). Interestingly, such *nanodomain* patterns occur in *any* low-dimensional ferroelectrics under compressive strain and under residual



19.12 Ground-state spontaneous polarization in dot (part (a)) and wire (part (b)), under a compressive strain  $-2.65\%$  in the  $(x, z)$  plane, as a function of the screening coefficient  $\beta$ . Right and left insets to both parts (a) and (b) show the projection of the dipole patterns on a chosen plane for perfect SC and OC conditions, respectively, in the corresponding nanostructure. (Note that these dipoles nearly lie in the plane shown in the insets, that is there is only a slight difference between the dipole vectors and their displayed projections.) The infinite direction of the wire is along the  $z$ -axes. The  $x$ -,  $y$ - and  $z$ -axis are chosen along the pseudo-cubic  $[100]$ ,  $[010]$  and  $[001]$  directions, respectively. (Reprinted with permission from Ponomareva *et al.*, 2005b.)



depolarizing field since they have also been found in ferroelectric thin films experiencing similar mechanical and electrical boundary conditions (see Section 19.3.1, Fong *et al.*, 2004, and Kornev *et al.*, 2004). Note, however, that the wires and films distinguish themselves from the dot in the sense that the former exhibit stripe domains that are (infinitely) repeated along a periodic direction, while the 3D-confinement of the nanodot results in a *finite* number of stripes. Furthermore, unlike for the stress-free and tensile mechanical boundary conditions in the dot, the ground-state dipole pattern in the compressively strained dot leads to a vanishing spontaneous (total) toroid moment of polarization – in addition to a vanishing spontaneous polarization – for small  $\beta$ .

## 19.5 Conclusions

Recent works have shown that it is now possible to study domain patterns occurring in ferroelectric nanostructures from *direct* first principles and first-principles-based techniques. In particular, we used the effective Hamiltonian approach (1) to describe a wide variety of dipole patterns that can exist in ultra-thin films, nanodots, and nanowires, depending on the interplay between film orientation and boundary conditions and (2) to provide detailed atomistic information of the peculiar domain evolution of epitaxial ultrathin films under an applied electric field.

We are thus confident that the use of the first-principles approaches for obtaining important quantitative information leads to a deeper understanding of low-dimensional ferroelectrics, in general, and will help in interpreting future experimental and phenomenological data, in particular.

## 19.6 Acknowledgments

This work was supported by ONR grants N 00014-01-1-0365 and N 00014-04-1-0413, NSF grants DMR-0404335, and DOE grant DE-FG02-05ER46188.

## 19.7 References

- Aitlamine, H., Abelmann, L. and Puchalska, I. B. (1991) *Journal of Applied Physics*, **71**, 353.
- Almahmoud, E., Navtsenya, Y., Kornev, I., Fu, H. and Bellaiche, L. (2004) *Physical Review B*, **70**, 220102.
- Arlt, G. and Sasko, P. (1980) *Journal of Applied Physics*, **51**, 4956–4960.
- Auciello, O., Scott, J. F. and Ramesh, R. (1998) *Physics Today*, **51**, 22.
- Bellaiche, L., Garcia, A. and Vanderbilt, D. (2000) *Physics Review Letters*, **84**, 5427.
- Bellaiche, L., Garcia, A. and Vanderbilt, D. (2002) *Ferroelectrics*, **266**, 41.
- Catalan, G., Scott, J. F., Schilling, A. and Gregg, J. M. (2006) *Journal of Applied Physics*, **19**, 022201.

- Cohen, R. E. (1992) *Nature*, **358**, 136.
- Dawber, M., Rabe, K. M. and Scott, J. F. (2005) *Reviews of Modern Physics*, **77**, 1083.
- Fong, D. D., Stephenson, G. B., Streiffer, S. K., Eastman, J. A., Auciello, O., Fuoss, P. H. and Thompson, C. (2004) *Science*, **304**, 1650.
- Fong, D. D., Cionca, C., Yacoby, Y., Stephenson, G. B., Eastman, J. A., Fuoss, P. H., Streiffer, S. K., Thompson, C., Clarke, R., Pindak, R. and Stern, E. A. (2005) *Physical Review B*, **71**, 144112.
- Ghosez, P. and Rabe, K. M. (2000) *Applied Physics Letters*, **76**, 2767.
- Glinchuk, M. D., Eliseev, E. A., Stephanovich, V. A. and Farhi, R. (2003) *Journal of Applied Physics*, **93**, 1150.
- Hubert, A. and Schafer, R. (1998) *Magnetic Domains: The Analysis of Magnetic Microstructures*, Springer, Berlin.
- Junquera, J. and Ghosez, P. (2003) *Nature*, **422**, 506.
- Junquera, J., Dieguez, O., Rabe, K. M., Ghosez, P., Lichtensteiger, C. and Triscone, J.-M. (2004) In *Fundamental Physics of Ferroelectrics*, NISTIR, Gaithersburg, Colonial Williamsburg, VA, pp. 86–87.
- Kanno, I., Kotera, H., Matsunaga, T., Kamada, T. and Takayama, R. (2003) *Journal of Applied Physics*, **93**, 4091.
- Kelman, M. B., Schloss, L. F., McIntyre, P. C., Hendrix, B. C., Bilodeau, S. M. and Roeder, J. F. (2001) *Applied Physics Letters*, **80**, 1258.
- Kittel, C. (1946) *Physical Review*, **70**, 965.
- Kopal, A., Bahník, T. and Fousek, J. (1997) *Ferroelectrics*, **202**, 267.
- Kornev, I., Fu, H. and Bellaiche, L. (2004) *Physics Review Letters*, **93**, 196104.
- Kornev, I. A., Fu, H. and Bellaiche, L. (2006) *Journal of Materials Science*, **41**, 137–145.
- Lai, B.-K., Kornev, I. A., Bellaiche, L. and Salamo, G. J. (2005) *Applied Physics Letters*, **86**, 132904.
- Lai, B.-K., Ponomareva, I., Naumov, I. I., Kornev, I., Fu, H., Bellaiche, L. and Salamo, G. J. (2006) *Physical Review Letters*, **96**, 137602.
- Lai, B.-K., Ponomareva, I., Kornev, I. A., Bellaiche, L. and Salamo, G. J. (2007) *Physical Review B (Condensed Matter and Materials Physics)*, **75**, 085412–7.
- Landau, L. and Lifshitz, E. (1935) *Physikalische Zeitschrift der Sowjetunion*, **8**, 153–169.
- Landau, L. D. and Lifshitz, E. M. (1984) *Electrodynamics of Continuous Media*, 2nd ed, Pergamon Press, Oxford, England, pp. 280–283.
- Li, Y. L., Hu, S. Y., Liu, Z. K. and Chen, L. Q. (2002) *Applied Physics Letters*, **81**, 427.
- Liang, C.-S. and Wu, J.-M. (2005) *Applied Physics Letters*, **87**, 022906.
- Liebmann, M., Schwarz, A., Kaiser, U., Wiesendanger, R., Kim, D.-W. and Noh, T.-W. (2005) *Physical Review B*, **71**, 104431.
- Maruyama, T., Saitoh, M., Sakai, I., Hidaka, A. T., Yano, Y. and Noguchi, T. (1998) *Applied Physics Letters*, **73**, 3524.
- Mehta, R. R., Silverman, B. D. and Jacobs, J. T. (1973) *Journal of Applied Physics*, **44**, 3379.
- Merz, W. J. (Aug, 1954) *Physical Review*, **95**, 690–698.
- Meyer, B. and Vanderbilt, D. (2001) *Physical Review B*, **63**, 205426.
- Meyer, B. and Vanderbilt, D. (2002) *Physical Review B*, **65**, 104111.
- Naumov, I. I., Bellaiche, L. and Fu, H. (2004) *Nature*, **432**, 737.
- Noheda, B., Cox, D. E., Shirane, G., Guo, R., Jones, B. and Cross, L. E. (2001) *Physical Review B*, **63**, 014103.
- O'Dell, T. H. (1986) *Reports on Progress in Physics*, **49**, 589.
- Patel, J. R., Jackson, K. A. and J. F. Dillon, J. (1968) *Journal of Applied Physics*, **39**, 3767.

- Pertsev, N. A., Kukhar, V. G., Kohlstedt, H. and Waser, R. (2003) *Physical Review B*, **67**, 054107.
- Ponomareva, I. and Bellaiche, L. (2006) *Physical Review B*, **74**, 064102.
- Ponomareva, I., Naumov, I., Kornev, I., Fu, H. and Bellaiche, L. (2005a) *Current Opinion in Solid State and Materials Science*, **9**, 114–121.
- Ponomareva, I., Naumov, I. I. and Bellaiche, L. (2005b) *Physical Review B*, **72**, 214118.
- Ponomareva, I., Naumov, I. I., Kornev, I., Fu, H. and Bellaiche, L. (2005c) *Physical Review B*, **72**, 140102.
- Rabe, K. M. (2005) *Current Opinion in Solid State and Materials Science*, **9**, 122–127.
- Ramesh, R., Aggarwal, S. and Auciello, O. (2001) *Materials Science and Engineering*, **32**, 191.
- Roitburd, A. L. (1976) *Physics Status Solidi A*, **37**, 329–39.
- Scott, J. F. (1998) *Annual Review of Material Science*, **28**, 79.
- Scott, J. F. (2000) *Ferroelectric Memories*, Springer Verlag.
- Setter, N., Damjanovic, D., Eng, L., Fox, G., Gevorgian, S., Hong, S., Kingon, A., Kohlstedt, H., Park, N. Y., Stephenson, G. B., Stolitchnov, I., Taganstev, A. K., Taylor, D. V., Yamada, T. and Streiffer, S. (2006) *Journal of Applied Physics*, **100**, 051606.
- Shur, V. Y. and Rumyantsev, E. L. (1997) *Ferroelectrics*, **191**, 319.
- Stachiotti, M. G. (2004) *Applied Physics Letters*, **84**, 251.
- Streiffer, S. K., Eastman, J. A., Fong, D. D., Thompson, C., Munkholm, A., Murty, M. V. R., Auciello, O., Bai, G. R. and Stephenson, G. B. (2002) *Physics Review Letters*, **89**, 067601.
- Tinte, S. and Stachiotti, M. G. (2001) *Physical Review B*, **64**, 235403.
- Tybell, T., Ahn, C. H. and Triscone, J.-M. (1999) *Applied Physics Letters*, **75**, 856.
- Wu, Z., Huang, N., Liu, Z., Wu, J., Duan, W., Gu, B.-L. and Zhang, X.-W. (2004) *Physical Review B*, **70**, 104108.
- Yacoby, Y., Girshberg, Y., Stern, E. A. and Clarke, R. (2006) *Physical Review B*, **74**, 104113–9.
- Zhong, W., Vanderbilt, D. and Rabe, K. M. (1994) *Physics Review Letters*, **73**, 1861.
- Zhong, W., Vanderbilt, D. and Rabe, K. M. (1995) *Physical Review B*, **52**, 6301.
- Zybill, C. E., Li, B., Koch, F. and Graf, T. (2000) *Physics Status Solidi*, **177**, 303.

---

I S Z A F R A N I A K - W I Z A, Poznan University of  
Technology, Poland and M A L E X E and D H E S S E,  
Max Planck Institute of Microstructure Physics, Germany

## 20.1 Introduction

Functional materials in real applications have the form of patterned structures rather than 2D infinite thin films. For example, piezoelectric micro-sensors and micro-actuators involve piezoelectric thin films patterned into structures of micrometer-range sizes. For future applications, e.g. memories, ferroelectric films should be patterned into structures with lateral sizes in the nanometer range. For example, in a prospective 10 Gbit non-volatile ferroelectric random access memory (NV-FeRAM), the lateral area of the whole memory cell, consisting of a capacitor and a transistor, should not exceed 100 nm, implying ferroelectric capacitors having lateral sizes well below 100 nm [1, 2]. It is well known that many materials change or even lose their useful properties as soon as their sizes fall below a certain limit [3, 4]. During the past decade a large amount of effort has been made to understand whether electroceramic cells of 100 nm lateral sizes can still show piezo- or ferroelectric properties. Most investigations were performed on ultra-thin films, but these can lead to conclusions that are not always true for geometrically confined structures such as islands, nanotubes or nanorods. In this case the relatively large proportion of surfaces and interfaces can lead to domain pinning or to other surface-related problems.

On the other hand the properties of nanostructures can also depend on the route of their preparation. Different preparation methods can impose a certain degree of specific defects, a certain porosity level, the incorporation of foreign atoms or, for example, hydroxyl groups, interfacial stresses, etc. Additional problems can occur during conventional and non-conventional patterning processes when part of the continuous film is removed in order to obtain separate structures [5–7]. Self-patterning methods seem to be appealing for the production of good-quality structures that can be used for basic investigations (e.g. for size–effect-related issues). Additional advantages of such methods are usually lower fabrication costs (compared with, e.g., lithography-based routes) and relatively fast preparation time (compared

with, e.g., direct e-beam processes) [8]. That can make them attractive from the point of view of potential applications. As one possible self-patterning route, the formation of islands during very early stages of film formation has been investigated [9–11].

In the middle of the 1990s, it was observed that the preparation of ultra-thin epitaxial films by chemical solution deposition (CSD) is hindered by a microstructural instability [12, 13]. Oxide thin films with a thickness below a critical value break into islands after a high-temperature annealing. The driving force of this process is an excess of the total free energy of the continuous film compared with a film that only partially covers the substrate. The free energy is minimized by (i) the film–substrate system through the formation of surfaces of low energy [14], and eventually (ii) the formation of islands, which lowers the interface area and thus the interface energy. Although this effect has initially been regarded as an undesirable effect occurring during the preparation of ultra-thin epitaxial films, it can favorably be applied for the preparation of nano-islands. First attempts were focused on the fabrication of lead titanate nanograins [15–17]. However, the choice of the substrate, which was platinum-coated silicon, resulted in a random orientation of the nanograins. The analysis of the size effect of such randomly oriented nanograins can be rather complicated if there is no information on the crystal orientation of each grain, because ferroelectric and piezoelectric properties are closely connected with the crystallographic orientation [18]. A detailed analysis of lead titanate and ferroelectric lead zirconate titanate nanostructures, prepared on Pt-coated Si wafers, has shown that they do not possess single-crystal quality, since twin boundaries were observed by transmission electron microscopy (TEM) [9]. Therefore, it can be difficult to distinguish between the intrinsic and extrinsic size effects associated with crystal imperfections. The best way to investigate size effects in ferroelectrics is to produce single-crystal, defect-free, monodomain nanostructures with controlled size and orientation. The present chapter considers the preparation and properties of single-crystal ferroelectric nanostructures obtained by the self-patterning method based on the instability of ultra-thin films.

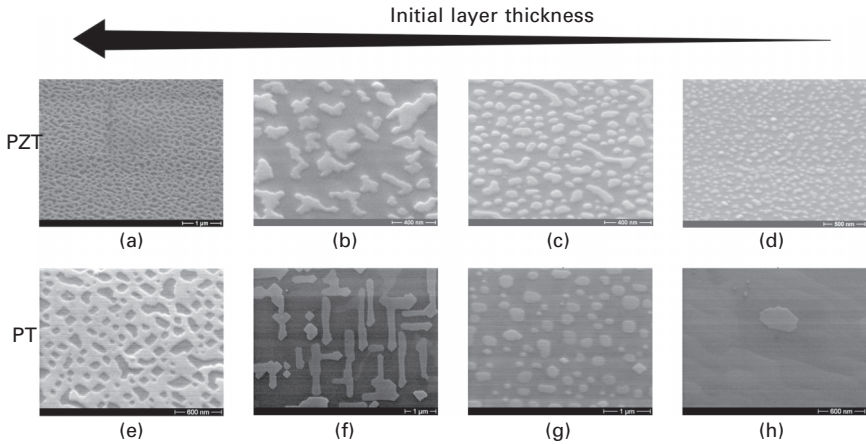
## 20.2 Preparation of nano-islands

Nanosize lead zirconate titanate epitaxial crystals were prepared by a conventional chemical solution deposition. However, the film thickness was much smaller compared with the conventional method, and the post-annealing treatment was performed at slightly higher temperatures than usual [19]. The amorphous ultra-thin films were deposited by spin-coating. Different single crystals such as (001)-oriented  $\text{SrTiO}_3$  (STO) (from CrysTec GmbH, Berlin), (001)-oriented  $\text{MgO}$  and (001)-oriented  $\text{LaAlO}_3$  (LAO) (both from Crystal GmbH, Berlin) were used as substrates. For electrical measurements, STO

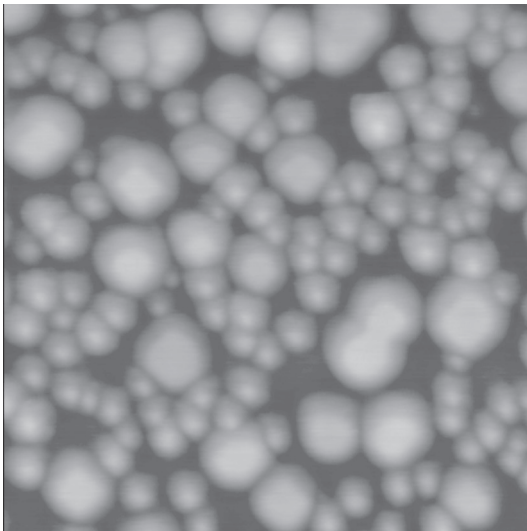
substrates with a niobium doping were used. The Nb concentration of 0.5% ensures some conductivity, so that the substrate can also take the role of a bottom electrode. Two types of solutions were used, *viz.* a commercial precursor (PZT9906, Chemat Technology, Inc.) for  $\text{Pb}(\text{Zr}_{0.52}\text{Ti}_{0.48})\text{O}_3$  (denoted as PZT 52/48) and metalorganic solutions for lead zirconate titanate with different Zr/Ti contents (denoted, e.g., PZT 20/80 for  $\text{Pb}(\text{Zr}_{0.2}\text{Ti}_{0.8})\text{O}_3$ ). The initial film thickness was determined by the degree of dilution of the raw precursors in their solvents (butanol in the case of the commercial precursor, and xylene for metalorganic ones) within a wide range (e.g. from 1:10 to 1:50 for  $\text{Pb}(\text{Zr}_{0.52}\text{Ti}_{0.48})\text{O}_3$ ), and by adjusting the spinning speed from 3000 to 6000 rpm. The gel film obtained was dried on a hot plate at 80 °C for 5 min, pyrolyzed at 300 °C for 5 min, and finally crystallized at 600–1100 °C for 5 min–10 h in a lead-rich atmosphere. Energy dispersive spectroscopy (EDS) analysis in a scanning electron microscope (SEM) was used to control the PZT compositions. In all cases the composition after crystallization agreed well with the nominal composition of the raw precursors.

### 20.2.1 The control of size and distribution of the nano-islands

The growth of nanostructures was firstly investigated as a function of the initial film thickness, the crystallization temperature, and the lattice mismatch between the substrate and the nano-islands. The initial thickness of the deposited amorphous layers has been adjusted by the combination of spinning speed and dilution of the raw precursors. After crystallization at 800 °C for 1 h, the final morphology of the layers was examined in SEM and by atomic force microscopy (AFM). Figure 20.1 shows the SEM images of the final structures of PZT 52/48 and lead titanate ( $\text{PbTiO}_3$ , denoted as PT). The deposition conditions were kept the same, only the precursor dilution was changed. All AFM investigations have shown that the nano-islands obtained by this method have similar height. As expected, thicker PZT 52/48 films, with an initial thickness below the critical value, have transformed into films with faceted holes after the crystallization. A deposition using a higher dilution results in ultra-thin films, which, after the high-temperature crystallization, break up into small single-crystal islands, as shown in Fig. 20.1. For the highest dilution (1:40) the resulting islands have a height of about 9 nm and lateral sizes of 40–90 nm with a relatively narrow distribution in size (Fig. 20.1d). The islands are distributed on the substrate with a high density of about 150 crystals on an area of  $1\ \mu\text{m}^2$ . Thicker layers obtained with lower dilution (1:25) result in islands that are both larger and higher (Fig. 20.1b). Their height increases to about 25 nm, and the distance between close neighbours increases as well, resulting in a low areal density of the islands of about  $30/\mu\text{m}^2$ . If the initial film thickness is just below a critical value, larger



20.1 Scanning electron images of final PZT 52/48 (a)–(d) and  $\text{PbTiO}_3$  (e)–(h) structures obtained after 1 h crystallization of ultra-thin films at 800 °C.



20.2 AFM image of the smallest PZT 52/48 islands on STO (image size  $500 \times 500 \text{ nm}^2$ , z range 10 nm).

islands of irregular shape form, as shown in Fig. 20.1a. The smallest structures obtained in this way have a height of about 3–4 nm and a lateral size of 30–40 nm according to the AFM investigation shown in Fig. 20.2.

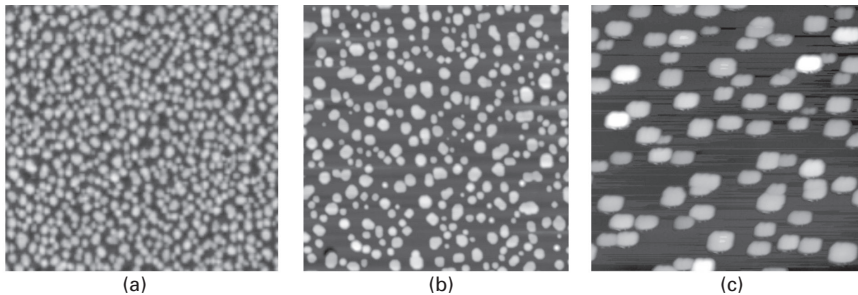
Similar behavior has been observed for the PT structures. If the initial film thickness is just above a critical value (dilution 1:5), faceted holes develop in the film (Fig. 20.1e). The thinner initial layer (1:10) has broken

up into relatively large islands. The islands have a different shape from the PZT islands; they have formed elongated stripes, as shown in Fig. 20.1f. The islands have an average height of 15 nm and a wide distribution in lateral sizes, up to more than a few hundred micrometres. As it was observed previously, thinner layers compared with thicker ones create more regular islands that are both higher and laterally larger up to a height of about 20 nm (Fig. 20.1g) and their areal density is lower. The smallest islands obtained from the 1:25 diluted precursor have a height of about 10 nm and lateral sizes of about 50 nm with a relatively narrow distribution in size (Fig. 20.1h).

### 20.2.2 The influence of the crystallization temperature

The crystallization temperature plays an important role in the morphology of the final structures. It was found that, in order to obtain uniform islands, a thermal treatment at 800 °C for 1 h is necessary. The annealing at higher temperature results in the formation of larger islands. For instance, as Fig. 20.3 shows, the height of nanocrystals obtained from the 1:40 diluted precursor increases from 9 nm after a treatment at 800 °C up to 20 nm after an annealing at 1100 °C. The area density drastically decreases down to 15–20 islands per  $1 \mu\text{m}^2$ . Most probably at higher temperature the mobility and surface diffusion are enhanced and that allows the deposited material to migrate and to coalesce into larger islands. As a result the PZT nano-islands are higher and more separated.

The mechanism of nano-island formation can be described similarly to that used to produce semiconductor quantum nanostructures in materials like Ge on Si, in which the shape and distribution obeys the Shchukin–Williams theory [20, 21]. This theory predicts the formation of three different kinds of structure (pyramids, domes and superdomes) as a function of the coverage



20.3 AFM images (size:  $2 \times 2 \mu\text{m}^2$ ) of PZT 52/48 nanocrystals on  $\text{SrTiO}_3$  crystallized at (a) 800 °C (z range 20 nm), (b) 950 °C (z range 20 nm), and (c) 1100 °C (z range 35 nm).

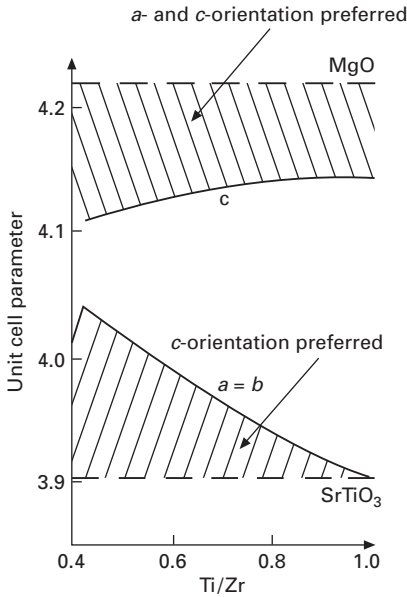


and the crystallization temperature. The detailed analysis of the influence of the thickness of the amorphous layer and the crystallization temperature on the final shape of the PZT islands was presented in Dawber *et al.* [22]. For large thicknesses superdomes are dominant; as the thickness is decreased the coexistence of domes and superdomes changes to a dominance of domes. The domes and superdomes can be distinguished both on the basis of size (superdomes are significantly larger than domes) and the kind of facets present (superdomes have steeper side facets and a larger flat top facet than domes). After processing at higher temperatures (e.g. 1100 °C) even for the thinnest amorphous layers the superdomes become dominant. This may be advantageous for the fabrication of an array of superdomes which are further spaced from each other, thus avoiding the formation of merged domes which drastically reduce the degree of registration in an array of nanocrystals.

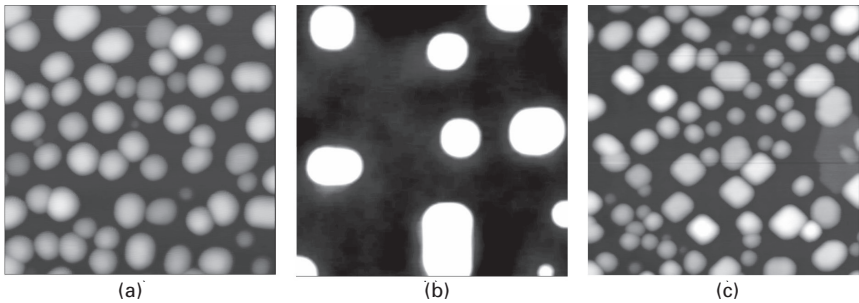
On the other hand a crystallization at higher temperatures can cause undesirable effects. Quite often losses of volatile elements or compounds, which become more important at higher temperature, have a big impact on the final composition and the phase contents (e.g. pyrochlore phases are formed instead of the perovskite phase). An additional disadvantage of this treatment is the possibility of diffusion through layer/substrate interfaces, which may result in the formation of solid solutions. Because of these facts the lowest possible crystallization temperature (e.g. 800 °C) was chosen for the fabrication of uniform nanostructures, the physical properties of which have been investigated.

### 20.2.3 The effect of the lattice mismatch

As is clear from Fig. 20.1, the shape of the islands depends on the composition of the deposited layer. The Zr/Ti ratio has an influence on the tetragonality (i.e. the ratio  $c/a$  of the lattice parameters) and therefore the lattice mismatch varies with the Zr/Ti composition (Fig. 20.4). The influence of the lattice mismatch on the growth mechanism has been the subject of detailed studies during recent decades [4]. The influence of the lattice mismatch on the formation of nanoislands was investigated as well. For these investigations several samples of different compositions were prepared, and all were crystallized at 800 °C for 1 h. The wide range of PZT compositions (Zr contents between 0 and 48%) of islands deposited on single crystal STO, LAO and MgO substrates provided a variation of the lattice mismatch  $\delta$  ( $\delta = (a_{\text{island}} - a_{\text{substrate}})/a_{\text{substrate}}$ , where  $a$  are the respective lattice constants of island or substrate) between 6.5% and 0.2%. It was shown that PT islands on (001) STO substrates formed elongated structures (see Fig. 20.1), whereas thin layers of PZT with higher Zr concentration broke up into smaller structures. In the case of PZT/STO and PZT/LAO, small structures were obtained with an average height of 10 nm and a lateral size of about 50 nm. The deposition



20.4 Schematic diagram of the lattice mismatch and possible orientations of PZT.



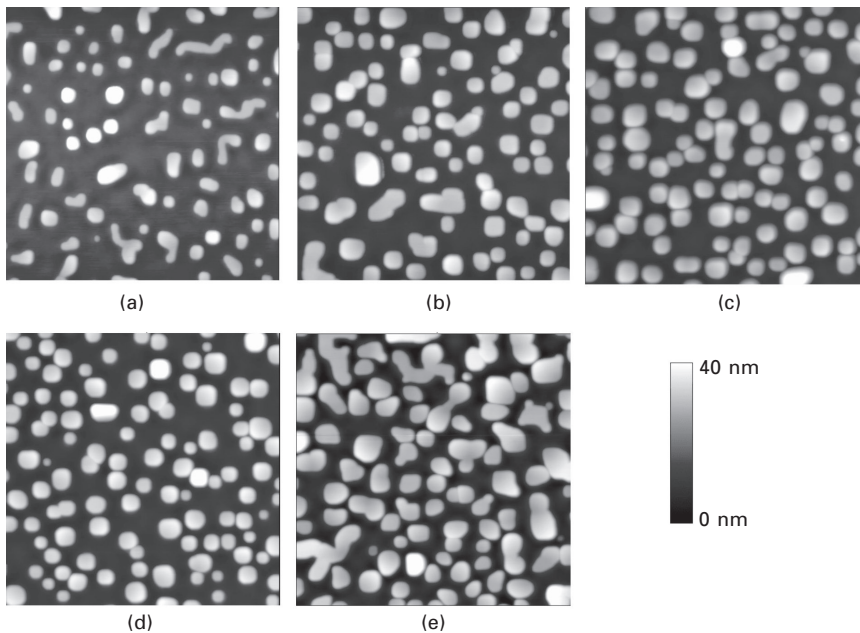
20.5 AFM images of PZT 20/80 nanoislands with the same initial thickness deposited on (a) (001) STO, (b) (001) MgO and (c) (001) LAO. The images were taken from  $500 \times 500 \text{ nm}^2$  area, z range is 20 nm.

of PZT onto LAO substrates produced two types of islands – smaller and larger ones having a more square shape (Fig. 20.5). In both cases the islands are distributed on the substrate with a high density of about 150–200 crystals on an area of  $1 \mu\text{m}^2$ . PZT islands on MgO substrates became both laterally larger and higher (Fig. 20.5). Their height increases to about 25 nm, and the lateral size may reach a few hundred nanometers. Again due to the conservation of the total volume, the distance between close neighbors increased resulting in a low area density of the islands.

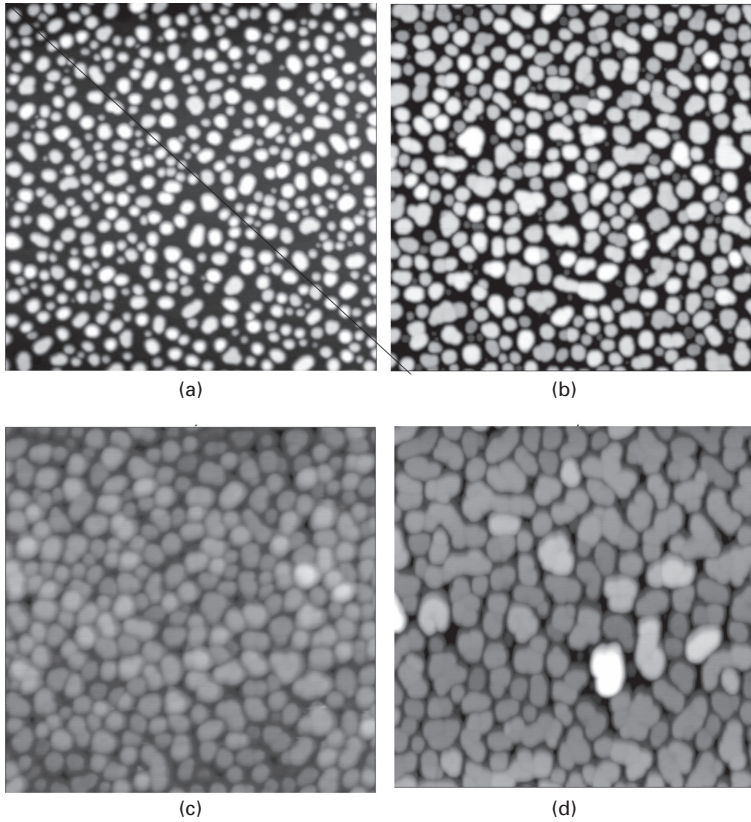
The results clearly show that a certain value of the lattice mismatch strain helps the total system to break up into islands. The smallest strain of PT/STO (0.2%) allows elongated stripe-like structures to be prepared. The islands obtained in such systems where the lattice mismatch is relatively large are usually bigger, and their density on the surface is smaller; however, in this case the islands usually possess two possible orientations (see Section 20.3.1 below).

#### 20.2.4 Multi-step deposition

In order to control the sizes of the nano-islands more precisely, a multi-step deposition procedure has been applied. Figure 20.6 shows the morphology of PZT 20/80 structures on MgO after each deposition step, whereas Fig. 20.7 shows the deposition of PZT 52/48 on STO. The first deposited amorphous layers with a thickness below the critical value were crystallized at 800 °C. The films broke up to form nano-islands during the crystallization stage and then samples were recoated with an amorphous layer having the same thickness as the first layer. Again the film broke up during the thermal treatment. It was observed that most of the ‘old’ islands increased their lateral size but



20.6 PZT 20/80 nano-islands after (a) first, (b) second, (c) third, (d) fourth and (e) fifth deposition on (001) MgO substrates. The scanning area was  $2 \times 2 \mu\text{m}^2$ .



20.7 PZT 52/48 nano-islands after (a) first, (b) second, (c) third and (d) fourth deposition on (001) STO substrates. The images were taken from  $2 \times 2 \mu\text{m}^2$  area, z-range 20 nm.

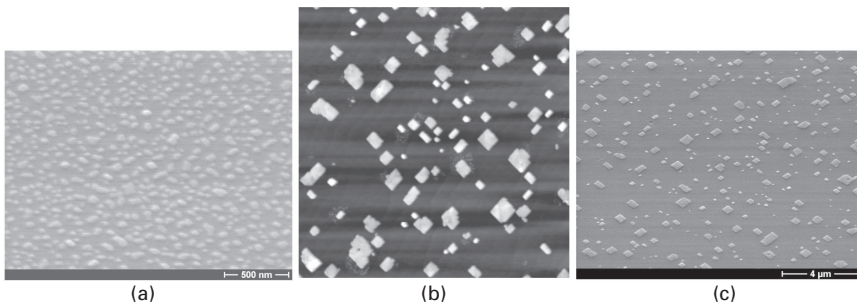
new ones appeared with the same lateral size as those obtained previously. It was possible to repeat this procedure several times until the islands started to coalesce. Owing to the lower density of relatively big islands on the MgO substrate it was possible to repeat the procedure up to five times, but in the case of the very dense islands on STO the procedure was limited because coalescence started already during the third step.

Generally this procedure can be repeated several times until a coalescence process starts. From a practical point of view it is easier to use a multi-step deposition procedure in the case of islands with a relatively large distance between neighbors. A precise control of the island size could be possible using a more diluted precursor; however, each deposition cycle (solution deposition, pyrolysis, and crystallization step) could also increase the number of dust particles and impurities on the sample surface. As a result such a thin film would not be deposited homogeneously, resulting in large structures,

often with a somewhat strange shape, or even in continuous films around imperfections.

### 20.2.5 Towards nano-island registration

One of the disadvantages of self-assembly methods is the random distribution of the final structures on the substrate. As expected, nanostructures obtained by this method did not show an ordered arrangement in their positions. The initial thin film broke up at random places, and formed a collection of irregularly spaced nanocrystals. Because nanostructures are formed as the result of film breaking, it is possible to introduce defects that could play an essential role in creating discontinuities in the film during thermal treatment before the crystallization process would start. Up to now the influence of two types of defects has been investigated. In both cases the initial thin layer of PZT 52/48 was deposited and dried at 80 °C. Then defect sites at regular spatial intervals were intentionally introduced. During the first experiment defects were created by mechanical imprint using a stamp with a regular array of pyramidal  $\text{SiN}_4$  structures. The height of the pyramids was about 260 nm and the spacing between them 0.5  $\mu\text{m}$ . In the second experiment the defect sites were imposed by an electron beam. In both cases the final structures obtained after defect introduction and crystallization (Fig. 20.8) are apparently different from the previous structures. The islands are larger and higher and they have a well-defined rectangular shape. Their edges are parallel to the  $[110]$  and  $[1\bar{1}0]$  crystallographic directions of the substrate. The distances between nearest neighbors are much larger than in the case of non-treated samples. It seems that the introduction of defects can be used as a method for registration; however, the presented registration is still relatively poor. Most probably it could be improved by optimizing the distance between the introduced defects



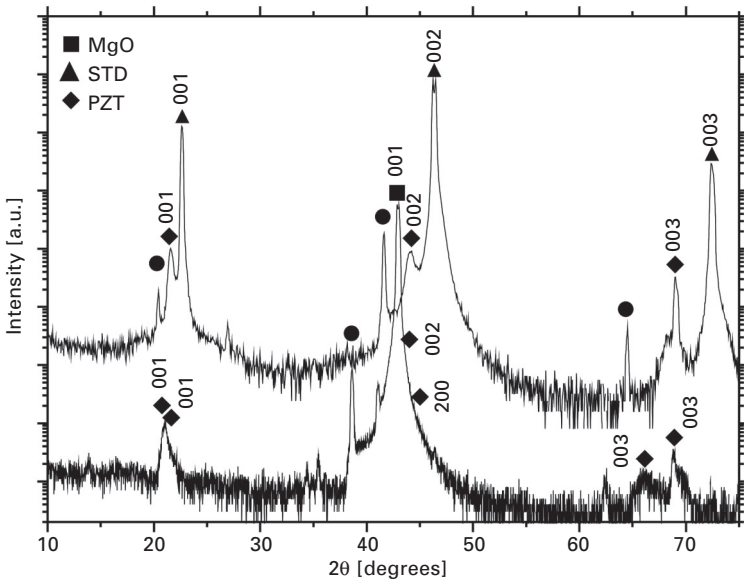
20.8 PZT 52/48 nanostructures obtained after crystallization of the same thick amorphous layer (a) not treated, (b) mechanically imprinted (area  $10 \times 10 \mu\text{m}^2$ , z range 50 nm), (c) periodically exposed with  $1000 \mu\text{C}/\text{cm}^2$  doses and 1  $\mu\text{m}$  pitch with the same initial thickness.

with respect to the island distribution (particularly the spacing between the self-patterning structures should be taken into account). The mechanical imprint technique seems to be very attractive due to its efficient (cheap and fast) way of application on a large-area scale.

## 20.3 Physical properties of the nano-islands

### 20.3.1 Structural investigation

For larger and smaller structures X-ray diffraction (XRD) analysis and/or high-resolution transmission electron microscopy (HRTEM), respectively, were performed to obtain structural information on the nanocrystals. XRD diffraction patterns of PZT/STO nano-islands, obtained at 800 °C, show the  $00l$  reflections from the STO substrate (cubic), and only the  $00l$  reflections of the tetragonal PZT (Fig. 20.9). This proves the epitaxial relationship between the substrate and the nanostructures. No secondary phase peaks were detected in the XRD patterns, confirming the formation of a good-quality perovskite phase. XRD has shown that the PZT islands on STO have a  $c$ -axis orientation. The XRD patterns obtained for PZT nano-islands grown on (001) MgO substrate showed more diffraction peaks that could be indexed as ( $h00$ ) and ( $00l$ ) reflections (Fig. 20.9). Obviously the larger lattice misfit

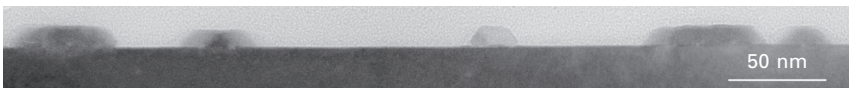


20.9 X-ray diffraction pattern of PZT 52/48 nanocrystals on (001) STO and (001) MgO substrates. The peaks labelled with circles indicate substrate peaks originating from the remaining Cu  $K_{\beta}$  radiation.

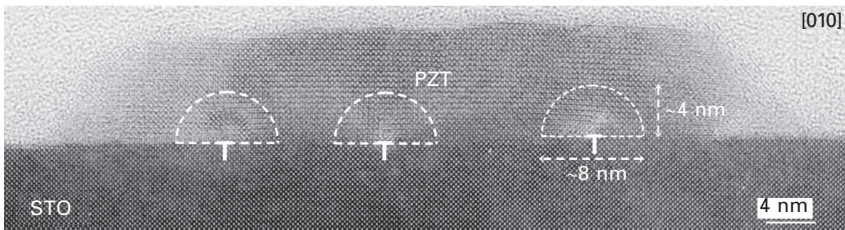
(PZT/MgO) results in the formation of epitaxial islands with both *a*- and *c*-axis orientations.

Further structural information about the nanoislands was obtained from TEM analysis (Figs 20.10 and 20.11). The low-magnification pictures (Fig. 20.10) show that all islands have a uniform height. Moreover, all the structures have a well-defined truncated pyramidal shape with relatively sharp facets. The facets preferably consist of {111} or {110} planes as the side walls of the nanocrystals. The top facet of the island is parallel to the {001} substrate plane. The appearance of such facets is related to previous research that showed the ultra-thin film breaking up into small structures with lower energy planes as result of microstructural instability and that in such a way the total energy is reduced [12–14].

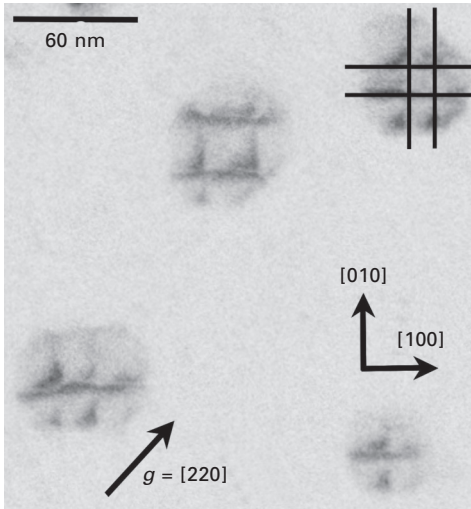
The HRTEM images of several PZT 52/48 /STO nano-islands have confirmed that they are single crystals which are uniformly *c*-domain-oriented without any 90° domains being present. All nano-islands have almost an atomically flat surface. The rare steps observed on the top facet are related to the substrate steps with a height of half a unit cell. The interface is atomically flat, which indicates that any diffusion between the nanocrystal and the substrate does not occur. The crystals are free from volume defects, and the only defects are dislocations concentrated along the interface. They are caused by stress relaxation-induced by the lattice mismatch between the STO substrate and the PZT islands. The distance *d* between the dislocations estimated on the basis of several tens of nano-islands gives values between 9 and 13 nm. This value is in agreement with the calculated spacing,  $d = a / \delta$  (where *a* is the lattice constant and  $\delta$  is the value of the lattice misfit), which is about 12 nm. It should be underlined that in each island there is a



20.10 Low-magnification electron micrograph of PZT 52/48 on STO.



20.11 Cross-section HRTEM image of a single PZT 52/48 nanocrystal. The distorted regions near misfit dislocations (showed by 'T') are marked by dotted line.



20.12 Plan-view HRTEM image of PZT 52/48 nano-islands on STO substrate (the dislocation network is marked in the upper right corner).

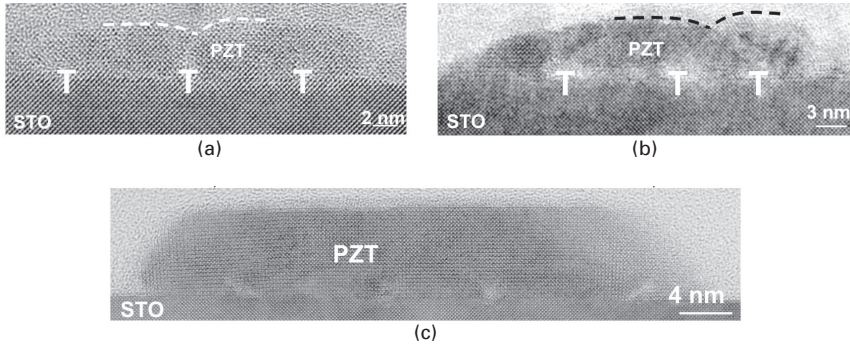
network of misfit dislocations present, the dislocations on average having a mutual distance of 12 nm. The dislocation network is clearly visible on plan-view TEM images (see Fig. 20.12).

### 20.3.2 The growth mechanism of the nano-islands

To investigate the growth mechanism of the PZT 52/48 nano-islands several samples were prepared under different conditions: the crystallization temperature was varied between 650 and 800 °C and the annealing time between 5 min and 10 h. All experiments were carried out on samples with the same thickness of the initial layer. Each sample was studied using HRTEM (Fig. 20.13). In the early stage of nucleation the pre-existing holes penetrate down to the substrate surface. As a result a non-faceted discontinuous layer of about 3–4 nm thickness is formed. During longer heat treatments (650 °C for 1 h) the nano-islands migrate on the substrate surface and coalesce into larger irregular structures. The nanostructures crystallized at higher temperatures (e.g. at 800 °C for 5 min) have a better thickness uniformity; however, the coalescence process is not finished. An annealing as long as 1 h at 800 °C is required to form the equilibrium shape and distribution of the islands. A thermal treatment at 800 °C longer than 1 h does not lead to significant changes in island morphology, shape and distribution.

As it was previously shown, the nanostructure formation is connected with the lowering of the interfacial energy [12–14]. In order to minimize the





20.13 Cross-sectional HRTEM micrographs of PZT nano-islands grown on STO substrates (a) at 650 °C for 1 h, (b) at 800 °C for 5 min and (c) at 800 °C for 1 h. The dashed lines in (a) and (b) show the coalescence of two neighboring islands.

PZT/STO interfacial energy, pre-existing ‘holes’ at the thin, amorphous CSD-prepared PZT layer accumulate during annealing and then grow through the PZT layer to uncover the STO substrate, leading to isolated islands with misfit dislocations at the interface. At longer annealing times at high temperatures, isolated PZT islands may coalesce into bigger ones, simultaneously forming energetically favorable  $\{111\}$  and  $\{110\}$  facets. However, a certain amount of thermal energy (equivalent to the 1 h treatment at 800 °C) is required to reach the equilibrium state in which well-defined facets appear.

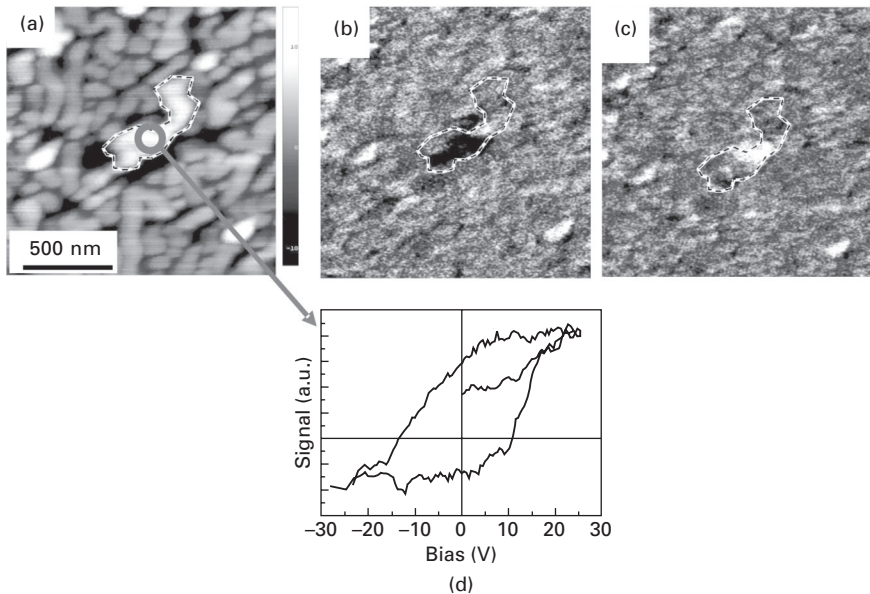
### 20.3.3 Ferroelectric properties

Owing to the small size of the nanocrystals, their characterization cannot be achieved using conventional measurement techniques. For this purpose, scanning probe techniques, in particular piezoresponse force microscopy (PFM), have proven to be most valuable. The local polarization state and the electromechanical properties of the ferroelectric nanostructures can be probed via the converse piezoelectric effect using the AFM technique combined with a lock-in technique. This method is based on the detection of local vibrations of a ferroelectric sample induced by a testing a signal applied between the conductive tip of the PFM and the bottom electrode of the sample [7, 23]. The role of the bottom electrode is usually played by a conductive substrate; in the case of PZT nano-islands Nb-doped STO substrates allowed to study the ferroelectric properties. Because of the strong relation between the piezoelectric coefficient and the spontaneous polarization the material expands or contracts under the applied electric field. The sign of the piezoelectric coefficient is determined by the direction of the spontaneous polarization with respect to that of the applied electric field.

The PZT 52/48/STO:Nb islands with heights above 25 nm or with a large lateral size show a well-developed piezoelectric hysteresis loop. Figure 20.14 shows the topography and piezoresponse images proving the switching of the polarization in crystals with a height of 15 nm. The grain marked by the dashed contour was successively polarized negatively (polarization pointing into the sample, Fig. 20.14b), and then positively (Fig. 20.14c) by the biased AFM tip. It was also possible to record a loop on an island of irregular shape. Similar loops were obtained for islands with heights above 25 nm and smaller lateral size and for the structures after mechanical imprint. For smaller structures (smaller island volume, e.g. low height and low lateral size) there were problems in obtaining a hysteresis loop.

### 20.3.4 Impact of the misfit dislocations on the ferroelectric switching

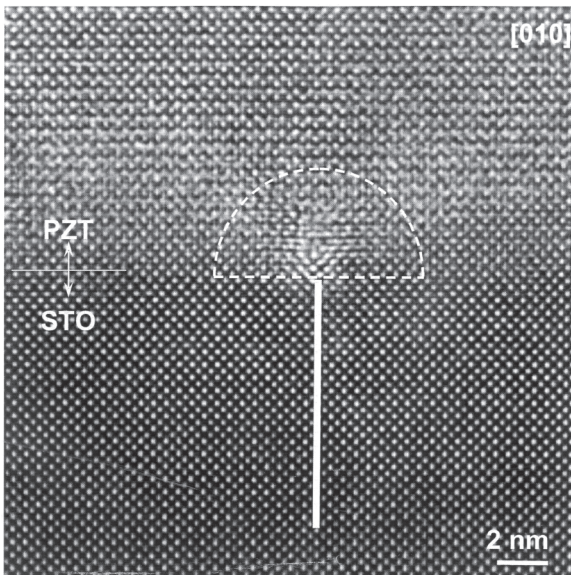
In order for switching to occur it is necessary that the crystal possesses more than a critical number of unit cells with the proper crystallographic structure. The PZT/STO nano-islands have relatively large regions affected by the dislocation network (see Figs 20.11 and 20.12). In order to investigate the long-range strain fields associated with the dislocation, a geometric phase



20.14 Switching of an individual nanocrystal by PFM: (a) topography (z-scale 25 nm) and piezoresponse images after applying (b) a negative and (c) a positive dc voltage. (d) Hysteresis loop recorded on the structure in the middle of the image (a).

analysis of HRTEM images was performed. Based on this analysis, the details of which are given in Chu *et al.* [24], the in-plane ( $\epsilon_{xx}$ ), shear ( $\epsilon_{xy}$ ) and out-of-plane ( $\epsilon_{yy}$ ) strain fields have been determined. The strain, associated with the misfit dislocations, is predominantly localized on the PZT side. The estimation has shown that the strain extends into the PZT phase for about 4 nm from the dislocation core (Fig. 20.15). Based on this value it is possible to calculate the partial volume ( $V_p$ ) affected by the dislocations. In the case of PZT 52/48 nano-islands on STO, with a base length of about 50 nm and a height of about 9 nm,  $V_p$  can be estimated to about 50% of the total volume of the island. Because ferroelectricity is a cooperative phenomenon of a sufficiently large number of non-centrosymmetric unit cells, this significant value could influence the ferroelectric properties. In the affected regions, the PZT lattice deviates from the regular tetragonal structure, and the long-range correlations of the local polarization may thus break down, leading to a polarization instability. As a result, ferroelectric switching was not observed in these nano-islands using PFM. By contrast, in PZT 52/48 islands with a double height of  $\sim 20$  nm,  $V_p$  is only about 25% and in this case a well-defined piezoresponse loop has been recorded (see Fig. 20.14).

To distinguish the impact of a purely intrinsic size effect (which in principle may occur in structures with a height of only about 10 nm) from the influence of dislocations, dislocation-free islands were fabricated and investigated.

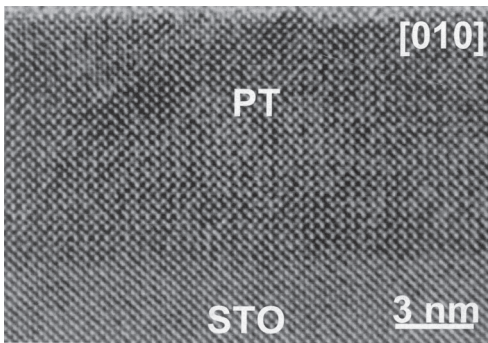


20.15 Cross-sectional HRTEM image of a PZT nano-island with the distorted regions near misfit dislocations (dashed line). The additional half-plane on the substrate side is marked as a solid line.

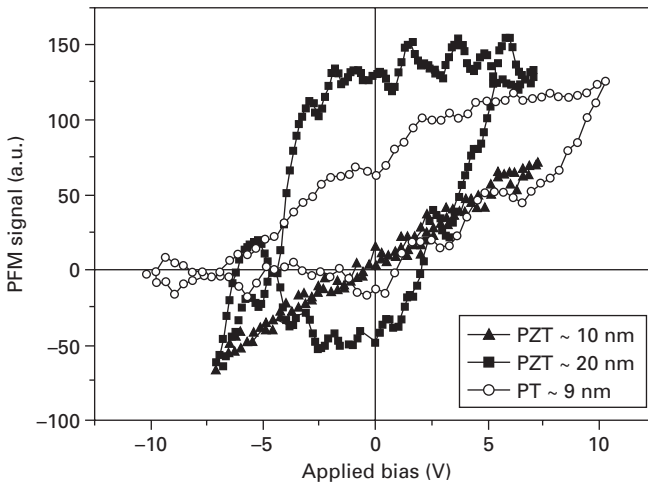
One of such systems is PT/STO, where the calculated spacing between misfit dislocations (about 195 nm) is much larger than the island size. HRTEM studies have proven that the PT/STO interface is atomically sharp and misfit dislocations are not present (see Fig. 20.16). An individual PT island on STO has shown a piezoelectric hysteresis loop, proving the switching behavior of 10 nm high PT structures (Fig. 20.17). This result is also in good agreement with recent results showing the ferroelectric properties of thin lead titanate film with thickness of several unit cells [25, 26].

### 20.3.5 Dislocations and domain wall formation

During the analysis of nanoislands with different interfacial strain, a few islands were found that contain a twin boundary [27]. The HREM image of



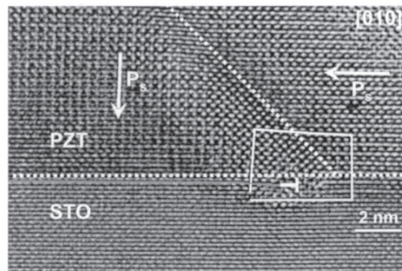
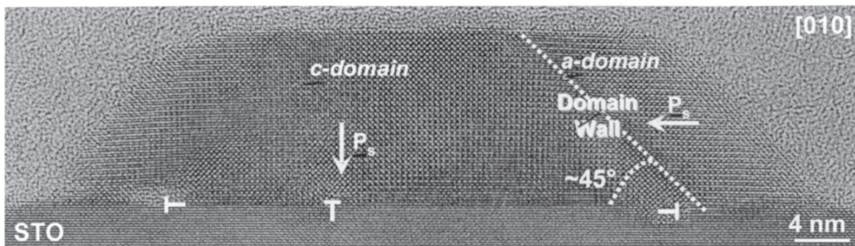
20.16 HRTEM image of PT nanocrystal on STO.



20.17 PFM measurements of local hysteresis loop of three different islands.

such an island is shown in Fig. 20.18. This island is slightly larger than those discussed before. The PZT 40/60 island shows an epitaxial  $c$ -axis orientation with respect to the substrate; however, a small region (on the top right on Fig. 20.18) possesses an  $a$ -axis orientation. Between these two regions a  $90^\circ$  domain wall is observed. The estimated angular separation ( $\alpha$ ) between these two regions is about  $1^\circ$  which is smaller than the calculated value of  $2^\circ$ . This suggests that the ferroelastic strain distribution near the domain wall is rather complex. The defect analysis has shown that – besides the dislocations related to the relaxation of the lattice mismatch (with an extra half plane on the substrate side) – there is a dislocation related to another extra half plane in the substrate which is parallel to the interface, i.e. a dislocation with a Burger's vector perpendicular to the plane of the interface.

The geometric phase analysis of HRTEM images was used in order to determine the strain near the domain wall. The corresponding details were published in Chu *et al.* [27]. In the region far from the interface the strain distorts both the  $a$ - and  $c$ -domain regions. The wall region exhibits a compressively strained area embedded in a relatively strain-free surrounding. The estimated thickness of the domain wall, based on this analysis, is about 1.5 nm (close to four unit cells). A more complicated situation prevails near the interface. The  $90^\circ$  domain wall does not end directly on the edge dislocation, but on a distance of about 2 nm from it. The strain distribution in this region



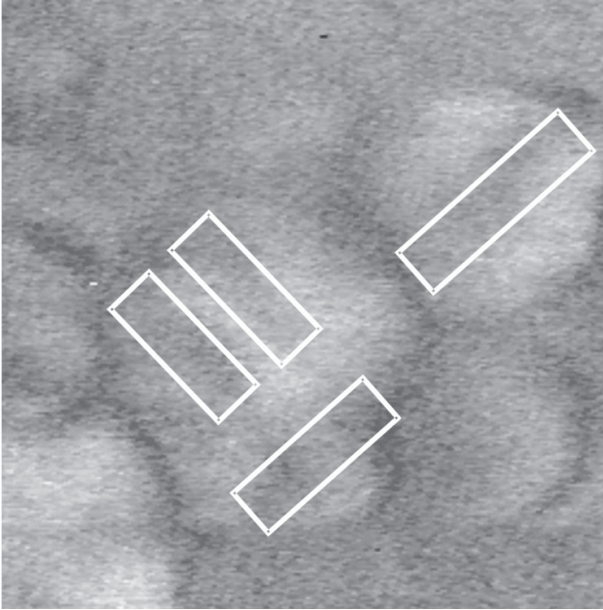
20.18 Cross-sectional HRTEM image of a PZT 40/60 island showing the twin wall. Bottom: Magnified section of the region close to the interfacial dislocation.

is more complicated. Near the edge dislocation with a perpendicular Burger's vector a tensile strain is observed. Near the interface and the wall, this tensile strain is reduced by the compressive strain caused by the presence of the twin wall. This elastic coupling by partial strain annihilation qualitatively minimizes the long-range electromechanical energy. The slight deviation between the calculated and the observed value of the angular separation and the gentle broadening of the wall width near the dislocation core can be understood as effects of the interaction of long-range strain fields of the twin wall and the dislocation core. More important for future PZT applications is the fact that the switching behavior of the islands containing a twin wall is different. If an electric field is applied perpendicularly to the interface of the island, switching of the single *c*-domain state has to be accomplished by removing the twin wall from the island. This electric field-driven movement is, however, difficult, since the long-range strain field of the interfacial dislocation imposes a potential barrier on the twin wall. This fact can cause difficulties in mobilizing the twin wall by applying electric fields. As a consequence, the twin wall in the islands should thus not be electrically active. Indeed the nano-islands, investigated by PFM, show large regions where the PFM signal is about zero (see Fig. 20.19a). This value suggests the presence of the 90° domains. Figure 20.19(b) shows the hysteresis loop acquired on the structure in the middle of the image. Its shape reveals the huge imprint, which can be associated also with the domain pinning.

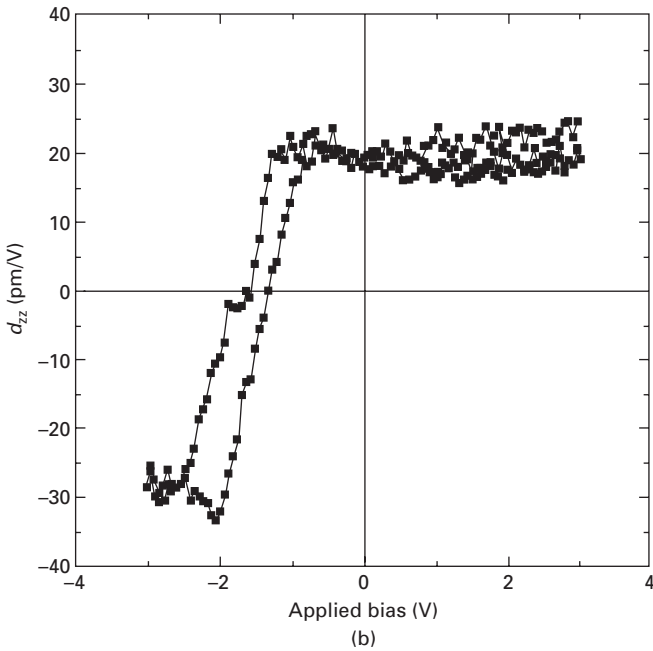
## 20.4      Conclusions and future trends

The self-patterning method is a new appealing way of nano-island fabrication. The lateral size and the height of the nanostructures can be controlled by adjustments of the deposited film thickness, of the crystallization conditions and a proper choice of the substrate. The dislocations present in such structures can have a large impact on the final properties. The network of misfit dislocations forming as a result of lattice mismatch relaxation affects a relatively large volume of the island. Such islands are not switchable and they lose the useful properties for an application as memories or storage devices. Dislocations with a Burger's vector perpendicular to the interface and connected with a twin wall can render the system electrically inactive. Thus the formation of such defects has to be avoided, if ferroelectric oxides with nanometer-size sizes are to be employed for future applications that require ferroelectric switching.

It appears that an 'interface engineering' is required for epitaxial nano-islands, if the latter should retain their ferroelectric properties, in particular polarization switchability. The substrate should be carefully chosen, not only under the aspect of chemical stability (avoiding interfacial diffusion and reaction processes at the processing temperatures), but also adapting the



(a)



(b)

20.19 (a) AFM image of PZT 40/60 nano-islands on STO ( $200 \times 200$  nm<sup>2</sup>,  $z$  range 10 nm). The marked regions have shown a PFM signal about zero. (b) Hysteresis loop recorded on the structure in the middle of the image (a).

crystal structure and lattice parameter of the substrate to those of the ferroelectric nano-islands, in this way minimizing the density of interfacial dislocations and other interfacial defects at the nanostructure/substrate interface. Nanosized ferroelectric crystals are thus another area of technology where interface engineering is indispensable.

## 20.5 Acknowledgments

This work has been performed in close collaboration with M.-W. Chu, M. Dawber, C. Harnagea, R. Scholz and J.F. Scott, to whom the authors are grateful for their respective contributions. Special thanks are due to U. Gösele for his continuous support.

## 20.6 References

1. Scott J F, *Ferroelectric Memories*, Berlin, Springer, 2000.
2. International FRAM roadmap; <http://public.itrs.net>.
3. Wang Y G, Zhong W L and Zhang P L, 'Surface and size effects on ferroelectric films with domain structures', *Phys Rev B*, 1995 **51** 5311.
4. Waser R (ed.), *Nanoelectronics and Information Technology: Advanced Electronic Materials and Novel Devices*, Weinheim, Wiley-VCH, 2003.
5. Ganpule C S, Stanishevsky A, Su Q, Aggarwal S, Melngailis J, Williams E and Ramesh R, 'Scaling of ferroelectric properties in thin films', *Appl Phys Lett*, 1999 **75** 409.
6. Harnagea C, Alexe M, Schilling J, Choi J, Wehrspohn R B, Hesse D and Gösele U, 'Mesoscopic ferroelectric cell arrays prepared by imprint lithography', *Appl Phys Lett*, 2003 **83** 1827.
7. Alexe M, Harnagea, C and Hesse D, 'Non-conventional micro- and nanopatterning techniques for electroceramics', *J Electroceramics*, 2004 **12** 69.
8. Alexe M, Harnagea C, Hesse D and Gösele U, 'Patterning and switching of nanosize ferroelectric memory cells', *Appl Phys Lett*, 1999 **75** 1793.
9. Fujisawa H, Shimizu M, Niu H, Honda K and Ohtani S, 'Observations of domain structure at initial growth stage of PbTiO<sub>3</sub> thin films growth by MOCVD', *Mat Res Soc Symp Proc*, 2000 **596** 321.
10. Fujisawa F, Morimoto K, Shimizu M, Niu H, Honda K and Ohtani S, 'Piezoresponse measurements of Pb(Zr,Ti)O<sub>3</sub> island structure using scanning probe microscopy', *Mat Res Soc Symp Proc*, 2001 **655** CC10.4.1.
11. Alexe M, Harnagea C, Visinoinu A, Pignolet A, Hesse D and Gösele U, 'Patterning and switching of nano-size ferroelectric memory cells', *Scripta Materialia*, 2001 **44** 1175.
12. Seifert A, Vojta A, Speck J S and Lange F F, 'Microstructural instability in single-crystal thin films', *J Mater Res*, 1996 **11** 1470.
13. Zhao L, Chien A T, Lange F F and Speck J S, 'Microstructural development of BaTiO<sub>3</sub> powders synthesized by aqueous methods', *J Mater Res*, 1996 **11** 1325.
14. Lee W T, Salje E K H and Dove M T, 'Effect of surface relaxations on the equilibrium growth morphology of crystals: platelet formation', *J Phys: Condens Matter*, 1999 **11** 7385.



15. Waser R, Schneller T, Hoffmann-Eifert S and Ehrhart P, 'Advanced chemical deposition techniques – from research to production', *Integr Ferroelectr*, 2001 **36** 3.
16. Roelofs A, Schneller T, Szot K and Waser R, 'Piezoresponse force microscopy of lead titanate nanograins possibly reaching the limit of ferroelectricity', *Appl Phys Lett*, 2002 **81** 5231.
17. Roelofs A, Schneller T, Szot K and Waser R, 'Towards the limit of ferroelectric nanosized grains', *Nanotechnology*, 2003 **14** 250.
18. Harnagea C, Pignolet A, Alexe M and Hesse D, 'Piezoresponse scanning force microscopy: what quantitative information can we really get out of piezoresponse measurements on ferroelectric thin films? *Integr Ferroelectr*, 2002 **44** 113.
19. Szafraniak I, Harnagea C, Scholz R, Bhattacharyya S, Hesse D and Alexe M, 'Ferroelectric epitaxial nanocrystals obtained by a self-patterning method', *Appl Phys Lett*, 2003 **83** 2211.
20. Shchukin V A and Bimberg D, 'Spontaneous ordering of nanostructures on crystal surfaces', *Rev Mod Phys*, 1999 **71** 1125.
21. Williams R S, Medeiros-Ribeiro G, Kamins T I and Ohlberg D A A, 'Thermodynamics of the size and shape of nanocrystals: epitaxial Ge on Si(001)', *Annu Rev Phys Chem*, 2000 **51** 527.
22. Dawber M, Szafraniak I, Alexe M and Scott J F, 'Self patterning of arrays of ferroelectric capacitors: description by theory of substrate mediated strain interactions', *J Phys: Condens Matter*, 2003 **15** L667.
23. Alexe M and Gruverman A (eds.), *Nanoscale Characterisation of Ferroelectric Materials – Scanning Probe Microscopy Approach*, Berlin, Springer, 2004.
24. Chu M-W, Szafraniak I, Harnagea C, Scholz R, Hesse D, Alexe M and Gösele U, 'Impact of misfit dislocations on polarization instability of epitaxial nanostructured ferroelectric perovskites', *Nature Materials*, 2004 **3** 87.
25. Streiffner S K, Eastman J A, Fong D D, Thompson C, Munkholm A, Ramana Murty M V, Auciello O, Bai G R and Stephenson G B, 'Observation of nanoscale 180° stripe domains in ferroelectric PbTiO<sub>3</sub> thin films', *Phys Rev Lett*, 2002 **89** 067601.
26. Fong D D, Stephenson G B, Streiffner S K, Eastman J A, Auciello O, Fuoss P H and Thompson C, 'Ferroelectricity in ultrathin perovskite films', *Science*, 2004 **304** 1650.
27. Chu M-W, Szafraniak I, Hesse D, Alexe M and Gösele U, 'Elastic coupling between 90° twin walls and interfacial dislocations in epitaxial ferroelectric perovskites', *Phys Rev B*, 2005 **72** 174112.

## 21.1 Introduction

In recent decades, domain engineering has become one of the most important areas of ferroelectric science and technology. The main target of domain engineering is the manufacturing of stable tailored domain patterns in commercially available ferroelectrics possessing characteristics important for applications. The ability to introduce the spatial modulation of the electro-optic, photorefractive, piezoelectric, and nonlinear optical properties by the creation of periodic domain structure opens wide possibilities in the manufacturing of devices with upgraded performance. The relatively low price of these devices can be achieved under mass production using lithographic electrode patterning for periodical poling. The potential for this technology is ready to expand into a wider market.

The optimization of the poling process resulting from the fundamental studies of the domain kinetics is expected to enable the fabrication of sub-micrometer-pitch gratings and engineered 1D and 2D structures, which could meet the demanding specifications for the photonic applications. The ultimate interest is the exploitation of fine (nanoscale) domain structures with capabilities for optical devices. It is necessary to keep in mind that for achieving high conversion efficiency the structure has to be precisely reproducible with the period dispersion about 10 nm.

The idea to optimize the ferroelectric properties by the creation of stable tailored domain structures was advanced 30 years ago by Newnham, Cross and coworkers (Newnham *et al.*, 1975), who discussed the ability to modify the crystal properties for piezoelectric devices by producing ‘domains which are not to be switched during device operation.’ In parallel the independent branch of the domain engineering aimed at creating the periodically poled nonlinear optical crystals for light frequency conversion and production of quasi-phase-matched devices has been developed. The original method of phase-matching by reversing the sign of the nonlinear coefficient every coherence length, when a phase difference over  $\pi$  is accumulated between

the interacting waves, was proposed by Armstrong *et al.* (1962) and was applied experimentally to an array of ferroelectric domains by Miller (1964). The  $\text{LiNbO}_3$  (LN) and  $\text{LiTaO}_3$  (LT) single crystals are the most popular materials because of their record electro-optic and nonlinear optical properties. LN and LT are favorable for the production of precise periodic domain structures, because  $180^\circ$  domain walls in both crystals are strictly oriented in proper crystallographic directions.

Feng *et al.* (1980) and Ming *et al.* (1982) were the first to produce periodically poled LN (PPLN) by growing doped LN crystals in periodically variable electric field conditions, giving rise to the artificially controlled growth striations, which led to the formation of the periodic domain structure. Many other methods were proposed later for the creation of PPLN, such as diffusion, proton exchange and, electron beam, but not all of them satisfy the requirements of industrial technology.

The most important step in the development of domain engineering in LN and LT occurred in 1993, when the poling of congruent composition LN (CLN) by electric field application using the photolithographic electrode pattern was realized by Yamada *et al.* (1993), thus opening the way to the mass production of quasi-phase-matched devices. It was pointed out by Byer (1997) that ‘the leverage of mass production made possible by lithographic patterning with subsequent domain inversion has led to a rapid transition from nonlinear crystals that cost thousands of dollars to fabricate to nonlinear chips that cost less than one dollar each to fabricate’. Further activities were directed to the improvement of the electrical poling method, the decrease of threshold fields, and the struggle with optical damage. The development of domain engineering requires the understanding of the main physical mechanisms governing the formation of the domain structure from micro- to nanoscale.

This chapter gives a review of the most important recent achievements in the experimental and theoretical study of the domain wall kinetics in single crystalline LN and LT. Our experimental study of the polarization reversal reveals that the stable tailored domain patterns are of a kinetic nature. The crucial result is that almost any domain pattern can be stabilized by the screening of a depolarization field (Shur, 1996, 2005). The developed approach based on the critical review of experimental facts allows us to achieve the essential improvement of the poling processes both for micro- and nanoscale domain patterning (Shur, 1996, 2005).

The chapter is organized in the following way. In Section 21.2 we introduce and discuss the main experimental stages of the domain structure evolution during polarization reversal. Section 21.3 reviews briefly the properties of the materials under investigation and the experimental methods for domain observation: from optics to scanning force microscopy. The general approach to the explanation of the experimentally observed variety of the domain

structure evolution scenarios is presented in Section 21.4. In Section 21.5 we discuss the evolution of the domain growth scenario from continuous motion of the plane domain wall to discrete switching due to the controlled change of the switching conditions from quasi-equilibrium to highly non-equilibrium. We demonstrate also how the effectiveness of screening and the domain merging can drastically change the shape of individual domains. In Section 21.6 the process of the formation of self-assembled nanoscale domain structures is systematically studied and discussed. Some modern tricks of nanoscale domain engineering are introduced in Section 21.7. The original kinetics of nanoscale domains in the heterophase media of relaxor ferroelectrics is discussed in Section 21.8.

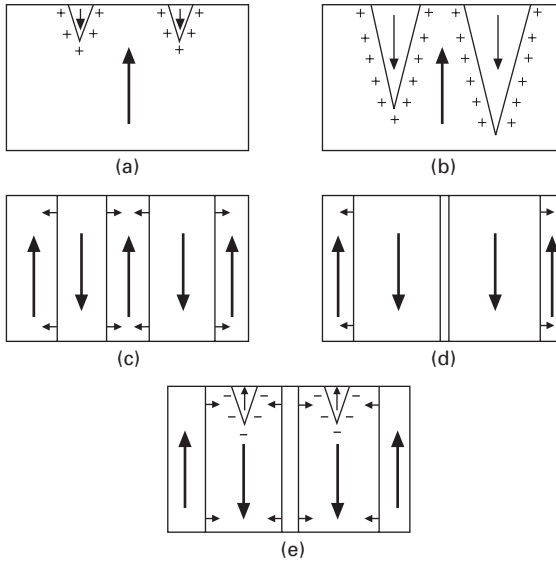
## 21.2 Main experimental stages of domain structure evolution during polarization reversal in normal ferroelectrics

The classical experimental investigations of domain dynamics during polarization reversal (switching) were realized by *in situ* optical methods (Merz, 1954; Little, 1955; Cameron, 1957; Miller and Savage, 1959). Later, systematic study of domain structure evolution was carried out in several uniaxial ferroelectric single crystals with optically distinguished domains, such as lead germanate  $\text{Pb}_5\text{Ge}_3\text{O}_{11}$  (PGO) (Newnham and Cross, 1974; Shur *et al.*, 1989), gadolinium molybdate  $\text{Gd}_2(\text{MoO}_4)_3$  (Kumada, 1969; Flippen, 1975; Shur *et al.*, 1990), LN (Shur *et al.*, 1999c; Gopalan *et al.*, 1999) and LT (Gopalan and Mitchell, 1998, 1999), which have been considered as model systems.

In the following we will restrict ourselves to the simplest case of the polarization reversal process in the  $180^\circ$  domain structures. This is done not only for the clarity of presentation, but also because the ferroelectrics LN and LT, which are discussed throughout this chapter, belong to uniaxial crystals. It must be understood that  $180^\circ$  switching is realized also in multiaxial ferroelectrics with *c*-domain structure.

The domain evolution occurring during the polarization reversal of a single-domain state by application of an external electric field pulse can be divided into the following main stages (Fatuzzo and Merz, 1967; Shur, 2005): (1) ‘nucleation of new domains’, (2) ‘forward growth’, (3) ‘sideways domain growth’, (4) ‘domain coalescence’ and (5) ‘spontaneous backswitching’ (Fig. 21.1). The division into these stages is based on the experimental observation of the domain dynamics by *in situ* optical methods (Merz, 1954; Little, 1955; Cameron, 1957; Miller and Savage, 1959).

‘Nucleation of new domains’ is the most mysterious stage, because it is practically impossible to visualize the appearance of individual nanoscale domains. It is a matter of discussion whether the initial domain state could



21.1 The main stages of the polarization reversal in ferroelectrics.

be completely single domain or it contains a large quantity of nanoscale irremovable residual domains (Shur, 1996). In the latter case the nucleation stage represents a transition of the invisible residual nano-domains into visible ones as a result of the field-induced domain growth.

In high-quality crystals the appearance of new domains is observed as a rule at the surface (Fig. 21.1a). The intrinsic surface dielectric gap existing in any ferroelectric capacitor provokes incomplete compensation of the depolarization field in the vicinity of the electrodes (Janovec, 1959; Shur, 1996). This residual field can provide the existence of residual ‘shallow’ domains and also facilitates the ‘nucleation’ process at the surface.

The second stage, ‘forward growth’ (domain tip propagation), represents a fast expansion of the formed ‘nuclei’ in the polar direction. The tip of the needle-like domain with charged domain walls rapidly moves through the sample (Fig. 21.1b). The direct observation of this short stage encounters experimental difficulties. That is the reason why this process is poorly explored. The method used to study this stage consists of partial switching by application of short pulses. It allows us to obtain and to study in detail the stable structure with charged domain walls consisting of needle-like domains which have not reached the opposite polar surface (Shur *et al.*, 2000b). The depolarization fields produced by bound charges result in pronounced optical contrast due to electro-optical effect. The formation of the quasi-regular clogged ‘charged domain wall’ and its expansion have been visualized in the

bulk of LN under continuous switching using the uniform metal electrodes (Shur *et al.*, 2000b).

The third stage, 'sideways domain growth' (spreading), is best studied experimentally by direct *in situ* methods of domain observation with high time resolution due to the remarkable optical contrast of the regions in the vicinity of the domain walls. At this stage the domain growth is achieved through the domain expansion in the direction transversal to the polar one (Fig. 21.1c). It has been shown experimentally that under 'equilibrium' switching conditions (see Section 21.6) the essential anisotropy of the sideways domain wall motion results in the growth of regular-shaped polygon domains with sides oriented along preferred crystallographic directions (Fatuzzo and Merz, 1967). The detailed study of this stage reveals that the domain shape depends crucially on the switching conditions (Shur, 2005a, 2006). The variation of the field pulse parameters and modification of the dielectric gap properties allow the domain shape to be governed and various regular and irregular shapes to be obtained (Shur *et al.*, 1984b, 1985, 2002b; Shur, 2006).

The fourth stage, 'coalescence of residual domains' (merging), is observed when the switching process is close to the completion (Fig 21.1d). At this stage the pronounced deceleration of the approaching walls is observed. The walls' motion stops and after definite rest-time the residual domains between these walls disappear very rapidly. This process leads to the jump-like switching behavior, which can be one of the sources of the switching current noise (Barkhausen noise) (Miller, 1960; Lines and Glass, 1977; Shur *et al.*, 2002a).

The fifth stage, 'spontaneous backswitching' (flip-back), represents partial revival of the initial domain state after the electric field switch off. This stage is poorly studied experimentally. Nevertheless, the role of this stage during cyclic switching is crucial. The backswitching represents the enlargement of the residual domains by the backward wall motion and the nucleation of the domains with the initial orientation of spontaneous polarization after abrupt decrease of the switching field (Fig. 21.1e). It is necessary to point out that the backswitching stage occurs under the action of the abnormally high field. That is the reason why various self-assembled nano-domain structures can be produced (Shur *et al.*, 2000a).

It must be understood that the different stages of the domain structure evolution can occur simultaneously in different parts of a real ferroelectric sample even during switching in uniform electric field. Moreover, during the given switching experiment it can happen that not all the stages discussed can be realized. For example, such stages as nucleation and forward growth (Fig. 21.1a,b) are not realized for switching from the multidomain initial state.

## 21.3 Materials and experimental conditions

### 21.3.1 LN and LT family: from congruent to stoichiometric

In this chapter the main attention will be paid to experimental study of the single crystals of LN and LT family owing, first of all, to practical reasons. LN and LT are the favourite materials of domain engineering. The production of periodically poled nonlinear chips for light conversion based on these materials opens wide possibilities for further upgrading of quasi-phase matching devices.

Moreover, LN and LT have recently become the recognized leaders in the study of the domain structure stimulated by practical reasons. It is possible to claim that now LN and LT can be used also as model crystals for the study of the domain kinetics as they possess the simplest domain structure and permit *in situ* optical domain visualization.

LN and LT are uniaxial crystals with  $C_{3V}$  ( $R_{3c}$ ) symmetry in ferroelectric phase, thus possessing the domain structure with  $180^\circ$  domain walls only. The direct study of the domain kinetics in LN and LT is due to optical contrast of the domain walls. The origin of the contrast is the essential change of the refractive index in the vicinity of the domain walls induced by incompletely compensated depolarization field in materials with a pronounced electro-optical effect.

In the most popular congruent compositions of LN (CLN) and LT (CLT) the coercive field is enormously high and attains 210 kV/cm. Thus, the application of the necessary threshold field to the sample is coupled with great experimental difficulty. For this reason both materials were named as ‘frozen ferroelectrics’ for many years. Recently, new representatives of LN and LT family closer to stoichiometric composition have become available for research and application (Furukawa *et al.*, 1998; Kitamura *et al.*, 1998; Niwa *et al.*, 2000; Huang *et al.*, 2001). The stoichiometric LN (SLN) and LT (SLT) demonstrate essentially lower values of the coercive field and substantially different domain kinetics as compared with the congruent ones (Kitamura *et al.*, 1998; Niwa *et al.*, 2000). In addition, we have studied domain kinetics in LN and LT doped by MgO in order to increase essentially the optical damage threshold, which is crucial for production of the periodical poled elements for high-energy light conversion.

The LN and LT single crystals of congruent composition were grown from the melt by the Czochralski method. The double-crucible modification of this method and top-seeded solution growth method allows the production of the near-stoichiometric LN and LT (Kitamura *et al.*, 1998; Niwa *et al.*, 2000; Huang *et al.*, 2001). Switching experiments were carried out in optical-grade single-domain wafers cut perpendicular to the polar axis. The typical thickness of the studied wafers ranges from 0.2 to 0.5 mm for CLN and CLT

and from 1 to 2 mm for SLN and SLT. The polar surfaces of all studied samples were carefully polished.

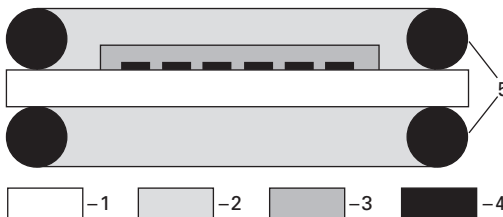
For *in situ* study of the domain kinetics in a uniform field we prepared two types of circular transparent electrodes: (1) liquid electrolyte (water solution of LiCl or pipe water) in a special fixture and (2)  $\text{In}_2\text{O}_3\text{:Sn}$  (ITO) films deposited by magnetron sputtering, with diameter down to 1 mm. The visualization by polarizing microscopy in transmitted and reflected light with simultaneous TV-recording and subsequent image processing was used for detailed study of the domain kinetics.

The LN and LT wafers, used for the periodical poling, were lithographically patterned with periodic stripe NiCr or Al electrodes deposited on Z+-surface only and oriented along one of Y-directions. The patterned surface was covered by a photoresist layer about 1  $\mu\text{m}$  thick. A high voltage pulse producing an electric field greater than the coercive one was applied to the structure through the fixture containing the liquid electrolyte (Fig. 21.2). To observe the domain patterns after partial poling both polar surfaces were etched with pure hydrofluoric (HF) acid at room temperature. The surface relief obtained was visualized by optical microscopy, scanning electron microscopy (SEM), and various modes of scanning probe microscopy (SPM).

### 21.3.2 Relaxors

Relaxor ferroelectrics are among the most intensively studied materials due to their unique properties which are useful for various important applications (Cross, 1994; Blinc *et al.*, 2006; Bokov and Ye, 2006a). They are included in our investigations for the practical reasons resulting from prominent electromechanical properties (Cross, 1994). Of course the domain kinetics in these materials is far from the ‘model’ one because of their complicated structure.

We have studied the hot-pressed high-density transparent lanthanum-doped lead zirconate–titanate ceramics ( $\text{Pb}_{1-x}\text{La}_x$ )( $\text{Zr}_{0.65}\text{Ti}_{0.35}$ ) $\text{O}_3$  PLZT (5-12)/65/35, which exhibits a classic relaxor behavior within a broad temperature range. The plate thickness varied from 90 to 300  $\mu\text{m}$ . Two types of electrodes



21.2 Experimental setup used for periodical poling: 1 wafer, 2 liquid electrolyte, 3 insulating layer, 4 periodic electrodes, 5 O-rings.



were used: (1) transparent ITO deposited by magnetron sputtering and (2) gold deposited by thermal evaporation.

The hysteresis loops were measured under the action of *ac* triangular field pulses in the frequency range from 0.02 to 0.2 Hz and the field amplitude up to 10 kV/cm. The switching charge has been obtained by digital integration of the recorded switching current. The frequency range was chosen to provide the ‘quasi-static switching regime’. The switching under the action of the series of rectangular unipolar pulses with rise time about 20  $\mu$ s, amplitude up to 10 kV/cm and duration ranging from 50  $\mu$ s to 5 s was carried out. The pulse frequency was chosen sufficiently low to provide the complete backswitching between subsequent pulses which results in good reproducibility of the current data. All experiments have been done in temperature range from 20 to 200 °C.

Piezo-response force microscopy (PFM) mode was realized on the basis of EXPLORER™ AFM. Conductive Co-coated silicon cantilevers with 75 kHz resonance frequency were used for visualization of domain patterns. The *ac* modulation voltage with amplitude 10 V and frequency 17 kHz was applied between the bottom electrode and the conductive tip being in contact with the surface. Local mechanical deformation at the frequency of the reference signal was induced by applied *ac* voltage due to reversed piezoelectric effect. The piezoelectric response was detected by analyzing the scanning probe microscopy (SPM) photodetector signal using the lock-in amplifier. The phase of recorded signal differed by 180° for domains with opposite polarization directions. The main PFM advantage is the ability to obtain the domain contrast even in the case of complete screening of the depolarization field at the surface.

### 21.3.3 Experimental methods of domain observation in LN and LT: from optics to SPM

The number of different techniques ranging from common optical microscopy to more sophisticated SPM has been widely used for the investigation of the static domain patterns and the kinetics of the domain structure in LN and LT family crystals. We shall only briefly discuss the most important visualization techniques. A review of modern experimental methods has been published (Soergel, 2005).

Selective chemical etching is one of the oldest and most popular techniques used for revealing the domain structure in ferroelectrics. The inherent difference in the etch rate for domains with opposite directions of spontaneous polarization leads to the formation of steps on the polished sample’s surface at the position of the domain walls. It has been revealed in LN and LT that the etching rates for the faces of anti-parallel domains are drastically different. The Z-face etches hundreds of times faster than Z+ one. This method is commonly used

for precise measurement of the period and duty cycle of the engineered periodic domain patterns in LN and LT using (HF) acid-based etchants (Ohnishi and Iizuki, 1975; Alekseeva *et al.*, 1986; Mizuuchi and Yamamoto, 1992; Sones *et al.*, 2002). The observation of revealed domain pattern can be carried out by optical or scanning electron microscopy (SEM). Moreover, the etch relief can be measured with high spatial resolution by the topographic mode of SPM. Nevertheless, the interpretation of obtained images must be done with care, because the etching relief for nanoscale domains can be essentially different from the domain pattern due to strong anisotropy of etching rate in the Y direction.

It is generally accepted that the etching procedure does not significantly affect the domain structure. Thus, the etched relief structure must correlate one-to-one with the existing stable domain pattern. It has been demonstrated recently that this statement is not always true (Shur *et al.*, 2005c). It has been shown experimentally using SPM measurements that in MgO-doped stoichiometric LT (MgO:SLT) crystals, contrary to current opinion, the domain walls can be shifted considerably (about tenths of micrometers) from their initial positions during etching. It has been found that the wall motion proceeded even after the termination of the etching procedure. It has been revealed that the whole consequence of the domain wall positions during etching is recorded in the etching relief height and can be extracted with high spatial and temporal resolution (Shur *et al.*, 2005c). The main drawback of the etching technique is that it is a destructive method, which is useless for *in situ* study of the domain kinetics, and gives information only about the surface domain structure.

The SPM methods can be used for visualization of the static domain patterns with nanoscale resolution even without preliminary etching. PFM analyzes the piezoelectric response of the volume fraction mechanically deforming under the locally applied ac electric field. Since any ferroelectric is piezoelectric, it is possible to obtain a two-dimensional (2D) map of the complete 3D piezoelectric tensor, which gives insight to the different ferroelectric domain structures. In the case of investigated LN and LT possessing the simple domain structure with  $180^\circ$  walls only the scanning of the polar face allows one to distinguish the domains with opposite polarization sign by recording the phase of the signal. The domain walls can be visualized by recording the signal amplitude.

The widely accessible optical methods which present the unique possibility of *in situ* observation of domain evolution using polarizing microscope are the most informative and suitable (Burfoot and Taylor, 1979). These methods are non-invasive, if the properly chosen intensity and wavelength of illumination do not affect the domain kinetics. Even super-fast switching can be investigated by using pulse lighting and high-speed photography (Malozemoff and Slonczewski, 1979; O'Dell, 1981). The time resolution is determined by the light pulse duration and can be above 10 ns. The domains separated by  $90^\circ$

walls can be easily distinguished by polarizing microscopy due to the different values of spontaneous birefringence (Blattner *et al.*, 1948; Matthias and Hippel, 1948). This effect has been used to study many ferroelectrics. But it is unusable for antiparallel domains with  $180^\circ$  walls because of the identity of optical indicatrix in neighboring domains. Some special techniques have been developed for optical visualization of such domains.

In  $\text{BaTiO}_3$  antiparallel domains become optically distinguished when the electric field (Little, 1955; Merz, 1956) or corresponding mechanical forces (Hooton and Meiz, 1955) are applied perpendicularly to the polar axis. The rotation of the optical axis in opposite directions in different domains leads to a difference between extinction positions of antiparallel domains, allowing their visualization.

Miller and Savage (1959) and Savage and Miller (1960) have shown that the antiparallel domains in  $\text{BaTiO}_3$  can be observed in transmitted polarized light during polarization reversal in a longitudinal field. Kobayashi *et al.* (1963) showed that in this case domains are distinguishable only under the illumination directed at small angles to the polar axis and explained this effect by the existence of strain-induced birefringence in the vicinity of domain walls.

The linear electro-optic effect is the versatile property making possible optical visualization of domains and/or domain boundaries. In the case of anti-parallel  $180^\circ$  domains the electric field applied along the optical axis induces the difference in refractive indices in Z+ and Z− domains. In LN and LT the perturbation of the refractive index in the area near the domain walls is induced by extremely high internal bias field. This effect allows the domains to be visualized using polarized and phase contrast modes of the optical microscopy. This also presents the unique opportunity of visualizing the domains with charged domain walls embedded in the bulk. The drawback of the optical methods imposed by the diffraction limiting the spatial resolution to  $0.5\ \mu\text{m}$  is outweighed by the ability to realize a high temporal resolution.

A promising new integral optical technique is based on the physical phenomenon of light deflection at the domain boundaries. In these experiments, a partially deflected laser beam produces, in the far-field, the light pattern which carries information about the orientation of the domain walls. In LN the light pattern is a six-point star, because in this material the individual domains are mainly hexagons. The same experiments carried out in LT demonstrate a three-point star pattern, because the observed domain shapes are usually triangles. This method can be used for the statistical characterization of the wall orientation in complicated multidomain patterns.

## 21.4 General consideration

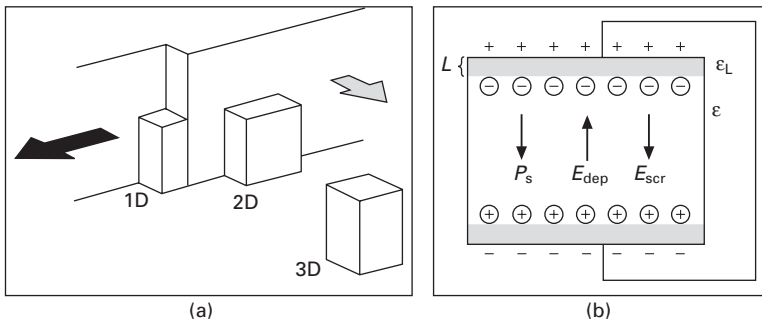
In this chapter all stages of the domain structure evolution will be considered from a unified point of view as a manifestation of the various nucleation

processes. This commonly accepted approach was proposed and developed by Fatuzzo and Merz (1967) and Miller and Weinreich (1960). The nucleation and growth approach is widely used for the description of the kinetics of aggregative state changes during first-order phase transformation, e.g. crystallization and melting (Shur, 2005). In our case the coexisting domains with different orientation of the spontaneous polarization are considered as an analogue of volumes occupied by different phases, while the domain walls represent the phase boundaries. It has been shown by direct experiments that the width of ferroelectric walls is a few unit cells (Lin and Bursill, 1982; Bursill and Lin, 1986). This result supports the consideration of the domain structure evolution as a discrete nucleation process. Following this approach the domain kinetics during all the above-mentioned stages has to be considered as a result of numerous elementary processes of thermally activated generation of nuclei with a preferred orientation of the spontaneous polarization.

### 21.4.1 The elementary nucleation processes

The domain kinetics, similar to any first-order phase transformation kinetics, is achieved through competitive formation of nuclei of three different dimensionalities (Fig. 21.3). Each nucleus represents the nanoscale domain with changed orientation of the spontaneous polarization.

The appearance of the optically observed new domains ('nucleation of new domains') is a result of the expansion of either newly formed or residual 3D nanoscale nuclei. Such 'invisible expansion' occurs by 1D- and 2D-nucleation (Fig. 21.3). In the real systems the heterogeneous nucleation takes place during first-order phase transformation, and the position of the nucleation sites is determined by imperfections and point defects. The predominance of the nucleation at the sample surface is the special feature of ferroelectrics caused by the existence of the intrinsic surface dielectric gap playing the role of the 'defect plane'.



21.3 Schemes: (a) of the nucleation processes of various dimensionalities, (b) of the ferroelectric with intrinsic dielectric surface layer.

The growth of visible domains by motion of the walls ('sideways domain growth') is achieved through 1D- and 2D-nucleation, as shown in Fig. 21.3. The elementary steps with the thickness about one unit cell are generated by 2D-nucleation at the wall. The subsequent motion of the steps along the wall is a result of 1D-nucleation. The crystal symmetry imposed the restrictions on the orientation of the elementary steps thus leads to experimentally observed anisotropy of the domain growth. The shape of isolated domains usually observed during 'equilibrium' switching conditions is defined by the crystal symmetry: e.g. square domains are formed in tetragonal phase of BaTiO<sub>3</sub> (Iona and Shirane, 1962) and hexagonal domains – in LN ( $C_3$  or  $R_{3c}$  symmetry) (Prokhorov and Kuzminov, 1990).

The nucleation probability determines the rates of all switching processes. For any first-order phase transformation it is determined by the driving force value. The electric field averaged over the volume of the order of the nucleus size (named in the following as 'local field',  $E_{loc}$ ) plays the role of the driving force of nucleation during polarization reversal in ferroelectrics (Shur, 1996).  $E_{loc}$  is macroscopic electric field obeying macroscopic electrodynamics equations with proper boundary conditions (Lifshitz *et al.*, 1985).  $E_{loc}$  is essentially spatially inhomogeneous and changes during polarization reversal. It is necessary to point out that  $E_{loc}$  has nothing in common with the local field which is analyzed while discussing the interaction of the crystal lattice ions.

$E_{loc}$  in a ferroelectric capacitor is the sum of: (1) the external field applied by electrode pattern, (2) the depolarization field produced by bound charges developing as a result of spatial inhomogeneity of the spontaneous polarization in multidomain state, (3) the external screening field originating from the redistribution of the charges at the electrodes, and (4) the bulk screening field governed by various bulk screening processes.

The external field is determined by the shape, sizes, and period of the electrode pattern. The field singularities in the surface layer at the electrode edges due to the fringe effect play the crucial role in the nucleation of the new domains. The switching process usually starts through formation of the nuclei at the electrode edge or at the tips of the stripe electrodes. Due to the fringe effect the real value of  $E_{loc}$  initiating the switching process in single-domain state (threshold field) essentially exceeds the field value calculated as potential difference divided by sample thickness. The pronounced field concentration in the vicinity of the ends and corners of the stripe electrodes must be accounted for while creating the tailored domain structures (Shur, 2005).

The depolarization field  $E_{dep}$  is produced by bound charges existing at the polar surfaces of the sample and at the charged walls of the encountering domains ('head to head' or 'tail to tail'). The bound charges density ( $\rho_b$ ) is determined by spontaneous polarization ( $P_s$ ) by the following equation:

$$\rho_b = -\operatorname{div} P_s \quad 21.1$$

For single-domain plate of typical ferroelectrics the depolarization field strength can reach  $10^8$  V/m. It is clear that  $E_{\text{dep}}$  far exceeding the experimentally observed threshold or coercive fields leads to break-up of the single domain state and fragmentation of the domain structure into narrow domains of opposite sign.

In the volume of the isolated domain of ellipsoid shape:

$$E_{\text{dep}} = L P_s / \epsilon \epsilon_0 \quad 21.2$$

where  $L$  is the depolarization factor, which is essentially reduced for the elongated domains. Thus, the wedge and needle-like shapes are the most favorable for new domains due to minimization of the depolarization energy.

The domain growth by nucleation at the existing domain wall is determined by the value of  $E_{\text{dep}}$  at the wall front in the interface between the dielectric gap and the 'ferroelectric bulk'. This field is essentially spatially inhomogeneous and strongly depends on the distance from the wall (Drougard and Landauer, 1959). For the sideways domain growth stage  $E_{\text{dep}}$  increases with domain enlargement, thus decreasing the nucleation probability at the moving wall. This effect leads to experimentally observed deceleration and termination of the wall motion (Drougard and Landauer, 1959; Shur, 1996, 2005a).

The effect of  $E_{\text{dep}}$  is reduced by screening processes. For effective screening of  $E_{\text{dep}}$  the complete switching can be achieved even in a comparatively low electric field. Only a small shift of the existing domain walls is observed for ineffective screening due to the screening retardation. The incomplete screening of  $E_{\text{dep}}$  is the main source of the spontaneous backswitching ('flip back') representing the partial recovering of the initial domain state after the external field switch off. Two types of screening processes must be distinguished: external and bulk.

External screening in ferroelectric capacitors is due to redistribution of charges in the electrodes (the current in external circuit). The screening rate is determined by the characteristic time of the external circuit  $\tau_{\text{ex}}$  (product of effective resistance and capacity). Usually  $\tau_{\text{ex}}$  ranges from a few nanoseconds to microseconds. The external screening field  $E_{\text{scr}}(r,t)$  effectively compensates  $E_{\text{dep}}(r,t)$  thus allowing the long-distance-shift of the domain wall and drastically diminishes the value of the applied external field  $E_{\text{ex}}(r)$ , which is necessary for the complete switching. The experimentally observed switching time  $t_s$  always exceeds  $\tau_{\text{ex}}$  as the complete switching can be obtained only if the depolarization field is sufficiently screened.

The fast external screening never completely compensates  $E_{\text{dep}}$  due to the existence of the intrinsic dielectric surface layer ('dielectric gap' or 'dead layer'), in which spontaneous polarization is absent (Fig. 21.3b) (Fridkin, 1980; Shur, 1996).

For a ferroelectric capacitor of thickness  $d$  the bulk residual depolarization field  $E_{rd}$  remains in the area freshly switched from one single-domain state to another one even after complete external screening due to existence of the intrinsic surface dielectric layer of the thickness  $L$  (Fridkin, 1980; Shur, 1996):

$$E_{rd} = E_{dep} - E_{scr} = 2L/d [P_S/(\epsilon_L \epsilon_0)] \quad 21.3$$

where  $\epsilon_L$  is the dielectric permittivity of the surface dielectric gap.

$E_{rd}$  is several orders of magnitude less than  $E_{dep}$ , but it is of the order of the experimentally observed threshold/coercive fields. Thus, the effective compensation of  $E_{rd}$  by comparatively slow bulk screening processes is necessary for complete switching. That is why bulk screening plays an essential role in the evolution of the domain structure.

Bulk screening is the only way to compensate  $E_{rd}$  existing after completion of the external screening. Three groups of the bulk screening mechanisms are usually considered: (1) redistribution of the bulk charges (Fridkin, 1980; Shur, 1996), (2) reorientation of the defect dipoles (Lambeck and Jonker, 1986), (3) injection of carriers from the electrode through the dielectric gap (Tagantsev *et al.*, 2001). All bulk screening mechanisms are considerably slower than the external ones, with typical time constants  $\tau_b$  ranging from milliseconds up to days and even months.

According to the above-discussed considerations the local electric field being the driving force of all nucleation processes is spatially inhomogeneous and time dependent. After completion of the external screening the local electric field at the given point and at the given moment  $E_{loc}(r,t)$  is the sum of the external field  $E_{ex}(r)$ , the residual depolarization field  $E_{rd}(r,t)$ , and bulk screening field  $E_b(r,t)$  (Shur, 1996, 1998; Shur and Rumyantsev, 1997 Shur):

$$E_{loc}(r,t) = E_{ex}(r) + E_{rd}(r,t) + E_b(r,t) \quad 21.4$$

That is why the application of the short field pulse, for which the bulk screening of the new state lags behind, is absolutely ineffective for the creation of a modified domain pattern. The cooperative action of  $E_{rd}$  and  $E_b$  remaining after the external field is switched off leads to the spontaneous backswitching process. This effect could be observed in the areas where the value of  $E_{loc}(r,t)$  exceeds the threshold field for the switching process  $E_{th}$ , i.e.:

$$E_{loc}(r,t) = -[E_{dep}(r,t) - E_{scr}(r,t) + E_b(r,t)] = -[E_{rd}(r,t) + E_b(r,t)] > E_{th} \quad 21.5$$

The initial domain state can even be completely reconstructed for ineffective screening of the modified  $E_{dep}$  produced by the domain pattern formed at the end of the electric field pulse. The conservation of the new domain configuration can be realized only when the duration of the external field pulse is long

enough for effective bulk screening. Thus for an appropriate duration of the field application it is possible to stabilize almost any domain pattern.

The systematic study of the polarization reversal in various ferroelectric single crystals reveals a great variety of the domain kinetics scenarios. The main problem in their classification lies in the fact that it is impossible to attribute the given scenario to a definite range of applied fields and switching rates. The critical values of the fields and rates corresponding to a replacement of one domain kinetics scenario by another differ drastically for different materials and experimental conditions.

Basing on the above-discussed approach we have chosen the ratio between switching rate ( $1/t_s$ ) and bulk screening rate ( $1/\tau_{scr}$ ) for quantitative characterization of the screening efficiency. This parameter is named screening effectiveness  $R$  (Shur, 2005, 2006(a)):

$$R = \tau_{scr}/t_s \quad 21.6$$

Three ranges for screening effectiveness must be distinguished: (1)  $R \ll 1$  – ‘complete screening’, (2)  $R \sim 1$  – ‘incomplete screening’ and (3)  $R \gg 1$  – ‘ineffective screening’. It was confirmed both experimentally and by computer simulation that the proposed ranges correspond to qualitatively different switching regimes (scenarios of domain kinetics).

The complete screening corresponds to quasi-equilibrium switching conditions when the reconstruction of the subsystem of the bulk screening charges is fast enough to keep pace with the changes of the domain structure. The retardation of the bulk screening makes the switching conditions non-equilibrium. Thus the equilibrium switching conditions corresponds to  $R \ll 1$  and the highly non-equilibrium ones to  $R \gg 1$ .

Sideways domain wall motion is a result of step generation (2D nucleation) and subsequent step growth (1D nucleation) along the wall (Fig. 21.3a). The shape and orientation of the moving wall strongly depend on the spatial distribution of the nucleation sites. Two limiting variants can be considered: stochastic and predetermined.

Stochastic nucleation with random position of the nucleation sites at the wall is the classical approach to the problem of the wall motion (Miller and Weinreich, 1960b; Hayashi, 1972). This approach assumes that the switching field is homogeneous and the step generation probability is independent of the position at the wall. As a result, the shape of the moving wall becomes irregular. In this case the deceleration of the wall by local pinning centers is ineffective. The wall easily flows around the pinning center, because the decrease of the nucleation probability occurs only in the vicinity of the center, while the rest of the wall continues to move. The shape of individual domains under stochastic nucleation is usually irregular and does not follow the crystal symmetry.

However, in many ferroelectrics switched under usual experimental conditions the domains demonstrate regular shape with walls strictly oriented

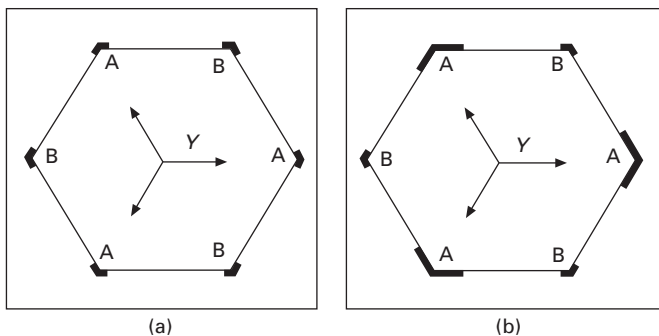


along definite crystallographic directions. In LN the domains demonstrate hexagon shape with walls strictly oriented along  $Y$  crystallographic directions. This behavior can be understood, if we assume that the predetermined nucleation prevails.

Predetermined nucleation means that the generation of the steps (2D-nucleation) along the wall is spatially inhomogeneous. The preferred nucleation at the given sites determined by field singularities can be produced both artificially and during growth of isolated domain.

For growth of isolated domain the switching field at the wall is decreased due to incomplete screening of the depolarization field. For a polygon domain shape this screening retardation leads to formation of the field singularities at the vertices leading to local increase of the step generation probability. In this case the predetermined nucleation at polygon vertices must be realized. The position of the nucleation sites for hexagon domains in LN is shown in the Fig. 21.4. The crystal symmetry imposes restrictions on the directions of the growth of the elementary steps, thus leading to anisotropy of the domain growth, which is observed experimentally (Shur, 2005). In LN crystal with  $C_{3V}$  ( $R_{3c}$ ) symmetry the step propagation along three allowed directions must prevail. The direct experimental observation of the domain kinetics allows us to state that the steps propagate along the  $Y$  direction only (Shur, 2005, 2006). The steps generated at three  $Y$  non-adjacent vertices are growing while the growth of the steps generated at three other vertices is completely suppressed. The experimentally observed hexagon shape is obtained when the step growth rate exceeds essentially the step generation rate.

The growth of the hexagon domain governed by predetermined nucleation is demonstrated on the schematic drawing presented in Fig. 21.4. It is clearly seen that the growing conditions for steps generated at the vertices A and B are essentially different. The growth probability for steps generated at vertex A must far exceed the probability at B, because the growth of the latter must occur in the directions opposite to the preferable ones.



21.4 Predetermined nucleation: (a) step generation at vertices and (b) step growth in three  $Y$  directions.

Within this consideration we have shown by computer simulation that the growing domain preserves its polygon shape, if the step generation probability at the faces is neglected (Lobov *et al.*, 2006). The additional experimental evidence of the proposed approach was obtained while observing the propagation of macro-steps along the wall in three  $Y$  directions only. These micrometer-scale steps formed as a result of interaction of the moving wall with the crystal defects can be easily visualized *in situ* by optical microscopy (Shur, 2005, 2006).

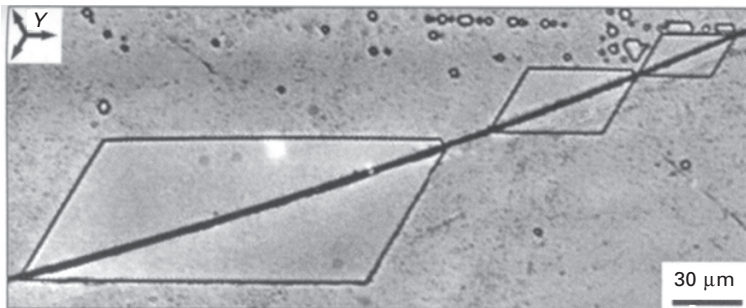
#### 21.4.2 Artificially produced nucleation sites

It is interesting to study the role of the predetermined nucleation on the domain shape when the nucleation sites are produced artificially. The scratching of the crystal polar surface is one of the possible ways to initiate the nucleation in the given place. In this case the predetermined position of the nucleation sites is caused by an artificial array of field concentrators produced by the scratch. The slow switching using the solid liquid electrode of the sample with a single scratch oriented along  $X$  axis produces the regular tetragons (Fig. 21.5). It is clearly seen that the walls are strictly oriented along the  $Y$  directions. Such behavior is an unequivocal experimental confirmation of the prevailing role of the predetermined nucleation in LN.

### 21.5 Domain growth: from quasi-equilibrium to highly non-equilibrium

#### 21.5.1 Growth of isolated domains

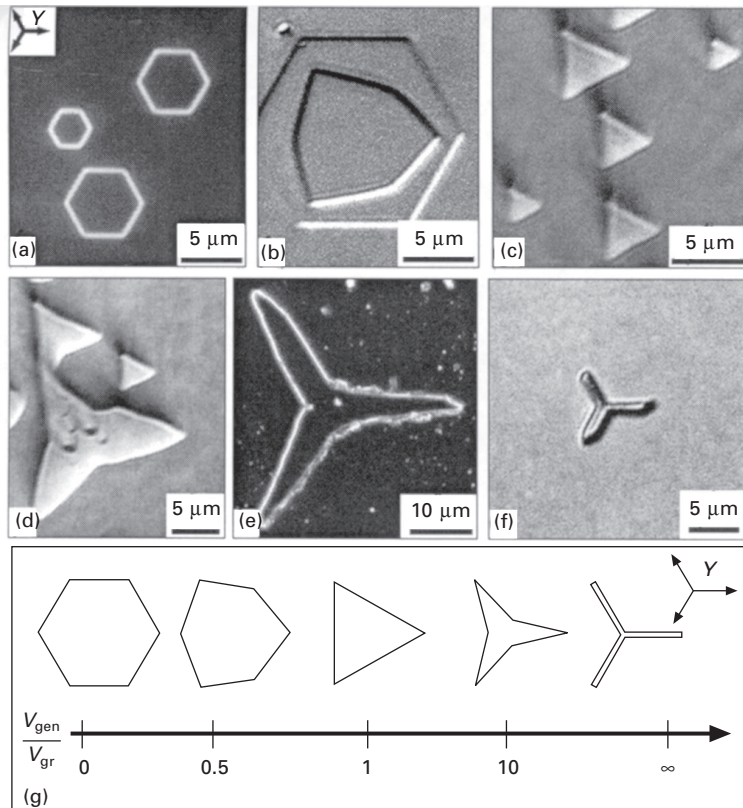
It has been shown that the shape of individual domains in LN essentially depends on experimental conditions and can differ from the above-discussed



21.5 Tetragon domains in CLN. Predetermined nucleation initiated by scratch oriented in  $X$  direction. Optical images of domains revealed by etching.

regular hexagon (Fig. 21.6). According to the mechanism of predetermined nucleation it is possible to explain all shapes observed in LN and LT in wide range of experimental conditions as a result of variation of the ratio between rates of step generation and step growth. It is convenient to characterize the step generation rate by experimentally measured vertex motion velocity  $V_{gen}$ , and the step growth – by motion velocity of the step edge  $V_{gr}$ . The hexagon shape is obtained, if condition  $V_{gen} \ll V_{gr}$  is fulfilled.

It has been shown that the ratio between  $V_{gen}$  and  $V_{gr}$  is the main parameter which governs the shape of isolated domain. The simulation of the domain growth for wide range of  $V_{gen}/V_{gr}$  values allows us to obtain the smooth variation of the domain shapes from equilateral hexagon to stars with three rays (Fig. 21.6f).

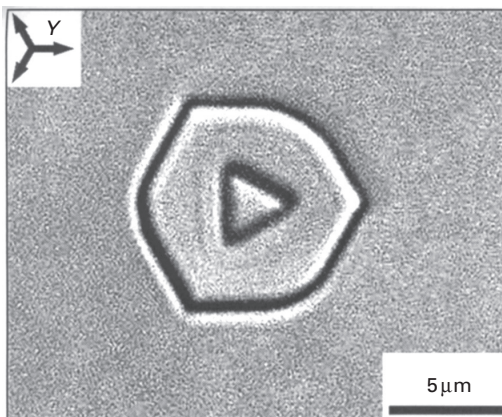


21.6 The domain shapes obtained as a result of switching in various conditions in CLN: (a) hexagons, (b) irregular hexagon, (c), (d) triangles, (d), (e) Mercedes stars, (f) star with three rays. Optical images of domains revealed by etching. (a), (e) – dark field mode. (g) Simulated dependence of domain shapes in LN on the ratio of step generation to step growth rates.

It has been revealed experimentally that the same domain shapes can be obtained in a wide range of applied fields and the switching times, so the ratio  $V_{\text{gen}}/V_{\text{gr}}$  demonstrates non-trivial dependence on the experimental conditions. According to my general approach the  $V_{\text{gen}}/V_{\text{gr}}$  ratio is determined by the screening efficiency, because the role of the residual depolarization fields increases for ineffective screening.

For incomplete screening the residual depolarization field hampers the step generation and growth processes. It can be shown that the influence of the train of uncompensated depolarization field is more pronounced for the step growth (1D nucleation) along the sides of a polygon as compared with the step generation (2D nucleation) at the vertices. Thus, under non-equilibrium conditions (for  $R \gg 1$ )  $V_{\text{gen}}$  can essentially exceed  $V_{\text{gr}}$  leading to increase of the step concentration at the wall, which determines the deviation of the wall orientation from  $Y$  directions. Formation of the regular hexagonal domain shape in LN can be observed only for the equilibrium switching conditions (for  $R \ll 1$ ) with complete screening, when the step concentration is negligible and the angles at the 'growing vertices' are close to  $120^\circ$ . The increase of  $R$  within this approach must lead to increase of the step concentration and to decrease of the angles at the 'growing vertices'. In this case the 'vicinal walls' formed essentially deviate from the  $Y$  directions imposed by crystal symmetry.

Based on the above-presented considerations we can state that the shape of individual domains is determined by domain kinetics which depends on the switching conditions. The convincing experimental proof of this statement is presented in Fig. 21.7, demonstrating that it is possible to produce domains with qualitatively different shapes in the same place on the CLN wafer. The



21.7 The shapes of domains formed by switching and spontaneous backswitching in CLN. Switching by short pulse with abrupt edge. Optical images of domains revealed by etching.

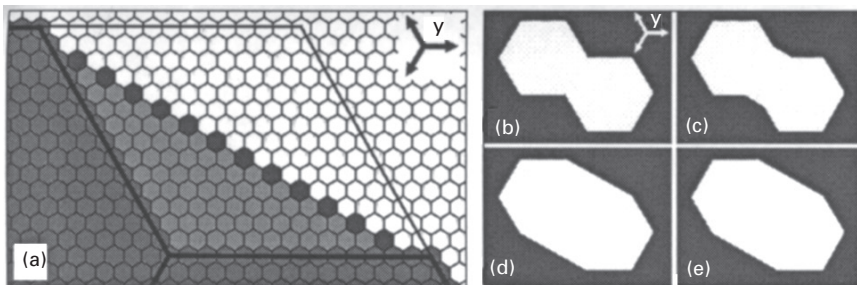
domain structure has been produced in single-domain CLN by application of short rectangular unipolar field pulse with abrupt edge. In this case the new domains appear within the already switched area as a result of backswitching after the external field has been switched off (Fig. 21.1e).

The domain structure was revealed by selective chemical etching. The dark curves on the image correspond to the position of the domain walls. The large hexagon domain was formed during application of the pulse. The subsequent backswitching after field switch off leads to formation of triangular domain in the center of the switched one. The usage of abrupt pulse edge allows the non-equilibrium conditions for backswitching to be realized.

### 21.5.2 Domain shape evolution during merging

The domain shape evolution after merging of hexagonal domains was studied by *in situ* observation. The most interesting result is the formation of the strictly oriented  $X$  wall after merging of two  $Y$  oriented domain walls (Fig. 21.8). The velocity of  $X$  wall motion far exceeds the velocity of  $Y$  walls. As a result, the ‘super-mobile’  $X$  wall disappears quickly. The limited lifetime hinders the direct observation of  $X$  wall in the course of the switching process in the constant field. Nevertheless, switching off the external field allows the unusual domain polygons with both  $Y$  and  $X$  walls to be fixed.

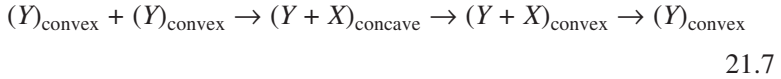
According to the above-discussed general approach, the sideways wall motion velocity is determined by generation rate of the elementary steps. The abnormally high velocity of the  $X$  wall is caused by the maximum possible density of the elementary steps remaining constant throughout the lifetime (Fig. 21.8a). The  $X$  wall motion velocity is determined by the growth velocity of elementary steps which reaches meters per second. It is about 1000 times faster than the average sideways  $Y$  wall motion velocity in the same switching conditions. The computer simulation of the domain shape



21.8 Schematic drawing of domain shape evolution as a result of domain merging; (a) formation of  $X$  wall, (b) two ( $Y$ ) hexagons before merging, (c) concave ( $Y + X$ ) shape, (d) convex ( $Y + X$ ) shape, (e) convex ( $Y$ ) shape.

evolution after merging based on the step growth mechanism allowed all experimentally observed ‘abnormal’ convex polygonal domains with side numbers ranging from 6 to 12 to be obtained.

The complete evolution of the domain shapes as a result of merging of two hexagonal domains with  $Y$  walls only ( $(Y)_{\text{convex}}$ ) (Fig. 21.8b) can be presented by the following scheme:



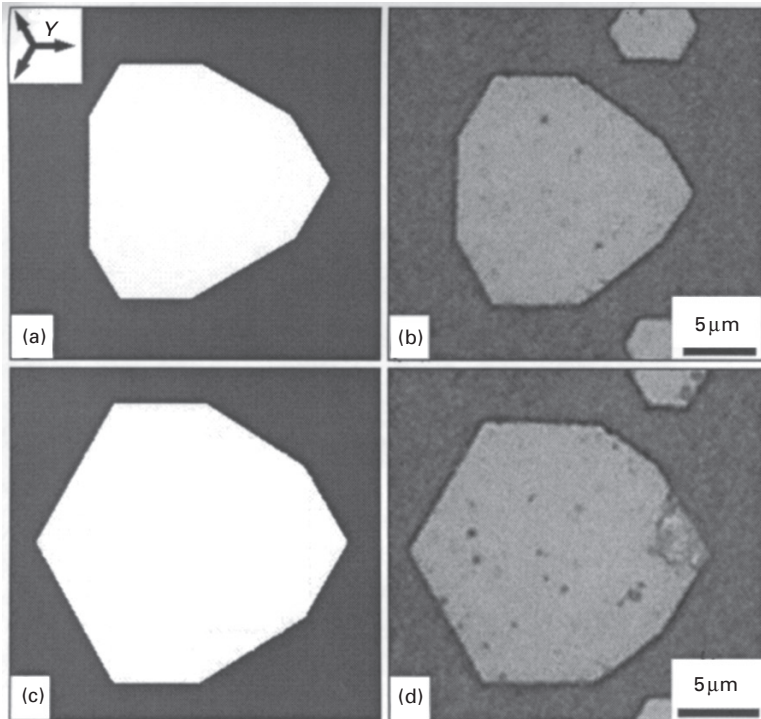
The concave domain shape  $(Y + X)_{\text{concave}}$  appears just after the merging of two convex ones (Fig. 21.8c). Such an unusual temporary shape transforms in a short time to the convex one  $(Y + X)_{\text{convex}}$  due to the fast motion of the  $X$  wall (Fig. 21.8d). At the concave domain stage the length of the  $X$  wall increases. Just after formation of convex domain, the length of the  $X$  wall starts to decrease and then disappears, thus forming the hexagonal domain with  $Y$  walls only (Fig. 21.8e).

The evolution during merging of the regular 2D domain structure produced by the hexagonal grid electrode pattern has been studied systematically. The merging of individual domains has been stimulated by artificial conducting defects between neighboring electrodes. The domain evolution after merging has been studied in detail both experimentally and by computer simulation (Fig. 21.9). It has been shown that the shapes of the domain polygons appeared at different stages of shape evolution are determined by the number and succession of merging events. The abrupt switching off of the applied field allows any intermediate domain shape to be stabilized. For example, the simultaneous merging of three hexagon domains leads to formation of the regular nonagon (Fig. 21.9a), while consecutive merging of the same domains results in formation of an octagon (Fig. 21.9b). The understanding of the origin of abnormal polygon domain shapes can be used to create desirable domain shapes choosing the proper electrode pattern.

### 21.5.3 Loss of the domain wall shape stability

The various effects of loss of the domain wall shape stability are observed for  $R \gg 1$ , when switching is realized under highly non-equilibrium conditions. The loss of stability in this case is caused by self-assembled nucleation and oriented growth of domain rays. The typical finger and dendrite structures formed due to wall shape instability in LN are presented in Fig. 21.10.

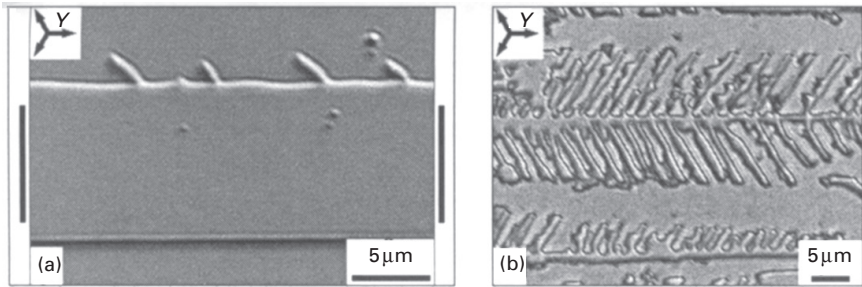
The non-equilibrium switching can be realized experimentally under different conditions. There are two ways to increase the role of the screening retardation effect. The first is to accelerate the polarization reversal process by application of a ‘super-strong’ external field.



21.9 Experimental (right) and simulated (left) domain polygons with X and Y walls formed as a result of merging of three regular hexagon domains: (a) nonagon and (b) octagon. Optical images of domains revealed by etching.

The second is to increase the input of residual depolarization field by deposition of the artificial surface dielectric layer. This layer effectively increases the thickness of the dielectric gap, thus increasing the value of the residual depolarization field remaining after completion of the fast external screening. This residual field hampers the motion of the domain wall as a whole.

This situation is realized during the conventional method of production of the tailored domain structures in LN and LT by application of electric field using periodical electrode pattern (Yamada *et al.*, 1993; Webjörn *et al.*, 1994; Zhu *et al.*, 1995; Myers *et al.*, 1995; Batchko *et al.*, 1999; Rozenman *et al.*, 1999). The area between the stripe electrodes is covered by photoresist and domain ‘broadening’ out of the electrodes is frequently accompanied by the loss of the regular wall shape (Shur, 2005, 2006). Various instabilities of the domain shape leading to formation of ‘fingers’ (Fig. 21.10a), ‘branches’ and ‘dendrites’ (Fig. 21.10b) were revealed (Shur, 2005, 2006). It must be stressed that all these self-assembled structures are formed as a result of



21.10 (a) Finger domain structure formed during periodical poling in CLN. (b) Dendrite structure formed during backswitching in MgO:LN. Z+ view. Black lines show the position of stripe electrode. Optical images of domains revealed by etching.

growth in strictly oriented directions. Such behavior is in accord with the above-discussed approach.

The uncompensated depolarization field suppresses the broadening of the strip domains by the sideways motion out of electrodes. Nevertheless, the alternative mechanism of the broadening through formation of ‘fingers’ can be observed. The individual finger is a ray oriented along the  $Y$  direction, which has been generated by perturbation at the domain wall. The regular distribution of the fingers is caused by the electrostatic interaction between the neighbors.

#### 21.5.4 Dendrite domain structures

The non-equilibrium switching is easily achieved during spontaneous polarization reversal after abrupt switching off of the external electric field (backswitching). In this case the retardation of the screening leads to the existence of strong switching field produced by an uncompensated depolarization field. The fast backward motion of the wall as a whole terminates after a small backward shift under the action of appearing residual depolarization field (Shur, 2005, 2006).

The alternative scenario of the backward wall motion is realized through the formation and propagation of the quasi-regular structure of fingers strictly oriented along allowed  $Y$  directions, which differ for different sides of the stripe domain. These two finger structures grow towards each other, but the electrostatic interaction between approaching fingers prevents their merging (Shur, 2005). The same effect prevents merging of the neighboring fingers. As a result, the ‘dendrite-like’ stable structure of residual domains remains at the end of backswitching (Fig. 21.10b). The complicated shape of individual fingers is caused by branching. It is seen from detailed analysis of the images that the branches are also oriented only along allowed  $Y$  directions. The

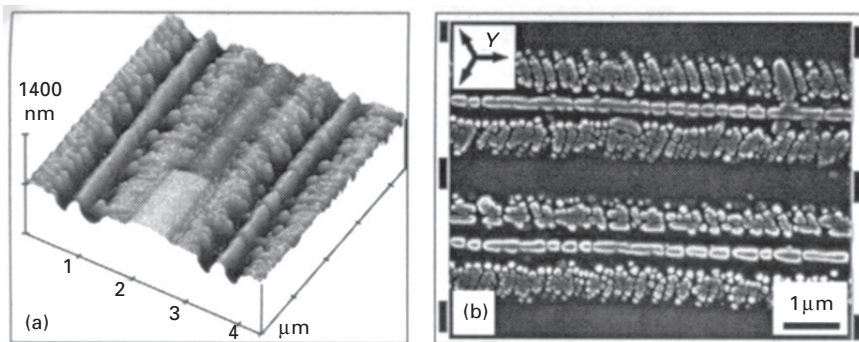


higher mobility of the front of finger structure as compared with the plane domain wall is due to the diminishing of the deceleration effect for quasi-periodic distribution of bound charges (Fatuzzo and Merz, 1967; Lines and Glass, 1977).

## 21.6 Self-assembled nanoscale domain structures

The rapid development of the new SPM methods with nanoscale resolution for visualization of the domain patterns has revolutionized our conception of the domain kinetics in the case of ineffective screening. A recent study (Shur *et al.*, 2000a) reveals that along with continuous domain growth (growth of fingers and dendrites) the discrete switching through the formation of structures consisting of isolated nanoscale domains can be observed during polarization reversal at the highly non-equilibrium conditions ( $R \gg 1$ ) (Fig. 21.11). It has been shown experimentally that the discrete switching through formation and enlargement of the ensemble of nano-domains occurs in LN. The self-assembled structures usually demonstrate quasi-regular spatial distribution of the monomers (isolated nano-domains).

We have discovered the effect of self-maintained spontaneous decay of the stripe domain structure in CLN through arising and growth of the oriented nanoscale domain arrays (Batchko *et al.*, 1999; Shur *et al.*, 2000a, 2001, 2003). The domain patterns, revealed by etching and visualized by AFM (Fig. 21.11a) and SEM (Fig. 21.11b), demonstrate the array-assisted reversal motion of the existing domain walls through propagation of the highly organized quasi-periodical structure of domain arrays strictly oriented along crystallographic directions. Each quasi-regular array is comprised of nano-domains with a diameter 30–100 nm and an average linear density exceeding

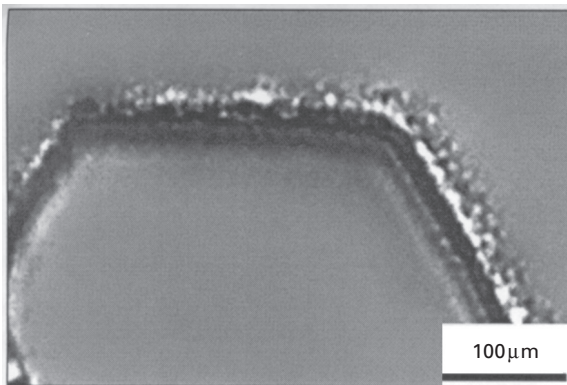


21.11 Stable nano-domain arrays in CLN formed as a result of backswitching during periodical poling. Black rectangles – electrode position. Z+ view. Domain patterns revealed by etching and visualized by (a) AFM and (b) SEM.

$10^4 \text{ mm}^{-1}$ . Such a domain evolution scenario was observed during switching using periodical stripe electrodes oriented along the  $Y$ -direction deposited on the  $Z$ -surface. It has been shown that for a sufficient domain spreading out of the electrodes (obtained for short switching pulse duration  $\Delta t_{\text{sp}} \sim 5 \text{ ms}$  and a small field-diminishing amplitude  $\Delta E \sim 2 \text{ kV/mm}$ ) the backswitched domain evolution represents self-maintained, self-organized growth of oriented nanoscale domain arrays.

The typical structure produced in CLN covered by artificial dielectric layer (photoresist) as a result of backswitching after the electric field switch-off is shown in Fig. 21.10. This domain pattern is stable (frozen-in) and does not undergo any evident changes for years. According to the optical visualization with low spatial resolution this structure consists of fingers strictly oriented along three crystallographic directions similar to the dendrite structures. But the detailed visualization of these stable domain patterns by SPM reveals that in this case each finger is an array of nanoscale monomers (Fig. 21.11). The statistical analysis of the monomer distribution along the array reveals that the distances between the neighboring monomers are highly correlated.

The effect of correlated nucleation was studied also during switching in uniform electric field in CLN with surface layer modified by proton exchange. The *in situ* recording of the set of instantaneous domain patterns reveals that the stripe area filled by isolated nanoscale domains propagates in front of the moving domain wall (Fig. 21.12). The domain growth in this case is achieved through the appearance of new chains of individual nano-domains in front of the stripe, while the trailing edge of the stripe is swept by the wall of the growing solid domain (Shur *et al.*, 2006). It is necessary to point out that in this experiment the non-equilibrium switching conditions ( $R \gg 1$ ) are fulfilled

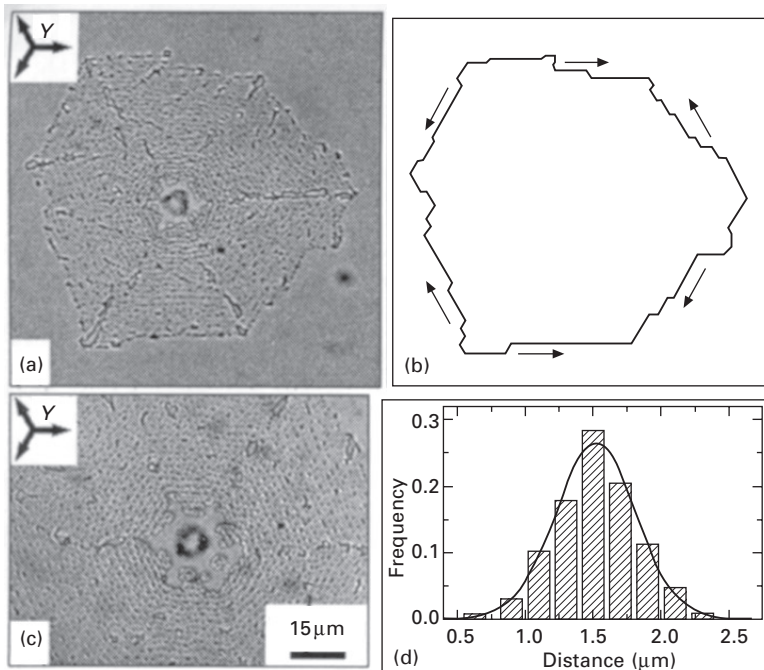


21.12 Propagation of the stripe area filled by isolated nano-scale domains in front of the moving domain wall during switching in CLN with proton-exchanged surface layer. Instantaneous optical image.

as the proton exchange leads to the formation of the thick surface dielectric layer (Shur *et al.*, 2004b).

Another clear demonstration of correlated nucleation effect was observed for switching in a uniform electric field in SLT completely covered by a thick artificial dielectric layer (2  $\mu\text{m}$ -thick photoresist) using liquid electrodes (Shur *et al.*, 2002b; Shur, 2005, 2006). In these conditions the web-like self-assembled domain structures appear around the pinholes in the dielectric layer (Fig. 21.13).

The switching process starts as the formation of a ‘hexagon’ domain around the pinhole. The visualization of the structure by optical microscope reveals that its subsequent growth is achieved through propagation of the quasi-regular ensemble of microscale isolated domains. It is possible to obtain the information about the domain structure evolution by analysis of the static domain pattern as the positions of the domain chains can be attributed to the subsequent locations of the ensemble boundary. Such analysis allows us to conclude that the growth of this structure (evolution of the ensemble



**21.13** Web-like self-assembled domain structures formed in SLT covered by photoresist. (a), (c) Optical images of structures revealed by etching. (b) Boundary of ensemble of microscale isolated domains. (d) Distributions function of the distances between the neighboring domains.

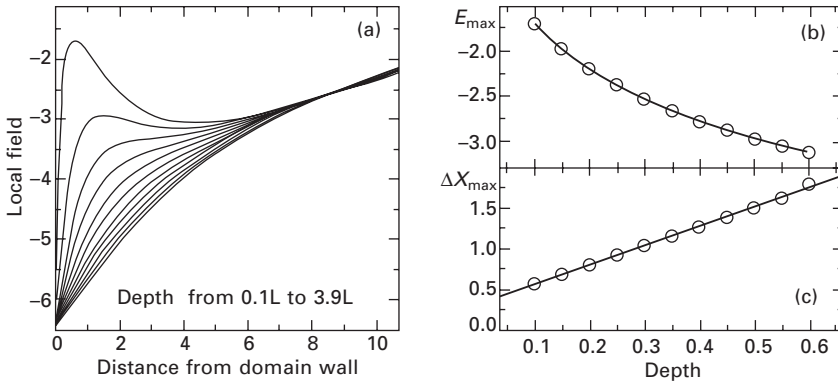
boundary) follows the same rules as the continuous growth of the isolated domain. For discrete switching the ensemble boundary shown in Fig. 21.13b plays the role of the domain wall. The shape of the switched area is the same regular polygon as in the case of isolated domain growth (see Section 21.5). The boundaries are oriented in strict crystallographic directions. One can observe the formation of the steps and their propagation along the boundary.

The spatial correlation of the individual domain distribution is clearly demonstrated by statistical analysis of the distances between the neighboring domains (Fig. 21.13d). The obtained averaged distance between domains is very close to the thickness of the artificial dielectric gap. This fact opens the possibility of evaluating the effective depth of the intrinsic dielectric layer for any material and any experimental condition by measuring the average period of the quasi-regular structure appearing during discrete switching for  $R \gg 1$ .

All the above-discussed self-assembled structures are formed as a result of correlated nucleation in the vicinity of the moving domain wall or the propagating boundary of the enlarging domain ensemble. The effect is caused by the influence on the nucleation probability of the trail of the uncompensated depolarization field behind the moving wall or propagating boundary. To explain the effect we have calculated the spatial distribution of the electric field in the vicinity of the domain wall with the trail in the ferroelectric capacitor (plate covered by uniform electrodes) with the surface dielectric layers. It has been shown that the distribution of the field value at the boundary between the ferroelectric and dielectric layer demonstrates a pronounced maximum at some distance from the wall (Fig. 21.14a). This distance is about the thickness of the surface dielectric layer  $L$ .

While the field maximum diminishes with the depth (Fig. 21.14), nevertheless the existence of the field maximum drastically changes the domain kinetics. On one hand, the trail of uncompensated depolarization field suppresses the nucleation at the wall, thus terminating the classical wall motion. On the other hand, it induces the field maximum, which increases the probability of nucleation at the definite distance in front of the wall. The growth of nuclei leads to the appearance along the wall of the isolated needle-like micro-domains with charged walls. The sideways growth of any isolated domains that arise is suppressed due to the same effect of the uncompensated depolarization field. The decrease of the local electric field in the vicinity of each isolated domain initiates the formation of new domains at some distance from each other. As a result, the quasi-regular domain chain aligns along the wall.

It has been calculated that the new field maximum appears at the distance from the formed domain chain thus initiating formation of the new chain, leading to self-maintained enlarging of the domain ensemble. It has been



21.14 (a) The simulated local field distributions near the stripe non-through domain for different depth under the dielectric surface layer. Depth dependences of (b) value of local field maximum  $E_{\max}$ , (c) distance between the wall and field maximum  $\Delta X_{\max}$ . The distance from the domain wall and depth are normalized by the thickness of the surface dielectric layer  $L$ .

shown experimentally that these self-assembled structures can cover areas of several square millimeters.

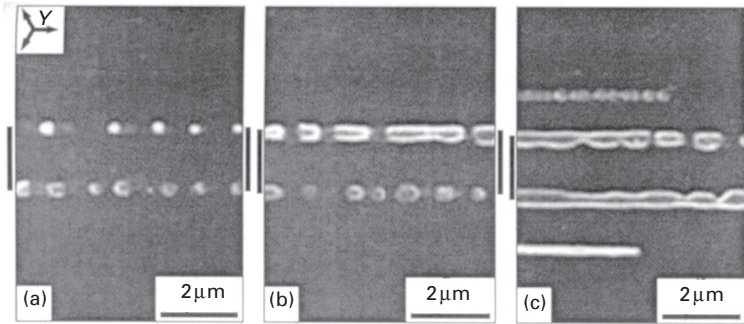
There are two ways to intensify the role of the correlated nucleation process. One of them has been realized by increasing the ratio  $R$ , by amplification of the switching field or by hindering the screening processes. This possibility has been demonstrated in the above-discussed backswitching experiments. The alternative possibility is the deposition of the artificial surface dielectric layer, thus increasing the residual depolarization field. The period of the quasi-regular structure increases accordingly in this case.

## 21.7 Modern tricks in nanoscale domain engineering

### 21.7.1 Backswitch poling

The backswitching process is always considered as undesirable one, because it destroys the tailored domain structure, but its detailed study is useful. An original poling method for creation of short-pitch periodical domain structures in LN and LT, so-called ‘backswitched poling’, has been proposed (Batchko *et al.*, 1999, 2003; Shur *et al.*, 2000a). The unique feature of backswitched poling is that the polarization reversal occurs without application of any external electric field. The domain kinetics is induced by internal source – residual depolarization field existing after abrupt switch-off of the external field due to retardation of the bulk screening.

Two distinguishable stages of domain evolution can be revealed during backswitched poling (Fig. 21.15). The process starts with nucleation of chains



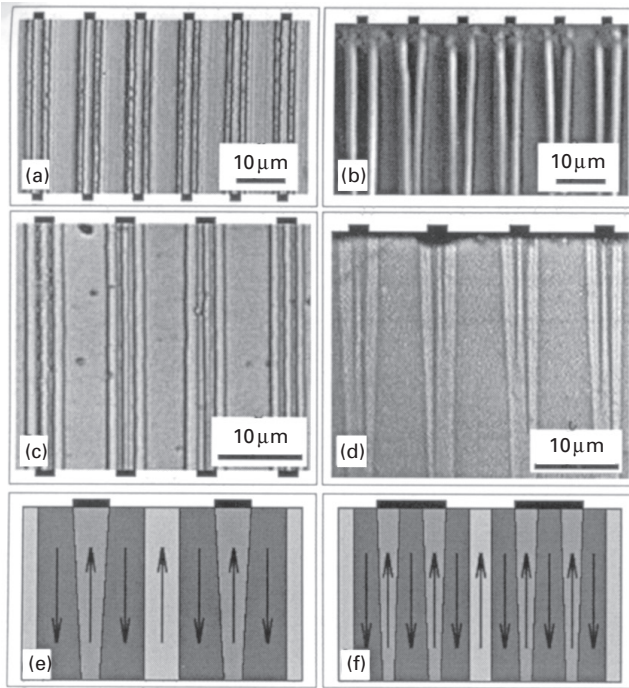
21.15 The stages of domain kinetics along the electrode edges during backswitching in CLN. Strip electrode oriented along Y direction covers the area between the black lines. SEM patterns of domains revealed by etching. Z+ view.

of the new needle-like domains at the Z+ surface along the electrode edges due to the field singularities caused by the fringe effect (Fig. 21.15a). During the second stage, these growing domains merge and propagate through the wafer, forming the lamellar domains with the initial orientation of  $P_s$  along the electrode edges (Fig. 21.15b).

The backswitched poling also allows the undesirable effect of domain broadening out of the electrode area to be overcome. This effect is a cause of essential difference between the lithographically defined electrode pattern and the periodical domain structure produced. For short domain periods the broadening effect limits the production of the short-pitch periodical domain patterns due to domain merging. For backswitched poling, the domains enlarged during the poling stage under application of the field pulse shrink by the backward wall motion.

The application of this improved poling method to LN demonstrates the spatial frequency multiplication of the domain patterns as compared with the spatial frequency of the electrodes and self-maintained formation of the oriented domain arrays consisting of individual nanoscale domains (Shur *et al.*, 2000a, 2001). The mechanism of frequency multiplication is based on domain formation along the electrode edges during backswitching. For ‘frequency tripling’ (Fig. 21.16c), the subsequent growth and merging of the domains lead to the formation of a couple of strictly oriented sub-micrometer-width domain stripes with depth about 20–50  $\mu\text{m}$  under the edges of wide electrodes (Fig. 21.16d). For narrow electrodes only the ‘frequency doubling’ can be obtained (Fig. 21.16a) with the depth of the backswitched domain stripes about 50–100  $\mu\text{m}$  (Fig. 21.16b).

Let us consider the stages of backswitched domain evolution for wide (about 3  $\mu\text{m}$ -width) electrodes (Fig. 21.17). The patterns were observed in different partially backswitched samples. The initial nucleation along electrode



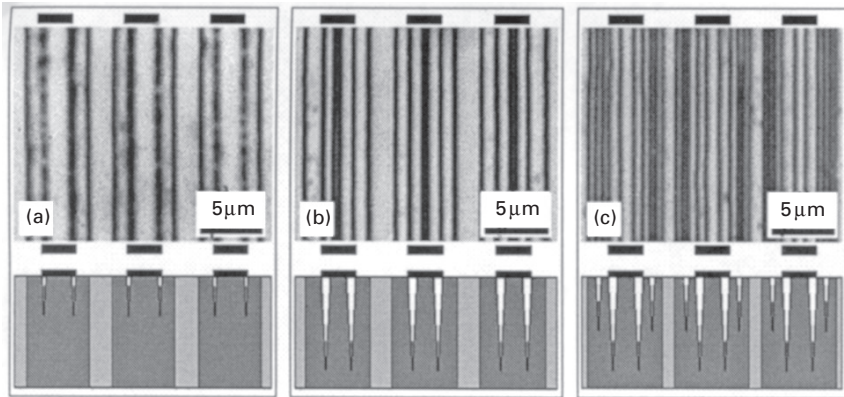
**21.16** Spatial frequency multiplication of the periodical domain patterns by backswitching in CLN. (a), (c), (e) ‘frequency doubling’; (b), (d), (f) ‘frequency tripling’. (a), (b) Z+ view; (c), (d), (e), (f) Y cross-sections. Optical images of domains revealed by etching. (e), (f) schematic drawing. Dark gray – switched domains, medium gray – backswitched, light gray – non-switched.

edges (Fig. 21.17a) and subsequent merging led to the formation of a couple of strictly oriented sub-micrometer-width domain stripes under each electrode (Fig. 21.17b). This process can be considered as ‘frequency tripling’. The width of the stripes can be controlled by duration of backswitching stage. The depth of the backswitched domains is about 20–50 μm.

For the longer backswitching stage a new couple of nano-domain arrays appears out of electroded area along the electrode edges (Fig. 21.17c). The ‘frequency pentaplication’ effect was observed in this way. It has been shown that the distance between secondary and initial stripes (structure period) is determined and can be controlled by the thickness of the artificial insulating layer.

The backswitching method has been applied to 2.6 μm periodical poling of the LN 0.5 mm-thick wafers. It is seen that the domain patterns on Z<sup>-</sup> prepared in fragments of 3-inch-diameter (75 mm) wafer are practically ideal (Fig. 21.18a).

The continuous-wave (CW) single-pass second harmonic generation (SHG) of blue light in 4 μm-period, 0.5 mm-thick, 50 mm-length backswitched-poled



21.17 Stages of the domain evolution during the domain frequency multiplication process in LN. Z+ view. Strip electrode oriented along Y direction covers the area between the black lines. Optical images of domains revealed by etching.

LN devices was obtained. Using the CW Ti:sapphire pump laser 6.1%/W efficient first-order generation of 61 mW at  $\lambda = 460$  nm was achieved, indicating an effective nonlinearity about one half of the nominal value. It has been shown that the sample phase matches over the full 50 mm length.

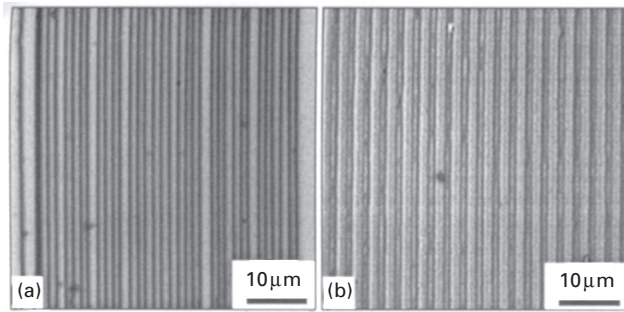
Moreover, laser-diode-pumped SHG was performed with InGaAs single-stripe diode master oscillator. The oscillator was single frequency and tunable from 874 to 936 nm, with maximum output of 20 mW at 930 nm. The pump power after the amplifier and two pairs of optical isolators was above 2 W. With 1.5 W of laser-diode power, 60 mW of SHG at 465 nm was produced, given a normalized conversion efficiency of 2.8%/W. An improved efficiency of 3.4%/W was obtained by expansion and spatial filtering of the diode beam before it was focused into the periodically poled LN.

The optimized method for 2.6  $\mu\text{m}$  has been applied periodical poling of the LT 0.3 mm-thick wafers. It is seen that the domain patterns prepared in fragments of 2-inch-diameter (50 mm) wafer on Z+ are practically ideal (Fig. 21.18b).

### 21.7.2 Formation of oriented quasi-regular domain rays by pulse UV irradiation

It has been shown recently that illumination of the polar face of CLN crystal by pulsed ultraviolet laser leads to the formation of the surface domain structure with the depth about a few micrometers (Valdivia *et al.*, 2005). Our detailed study of the domain kinetics under these highly non-equilibrium conditions reveals that arising of self-assembled structures is also achieved through the discrete switching.





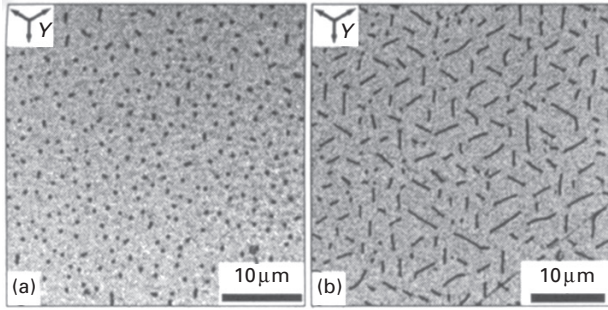
21.18 Domain patterns with  $2.6\mu\text{m}$  period (a) Z- view in CLN and (b) Z+ view in CLT revealed by etching and visualized by optical microscopy.

The studied  $0.5\text{ mm}$ -thick single-domain wafers of congruent LN were cut normally to the polar axis. Both polar surfaces (Z+ and Z-) were UV-irradiated using eximer gas pulsed laser LGE-4 (wavelength  $308\text{ nm}$ , pulse duration  $25\text{ ns}$ ) produced by the laboratory of Quantum Electronics, Institute of Electrophysics, Ural Branch of Russian Academy of Science. The diameter of irradiated area was about  $3\text{ mm}$ . The applied energy density ranged from  $0.5$  to  $1.5\text{ J/cm}^2$ .

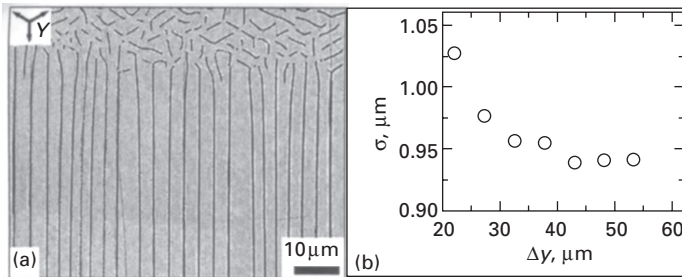
The optical microscopy and AFM in contact mode were used for visualization of the domain patterns revealed by shallow etching. Additionally, the surface domain structure was visualized with high spatial resolution without etching by piezoelectric force microscopy (PFM). It has been shown that the obtained domain patterns and their dependence on the energy density are qualitatively different for Z+ and Z- polar surfaces.

In all the used range of energy density the irradiated area at the Z-surface is covered by isolated nano-domains ('dots'). In contrast, the types of domain patterns appeared at Z+ surface depend essentially on the energy density. Systematic analysis of domain images allows us to distinguish three types of the surface domain structures at the Z+ surface: (1) 'dots' – isolated domain patterns appearing in the narrow region along the boundary of the irradiated area (Fig. 21.19a); (2) 'lines' – quasi-periodic domain patterns, consisting of parallel rays, forming inside the irradiated area (Fig. 21.20); (3) 'fractals' – self-similar domain patterns appearing inside the irradiated area (Fig. 21.21).

Dotted patterns represent the quasi-regular structure. The average distance between the neighboring isolated domains is about  $2.4\mu\text{m}$  while the shortest distance between neighboring domains is  $0.6\mu\text{m}$ . The obtained correlated spatial distribution is caused by above-discussed effect of correlated nucleation (Shur, 2005). The dotted pattern can be essentially changed by second pulse irradiation using higher energy density. The anisotropic growth of isolated domains leads to the formation of dash-like domains strictly oriented along



21.19 Isolated domain patterns formed in CLN under pulsed UV laser irradiation on Z+ face: (a) dots, (b) dashes. Optical images of domains revealed by etching.

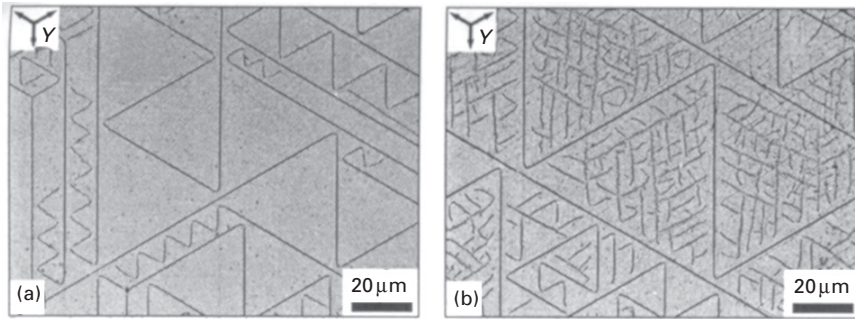


21.20 (a) Quasi-periodic lines pattern formed in CLN under pulsed UV laser irradiation on Z+ face. (b) Dependence of the period dispersion on the distance from boundary of irradiated area. Optical images of domains revealed by etching.

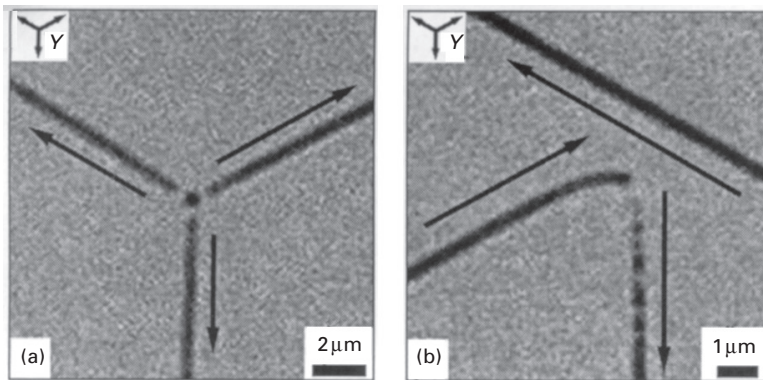
*Y* crystallographic directions (Fig. 21.19b). The anisotropic growth is similar to the above-discussed formation of the finger structure and can be attributed also to the ineffective screening.

Line patterns consisting of long domain rays strictly oriented along *Y*+ directions are the typical domain patterns inside the irradiated area. The average period of quasi-periodic structures is about  $3.9 \pm 0.8 \mu\text{m}$ , while the ray thickness is about 200 nm (Fig. 21.20a). The rays start to grow from the isolated domains situated along the boundary of the irradiated area. During propagation from the boundary to the center, the averaged period remains almost constant, while the dispersion essentially decreases (Fig. 21.20b).

Fractal patterns appear as a result of ray interaction. The rays start to grow along all three allowed directions from the isolated domains situated in the center of the area and form the ‘three-ray stars’ (Fig. 21.22a). The rays never cross each other and their interaction leads to ‘reflection’ (Fig. 21.22b). The ray growing in one *Y* direction changes the growth direction by  $120^\circ$ , when the ray tip approaches the already existing ray oriented in another *Y* direction.



21.21 Typical fractal domain patterns formed in CLN under pulsed UV laser irradiation on Z+ face: (a) without branching, (b) with branching. Optical images of domains revealed by etching.

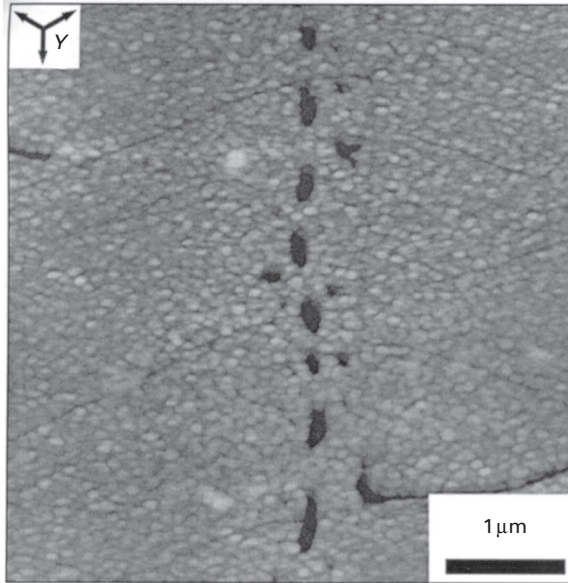


21.22 Elementary fragments of domain patterns formed in CLN under pulsed UV laser irradiation on Z+ face: (a) 'three-ray star', (b) interaction of growing domain rays - 'reflection'. Optical images of domains revealed by etching.

The direction of further growth corresponds to the third Y direction (Fig. 21.22b). The multiple ray reflections result in the formation of 'triangles' and 'zigzags' (Fig. 21.21).

Denser fractal patterns appear for higher radiation energy due to the branching effect (Fig. 21.21b) representing the growth of rays of next generation from already existing ones. The branches fill the empty space inside the large triangles of the previous generations. The fractal analysis of the domain structures shows their self-similarity in wide size range with the fractal dimension about 1.8 calculated by the box-counting method (Feder, 1988).

While according to optical microscopy observations the domain rays are continuous or dash-like, AFM images reveal that in many cases these rays represent the chains/arrays of nano-domains with average size about 200 nm (Fig. 21.23). The average period of nano-domains in a chain is about 400 nm.



21.23 Fragment of nano-domain array formed in CLN under pulsed UV laser irradiation on Z+ face. AFM images of domains revealed by etching.

It is necessary to reveal the origin of the electric field that is the driving force of the polarization reversal under the action of the pulse laser irradiation. Two models can be proposed. First, the switching field is caused by the laser ablation, which partially removes the screening charges compensating the depolarization field in stable conditions. The uncompensated depolarization field that arises becomes high enough for polarization reversal. The effect is similar to the recently observed spontaneous backswitching induced by the chemical etching (Shur *et al.*, 2005c). Second, the switching field of pyroelectric nature appears during cooling. The polarization reversal under the action of the pyroelectric field is well known (Miyazawa, 1979; Nakamura and Tourlog, 1993; Zhu *et al.*, 1994).

The next issue to be addressed is why the ‘discrete switching’ is observed. According to previous experiments, such anomalous switching is caused by highly non-equilibrium switching conditions due to ineffective screening of the depolarization field (Shur, 2005). In contrast to switching under application of external electric field the surface in these experiments remains free of electrodes. It is clear that in such conditions the external screening is ineffective and the residual depolarization field is abnormally high.

The formation of the nanoscale domain chains and other effects of self-assembling is due to electrostatic domain–domain interaction, which is abnormally strong due to ineffective screening. The reflection effect can be

understood as a result of suppression of the nucleation process in initial direction due to the electrostatic domain–domain interaction. I believe that the tailored self-similar nanoscale structures produced by pulse laser illumination can be used for the production of the nano-domain structures with sub-micron meter periods for various applications.

## 21.8 Polarization reversal in relaxors

The heterophase state exists in relaxor ferroelectrics over a wide temperature interval. It has been shown by high-resolution electron microscopy that the heterophase structure just below the transition from non-polar to relaxor phase consists of polar nanoregions embedded in a non-polar medium (matrix) (Cross, 1994; Bokov and Ye, 2006b). The polar microregions with a complicated structure of nanoscale domains appear during subsequent cooling (Dai *et al.*, 1994; Egami *et al.*, 1997; Lehnen *et al.*, 2001; Terabe *et al.*, 2002). The random orientation of spontaneous polarization  $P_S$  in individual polar nanoregions leads to zero value of  $P_S$  averaged over microregions. The irreversible switching to the state with electrical field-induced macroscopic polarization is observed in such canonical relaxors as PMN over a wide temperature range below the temperature of the dielectric permittivity maximum (Cross, 1994; Bokov and Ye, 2006b).

In PLZT ceramics the irreversible switching is observed below the so-called freezing temperature  $T_f$ . The unusual reversible switching behavior was discovered and studied in PLZT ceramics in the temperature range just above the freezing temperature (Shur *et al.*, 1999b, 2004a, 2005a,b). In this case, the application of a strong electric field induces averaged  $P_S$ , but in contrast with the normal ferroelectrics, this state is unstable without electric field. The restoration of the initial state (complete spontaneous ‘backswitching effect’) is observed after external field switch-off (Shur *et al.*, 1999b, 2004a, 2005a,b). Special attention has been paid to this phenomenon because it demonstrates the original kinetics of nanoscale domain structure and can be discussed within general approach presented above.

According to the classical concepts of relaxor ferroelectrics (Isupov, 1983; Cross, 1994; Kleemann and Lindner, 1997; Marssi *et al.*, 1998), the temperature increase leads to transition from the homogeneous ferroelectric state to the heterogeneous (heterophase) one. The heterophase structure just above this transition represents a ferroelectric multidomain matrix with isolated nanoscale inclusions of the non-polar phase. The depolarization fields produced by bound charges (the polarization jumps at the interfaces) prevent formation of macro-domains and stimulate appearance of the nanoscale domain structure. There exists the essential difference between screening of the depolarization fields produced by bound charges situated at the surface (in normal ferroelectrics) and at the interfaces in the bulk (in relaxors). The above-

discussed surface  $E_{\text{dep}}$  (see Section 21.4) is compensated for substantially by fast external screening (charge redistribution at the electrodes), while the bulk  $E_{\text{dep}}$  in relaxors can be compensated for by slow bulk screening only (Shur *et al.*, 1984a, 1997; Shur, 1998). This feature explains the peculiarities of the domain kinetics in relaxors.

The nanoscale domains have been observed recently in several relaxors using high-resolution microscopy (Dai *et al.*, 1994; Lehnen *et al.*, 2001; Terabe *et al.*, 2002; Abplanalp *et al.*, 2002; Bdikin *et al.*, 2003; Shvartsman and Kholkin, 2004; Bai *et al.*, 2004). It has been shown in PLZT by high-resolution transmission electron microscopy that the relaxor state in some temperature range is the heterophase structure consisting of polar nanoregions with diameters down to 10 nm embedded in a non-polar matrix (Dai *et al.*, 1994). The complicated nanoscale domain structure was observed in pure and doped single crystals of strontium-barium niobate (Sr,Ba)Nb<sub>2</sub>O<sub>6</sub> by PFM (Lehnen *et al.*, 2001; Terabe *et al.*, 2002). The ‘fingerprint’ sub-microscale domain patterns have also been observed in single-crystalline Pb(Mg<sub>1/3</sub>Nb<sub>2/3</sub>)O<sub>3</sub>–PbTiO<sub>3</sub> (PMN–PT) and Pb(Zn<sub>1/3</sub>Nb<sub>2/3</sub>)O<sub>3</sub>–PbTiO<sub>3</sub> (PZN–PT) using PFM (Abplanalp *et al.*, 2002; Bdikin *et al.*, 2003; Shvartsman and Kholkin, 2004; Bai *et al.*, 2004). The domain patterns of similar geometry have been revealed recently in PLZT ceramics by scanning force microscopy in acoustic mode (Yin *et al.*, 2004) and PFM (Shvartsman *et al.*, 2005).

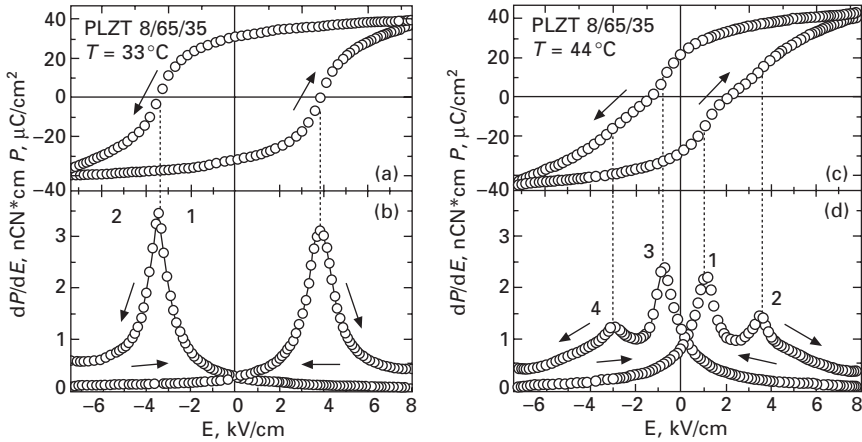
It is necessary to stress that all performed experiments allow us to visualize the domain patterns only at the surface. Thus, the geometry of the nanoscale structure in the bulk remains unknown. It has been shown that the information about the geometry of the initial domain structure and its evolution during switching can be extracted by analysis of the switching current shape proposed in Shur *et al.* (1998). This analysis is valid for characterization of nanoscale structures, because it provides unique scale-free information about dimensionality of the domain growth.

In this section we present the results of experimental investigation of the geometry of nanoscale domain structures using analysis of the switching current shape and visualization of the surface domain patterns by PFM in PLZT ceramics chosen as a model relaxor ferroelectric.

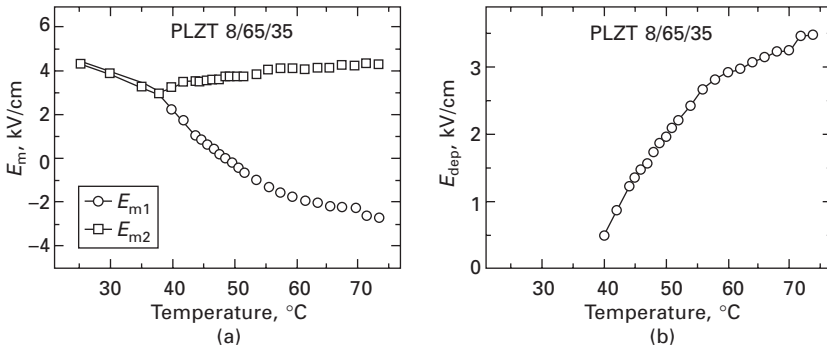
### 21.8.1 Hysteresis loops

The temperature evolution of the hysteresis loops in PLZT has been measured during quasi-static bipolar switching. It has been shown that the shape of loop changes qualitatively during heating/cooling in the vicinity of proper temperature  $T_f$  (Fig. 21.24). The classical ferroelectric loop observed at low temperatures transforms during heating to the ‘double loop’.

The temperature evolution was studied by analyzing of the field dependence of the derivative of the switched charge on field  $dQ/dE$ , which is proportional



21.24 (a), (c) Hysteresis loops and (b), (d) field dependences of the derivative of the switched charge on field  $dQ/dE$  measured in PLZT 8/65/35 ceramics at different temperatures. (a), (b)  $T < T_f$ , (c), (d)  $T > T_f$ .



21.25 Temperature dependences of averaged coercive fields for PLZT 8/65/35 ceramics.

to the switching current for polarization reversal in linear increasing field. Two peaks of  $dQ(E)/dE$  observed in the ferroelectric phase are caused by classical polarization reversal typical for normal ferroelectrics. The maxima of  $dQ(E)/dE$  are observed at the fields, which are close to the coercive fields  $E_c$  determined by conventional methods. For the double loop obtained in the relaxor state (for  $T > T_f$ ) both peaks demonstrate splitting (Fig. 21.24d). The positions of the four peak maxima  $E_{mi}$  (Fig. 21.25a) are very sensitive to temperature variation.

The special feature of the switching in relaxor state can be discussed in the framework of the above approach underlining the crucial role of bulk screening. In a strong enough applied negative field the ferroelectric matrix

is poled almost completely in the direction determined by this field. It is clear that the main volume of the sample being in the ferroelectric state will demonstrate the usual switching behavior. The influence of non-polar inclusions are essential only in the regions close to the interfaces (boundaries of non-polar inclusions). The backswitching (switching in negative field) takes place in these regions under the action of  $E_{\text{dep}}$  (produced by bound charges at the boundaries of non-polar inclusions), which stimulates the switching to the multidomain state in the bulk. This first switching stage is characterized by the averaged value of the local coercive field  $E_{m1}$ . The transition from the multidomain state to the single domain one in the regions close to interfaces is hindered by increasing of  $E_{\text{dep}}$ . Thus, the final switching stage is characterized by averaged value of the local coercive field  $E_{m2}$ . It is clear that the single domain state existing in high applied field is unstable and will be destroyed by  $E_{\text{dep}}$  after external field switch-off. Thus, the splitting  $0.5 (E_{m2} - E_{m1})$  is determined by the value of  $E_{\text{dep}}$ :

$$E_{\text{dep}} = 0.5 (E_{m2} - E_{m1}) \quad 21.8$$

The critical temperature dependence of  $E_{\text{dep}}$  (Fig. 21.25b) allows us to define the temperature  $T_f$ , which characterizes transition to the unstable field-induced state caused by the appearance of non-polar inclusions. For PLZT 8/65/35  $T_f = 38^\circ\text{C}$  has been obtained.

## 21.8.2 Switching by rectangular pulses

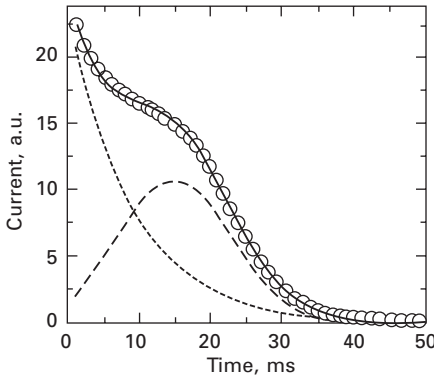
It is well known that recording of the switching current under application of the rectangular pulses is the most effective for quantitative characterization of the domain kinetics (Merz, 1956). The analysis of the switching current data based on the Kolmogorov–Avrami (K-A) approach (Kolmogorov, 1937; Avrami, 1939) to the description of the phase growth during phase transformation was proposed by Ishibashi and Takagi (1971). The modification of the K-A approach for polarization reversal in finite media (Shur *et al.*, 1998) allows us to find out the domain growth dimensionality. As a result, it is possible to distinguish between two main variants of nucleation processes and to reveal the geometry of the domain structure without direct visualization (Shur *et al.*, 1998).

The switching current data (Fig. 21.26) recorded under the action of rectangular pulses for the relaxor phase ( $T > T_{fd}$ ) have been fitted using the following formula:

$$j(t) = j_c(t) + j_s(t) \quad 21.9$$

where  $j_c(t) = j_0 \exp(-t/\tau_c)$  is due to charging of ferroelectric capacitor,  $\tau_c$  depends on the parameters of the external circuit,  $j_s$  is the proper switching current caused by polarization reversal in ferroelectric regions.





21.26 Switching current under application of rectangular pulses for PLZT 7/65/35. Experimental points are fitted by Equations [21.9] and [21.10]. Short dashes –  $j_c(t)$ , charging of ferroelectric capacitor; long dashes –  $j_s(t)$ , switching current caused by polarization reversal in ferroelectric regions.  $E = 7.6 \text{ kV/cm}$ .  $T = 89^\circ\text{C}$ .

The switching current component  $j_s$  has been fitted by K-A formula modified for switching in finite media, which accounts for existence of the heterophase structure of relaxors (Fig. 21.26) (Shur *et al.*, 1998, 1999a):

$$j_s(t) = 2P_s \, dq(t)/dt \tag{21.10}$$

where  $q(t) = \exp[-(t/t_0)^n (1 - t/t_m)]$ ,  $t_0$  and  $t_m$  are time constants,  $t_m$  accounts for the impingement of the growing domains on the switched volume boundary. Exponent  $n$  is so-called growth dimensionality.

Two limiting situations of the nucleation process are usually considered following Kolmogorov classification. The first,  $\alpha$  model, when the nuclei are arising through the whole process with nucleation probability  $\alpha(t)$ , and the second,  $\beta$  model, when all nuclei have arisen at the very beginning of the process with the density  $\beta$  (Shur *et al.*, 1998).  $n = d + 1$  for  $\alpha$  model, and  $n = d$  for  $\beta$  model, where  $d$  is the topological dimensionality. In our approach the meaning of  $d$  is changed and it is interpreted as the growth dimensionality equal to 1, 2, or 3.  $d = 3$  for growth of new domains in the bulk,  $d = 2$  for sideways growth of cylinder domains, and  $d = 1$  for parallel shift of the walls of domains organized in the maze-like structure (Ishibashi and Tagaki, 1971; Shur *et al.*, 1998).

It has been found out by analysis of the switching current data measured in PLZT ceramics in all experimental conditions that the best-fit value of the growth dimensionality is equal to 2 and can be classified as  $\alpha(1D)$  process. It means that the parallel shift of the domain walls is the predominant mechanism of the domain kinetics. Thus, the polarization reversal in relaxor ceramics is the result of the evolution of the maze domain structure, which is in accordance with interpretation of the hysteresis loop data.

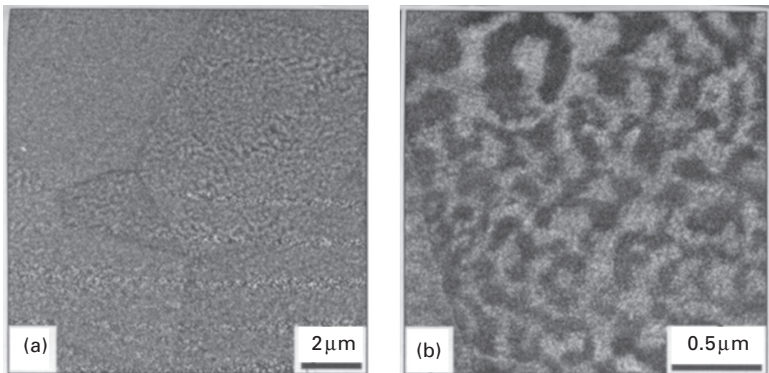
### 21.8.3 Visualization of the nano-domain structure

The nanoscale domain structure has been visualized with good contrast by PFM (Fig. 21.27b). The typical domain pattern of PLZT ceramics after zero-field-cooling represents the quasi-regular nanoscale maze ('fingerprint' pattern). Light and dark areas correspond to domains with different polarization directions. It has been shown that the fractions of the areas occupied by different domains are almost equal.

The PFM images contain the piezoelectric response of the domain structure integrated over the volume, the depth of which depends on the applied voltage. Thus, the observed diffused boundaries between neighboring domains are caused by randomly oriented charged domain walls. It is an evidence of the existence of 3D maze structure, predicted by our interpretations of the switching data. The similarity of the structures in grains with different orientations is the additional argument in favor of 3D maze geometry (Fig. 21.27a).

The main characteristics of the maze domain structure have been extracted by statistical analysis of the PFM images. It has been found that the average value of the maze segment width ('period') is essentially dependent on the La concentration. For  $x = 9.75\%$  the maze period is 170 ~ 220 nm, while for  $x = 7\%$  the period is 30 ~ 40 nm.

A fractal analysis was carried out by so-called 'island method' of PFM images considered as the section of 3D domain structure (Feder, 1988). The obtained value of fractal dimension is equal to  $2.5 \pm 0.1$ . Such a result allows us to suppose that the formation of the nanoscale domain structure during zero-field cooling is the random spatially non-correlated process (Feder, 1988).



21.27 (a) Nanoscale structure in different grains and (b) maze domain structure visualized by PFM in PLZT 9.75/65/35 ceramics.

## 21.9 Conclusions and future trends

In this chapter, we have formulated the unified approach to the domain kinetics based on the nucleation mechanism of the polarization reversal and demonstrated its validity for understanding the variety of experimentally observed domain evolution scenarios in LN and LT single crystals. It has been proved that the kinetics of the ferroelectric domain structure essentially depends upon the effectiveness of the screening processes. Original scenarios of the domain structure evolution were revealed experimentally and discussed within unified approach accounting for the decisive role of the retardation of the screening process. It has been shown that the predetermined nucleation effect plays the key role in the growth of the polygon domains in LN and LT. It has been demonstrated that the degree of screening effectiveness determines the formation of the whole variety of the shapes of isolated domains experimentally observed in LN and LT from regular hexagons to three-ray stars. The role of merging in formation of super-fast X domain walls was revealed experimentally and by computer simulation. We have demonstrated that the evolution of a domain structure in LN and LT under the highly non-equilibrium switching conditions proceeds through the formation of the self-assembled nanoscale structures.

The results of the fundamental investigations were used as a physical basis of ‘domain engineering’. The proposed and realized new techniques allow the production of the short-pitch regular domain patterns with record periods in LN and LT single crystals. The modern tricks in nanoscale domain engineering (formation of nanoscale quasi-regular domain structures) have been reviewed. The elements with tailored domain structures demonstrate nonlinear optical properties required for modern coherent light frequency conversion devices with upgraded characteristics. The application of the proposed approach to the analysis of the hysteresis loops and switching current data in relaxor PLZT ceramics enables us to reveal the key role of nanoscale non-polar inclusions in polarization reversal in relaxor state.

The recent achievements in studying the domain kinetics with nanoscale resolution allow predicting that the future of the domain engineering lies in the production of the tailored nano-domain structure and the structures possessing the nanoscale period accuracy. Several approaches to creation of the regular nanoscale structures can be singled out. The precise periodic structures can be produced as a result of the local switching of the single-domain using application of the inhomogeneous electric field by the nanoscale electrode pattern, conductive tip of SPM or electron beam. According to the experimental results discussed above the periodic nanoscale heterogeneous modification of the surface layer by various alternative methods looks very promising. The most interesting and effective methods are those that are based on formation of self-assembled structures. Some examples of

quasi-regular self-assembled structures and ways to produce them were discussed in this chapter.

It is clear that the future development of nanoscale engineering requires deep investigations of the polarization kinetics in normal and relaxor ferroelectrics using modern sophisticated experimental methods with nanoscale resolution including elaborate modes of SPM, scanning electron and ion microscopy, and focused ion beam (FIB). The development of a reliable technology for domain engineering at the submicrometer scale would be a major breakthrough, leading to a brand new generation of photonic devices. In this chapter I have attempted to show how these two aims are interconnected. The occurrence of nano-domain chains destroying the duty cycle and that of nano-domain ensembles occur under the same highly non-equilibrium conditions.

## 21.10 Acknowledgments

The research was made possible in part by INTAS (Grant 03-51-6562); by Federal Agency of Science and Innovation (Contract 02.513.11.3128); by Program ‘Development of the Scientific Potential of High Education’ of the Federal Agency of Education (Grant RNP 2.1.1.8272); by RFBR-CNRS (Grant 05-02-19648), and by RFBR (Grants 06-02-08149-ofr and 07-02-96033-r\_ural). It is a pleasure to acknowledge the many helpful stimulating discussions with A. Alexandrovski, A. Bratkovski, R.L. Byer, L.E. Cross, M.M. Fejer, J. Fousek, V.M. Fridkin, K. Kitamura, A.L. Korzhenevskii, A.P. Levanyuk, A.L. Roytbourd, E.L. Rumyantsev, J.F. Scott and L.A. Shuvalov in the course of preparation of this publication.

## 21.11 References

- Abplanalp M, Baroshava D, Bridenbaugh P, Erhart J, Fousek J, Guenter P, Nosek J, Shulc M (2002), ‘Scanning force microscopy of domain structures in  $\text{Pb}(\text{Zn}_{1/3}\text{Nb}_{2/3})\text{O}_3$ –8%  $\text{PbTiO}_3$  and  $\text{Pb}(\text{Mg}_{1/3}\text{Nb}_{2/3})\text{O}_3$ –29%  $\text{PbTiO}_3$ ’, *J Appl Phys*, **91** (6), 3797–3805.
- Alekseeva Z E, Vorobieva L B, Yevlanova N F (1986), ‘Selective chemical etching of lithium niobate doped with iron’, *Inorg Mats*, **22**, 1384–1387.
- Armstrong J A, Bloembergen N, Ducuing J, Perhsan P S (1962), ‘Interactions between light waves in a nonlinear dielectric’, *Phys Rev*, **127** (6) 1918–1939.
- Avrami M (1939), ‘Kinetics of phase change. 1. General theory’, *J Chem Phys*, **7**, 1103–1112.
- Bai F, Li J F, Viehland D (2004), ‘Domain hierarchy in annealed (001)–oriented  $\text{Pb}(\text{Mg}_{1/3}\text{Nb}_{2/3})\text{O}_3$ – $x\%$  $\text{PbTiO}_3$  single crystals’, *Appl Phys Lett*, **85**, 2313–2315.
- Batchko R G, Shur V Ya, Fejer M M, Byer R L (1999), ‘Backswitch poling in lithium niobate for high-fidelity domain patterning and efficient blue light generation’, *Appl Phys Lett*, **75** (12), 1673–1675.
- Batchko R, Miller G, Byer R, Shur V, Fejer M (2003), ‘Backswitch poling method for domain patterning of ferroelectric materials’, United States Patent No. 6,542,285 B1, April 1.

- Bdikin I K, Shvartsman V V, Kholkin A L (2003), 'Nanoscale domains and local piezoelectric hysteresis in  $\text{Pb}(\text{Zn}_{1/3}\text{Nb}_{2/3})\text{O}_3$ -4.5% $\text{PbTiO}_3$  single crystals', *Appl Phys Lett*, **83** (20), 4232-4234.
- Blattner H, Kanzig W, Merz W, Sutter H (1948), 'Domain structure of barium titanate crystals', *Helv Phys Acta*, **21**, 207-209.
- Blinic R, Laguta V V, Zalar B, Banys J (2006), 'Polar nanoclusters in relaxors', *J Mat Sci*, **41** (1), 27-30.
- Bokov A A, Ye Z-G (2006a), 'Recent progress in relaxor ferroelectrics with perovskite structure', *J Mat Sci*, **41** (1), 31-52.
- Bokov A A, Ye Z-G (2006b), 'Double freezing of dielectric response in relaxor  $\text{Pb}(\text{Mg}_{1/3}\text{Nb}_{2/3})\text{O}_3$  crystals', *Phys Rev B*, **74**, 132102.
- Burfoot J C, Taylor G W (1979), *Polar Dielectrics and their Applications*, London, Macmillan Press Ltd.
- Bursill L A, Lin P J (1986), 'Electron microscopic studies of ferroelectric crystals', *Ferroelectrics*, **70**, 191-203.
- Byer R L (1997), 'Quasi-phases-matched nonlinear interactions and devices', *J Nonl Opt Phys & Mats*, **6**, 549-592.
- Cameron D P (1957), 'Domain orientation in barium titanate single crystals', *IBM J Res Developm*, **1**, 2-6.
- Cross L E (1994), 'Relaxor ferroelectrics: an overview', *Ferroelectrics*, **151**, 305-320.
- Dai X, Xu Z, Viehland D (1994), 'The spontaneous relaxor to normal ferroelectric transformation in La-modified lead zirconate titanate', *Phil Mag B*, **70**, 33-48.
- Drougard M E, Landauer R (1959), 'On the dependence of the switching time of barium titanate crystals on their thickness', *J Appl Phys*, **30**, 1663-1668.
- Egami T, Teslic S, Dmowski W, Viehland D, Vakhrushev S (1997), 'Local atomic structure of relaxor ferroelectric solids determined by pulsed neutron and X-ray scattering', *Ferroelectrics*, **199**, 103-113.
- Fatuzzo E, Merz W J (1967), *Ferroelectricity*, Amsterdam, North-Holland Publishing Company.
- Feder J (1988), *Fractals*, New York, Plenum Press.
- Feng D, Ming N B, Hong J F, Yang Y S, Zhu J S, Wang Y N (1980), 'Enhancement of second-harmonic generation in  $\text{LiNbO}_3$  crystals with periodic laminar ferroelectric domains', *Appl Phys Lett*, **37**, 607-609.
- Flippen R B (1975), 'Domain wall dynamics in ferroelectric/ferroelastic molybdate', *J Appl Phys*, **46**, 1068-1071.
- Fridkin V M (1980), *Ferroelectrics Semiconductors*, New York and London, Consult. Bureau.
- Furukawa Y, Kitamura K, Takekawa S, Niwa K, Hatano H (1998), 'Stoichiometric  $\text{Mg}:\text{LiNbO}_3$  as an effective material for nonlinear optics', *Opt Lett*, **23**, 1892-1894.
- Gopalan V, Mitchell T (1998), 'Wall velocities, switching times, and the stabilization mechanism of  $180^\circ$  domains in congruent  $\text{LiTaO}_3$  crystals', *J Appl Phys*, **83**, 941-954.
- Gopalan V, Mitchell T (1999), '*In-situ* video observation of  $180^\circ$  domain switching in  $\text{LiTaO}_3$  by electro-optic imaging microscopy', *J Appl Phys*, **85**, 2304-2311.
- Gopalan V, Jia Q, Mitchell T (1999), '*In situ* video observation of  $180^\circ$  domain kinetics in congruent  $\text{LiNbO}_3$ ', *Appl Phys Lett*, **75**, 2482-2484.
- Hayashi M (1972), 'Kinetics of domain wall motion in ferroelectric switching. Pt. 1. General formulation', *J Phys Soc Jpn*, **33**, 616-628.
- Hooton J A, Merz W J (1955), 'Etch patterns and ferroelectric domains in  $\text{BaTiO}_3$  single crystals', *Phys Rev*, **98** (2), 409-413.

- Huang L, Hui D, Bamford D J, Field S J, Mnushkina I, Myers L E, Kayser J V (2001), 'Periodic poling of magnesium-oxide-doped stoichiometric lithium niobate grown by the top-seeded solution method', *Appl Phys B*, **72**, 301–306.
- Iona F, Shirane G (1962), *Ferroelectric Crystals*, London, Pergamon.
- Ishibashi Y, Takagi Y (1971), 'Note on ferroelectric domain switching', *J Phys Soc Jpn*, **31** (2), 506–510.
- Ispov V A (1983), 'Physical phenomena in complex ferroelectric perovskites', *Izv Akad Nauk SSSR, Ser Fiz*, **47** (3), 559–565.
- Janovec V (1959), 'Anti-parallel ferroelectric domain in surface space-charge layers of BaTiO<sub>3</sub>', *Czechosl J Phys*, **9**, 468–480.
- Kitamura K, Furukawa Y, Niwa K, Gopalan V, Mitchell T (1998), 'Crystal growth and low coercive field 180° domain switching characteristics of stoichiometric LiTaO<sub>3</sub>', *Appl Phys Lett*, **73**, 3073–3075.
- Kleemann W, Lindner R (1997), 'Dynamic behavior of polar nanodomains in PbMg<sub>1/3</sub>Nb<sub>2/3</sub>O<sub>3</sub>', *Ferroelectrics*, **199**, 1–10.
- Kobayashi J, Yamada N, Nakamura T (1963), 'Origin of the visibility of the antiparallel 180° domains in barium titanate', *Phys Rev Lett*, **11**, 410–415.
- Kolmogorov A N (1937), 'The statistical theory of metal crystallization', *Izv Akad Nauk USSR, Ser Math*, **3**, 355–359.
- Kumada A (1969), 'Domain switching in Gd<sub>2</sub>(MoO<sub>4</sub>)<sub>3</sub>', *Phys Lett*, **30A**, 186–187.
- Lambeck P V, Jonker G H (1986), 'The nature of domain stabilization in ferroelectric perovskites', *J Phys Chem Solids*, **47**, 453–461.
- Lehnen P, Kleemann W, Wöike Th, Pankrath R (2001), 'Ferroelectric nanodomains in the uniaxial relaxor system Sr<sub>0.61-x</sub>Ba<sub>0.39</sub>Nb<sub>2</sub>O<sub>6</sub>:Ce<sub>x</sub><sup>3+</sup>', *Phys Rev B*, **64**, 224109.
- Lifshitz E M, Pitaevskii L P, Landau L D (1985), *Electrodynamics of Continuous Media, Theoretical Physics*, 2nd ed., Vol. 8, New York, Elsevier Science.
- Lin P J, Bursill L A (1982), 'High-resolution study of ferroelectric domain boundaries in lithium tantalate', *Phil. Magazine A*, **45** (6), 911–928.
- Lines M E, Glass A M (1977), *Principles and Application of Ferroelectrics and Related Materials*, Oxford, Clarendon Press.
- Little E A (1955), 'Dynamic behavior of domain walls in barium titanate', *Phys Rev*, **98**, 978–984.
- Lobov A I, Shur V Ya, Baturin I S, Shishkin E I, Kuznetsov D K, Shur A G, Dolbilov M A, Gallo K (2006), 'Field induced evolution of regular and random 2D domain structures and shape of isolated domains in LiNbO<sub>3</sub> and LiTaO<sub>3</sub>', *Ferroelectrics*, **341**, 109–116.
- Malozemoff A P, Slonczewski J S (1979), *Magnetic Domain Walls in Bubble Materials*, New York, Academic Press.
- Marssi M El, Farhi R, Dellis J-L, Glinchuk M D, Seguin L, Viehland D (1998), 'Ferroelectric and glassy states in La-modified lead zirconate titanate ceramics: a general picture', *J Appl Phys*, **83**, 5371–5380.
- Matthias B, Hippel A (1948), 'Domain structure and dielectric response of barium titanate single crystals', *Phys Rev*, **73** (11), 1378–1384.
- Merz W J (1954), 'Domain formation and domain wall motions in ferroelectric BaTiO<sub>3</sub> single crystals', *Phys Rev*, **95**, 690–698.
- Merz W J (1956), 'Switching time in ferroelectric BaTiO<sub>3</sub> and its dependence on crystal thickness', *J Appl Phys*, **27** (8), 938–943.
- Miller R C (1960), 'On the origin of Barkhausen pulses in BaTiO<sub>3</sub>', *J Phys Chem Solids*, **17**, 93–100.

- Miller R C (1964), 'Optical harmonic generation in single crystal BaTiO<sub>3</sub>', *Phys Rev*, **134** (5A), 1313–1319.
- Miller R C, Savage A (1959), 'Direct observation of antiparallel domains during polarization reversal in single crystal barium titanate', *Phys Rev Lett*, **2**, 294–296.
- Miller R C, Weinreich G (1960), 'Mechanism for the sidewise motion of 180° domain walls in barium titanate', *Phys Rev*, **117**, 1460–1466.
- Ming N B, Hong J F, Feng D (1982), 'The growth striations and ferroelectric domain structures in Czochralski-grown LiNbO<sub>3</sub> single crystals', *J Mater Sci*, **17** (6), 1663–1670.
- Miyazawa S (1979), 'Ferroelectric domain inversion in Ti-diffused LiNbO<sub>3</sub> optical waveguide', *J Appl Phys*, **50**, 4599–4603.
- Mizuuchi K, Yamamoto K (1992), 'Characteristics of periodically domain-inverted LiTaO<sub>3</sub>', *J Appl Phys*, **72** (11), 5061–5069.
- Myers L E, Eckardt R C, Fejer M M, Byer R L, Bosenberg W R, Pierce J W (1995), 'Quasi-phase-matched optical parametric oscillators in bulk periodically poled LiNbO<sub>3</sub>', *J Opt Soc Am B*, **12** (11), 2102–2116.
- Nakamura K, Tourlog A (1993), 'Single-domain surface layers formed by heat treatment of proton-exchanged multidomain LiTaO<sub>3</sub> crystals', *Appl Phys Lett*, **63**, 2065–2066.
- Newnham R E, Cross L E (1974), 'Ambidextrous crystals', *Endeavour*, **33**, 18–22.
- Newnham R E, Miller C S, Cross L E, Cline T W (1975), 'Tailored domain patterns in piezoelectric crystals', *Phys Stat Sol (A)*, **32**, 69–78.
- Niwa K, Furukawa Y, Takekawa S, Kitamura K (2000), 'Growth and characterization of MgO doped near stoichiometric LiNbO<sub>3</sub> crystals as a new nonlinear optical material', *J Crystal Growth*, **208**, 493–500.
- O'Dell T H (1981), *Ferromagnetodynamics*, London, Macmillan Press Ltd.
- Ohnishi N, Iizuka T (1975), 'Etching study of microdomains in LiNbO<sub>3</sub> single crystals', *J Appl Phys*, **46** (3), 1063–1067.
- Prokhorov A M, Kuzminov Y S (1990), *Physics and Chemistry of Crystalline Lithium Niobate*, Bristol, Adam Hilger.
- Rosenman G, Skliar A, Arie A (1999), 'Ferroelectric domain engineering for quasi-phases-matched nonlinear optical devices', *Ferroelectrics Review*, **1**, 263–326.
- Savage A, Miller R C (1960), 'Temperature dependence of the velocity of sidewise 180° domain-wall motion in BaTiO<sub>3</sub>', *J Appl Phys*, **31** (9), 1546–1549.
- Shur V Ya (1996), 'Fast polarization reversal process: evolution of ferroelectric domain structure in thin films', in Paz de Araujo C A, Scott J F, Taylor G W, *Ferroelectric Thin Films: Synthesis and Basic Properties*, New York, Gordon and Breach, 153–192.
- Shur V Ya, Romyantsev E L (1997), 'Kinetics of ferroelectric domain structure: retardation effects', *Ferroelectrics*, **191**, 319–333.
- Shur V Ya (1998), 'Kinetics of polarization reversal in normal and relaxor ferroelectrics: relaxation effects', *Phase Trans*, **65**, 49–72.
- Shur V Ya (2005), 'Correlated nucleation and self-organized kinetics of ferroelectric domains', in Schmelzer J W P, *Nucleation Theory and Applications*, Weinheim, Wiley-VCH, 178–214.
- Shur V Ya (2006), 'Kinetics of ferroelectric domains: application of general approach to LiNbO<sub>3</sub> and LiTaO<sub>3</sub>', *J Mat Sci*, **41** (1), 199–210.
- Shur V Ya, Popov Yu A, Korovina N V (1984a), 'Bound internal field in lead germinate', *Sov Phys Solid State*, **26**, 471–474.
- Shur V Ya, Letuchev V V, Romyantsev E L (1984b), 'Field dependence of the polarization

- switching parameters and shape of domains in lead germanate', *Sov Phys Solid State*, **26**, 1521–1522.
- Shur V Ya, Letuchev V V, Rumyantsev E L, Ovechkina I V (1985), 'Triangular domains in lead germanate', *Sov Phys Solid State*, **27**, 959–960.
- Shur V Ya, Gruverman A L, Letuchev V V, Rumyantsev E L, Subbotin A L (1989), 'Domain structure of lead germanate', *Ferroelectrics*, **98**, 29–49.
- Shur V Ya, Gruverman A L, Kuminov V P, Tonkachyova N A (1990), 'Dynamics of plane domain walls in lead germanate and gadolinium molybdate', *Ferroelectrics*, **111**, 197–206.
- Shur V Ya, Rumyantsev E L, Makarov S D (1998), 'Kinetics of phase transformations in real finite systems: application to switching in ferroelectrics', *J Appl Phys*, **84**, 445–451.
- Shur V Ya, Rumyantsev E L, Makarov S A, Kozhevnikov V L, Nikolaeva E V, Shishkin E I (1999a), 'How to learn the domain kinetics from the switching current data', *Int Ferroelectrics*, **27**, 179–194.
- Shur V Ya, Lomakin G G, Kuminov V P, Pelegov D V, Beloglazov S S, Slovikovski S V, Sorkin I L (1999b), 'Fractal-cluster kinetics in phase transformations in relaxor ceramic PLZT', *Phys Solid State*, **41**, 453–456.
- Shur V Ya, Rumyantsev E L, Batchko R G, Miller G D, Fejer M M, Byer R L (1999c), 'Domain kinetics during periodic domain patterning in lithium niobate', *Phys Solid State*, **41**, 1681–1687.
- Shur V Ya, Rumyantsev E L, Nikolaeva E V, Shishkin E I, Fursov D V, Batchko R G, Eyres L A, Fejer M M, Byer R L (2000a), 'Nanoscale backswitched domain patterning in lithium niobate', *Appl Phys Lett*, **76** (2) 143–145.
- Shur V Ya, Rumyantsev E L, Nikolaeva E V, Shishkin E I (2000b), 'Formation and evolution of charged domain walls in congruent lithium niobate', *Appl Phys Lett*, **77** (22), 3636–3638.
- Shur V Ya, Rumyantsev E, Nikolaeva E, Shishkin E, Batchko R G, Miller G D, Fejer M M, Byer R L (2000c), 'Micro- and nanoscale domain engineering in lithium niobate and lithium tantalate', *SPIE Proceedings on Smart Structures and Materials*, **3992**, 143–154.
- Shur V Ya, Rumyantsev E L, Nikolaeva E V, Shishkin E I, Fursov D V, Batchko R G, Eyres L A, Fejer M M, Byer R L, Sindel J (2001), 'Formation of self-organized nanoscale domain patterns during spontaneous backswitching in lithium niobate', *Ferroelectrics*, **253**, 105–114.
- Shur V Ya, Rumyantsev E L, Pelegov D V, Kozhevnikov V L, Nikolaeva E V, Shishkin E I, Chernykh A P, Ivanov R K (2002a), 'Barkhausen jumps during domain wall motion in ferroelectrics', *Ferroelectrics*, **267**, 347–353.
- Shur V Ya, Nikolaeva E V, Shishkin E I, Chernykh A P, Terabe K, Kitamura K, Ito H, Nakamura K (2002b), 'Domain shape in congruent and stoichiometric lithium tantalate', *Ferroelectrics*, **269**, 195–200.
- Shur V Ya, Nikolaeva E V, Shishkin E I (2003), 'Ferroelectric nanodomain structures in LiNbO<sub>3</sub> and LiTaO<sub>3</sub>: investigation by scanning probe microscopy', *Phys Low-Dim Str*, **3** (4), 139–148.
- Shur V Ya, Lomakin G G, Rumyantsev E L, Beloglazov S S, Pelegov D V, Sternberg A, Krumins A (2004a), 'Fractal clusters in relaxor PLZT ceramics: evolution in electric field', *Ferroelectrics*, **299**, 75–81.
- Shur V, Shishkin E, Rumyantsev E, Nikolaeva E, Shur A, Batchko R, Fejer M, Gallo K, Kurimura S, Terabe K, Kitamura K (2004b), 'Self-organization in LiNbO<sub>3</sub> and



- LiTaO<sub>3</sub>: formation of micro- and nanoscale domain patterns', *Ferroelectrics*, **304**, 111–116.
- Shur V Ya, Lomakin G G, Romyantsev E L, Yakutova O V, Pelegov D V, Sternberg A, Kosec M (2005a), 'Polarization reversal in heterophase nanostructures: relaxor PLZT ceramics', *Phys Solid State*, **47** (7), 1340–1345.
- Shur V Ya, Romyantsev E L, Lomakin G G, Yakutova O V, Pelegov D V, Sternberg A, Kosec M (2005b), 'Field induced evolution of nanoscale structures in relaxor PLZT ceramics', *Ferroelectrics*, **316**, 23–29.
- Shur V Ya, Lobov A I, Shur A G, Kurimura S, Nomura Y, Terabe K, Liu X Y, Kitamura K (2005c), 'Rearrangement of ferroelectric domain structure induced by chemical etching', *Appl Phys Lett*, **87** (2), 022905.
- Shur V Ya, Shishkin E I, Kuznetsov D K, Lobov A I, Dolbilov M A, Tascu S, Baldi P, De Micheli M P, Gallo K (2006), 'Modification of the domain kinetics in congruent lithium niobate by proton exchanged surface layers', *The Abstract Book of the 8th European Conference on Applications of Polar Dielectrics, Metz, France, Sept. 4–8, 2006*, 224.
- Shvartsman V V, Kholkin A L (2004), 'Domain structure of 0.8Pb(Mg<sub>1/3</sub>Nb<sub>2/3</sub>)O<sub>3</sub>–0.2PbTiO<sub>3</sub> studied by piezoresponse force microscopy', *Phys Rev B*, **69**, 014102.
- Shvartsman V V, Kholkin A L, Orlova A, Kiselev D, Bogomolov A A, Sternberg A (2005), 'Polar nanodomains and local ferroelectric phenomena in relaxor lead lanthanum zirconate titanate ceramics', *Appl Phys Lett*, **86** (20), 202907.
- Soergel E (2005), 'Visualization of ferroelectric in bulk single crystals', *Appl Phys B*, **81**, 729–752.
- Sones C L, Mailis S, Brocklesby W S, Eason R W, Owen J R (2002), 'Differential etch rates in z-cut LiNbO<sub>3</sub> for variable HF/HNO<sub>3</sub> concentrations', *J Mater Chem*, **12** (2), 295–298.
- Tagantsev A K, Stolichnov I, Colla E L, Setter N (2001), 'Polarization fatigue in ferroelectric films: basic experimental findings, phenomenological scenarios, and microscopic features', *J Appl Phys*, **90**, 1387–1402.
- Terabe K, Takekawa S, Nakamura M, Kitamura K, Higuchi S, Gotoh Y, Gruverman A (2002), 'Imaging and engineering the nanoscale-domain structure of a Sr<sub>0.61</sub>Ba<sub>0.39</sub>Nb<sub>2</sub>O<sub>6</sub> crystal using a scanning force microscope', *Appl Phys Lett*, **81**, 2044–2046.
- Valdivia C E, Sones C L, Scott J G, Mailis S, Eason R W, Scrymgeour D A, Gopalan V, Jungk T, Soergel E, Clark I (2005), 'Nanoscale surface domain formation on the +z face of lithium niobate by pulsed ultraviolet laser illumination', *Appl Phys Lett*, **86**, 022906.
- Webjörn J, Pruneri V, Russell P St J, Barr J R M, Hanna D C (1994), 'Quasi-phase-matched blue light generation in bulk lithium niobate, electrically poled via periodic liquid electrodes', *Electron Lett*, **30** (11), 894–895.
- Yamada M, Nada N, Saitoh M, Watanabe K (1993), 'First-order quasi-phase matched LiNbO<sub>3</sub> waveguide periodically poled by applying an external field for efficient blue second-harmonic generation', *Appl Phys Lett*, **62**, 435–436.
- Yin Q R, Li G R, Zeng H R, Liu X X, Heiderhoff R, Balk L J (2004), 'Ferroelectric domain structures in (Pb,La)(Zr,Ti)O<sub>3</sub> ceramics', *Appl Phys A*, **78** (5), 699–702.
- Zhu S-N, Zhu Y-Y, Zhang Z-Y, Shu H, Wang H-F, Hong J-F, Ge C-Z, Ming N-B (1995), 'LiTaO<sub>3</sub> crystal periodically poled by applying an external pulsed field', *J Appl Phys*, **77** (10), 5481–5483.
- Zhu Y-Y, Zhu S-N, Hong J-F, Ming N-B (1994), 'Domain inversion in LiNbO<sub>3</sub> by proton exchange and quick heat treatment', *Appl Phys Lett*, **65**, 558–560.

## Interface control in 3D ferroelectric nanocomposites

---

C ELISSALDE and M MAGLIONE,  
University of Bordeaux 1, France

### 22.1 Introduction

Thanks to their high polarisability, ferroelectric materials are very sensitive to charged defects such as vacancies or substituted ions. In this respect, oxide perovskites of general formula  $ABO_3$  display very specific features:

- their ferroelectric transition temperature can be tuned continuously across room temperature;
- the density of oxygen vacancies that they can host may be tuned on annealing under well-defined reducing/oxidising atmospheres;
- a large number of heterovalent substitutions can be performed so as to tune the local charge.

As expected, interfaces play a major role in localising charged defects in ferroelectrics. The surface and the electrode/ferroelectric boundary are the first macroscopic locations where charge accumulation can influence dielectric properties. Mesoscopic space charges can be found in single crystals and ceramics. In the former case, a well-modulated space charge can be produced and released by laser irradiation; in the latter, solid-state chemistry is able to fix charge gradients at the grain boundaries. As a consequence, the overall dielectric permittivity and conductivity of electroceramics can be tuned. In some cases, the tuning of dielectric properties through interfaces has met real world applications. Sometimes, the use of a single ferroelectric compound is not enough to comply with industry needs. In such instances, composites made of a ferroelectric material mixed with a simple dielectric are used. Solid-state chemistry and soft chemistry have been used in order to monitor the architecture of these composites and thus the density of interfaces even on the nanoscopic scale.

In Section 22.2, we will recall the basics of charged defects chemistry in perovskites taking the  $BaTiO_3$ -type compounds as an example and moving to the  $CaCu_3Ti_4O_{12}$  double perovskite which has been the focus of a great deal of research effort in recent years. In Section 22.3, we will address the ionic

concentration gradient, whether controlled or not, in ceramics and composites, including a ferroelectric phase. We will then describe the most recent routes that have been used to control the microstructure in micro- and nanocomposites including a ferroelectric phase.

## 22.2 Interface defects and dielectric properties of bulk ferroelectric materials

Charged defect chemistry in ferroelectric perovskites is a long-standing topic which has stimulated a lot of research with special emphasis on BaTiO<sub>3</sub>-based compounds (Chan *et al.*, 1981; Vollman and Waser, 1994; Smyth 2000). General agreement has been reached when the density of such defects is small but the heavily doped case is still a matter of debate which is mostly about the compensation mechanism of charged defects (Morrison *et al.*, 2001; Smyth, 2002). In this section, we will review the various contributions of charged defects to the overall dielectric permittivity of perovskites.

### 22.2.1 Charged defects at electrode/ferroelectric interfaces

Like any dielectric material, ferroelectrics can be considered as broadband gap semiconductors at least in their paraelectric state where no polarisation or ferroelectric domain contribution are to be included. When semiconductor models apply, the electrode/ferroelectric interface can be considered as a metal/semiconductor junction (Sze, 1969). Such semiconductor models were used in the 1960s particularly in the case of Nb-doped SrTiO<sub>3</sub> which shows appealing conductivity behaviour (Wemple *et al.*, 1969). Very early on, numerical models were used to solve the tricky problem of band bending and charge localisation at the metal/ferroelectric interface (Bardet, 1979). More recently, such analytical and computer simulations have been greatly renewed in the context of ferroelectric thin films (Ishibashi, 1990; Stolichnov and Tagantsev, 1998; Baudry, 1999; Dawber and Scott, 2000). The main result of these investigations is that the density of charged defects such as oxygen vacancies can greatly increase the penetration length of the space charge in the ferroelectric material. With a defect density of 0.1%, a space charge could be extended to more than 25% in depth of submicrometre films (Baudry, 1999). When going to the ferroelectric state, the depolarising electric field and the polarisation decay length (Kretschmer and Binder, 1979) have to be added in the equations which lead to very unusual behaviour. Recently, *ab initio* computations have clearly shown that not only does the ferroelectric material undergo a continuous decrease of the local electric field but a space charge is also induced in the metal electrode (Junquera and Ghosez, 2003). This means that even without charged defects in the ferroelectric material,

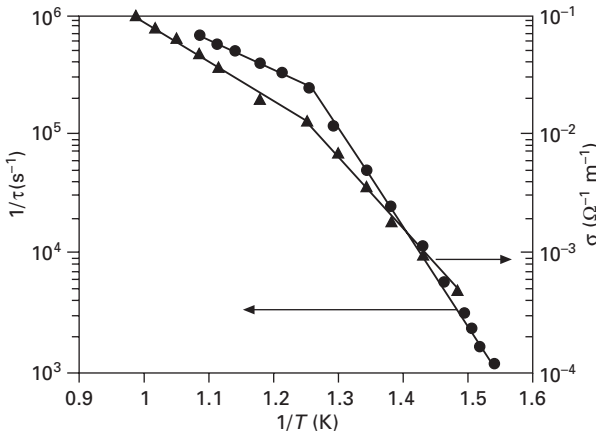
space charge must be taken into account. The effect of charge depletion on the ferroelectric properties of thin films has also been investigated (Bratkovsky and Levanyuk, 2000).

### 22.2.2 Space charge relaxation in bulk ferroelectric perovskites

Experimental probing of space charge at metal/ferroelectric interfaces is not an easy task since the broadband gap and the low electronic density of states precludes the use of standard dc current techniques which are efficient in usual semiconductors. Triggered by the reliability issues of ferroelectric films, improved experimental methods and models have been used to explain the dc current behaviours of such devices which can change their polarisation switching (Waser and Klee, 1992; Dawber and Scott, 2000). Even if all the issues have not yet been settled, general agreement is being reached as to the band bending and charged defects at metal–ferroelectric interfaces. One of the key ingredient is the density of oxygen vacancies which can reach levels as high as  $10^{21}\text{cm}^{-3}$  at the very top atomic layers. A long time ago, dielectric spectroscopy was able to show that such charged interfaces can lead to large dielectric relaxation, in many ferroelectric perovskites whatever their chemical composition, morphology and ferroelectric properties. A monodispersive Debye-type relaxation was recorded in the temperature range 500–100 K and frequency range 1 kHz–10 MHz, leading to an activation energy of about 1 eV (Maglione and Belkaoumi, 1992; Bidault *et al.*, 1994). The close connection of this activation energy with the one of the static conductivity showed that macroscopic space charges at the metal/ferroelectric interfaces are contributing to the dielectric permittivity (Fig. 22.1). Such relaxation has been evidenced in numerous bulk ferroelectrics, most of them including heterovalent substitutional cations like  $\text{BaFe}_{1/2}\text{Nb}_{1/2}\text{O}_3$  (Raevski *et al.*, 2003; Abdelkafi *et al.*), as well in thin films.

### 22.2.3 Charged boundaries in ceramics and single crystals

Away from the surface and from the electrode/ferroelectric interfaces, charged defects can be induced in the bulk of ceramics and single crystals. Before addressing the grain boundary localisation of such charged defects, one has to recall that the basic equations for bulk ceramics rely on the mass action law and the charge neutrality conditions (Chan *et al.*, 1981). The charge state of host lattice ions and dopants may be tuned under annealing and oxidation/reduction at several oxygen partial pressures. As a consequence the density of free holes and electrons can be systematically varied. The resulting Kröger–Vink diagrams in pure and doped  $\text{BaTiO}_3$  have been probed through isothermal



22.1 Relaxation time (left scale) and dc conductivity (right scale) in BaTiO<sub>3</sub> single crystals on an Arrhenius scale showing the similarity between the thermal activation of both processes.

resistance experiments (Chan *et al.*, 1981). This average bulk model for impurities is refined in the case of ceramics. As was clearly evidenced by Waser and coworkers, even the most perfect grain boundary between two grains in a ceramic carries a positive charge (Waser and Klee, 1992; Vollman and Waser, 1994). As a consequence, negatively depletion layer called space charge is created in the grains close to the grain boundary. Such a grain boundary space charge has been probed through time domain relaxation as well as impedance spectroscopy and its width estimated in Ni-doped SrTiO<sub>3</sub> through a Schottky model (Vollman and Waser, 1994). One of the main assumptions in such a model is that the grain boundaries are perfect, which means that there is a crystallographic continuity between two adjacent grains. Even if this is close to reality in the most dense ceramics, imperfect grain boundaries are increasing as the grain size decreases to the nanometre scale.

There is one case where micrometre size space charges are well controlled in ferroelectric materials, which is the storage of laser interference patterns in bulk single crystals: the so-called photorefractive activity of ferroelectrics. The spatial periodic modulation of the light intensity localises the free charges in the selected part of the single crystals, leading to strong space charges. When the input laser beams are in the visible range, the resulting spatial modulation of space charges takes place on the micrometre size. The effect of pre-existing charged defects such as iron on the ability of single crystals to store large space charges has been studied in great detail (Schwartz *et al.*, 1992). For example, it was only when the density of residual Fe defects could be brought down to a few ppm that the contribution of intentionally introduced defects could be investigated (Rytz *et al.*, 1990). The contribution

from oxygen vacancy-related centres could be evidenced through electron spin resonance (ESR) (Vanhorst *et al.*, 1996).

In the two cases reviewed in this section, the space charged localised at boundaries does not affect the low-frequency dielectric permittivity. We will show in the next section that grain boundaries are able to artificially increase this permittivity up to giant effective values.

#### 22.2.4 Grain boundary enhancement of the effective dielectric permittivity: the case of $\text{CaCu}_3\text{Ti}_4\text{O}_{12}$

When the density of multivalent cations such as copper is high, as in the multiple perovskite  $\text{CaCu}_3\text{Ti}_4\text{O}_{12}$ , the probability of increased localisation of charged defects increases. In ceramics and single crystals of this composition, a huge dielectric permittivity (up to more than  $10^5$ ) was recorded with a sharp decrease in the MHz frequency range (Subramanian *et al.*, 2000). The thermal activation of this relaxation as well as its link with the inner grain conductivity showed that the giant permittivity originated in barrier layer at grain boundaries (Morrison *et al.*, 2001). In this way, the giant dielectric properties of  $\text{CaCu}_3\text{Ti}_4\text{O}_{12}$  could be ascribed to space charges analogous to the macroscopic one already mentioned but on a more local scale. In any instance, the giant permittivity can hardly be attributed to a lattice polarisability which could result from soft-phonon modes or from ionic dipoles. In this respect, the recent description of  $\text{CaCu}_3\text{Ti}_4\text{O}_{12}$  in terms of a relaxor model (Ke *et al.*, 2006) is questionable. On the other hand, this example shows that the control of charged defects at interfaces is of key relevance to the effective macroscopic dielectric properties. This opens the route towards the use of grain boundary engineering as a tool to control the dielectric properties. Some examples of such engineering will be described in the following sections.

### 22.3 Interdiffusion in bulk ceramics and composites

As mentioned above, tuning the macroscopic properties of polycrystalline ferroelectric materials is desirable for a targeted application. From the early investigations up to now, such improvements largely rely on the bulk chemistry as well as on the standard shaping of ferroelectric ceramics. Recently, alternative routes have been proposed as to overcome some intrinsic drawbacks of ferroelectrics. The first one, which will be described below, is the use of ferroelectrics for telecommunications in the GHz frequency range. To reduce the dielectric losses, composites have been proposed that include ferroelectric and dielectric components. The improved control of these composites on the nanometre scale is the most recent achievement in this field. The second one is the use of ferroelectric materials in multilayer capacitors which require very low-temperature sensitivity, a requirement that is not fulfilled in

ferroelectrics. Composition gradients in individual ferroelectric grains are a way to decrease their temperature sensitivity. Again, the control of compositions on the nanoscale is the ultimate way to provide stable and reliable ferroelectric ceramics.

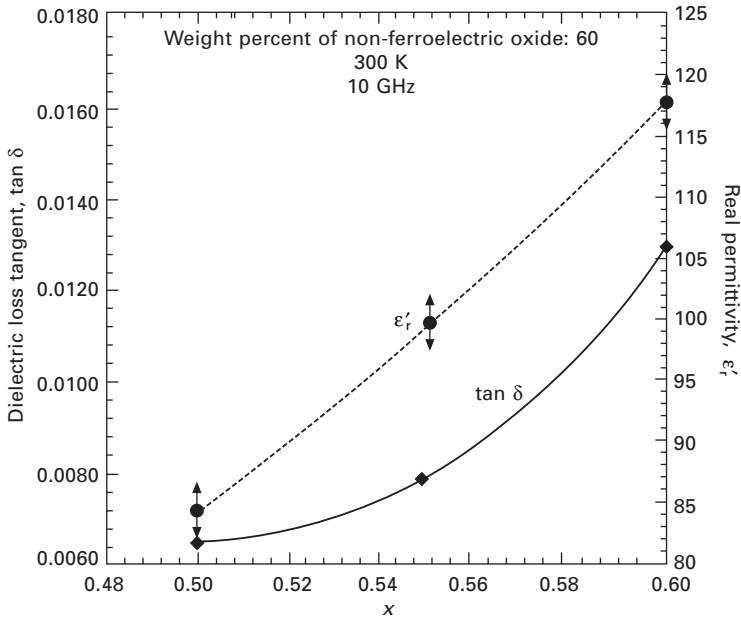
### 22.3.1 Interdiffusion in BST/MgO and BST/MgTiO<sub>3</sub> ceramic composites

Ferroelectric materials are the topic of a great deal of research and development in the high-frequency range (between 100 MHz and 10 GHz) due to the increasing interest in applications in telecommunication and radar fields. Low dielectric losses are required in order to allow for their integration as low dimension capacitors in electronic devices and even microwave devices. Close to their transition temperature, ferroelectrics usually display non-linear properties under a dc electric field: the permittivity can be easily changed by applying a dc bias. Such property is used for agile devices such as tunable capacitors, tunable resonators and phase shifter in radars.

The required performances in the GHz frequency range for integration in telecommunication electronic devices are: (i) a moderate permittivity (100–1000), (ii) low insertion losses ( $\tan \delta \ll 1\%$ ), (iii) a good thermal stability and (iv) a high tunability of the dielectric permittivity ( $>10\%$ ). Ferroelectric materials such as BaTiO<sub>3</sub> (BT) show high permittivity but strong temperature sensitivity at temperatures close to phase transition ( $T\epsilon'_{\max}$ ). Moreover, it has been shown that the maximal tunability is reached at  $T\epsilon'_{\max}$  and that losses increase in the GHz range. The challenge is to find a balance between all these mismatched specifications.

It is now well recognised that ferroelectric materials with transition temperatures close to, but below, room temperatures are of key interest. That is the reason why mixed perovskites such as Ba<sub>0.6</sub>Sr<sub>0.4</sub>TiO<sub>3</sub> (BST) attract so much interest. BST displays a Curie temperature close to 280 K, permittivity values usually about 2000 at room temperature for micrometre grain ceramics, high tunability ( $>10\%$  for a 20 kV/cm field at room temperature) and dielectric losses higher than 1% up to high frequency (Sengupta and Sengupta, 1999). To reduce the temperature sensitivity, decrease the permittivity and lower dielectric losses, ceramic/ceramic composites were processed. Composite materials such as BST combined with low permittivity and low-loss non-ferroelectric oxides (MgO, MgTiO<sub>3</sub>) are excellent candidates for telecommunications devices (Fig. 22.2) (Weil *et al.*, 1998). Pioneer works in the field of BST composites with tunable properties are attributed to Sengupta *et al.* (1995a,b).

BST–alumina (Liang *et al.*, 2003), zirconia and magnesia ceramic composites have also been studied. Interesting performances in terms of tunability and losses were reported. However, the properties improvement is



22.2 Measured complex permittivity data for a BST/non ferroelectric oxide composite as a function of Ba/Sr ratio for BST phase (Weil *et al.*, 1998).

limited due to interdiffusion between the ferroelectric and non-ferroelectric phases (Sengupta *et al.*, 1996; Nagai *et al.*, 2000; Chang and Sengupta, 2002). As a result, the cubic–tetragonal phase transition peak shifted to a lower temperature, leading to a decrease in both permittivity and tunability of the composite at room temperature. Such an interdiffusion was also reported for the BST/MgO and BST/MgTiO<sub>3</sub> ceramic composites by Nenez *et al.* (2002) In this latter case, a secondary phase BaMg<sub>6</sub>Ti<sub>6</sub>O<sub>19</sub> was detected. In addition, ceramics with nanometre grain size were compared with micrometre grain size ones. No improvement of the dielectric performance was obtained. The reduction of the grain size allowed the reduction of the permittivity values but to the detriment of both tunability and losses (Nenez, 2001). These results underline the influence of sintering temperature, grain boundary control and microstructure on the dielectric performance of these composites.

Improvements have been proposed in the literature. As an example, several authors have reported the preparation of BST/MgO in the forms of thick and thin films as an interesting alternative to increase the tunability (Sengupta *et al.*, 2000; Joshi and Cole, 2000). Tunability enhancement was also obtained by mixing micrometre-size BST with nano-size MgO (Yu *et al.*, 2003). In order to decrease the synthesis temperature and thus to limit interdiffusion, sol–gel processes have been also used (Jain *et al.*, 2002; Synowczynski *et*



*al.*, 2002). However, the downshift of the Curie temperature resulting from the interdiffusion in such composite materials is still hard to avoid.

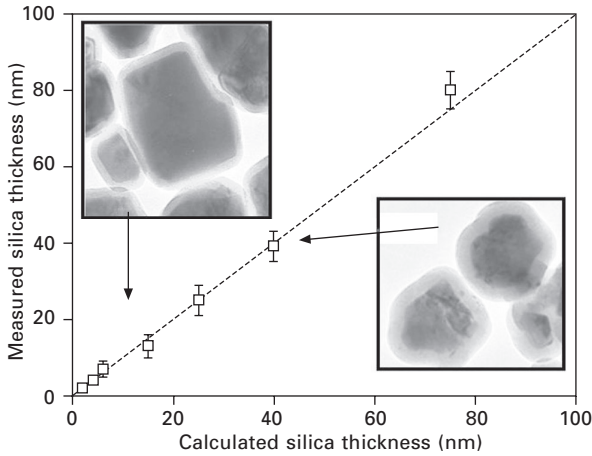
### *Improved control of interfaces in ceramic composites*

In the field of nanosciences, it is well established that surfaces and interfaces play a key role in affecting the properties of materials. Full control of interfaces is needed to monitor the interdiffusion occurring during the solid-state synthesis of composites. This can be achieved via a multidisciplinary approach involving nanoscale wet chemistry, solid-state chemistry and materials science. Our strategy was to use nanoparticle technology to process ferroelectric/dielectric composites with controlled interfaces between the two components. Nanoscience applied to ferroelectrics thus opens great opportunities for the design of new functional materials for microelectronics and telecommunications. Another way to decrease the chemical reactivity between the ferroelectric and the non-ferroelectric phases is to control the microstructure using an advanced sintering process.

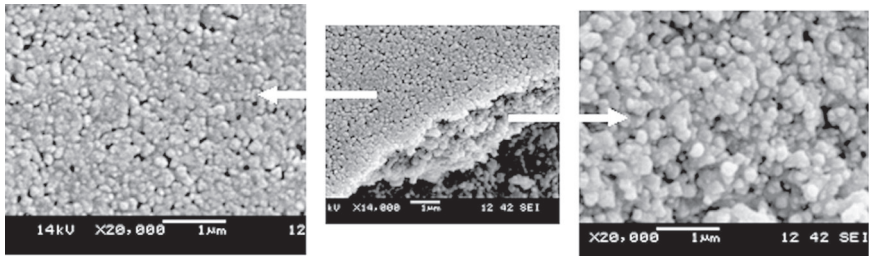
### The core–shell concept applied to ferroelectric/non-ferroelectric composites

The proposed concept is to achieve a network made of individual ferroelectric particles coated with a dielectric shell (written in the following as core@shell) with a full control of both the size of the ferroelectric core (BT, BST) and the thickness of the non-ferroelectric shell ( $\text{SiO}_2$ ). This concept has already been applied to various inorganic materials from magnetic materials ( $\text{Fe}_2\text{O}_3@ \text{SiO}_2$ ) to structural oxides ( $\text{Al}_2\text{O}_3@ \text{SiO}_2$ ) coated with silica. We successfully adopted this approach to ferroelectric materials (Huber *et al.*, 2003; Mornet *et al.*, 2005). Note that enhancement of the BT particle stability in acidic media by silica coating had already been demonstrated by Shih *et al.* (1995). Our method based on seeded growth process was developed to coat ferroelectric particles (from 50 nm to 1  $\mu\text{m}$  size) and has allowed the control of the silica shell thickness from 2 to 80 nm with an accuracy of 1–2 nm (Fig. 22.3).

In order to improve both the microstructure and the dielectric performance of the final composites, we took advantage of the self-assembly properties of size-sorted BST, BT@silica particles. Thanks to the silica shell, SEM observations show neck formation at only 1000 °C (Fig. 22.4). Reliable dielectric characterisation was thus possible on as-calcined colloidal composites. The ferroelectric transition temperature was kept in the final composite, the dielectric permittivity reached expected values and the dielectric losses were very low and stable in the temperature range of 100–400 K (Fig. 22.5). This last result confirmed that the silica shell acts as a dielectric loss



22.3 Thickness evolution of the silica shell as determined by transmission electron microscopy (TEM) as a function of the calculated thickness.

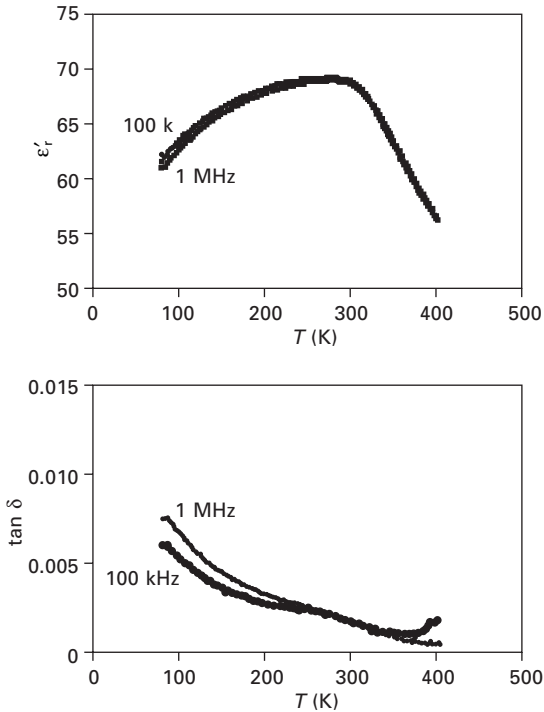


22.4 SEM micrographs of BST@silica composites as obtained after sintering at 1000 °C for 3 h of size-sorted BST–silica nanoparticles.

barrier while keeping the intrinsic properties of the ferroelectric cores, i.e. interdiffusion is avoided, which was difficult to achieve in standard ferroelectric/dielectric composites. Sintering studies on nano-sized  $\text{BaTiO}_3$  (30 nm) coated with silica showed complex densification behaviour as a function of  $\text{SiO}_2$  content (Park and Han, 2005).

The core–shell approach was also investigated using a solvothermal synthesis route.  $\text{BaTiO}_3$  nanoparticles were coated with an amorphous  $\text{Al}_2\text{O}_3$  shell of few nanometres using a chemical fluid deposition process in supercritical state. After sintering of the core–shell nanoparticles, the final ceramic material exhibited significant improvement in the lowering of dielectric losses while keeping the Curie temperature unchanged (Fig. 22.6) (Aymonier *et al.*, 2005).

More recently, a modified hydrothermal process was developed to synthesized BST nanoscaled powder (17–20 nm) and a core–shell structure was formed by self-wrapping with MgO oxide. However, a radial composition



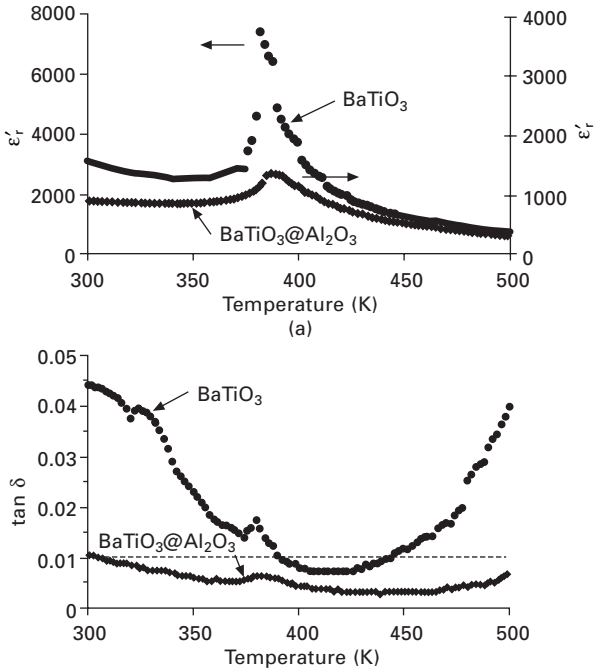
22.5 Dielectric permittivity and losses versus temperature measured at 100 kHz and 1 MHz on sintered colloidal BST@silica (5 nm) composite.

gradient from the shell to the core was revealed and no dielectric investigation was performed (Tian *et al.*, 2005).

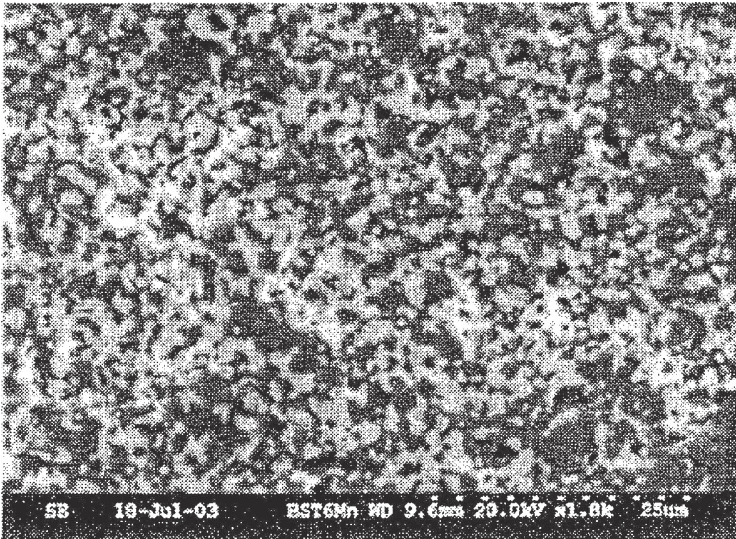
#### *Ferroelectric composites obtained by non-conventional sintering method*

One of the problems in the fabrication of BST/MgO composites via the conventional route is the high sintering temperature required to densify the ceramics due to the refractory character of MgO ( $T_{\text{sint}} > 1600^\circ\text{C}$ ). As a result of high thermal treatment, grain growth and interdiffusion between the two components are hard to avoid. To overcome these drawbacks, non-conventional sintering processes which provide rapid heating, short sintering time and low sintering temperature are particularly well suited.

The BST/MgO composites fabricated by microwave processing were reported by Agrawal *et al.* (2004) (Fig. 22.7). The aim of this study was to obtain a well-defined phase boundary and a fine grain size in the sintered composites by lowering the chemical reactivity. Thanks to uniform connectivity obtained between the BST grains, enhanced tunability was reached (maximum



22.6 Thermal dependences of (a)  $\epsilon'_r$  (real part of the permittivity) and (b)  $\tan \delta$  (dielectric losses) of  $\text{BaTiO}_3@/\text{Al}_2\text{O}_3$  and standard  $\text{BaTiO}_3$  ceramics at 100 kHz.

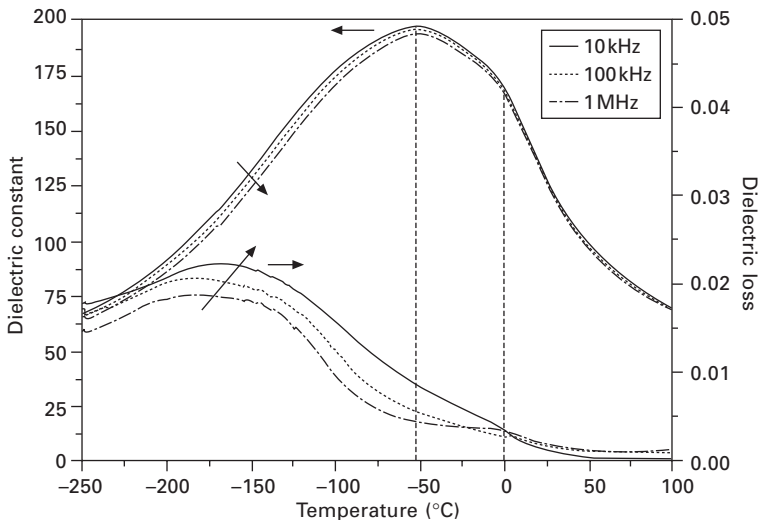


22.7 Scanning electron microscopy (SEM) micrograph of BST-MgO composite of polished surface showing uniform distribution of BST and MgO grains (Agrawal *et al.*, 2004).

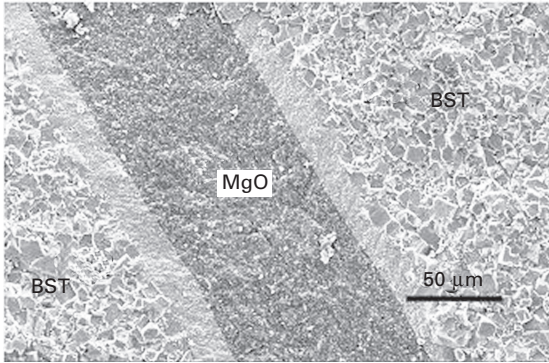
tunability 38% and  $\epsilon' \sim 220$  close to the room temperature at  $\pm 80$  kV/cm at 100 kHz). However, the addition of MgO in BST shifted the Curie temperature from 2 to  $-52^\circ\text{C}$  as shown in Fig. 22.8.

More recently, a straightforward and simple way to produce well-densified ferroelectric ceramic composites with a full control of both architecture and properties using spark plasma sintering (SPS) was proposed (Elissalde *et al.*, 2007). In the SPS process, the combination of high pressure, pulsed electrical current and plasma generation leads to efficient heat transfer (Nygren and Zhen, 2003; Anselmi-Tamburini *et al.*, 2005a,b; Chen *et al.*, 2005). The heating source is not external as the electric current applied passes through the conductive pressurised die containing the powder. Consequently very high heating rates were reached. SPS consolidation enhances the sintering kinetics and temperature and the processing time can be significantly reduced compared to conventional sintering. Thus, the interdiffusion of cations from the different layers is limited, allowing the preservation of clean interfaces. Highly densified BST/MgO/BST multilayer ceramics (97%) were obtained via SPS (Fig. 22.9). Suppression of interdiffusion between the ferroelectric and the non-ferroelectric phases was possible. The composite exhibited dielectric losses well below 1% while keeping the Curie temperature of the ferroelectric part unchanged (Fig. 22.10).

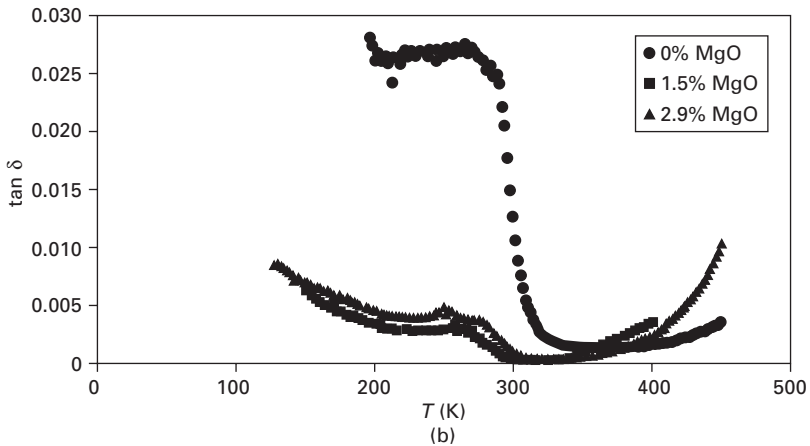
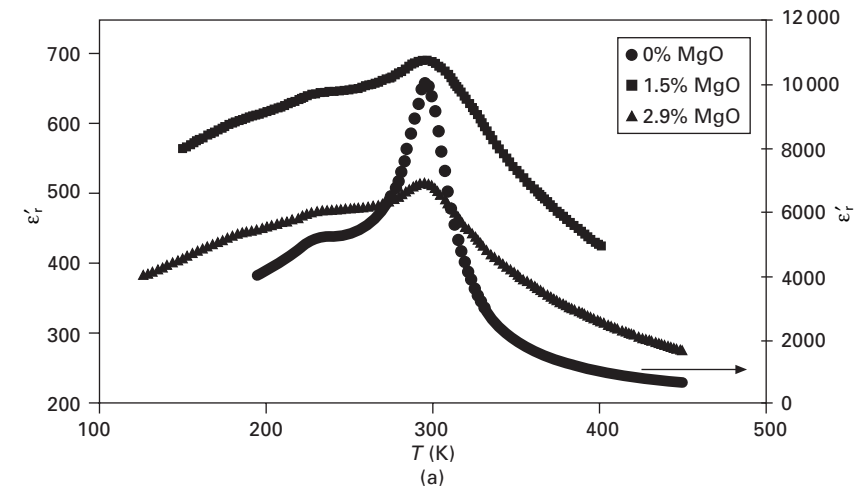
A multilayer design had already been investigated for tunable microwave devices in the case of  $\text{Ba}_{0.5}\text{Sr}_{0.5}\text{TiO}_3/\text{MgO}$  thin film composites (Jain *et al.*, 2003). Rutherford backscattering (RBS) analysis and SEM observations



22.8 Temperature and frequency dependences of dielectric constant and loss factor of  $\text{Ba}_{0.6}\text{Sr}_{0.4}\text{TiO}_3\text{-MgO}$  composite with 40:60 wt ratio (Agrawal *et al.*, 2004).



22.9 SEM micrograph of the fracture surface of sandwiched BST/MgO/BST ceramic obtained by SPS.



22.10 Dielectric permittivity (a) and losses (b) of SPS-sintered BST/MgO/BST stack as a function of the thickness ratio MgO/BST.

revealed the annealed multilayer film as a 3-0 connectivity composite having micro-MgO single crystals dispersed in a three-dimensionally connected BST matrix. The dielectric data, given only at room temperature as a function of frequency, showed reduced dielectric loss values. Improvement of both the dielectric losses and quality factor was also reported in sputtered BST@SiO<sub>2</sub> multilayers (Reymond *et al.*, 2004).

It is worth noting that improvement in these materials in terms of loss tangent reduction is limited simply because of the ferroelectric materials' intrinsic losses. A number of studies on bulk microwave ceramics have shown the possibility of estimating the unavoidable intrinsic microwave losses using the extrapolation from far IR range (Petzelt and Kamba, 2003). Petzelt *et al.* (2003) demonstrated that measurement of dielectric response in a very wide frequency range including low and high frequencies, microwaves, submillimetre and IR region is very helpful in understanding the origin of the dielectric losses in ferroelectric ceramics (Zurmülhen *et al.*, 1995; Petzelt *et al.*, 2003; Kamba *et al.*, 2004). The main contribution to the dielectric losses has an extrinsic origin (lattice disorder, point defects, grain boundaries, etc.). Intrinsic losses are due to phonon-related absorption. In the frequency range 500–1200 GHz, the measured losses are assumed to be of intrinsic origin and can be described using the phonon parameters defined by R-FTIR (Fourier transform infrared spectroscopy) measurements near the phonon resonance. Determination and fitting of the dielectric losses frequency dependence would then allow extrapolating and predicting the minimum loss expected down to the microwave range.

### 22.3.2 Concentration gradients in ceramics

Temperature-stable BaTiO<sub>3</sub>-based dielectric materials have found extensive application in the fabrication of multilayer ceramic capacitors (MLCC). To comply with the X7R specification (Hennings and Rosenstein, 1984), the main objective is to modify the ferroelectric properties by broadening the dielectric constant–temperature profile. The relative dielectric constant must not change by more than  $\pm 15\%$  from the room temperature value, over a temperature range from  $-55$  to  $125$  °C. Small grain size and chemical inhomogeneity were found to be the main features important in obtaining such X7R dielectric materials (Rawal *et al.*, 1981). The most popular example is the gradual increase of ionic substitution on the titanium site of BaTiO<sub>3</sub> grains from the centre to the surface of each grain. This graded structure, usually called core–shell structure, is obtained during the processing of the ceramics through a radial chemical gradient from the core of the grains to the grain boundary. The local gradient within the shell leads to a distribution of the Curie temperature. A smearing of the thermal variation of the ferroelectric properties of BaTiO<sub>3</sub> (BT) is thus achieved with a highly stable dielectric

susceptibility. The literature is rich in studies based on both solid state chemistry and materials science. Hennings and Rosenstein (1984) studied  $\text{BaTiO}_3$  materials sintered with addition of the pseudophase 'CdBi<sub>2</sub>Nb<sub>2</sub>O<sub>9</sub>'. A complex core-shell microstructure was determined and the chemical inhomogeneity was shown to emerge during a process of reactive liquid phase sintering. Chemical substitutions using oxides such as NiO, ZrO<sub>2</sub> and Nb<sub>2</sub>O<sub>5</sub> are well known to modify the  $\text{BaTiO}_3$  ferroelectric properties by controlling grain size and flattening the transition peak. According to several authors, the transition temperatures in  $\text{BaTiO}_3$  were also found to be modified by the ZrO<sub>2</sub> addition. It was shown that an accumulation of ZrO<sub>2</sub> at the grain boundaries leads to suppression of grain growth during sintering which flattened dielectric response (Maurice, 1984; Armstrong *et al.*, 1989). Depending on the sintering temperature, ZrO<sub>2</sub> particles at the grain boundaries or core-shell grains composed of a pure BT core surrounded by a shell of Zr-modified material were observed. Flat permittivity in the temperature range 30–125 °C and significantly reduced dielectric losses were reported. The dielectric results were discussed on the basis of the microstructural considerations.

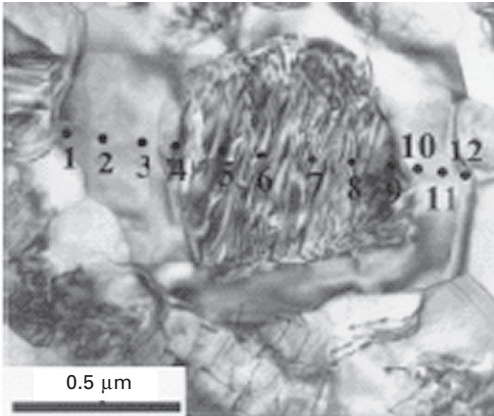
Sintering characteristics in the  $\text{BaTiO}_3$ -Nb<sub>2</sub>O<sub>3</sub>-Co<sub>3</sub>O<sub>4</sub> system have been studied in order to understand the formation mechanism and the stability of the core-shell microstructure according to the donor/acceptor ratio (Hennings and Schreinemacher, 1994; Chazono and Kishi, 2000). Yoon *et al.* (2002) also studied the core-shell structure in donor (Nb)-rich  $\text{BaTiO}_3$  and acceptor (Mg)-rich  $\text{BaTiO}_3$  compositions (Fig. 22.11). The grain-coarsening behaviour during  $\text{BaTiO}_3$  sintering is strongly affected by the donor/acceptor ratio and, as a result, different dielectric performances are observed. Donor-rich ceramics exhibit fine-grained microstructure and stable dielectric constant with temperature. In contrast, a coarse-grained structure is observed in acceptor-rich ceramics. In this last case, the peak value of the dielectric constant can be explained by the undoped core region of the grain and the dopant concentration of the shell.

The sintering behaviour of BT in terms of grain coarsening is modified by the nature of the dopant. The determination of the dopant's diffusion mechanism (diffusion through liquid phase or solid state bulk diffusion) is of main importance to control both the core-shell structure and the grain growth during the sintering process. The dielectric performance is closely related to such microstructural features. It becomes clear that full control of the interfaces, during both the synthesis and the sintering steps, is essential to obtain tunable dielectric properties.

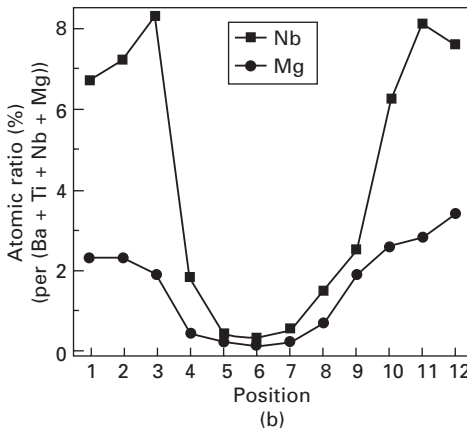
#### *Improved control of interfaces in ceramic with compositional gradient*

A tentative design on the nanoscale was recently proposed with X7R dielectric materials prepared by adding Nb<sub>2</sub>O<sub>5</sub>-Co<sub>3</sub>O<sub>4</sub> nanometre oxides to BT powder





(a)



(b)

22.11 (a) TEM image of the core-shell structure of 6.2. Nb-2.8Mg-BT, (b) scanning TEM energy dispersive X-ray spectroscopy (STEM/EDS) results for the Nb and Mg concentrations at the points indicated in (a) (Yoon *et al.*, 2002).

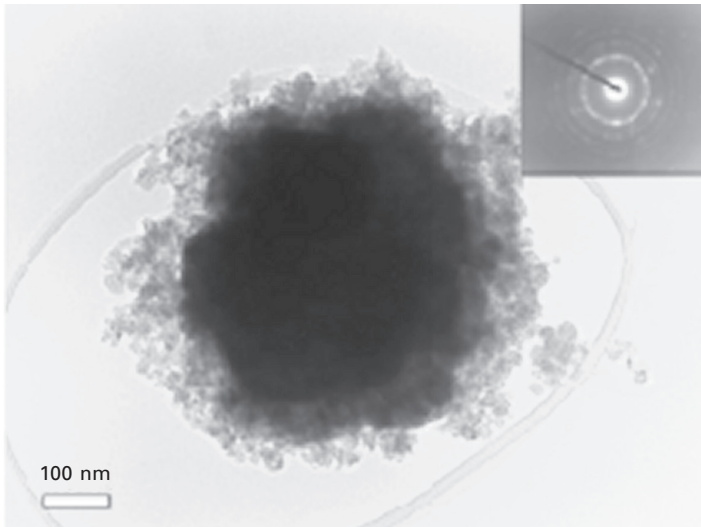
(Yuan *et al.*, 2004). The enhanced dielectric constant and depressed dielectric losses obtained were attributed to a more uniform distribution of nanometre dopants in BT grains with as a result the formation of core-shell structure with thin grain shell. However this work was not supported by SEM or TEM investigations.

The multidisciplinary approach, described above in the case of ferroelectric-non-ferroelectric composites, was successfully applied to ceramics with gradient concentration. Limited interdiffusion between the core and the shell can be achieved in dense ceramics thanks to a full control of both the design during synthesis and sintering. This is illustrated by one of the latest improvements on the fabrication of dielectric ceramics with locally graded structure proposed

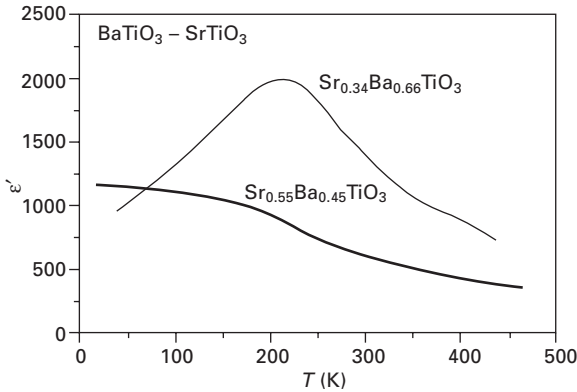
by Buscaglia *et al.* (2006a). Their approach consists of the coating of BT particles with a shell made of  $\text{SrTiO}_3$  or  $\text{BaZrO}_3$  through a precipitation process (Fig. 22.12). Coagulation of  $\text{SrTiO}_3/\text{BaZrO}_3$  nanocrystals on the BT cores was then obtained. Controlled sintering of the as-obtained core–shell structure was possible thanks to the use of SPS which allows limited interdiffusion during the thermal treatment (Fig. 22.13). The dielectric investigations indicate that the dielectric constant can be tuned by adjusting both the size of the core and the composition of the material via the amount of coating material. The well-known grain size effect of the BT core on the final dielectric properties was also considered. Effectively, broadening and flattening of the dielectric constant–temperature profile arises when the grain size of the BT is reduced below  $1\ \mu\text{m}$ . Besides the specific X7R requirements, continuous advances in the field of Multilayer Ceramic Capacitors (MLCCs) towards miniaturisation have spectacularly renewed the interest focused on size effect in nanocrystalline ceramics. Indeed, the need to reduce the layer thickness while increasing the total number of layers entails a drastic decrease of ferroelectric grain size (Randall, 2001; Buscaglia *et al.*, 2006b).

## 22.4     Summary and future trends

The dielectric properties of ferroelectric ceramics were shown to be highly sensitive to the various interfaces, particularly to charged defect localisation at grain boundaries. When the materials were prepared in the form of graded



22.12 TEM image of a typical  $\text{BaTiO}_3@ \text{SrTiO}_3$  particle (Buscaglia *et al.*, 2006a).



22.13 Relative dielectric constant of ceramics with local graded structure obtained by sintering BaTiO<sub>3</sub>-SrTiO<sub>3</sub> core-shell particles (Buscaglia *et al.*, 2006a).

materials and composites, this became even more drastic and thus raised some technological drawbacks. We have reviewed such drawbacks in the contexts of composites for telecommunications and graded ceramics for multilayer ceramic capacitors. In both cases, improved control of interfaces could be achieved through both the softening conditions of processing and sintering. Soft chemistry routes have been used to prepare core-shell grains as starting building blocks for composites of well-controlled architecture. This was useful to decrease the dielectric losses, which are an intrinsic limitation of ferroelectric ceramics.

Such a control of the nanoscale architecture of ferroelectric-based composites will be helpful to achieve improved functionality. The first example of this is the intimate mixing of ferroelectric cores with magnetic nanograins, thus leading to the coexistence of ferroelectricity and magnetism in a given bulk composite (Mornet *et al.*, 2007). The next steps will be the tuning of interface parameters in such composites, thus allowing for a better understanding of grain boundaries contribution to the effective dielectric parameters in ceramics.

## 22.5 References

- Abdelkafi Z, Abdelmoula N and Khemakhem H, Bidault O and Maglione M (2006), Dielectric relaxation in BaTi<sub>0.85</sub>(Fe/2Nb/2)0.15O<sub>3</sub>, *J. of Appl. Phys.* 100, 114111.
- Agrawal S, Guo R, Agrawal D and Bhalla A S (2004), 'Tunable BST:MgO dielectric composite by microwave sintering', *Ferroelectrics*, **306**, 155–163.
- Anselmi-Tamburini U, Gennari S, Garay J E and Munir Z A (2005a), 'Fundamental investigations on the spark plasma sintering/synthesis process: II. Modelling of current and temperature distributions', *Mater. Sci. Eng. A*, **394** (Issues 1–2), 139–148.
- Anselmi-Tamburini U, Garay J E and Munir Z A (2005b), 'Fundamental investigations on the spark plasma sintering/synthesis process: III. Current effect on reactivity', *Mater. Sci. Eng. A*, **407** (Issues 1–2), 24–30.

- Armstrong T R, Morgens L E, Maurice A K and Buchanan R C (1989), 'Effects of zirconia on microstructure and dielectric properties of barium titanate ceramics', *J. Am. Ceram. Soc.*, **72**(4), 605–611.
- Aymonier C, Elissalde C, Reveron H, Weill F, Maglione M and Cansell F (2005), 'Supercritical fluid technology of nanoparticles coating for new ceramic materials', *J. Nanosci. Nanotech.*, **5**(6), 980–983.
- Bardet J P (1979), 'Etats stationnaires et régimes évolutifs de la charge d'espace dans les diélectriques', *J. Phys. IV Paris*, **40**, 607–615 (in French).
- Baudry L (1999), 'Theoretical investigation of the influence of space charges on ferroelectric properties of PbZrTiO<sub>3</sub> thin film capacitor', *J. Appl. Phys.*, **86**, 1096–1105.
- Bidault O, Goux P, Kchikech M, Belkaoumi M and Maglione M (1994), 'Space charge relaxation in perovskites', *Phys. Rev. B*, **49**(12), 7868–7873.
- Bratkovsky A and Levanyuk A P (2000), 'Ferroelectric phase transitions in films with depletion charge', *Phys. Rev. B*, **61**(22), 15042–15050.
- Buscaglia M T, Viviani M, Zhao Z, Buscaglia V and Nanni P (2006a), 'Synthesis of BaTiO<sub>3</sub> core-shell particles and fabrication of dielectric ceramics with local graded structure', *Chem. Mater.*, **18**, 4002–4010.
- Buscaglia M T, Viviani M, Buscaglia V, Mitoseriu L, Testino A, Nanni P, Zao Z, Nygren M, Harnagea C, Piazza D and Galassi C (2006b), 'High dielectric constant and frozen macroscopic polarization in dense nanocrystalline BaTiO<sub>3</sub> ceramics', *Phys. Rev. B*, **73**, 064114-1–064114-10.
- Chan N H, Sharma R K and Smyth D M (1981), 'Nonstoichiometry in undoped barium titanate', *J. Am. Ceram. Soc.*, **64**(9), 556–562.
- Chang W and Sengupta L (2002), 'MgO-mixed Ba<sub>0.6</sub>Sr<sub>0.4</sub>TiO<sub>3</sub> bulk ceramics and thin films for tunable microwave applications', *J. Appl. Phys.*, **92**(7), 3941–3946.
- Chazono H and Kishi H (2000), 'Sintering characteristics in the BaTiO<sub>3</sub>-Nb<sub>2</sub>O<sub>5</sub>-Co<sub>3</sub>O<sub>4</sub> ternary system: II, stability of so-called 'core-shell' structure', *J. Am. Ceram. Soc.*, **83**(1), 101–106.
- Chen W, Anselmi-Tamburini U, Garay J E, Groza J R and Munir Z A (2005), 'Fundamental investigations on the spark plasma sintering/synthesis process: I. Effect of dc pulsing on reactivity', *Mater. Sci. Eng. A*, **394** (Issues 1–2), 132–138.
- Dawber M and Scott J (2000), 'A model for fatigue in ferroelectric perovskite thin films', *Appl. Phys. Lett.* **76**(8), 1060–1062.
- Elissalde C, Estournès C and Maglione M (2007), 'Tailoring dielectric properties of multilayer composites using spark plasma sintering', *J. Am. Ceram. Soc.*, **90**(3), 973–976.
- Hennings D and Rosenstein G (1984), 'Temperature-stable dielectric based on chemically inhomogeneous BaTiO<sub>3</sub>', *J. Am. Ceram. Soc.*, **67**, 249–254.
- Hennings D and Schreinemacher B (1994), 'Temperature-stable dielectric materials in the system BaTiO<sub>3</sub>-Nb<sub>2</sub>O<sub>5</sub>-Co<sub>3</sub>O<sub>4</sub>', *J. Eur Ceram. Soc.*, **14**, 463–471.
- Huber C, Treguer-Delapierre M, Elissalde C, Weill F and Maglione M (2003), 'New application of the core-shell concept to ferroelectric nanopowder', *J. Mater. Chem.*, **13**, 650–653.
- Ishibashi Y (1990), 'A model of polarization reversal in ferroelectrics', *J. Phys. Soc. Jpn.*, **59**(11), 4148–4154.
- Jain M, Majumder S B, Katiyar R S, Agrawal D C and Bhalla A S (2002), 'Dielectric properties of sol-gel derived MgO : Ba<sub>0.5</sub>Sr<sub>0.5</sub>TiO<sub>3</sub> thin film composites', *Appl. Phys. Lett.*, **81**(17), 3212–3214.
- Jain M, Majumder S B, Katiyar R S and Bhalla A S (2003), 'Novel barium strontium

- titanate  $\text{Ba}_{0.5}\text{Sr}_{0.5}\text{TiO}_3/\text{MgO}$  thin film composites for tunable microwave devices', *Mater. Lett.*, **57**, 4232–4236.
- Joshi P C and Cole M W (2000), 'Mg-doped  $\text{Ba}_{0.6}\text{Sr}_{0.4}\text{TiO}_3$  thin films for tunable microwave applications', *Appl. Phys. Lett.*, **77**(2), 289–291.
- Junquera J and Ghosez P (2003), 'Critical thickness for ferroelectricity in ultra thin films', *Nature*, **422**, 506–509.
- Kamba S, Hughes H, Noujni D, Surendran S, Pullar R C, Samoukhina P, Petzelt J, Freer R, McN Alford N and Iddles D M (2004), 'Relationship between microwave and lattice vibration properties in  $\text{Ba}(\text{Zn}_{1/3}\text{Nb}_{2/3})\text{O}_3$ -based microwave dielectric ceramics', *J. Phys. D: Appl. Phys.*, **37**, 1980–1986.
- Ke S, Huang H and Fan H (2006), 'Relaxor behaviour in  $\text{CaCu}_3\text{Ti}_4\text{O}_{12}$ ', *Appl. Phys. Lett.*, **89**, 182904-1–182904-3.
- Kretschmer K and Binder K (1979), 'Surface effects on phase transitions in ferroelectrics and dipolar magnets', *Phys. Rev. B*, **20**(3), 1065–1076.
- Liang X, Wu W and Meng Z (2003), 'Dielectric and tunable characteristics of barium strontium titanate modified with  $\text{Al}_2\text{O}_3$  addition', *Mater. Sci. Eng.*, **B99**, 366–369.
- Maglione M and Belkaoui M (1992), 'Electron relaxation mode interaction in  $\text{BaTiO}_3:\text{Nb}$ ', *Phys. Rev. B*, **45**(5), 2029–2034.
- Maurice A K (1984), 'Powder synthesis, stoichiometry, and processing effects on properties of high purity barium titanate', MS Thesis, University of Illinois, Urbana, IL.
- Mornet S, Elissalde C, Hornebecq V, Bidault O, Duguet E, Brisson A and Maglione M (2005), 'Controlled growth of silica shell on  $\text{Ba}_{0.6}\text{Sr}_{0.4}\text{TiO}_3$  nanoparticles used as precursors of ferroelectric composites', *Chem. Mater.*, **17**, 4530–4536.
- Mornet S, Elissalde C, Bidault O, Weill F, Sellier E, Nguyen O and Maglione M (2007), 'Ferroelectric-based nanocomposites: towards multifunctional materials', *Chem. Mater.*, **19**(5), 987–992.
- Morrison F D, Coats A M, Sinclair D C and West A R (2001), 'Charge compensation mechanisms in La-doped  $\text{BaTiO}_3$ ', *J. Electroceram.*, **6**, 219–232.
- Nagai T, Iijima K, Hwang H J, Sando M, Sekino T and Niihara K (2000), 'Effect of MgO doping on the phase transformations of  $\text{BaTiO}_3$ ', *J. Am. Ceram. Soc.*, **83**, 107–112.
- Nenez S (2001), 'Céramiques diélectriques commandables pour applications micro-ondes: composites à base de titanate de baryum strontium et d'un oxyde non ferroélectrique', Thesis, Université de Bourgogne.
- Nenez S, Morell A, Paté M, Maglione M, Niepce J C and Ganne J P (2002), 'Dielectric properties of barium strontium titanate/non ferroelectric oxide ceramic composites', *Key Eng. Mater.*, **206–213**, 1513–1518.
- Nygren M and Zhen S (2003), 'On the preparation of bio-, nano- and structural ceramics and composites by spark plasma sintering', *Solid State Sci.*, **5**, 125–131.
- Park J S and Han Y H (2005), 'Nano size  $\text{BaTiO}_3$  coated with silica', *Ceram. Int.*, **31**, 777–782.
- Petzelt J and Kamba S (2003), 'Submillimetre and infrared response of microwave materials: extrapolation to microwave properties', *Mater. Chem. Phys.*, **79**, 175–180.
- Petzelt J, Ostapchuk T, Pashkin A and Rychetský I (2003), 'FIR and near-millimetre dielectric response of  $\text{SrTiO}_3$ ,  $\text{BaTiO}_3$  and BST films and ceramics', *J. Eur. Ceram. Soc.*, **23**, 2627–2632.
- Raevski I P, Prosandeev S A, Bogatin A S, Malitskaya M A and Jastrabik L (2003), 'High dielectric permittivity in  $\text{AFe}_{1/2}\text{B}_{1/2}\text{O}_3$  non ferroelectric perovskite ceramics (A = Ba, Sr, Ca; B = Nb, Ta, Sb)', *J. Appl. Phys.*, **93**(7), 4130–4136.

- Randall C (2001), 'Scientific and engineering issues of the state-of-the-art and future multilayer capacitors', *J. Ceram. Soc. Jpn.*, **109**, S2–S6.
- Rawal B S, Khan M and Buessem W R (1981), 'Grain core–grain shell structures in barium titanate-based dielectrics', *Advances in Ceramics*, The American Ceramic Society Columbus, Ohio, 1, 172–188.
- Reymond V, Michau D, Payan S and Maglione M (2004), 'Strong improvement of the dielectric losses of  $\text{Ba}_{0.6}\text{Sr}_{0.4}\text{TiO}_3$  thin films using a  $\text{SiO}_2$  barrier layer', *J. Phys.: Condensed Matter*, **16**, 9155–9162.
- Rytz D, Wechsler A, Garrett M H, Nelson C C and Schwartz R N (1990), 'Photorefractive properties of cobalt-doped barium titanate ( $\text{BaTiO}_3$ )', *J. Opt. Soc. Am. B*, **7**(12), 2245–2254.
- Schwartz R N, Wechsler B A and MacFarlane R A (1992), 'Photo-EPR study of light-sensitive impurity and defects centers in photorefractive  $\text{BaTiO}_3$ ', *Phys. Rev. B*, **46**(6), 3263–3272.
- Sengupta L C and Sengupta S (1999), 'Breakthrough advances in low loss, tunable dielectric materials', *Mat. Res. Innov.*, **2**, 278–282.
- Sengupta L C, Stowell S, Ngo E and O'Day M E (1995a), 'Barium strontium titanate and non-ferroelectric oxide ceramic composites for use in phase array antennas', *Integrated Ferroelectrics*, **8**, 77–88.
- Sengupta L C, Ngo E, Stowell S, and O'Day M E (1995b), 'Ceramic ferroelectric composite material BSTO-MgO', US Patent 5 427 988.
- Sengupta L, Ngo E, Stowell S, O'Day M and Lancto R (1996), 'Ceramic ferroelectric composite material BSTO-ZrO<sub>2</sub>', US Patent 5 486 491.
- Sengupta S, Stowell S, Sengupta L and Joshi P C (2000), 'Ferroelectric thin film composites made by metalorganic decomposition', US Patent 6 071 555.
- Shih W H, Kisailus D and Wei Y (1995), 'Silica coating on barium titanate particles', *Mat. Lett.*, **24**, 13–15.
- Smyth D M (2000), 'The effects of dopants on the properties of metal oxides', *Solid State Ionics*, **129**, 5–12.
- Smyth D M (2002), 'The defect chemistry of donor-doped  $\text{BaTiO}_3$ : a rebuttal', *J. Electroceram.*, **9**, 179–186.
- Stolichnov I and Tagantsev A (1998), 'Space charge influenced-injection model for conduction in  $\text{Pb}(\text{Zr}_x\text{Ti}_{1-x})\text{O}_3$  thin films', *J. Appl. Phys.*, **84**(6), 3216–3225.
- Subramanian M A, Dong L, Duan N, Reisner B A, and Sleight A W (2000), 'High dielectric constant in  $\text{ACu}_3\text{Ti}_4\text{O}_{12}$  and  $\text{ACu}_3\text{Ti}_3\text{FeO}_{12}$  phases', *J. Solid State Chem.*, **151**(2), 323–325.
- Synowczynski J, Hirsch S and Gersten B (2002), 'Rapid gel cast prototyping of complex paraelectric (Ba, Sr) $\text{TiO}_3$ /MgO composites', *Materials Research Society Symposium Proceedings*, **720**, 203–208.
- Sze S M (1969), *Physics of Semiconductor Devices*, Wiley International, New York.
- Tian H Y, Qi J Q, Wang Y, Chan H L W and Choy C L (2005), 'Core–shell structure of nanoscaled  $\text{Ba}_{0.5}\text{Sr}_{0.5}\text{TiO}_3$  self-wrapped by MgO derived from a direct solution synthesis at room temperature', *Nanotechnology*, **16**, 47–52.
- Vanhorst T, Schirmer O F, Kröse H, Scharfschwerdt R and Kool T W (1996),  $\text{O}^{2-}$  holes associated with alkali acceptors in  $\text{BaTiO}_3$ ', *Phys. Rev. B*, **53**(1), 116–125.
- Vollman M and Waser R (1994), 'Grain boundary defect chemistry of acceptor-doped titanates: space charge layer width', *J. Am. Ceram. Soc.*, **77**, 235–243.
- Waser R and Klee M (1992), 'Theory of conduction and breakdown in perovskite thin films', *Integrated Ferroelectrics*, **2**, 23–40.

- Weil C M, Geyer R G and Sengupta L (1998), 'Microwave dielectric characterization of bulk ferroelectrics', *J. Phys. IV*, **8**, 9-113-9-116.
- Wemple S H, Di Domenico M and Jarayaman A (1969), 'Electron scattering in perovskite-oxide ferroelectric semiconductors', *Phys. Rev.* **180**, 547-556.
- Yoon S H, Lee J H and Kim D Y (2002), 'Core-shell structure of acceptor-rich, coarse barium titanate grains', *J. Am. Ceram. Soc.*, **85**(12), 3111-3113.
- Yu Z, Ang C, Guo R and Bhalla A S (2003), 'Dielectric properties and tunability of (Sr, Bi)TiO<sub>3</sub> with MgO additives', *Mater. Lett.*, **57**, 2927-2931.
- Yuan Y, Zhang S and You W (2004), 'Preparation of BaTiO<sub>3</sub>-based X7R ceramics with high dielectric constant by nanometer oxides doping method', *Mater. Lett.*, **58**, 1959-1963.
- Zurmühlen R, Petzelt J, Kamba S, Kozlov G, Volkov A, Gorshunov B, Dube D, Tagantsev A and Setter N (1995), Dielectric spectroscopy of Ba(B'<sub>1/2</sub>B''<sub>1/2</sub>)O<sub>3</sub> complex perovskite ceramics: correlations between ionic parameters and microwave dielectric properties. II Studies below the phonon eigenfrequencies (10<sup>-2</sup>-10<sup>-12</sup> Hz) *J. Appl. Phys.*, **77** (10), 5351-5364.

## Single crystalline PZT films and the impact of extended structural defects on the ferroelectric properties

I VREJOIU, D HESSE and M ALEXE,  
Max Planck Institute of Microstructure Physics, Germany

### 23.1 Introduction

In most materials of technological interest structural defects play detrimental roles. Therefore, the heteroepitaxial growth of thin films free from structural defects, especially of semiconductors, has received a great deal of attention in the last decades. In mismatched epitaxial films, which grow in a two-dimensional mode (i.e. step flow or layer-by-layer growth), biaxial stress is built up. Usually the stress relaxation in mismatched epitaxial films leads to the formation of misfit dislocations (MDs) at the film/substrate interface, which are commonly accompanied by threading dislocations (TDs) that extend across the film. Structural defects, such as MDs and TDs, are well known to significantly influence the physical properties of semiconductor thin films and heterostructures (Fitzgerald, 1991; Queisser and Haller, 1998). For example, epitaxial film quality is of great importance to the success of all III–V semiconductor devices. Dislocation densities above  $\approx 10^4 \text{ cm}^{-2}$  significantly reduce the efficiency of GaP and GaAs optoelectronic devices. The threading dislocation density depends only marginally on the substrate material (and hence on the misfit between the substrate and the layer) but rather on the growth technique and conditions (Matthews, 1975; Miguel and Kardar, 1997; Kaganer *et al.*, 2005; Kapolnek *et al.*, 1995).

Although the presence of TDs in functional ternary-oxide thin films, including ferroelectric perovskite thin films and heterostructures has been reported (Heying *et al.*, 1999; Alpay *et al.* 1999; Canedy *et al.*, 2000; Misirlioglu *et al.*, 2006a,b), details on their origin, role and particularly on their avoidance (Romanov *et al.*, 1999) are not sufficiently understood. If large single crystals cannot be grown easily, as in case of the ferroelectric  $\text{PbZr}_x\text{Ti}_{1-x}\text{O}_3$  (PZT) perovskite, for a broad range of compositions (Clarke and Whatmore, 1976; Clarke *et al.*, 1976; Haun *et al.*, 1989), the intrinsic properties can be studied on single-crystalline films, if the quality of growth permits to achieve films that are free from extended defects. This chapter presents very recent results regarding heteroepitaxial ferroelectric ( $\text{PbTiO}_3$ , PZT) thin films synthesized



by pulsed-laser deposition (PLD), emphasizing the role of extended structural defects for their ferroelectric performance by comparing thin films with and without defects.

### **23.2      Pulsed laser deposition of epitaxial ferroelectric oxide thin films**

Pulsed-laser deposition (Chrissey and Hubler, 1994; Bäuerle, 2000; Willmott and Huber, 2000) is a thin film synthesis technique based on laser ablation, in which the energy of, typically, ultraviolet (UV) photons produced by excimer lasers is coupled to the bulk starting material via electronic processes. An intense laser pulse is focused onto a target placed in a vacuum chamber, where it is partially absorbed and results in material ejection in the form of a luminous plume, when the power density exceeds a certain threshold. The threshold power density depends on the properties of the target material and its morphology, and on the laser pulse wavelength and duration. The ablated material is then allowed to condense on a suitable substrate, which may be heated when crystalline films are desired, and thus thin film growth occurs. The deposition process may be performed in high vacuum or in a background of an inert (argon) or reactive (oxygen, nitrogen,  $N_2O$ , etc.) gas. The latter may affect the ablated plume species in the gas phase or the surface reactions on the substrate, resulting in reactive PLD.

Among the several well-established techniques for thin film fabrication, PLD offers some important advantages: (i) the energy source (laser photons) is outside the vacuum chamber; (ii) almost any condensed matter material can be ablated; (iii) the pulsed nature of PLD enables flexible control over the film growth rate; (iv) the vaporized material originates only from the area defined by the laser focus; (v) under optimal conditions, the ratios of the elemental components of the target and the film are the same, even for multi-elemental systems with complex stoichiometry; and (vi) the possibility to produce species in energetic states far from chemical equilibrium may lead to the production of novel or metastable materials that are unattainable under thermal equilibrium. There are also several technical and fundamental drawbacks one has to deal with when employing PLD: (i) the possible production of up to micrometre-sized particles and droplets during the ablation process; (ii) impurities in the ceramic/single crystal target material; (iii) the limited size (around  $1\text{ cm}^2$ ) of thin film uniform thickness (Chrissey and Hubler, 1994; Bäuerle, 2000; Willmott and Huber, 2000), unless specific methods are applied (Pignolet *et al.*, 1996; Lorenz *et al.*, 1997). Additionally, special care should be involved, when thin films with multicomponent stoichiometry are synthesized by PLD. The angular distribution in the ablation plume may vary for the different chemical elements (Ma *et al.*, 1996). Several studies dedicated to XeCl laser ablation of  $PbZr_xTi_{1-x}O_3$  indicated that the

spatial distribution of the PZT film constituents has two components, one resulting from thermal evaporation and the other from the photoablative process, and are strongly dependent on the laser fluence and the ambient oxygen pressure. The distribution profiles of Pb, the volatile element, exhibit a dip at the centre for fluences higher than  $0.2 \text{ J/cm}^2$  and it has been concluded that the Pb deficiency in PZT thin films may be caused by resputtering with energetic Zr atoms and ions bombarding the growing deposit (Hau *et al.*, 1992, 1995).

PLD has been employed successfully for the fabrication of high-quality thin films of ferroelectrics. A broadly documented review related to the PLD synthesis of ferroelectrics is given in Leuchtner and Grabowski (1994). Deposition of ferroelectric films of the correct stoichiometry is fundamental for their utility. However, the synthesis is rather complicated, because often the ferroelectric material involves volatile components such as Pb, Li or K. Therefore, the most critical parameters that influence the film composition are substrate temperature, ambient gas pressure and target composition itself, whereas the laser energy density (fluence) can affect the chemical composition to a less important extent. Since 1995, much progress has been made in the controlled PLD-epitaxy of ferroelectric perovskites on single crystalline substrates, such as  $\text{SrTiO}_3$ ,  $\text{LaAlO}_3$ ,  $\text{DyScO}_3$ , or  $\text{MgO}$ , with various orientations. PLD systems equipped with high-pressure reflection high-energy electron diffraction (RHEED) became available to monitor the layer-by-layer growth of homoepitaxial and heteroepitaxial thin films and superlattices *in situ* (Neave *et al.*, 1985; Tarsa *et al.*, 1996; Blank *et al.*, 1999; Lee *et al.*, 2005). Additionally, a novel growth method, pulsed laser interval deposition, has been developed to enable layer-by-layer growth in a regime (temperature, pressure) where otherwise island formation would dominate the growth (Koster *et al.*, 1999). X-ray reflectivity and scattering, and optical reflectivity measurements, can also be employed for *in situ* monitoring the growth regime of perovskites, shedding light on the fundamental aspects (atomic level) of the PLD growth process (Fei *et al.*, 2004; Wang *et al.* 2004).

### **23.3 Epitaxial ferroelectric oxide thin films and nanostructures with extended structural defects**

Great effort has been devoted to growing epitaxial thin films on lattice-mismatched substrates for device application. When the epilayer exceeds a certain critical thickness, misfit dislocations are generated to reduce the mismatch strain and are usually accompanied by threading dislocations that extend across the thin film (Matthews, 1975). The possibilities for the generation of threading dislocations during epitaxial growth are:

- the extension of substrate dislocations;
- the accommodation of translational and rotational displacements between agglomerating islands that are close to epitaxial orientation;
- the formation of dislocation loops by the aggregation of point defects;
- plastic deformation of the film, during growth and subsequent cooling.

In the case of oxide ferroelectrics, it has been demonstrated that misfit and threading dislocations have an important impact on the ferroelectric properties of thin films and nanostructures. The strain field surrounding dislocations is predicted to significantly perturb the ferroelectric and dielectric properties of the neighbouring material (Alpay *et al.*, 2004; Nagarajan *et al.*, 2005; Misirlioglu *et al.*, 2006b). In nanostructures, owing to their confined dimensions, the influence of defects is even more pronounced, because of the relatively enhanced volume of the defective regions. In a joint study by quantitative high-resolution electron microscopy and piezo-force microscopy (PFM), Chu *et al.* (2004) showed that epitaxial  $\text{PbZr}_{0.52}\text{Ti}_{0.48}\text{O}_3$  nano-islands exhibited edge-type misfit dislocations, whose strain fields were affecting relatively large tubular regions of PZT with a cross-section of 4 nm (height)  $\times$  8 nm (width). Therefore, PZT islands that were only  $\sim 10$  nm high showed an apparent polarization instability, associated with the distorted PZT lattice within the strain fields. The PZT lattice deviated from the expected tetragonal structure and the long-range correlations of local polarizations might thus break down, resulting in polarization instability.

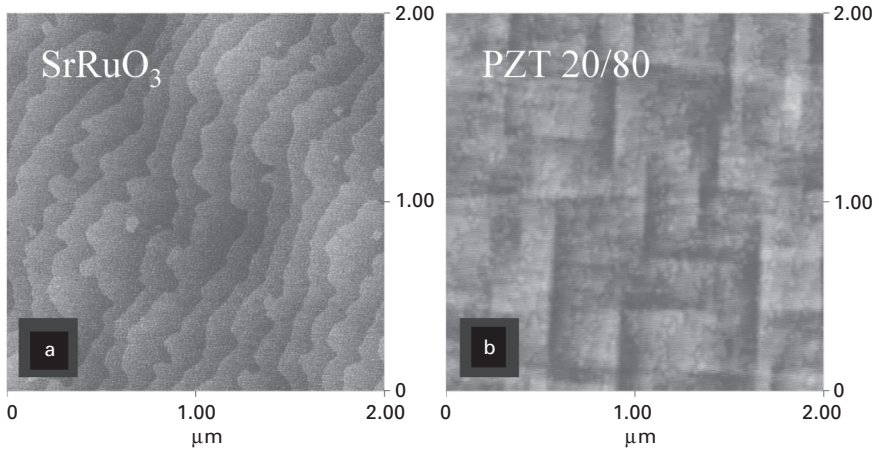
In epitaxial thin films, although it is unanimously accepted that TDs and MDs have an important impact, it is more difficult to correlate directly the presence of various types of dislocations with the ferroelectric and dielectric properties of the material (Nagarajan *et al.*, 1999, 2005; Ryen *et al.*, 1999; Canedy *et al.*, 2000; Balzar *et al.*, 2002; Misirlioglu 2006a). Nagarajan *et al.* (2005) reported a quantitative study of the thickness dependence of the polarization and piezoelectric properties of epitaxial PZT films with two compositions,  $\text{PbZr}_{0.52}\text{Ti}_{0.48}\text{O}_3$  (PZT 52/48) and  $\text{PbZr}_{0.2}\text{Ti}_{0.8}\text{O}_3$  (PZT 20/80), grown on  $\text{SrRuO}_3$ -coated (001)  $\text{SrTiO}_3$ . Cross-section transmission electron microscopy (TEM) micrographs of 20 nm thin PZT films of both compositions showed that dislocations were present in the PZT films. However dislocations formed in a much higher density for the PZT 52/48 film, which has a larger in-plane lattice mismatch with the  $\text{SrTiO}_3$  substrate ( $-3.9\%$  for PZT 52/48, about only  $-0.7\%$  for PZT 20/80, at growth temperature). As a consequence, a drastic decrease of both the switchable polarization  $\Delta P$  and piezoelectric coefficient  $d_{33}$  was observed for PZT 52/48 films thinner than 100 nm. The lattice-matched PZT 20/80 films, with low density of dislocations, showed no scaling in  $\Delta P$  or  $d_{33}$  down to 15 nm. The severe drop in  $\Delta P$  and  $d_{33}$  values in the PZT 52/48 systems occurring for much thicker layers indicated the overriding role of dislocations in the size effects in ferroelectrics.

Another important aspect is the polydomain formation, which is inherent to heteroepitaxial ferroelectric films. The formation of polydomains relaxes the total strain energy during the paraelectric–ferroelectric phase transformation. Ferroelectric thin films, deposited at elevated temperature, undergo this transition, when cooled down to room temperature through the phase transition (Roytburd 1998a,b; Alpay and Roytburd, 1998; Roytburd *et al.*, 2001; Foster *et al.*, 1996a; Nagarajan *et al.*, 1999; Li *et al.*, 2005; Pertsev *et al.*, 2003; Kukhar *et al.*, 2006). The existence of dislocations influences the ferroelectric domain patterns and movement as well (Speck and Pompe, 1994; Speck *et al.*, 1994; Emelyanov and Pertsev, 2003). Hu *et al.* (2003) found that the presence of interfacial dislocations in tetragonal ferroelectric thin films locally changes the ferroelectric transition temperature and leads to preferential formation of ferroelectric domains around misfit dislocations.

The formation of domains can be regarded as a drawback, if single-domain thin films are desired, when studying intrinsic ferroelectric properties of materials. On the other hand, the domains can be employed for device fabrication, exploiting the extrinsic contribution of domain wall motion to the enhancement of dielectric and piezoelectric response of the material (Nagarajan *et al.*, 2003; Le Rhun *et al.*, 2006).

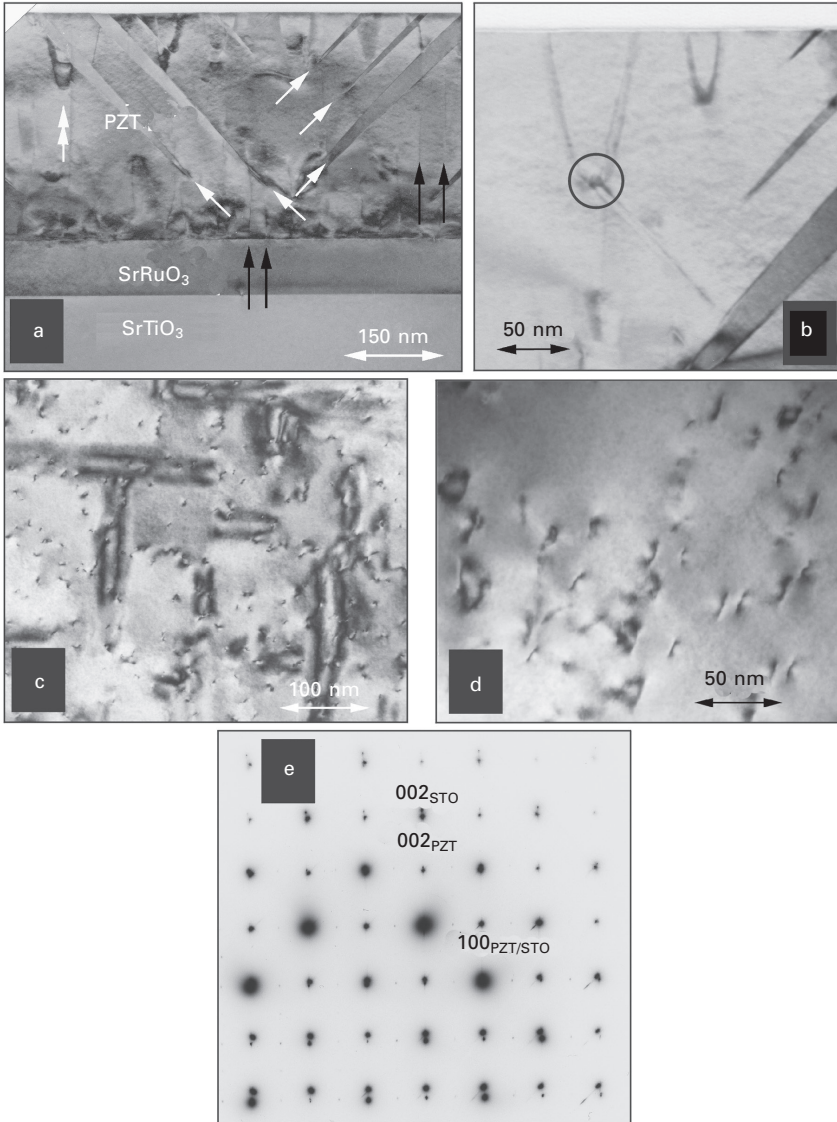
### 23.3.1 TEM and HRTEM analyses of the defects in epitaxial PZT 20/80 films

Vrejoiu *et al.* (2006a) reported on the PLD synthesis of ferroelectric epitaxial PZT 20/80 films and analyzed in detail the defects exhibited by the PZT layers and their effect on the polarization backswitching. PZT 20/80 films have a tetragonal crystal structure. Vicinal single crystalline SrTiO<sub>3</sub> (100) (STO) substrates with a miscut angle of 0.1–0.2° (CrysTec, Berlin, Germany) were etched in buffered hydrofluoric acid and annealed so that single-unit-cell stepped terraces with uniform TiO<sub>2</sub>-termination were formed (Koster *et al.*, 2000). A single-crystalline conductive SrRuO<sub>3</sub> (SRO) layer of a thickness of 20–75 nm was first grown in a step-flow growth regime (Hong *et al.*, 2005) onto the SrTiO<sub>3</sub> substrate. The SRO layer is to be used as bottom electrode for the future metal–ferroelectric–metal heterostructure. Subsequently, PZT layers up to 350 nm thick were deposited at a substrate temperature  $T_g = 575\text{--}600^\circ\text{C}$  in 150–300 mtorr O<sub>2</sub>, on top of the SRO-coated STO (001). A ceramic Pb<sub>1.1</sub>Zr<sub>0.2</sub>Ti<sub>0.8</sub>O<sub>3</sub> target purchased from SCI Engineered Materials (Columbus, OH) was used for PLD. Atomic force microscopy (AFM) images taken on 2 μm × 2 μm areas on the surface of such SRO and PZT layers are shown in Fig. 23.1. The surface of the 250 nm thick PZT layer exhibited a 90° grid that indicated the formation of 90° twin *a*–*c* domains, typical for tetragonal ferroelectric thin films (Foster *et al.*, 1996b; Alpay and Roytburd, 1998; Nagarajan *et al.*, 1999; Li *et al.*, 2005).



23.1 Atomic force microscopy (AFM) images taken on  $2\mu\text{m} \times 2\mu\text{m}$  areas on the surface of (a) a 70 nm thick step-flow grown SRO film and (b) a 250 nm thick defective PZT 20/80 film.

TEM samples were fabricated by standard mechanical and ion milling procedures. Plan view and two types of cross-section TEM samples were prepared from the PZT/SRO/STO heterostructures. The cross-sections were cut in such a way that the electron beam was incident to the TEM sample either from the [010] or the [110] direction. Conventional TEM was performed in a Philips CM20T electron microscope at 200 keV primary energy of the electrons, and high resolution (HR)TEM in a Jeol 4010 high-resolution electron microscope at 400 keV. Some of the HRTEM images were Fourier-filtered to reveal the nature of the observed defects. Figure 23.2(a) shows a cross-section TEM micrograph of a PZT/SRO/STO heterostructure, seen from the [010] direction. The tetragonal film was  $c$ -axis oriented, as shown by the electron diffraction pattern (Fig. 23.2e), but contained narrow  $90^\circ$   $a$ -domains bounded by  $\{101\}$  twin planes ( $90^\circ$   $a$ - $c$  boundaries) (see Fig. 23.2a, where the tilted white arrows are inserted). Typically two types of vertical TDs were discovered in the PZT film. There exist pairs of partial dislocations (partial dislocation dipoles) that run across the entire layer (Alpay *et al.*, 1999; Misirlioglu *et al.*, 2006a) (indicated by the black arrows in Fig. 23.2a) and half-loops (Matthews, 1975; Fitzgerald, 1991; Suzuki *et al.*, 1999; Sun *et al.* 2004) (indicated by the white double-arrow in the figure) that come from the top surface and end in the bulk of the PZT film. The TD dipoles that cross the whole PZT layer go through the  $a$ -domains as well, which indicates that the TD dipoles are already formed at the growth temperature (Foster *et al.*, 1996b; Alpay *et al.*, 1999; Misirlioglu *et al.*, 2006a). The twin domains start being formed during the cooling of the heterostructure through the cubic-to-tetragonal structural phase transition (Foster *et al.*, 1996a,b). The temperature at which the PZT layers are usually

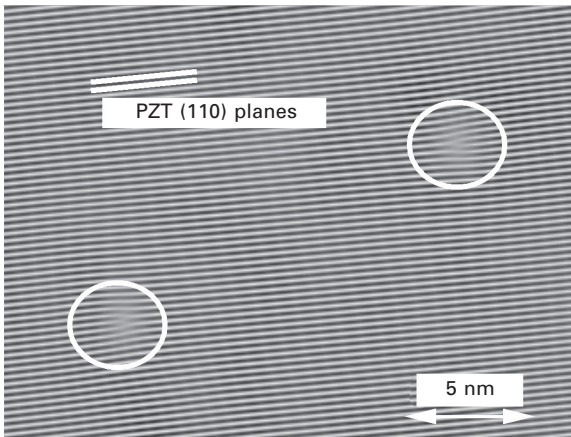


23.2 Cross-section (a, b, seen from [010]) and plan view (c, d, seen from [001]) TEM micrographs of PZT/SRO/STO (001) heterostructures. In (b) a detailed view is shown, and the circle points out that the half-dislocation loop pins a  $90^\circ$   $a$ -domain. The plan view TEM image in (c) reveals the  $90^\circ$  domains, and the dark spots are the terminations of threading dislocations on the PZT top surface, which can be better seen in (d). In (e) a contrast-inverted cross-sectional electron diffraction pattern (beam direction [010]), correctly rotated with respect to (a), is given. Three reflections are indexed, on the bottom right  $45^\circ$ -oriented streaks due to the habit planes of the  $90^\circ$   $a$ - $c$ -boundaries are seen (from Vrejoiu *et al.*, 2006a, <http://www.tandf.co.uk/journals>).

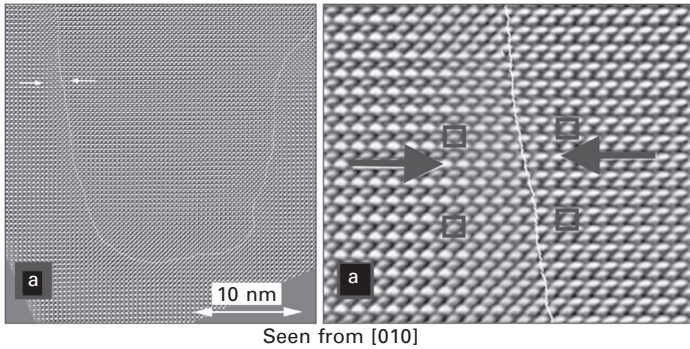
grown,  $T_g$ , significantly exceeds the phase transition temperature for the bulk PZT 20/80 ( $T_C \approx 450^\circ\text{C}$ ). It can be seen that sometimes the half-loop dislocations may pin a  $90^\circ$  domain (Fig. 23.2b).

Plan view TEM micrographs are shown in Fig. 23.2(c) and (d).  $90^\circ$  domains (partly etched away during the TEM sample thinning process) are visible in Fig. 23.2(c), as well as black spots that are spread over the entire viewed area. These spots can be better seen in the higher magnified image, given in Fig. 23.2(d). They turned out to be dislocation dipoles with a typical separation distance of 10–50 nm. To further elucidate the nature of these threading dislocation dipoles, (110)-Fourier filtered plan view HRTEM images were taken. Figure 23.3 shows such an image. It reveals that the TD dipole consists of two partial edge dislocations of equal in-plane Burgers' vector component,  $\mathbf{b}_{\parallel} = (a/2)[110]$  (Matthews, 1975; Fitzgerald, 1991; Wunderlich *et al.*, 2000) (0.28 nm), but of opposite sign, separated by a distance of about 15 nm. The vector  $(a/2)[110]$  represents half of a lattice vector, in view of the primitive cubic unit cell of PZT. As indicated by cross-sectional HRTEM of a single half-loop TD (Fig. 23.4a,b), half-loop TDs have an out-of-plane Burgers' vector component  $\mathbf{b}_{\perp} = (c/2)[001]$  and thus represent partial dislocations, too. Although neither the half-loops nor the dipoles have been entirely characterized in terms of their Burgers' and line vectors, we may state that partial in-plane Burgers' vector components  $\mathbf{b}_{\parallel} = (a/2)[110]$  and partial out-of-plane components  $\mathbf{b}_{\perp} = (c/2)[001]$  have been detected.

Misirlioglu *et al.* (2006a) studied the microstructure of epitaxial PZT 20/80 films of  $\sim 300$  nm thickness grown directly on (001) SrTiO<sub>3</sub> by pulsed laser deposition. Their TEM observations revealed that the films were



23.3 (110)-Fourier filtered plan-view HRTEM of a single TD dipole, with a separation distance of about 15 nm (from Vrejoiu *et al.*, 2006a, <http://www.tandf.co.uk/journals>).

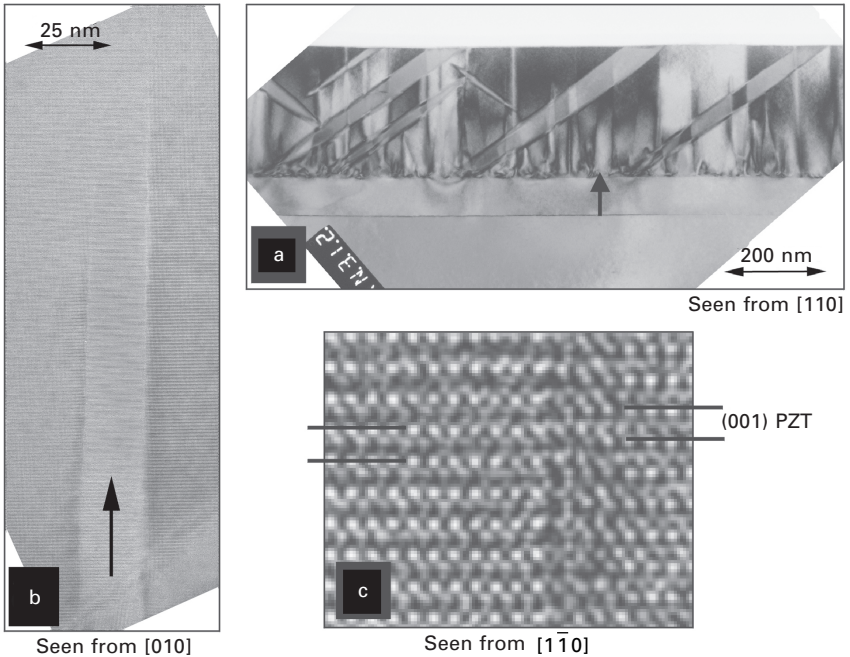


23.4 HRTEM of a single threading dislocation half-loop, with a separation distance of about 20 nm, seen from the [010] direction in (a), and a detailed view in (b). In (a) the white line is added as a guide to the position of the dislocation. The black boxes and arrows in (b) designate the vertical position of the unit cells on the left and right of the stacking fault (from Vrejoiu *et al.*, 2006a, <http://www.tandf.co.uk/journals>).

predominantly  $c$ -oriented with  $a_1$ - and  $a_2$ -oriented domains (Li *et al.*, 2005) lying on {101} planes. The substrate/film interface contained arrays of edge-type misfit dislocations and there was a high density of TDs ( $\gg 10^{10} \text{ cm}^{-2}$ ). Dai *et al.* (1996) showed that interface dislocations in  $\text{BaTiO}_3/\text{LaAlO}_3$  were directly linked up with the  $90^\circ$  domain boundaries in  $\text{BaTiO}_3$  and thus the domain boundaries were likely to be pinned at the dislocation site. Lu *et al.* (2003a) studied the defect structure of a 350 nm-thick epitaxial  $\text{Ba}_{0.3}\text{Sr}_{0.7}\text{TiO}_3$  film grown on (001)  $\text{LaAlO}_3$  and revealed that the dominant defects in the BSTO film were edge-type TDs with Burgers' vectors  $\mathbf{b} = \langle 100 \rangle$  and  $\langle 110 \rangle$ .

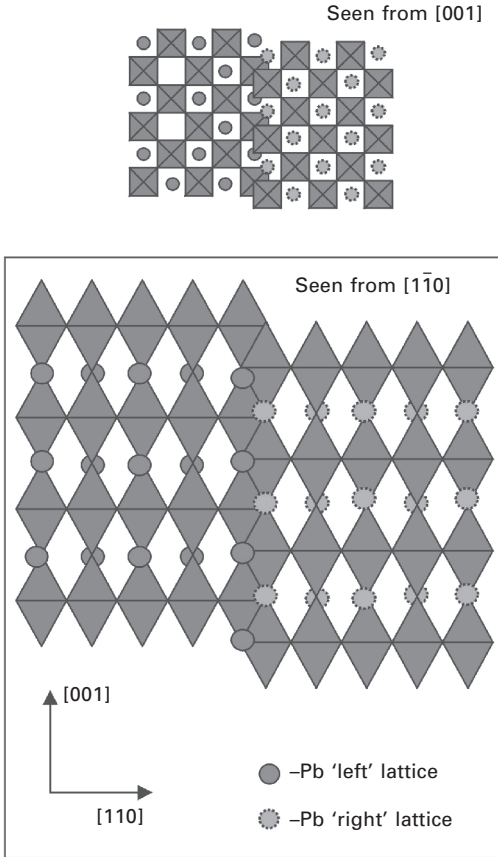
Diffraction contrast TEM and HRTEM images of the PZT/SRO/STO heterostructures on which Vrejoiu *et al.* (2006a) reported showed that the partial dislocation dipoles include a stacking fault (SF) in between (Matthews, 1975; Suzuki *et al.*, 1999; Wunderlich *et al.*, 2000; Lu *et al.*, 2003a,b), as seen in Fig. 23.5(a) and (b). The black arrow indicates the location of one of the numerous SFs. Figure 23.5(c) is a HRTEM image seen from the  $[1\bar{1}0]$  direction, so that the (001) PZT planes and the SF are visible edge-on. This image was taken on a very thin sample area (weak phase object) at Scherzer defocus ( $-40 \text{ nm}$ ), which allows one to assume that cations are visualized as dark spots ('intuitively interpretable image', *cf.* van Dyck, 1997). In view of these imaging conditions, the very dark elongated contrast spots, which occur along the stacking fault, can most probably be assigned to pairs of lead cations. Thus the stacking faults are most probably lead-rich. An unambiguous allocation of the elongated contrast spots to lead ions would, however, require some detailed contrast simulation work; thus the possibility of a titanium-rich stacking fault, as described by Lu *et al.* (2003b), cannot be entirely





23.5 Threading dislocation dipoles with a stacking fault (SF), indicated by the black arrow. (a) Diffraction contrast cross-section TEM image (seen from  $[110]$  direction) and (b) cross-section HRTEM micrograph (seen from  $[110]$  direction). A HRTEM micrograph (seen from  $[1\bar{1}0]$  direction), where the (001) PZT planes and the stacking fault are seen edge-on, is given in (c) (from Vrejoiu *et al.*, 2006a, <http://www.tandf.co.uk/journals>).

excluded. In any case, the stacking fault should be metal-rich in nature. In Fig. 23.6, a schematic model is given which refers to the possibility of a lead-rich stacking fault. This model involves an in-plane displacement vector component  $\mathbf{R}_{\parallel} = (a/2)[110]$  (schematic top) and an out-of-plane displacement vector component  $\mathbf{R}_{\perp} = (c/2)[001]$  and is thus in accordance with the experimental findings for the respective Burgers' vector components. The changed linking of the oxygen-octahedra at the stacking fault is equivalent to an oxygen deficiency (see Fig. 23.6, schematic seen from  $[1\bar{1}0]$  direction). In our case, the dislocation loops may form by aggregation of point defects (i.e. oxygen vacancies) (Matthews, 1975; Fitzgerald, 1991; Suzuki *et al.*, 2000). Because the growth of the thin film often occurs under non-equilibrium and high supersaturation conditions, as it is certainly the case for typical PLD conditions (Chrisney and Hubler, 1994; Bäuerle, 2000; Willmott and Huber, 2000), it can be anticipated that an excess of vacancies or gas atoms could be trapped in a growing film. These point defects could aggregate to form dislocation loops that would subsequently grow and coalesce to form



23.6 A possible schematic model of the stacking fault seen from  $[1\bar{1}0]$  direction: along the SF edge, oxygen ions are missing and metallic Pb atoms are paired. The small top schematic is seen from the [001] direction (from Vrejoiu *et al.*, 2006a, <http://www.tandf.co.uk/journals>).

dislocations threading the thin film. Therefore, it is likely that non-stoichiometry of the growing film could lead to dislocations being produced by the mechanism under discussion (Matthews, 1975).

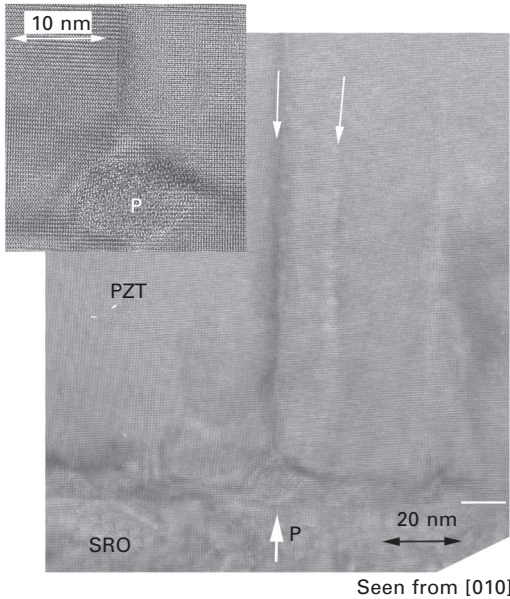
The PZT target we employed for PLD, although of  $\text{Pb}_{1.1}(\text{Zr}_{0.2}\text{Ti}_{0.8})\text{O}_3$  nominal composition, may have already been oxygen-deficient, as it is suggested by its dark grey colour, and this may have contributed to the slightly non-stoichiometric deposits. The target was deliberately purchased with 10% PbO excess, as a precaution for the possible loss of PbO during the deposition, because PbO is highly volatile at the usually elevated growth temperature. Moreover, the correct oxygen content of the growing film was

expected to be ensured by the background oxygen atmosphere, as the depositions were performed in 150–200 mtorr  $O_2$ . As mentioned in Section 23.1, PLD is known to be a deposition technique that, under favorable conditions, allows for stoichiometric transfer of the material from the bulk target to the growing thin film (Chrissey and Hubler, 1994; Bäuerle, 2000; Willmott and Huber, 2000). However, we would expect that small deviations from the nominal composition are likely to be exhibited by these PZT films. Electron-energy loss spectroscopy (EELS) and energy dispersive X-ray (EDX) analyses performed along the entire cross-section of the PZT layers ascertained that the Ti/Zr ratio stays within  $4 \pm 1$ .

Suzuki *et al.* (2000) reported on the effect of non-stoichiometry on the microstructure of epitaxial  $BaTiO_3$  thin films grown by PLD. They varied the cation non-stoichiometry over a wide range (up to 50% excess of either Ti or Ba) and observed the modification of the microstructure. Based on the observation that the defect structures were characteristic to the titanium-excess films and were not seen in stoichiometric films (Suzuki *et al.*, 1999), the authors drew the conclusion that the dislocation cores could act as a sink for insoluble excess cations and for relevant point defects such as barium and oxygen vacancies. In titanium-excess films ( $BaTi_{1.2}O_{3.4}$ ), planar defects were found and described as being terminated by a pair of partial dislocations with projected Burgers' vectors of type  $a/2$  [110]. These planar defects with the (001)-projected shear vector component of  $a/2$  [110] formed the so-called crystallographic shear (CS) structure described by the (100) stacking irregularity of either double  $TiO_2$ -layers or double  $BaO$ -layers, closely related to non-stoichiometry. Lu *et al.* (2003b) argued that the formation of stacking faults with a double layer of edge-sharing  $TiO_6$ -octahedra in epitaxial  $Ba_{0.3}Sr_{0.7}TiO_3$  films was probably related to a small amount of Ti excess during the PLD growth of the film as well.

In the case of Aurivillius-phase ferroelectrics, such as  $SrBi_2Nb_2O_9$  and  $SrBi_2Ta_2O_9$ , bismuth volatility makes the growth of phase-pure films difficult (Zurbuchen *et al.*, 2003). Loss of Bi during the slow cooling of a  $SrBi_2Ta_2O_9$  film resulted in a 5% Bi-deficient film and the generation of a high density of out-of-phase boundaries (OPBs). These OPBs, by symmetry, were demonstrated to be ferroelectrically inactive. Although the OPBs did not represent a considerable volume of material, the film had severely reduced ferroelectric properties compared with stoichiometric films, even though it appeared to be of very good quality by XRD. This could explain why many reported films of apparent high quality by XRD have such poor ferroelectric properties.

Another observation related to the formation of TDs starting from the PZT/SRO interface shows that the TDs may originate on particulates, as it can be seen in Fig. 23.7. This can be a source for heterogeneous nucleation of dislocation dipoles (Fitzgerald, 1991). The particle 'P' (10–15 nm in diameter)

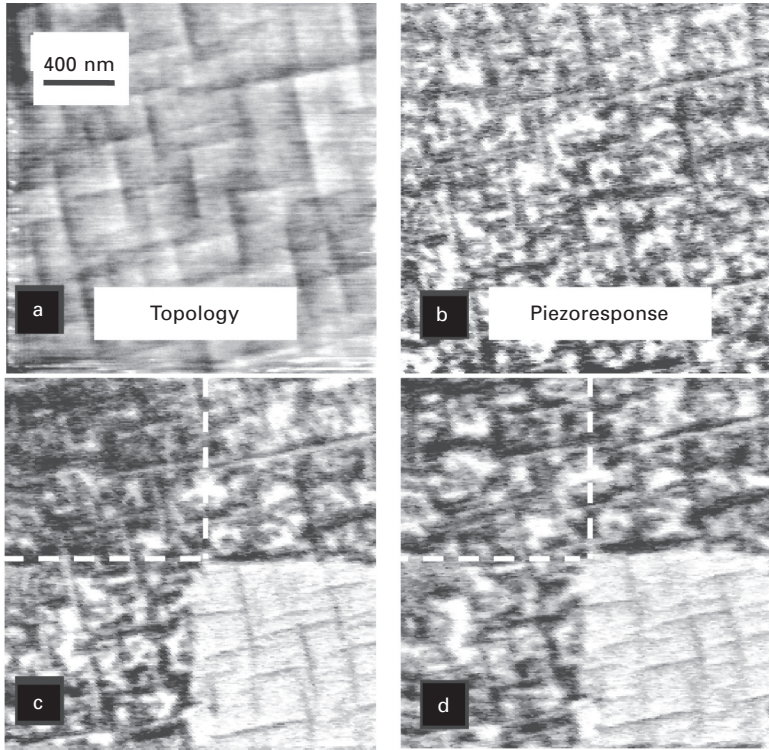


23.7 Cross-section HRTEM micrograph revealing that a threading dislocation dipole may nucleate on an amorphous particle 'P' at the PZT/SRO interface that can be better seen in the inset (upper left corner) (from Vrejoiu *et al.*, 2006a, <http://www.tandf.co.uk/journals>).

appeared to be amorphous (better visible in the top left inset of Fig. 23.7) and may be either an impurity, a particulate ejected from the PLD target or formed on the SRO surface at the initial stage of the PZT layer growth. It is assumed that the presence of such a particle or impurity results in stress concentrations which can extend into the epilayer.

### 23.3.2 Piezo-force microscopy investigations on defective epitaxial PZT 20/80 films

Piezo-force microscopy (PFM) investigations, performed on that PZT/SRO/STO heterostructure whose TEM is given in Fig. 23.5, revealed some intriguing aspects regarding the switching of  $180^\circ$  ferroelectric domains (Vrejoiu *et al.*, 2006a). Figure 23.8a shows the surface topography of a  $2\ \mu\text{m} \times 2\ \mu\text{m}$  area of the as-grown PZT film. The two-dimensional grid exhibited by the surface confirmed that  $90^\circ$  twin  $a$ - $c$  domains (Ganpule *et al.*, 2000; Le Rhun *et al.*, 2006) were formed in the PZT layer. The piezoresponse image of the as-grown PZT film, associated with the topography image is given in Fig. 23.8(b). The piezoresponse image confirms the existence of  $90^\circ$  domains, with the dark lines (forming a grid) representing the  $a$ -domains (i.e. domains with the polar  $c$ -axis lying in the plane of the film) (Ganpule *et al.*, 2000;



23.8 PFM investigations on a  $\text{PbZr}_{0.2}\text{Ti}_{0.8}\text{O}_3/\text{SrRuO}_3/\text{SrTiO}_3$  (001) heterostructure: (a) image of the PZT surface topography ( $2\ \mu\text{m} \times 2\ \mu\text{m}$ ) and (b) piezoresponse image acquired by scanning the area shown in (a); (c) piezoresponse image acquired in the very same area, immediately after poling the top left corner ( $1\ \mu\text{m} \times 1\ \mu\text{m}$ ) with  $-4\ \text{V}$  and the bottom right corner by  $+4\ \text{V}$ ; (d) piezoresponse image of the very same area acquired by scanning 15 hours after the poling. In (c) and (d) the dashed lines were added to guide the reader's eye. (From Vrejoiu *et al.*, 2006a, <http://www.tandf.co.uk/journals>).

Roelofs *et al.*, 2002; Le Rhun *et al.*, 2006).  $180^\circ$  domains of 'up' preferential orientation of the polarization are present in the PZT film (Alpay *et al.*, 1999; Le Rhun *et al.*, 2006; Vrejoiu *et al.*, 2006b), their piezoresponse being displayed as bright irregular spots with various lateral sizes between about 50 and 200 nm. In order to investigate the switching behaviour of these  $180^\circ$  domains, the following experiment was performed. The top left quadrant ( $1\ \mu\text{m} \times 1\ \mu\text{m}$ ) of the  $2\ \mu\text{m} \times 2\ \mu\text{m}$  area was poled by  $-4\ \text{V}$ , and the bottom right quadrant ( $1\ \mu\text{m} \times 1\ \mu\text{m}$ ) was poled oppositely by  $+4\ \text{V}$ . The piezoresponse image of the overall area, acquired immediately after the poling procedure is shown in Fig. 23.8(c). Complete switching to positive polarization occurred in the positively biased area, whereas in the negatively poled area, some of

the positive  $180^\circ$  domains did not completely switch to negative polarization. The sample was left on the PFM stage for 15 hours and the same  $2\mu\text{m} \times 2\mu\text{m}$  area was scanned again, the resulting image being displayed in Fig. 23.8(d). In the previously positively poled quadrant, no modification of the polarization pattern was observed. However, in the negatively poled area backswitching from the negative polarization to the positive polarization state took place, as many of the initial bright spots reappeared at the very same location.

According to up-to-date observations, TD half loops, TD dipoles and backswitching  $180^\circ$  domains are all absent in layer-by-layer grown, defect-free  $\text{PbZr}_{0.2}\text{Ti}_{0.8}\text{O}_3$  films deposited on  $\text{SrRuO}_3/\text{SrTiO}_3$  (001) (Vrejoiu *et al.*, 2006b). Since they all show up simultaneously in the present films, it is reasonable to assume that TD half loops and/or TD dipoles (with their lead-rich stacking faults) may represent pinning centres for backswitching  $180^\circ$  domains. The lateral spacing between 20 nm and about 120 nm of the TD dipoles and of the TD half loops at the surface of the films, and the lateral dimension of the backswitching ferroelectric  $180^\circ$  domains (which is between 50 and about 200 nm) are also in accordance with this assumption.

### 23.4 Single crystalline $\text{PbTiO}_3$ and PZT 20/80 films free from extended structural defects

The fabrication of single crystalline ferroelectric thin films that are free from extended structural defects requires the careful choice of a single crystalline substrate and its crystallographic surface termination, a suitable growth technique and – most important – appropriate growth parameters. It is necessary to employ a single crystalline substrate with closely matched lattice constants, because in mismatched epitaxial films which grow in a two-dimensional mode (i.e. step flow or layer-by-layer growth), biaxial stress is generated. If the thickness of the epitaxial film is below a certain critical value (Matthews, 1975) it may be expected that the misfit strain is not relaxed and the epilayer is coherently grown on the substrate. When the layer-by-layer growth regime is achieved, the indications are that epitaxy results in almost all circumstances provided that the substrate surface is clean enough and well prepared. In this regime the substrate has a very strong influence on the form of the film produced, and the growing film has little option but to choose the best (i.e. necessarily epitaxial) orientation in which to grow.

PLD is a suitable technique for synthesis of high-quality homo- and heteroepitaxial films. This is due to the highly supersaturated ablation plasma plume, its pulsed nature and the adjustable deposition rate attainable by changing the laser energy density, laser repetition rate, background reactive gas pressure and target-to-substrate distance.

Bearing in mind the aforementioned reasoning, Vrejoiu *et al.* (2006b)

chose to grow epitaxial  $\text{PbTiO}_3$  and  $\text{PbZr}_{0.2}\text{Ti}_{0.8}\text{O}_3$  films onto well-defined vicinal  $\text{SrTiO}_3$  (001) (STO) substrates of uniform surface termination by PLD. First the necessary bottom electrode consisting of  $\text{SrRuO}_3$  (SRO) was deposited on STO (001) by PLD. SRO is an excellent template for the heteroepitaxial growth of high-quality ferroelectric perovskites. For thickness below  $\sim 75$  nm (Oh and Park, 2004) (the value also depends upon the growth technique and conditions), SRO can grow in a single crystalline manner, with an atomically flat surface and coherently strained on vicinal STO (001) substrates (Hong *et al.*, 2005). Bulk tetragonal  $\text{PbTiO}_3$  (PTO) has the in-plane lattice parameter  $a = 3.904 \text{ \AA}$  (Lichtensteiger *et al.*, 2005), which perfectly matches the lattice parameter of the cubic STO substrate ( $3.905 \text{ \AA}$ ). Concerning PZT, Vrejoiu *et al.* focused on the PZT 20/80 composition, because it has a room temperature *bulk* in-plane lattice parameter of  $3.935 \text{ \AA}$  (Li *et al.*, 2002a), which is closely matched to that of pseudocubic SRO ( $3.93 \text{ \AA}$ ), and has a rather small misfit to the slightly smaller lattice parameter of the STO substrate. Nevertheless, under such circumstances, it is expected that compressive biaxial strain would build up in the heteroepitaxially grown SRO and PZT 20/80 layers, which may enhance the tetragonality of the PZT 20/80 thin films.

The critical thickness for misfit dislocation formation for  $\text{PbTiO}_3$  epitaxial films grown by PLD directly on  $\text{SrTiO}_3$  (001) crystals was calculated (Stemmer *et al.*, 1995), following the equilibrium theory of MD formation proposed by Matthews and Blakeslee (Matthews, 1975). For dislocations with a Burgers' vector  $\mathbf{b} = [010]$ , the PTO critical thickness at room temperature (where the in-plane lattice mismatch was  $+0.16\%$ ) was estimated to be  $57$  nm. However, at the deposition temperature (i.e.  $600^\circ\text{C}$ ), the lattice mismatch becomes compressive and much larger,  $-1.3\%$  (the biaxial strain due to the lattice mismatch changes from tensile to compressive at about  $200^\circ\text{C}$ ). Therefore, the critical thickness is much smaller, around  $5\text{--}6$  nm at the growth temperature and most of the misfit is thus expected to be relaxed by MD formation at the deposition temperature for the  $87$  nm thick PTO film investigated by Stemmer *et al.* (1995). As a further example, in the case of a  $\text{SrTi}_{0.5}\text{Zr}_{0.5}\text{O}_3$  epitaxial film grown on  $\text{SrTiO}_3$  (001) the misfit is  $-2.5\%$  and Matthews and Blakeslee (MB) theory predicts a critical thickness of  $1.6$  nm ( $\sim$ four unit cells) (Langjahr *et al.*, 1998).

The misfit relaxation by dislocations for  $\text{SrRuO}_3$  grown epitaxially on  $\text{SrTiO}_3$  (001) was studied by Oh and Park (2004). In this case the in-plane lattice mismatch is  $-0.64\%$  at room temperature and, based on the same MB equilibrium theory, the authors estimate that for a  $20$  nm SRO film the misfit will be shared between elastic strain and dislocations and a  $75$  nm SRO film approaches complete relaxation but is still somewhat elastically strained.

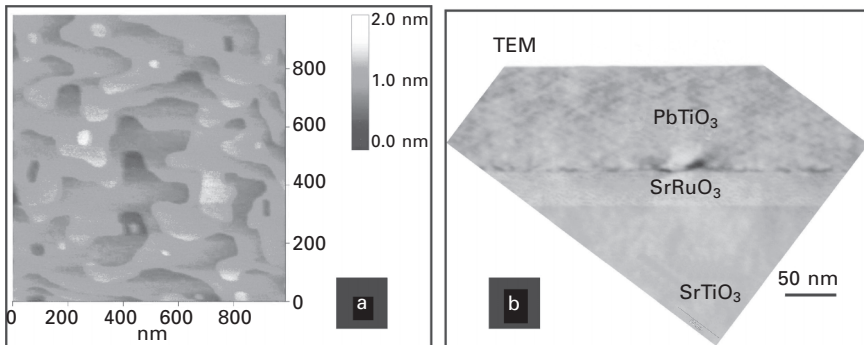
However, we note here that the growth of thin films by PLD is typically a strong non-equilibrium process (Bäuerle, 2000) and therefore the MB

theory may not be entirely valid for this case. Thus films with thicknesses well beyond the predicted critical thickness can be actually grown coherently on dissimilar substrates.

Figure 23.9 shows AFM and TEM investigations performed on a  $\text{PbTiO}_3/\text{SrRuO}_3/\text{SrTiO}_3$  (001) heterostructure grown by PLD by Vrejoiu *et al.* The SRO layer was deposited at  $700^\circ\text{C}$  in 0.14 mbar  $\text{O}_2$  and the  $\text{PbTiO}_3$  (PTO) layer at  $575^\circ\text{C}$  in 0.3 mbar  $\text{O}_2$  (see details about the fabrication of SRO in Vrejoiu *et al.*, 2006b). The AFM image in Fig. 23.9(a) shows that the PTO layer grew in a layer-by-layer regime onto the SRO-coated STO. The TEM cross-section micrograph of such a heterostructure (different sample, with similar thickness of the PTO and SRO layers) (Fig. 23.9b) proved that the  $\sim 100$  nm thick PTO thin film grown on top of an  $\sim 30$  nm thick SRO had very low density of MDs and no threading dislocations or  $90^\circ a-c$  domains (compare with the TEM micrographs shown by Foster *et al.*, 1996b), and it was fully  $c$ -axis oriented and almost coherently grown on STO (001).

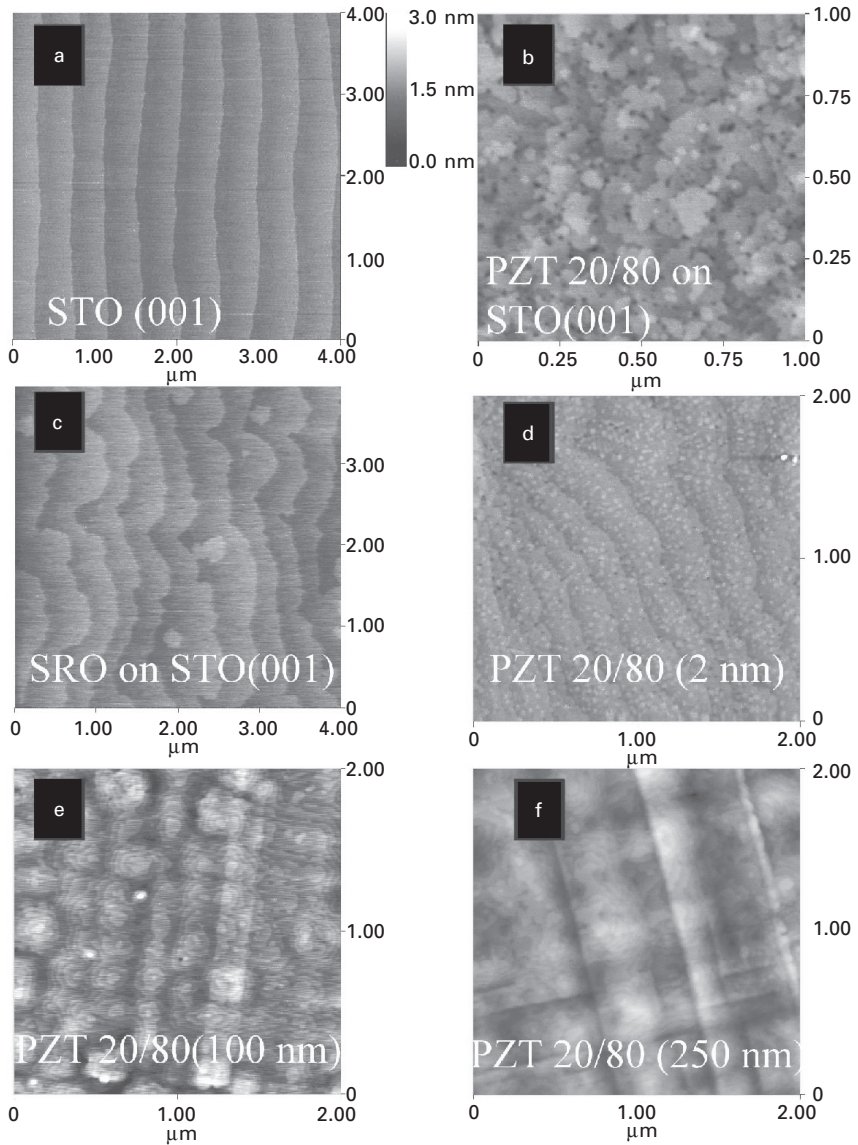
Morita and Cho (2004) reported on a similar  $\text{PbTiO}_3/\text{SrRuO}_3/\text{SrTiO}_3$  (001) heterostructure, synthesized by the hydrothermal method (see also Jung *et al.*, 2005), in which the 100 nm thick  $\text{PbTiO}_3$  film was also fully  $c$ -axis oriented, having no twins. However, a time as long as 24 h was required to grow a 100 nm thick PTO layer by Morita's method, whereas it took only 10–20 min by PLD. In a more recent report, Morita and Cho (2006) mentioned that at the interface between the 100 nm thick hydrothermally synthesized PTO film and the 50 nm thick SRO bottom electrode, a 20 nm thin interface layer that was a mixture between PTO and SRO formed, which is not the case for the sharp interfaces of the PLD-fabricated PTO/SRO/STO (001) heterostructures (Fig. 23.9b).

Figure 23.10 shows detailed AFM investigations performed on top of  $\text{SrRuO}_3/\text{SrTiO}_3$  (001),  $\text{PbZr}_{0.2}\text{Ti}_{0.8}\text{O}_3/\text{SrTiO}_3$  (001) and  $\text{PbZr}_{0.2}\text{Ti}_{0.8}\text{O}_3/\text{SrRuO}_3/$



23.9 (a) AFM image taken on the surface of a layer-by-layer grown  $\text{PbTiO}_3/\text{SrRuO}_3/\text{SrTiO}_3$  (001) heterostructure; (b) a TEM cross-section micrograph, seen from [010] direction, of such a heterostructure, with a 100 nm thick  $\text{PbTiO}_3$  layer and a 30 nm thick  $\text{SrRuO}_3$  layer.

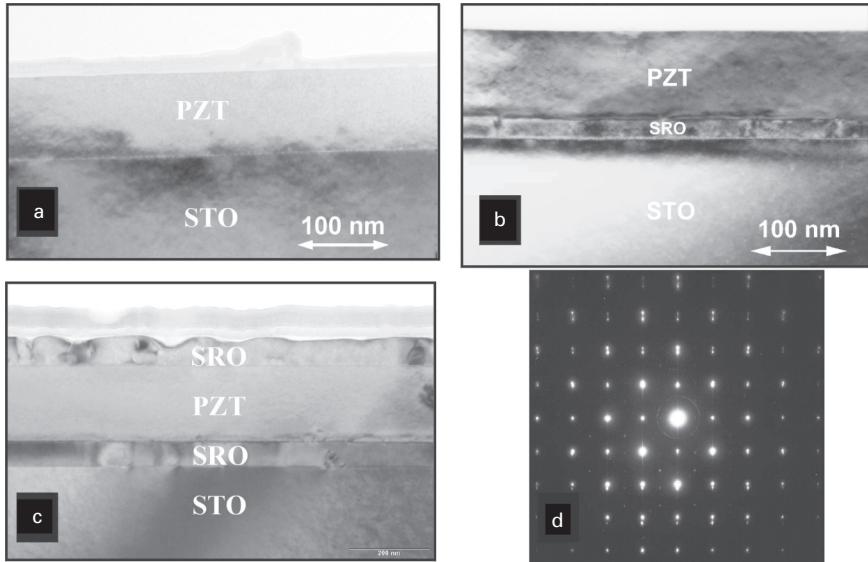




**23.10** AFM images of (a) a vicinal STO (001) substrate with single-unit-cell stepped terraces of uniform  $\text{TiO}_2$  termination; (b) a 100 nm thick PZT 20/80 film grown directly on a vicinal STO substrate; (c) an ~50 nm step-flow grown SRO film on a vicinal STO substrate; (d) an ultrathin PZT 20/80 film (2–3 nm) grown on top of a SRO-coated STO; (e) a PZT 20/80 film (100 nm) grown on top of a SRO-coated STO; (f) a PZT 20/80 film (250 nm) grown on top of a SRO-coated STO.

SrTiO<sub>3</sub> (001) heterostructures grown by PLD by Vrejoiu *et al.* (details about the fabrication procedure are given in Vrejoiu *et al.*, 2006b). Figure 23.10(a) displays the AFM image taken on the surface of a vicinal STO (001) substrate with single-unit-cell stepped terraces formed after etching and annealing. On such a STO (001) substrate, a PZT 20/80 layer (100 nm thick) was deposited in a layer-by-layer regime, as shown in Fig. 23.10(b), for further XRD and reciprocal space mapping (RSM) investigations. For metal–ferroelectric–metal devices, a SRO layer (20–75 nm thick) was deposited on thus prepared vicinal STO (001) substrate in step-flow growth regime, as shown in Fig. 23.10(c) for an ~50 nm thick SRO film. The morphology of the top surface of PbZr<sub>0.2</sub>Ti<sub>0.8</sub>O<sub>3</sub>/SrRuO<sub>3</sub>/SrTiO<sub>3</sub> (001) heterostructures is presented in Fig. 23.10(d)–(f), for PZT 20/80 layers of various thickness, from 2 nm up to 250 nm, grown in a layer-by-layer regime. The 90° grid of traces that one can see in the AFM image of the 250 nm thick film indicates that MDs and 90° domains were formed, which one expected for this rather thick PZT 20/80 film that must have partially relaxed via the formation of MDs and 90° *a*–*c* domains. Such traces were not observed for PZT 20/80 films with thicknesses of up to 100 nm, however.

TEM cross-section investigations of three types of heterostructures based on PZT 20/80 revealed that the PZT 20/80 layers are free from extended structural defects, such as TDs and SFs (unlike the heterostructures presented in Section 23.3.1). Figure 23.11 summarizes TEM micrographs taken on the cross-sections of PbZr<sub>0.2</sub>Ti<sub>0.8</sub>O<sub>3</sub>/SrTiO<sub>3</sub> (001) (Fig. 23.11a), PbZr<sub>0.2</sub>Ti<sub>0.8</sub>O<sub>3</sub>/SrRuO<sub>3</sub>/SrTiO<sub>3</sub> (001) (Fig. 23.11b) and SrRuO<sub>3</sub>/PbZr<sub>0.2</sub>Ti<sub>0.8</sub>O<sub>3</sub>/SrRuO<sub>3</sub>/SrTiO<sub>3</sub> (001) (Fig. 23.11c). The PZT 20/80 layer of the heterostructure given in Fig. 23.11(c) was sandwiched between top and bottom SRO electrodes, the top SRO electrode being epitaxially grown at 575 °C, immediately after finishing the deposition of the PZT layer. Thus the entire SRO/PZT/SRO/STO (001) heterostructure was cooled to room temperature in short-circuit conditions and, although ~200 nm thick, the PZT 20/80 film is fully *c*-axis oriented, with no twin 90° domains (Li *et al.*, 2002b). Electron diffraction patterns (Fig. 23.11d) of the three heterostructures showed that the PZT 20/80 layers are single-crystalline tetragonal, coherently grown with the in-plane lattice parameter *a* matching that of the STO substrate and the out-of-plane lattice parameter *c* undergoing an enlargement, so that a tetragonality ratio *c/a* ≈ 1.07–1.075 resulted. This value of the tetragonality ratio was confirmed by our X-ray diffraction reciprocal space mapping (XRD-RSM) measurements (Ishida *et al.*, 2002; Morioka *et al.*, 2003). Figure 23.12 displays the XRD-RSM measured for the (422) and (303) reflections of a PZT/STO (001) heterostructure with a PZT 20/80 layer of 100–120 nm thickness, whose TEM micrograph is given in Fig. 23.11(a). These XRD-RSM patterns confirmed that the PZT 20/80 film was fully *c*-axis oriented, without *a*–*c* twin domains and only partly relaxed.

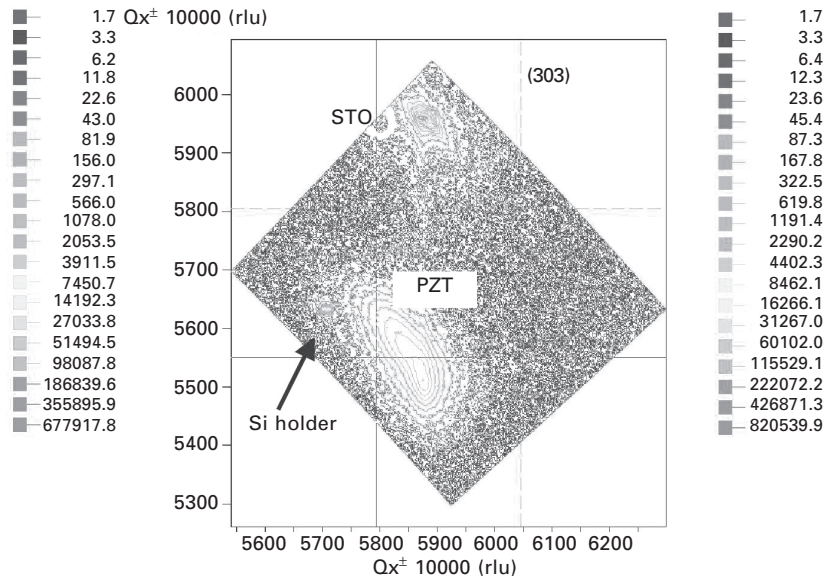
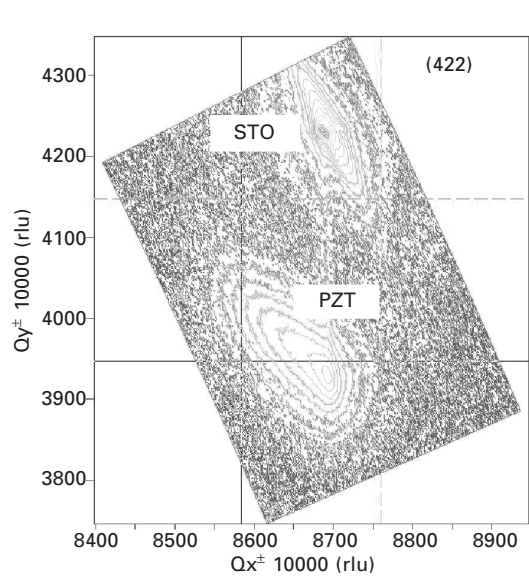


23.11 TEM cross-section micrographs, seen from [010] direction of heterostructures involving defect-free single-crystalline  $\text{PbZr}_{0.2}\text{Ti}_{0.8}\text{O}_3$  thin films: (a)  $\text{PbZr}_{0.2}\text{Ti}_{0.8}\text{O}_3$  on STO (001); (b)  $\text{PbZr}_{0.2}\text{Ti}_{0.8}\text{O}_3$  on  $\text{SrRuO}_3/\text{SrTiO}_3$  (001); (c)  $\text{PbZr}_{0.2}\text{Ti}_{0.8}\text{O}_3$  film sandwiched between epitaxial SRO bottom and top electrodes. The electron diffraction pattern of the heterostructure shown in (b) is given in (d) and was correctly rotated with respect to (b).

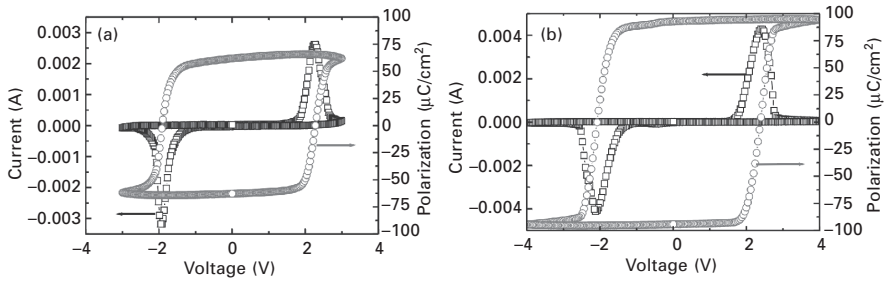
In contrast with the PZT 20/80 layers with high density of structural defects, presented in the previous paragraphs, these PZT 20/80 layers free from threading dislocations and stacking faults were synthesized from a different PZT 20/80 target, purchased from PRAXAIR (Woodinville, WA). Careful optimization of the PLD parameters and the obviously good stoichiometry and density of this PLD target led to the outstanding improvement of the PZT film quality.

### 23.5 Comparison of ferroelectric properties of PZT 20/80 films with and without extended structural defects

In order to determine the ferroelectric and dielectric properties of  $\text{PbZr}_{0.2}\text{Ti}_{0.8}\text{O}_3/\text{SrRuO}_3/\text{SrTiO}_3$  (001) heterostructures, Vrejoiu *et al.* (2006a,b) deposited top electrodes through a shadow mask. First SRO was deposited at room temperature by PLD; subsequently Pt was sputtered to ease the contacting of the individual capacitors. Figure 23.13 compares the polarization and switching current loops measured on two types of PZT 20/80-based heterostructures. We stress that these samples were prepared in the same PLD chamber,



23.12 XRD-RSM measurements performed on a 100 nm  $\text{PbZr}_{0.2}\text{Ti}_{0.8}\text{O}_3$  film grown on STO (001): (422) reflection (left) and (303) reflection (right).



23.13 Polarization and switching current hysteresis loops (as indicated by the arrows) measured on (a) a defective PZT 20/80 film (250 nm thick) and (b) a PZT 20/80 film (215 nm thick) free of extended structural defects, both with  $90^\circ$  *a-c* domains.

employing the same PLD set-up, under similar deposition parameters. The only difference in the synthesis procedure was the use of two different PZT targets, purchased from two vendors, which are of nominally the same composition,  $\text{Pb}_{1.1}\text{Zr}_{0.2}\text{Ti}_{0.8}\text{O}_3$ . Nevertheless, we suspect that the target quality was significantly different, as the target from which the defective films were produced exhibited a dark grey colour, unlike the PRAXAIR target which was light yellow.

Figure 23.13(a) shows polarization and switching current hysteresis curves, measured on a heterostructure whose PZT 20/80 layer of 250 nm thickness was defective (exhibiting TDs, SFs and a high density of  $90^\circ$  domains), and whose TEM and PFM analyses are given in Fig. 23.5 and 23.10, respectively. The remnant polarization of this MFM heterostructure was  $P_r = 65 \pm 10 \mu\text{C}/\text{cm}^2$ . Figure 23.13(b) displays the hysteresis curves measured on a heterostructure with a 215 nm thick PZT 20/80 layer that was free from TDs and had only a low fraction of  $90^\circ$  domains. The remnant polarization of this MFM heterostructure is significantly higher,  $P_r = 95 \pm 10 \mu\text{C}/\text{cm}^2$ , which, to the best of our knowledge, is the highest polarization value reported for PZT 20/80 thin films. We note that the formation of twin *a*-domains did not affect severely the value of the remnant polarization, as both PZT films with and without twins have  $P_r$  in the range 80–100  $\mu\text{C}/\text{cm}^2$ , thus considerably higher than the  $P_r$  of the PZT films with TDs and SFs. The shape of the polarization hysteresis curve is more square-like in the case of the PZT 20/80 layer without dislocations. The reduced value of the polarization that the defective PZT 20/80 layers show correlates with the observation that the  $180^\circ$  domains were pinned by the structural defects, such as the metal-rich SFs, and were undergoing backswitching when analysed by PFM (Vrejoiu *et al.*, 2006a).

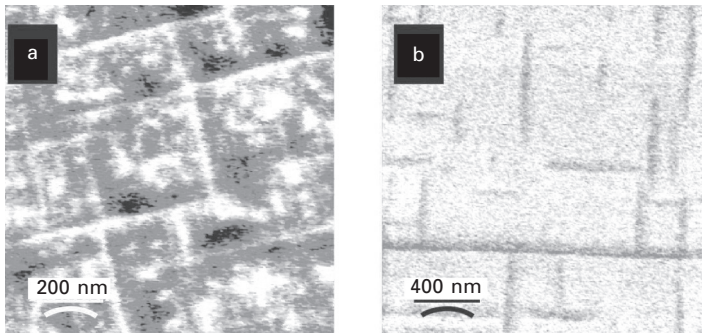
The value of the dielectric constant calculated assuming the plane-parallel capacitor model was also significantly different for the two types of heterostructures, although they have a similar thickness of the ferroelectric

layer and a similar electrode area. At 100 kHz, the defective layer, with high density of TDs and  $90^\circ$  domains, has an effective dielectric constant of about 235. The layer without TDs and SFs, but a minor fraction of  $90^\circ$  domains, has an effective dielectric constant of 170. The higher values of the dielectric constant measured on the defective PZT layers are assumed to arise from extrinsic contributions of extended structural defects and  $a$ - $c$  twin domains to the effective dielectric response of the material (Kim *et al.*, 2005; Li *et al.*, 2005). For the defect-free PZT 20/80 thin films, which do not have  $90^\circ$  domains (films thinner than 100 nm), the dielectric permittivity  $\epsilon_{33}$  calculated from the plane-parallel capacitor model decreases to  $\epsilon_{33} \approx 75$  (Pintilie *et al.*, 2007).

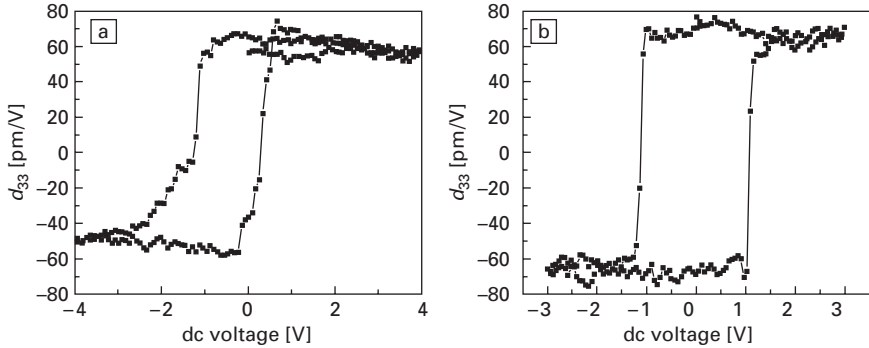
Piezoresponse atomic-force microscopy (PFM) measurements were performed either on the free surface of the epitaxial PZT 20/80 layers or on top of the electrode pads that were employed for macroscopic measurements (Le Rhun *et al.*, 2006; Vrejoiu *et al.*, 2006a,b). Figure 23.14 shows the piezoresponse images taken on the free surface of a defective PZT 20/80 layer (250 nm thick, whose TEM cross-section is displayed in Fig. 23.5(a) and detailed PFM scans are shown in Fig. 23.8) and of a PZT 20/80 layer without TDs and SFs (215 nm thick). The hysteresis loops of the piezoelectric coefficient  $d_{33}$ , acquired on top of Pt/SRO contact pads (50–75  $\mu\text{m}$  in diameter), are given in Fig. 23.15. The piezo-hysteresis loop of the PZT film free from TDs is more squared and saturated (Fig. 23.15b) in comparison with the piezo-hysteresis of the PZT film with TDs and SFs (Fig. 23.15a).

## 23.6 Summary

The incongruent melting of  $\text{PbZrO}_3$  and  $\text{PbTiO}_3$  as well as the high volatility of  $\text{PbO}$  at growth temperatures pose a challenge in establishing the equilibrium



23.14 Piezo-response images taken on the surface of a PZT 20/80 film with threading dislocations (250 nm thick) (a) and on the surface of a PZT 20/80 film (215 nm thick) without threading dislocations (b), both with  $90^\circ$   $a$ - $c$  domains.



23.15 Piezo-coefficient  $d_{33}$  hysteresis loops of a PZT 20/80 film with threading dislocations (250 nm thick) (a) and of a PZT 20/80 film without threading dislocations (215 nm thick) (b), both with  $90^\circ$   $a$ - $c$  domains.

of bulk crystals of PZT. Therefore, large single-domain single crystals of PZT have never been synthesized for a significant compositional range across the solid solution phase. This leaves the intrinsic properties of single domain PZT crystals under debate. Hence, the growth of single crystalline and defect-free PZT thin films may enable the study of fundamental physical properties. For instance, the spontaneous polarization  $P_S$ , which is a fundamental parameter that defines the performance of a ferroelectric material, is rarely reported due to the lack of single crystals and perfectly polar-axis-oriented films. Although the macroscopic polarization is the basic quantity used to describe ferroelectrics, it has long escaped precise microscopic definition. Novel concepts such as polarization as a Berry phase of the electronic Bloch wavefunctions have been recently introduced (Resta, 1997; Sai *et al.*, 2002).

Additionally, accurate investigations of the highly debated issue of size effects in nanostructured ferroelectrics demand the growth of materials free from extended defects, to rule out the extrinsic contribution of defects to the disappearance/suppression of ferroelectricity below a certain critical size.

Epitaxially grown ferroelectric films often exhibit misfit and threading dislocations, twins and anti-phase boundaries that generally have a negative impact on their ferroelectric performance. The existence of threading dislocations and stacking faults in epitaxial PZT 20/80 films was shown to be correlated with the polarization backswitching.

The herein reported single crystalline defect-free PZT 20/80 thin films grown by PLD show excellent ferroelectric performance, with remnant polarization as high as  $P_r \approx 100 \mu\text{C}/\text{cm}^2$  that clearly stems from their high-quality microstructure.

## 23.7 Acknowledgments

The authors are grateful to Drs Nikolai D. Zakharov, Gwenaël Le Rhun, Steffen Schmidt, Lucian Pintilie, Eckhard Pippel, Stephan Senz and Andreas Schubert for their contributions to the characterization of the PZT films and to Professor Ulrich Gösele for fruitful discussions. Partial financial support from Volkswagen Foundation, through the ‘Nanosized ferroelectric hybrids’ project no I/80897, is gratefully acknowledged.

## 23.8 References

- Alpay S P and Roytburd A L (1998), ‘Thermodynamics of polydomain heterostructures. III. Domain stability map’, *J. Appl. Phys.* **83**, 4714–4723.
- Alpay S P, Nagarajan V and Bendersky L A (1999), ‘Effect of the electrode layer on the polydomain structure of epitaxial  $\text{PbZr}_{0.2}\text{Ti}_{0.8}\text{O}_3$  thin films’, *J. Appl. Phys.* **85**, 3271–3277.
- Alpay S P, Misirlioglu I B, Nagarajan V and Ramesh R (2004), ‘Can interface dislocations degrade ferroelectric properties?’, *Appl. Phys. Lett.* **85**, 2044–2047.
- Balzar D, Ramakrishnan P A, Spagnol P, Mani S, Hermann A M and Matin M A (2002), ‘Influence of strains and defects on ferroelectric and dielectric properties of thin-film barium–strontium titanates’, *Jpn. J Appl. Phys.* **41**, 6628–6632.
- Bäuerle D (2000), *Laser Processing and Chemistry*, Berlin, Springer.
- Blank D H A, Rijnders G J H M, Koster G and Rogalla H (1999), ‘*In-situ* monitoring by reflective high energy electron diffraction during pulsed laser deposition’, *Appl. Surf. Sci.* **138–139**, 17–23.
- Canedy C L, Li H, Alpay S P, Salamanca-Riba L, Roytburd A L and Ramesh R (2000), ‘Dielectric properties in heteroepitaxial  $\text{Ba}_{0.6}\text{Sr}_{0.4}\text{TiO}_3$  thin films: effect of internal stresses and dislocation type-defects’, *Appl. Phys. Lett.* **77**, 1695–1698.
- Chrisey D B and Hubler G K (1994), *Pulsed Laser Deposition of Thin Films*, New York, John Wiley & Sons.
- Chu M-W, Szafraniak I, Scholz R, Harnagea C., Hesse D, Alexe M, Gösele U (2004), ‘Impact of misfit dislocations on the polarization instability of epitaxial nanostructured ferroelectric perovskites’, *Nat. Mater.* **3**, 87–90.
- Clarke R and Whatmore R W (1976), ‘The growth and characterization of  $\text{PbZr}_x\text{Ti}_{1-x}\text{O}_3$  single crystals’, *J. Cryst. Growth* **33**, 29–38.
- Clarke R, Whatmore R W and Glazer A M (1976), ‘Growth and characterization of  $\text{PbZr}_x\text{Ti}_{1-x}\text{O}_3$  single crystals’, *Ferroelectrics* **13**, 497–500.
- Dai Z R, Wang Z L, Duan X F and Zhang J (1996), ‘Link-up of  $90^\circ$  domain boundaries with interface dislocations in  $\text{BaTiO}_3/\text{LaAlO}_3$ ’, *Appl. Phys. Lett.* **68**, 3093–3095.
- Emelyanov A Y and Pertsev N A (2003), ‘Abrupt changes and hysteretic behavior of  $90^\circ$  degrees domains in epitaxial ferroelectric thin films with misfit dislocations’, *Phys Rev. B* **68**, 214103.
- Fei Y Y, Zhu X D, Liu L F, Lu H B, Chen Z H and Yang G Z (2004), ‘Oscillations in oblique-incidence optical reflection from a growth surface during layer-by-layer epitaxy’, *Phys. Rev. B* **69**, 2334051–4.
- Fitzgerald E A (1991), ‘Dislocations in strained-layer epitaxy: theory, experiment, and applications’, *Matter. Sci. Rep* **7**, 87–142.
- Foster C M, Pompe W, Daykin A C and Speck J S (1996a), ‘Relative coherency strain and



- phase transformation history in epitaxial ferroelectric thin films', *J. Appl. Phys.* **79**, 1405–1415.
- Foster C M, Bai G-R, Csencsits R, Vetrone J, Jammy R, Willis L A, Carr E and Amano J (1996b), 'Single-crystal  $\text{Pb}(\text{Zr}_x\text{Ti}_{1-x})\text{O}_3$  thin films prepared by metal-organic chemical vapor deposition: systematic compositional variation of electronic and optical properties', *J. Appl. Phys.* **81**, 2349–2357.
- Ganpule S, Nagarajan V, Li H, Ogale A S, Steinhauer D E, Aggarwal S, Williams E, Ramesh R and De Wolf P (2000), 'Role of  $90^\circ$  domains in lead zirconate titanate thin films', *Appl. Phys. Lett.* **77**, 292–294.
- Hau S K, Wong K H, Chan P W, Choy C L and Wong H K (1992), 'Angular distribution of XeCl laser deposition of  $\text{Pb}(\text{Zr}_{0.48}\text{Ti}_{0.52})\text{O}_3$  films', *J. Mater. Sci. Lett.* **11**, 1266–1268.
- Hau S K, Wong K H, Chan P W and Choy C L (1995), 'Intrinsic resputtering in pulsed-laser deposition of lead–zirconate–titanate thin films', *Appl. Phys. Lett.* **66**, 245–247.
- Haun M J, Furman E, Jang S J and Cross L E (1989), 'Thermodynamic theory of the lead–zirconate–titanate solid solution system, part V: theoretical calculations', *Ferroelectrics* **99**, 63–86.
- Heying B, Tarsa E J and Elsass C R (1999), 'Dislocation mediated surface morphology of GaN', *J. Appl. Phys.* **85**, 6470–6476.
- Hong W, Lee H N, Yoon M, Christen H M, Lowndes D H, Suo Z and Zhang Z (2005), 'Persistent step-flow growth of strained films on vicinal substrates', *Phys. Rev. Lett.* **95**, 095501 1–4.
- Hu S Y, Li Y L and Chen L Q (2003), 'Effect of interfacial dislocations on ferroelectric phase stability and domain morphology in a thin film – a phase-field model', *J. Appl. Phys.* **94**, 2542–2547.
- Ishida J, Yamada T, Sawabe A, Okuwada K and Saito K (2002), 'Large remanent polarization and coercive force by 100%  $180^\circ$  domain switching in epitaxial  $\text{Pb}(\text{Zr}_{0.5}\text{Ti}_{0.5})\text{O}_3$  capacitor', *Appl. Phys. Lett.* **80**, 467–469.
- Jung W W, Lee H C, Ahn W S, Ahn S H and Choi S K (2005), 'Switchable single *c*-domain formation in a heteroepitaxial  $\text{PbTiO}_3$  thin film on a (001) Nb-SrTiO<sub>3</sub> substrate fabricated by means of hydrothermal epitaxy', *Appl. Phys. Lett.* **86**, 252901.
- Kaganer V M, Brandt O, Trampert A and Ploog K H (2005), 'X-ray diffraction peak profiles from threading dislocations in GaN epitaxial films', *Phys. Rev. B* **72**, 045423 1–12.
- Kapolnek D, Wu X H, Heying B, Keller S, Keller B P, Mishra U K, DenBaars S P and Speck J S (1995), 'Structural evolution in epitaxial metalorganic chemical vapor deposition grown GaN films on sapphire', *Appl. Phys. Lett.* **67**, 1541–1543.
- Kim Y K, Morioka H, Ueno R, Yokoyama S and Funakubo H (2005), 'Domain structure control of (001)/(100)-oriented epitaxial  $\text{Pb}(\text{Zr},\text{Ti})\text{O}_3$  films grown on (100)<sub>c</sub> SrRuO<sub>3</sub>/(100) SrTiO<sub>3</sub> substrates', *Appl. Phys. Lett.* **86**, 212905.
- Koster G, Rijnders G J H M, Blank D H A and Rogalla H (1999), 'Imposed layer-by-layer growth by pulsed laser interval deposition', *Appl. Phys. Lett.* **74**, 3729–3731.
- Koster G, Rijnders G, Blank D H A and Rogalla H (2000), 'Surface morphology determined by (001) single-crystal SrTiO<sub>3</sub> termination', *Physica C* **339**, 215–230.
- Kukhar V G, Pertsev N A, Kohlstedt H and Waser R (2006), 'Polarization states of polydomain epitaxial  $\text{Pb}(\text{Zr}_{1-x}\text{Ti}_x)\text{O}_3$  thin films and their dielectric properties', *Phys. Rev. B* **73**, 214103 1–9.
- Langjahr P A, Lange F F, Wagner T and Rhüle M (1998), 'Lattice mismatch accommodation in perovskite films on perovskite substrates', *Acta Mater.* **46**, 773–785.

- Lee H N, Christen H M, Chisholm M F, Rouleau C M and Lowndes D H (2005), 'Strong polarization enhancement in asymmetric three-component ferroelectric superlattices', *Nature* **433**, 395–399.
- Le Rhun G, Vrejoiu I, Pintilie L, Hesse D, Alexe M and Gösele U, (2006), 'Increased ferroelastic domain mobility in ferroelectric thin films and its use in nano-patterned capacitors', *Nanotechnology* **17**, 3154–3159.
- Leuchtner R E and Grabowski K S (1994), 'Ferroelectrics', in Chrisey D B and Hubler G K, *Pulsed Laser Deposition of Thin Films*, New York, John Wiley & Sons, 473–508.
- Li Y, Nagarajan V, Aggarwal S, Ramesh R, Salamanca-Riba L G and Martinez-Miranda L J (2002a), 'Depth profile study of ferroelectric  $\text{PbZr}_{0.2}\text{Ti}_{0.8}\text{O}_3$  films', *J. Appl. Phys.* **92**, 6762–6767.
- Li Y L, Hu S Y, Liu Z K and Chen L Q (2002b), 'Effect of electrical boundary conditions on ferroelectric domain structures in thin films', *Appl. Phys. Lett.* **81**, 427–429.
- Li Y L, Hu S Y and Chen L Q (2005), 'Ferroelectric domain morphologies of (001)  $\text{PbZr}_x\text{Ti}_{1-x}\text{O}_3$  epitaxial thin films', *J. Appl. Phys.* **97**, 034112 1–7.
- Lichtensteiger C, Triscone J M-, Junquera J and Ghosez P (2005), 'Ferroelectricity and tetragonality in ultrathin  $\text{PbTiO}_3$  films', *Phys. Rev. Lett.* **94**, 047603.
- Lorenz M, Hochmuth H, Natusch D, Börner H, Thäringen T, Patrikarakos D G, Frey J, Kreher K, Senz S, Kästner G, Hesse D, Steins M and Schmitz W (1997), 'Large-area and double-sided pulsed laser deposition of Y-Ba-Cu-O thin films applied to HTSC microwave devices', *IEEE Trans. Appl. Supercond.* **7**, 1240–1243.
- Lu C J, Bendersky L A, Chang K and Takeuchi I (2003a), 'Dissociation and evolution of threading dislocations in epitaxial  $\text{Ba}_{0.3}\text{Sr}_{0.7}\text{TiO}_3$  thin films grown on (001)  $\text{LaAlO}_3$ ', *J. Appl. Phys.* **93**, 512–521.
- Lu C J, Bendersky L A, Chang K and Takeuchi I (2003b), 'High-resolution identification of  $\frac{1}{2}\langle 110 \rangle$  stacking faults in epitaxial  $\text{Ba}_{0.3}\text{Sr}_{0.7}\text{TiO}_3$  thin films', *Phil. Mag.* **83**, 1565–1586.
- Ma C S, Hau S K, Wong K H, Chan P W and Choy C L (1996), 'The role of ambient gas scattering effect and lead oxide formation in pulsed laser deposition of lead-zirconate-titanate thin films', *Appl. Phys. Lett.* **69**, 2030–2032.
- Matthews J W (1975), *Epitaxial Growth. Part B*, New York Academic Press.
- Miguel M -C and Kardar M (1997), 'Threading dislocation lines in two-sided flux-array decorations', *Phys. Rev. B* **56**, 11903–11906.
- Misirlioglu I B, Vasiliev A L and Alpay S P (2006a), 'Defect microstructures in epitaxial  $\text{PbZr}_{0.2}\text{Ti}_{0.8}\text{O}_3$  films grown on (001)  $\text{SrTiO}_3$  by pulsed laser deposition', *J. Mater. Sci.* **41**, 697–707.
- Misirlioglu I B, Alpay S P, Aindow M and Nagarajan V (2006b), 'Thermodynamic and electrostatic analysis of threading dislocations in epitaxial ferroelectric films', *Appl. Phys. Lett.* **88**, 102906 1–3.
- Morioka H, Asano G, Oikawa T, Funakubo H and Saito K (2003), 'Large remanent polarization of 100% polar-axis-oriented epitaxial  $\text{Pb}(\text{Zr}_{0.35}\text{Ti}_{0.65})\text{O}_3$  thin films', *Appl. Phys. Lett.* **82**, 4761–4763.
- Morita T and Cho Y (2004), 'A hydrothermally deposited epitaxial lead titanate thin film on strontium ruthenium oxide bottom electrode', *Appl. Phys. Lett.* **85**, 2331–2333.
- Morita T and Cho Y (2006), 'Piezoelectric property of an epitaxial lead titanate thin film deposited by the hydrothermal method', *Appl. Phys. Lett.* **88**, 112908.
- Nagarajan V, Jenkins I G, Alpay S P, Li H, Aggarwal S, Salamanca-Riba L, Roytburd A L and Ramesh R (1999), 'Thickness dependence of structural and electrical properties of epitaxial lead zirconate titanate films' *J. Appl. Phys.* **86**, 595–602.

- Nagarajan V, Roytburd A, Stanishevski A, Prasertchoung S, Zhao T, Chen L, Melngailis J, Auciello O and Ramesh R (2003), 'Dynamics of ferroelastic domains in ferroelectric thin films' *Nat. Mater.* **2**, 43–47.
- Nagarajan V, Lia C J, Kohlstedt H, Waser R, Misirlioglu I B, Alpay S P and Ramesh R (2005), 'Misfit dislocations in nanoscale ferroelectric heterostructures', *Appl. Phys. Lett.* **86**, 192910.
- Neave J H, Dobson P J, Joyce B A and Zhang J (1985), 'Reflection high-energy electron diffraction oscillations from vicinal surfaces – a new approach to surface diffusion measurements', *Appl. Phys. Lett.* **47**, 100–102.
- Oh S H and Park C G (2004), 'Misfit strain relaxation by dislocations in SrRuO<sub>3</sub>/SrTiO<sub>3</sub> (001) heteroepitaxy', *J. Appl. Phys.* **95**, 4691–4704.
- Pertsev N A, Kukhar V G, Kohlstedt H and Waser R (2003), 'Phase diagrams and physical properties of single-domain epitaxial Pb(Zr<sub>1-x</sub>Ti<sub>x</sub>)O<sub>3</sub> thin films', *Phys. Rev. B* **67**, 054107 1–10.
- Pignolet A, Curran C, Welke S, Senz S, Alexe M, Hesse D and Gösele U (1996), 'Large area pulsed laser deposition of Aurivillius-type layered perovskite thin films', *Mater. Res. Soc. Symp. Proc.* **433**, 125–130.
- Pintilie L, Vrejoiu I, Hesse D, Le Rhun G and Alexe M (2007), 'Extrinsic contributions to the apparent thickness dependence of the dielectric constant in epitaxial Pb(Zr,Ti)O<sub>3</sub> thin films', *Phys. Rev. B* **75**, 224113, 1–12.
- Queisser H J and Haller E E (1998), 'Defects in semiconductors: some fatal, some vital', *Science* **281**, 945–950.
- Resta R (1997), 'Polarization as a Barry phase', *Europhysics News* **28**, 18–20.
- Roelofs A, Pertsev N A, Waser R, Schlaphof F, Eng L M, Ganpule C, Nagarajan V and Ramesh R (2002), 'Depolarizing-field mediated 180° switching in ferroelectric thin films with 90° domains', *Appl. Phys. Lett.* **80**, 1424–1426.
- Romanov A E, Pompe W, Mathis S, Beltz G E and Speck J S (1999), 'Threading dislocation reduction in strained layers', *J. Appl. Phys.* **85**, 182–192.
- Roytburd A L (1998a), 'Thermodynamics of polydomain heterostructures. I. Effect of macrostresses', *J. Appl. Phys.* **83**, 228–238.
- Roytburd A L (1998b), 'Thermodynamics of polydomain heterostructures. II. Effect of microstresses', *J. Appl. Phys.* **83**, 239–245.
- Roytburd A L, Alpay S A, Bendersky L A, Nagarajan V and Ramesh R (2001), 'Three-domain architecture of stress-free epitaxial ferroelectric films', *J. Appl. Phys.* **89**, 553–556.
- Ryen L, Wang X, Petrov P, Carlsson E, Helmersson U and Olsson E (1999), 'Reduction of density of subgrain boundaries and misfit dislocations in epitaxial (001) SrTiO<sub>3</sub> thin films: effect on dielectric tunability', *J. Appl. Phys.* **85**, 3976–3983.
- Sai N, Rabe K M and Vanderbilt D (2002), 'Theory of structural response to macroscopic electric fields in ferroelectric systems', *Phys. Rev. B* **66**, 104108 1–17.
- Speck J S and Pompe W (1994), 'Domain configurations due to multiple misfit relaxation mechanisms in epitaxial ferroelectric thin films. I. Theory', *J. Appl. Phys.* **76**, 466–476.
- Speck J S, Steifert A, Pompe W and Ramesh R (1994), 'Domain configurations due to multiple misfit relaxation mechanisms in epitaxial ferroelectric thin films. II. Experimental verification and implications', *J. Appl. Phys.* **76**, 477–483.
- Stemmer S, Streiffner S K, Ernst F and Rhüle M (1995), 'Dislocations in PbTiO<sub>3</sub> thin films', *Phys. Stat. Sol. (a)* **147**, 135–154.
- Sun H P, Tian W, Pan X Q, Haeni J H and Schlom D G (2004), 'Evolution of dislocation

- arrays in epitaxial BaTiO<sub>3</sub> thin films grown on (100) SrTiO<sub>3</sub>', *Appl. Phys. Lett.* **84**, 3298–3300.
- Suzuki T, Nishi Y and Fujimoto M (1999), 'Analysis of misfit relaxation in heteroepitaxial BaTiO<sub>3</sub> thin films', *Phil. Mag. A* **79**, 2461–2483.
- Suzuki T, Nishi Y and Fujimoto M (2000), 'Effect of nonstoichiometry on microstructure of epitaxially grown BaTiO<sub>3</sub> thin films', *Jpn. J. Appl. Phys.* **39**, 5970–5976.
- Tarsa E J, Hackfeld E A, Quinlan F T, Speck J S and Eddy M (1996), 'Growth-related stress and surface morphology in homoepitaxial SrTiO<sub>3</sub> films', *Appl. Phys. Lett.* **68**, 490–492.
- van Dyck D (1997), 'High-resolution electron microscopy', in *Electron Microscopy – Principles and Fundamentals*, edited by S. Amelinckx, D van Dyck, J van Landuyt and G van Tendeloo, Weinheim, VCH-Wiley, 125ff.
- Vrejoiu I, Le Rhun G, Zakharov N D, Hesse D, Pintilie L and Alexe M (2006a), 'Threading dislocations in epitaxial ferroelectric PbZr<sub>0.2</sub>Ti<sub>0.8</sub>O<sub>3</sub> films and their effect on polarization backswitching', *Phil. Mag.* **86**, 4477–4486.
- Vrejoiu I, Le Rhun G, Pintilie L, Hesse D, Alexe M and Gösele U (2006b), 'Intrinsic ferroelectric properties of strained tetragonal PbZr<sub>0.2</sub>Ti<sub>0.8</sub>O<sub>3</sub> obtained on layer-by-layer grown, defect-free single-crystalline films', *Adv. Mater.* **18**, 1657–1661.
- Wang H -H, Fleet A, Brock J D, Dale D and Suzuki Y (2004), 'Nearly strain-free heteroepitaxial system for fundamental studies of pulsed-laser deposition: EuTiO<sub>3</sub> on SrTiO<sub>3</sub>', *J. Appl. Phys.* **96**, 5324–5328.
- Willmott P R and Huber J R (2000), 'Pulsed laser vaporisation and deposition', *Rev. Mod. Phys.* **72**, 315–328.
- Wunderlich W, Fujimoto M and Ohsato H (2000), 'Molecular dynamics calculations about misfit dislocations at the BaTiO<sub>3</sub>/SrTiO<sub>3</sub>-interface', *Thin Solid Films* **375**, 9–14.
- Zurbuchen M A, Lettieri J, Fulk S J, Jia Y, Carim A H, Schlom D G and Streiffer S K (2003), 'Bismuth volatility effects on the perfection of SrBi<sub>2</sub>Nb<sub>2</sub>O<sub>9</sub> and SrBi<sub>2</sub>Ta<sub>2</sub>O<sub>9</sub> films', *Appl. Phys. Lett.* **82**, 4711–4713.

## Piezoelectric thick films for MEMS application

---

Z WANG, W ZHU and J MIAO, Nanyang Technological University, Singapore

### 24.1 Introduction

Piezoelectric thick films integrated on silicon substrate have attracted considerable attention in recent years for potential applications in micro-electromechanical systems (MEMS) devices, such as sensors and actuators used in liquid, micro-pumps for micro-fluidic devices, ultrasonic transducers for high-frequency medical imaging, and so on. Although much attention has been paid to prepare thick piezoelectric films on silicon substrate<sup>1-6</sup> in the past decade, integration of high-performance piezoelectric thick films with a uniform thickness of up to 10  $\mu\text{m}$  on a wafer scale, either by deposition or patterning, is still a main challenge in the micromachining of piezoelectric MEMS. This is because piezoelectric films of such thickness are unfortunately located within a technological gap between the processing capabilities of thin film deposition techniques and the machining of bulk ceramics. In addition, the dry etching of  $\text{Pb}(\text{Zr},\text{Ti})\text{O}_3$  (PZT) film is not well developed because there is no common halogenous gas that can form volatile compounds with all three elements (Pb, Zr, Ti) to guarantee the residue-free removal of film.

A composite thick film deposition technique is capable of producing thick films at low temperatures<sup>5-10</sup> compatible with integrated unit (IC) technology. The process is featured at producing composite slurry consisting of a PZT ceramic powder and a PZT-producing sol. The composite slurry is then deposited onto an electroded silicon substrate using a spin-coating process. The added PZT powder can reduce the stress generated within the film during processing and therefore a thick film can be achieved. A final heat treatment as low as 650  $^{\circ}\text{C}$  is sufficient to develop the piezoelectric films. In this chapter, we will first introduce the novel composite route<sup>7-9</sup> to integrate thick PZT films with uniform microstructure on silicon substrate and the corresponding properties of the films; the design concept of piezoelectric micromachined ultrasonic transducer (pMUT) based on thus-prepared thick composite PZT films; and some key issues of the microfabrication process

of pMUTs. Finally, the performances of the fabricated pMUT devices have been presented as an application example of piezoelectric MEMS.

## 24.2 A composite coating process for preparing thick film on silicon wafer

The key technique of the composite coating process is how to prepare uniform slurry by dispersing PZT powder (APC 850 from APC International Ltd) of the desired size into PZT sol–gel precursor solution (Zr/Ti = 53/47). In this section, the slurry preparation and film deposition will be described in detail.

### 24.2.1 Preparation of PZT xerogel and precursor solution

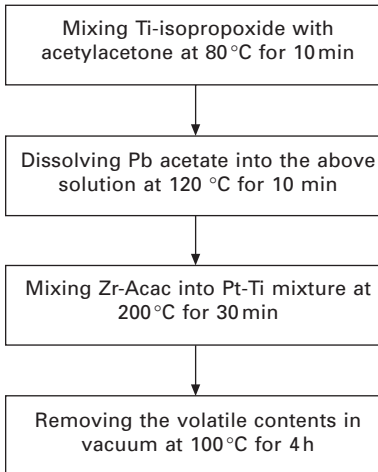
A chelate method<sup>9,11,12</sup> was used to prepare PZT xerogel. This ‘chelate’ method is essentially a molecularly modified alkoxide precursors approach to create moisture tolerant metal–organic precursors by changing the molecular structure of the precursor. The moisture-tolerant precursors created in this way can be used to prepare stable sol and slurry. The raw chemicals used in this process are listed in Table 24.1. Acetylacetone was used as a chelating agent for titanium isopropoxide. The xerogel preparation procedure is schematically shown in Fig. 24.1.

Firstly, the titanium isopropoxide is chelated with acetylacetone in a molar ratio of 1:1 by heating and stirring the mixture at 80 °C for 10 min. Before heating, titanium isopropoxide was slowly dripped into the acetylacetone with a transfer to avoid the effect of moisture. This reaction is an exothermic reaction so that white fumes were observed during stirring. The hydrolysis speed of the modified titanium isopropoxide was greatly reduced after one isopropoxide group was replaced with acetylacetone group. This step was the key process for the xerogel preparation.

Secondly, the lead acetate trihydrate with 10 wt% excess was added into the modified titanium isopropoxide solution. The Ti-Pb mixture was obtained

*Table 24.1* Chemicals and solvents used for preparing PZT xerogel and sol

Chemical	Formula	Molar mass	Purity
Tetraisopropyl titanate	$[(\text{CH}_3)_2\text{CHO}]_4\text{Ti}$	284.22	97%
Zirconium acetylacetonate	$[\text{CH}_3\text{COCH}=\text{C}(\text{O}-)\text{CH}_3]_4\text{Zr}$	487.66	98%
Lead acetate	$(\text{CH}_3\text{COO})_2\text{Pb}\cdot 3\text{H}_2\text{O}$	379.33	>99.5%
Acetylacetone	$\text{CH}_3\text{COCH}_2\text{COCH}_3$	100.12	>99.0%
2-methoxyethanol	$\text{CH}_3\text{OC}_2\text{H}_4\text{OH}$		



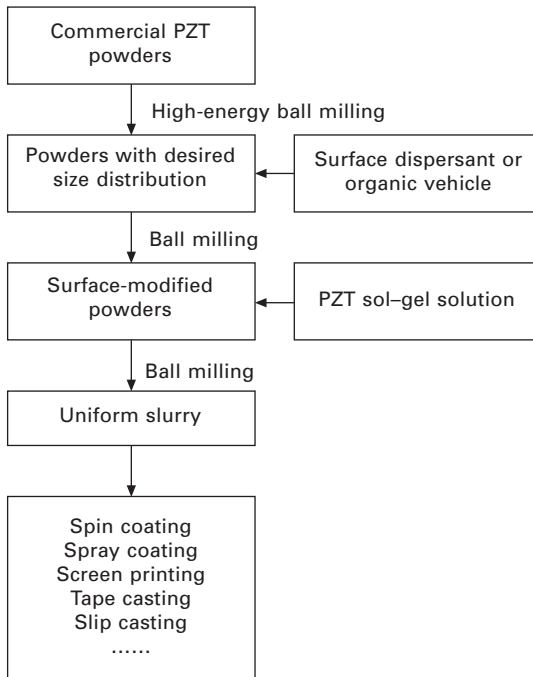
24.1 Flowchart of PZT 53/47 xerogel preparation process using chelating method.

by stirring at 120 °C for 10 mins. After lead acetate trihydrate was added, oil-like coacervation was observed.

Thirdly, the zirconium acetylacetonate was dissolved into the Ti-Pb mixture. By stirring at 200 °C for 30 min, a yellow clear sticky solution was obtained. After that, the sticky solution was placed into a vacuum drying oven to remove volatile products under reduced pressure at 100 °C for more than 4 h. The xerogel, a light yellow coloured powder, can thus be obtained. The xerogel is insensitive to moisture and can be steadily stored for very long time. By dissolving 10–40 wt% xerogel into 2-methoxyethanol solvent, PZT precursor solution can be obtained.

#### 24.2.2 Preparation of uniform slurry

High-energy ball milling is effective in getting well-dispersed slurry.<sup>7–9</sup> The preparation procedure is summarized in Fig. 24.2. First, commercially available PZT powders (APC 850) were high-energy ball milled to get the desired particle size. Secondly, a selected dispersant was added to the milled powders to get the surface-modified powders. The smaller the powder, the more important this procedure. Afterwards, PZT precursor solution was added to these surface-modified powders and mixed by further ball milling. Finally, the resultant uniform slurry was ready for further processing, such as spin coating, tape casting, screen printing and molding. The recipe for the slurry, including the concentration of xerogel solution and powder to solution mass ratio, depends on the further processing method employed. For our convenience, the recipes for the slurry were given four numbers with regard to the above



24.2 Flowchart for preparing uniform slurry.

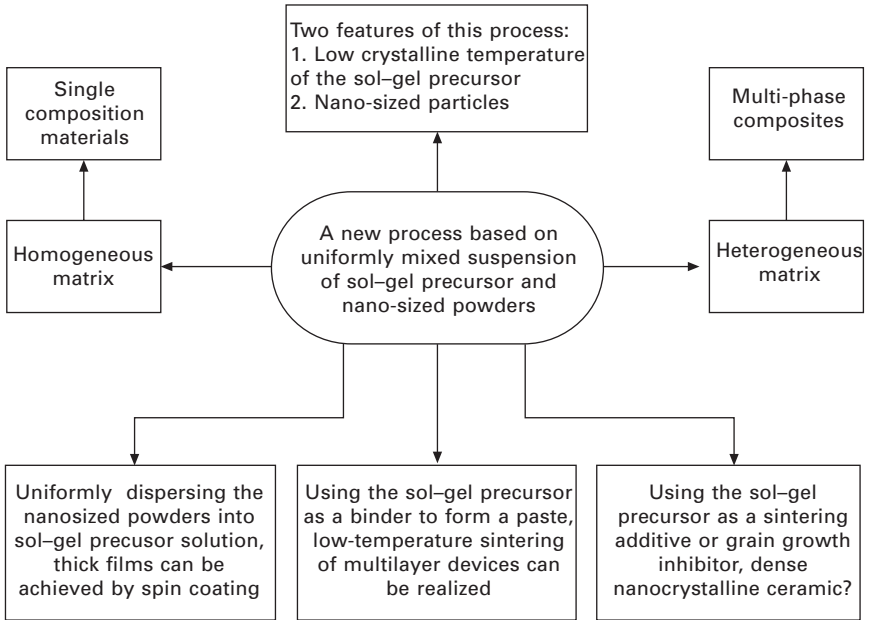
two important parameters. For example, in 3025, the first two numbers represent the concentration of the xerogel solution<sup>9</sup> in weight percent, i.e. 30 wt%, and the last two numbers represent the mass ratio of the added PZT powder to xerogel solution, namely 2 to 5.

### 24.2.3 The features of the composite process <sup>7</sup>

Figure 24.3 outlines the remarkable features of this route. All the features result from the basic characteristic of this technique, i.e. the combination of the sol-gel precursor and powder. If the calcinated sol-gel precursor has the same composition as the powder, we call the mixture a homogeneous matrix; therefore, the resulting material will have single composition. On the other hand, if we mix the precursor solution and powder with different compositions, a multiphase composite will be produced from the heterogeneous matrix. With this method, a uniformly distributed multi-phase composite can be obtained easily.

Moreover, if nanosized powder is used, the matrix should exhibit all the merits of the nanopowder and sol-gel precursor. We can find different applications of this route by utilizing its respective merits. For example, by using the uniformly dispersed nanopowders in the sol-gel solution we could





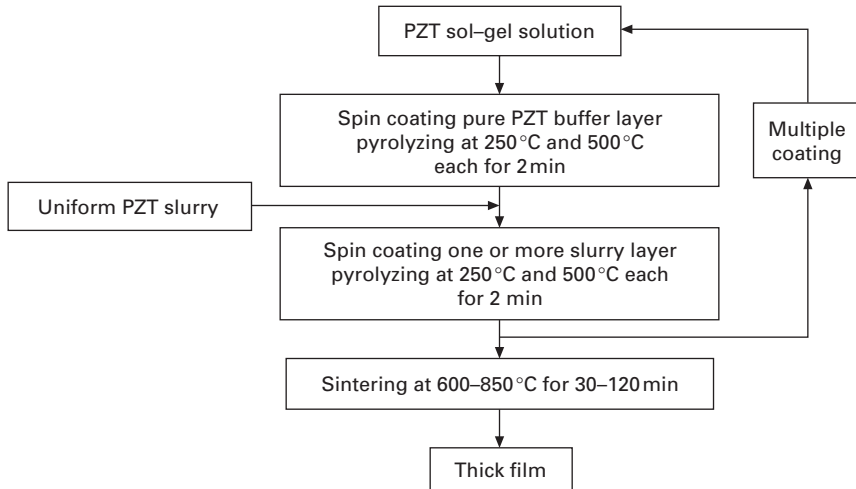
24.3 Illustration of the features of the nanocomposite process.

obtain homogeneous thick films by spin coating. Also, by using the sol-gel precursor as a binder, the density of the green compact can be increased and the sintering temperature of nano-scaled powders can be further reduced. Thus, we can expect low-temperature sintering of the screen-printing films. This unique feature is particularly useful to low-temperature co-firing of a multilayer device because cheap internal electrode paste can be used if this idea can be realized. The simplicity of this approach should make it useful to most ceramic processes. However, in this chapter, we will only report the results of our attempts on spin coating thick films.

#### 24.2.4 Thick film deposition by spin coating

Figure 24.4 shows the flowchart for processing the slurry by spin coating. The pure sol-gel thin films and slurry-derived thick films are deposited alternately. The first layer pure thin film is deposited on the bottom electrode as a buffer layer to enhance the adhesion between the thick film and the substrate. After depositing one or more slurry layers, another pure thin film is deposited subsequently. The intermediate pure sol-gel layers can infiltrate the pore in the slurry layers to increase the film density.

The processing parameters of the composite route include the properties of the powder, the recipe of the slurry and the deposition conditions. The optimized processing parameters have been summarized below.



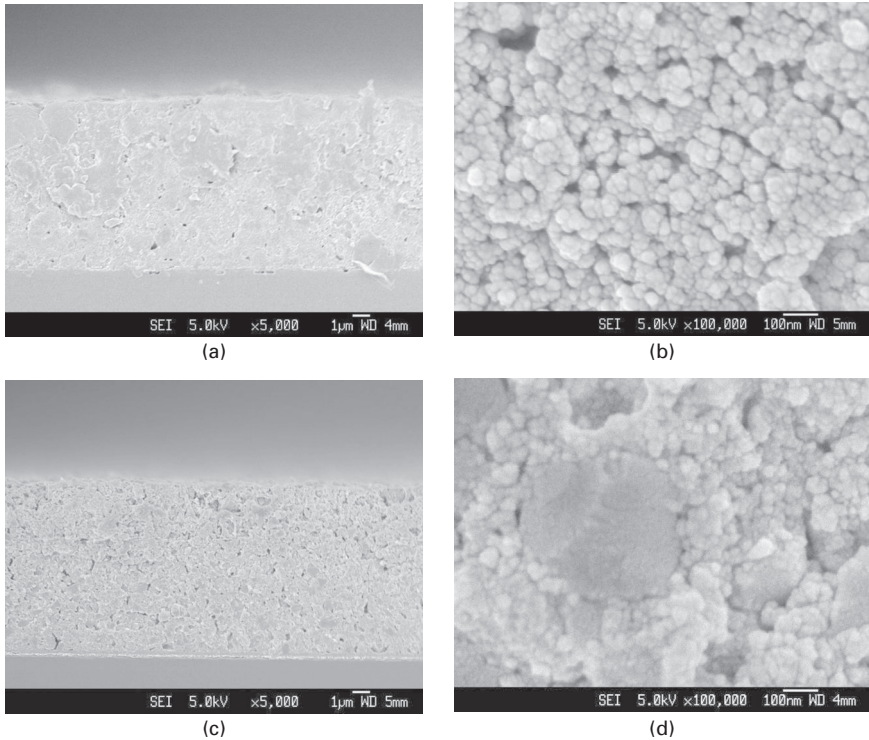
24.4 Flowchart for depositing thick film on silicon wafer by spin coating.

- *Powder properties.* The commercial available powder should be presintered at 1200–1300 °C to improve its crystallinity before being mixed with precursor solution and the powder size should be in the range of 100–300 nm.
- *Slurry recipe.* Concentration of the sol–gel solution: 30 to 40 wt%; powder/solution mass ratio: 2/5 to 2/3; vehicle content: 5 wt%.
- *Deposition procedure.* Deposited at 3000 RPM, preheated at 250 °C and 500 °C on a hot plate, and finally annealed at 650–750 °C for 30 min in a tube furnace.

## 24.3 Characterization of spin-coated thick films

### 24.3.1 Microstructure of the thick film

Since the resultant films are composite and the added powder occupies the majority of the volume fraction, the microstructure of the resultant film is mainly determined by the size of the added powder. Figure 24.5 shows two typical microstructures of the composite films using nano-sized (10–30 nm) and submicrometer-sized (150–300 nm) PZT powder, respectively. The surfaces of both films are sufficiently smooth for device fabrication. Nanocomposite film has relatively dense microstructure in comparison with that of the film prepared with submicrometer-sized powder. Because the aggregation of the nano-sized powder in slurry has been successfully eliminated by using dispersant, the obtained microstructure is quite uniform and dense. From the cross-section image of the film prepared by using nano-sized powders shown



24.5 Cross-section images of two 10  $\mu\text{m}$ -thick composite films: (a) and (b) film 4012 prepared with nano-sized powder; (c) and (d) film 4023 prepared with submicrometre-sized powder.

in Fig. 24.5(b), one can hardly identify the added powders from the sol–gel derived crystallites. However, the added submicrometer-sized powder can be clearly seen from Fig. 24.5(c) and (d). The powder is uniformly distributed in the matrix nano-grains derived from the sol–gel solution. It is because the thick films obviously have the two phases (the added powder and the sol–gel nano-grains) in the microstructure that thick films are called composite films.

From Fig. 24.5(d) we can also see that, for the submicrometer-sized powder, only the sol–gel phase was sufficiently processed or crystallized at the annealing temperature above 600 °C, no substantial grain growth of the added powders occurred during annealing of the film at temperatures below 700 °C. Thus the most important approach to obtain good properties in resultant composite films is presintering the added powder to ensure it has good crystallinity and sufficient size, and thereby will exhibit good ferroelectricity.

A high-quality microstructure can be obtained within a relatively broad range of the slurry recipe. This flexibility much benefits the preparation of the slurry and the adjustment of the single layer thickness. By using this composite route, we can conveniently prepare crack-free composite film in

the thickness range of several micrometers to several ten micrometers within ten spin-coating steps.

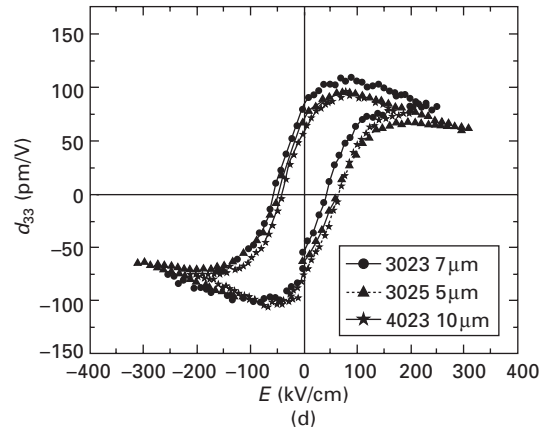
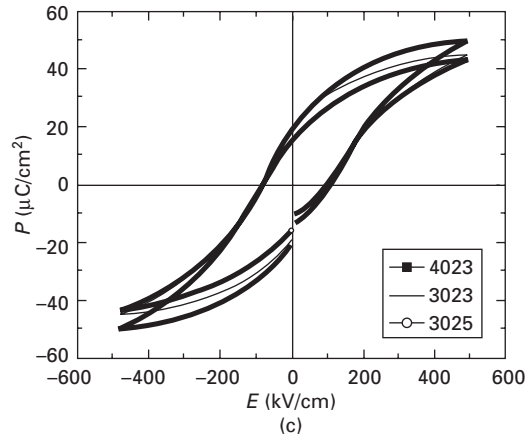
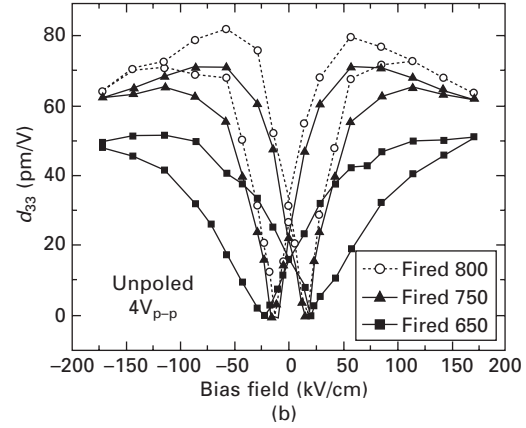
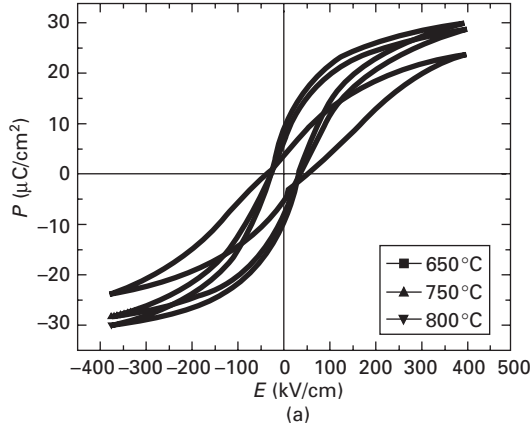
### 24.3.2 Ferroelectric and piezoelectric properties

Figure 24.6 compares  $P$ - $E$  hysteresis curves and effective piezoelectric coefficients of the above-mentioned two composite films. The  $P$ - $E$  hysteresis loops of the composite films were measured using Precision Pro Ferroelectric Analyzer (Radiant Technology Inc.) with a high-voltage interface at 1 kHz. For films prepared with submicrometer-sized powder, the relations between effective longitudinal piezoelectric coefficients ( $d_{33}$ ) of the films and applied dc bias were measured with a home-developed scanning modulated interferometer<sup>13-15</sup>. A 12 V<sub>p-p</sub> alternating current driving signal was applied on the film during measurement. For nanocomposite films, the  $d_{33}$  were measured with a PSV-300 scanning vibrometer.<sup>16,17</sup> A 4 V<sub>p-p</sub> alternating current voltage was applied as a driving signal.

It can be seen from Fig. 24.6 that the average remanent polarization ( $(P_r - (-P_r))/2$ ) of the films prepared with submicrometer-sized powder were 20.0, 18.8 and 15.0  $\mu\text{C}/\text{cm}^2$  for the recipe of 4023, 3023 and 3025, respectively (see Fig. 24.6c), much higher than that (around 7  $\mu\text{C}/\text{cm}^2$ ) of the films prepared with nanocomposite process (see Fig. 24.6a).

Figure 24.6(d) shows the effective  $d_{33}$  of the film at zero bias is around 75 pm/V, and the highest  $d_{33}$  values are around 120 pm/V without considering the clamping effect of the substrate. Note that the films were not poled before the measurement, which implies that the saturated  $d_{33}$  will be higher if the film is well poled. Again, the piezoelectric performances of these films are quite good compared with those of the nanocomposite films shown in Fig. 24.6(b). In that case, the  $d_{33}$  at 0 bias ranged from 20 to 30 pm/V, and the highest  $d_{33}$  at certain bias was around 80 pm/V for films sintered at between 650 and 800 °C.

These results reveal that the piezoelectric and ferroelectric properties of the nanocomposite film are not as good as expected, although the use of the nano-sized powder is of great benefit to the uniformity and density of the PZT film. The film exhibits lower remanent polarization and thus lower piezoelectric coefficient. This is reasonable because too small a grain size in the nanometer range does not allow the grain to split into domains. Using submicrometer-sized PZT powder is an effective way to improve ferroelectric and piezoelectric performances of the composite films. Therefore, we have to compromise between uniformity of the microstructure and the piezoelectric performances of the thick film when selecting the powder size. Considering the comprehensive properties of the films, the submicrometer-sized PZT powder was employed to prepare the slurry for device fabrication.



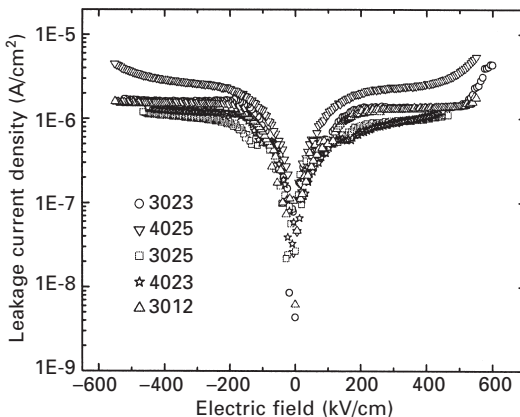
24.6 P-E hysteresis loops and effective piezoelectric coefficients of the composite films: (a) and (b) nanocomposite film 3025 prepared with nano-sized powder sintered at different temperature; (c) and (d) films with different recipe prepared with submicrometer-sized powder sintered at 650 °C.

### 24.3.3 Leakage current density and dielectric properties

The data presented in Fig. 24.7 are dependence of leakage current density on applied field of the films measured with a Precision Pro Ferroelectric Analyzer. The mean leakage current density of the films is around  $2 \times 10^{-6}$  A/cm<sup>2</sup> and the breakdown field is higher than 500 kV/cm for all the investigated recipes. The data also indicate that the driving field of 200 kV/cm, i.e. 20 V/ $\mu$ m, is definitely safe for the composite thick film. Besides, the measured relative permittivity of the films ranges from 600 to 1000 at 1 kHz, and the nanocomposite film has relatively higher permittivity. The dielectric loss is less than 0.02 within the investigated slurry recipe range. These dielectric properties are also quite acceptable for device application.

## 24.4 Piezoelectric micromachined ultrasonic transducer (pMUT) based on thick PZT film

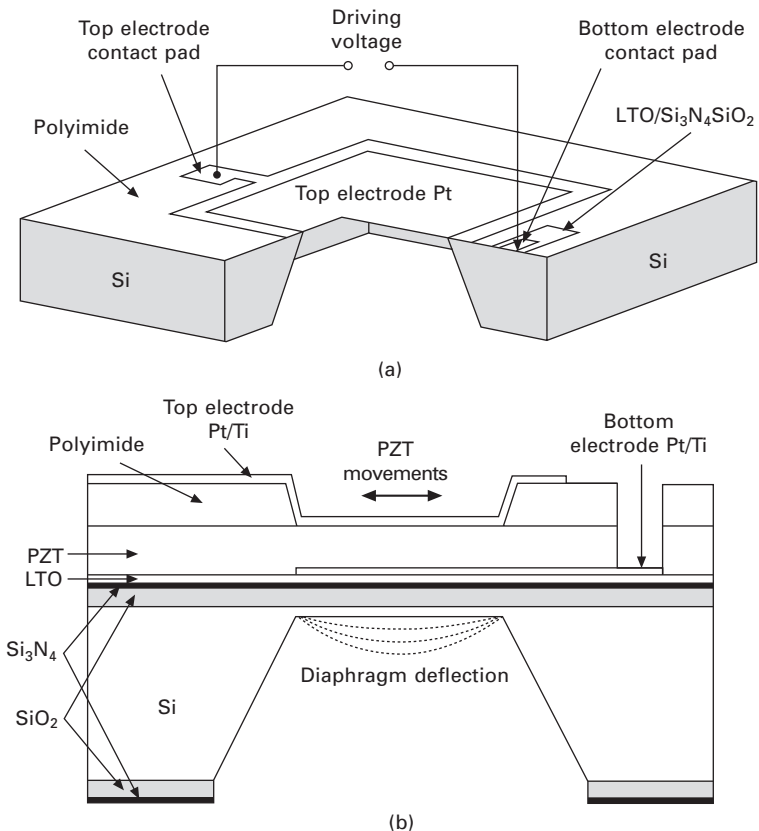
Miniaturized MUTs represent a promising approach to ultrasound detection and generation. They are of particular interest in high-frequency medical imaging systems,<sup>18,19</sup> non-destructive evaluation, underwater exploration<sup>20</sup> and low-frequency airborne ultrasound applications,<sup>21,22</sup> such as vehicle control and object detection for robots. In the diaphragm-type pMUTs, the individual transducer element consists of a micromachined membrane embedded with a PZT film. The PZT film, sandwiched between two electrode layers is poled in the thickness direction and only the transverse mode of  $d_{31}$  is utilized. The laminated inert membrane, which forms the supporting structure layer of the so-called bi-morph structure of PZT/silicon, is necessary to realize the ultrasound reception or transmission. The schematic structure of the pMUT



24.7 Dependence of leakage current density on electric field of the composite films prepared with submicrometer-sized powder.

and its cross-section is sketched in Fig. 24.8. A PZT thick film as the active layer was deposited on Pt/Ti(TiO<sub>2</sub>)/LTO/Si<sub>3</sub>N<sub>4</sub>/SiO<sub>2</sub>/Si wafer. The uppermost layer is Pt/Ti top electrode with an intermediate layer of polyimide as an isolation layer to define the effective top electrode area of an individual transducer element. The descriptions of each layer within the multilayer diaphragm and relevant materials processing steps are listed in Table 24.2.

As shown in Fig. 24.8, a square diaphragm will be fabricated as the active pMUT element when the substrate is anisotropically etched by KOH. For pMUT array operating at high frequency, deep reactive ion etching (DRIE) is preferred for silicon etching. In this case, the shape of the diaphragms is no longer limited to square. Various element shapes, e.g. circular dots and rectangular bars, can be achieved. To simplify electrical interconnection, the top electrode in a pMUT array is designed as the common electrode for all the elements. Only the overlapping part sandwiched between top electrode



24.8 Schematic drawings of a diaphragm-type pMUT: (a) perspective view and (b) cross-section of multilayer structure.

*Table 24.2* Multilayer structure descriptions and materials processing steps in pMUT fabrication

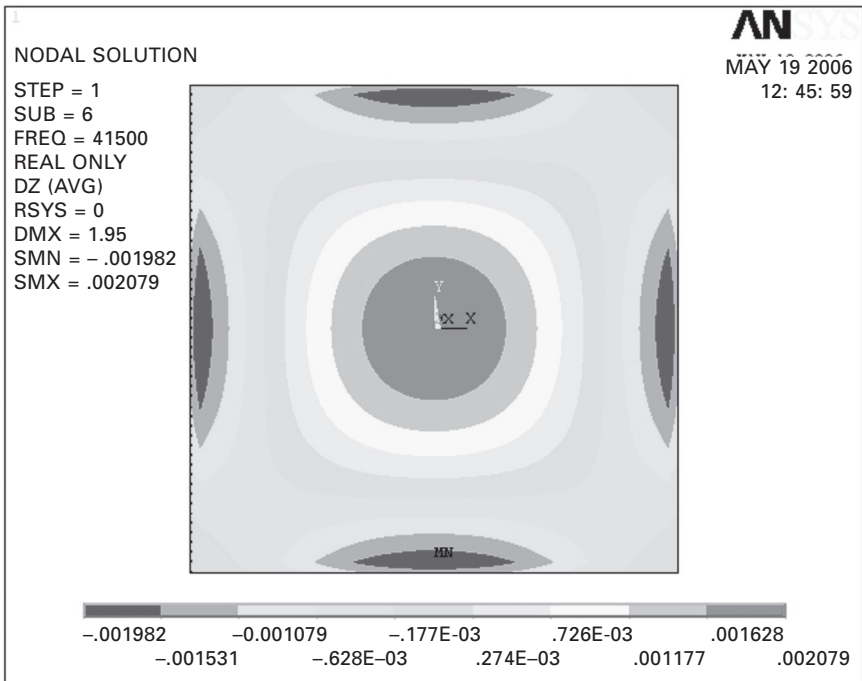
Layer type	Typical composition	Thickness	Purpose of the layer	Fabrication methods and issues
Top electrode	Pt	160 nm	Electrical contact	Sputtering, lift-off
Adhesion layer	Ti	60 nm	To improve adhesion of Pt to PZT	Sputtering, lift-off
Isolation layer	Polyimide	4 μm	To isolate and reduce parasitic capacitance	Spin-coating, open contact holes to bottom electrode
Piezoelectric layer	PZT53/47	2 ~ 20 μm	Active layer	Composite thick film process. Patterning of dense thick PZT film,
Bottom electrode	Pt	200 nm	Electric contact	Lift-off, precise patterning
Adhesion layer	Ti or TiO <sub>2</sub>	20 nm or 100 nm	To prevent delamination of the electrode	Oxidation control: to avoid Ti migration through grain of the electrodes
Support membrane	LTO	350 nm	To avoid crack of PZT films	LPCVD
	Si <sub>3</sub> N <sub>4</sub>	200 nm	Etching mask, stress control	LPCVD
	SiO <sub>2</sub>	1.8 μm	Mechanical support	Dry and wet thermal oxidation
	Si (100)	0–20 μm		Thickness control, SOI wafer

LTO = Low temperature oxide; LPCVD = Low pressure chemical vapor deposition; SOI = silicon on insulator



and patterned bottom electrode can be excited and thus becomes the active part of the transducer element. Piezoelectric response and parasitic capacitance, caused by the overlapping part between the top electrode and patterned leading wire of the bottom electrode, were minimized by using a polyimide layer.

A pMUT can operate either as ultrasonic transmitter or receiver. By applying an ac electric field across the thickness of the PZT film, the induced lateral deformation of the piezoelectric film causes structure vibration; thus generating a pressure sound wave to propagate in the medium in contact. When it is used as a receiver, the multilayer diaphragm turns an input sound pressure into charge generation. Figure 24.9 shows the ANSYS finite element analysis (FEA) result of flux density in response to a uniform pressure of 10 Pa. The result indicates that the induced charge changes its sign at around 70% of its side length of square diaphragm. Therefore, in the pMUT design, the active electrode should not cover the whole area of the diaphragm. Otherwise, the induced charges in the inner part and outer part will be partially neutralized and thus reduce the receiving sensitivity of the pMUT.

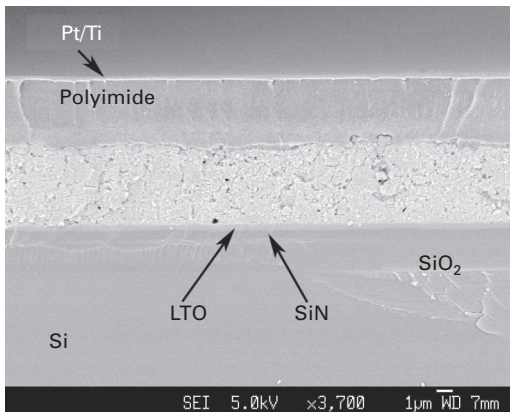


24.9 FEA simulation result of flux density in response to a uniform pressure of 10 Pa, indicating that the induced charge changes its sign at around 70% of its side length of the square diaphragm.

## 24.5 Microfabrication of thick film pMUT

PMUTs were fabricated using standard bulk micromachining fabrication techniques with some minor modifications needed for the PZT thick film deposition.<sup>23</sup> The fabrication processes are depicted with reference to Fig. 24.8(b) and Table 24.2. A layer of  $1.8\text{ }\mu\text{m}$ -thick thermal silicon oxide was first grown on a 4-inch (100mm) double side polished silicon or SOI wafer as supporting structure layer. A LPCVD silicon nitride layer of 200nm and an LTO layer of 350nm were then deposited on both sides of the wafer. The silicon nitride layer is used as the etching mask layer during the KOH wet etching of backside silicon; this layer can be omitted if DRIE is used to etch the silicon. A window on the backside is opened for silicon etching after wet etching of LTO by buffered oxide etch (BOE), dry etching of  $\text{Si}_3\text{N}_4$  and  $\text{SiO}_2$  by RIE using  $\text{CF}_4 + \text{O}_2$ . Backside silicon was anisotropically wet etched by KOH first until the remaining thickness of silicon is reached at about  $50\text{ }\mu\text{m}$ . Ti/Pt or  $\text{TiO}_2/\text{Pt}$  layers of 20 nm/200 nm as bottom electrode are sputtered and patterned by a lift-off process. Thick PZT layer was deposited using the composite thick film deposition technique described in Section 24.2. Wet etching of PZT was performed in diluted HCl : HF solution with a photoresist mask to open a window for the access to the bottom electrode pad. A polyimide layer is spin-coated, patterned and cured as an insulation layer. Ti (20nm)/Pt (200nm) as the top electrode were sputtered and patterned on the front side by lift-off process. After that, the backside silicon was etched off by KOH or DRIE until the required silicon thickness was reached.

Figure 24.10 shows the SEM cross-section image of the multilayer structure on the front side of a fabricated pMUT, where the composite PZT layer is



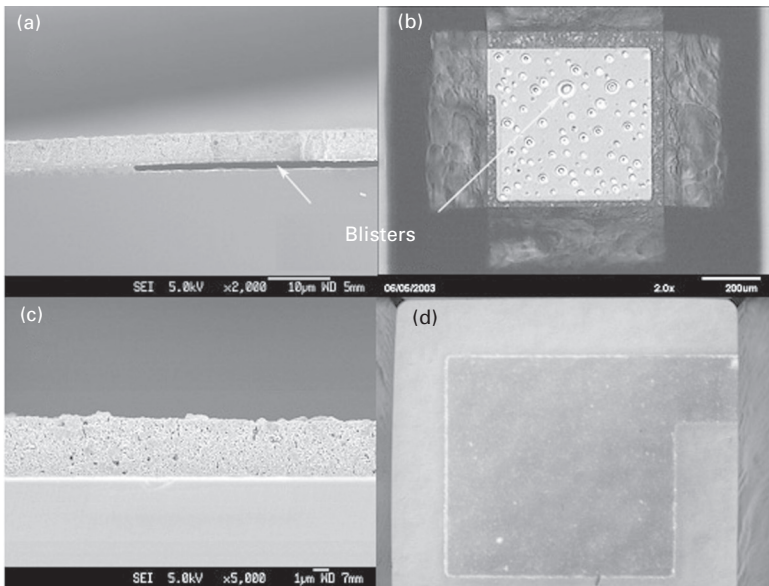
24.10 SEM cross-section image of a multilayer structure fabricated on the front side of the silicon wafer. The dense polyimide layer of around  $4\text{ }\mu\text{m}$  is coated on the  $5\text{ }\mu\text{m}$ -thick composite PZT layer for the protection purpose. The smooth surface of polyimide facilitates the wiring of the top electrode.

about  $5\mu\text{m}$  in thickness. Some important process issues will be further addressed in the following subsections.

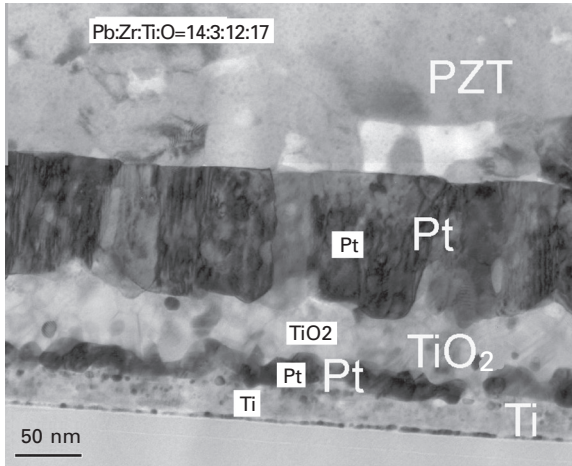
### 24.5.1 Buffer layer of bottom electrode

After the multiple coating steps, the PZT film together with its underlayer structure has to be sintered at relatively higher temperature. Pt/Ti/SiO<sub>2</sub>/Si is usually adopted as the substrate of PZT films. Initially, we also used Ti as the buffer layer of bottom electrode Pt. However, after pMUT fabrication, we found that the Pt/Ti bilayer cannot withstand a high sintering temperature. Blister occurs within the bottom electrode when the sintering temperature exceeds  $700^\circ\text{C}$ .

Figure 24.11(a) and (b) shows the blisters within the Ti/Pt bottom electrode and a pMUT element. The picture of the pMUT was taken through the transparent SiO<sub>2</sub> and Si<sub>3</sub>N<sub>4</sub> layers from the backside. TEM observation of the electrode interface shown in Fig. 24.12 reveals that the possible cause of the blisters can be attributed to the diffusion of the Ti and oxygen into the Pt layer and the formation of TiO<sub>2</sub> in the Pt grain boundaries during high-



24.11 (a) A blister occurs within Pt/Ti bottom electrode due to high annealing temperature at  $700^\circ\text{C}$ . (b) Backside view of a pMUT element shows blisters within Pt/Ti bottom electrode after annealing at  $700^\circ\text{C}$ . (c) Cross-section of a composite film on Pt/TiO<sub>2</sub> bottom electrode sintered at  $800^\circ\text{C}$ . (d) Backside view of a pMUT element with Pt/TiO<sub>2</sub> bottom electrode. No blister occurs after the final annealing of PZT composite film at  $750^\circ\text{C}$ .



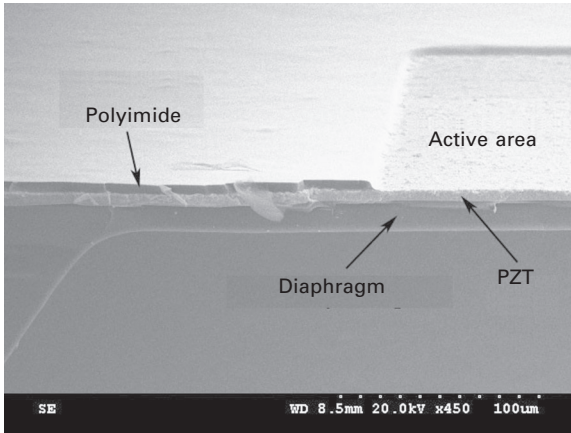
24.12 TEM image shows the formation of  $\text{TiO}_2$  within the Pt layers.

temperature annealing in oxidizing atmosphere. High compressive stress within the  $\text{TiO}_2$  layer results in the occurrence of the blister. Therefore, we attempted incorporating a well-reacted  $\text{TiO}_2$  layer instead of a pure metallic Ti layer as the adhesion layer to avoid the formation of the blister.

The  $\text{TiO}_2$  buffered layer was deposited onto a thermal-oxidized silicon wafer at  $400^\circ\text{C}$  using radio frequency (RF) magnetron sputtering. The 100 nm-thick  $\text{TiO}_2$  layer is reactively sputtered from the titanium target at 500 W and  $1.8 \times 10^{-3}$  mbar with an  $\text{O}_2/\text{Ar}$  ratio of 1:9. The Pt layer is then sputtered at 200 W and  $1.8 \times 10^{-3}$  mbar in argon. Figure 24.11(c) and (d) shows a film cross-section and a square pMUT element with a Pt/ $\text{TiO}_2$  bottom electrode sintered at high temperature. The result reveals that the Pt/ $\text{TiO}_2$  combination significantly improves the heat resistance of the bottom electrode. By employing the Pt/ $\text{TiO}_2$ / $\text{SiO}_2$ /Si substrate, the composite thick films can be finally sintered up to  $800^\circ\text{C}$  without the occurrence of the blister.

### 24.5.2 Polyimide layer

PI2542 wet etch polyimide and PI2771 photosensitive polyimide were used in the pMUT fabrication to protect the PZT films. As mentioned before, the top electrode of the pMUT array is a common electrode of all the elements in the array. The effective top electrode of each element is actually defined by an etch window patterned on polyimide layer. In the window area, the top electrode is directly deposited on PZT film as shown in Fig. 24.13. Since the dielectric constant of polyimide layer is much smaller than that of PZT layer, the induced parasitic capacitance is very small compared with the total capacitance, even if the electric interconnections of top and bottom electrode overlapped each other.

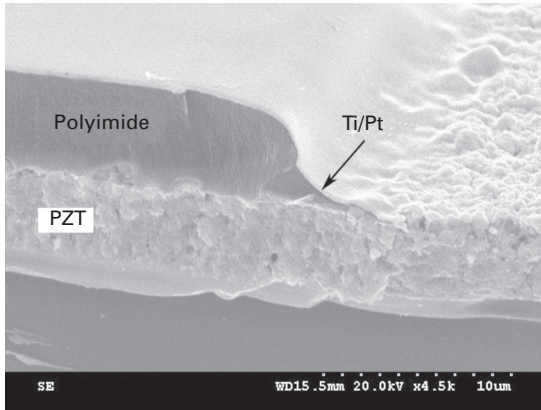


24.13 Top profile image of a fabricated pMUT diaphragm. Backside silicon is wet etched by the KOH. The PZT film is  $5\mu\text{m}$  in thickness and the total thickness of the support layer is  $13\mu\text{m}$ . The effective top electrode area of the element is defined by an opened window on polyimide layer.

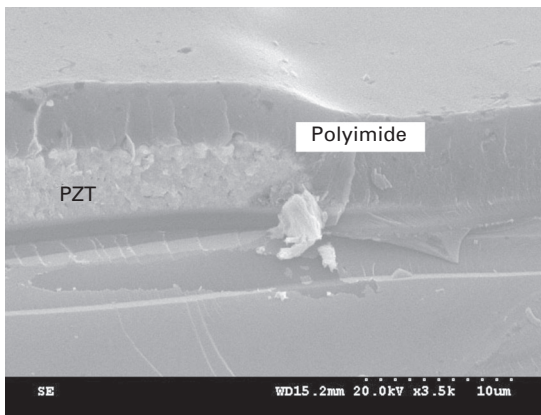
Usually, the PZT film, especially the thin sol-gel film, tends to crack at the edge of the bottom electrode. Electric short-circuit occurs when the patterned top electrode interconnection passes across the edge of the bottom electrode although this part is often designed to be covered by PZT film. Therefore, making a good interconnection between the top electrode and its electric contact pad is one of the challenges in pMUT fabrication. In our design, a polyimide layer is utilized to cover the top of the PZT film at the edge part to overcome this problem. Figure 24.14 shows that the smooth surface and well-curved slope covered at the edge of PZT layer facilitate the interconnection of the top electrode. In addition, the very dense polyimide layer prevents the electric short-circuit at the edge part of the bottom electrode.

### 24.5.3 Etching of the PZT thick film

In general, there are two approaches to micromachine the PZT film: dry etching and wet etching. Reactive ion etching (RIE), inductively coupled plasma (ICP) and electron cyclotron resonance (ECR) excitation, have been reported to etch PZT films. These studies are driven primarily by ferroelectric memory applications, where the film thickness generally does not exceed  $250\text{nm}$ . However, the dry PZT etching technique is not well developed because there is no common halogenous gas that forms a volatile compound with all three elements (Pb, Zr, Ti) to guarantee the residue-free removal of the film. The volatility of the reactive products of individual Pb, Zr and Ti is different. Heating the substrate or increasing the ion bombardment is often



(a)



(b)

24.14 Polyimide layers on the fabricated pMUT facilitate the electric interconnection of the top electrode and reduce the parasitic capacitance. (a) Isolation layer for defining the effective top electrode area. (b) Polyimide protection layer at the device edge.

a way to obtain a uniform etch of PZT layer. It is very difficult to achieve a high etch rate of the PZT with adequate etch selectivity to electrode materials and photoresist mask. As a result, the dry etching technique is too slow to etch thick composite PZT films with thickness up to  $20\mu\text{m}$ . The wet etching of PZT films remains the only good choice for thick PZT etching in our pMUT fabrication.

Since the wet etching process is isotropic, lateral etching cannot be avoided. We define the active pMUT element with patterned bottom electrode together with an open window through polyimide layer to avoid the etching of small lateral PZT patterns. Large ‘V’s are etched on PZT films for the access to bottom electrode bonding pads. Since this bonding pads area is far away

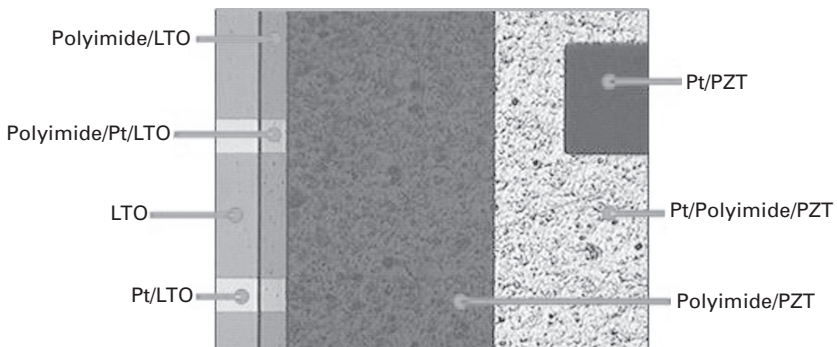
from the active part of the pMUT element, undercutting does not affect the operation of the pMUT.

In our work, 50 ml concentrated HCl (37%), 50 ml water and 0.1 ml HF (48%) were mixed as the etch solution. A 5  $\mu\text{m}$ -thick AZ9260 photoresist was patterned as an etching mask. The etching process was conducted before the final annealing of the composite PZT film because the etching is relatively faster if the PZT film is not fully crystallized. The etch rate at room temperature was about 0.8  $\mu\text{m}/\text{min}$ . The whitish metal-fluoride residues formed on the etch area during PZT film etching were rinsed off by de-ionized (DI) water after every minute of etching. The residue-free etching of PZT film can be achieved in few etch–rinse cycles. Figure 24.15 shows an optical image of a wet etched composite film covered by polyimide layer. It can be seen that the etching edge is neat and straight at this magnification. However, under etching as large as 20  $\mu\text{m}$  and some profile irregularity can be observed, which means small etching patterns less than 40  $\mu\text{m}$  are impossible by using wet etching. Fortunately, for our pMUT design, the achieved wet etching results are good enough at the device edge which is far away from the pMUT diaphragm.

## 24.6 Performances of thick film pMUT

### 24.6.1 Piezoelectric response and simulated properties of the fabricated thick film

As a transducer, the pMUT is supposed to work at around its resonance frequency. Thus the dynamic piezoelectric response of the fabricated pMUT was investigated. The resonance frequency of a multilayer PZT/silicon diaphragm is basically determined by the dimension and the mechanical

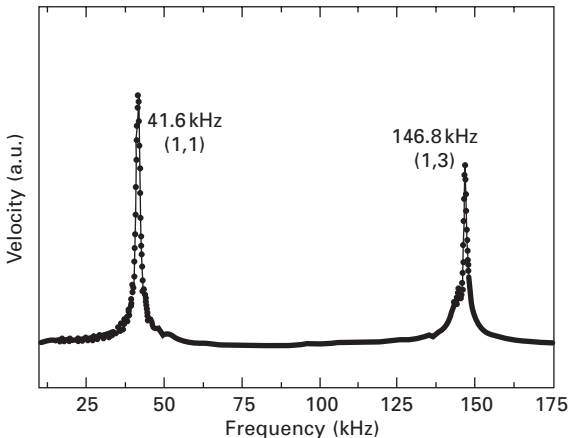


24.15 Optical image of the edge part of a fabricated pMUT element. The wet etched composite film is covered by a transparent polyimide layer. The etching edge of PZT is clear and straight. The area marked with Pt/PZT is the active part of a  $250 \times 250 \mu\text{m}^2$  pMUT element.

properties of the PZT and silicon. As long as the fundamental resonance frequency of the PZT/silicon diaphragm is measured, the mechanical properties of the thick PZT film can be extracted based on the ANSYS modal analysis method.

A fabricated  $2 \times 2 \text{ mm}^2$  pMUT diaphragm was measured and used for FEA. The measured thicknesses of the PZT film and support layer are  $5 \mu\text{m}$  and  $13 \mu\text{m}$ , respectively, as shown in Fig. 24.13. An external ac electric field with sweeping frequency was used to excite the vibration of the pMUT and the vibration velocity at the central point was recorded as the function of the frequency. Figure 24.16 shows the measured velocity response by using a Polytec PSV300 scanning laser vibrometer. Only two vibration modes at 41.6 kHz (fundamental mode) and 146.8 kHz (sixth mode) were detected. Assuming the density and Poisson's ratio of the PZT film are  $7500 \text{ kg/m}^3$  and 0.25, respectively, the Young's modulus of the film was determined as 75.2 GPa when the simulated fundamental resonance frequency equals 41.6 kHz. The bulk silicon material properties used for the simulation and the estimated mechanical properties of the thick composite film are listed in Table 24.3. In the FEA simulation, the influence of the thin electrode and  $\text{SiO}_2$  layers was ignored.

After determining the mechanical properties of the composite PZT film, we further estimated the piezoelectric stress coefficient of the film based on its quasi-static piezoelectric response. Figure 24.17 shows the quasi-static piezoelectric displacement at the center of the same pMUT element driven by a sine wave voltage of 500 Hz, which is much lower than its resonance frequency. The bias dc voltage is 20 V and the peak-to-peak driving voltage

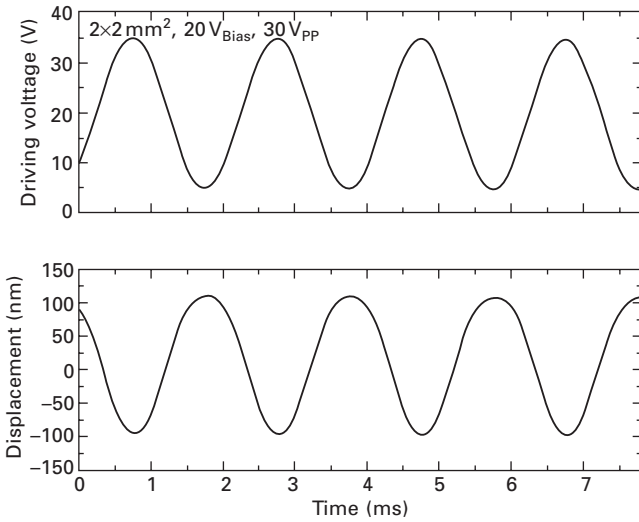


24.16 Frequency response of vibration velocity at central point of a square  $2 \text{ mm} \times 2 \text{ mm}$  diaphragm driven by  $5 \mu\text{m}$ -thick PZT film. About  $13 \mu\text{m}$ -thick support layer was left after DRIE.



Table 24.3 Estimated mechanical properties of PZT film from mode analysis and material properties of silicon used in simulation

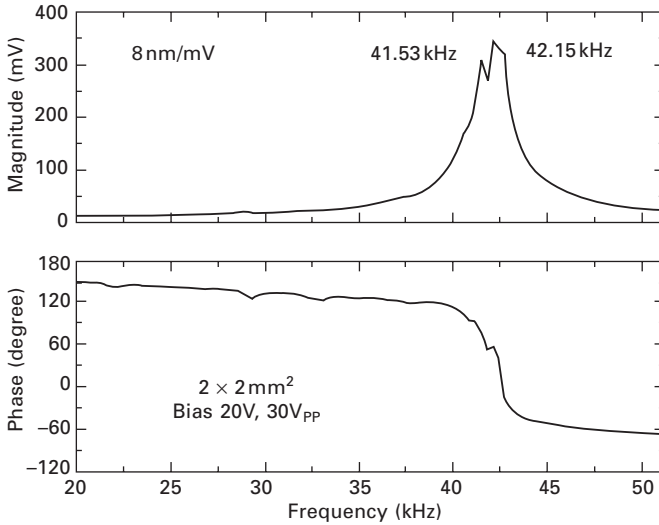
Materials	Young's modulus (GPa)	Poisson's ratio	Density (kg/m <sup>3</sup> )
PZT	75.2	0.25	7500
Silicon	150	0.17	2330



24.17 Quasi-static piezoelectric center displacement of the  $2 \times 2 \text{ mm}^2$  diaphragm measured at 500 Hz for estimation of piezoelectric properties of the thick PZT film.

is 30 V, resulting in a peak-to-peak center displacement of the PZT/silicon diaphragm at about 200 nm, corresponding to a quasi-static piezoelectric center displacement/voltage sensitivity of 6.67 nm/V. This deflection/voltage sensitivity was then used to estimate the piezoelectric stress coefficients of the composite PZT films. The other materials properties determined by model analysis shown in Table 24.3 remained unchanged during simulation. The obtained piezoelectric coefficients  $e_{31}$  and  $e_{33}$  of the composite PZT film were  $-14.8$  and  $18.8 \text{ C/m}^2$ , respectively, quite close to those of the bulk PZT ceramics. The good piezoelectric properties are attributable to the applied dc bias voltage.

Figure 24.18 shows the displacement magnitude/phase-frequency properties of the same pMUT around the fundamental resonance frequency. During the measurement, a dc bias of 20 V was applied to ensure the film has sufficient polarization. A 30 V peak-to-peak ac voltage was superimposed on the dc bias as a driving voltage. It is seen that in the vicinity of the resonance



24.18 Frequency spectra of magnitude/phase of the  $2 \times 2 \text{ mm}^2$  diaphragm at around fundamental resonance frequency.

frequency, the deflection amplitude of the central point of the diaphragm reaches about  $2.8 \mu\text{m}$ , and the phase shifts about  $180^\circ$ . The fundamental vibration mode is the interested mode which can be utilized as both ultrasound transmitters and receivers.

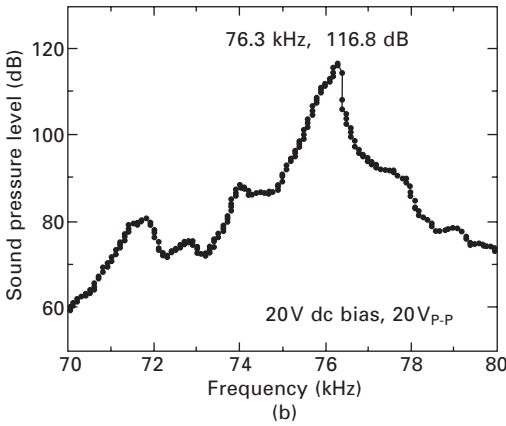
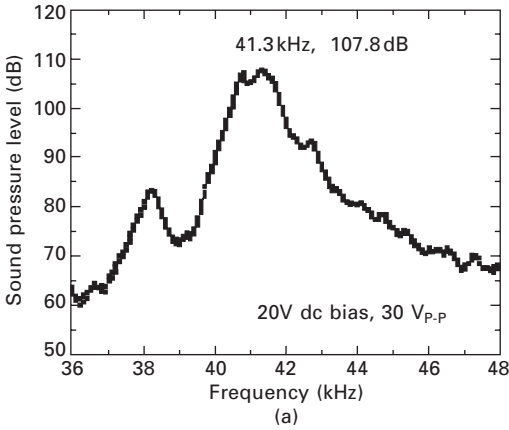
#### 24.6.2 Output sound pressure level<sup>23,24</sup>

The performance of the pMUT as an ultrasound transmitter can be evaluated by output sound pressure level (*SPL*), which is expressed by

$$\text{SPL} = 20 \log \left( \frac{P_{\text{rms}}}{P_{\text{ref}}} \right) \quad 24.1$$

where  $P_{\text{rms}}$  is the output sound pressure at the measuring point which should be far away from the transmitter,  $P_{\text{ref}}$  is reference sound pressure and equals  $2 \times 10^{-5} \text{ Pa}$ .

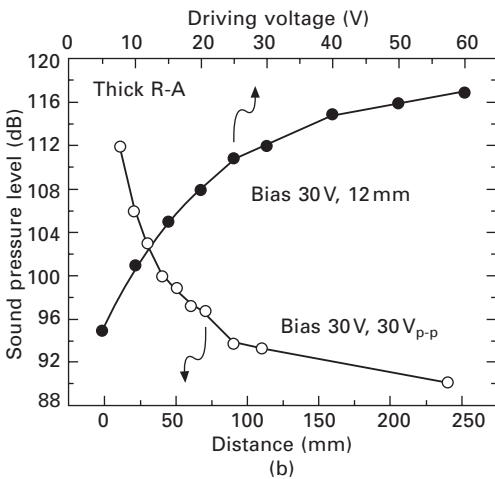
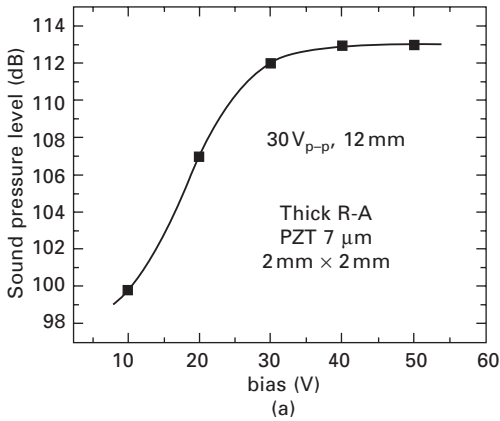
The continuous ultrasound wave emitted by the transmitter is measured in air with Brüel and Kjær 2825 test system, including a 7521 signal analyzer interface module, 3016 input module, and 2670 microphone. The highest frequency of the system can reach 100 kHz. The output SPL of the same transmitter as shown in Fig. 24.18 is measured at the same driving conditions. Figure 24.19(a) shows the test result. The distance between the transmitter and the microphone is 12 mm. In comparison with Fig. 24.18, Fig. 24.19(a) indicates that the output SPL of a pMUT also reaches its maximum at the resonance frequency. The output SPL is 107.8 dB at 41.3 kHz. Among the



24.19 Frequency dependence of output sound pressure level of pMUTs with different diaphragm sizes: (a)  $2\text{ mm} \times 2\text{ mm}$ , (b)  $1.5\text{ mm} \times 1.5\text{ mm}$ .

fabricated pMUTs, the highest SPL obtained is around 120 dB at a distance of 12 mm. Figure 24.19(b) shows another example. The SPL is 116.8 dB at 76.3 kHz for a square pMUT element with side length of 1.5 mm. As an ultrasonic transmitter, this output SPL is quite good.

We also investigated the effect of the dc bias, the driving voltage and the measuring distance on the output SPL and resonance frequency of a pMUT with  $7\text{ }\mu\text{m}$ -thick composite PZT layer. Figure 24.20 shows the results. The output SPL increases with the increase of the applied dc bias and saturated at certain dc bias level (30 V as shown in Fig. 24.20a) at which the polarization of the film approaches saturation. Figure 24.20(b) shows that the output SPL increases with the driving voltage and decreases with the increase of the measuring distance.



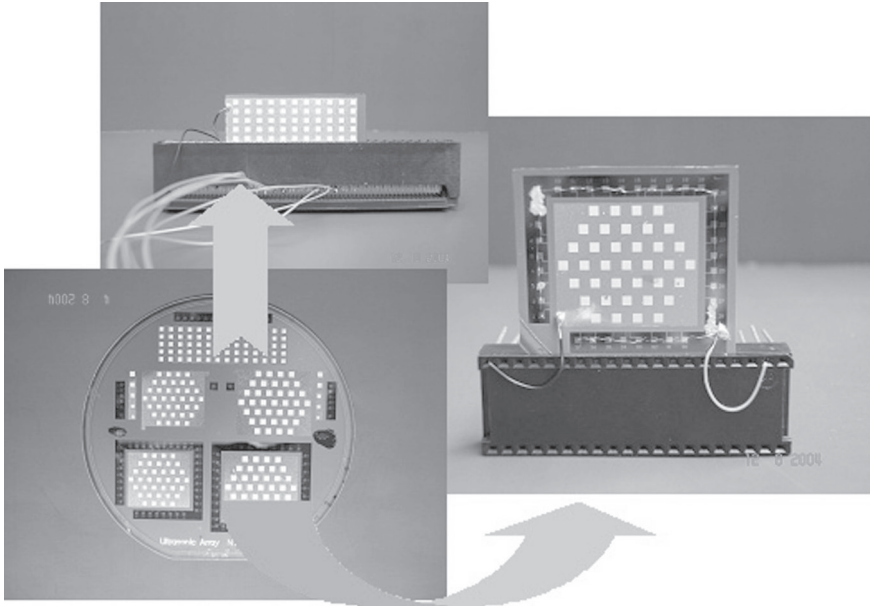
24.20 Output sound pressure level at resonance frequency versus (a) dc bias (at driving voltage of 30 V<sub>p-p</sub>), (b) peak to peak driving voltage (at dc bias of 30V) and distance between measuring point and transmitter (bias 30V, 30 V<sub>p-p</sub>).

### 24.6.3 Directivity of 2D pMUT array<sup>25</sup>

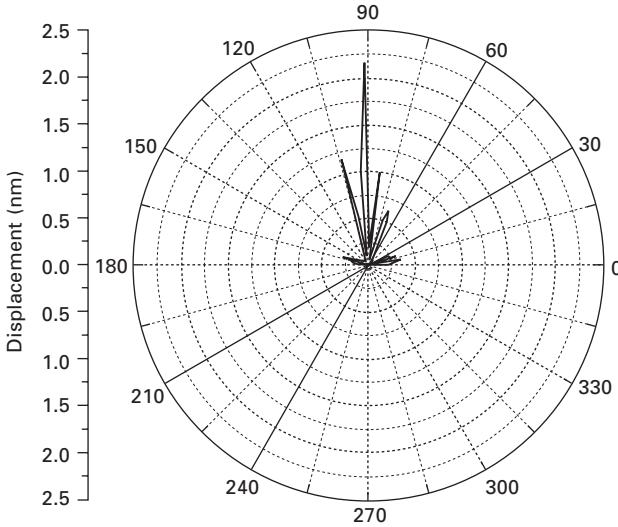
The pMUT array has potential applications in object detection and environmental recognition, either at low ultrasonic frequency in air or at high frequency in liquid medium or human body. In the design of pMUT array for these applications, the number of elements in the array has to be increased to meet the requirement of the resolution and signal to noise ratio. As a result, the whole array will occupy a large area on the silicon wafer. In this case, it would be increasingly difficult to maintain uniform thickness of the diaphragm throughout a whole array by wet silicon etching. This problem can be solved by making use of SOI wafers and DRIE etching since the

etching will stop automatically at the  $\text{SiO}_2$  layer and the diaphragm thickness will be determined by the device layer of the SOI wafer. This can ensure a very uniform diaphragm thickness over the whole wafer, resulting in a uniform resonance frequency of the individual elements of pMUT array. Figure 24.21 shows fabricated pMUT arrays on a 4-inch (100 mm) SOI wafer for ultrasound beam forming and beam steering applications. The individual devices were separated by wafer dicing and electrically connected by wire bonding.

We investigated the directivity of the ultrasound beam emitted by the pMUT array at resonance frequency. The tested array consists of 37 elements with a size of  $1.5 \times 1.5 \text{ mm}^2$ . An ac driving voltage of  $10 \text{ V}_{\text{p-p}}$  superimposed on a dc bias of  $30 \text{ V}$  is applied across the  $6 \mu\text{m}$ -thick piezoelectric layer. The support silicon layer is  $40 \mu\text{m}$  thick. The array surface is rotated from  $-90^\circ$  to  $+90^\circ$  with respect to the normal direction of an acousto-optic sensor. The displacement output of the sensor in response to the radiated ultrasound from the array was recorded at every rotation step of  $1^\circ$  and was utilized as the measure of sound pressure. The ultrasound radiation pattern of the array measured at its resonant frequency of  $160 \text{ kHz}$  is shown in Fig. 24.22. It can be seen that the main lobe is very sharp and tall, which reveals that the fabricated transmitter array can be employed in beam forming and beam steering applications.



24.21 Piezoelectric ultrasonic transmitter arrays fabricated on a 4-inch (100 mm) silicon wafer and a separate array device after wafer dicing and wire bonding.



24.22 The directivity pattern of a pMUT array fabricated with SOI wafer and measured by using a diaphragm type acousto-optic sensor.

#### 24.6.4 Electromechanical coupling coefficient

The effective electromechanical coupling coefficient  $k^2$  of pMUT is defined as

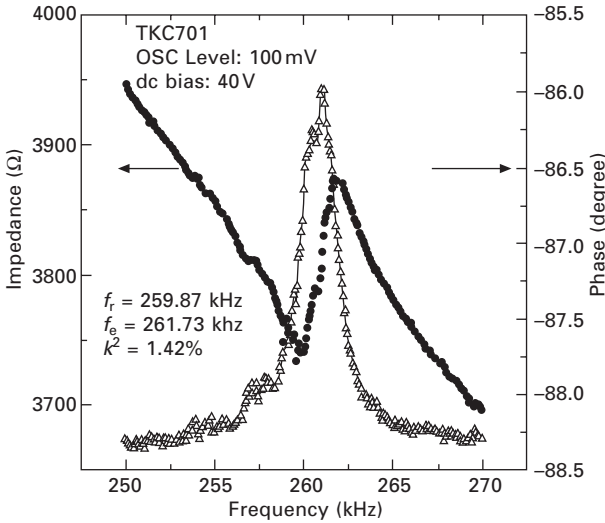
$$k^2 = 1 - (f_r/f_a)^2 \quad 24.2$$

where  $f_r$  means the resonance frequency and  $f_a$  the anti-resonance frequency in an impedance frequency spectrum, respectively.

Figure 24.23 shows the measurement results of the impedance and phase frequency spectrum for a  $0.5 \times 0.5 \text{ mm}^2$  pMUT element with a  $7 \mu\text{m}$ -thick PZT film and  $10 \mu\text{m}$ -thick support layer. The impedance frequency spectrum of the pMUT was characterized using an Agilent 4294A Precision Impedance Analyzer. The measured  $f_r$  and  $f_a$  are 259.87 and 261.73 kHz, respectively, resulting in a coupling coefficient of 1.42% as calculated according to equation (24.2). The measured value is similar to that of a diaphragm prepared with sol-gel PZT film.<sup>26</sup> With optimum thicknesses of PZT and silicon in the diaphragm, a better coupling coefficient can be expected by using our thick composite PZT film.

#### 24.6.5 Equivalent circuit parameters of the pMUT

The  $Q$  factor of the pMUT can be determined by the real part of the impedance frequency spectrum, which is defined as  $Q = f_r/\Delta f$ , where the resonance frequency  $f_r$  is the frequency at which the real part of the impedance reaches its maximum,  $\Delta f$  is the width of the peak at its half height, so-called 3 dB



24.23 Measurement results impedance frequency spectrum of a pMUT element with a diaphragm size of  $0.5 \times 0.5 \text{ mm}^2$  of  $7 \mu\text{m}$ -thick PZT and  $10 \mu\text{m}$ -thick support layer.

bandwidth. Figure 24.24 shows the real part of the impedance frequency spectrum of the pMUT as shown in Fig. 24.23. The measurement data was fitted using the Lorentz function. The fitted parameters  $f_r$  and  $\Delta f$  were used to estimate the  $Q$  value. The estimated  $Q$  value is about 110.

The equivalent circuit of the pMUT element can be modeled as shown in Fig. 24.25. The static capacitance  $C_0$  of the pMUT is around 200 pF measured with HP4284 LCR meter at 1 kHz. Based on the measurement results of the coupling coefficient  $k$  and the  $Q$  value, the dynamic equivalent circuit parameters of the pMUT can be calculated as  $C_1 = 2.88 \text{ pF}$ ,  $R_1 = 1926 \Omega$  and  $L_1 = 0.1293 \text{ H}$ , according to the equations listed below.

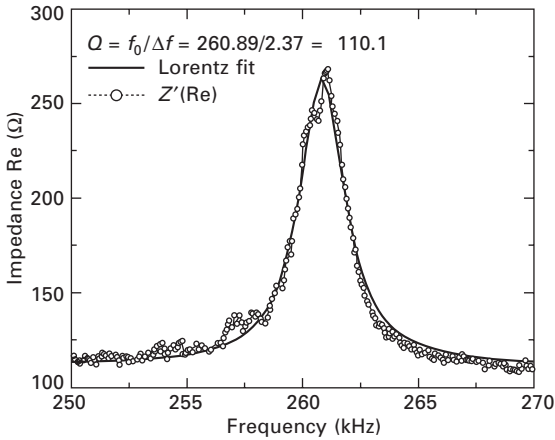
$$k^2 = \frac{C_1}{C_0 + C_1} \Rightarrow C_1 = C_0 \frac{k^2}{1 - k^2} \quad 24.3$$

$$f_r = \frac{1}{2\pi\sqrt{L_1 C_1}} \Rightarrow L_1 = \frac{1}{(2\pi f_r)^2 C_1} \quad 24.4$$

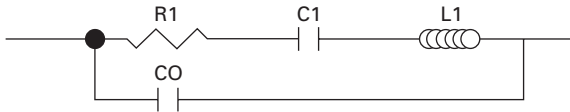
$$Q = \frac{2\pi f_r L_1}{R_1} \Rightarrow L_1 = \frac{2\pi f_r L_1}{Q} \quad 24.5$$

### 24.6.6 Size dependence of resonance frequency<sup>24</sup>

The relationship between the resonance frequency of the diaphragm and its size was investigated by employing the pMUT prepared with nanocomposite PZT film. Three contiguous square diaphragms with respective side lengths



24.24 Measured real part of the impedance frequency spectrum of the pMUTs element with a diaphragm size of  $0.5 \times 0.5 \text{ mm}^2$  of  $7 \text{ }\mu\text{m}$ -thick PZT layer and  $10 \text{ }\mu\text{m}$ -thick silicon, fitted with Lorentz function for calculation of the  $Q$  value.



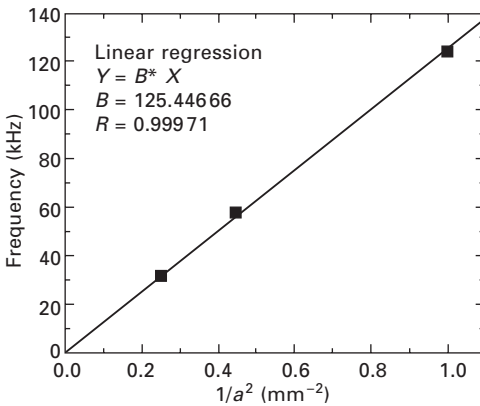
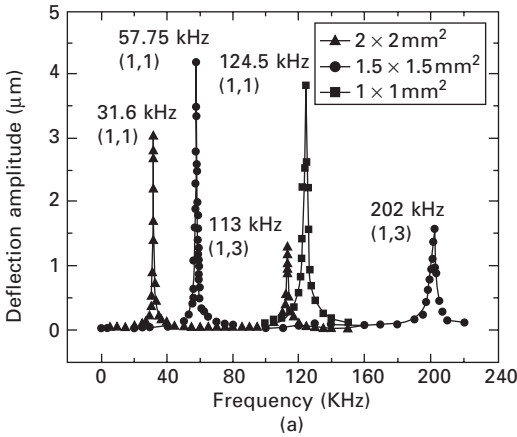
24.25 Equivalent circuit of the resonant pMUT element.

of 2, 1.5 and 1 mm were measured. Figure 24.26 shows the result. Their fundamental resonance frequencies were 31.6, 57.8 and 124.5 kHz, respectively. The sixth order harmonic modes of the two large diaphragms were also detected. Figure 24.26(b) reveals that the resonance frequency of the diaphragm is inversely proportional to the square of the side length, expressed as  $a$ , provided that the diaphragms have the same multilayer structure and thickness. This test confirms that the thick film diaphragms operate as clamped plates. This result is significant because it reveals that the thickness of the PZT layer is not the sole parameter that dictates the operating frequency (the membrane resonance frequency), as it is the case in conventional ceramic transducers. Instead, frequency is governed by the dimensions and the layering materials of the diaphragm and can thus be controlled independent of the PZT layer thickness, offering more design flexibility and control over the frequency.

## 24.7 Summary

Thick piezoelectric film pMUTs with operating frequency of tens to hundreds kilohertz have been developed by combining silicon micromachining and





24.26 (a) Frequency dependence of deflection at central point of square pMUT diaphragms driven by  $3.5\mu\text{m}$ -thick nanocomposite PZT film under 30V dc bias voltage. The backside Si was completely etched off. (b) Relationship between measured resonance frequency and the side length  $a$  of the diaphragm. A linear regression analysis based on  $Y = B * X$  is applied to the data points, where  $Y$  is frequency, and  $X$  equals  $1/a^2$ . The linear regression coefficient  $R$  equals 0.9997.

the composite thick PZT film deposition technology. The success of the fabrication of the pMUT is mainly due to the thick, crack-free and homogeneous composite thick film. Preparing the slurry with submicrometer-sized PZT powder is an effective way to improve the remanent polarizations, and thus the piezoelectric coefficient of the composite film at the expense of the film density. The leakage current density and breakdown field of the film, however, are quite acceptable for MEMS device application in spite of relatively higher porosity of the film in comparison with nanocomposite film. Using a well-reacted  $\text{TiO}_2$  layer instead of a pure metallic Ti layer as the adhesion layer of the bottom electrode is an effective way to avoid the formation of

the blister. The resonance frequency of the square transmitter is inversely proportional to the area of the membrane. At the resonance frequency the oscillation amplitude at the center of the diaphragm can reach several micrometers and the output sound pressure also reaches its maximum. The generated SPL of up to 120 dB indicates that the developed pMUT has quite good ultrasound-radiating performance and the pMUT array has potential applications in ultrasound beam forming and beam steering, either at low ultrasonic frequency in air or high frequency in liquid medium or human body.

## 24.8 Future perspective

Although the good materials properties and processing compatibility of the composite PZT films have been demonstrated in this chapter, there is still the potential to further improve the performance of the films. Regarding the material's properties, because the resultant films are composite and the added powder occupies the majority of the volume fraction, the performances of the films are dominated by the properties of the added powder. This feature facilitates the property optimization of the composite films. For example, according to the specific application, we can directly select the most suitable commercial available piezoelectric ceramic (either a hard or soft composition) as the added powder phase to prepare the slurry, which is a unique advantage of the composite thick film technology. In comparison with the ordinary modification methods by adding dopant or low melting point sintering aids to the slurry, this advantage provides us with a very straightforward and effective way to optimize the piezoelectric properties of the films. As to the troublesome etching problem of the thick composite film, directly depositing patterned thick film on silicon substrate can eliminate the need to etch the film after deposition. Electrophoretic deposition is capable of coating complex geometries. By combining composite slurry and electrophoretic deposition, the PZT film will be deposited only on the patterned electrode and we expect that the sintering temperature of the resultant film can be significantly reduced. This will be an important extension of the composite thick film technology. Regarding the application, the composite thick film is promising in sensors and actuators field. We have demonstrated in this chapter that the thick film pMUT are suited for applications at relatively low ultrasonic frequency. However, there are still a number of challenges if the pMUT aims at high-frequency (MHz) ultrasonic imaging.

## 24.9 References

1. Kurchania R and Milne S J, 'Characterization of sol-gel  $\text{Pb}(\text{Zr}_{0.53}\text{Ti}_{0.47})\text{O}_3$  films in the thickness range 0.25–10  $\mu\text{m}$ ', *J. Mater. Res.*, 1999 **14**(5) 1852–59.

2. Akedo J and Lebedev M, 'Influence of carrier gas conditions on electrical and optical properties of Pb(Zr,Ti)O<sub>3</sub> thin films prepared by aerosol deposition method', *Jpn. J. Appl. Phys.*, 2001 **40**(9B) 5528–32.
3. Yasuda Y, Akamatsu M, Tani M, Yoshida M, Kondo K and Iijima T, 'Preparation of lead zirconate titanate thick films by arc-discharged reactive ion-plating method', *Jpn. J. Appl. Phys.*, 2001 **40**(9B) 5518–22.
4. Tsurumi T, Ozawa S, Abe G, Ohashi N, Wada S and Yamane M, 'Preparation of Pb(Zr<sub>0.53</sub>Ti<sub>0.47</sub>)O<sub>3</sub> thick films by an interfacial polymerization method on silicon substrates and their electrical and piezoelectric properties', *Jpn. J. Appl. Phys.*, 2000 **39**(9B) 5604–8.
5. Barrow D A, Petroff T E, Tandon R P and Sayer M, 'Characterization of thick lead zirconate titanate films fabricated using a new sol–gel based process', *J. Appl. Phys.*, 1997 **81**(2) 876–81.
6. Sayer M, Lockwood G R, Olding T R, Pang G, Cohen L M, Ren W and Mukherjee B K, 'Macroscopic actuators using thick piezoelectric coatings', *Mat. Res. Soc. Proc.* 2001 **655** cc13.6.1–11.
7. Zhu W, Wang Z, Zhao C, Tan O K and Hng H, 'Low temperature sintering of piezoelectric thick films derived from a novel sol–gel route', *Jpn. J. Appl. Phys.*, 2002 **41**(11B) 6969–75.
8. Wang Z, Zhu W, Zhao C and Tan O K, 'Dense PZT thick films derived from sol–gel based nanocomposite process', *Mater. Sci. Eng.*, 2003 **B99**(1–3) 56–62.
9. Zhao C, Wang Z, Zhu W, Yao X and Liu W, 'PZT thick films fabrication using a sol–gel based 0-3 composite processing', *Int. J. Mod. Phys. B.*, 2002 **16**(1&2) 242–248.
10. Dorey R A, Stringfellow S B and Whatmore R W, 'Effect of sintering aid and repeated sol infiltrations on the dielectric and piezoelectric properties of a PZT composite thick film', *J. Eur. Ceram. Soc.*, 2002 **22**(16) 2921–6.
11. Liu W, Zhu W and Tan O K, 'Preparation of PZT thin films by a solid precursor sol–gel routine', in Hing P (Ed), *Proceedings of the First International Conference on Thermophysical Properties of Materials*, Singapore, 1999, pp. 187–90.
12. Sporn D, Merklein S, Grond W, Seifert S, Wahl S and Berger A, 'Sol-gel processing of perovskite thin films', *Microelectronic Eng.*, 1995 **29** 161–8.
13. Chao C, Wang Z and Zhu W, 'Scanning homodyne interferometer for characterization of piezoelectric films and MEMS devices', *Rev. Sci. Instrum.*, 2005 **76**(6) 063906.
14. Chao C, Wang Z and Zhu W, 'Measurement of piezoelectric displacement of PZT using a modified double-beam interferometer', *Rev. Sci. Instrum.*, 2004 **75**(11) 4641–5.
15. Wang Z, Zhu W, Miao J, Chao C and Tan O K, 'Measurement of longitudinal piezoelectric coefficient of film with scanning-modulated interferometer', *Sens. Actuators* 2006 **A128**(2), 327–32.
16. Yao K and Tay F E H, 'Measurement of longitudinal piezoelectric coefficient of thin films by a laser-scanning vibrometer', *IEEE Trans Ultrason. Ferroelectr. Freq. Control.* 2003 **50**(2) 113–16.
17. Wang Z, Zhu W, Chao C, Zhao C and Chen X, 'Characterization of composite piezoelectric thick film for MEMS application', *Surf. Coat. Tech.* 2005 **198**(1–3) 384–8.
18. Oralkan Ö, Ergun A S, Johnson J A, Karaman M, Demirci U, Kaviani K, Lee T H and Khuri-Yakub B T, 'Capacitive micromachined ultrasonic transducers: next-generation arrays for acoustic imaging?', *IEEE Trans. Ultrason. Ferroelectr. Freq. Control.* 2002 **49**(11) 1596–610.

19. Akasheh F, Myers T, Fraser J D, Bose S and Bandyopadhyay A, 'Development of piezoelectric micromachined ultrasonic transducers', *Sens. Actuators*, 2004 **A111**(2-3). 275-287.
20. Bernstein J J, Finberg S L, Houston K, Niles L C, Chen H D, Cross L E, Li K K and Udayakumar K, 'Micromachined high frequency ferroelectric sonar transducers', *IEEE Trans. Ultrason. Ferroelectr. Freq. Contr.*, 1997 **44**(5) 960-69.
21. Yamashita K, Katata H, Okuyama M, Miyoshi H, Kato G, Aoyagi S and Suzuki Y, 'Arrayed ultrasonic microsensors with high directivity for in-air use using PZT thin film on silicon diaphragms', *Sens. Actuators*, 2002 **A97-98** 302-7.
22. Yamashita K, Chansomphou L, Murakami H and Okuyama M, 'Ultrasonic micro array sensors using piezoelectric thin films and resonant frequency tuning', *Sens. Actuators*, 2004 **A114**(2-3) 147-153.
23. Wang Z, Zhu W, Zhu H, Miao J, Chao C, Zhao C and Tan O K, 'Fabrication and characterization of piezoelectric micromachined ultrasonic transducers with thick composite PZT films', *IEEE Trans. Ultrason. Ferroelect. Freq. Contr.* 2005 **52**(12) 2289-297.
24. Wang Z, Zhu H, Zhu W, Miao J, Chao C and Tan O K, 'Ultrasound radiating performances of piezoelectric micromachined ultrasonic transmitter', *Appl. Phys. Lett.*, 2005 **86**(3) art. no. 033508.
25. Wang Z, Zhu W, Miao J, Zhu H, Chao C and Tan O K, 'Micromachined thick film piezoelectric ultrasonic transducer array', in *Digest of Technical Paper, Transducers'05*, Seoul, Korea, June 5-9, 2005, 883-6.
26. Murali P, Ledermann N, Baborowski J, Barzegar A, Gentil S, Belgacem B, Petitgrand S, Bosseboeuf A and Setter N, 'Piezoelectric micromachined ultrasonic transducers based on PZT thin films', *IEEE Trans. Ultrason. Ferroelect. Freq. Contr.* 2005 **52**(12) 2276-88.

## Symmetry engineering and size effects in ferroelectric thin films

---

B NOHEDA, University of Groningen, The Netherlands and  
G CATALAN, University of Cambridge, UK

### 25.1 Introduction

Ferroelectricity and symmetry are intimately related. Indeed, the lack of a centre of symmetry is a necessary condition for the existence of ferroelectricity, the other condition being that the electric field needed to switch the polarization be smaller than the breakdown field. It is therefore not surprising that subtle changes in crystal symmetry can have enormous effects on the functional properties of ferroelectric and piezoelectric materials. This justifies the large research effort that is currently being invested in modifying crystal symmetries (e.g. by using externally imposed strains) to tune and enhance the functional properties of ferroelectric thin films.

In this chapter we give a short overview on the interplay between strain, symmetry and functional properties of perovskite ferroelectrics. We have limited ourselves to perovskites because their relative structural simplicity and ease of fabrication make them the preferred model system in most academic studies. Moreover, perovskites are also the basis for some of the most industrially relevant ferroelectrics such as  $\text{Pb}(\text{Zr},\text{Ti})\text{O}_3$  and  $(\text{Ba},\text{Sr})\text{TiO}_3$ . We warn the reader that, though we believe that all the works described in this chapter are important, they are by no means exhaustive in this rapidly growing and exciting field.

This chapter is organized as follows. In Sections 25.2 and 25.3 we review some of the most important results to date on the physics of ferroelectric thin films, including finite-size effects, domains, superlattices and strain relaxation. In Section 25.4 we review the current views on the origin of the large piezoelectric coefficients of low-symmetry perovskite-like systems, such as morphotropic-boundary  $\text{Pb}(\text{Zr},\text{Ti})\text{O}_3$  and lead-based relaxors. Section 25.5 will connect the previous, by summarizing the most important experimental and theoretical results on symmetry-tuning through epitaxial strain in ferroelectric thin films. This lowering of symmetry is a recurrent theme that will also emerge in connection with recent results in multiferroics such as  $\text{BiFeO}_3$ . The last two sections contain the authors' view of what are likely to

be the next ‘hot topics’ in ferroelectric thin film research, and a suggested list of further reading.

## 25.2 Size effects

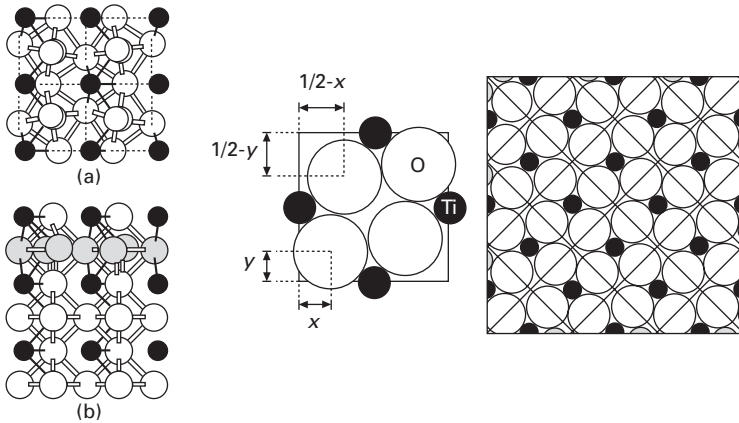
### 25.2.1 The ferroelectric size effect

The convergence between increasingly sophisticated experimental techniques and larger computer capacity for *ab-initio* calculations, together with the ever-present drive for device miniaturization, has in recent times spawned a wealth of research looking at the science of ferroelectric thin and ultra-thin films. Since the length scales at which ferroelectric films can be made and measured are beginning to coincide with those that can be modelled, the advancements in theory and experiment go hand-in-hand and feed off each other [1]. One of the core areas of interest has been the physics of the ferroelectric size effect, i.e. the change in symmetry and properties as the thickness/size of a ferroelectric is reduced. Ferroelectricity is a collective phenomenon which depends on the interaction between many unit cells, so the first question that one may ask is: is there a thickness limit below which a ferroelectric thin film stops being ferroelectric?

When decreasing the thickness of ferroelectric thin films, the surfaces begin to dominate the behaviour. The structure of the epilayer of a film may be different from that of the core due to the uncompensated atomic bonds at the surface (surface tension), which can result in different polarization near the surface [2–4], and/or in the appearance of surface symmetries different from those at the core [4,5] (Fig. 25.1).

By far the most important surface effect is depolarization. The permanent dipoles of a ferroelectric yield a charge density at the surfaces. This charge creates an electric field that opposes the polarization and, eventually, should lead to its cancellation. If the films have good metallic electrodes, or if they have polarization in-plane, depolarization fields do not play a role, and ferroelectricity may remain stable down to thickness of the order of a couple of monolayers [6]. On the other hand, when the polarization is perpendicular to the surface, and in the absence of screening charge, the depolarization field does tend to cancel the ferroelectricity. Electrostatic considerations (assuming a monodomain state) lead to estimates for the critical thickness of a ferroelectric as high as tens or even hundreds of nanometres [7]. Probably one of the most stunning results of the recent years has been the observation of out-of-plane ferroelectricity in non-electroded films of lead titanate only three unit cells thick [8] (Fig. 25.2), well below what was previously thought to be the limit posed by the electrostatic calculations. So how is that possible?

The answer is that the depolarization field in real ferroelectric crystals is not as big as assumed in the calculations. This is principally for two reasons: domain formation and charge screening.



**25.1** Surface antiferrodistortive structure in  $\text{PbTiO}_3$  (PTO). The surface has a different symmetry and polarization than the bulk. Left: results from *ab-initio* simulations (plan view (a) and cross-section (b)); [4] right: experimental results (plan view) from grazing incidence diffraction.[5] As the thickness of the  $\text{PbTiO}_3$  decreases, the relative importance of these surface states will increase. Reprinted figures with permission from [4] and [5]. Copyright 2002 and 2005 by the American Physical Society.

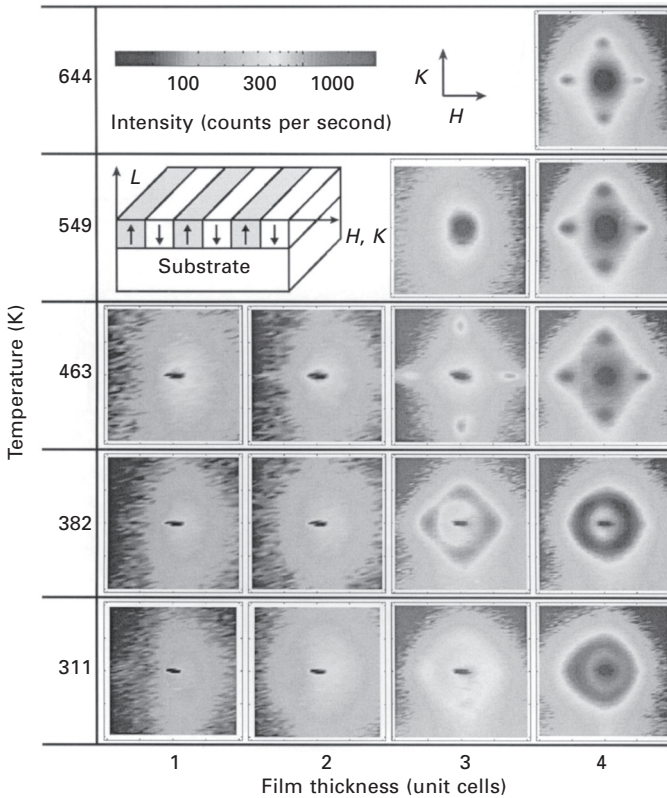
### Domains

Ferroelectrics can reduce the depolarization field by creating domains of opposite polarization, also known as  $180^\circ$  domains [9]: by alternating regions of positive and negative charge at the surface, the net electrostatic energy is reduced. This, however, is not a free trick, because the domains have an energy cost (if it was free to have anti-parallel polarization, the material would actually be anti-ferroelectric!). There is thus a balance between depolarization energy (proportional to domain size) and domain wall energy (proportional to the number of walls and hence inversely proportional to domain size). The domain wall energy is also proportional to the wall size, and hence to the film thickness  $d$ . For a pattern of regular, parallel-sided domains of width  $w$ , the free energy  $F$  per unit surface of crystal due to both contributions is

$$F = Uw + \gamma \frac{d}{w} \quad 25.1$$

where  $U$  is proportional to the volume energy density of the domains and  $\gamma$  is the energy density per unit surface of the domain wall. Minimization of this energy balance leads to the well-known expression

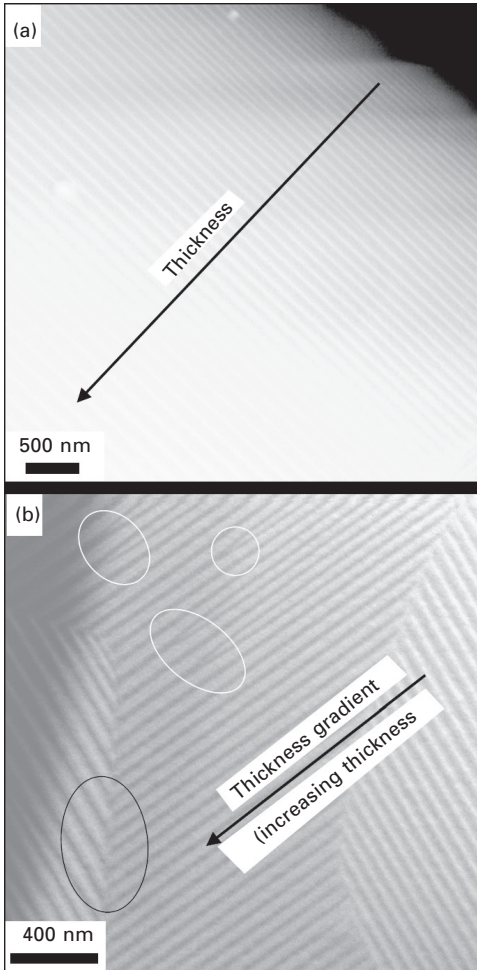
$$w^2 = \frac{\gamma}{U} d \quad 25.2$$



25.2 Area scans in the  $HK0$  scattering plane around the  $(303)$  Bragg reflection of  $\text{PbTiO}_3$  ultra-thin films with different thickness (1, 2, 3 and 4 unit cells) at different temperatures, as measured by synchrotron X-ray diffraction by Fong *et al.*[8] The measurements are taken *in situ* during the growth by MOCVD and cool down of the films. Modulations in the diffuse scattering for thickness of three unit cells and above signal the presence of periodic polar domains, the analysis of which indicates that the polarization in the stripes is perpendicular to the substrate plane. Figure from ref.[9] Reprinted with permission from AAA.

The proportionality  $w^2 = Ad$  was first proposed for ferromagnets by Landau and Lifshitz [10], and later by Kittel [11] known as Kittel's law sometimes, but it is also valid for ferroelectrics [9], ferroelastics [12] and even non-ferroic materials such as martensitic steels [13]: the only difference is the value and the physical nature of  $U$  and  $\gamma$  in equation 25.2. It is important to bear this in mind because most ferroelectrics are also ferroelastic, and thus domains can be due to either depolarization or to strain minimization. This is illustrated in Fig. 25.3, where we show stripe domains in single crystal thin films of ferroelectric  $\text{BaTiO}_3$ . These domains are  $90^\circ$  domains and





25.3 TEM images of 90° domains in single crystal films of BaTiO<sub>3</sub>. The orientation of the polarization is in-plane, and hence the domains are not due to depolarization but to stress (ferroelastic). The films were not parallel-faced but wedge-shaped, so that there is a gradient of thicknesses within the sample: the domains are wider in the thicker side of the wedge, according to Kittel's law. The figure also illustrates the mechanisms for domain width change: continuous change when the domain walls are perpendicular to the thickness gradient(a), discrete bifurcation when they are parallel to it (b)[14]. Reprinted with permission from. Copyright 2006 by the American Physical Society.

correspond to polarization in-plane. Their origin is thus not polar but elastic. This figure also illustrates how the domain width grows with the thickness of the crystal.

The proportionality constant between domain size and film thickness is

different for ferroelectrics and for ferromagnets, being usually bigger for the latter [14]. In fact, the scaling factor is proportional to the width of the domain wall [15–17]. It is thus possible to rewrite Kittel’s law by renormalizing the square of the domain size by the domain wall thickness. If this is done, all ferroics (whether ferromagnetic or ferroelectric) fall in the same parent curve (see Fig. 25.3), meaning that the renormalized (adimensional) scaling factor for 180 domains is the same for ferroelectrics and ferromagnets. This scaling factor can be calculated analytically, and is [17]:

$$G \equiv \frac{w^2}{d\delta} = \frac{2}{3} \frac{\pi^3}{7\zeta(3)} \sqrt{\frac{\chi_a}{\chi_c}} \cong 2.455 \sqrt{\frac{\chi_a}{\chi_c}} \quad 25.3$$

(where  $\chi_a$ ,  $\chi_c$  are the dielectric permittivities perpendicular and parallel to the direction of the polarization and  $\delta$  is the domain wall halfwidth  $\zeta$  is Reimains zeta function,  $\zeta(3) \cong 1.202$ ). The interest of this equation is that it provides a simple (though indirect) way of measuring domain wall thickness: one needs only measure the domain size and the dielectric anisotropy instead. For ferroelectrics, domain wall thickness turns out to be of the order of only a few angstrom.

For ferroelectrics, Kittel’s law is valid down to a thickness of only a few nanometres [8, 14]. Nevertheless, the energy cost of introducing domain walls still causes the critical temperature ( $T_c$ ) of the ferroelectric material to decrease [18]:

$$T_c = T_{c0} \left( 1 - \pi \sqrt{\frac{\chi_c}{\chi_a}} \frac{\delta}{d} \right) \quad 25.4$$

Therefore, ferroelectricity will still disappear below a critical thickness ( $d_c$ ):

$$d_c = \pi \sqrt{\frac{\chi_c}{\chi_a}} \delta \quad 25.5$$

This critical thickness is proportional to the domain wall half-width, which in ferroelectrics is thin: about 2.5 Å for PbTiO<sub>3</sub> [17], for which  $d_c$  turns out to be of the order of only ~6 Å.

The above equations consider a ferroelectric where  $d \gg w$ , so that the two surfaces of the ferroelectric can be treated as independent. For very small thicknesses this is not true, and the interaction between the two surfaces can actually lower the depolarization field and thus prevent the formation of domains [19].

### Screening

The other mechanism for preventing depolarization is charge screening. This can happen naturally when ionic impurities aggregate at the exposed surfaces

of a ferroelectric [9]. Likewise, if the ferroelectric has electrodes and these are connected in short-circuit, the charges at the electrodes neutralize the depolarization field. This, however, is true only for films with perfect electrodes. In reality, electrodes have a finite Thomas–Fermi screening length, which the depolarization field can penetrate [20]. Consequently, the depolarization field is not completely screened in real systems. Calculations for monodomain  $\text{BaTiO}_3$  ferroelectric films with realistic  $\text{SrRuO}_3$  electrodes predict a depolarization-induced critical thickness of six unit cells [21]. These calculations, however, do not incorporate the extra screening that comes from the displacement of the ionic charges in the electrodes. Calculations that incorporate these yield a considerably lower critical thickness of only three unit cells [22].

The above works analyse either domain formation in unscreened ferroelectrics, or screening in mono-domain ferroelectrics. The work of Bellaiche and coworkers [23] looks at both effects simultaneously and shows that, if domain formation is incorporated to realistic models of ultra-thin films, the local structure of the dipoles within the domains shows new types of arrangements, with rotational gradients of polarization as a function of depth within the film. Such structures depend on both the screening efficiency of the electrode and the strain state of the film.

### 25.2.2 The dielectric size effect

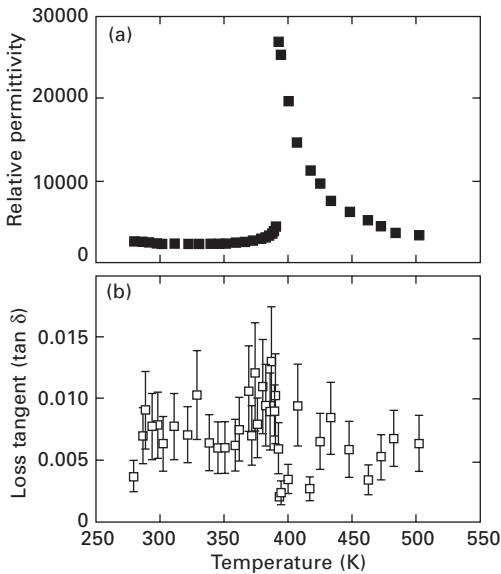
From the above discussion one might conclude that the size effect is irrelevant for real ferroelectric film devices, which operate at bigger thickness (typically tens or hundreds of nanometres), and have electrodes. Yet, in reality, ferroelectric thin films are generally seen to behave differently from their bulk counterparts even at such relatively large thicknesses. One of the most ubiquitous effects is the ‘dielectric size effect’, i.e. the progressive lowering of the dielectric constant in thin films with respect to their bulk counterparts.

Bulk ferroelectric materials normally show a sharp dielectric anomaly at the critical temperature of the ferroelectric transition. But, for thin films, the peak essentially disappears and the dielectric constant can decrease by one or two orders of magnitude, even for thicknesses of the order of hundreds of nanometres. Quite often, too, the decrease in permittivity with decreasing thickness is such that it can be quantitatively described as if there were a low-permittivity ‘dead’ layer at the interface between the dielectric and the electrode. The ‘dead layer’ model seems to hold down to thickness of only a few nanometres [24] even when there is no evidence of the actual existence of an actual dead layer chemically or morphologically distinct from the rest of the film. There have been several proposed explanations for the dielectric size effect: dead layers in the ferroelectric [25], finite screening

length in the electrode [26], Schotky barriers [27], phonon hardening [28], dissimilar electrodes [29] and strain gradients [30] are but a few.

One challenge is to assess how much of the decrease in dielectric constant is intrinsic, and thus impossible to get rid of, and how much is extrinsic. This was addressed by the group of Marty Gregg in Belfast, who analysed the dielectric behaviour of free-standing ferroelectric single crystal lamellae only 70 nm thick [31]. The dielectric behaviour was found to be essentially identical to that of the bulk crystal (see Fig. 25.4), thus proving that the dielectric smearing previously seen in other thin films was not due to intrinsic properties of the films or the film–electrode interface, but rather to extrinsic effects. Two strong contributors to the extrinsically generated dielectric size effect are dissimilar electrodes [29] and strain gradients [30] which may arise from epitaxial strain relaxation [30, 32] or from local strain gradients caused by point defects [33].

Intrinsic effects can nevertheless still play a role, as recently shown by the *ab-initio* calculations of the dielectric constant of SrTiO<sub>3</sub> with symmetric SrRuO<sub>3</sub> electrodes [34], which show that the screening length in the electrodes acts as a dielectric ‘dead layer’ of low dielectric constant in series with the ‘proper’ dielectric SrTiO<sub>3</sub>. Although the effect of this dead layer is big for films with a thickness of a few unit cells, a film of 70 nm (such as the one experimentally analysed by Saad *et al.* [31]), would experience a reduction in



25.4 Dielectric constant of a free-standing thin single crystal of BaTiO<sub>3</sub> with a thickness of 70 nm, by M. Saad *et al.* [31]. The dielectric response is identical to that of bulk. Figure from [31]. Reproduced with permission from IOP Publishing Limited.

dielectric constant of only 15%, which is negligible in comparison with the effect of the other extrinsic ingredients.

## 25.3 Heterogeneous thin films: superlattices and gradients

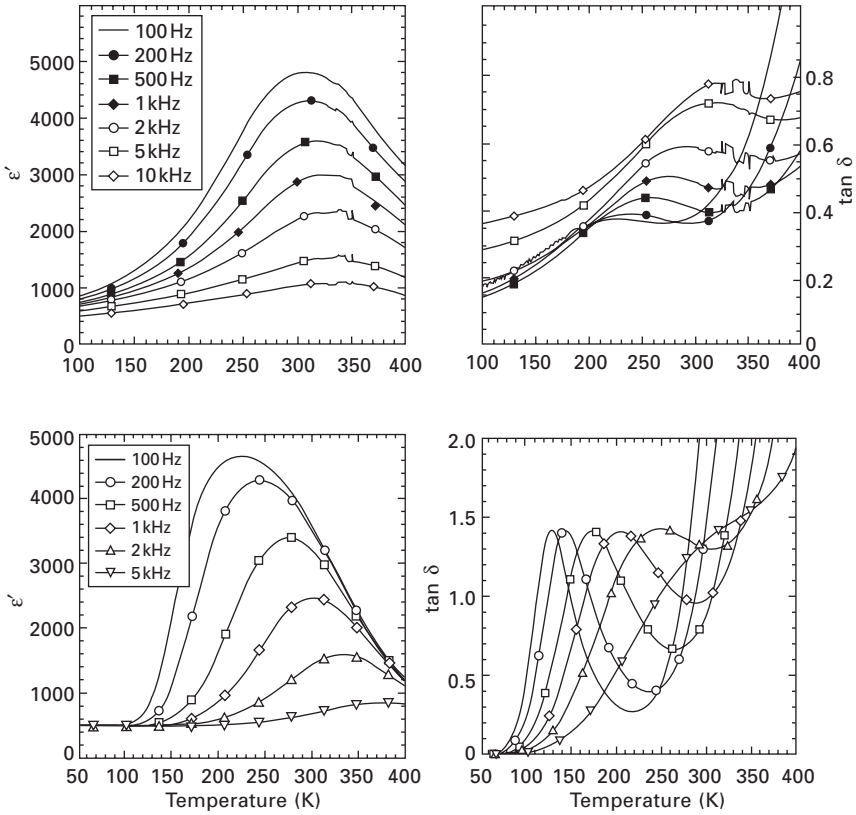
### 25.3.1 Superlattices

Heterogeneity can be artificially introduced in ferroelectrics by, for example, fabricating superlattices. These have been an object of very active research over the last dozen years or so [35–45]. The initial impetus for fabricating these structures was to try to replicate some of the advantages of relaxors such as high dielectric constant with smooth temperature dependence. Initial results were promising, as indeed the large, frequency-dependent dielectric characteristics of relaxors were reproduced, roughly at the same stacking periodicity as the naturally occurring heterogeneity of relaxors (a few nanometres). However, most of these early results were later shown to be probably influenced by conductive artefacts: oxygen vacancies may accumulate at the interfaces between each slab [40–43], and thus the space charge dominates the dielectric behaviour through the Maxwell–Wagner effect (see Fig. 25.5) [39, 40].

More recent works are being more careful in trying to eliminate conductive artefacts, and also are using alternative means of exploration which are not affected by these, such as structural, rather than electric, characterization techniques. Among the more sound results is the observation that when the superlattice period is decreased, the material may have a transition in which it goes from behaving as two separate components to behaving as a single compound [38, 41]. The mechanisms for this inter-layer coupling are the depolarization field [46] and strain [35, 42], which depend on material parameters such as spontaneous polarization and lattice mismatch, as well as on the stacking periodicity. The interplay between these parameters has also yielded several new and unexpected phenomena, such as an orthorhombic phase in normally cubic STO when it is superlatticed with BTO [42], and an anomalous enhancement of polarization for small-period superlattices [45].

### 25.3.2 Gradients

Another type of heterogeneous structure is achieved by introducing a compositional gradient across the thickness of a planar capacitor structure. By growing films in which the composition is gradually changed from, say, pure  $\text{BaTiO}_3$  to pure  $\text{SrTiO}_3$ , or from  $\text{PbTiO}_3$  to  $\text{PbZrO}_3$ , one introduces a built-in bias field that self-poles the sample. This leads to rather unusual behaviour of the polarization vs. field loops [47], although it is as yet unclear



25.5 Comparison between measured relaxor-like dielectric properties in ferroelectric superlattices (above) and calculated properties assuming Maxwell–Wagner behaviour due to interfacial space-charge (below), showing that the relaxor-like properties are due to conductive artefacts. Figures adapted from ref[40]. Reused with permission from G. Catalan, D. O’Neill, R. M. Bowman, and J. M. Gregg, *Applied Physics Letters*, **77**, 3078 (2000). Copyright 2000, American Institute of Physics.

how much of this is intrinsic and how much is due to conductivity artefacts [48]. It seems that such graded ferroelectrics may present very large pyroelectric [49] and piezoelectric coefficients [50] without the need to externally pole the material.

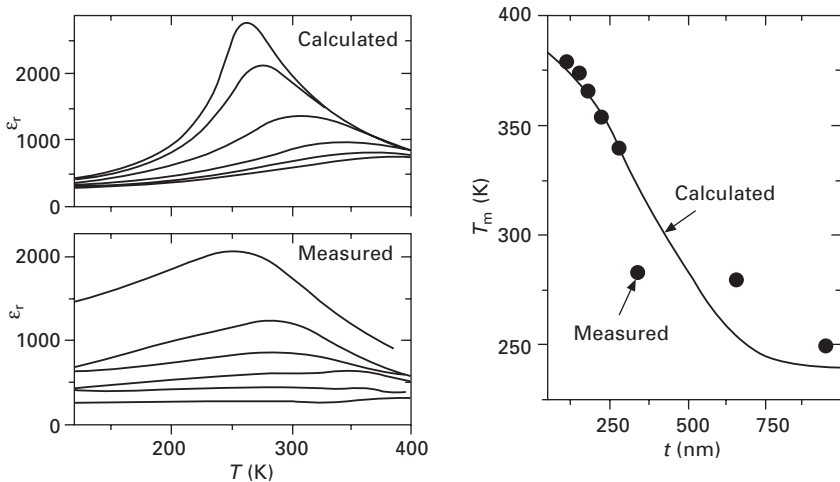
Sometimes, however, the gradients are not deliberate but accidental. Thin films grown on substrates with a different lattice parameter will try to accommodate the strain. There are several ways to do this: twin domains [51, 52], dislocations [52–54] and compositional segregation [55] are but a few. It has been observed that strain relaxation may not always be homogeneous throughout the thickness of the film, but rather it may take place in a gradual

manner, leading to vertical strain gradients across the dielectric layer [32, 55]. Such strain gradients break the inversion symmetry, and can couple to the ferroelectric properties through the so-called flexoelectric effect [56–58]. Because strain gradients break the inversion symmetry, flexoelectric polarization can actually be induced in any material, even those that are not ferroelectric. The introduction of flexoelectricity in the thermodynamic potential leads to an equation of state of the form [30]:

$$E + \frac{\mu}{\chi} \frac{d\varepsilon}{dz} = aP + bP^3 \quad 25.6$$

where  $E$  is the electric field,  $P$  is the polarization,  $\mu$  is the flexoelectric coefficient,  $\chi$  the permittivity and  $d\varepsilon/dz$  is the strain gradient;  $a$  and  $b$  are the first two coefficients of the Landau thermodynamic potential. From this equation it can immediately be seen that the effect of strain gradient is analogous to that of an external DC electric field. Accordingly, two effects can be predicted:

- 1 There will be a preferential direction of the polarization in the film (self-poling or imprint) [59].
- 2 In much the same way that a dc voltage would lowers the capacitance in a  $C(V)$  measurement, the strain gradient lowers the capacitance and smears the dielectric peak. Calculations based on this idea reproduce experimental results very well, as shown in Fig. 25.6 [32].



25.6 Comparison between experimental dielectric properties of (Ba, Sr)  $\text{TiO}_3$  thin films and flexoelectric calculations using the strain gradients measured by X-ray diffraction in the same samples. Reprinted with permission from ref. [32]. Copyright 2005 by the American Physical Society

In all the above discussions, we have deliberately left out what is possibly the most important factor in the rationalization of ferroelectric thin film properties: the biaxial strain induced by the substrate. This will be the subject of Section 25.5.

## 25.4 Symmetry and ferroelectric properties: polarization rotation and lattice softening

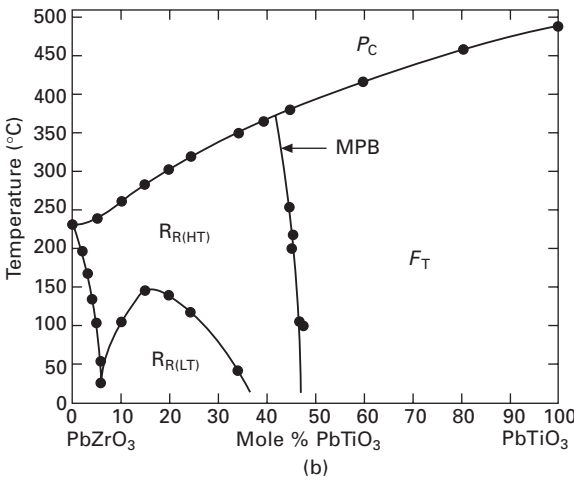
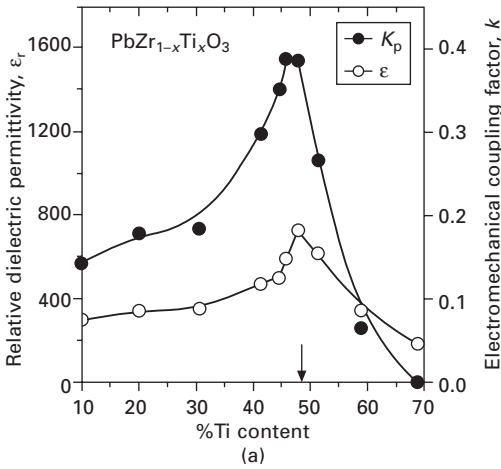
### 25.4.1 Piezoelectricity and phase coexistence

Ferroelectric materials are not only interesting because of the properties directly derived from their remnant polarization. The best piezoelectrics are also to be found among ferroelectric perovskites due to the strong coupling between the polarization and the lattice existing in most of these compounds. Moreover, a few of these ferroelectrics show astonishingly high dielectric and piezoelectric responses, whose mechanisms are not totally understood. In particular, the ceramic lead titanate–lead zirconate solid solution,  $\text{PbZr}_{1-x}\text{Ti}_x\text{O}_3$  (PZT), has been for decades the most popular piezoelectric in the actuator market. This is because, next to the low price and ease of fabrication and handling of the ceramics, the effective longitudinal piezoelectric coefficient ( $d_{33}^{\text{eff}}$ ) of the  $x = 0.48$  composition (PZT48) is as high as  $\sim 600$  pm/V [60], two orders of magnitude larger than that of quartz. The highly responsive PZT48 lies just at the boundary between the tetragonal (T) and the rhombohedral (R) phase fields, the so-called *morphotropic phase boundary* (MPB), in the phase diagram depicted in Fig. 25.7(b) [60–62]. But the relevance of this fact to explain the unusually large electromechanical response in this compound is, only recently, beginning to be understood.

As shown in Fig. 25.7(b), the MPB has a very weak temperature dependence and thus only an exquisite compositional homogeneity of the ceramics and the extension of the temperature range (by measuring at lower temperatures) allows us to investigate the R-to-T phase transition in detail by means of temperature variations. Changes in composition away from  $x = 0.48$  lead to a decrease in the piezoelectric coefficients and the electromechanical coupling factor, as well as in the dielectric permittivity. The decrease is dramatic for increasing Ti content (towards the tetragonal side), while relatively high dielectric and piezoelectric responses are found in the rhombohedral part of the phase diagram (see Fig. 25.7a).

Because of the lack of group–subgroup relationship between the rhombohedral and tetragonal space groups ( $R3m$  and  $P4mm$ , respectively), a T-to-R phase transition must be of first order and therefore a phase coexistence region is expected. A coexistence region is indeed often observed around the MPB but it is not straightforward to interpret this as a signature of a first-order phase transition in the presence of even slight compositional fluctuations (according to Fig. 25.7b, fluctuations in composition of  $\Delta x = 0.01$  at the





25.7 (a) Relative dielectric permittivity (open symbols) and electromechanical coupling factor (solid symbols) of  $\text{PbZr}_{1-x}\text{Ti}_x\text{O}_3$  (PZT) at room temperature, as a function of Ti content, showing a large enhancement of both properties at the MPB composition,  $x = 0.48$ . (b) Phase diagram of PZT as determined by Jaffe *et al.* [60] from measurements of the elastic moduli. Figures (a) and (b) modified and reprinted, respectively, from ref. [60] with permission of Elsevier.

MPB can give place to a change of about 100 K in the transition temperature). Whatever the origin, such a coexistence region allows for a large number of available polarization orientations of domains (8 for the R phase plus 6 for the T phase) and this was believed to cause the huge response enhancement observed at the MPB compositions [63].

However, the width of the coexistence region seemed to be determined not only by the compositional uncertainty [64], but also by grain size effects

[65]. In particular, large grain ceramics were shown to display coexistence regions of less than 0.1 mole% [64]. More interestingly, the maximum electromechanical response was found always at a very specific composition ( $x = 0.48$  at RT) independently of the extent of the coexistence region and the phase population. In other words, the MPB appeared as an amazingly robust line. This was early realised by Jaffe *et al.* [60] and it was, in fact, by measuring the maxima of the piezoelectric response how the MPB in the phase diagram of Fig. 25.7(b) was determined. The same authors already remarked that the composition of maximum dielectric response ( $x = 0.48$ ) was shifted towards the tetragonal side with respect to that for which the rhombohedral and tetragonal compositions appeared at equal ratios ( $x = 0.465$ ). Later it was reported that, in very homogeneous ceramics, the maximum response was indeed located in the tetragonal side of the MPB and, unexpectedly, it was outside the coexistence region [66]. This worked against the argument of the maximum number of available domains being the main origin of the large observed piezoelectricity. Moreover, a significant dependence of the effective  $d_{33}$  with doping and changes from sample to sample had suggested a different extrinsic origin, such as domain wall contributions, for this remarkable behaviour.

PZT was considered a fortunate rare case for many years, leading the actuator market in isolation. However, since 1995, other related solid solutions, such as  $\text{Pb}(\text{Mg}_{1/3}\text{Nb}_{2/3})_{1-x}\text{Ti}_x\text{O}_3$  (PMN-PT),  $\text{Pb}(\text{Zn}_{1/3}\text{Nb}_{2/3})_{1-x}\text{Ti}_x\text{O}_3$  (PZN-PT) and  $\text{Pb}(\text{Sc}_{1/2}\text{Nb}_{1/2})_{1-x}\text{Ti}_x\text{O}_3$  (PSN-PT), with very similar phase diagrams to that of PZT, have been shown to display even larger piezoelectric coefficients (of about 2500 pm/V) for compositions lying at the boundary between the tetragonal and rhombohedral phases [67–69]. A detailed structural investigation of the MPBs then seemed necessary and the study of these materials by high-resolution X-ray and neutron diffraction in an extended temperature range was systematically carried out [70–74].

It is well known that the piezoelectric response of materials is highly anisotropic. The most commonly reported piezoelectric coefficients are the longitudinal  $d_{33}$ , for which the induced polarization and the normal stress are collinear, and the transversal one,  $d_{31}$ , in which the direction of the induced polarization is perpendicular to the normal stress. Configurations exploiting other piezoelectric components, as those that involve shear strain, require less straightforward geometries and have been less investigated. However, for polycrystalline materials, the ones commonly used in applications, the measured effective coefficients are an average of the components of the single-crystal piezoelectric tensor. In the tetragonal case, the effective

longitudinal coefficient can be written as  $d_{33}^{\text{eff}} = \int_0^{\pi/2} (d_{15}\sin^2\theta + d_{31}\sin^2\theta + d_{33}\cos^2\theta) \cos\theta\sin\theta d\theta$ , where  $\theta$  is the angle between the crystallites polar axis and the poling axis of the ceramic pellet [75]. The prominence of

piezoelectric ceramics versus single crystals is, probably, the reason why it was not widely known that the main contribution to the  $d_{33}^{\text{eff}}$  in well-known piezoelectrics such as PZT, comes from the  $d_{15}$  piezoelectric modulus [75], which relates the induced transversal polarization to the shear stress. Had we carefully considered the implications of this result, already reported in the 1970s [60], the behaviour of the MPB piezoelectrics would have been understood earlier.

### 25.4.2 Polarization rotation

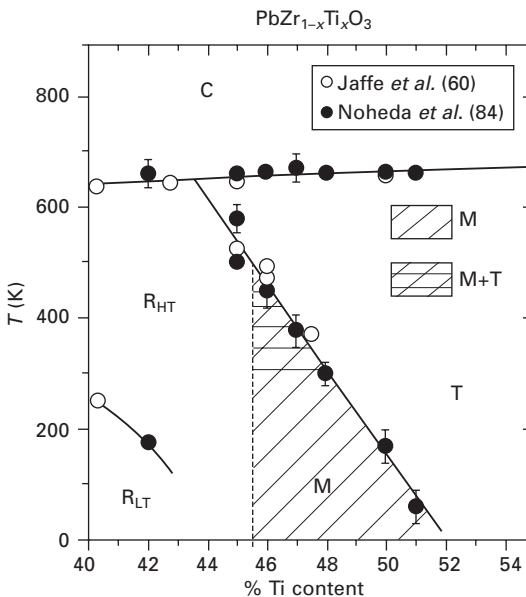
The first step into the new understanding was offered by the seminal work of Park and Shrout [67] on rhombohedral PZN–PT and PMN–PT single crystals showing unprecedented high-strain values of 1.5% and high electromechanical performance ( $d_{33} = 2500$  pm/V) with virtually no hysteresis. Lack of hysteresis implies no domain wall motion, and this was not possible to understand in the context of phase coexistence and multiple accessible polar domains. The concept of *engineered domain configuration* was then developed. According to this model, poling a rhombohedral crystal with a field along the  $[001]_{\text{pc}}$  (pseudo-cubic) direction will favour four of the eight possible rhombohedral domains. Upon increasing the electrical field, domain wall motion will not take place because the four domains are symmetrically oriented with respect to the field. Instead, the unit cell will elongate along  $[001]_{\text{pc}}$ , forcing the polarization to rotate away from the rhombohedral polarization direction  $[111]_{\text{pc}}$ .

The possibility of polarization rotation under electric field was investigated by Fu and Cohen using calculations based on first principles [76]. They showed that, in a monodomain rhombohedral  $\text{BaTiO}_3$  crystal (easier to deal with than the chemically complex MPB solid solutions), the minimum energy path for the polarization to change between the rhombohedral and the tetragonal orientations under an  $[001]$ -oriented electric field, corresponds to the continuous rotation of the polarization from the  $[111]_{\text{pc}}$  to the  $[001]_{\text{pc}}$  direction. This mechanism produces a hysteresis-free strain vs. field dependence (very similar to those observed for the high-strain piezoelectrics [68]) and generates very large strain values and piezoelectric coefficients. However, the electric fields at which polarization rotation would take place are huge and less accessible than those experimentally found for the lead MPB compounds. That was probably the reason why this predicted behaviour was not observed in  $\text{BaTiO}_3$ . Thus, polarization rotation at the unit cell level was presented as a new mechanism to enhance the electromechanical responses of ferroelectric materials. It is very likely, for the compositions close to MPBs, that the threshold electric fields for polarization rotation were unusually low, due to lattice softening at the phase boundary [77–79], allowing this effect to be experimentally observed at relatively low electric fields. These ideas were in

tune with an earlier report by Du and colleagues in which, by using a phenomenological Landau–Devonshire approach, they showed that rhombohedral PZT single crystals poled along the non-polar  $[001]_{pc}$  direction would show enhanced dielectric and electromechanical properties [80]. Unfortunately no single crystals of PZT were available to test this result but, two years later, Taylor and Damjanovic were able to observe this behaviour on differently oriented PZT thin films [81].

### 25.4.3 Low-symmetry ferroelectric phases

Around this time, a third phase was unexpectedly observed in PZT by using high-resolution synchrotron X-ray diffraction [82–84]. The new phase extends over a narrow region of compositions next to the MPB, just in between the R and T phases [83] (Fig. 25.8). This phase, with monoclinic symmetry (space group  $Cm$ ), has a mirror plane as the only symmetry element and it is, thus, fundamentally different from other known ferroelectric phases with symmetry axes. A symmetry axis determines the direction of the polarization

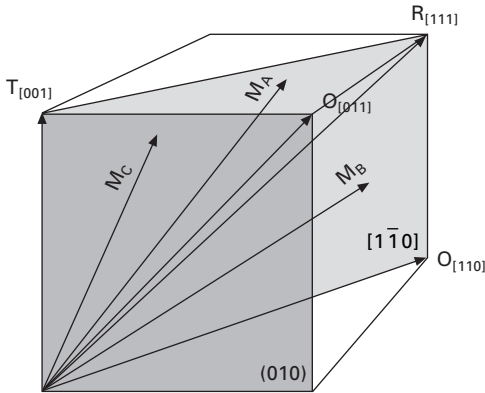


25.8 Phase diagram of PZT around the MPB, down to low temperatures, as determined from synchrotron X-ray powder diffraction (solid symbols). The phase boundaries are compared with those reported by Jaffe *et al.* [60] (open symbols), also shown in Fig. 25.1(b). The MPB appears as a straight, slightly slanted line separating the tetragonal (T) and the monoclinic (M) phases. Figure reprinted with permission from [84]. Copyright 2001 by the American Physical Society.

(any component perpendicular to that axis would cancel out by symmetry). In an un-twinned ferroelectric crystal with such a well-defined polar axis, two equivalent polarization directions exist,  $180^\circ$  apart from each other. During switching, relatively high electric fields are needed to invert the polarization direction. This well-known scenario of a symmetric double-well potential with a relatively large potential barrier, becomes elusive in the monoclinic  $Cm$  case, in which the symmetry imposes minimal constraints to the polarization direction (namely to lie within the mirror plane,  $m$ ). Switching fields can be very small and under the application of a non-collinear electric field contained in  $m$ , the polarization is able to rotate to align parallel to the field.

Interestingly, the  $m$  plane in monoclinic PZT is the  $(1-10)_{pc}$  [83], which contains both the  $[111]_{pc}$  and the  $[001]_{pc}$  directions, that is the polar axes of the R and T phases (see Fig. 25.9). Therefore, the rotation of the polarization between  $[111]_{pc}$  and  $[001]_{pc}$  is possible in the presence of this bridging phase and domain wall motion is not required in order to change the polarization direction. In this way, the link between the hysteresis-free strain curves, the high electromechanical responses and the MPB compositions was made through the polarization rotation mechanism in low symmetry phases.

From symmetry arguments [79, 85], the T-to-M phase transition can be of second order (with continuous change in the order parameters). However, the transformation between the M and R phases has to be, also by symmetry arguments, discontinuous. Thus, although the polarization can rotate continuously from  $[001]$  towards  $[111]$  by changing composition across the



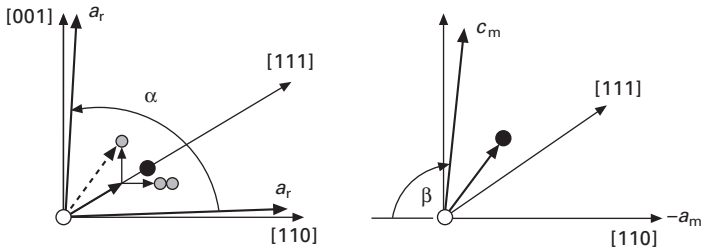
25.9 Sketch of the orientations of the polarization ( $P$ ) for the different monoclinic phases of a ferroelectric perovskite: in  $M_A$  and  $M_B$ ,  $P$  is contained in the  $(1-10)_{pc}$  plane (light grey), while in  $M_C$ ,  $P$  is contained in the  $(010)_{pc}$  plane (dark grey).  $M_A$ ,  $M_B$  and  $M_C$  allow rotations of  $P$  between the polar axes of the tetragonal and rhombohedral, rhombohedral and orthorhombic and orthorhombic and tetragonal phases, respectively.

MPB, it cannot reach a truly rhombohedral phase in a continuous way. Indeed, there is sufficient evidence to propose that the so-called rhombohedral phase in PZT and related systems may be only rhombohedral in average but monoclinic at the unit cell level [83, 86–91]. This would explain the fact that no second phase boundary limiting the monoclinic and the rhombohedral phase has been directly observed [90] (see dashed line in Fig. 25.8).

The intermediate monoclinic phase in PZT (at zero electric field) has been observed by other experimental techniques [92, 93] and has been reproduced by first-principles calculations [75, 94–96]. Ginzburg–Landau–Devonshire phenomenological calculations are also able to reproduce monoclinic, and even triclinic, phases, if higher order terms (eighth order for monoclinic and twelfth order for triclinic) are taken into account [79]. This reflects the fact that low symmetry phases are expected in the presence of highly anharmonic energy potentials or flat energy landscapes, as are known to exist in the proximity of a phase transition [77, 78], or in lead oxides, due to disorder [97, 98].

The tendency of Pb to form four, instead of three, short Pb–O bonds favours the monoclinic phase at the local level, even for Zr-rich compositions, which show an average rhombohedral phase. It has been repeatedly shown by synchrotron and neutron diffraction that the rhombohedral phase in PZT, although rhombohedral on average, contains a large degree of disorder. This disorder is very anisotropic [86]. The diffraction data could well be explained by a model in which the lead shifts are displaced away from the [111] direction. This deviation can be described by three equal components along the main crystallographic axes (see Fig. 25.10). In the ‘rhombohedral’ phase the three components are randomly distributed in such a way that the average polarization still points along  $[111]_{pc}$  [88]. With increasing Ti content, the [001] component is gradually preferred against the other two, favouring the monoclinic phase, and providing the structural bridge to the tetragonal phase [83]. The disorder existing at higher Zr contents diminishes towards the MPB and in the monoclinic phase there is no discrepancy between the local and the average structure. It can be said then that, by increasing Ti content, the solid solution transforms gradually from short-range to long-range monoclinic ordering without crossing any phase boundaries [90].

Deeper insight into the local order of these materials has been obtained using density functional calculations by Grinberg *et al.* [94, 95]. They showed that the local structure in PZT is indeed very different from the average one offered by conventional diffraction refinements: the shifts of Zr, Ti and Pb cations are not collinear. The most striking behaviour is displayed by the Pb cations: shifts along  $[100]_{pc}$ ,  $[211]_{pc}$  or  $[110]_{pc}$  pseudo-cubic directions are preferred over the  $[111]_{pc}$  shifts, even in the rhombohedral phase, where the average polarization is along [111]. Moreover, the Pb cations are highly sensitive to their local environment. In particular, Pb displacements tend to



25.10 In order to explain the disorder typically observed in the rhombohedral phase (R) of PZT, Corker *et al.* [88] proposed a model in which Pb can randomly occupy three different sites (grey dots), while keeping the macroscopic polarization along the [111] direction. These random positions are defined by a common component along [111] and three shifts of the same magnitude but directed along [100], [010] and [001], respectively. One of these sites, which can be described as  $(x, x, x) + (00z)$  coincides with the position of Pb in the monoclinic phase, M (right). The transition from R to M corresponds to the preference of the [001] Pb displacement against the [100] and [100] ones, upon decreasing Zr content. Figure adapted and reprinted with permission from [83]. Copyright 2000 by the American Physical Society.

point towards the Ti neighbours and away from their larger Zr neighbours, governed by simple electrostatics reasons.

At relatively low Zr contents, in the tetragonal phase, local Pb shifts will tend to follow the average [001] polarization. However, in the rhombohedral phase, shifts of the Pb along the overall macroscopic polarization  $[111]_{pc}$  bring the Pb and Zr neighbours closer together and are energetically unfavourable, forcing the Pb atoms to deviate from the average polarization direction. Clearly, this balance becomes more difficult the larger the Zr content. These authors also show that at around the  $x = 0.50$  composition, a monoclinic phase made of  $[001]_{pc}$  (for Pb cations undisturbed by a Zr neighbour) and  $[211]_{pc}$  Pb distortions (of those trying to avoid a Zr) is expected, in agreement with the experimental finding.

In other solid solutions, intermediate low symmetry phases have also been observed, some of them different from that in PZT (the so-called  $M_A$  phase [79]), which gives a polarization  $P_x = P_y < P_z$ , where  $P_x$ ,  $P_y$  and  $P_z$  are the Cartesian components of the polarization along the pseudo-cubic perovskite directions (see Fig. 25.9). The intermediate monoclinic phase that can bridge the tetragonal and orthorhombic phases is called  $M_C$  and supports polarization with  $P_x < P_z$ ;  $P_y = 0$ . The symmetry plane in this case is the  $(010)_{pc}$  and the space group is  $Pm$ . The intermediate monoclinic phase between the rhombohedral and the orthorhombic phases ( $M_B$ ) has the same symmetry as  $M_A$  phase but in this case  $P_x = P_y > P_z$ . These three phases have been predicted by a Ginzburg–Landau–Devonshire approach [79], as well as by

first-principles calculations [75, 96] and all of them have been also found experimentally in different systems. The richest solid solutions seem to be PMN- $x$ PT [99] and PSN-PT [100, 101], in which both  $M_B$  and  $M_C$  phases are observed at the MPB.

The availability of single crystals of PMN-PT and PZN-PT [102] made it possible to observe directly the polarization rotation by detecting monoclinic phases by X-ray and neutron diffraction. This was done in rhombohedral compositions by applying a [001]-electric field *in situ* and observing the lattice distortion. Low symmetry M phases were observed under electric fields [103, 104] and at large enough fields a tetragonal phase was induced. The R-M-T transformation path is irreversible [105] and the crystals remain monoclinic upon removal of the electric field (at least during a time scale of months). This seems to argue in favour of the stability of the intermediate monoclinic phase, in agreement with first-principles calculations in PZT [106]. There is, however, still some disagreement in the community and it has been argued that these are not proper monoclinic phases but rather monoclinic metastable states induced by strain and/or electric field [107, 108].

Other authors have explained the intermediate structures as 'adaptive phases' similar to those taking place in martensites [109, 110]. According to this model, crystallographic nano-twins with tetragonal or rhombohedral symmetry exist and will appear as a uniform monoclinic phase under long-range probes such as X-ray diffraction. The macroscopic rotation of the polarization occurs under electric field by means of de-twinning. Nano-twinning is indeed expected close to the MPBs, and also in truly monoclinic phases, due to the very small anisotropy, which gives place to a low domain wall formation energy. Recently, it has also been suggested that domain wall broadening occurs under an electric field and that the intrinsic piezoelectric response of the domain walls are at the origin of the unusual behaviour observed in morphotropic systems [111], in which there is a high density of domain walls.

As it seems, first-principles calculations and local probe techniques in PZT favour truly monoclinic phases, while structural and optical investigations on PMN-PT and PZN-PT single crystals seem to be in good agreement with the postulates of the adaptive theory. The diffraction patterns of PZT48 at low temperatures show clear monoclinic peak splitting [83], while the monoclinic distortion in the diffraction patterns of PMN-PT or PSN-PT appears more often as peak broadening and asymmetry in the diffraction peaks, due to a larger amount of disorder in this chemically more complex systems.

As reminded [112], the phase boundary between two different ferroelectric phases (with different direction of the polarizations), as in the case of the MPBs, involves the softening of the lattice in a direction different from the



polar direction and, therefore, causes large dielectric anomalies that are responsible for the ease of rotation of the polarization and for the enhancement of the piezoelectric response due to shear tensor components [113–115]. The proximity of a critical point will also have the effect of softening the lattice and allowing anomalously high piezoelectric deformations [116]. And, as has been recently pointed out, these descriptions are not unrelated to one another [117]. Thus, over the past years it has become clear that very large dielectric (and piezoelectric) responses are expected when polarization rotation is allowed, either at the unit cell level (by the softening of the lattice at a phase transition, and/or by inducing phases with no symmetry axis) or macroscopically (by de-twinning of  $90^\circ$ -like domains).

Despite the recent understanding, it is still puzzling that so very few materials actually display the above behaviour. Moreover, the ones that do so are chemically complex and thus difficult to control and model. It would be desirable to find simple materials behaving in such a responsive way. As described above,  $\text{BaTiO}_3$  is one such material but polarization rotation happens at impractically high electric fields. Rotation can become easy close to the transition temperatures [112] but this strong temperature dependence is also not practical.

The question then arises whether it is possible to design and build new materials displaying any of the polarization rotation mechanisms so far detected. One possible approach is using strain engineering by means of thin film deposition techniques, as described in the next section. The advantage of this approach is that it provides us with very thin films for integration and miniaturization of dielectric, ferroelectric and piezoelectric components, which are still missing in the applications market. The disadvantages are related to high production costs, clamping effects and size effects that, as shortly reviewed in the previous section, are an interesting topic on their own.

## 25.5      Strain effects on ferroelectric thin films

As described in Section 25.4, substituting  $\text{Ti}^{4+}$  in the classical ferroelectric perovskite  $\text{PbTiO}_3$  with a larger size isovalent cation, such as  $\text{Zr}^{4+}$  or a mixture of  $(\text{Mg}_{1/3}\text{Nb}_{2/3})^{4+}$ ,  $(\text{Zn}_{1/3}\text{Nb}_{2/3})^{4+}$ ,  $(\text{In}_{1/2}\text{Nb}_{1/2})^{4+}$  and  $(\text{Sn}_{1/2}\text{Nb}_{1/2})^{4+}$ , the tetragonal ferroelectric ground state, with polarization along  $[001]_{\text{pc}}$ , transforms into a rhombohedral ferroelectric phase with polarization along  $[111]_{\text{pc}}$ . At the boundary between these two, the electromechanical and dielectric responses are astonishingly large. It seems plausible that a similar effect could be attained by enlarging the unit cell via external pressure or epitaxial stress. Indeed, first-principles calculations on  $\text{PbTiO}_3$  [118] and PZT [119] under hydrostatic pressure, as well as structural and Raman experiments [119, 120], confirm that polarization rotation also takes place under external pressure.

In thin film crystals, biaxial strain provided by a crystalline substrate can be applied permanently in the plane of the film. The perpendicular lattice parameter will be strained in the opposite direction according to the Poisson ratio:

$$s_z = (s_x + s_y) \frac{\nu}{1 - \nu} = s_m \frac{2\nu}{1 - \nu} \quad 25.7$$

where  $s_z$  is the out-of-plane strain (with respect to the unclamped structure), and  $s_x, s_y$  are the lattice mismatches between the in-plane lattice parameters of the film and those of the substrate, which reduce to a single mismatch value  $s_m$  in the particular case of square in-plane lattices for both substrate and film. Parenthetically, it is worth noting here that reliable values of the Poisson's ratio of perovskites are hard to come by. The convention is to cite values in the region of 0.3–0.4, but these are often based on hearsay. It is easier to find reliable values for the elastic compliances. The Poisson's ratio can then be related to the elastic compliances using  $\nu = S_{12}/S_{11}$ . For SrTiO<sub>3</sub> (STO) single crystals, the Poisson's ratio is actually about 0.22–0.24, considerably lower than often assumed.

Thin films are normally grown (or crystallized) at high temperatures on rigid substrates. Since the film and substrate rarely have the same thermal expansion coefficient, strains will generally develop upon cooling from the deposition temperature. In the case of epitaxial films, this process can be controlled by selecting substrates with a structure and lattice parameters closely matched to those of the film. In this way one can achieve coherent growth and hence, provided there is no relaxation, gain complete control over the in-plane strain state of the film. Thus, in any phase transition where there is a degree of spontaneous strain associated, one can use epitaxial strain to control, to some extent, the film properties. This trick has been used in the past to change critical temperatures in superconductors [121, 122], metal-insulator transitions [123, 124] and, of course, ferroelectrics [125–127].

Polarization requires a relative displacement of the ions in the unit cell, and hence a structural deformation. Accordingly, the onset of spontaneous polarization in ferroelectrics causes a spontaneous strain with respect to the paraelectric, more symmetric phase. Conversely, externally induced deformations of the crystal can change the polarization state and/or the polar symmetry. In the case of perovskite ferroelectrics (by far the most studied family), the onset of ferroelectricity is generally associated with a stretching of the unit cell along the polar direction, usually in a cubic–tetragonal transition. Trivially, then, if one forces the unit cell to be tetragonal by the use of compressive in-plane strains, the Curie temperature will rise and the room temperature polarization will also increase. Using standard Landau theory of phase transitions, it is possible to quantify the shift as a function of strain, which is given by the formula [30, 125, 126]:

$$\Delta T_C = 2C\epsilon_0 Q_{12} \frac{2}{S_{11} + S_{12}} s_m = 4C\epsilon_0 Q_{12} \frac{Y}{1 - \nu} s_m \quad 25.8$$

where  $C$  is the Curie constant,  $s_m$  is the lattice mismatch between the in-plane lattice parameters of the film and the substrate,  $Q_{12}$  and  $S_{ij}$  are the transverse electrostrictive coefficient and elastic compliances, and  $Y$ ,  $\nu$  are Young's modulus and the Poisson ratio, respectively. Since both  $Q_{12}$  and  $s_m$  are negative, compressive in-plane strains will increase the critical temperature of the ferroelectric. This effect has been known for a while [125–129], but it has recently been taken to new extremes, with shifts in the critical temperature of  $\text{BaTiO}_3$  from  $\sim 125$  to  $\sim 540$  °C [126]. A tensile in-plane strain, on the other hand, has been used to achieve room temperature ferroelectricity in  $\text{SrTiO}_3$  (STO) [130]. Since this material is normally paraelectric at all temperatures, this implies a shift in  $T_C$  from 0 to around 300 K. The shifts in  $T_C$  for strained  $\text{BaTiO}_3$  (BTO) and STO films are the biggest ever reported for any material.

The recent research on  $\text{SrTiO}_3$  also illustrates another of the potential uses of strain, which is to achieve crystallographic symmetries in the film that do not exist in bulk form [131]. This possibility was first theoretically predicted by Pertsev *et al.* [126], and has so far been experimentally achieved in STO [131],  $\text{BiFeO}_3$  (BFO) [132, 133] and  $\text{PbTiO}_3$  (PTO) [134].

The case of  $\text{BiFeO}_3$ , a ferroelectric antiferromagnet, has attracted much attention in the past few years for being one of the few simple materials displaying ferroelectric and magnetic order at room temperature. Although  $\text{BiFeO}_3$  is rhombohedral (space group  $R3c$ ) in bulk and, therefore, has the spontaneous polarization along the  $[111]_{\text{pc}}$  direction, the epitaxial growth of  $\text{BiFeO}_3$  films on  $[001]$ -oriented  $\text{SrTiO}_3$  substrates, which infer a misfit compressive strain of 1.1%, induces the tetragonal symmetry in very thin films, in which the polarization aligns normal to the film plane. Partial relaxation of the strain as the thickness is increased tilts the polarization and reduces the symmetry down to monoclinic [132, 133, 135], with a unit cell of the same type than that of monoclinic PZT (space group  $Cm$ , see Section 25.4). Further increment of the thickness to about 100 nm can rotate the polarization completely to lie along the  $[111]_{\text{pc}}$  direction and relax the structure to the bulk rhombohedral symmetry. Therefore, compressive biaxial strain in rhombohedral  $\text{BiFeO}_3$  has the same effect as chemical pressure in rhombohedral  $\text{PbZr}_{1-x}\text{Ti}_x\text{O}_3$  (increasing Ti content). Surprisingly, the strain and the associated change of symmetry barely affect the functional properties – or at least the remnant polarization – compared to bulk. While early works suggested a very low bulk polarization of only  $5 \mu\text{C}/\text{cm}^2$  in bulk [136], recent investigations in single crystals have shown polarizations of  $60 \mu\text{C}/\text{cm}^2$  along the  $[001]_{\text{pseudocubic}}$  direction, which correspond to  $\sim 100 \mu\text{C}/\text{cm}^2$  along the polar  $[111]$  direction [137] and which are almost identical to those measured in thin films. In spite of the large polarization, no huge piezoelectric responses have been detected in BFO, which may be due to the small

polarization–strain coupling in BiFeO<sub>3</sub> compared with that of PbTiO<sub>3</sub> or BaTiO<sub>3</sub> [138]. There are still many unknowns about this interesting ferroelectric, but the large number of groups currently dedicated to investigating it may change this picture soon.

Because of the clamping to the substrate, strain may change the polar symmetry of the films without changing the symmetry of the unit cell. The decoupling between the unit cell parameters (micro-strain) and the polarization due to substrate clamping has been observed in SrTiO<sub>3</sub> [131] and in PbTiO<sub>3</sub> thin films [134]. This means that  $(c/a-1)$ ,  $a$  and  $c$  being the tetragonal lattice parameters, is no longer an order parameter of the ferroelectric transition, which complicates characterization of ferroelectricity in very thin films.

### 25.5.1 Fully strained films: novel crystal symmetries and depolarizing fields

The discussion in the introduction focuses on a rather simplified picture, where every unit cell of the film experiences a strain equal to the mismatch with the substrate or misfit strain ( $s_m = a_{\text{subs}}/a_{\text{bulk}}-1$ ). This is true for non-relaxed, un-twinned films. For relaxation not to take place, the mismatch with the substrate ought to be small enough. Even for low misfits, because the strain energy scales with thickness, there will be a certain critical thickness above which formation of dislocations or formation of twin walls will take place to relax the strain. The critical thickness for the appearance of dislocations ( $t_c$ ) is smaller for larger misfit strain values, according to the equation [53, 54]:

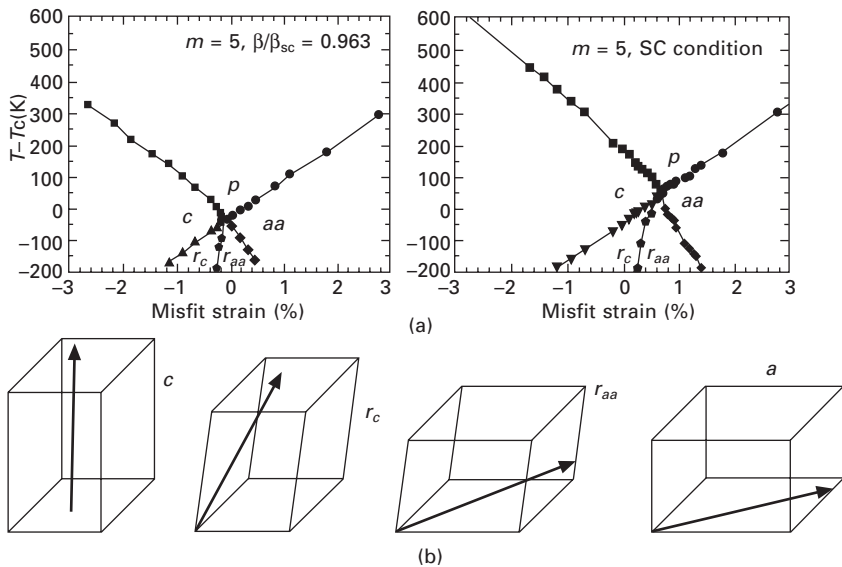
$$s_m = \frac{[b_x^2 + b_y^2 + (1 - \nu)b_z^2]}{8\pi(1 + \nu)b_x} \frac{1}{t_c} \ln\left(\beta \frac{t_c}{r_0}\right) \quad 25.9$$

where  $b_i$  are the coordinates of the Burger's vector of the dislocation,  $r_0$  is the lattice parameter, and  $\beta$  is an adimensional factor that is approximately 4 for perovskites [54]. Since there is not much choice of substrates, having fully strained and dislocation-free films is not easy and, when possible, it usually means dealing with very thin films, whose properties and structure are difficult to characterize.

Predictions about untwinned, defect-free films are somewhat easier (or so we believe) for theorists. Phenomenological Landau–Devonshire calculations, full first principles, as well as first-principles-based methods combined with Monte Carlo simulations have been used to predict phase stability under strain and/or the temperature vs. strain phase diagrams of single domain slabs of ferroelectric perovskites such as BaTiO<sub>3</sub>, PbTiO<sub>3</sub> and PbZr<sub>1-x</sub>Ti<sub>x</sub>O<sub>3</sub> [126, 136–142]. For BaTiO<sub>3</sub> single-domain films, most of the reported methods agree qualitatively on the strain phase diagram [126, 136, 142]. For relatively large compressive misfit strain values, the films have tetragonal symmetry

with the polarization aligned perpendicular to the film's plane ( $c$ -phase), while for relatively large tensile strain values the polarization lies down in-plane along the  $[110]_{pc}$  direction and the symmetry is orthorhombic ( $aa$ -phase) (see Fig. 25.11). For zero and intermediate strain values and at low temperatures, a low-symmetry phase ( $r$ -phase) occurs, which is, again, very similar to that observed at the MPBs of PZT and related materials, discussed in Section 25.4: it has no fixed symmetry axis so the polarization can rotate in the plane defined by the  $[001]_{pc}$  and  $[110]_{pc}$  directions. The  $r$ -phase is another example of a novel phase that does not exist in bulk  $\text{BaTiO}_3$  but could be stabilized in very thin films by strain engineering.

The case of  $\text{PbTiO}_3$  has proved to be more complex and the different predictions do not always agree with each other. While a similar  $r$ -phase is predicted by the Landau–Devonshire approach (when single-domain films are considered), in between the  $c$ -phase and the so-called  $a$ -phase (with polarization in plane along  $[100]_{pc}$ ) [126], the first-principles-based methods predict the coexistence of the  $c$  and  $a$  phases at intermediate strain values, with no  $r$ -phase [140, 141].



25.11 a) Temperature-misfit strain phase diagram of a single-domain, five unit cell thick film of  $\text{BaTiO}_3$  with realistic electrical boundary conditions (96.3% charge compensation at the surfaces) and short circuit conditions (no depolarizing field), as reported by Bo-Kuai Lai *et al.* [142] (b) The orientation of the polarization in the different phases. Reused with permission from Bo-Kuai Lai, Igor A. Kornev, L. Bellaiche, and G. J. Salamo, *Applied Physics Letters*, 86, 132904 (2005). Copyright 2005, American Institute of Physics.

For thin films, the electrical boundary conditions are also important in order to determine the polarization state, as discussed in Sections 25.2 and 25.3. Formation of periodic stripe domains with opposite polarizations is predicted in open-circuit conditions, in which the surface charges are not compensated and large depolarizing fields are created. These domain variants are elastically equivalent and the strain energy is, therefore, not modified (the film is not relaxed) by the formation of stripes of  $180^\circ$  domains. In this situation the net polarization of the materials is zero and, therefore, the film is strictly speaking non-ferroelectric, despite the ferroelectric alignment of the unit cells within each domain. It has been recently observed that the  $c/a$  ratio of the films, typically linked to the squared polarization via  $c/a = (c/a)_0 + aP^2$  does not decrease monotonously with decreasing thickness (as expected due to the increasing depolarizing field), but increases at very low thickness (a few unit cells) [143]. This has been associated with the creation of stripe domains at sufficiently large depolarizing fields. With the depolarizing fields avoided in this way, the dipole moment per unit cell and the  $c/a$  ratio are restored.

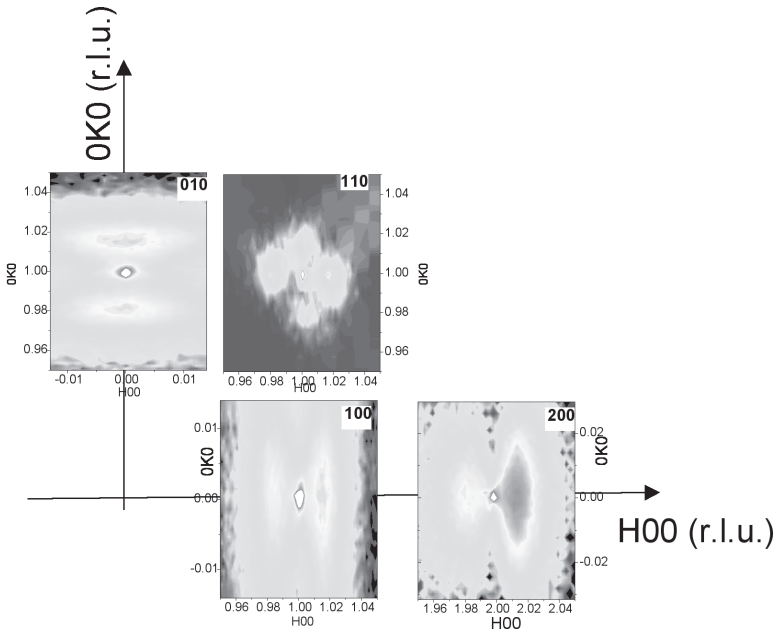
Other examples of the important influence of the electrical boundary conditions when dealing with very thin films are given by first-principles methods in  $\text{BaTiO}_3$  [21, 142] and  $\text{PbZr}_{0.5}\text{Ti}_{0.5}\text{O}_3$  [23] where the amount of compensating charges is shown to influence the phase stability greatly. In Fig. 25.11 the phase diagram of BTO has been calculated by Lai *et al.* for the case with no depolarizing field (ideal short circuit conditions) and for a situation in which 96.3% of the surface charges are compensated. It can be seen that such a seemingly small difference changes the phase diagram considerably [142].

## 25.5.2 $\text{PbTiO}_3$ under tensile strain

Fully strained 5 nm thin films of  $\text{PbTiO}_3$  under small tensile strain have been grown on  $\text{DyScO}_3$  substrates, by using RHEED-assisted pulsed laser deposition [134]. With this technique, thin films can be built unit cell-by-unit cell, allowing a great control at the atomic level [144].

A mapping of the reciprocal space performed by synchrotron X-ray diffraction on those films (see Fig. 25.12) has revealed an intensity modulation with in-plane periodicity of about 30 nm (70 unit cells), which is due to polar stripe domains, similar to those observed by Streiffer and coworkers [8, 145]. The reciprocal space points around which the satellites are shown reveal the symmetry of the polarization inside the stripes, while the direction of the modulation tells us about the orientation of the stripes.

The measurements have revealed that the stripes carry in-plane, as well as out-of-plane components of the polarization. Thus, it is shown that when  $\text{PbTiO}_3$  is grown under a small tensile strain (of about 1%), the polarization



**25.12** Selected regions of the reciprocal space in the  $(hk0)$  plane, around  $(100)$ ,  $(200)$ ,  $(010)$  and  $(110)$  Bragg peaks, of a  $\text{PbTiO}_3$  thin film deposited under tensile strain on a  $\text{DyScO}_3$  substrate. The measurements were obtained by synchrotron X-ray scattering in grazing incidence geometry. Next to the sharp Bragg reflections, broad intensity maxima are observed revealing a second periodicity of about 30 nm, which is due to polar stripe  $180^\circ$  domains. The same in-plane periodicity is observed in the  $(h0l)$  scattering plane. The orientation of these modulations and the Bragg peaks around which they appear indicate that the polarization in the stripes has both in-plane and out-of-plane component and it is, therefore, tilted away from the substrate normal (see ref. [134]).

tilts away from the substrate normal but does not reach a full in-plane configuration. This would be consistent with a phase of the type  $r$ , as the one predicted for  $\text{BaTiO}_3$ . As explained above, if the polarization has a larger freedom to deform, piezoelectric and dielectric responses could be drastically enhanced. Work is in progress to determine whether this is the case.

This work demonstrates that controlling the growth of thin films at the atomic level allows novel phases to be created even in chemically simple compounds. Some of these phases do not exist in bulk or cannot be synthesized by standard means. The epitaxial growth of thin films gives us access to tune the symmetry of materials at the unit cell level, which is crucial for defining their functional responses and to build model materials designed for specific functionalities.

### 25.5.3 Strain relaxation and domain formation

As already discussed, above certain critical thickness, the strain will relax. The system  $\text{PbTiO}_3$  on  $\text{DyScO}_3$  described above is a very special one because at the growth temperature (around 600 °C), above the Curie temperature, the in-plane lattices parameters of a [110]-oriented  $\text{DyScO}_3$  substrate and the bulk  $\text{PbTiO}_3$  are very close to each other [146]. This means that the films can grow coherently and without forming dislocations. Upon cooling below  $T_C$  the spontaneous strain will appear, but by then there is not enough energy to nucleate the dislocations. Hence, strain will be relaxed either through a transition to a new phase with tilted polar vectors, as in the ultra-thin films described in the previous section, or, for sufficiently thick films (above 5 nm) relaxation may take place by forming twins or 90° domains [147].

As explained by Pompe and collaborators in a series of seminal papers, a configuration of periodic *a/c/a* domain (with the *c* and *a* domains having polarization perpendicular and parallel, respectively, to the plane of the films) can relax the lattice mismatch [52, 148, 149]. The volume ratio of *a*-domains will depend on the so-called effective mismatch strain, with which dislocations that are created above the ferroelectric phase transition are taking into account to lower the nominal mismatch [52, 148, 149].

Recently, phase field models have been used to predict domain patterns under different strain conditions: under biaxial strain, under anisotropic substrates, etc. [150–152]. On the face of it, theory would appear to be slightly ahead of experiment; this is partly because it is difficult to find the right combination of real substrates and films that will allow the growth under the necessary conditions to replicate the theoretical calculations. On top of that, in the real world dislocations appear which relax strain, and adsorbates stick to the surfaces screening depolarizing fields, so results can, and often do, differ from predictions. Furthermore, even if dislocations can be prevented (as in [134]) and adsorbates minimized (as in [8, 144]), other subtle effects such as surface symmetry [4, 5] and electrode screening length [143] all contribute to the final polarization state of the films, so experimental results may disagree with theoretical predictions even under ideal growth conditions. Resolving the problem of domain states and polar symmetry in ferroelectric thin films is therefore going to require a two-way approach with experimentalists and theoreticians feeding off each other's findings and ideas. But then, that is the way it always has been in science.

## 25.6 Conclusion and future trends

This chapter aims at showing some of the current research trends regarding the interplay between size, symmetry and functional properties in ferroelectric thin films. It seems clear that, at the laboratory level, the ultimate limits for



size minimization in ferroelectric thin films have been reached (basically, there is no limit!). And the basic ingredients of the physics of ferroelectric thin films are also known: strain, strain relaxation and depolarization fields. The interplay between these can lead to new polar symmetries and/or new domain geometries, while the domain size is dictated by Kittel's law down to the nanometre regime.

In recent times some new research trends are emerging in the area of ferroelectrics. At present these are incipient, but look likely to grow in importance; below we list a few, with the aim not so much of discussing their physics, but rather inspiring the reader along new lines of work.

- *Non-planar nanoferroelectrics*: pioneering work has been done on ferroelectric nanotubes [153, 154], ferroelectric nanorods [155] and ferroelectric nanocolumns [156]. At present most of the work is just 'proof of principle' showing that these structures can be made and are indeed ferroelectric. Almost nothing is known yet, however, about the polar orientation, the depolarization effects, the existence of new polar symmetries, including vortex states [157], and the ultimate ferroic size limit in these confined geometries. One of the first new insights has been the analysis of domain size scaling in single-crystal 3D nanoferroelectrics, where an extension of the original Kittel's law has been proposed [158].

Three-dimensional effects in small ferroelectrics have more than just academic interest. As the size of planar ferroic structures is laterally reduced in order to increase the storage density of devices, even planar geometries begin to experience edge effects. Furthermore, in order to increase the storage density, 3D nanostructures are the only way forward, and indeed the International Technology Roadmap for Semiconductors indicates that these should reach the prototype stage by 2010 [159].

- *Self-organized ferrodevices*: as the drive towards miniaturization pushes on, new strategies for the fabrication of large arrays of very small ferrodevices become more urgent. An interesting idea is the use of self-organization or self-patterning. Self-organized arrays of ferroelectric islands [160, 161] and metallic electrodes on top of ferroelectric films [162] have been reported. The self-patterning in these structures is achieved through strain interactions via the substrate, leading to a distinct size and shape distribution of the resulting nano-islands [161].

But there are other approaches. Gregg and co-workers have achieved self-organized Tbit/inch<sup>2</sup> arrays by filling in self-organized nanoporous alumina with Pt electrodes [163]. They are also actively working with other strategies such as the use of close-packing spheres as templates. The achievement of well-registered self-organized nano-patterns is as much an engineering problem as a scientific one, with difficulties ranging from the mere fabrication to the addressing of the individual devices and

the modelling of the properties. But overcoming the difficulties has a big prize in terms of potential economic impact, so it is expected that research in this area will continue.

- *Domain walls*: domain walls have their own symmetry, distinct from that of the domains. They also have, accordingly, their own properties: recent reports suggest that domain walls in some piezoceramics have enhanced electromechanical properties owing to their low dimensionality. And while domain walls are very thin in typical ferroelectrics, there is reason to suspect that they may not be so in relaxors and multi-ferroics. Moreover, they can be broadened by the applied electric field [110]. Furthermore, according to Kittel's law, the density of domain walls increases as film thickness decreases, so in very thin films of the right materials the properties of the domain walls may dominate the physics. This idea is already being explored in relation to multi-ferroics [164], and it is likely to attract increased attention in the near future.

The above list is by no means exhaustive: hybrid materials and nanocomposites, flexoelectricity and graded ferroelectrics, integration with carbon nanotubes, non-oxide multiferroics, etc. are other promising areas of incipient research. The number of scientists working in ferroelectrics or multi-ferroics, and the number of high-impact articles being published suggest that this is a very dynamic and exciting area of research at the moment. Whether the interest will be sustained or whether it will fizzle out remains to be seen. But, from our point of view, there is promise in the factor that ferroelectric nanodevices (memories, micro-electromechanical sensors and actuators (MEMS), etc.) are already being made and marketed. The combination of exciting physics and commercial applications offers a solid platform to build upon. Our bet is that nanoferroelectrics are here to stay.

## 25.7 Further reading

In order to expand in the topics discussed here, we advise reading the following books on thin films and heteroepitaxy, deposition techniques and X-ray diffraction techniques applied to thin films:

*Thin Films: Heteroepitaxial Systems*, edited by W.K. Liu and M.B. Santos (Series on Directions in Condensed Matter Physics, vol. 15), World Scientific UK, 1999.

*Thin Films and Heterostructures for Oxide Electronics* by Satishchandra B. Ogale (Multifunctional Thin Films Series, Editors: O. Auciello and R. Ramesh), Springer, 2005.

*High Resolution X-Ray Scattering: From Thin Films to Lateral Nanostructures* by U. Pietsch, V. Holy and T. Baumbach (Series: Advanced Texts in Physics), Springer-Verlag, Second Edition, 2004.

We also recommend reading the following excellent, recent review articles (some of which are also referred to in the general list of references):

M. Dawber, K. M. Rabe, J. F. Scott, 'Physics of thin-film ferroelectric oxides', *Rev. Mod. Phys.* **77**, 1083 (2005).

D. Damjanovic, 'Contributions to the piezoelectric effect in ferroelectric single crystals and ceramics', *Journal of the American Ceramic Society*, **88**, 2663 (2005).

N. Setter *et al.* 'Ferroelectric thin films: Review of materials, properties, and applications', *J. Appl. Phys.* **100**, 051606 (2006).

J. F. Scott, 'Applications of modern ferroelectrics', *Science* **315**, 955 (2007).

M. Davis, 'Picturing the elephant: giant piezoelectric activity and the monoclinic phases of relaxor-ferroelectric single crystals', *Journal of Electroceramics* (2007) DOI: 10.1007/s 10832-007-9046-1.

Other reviews on the subject of Section 25.4 include:

B. Noheda, 'Structure and high-piezoelectricity in lead oxide solid solutions', *Current Opinion in Solid State & Materials Science*, **6**, 27 (2005)

B. Noheda and D. E. Cox, 'Bridging phases at the morphotropic boundaries of lead oxide solid solutions', *Phase Transitions*, **79**, 5–20 (2006)

## 25.8 Acknowledgements

Much of our pulsed laser deposition work has been done in collaboration with Arjen Janssens, Guus Rijnders and Dave H. A. Blank, of the University of Twente, and Ard Vlooswijk, Gijsbert Rispen and Christophe Daumont of the University of Groningen. Section 25.4 is based on an intensive collaboration with Dave E. Cox and the late Gen Shirane, which has been most rewarding from professional and personal points of view. We are also grateful to Oliver Seeck and Wolfgang Caliebe for their help at the beamline W1 in HASYLAB (DESY-Hamburg). We acknowledge the support of the Dutch Foundation for Fundamental Research (FOM) and the Dutch Science Organization (NWO). One of us (G.C.) acknowledges the financial support of a Marie Curie Fellowship.

## 25.9 References

1. M. Dawber, K. M. Rabe and J. F. Scott, 'Physics of thin-film ferroelectric oxides', *Rev. Mod. Phys.* **77**, 1083 (2005).
2. J. Padilla and D. Vanderbilt, 'Ab initio study of BaTiO<sub>3</sub> surfaces', *Phys. Rev. B* **56**, 1625 (1997).
3. B. Meyer, J. Padilla and D. Vanderbilt, 'Theory of PbTiO<sub>3</sub>, BaTiO<sub>3</sub>, and SrTiO<sub>3</sub> surfaces', *Faraday Discuss.* **114**, 395 (1999).
4. C. Bungaro and K. M. Rabe, 'Coexistence of antiferrodistortive and ferroelectric distortions at the PbTiO<sub>3</sub> (001) surface', *Phys. Rev. B* **71** 035420 (2005).

5. A. Munkholm, S. K. Streiffer, M. V. Ramana Murty, J. A. Eastman, C. Thompson, O. Auciello, L. Thompson, J. F. Moore and G. B. Stephenson, 'Antiferrodistortive Reconstruction of the  $\text{PbTiO}_3(001)$  Surface', *Phys. Rev. Lett.* **88**, 016101 (2002).
6. A. V. Bune, V. M. Fridkin, S. Ducharme, L. M. Blinov, S. P. Palto, A. V. Sorokin, S. G. Yudin and A. Zlatkin, 'Two-dimensional ferroelectric films', *Nature* **391** 874–877 (1998).
7. I. P. Batra and B. D. Silverman, 'Thermodynamic stability of thin ferroelectric films', *Sol. St. Commun.* **11**, 291 (1972).
8. D. D. Fong, G. B. Stephenson, S. K. Streiffer, J. A. Eastman, O. Auciello, P. H. Fuoss and C. Thompson, 'Ferroelectricity in ultrathin perovskite films', *Science* **304**, 1650–1653 (2004).
9. T. Mitsui and J. Furuichi, 'Domain structure of Rochelle salt and  $\text{KH}_2\text{PO}_4$ ', *Phys. Rev.* **90**, 193 (1953).
10. L. Landau and E. Lifshitz, 'Theory of the dispersion of magnetic permeability in ferromagnetic bodies', *Physikalische Zeitschrift der Sowjetunion* **8**, 153 (1935).
11. C. Kittel, 'Theory of the structure of ferromagnetic domains in films and small particles', *Phys. Rev.* **70**, 965 (1946).
12. N. A. Pertsev and A. G. Zembilgotov, 'Energetics and geometry of  $90^\circ$  domain structures in epitaxial ferroelectric and ferroelastic films', *J. Appl. Phys.* **78**, 6170 (1995).
13. A. G. Khachaturyan, *The Theory of Structural Transformations in Solids* (Wiley, New York, 1983).
14. A. Schilling, T. B. Adams, R. M. Bowman, J. M. Gregg, G. Catalan and J. F. Scott, 'Scaling of domain periodicity with thickness in  $\text{BaTiO}_3$  single crystal lamellae and other ferroics', *Phys. Rev. B* **74**, 024115 (2006).
15. V. A. Zhirnov, 'A contribution to the theory of domain walls in ferroelectrics', *Soviet Physics JETP* **35**, 822 (1959).
16. J. F. Scott, 'Nanoferroelectrics: statics and dynamics', *J. Phys.: Condens. Matter* **18** R361–R386 (2006).
17. G. Catalan, J. F. Scott, A. Schilling and J. M. Gregg, 'Wall thickness dependence of the scaling law for ferroic stripe domains', *J. Phys.: Condens. Matter* **19**, 132201 (2007).
18. F. De Guerville, I. Luk'yanchuk, L. Lahoche and M. El Marssi 'Modeling of ferroelectric domains in thin films and superlattices', *Mater. Sci. Eng. B* **120** 16–20 (2005).
19. A. Kopal, T. Bahnik and J. Fousek, 'Domain formation in thin ferroelectric films: the role of depolarization energy', *Ferroelectrics* **202**, 267 (1997).
20. R. Mehta, B. Silverman and J. T. Jacobs, 'Depolarization fields in thin ferroelectric films', *J. Appl. Phys.* **44**, 3379 (1973).
21. J. Junquera and P. Ghosez, 'Critical thickness for ferroelectricity in perovskite ultrathin films', *Nature* **422**, 506 (2003).
22. G. Gerra, A. K. Tagantsev, N. Setter and K. Parlinski, 'Ionic polarizability of conductive metal oxides and critical thickness for ferroelectricity in  $\text{BaTiO}_3$ ', *Phys. Rev. Lett.* **96** 107603 (2006).
23. I. Kornev, H. X. Fu and L. Bellaiche, 'Ultrathin films of ferroelectric solid solutions under a residual depolarizing field', *Phys. Rev. Lett.* **93**, 196104 (2004).
24. L. J. Sinnamon, R. M. Bowman and J. M. Gregg, 'Investigation of dead-layer thickness in  $\text{SrRuO}_3/\text{Ba}_{0.5}\text{Sr}_{0.5}\text{TiO}_3/\text{Au}$  thin-film capacitors', *Appl. Phys. Lett.* **78**, 1724 (2001).

25. K. Amanuma, T. Mori, T. Hase, T. Sakuma, A. Ochi and Y. Miyasaka, 'Ferroelectric properties of sol-gel derived  $\text{Pb}(\text{Zr}, \text{Ti})\text{O}_3$  thin films', *Jpn. J. Appl. Phys., Part 1* **32**, 4150 (1993).
26. M. Dawber and J. F. Scott, 'Models of electrode-dielectric interfaces in ferroelectric thin-film devices', *Jpn. J. Appl. Phys. Part 1* **41**, 6848 (2002).
27. C. S. Hwang, B. T. Lee, C. S. Kang, K. H. Lee, H. Cho, H. Hideki, W. D. Kim, S. I. Lee and M. Y. Lee, 'Depletion layer thickness and Schottky type carrier injection at the interface between Pt electrodes and  $(\text{Ba}, \text{Sr})\text{TiO}_3$  thin films', *J. Appl. Phys.* **85**, 287 (1999).
28. A. A. Sirenko, C. Bernhard, A. Golnik, A. M. Clark, J. Hao, W. Si and X. X. Xi, 'Soft-mode hardening in  $\text{SrTiO}_3$  thin films', *Nature (London)* **404**, 373 (2000).
29. A. M. Bratkovsky and A. P. Levanyuk, 'Smearing of phase transition due to a surface effect or a bulk inhomogeneity in ferroelectric nanostructures', *Phys. Rev. Lett.* **94**, 107601 (2005).
30. G. Catalan, L. J. Sinnamon and J. M. Gregg, 'The effect of flexoelectricity on the dielectric properties of inhomogeneously strained ferroelectric thin films', *J. Phys.: Condens. Matter* **16**, 2253 (2004).
31. M. M. Saad, P. Baxter, R. M. Bowman, J. M. Gregg, F. D. Morrison and J. F. Scott 'Intrinsic dielectric response in ferroelectric nano-capacitors', *J. Phys.: Condens. Matter* **16**, L451 (2004).
32. G. Catalan, B. Noheda, J. McAneney, L. J. Sinnamon and J. M. Gregg, 'Strain gradients in epitaxial ferroelectrics', *Phys. Rev. B* **72**, 020102(R) (2005).
33. S. P. Alpay, I. B. Misirlioglu, V. Nagarajan and R. Ramesh, 'Can interface dislocations degrade ferroelectric properties?', *Appl. Phys. Lett.* **85**, 2044 (2004).
34. M. Stengel and N. A. Spaldin, 'Origin of the dielectric dead layer in nanoscale capacitors', *Nature* **443**, 679-682 (2006).
35. H. Tabata, H. Tanaka and T. Kawai, 'Formation of artificial  $\text{BaTiO}_3/\text{SrTiO}_3$  superlattices using pulsed-laser deposition and their dielectric-properties', *App. Phys. Lett.* **65**, 1970 (1994).
36. B. D. Qu, M. Evstigneev, D. J. Johnson and R. H. Prince, 'Dielectric properties of  $\text{BaTiO}_3/\text{SrTiO}_3$  multilayered thin films prepared by pulsed laser deposition', *Appl. Phys. Lett.* **72**, 1394 (1998).
37. A. Erbil, Y. Kim and R. A. Gerhardt, 'Giant permittivity in epitaxial ferroelectric heterostructures', *Phys. Rev. Lett.* **77**, 1628 (1996).
38. H. M. Christen, E. D. Specht, D. P. Norton, M. F. Chisholm and L. A. Boatner, 'Long-range ferroelectric interactions in  $\text{KTaO}_3/\text{KNbO}_3$  superlattice structures', *Appl. Phys. Lett.* **72**, 2535 (1998).
39. D. O'Neill, R. M. Bowman and J. M. Gregg, 'Dielectric enhancement and Maxwell-Wagner effects in ferroelectric superlattice structures', *Appl. Phys. Lett.* **77**, 1520 (2000).
40. G. Catalan, D. O'Neill, R. M. Bowman and J. M. Gregg, 'Relaxor features in ferroelectric superlattices: a Maxwell-Wagner approach', *Appl. Phys. Lett.* **77**, 3078 (2000).
41. M. H. Corbett, R. M. Bowman, J. M. Gregg and D. T. Foord., 'Enhancement of dielectric constant and associated coupling of polarization behavior in thin film relaxor superlattices', *Appl. Phys. Lett.* **79**, 815 (2001).
42. S. Ríos, A. Ruediger, A. Q. Jiang, J. F. Scott, H. Lu and Z. Chen, 'Orthorhombic strontium titanate in  $\text{BaTiO}_3$ - $\text{SrTiO}_3$  superlattices', *J. Phys.: Condens. Matter* **15**, L305-L309 (2003).

43. J. Zhang, A. Visinoiniu, F. Heyroth, F. Syrowatka, M. Alexe, D. Hesse and H. S. Leipner, 'High-resolution electron energy-loss spectroscopy of BaTiO<sub>3</sub>/SrTiO<sub>3</sub> multilayers', *Phys. Rev. B* **71**, 064108 (2005).
44. H. N. Lee, H. M. Christen, M. F. Chisholm, C. M. Rouleau and D. H. Lowndes, 'Strong polarization enhancement in asymmetric three-component ferroelectric superlattices', *Nature* **433**, 395 (2005).
45. M. Dawber, C. Lichtensteiger, M. Cantoni, M. Veithen, P. Ghosez, K. Johnston, K. M. Rabe and J. M. Triscone, 'Unusual behavior of the ferroelectric polarization in PbTiO<sub>3</sub>/SrTiO<sub>3</sub> superlattices', *Phys. Rev. Lett.* **95**, 177601 (2005).
46. V. A. Stephanovich, I. A. Luk'yanchuk and M. G. Karkut, 'Domain-enhanced interlayer coupling in ferroelectric/paraelectric superlattices', *Phys. Rev. Lett.* **94**, 047601 (2005).
47. J. V. Mantese, N. W. Schubring, A. L. Micheli, A. B. Catalan, M. S. Mohammed, R. Naik and G. W. Auner, 'Slater model applied to polarization graded ferroelectrics', *Appl. Phys. Lett.* **71**, 2047 (1997).
48. G. Poullain, R. Bouregba, B. Vilquin, G. Le Rhun and H. Murray, 'Graded ferroelectric thin films: possible origin of the shift along the polarization axis', *Appl. Phys. Lett.* **81**, 5015 (2002).
49. F. Jin, G. W. Auner, R. Naik, N. W. Schubring, J. V. Mantese, A. B. Catalan and A. L. Micheli, 'Giant effective pyroelectric coefficients from graded ferroelectric devices', *Appl. Phys. Lett.* **73**, 2838 (1998).
50. S. Zhong, Z.-G. Ban, S. P. Alpay and J. V. Mantese, 'Large piezoelectric strains from polarization graded ferroelectrics', *Appl. Phys. Lett.* **89**, 142913 (2006).
51. B. S. Kwak, A. Erbil, B. J. Wilkens, J. D. Budai, M. F. Chisholm and L. A. Boatner, 'Strain relaxation by domain formation in epitaxial ferroelectric thin films', *Phys. Rev. Lett.* **68**, 3733–3736 (1992).
52. J. S. Speck and W. Pompe, 'Domain configurations due to multiple misfit relaxation mechanisms in epitaxial ferroelectric thin films. I. Theory', *J. Appl. Phys.* **76**, 466 (1994).
53. J. W. Mathews and A. E. Blackeslee, 'Defects in epitaxial multilayers. I. Misfit dislocations', *J. Cryst. Growth* **27**, 118 (1974).
54. P. A. Langjahr, F. F. Lange, T. Wagner and M. Rühle, 'Lattice mismatch accommodation in perovskite films on perovskite substrates', *Acta Mater.* **46**, 773 (1998).
55. J.-L. Maurice, F. Pailloux, A. Barthélémy, O. Durand, D. Imhoff, R. Lyonnet, A. Rocher, J.-P. Contour, 'Strain relaxation in the epitaxy of La<sub>2/3</sub>Sr<sub>1/3</sub>MnO<sub>3</sub> grown by pulsed-laser deposition on SrTiO<sub>3</sub>(001)', *Philos. Mag.* **83**, 3201 (2003).
56. Sh. Kogan, 'Piezoelectric effect during inhomogeneous deformation and acoustic scattering of carriers in crystals', *Sov. Phys. – Solid State* **5**, 2069 (1964).
57. A. K. Tagantsev, 'Theory of flexoelectric effect in crystals', *Sov. Phys. JETP* **61**, 1246 (1985).
58. L. E. Cross, 'Flexoelectric effects: charge separation in insulating solids subjected to elastic strain gradients', *J. Mat. Sci.* **41**, 53 (2006).
59. A. Gruverman, B. J. Rodriguez, A. I. Kingon, R. J. Nemanich, A. K. Tagantsev, J. S. Cross and M. Tsukada 'Mechanical stress effect on imprint behavior of integrated ferroelectric capacitors', *Appl. Phys. Lett.* **83**, 728 (2003).
60. B. Jaffe, W. R. Cook and H. Jaffe, *Piezoelectric Ceramics* (Academic Press, London, 1971).
61. G. Shirane and A. Takeda, 'Phase Transitions in Solid Solutions of PbZrO<sub>3</sub> and PbTiO<sub>3</sub>', *J. Phys. Soc. Jpn* **7**, 5 (1952).

62. G. Shirane and K. Suzuki, 'Crystal structure of  $\text{Pb}(\text{Zr-Ti})\text{O}_3$ ', *J. Phys. Soc. Jpn* **7**, 333 (1952).
63. K. Carl and K. H. Hardtl, 'Origin of the maximum in electromechanical activity in  $\text{Pb}(\text{Zr}_x\text{Ti}_{1-x})\text{O}_3$  ceramics near morphotropic phase boundary', *Phys. Status Solidi A Appl. Res.* **8**, 87 (1971).
64. K. Kakegawa *et al.*, 'Compositional fluctuation and properties of  $\text{Pb}(\text{Zr,Ti})\text{O}_3$ ', *Solid State Commun.* **24**, 769 (1977).
65. W. W. Cao and L. E. Cross, 'Theoretical-model for the morphotropic phase-boundary in lead zirconate lead titanate solid-solution', *Phys. Rev. B* **47**, 4825 (1993).
66. S. K. Mishra, D. Pandey and A. P. Singh, 'Effect of phase coexistence at morphotropic phase boundary on the properties of  $\text{Pb}(\text{Zr}_x\text{Ti}_{1-x})\text{O}_3$  ceramics', *Appl. Phys. Lett.* **69**, 1707 (1996).
67. T. R. Shrout *et al.*, 'Dielectric behavior of single-crystals near the  $(1-X)\text{Pb}(\text{Mg}_{1/3}\text{Nb}_{2/3})\text{O}_3$ - $(X)\text{PbTiO}_3$  morphotropic phase-boundary', *Ferroelectrics Letters Section* **12**, 63 (1990).
68. S.-E. Park and T. R. Shrout, 'Ultrahigh strain and piezoelectric behavior in relaxor based ferroelectric single crystals', *J. Appl. Phys.* **82**, 1804 (1997).
69. G. S. Xu *et al.*, 'Third ferroelectric phase in PMNT single crystals near the morphotropic phase boundary composition', *Phys. Rev. B* **64**, 020102 (2001).
70. Z. G. Ye *et al.*, 'Monoclinic phase in the relaxor-based piezoelectric/ferroelectric  $\text{Pb}(\text{Mg}_{1/3}\text{Nb}_{2/3})\text{O}_3$ - $\text{PbTiO}_3$  system', *Phys. Rev. B* **64**, 184114 (2001).
71. A. K. Singh and D. Pandey, 'Structure and the location of the morphotropic phase boundary region in  $(1-x)[\text{Pb}(\text{Mg}_{1/3}\text{Nb}_{2/3})\text{O}_3]$ - $x\text{PbTiO}_3$ ', *J. Phys. Condensed Matter* **13**, L931 (2001).
72. B. Noheda *et al.*, 'Phase diagram of the ferroelectric relaxor  $(1-x)\text{PbMg}_{1/3}\text{Nb}_{2/3}\text{O}_3$ - $x\text{PbTiO}_3$ ', *Phys. Rev. B* **66**, 054104, (2002).
73. J. M. Kiat *et al.*, 'Monoclinic structure of unpoled morphotropic high piezoelectric PMN-PT and PZN-PT compounds', *Phys. Rev. B* **65**, 064106 (2002).
74. R. Haumont *et al.*, 'Cationic-competition-induced monoclinic phase in high piezoelectric  $(\text{PbSc}_{1/2}\text{Nb}_{1/2}\text{O}_3)(1-x)-(\text{PbTiO}_3)(x)$  compounds', *Phys. Rev. B* **68**, 014114 (2003).
75. L. Bellaiche, A. Garcia and D. Vanderbilt, 'Finite-temperature properties of  $\text{Pb}(\text{Zr}_{1-x}\text{Ti}_x)\text{O}_3$  alloys from first principles', *Phys. Rev. Lett.* **84**, 5427(2000).
76. H. Fu and R. E. Cohen, 'Polarization rotation mechanism for ultrahigh electromechanical response in single-crystal piezoelectrics', *Nature* **403**, 281 (2000).
77. Y. Ishibashi and M. Iwata, 'Morphotropic phase boundary in solid solution systems of perovskite-type oxide ferroelectrics', *Jpn. J. Appl. Phys. (Part 2)* **37**, L985 (1998).
78. Y. Ishibashi and M. Iwata, 'A theory of morphotropic phase boundary in solid-solution systems of perovskite-type oxide ferroelectrics', *Jpn J. Appl. Phys. (Part 1)* **38**, 800 (1999).
79. D. Vanderbilt and M. H. Cohen, 'Monoclinic and triclinic phases in higher-order Devonshire theory', *Phys. Rev. B* **63**, 094108 (2001).
80. X. H. Du *et al.*, 'Crystal orientation dependence of piezoelectric properties of lead zirconate titanate near the morphotropic phase boundary', *Appl. Phys. Lett.* **72**, 2421 (1998).
81. D. V. Taylor and D. Damjanovic, 'Piezoelectric properties of rhombohedral  $\text{Pb}(\text{Zr}, \text{Ti})\text{O}_3$  thin films with (100), (111), and "random" crystallographic orientation', *Appl. Phys. Lett.* **76**, 1615 (2000).

82. B. Noheda *et al.*, 'A monoclinic ferroelectric phase in the  $\text{Pb}(\text{Zr}_{1-x}\text{Ti}_x)\text{O}_3$  solid solution', *Appl. Phys. Lett.* **74**, 2059 (1999).
83. B. Noheda *et al.*, 'Tetragonal-to-monoclinic phase transition in a ferroelectric perovskite: the structure of  $\text{PbZr}_{0.52}\text{Ti}_{0.48}\text{O}_3$ ', *Phys. Rev. B* **61**, 8687 (2000).
84. B. Noheda *et al.*, 'Stability of the monoclinic phase in the ferroelectric perovskite  $\text{PbZr}_{1-x}\text{Ti}_x\text{O}_3$ ', *Phys. Rev. B* **63**, 014103 (2001).
85. L. D. Landau and E. M. Lifshitz, *Statistical Physics*, Part 1, 3rd ed. (Pergamon Press, New York, 1980).
86. A. M. Glazer, S. A. Mabud and R. Clarke, 'Powder profile refinement of lead zirconate titanate at several temperatures. 1.  $\text{PbZr}_{0.9}\text{Ti}_{0.1}\text{O}_3$ ', *Acta Crystallographica Section B*, **34**, 1060 (1978).
87. S. Teslic, T. Egami and D. Viehland, 'Local atomic structure of PZT and PLZT studied by pulsed neutron scattering', *J. Phys. Chem. Solids* **57**, 1537 (1996).
88. D. L. Corker *et al.*, 'A neutron diffraction investigation into the rhombohedral phases of the perovskite series  $\text{PbZr}_{1-x}\text{Ti}_x\text{O}_3$ ', *J. Phys.: Condens. Matter* **10**, 6251 (1998).
89. R. R. Ragini, S. K. Mishra and D. Pandey, 'Room temperature structure of  $\text{Pb}(\text{Zr}_x\text{Ti}_{1-x})\text{O}_3$  around the morphotropic phase boundary region: a Rietveld study', *J. Appl. Phys.* **92**, 3266 (2002).
90. A. M. Glazer *et al.* 'Influence of short-range and long-range order on the evolution of the morphotropic phase boundary in  $\text{Pb}(\text{Zr}_{1-x}\text{Ti}_x)\text{O}_3$ ', *Phys. Rev. B* **70** 184123 (2004).
91. W. Dmowski *et al.*, 'Structure of  $\text{Pb}(\text{Zr}, \text{Ti})\text{O}_3$  near the morphotropic phase boundary', in *Fundamental Physics of Ferroelectrics 2001*, edited by H. Krakauer, AIP Conf. Proc. 582 (AIP, Melville, New York, 2001), pp. 33–44.
92. D. Cao *et al.*, 'Local structure study of the off-center displacement of Ti and Zr across the morphotropic phase boundary of  $\text{PbZr}_{1-x}\text{Ti}_x\text{O}_3$  ( $x = 0.40, 0.47, 0.49, 0.55$ )', *Phys. Rev. B* **70**, 224102 (2004).
93. A. G. Souza *et al.*, 'Monoclinic phase of  $\text{PbZr}_{0.52}\text{Ti}_{0.48}\text{O}_3$  ceramics: Raman and phenomenological thermodynamic studies', *Phys. Rev. B* **61**, 14283 (2000).
94. I. Grinberg, V. R. Cooper and A. M. Rappe, 'Relationship between local structure and phase transitions of a disordered solid solution', *Nature* **419**, 909 (2002).
95. I. Grinberg, V. R. Cooper and A. M. Rappe, 'Oxide chemistry and local structure of  $\text{PbZr}_x\text{Ti}_{1-x}\text{O}_3$  studied by density-functional theory supercell calculations', *Phys. Rev. B* **69** 144118 (2004).
96. Z. Wu and H. Krakauer, 'First-principles calculations of piezoelectricity and polarization rotation in  $\text{Pb}(\text{Zr}_{0.5}\text{Ti}_{0.5})\text{O}_3$ ', *Phys. Rev. B* **68**, 014112 (2003).
97. J. M. Kiat *et al.*, 'Anharmonicity and disorder in simple and complex perovskites: a high energy synchrotron and hot neutron diffraction study'. *J. Phys. Condensed Matter* **12**, 8411 (2000).
98. C. Malibert *et al.*, 'Order and disorder in the relaxor ferroelectric perovskite  $\text{PbSc}_{1/2}\text{Nb}_{1/2}\text{O}_3$  (PSN): comparison with simple perovskites  $\text{BaTiO}_3$  and  $\text{PbTiO}_3$ ', *J. Phys. Condensed Matter* **9**, 7485 (1997).
99. A. K. Singh and D. Pandey, 'Evidence for  $M_B$  and  $M_C$  phases in the morphotropic phase boundary region of  $(1-x)[\text{Pb}(\text{Mg}_{1/3}\text{Nb}_{2/3})\text{O}_3]_x\text{PbTiO}_3$ : a Rietveld study', *Phys. Rev. B* **67**, 064102 (2003).
100. R. Haumont *et al.*, 'Cationic-competition-induced monoclinic phase in high piezoelectric  $(\text{PbSc}_{1/2}\text{Nb}_{1/2}\text{O}_3)_{(1-x)}-(\text{PbTiO}_3)_x$  compounds', *Phys. Rev. B* **68**, 014114 (2003).



101. R. Haumont *et al.*, 'Morphotropic phase boundary of heterovalent perovskite solid solutions: experimental and theoretical investigation of  $\text{PbSc}_{1/2}\text{Nb}_{1/2}\text{O}_3\text{-PbTiO}_3$ ', *Phys. Rev. B* **71**, 104106 (2005).
102. Z. G. Ye, 'Crystal chemistry and domain structure of relaxor piezoerystals', *Current Opin. Solid State Mater. Sci.* **6**, 35 (2002).
103. B. Noheda *et al.*, 'Polarization rotation via a monoclinic phase in the piezoelectric 92%  $\text{PbZn}_{1/3}\text{Nb}_{2/3}\text{O}_3\text{-8% PbTiO}_3$ ', *Phys. Rev. Lett.* **86**, 3891 (2001).
104. B. Noheda *et al.*, 'Electric-field-induced phase transitions in rhombohedral  $\text{Pb}(\text{Zn}_{1/3}\text{Nb}_{2/3})(1-x)\text{Ti}_x\text{O}_3$ ', *Phys. Rev. B* **65**, 224101 (2002).
105. K. Ohwada *et al.*, 'Neutron diffraction study of the irreversible  $\text{R-M}_A\text{-M}_C$  phase transition in single crystal  $\text{Pb}[(\text{Zn}_{1/3}\text{Nb}_{2/3})(1-x)\text{Ti}_x]\text{O}_3$ ' *J. Phys. Soc. Jap* **70**, 2778 (2001).
106. L. Bellaiche, A. Garcia and D. Vanderbilt, 'Electric-field induced polarization paths in  $\text{Pb}(\text{Zr}_{1-x}\text{Ti}_x)\text{O}_3$  alloys', *Phys. Rev. B* **64**, 060103 (2001).
107. E. H. Kisi *et al.*, 'The giant piezoelectric effect: electric field induced monoclinic phase or piezoelectric distortion of the rhombohedral parent', *J. Phys. Condensed Matter* **15**, 3631 (2003).
108. M. Davis, D. Damjanovic and N. Setter, 'Electric-field-, temperature-, and stress-induced phase transitions in relaxor ferroelectric single crystals', *Phys. Rev. B* **73**, 014115 (2006).
109. Y. M. Jin *et al.*, 'Conformal miniaturization of domains with low domain-wall energy: monoclinic ferroelectric states near the morphotropic phase boundaries', *Phys. Rev. Lett.* **91**, 197601 (2003).
110. Y. M. Jin *et al.*, 'Adaptive ferroelectric states in systems with low domain wall energy: tetragonal microdomains', *J. Appl. Phys.* **94**, 3629 (2003).
111. W. F. Rao and Y. U. Wang, 'Domain wall broadening mechanism for domain size effect of enhanced piezoelectricity in crystallographically engineered ferroelectric single crystals', *Appl. Phys. Lett.* **90**, 041915 (2007).
112. D. Damjanovic, F. Brem and N. Setter, 'Crystal orientation dependence of the piezoelectric  $d_{33}$  coefficient in tetragonal  $\text{BaTiO}_3$  as a function of temperature', *Appl. Phys. Lett.* **80**, 652 (2002).
113. M. Budimir, D. Damjanovic and N. Setter, 'Piezoelectric anisotropy-phase transition relations in perovskite single crystals', *J. Appl. Phys.* **94**, 6753 (2003).
114. M. Budimir, D. Damjanovic and N. Setter, 'Large enhancement of the piezoelectric response in perovskite crystals by electric bias field antiparallel to polarization', *Appl. Phys. Lett.* **85**, 2890 (2004).
115. M. Budimir, D. Damjanovic and N. Setter, 'Enhancement of the piezoelectric response of tetragonal perovskite single crystals by uniaxial stress applied along the polar axis: a free-energy approach', *Phys. Rev. B* **72**, 064107 (2005).
116. Z. Kutnjak, J. Petzelt and R. Blinc, 'The giant electromechanical response in ferroelectric relaxors as a critical phenomenon', *Nature* **441**, 956 (2006).
117. M. Davis, 'Picturing the elephant: giant piezoelectric activity and the monoclinic phases of relaxor-ferroelectric single crystals', *J. Electroceramics* **19**, 25–47 (2007).
118. Z. Wu and R. E. Cohen, 'Pressure-induced anomalous phase transitions and colossal enhancement of piezoelectricity in  $\text{PbTiO}_3$ ', *Phys. Rev. Lett.* **95**, 037601 (2005).
119. Sani *et al.*, 'High-pressure phases in highly piezoelectric  $\text{PbZr}_{0.52}\text{Ti}_{0.48}\text{O}_3$ ', *Phys. Rev. B* **69**, 020105 (2004).
120. J. Rouquette *et al.*, 'Pressure-induced rotation of spontaneous polarization in monoclinic and triclinic  $\text{PbZr}_{0.52}\text{Ti}_{0.48}\text{O}_3$ ', *Phys. Rev. B* **71**, 024112 (2005).

121. J.-P. Locquet, J. Perret, J. Fompeyrine, E. Machler, J. W. Seo and G. Van Tendeloo, 'Doubling the critical temperature of  $\text{La}_{1.9}\text{Sr}_{0.1}\text{CuO}_4$  using epitaxial strain', *Nature* **394**, 453 (1998).
122. G. Rijnders, S. Curras, M. Huijben, D. H. A. Blank and H. Rogalla, 'Influence of substrate-film interface engineering on the superconducting properties of  $\text{YBa}_2\text{Cu}_3\text{O}_7$ ', *Appl. Phys. Lett.* **84**, 1150 (2004).
123. S. Jin, T. H. Tiefel, M. McCormack, R. A. Fastnacht, R. Ramesh and L. H. Chen, 'Thousandfold Change in Resistivity in Magnetoresistive La-Ca-Mn-O Films', *Science* **264**, 413 (1994).
124. G. Catalan, R. M. Bowman and J. M. Gregg, 'Metal-insulator transitions in  $\text{NdNiO}_3$  thin films', *Phys. Rev. B* **62**, 7892–7900 (2000).
125. G. A. Rossetti, L. E. Cross and K. Kushida, 'Stress induced shift of the Curie point in epitaxial  $\text{PbTiO}_3$  thin films', *Appl. Phys. Lett.* **59**, 2524 (1991).
126. N. A. Pertsev, A. G. Zembilgotov and A. K. Tagantsev, 'Effect of mechanical boundary conditions on phase diagrams of epitaxial ferroelectric thin films'. *Phys. Rev. Lett.* **80**, 1988–1991 (1998).
127. K. J. Choi, M. Biegalski, Y. L. Li, A. Sharan, J. Schubert, R. Uecker, P. Reiche, Y. B. Chen, X. Q. Pan, V. Gopalan, L.-Q. Chen, D. G. Schlom and C. B. Eom, 'Enhancement of ferroelectricity in strained  $\text{BaTiO}_3$  thin films', *Science* **306**, 1005 (2004).
128. C. L. Canedy, Hao Li, S. P. Alpay, L. Salamanca-Riba, A. L. Roytburd and R. Ramesh, 'Dielectric properties in heteroepitaxial  $\text{Ba}_{0.6}\text{Sr}_{0.4}\text{TiO}_3$  thin films: Effect of internal stresses and dislocation-type defects', *Appl. Phys. Lett.* **77**, 1695 (2000).
129. L. J. Sinnamon, R. M. Bowman and J. M. Gregg, 'Thickness-induced stabilization of ferroelectricity in  $\text{SrRuO}_3/\text{Ba}_{0.5}\text{Sr}_{0.5}\text{TiO}_3/\text{Au}$  thin film capacitors', *Appl. Phys. Lett.* **81**, 889 (2002).
130. J. H. Haeni *et al.*, 'Room-temperature ferroelectricity in strained  $\text{SrTiO}_3$ ', *Nature* **430**, 758 (2004).
131. F. He, B. O. Wells and S. M. Shapiro, 'Strain phase diagram and domain orientation in  $\text{SrTiO}_3$  thin films', *Phys. Rev. Lett.* **94**, 176101 (2005).
132. J. Wang, J. B. Neaton, H. Zheng, V. Nagarajan, S. B. Ogale, B. Liu, D. Viehland, V. Vaithyanathan, D. G. Schlom, U. V. Waghmare, N. A. Spaldin, K. M. Rabe, M. Wuttig and R. Ramesh, 'Epitaxial  $\text{BiFeO}_3$  multiferroic thin film heterostructures', *Science* **299**, 1719 (2003).
133. J. Li, J. Wang, M. Wuttig, R. Ramesh, N. Wang, B. Ruetter, A. P. Pyatakov, A. K. Zvezdin and D. Viehland, 'Dramatically enhanced polarization in (001), (101), and (111)  $\text{BiFeO}_3$  thin films due to epitaxial-induced transitions', *Appl. Phys. Lett.* **84**, 5261 (2004).
134. G. Catalan, A. Janssens, G. Rispens, S. Csiszar, O. Seeck, G. Rijnders, D. H. A. Blank and B. Noheda, 'Polar domains in lead titanate films under tensile strain', *Phys. Rev. Lett.* **96**, 127602 (2006).
135. H. Bea, M. Bibes, S. Petit, J. Kreisel and A. Barthelemy, 'Structural distortion and magnetism of  $\text{BiFeO}_3$  epitaxial thin films: a Raman spectroscopy and neutron diffraction study', *Phil. Mag. Letters* **87**, 165–174, (2007).
136. J. R. Teague, R. Gerson and W. J. James, 'Dielectric hysteresis in single crystal  $\text{BiFeO}_3$ ', *Solid State Commun.* **8**, 1073 (1970).
137. D. Lebeugle, D. Colson, A. Forget and M. Viret, 'Very large spontaneous electric polarization in  $\text{BiFeO}_3$  single crystals at room temperature and its evolution under cycling fields', *Appl. Phys. Lett.* **91**, 22907 (2007).

138. C. Ederer and N. A. Spaldin, 'Influence of strain and oxygen vacancies on the magnetoelectric properties of bismute ferrite', *Phys. Rev. B* **71**, 224103 (2005).
139. O. Diéguez, S. Tinte, A. Antons, C. Bungaro, J. B. Neaton, K. M. Rabe and D. Vanderbilt, 'Ab initio study of the phase diagram of epitaxial BaTiO<sub>3</sub>', *Phys. Rev. B* **69**, 212101 (2004).
140. C. Bungaro and K. M. Rabe, 'Epitaxially strained [001]-(PbTiO<sub>3</sub>)<sub>1</sub>-(PbZrO<sub>3</sub>)<sub>1</sub> superlattice and PbTiO<sub>3</sub> from first principles', *Phys. Rev. B* **69**, 184101 (2004).
141. O. Diéguez, K. M. Rabe and D. Vanderbilt, 'First-principles study of epitaxial strain in perovskites', *Phys. Rev. B* **72**, 144101 (2005).
142. B.-K. Lai, I. A. Kornev, L. Bellaiche and G. J. Salamo, 'Phase diagrams of epitaxial BaTiO<sub>3</sub> ultrathin films from first principles', *Appl. Phys. Lett.* **86**, 132904 (2005).
143. C. Lichtensteiger, M. Dawber, N. Stucki, J.-M. Triscone, J. Hoffman, J.-B. Yau, C. H. Ahn, L. Despont and P. Aebi, 'Monodomain to polydomain transition in ferroelectric PbTiO<sub>3</sub> thin films with La<sub>0.67</sub>Sr<sub>0.3</sub>MnO<sub>3</sub> electrodes', *Appl. Phys. Lett.* **90**, 052907 (2006).
144. D. H. A. Blank, G. Koster, G. J. H. M. Rijnders and H. Rogalla, 'In-situ monitoring by RHEED during pulsed laser deposition', *Appl. Surface Sci.* **138**, 17 (1999).
145. S. K. Streiffer, J. A. Eastman, D. D. Fong, Carol Thompson, A. Munkholm, M. V. Ramana Murty, O. Auciello, G. R. Bai and G. B. Stephenson, 'Observation of nanoscale 180° stripe domains in ferroelectric PbTiO<sub>3</sub> thin films', *Phys. Rev. Lett.* **89**, 067601 (2002).
146. M. D. Biegalski, J. H. Haeni, S. Trolier-McKinstry, D. G. Schlom, C. D. Brandle, A. J. Ven Graitis, 'Thermal expansion of the new perovskite substrates DySCO<sub>3</sub> and GdSCO<sub>3</sub>', *J. Mat. Res.* **20**, 952 (2005).
147. A. H. G. Vlooswijk, B. Noheda, G. Catalan, A. Janssens, B. Barcones, G. Rijnders and D. H. A. Blank, 'Smallest 90 degrees domains in epitaxial ferroelectric films', *Applied Physics Letters* **91**, 112901 (2007).
148. J. S. Speck, A. Seifert, W. Pompe and R. Ramesh, 'Domain configurations due to multiple misfit relaxation mechanisms in epitaxial ferroelectric thin films. II. Experimental verification and implications', *J. Appl. Phys.* **76**, 477 (1994).
149. J. S. Speck, A. C. Daykin, A. Seifert, A. E. Romano and W. Pompe, 'Domain configurations due to multiple misfit relaxation mechanisms in epitaxial ferroelectric thin films. III. Interfacial defects and domain misorientations', *J. Appl. Phys.* **78**, 1696 (1995).
150. J. Slutsker, A. Artemev and A. L. Roytburd, 'Engineering of elastic domain structures in a constrained layer', *Acta Materialia* **52**, 1731 (2004).
151. A. Artemev, J. Slutsker and A. L. Roytburd, 'Phase field modeling of self-assembling nanostructures in constrained films', *Acta Materialia* **53** 3425 (2005).
152. Y. L. Li, S. Y. Hu and L. Q. Chen, 'Ferroelectric domain morphologies of (001) PbZr<sub>1-x</sub>Ti<sub>x</sub>O<sub>3</sub> epitaxial thin films', *J. Appl. Phys.* **97**, 034112 (2005).
153. F. D. Morrison, L. A. Ramsay and J. F. Scott, 'High-aspect-ratio piezoelectric strontium-bismuth-tantalate nanotubes', *J. Phys.: Cond. Matter* **15**, 527 (2003).
154. Y. Luo, I. Szafraniak, N. D. Zakharov, V. Nagarajan, M. Steinhart, R. B. Wehrspohn, J. H. Wendorff, R. Ramesh and M. Alexe, 'Nanoshell tubes of ferroelectric lead zirconate titanate and barium titanate', *Appl. Phys. Lett.* **83**, 440 (2003).
155. J. E. Spanier, A. M. Kolpak, J. J. Urban, I. Grinberg, L. Ouyang, W. Soo Yun, A. M. Rappe and H. Park, 'Ferroelectric phase transition in individual single-crystalline BaTiO<sub>3</sub> nanowires', *Nano Letters* **6**, 735 (2006).

156. A. Schilling, R. M. Bowman, J. M. Gregg, G. Catalan and J. F. Scott, 'Ferroelectric domain periodicities in nanocolumns of single crystal barium titanate', *Appl. Phys. Lett.* **89**, 212902 (2006).
157. I. I. Naumov, L. Bellaiche and H. X. Fu, 'Unusual phase transitions in ferroelectric nanodisks and nanorods', *Nature* **432**, 7018 (2004).
158. G. Catalan, A. Schilling, J. F. Scott and J. M. Gregg, 'Domains in three-dimensional ferroelectric nanostructures: theory and experiment', *J. Phys.: Cond. Matter* **19**, 132201 (2007).
159. <http://www.itrs.net/Links/2005ITRS/PIDS2005.pdf>
160. I. Szafraniak, C. Harnagea, R. Scholz, S. Bhattacharyya, D. Hesse and M. Alexe, 'Ferroelectric epitaxial nanocrystals obtained by a self-patterning method', *Appl. Phys. Lett.* **83**, 2211 (2003).
161. M. Dawber, I. Szafraniak, M. Alexe and J. F. Scott, 'Self-patterning of arrays of ferroelectric capacitors: description by theory of substrate mediated strain interactions', *J. Phys.: Cond. Matter.* **15**, L677 (2003).
162. M. Alexe, J. F. Scott, C. Curran, N. D. Zakharov, D. Hesse and A. Pignolet, 'Self-patterning nano-electrodes on ferroelectric thin films for gigabit memory applications', *Appl. Phys. Lett.* **73**, 1592 (1998).
163. P. R. Evans, X. Zhu, P. Baxter, M. McMillen, J. McPhillips, F. D. Morrison, J. F. Scott, R. J. Pollard, R. M. Bowman and J. M. Gregg, 'Toward self-assembled ferroelectric random access memories: hard-wired switching capacity arrays with almost  $\text{Tb}/\text{in}^2$  densities', *Nano. Letters* **7**, 1134–1137 (2007).
164. M. Mostovoy, 'Ferroelectricity in spiral magnets', *Phys. Rev. Lett.* **96**, 067601 (2006).

## Processing of textured piezoelectric and dielectric perovskite-structured ceramics by the reactive-templated grain growth method

---

T KIMURA, Keio University, Japan

### 26.1 Enhancement of piezoelectric properties of perovskite-structured ceramics by texture formation

The physical properties of sintered ceramics are determined not only by composition but also by microstructure. The methods to enhance the physical properties of ceramics include (1) the search for new materials, (2) the selection of additives and (3) the optimization of microstructure. The development of texture is a technique belonging to category (3). The orientation of each grain in sintered compacts determines the physical properties of the compacts, because many physical properties are tensors and depend on the direction of measurement with respect to the crystal axes (Newnham, 2005). Texture engineering intends to enhance the performance of ceramics by controlling grain orientation. The constants that describe piezoelectric properties are third rank tensors. Therefore, the magnitude of piezoelectric properties depends on the orientation of grains composing sintered compacts.

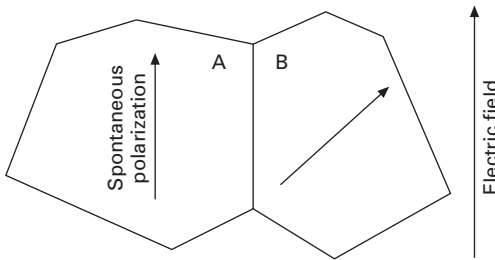
The enhancement of piezoelectric properties by texture formation has been reported for several compounds belonging to bismuth layer structure, tungsten bronze and perovskite families (Kimura, 2006). Among these families, the former two have a highly anisotropic crystal structure and spontaneous polarization is restricted along a specific direction (Jaffe *et al.*, 1971). Therefore, the formation of texture enhances the piezoelectric properties of compounds belonging to these families by aligning the direction of spontaneous polarization (Takenaka and Sakata, 1980; Granahan *et al.*, 1981).

The perovskite structure is relatively isotropic and has many equivalent directions of spontaneous polarization: 6 for tetragonal, 12 for orthorhombic and 8 for rhombohedral, and the benefit of texture is thought to be not so great. However, large increases in the piezoelectric constants have been reported (Table 26.1). The possible origins of these increases are explained as follows:

Table 26.1 Enhancement of piezoelectric properties by texture formation

Compounds	Properties	Random	Textured	References
$\text{Bi}_{0.5}(\text{Na}_{0.85}\text{K}_{0.15})_{0.5}\text{TiO}_3$	$k_p$ (%)	0.295	0.402	Tani (1998)
	$d_{31}$ (pC/N)	-36.7	-57.4	Tani (1998)
	$g_{31}$ ( $10^{-3}\text{V m/N}$ )	7.21	11.2	Tani (1998)
$94.5\text{Bi}_{0.5}\text{Na}_{0.5}\text{TiO}_3-5.5\text{BaTiO}_3$	$d_{33}$ (pC/N)	110	200	Yilmaz <i>et al.</i> (2003b)
	$d_{33}$ (pC/N)	580	1310	Kwon <i>et al.</i> (2005)
$0.675\text{Pb}(\text{Mg}_{1/3}\text{Nb}_{2/3})\text{O}_3-0.325\text{PbTiO}_3$	$d_{31}$ (pC/N)	-195	-282	Sabolsky <i>et al.</i> (2003)
	$k_{33}$ (%)	0.673	0.755	Sabolsky <i>et al.</i> (2003)
	$d_{33}$ (pC/N)	300	416	Saito <i>et al.</i> (2004)
$(\text{K}_{0.44}\text{Na}_{0.52}\text{Li}_{0.04}) \times (\text{Nb}_{0.86}\text{Ta}_{0.10}\text{Sb}_{0.04})\text{O}_3$	$d_{33}$ (pC/N)			

$k_p$ ,  $k_{33}$ , coupling factors;  $d_{33}$ ,  $d_{31}$ ,  $g_{31}$ , piezoelectric coefficients.



26.1 Direction of spontaneous polarization of grains A and B and that of external electric field.

- The magnitude of strain caused by an external electric field is dependent on the angle between the directions of spontaneous polarization and external field, and the development of texture reduces the misorientation angle (Takenaka and Sakata, 1980). Figure 26.1 shows two adjacent grains, A and B. The direction of spontaneous polarization is parallel to that of the external electric field in grain A but not in grain B. Grain A has the largest strain. Therefore, a larger strain is expected in textured materials than materials with randomly oriented grains, because all grains in the textured materials have the orientation of grain A.
- The difference in the magnitude of strain of two adjacent grains lowers overall strain; grain B with a smaller strain suppresses the deformation of grain A with a larger strain, resulting in a small overall strain. In textured materials, the difference in the magnitude of strain of two adjacent

grains is small, and a large overall strain is expected. This results in large piezoelectric coefficients.

- Another origin is attributed to engineered domain configuration (Kwon *et al.*, 2005). Higher piezoelectric constants along a certain direction than along the direction of spontaneous polarization are expected for materials with the engineered domain configuration (Wada *et al.*, 1999). For a tetragonal BaTiO<sub>3</sub> single crystal, for example, the piezoelectric constant  $d_{33}$  is higher when an electric field is applied along the [111] direction than the [001] direction. In polycrystalline materials with randomly oriented grains, the direction of the applied electric field with respect to the crystallographic axes is dependent on the orientation of each grain and  $d_{33}$  of overall compact is the average value of  $d_{33}$  for each grain. In textured materials, an electric field is applied along a certain direction, and the materials textured with the engineered domain configuration are expected to have high piezoelectric properties.

## 26.2 Reactive-templated grain growth method

The methods to prepare textured ceramics are based on the conventional ceramic processing processes: preparation of powder particles, consolidation of the particles and sintering of the compacts. The techniques to develop texture are (1) the application of pressure during heating, i.e. hot pressing (Igarashi *et al.*, 1978) and hot forging (Takenaka and Sakata, 1980) and (2) the alignment of particles in green compacts. In the latter technique, the particles are aligned during consolidation of powder particles by the application of magnetic field (Bedoya *et al.*, 2002; Makiya *et al.*, 2003) or under flow velocity gradient (Holmes *et al.*, 1979). This chapter deals with the preparation of textured materials by the flow velocity gradient, i.e. tape casting of slurries containing anisometric particles by a doctor-blade process. When the slurry passes under the blade, a flow velocity gradient develops. This gradient causes the alignment of anisometric particles in concentrated slurries (Watanabe *et al.*, 1989). Thus, a cast sheet with aligned anisometric particles is obtained. Sintered compacts are prepared from the cast sheet by a method similar to that used for the fabrication of multilayer ceramic capacitors (Kahn *et al.*, 1988).

Anisometric particles are easily prepared by molten salt synthesis (Kimura and Yamaguchi, 1987). Salt such as NaCl, KCl, Na<sub>2</sub>SO<sub>4</sub> and K<sub>2</sub>SO<sub>4</sub> is used as molten salt. Starting oxides (and carbonates) are mixed with the salt and heated at temperatures above the melting point of the salt. In the Bi<sub>4</sub>Ti<sub>3</sub>O<sub>12</sub> case, for example, Bi<sub>2</sub>O<sub>3</sub> and TiO<sub>2</sub> with the stoichiometric ratio are mixed with KCl or a mixture of NaCl and KCl. The product phase (Bi<sub>4</sub>Ti<sub>3</sub>O<sub>12</sub>) is formed by the reaction between starting oxides in molten salt. Prolonged heating at high temperatures causes particle growth by Ostwald ripening

(Rahaman, 2003) and particles with a well-developed crystal habit are obtained. When the compound has a highly anisotropic crystal structure, anisometric particles are obtained; for the compounds belonging to the bismuth layer structure and tungsten bronze families, plate-like and needle-like particles are formed, respectively (Kimura and Yamaguchi, 1987). Figure 26.2 shows the photomicrograph of plate-like  $\text{Bi}_4\text{Ti}_3\text{O}_{12}$  particles prepared using molten KCl. Generally speaking, the particle size and aspect ratio are determined mainly by the heating temperature and the chemical species of the salt (Kimura and Yamaguchi, 1987).

The anisometric particles are mixed with small equiaxed particles with the same composition to make slurries (Horn *et al.*, 1999; Duran *et al.*, 2000). In green compacts, the anisometric particles are dispersed in the small equiaxed particles (matrix particles). Furthermore, they align with specific particle orientation; for plate-like particles, their plate face is aligned parallel to the sheet surface, and for needle-like particles, their needle axis is aligned parallel to the casting direction. Sintering of green compact causes densification and grain growth. In many cases, the anisometric particles grow at the expense of matrix particles. Thus, the volume fraction of grains with the desired orientation increases and textured materials are obtained. Ideally, all the matrix particles are consumed. This process is called templated grain growth (TGG), because the anisometric particles act as templates for texture development (Messing *et al.*, 2004).

The application of the TGG process to compounds with the perovskite structure has been limited because of the lack of appropriate templates. Platelike  $\text{BaTiO}_3$ ,  $\text{SrTiO}_3$  and  $\text{Ba}_6\text{Ti}_{17}\text{O}_{40}$  are prepared and used as templates for  $\langle 001 \rangle$ -textured  $\text{Pb}(\text{Mg}_{1/3}\text{Nb}_{2/3})\text{O}_3\text{-PbTiO}_3$  (Sabolsky *et al.*, 2001a,b),  $\langle 001 \rangle$ -textured  $\text{Bi}_{0.5}\text{Na}_{0.5}\text{TiO}_3\text{-BaTiO}_3$  (Yilmaz *et al.*, 2003a) and  $\langle 111 \rangle$ -textured  $\text{BaTiO}_3$  (Kimura *et al.*, 2005) by the TGG process. However,  $\text{SrTiO}_3$  and  $\text{Ba}_6\text{Ti}_{17}\text{O}_{40}$  are non-piezoelectric and the presence of these particles in

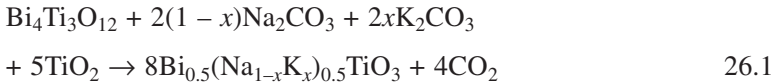


26.2 Photomicrograph of plate-like  $\text{Bi}_4\text{Ti}_3\text{O}_{12}$  particles prepared in molten KCl.

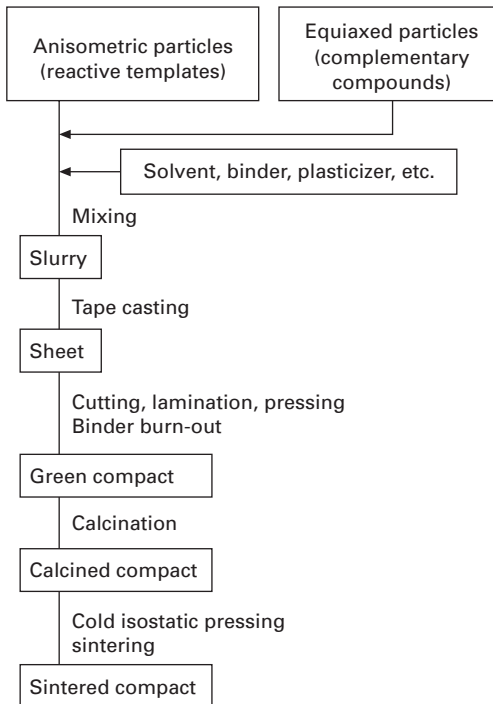


the sintered compacts reduces the piezoelectric constants (Yang *et al.*, 1998; Nakai and Fukuoka, 1999). It is desirable to obtain textured ceramics using the template particles with the same composition as the matrix particles. This is made possible by a reactive-templated grain growth (RTGG) process (Tani and Kimura, 2006; Kimura, 2006).

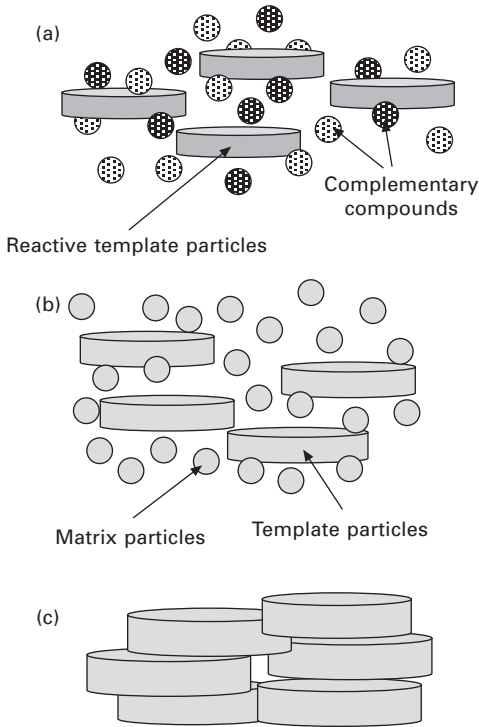
Figure 26.3 shows the flowchart of the preparation of textured ceramics by the RTGG process, using  $\text{Bi}_{0.5}(\text{Na}_{1-x}\text{K}_x)_{0.5}\text{TiO}_3$  (BNKT) as an example. At first, a precursor (reactive template) of a target compound is selected. The reactive template must be anisometric and contain the elements of the target compound; in the BNKT case, plate-like  $\text{Bi}_4\text{Ti}_3\text{O}_{12}$  particles (Fig. 26.2) are selected. Then, the reaction to form the target compound is designed, and complementary compounds for the target compound are determined. In the BNKT case, the reaction is



and the complementary compounds are  $\text{Na}_2\text{CO}_3$ ,  $\text{K}_2\text{CO}_3$  and  $\text{TiO}_2$ . The mixture of reactive template and complementary compounds is mixed with solvent, of reactive template and complementary compounds is mixed with solvent,



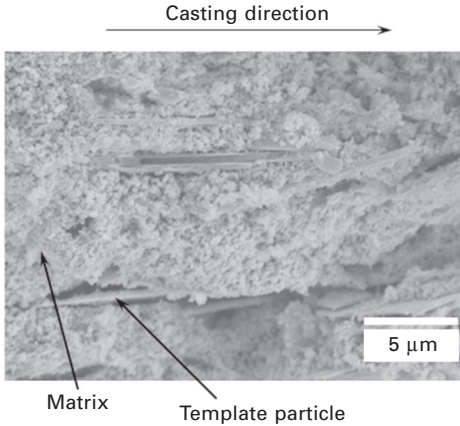
26.3 Flowchart of RTGG process.



26.4 Structures of (a) green compact, (b) calcined compact and (c) sintered compact.

binder, plasticizer and other materials to form slurry. The slurry is tape cast to form thin sheets in which plate-like  $\text{Bi}_4\text{Ti}_3\text{O}_{12}$  particles are aligned with their plate face parallel to the sheet surface (Fig. 26.4a). The sheets are cut, laminated and pressed to form a green compact with the desired dimensions. The compact is heated to remove organic ingredients and, most importantly, to form the target compound (BNKT) by an *in situ* reaction [26.1]. Figure 26.4(b) schematically shows the structure of a calcined compact, and Fig. 26.5 shows the microstructure of a calcined BNKT compact. The large plate-like and small equiaxed grains are present in the calcined compact. These grains are BNKT. The plate-like grains are oriented with their plate face parallel to the sheet surface.

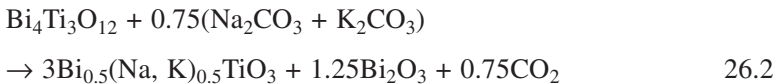
It is well known that volume expansion is accompanied by the formation of perovskite phase from the starting materials (Tsutai *et al.*, 2001). This is the situation for the BNKT case. The volume expansion reduces the density of compact after calcination, and causes slow densification during sintering. Therefore, the compact after calcination is subject to cold isostatic pressing (CIP). By this procedure, the green compacts with about 60% of the theoretical density are obtained.



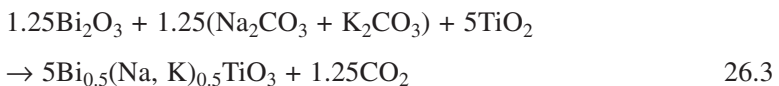
26.5 Microstructure of calcined compact of BNKT.

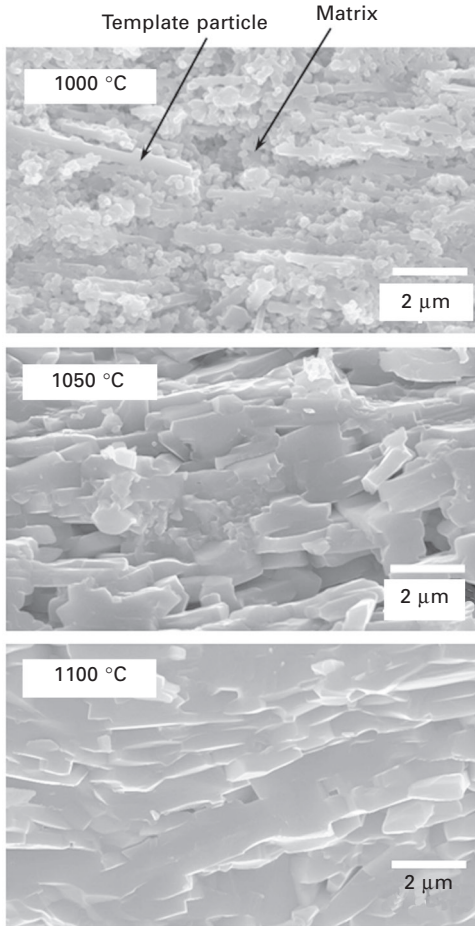
The compact after CIP is sintered at appropriate temperatures. Figure 26.4(c) schematically shows the structure of a sintered compact and Fig. 26.6 shows the microstructure development during sintering of BNKT. The comparison of these microstructures with the microstructure of the calcined compact (Fig. 26.5) indicates the growth of template grains. In the BNKT case, the template grains are plate-like and have a rectangular cross-section. Sintering increases mainly their thickness without changing cross-sectional shape, and finally, the compact is composed of only plate-like grains. Figure 26.7 shows their X-ray diffraction patterns; the intensity of (100) and (200) peaks increases as the sintering temperature is increased, indicating the development of <100> texture. These results indicate that the BNKT template grains with their <100> direction perpendicular to the compact surface grow at the expense of randomly oriented matrix grains, leading to an increase in the degree of orientation.

Because texture development is caused by the growth of template grains, their relative amount and growth rate are important to obtain highly textured compacts. The relative amount of template and matrix grains is determined by the formation reaction of target compound. In the case of reaction [26.1], template BNKT grains are formed by the diffusion of Na<sub>2</sub>O and K<sub>2</sub>O into Bi<sub>4</sub>Ti<sub>3</sub>O<sub>12</sub> particles by reaction [26.2] (Seno and Tani, 1999):



Bi<sub>2</sub>O<sub>3</sub> produced by reaction [26.2] reacts with Na<sub>2</sub>CO<sub>3</sub>, K<sub>2</sub>CO<sub>3</sub>, and TiO<sub>2</sub> and forms equiaxed BNKT grains by reaction [26.3]:

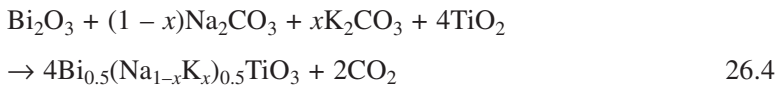




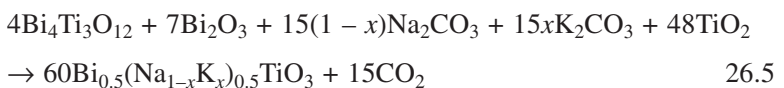
26.6 Microstructures of sintered compact of BNKT.

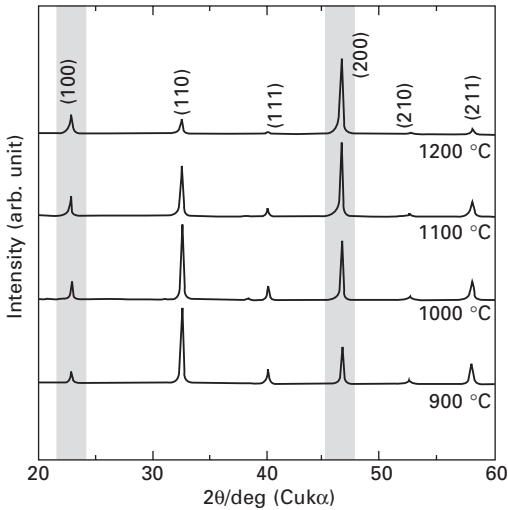
These grains are matrix grains. Therefore, the ratio of template to matrix grains is 3:5.

It is impossible to increase the relative amount of template grains, but the relative amount of matrix grains can be increased by adding the predetermined amount of starting materials which are shown in reaction [26.4]:



When the amount of template grains is designed to be 20%, the reaction is expressed by [26.5]:





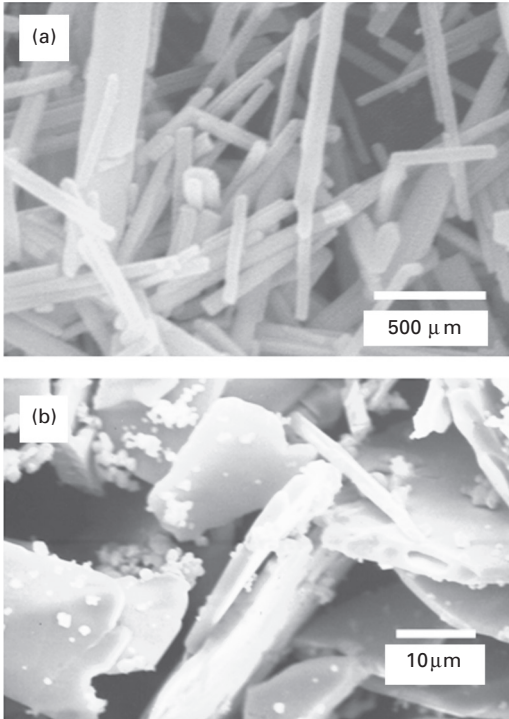
26.7 X-ray diffraction patterns of textured BNKT ceramics sintered at various temperatures.

### 26.3 Selection of reactive templates

The selection of reactive templates is important to prepare textured ceramics by the RTGG process (West and Payne, 2003). The conditions required for the reactive template are that (1) it contains all or a part of elements composing the target compound, (2) its crystal structure is highly anisotropic and anisometric particles can be obtained, (3) it has crystallographic relations with the target compound and (4) the target compound is formed by the unidirectional diffusion of complementary compound into the reactive template.

$\text{Bi}_4\text{Ti}_3\text{O}_{12}$  fulfills all these conditions required for the reactive template of  $\langle 100 \rangle$ -textured BNKT: (1) it contains Bi and Ti, (2) it has a layer structure and plate-like particles can be easily obtained (Fig. 26.2), (3) it contains perovskite blocks sandwiched by  $\text{Bi}_2\text{O}_2$  layers and the perovskite blocks have a structure similar to that of BNKT (Jaffe *et al.*, 1971) and (4) BNKT is formed by the unidirectional diffusion of  $\text{Na}_2\text{O}$  and  $\text{K}_2\text{O}$  into  $\text{Bi}_4\text{Ti}_3\text{O}_{12}$  and the structure of perovskite blocks is preserved (Seno and Tani, 1999).

Reactive templates other than  $\text{Bi}_4\text{Ti}_3\text{O}_{12}$  are required for target compounds containing elements other than Bi and Ti. The data reporting topotaxy are useful for selecting the reactive templates. In the  $\text{BaTiO}_3$  case, for example,  $\text{TiO}_2$  and  $\text{Ba}_6\text{Ti}_{17}\text{O}_{40}$  are used for  $\langle 110 \rangle$  and  $\langle 111 \rangle$  texture, respectively (Sugawara *et al.*, 2001; Kimura, 2006). In the  $\text{TiO}_2$  case, the topotaxial relation of  $[001]_{\text{rutile}} // [110]_{\text{BaTiO}_3}$  and  $[100]_{\text{rutile}} // [111]_{\text{BaTiO}_3}$  has been reported (Suyama *et al.*, 1979). Furthermore,  $\text{BaTiO}_3$  is formed by the unidirectional diffusion of BaO into  $\text{TiO}_2$  (Suyama and Kato, 1977), and needle-like  $\text{TiO}_2$  particles with  $\langle 001 \rangle$  parallel to the needle axis are commercially available

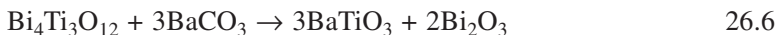


26.8 Photomicrographs of (a) needle-like  $\text{TiO}_2$  and (b) plate-like  $\text{Ba}_6\text{Ti}_{17}\text{O}_{40}$  particles.

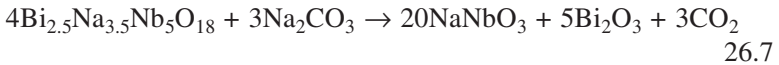
(Fig. 26.8a). In the  $\text{Ba}_6\text{Ti}_{17}\text{O}_{40}$  case, the relation of  $(001)_{\text{Ba}_6\text{Ti}_{17}\text{O}_{40}} // (111)_{\text{BaTiO}_3}$  and  $(010)_{\text{Ba}_6\text{Ti}_{17}\text{O}_{40}} // (110)_{\text{BaTiO}_3}$  has been reported (Kravec *et al.*, 1987; Senz *et al.*, 1998). Plate-like  $\text{Ba}_6\text{Ti}_{17}\text{O}_{40}$  particles with  $\langle 001 \rangle$  perpendicular to the plate face can be easily obtained by molten salt synthesis (Fig. 26.8b) (Sugawara *et al.*, 2001; Kimura *et al.*, 2005).

Plate-like  $\text{BaTiO}_3$  particles made by the Remeika method are one of the candidates for the template of  $\text{BaTiO}_3$ -containing materials (Sabolsky *et al.*, 2001a). The  $\langle 100 \rangle$  direction lies perpendicular to the plate face and the particles can be used as templates for  $\langle 100 \rangle$  texture. The problem is their low aspect ratio.

The plate-like particles with a high aspect ratio can be easily obtained by molten salt synthesis for compounds belonging to the bismuth layer structure family,  $\text{Bi}_4\text{Ti}_3\text{O}_{12}$ ,  $\text{CaBi}_4\text{Ti}_4\text{O}_{15}$ ,  $\text{SrBi}_4\text{Ti}_4\text{O}_{15}$ ,  $\text{BaBi}_4\text{Ti}_4\text{O}_{15}$  and so forth. However, these compounds contain  $\text{Bi}_2\text{O}_3$  as one of the constituents, and this must be removed before use as the reactive template for compounds that do not contain Bi. Sintering under vacuum is necessary for the preparation of  $\langle 100 \rangle$ -textured  $\text{BaTiO}_3$  (Sugawara *et al.*, 2004) using reaction [26.6]:



$\text{Bi}_2\text{O}_3$  formed by reaction [26.6] is removed from the product phase by heating under vacuum because of the high vapor pressure of  $\text{Bi}_2\text{O}_3$ . The reaction in molten salt is another route (Saito *et al.*, 2004). Plate-like  $\text{NaNbO}_3$  particles are prepared from plate-like  $\text{Bi}_{2.5}\text{Na}_{3.5}\text{Nb}_5\text{O}_{18}$  particles, which is a member of the bismuth layer structure family. At first plate-like  $\text{Bi}_{2.5}\text{Na}_{3.5}\text{Nb}_5\text{O}_{18}$  particles are prepared by molten salt synthesis and then reacted with  $\text{Na}_2\text{CO}_3$  in molten salt to form plate-like  $\text{NaNbO}_3$  particles, which are used as reactive templates for  $(\text{Na},\text{K})\text{NbO}_3$ -based materials. The reaction in molten salt is



and  $\text{Bi}_2\text{O}_3$  produced is removed by washing the reaction product with acid. A similar technique is applied to the preparation of plate-like  $\text{SrTiO}_3$  particles (Saito and Takao, 2006).

## 26.4 Factors determining texture development

The degree of orientation is determined by several factors. The most important factor is the alignment of reactive template particles in the cast sheets, which is determined by the motion of particles in the slurries. When the particles are well dispersed in the slurries, the particles are easily aligned by tape casting (Watanabe *et al.*, 1989). However, when the particles are agglomerated (coagulated) in the slurries, the alignment of particles is difficult (Sugawara *et al.*, 2001). For example, plate-like  $\text{Ba}_6\text{Ti}_{17}\text{O}_{40}$  particles form agglomerates with  $\text{BaCO}_3$ , and these agglomerates have an equiaxed shape and have no tendency to align by flow velocity gradient. The dispersion of particles is controlled by several parameters (Pugh, 1994). In a single component system, the control of particle dispersion is rather easy. However, the RTGG process uses slurries containing multicomponents (reactive template and complementary compounds), resulting in the possibility of heterocoagulation (Hunter, 1993). The proper selection of dispersant is necessary to prepare well-dispersed slurries. Therefore, the confirmation of particle orientation in the cast sheets by X-ray diffraction is necessary before further processing.

In the RTGG process, calcined compacts are composed of template and matrix grains as shown in Figs 26.4(b) and 26.5, and texture develops by the growth of template grains at the expense of matrix grains (Fig. 26.6). Therefore, the degree of orientation is determined by the relative amount of template grains and their growth rate. In this sense, the situation is the same as that occurred in the TGG process (Messing *et al.*, 2004).

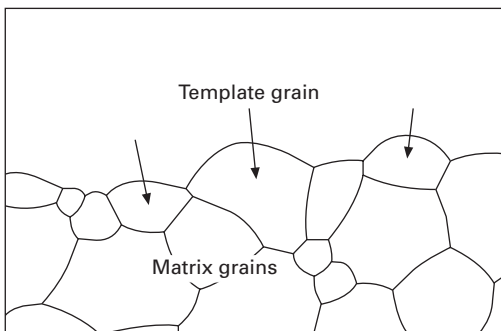
Because piezoelectric ceramics are subject to poling before use, their density must be high; at least 95% of the theoretical density is desired. Therefore, the sintered density as well as the degree of orientation is an

important parameter. The densification rate is determined by the particle size; powders with small particle sizes are usually desired. The size of template grains is determined by the size of reactive template particles. The reactive template particles are usually made by molten salt synthesis, and the synthesis at high temperatures results in particles of large sizes. For example, the diameter and thickness are about 10 and 0.5  $\mu\text{m}$ , respectively, for plate-like particles, whereas the particle size of matrix particles is usually submicrometer.

Calcined compacts used in the RTGG process are composed of anisometric template grains and equiaxed matrix grains. Large template grains act as rigid inclusions in the densification process and hinder the densification of the matrix phase (Belmonte *et al.*, 1995; Rahaman, 2003; Ozer *et al.*, 2006). The degree of hindrance is proportional to the amount of template grains (De Jonghe *et al.*, 1986). Therefore, a small amount of template grains is desirable from the viewpoint of densification. However, too small an amount results in the limited development of texture. Densification and texture development are in a trade-off relationship, and the optimum template amount is determined by experiments. Usually, 5–20 volume % is selected.

Texture develops by the selective growth of template grains (Fukuchi *et al.*, 2002). When a large template grain is surrounded by small matrix grains, the template grain is surrounded by concave grain boundaries (Fig. 26.9). The grain boundaries migrate towards the center of curvature, resulting in the growth of template grain. The rate of grain boundary migration is inversely proportional to the radius of curvature, which is proportional to the matrix grain size. Therefore, it is desirable to use small matrix particles for texture development. A small particle size is also desirable for densification.

When the matrix particles are formed by *in situ* reaction in green compacts as in the BNKT case (reaction [26.3]), the selection of particle sizes of starting materials is important. There is a certain compound that determines the matrix particle size of the target compound. In the BNKT case,  $\text{TiO}_2$  determines the particle size of matrix BNKT, and small  $\text{TiO}_2$  is favorable for texture development (Fuse and Kimura, 2006).



26.9 Migration of boundary between template and matrix grains.



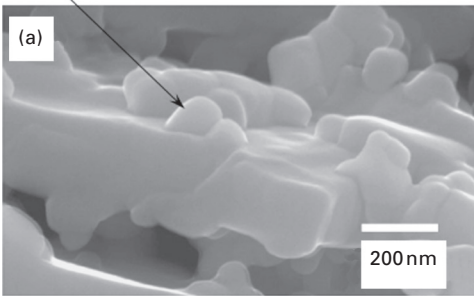
The most widely used technique to increase grain boundary mobility is the addition of a liquid phase (Rahaman, 2003). The liquid phase promotes material transport by a solution-precipitation mechanism. Therefore, the use of liquid phase is reported for  $\text{Al}_2\text{O}_3$  (Seabaugh *et al.*, 1997), mullite (Hong and Messing, 1999),  $\text{Pb}(\text{Mg}_{1/3}\text{Nb}_{2/3})\text{O}_3\text{-PbTiO}_3$  (Sabolski *et al.*, 2001b) and  $\text{Sr}_{0.53}\text{Ba}_{0.47}\text{Nb}_2\text{O}_6$  (Duran *et al.*, 2000).

BNKT was the first material to which the RTGG process was applied (Tani, 1998). In this system, a special mechanism is operative for the promotion of selective growth of template grains. The shape of matrix grains is irregular with curved surfaces, whereas template grains have flat (100) surfaces, as shown in Fig. 26.10 (Fuse and Kimura, 2006). In this system, the surface energy of (100) is lower than that of other faces (*hkl*). In general, the driving force of grain growth is the reduction of total grain boundary energy which is the product of boundary area and boundary energy per unit area ( $\gamma$ ). In ordinary cases,  $\gamma$  is almost the same for various (*hkl*) planes and the driving force is caused by the reduction of boundary area. In the present BNKT case, on the other hand, the reduction in  $\gamma$  is also accompanied as shown in Fig. 26.10. Therefore, the growth of template grains with low  $\gamma$  is favorable, causing the selective growth of template grains (Fuse and Kimura, 2006). The (Na,K) $\text{Nb}_2\text{O}_6$ -based ceramics for lead-free piezoelectrics also have flat grain boundaries and this driving force of grain growth is operative (Saito *et al.*, 2004).

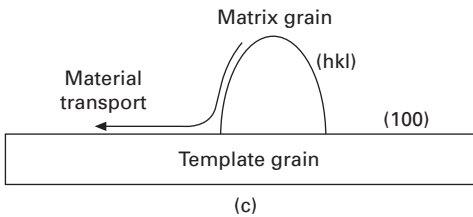
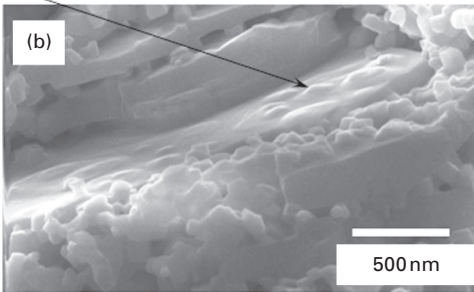
## 26.5 Application to solid solutions

The RTGG method has two advantages; this method can develop texture in compounds with an isotropic crystal structure, as already mentioned, and can be applicable to solid solutions with complex compositions, as exemplified for the systems  $\text{Bi}_{0.5}(\text{Na,K})_{0.5}\text{TiO}_3$  (Fukuchi *et al.*, 2002),  $\text{Bi}_{0.5}(\text{Na,K})_{0.5}\text{TiO}_3\text{-Pb}(\text{Zr, Ti})\text{O}_3$  (Abe and Kimura, 2002),  $\text{Bi}_{0.5}(\text{Na, K})_{0.5}\text{TiO}_3\text{-BaTiO}_3$  (Kimura *et al.*, 2004),  $\text{Bi}_{0.5}(\text{Na,K})_{0.5}\text{TiO}_3\text{-BiFeO}_3$  (Kato and Kimura, 2006) and  $(\text{Na,K,Li})(\text{Nb,Sb,Ta})\text{O}_3$  (Saito *et al.*, 2004). In the titanate systems, the reactive template is  $\text{Bi}_4\text{Ti}_3\text{O}_{12}$  and the end member of the solid solutions is added into the matrix phase except for  $\text{Bi}_{0.5}(\text{Na,K})_{0.5}\text{TiO}_3$ . The calcine compacts are composed of template grains of BNKT and matrix phase containing both BNKT and the end member compound. The ions in matrix grains must diffuse into template grains to form textured ceramics. Figure 26.11 shows the effect of the direction of material transport on the growth and disappearance of template grains. When the materials of matrix phase diffuse into template grains (Fig. 26.11a), the template grains grow and the matrix grains disappear, resulting in the development of texture. When the diffusion direction is the opposite (Fig. 27.11b), on the other hand, the template grains disappear and textured materials cannot be obtained.

Matrix grain attached to template grain

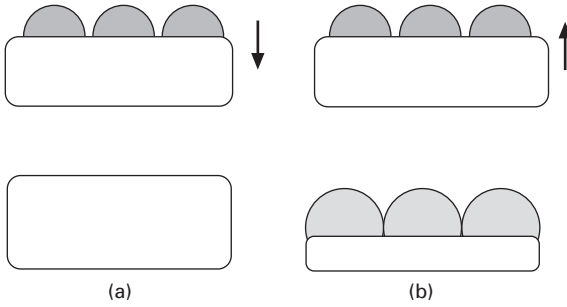


Matrix grain spreading over template grain

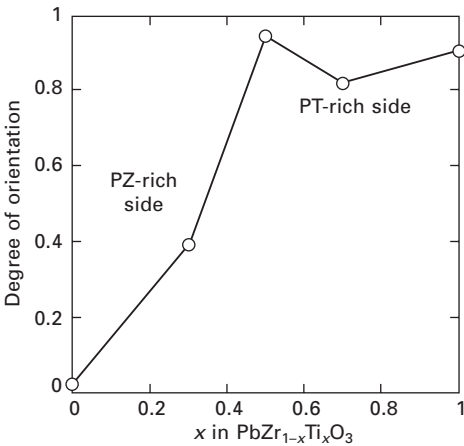


**26.10** Growth of template grains at the expense of matrix grains. Contact between template and matrix grains is formed (a). Matrix grains spread over (100) face of template grains and incorporate with template grain (b). Material transport from matrix (hkl) plane to template (100) plane reduces total surface free energy, because  $\gamma_{(100)}$  is much less than  $\gamma_{(hkl)}$  for BNKT (c).

The diffusion direction is dependent on the chemical composition. For the BNKT–PZT case, as an example, the PZT composition determines the diffusion direction and therefore texture development as shown in Fig. 26.12 (Abe and Kimura, 2002). In this case, the template grains are BNKT and matrix grains are PZT. When PZT is Ti-rich, the components of PZT have a large diffusion rate and diffuse into BNKT template grains. When PZT is Zr-rich, on the other hand, the diffusivity of PZT components is small and the components of BNKT diffuse into PZT grains, resulting in the disappearance of template grains. In the  $\text{Bi}_{0.5}(\text{Na},\text{K})_{0.5}\text{TiO}_3\text{–BiFeO}_3$  case, the direction of material



26.11 Effect of diffusion direction on the disappearance of (a) matrix and (b) template grains. The arrows indicate the diffusion direction.



26.12 Effect of PZT composition on texture development in BNKT-PZT solid solutions sintered at 1200 °C.

transport is determined by the chemical composition of template grains. When the template grains are BNT, they diffuse into  $\text{BiFeO}_3$ , resulting in the disappearance of template grains. When the template grains are BKT, on the other hand, the diffusivity of BKT is smaller than that of  $\text{BiFeO}_3$  and  $\text{BiFeO}_3$  diffuses into BKT template grains, resulting in the formation of textured materials.

## 26.6 Conclusions and future trends

The control of texture is necessary to develop high-performance, lead-free piezoelectric ceramics, because the performance of PZT-based materials is quite excellent and it is difficult to develop lead-free materials with performance comparable to or better than PZT by compositional design on its own. The methods other than the RTGG process can be applicable to the preparation

of piezoelectric materials with anisotropic crystal structures. These methods are hardly applicable to materials with the perovskite structure. The RTGG process is the most convenient preparation method of such materials.

In the RTGG process, the reactive template of a target compound is selected, and mixed with complementary compound(s) for the target compound to make slurry. The slurry is tape cast to form thin sheets, in which reactive template particles are aligned. A green compact made from the cast sheets is calcined to cause a reaction between the reactive template and the complementary compound(s). The calcined compact is composed of template and matrix grains of the target compound. Sintering causes the growth of template grains at the expense of matrix grains, resulting in the development of texture.

The RTGG process was proposed in 1998 and research to this date is mainly focused on the search for reactive templates because the compounds that fulfill the requirement for reactive templates are limited. The performance is determined by the microstructure of sintered compacts as well as by the chemical composition. Texture is one of the elements of microstructure. The optimization of all elements of microstructure, which includes density and grain size as well as the uniformity of microstructure, is required. Because the calcined compact is composed of template and matrix grains, it is necessary to understand the densification behavior and microstructure development in such a compact with a non-uniform microstructure. Furthermore, the change from starting materials (reactive template and complementary compound(s)) to template and matrix grains must be fully understood to select starting materials with optimum powder characteristics.

The application of the RTGG process is not restricted to piezoelectric ceramics. The establishment of high performance through RTGG process is reported for thermoelectrics (Tani, 2006).

## 26.7 References

- Abe Y and Kimura T (2002), 'Factors determining grain orientation in bismuth sodium potassium titanate–lead zirconate titanate solid solutions made by reactive templated grain growth method', *J. Am. Ceram. Soc.*, **85** (5) 1114–1120.
- Bedoya C, Muller C, Jacob F, Gagou Y, Freymy M A and Elkaim E (2002), 'Magnetic-field-induced orientation in Co-doped SrBi<sub>2</sub>Ta<sub>2</sub>O<sub>9</sub> ferroelectric oxide', *J. Phys.: Condens. Matter*, **14** (45) 11849–11857.
- Belmonte M, Moya J S and Miranzo P (1995), 'Bimodal sintering of Al<sub>2</sub>O<sub>3</sub>/Al<sub>2</sub>O<sub>3</sub> platelet ceramic composites', *J. Am. Ceram. Soc.*, **78** (6) 1661–1667.
- De Jonghe L C, Rahaman M N and Hsueh C H (1986), 'Transient stresses in bimodal compact during sintering', *Acta Metall.*, **34**(7) 1467–1471.
- Duran C, Trolrier-McKinstry S and Messing G L (2000), 'Fabrication and electrical properties of textured Sr<sub>0.53</sub>Ba<sub>0.47</sub>Nb<sub>2</sub>O<sub>6</sub> ceramics by templated grain growth', *J. Am. Ceram. Soc.*, **83** (9) 2203–2213.

- Fukuchi E, Kimura T, Tani T, Takeuchi T and Saito Y (2002), 'Effect of potassium concentration on the grain orientation in bismuth sodium potassium titanate', *J. Am. Ceram. Soc.*, **85** (6) 1461–1466.
- Fuse K and Kimura T (2006), 'Effect of particle sizes of starting materials on microstructure development in textured  $\text{Bi}_{0.5}(\text{Na}_{0.5}\text{K}_{0.5})\text{TiO}_3$ ', *J. Am. Ceram. Soc.*, **89** (6) 1957–1964.
- Granahan M, Holmes M, Shulze W A and Newnham R E (1981), 'Grain-oriented  $\text{PbNb}_2\text{O}_6$  ceramics', *J. Am. Ceram. Soc.*, **64** (4) C-68–C-69.
- Holmes M, Newnham R E and Cross L E (1979), 'Grain-oriented ferroelectric ceramics', *Am. Ceram. Soc. Bull.*, **58** (9) 872.
- Hong S H and Messing G L (1999), 'Development of textured mullite by templated grain growth', *J. Am. Ceram. Soc.*, **82** (4) 867–872.
- Horn J A, Zhang S C, Selvaraj U, Messing G L and Trolrier-McKinstry S (1999), 'Templated grain growth of textured bismuth titanate', *J. Am. Ceram. Soc.*, **82** (4) 921–926.
- Hunter R J (1993), *Introduction to Modern Colloid Science*, Oxford, Oxford University Press.
- Igarashi H, Matsunaga K, Taniai T and Okazaki K (1978), 'Dielectric and piezoelectric properties of grain-oriented  $\text{PbBi}_2\text{Nb}_2\text{O}_9$  ceramics', *Am. Ceram. Soc. Bull.*, **57** (9) 815–817.
- Jaffe B, Cook, Jr. W R and Jaffe H (1971), *Piezoelectric Ceramics*, London, Academic Press.
- Kahn M, Burks D, Burn I and Schulze W A (1988), 'Ceramic capacitor technology', in Levinson L M, *Electronic Ceramics*, New York, Marcel Dekker, 191–274.
- Kato K and Kimura T (2006), 'Preparation of textured  $\text{Bi}_{0.5}(\text{Na},\text{K})_{0.5}\text{TiO}_3$ - $\text{BiFeO}_3$  solid solutions by reactive-templated grain growth process', *J. Korean Ceram. Soc.*, **43** (11) 693–699.
- Kimura T (2006), 'Application of texture engineering to piezoelectric ceramics – a review', *J. Ceram. Soc. Jpn.*, **114** (1) 15–25.
- Kimura T and Yamaguchi T (1987), 'Morphology control of electronic ceramic powders by molten salt synthesis', *Adv. Ceram.*, **21**, 169–177.
- Kimura T, Takahashi T, Tani T and Saito Y (2004), 'Crystallographic texture development in bismuth sodium titanate by reactive templated grain growth method', *J. Am. Ceram. Soc.*, **87** (8) 1424–1429.
- Kimura T, Miura Y and Fuse K (2005), 'Texture development in barium titanate and PMN-PT using hexabarium 17-titanate heterotemplates', *Int. J. Appl. Ceram. Technol.*, **2** (1) 15–23.
- Krasevec V, Drogenik M and Kolar D (1987), 'Topotaxy between  $\text{BaTiO}_3$  and  $\text{Ba}_6\text{Ti}_{17}\text{O}_{40}$ ', *J. Am. Ceram. Soc.*, **70** (5) C-193–C-195.
- Kwon S, Sabolsky E M, Messing G L and Trolrier-McKinstry S (2005), 'High strain,  $\langle 001 \rangle$  textured  $0.675\text{Pb}(\text{Mg}_{1/3}\text{Nb}_{2/3})\text{O}_3$ - $0.325\text{PbTiO}_3$  ceramics: templated grain growth and piezoelectric properties', *J. Am. Ceram. Soc.*, **88** (2) 312–317.
- Makiya A, Kusano D, Tanaka S, Uchida N, Uematsu K, Kimura T, Kitazawa K and Doshida Y (2003), 'Particle oriented bismuth titanate ceramics made in high magnetic field', *J. Ceram. Soc. Jpn.*, **111** (9) 702–704.
- Messing G L, Trolrier-McKinstry S, Sabolsky E M, Duran C, Kwon S, Brahmarrout B, Park P, Yilmaz H, Rehrig P W, Eitel K B, Suvaci E, Seabaugh M and Oh K S (2004), 'Templated grain growth of textured piezoelectric ceramics', *Crit. Rev. Solid State Mater. Sci.*, **29**, 45–96.
- Nakai Y and Fukuoka S (1999), 'Piezoelectric and mechanical properties of  $\text{BaBi}_4\text{Ti}_4\text{O}_{15}/\text{Ba}_4\text{Ti}_{13}\text{O}_{30}$  ceramics', *Jpn. J. Appl. Phys. Part 1*, **38** (9B) 5568–5571.

- Newnham R E (2005), *Properties of Materials*, New York, Oxford University Press.
- Ozer I O, Suvaci E, Karademir B, Missiaen J M, Carry C P and Bouvard D (2006), 'Anisotropic sintering shrinkage in alumina ceramics containing oriented platelets', *J. Am. Ceram. Soc.*, **89** (6) 1972–1976.
- Pugh R J (1994), 'Dispersion and stability of ceramic powders in liquid', in Pugh R J and Bergstrom L, *Surface and Colloid Chemistry in Advanced Ceramics Processing*, New York, Marcel Dekker, 127–192.
- Rahaman M N (2003), *Ceramic Processing and Sintering*, New York, Marcel Dekker.
- Sabolsky M, James A R, Kwon S, Trolier-McKinstry S and Messing G L (2001a), 'Piezoelectric properties of <001> textured  $\text{Pb}(\text{Mg}_{1/3}\text{Nb}_{2/3})\text{O}_3$ – $\text{PbTiO}_3$  ceramics', *Appl. Phys. Lett.*, **78** (17) 2551–2553.
- Sabolsky E M, Messing G L and Trolier-McKinstry S (2001b), 'Kinetics of templated grain growth of  $0.65\text{Pb}(\text{Mg}_{1/3}\text{Nb}_{2/3})$ – $0.35\text{PbTiO}_3$ ', *J. Am. Ceram. Soc.*, **84** (11) 2507–2513.
- Sabolsky E M, Trolier-McKinstry S and Messing G L (2003), 'Dielectric and piezoelectric properties of <001> fiber-textured  $0.675\text{Pb}(\text{Mg}_{1/3}\text{Nb}_{2/3})\text{O}_3$ – $0.325\text{PbTiO}_3$  ceramics', *J. Appl. Phys.*, **93** (7) 4072–4080.
- Saito Y and Takao H (2006), 'Synthesis of Platelike {100}  $\text{SrTiO}_3$  particles by topochemical microcrystal conversion and fabrication of grain-oriented ceramics', *Jpn. J. Appl. Phys.*, **45** (9B) 7377–7381.
- Saito Y, Takao H, Tani T, Nonoyama T, Takatori K, Homma T, Nagaya T and Nakamura M (2004), 'Lead-free piezoceramics', *Nature*, **432**, 84–87.
- Seabaugh M M, Kerscht I H and Messing G L (1997), 'Texture development by templated grain growth in liquid-phase-sintered  $\alpha$ -alumina', *J. Am. Ceram. Soc.*, **80** (5) 1181–1188.
- Seno Y and Tani T (1999), 'TEM observation of a reactive template for textured  $\text{Bi}_{0.5}(\text{Na}_{0.87}\text{K}_{0.13})_{0.5}\text{TiO}_3$  polycrystals', *Ferroelectrics*, **224** (1–4) 793–800.
- Senz S, Graff A, Blum W and Hesse D (1998), 'Orientation relationship of reactively grown  $\text{Ba}_6\text{Ti}_{17}\text{O}_{40}$  and  $\text{Ba}_2\text{TiSi}_2\text{O}_8$  on  $\text{BaTiO}_3$  (001) determined by X-ray diffractometry', *J. Am. Ceram. Soc.*, **81** (5) 1317–1321.
- Sugawara T, Nomura Y, Kimura T and Tani T (2001), 'Fabrication of <111> oriented  $\text{BaTiO}_3$  bulk ceramics by reactive templated grain growth', *J. Ceram. Soc. Jpn.*, **109** (10) 897–890.
- Sugawara T, Shimizu M, Kimura T, Takatori K and Tani T (2004), 'Fabrication of grain oriented barium titanate', *Ceram. Trans.*, **136**, 389–406.
- Suyama Y and Kato A (1977), 'Solid-state reaction between CVD- $\text{TiO}_2$  and  $\text{BaCO}_3$ ', *Bull. Chem. Soc. Jpn.*, **50** (6) 1361–1366.
- Suyama Y, Oda Y and Kato A (1979), 'Topotaxy between  $\text{TiO}_2$  and  $\text{BaTiO}_3$ ', *Chem. Lett.*, **8**, 987–988.
- Takenaka T and Sakata K (1980), 'Grain orientation and electrical properties of hot-forged  $\text{Bi}_4\text{Ti}_3\text{O}_{12}$  ceramics', *Jpn. J. Appl. Phys.*, **19** (1) 31–39.
- Tani T (1998), 'Crystalline-oriented piezoelectric bulk ceramics with a perovskite-type structure', *J. Korean Phys. Soc.*, **32**, S1217–S1220.
- Tani T (2006), 'Texture engineering of electronic ceramics by the reactive-templated grain growth method', *J. Ceram. Soc. Jpn.*, **114** (5) 363–370.
- Tani T and Kimura T (2006), 'Reactive templated grain growth processing for lead free piezoelectric ceramics', *Adv. Appl. Ceram.*, **105** (1) 55–63.
- Tsutai S, Hayashi T, Hayashi S and Nakagawa Z (2001), 'Reaction mechanism of  $\text{BaTiO}_3$  from powder compacts,  $\text{BaCO}_3$  and  $\text{TiO}_2$  and expansion phenomena during the formation process', *J. Ceram. Soc. Jpn.*, **109**(12) 1028–1034 (in Japanese).

- Wada S, Suzuki S, Noma T, Suzuki T, Osada M, Kakihana M, Park S E, Cross L E and Shrout T R (1999), 'Enhanced piezoelectric property of barium titanate single crystals with engineered domain configuration', *Jpn. J. Appl. Phys. Part 1*, **38** (9B) 5505–5511.
- Watanabe H, Kimura T and Yamaguchi T (1989), 'Particle orientation during tape casting in the fabrication of grain-oriented bismuth titanate', *J. Am. Ceram. Soc.*, **72** (2) 289–293.
- West D L and Payne D A (2003), 'Microstructure development in reactive-templated grain growth of  $\text{Bi}_{1/2}\text{Na}_{1/2}\text{TiO}_3$ -based ceramics: template and formulation effect', *J. Am. Ceram. Soc.*, **86** (5) 769–774.
- Yang J S, Chen X M, Aizawa T and Kuwabara M (1998), 'PZT based piezoelectric ceramics with enhanced fracture toughness', *Solid State Ionics*, **108** (1–4) 117–121.
- Yilmaz H, Messing G L and Trolrier-McKinstry S (2003a), '(Reactive) Templated grain growth of textured sodium bismuth titanate ( $\text{Na}_{1/2}\text{Bi}_{1/2}\text{TiO}_3$ - $\text{BaTiO}_3$ ) ceramics – I Processing', *J. Electroceramics*, **11** (3) 207–215.
- Yilmaz H, Messing G L and Trolrier-McKinstry S (2003b), '(Reactive) Templated grain growth of textured sodium bismuth titanate ( $\text{Na}_{1/2}\text{Bi}_{1/2}\text{TiO}_3$ - $\text{BaTiO}_3$ ) ceramics – II Dielectric and piezoelectric properties', *J. Electroceramics*, **11** (3) 217–226.

## Grain orientation and electrical properties of bismuth layer-structured ferroelectrics

T TAKENAKA, Tokyo University of Science, Japan

### 27.1 Introduction

Important ferroelectric or antiferroelectric oxide ceramics for dielectric, ferroelectric, piezoelectric, electrostrictive and/or pyroelectric applications are restricted to perovskite-type, tungsten bronze-type and bismuth layer-structured compounds. One recent trend in the study on piezoelectric and/or pyroelectric ceramic compounds is the use of lead-free materials. The other trend is the use of grain orientation techniques as the ceramic fabrication methods.

Recently, bismuth layer-structured ferroelectrics (BLSF), which form one of the  $\text{BO}_6$  octahedral ferroelectric groups, have been extensively studied in the form of thin films because BLSF seem to be excellent candidate materials for non-volatile FeRAM (ferroelectric random access memory) in various commercial applications. For example, one BLSF,  $\text{SrBi}_2\text{Ta}_2\text{O}_9$  shows very high-quality characteristics with fatigue-free property for FeRAM.

The family of BLSF is a group of important ferroelectric oxide materials for dielectric, ferroelectric, piezoelectric and pyroelectric applications because BLSF such as  $\text{Bi}_4\text{Ti}_3\text{O}_{12}$  (BIT),  $\text{PbBi}_2\text{Nb}_2\text{O}_9$  (PBN), and  $\text{Na}_{0.5}\text{Bi}_{4.5}\text{Ti}_4\text{O}_{15}$  (NBT) are characterized<sup>1-3</sup> by their low dielectric constant  $\epsilon_s$ , high Curie temperature  $T_c$ , and large anisotropy in electromechanical coupling factors  $k_t/k_p$  or  $k_{33}/k_{31}$  compared with those of PZT family. Furthermore, these characteristics can be easily enhanced by a grain orientation technique such as the hot-forging (HF) method.<sup>4-6</sup> Therefore, grain-oriented BLSF ceramics seem to be a superior candidate for the lead-free or low-lead-content piezoelectric materials with high  $T_c$  and anisotropic characteristics<sup>7,8</sup>, or for pyroelectric sensor materials with a large figure of merit.<sup>9,10</sup> BLSF ceramics can be used as stable and high- $Q$  piezoelectric materials to be operated at high temperatures and at high frequencies.

Piezoelectric activities of conventionally sintered BLSF ceramics, however, are not as large as expected from those of the single crystals.<sup>11,12</sup> One reason for the low piezoelectric activity in such ceramics may be due to the two-



dimensional restriction on the permissible rotations of the spontaneous polarization, in comparison with three-dimensionally permitted ones in perovskite-type ferroelectrics. Thus, ferroelectric ceramics whose grain crystallites have such lower symmetry as bismuth layer-type compounds may have an essentially weak point in that a satisfactorily large remanent polarization cannot be obtained by electric poling.

In order to solve this problem, new fabrication processes of piezoelectric ceramics are desirable through which the texture of the ceramics can be well controlled to give preferred grain orientations. There are usually two fabrication methods for orientating the grains in oxide ceramics: one is a hot working technique which makes use of the motion of dislocations in the grains and of the slip in the grain boundaries at high temperatures, and the other is a topotaxial reaction which is based on the shape of the powder of the raw material.

The grain orientation technique, which is one of several ceramic preparation methods with a controlled grain structure during the ceramic sintering process, gives the ceramics an anisotropic single-crystal-like behavior. Of many hot-working methods such as hot-forging, hot-rolling, hot-extrusion, and super plastic deformation, the HF method<sup>4-6</sup> seems to be the most advantageous grain orientation technique in laboratories for lower symmetric materials with a large anisotropic crystal structure such as the bismuth layer-structured type and the tungsten bronze type. The HF samples have a higher plastic deformation than those produced by hot-pressing. A slip between ( $\text{Bi}_2\text{O}_2$ ) layers and perovskite-like layers in the  $c$ -plane of BLSF ceramics occurs during the hot-forging process and finally the  $c$ -axis is aligned almost parallel to the forging axis with a well-oriented grain structure. The HF-BLSF ceramics whose spontaneous polarization lies in the grain-oriented  $c$ -plane normal to the forging axis display the piezoelectric and pyroelectric properties that are enhanced by the grain orientation effects. Studies of the grain orientations in piezoelectric and pyroelectric ceramics have been systematically carried out for more than 30 years. The author has been able to obtain ceramics with a high degree of preferred grain orientation by using HF in many BLSF which have shown greatly enhanced dielectric, ferroelectric, piezoelectric and pyroelectric properties.

This chapter describes the effects of grain orientation on electrical properties such as dielectric, ferroelectric, piezoelectric, and pyroelectric properties of some grain-oriented BLSF ceramics by the HF method, comparing them with ordinarily fired (OF) non-oriented ones.

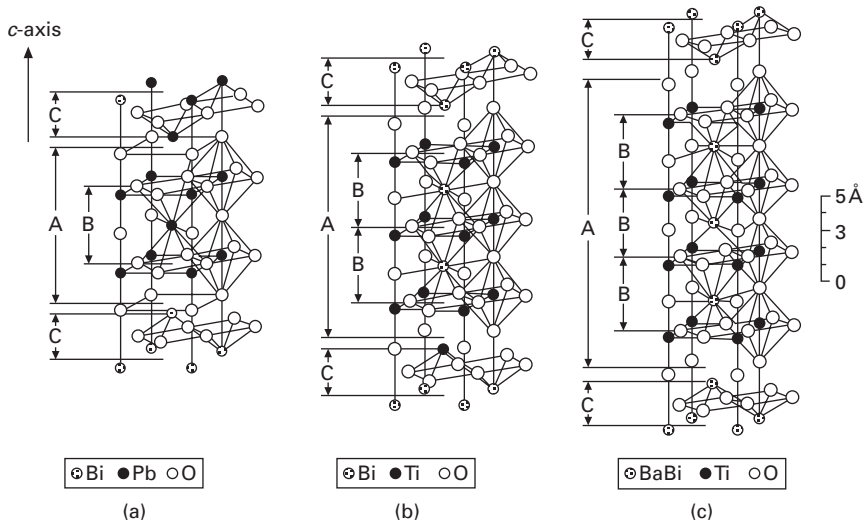
## 27.2 Bismuth layer-structured ferroelectrics (BLSF)

More than 50 years ago Aurivillius<sup>13</sup> discovered a family of bismuth compounds with a layer structure, and to date more than 50 compounds in

the group have been investigated; a large number have been found to be ferroelectric.<sup>14-20</sup> Crystallographic studies of bismuth-layered oxides have been made by many workers,<sup>13-20</sup> the dielectric properties have been examined in detail by Subbarao,<sup>18</sup> and ferroelectric and piezoelectric properties have been studied by some Japanese scientists.<sup>2,3,7-8</sup>

The bismuth layer-structured oxides (BLSO) have a generalized chemical formula of  $A_{m-1}Bi_2B_mO_{3m+3}$  where A is mono-, di-, or trivalent ions or a mixture of them and B is tetra-, penta-, or hexavalent ions, or a mixture of them, and the integer  $m$  takes any value from 1 to 5. Examples of their crystal structures are shown in Fig. 27.1, where A shows  $(A_{m-1}B_mO_{3m+1})$  which consists of  $(m-1)$  layers of perovskite-like units (B) and is sandwiched between  $(Bi_2O_2)$  layers (C). Bismuth titanate,  $Bi_4Ti_3O_{12}$  (BIT) (Fig. 27.1b), is a prototype of many bismuth layer structure oxides with the simplest chemical composition ( $m = 3$ ) and has a high Curie point of  $680^\circ\text{C}$ .<sup>11,12</sup>

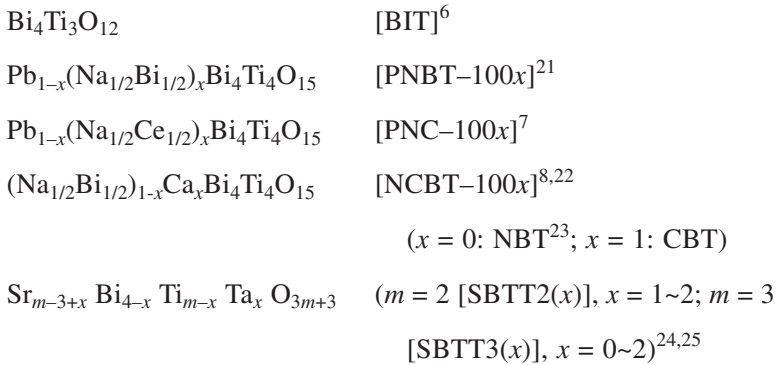
BLSO have  $BO_6$  octahedra like perovskite, pyrochlore, and tungsten-bronze structures and many of them are ferroelectric. An electrically neutral condition gives the following formula,  $(m-1)N(A) + mN(B) = 6m$ , where  $N(A)$  and  $N(B)$  indicate the mean valencies of the A and the B ions, respectively. However, BLSO have a great variety of available combinations of A and B ions, respectively. For example, the basic BLSF are  $Bi_4Ti_3O_{12}$  (BIT) ( $m = 3$ ),  $PbBi_2Nb_2O_9$  (PBN) ( $m = 2$ ),  $Bi_3TiNbO_9$  (BTN) ( $m = 2$ ),  $Na_{0.5}Bi_{4.5}Ti_4O_{15}$



27.1 Schematic drawings of (a)  $PbBi_2Nb_2O_9$  (PBN) ( $m = 2$ ), (b)  $Bi_4Ti_3O_{12}$  (BIT) ( $m = 3$ ) and (c)  $BaBi_4Ti_4O_{15}$  (BBT) ( $m = 4$ ) structures (one-half of the unit cell). A: The perovskite layer of  $(Bi_2Ti_3O_{10})^{2-}$  in BIT, B: a unit cell of the hypothetical perovskite structure  $BiTiO_3$  in BIT, C: the layer of  $(Bi_2O_2)^{2+}$  (after Aurivillius<sup>13</sup>).

(NBT) ( $m = 4$ ),  $\text{PbBi}_4\text{Ti}_4\text{O}_{15}$  (PBT) ( $m = 4$ ), and  $\text{Pb}_2\text{Bi}_4\text{Ti}_5\text{O}_{18}$  (P2BT) ( $m = 5$ ). Many derivative solid solutions have also been studied, mainly in grain-oriented piezoelectric and pyroelectric ceramics.

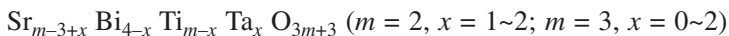
Among a great number of the BLSF compounds, the following solid solution systems were selected in this chapter on the basis of the results of the electrical properties:



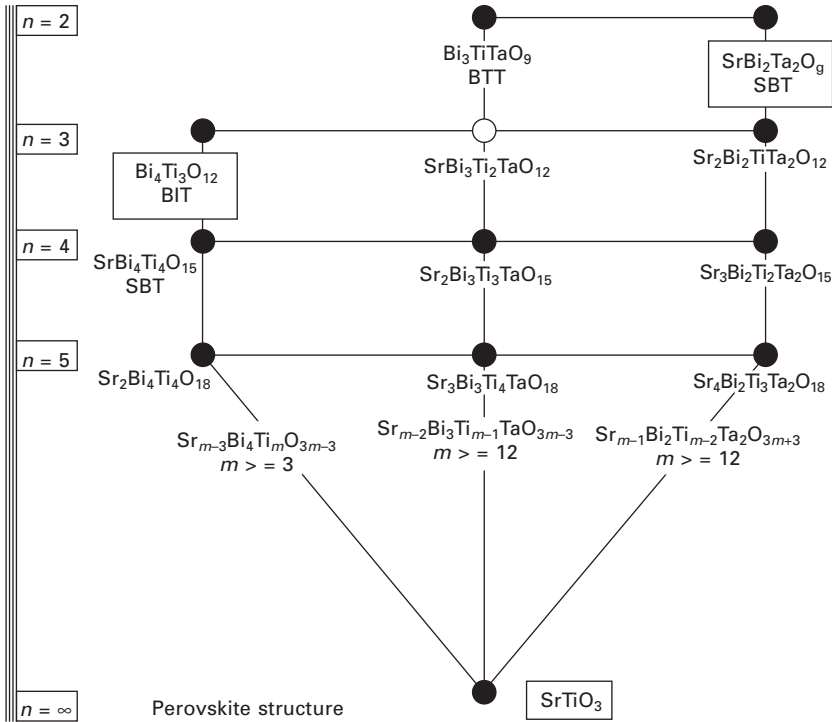
where [ ] shows the abbreviation of the respective systems.

Among a great number of the BLSF compounds, the  $\text{Na}_{0.5}\text{Bi}_{4.5}\text{Ti}_4\text{O}_{15}$  (NBT) ( $m = 4$ ) ceramic displays excellent piezoelectric properties.<sup>2,23</sup> On the other hand, substituted perovskite compounds by Ca for A-site ions are expected to have large anisotropic piezoelectric properties because the calcium ionic radius is the smallest in the A-site ion group of the perovskite compounds. Due to an enhanced anisotropy, the electromechanical coupling factor  $k_p$  or  $k_{31}$  in the radial or transverse mode of 24 mol% calcium-modified  $\text{PbTiO}_3$  (PT) ceramics is almost negligible,<sup>26</sup> in contrast with the large coupling factor  $k_t$  or  $k_{33}$  in the thickness expansion or longitudinal expansion mode, resulting in a very large anisotropy in the coupling factor,  $k_t/k_p$  or  $k_{33}/k_{31}$ . The Ca-modified NBT, namely,  $(\text{Na}_{1/2}\text{Bi}_{1/2})_{1-x}\text{Ca}_x\text{Bi}_4\text{Ti}_4\text{O}_{15}$  [NCBT], ceramics can be expected to show the most excellent piezoelectric and/or pyroelectric properties.

Figure 27.2 shows the phase relation between well-known bismuth layer-structured ferroelectrics such as  $\text{Bi}_3\text{TiTaO}_9$  (BTT) ( $m = 2$ ),  $\text{SrBi}_2\text{Ta}_2\text{O}_9$  (SBT) ( $m = 2$ ) and  $\text{Bi}_4\text{Ti}_3\text{O}_{12}$  (BIT) ( $m = 3$ ), including a perovskite compound  $\text{SrTiO}_3$ . The general formula of phase relation in Fig. 27.2 is as follows:



where  $x$  corresponds to the amount of Ta ions in the layer structure and  $1 \leq x \leq 2$  for  $m = 2$  and  $0 \leq x \leq 2$  for  $3 \leq m \leq 5$ . Hereafter the formula is abbreviated to  $\text{SBTT}m(x)$ , especially the series of  $m = 2$  and 3 are abbreviated to  $\text{SBTT2}(x)$  ( $1 \leq x \leq 2$ ) and  $\text{SBTT3}(x)$  ( $0 \leq x \leq 2$ ).



27.2 The phase relation between well-known bismuth layer-structured ferroelectrics such as  $\text{Bi}_3\text{TiTaO}_9$  (BTT) ( $m = 2$ ),  $\text{SrBi}_2\text{Ta}_2\text{O}_9$  (SBT) ( $m = 2$ ) and  $\text{Bi}_4\text{Ti}_3\text{O}_{12}$  (BIT) ( $m = 3$ ) including a perovskite compound  $\text{SrTiO}_3$ .

### 27.3 Grain orientation and HOT-Forging (HF) method

#### 27.3.1 Ceramic sample preparations

OF (non-oriented) ceramic samples were prepared by the conventional ceramic technique. Reagent grade oxide or carbonate powders of  $\text{Bi}_2\text{O}_3$ ,  $\text{PbO}$ ,  $\text{Na}_2\text{CO}_3$ ,  $\text{CaCO}_3$ ,  $\text{TiO}_2$ , and  $\text{Nb}_2\text{O}_5$  with 99+% purity were used as the starting materials. To prepare the perovskite type  $(\text{Na}_{1/2}\text{Ce}_{1/2})\text{TiO}_3$  powders for the PNC system, raw materials of  $\text{CeO}_2$ ,  $\text{Na}_2\text{CO}_3$ , and  $\text{TiO}_2$  were pre-calcined in a reduced atmosphere using carbon graphite powders. The materials mixed using ball milling were calcined at  $850^\circ\text{C}$  for 2 h. After calcining, the ground and ball-milled powders were pressed into a disc of 20 mm in diameter and about 10 mm in thickness. Pressed discs were finally sintered at  $1000\text{--}1250^\circ\text{C}$  for 1–2 h in air.

### 27.3.2 Grain orientation by hot-forging method

Grain-oriented samples were prepared by the HF method as described in detail elsewhere.<sup>6</sup> Cylinder bodies 15 mm in diameter and about 30–40 mm in height were pre-pressed in a steel die at a pressure of about 800 kg/cm<sup>2</sup>, and were used as starting bodies in the HF process. The pre-pressed cylinder (green body) was sandwiched between two platinum plates to prevent the sample from reacting with alumina plungers. A uniaxial compressive load of about 200 kg/cm<sup>2</sup> for the area of  $\pi (15/2)^2$  mm<sup>2</sup> was applied along the thickness of the sample (the forging axis) using oil pressure. After ordinary firing at 1000–1200 °C for 2 h, the sample was gradually pressed by two alumina plungers, since abrupt pressing will produce cracks in the sample. Then a constant pressure and a maximum temperature were maintained for a variable time. A lower temperature and abrupt pressing will produce cracks in the sample. Four conditions are most critical:  $T_m$ , the maximum temperature;  $P_h$ , the maximum total pressure;  $t_p$ , the soaking time when the maximum pressure is maintained; and  $t_a$ , the annealing time. A degree of deformation in HF ceramics is expressed in terms of an area ratio  $\gamma$ , and a thickness contraction rate  $\lambda$ ; i.e.  $\gamma = S_f/S_i$ , and  $\lambda = (h_i - h_f)/h_i$ , where  $S_i$  and  $S_f$  are cross-section areas, and  $h_i$ ,  $h_f$  thickness, of pre-sintered and hot-forged samples, respectively. The value of  $h_i$  is estimated by a relation of  $h_i = (1 - \alpha)h_{gb}$ , where  $h_{gb}$  is a thickness of the green body and  $\alpha$  is a linear shrinkage of the ordinarily fired pellet which was sintered at the same temperature. The plastic deformations, namely  $\gamma$  and  $\lambda$ , depend heavily on the forging temperature and the composition of the sample. For example, HF BLSF ceramics showed an area ratio,  $\lambda$ , of about 2–10, and a thickness contraction rate,  $\lambda$ , of about 50–90%, respectively. A measured density of 7.78 g/cm<sup>3</sup> in HF samples was 97% of the X-ray density 8.04 g/cm<sup>3</sup>, and it increased to 99% if further hot-pressing was applied after the hot-forging.

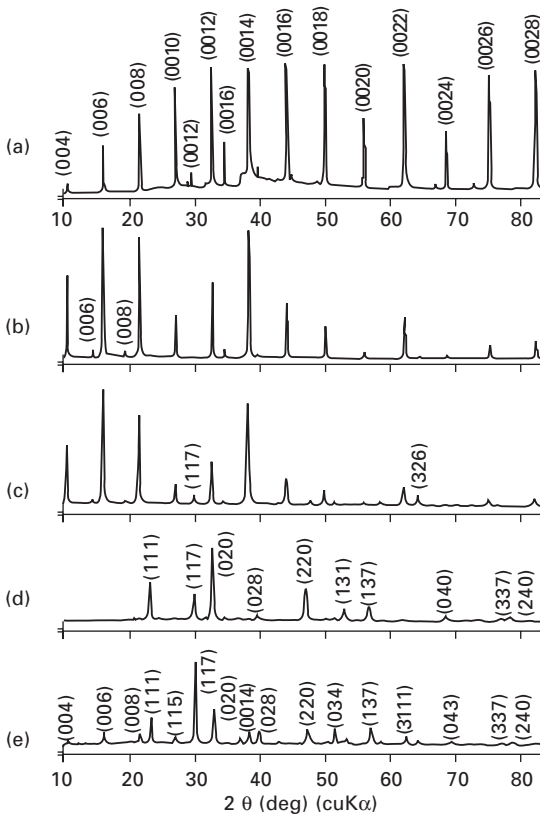
## 27.4 Grain orientation effects on electrical properties

### 27.4.1 Grain orientation and microstructure

The crystalline structure was confirmed by X-ray powder diffraction analysis using a Ni-filtered CuK $\alpha$  radiation at a scanning speed of 1 deg/min. Evaluation of the HF samples was performed for the grain orientation factor,  $F$ , obtained from X-ray diffraction patterns compared with that from the powder diffraction patterns of the OF sample using the Lotgering method.<sup>27</sup> The texture of HF samples was observed with a scanning electron microscope (SEM). For preparing samples, ceramics were polished with successively finer carborundum, were finished with 3  $\mu$ m diamond paste, and then were thermally etched at 1000–1100 °C for 30 min.

In the growth of BIT single crystals,<sup>11,12</sup> it is known that the *c*-plate grows into a mica-like shape. Furthermore, Ikegami and Ueda<sup>2</sup> reported that grain boundaries in OF BIT ceramics are of nearly rectangular in shape and fine stripes are observed in each grain, always parallel to the length of each rectangular grain boundary, which will be related closely to the crystal structure with  $\text{Bi}_2\text{O}_2$  layers. Therefore, when X-rays are reflected by the plane perpendicular to the forged direction of the ceramic, (00*l*) reflections are expected to increase and others to decrease compared with those of OF ceramics. Figure 27.3 shows X-ray diffraction patterns, reflected by the perpendicular plane (b), (c) and by the parallel plane (d), respectively, in the HF samples; reflected by the *c*-plate of a single crystal (a), and by OF ceramics (e).

As shown in Fig. 27.3, (00*l*) reflections increase in the perpendicular plane (b), (c) whose patterns resemble that of the *c*-plate of a single crystal



27.3 X-ray diffraction patterns for  $\text{Bi}_4\text{Ti}_3\text{O}_{12}$  (BIT), for (a) the *c*-plate of a single crystal, (b) the perpendicular plane (non-polished), (c) the perpendicular plane (polished) and (d) the parallel plane of hot-forged ceramics, and (e) the ordinarily fired ceramics.<sup>6</sup>

(a), and (00*l*) reflections in the parallel plane (d) almost disappear, in comparison with OF ceramics (e). Thus, in the HF ceramics, the grains are found to be oriented with *c*-axes along a forged direction. The degree of grain orientation, *F*, can be estimated by comparing the X-ray diffraction patterns with those of non-oriented (OF) ceramics as follows.<sup>27</sup> First, a ratio *p* of the sum of the intensities *I* (00*l*) of the (00*l*) reflections to the sum of the intensities *I* (*hkl*) including (00*l*) is calculated over the range between 10° and 84° of 2θ. Namely,

$$p = \frac{\sum I(00l)}{\sum I(hkl)} \quad 27.1$$

As the degree of orientation is increased, the value of *p* is increased from *p*<sub>0</sub> (a value for a non-oriented case) to 1 (a value for a completely oriented case). Hence, if *F* is defined as

$$F = \frac{p - p_0}{1 - p_0} \quad 27.2$$

*F* varies from 0 (non-oriented) to 1 (completely oriented) and *F* may be used as a measure of the grain orientation. In this way, *F* is estimated as 1, 0.98 and 0.95 for Fig. 27.3(a), (b) and (c), respectively, and *F* increased as the area ratio *γ* increased (for example, *γ* = 8 in Fig. 27.3b and 27.3c).

The HF NCBT-5 sample was almost smoothly deformed at temperatures of 1100–1150°C, and a thickness contraction rate *λ* of about 90% was obtained with good reproducibility. The grain orientation factor *F* of the Mn-doped NCBT system was more than 90%. The *F* values of the respective samples are given in Table 27.1, with other related values.

## 27.4.2 Dielectric properties

The anisotropies in the electrical properties of HF samples were measured by applying an electric field perpendicular [⊥] and parallel [//] to the forging axis, that is, the electrodes of the HF samples<sup>6,7</sup> were adhered to the faces to which were applied electric fields perpendicular and parallel to the forging axis, respectively. Electrodes for studying the temperature dependence of dielectric properties were made with fired-on silver–palladium (Ag-Pd) paste.

The temperature dependence of the dielectric constant, *ε*<sub>s</sub>, and dielectric loss tangent, tan δ, was measured at 1 or 10 MHz by an automated dielectric measurement system with a multi-frequency LCR meter (YHP 4275A) in the temperature range of room temperature to 800°C.

The dielectric constants *ε*<sub>s</sub> [⊥] and *ε*<sub>s</sub> [//] of HF BIT ceramics are approximately 160 and 130, respectively, at room temperature. The *ε*<sub>s</sub> [⊥] increases steeply above 500°C and reaches about 1170 at ca. 680°C, which

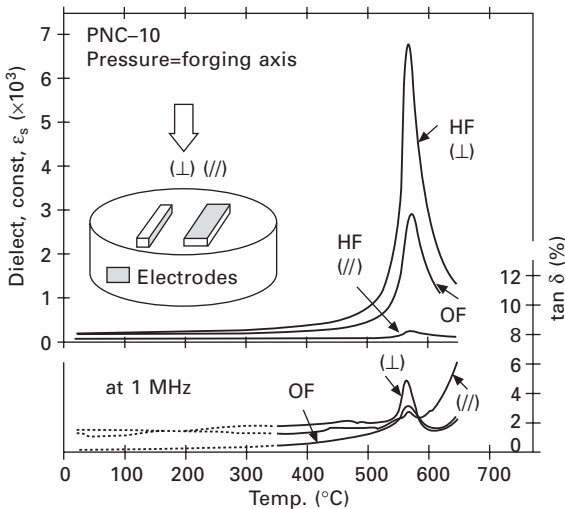
Table 27.1 Elastic, piezoelectric, and dielectric (EPD) constants of the OF and HF (Na<sub>1/2</sub>Bi<sub>1/2</sub>)<sub>1-x</sub>Ca<sub>x</sub>Bi<sub>4</sub>Ti<sub>4</sub>O<sub>15</sub> (NCBT-100x) ceramics

Sample	NBT + Mn (0.1)		NCBT-5 + Mn (0.1)		NCBT-5 + Mn (0.2)	
	HF	OF	HF	OF	HF	OF
Grain orientation factor $F_i$	0.98	/	0.91	/	0.93	/
Measured density $\rho_0$ (g/cm <sup>3</sup> )	7.29	7.01	6.92	6.88	7.20	6.65
Curie temperature $T_c$ (°C)	660	658	665	680	–	677
Dielectric constant $\epsilon_{33}^T/\epsilon_0$	149	140	134	148	132	135
Coupling factor (%)						
$k_{33}$	32.5	14.7	35.6	16.1	40.0	18.8
$k_{31}$	2.8	3.3	2.75	2.85	2.34	2.39
Frequency constant (Hzm)						
$N_{33}$	2170	2000	2260	1950	2290	1950
$N_{31}$	2130	1990	2180	1980	2170	1970
Piezoelectric constant						
$d_{33}$ (10 <sup>-12</sup> C/N)	33.7	15.6	34.9	18.3	38.3	20.8
$d_{31}$	2.80	3.49	2.61	3.15	2.17	2.58
$g_{33}$ (10 <sup>-3</sup> V m/N)	25.6	12.6	29.4	13.9	32.8	17.4
$g_{31}$	2.12	2.81	2.20	2.40	1.86	2.16
$d_h g_h$ (10 <sup>-15</sup> m <sup>2</sup> /N)	600	60	742	109	988	205
Elastic constant (10 <sup>-12</sup> m <sup>2</sup> /N)						
$s_{33}^E$	8.17	9.13	8.11	9.84	7.85	10.2
$s_{11}^E$	7.56	9.01	7.58	9.32	7.38	9.72



corresponds to the Curie temperature of single crystal. On the other hand,  $\epsilon_s$  [//] depends to some degrees on temperature over the whole temperature range and has a small peak of 270 at ca. 680 °C. Dielectric constant  $\epsilon_s$  [OF] of OF ceramics shows an intermediate value between  $\epsilon_s$  [ $\perp$ ] and  $\epsilon_s$  [//]. The symmetry of BIT is monoclinic below the Curie temperature of 675 °C.<sup>11,12</sup> In a BIT single crystal,<sup>28</sup> the dielectric constants  $\epsilon_a$  and  $\epsilon_b$  are about 100 and 200, respectively, at room temperature, and their temperature dependences show sharp peaks of about 1750 at the Curie point, while  $\epsilon_c$  has a value of 100 at room temperature and shows no peak up to 750 °C. The dielectric constants  $\epsilon_s$  [ $\perp$ ] and  $\epsilon_s$  [//] of HF ceramics have similar temperature dependences to those of  $\epsilon_a$  (or  $\epsilon_b$ ) and  $\epsilon_c$  of a single crystal, respectively, so that a large anisotropy in the dielectric constant was observed, the ratio of  $\epsilon_s$  [ $\perp$ ] to  $\epsilon_s$  [//] being about 5 at the Curie point.

Figure 27.4 shows the temperature dependence of  $\epsilon_s$  and  $\tan \delta$  of the HF PNC-10 ([ $\perp$ ] and [//]), together with that of the OF sample for the sake of comparison. A remarkable anisotropy in  $\epsilon_s$  [ $\perp$ ] and  $\epsilon_s$  [//] is observed. The ratio of  $\epsilon_s$  [ $\perp$ ] to  $\epsilon_s$  [//] increases with temperature rise and reaches a maximum at  $T_c$ . In our previous paper<sup>29</sup> it has been shown that the ratio  $\epsilon_s$  [ $\perp$ ]/ $\epsilon_s$  [//] can be considered to be proportional to the degree of grain orientation  $F$  and has various values from 4 to 12 at  $T_c$  depending on the magnitude of  $F$ . In our present measurement on PNC-10, for example, this ratio is found to be 2.0 at room temperature and 26.5 at  $T_c$ , with  $F = 0.97$ . This suggests that PNC solid solution can be an attractive member of a BLSF family because of its large anisotropy.



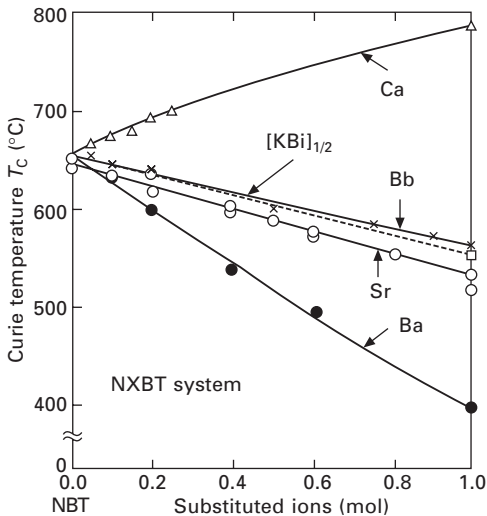
27.4 Temperature dependence of  $\epsilon_s$  and  $\tan \delta$  for the HF PNC-10, compared with those of the OF samples.

Figure 27.5 shows the  $T_c$  of the  $(\text{Na}_{1/2}\text{Bi}_{1/2})_{1-x}\text{M}_x\text{Bi}_4\text{Ti}_4\text{O}_{15}$  ( $\text{M} = \text{Ba}, \text{Ca}, \text{Pb}, \text{Sr}, \text{and } \text{K}_{1/2}\text{Bi}_{1/2}$ ) (NXBT) system as a function of the amount ( $x$ ) of the substituted ions. The  $T_c$ , except the case of  $\text{M} = \text{Ca}$  (NCBT), decrease as the concentration,  $x$ , of the substituted ions increases. On the other hand, the  $T_c$  of  $\text{M} = \text{Ca}$  (NCBT) increases as the Ca concentration,  $x$ , increases. This suggests<sup>22</sup> that the  $T_c$  is related to the change of the lattice distortion  $b/a$  as mentioned above. The  $T_c$  of  $\text{CaBi}_4\text{Ti}_4\text{O}_{15}$  CBT ( $x = 1$ : Ca substituting for  $\text{Na}_{1/2}\text{Bi}_{1/2}$ ) reaches a high of  $785^\circ\text{C}$ .

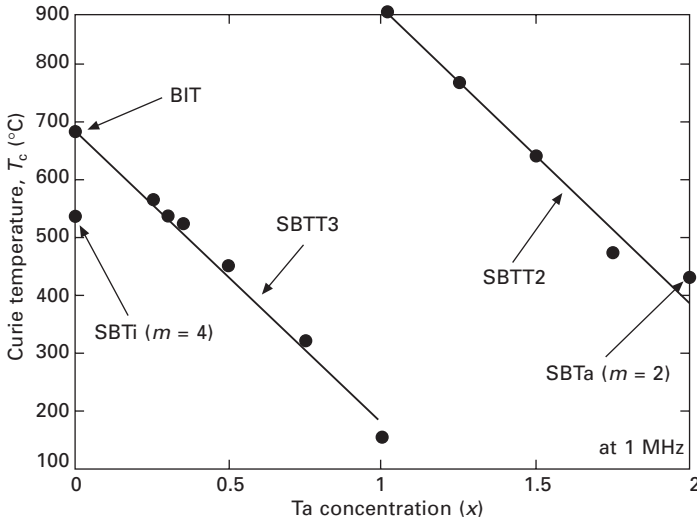
Figure 27.6 shows the Curie temperature  $T_c$  of SBTT2 ( $x$ ) and SBTT3 ( $x$ ) as a function of Ta concentration ( $x$ ). The  $T_c$  of the BIT ( $x = 0$ ) ceramic in SBTT3 is  $680^\circ\text{C}$ , and becomes lower gradually with the increasing amount of Ta concentration ( $x$ ). In other words, the ferroelectricity becomes weak with the increasing amount of Sr and Ta ions, compared with that of the BIT ceramic. The reason why the  $T_c$  becomes lower is the increase of the amount of modified  $\text{SrTiO}_3$ , which has a paraelectric phase at room temperature, for the perovskite-like unit in BLSF. The  $T_c$  of the SBTT2 is higher than those of the SBTT3. On the other hand, the  $T_c$  of SBTT4(0) ( $m = 4$ ,  $\text{SBTi}$ ) is lower than those of the SBTT3(0) (BIT). It is thought that this tendency of the  $T_c$  may be caused by the effects of the  $\text{Bi}_2\text{O}_2$  layer.

### 27.4.3 Resistivities

Temperature dependence of resistivity,  $\rho$ , was measured by using a high-resistance meter (YHP 4329A and 4339B). Resistivity measurements were



27.5 Curie temperature,  $T_c$ , of the  $(\text{Na}_{1/2}\text{Bi}_{1/2})_{1-x}\text{M}_x\text{Bi}_4\text{Ti}_4\text{O}_{15}$  ( $\text{M} = \text{Ba}, \text{Ca}, \text{Pb}, \text{Sr}$  and  $\text{K}_{1/2}\text{Bi}_{1/2}$ ) (NXBT) system as a function of the amount ( $x$ ) of the substituted ions.

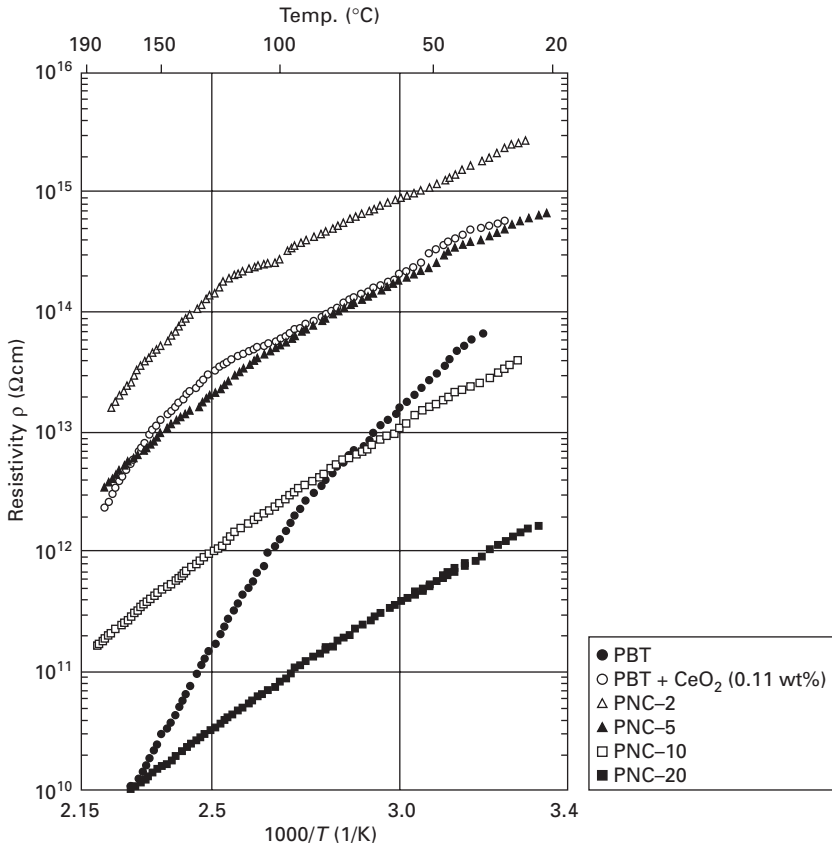


27.6 Curie temperature  $T_c$  of SBTT2 (x) and SBTT3 (x) as a function of Ta concentration (x).

made on unpoled specimens. In general, the conductivity of most dielectric materials increases with increasing temperature. It is essential for the high-temperature poling process that the conductivity of the material should somehow be suppressed, otherwise it becomes very difficult for a large electric field to be built up across the material at a high temperature. Also, piezoceramics having a high Curie temperature or large coercive field such as BLSF or  $\text{PbTiO}_3$  must have high resistivity at high temperatures to avoid thermal breakdown during the poling process.

Figure 27.7 shows the temperature dependence of the resistivity  $\rho$  of the  $\text{Pb}_{1-x}(\text{Na}_{1/2}\text{Ce}_{1/2})_x\text{Bi}_4\text{Ti}_4\text{O}_{15}$  [PNC-100x]<sup>7</sup> system as a function of the reciprocal absolute temperature. The resistivities of PNC-2 and PNC-5 are  $10^2$  or  $10^3$  times larger than those of conventional piezoceramics such as PZT and  $\text{BaTiO}_3$ . The resistivity at room temperature has a very high value of about  $10^{15}\ \Omega\ \text{cm}$ . Even at  $150^\circ\text{C}$ , it ranges from  $10^{12}$  to  $10^{13}\ \Omega\ \text{cm}$ . In Fig. 27.7, the amount of  $\text{Ce}^{4+}$  in PBT +  $\text{CeO}_2$  (0.11 wt.%) corresponds to that of  $\text{Ce}^{3+}$  in PNC-2. PNC solid solution is more effective for realizing high resistivity than using  $\text{CeO}_2$  as an additive. It seems to suggest that the trivalent cerium ion  $\text{Ce}^{3+}$  contributes to suppress the increase of electrical conductivity.

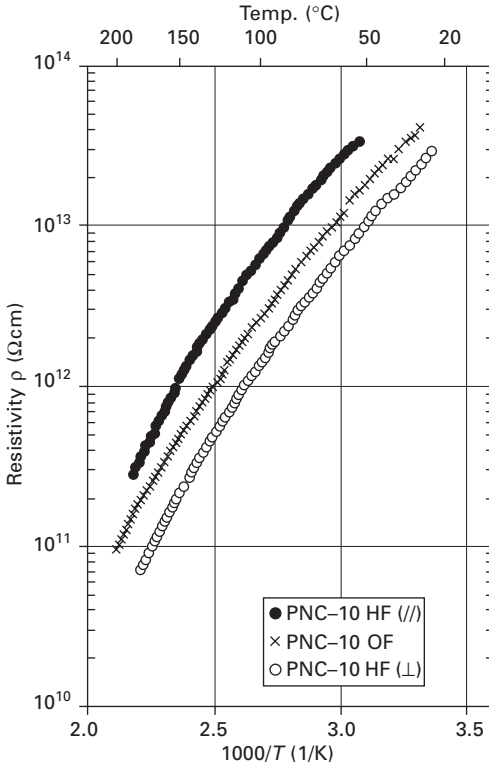
As shown in Fig. 27.8, the resistivity  $\rho$  [//] of hot-forged samples in the parallel direction to the forging axis is higher than  $\rho$  [ $\perp$ ] in the perpendicular direction. We find the value of  $\rho$  [OF] for ordinarily fired ones midway between  $\rho$  [//] and  $\rho$  [ $\perp$ ]. The parallel resistivity  $\rho$  [//] is about five times as large as the perpendicular resistivity  $\rho$  [ $\perp$ ] over the range of measurements that is,  $\rho$  [//]/ $\rho$  [ $\perp$ ] =  $\rho$  [ $\perp$ ]/ $\rho$  [//]  $\cong 5$ , where  $\sigma$  [ $\perp$ ] and  $\sigma$  [//] are conductivities.



27.7 Temperature dependence of resistivity  $\rho$  in the OF PNC system.

This anisotropy in resistivity of the HF sample can be explained as follows.

In our previous report,<sup>6</sup> we have shown SEM photographs of the perpendicular plane and the parallel plane in the HF Bi<sub>4</sub>Ti<sub>3</sub>O<sub>12</sub> ceramics, and concluded that thin plates of the crystallite are piled up along the forging axis and that the grains have a high degree of orientation in the ceramics. Therefore, if the influence of grain boundaries and porosity can be ignored, the resistivity  $\rho$  [//] or  $\rho$  [ $\perp$ ] in the parallel [//] or perpendicular [ $\perp$ ] direction to the forging axis corresponds, respectively, to  $\rho_c (= \rho_{33})$  or  $\rho_a$  (or  $\rho_b$ ) ( $= \rho_{11}$ ) in  $c$  axis or  $a$  (or  $b$ ) axis of the single crystal with bismuth oxide layer structure. In earlier treatments<sup>30</sup> of conduction in Bi<sub>4</sub>Ti<sub>3</sub>O<sub>12</sub> single crystal, an anisotropy in electrical conductivity  $\sigma_a$  (or  $\sigma_b$ ) and  $\sigma_c$  in  $a$  (or  $b$ ) axis and  $c$  axis was observed, whose  $\sigma_c (= \sigma_{33})$  is significantly smaller than  $\sigma_a$  (or  $\sigma_b$ ) ( $= \sigma_{11}$ ) in the single crystal due to the layered structure. The observed value<sup>30</sup> of  $\sigma_a$  (or  $\sigma_b$ ) at room temperature to about 250 °C was four to five times as



27.8 Temperature dependence of resistivity  $\rho$  in the HF PNC-10 (HF  $\perp$ ],  $\parallel$ ]), with that of the OF ones.

large as that of  $\sigma_c$ , namely,  $\sigma_a/\sigma_c = \sigma_{11}/\sigma_{33} = \rho_{33}/\rho_{11} = 4 \sim 5$ . Thus the anisotropy in conductivity of the HF ceramics as well as the dielectric properties can be estimated from those of the single crystals.

The anisotropy in the conductivity between the OF ceramics and the HF ones is less than that of single crystals, but the anisotropy in resistivity found in our present measurement is 2 to 3 for both  $\rho [\parallel]/\rho [\text{OF}]$  and  $\rho [\text{OF}]/\rho [\perp]$ . To account for this anisotropy, it is assumed<sup>31</sup> that the  $\parallel\perp$  aggregate is statistically homogeneous and isotropic and that there neither exists an additional phase at crystal boundaries nor that surface effects occur at these boundaries. Then the two most commonly used estimates for macroscopic conductivity  $\sigma^*$  in ceramic specimens are given<sup>31</sup> by Eqs (27.3) and (27.4).

$$\sigma^* = \frac{1}{3}(\sigma_{11} + \sigma_{22} + \sigma_{33}) \tag{27.3}$$

$$\frac{1}{\sigma^*} = \frac{1}{3} \left( \frac{1}{\sigma_{11}} + \frac{1}{\sigma_{22}} + \frac{1}{\sigma_{33}} \right) \tag{27.4}$$

where  $\sigma_{11} = \sigma_a$ ,  $\sigma_{22} = \sigma_b$ , and  $\sigma_{33} = \sigma_c$  are conductivity in the single crystal. It can be shown that Eqs. (27.3) and (27.4) are actually upper and lower bounds, respectively, on effective macroscopic conductivity. If  $\sigma_{11} \cong \sigma_{22}$  and  $\sigma_{11}/\sigma_{33} = \sigma_a/\sigma_c \cong 4.5$ , then Eq. (27.3) easily leads to the following equation:

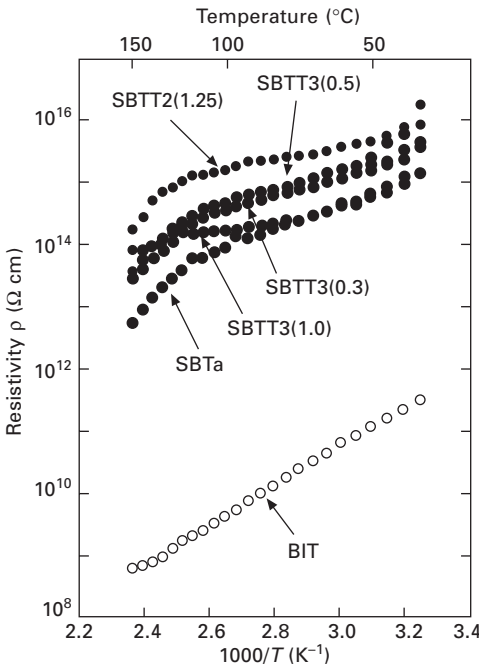
$$\frac{\sigma^*}{\sigma_{33}} \cong \frac{2\left(\frac{\sigma_{11}}{\sigma_{33}}\right) + 1}{3} \cong 3.3 \tag{27.5}$$

Also, Eq. (27.4) can be rewritten as follows:

$$\frac{\sigma^*}{\sigma_{33}} \cong \frac{3}{2\left(\frac{\sigma_{33}}{\sigma_{11}}\right) + 1} \cong 2.1 \tag{27.6}$$

Hence, the effective conductivity  $\sigma^*/\sigma_{33}$  in OF (non-oriented) ceramics can be estimated from Eqs. (27.5) and (27.6) to have some value between 2.1 and 3.3. The observed value of  $\sigma^*/\sigma_{33} = \rho [//]/\rho [OF]$  over the temperature range of 50 to 150 °C is approximately 2.5, showing close agreement between the measured and calculated results.

Figure 27.9 shows the temperature dependence of the resistivity of SBTT2 (x) and SBTT3 (x). The resistivity,  $\rho$ , of the BIT ( $m = 3, x = 0$ ) ceramic was



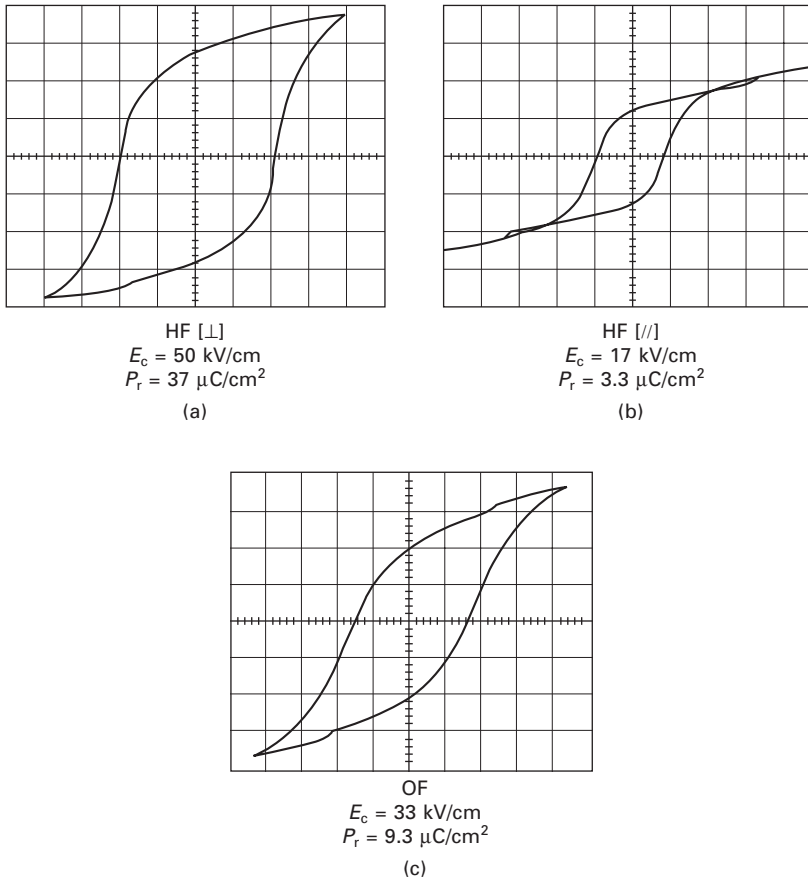
27.9 Temperature dependence of the resistivity of SBTT2 (x) and SBTT3 (x).

about  $10^{11}\Omega\text{cm}$ . SBTT ceramics have the high value of about  $10^{14}\text{--}10^{15}\Omega\text{cm}$  except for the SBTT3 (0) (BIT) ceramic. It is thought that a reason of this improvement is due to substitution of unstable  $\text{Ti}^{4+}$  ions by stable  $\text{Ta}^{5+}$  ions. From the result of  $\rho$ , SBTT ceramics except BIT seem to be suitable for heavy poling conditions with high applied fields at high temperatures.

#### 27.4.4 $D$ – $E$ hysteresis loops and remanent polarization

$D$ – $E$  hysteresis loops for HF and OF ceramics were observed by a standard Sawyer–Tower circuit at 50Hz. Samples for hysteresis loop measurements have a thickness of 0.3–0.5 mm and an area of 10–50 mm<sup>2</sup> with fired-on silver paste or vacuum-evaporated silver electrodes.

As shown in Fig. 27.10, hysteresis loops of both HF and OF BIT ceramics



27.10 Typical hysteresis loops of HF and OF ceramics at room temperature (at 50Hz), (a) the perpendicular [ $\perp$ ], (b) the parallel [ $\parallel$ ] and (c) OF.

were observed at room temperature. The shapes of the hysteresis loops in Fig. 27.10 resemble those of BIT thin films which were prepared by an RF sputtering method.<sup>32</sup> The spontaneous polarization  $P_s$ ,<sup>12</sup> lying in the monoclinic  $a_m$ - $c_m$  plane with an angle of about  $5^\circ$  to the  $a_m$ -axis, exhibits two components,  $P_{sa} = 50 \pm 10 \mu\text{C}/\text{cm}^2$  along the  $a_m$ -axis and  $P_{sc} = 4 \pm 0.1 \mu\text{C}/\text{cm}^2$  along the  $c_m$ -axis, approximately. When a strong electric field is applied, the spontaneous polarization direction in each crystal tends to switch to the equivalent direction nearest to that of the applied field. In the case of the perovskite-type structure, a simplified assumption has usually been adopted that under a strong poling field each randomly oriented crystallite becomes a single domain polarized in the closest direction of the 6, 12 or 8 directions possible in the tetragonal, orthorhombic or rhombohedral state, respectively. The reduced saturated remanent polarization  $P_r/P_s$  is calculated as:  $(3\sqrt{2}/8) \tan^{-1}(1/\sqrt{2}) = 0.831$ ,  $(3/\pi) \tan^{-1}\sqrt{2} = 0.912$  or  $(\sqrt{3}/2) = 0.866$ , respectively.<sup>33</sup>

On another assumption – that only  $180^\circ$  switching, which is accompanied by no mechanical strain, takes place – the remanent polarization is  $1/2$  of  $P_s$ , since every axis is randomly distributed over every direction.<sup>34</sup> Thus, a considerably high percentage of domains are oriented along the polarizing field, in fully polarized ferroelectric ceramics with perovskite type structure.

For the case of bismuth layer structure ferroelectric ceramics, completely saturated remanent polarization is calculated in a similar way. Though a  $90^\circ$  switching is accompanied by mechanical strains (elongation, contraction, and heat), their effects are neglected in the calculations. The results are as follows:

- *Perfect orientation* ( $F = 1$ ). Here, every  $c_m$ -axis is oriented along the forging axis and every  $a_m$ -axis lies randomly in the plane perpendicular to the forging axis.

- *Poling along the forging axis.* Every  $c_m$ -axis switched ( $180^\circ$ -reversal), and remanent polarization  $P_r$  [ $//$ ] is calculated as

$$P_r [//] = P_{sc}$$

- *Poling perpendicular to the forging axis in the case of only  $180^\circ$  switching:* Every  $a_m$ -axis is switched ( $180^\circ$ -reversal), and remanent polarization  $P_r$  [ $\perp$ ] is calculated as

$$P_r [\perp] = (2/\pi) P_{sa} = 0.637 P_{sa}$$

- *Poling perpendicular to the forging axis in the case of both  $180^\circ$  and  $90^\circ$  switchings:* Every  $a_m$ -axis is switched to one of four directions, namely along one of the  $\pm a_m$  and  $\pm b_m$ -axes, which is located closest to the poling field. Hence,

$$P_r [\perp] = \left( \frac{2\sqrt{2}}{\pi} \right) P_{sa} = 0.900 P_{sa}$$



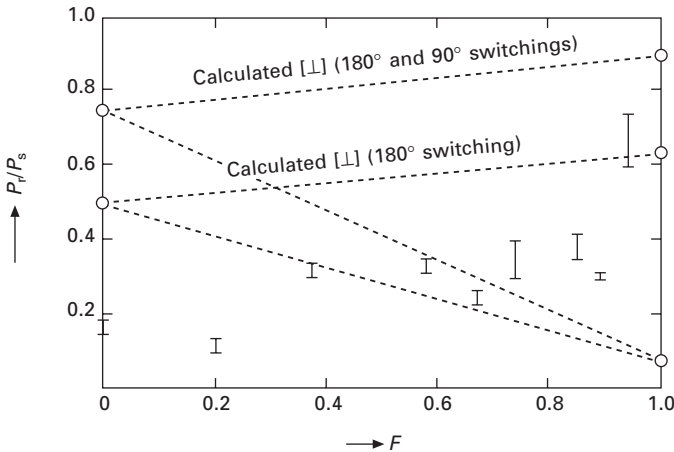
- Random orientation ( $F = 0$ ).
  - Case of only  $180^\circ$  switching:

$$P_r = \frac{(P_{sa} + P_{sc})}{2} = 0.500 (P_{sa} + P_{sc})$$

- Case of both  $180^\circ$  and  $90^\circ$  switchings:

$$P_r = \left(\frac{1}{\sqrt{2}}\right)P_{sa} + \left(\frac{1}{2}\right)P_{sc} = 0.707P_{sa} + 0.500P_{sc}$$

Figure 27.11 shows the dependence of  $P_r/P_s$  on the degree of orientation  $F$ . Observed values are obtained from 50 Hz hysteresis loops. Samples of intermediate value of  $F$  (0.2–0.7) are particularly fabricated by controlling the soaking time  $t_p$  in the HF process. Calculated values are given only for  $F = 0$  and  $F = 1$ . They are connected tentatively by straight dotted lines, though the relation between  $P_r$  and  $F$  is unknown. The value of 50 ( $\cong \sqrt{(50^2 + 4^2)}$ )  $\mu\text{C}/\text{cm}^2$  is used as  $P_s$  ( $= \sqrt{(P_{sa}^2 + P_{sc}^2)}$ ). Namely, the observed value of the remanent polarization  $P_r$  [ $\perp$ ] for  $F = 0.95$  is estimated to be about 82% of the calculated one in  $F = 1$  for both  $180^\circ$  and  $90^\circ$  switchings, which is supposed to be the case in the observation of the hysteresis loop. This seems to be due mainly to the lack of saturation in the loops (Fig. 27.10), since a sufficiently strong voltage cannot be applied. At all events, it is apparent that the HF process is more effective in producing a high remanent polarization than the OF process, the ratio  $P_r$  [ $\perp$ ]/ $P_r$  [//] and  $P_r$  [ $\perp$ ]/ $P_r$  [OF] being about 11 and 4, respectively, for  $F = 0.95$  at room temperature. Thus



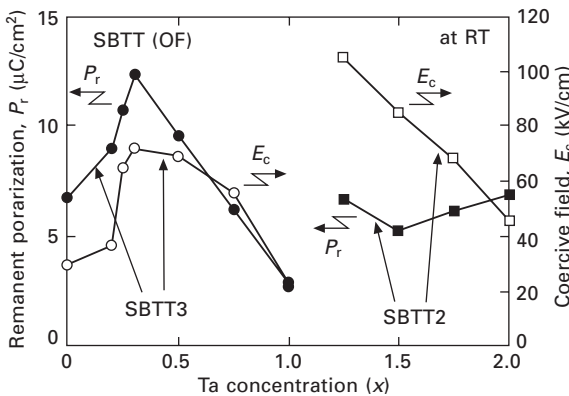
27.11 The dependence of  $P_r/P_s$ , on the degree of orientation  $F$  ( $\circ$  calculated, | observed).

HF is expected to be more useful for piezoelectric and pyroelectric applications. In these applications, however, the ceramics are poled and kept without electric fields, and  $P_r$  will be less than the value measured from the hysteresis loop, and may correspond to the case for only  $180^\circ$  switchings since  $90^\circ$  switchings tend to be depoled by mechanical strains induced in their switchings.

Figure 27.12 shows the remanent polarization,  $P_r$  of SBTT2( $x$ ) and SBTT3( $x$ ) at RT as a function of Ta concentration ( $x$ ). The values of  $P_r$  and  $E_c$  in SBTT2 decrease sharply with increasing of Sr or Ta concentration ( $x$ ). This tendency almost corresponds to the compositional dependence of  $T_c$ . The  $P_r$  of SBTT3 (0.3) was the largest ( $P_r = 12.3 \mu\text{C}/\text{cm}^2$ ) in the SBTT system. The  $D-E$  hysteresis loop of the BIT ceramic was not saturated sufficiently because of the electrical breakdown at about  $70 \text{ kV}/\text{cm}$ . On the other hand, the electrical breakdown of the SBTT3 (0.3) ceramic did not occur up to about  $140 \text{ kV}/\text{cm}$  because the resistivity was very high. Therefore, large piezoelectricity is expected for this composition. On SBTT2 ceramics, the  $E_c$  becomes higher with the decreasing concentration of Ta. Therefore, the  $D-E$  hysteresis loop of the SBTT2 ceramics was not saturated sufficiently.

#### 27.4.5 Piezoelectric properties

The electromechanical properties of poled ferroelectric ceramics depend strongly on the poling conditions, namely, poling temperature, poling field, and poling time. The high-temperature poling process seems to be very effective for activating piezo- and pyroceramics with a high Curie temperature or large coercive field such as BLSF or  $\text{PbTiO}_3$ -based materials. To pole at a high temperature, the BLSF ceramics must have high resistivity at that

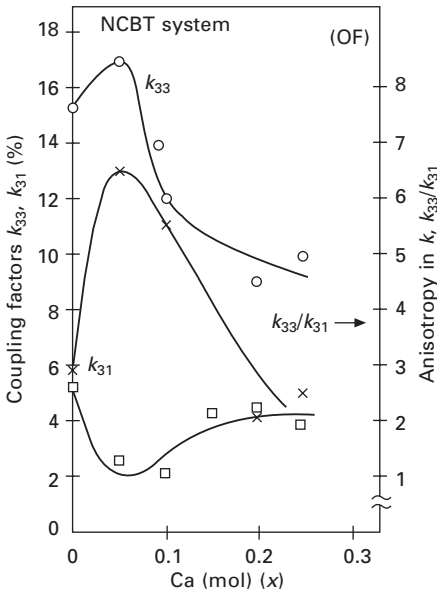


27.12 Remanent polarization,  $P_r$ , and coercive field,  $E_c$ , of the SBTT2( $x$ ) and SBTT3( $x$ ) as a function of Ta concentration ( $x$ ) at room temperature and 50 Hz.

temperature to avoid thermal breakdown or damage during the poling process. The empirical data show that the Mn-dopant is very effective in reducing conductivity at high temperatures.

Specimens for piezoelectric and pyroelectric measurements were poled in a stirred silicone oil. Poling conditions of applied field,  $E_p$ , temperature,  $T_p$ , and time,  $t_p$ , are about 5–30 kV/mm, 150–200 °C and 1–15 min, respectively. Piezoelectric properties were measured by means of a resonance–antiresonance method on the basis of IEEE standards using an impedance analyzer (YHP 4192A and 4194A). The electromechanical coupling factor,  $k_{33}$ , was calculated from the resonance and antiresonance frequencies. The free permittivity,  $\epsilon_{33}^T$ , and the loss tangent,  $\tan \delta_{33}$ , were determined from the capacitance measurement at 1 or 10 kHz of the poled specimen. The piezoelectric strain constants,  $d_{ij}$ , the piezoelectric voltage constants,  $g_{ij}$ , and the elastic constants,  $s_{ij}^E$ , were calculated from the coupling factor,  $k_{ij}$ , the free permittivity,  $\epsilon_{ii}^T$ , the frequency constant,  $N_{ij}$ , and the measured density,  $\rho_0$ .

Figure 27.13 shows electromechanical coupling factors,  $k_{33}$  and  $k_{31}$ , of the longitudinal and the transverse modes, along with the anisotropy,  $k_{33}/k_{31}$ , in the coupling factor  $k$  of the NCBT (OF) system as a function of Ca concentration ( $x$ ) in mol. The  $k_{33}$  shows a peak at  $x = 0.05$ , corresponding to the maximum of  $\epsilon_s$  (at  $T_c$ ), while the  $k_{31}$  has a minimum value at this composition, resulting in a high value for the anisotropy,  $k_{33}/k_{31}$ . This composition ( $x = 0.05$ ) seems



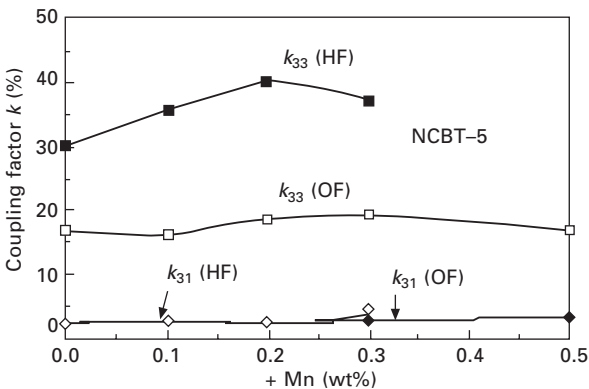
27.13 Electromechanical coupling factors,  $k_{33}$  and  $k_{31}$ , for each vibration mode and the anisotropy,  $k_{33}/k_{31}$ , in the  $k$  of the NCBT system (OF) as a function of Ca mol ( $x$ ).

to be the most suitable for piezoelectric properties.

Since the grain orientation effects on the piezo- and pyroelectric properties by the HF technique give almost proportional enhancements to those of non-oriented (OF) samples, the preparation of grain-oriented (HF) samples was made only for the composition with 5 mol% Ca concentration ( $x = 0.05$ ), which seems to be the most favourable for piezoelectric and pyroelectric activities (Fig. 27.13). The HF samples were almost smoothly deformed at temperatures of 1100–1200 °C. The grain orientation factor,  $F$ , of the HF ceramics is more than 90% and the values of the respective samples are given in Table 27.1.

Figure 27.14 shows the coupling factors,  $k_{33}$  and  $k_{31}$ , of the Mn-doped NCBT-5 (+Mn(wt%)) (HF and OF) as a function of Mn doping concentration in wt%. The  $k_{33}$  of the HF sample has a maximum value of about 0.4 at 0.2 wt% of Mn. On the other hand, the  $k_{31}$  of the HF or the OF sample shows low values of about 0.03 or less. As a result, the anisotropy,  $k_{33}/k_{31}$ , in the coupling factor  $k$  of the HF NCBT-5 + Mn(0.2) reaches about 17, which is three or more times larger than that of the non-oriented (OF) samples or the usual PZT piezoelectric ceramics.

Table 27.1 gives typical values of the elastic, piezoelectric, and dielectric (EPD) constants of the NCBT+Mn ceramics, comparing grain-oriented (HF) samples with non-oriented (OF) ones. The  $T_c$  is higher than 660 °C. The  $\epsilon_{33}^T$  is one-third of that of the conventional PZT ceramics. The values of  $k_{33}$ ,  $d_{33}$ , or  $g_{33}$  of the grain-oriented (HF) ceramics are more than two times as large as that of non-oriented (OF) ceramics, while their values of the (31) mode show few changes. The large anisotropy,  $k_{33}/k_{31}$  or  $d_{33}/d_{31}$ , was enhanced by the grain orientation. This means that the HF NCBT ceramics have a larger  $d_{hgh} (= (d_{33} - 2d_{31})(g_{33} - 2g_{31}))$  constant than that of the OF ones or the



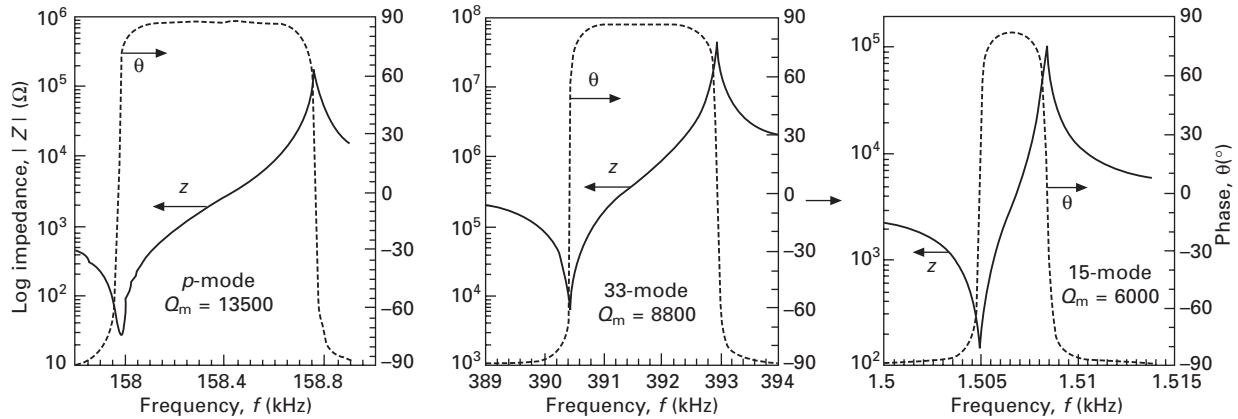
27.14 Coupling factors,  $k_{33}$  and  $k_{31}$ , of the NCBT-5 (HF and OF) as a function of Mn doping concentration (wt%).

conventional PZT ceramics. Therefore, these piezoceramic materials are preferable for the hydrophone application at high temperatures, or for high-frequency resonators.

The high mechanical quality factor,  $Q_m$ , was obtained for BLSF ceramics in some previous reports. For example, Nanao *et al.* [35] and Shibata *et al.* [36] reported that the  $Q_m$  shows 9000 in thickness (t)-mode for  $\text{Bi}_3\text{TiNbO}_9$ – $\text{BaBi}_2\text{Nb}_2\text{O}_9$  solid solution and 11000 in planar (p)-mode for  $\text{SrBi}_2\text{Ta}_2\text{O}_9$ – $\text{CaBi}_2\text{Ta}_2\text{O}_9$  solid solution, respectively. The common features of these reports are that the end members of these systems,  $\text{Bi}_3\text{TiNbO}_9$  and  $\text{CaBi}_2\text{Ta}_2\text{O}_9$ , have a very high  $T_c$  above 800 °C. These data suggest the possibility of high  $Q_m$  can be obtained by BLSF materials with high  $T_c$ . By this concept, the piezoelectric properties of  $\text{Bi}_3\text{TiTaO}_9$  (BTT) ( $m = 2$ ) (SBTT2(1)) based solid solution systems such as SBTT2 and SBTT3 with high Curie temperatures seem to have high  $Q_m$  values.

About the SBTT2 system, the  $T_c$  of the SBT (SBTT2(2)) ceramic is 280 °C and becomes higher with the increasing amount of modified BTT so that the  $T_c$  is higher than 900 °C. The  $Q_m$  and  $k_p$  were enhanced with the maximum value of 9000 and 0.12, respectively, on the SBTT2 (1.375) with poling conditions of  $E_p = 7$ –10 kV/mm,  $T_p = 250$  °C, and  $t_p = 7$  min. On the other hand, SBTT2 (1.25) with the poling condition of  $T_p = 300$  °C shows the maximum  $Q_m$  of 13500 in the (p)-mode. This value is extremely high in usual piezoelectric ceramics. Figure 27.15 shows the frequency dependence of impedance,  $Z$  (magnitude  $|Z|$ , and phase  $\theta$ ), of (p)-, (33)- and (15)-vibration modes for the SBTT2 (1.25) ceramic. Using the same poling conditions,  $Q_m$  values of (33) and (15) modes for SBTT2 (1.25) were about 8800 and 6000, respectively. The  $Q_m$  of SBTT2 ceramic is higher than 6000. It is thought that high  $Q_m$  of SBTT2 causes the high  $T_c$  and large  $E_c$  shown in Figs. 27.6 and 27.12, respectively. Temperature coefficients of the resonance frequency,  $\text{TC-}f_r$ , of SBTT2 (1.25) were  $-82$  ppm/°C for (33) mode and  $-97$  ppm/°C for (15) mode, respectively.

Table 27.2 summarizes the piezoelectric properties of OF and HF SBTT ceramics. The orientation factor,  $F_i$  of the SBTT3 (0.3) ceramic is 70% which is relatively low. The  $k_{33}$  value of the HF SBTT3 (0.3) ceramic is 0.37. This value is about three times larger than that of the non-oriented sample. Comparing with  $k_{33}$  value between the HF BIT and SBTT3 (0.3) ceramic, the  $k_{33}$  of SBTT3 (0.3) shows larger than that of BIT. It is thought that these results are caused by the change of the resistivity. In other words, through the poling treatment, the saturated  $k_{33}$  value is not observed on the BIT ceramic because of electrical breakdown in this study. The piezoelectric constant,  $d_{33}$ , of the HF SBTT3 (0.3) ceramic shows 45.3 pC/N. This  $d_{33}$  is relatively large in the BLSF and is larger than that of the HF BIT ceramic. If the saturated  $k_{33}$  can be obtained on the BIT ceramic, the  $k_{33}$  must be larger than that of SBTT3 (0.3) ceramic. Poling treatments of



27.15 Frequency dependence of impedance,  $Z$  (magnitude  $|Z|$ , and phase  $\theta$ , of (p)-, (33)- and (15)-modes for the SBT2 (1.25) ceramic.

Table 27.2 Piezoelectric properties of HF and/or OF SBTT3(0) (BIT), SBTT3 (0.3) and SBTT2 (1.25) ceramics

Composition (SBTT <i>m</i> ( <i>x</i> ))	BIT	SBTT3 (0.3)		SBTT2 (1.25)
	HF	OF	HF	OF
Curie temperature, $T_c$ (°C)	675	540	540	770
Density, $\rho_0$ (g/cm <sup>3</sup> )	7.90	7.75	7.77	8.66
Orientation factor, $F_i$ (%)	80	–	70	–
Dielectric constant, $\epsilon_{33}^T/\epsilon_0$	129	188	187	122
Coupling factor, $k_{33}$ (%)	25.5	12.8	37.1	15.7
$k_{31}$ (%)	3.20	3.73	3.40	5.99
$k_p$ (%)	–	4.61	–	8.99
Quality factor, $Q_m$ ( <i>p</i> -mode)	–	1243	–	2848
Piezoelectric anisotropy, $k_{33}/k_{31}$	7.96	3.43	10.9	2.61
Piezoelectric constant, $d_{33}$ (pC/N)	25.3	14.6	45.3	15.7
Frequency constant, $N_{33}$ (Hz m)	1990	2026	2046	1791

SBTT2 ceramics were very difficult because of the very high  $E_c$ . On the other hand, the  $Q_m$  values of SBTT2 ceramics are larger than those of SBTT3 ceramics.

#### 27.4.6 Pyroelectric properties

Temperature dependences of the pyroelectric coefficient,  $p$ , were measured by the modified Byer–Roundy technique,<sup>9,37,38</sup> over the temperature range from  $-20$  to  $200^\circ\text{C}$ . The coefficient,  $p$ , was calculated from the relation  $p = (i/A)/(dT/dt)$ , as a function of temperature, where  $i$  is the pyroelectric current,  $A$  the electroded area of the specimen and  $dT/dt$  the heating rate. The measurements were made during the heating cycles with a typical heating rate of  $2\text{--}3^\circ\text{C}/\text{min}$ . The room temperature value of the  $p$  was obtained from the average value of  $20\text{--}25^\circ\text{C}$ .

The suitability of a pyroelectric material for infrared sensing is usually judged by its figures of merit,  $F_V$  and  $F_D$ , which can be calculated using the material constants and the expressions as follows:  $F_V = [p/(C_v\epsilon)]$  and  $F_D = [p/(C_v\sqrt{\epsilon \tan \delta})]$ , where  $\epsilon = \epsilon_{33}^T/\epsilon_0$  is free dielectric constant,  $C_v = C_s\rho_0$  the volume specific heat,  $C_s$  specific heat and  $\rho_0$  measured density.

Table 27.3 summarizes the pyroelectric properties of the NCBT ceramics, along with the figures of merit,  $F_V$  and  $F_D$ , comparing HF values with OF ones. In these calculations, the  $C_s$  of the NCBT ceramics was assumed to be the same value as that ( $C_s = 0.41\text{ J/g}^\circ\text{C}$ ) of the PT-based ceramics, because no data on the  $C_s$  values of NCBT ceramics exist. The  $F_V$  and  $F_D$  of HF samples are two times larger than those of OF ones, having the same enhancement<sup>21,23</sup> as that of the piezoelectric properties. The  $F_V$  of HF NCBT ceramics is comparable to the typical values obtained for the PT-based ceramics, but the  $F_D$  is smaller compared with the values for the PZ-based ceramics. This is mainly due to the fact that the pyro-coefficient,  $p$ , in the case of

Table 27.3 Pyro-coefficient,  $p$ , dielectric constant,  $\epsilon$ , loss tangent,  $\tan \delta$ , volume heat capacity,  $C_v$ , figure of merit,  $F_v$  and  $F_D$ , and Curie temperature,  $T_C$ , of the OF and HF  $(\text{Na}_{1/2}\text{Bi}_{1/2})_{1-x}\text{Ca}_x\text{Bi}_4\text{Ti}_4\text{O}_{15}$  (NCBT-100x) ( $x = 0$ : NBT) ceramics

Sample		$p$ ( $\times 10^{-8}$ ) C/cm <sup>2</sup> °C	$\epsilon$	$\tan \delta$ (%)	$C_v$ J/cm <sup>3</sup> °C	$F_v$ ( $\times 10^{-11}$ ) C cm/J	$F_D$ ( $\times 10^{-9}$ ) C cm/J	$T_c$ °C
NBT	(HF)	1.3	149	0.32	2.99	2.9	6.3	660
+ Mn(0.1)	(OP)	0.56	140	0.29	2.87	1.4	3.1	658
NCBT-5	(HF)	1.1	149	0.38	2.95	2.5	5.0	670
	(OF)	0.68	151	0.33	2.86	1.6	3.4	674
NCBT-5	(HF)	1.0	134	0.17	2.84	2.6	7.4	665
+Mn(0.1)	(OF)	0.82	148	0.16	2.82	2.0	6.0	680
PT		1.8	190		3.2	3.0		460
PZ		3.5	250	0.5	2.6	5.4	12	200

$$F_v = \frac{p}{C_v \cdot \epsilon}, F_D = \frac{p}{C_v \sqrt{\epsilon \tan \delta}}, \text{ where } \epsilon = \frac{\epsilon_{33}^T}{\epsilon_0} \text{ and } C_v = C_s \cdot \rho_0.$$

$\rho_0$  : measured density,  $C_s = 0.41$  J/g °C (PbTiO<sub>3</sub>).

+Mn(0.1) : + MnCO<sub>3</sub> (0.1 wt%).

PT = PbTiO<sub>3</sub>-based ceramics, PZ = PbZrO<sub>3</sub>-based ceramics.



NCBT ceramics is smaller than that obtained in PZ-based or PT-based compositions.

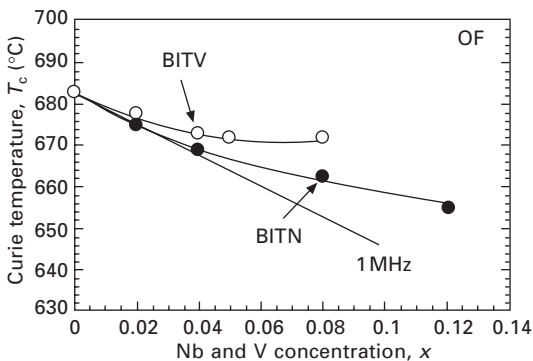
Grain-oriented (HF) NCBT ceramics with a large pyroelectric coefficient, low dielectric constant, low loss tangent, and high Curie temperature produce a superior candidate for excellent pyroelectric sensor materials to be used as highly stabilized infrared temperature detectors.

### 27.4.7 Recent progress on $\text{Bi}_4\text{Ti}_3\text{O}_{12}$ -based system

Bismuth titanate,  $\text{Bi}_4\text{Ti}_3\text{O}_{12}$  (BIT) is a typical well-known BLSF<sup>1,20,28,39</sup> and the BIT single crystal has a good piezoelectricity. However, it is difficult to measure piezoelectric properties on the BIT single crystal because the shape of the grown BIT single crystals is always platelet and usually very thin. On the other hand, fully reliable piezoelectric properties of BIT ceramics have not been reported because of some problems such as the low resistivity and the large coercive field.<sup>2,3,6,12,40-43</sup> To solve these problems,  $\text{Nb}^{5+}$  and  $\text{V}^{5+}$  ions were doped into BIT ceramic to obtain higher resistivities.<sup>44,45</sup> Recently,  $\text{Bi}_4\text{Ti}_{3-x}\text{Nb}_x\text{O}_{12}$  [BITN- $x$ ] and  $\text{Bi}_4\text{Ti}_{3-x}\text{V}_x\text{O}_{12}$  [BITV- $x$ ] ceramics are studied regarding on their dielectric, ferroelectric, and piezoelectric properties. Furthermore, the grain orientation effects of BITN and BITV ceramics on their piezoelectric properties are discussed using the grain-oriented ceramics prepared by the HF method.

X-ray diffraction patterns for BITN and BITV ceramics (OF) show a single phase of bismuth layer-structured compounds with the layer number,  $m = 3$ . No peaks of  $\text{Nb}_2\text{O}_5$  and  $\text{V}_2\text{O}_5$  were observed within  $x \leq 0.12$ . Both BITN and BITV ceramics have relative density ratios higher than 95% of the theoretical density.

Figure 27.16 shows  $T_c$  as a function of Nb and V concentration. The  $T_c$  of the BIT ( $x = 0$ ) ceramic is 683 °C and gradually decreases lower with increasing

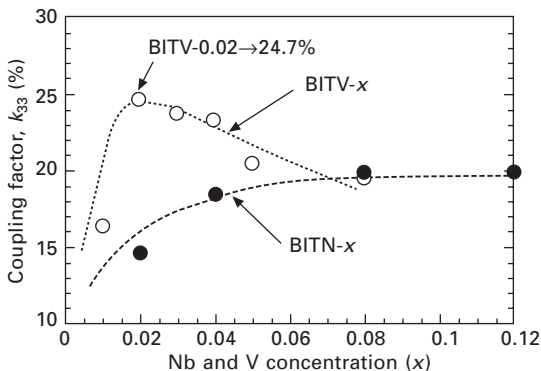


27.16 Curie temperature,  $T_c$ , of BITN and BITV ceramics as a function of Nb and V concentrations.

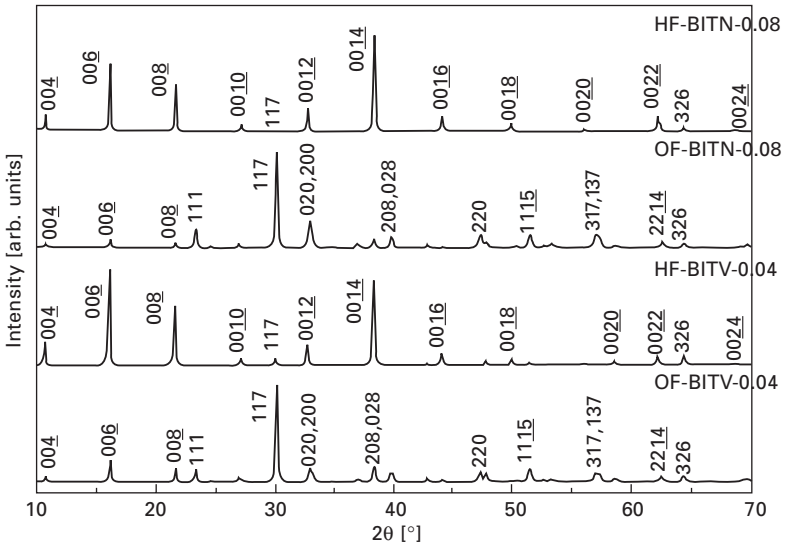
Nb and V concentration. Therefore, it is thought that the Nb and V ions occupy the B-site of the pseudo-perovskite cell in the bismuth layer-structure. However, the  $T_c$  of BITV has a tendency to saturate with the increasing V concentration, compared with the BITN ceramics. Therefore, it is thought that V ions to be in the place of Ti ions. Excess V ions seem to exist on the grain boundary and/or the triple point when the V concentration increases. This consideration is estimated by the ionic radii of Ti, Nb, and V ions. The ionic radii of  $Ti^{4+}$  (IV coordination),  $Nb^{5+}$  (IV coordination), and  $V^{5+}$  (IV coordination) are 0.605, 0.64, and 0.54 Å, respectively, according to Shannon.<sup>46</sup> It is thought that the ionic radius of the V ion is too small to substitute on the B-site of the pseudo-perovskite cell in the bismuth layer-structure. The resistivity,  $\rho$ , of BIT ( $x = 0$ ) is about  $10^{10}$ – $10^{11}$  Ω cm, and, those of BITN and BITV ceramics are about  $10^{13}$ – $10^{14}$  Ω cm. It is clear that  $\rho$  is enhanced by some donor-dopings. The optimum charge neutrality was observed for each composition of BITN-0.08 and BITV-0.01, respectively. Figure 27.17 shows the compositional dependences of the electromechanical coupling factor  $k_{33}$  on the dopant Nb and V concentration ( $x$ ). The  $k_{33}$  of BITN reaches the saturated value (0.20) for the composition of  $x = 0.08$ , while the  $k_{33}$  of BITV-0.02 is 0.25, which is a relatively high value for BLSF ceramics with random orientations.

Figure 27.18 shows X-ray diffraction patterns of BITN-0.08 and BITV-0.04 ceramics for the perpendicular plane (polished) of the HF ceramics and the OF ones. It is very clear that grains in the HF ceramics were oriented along the  $c$ -axis because the intensities of the (00 $l$ ) planes of the HF samples are very high. The grain orientation factors,  $F$ , of BITN-0.08 and BITV-0.04 were 0.91 and 0.75, respectively.

Figure 27.19 shows the frequency dependence of the impedance,  $Z$  (magnitude  $|Z|$  and phase  $\theta$ ), of HF BITN-0.08 and HF BITV-0.04 ceramics.



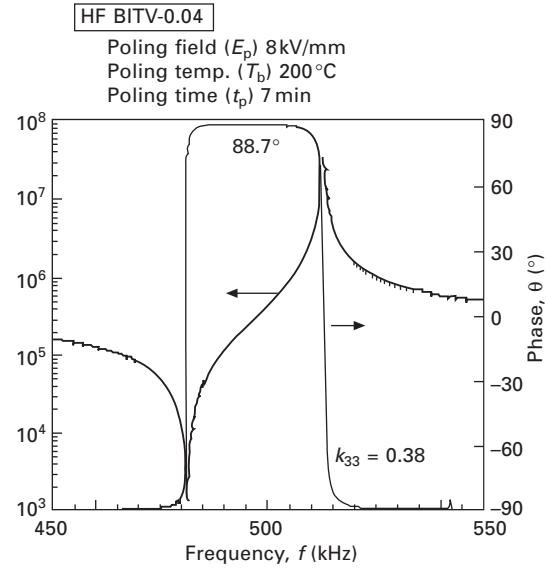
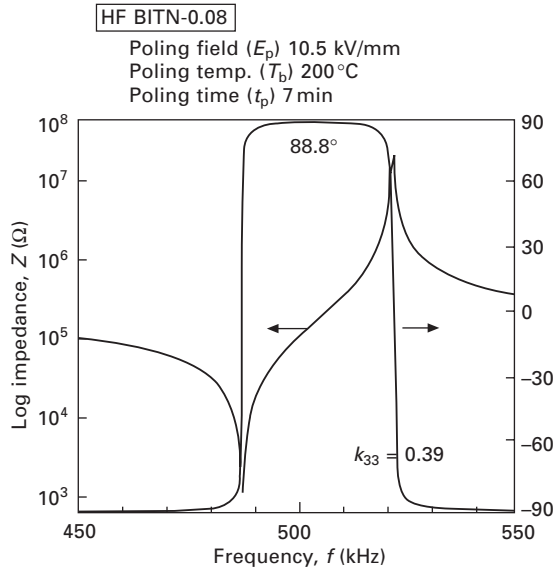
27.17 Electromechanical coupling factor  $k_{33}$  of BITN (OF) and BITV (OF) as a function of the dopant concentration ( $x$ ).



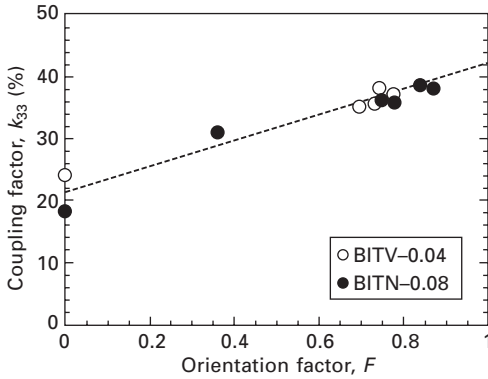
27.18 X-ray diffraction patterns of BITN-0.08 and BITV-0.04 ceramics for the perpendicular plane (polished) of the HF and the OF.

Good profiles were obtained and their  $k_{33}$  values were enhanced to 0.39 and 0.38 for BITN-0.08 and BITV-0.04, respectively. These values are about twice as large as those of non-oriented (OF) ones, and are larger than the reported value ( $k_{33} = 0.27$ )<sup>21</sup> of HF BIT ceramics. In this investigation, a saturated  $k_{33}$  value of the BIT ceramic was not observed because of an electrical breakdown during the poling process. Figure 27.20 shows the  $k_{33}$  of the HF BITN-0.08 and the BITV-0.04 as a function of the orientation factor,  $F$ . Accurate  $F$  was obtained using the X-ray diffraction (XRD) patterns for the  $k_{33}$  specimen, that is, XRD was performed directly on the  $k_{33}$  specimen shown in Fig. 27.21. From this measurement, the relationship between  $k_{33}$  and  $F$  is clear:  $k_{33}$  increases linearly with the increasing orientation factor,  $F$ . From this figure, the  $k_{33}$  value for the specimen with a perfect orientation ( $F = 1$ ) could be extrapolated to be almost 0.42.

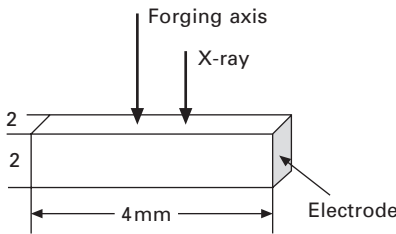
Figure 27.22 shows the temperature dependence of the  $k_{33}$  and the ratio of impedance peak/depth,  $P/D$ , obtained from the resonance and antiresonance curve for the HF BITN-0.08 ceramic. The  $k_{33}$  higher than 0.35 was maintained from room temperature up to 650 °C. However, the  $P/D$  decrease rapidly at temperatures higher than 350 °C. In other words, sharp resonance and antiresonance peaks with high  $P/D$  greater than 1000 was kept up to 350 °C. It is clear that the HF BITN-0.08 ceramic maintains high piezoelectric properties from RT up to 350 °C. The donor doped-BIT ceramics seem to be a superior candidate for lead-free high-temperature piezoelectric materials.



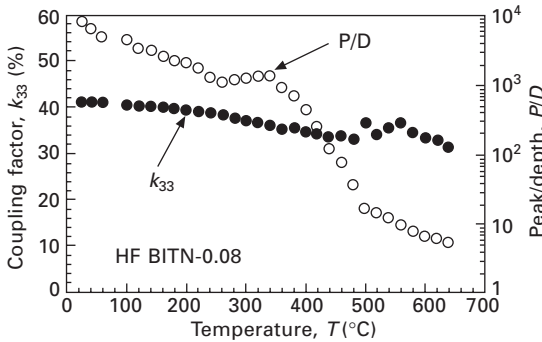
27.19 Frequency dependence of the impedance,  $Z$  (magnitude  $|Z|$ , and phase  $\theta$ , of HF BITN-0.08 and HF BITV-0.04.



27.20 Coupling factor,  $k_{33}$ , of HF BITN-0.08 and BITV-0.04 as a function of orientation factor,  $F$ .



27.21 Shape for measuring of the orientation factor,  $F$ , and the coupling factor,  $k_{33}$ .



27.22 Temperature dependence of  $k_{33}$  and the ratio of impedance peak/depth,  $P/D$ , of the HF BITN-0.08.

## 27.5 Conclusions and future trends

The results of our investigations on hot-forged (HF) ceramics indicate that the HF method produces strongly preferred grain orientation, which was confirmed by X-ray diffraction patterns, SEM observation and electrical measurements.

The degree of grain orientation  $F$  calculated from X-ray diffraction patterns increases as an area ratio  $\gamma$  (or a thickness contraction rate  $\lambda$ ), and is found to be as large as  $F = 0.95$  when  $\gamma = 8$  in  $\text{Bi}_4\text{Ti}_3\text{O}_{12}$  (BIT). Considerable anisotropy in the dielectric constant  $\epsilon_s$  of HF BIT ceramics was observed, and the value of  $\epsilon_s [\perp]/\epsilon_s [//]$  was 5 at the Curie temperature of  $680^\circ\text{C}$ . Moreover, we have noted that remanent polarizations  $P_r [\perp]$  and  $P_r [//]$  in the HF BIT ceramics correspond to the components  $P_{sa}$  along the  $a_m$ -axis and  $P_{sc}$  along the  $c_m$ -axis, respectively, of the spontaneous polarization  $P_s$  of a single crystal. It was made clear that the remanent polarization  $P_r [\perp]$  in the HF ceramics is much larger than that of the non-oriented (OF) ones, the ratio  $P_r[\perp]/P_r[//]$  and  $P_r [\perp]/P_r [\text{OF}]$  being about 11 and 4 in BIT, respectively, for  $F = 0.95$  at room temperature. The value of the remanent polarization  $P_r [\perp]$  for  $F = 0.95$  is estimated to be 82% of the calculated value.

Grain orientation of calcium modified  $(\text{Na}_{1/2}\text{Bi}_{1/2})_{1-x}\text{Ca}_x\text{Bi}_4\text{Ti}_4\text{O}_{15}$  (NCBT) system enhanced their piezoelectric and pyroelectric properties by two or more times. From the viewpoint of piezoelectric applications, 5 mol% Ca-modified, Mn-doped and grain-oriented NCBT (HF NCBT-5 + Mn) ceramics are superior, with a lower free permittivity,  $\epsilon_{33}^T/\epsilon_0$  ( $\cong 130$ ) and a higher electromechanical coupling factor,  $k_{33}$  ( $= 0.36\text{--}0.40$ ), along with a higher anisotropy,  $k_{33}/k_{31}$  ( $= 13\text{--}17$ ). Therefore, the HF NCBT-5 + Mn ceramics seem to be potential candidate materials for hydrophone applications or for high-frequency ultrasonic transducers at high temperatures. Pyroelectric properties of the HF NCBT-5 + Mn are also very interesting and the figure of merit ( $F_V$ ) is comparable to that of the PZ-based or PT-based materials.

One of the bismuth layer-structured ferroelectrics (BLSF) series,  $\text{Sr}_{m-3+x}\text{Bi}_{4-x}\text{Ti}_{m-x}\text{Ta}_x\text{O}_{3m+3}$  ( $1 \leq x \leq 2$  for  $m = 2$ ,  $0 \leq x \leq 2$  for  $m = 3$ ) (SBTT $m$  ( $x$ )) has very interesting dielectric, ferroelectric, and piezoelectric properties. It is clear that SBTT2 (1.25) ( $m = 2$ ) ceramic has high Curie temperature ( $=785^\circ\text{C}$ ) and is considered as a superior candidate for piezo- or pyroelectric sensor materials with high  $T_C$ . The SBTT3 (0.3) ceramic shows a relatively large remanent polarization,  $P_r$  ( $=12.3 \mu\text{C}/\text{cm}^2$ ), compared with SBT ( $m = 2$ ,  $x = 0$ ) and BIT ( $m = 3$ ,  $x = 0$ ). The SBTT3 (0.3) ceramic shows strong ferroelectricity and high piezoelectricity. The electromechanical coupling factor,  $k_{33}$  and piezoelectric constant,  $d_{33}$ , of the grain-oriented SBTT3 (0.3) ceramic were relatively high:  $k_{33} = 0.37$  and  $d_{33} = 45.3 \text{ pC}/\text{N}$ , respectively. The mechanical quality factor,  $Q_m$ , of the SBTT2 (1.5) ceramic was higher than 6000. The SBTT ceramics seem to be a superior candidate for lead-free piezoelectric resonator materials with high mechanical quality factors,  $Q_m$ , or high-temperature piezoelectric sensor materials with high Curie temperatures.<sup>47,48</sup>

Future trends of the research in bismuth layer-structured ferroelectrics (BLSFs) seem to be focused on environmentally gentle lead-free piezoelectric materials for high-temperature sensors, high-frequency applications and

temperature-stable ceramic resonators. Also textured grain orientations such as the templated grain growth (TGG) and the seeded polycrystal conversion (SPC) methods are other important keywords for the future trends of BLSF research and developments. Trend toward the thick and thin films is important for film bulk acoustic wave (FBAW) and micro-electro-mechanical systems (MEMS) applications.

## 27.6 Acknowledgments

This work was partially supported by a Grant-in-Aid for Scientific Research (C) (Nos. 07650790, 09650737) and (B) (Nos. 11555168, 13555176, 15360352, and 17360327) from the Japan Society for the Promotion of Science.

The author would like to express sincere thanks to the late Professor Masakazu Marutake of University of Electro-Communications for valuable discussion, particularly on the calculation of the remanent polarization. He would also like to thank Professor Emeritus Koichiro Sakata of Tokyo University of Science for encouraging this work for many years.

## 27.7 References

1. Subbarao E C (1962), 'Crystal chemistry of mixed bismuth oxides with layer-type structure', *J. Am. Ceram. Soc.* **45** (4), 166–169.
2. Ikegami S and Ueda I (1974), 'Piezoelectricity in ceramics of ferroelectric bismuth compound with layer structure', *Jpn. J. Appl. Phys.* **13** (10), 1572–1579.
3. Takenaka T and Sakata K (1982), 'Dielectric and piezoelectric properties of some bismuth layer-structured ferroelectric ceramics', *Jpn. J. IEEE (C)*, **J65-C** (7), 514–521 [in Japanese].
4. Takenaka T, Shoji K, Takai H and Sakata K (1976), 'Ferroelectric and dielectric properties of press forged  $\text{Bi}_4\text{Ti}_3\text{O}_{12}$  ceramics', *Proc. 19th Jap. Cong. Materials Research, Tokyo, 1975* (The Society of Materials Science, Kyoto, 1976), 230–233.
5. Takenaka T, Shoji K and Sakata K (1977), 'Grain orientation and microstructure of hot-forged  $\text{Bi}_4\text{Ti}_3\text{O}_{12}$  ceramics', *Proc. 20th Jap. Cong. Materials Research, Kyoto, 1976* (The Society of Materials Science, Kyoto, 1977), 212–214.
6. Takenaka T and Sakata K (1980), 'Grain orientation and electrical properties of hot-forged  $\text{Bi}_4\text{Ti}_3\text{O}_{12}$  ceramics', *Jpn. J. Appl. Phys.* **19** (1), 31–39.
7. Takenaka T and Sakata K (1984), 'Grain orientation effects on electrical properties of bismuth layer-structured ferroelectric  $\text{Pb}_{(1-x)}(\text{NaCe})_{x/2}\text{Bi}_4\text{Ti}_4\text{O}_{15}$  solid solution', *J. Appl. Phys.* **55** (4), 1092–1099.
8. Takenaka T and Sakata K (1989), 'Piezoelectric and pyroelectric properties of calcium-modified and grain-oriented  $(\text{NaBi})_{1/2}\text{Bi}_4\text{Ti}_4\text{O}_{15}$  ceramics', *Ferroelectrics* **94**, 175–181.
9. Takenaka T and Sakata K (1983), 'Pyroelectric properties of grain-oriented bismuth layer-structured ferroelectric ceramics', *Jpn. J. Appl. Phys.* **22** (Suppl. 22-2), 53–56.
10. Takenaka T and Sakata K (1991), 'Pyroelectric properties of bismuth layer-structured ferroelectric ceramics', *Ferroelectrics* **118**, 123–133.
11. Cummins S E and Cross L E (1967), 'Crystal symmetry, optical properties, and

- ferroelectric polarization of  $\text{Bi}_4\text{Ti}_3\text{O}_{12}$  single crystals', *Appl. Phys. Lett.* **10** (1), 14–16.
12. Cummins S E and Cross L E (1968), 'Electrical and optical properties of ferroelectric  $\text{Bi}_4\text{Ti}_3\text{O}_{12}$  single crystals', *J. Appl. Phys.*, **39** (5), 2268–2274.
  13. Aurivillius B (1949) 'Mixed bismuth oxides with layer lattices-I. The structure type of  $\text{CaNb}_2\text{Bi}_2\text{O}_9$ ', *Arkiv Kemi* **1**, 463–480; *ibid.* (1949), 'Mixed bismuth oxides with layer lattices-II. Structure of  $\text{Bi}_4\text{Ti}_3\text{O}_{12}$ ', **1**, 499–512; *ibid.* (1950), 'Mixed bismuth oxides with layer lattices-III. Structure of  $\text{BaBi}_4\text{Ti}_4\text{O}_{15}$ ', **2**, 519–527.
  14. Smolenskii G A, Isupov V A and Agranoskaya A I (1959), 'A new group of ferroelectrics (with layered structure)', *Sov. Phys. Solid State* **1**, 149–150.
  15. Subbarao E C (1961), 'Ferroelectricity in  $\text{Bi}_4\text{Ti}_3\text{O}_{12}$  and its solid solutions', *Phys. Rev.* **122** (3), 804–807.
  16. Fang P H, Robbins C R and Aurivillius B (1962), 'Ferroelectricity in the compound  $\text{Bi}_4\text{Ti}_3\text{O}_{12}$ ', *Phys. Rev.* **126** (3), 892–896.
  17. Aurivillius B and Fang P H (1962), 'Ferroelectricity in the compound  $\text{Ba}_2\text{Bi}_4\text{Ti}_5\text{O}_{18}$ ', *Phys. Rev.* **126**, 893–896.
  18. Subbarao E C (1962), 'A family of ferroelectric bismuth compounds', *J. Phys. Chem. Solids* **23**, 665–676.
  19. Newnham R E, Wolfe R W and Dorrian J F (1971), 'Structural basis of ferroelectricity in the bismuth titanate family', *Mater. Res. Bull.* **6**, 1029–1039.
  20. Armstrong R A and Newnham R E (1972), 'Bismuth titanate solid solutions', *Mater. Res. Bull.* **7** (10), 1025–1034.
  21. Takenaka T and Sakata K (1986), 'Piezoelectric properties of grain-oriented bismuth layer-structured ferroelectric ceramics', *Proc. 6th Inter. Symp. Appl. Ferro, IEEE*, 414–417.
  22. Takenaka T and Sakata K (1988), 'Grain-oriented and Mn-doped  $(\text{NaBi})_{(1-x)/2}\text{Ca}_x\text{Bi}_4\text{Ti}_4\text{O}_{15}$  ceramics for piezo- and pyrosensor materials', *Sensors and Materials*, **1**, 35–46.
  23. Takenaka T, Sakata K and Toda K (1985), 'Piezoelectric properties of bismuth layer-structured ferroelectric  $\text{Na}_{0.5}\text{Bi}_{4.5}\text{Ti}_4\text{O}_{15}$  Ceramic', *Jpn. J. Appl. Phys.* **24** (Suppl. 24–2), 730–732.
  24. Nagata H, Takahashi T, Chikushi N and Takenaka T (2000), 'A series of bismuth layer-structured ferroelectrics', *Ferroelectrics* **241**, 309–316.
  25. Nagata H, Takahashi T, Yano Y and Takenaka T (2001), 'Electrical properties of bismuth layer-structured ferroelectrics  $\text{Sr}_{m-3+x}\text{Bi}_{4-x}\text{Ti}_{m-x}\text{Ta}_x\text{O}_{3m+3}$  ( $m = 2, x = 1\sim 2$ ;  $m = 3, x = 0\sim 2$ )', *Ferroelectrics* **261**, 219–224.
  26. Yamashita Y, Yoshida S and Takahashi T (1983), 'Effects of MnO additive on piezoelectric properties in modified  $(\text{PbCa})\text{TiO}_3$  ferroelectric ceramics', *Jpn. J. Appl. Phys.* **22** (Suppl. 22–2), 40–42.
  27. Lotgering F K (1959), 'Topotactical reactions with ferrimagnetic oxides having hexagonal crystal structures – I', *J. Inorg. Nucl. Chem.* **9** (2), 113–123.
  28. Cross L E and Pohanka R C (1971), 'Ferroelectricity in bismuth oxides type layer structure compounds', *Mater. Res. Bull.* **6**, 939–949.
  29. Takenaka T and Sakata K (1981), 'Electrical properties of grain-orientated piezoelectric ceramics in layer-structure oxide family', *Jpn. J. Appl. Phys.* **20** (Suppl. 20–3), 161–163.
  30. Fouskova A and Cross L E (1970), 'Dielectric properties of bismuth titanate', *J. Appl. Phys.* **41** (7), 2834–2838.
  31. Schulgasser K: (1976) 'Relationship between single-crystal and polycrystal electrical conductivity', *J. Appl. Phys.* **47** (5), 1880–1886.



32. Wu S Y, Takei W J, Francombe M H and Cummins S E (1972), 'Domain structure and polarization reversal in films of ferroelectric bismuth titanate', *Ferroelectrics* **3**, 217–224.
33. Baerwald H G (1957), 'Thermodynamic theory of ferroelectric ceramics', *Phys. Rev.* **105** (2), 480–486.
34. Marutake M (1956), 'A calculation of physical constants of ceramic barium titanium' *J. Phys. Soc. Jpn.* **11**, (8), 807–814.
35. Nanao M, Hirose M and Tsukada T (2001), 'Piezoelectric properties of  $\text{Bi}_3\text{TiNbO}_9$ – $\text{BaBi}_2\text{Nb}_2\text{O}_9$  ceramics', *Jpn. J. Appl. Phys.*, **40** (9B), 5727–5730.
36. Shibata K, Shoji K and Sakata K (2001), ' $\text{Sr}_{1-x}\text{Ca}_x\text{Bi}_2\text{Ta}_2\text{O}_9$  piezoelectric ceramics with high mechanical quality factor', *Jpn. J. Appl. Phys.*, **40** (9B), 5719–5721.
37. Byer R L and Roundy C B (1972), 'Pyroelectric coefficient direct measurement technique and application to a NSEC response time detector', *Ferroelectrics* **3**, 333–338.
38. Dougherty J P and Seymour R J (1980), 'Automated simultaneous measurement of electrical properties of pyroelectric materials', *Rev. Sci. Instrum.* **51** (2), 229–233.
39. Smolenskii G A, Isupov V A and Agranovskaya A I (1961), 'Ferroelectrics of the oxygen-octahedral type with layered structure', *Sov. Phys. Solid State*, **3** (3), 651–655.
40. Takeuchi T, Tani T and Saito Y (1999), 'Piezoelectric properties of bismuth layer-structured ferroelectric ceramics with a preferred orientation processed by the reactive templated grain growth method', *Jpn. J. Appl. Phys.*, **38** (9B), 5553–5556.
41. Nagata H, Takahashi T and Takenaka T (2000), 'Piezoelectric anisotropies of bismuth layer-structured ferroelectrics', *Trans. Mater. Res. Jpn.*, **25** (1), 273–276.
42. Dorrian J F, Newnham R E, Smith D K and Kay M I (1971), 'Crystal structure of  $\text{Bi}_4\text{Ti}_3\text{O}_{12}$ ', *Ferroelectrics*, **3**, 17–27.
43. Villegas M, Caballero A C, Moure C, Duran P and Fernandez J F (1999), 'Factors affecting the electrical conductivity of donor-doped  $\text{Bi}_4\text{Ti}_3\text{O}_{12}$  piezoelectric ceramics', *J. Am. Ceram. Soc.*, **82** (9), 2411–2416.
44. Shulman H S, Testorf M, Damjanovic D and Setter N (1996), 'Microstructure, electrical conductivity, and piezoelectric properties of bismuth titanate', *J. Am. Ceram. Soc.*, **79** (12), 3124–3128.
45. Noguchi Y and Miyayama M (2001), 'Large remanent polarization of vanadium-doped  $\text{Bi}_4\text{Ti}_3\text{O}_{12}$ ', *Appl. Phys. Lett.*, **78** (13), 1903–1905.
46. Shannon R D (1976), 'Revised effective ionic radii and systematic studies of interatomic distances in halides and chalcogenides', *Acta Cryst.* **A 32** (5), 751–767.
47. Suzuki M, Nagata H, Ohara J, Funakubo H and Takenaka T (2003), ' $\text{Bi}_{3-x}\text{M}_x\text{TiTaO}_9$  ( $\text{M} = \text{La}$  or  $\text{Nd}$ ) ceramics with high mechanical quality factor  $Q_m$ ', *Jpn. J. Appl. Phys.* **42** (9B), 6090–6093.
48. Nagata H, Fujita Y, Enosawa H and Takenaka T (2004), 'Piezoelectric properties of Nb and V substituted  $\text{Bi}_4\text{Ti}_3\text{O}_{12}$  ferroelectric ceramics', in *Ceramic Materials and Multilayer Electronic Devices*, Ceramic Transactions, Vol. **150**, The American Ceramic Society, 253–263.

## Novel solution routes to ferroelectrics and relaxors

---

K BABOORAM and  
Z-G YE, Simon Fraser University, Canada

### 28.1 Introduction

Conventional processing of perovskite and perovskite-related materials is usually carried out by solid-state reactions of metal carbonates, hydroxides and oxides. These reactions require a long grinding time and high-temperature treatment so that the starting ingredients are provided with sufficient energy to come together and react. This process may lead to the formation of multiple phases in the final product because of incomplete reaction. The final product, if not homogeneous, usually suffers a decrease in its physical properties. For this reason, soft chemistry has forged its way into the synthesis of mixed oxides. Soft chemical routes to mixed oxide compounds are based on transformations that take place in solution. These methods allow the starting materials to homogeneously mix in solution and, therefore, react at the atomic or molecular level to give rise to precursors that can be converted to the final oxide under milder conditions than those required by solid-state synthesis. The sol-gel process and the co-precipitation method are two commonly used soft chemical routes for the synthesis of a variety of mixed oxides including perovskite and perovskite-related materials.

This chapter will focus on two soft chemical methods, namely, the sol-gel process and the co-precipitation method, and their roles in the synthesis of perovskite compounds exhibiting ferroelectric and relaxor ferroelectric properties, useful for a wide range of technological applications. Sections 28.2.1 and 28.2.2 will describe the principles of the sol-gel and co-precipitation methods, respectively, highlighting the advantages they offer to the synthesis of mixed oxide compounds. In Section 28.3, a new room temperature sol-gel method for the synthesis of the relaxor ferroelectric-based lead magnesium niobate-lead titanate solid solution system,  $(1-x)\text{Pb}(\text{Mg}_{1/3}\text{Nb}_{2/3})\text{O}_3-x\text{PbTiO}_3$  (with  $x = 0.10$  and  $0.35$ ) is described. Section 28.4 will deal with two new soft chemical processes, namely a sol-gel and a co-precipitation method for the synthesis of ferroelectric strontium bismuth tantalite,  $\text{SrBi}_2\text{Ta}_2\text{O}_9$  (SBT), of layered perovskite structure. The sol-gel method developed for the synthesis

of SBT has been extended to the synthesis of ferroelectric bismuth titanate,  $\text{Bi}_4\text{Ti}_3\text{O}_{12}$  (BT), and the lanthanum-doped system, bismuth lanthanum titanate,  $\text{Bi}_{4-x}\text{La}_x\text{Ti}_3\text{O}_{12}$  (BLT). The details of the synthesis and characterization of BT and a series of BLT compounds ranging from  $x = 0.2$  to  $0.75$  will be described in Section 28.5. Finally, Section 28.6 will be dedicated to the future development in this exciting field of soft chemical approaches to ferroelectric and relaxor ferroelectric materials.

## 28.2 Soft chemical methods for the synthesis of mixed metal oxides

### 28.2.1 Sol-gel process

The sol-gel process has gained considerable attention and popularity in recent years. The ability to homogeneously mix (and dissolve) the starting materials, commonly metal alkoxides, in solution is one of the major benefits of the sol-gel processing method [1]. Developed in 1845 by Ebelman who made the first silica gels, this technique has extensively been employed in the synthesis of inorganic mixed oxides because of the numerous advantages it offers over the conventional solid state reactions [2]. Sol-gel processing has highlighted the importance of chemistry in the fabrication of materials starting from chemical precursors. It was not until 1950 that the first non-silicate ceramics, the perovskites, were synthesized using the sol-gel process. In the last two decades, this soft chemical technique has attracted considerable interest and has been used for a major development in the synthesis of mixed oxides in the form of glass, ceramics, and thin films. Using the sol-gel method, the syntheses of electronic and ionic conductors, and ferroelectric and magnetic materials in the form of high-purity submicrometer powders, have been accomplished [2,3].

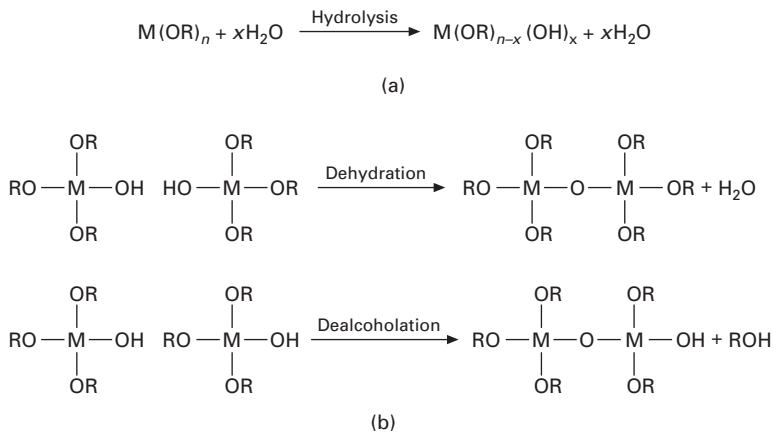
The basic requirement of this type of processing is the formation of a homogeneous solution (sol) containing all the necessary cationic ingredients in the desired stoichiometry. Therefore, it is very important to choose the right solvent, one that is capable of effectively dissolving all the starting chemicals in question. This allows for a good mixing of the reactants at the molecular level and, once this has been achieved, the next step of progressively forming a network of oxide in solution through polymerization of the dispersed constituents becomes a lot easier. Broadly speaking, the sol-gel method consists of polymerization reactions which are based on the hydrolysis and condensation of metal alkoxides  $\text{M}(\text{OR})_n$ , where M is a metal having an oxidation state of  $n^+$  and R is an alkyl group. Briefly, in the first step of the reaction, the metal alkoxide is hydrolyzed by a water molecule. Once the hydrolysis step has been initiated, the next reaction that follows is condensation of the hydrolyzed molecules to produce M-O-M linkages or networks. Further

condensation reactions can then take place, leading to the formation of longer chains or oligomers. The processes can be summarized in the reaction sequence in Fig. 28.1. The formation of more extended networks in the sol through further polymerization of the chains and oligomers causes gelation to occur. The homogeneous network of M–O–M units then decomposes at a much lower temperature to give rise to the desired inorganic oxide that is required in solid-state reactions. One of the key features of the sol–gel method is the ability to produce small particles, as small as nanometer size. The precursor powder obtained by the decomposition of the homogeneous gel is actually much finer than powders obtained by the solid-state reactions and this explains the increased reactivity of the former [3].

In summary, the sol–gel process offers a better control of stoichiometry and homogeneity, a higher purity and reactivity of the precursor powders, and a significantly reduced temperature of ceramic densification when compared with solid state synthesis. By allowing the preparation of stable sols, the sol–gel method also opens opportunities to the fabrication of thin and thick films through, e.g., spin-coating and other methods. The main disadvantages of the sol–gel process are the cost of the metal alkoxide precursors and the complexity of the processing.

### 28.2.2 Co-precipitation method

The co-precipitation method, often referred to as the solid-state analog or a side-branch of the sol–gel process, is another efficient soft chemical route to mixed oxide materials [4]. Briefly, this method, also starting from solution, involves dissolving the starting materials in a common solvent and then



28.1 (a) Hydrolysis of metal alkoxides and (b) condensation of the hydrolyzed species through dehydration or dealcoholation steps.

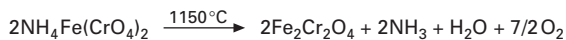
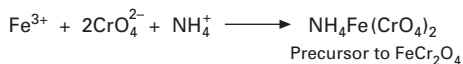
adding a precipitating agent so as to form a homogeneous and single phase inorganic solid. The precipitate can then be decomposed at a high temperature to produce the target mixed oxide material. Co-precipitation helps to hold the required cations close together in the reaction medium and lowers the temperature of decomposition, just as in the case of the sol-gel process. The starting materials can be simple metal salts that can easily be dissolved in water or other appropriate solvents.

Figure 28.2 shows, as an example, the synthesis of the complex metal oxide,  $\text{FeCr}_2\text{O}_4$ , by the co-precipitation method. The first step involves dissolving an iron(III) salt and a chromate in water to obtain  $\text{Fe}^{3+}$  and  $\text{CrO}_4^{2-}$  ions in solution. These ions are then precipitated in a complex form by an ammonium solution ( $\text{NH}_4^+$ ), and the resulting precipitate can be decomposed at high temperature into the target  $\text{FeCr}_2\text{O}_4$ .

### 28.3 Polyethylene glycol-based new sol-gel route to relaxor ferroelectric solid solution (1 - x)Pb(Mg<sub>1/3</sub>Nb<sub>2/3</sub>)O<sub>3</sub>-xPbTiO<sub>3</sub> (x = 0.1 and 0.35)

#### 28.3.1 Background

The relaxor ferroelectric-based solid solution system  $(1 - x)\text{Pb}(\text{Mg}_{1/3}\text{Nb}_{2/3})\text{O}_3$ - $x\text{PbTiO}_3$  ( $(1 - x)\text{PMN}$ - $x\text{PT}$ ) has attracted considerable interest because of its remarkable dielectric and electromechanical properties in the form of ceramics and single crystals [5–7].  $\text{Pb}(\text{Mg}_{1/3}\text{Nb}_{2/3})\text{O}_3$  (PMN) is well known to exhibit typical relaxor ferroelectric behavior characterized by a broad and frequency-dependent dielectric maximum at  $T_{\text{max}}$  (around  $-15^\circ\text{C}$  at 1 kHz) [8]. Addition of the normal ferroelectric  $\text{PbTiO}_3$  (PT) to PMN induces a long-range ferroelectric order, shifts the transition temperature upwards and enhances the dielectric, piezoelectric and ferroelectric properties of the solid solution [9, 10]. A morphotropic phase boundary (MPB) appears in the composition region of 30–37 mol% PT with the presence of a rhombohedral, a tetragonal, and/or a monoclinic phase [11]. The  $(1 - x)\text{PMN}$ - $x\text{PT}$  system embraces a wide range of compositions which find important applications in multilayer dielectric capacitors, electromechanical sensors and actuators [12]. Compositions within the MPB (e.g. 0.65PMN–0.35PT)



28.2 Synthesis of  $\text{FeCr}_2\text{O}_4$  by the co-precipitation method.

exhibit typical ferroelectric hysteretic character, with a large spontaneous polarization and a low coercive field, showing great potential for advanced electromechanical applications both in the forms of electroceramics and thin or thick films [13]. Recently, single crystals of  $(1-x)\text{PMN}-x\text{PT}$  solid solutions have been found to exhibit electromechanical performance superior to that of the  $(1-x)\text{PbZrO}_3-x\text{PbTiO}_3$  (PZT) ceramics [14,15] which have been used for decades as piezoelectric materials for transducers and actuators [16]. On the other hand, being more on the PMN side of the solid solution system, 0.90PMN–0.10PT is a typical relaxor ferroelectric material with a weak rhombohedral distortion [10]. It exhibits a diffuse dielectric constant maximum at about 40 °C ( $T_{\text{max}}$ ) and its dielectric constant at room temperature is very high ( $\epsilon' \sim 10\,000$ ), making it a potential candidate for multilayer high-power density capacitor applications [16,17].

The synthesis of pure perovskite 0.90PMN–0.10PT and 0.65PMN–0.35PT by conventional solid-state reactions can be challenging because of the formation of a more stable but undesired impurity phase of pyrochlore structure which considerably impairs the dielectric properties of the materials [18]. For this reason, soft chemical methods have emerged as the best alternatives for the synthesis of the  $(1-x)\text{PMNT}-x\text{PT}$  ceramics.

Among the various routes to homogeneous multi-component oxides that have recently been developed, the polymeric precursor method has drawn a lot of attention [19]. Pioneered by Pechini in the 1960s, this method provides a simple way to oxide powders by first making a solution containing all the cations in the form of polymer–cation complexes in the desired stoichiometry, and then firing this solution to drive off any organic moieties and to form the target oxides [20]. Chelation and entrapment of the cations by the polymer chains give rise to crystalline powders with better chemical homogeneity and smaller particle size. This is explained from the fact that chelation considerably lowers the mobility of the cations, thereby stabilizing the cations against precipitation [21], which is the key requirement to obtaining a stable precursor solution that can be used for making thin films.

Several researchers have reported the synthesis of multi-component ceramic oxides via the oxidation of polyethylene glycol– or poly(vinyl alcohol)–cation complexes [19,21–24]. The Pechini method, which uses  $\alpha$ -hydroxycarboxylic acids such as citric and lactic acids together with polyhydroxyl alcohols such as ethylene glycol to make a polymer resin, has been modified to some extent to the use of water-soluble sources such as metal nitrates and chlorides. This has now become a very common method because these inorganic salts are more stable than the corresponding alkoxides and, hence, relatively easy to handle. Polyethylene glycol (PEG) has proved to be a very suitable polymer for use in the polymeric precursor method in the preparation of mixed oxide powders and ceramics. The reason for this is the coordination of the ether oxygen atoms in PEG to the metal cations,

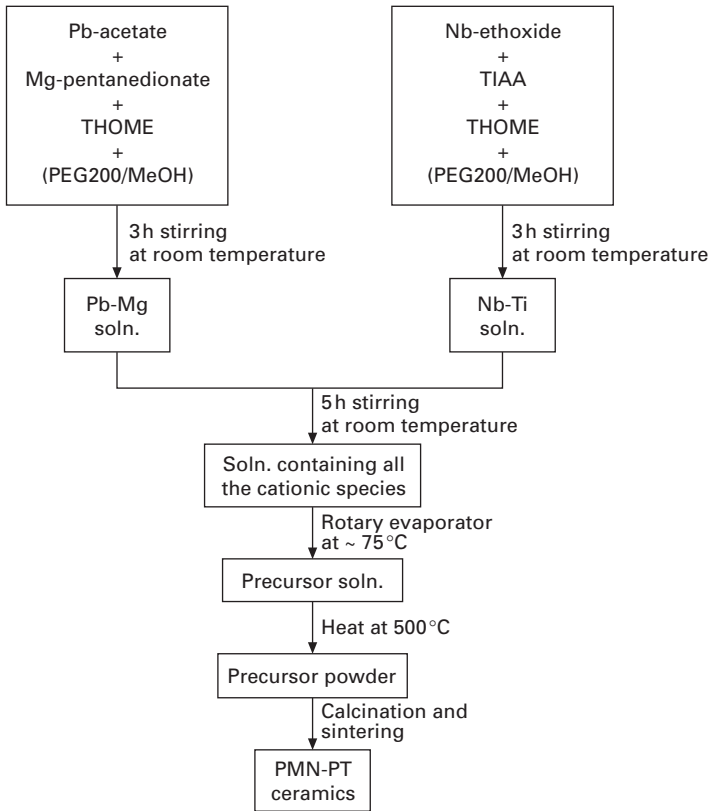
which allows it to dissolve a number of inorganic salts as well as metal alkoxides. Commonly, sol-gel processes using alkoxides require refluxing at temperatures usually above 100 °C to allow for hydrolysis and condensation reactions to take place and to form the cross-linked structures.

Besides polymer-binding, cross-linking can also greatly help in obtaining a very homogeneous distribution of cations in solutions. This is achieved by forming extended structures in solution by crosslinking the cations using a molecule with several binding sites. Sriprang and coworkers [25] demonstrated this through a triol-based route to PZT thin films in which 1,1,1-tris(hydroxy)methylethane (THOME) was used as the complexing agent. They demonstrated that, with its three hydroxyl groups, THOME could bind to up to three metal ions at a time, forming oligomeric species that were then oxidized to form the final mixed oxide compound. However, to the best of our knowledge, no application of such technique was made to the synthesis of the  $(1 - x)\text{PMN}-x\text{PT}$  system.

### 28.3.2 Results and discussion

We have developed a novel soft chemical route for the synthesis of 0.90PMN–0.10PT and 0.65PMN–0.35PT ceramics [26,27]. Using a 1:2 volume mixture of polyethylene glycol-200 (PEG200) and methanol as solvent for the starting materials, and THOME as a complexing agent, we were able to perform a room temperature reaction to produce the precursor solution, as well as to obtain the pure (pyrochlore-free) perovskite phase for the PMN–PT ceramics. The flowchart shown in Fig. 28.3 details the steps involved in the new sol-gel method. An interesting feature of this method is that the precursor solutions to the target PMN–PT ceramics were formed at room temperature under simple mixing and stirring conditions, thus avoiding the reflux and distillation steps usually required in sol-gel reactions. Moreover, the sol is not moisture sensitive and shows very good stability against precipitation, which makes it a very promising stock solution for depositing thin films. Furthermore, this new route to PMN–PT ceramics does not require the use of any excess of lead starting material, which is necessary in all conventional and most of soft chemical syntheses in order to compensate for lead oxide loss during sintering at high temperatures.

In the case of the 0.65PMN–0.35PT system, ceramics of pure perovskite phase, high density, high dielectric constant and excellent ferroelectric properties were obtained from a stoichiometric amount of the lead starting material in the preparation of the sol. A decrease in the ceramic quality in terms of the perovskite phase purity and dielectric properties was observed in those ceramics prepared without using the triol molecule, THOME, in the reaction. Figure 28.4 shows the positive effect of THOME on the perovskite phase formation by comparing the 0.65PMN–0.35PT powders prepared with

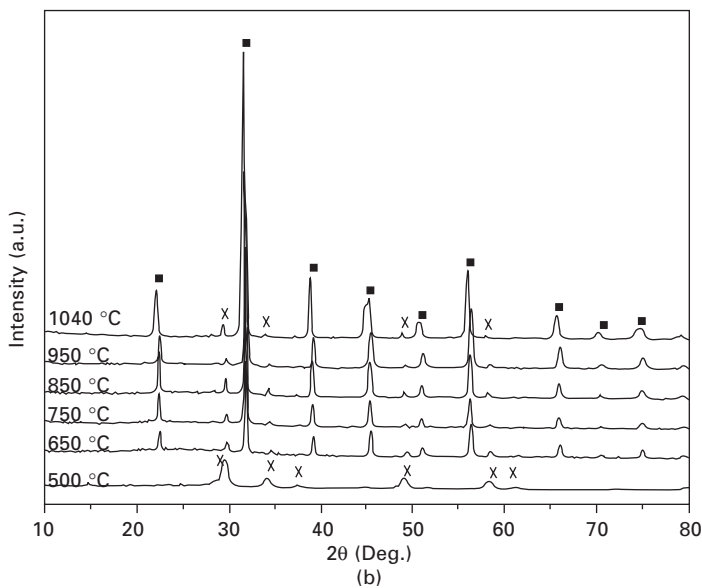
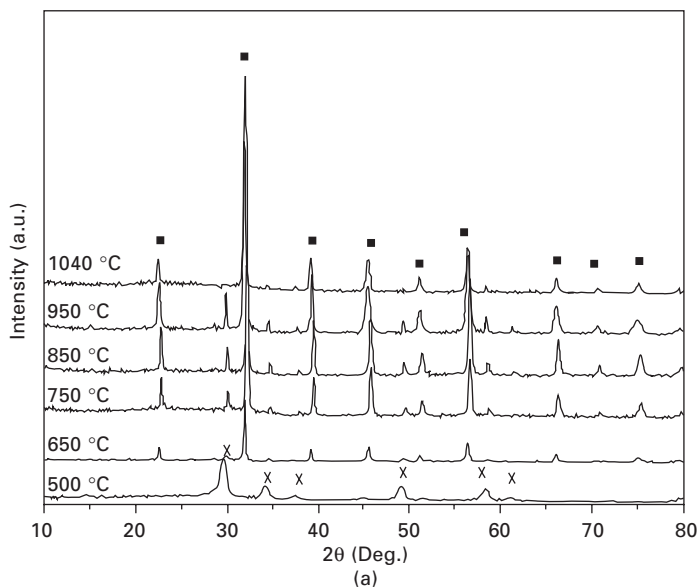


28.3 Flowchart for the preparation of precursor solutions and ceramics of  $(1-x)\text{PMN}-x\text{PT}$  ( $x = 0.10$  and  $0.35$ ). (Reproduced with permission from *Chem. Mater.* 2004, **16**(25), 5365–5371.)

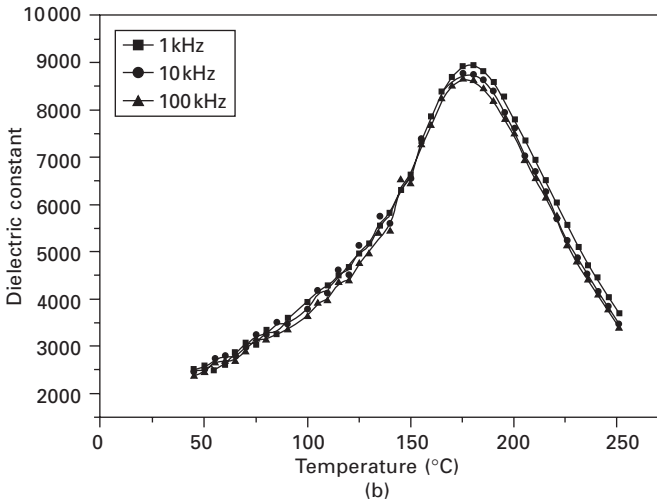
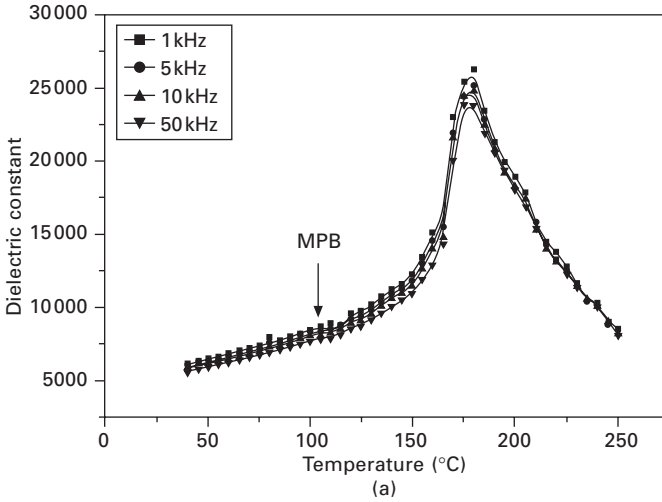
(PEG(S)T) and without (PEG(S)) the triol molecule and calcined at different temperatures.

The presence of THOME in the system during the synthesis of precursor solution has not only led to the formation of a pure perovskite phase, but also greatly improved the dielectric and ferroelectric properties of the  $0.65\text{PMN}-0.35\text{PT}$  ceramics with a maximum dielectric constant,  $\epsilon'_{\text{max}}$  of  $\sim 27\,000$  and a remnant polarization,  $P_r = 21\ \mu\text{C}/\text{cm}^2$ , as compared with  $\epsilon'_{\text{max}} = 9\,000$  and  $P_r = 7.5\ \mu\text{C}/\text{cm}^2$  for the ceramics prepared without THOME. The temperature and frequency dependences of the real part of dielectric permittivity ( $\epsilon'$ ) of the ceramic prepared with THOME (PEG(S)T) and the one prepared without THOME ([PEG(S)]), both sintered at  $1140\ ^\circ\text{C}$ , are shown in Fig. 28.5. The arrow (MPB) in Fig. 28.5(a) indicates the morphotropic phase transition from the rhombohedral or monoclinic to the tetragonal phase. The higher maximum dielectric constant with a sharp peak in the  $\epsilon'$  versus temperature curve is associated with a larger grain size ( $>2\ \mu\text{m}$ ) in the ceramic prepared



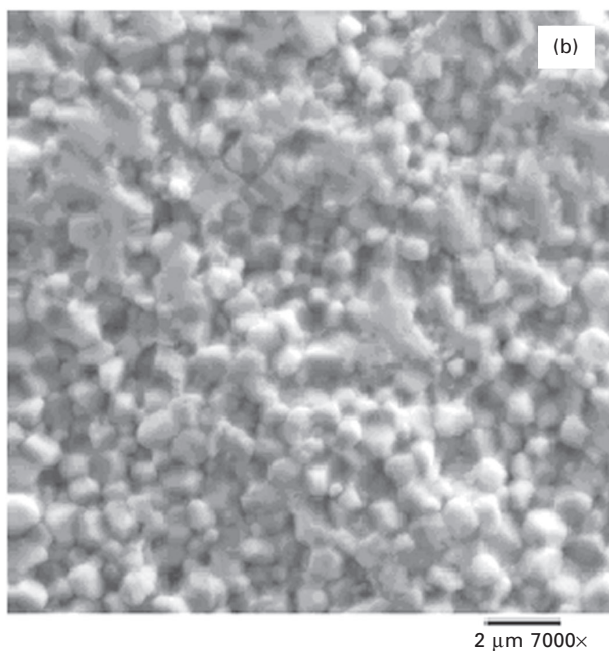
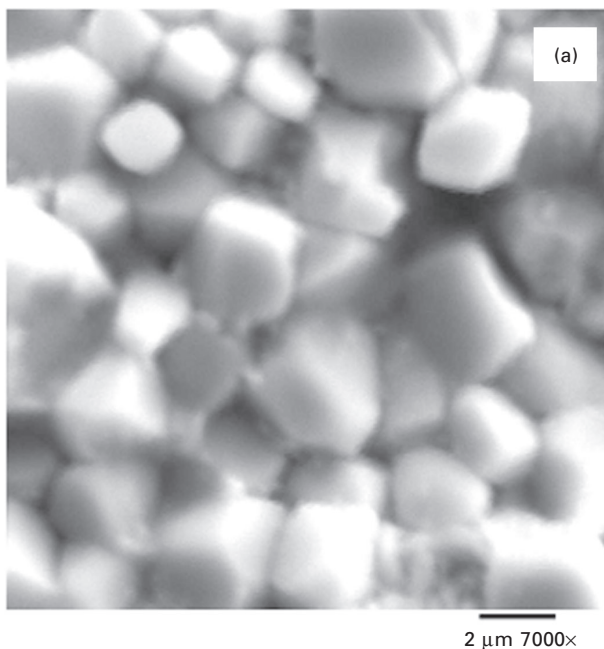


28.4 X-ray diffraction patterns of (a) PEG(S)T and (b) PEG(S) precursor powders of 0.65PMN–0.35PT calcined at different temperatures for a period of 8 h. (Reproduced with permission from *Chem. Mater.* 2004, **16**(25), 5365-5371.)

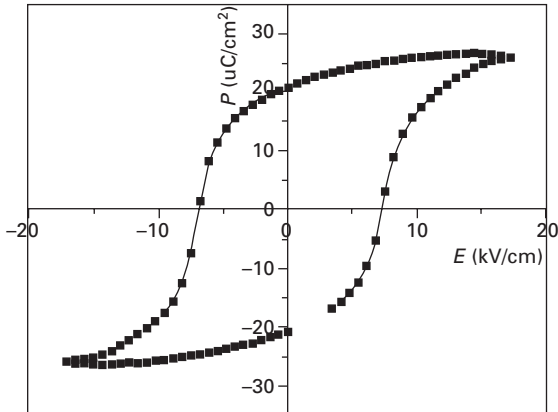


28.5 Dielectric constant as a function of temperature and frequency for (a) PEG(S)T and (b) PEG(S) ceramics of 0.65PMN–0.35PT sintered at 1140°C for 8 h. (Reproduced with permission from *Chem. Mater.* 2004, **16**(25), 5365–5371.)

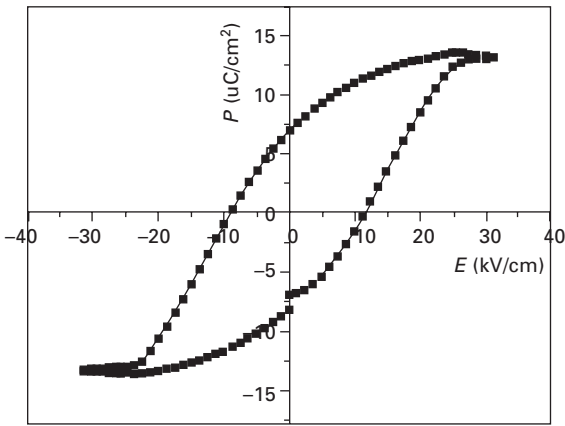
with THOME, as revealed by the scanning electron microscopy (SEM) pictures in Fig. 28.6. In comparison, the ceramics prepared without THOME exhibits a finer particle size ( $< 1 \mu\text{m}$ ), giving rise to a broad maximum in the dielectric peak. The polarization–electric field relations of the PEG(S)T and PEG(S) ceramics sintered at 1140°C are displayed in Fig. 28.7. It can be seen that the PEG(S)T ceramic shows improved ferroelectric properties as compared with the PEG(S) ceramic, with a well-defined and saturated hysteresis loop and a



28.6 Scanning electron microscopy images of (a) PEG(S)T and (b) PEG(S) ceramics of 0.65PMN–0.35PT sintered at 1140°C for 8 h. (Reproduced with permission from *Chem. Mater.* 2004, **16**(25), 5365–5371.)



(a)



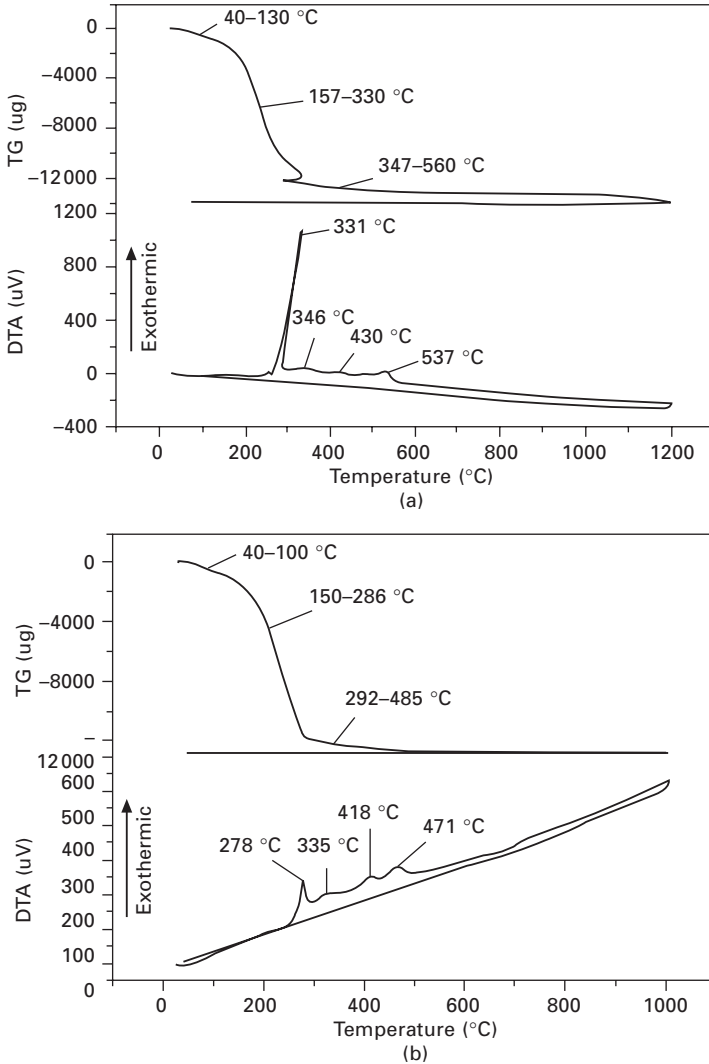
(b)

28.7 Variation of electrical polarization as a function of bipolar electric field showing ferroelectric hysteresis loops for (a) PEG(S)T and (b) PEG(S) ceramics of 0.65PMN–0.35PT sintered at 1140°C for 8h. (Reproduced with permission from *Chem. Mater.* 2004, **16**(25), 5365–5371.)

higher remnant polarization, i.e.  $P_r = 21 \mu\text{C}/\text{cm}^2$  in PEG(S)T, as compared with  $P_r = 14 \mu\text{C}/\text{cm}^2$  in PEG(S). The excellent ferroelectric properties of PEG(S)T ceramics make the material a very promising candidate for applications in advanced electromechanical devices.

The beneficial effects, demonstrated in this work, of the triol molecule (THOME) on the formation and the performance of the perovskite 0.65PMN–0.35PT ceramics, can be related to its ability as a very good metal complexing agent [25]. With three hydroxyl groups in its structure, the THOME molecule can bind to up to three metal centres at a time, thereby forming linear oligomeric

species in the solution. This has an influence on the arrangement of the M–O–M networks in the precursor powder. It has been shown by infrared spectroscopic studies that different M–O–M arrays exist in the precursor powder when THOME was used or not in the sol–gel process [27]. Thermogravimetric/differential thermal analysis (TG/DTA) on the precursor solutions (Fig. 28.8) has revealed that both PEG and THOME were bound to



28.8 Thermogravimetric/differential thermal analysis (TG/DTA) curves from room temperature to 1000 °C at a heating rate of 5 °C/min for (a) PEG(S)T and (b) PEG(S) precursor solutions. (Reproduced with permission from *Chem. Mater.* 2004, **16**(25), 5365–5371.)

the cations in the PEG(S)T solution, making the resulting complexes decompose at a higher temperature than those in the PEG(S) solution. As a result, the mechanisms of decomposition of the metal–organic complexes in PEG(S)T and PEG(S) during the high-temperature heat treatment become different, thereby making the rearrangements of the metal–oxygen–metal network also proceed through different pathways. This may be the main reason why a pure perovskite phase has been obtained in PMN–PT ceramics made from the PEG(S)T precursor solution, while some pyrochlore still exists in the ceramics synthesized from the PEG(S) solution.

In the case of relaxor ferroelectric 0.90PMN–0.10PT system, the effects, on the ceramic quality and properties, of using the complexing agent, 1,1,1-tris(hydroxymethyl)ethane (THOME) and the stoichiometric amount of the lead starting material (10PEG(S)T), have been studied, as compared with using (i) a stoichiometric amount of lead and no THOME (10PEG(S)), (ii) a 5% mol excess of lead and no THOME (10PEG(5)), and (iii) a 5% mol excess of lead and THOME (10PEG(5)T). The results, summarized in Table 28.1, show that better electrical properties were obtained in the ceramics synthesized with a stoichiometric amount of lead. On the other hand, the presence of an excess of lead in the ceramics was found to impair the electrical properties even though it leads to a slightly higher percentage of the perovskite phase. These ceramics (10PEG(5)) show lower values of room temperature and maximal dielectric constants, and remnant polarization ( $\epsilon'_{rt} = 8000$ ,  $\epsilon'_{max} = 10000$  and  $P_r = 11 \mu\text{C}/\text{cm}^2$ , respectively), as compared with the values of  $\epsilon'_{rt} = 25000$ ,  $\epsilon'_{max} = 33000$  and  $P_r = 18 \mu\text{C}/\text{cm}^2$  obtained for the ceramics prepared with THOME and without excess of lead (10PEG(S)T). The ceramics synthesized from precursor solutions containing stoichiometric amount of lead and no THOME (10PEG(S)) exhibit the values of  $\epsilon'_{rt} = 12500$ ,  $\epsilon'_{max} = 19500$ , and  $P_r = 19 \mu\text{C}/\text{cm}^2$ , which are in between those of 10PEG(S)T and 10PEG(5). It can be seen that of the ceramics prepared with a stoichiometric amount of lead, the one containing THOME in the sol–gel process (10PEG(S)T)

Table 28.1 Phase formation and properties of 0.90PMN–0.10PT ceramics prepared under various conditions

	Phase		Properties				
	Max.% perovskite	Sintering temperature (°C)	$\epsilon'_{rt}$ (Rt)	$\epsilon'_{max}$	$T_{max}$	$P_r$ (Rt)	Rank*
10PEG(S)T	90.3	950	25000	33000	40	18	1
10PEG(S)	91.7	1000	12500	19700	42	19	2
10PEG(5)	96.4	1000	8000	10000	40	11	3
10PEG(5)T	85.9	750	–	–	–	–	4

\* 1 best; 4 worst.

shows the best dielectric properties. These results confirm the beneficial role of the triol molecule in the synthesis and properties of both the 0.90PMN–0.10PT and the 0.65PMN–0.35PT solid solution compounds.

## 28.4 New soft chemical methods for the synthesis of ferroelectric $\text{SrBi}_2\text{Ta}_2\text{O}_9$

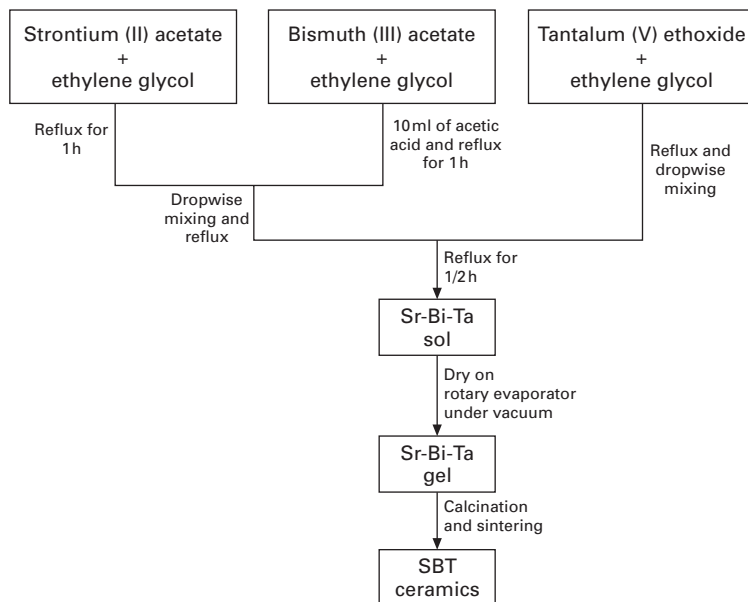
### 28.4.1 Background

Growing interest and attention have been invested in the study of ferroelectric materials with a view to applications in non-volatile random access memory devices (FRAM) [28–30]. In this respect,  $\text{Pb}(\text{Zr}_x\text{Ti}_{1-x})\text{O}_3$  (PZT) appeared first to be a promising candidate. However, PZT has been faced with serious problems such as fatigue, leakage current and aging, which may significantly degrade the performance of the material and the lifetime of the devices [31,32]. Among these problems, fatigue, which is a decrease in the switchable polarization as the number of read/write cycles is increased, is a major issue. Therefore, a great amount of effort has been put into searching for alternatives to PZT, and in this context  $\text{SrBi}_2\text{Ta}_2\text{O}_9$  (SBT) has emerged as a very promising candidate for non-volatile ferroelectric memory applications [28–30]. SBT is a member of the Aurivillius family [33] of compounds with the general formula  $(\text{Bi}_2\text{O}_2)^{2+}(\text{A}_{n-1}\text{B}_n\text{O}_{3n+1})^{2-}$ , where  $n = 2$  represents the number of corner-sharing perovskite units, and it has a layered structure in which  $(\text{Bi}_2\text{O}_2)^{2+}$  layers are sandwiched between the perovskite units. SBT has been identified as a fatigue-free material that can retain its remnant polarization even up to  $10^{12}$  switching cycles, and also has very good data retention of up to 10 years [29,30,34,35].

The literature contains a large number of reports on the synthesis and characterization of SBT thin films. These films were deposited using a number of different techniques, namely sol–gel, pulsed laser deposition (PLD) and metallorganic chemical vapour deposition (MOCVD) [36–40]. As far as SBT ceramics are concerned, they were mostly synthesized using the conventional solid-state reactions in which relatively high sintering temperature, usually exceeding 1200 °C, and/or long sintering time (12–30 h) were required [41–44]. On the soft chemistry side, most of the sol–gel methods documented so far in the literature for the synthesis of SBT made use of 2-methoxyethanol as solvent because of its versatility in dissolving a range of the alkoxide starting materials [37,45–47]. However, 2-methoxyethanol is also very well known to be a possible teratogen (potential birth defect causing substance), and its use in sol–gel processes should be limited, if not prohibited. Therefore, the objective of our study was to find alternative new soft chemical routes that require mild conditions and utilize less harmful reagents to synthesize SBT ceramics for the study of the bulk properties.

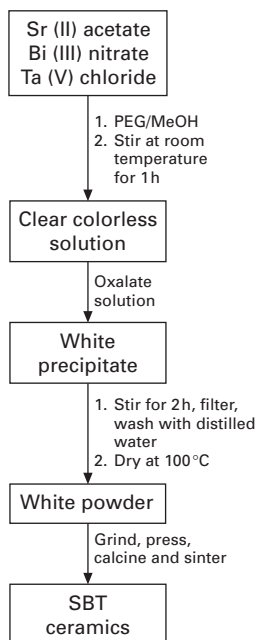
## 28.4.2 Results and discussion

We have developed two new soft chemical routes, namely a sol–gel and a co-precipitation method, to synthesize pure phase SBT ceramics at a calcination temperature as low as 750 °C. The flowcharts detailing the synthesis of SBT ceramics by the sol–gel and co-precipitation methods are shown in Figs 28.9 and 28.10, respectively. Ethylene glycol was employed as the solvent in the sol–gel process, while a mixture of polyethylene glycol 200 and methanol proved to be the right solvent for the co-precipitation method. In this sol–gel route ethylene glycol was found to be a very good solvent for all the starting materials. This is because the presence of two terminal hydroxyl groups in the molecule makes it easier for ethylene glycol to readily exchange with the alkoxy groups on the metals in a hydrolysis step. Once this has been achieved, the hydrolyzed metal alkoxides can then undergo condensation reactions which lead to the progressive formation of metal–oxygen oligomers or polymers in solution. The possible hydrolysis and condensation reactions of strontium acetate in ethylene glycol are illustrated in Fig. 28.11. Similar reactions are possible between the other two metal alkoxides (bismuth acetate and tantalum ethoxide) and ethylene glycol. When all the solutions are finally mixed together, further hydrolysis and condensation reactions might occur, leading



28.9 Flowchart for the synthesis of SBT ceramics by the sol–gel process (reproduced with permission from *Chem. Mater.* 2006, **18**(2), 532–540).



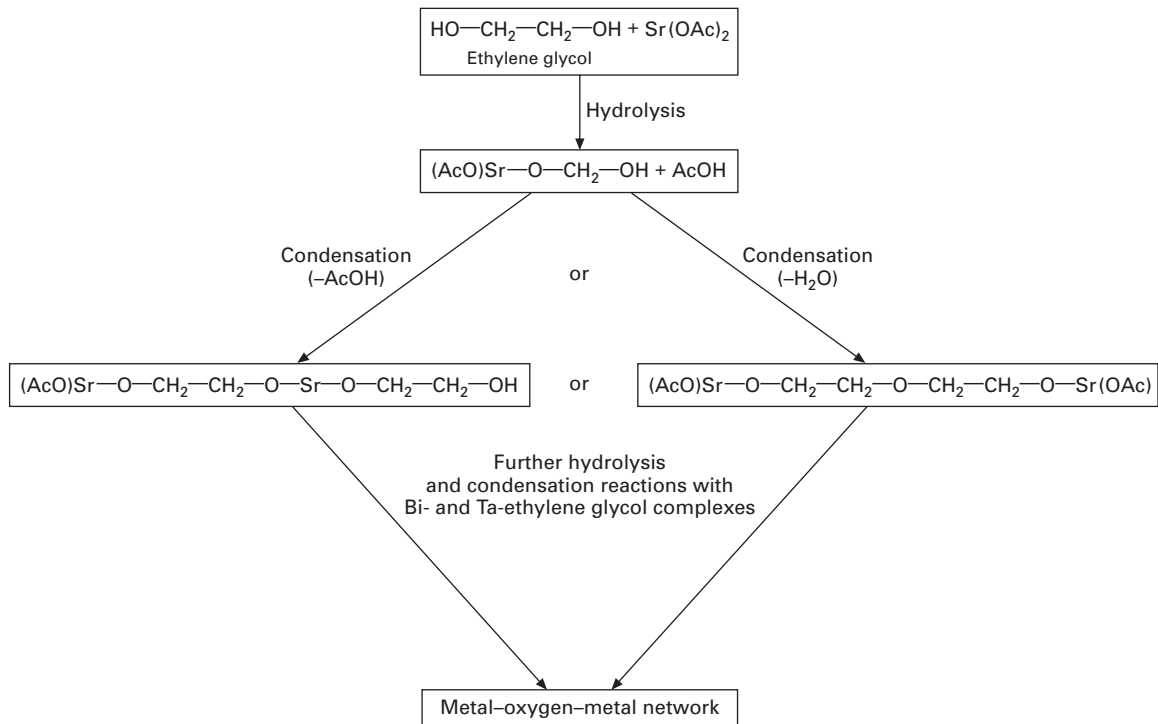


28.10 Flowchart for the synthesis of SBT ceramics by the co-precipitation method (reproduced with permission from *Chem. Mater.* 2006, **18**(2), 532–540).

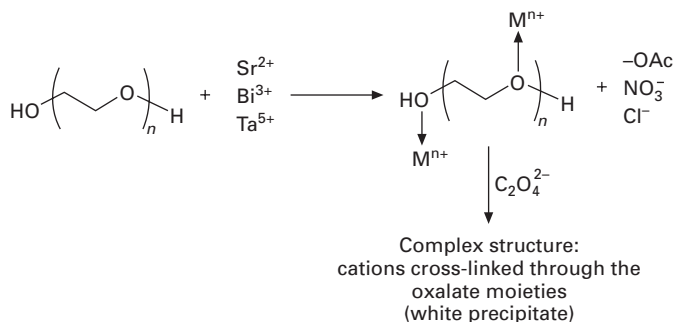
to the formation of an extended and/or cross-linked metal–oxygen–metal network.

Based on the successful room temperature sol–gel synthesis of the relaxor ferroelectric  $(1-x)\text{Pb}(\text{Mg}_{1/3}\text{Nb}_{2/3})\text{O}_3-x\text{PbTiO}_3$  solid solution in PEG-200, as discussed in Section 28.3, the usefulness of this solvent is once again proven in completely dissolving all the starting materials of SBT at room temperature, allowing thereby a homogeneous co-precipitation of the cations using an oxalate solution. Recently, there have been a few reports in the literature on the emulsion process which may be a promising chemical route to fine ceramic powders [48–50]. Basically, this method involves the mechanical dispersion of an aqueous medium, consisting of inorganic salts, into an organic phase. Different kinds of surfactants are also used in order to stabilize the emulsion before the cations are finally co-precipitated to give the stoichiometric precursor powder. In the co-precipitation method that we have developed, the use of PEG-200 eliminates the need of a surfactant by stabilizing all the cations in solution, possibly through interactions between the metals and both the ether oxygen and terminal hydroxyl groups present in the PEG chains [23], as illustrated in Fig. 28.12.

Of the two approaches, the sol–gel route produces ceramics with better dielectric and ferroelectric properties, while ceramics obtained from the



28.11 Proposed possible hydrolysis and condensation reactions of strontium acetate  $[\text{Sr}(\text{OAc})_2]$  in ethylene glycol  $[\text{HO}(\text{CH}_2)_2\text{OH}]$  (reproduced with permission from *Chem. Mater.* 2006, **18**(2), 532–540).



28.12 Proposed possible interactions between the PEG chains and the metal ions in solution before their co-precipitation by the oxalate ions (reproduced with permission from *Chem. Mater.* 2006, **18**(2), 532–540).

co-precipitation method show remarkable preferential grain orientation just through normal sintering procedure. Ferroelectric bismuth-containing layer-structured perovskites generally have their major component of spontaneous polarization along the *a*-axis, with a much smaller component of polarization lying along the *c*-direction. Other properties such as dielectric and piezoelectric properties are also anisotropic in a similar way (i.e. the best properties are obtained in the *a*-oriented grains) [51]. For this reason, much effort has been made in order to achieve grain control in these layer-structured ferroelectric perovskites. The most commonly used grain orientation technique in the literature is the hot-forging method which results in the spontaneous polarization being in the grain-oriented *c*-plane [52–55]. As a result, enhanced dielectric, piezoelectric, and pyroelectric properties have been observed in the hot-forged bismuth layered ceramics. It has been shown by Desu *et al.* [38] that highly *c*-axis oriented SBT thin films exhibit a decrease in polarization and coercive field as opposed to randomly oriented polycrystalline films. Therefore, it is desirable to synthesize SBT ceramics and thin films with preferred grain orientation, if possible, along the *a*-axis, for improved properties.

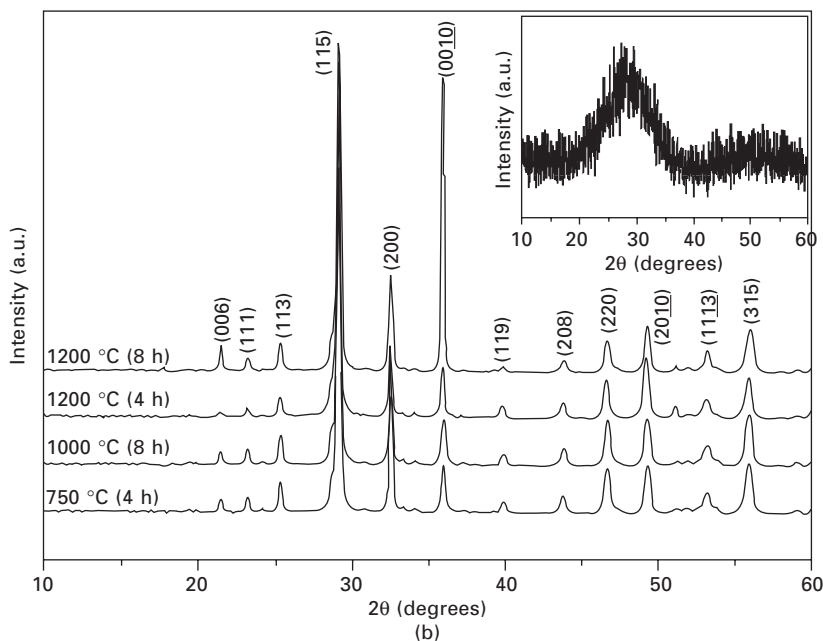
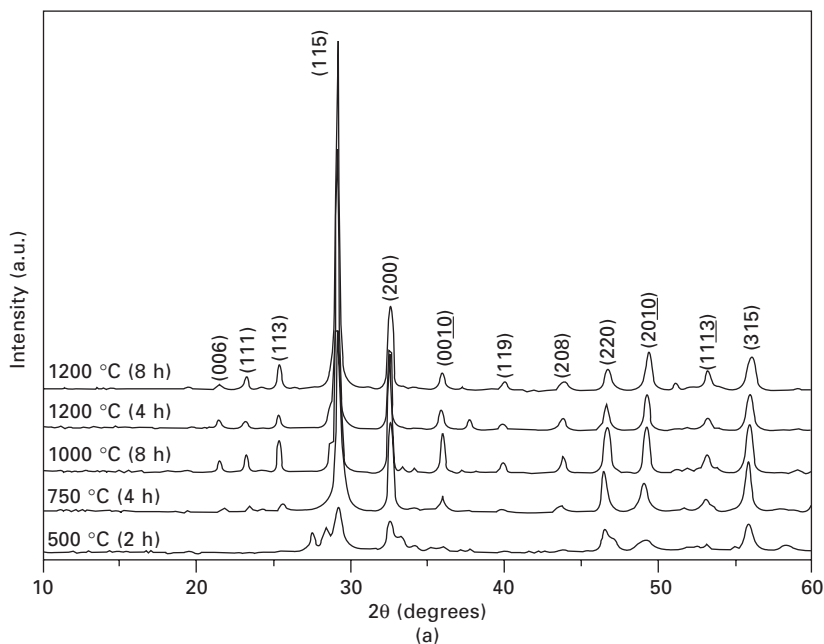
The co-precipitation method developed in this work leads to SBT ceramics with remarkable preferred grain orientation along the *c*-axis and therefore a lower remnant polarization value, while the sol–gel derived SBT ceramics show higher dielectric constant and  $P_r$  values. This is a very interesting feature of the newly designed sol–gel process which minimizes grain orientation along the *c*-axis without the need for special grain orientation techniques, thereby improving the dielectric and ferroelectric properties of the SBT ceramics. It is found that the sol–gel derived ceramics are much denser (93–96% of theoretical density) and also have smaller and more homogeneous grain sizes when compared with those obtained from the co-precipitation process (=85% of theoretical density). The ceramics obtained from the

co-precipitation method also tend to have a microstructure with plate-like anisotropic grains preferentially oriented parallel to the (0010) plane. This can clearly be seen on the X-ray diffraction (XRD) patterns in Fig. 28.13 in which a considerable increase in the intensity of the (0010) peak is observed for the ceramic synthesized by the co-precipitation method. The preferential grain orientation occurs when the sintering temperature and time are increased to 1200 °C and 8 h, and it is a possible reason for a lower measured density. The effects of the two different soft chemical methods on the grain size and orientation of ceramics sintered at different temperatures for different times are depicted by the SEM pictures in Fig. 28.14.

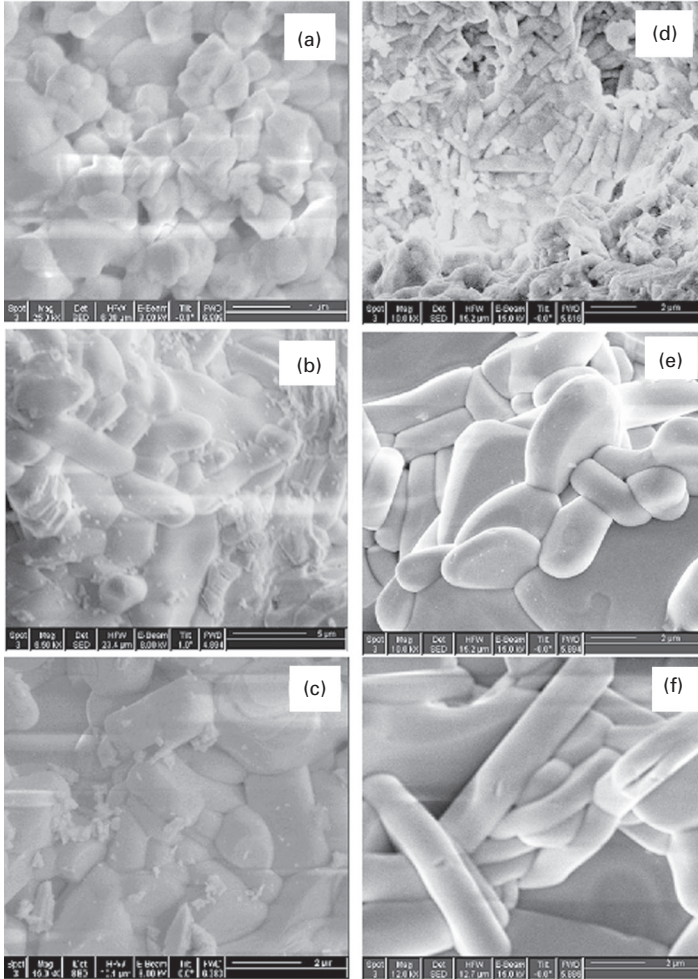
A comparison of the dielectric properties of SBT samples prepared by different methods is given in Table 28.2. It shows the advantage of both these soft chemical processes in improving the room temperature dielectric constant as well as the dielectric maximum at the Curie temperature,  $T_C$ , when compared with solid-state synthesis. The soft chemical routes are therefore the answer to the many shortcomings of the solid-state reaction method for the preparation of SBT and related materials.

Typical ferroelectric behaviour is revealed in the SBT ceramics prepared by the sol-gel method and sintered at 1000 °C for 8 h (SG1000(8)), 1200 °C for 4 h (SG1200(4)) and 1200 °C for 8 h (SG1200(8)), by the dielectric hysteresis loops displayed in Fig. 28.15(a)–(c), respectively. The values of the remnant polarization and coercive field are extracted and shown in Table 28.3. They are compared with the values reported in the literature for ceramics prepared from solid-state reaction processes, and for single crystals. An increase in the remnant polarization ( $P_r$ ) and a decrease in the coercive field ( $E_C$ ) are achieved with increasing sintering temperature and time.  $P_r$  increases from  $\sim 3.40 \mu\text{C}/\text{cm}^2$  in SG1000(8) to  $6.0 \mu\text{C}/\text{cm}^2$  in SG1200(4), and to  $7.6 \mu\text{C}/\text{cm}^2$  in SG1200(8). SG1200(4) and SG1200(8) show an  $E_C$  of 23 and 22 kV/cm, respectively, while SG1000(8) has the highest coercive field  $E_C = 34.5 \text{ kV}/\text{cm}$ , and its polarization is only saturated at a field as high as  $\sim 100 \text{ kV}/\text{cm}$ . Figures 28.15(d)–(e) illustrate the ferroelectric hysteresis loops of the ceramics synthesized by the co-precipitation method and sintered at 1200 °C for 4 h (PR1200(4)) and 1200 °C for 8 h (PR1200(8)), respectively. PR1200(4) and PR1200(8) yield almost the same values of the  $P_r$  and  $E_C$ : 3.5 and 3.7  $\mu\text{C}/\text{cm}^2$  and 19.5 and 21 kV/cm, respectively. However, the  $P_r$  values for these ceramics obtained from the co-precipitation method are only half of those observed in ceramics prepared by the sol-gel process and sintered under the same conditions.

The lower  $P_r$  values observed in the ceramics prepared by the co-precipitation method can be attributed to the preferred orientation along the [0010] direction of the grains, as depicted in the XRD pattern of the PR1200(8) ceramic (Fig. 28.13b). The spontaneous polarization in SBT is known to be parallel to the  $a$ -axis because the O-Ta-O chains in the  $a$ - $b$  plane have high polarizability



28.13 XRD patterns of SBT ceramic samples prepared by (a) the sol-gel process and (b) the co-precipitation method, and sintered at different temperatures for different times. The inset in (b) is the XRD pattern of the precursor powder obtained by the co-precipitation method (reproduced with permission from *Chem. Mater.* 2006, **18**(2), 532–540).



28.14 Scanning electron microscopy images of SBT ceramics prepared by the sol-gel process (a–c) and the co-precipitation method (d–e) and sintered at 1000°C for 8 h (a) and (d), 1200°C for 4 h (b) and (e), and 1200°C for 8 h (c) and (f) (reproduced with permission from *Chem. Mater.* 2006, **18**(2), 532-540).

and, hence, is responsible for the polarization [29]. Therefore, the polarization measured in ceramics containing more grains with the polarization oriented along the  $a$ -axis parallel to the field direction is larger than in those containing mostly grains with the  $c$ -axis along the field direction (i.e. perpendicular to the electrode surfaces) [56,57]. Moreover, the measured densities of the SG1200(4) and SG1200(8) ceramics are much higher than those of PR1200(4) and PR1200(8), which is another reason for their higher  $P_r$  values. The

**Table 28.2** Comparison of the dielectric properties of SBT prepared by different methods (reproduced with permission from *Chem. Mater.* 2006, **18**(2) 532–540)

Method	$\epsilon'_{RT}$ (100 kHz)	$\epsilon'_{max}$ (100 kHz)	$T_C$ (°C)
Sol-gel*	207	900	330
Co-precipitation*	219	800	330
Single crystals [14]**	135	127	320
Single crystals [38]†	105	130	355
Single crystals [38]‡	110	1325	355
Solid state reactions [35]	~100	~500	315

\*This work.

\*\*Single crystals with dominant (001) orientation and about 1–3% of (113) orientation.

†Perfectly *c*-oriented single crystals.

‡Single crystals oriented in the *ab*-plane.

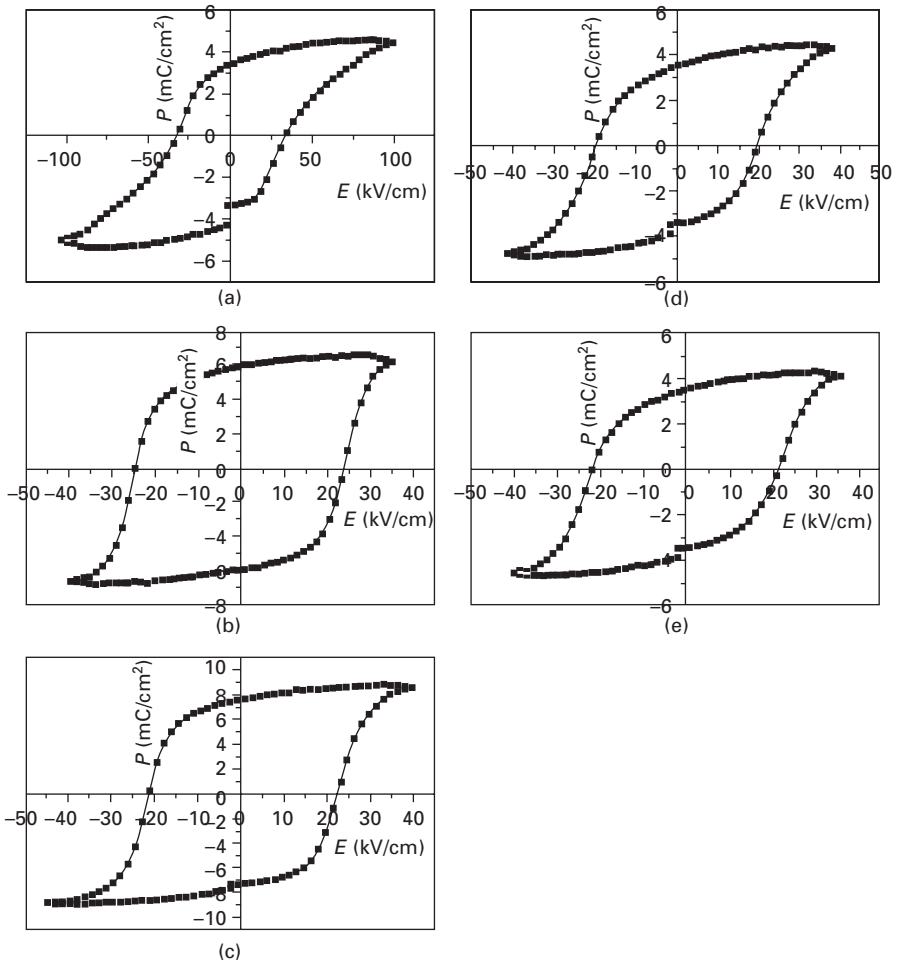
relationship between the high preferential orientation, relatively low density and low  $P_r$  value observed in the PR1200(8) ceramic is consistent with the previous report that excessive directional grain growth in SBT and  $\text{BaBi}_2\text{Ta}_2\text{O}_9$  ceramics leads to a lower density resulting from a loosely packed microstructure [43,58].

Overall, the sol-gel process produces ceramics with much better dielectric and ferroelectric properties because it allows more homogeneous grain distribution by reducing *c*-oriented grains in the materials, thus achieving the purpose of ‘grain-control’. This method therefore shows promising potential for depositing SBT thin films with minimized *c*-axis orientation and hence, improved remnant polarization, which is a key performance interesting for non-volatile memory applications.

## 28.5 Novel sol-gel route to ferroelectric $\text{Bi}_4\text{Ti}_3\text{O}_{12}$ and $\text{Bi}_{4-x}\text{La}_x\text{Ti}_3\text{O}_{12}$ ceramics

### 28.5.1 Background

As discussed in Section 28.4,  $\text{SrBi}_2\text{Ta}_2\text{O}_9$  (SBT) was found to be a promising alternative to PZT-based materials because of its excellent fatigue resistance and very good data retention over a long period of time [28,29]. However, the relatively low remnant polarization and the higher processing temperature of SBT may limit its application in FRAM [59]. This has led to research on other lead-free ferroelectric materials with better properties, and  $\text{Bi}_4\text{Ti}_3\text{O}_{12}$  (BIT) has emerged as a possible solution to the problem. BIT also belongs to the Aurivillius family of compounds [33] with a layered structure in which  $n$  perovskite-like  $(\text{A}_{n-1}\text{B}_n\text{O}_{3n+1})^{2-}$  blocks alternate with  $(\text{Bi}_2\text{O}_2)^{2+}$  layers. In BIT, three perovskite  $(\text{Bi}_2\text{Ti}_3\text{O}_{10})^{2-}$  units are stacked with the bismuth-oxygen layers, and the major component of spontaneous polarization is along the *a*-



28.15 Ferroelectric hysteresis loops of SBT ceramics derived from the sol-gel process and the co-precipitation method, and sintered at different temperatures and times: (a) SG1000(8), (b) SG1200(4), (c) SG1200(8), (d) PR1200(4), and (e) PR1200(8) (reproduced with permission from *Chem. Mater.* 2006, **18**(2), 532–540).

axis (only a much smaller component along the  $c$ -axis). As a lead-free ferroelectric with a high Curie temperature ( $T_C = 675^\circ\text{C}$ ) and a high remnant polarization ( $P_r = 50\ \mu\text{C}/\text{cm}^2$ ) along the main polar crystallographic  $a$ -axis [60], BIT appears to be a promising candidate for applications in piezoelectric transducers and memory devices over a wide temperature range [55,61]. However, BIT, especially in the form of thin film, is known to suffer from serious fatigue failure after only about  $10^6$  switching cycles [62]. The high  $T_C$  in BIT results in a large coercive field ( $E_C$ ) at room temperature, making



**Table 28.3** Comparison of the ferroelectric properties of SBT ceramics synthesized by the sol-gel process and the co-precipitation method with the literature data on single crystals and ceramics prepared by the solid state reaction (reproduced with permission from *Chem. Mater.* 2006, **18**(2) 532–540)

Samples	Sol-gel method			Co-precipitation		Single crystals [14]*	Single crystals [39]**	Solid-state reaction [44]
	1000(8)	1200(4)	1200(8)	1200(4)	1200(8)			
$E_C$	34.5	23	22	19.5	21	1	22	30
$P_r$	3.4	6.0	7.6	3.5	3.7	0.01	14	4.5

\*Single crystals with dominant (001) orientation and about 1–3% of (113) orientation.

\*\*Single crystals oriented in the *ab*-plane.

the poling of the material difficult. To lower  $E_C$ ,  $T_C$  must be decreased. Wolfe and Newnham [63] found that substituting trivalent rare earth ions for  $\text{Bi}^{3+}$  in the perovskite slabs of the Bi-layered ferroelectrics has the effect of decreasing  $T_C$ . Takenaka and Sakata [64] studied the effect of the  $\text{La}^{3+}$  substitution for  $\text{Bi}^{3+}$  in BIT, i.e.  $\text{Bi}_{4-x}\text{La}_x\text{Ti}_3\text{O}_{12}$  (*x*BLT), and found that  $T_C$  decreases with the increasing amounts of  $\text{La}^{3+}$  from 675 °C for  $x = 0$  to about –150 °C for  $x = 1.5$ .

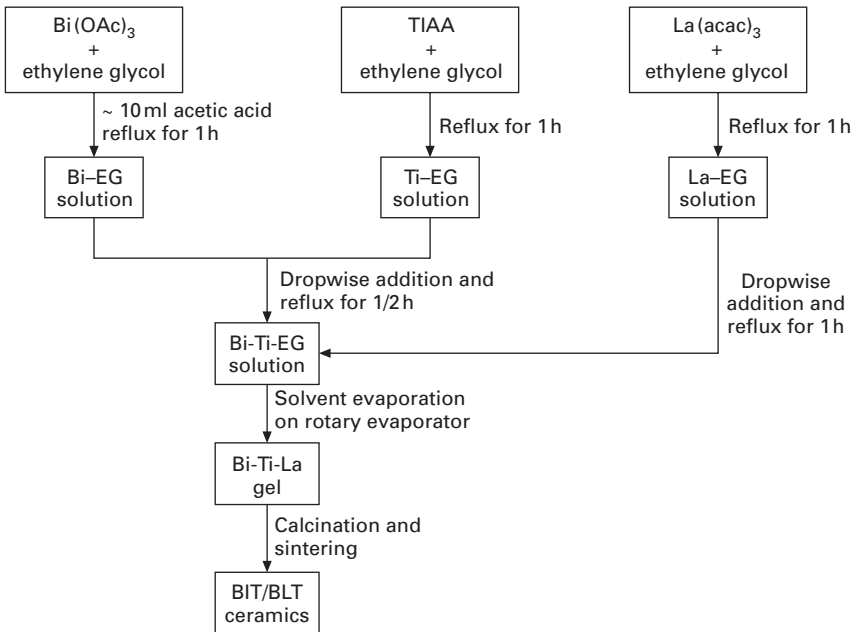
In the wake of intensive research efforts, it was found that replacing some of the  $\text{Bi}^{3+}$  ions in the perovskite slabs by the  $\text{La}^{3+}$  ions greatly improves the properties of BIT and also lowers the processing temperature [64]. For instance, thin films of  $\text{Bi}_{4-x}\text{La}_x\text{Ti}_3\text{O}_{12}$  ( $x = 0.75$ ) were prepared at a relatively low temperature of 650 °C, which exhibit good fatigue endurance even after  $3 \times 10^{10}$  switching cycles [65]. With its lower processing temperature and higher remnant polarization compared with SBT,  $\text{Bi}_{3.25}\text{La}_{0.75}\text{Ti}_3\text{O}_{12}$  stands as a better candidate for FRAM application. A number of different techniques were reported for the synthesis of BIT and BLT ceramics and thin films. The metal-organic chemical vapor deposition, the metal-organic deposition and the sol-gel process are among the most commonly used methods for preparing the thin films of these materials. Solid-state reactions employed for the synthesis of BIT powders require relatively high temperatures (>1100 °C) [66]. Several soft chemical routes were used for the preparation of BIT ceramics, including the co-precipitation method [67,68], the molten salt synthesis [69] and the sol-gel process [70,71]. In contrast, there have been only a few reports on the soft chemical synthesis of BLT powders and ceramics. Shen *et al.* [72] reported the sol-gel preparation of  $\text{Bi}_{4-x}\text{La}_x\text{Ti}_3\text{O}_{12}$  ( $x = 0.4$ ) powders and ceramics using ethylene glycol as a solvent. This method led to the preparation of fine BLT powders at a calcination temperature of 750 °C. However, it required drying the sol at 95–105 °C over a period of 5 days in order to obtain the gel.

Following our recent work on the soft chemical synthesis of SBT ceramics [73], as described in Section 28.4, we have synthesized  $\text{Bi}_4\text{Ti}_3\text{O}_{12}$  (BIT) and

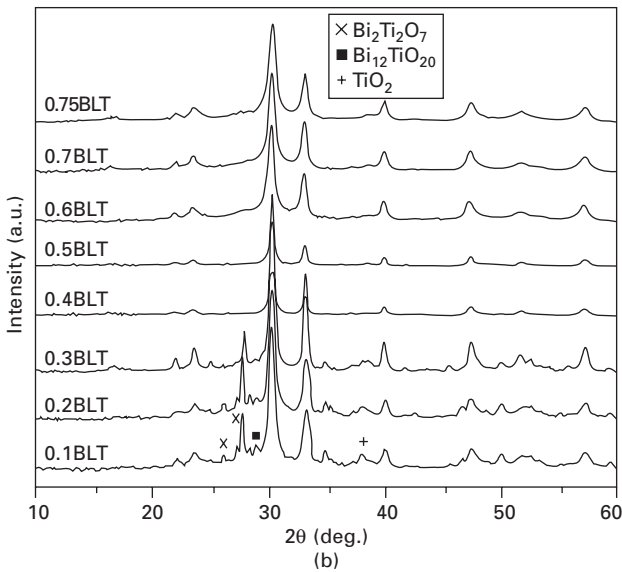
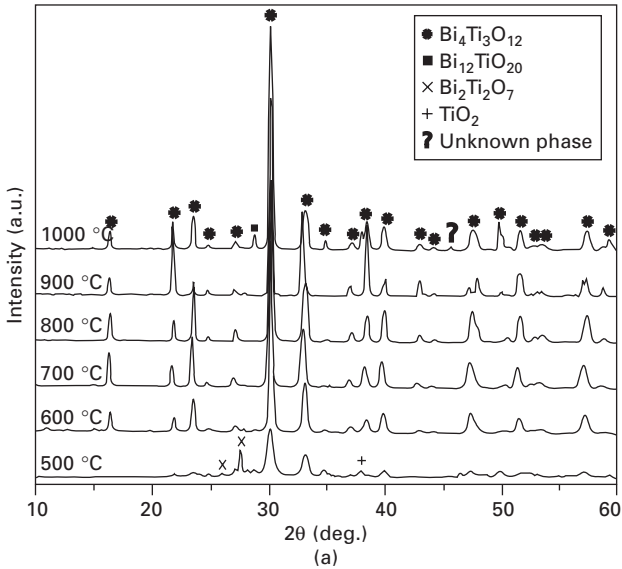
$\text{Bi}_{4-x}\text{La}_x\text{Ti}_3\text{O}_{12}$  ( $x\text{BLT}$ ) ceramics by an improved sol–gel method based on ethylene glycol. The flowchart in Fig. 28.16 outlines the procedure for the synthesis of precursor solutions, gels and ceramics of BIT and BLT. Our main objective was to study the effect of sol–gel processing parameters and La-doping on the phase formation and dielectric properties of the BLT compounds. It has been shown that, once again, ethylene glycol proves to be a good solvent for the starting materials, and this new method allows the synthesis of the  $x\text{BLT}$  powders and ceramics at relatively low temperatures with good dielectric properties. With this new sol–gel method, the formation of the pure Bi-layered phase has been achieved at a temperature as low as  $600^\circ\text{C}$  for BIT and  $x\text{BLT}$  with  $x = 0.1, 0.2$  and  $0.3$ , and  $500^\circ\text{C}$  for  $x\text{BLT}$  with  $x = 0.4\text{--}0.75$ , after heat treatment of the gels for 2 h. The X-ray diffraction (XRD) patterns are shown in Fig. 28.17. The sols obtained are stable over a period of 3–5 days, which points to the potential of this sol–gel process for the deposition of the thin films of BIT and  $x\text{BLT}$  for device applications.

## 28.6 Future trends

The exciting field of soft chemistry will continue to attract considerable attention in the area of materials science and engineering, more specifically



28.16 Flowchart for the preparation of precursor solutions, gels, and ceramics of  $\text{Bi}_4\text{Ti}_3\text{O}_{12}$  (BIT) and  $\text{Bi}_{4-x}\text{La}_x\text{Ti}_3\text{O}_{12}$  (BLT).



28.17 X-ray diffraction patterns of (a) BIT samples treated at different temperatures, and (b) xBLT samples treated at 500 °C.

in the synthesis of thin and thick films. In addition to the intensive research on dielectric and ferroelectric thin films initiated mainly for ferroelectric random access memory (FRAM) and dynamic random access memory (DRAM) device applications, recent emphasis is put more towards micro-electro-mechanical systems (MEMS). The strong piezoelectric effect and

high energy density of ferroelectric materials which result from their remarkably high dielectric constant make them very important materials for MEMS applications in the form of thin films [74]. PZT thin films deposited by several techniques such as physical deposition (e.g. PLD), chemical vapor deposition (e.g. MOCVD) and solution deposition (e.g. sol-gel process) are currently being used in a number of MEMS devices such as micro-accelerometers [75], force sensors [76], micropumps [74] and micromotors [77]. The solution deposition has become the preferred method because of its cost-effectiveness compared with the former two techniques, excellent control on stoichiometry in multiple-cation systems, good homogeneity and ability to make films with a thickness of several micrometers. Moreover, solution deposition routes are simple and do not require, for example, vacuum or reactor chambers.

The novel sol-gel routes that we have developed for the synthesis of  $(1 - x)\text{PMN}-x\text{PT}$  ( $x = 0.10$  and  $0.35$ ), SBT and BLT ceramics allow the formation of stable sols which can have tremendous potential for the fabrication of ferroelectric thin films for MEMS and FRAM applications. The room temperature synthesized PMN-PT sols are promising candidates for the deposition of thin and thick films with excellent piezo- and ferroelectric properties that can replace the currently used PZT films in MEMS. On the other hand, the sol-gel-derived SBT sol will offer the possibility of depositing thin films with reduced  $c$ -axis orientation and thereby improved remnant polarization, which will make them interesting for non-volatile memories. The SBT and BLT thin films can be outstanding lead-free and fatigue-free alternatives to the PZT films.

Single crystals of the  $(1 - x)\text{PMN}-x\text{PT}$  solid solution with compositions near the morphotropic phase boundary (MPB) have shown some of the highest piezoelectric properties, making them excellent materials for electromechanical transducer applications [6]. The ceramics of  $(1 - x)\text{PMN}-x\text{PT}$  are expected to be a viable alternative to the single crystals if their piezo- and ferroelectric properties can be optimized. The novel sol-gel process developed in this work has led to the  $0.65\text{PMN}-0.35\text{PT}$  ceramics of high density and good dielectric and ferroelectric properties. However, the piezoelectric performance of the ceramics remains to be assessed. Moreover, ceramics of other PMN- $x\text{PT}$  compositions, especially those in the rhombohedral phase but close to the MPB ( $x = 28-32\%$ ), need to be prepared with a view to achieving the optimum piezoelectric response and electromechanical properties (as referred to the performance of the single crystals).

The ability to make the powders or particles of nanometric size represents another feature of the new soft-chemical routes, which remains to be explored. Ferroelectric nano-powders have been given a great deal of attention in the past few years, not only because of the fundamental interest related to particle

size effects on the structure and properties of the materials, but also because of the practical applications arising from the enhanced properties of the nano-powders. For instance, ferroelectric BaTiO<sub>3</sub>-based fine particles have been used as raw materials for electronic devices such as multilayered ceramic capacitors (MLCC). The size dependence of the dielectric constant of BaTiO<sub>3</sub> particles reveals a maximum of 15 000 with a particle size of about 68 nm [78] or a maximum of 5 000 with a size of 140 nm [79]. Since the ceramics and single crystals of PMN-*x*PT, especially PMN-10PT, exhibit a very high dielectric constant around room temperature, it is expected that the nano-powders/particles of PMN-*x*PT can greatly improve the performance of miniaturized MLCC, more than the BaTiO<sub>3</sub> counterpart does, with enhanced capacitance and higher power density for micro-capacitors.

## 28.7 Acknowledgments

This work was supported by the Natural Science and Engineering Research Council of Canada (NSERC) and the US Office of Naval Research (Grant No. N00014-1-06-0166).

## 28.8 References

1. Bradley D C (1989), 'Metal alkoxides as precursors for electronic and ceramic materials', *Chem. Rev.*, **89**, 1317–1322.
2. Alain C P (1998), *Introduction to Sol-Gel Processing*, Boston/Dordrecht/London, Kluwer Academic Publishers.
3. Payne D A (1994), 'Powderless processing of ceramics: thin-layer electroceramics', *J. Sol-gel Sci. Techn.*, **2**, 311–315.
4. West A R (1996), *Basic Solid State Chemistry*, 2nd edition, New York, John Wiley & Sons Ltd.
5. Jang S J, Uchino K, Nomura S, and Cross L E (1980), 'Electrostrictive behavior of lead magnesium niobate based ceramic dielectrics', *Ferroelectrics*, **27**, 31–34.
6. Park S E, and Shrout T R (1997), 'Ultrahigh strain and piezoelectric behavior in relaxor based ferroelectric single crystals', *J. Appl. Phys.*, **82**(4), 1804–1811.
7. Ye Z-G, and Dong M (2000), 'Morphotropic domain structures and phase transitions in relaxor-based piezo-/ferroelectric (1 - *x*)Pb(Mg<sub>1/3</sub>Nb<sub>2/3</sub>)O<sub>3</sub>-*x*PbTiO<sub>3</sub> single crystals', *J. Appl. Phys.*, **87**(5), 2312–2319.
8. Ye Z-G (1998), 'Relaxor ferroelectric complex perovskites: structure, properties and phase transitions', *Key Eng. Mater.*, **155–156**, 81–122.
9. Shrout T R, Chang Z P, Kim N, and Markgraf S (1990), 'Dielectric behavior of single crystals near the (1 - *x*)Pb(Mg<sub>1/3</sub>Nb<sub>2/3</sub>)O<sub>3</sub>-*x*PbTiO<sub>3</sub> morphotropic phase boundary', *Ferroelectric Lett.*, **12**, 63–69.
10. Ye Z-G, Bing Y, Gao J, Bokov A A, Stephens P, Noheda B, and Shirane G (2003), 'Development of ferroelectric order in relaxor (1 - *x*)Pb(Mg<sub>1/3</sub>Nb<sub>2/3</sub>)O<sub>3</sub>-*x*PbTiO<sub>3</sub> (0 ≤ *x* ≤ 0.15)', *Phys. Rev. B.*, **67**, 104104-1-8.
11. Noheda B, Cox D E, Shirane G, Gao J, and Ye Z-G (2002), 'Phase diagram of the ferroelectric relaxor (1 - *x*)PbMg<sub>1/3</sub>Nb<sub>2/3</sub>O<sub>3</sub>-*x*PbTiO<sub>3</sub>', *Phys. Rev. B*, **66**, 054104.

12. Newnham R E, Xu Q C, Kumar S, and Cross L E (1990), 'Smart ceramics', *Ferroelectrics*, **102**, 259.
13. Park J H, Kang D H, and Yoon K H (1999), 'Effects of heating profiles on the orientation and dielectric properties of  $0.5\text{Pb}(\text{Mg}_{1/3}\text{Nb}_{2/3})\text{O}_3$ - $0.5\text{PbTiO}_3$  thin films by chemical solution deposition', *J. Am. Ceram. Soc.*, **82**(8), 2116–2120.
14. Service R F (1997), 'Materials science: shape-changing crystals get shiftier', *Science*, **275**, 1878–1880.
15. Park S-E, and Shrout T R (1997), 'Ultrahigh strain and piezoelectric behavior in relaxor based ferroelectric single crystals', *J. Appl. Phys.*, **82**(4), 1804–1811.
16. Jaffe B, Cook W R, and Jaffe H (1971), *Piezoelectric Ceramics*, London, Academic Press.
17. Francis L F, and Payne D A (1991), 'Thin-layer dielectrics in the  $\text{Pb}[(\text{Mg}_{1/3}\text{Nb}_{2/3})_{1-x}\text{Ti}_x]\text{O}_3$  system', *J. Am. Ceram. Soc.*, **74**(12), 3000–3010.
18. Nijmeijer A, Kruidhof H, and Hennings D (1997), 'Synthesis and properties of lead magnesium niobate zirconate relaxor materials', *J. Am. Ceram. Soc.*, **80**(10), 2717–2721.
19. Uekawa N, Sukegawa T, Kakegawa K, and Sasaki Y (2002), 'Synthesis of lead nickel niobate–barium titanate system by oxidation of polyethylene glycol–cation complex', *J. Am. Ceram. Soc.*, **85**(2), 329–334.
20. Pechini M P (1967), 'Method of preparing lead and alkaline earth titanates and niobates and coating method using the same to form a capacitor' US Pat. No. 3 330 697.
21. Nguyen M H, Lee S-J, and Kriven W M (1999), 'Synthesis of oxide powders by way of a polymeric steric entrapment precursor route', *J. Mater. Res.*, **14**(8), 3417–3426.
22. Gülgün M A, Nguyen M H, and Kriven W M (1999), 'Polymerized organic-inorganic synthesis of mixed oxides', *J. Am. Ceram. Soc.*, **82**(3), 556–560.
23. Uekawa N, Endo M, Kakegawa K, and Sasaki Y (2000), 'Homogeneous precipitation of  $\text{Cr}^{3+}$ - $\text{M}^{2+}$  ( $\text{M} = \text{Ni}, \text{Zn}, \text{Co}, \text{Cu}$ ) oxalate by oxidation of the polyethylene glycol–cation complex', *Phys. Chem. Chem. Phys.*, **2**, 5485–5490.
24. Shimizu Y, and Murata T (1997), 'Sol–gel synthesis of perovskite-type lanthanum manganite thin films and fine powders using metal acetylacetonate and poly(vinyl alcohol)', *J. Am. Ceram. Soc.*, **80**(10), 2702–2704.
25. Sriprang N, Kaewchinda D, Kennedy J D, and Milne S J (2000), 'Processing and sol chemistry of a triol-based sol–gel route for preparing lead zirconate titanate thin films', *J. Am. Ceram. Soc.*, **83**(8), 1914–1920.
26. Babooram K, Tailor H, and Ye Z-G (2004), 'Phase formation and dielectric properties of 0.9PMN–0.1PT ceramics prepared by a new sol–gel method', *Ceramics Int.*, **30**, 1411–1417.
27. Babooram K, and Ye Z-G (2004), 'Polyethylene glycol-based new solution route to relaxor ferroelectric  $0.65\text{Pb}(\text{Mg}_{1/3}\text{Nb}_{2/3})\text{O}_3$ - $0.35\text{PbTiO}_3$ ', *Chem. Mater.*, **16**, 5365–5371.
28. Scott J F, and De Araujo Paz C A (1989), 'Ferroelectric memories', *Science*, **246**, 1400–1405.
29. De Araujo Paz C A, Cuchiari J D, Scott M C, McMillan L D, and Scott J F (1995), 'Fatigue-free ferroelectric capacitors with Pt electrodes', *Nature*, **374**(13), 627.
30. Scott J F, Ross F M, De Araujo Paz C A, Scott M C, and Huffman M (1996), 'Structure and device characteristics of  $\text{SrBi}_2\text{Ta}_2\text{O}_9$ -based nonvolatile random-access memories', *Mater. Res. Soc. Bull.*, **21**, 33–39.

31. Chang J F, and Desu S B (1994), 'Effects of dopants in PZT films', *J. Mater. Res.*, **9**, 955–969.
32. Warren W L, Dimos D, Tuttle B A, Nasby R D, and Pike G E (1994), 'Electronic domain pinning in Pb(Zr,Ti)O<sub>3</sub> thin films and its role in fatigue', *Appl. Phys. Lett.*, **65**, 1018–1020.
33. Aurivillius B (1949), 'Mixed bismuth oxides with layer lattices. I. Structure type of CaCb<sub>2</sub>Bi<sub>2</sub>O<sub>9</sub>', *Arki. Kemi*, **1**, 463–480.
34. Desu S B, and Li T K (1995), 'Fatigue-free SrBi<sub>2</sub>(Ta<sub>x</sub>Nb<sub>1-x</sub>)<sub>2</sub>O<sub>9</sub> ferroelectric thin films', *Mater. Sci. Eng. B*, **34**, L4–L8.
35. Lee J J, Thio C L, and Desu S B (1995), 'Electrode contacts on ferroelectric Pb(Zr<sub>x</sub>Ti<sub>1-x</sub>)O<sub>3</sub> and SrBi<sub>2</sub>Ta<sub>2</sub>O<sub>9</sub> thin films and their influence on fatigue properties', *J. Appl. Phys.*, **78**(8), 5073–5078.
36. Calzada M L, Jimenez R, Gonzalez A, and Mendiola J (2001), 'Air-stable solutions for the low-temperature crystallization of strontium bismuth tantalate ferroelectric films', *Chem. Mater.*, **13**, 3–5.
37. Kato K, Zheng C, Finder J M, Dey S K, and Torii K (1998), 'Sol-gel route to ferroelectric layer-structured perovskite SrBi<sub>2</sub>Ta<sub>2</sub>O<sub>9</sub> and SrBi<sub>2</sub>Nb<sub>2</sub>O<sub>9</sub> thin films', *J. Am. Ceram. Soc.*, **81**(7), 1869–1875.
38. Desu S B, Vijay D P, Zhang X, and He B P (1996), 'Oriented growth of SrBi<sub>2</sub>Ta<sub>2</sub>O<sub>9</sub> ferroelectric thin films', *Appl. Phys. Lett.*, **69**(12), 1719–1721.
39. Calzada M L, Gonzalez A, Jimenez R, Alemany C, and Mendiola J (2001), 'Rapid thermal processing of strontium bismuth tantalate ferroelectric thin films prepared by a novel chemical solution deposition technique', *J. Eur. Ceram. Soc.*, **21**, 1517–1520.
40. Zurbuchen M A, Lettieri J, Fulk S J, Jia Y, Carim A H, Schlom D G, and Streiffer S K (2003), 'Bismuth volatility effects on the preparation of SrBi<sub>2</sub>Nb<sub>2</sub>O<sub>9</sub> and SrBi<sub>2</sub>Ta<sub>2</sub>O<sub>9</sub> Films', *Appl. Phys. Lett.*, **82**(26), 4711–4713.
41. Lee J-K, Park B, and Hong K-S (2000), 'Effect of excess Bi<sub>2</sub>O<sub>3</sub> on the ferroelectric properties of SrBi<sub>2</sub>Ta<sub>2</sub>O<sub>9</sub> ceramics', *J. Appl. Phys.*, **88**(5), 2825–2829.
42. Yang J S, and Chen X M (1996), 'Preparation and dielectric characteristics of SrBi<sub>2</sub>Ta<sub>2</sub>O<sub>9</sub> ceramics', *Mater. Lett.*, **29**, 73–75.
43. Murugan G S, and Varma K B R (2002), 'Microstructural, dielectric, pyroelectric, and ferroelectric studies on partially grain-oriented SrBi<sub>2</sub>Ta<sub>2</sub>O<sub>9</sub> ceramics', *J. Electroceram.*, **8**, 37–48.
44. Shimakawa Y, Kubo Y, Nakagawa Y, Kamiyama T, Asano H, and Izumi F (1999), 'Crystal structure and ferroelectric properties of SrBi<sub>2</sub>Ta<sub>2</sub>O<sub>9</sub> and Sr<sub>0.8</sub>Bi<sub>2.2</sub>Ta<sub>2</sub>O<sub>9</sub>', *Appl. Phys. Lett.*, **74**(13), 1904–1906.
45. Luk C H, Mak C L, and Wong K H (1997), 'Characterization of strontium barium niobate films prepared by sol-gel process using 2-methoxyethanol', *Thin Solid Films*, **298**, 57–61.
46. Anilkumar G M, and Sung Y-M (2003), 'Phase formation kinetics of nanoparticle-seeded strontium bismuth tantalate powder', *J. Mater. Sci.*, **38**, 1391–1396.
28. Kim Y, Chae H K, Lee K S, and Lee W I (1998), 'Preparation of SrBi<sub>2</sub>Ta<sub>2</sub>O<sub>9</sub> thin films with a single alkoxide sol-gel precursor', *J. Mater. Chem.*, **8**, 2317–2320.
48. Ramamurthi S D, Xu Z, and Payne D A (1990), 'Nanometer-sized ZrO<sub>2</sub> particles prepared by a sol-emulsion-gel method', *J. Am. Ceram. Soc.*, **73**(9), 2760–2763.
49. Maher G H, Hutchins C E, and Ross S D (1993), 'Preparation and characterization of ceramic fine powders produced by the emulsion process', *Am. Ceram. Soc. Bull.*, **72**(5), 72–76.

50. Lu C-H, and Saha S K (2000), 'Colloid emulsion of nanosized strontium bismuth tantalate powder', *J. Am. Ceram. Soc.*, **83**(5), 1320–1322.
51. Ramesh R, and Schlom D G (2002), 'Orienting ferroelectric films', *Science*, **296**, 1975–1976.
52. Sakata K, Takenaka T, and Shoji K (1978), 'Hot-forged ferroelectric ceramics of some bismuth compounds with layer structure', *Ferroelectrics*, **22**, 825–826.
53. Takenaka T, and Sakata K (1980), 'Grain orientation and electrical properties of hot-forged  $\text{Bi}_4\text{Ti}_3\text{O}_{12}$  ceramics', *Jpn. J. Appl. Phys.*, **19**, 31–39.
54. Takenaka T, and Sakata K (1991), 'Pyroelectric properties of bismuth layer-structured ferroelectric ceramics', *Ferroelectrics*, **118**, 123–133.
55. Seth V K, and Schulze W A (1989), 'Grain-oriented fabrication of bismuth titanate ceramics and its electrical properties', *IEEE Trans. Ultrason., Ferroelec. Freq. Contr.*, **36**(1), 41–49.
56. Smolenskii G A, Isupov V A, and Agranovskaya A I (1961), 'Ferroelectrics of the oxygen-octahedral type with layered structure', *Sov. Phys. Solid State*, **3**, 651.
57. Subbarao E C (1962), 'Family of ferroelectric bismuth compounds', *Phys. Chem. Solids*, **23**, 665–676.
58. Lu C H, and Fang B K (1998), 'Synthesis processes and synthesis behaviour of layered-perovskite barium bismuth tantalate ceramics', *J. Mater. Res.*, **13**, 2262–2268.
59. Auciello O, and Ramesh R (1996), 'Laser-ablation deposition and characterization of ferroelectric capacitors for nonvolatile memories', *Mater. Res. Bull.*, **21**, 31.
60. Dorrian J F, Newnham R E, Smith D K, and Kay M I (1971), 'Crystal structure of bismuth titanate', *Ferroelectrics*, **3**, 17–27.
61. Ding Y, Liu J S, Qin H X, Zhu J S, and Wang Y N (2001), 'Why lanthanum-substituted bismuth titanate becomes fatigue free in a ferroelectric capacitor with platinum electrodes', *Appl. Phys. Lett.*, **78**, 4175–4177.
62. Joshi P C, Krupanidhi S B, and Mansingh A (1992), 'Rapid thermally processed ferroelectric  $\text{Bi}_4\text{Ti}_3\text{O}_{12}$  thin films', *J. Appl. Phys.*, **72**, 5517–5519.
63. Wolfe R W, and Newnham R E (1969), 'Rare earth bismuth titanates', *J. Electrochem. Soc.*, **116**, 832–835.
64. Takenaka T, and Sakata K (1981), 'Electrical properties of grain-oriented ferroelectric ceramics in some lanthanum modified layer-structure oxides', *Ferroelectrics*, **38**, 769–772.
65. Park B H, Kang B S, Bu S D, Noh T W, Lee J, and Jo W (1999), 'Lanthanum-substituted bismuth titanate for use in non-volatile memories', *Nature (London)*, **401**, 682–684.
66. Villegas M, Caballero A C, Moure C, Duran P, and Fernandez J F (1999), 'Factors affecting the electrical conductivity of donor-doped  $\text{Bi}_4\text{Ti}_3\text{O}_{12}$  piezoelectric ceramics', *J. Am. Ceram. Soc.*, **82**(9), 2411–2416.
67. Umabala A M, Suresh M, and Prasadarao A V (2000), 'Bismuth titanate from coprecipitated stoichiometric hydroxide precursors', *Mater. Lett.*, **44**, 175–180.
68. Jiang A Q, Li H G, and Zhang L D (1998), 'Dielectric study in nanocrystalline  $\text{Bi}_4\text{Ti}_3\text{O}_{12}$  prepared by chemical coprecipitation', *J. Appl. Phys.*, **83**, 4878–4883.
69. Takeuchi T, Tani T, and Saito Y (2000), 'Unidirectionally textured  $\text{CaBi}_4\text{Ti}_4\text{O}_{15}$  ceramics by the reactive templated grain growth with an extrusion', *Jpn. J. Appl. Phys.*, **39**, 5577–5580.
70. Joshi P C, Mansingh A, Nkanalasanan M, and Chandra S (1991), 'Structural and optical properties of ferroelectric  $\text{Bi}_4\text{Ti}_3\text{O}_{12}$  thin films by sol-gel technique', *Appl. Phys. Lett.*, **59**, 2389–2390.



71. Prasada Rao A V, Robin A I, and Komarnani S (1996), 'Bismuth titanate from nanocomposite and sol-gel processes', *Mater. Lett.*, **28**, 469–473.
72. Shen L, Xiao D, Zhu J, Yu P, Zhu J, and Gao D (2002), 'Study of  $(\text{Bi}_{4-x}\text{La}_x)\text{Ti}_3\text{O}_{12}$  powders and ceramics prepared by sol-gel method', *J. Mater. Syn. Proc.*, **9**(6), 369–373.
73. Babooram K, and Ye Z-G (2006), 'New soft chemical routes to ferroelectric  $\text{SrBi}_2\text{Ta}_2\text{O}_9$ ', *Chem. Mater.*, **18**, 532–540.
74. Polla D L, and Francis L F (1996), 'Ferroelectric thin films in microelectromechanical systems applications', *MRS Bull.*, **21**(7), 59–65.
75. Yoon Y S, Kim J H, Hsieh M T, and Polla D L (1998), *J. Korean Phys. Soc.*, **32**, S1760–S1762.
76. Lee C, Itoh T, and Suga T (1996), 'Micromachined piezoelectric force sensors based on PZT thin films', *IEEE Trans. Ultrason. Ferroelec. Freq. Contr.*, **43**, 553–559.
77. Udayakumar K R, Chen J, Flynn A M, Bart S F, Tavrow L S, Ehrlich D J, Cross L E, and Brooks R A (1994), 'Ferroelectric thin films for piezoelectric micromotors', *Ferroelectrics*, **160**, 347–356.
78. Wada S, Yasuno H, Hoshina T, Nam S-M, Kakemoto H, and Tsurumi T (2003), 'Preparation of nm-sized barium titanate fine particles and their powder dielectric properties', *Jpn. J. Appl. Phys.*, **42**, 6188–6195.
79. Hoshina T, Kakemoto H, and Tsurumi T, and Wada S (2006), 'Size and temperature induced phase transition behaviours of barium titanate nanoparticles', *J. Appl. Phys.*, **99**, 054311/1–8.

## Room temperature preparation of $\text{KNbO}_3$ nanoparticles and thin film from a perovskite nanosheet

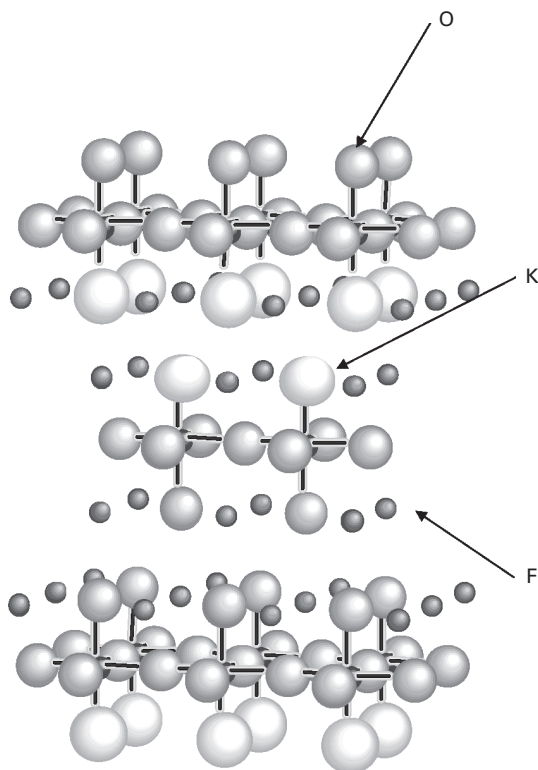
K TODA and M SATO, Niigata University, Japan

### 29.1 Introduction

The future use of piezoelectric materials containing lead, which is extensive at present, is likely to be restricted because of environmental regulations. Anticipating that situation, it is necessary for lead-free piezoelectric materials to be developed. Potassium niobate ( $\text{KNbO}_3$ ) is a material that has extremely high nonlinear optical characteristics and a high electromechanical coupling coefficient (efficiency of conversion between electrical energy and mechanical energy). Therefore, it is considered to be most promising for use as an alternative to current lead-based piezoelectric materials<sup>1,2</sup>. Nevertheless,  $\text{KNbO}_3$  poses many practical disadvantages for use in piezoelectric and ferroelectric materials.

First, polycrystal  $\text{KNbO}_3$  is a poorly sinterable material<sup>3</sup>. It is difficult to obtain sintered ceramics that are suitable for practical applications, even if special methods such as hot press are used. Although attempts have been made to improve the sintering using various additives, many additives degrade the electrical properties of the  $\text{KNbO}_3$  itself. Utilization of single crystals also involves such problems as difficulty in growing the stoichiometric single crystals.  $\text{KNbO}_3$  shows incongruent melting at high-temperature; moreover, fine cracks occur as a result of the phase transition from the high-temperature phase to the room temperature phase upon cooling, thereby engendering deterioration of the single-crystal quality.

To overcome these disadvantages, we specifically examined the layered perovskite  $\text{K}_2\text{NbO}_3\text{F}$ , with the structure as shown in Fig. 29.1, for use as a precursor for producing nanoparticles, single crystals in plate-shaped and thin films<sup>4</sup>. A distinctive feature of this compound is its unique layered perovskite structure, which includes an ordered KF block and a KO block between layers. An interlayer KF block composed of fluorine of negative charge one has weaker bonding than a perovskite block. For that reason, the potassium ions and fluorine ions in  $\text{K}_2\text{NbO}_3\text{F}$  are desorbed easily when stirred into water or calcinated at low temperature. Using this characteristic,



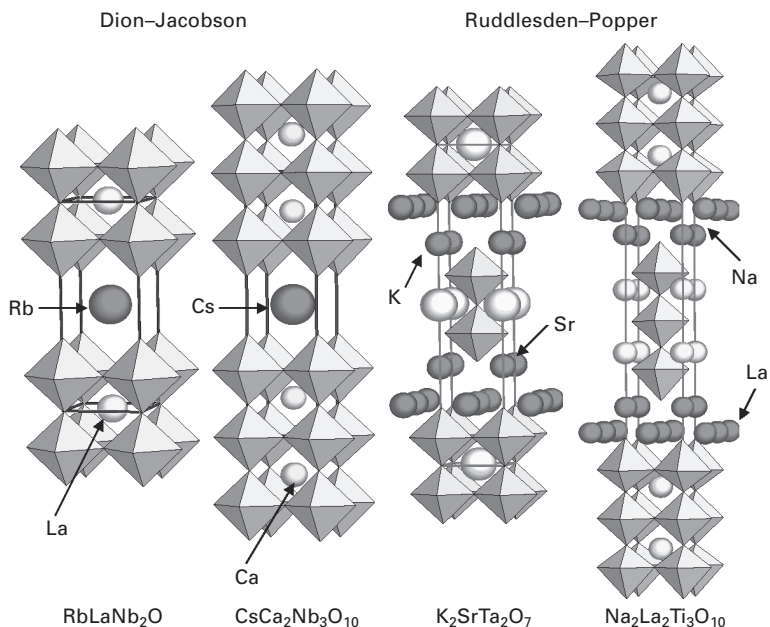
29.1 Crystal structure of layered perovskite  $\text{K}_2\text{NbO}_3\text{F}$ .

we obtained  $\text{KNbO}_3$  nanoparticles and formed a crystalline  $\text{KNbO}_3$  thin film at room temperature. This paper describes the reaction mechanism and formation of thin films.

## 29.2 Mechanisms of generation of $\text{KNbO}_3$ nanoparticles

### 29.2.1 Ion exchangeable layered perovskite

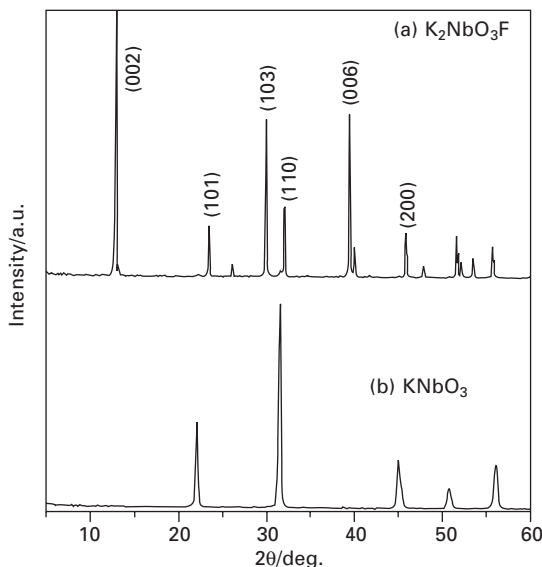
Since the late 1980s, we have been engaged in explorative research of ion exchangeable layered perovskite compounds, in which interlayer ions include alkali metals with lower valence that are readily exchangeable with other ions. Typical ion exchange layered perovskite compounds are the Dion–Jacobson phase and the Ruddlesden–Popper phase, as shown in Fig. 29.2<sup>5,6</sup>. The difference between the two structures lies in the charge amount of interlayer ions. These materials attract attention because manipulations on the nano-scale, such as conversion to a nanosheet by cleavage of layers, can be realized in easy-to-handle environments such as in a beaker. Moreover,



29.2 Model structure of typical Dion–Jacobson phase and Ruddlesden–Popper phases.

metastable compounds, which cannot be obtained by conventional solid-state high-temperature reactions, are obtainable through ion exchange reaction. These nanostructures are expected to form photocatalysts, phosphors, ionic conductors and superconducting materials which will find applications in new devices.

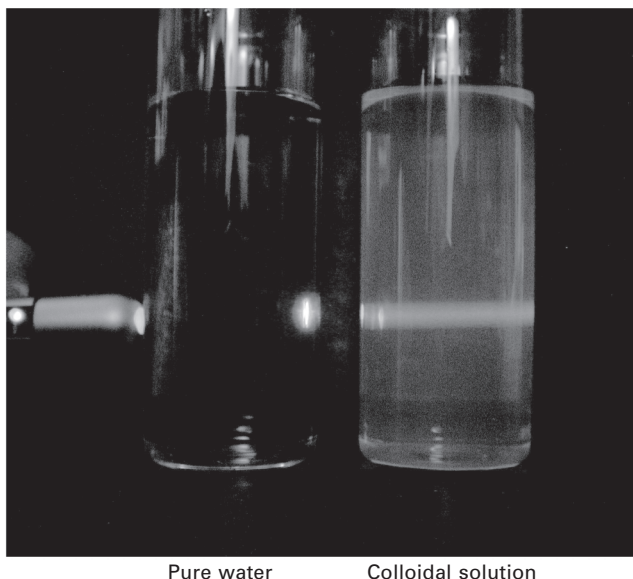
We have discovered the conversion of the layered perovskite  $K_2NbO_3F$ , a precursor phase, to perovskite  $KNbO_3$  at room temperature. Figure 29.3 shows the X-ray diffraction (XRD) patterns before and after the conversion. It is clear from Fig. 29.3 that  $KNbO_3$  obtained at room temperature is a crystalline compound. The synthesis of  $K_2NbO_3F$  was first reported by Galasso and Darby in 1962<sup>7</sup>. Its crystal structure is presumed to be a layered perovskite structure of  $K_2NiF_4$  type in which 50% of the apex oxygen is replaced by fluorine. In 1998, from the experiments using  $^{19}F$  NMR (nuclear magnetic resonance), Du *et al.* found that the averagely positioned fluorine model is incorrect. Instead, they proposed a structural model in which the KO block and KF block are built in a perfect order, as depicted in Fig. 29.1<sup>8</sup>. This peculiar pyramidal coordination structure plays an important role in the low-temperature reaction, as described in the following section.



29.3 Powder XRD pattern of layered perovskite  $\text{K}_2\text{NbO}_3\text{F}$  and  $\text{KNbO}_3$  prepared after immersion into water.

### 29.2.2 Conversion of $\text{K}_2\text{NbO}_3\text{F}$ to nanosheets in water and re-stacking

When the layered perovskite  $\text{K}_2\text{NbO}_3\text{F}$  is immersed in water at room temperature, exfoliation occurs first. Figure 29.4 shows a photograph of the solution together with pure water. Because the light path of a laser pointer is visible, this solution is inferred to be a colloidal solution. Observation by transmission electron microscopy (TEM) reveals that the colloid particles are uniform nanosheets of approximately 100 nm size. Such a size coincides with the crystallite size of the precursor phase. The conversion to nanosheets occurs rapidly and is almost completed within minutes. The insertion of bulky molecules to assist peeling, as is needed in the formation of nanosheet by ordinary cleavage of layers, is found to be unnecessary. This process is usually confused with the hydrothermal method. However, in contrast to the hydrothermal method, in which the formation of a crystal lattice occurs in hot water under high pressure, this method shows its characteristic in that the perovskite block is maintained, even in the solution. Therefore, there is no need for an external field for crystallization. Instead, voltage application or heating might hinder the self-organizing re-stacking of nanosheets. The simplest method, which is also effective for collecting powders, is centrifugation. Such a selective dissolution takes place between layers because of their binding characteristics: KF maintains higher solubility with regard to water, even at room temperature. For that reason, the KF block is dissolved solely

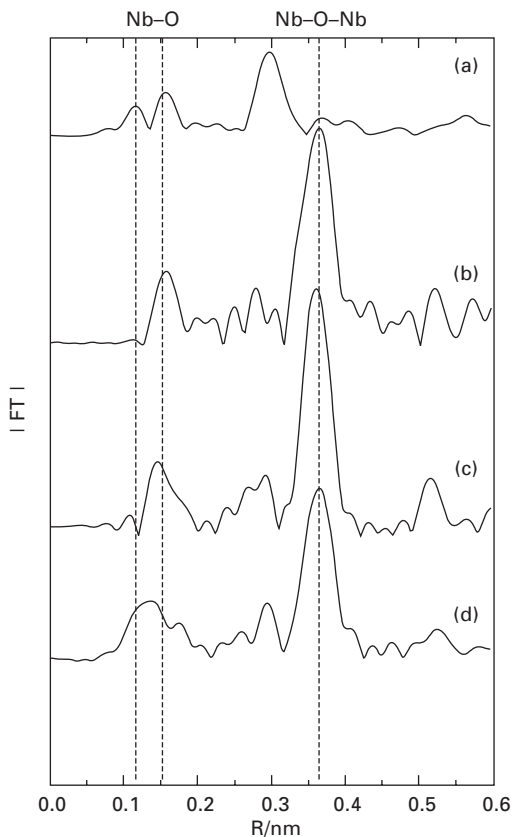


29.4 Colloidal solution obtained after immersion of layered perovskite  $K_2NbO_3F$  into water, as compared with pure water.

from  $K_2NbO_3F$  in water, but the perovskite block is held, strongly bound to pentavalent Nb. In fact, the conversion to nanosheets is not promoted because the KF block is not dissolved in the saturated aqueous solution of KF.

### 29.2.3 Re-stacking of nanosheets

Formation of  $KNbO_3$  from nanosheets occurs through self-organizing re-stacking. In this process, the layered perovskite is peeled to a monolayer perovskite nanosheet at room temperature; then a restructuring of the perovskite lattice occurs without any artificial manipulation. This self-organization is driven by the difference in the stability of lattice between the precursor and the intermediate product in a transition state in aqueous solution. The instability of the nanosheets, an intermediate product, is attributable to their peculiar pyramidal coordination structure, as mentioned previously. The nanosheets from which the KF block is dissolved selectively in water maintain a pyramidal-type coordination of  $NbO_5$  type because they lack apex oxygen. Figure 29.5 shows the extended X-ray absorption fine structure (EXAFS) data of nanosheets in an aqueous solution. Because the bonding state of Nb–O–Nb in the solution is different, it is known that the coordination of the nanosheets differs from that of  $KNbO_3$ , which is the final product. Furthermore, Fig. 29.6 shows the Raman spectra of the colloidal solution, the  $KNbO_3$  product and the  $K_2NbO_3F$  precursor for comparison. The electronic state of  $K_2NbO_3F$  changes because of the ordering of KO and KF, and a peak of Nb=O appears at  $822\text{ cm}^{-1}$  in

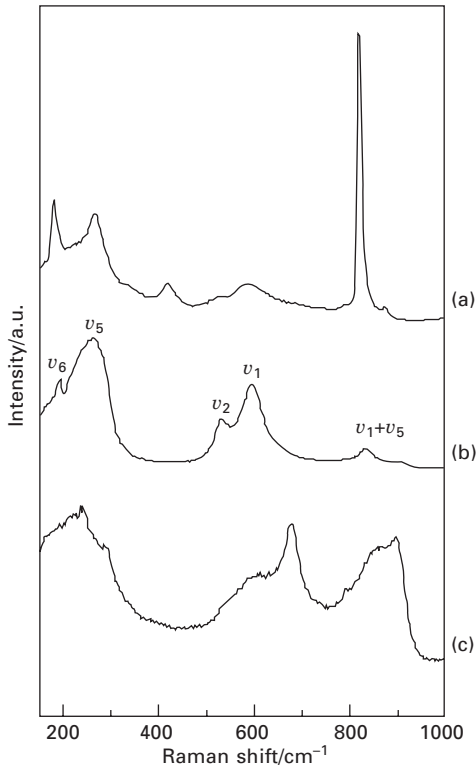


29.5 EXAFS data of (a) colloidal solution, (b)  $\text{KNbO}_3$  powder produced using the present process, (c)  $\text{KNbO}_3$  nano-powder annealed at  $1000^\circ\text{C}$  and (d)  $\text{KNbO}_3$  powder synthesized using a solid state reaction.

double-bond character<sup>9</sup>. The peak in the colloidal solution resembles that of  $\text{KNbO}_3$  of the final product, indicating the formation of a Nb–O polyhedron, although a slight shift of the peak position is observed<sup>10</sup>. These data imply that the nanosheets in the aqueous solution exhibit a distorted structure such that the  $\text{NbO}_5$  pyramids are turned to each other, as shown in Fig. 29.7. Such a peculiar five-coordinate structure is unstable. Therefore, more unstable  $\text{KNbO}_3$  is formed. A schematic representation of these structural changes is shown in Fig. 29.8.  $\text{KNbO}_3$  is obtained as nanoparticles in plate-shape, high-density sintered ceramics with a density of 98–99%, even under pressure-free conditions.

### 29.3 Fabrication of $\text{KNbO}_3$ thin film

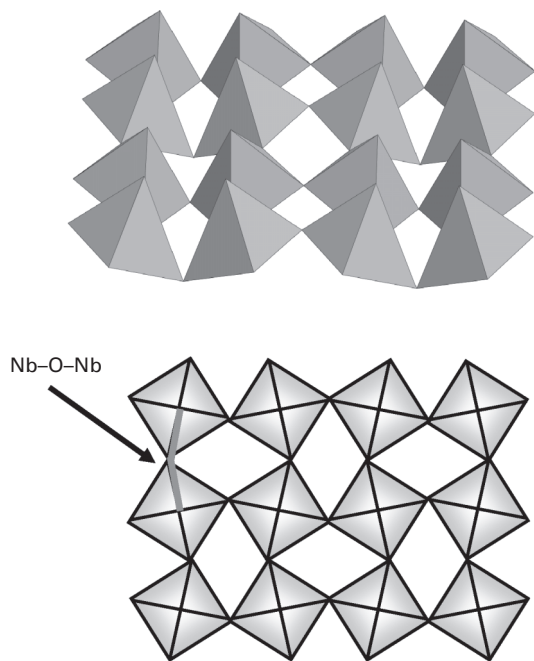
The precursor aqueous solution is a uniform colloidal solution. Using this solution in a simple process, we attempted to produce uniform thin films at



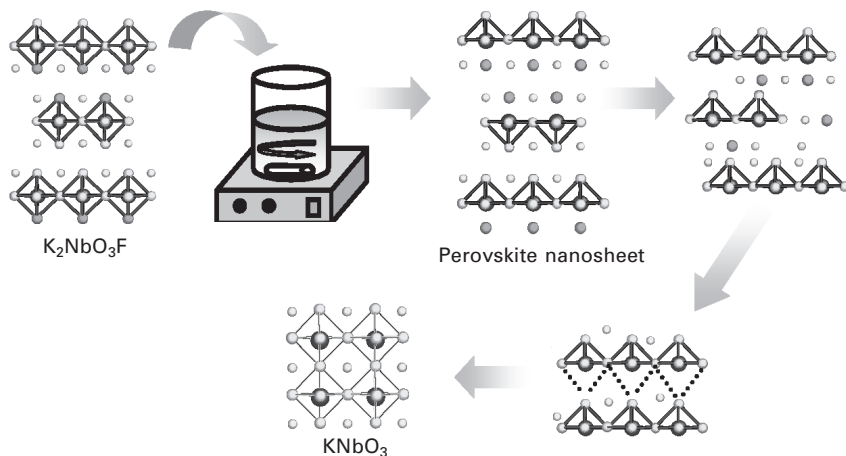
29.6 Raman spectra of (a) precursor  $K_2NbO_3F$  and (b) nano- $KNbO_3$  powders produced using the process described in the text, and (c) colloidal solution.

room temperature. A quartz substrate was immersed into the colloidal solution, raised up from it, and then air-dried. Figure 29.9 shows the photograph of a  $KNbO_3$  thin film produced on a glass substrate. A transparent and uniform thin film of polycrystals is formed, as is apparent in the figure. Observation by atomic force microscopy of the thin film before drying revealed a film that comprised plate-shaped particles in the order of 100–300 nm, in which the nanosheets are coagulated. The film orientation was not confirmed clearly, probably because the thermal disturbance at room temperature dominates the orientation as a result of the overly small nanosheets in the solution. Figure 29.10 shows a scanning electron microscopy (SEM) micrograph of the thin film cross-section and Fig. 29.11 shows its XRD pattern. A crystalline  $KNbO_3$  thin film is thus obtained without heat treatment. The effects of the immersion time on the film thickness are less significant because the nanosheets in the colloidal solution are used for the formation of the thin film at the beginning and the film showed little growth afterward. To control the film thickness, the initial concentration of the solution should merely be adjusted.



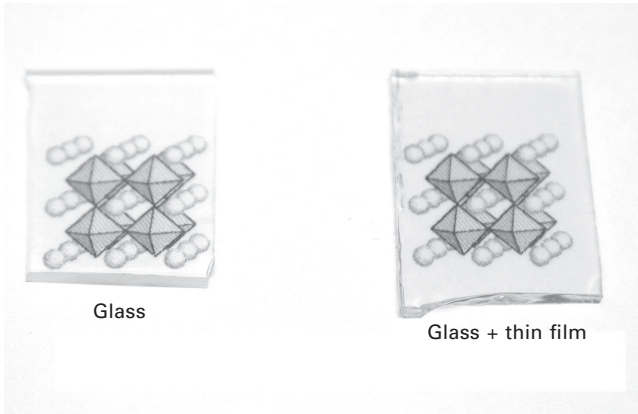


29.7 Structural model of deduced nanosheets.

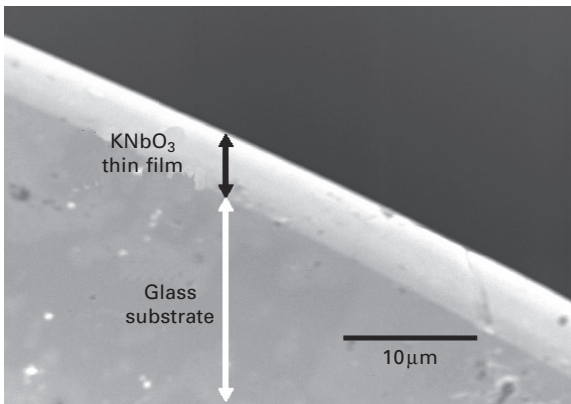


29.8 Schematic diagram of the reaction mechanism.

The use of a colloidal solution with a concentration of approximately 1 mass percent allows the formation of a thick film of 1–3  $\mu\text{m}$  after several hours of immersion. Because heating is not required for crystallization, various materials including glasses and plastics can be used as substrates.

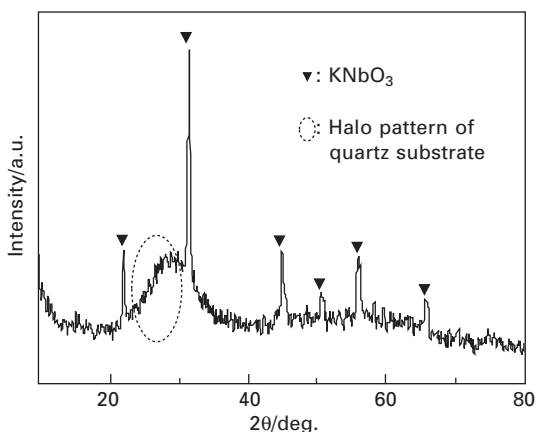
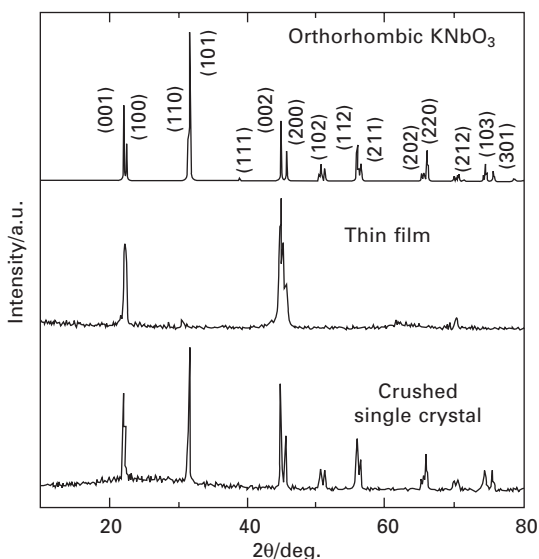


29.9 Photograph of transparent  $\text{KNbO}_3$  thin film produced on a glass substrate.

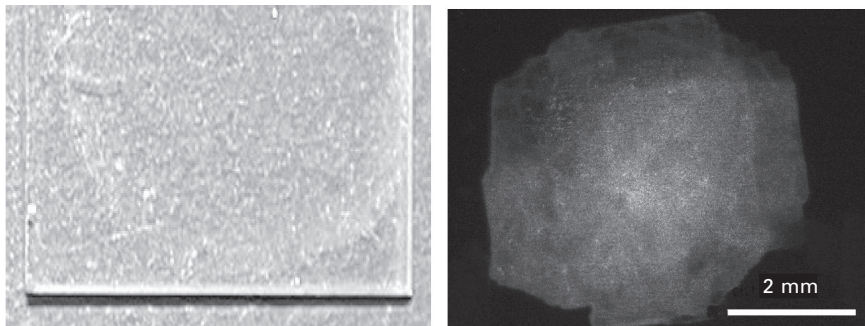


29.10 SEM image of a  $\text{KNbO}_3$  thin film cross-section.

Next, we attempted the fabrication of the  $\text{KNbO}_3$  thin film using a  $\text{K}_2\text{NbO}_3\text{F}$  single crystal. This process is also simple in that the  $\text{K}_2\text{NbO}_3\text{F}$  single crystal is obtained using  $\text{K}_2\text{CO}_3\text{--KF}$  as the flux which is placed on the substrate and left under a saturated water-vapor atmosphere (a sealed container with water). The  $\text{K}_2\text{NbO}_3\text{F}$  single crystal grows at temperatures lower than  $800^\circ\text{C}$ . Figure 29.12 shows the XRD pattern after the  $\text{K}_2\text{NbO}_3\text{F}$  single crystal was subjected to water vapor processing. It is noteworthy that the water vapor processing at room temperature causes the decomposition of the layered perovskite  $\text{K}_2\text{NbO}_3\text{F}$ , which undergoes a structural change. Unlike the reaction in water, the nanostructuring of particles does not occur in the water vapor processing. The configuration of the original single crystal is retained. Because the single crystal is plate-shaped,  $\text{KNbO}_3$  obtained after water vapor processing is also present as a thick film on the substrate. A feature of the resultant film

29.11 X-ray diffraction pattern of a  $\text{KNbO}_3$  thin film.29.12 X-ray diffraction pattern of a  $\text{KNbO}_3$  film produced from a  $\text{K}_2\text{NbO}_3\text{F}$  single crystal.

is that the single-crystal  $\text{KNbO}_3$  film grown is also oriented in the  $c$ -axis direction because the oriented single crystal is used as a precursor. Evaluation of nonlinear optical properties was carried out for the resultant film. Figure 29.13 shows a photograph of a single crystal film after irradiation with a YAG : Nd laser of 1064 nm wavelength. A second harmonic generation (SHG) is distinctly noted, indicating the possibility that a single-crystal film produced at room temperature can be used in nonlinear optical devices.



29.13 Photograph of a single crystal film on a glass substrate (left). Micrograph shows a spot of SHG signal with half wavelength (532 nm) of irradiated 1064 nm YAG: Nd laser (right).

## 29.4 Conclusions and future trends

The solution process that we have developed is characteristic in that it uses water, the most common solvent, and furthermore, the process proceeds under very mild room temperature conditions. It must be emphasized that the process takes place in a nearly closed system that uses neither high temperatures nor high energy. It does not even emit a gas, making this a truly ‘environmentally friendly’ process. The uniqueness of the developed process is further supported by the fact that perovskite  $\text{KNbO}_3$ , which is useful as an electroceramic material, can be synthesized in only one step, such that the solution reaction is performed at room temperature, by selectively dissolving a layered perovskite precursor, a solid in water. Therefore, to obtain highly crystalline and morphologically controlled materials, neither electrochemical processing nor additional processing such as heating is necessary, as required by conventional solution processes, thereby ensuring an environmentally sound and cost-effective process.

Furthermore, precursors that change to a perovskite structure through a self-organizing process are not limited to  $\text{K}_2\text{NbO}_3\text{F}$ . In fact, our preliminary study has revealed that layered perovskite  $\text{Sr}_2\text{CoO}_3\text{Cl}$  possesses an ordered structure that selectively includes halogen ions between layers, similar to  $\text{K}_2\text{NbO}_3\text{F}$ , and exhibits a selective interlayer dissolution process in an acidic aqueous solution. Therefore, the soft chemical route of selective dissolution from the layered perovskite precursors is a general and powerful tool for low-temperature synthesis of perovskite materials.

## 29.5 References

1. K. Yamanouchi, H. Odagawa, T. Kojima and T. Matsumura, *Electronic Letters*, **33**, 193 (1997).

2. K. Nakamura and Y. Kawamura, *IEEE Trans. Ultrason. Ferroelect. Freq. Contr.*, **47**, 750 (2000).
3. U. Fluckinger, H. Arend and H. R. Oswald, *J. Am. Ceram. Soc.*, **56**, 575 (1977).
4. K. Toda, N. Sakai, H. Ohnuma, Y. Aoyama, S. Tokuoka and M. Sato, *Ext. Abstr. (The 25th Symposium on Solid State Ionics in Japan 1999)*; The Solid State Ionics Society of Japan, 2A9.
5. M. Dion, M. Ganne and M. Tournoux, *Mater. Res. Bull.*, **16**, 1429 (1981).
6. J. Gopalakrishnan and V. Bhat, *Inorg. Chem.*, **26**, 4299 (1987).
7. F. Galasso and W. Darby, *J. Phys. Chem.*, **66**, 1318 (1962).
8. L-S. Du, F. Wang and C. P. Grey, *J. Solid State Chem.*, **140**, 285 (1998).
9. A. F. Vik, V. Dracopoulos, G. N. Papatheodorou and T. Ostvold, *J. Alloys Compd.*, **321**, 284 (2001).
10. A. M. Quittet, M. I. Bell, M. Karauzman and P. M. Raccah, *Phys. Rev. B*, **14**, 5068 (1976).

---

A SIMON and J RAVEZ, University Bordeaux1, France

### 30.1 Introduction

So-called ferroelectric materials may be divided into two classes: ferroelectrics and relaxors (Table 30.1) [1]. Typically, relaxors have at least one crystallographic site that is occupied by two or more ions. Unlike ferroelectrics, relaxors exhibit what is known as a diffuse transition: the real part of the permittivity  $\epsilon'_r$  is high but the maximum of  $\epsilon'_r = f(T)$  is wide. In relaxors, there is a strong influence of the frequency  $f$  of the electric field on the  $\epsilon'_r = f(T)$  curves; when  $f$  increases,  $\epsilon'_r$  decreases and the  $\epsilon'_r$  maximum temperature increases [1]. The latter refers to  $T_m$  (not  $T_C$ ) owing to its large variation with  $f$ . Concerning the  $\epsilon''_r = f(T)$  curve, when  $f$  increases, the imaginary part of the permittivity  $\epsilon''_r$  increases and the  $\epsilon''_r$  maximum temperature increases. The dielectric curve of a  $\text{Pb}(\text{Mg}_{1/3}\text{Nb}_{2/3})\text{O}_3$  (PMN) ceramic is a good example [2]. In many relaxors, the relationship between  $f$  and  $T_m$  can be described using the Vogel–Fulcher (VF) relationship [3, 4]:

$$\text{Log } f = \text{log } f_0 - \frac{E_a}{k(T_m - T_{VF})} \quad 30.1$$

where  $f_0$  is the Debye frequency,  $T_m$  the temperature of  $\epsilon'_r$  max at the given frequency  $f$ ,  $T_{VF}$  the static freezing temperature,  $E_a$  the activation energy and  $k$  the Boltzmann constant [5, 6]. In addition, there is a deviation from the Curie–Weiss law ( $\epsilon'_r = C/(T - T_0)$ ). The value of the Curie–Weiss temperature  $T_0$  is greater than that of  $T_m$ . To date, various physical models have been proposed to explain the properties of relaxors [7]: compositional fluctuations and diffuse phase transition [8, 9], the superparaelectric model [10], the nanostructure-octahedral model [11–17], the dipole-glass or the more recently derived model [18, 19], the random-field model [20, 21], the domain-wall model [22] and the random-layer model [23, 24]. Solid-state chemistry aspects of lead-free relaxor ferroelectrics have also been developed [25, 26].

In addition to the usual applications for ferroelectrics, relaxors are of great interest as dielectrics in capacitors and actuators [27]. Most relaxors

Table 30.1 Some physical properties of ferroelectrics or relaxors of perovskite type

	Ferroelectrics	Relaxors
Octahedral site occupation	–	More than one different cation
Composition heterogeneity	–	Nanoscopic scale
Polar region size	Microdomains	Nanodomains
Symmetry for $T \leq T_C$ (or $T_m$ )	Tetragonal, orthorhombic or rhombohedral	Macroscopically cubic (optical or X-ray diffraction studies)
Ferroelectric–paraelectric transition	Sharp	Diffuse
Frequency $f$ dispersion of $\epsilon'_r$ or $\epsilon''_r$ for $T \leq T_C$ (or $T_m$ )	$\epsilon'_r$ not dependent on $f$	$\epsilon'_r$ decreases when $f$ increases
	$\epsilon''_r$ not dependent on $f$	$\epsilon''_r$ increases when $f$ increases
Frequency dependence of $T_C$ (or $T_m$ )	$T_C$ not dependent on $f$	$T_m$ increases when $f$ increases
Thermal variation of $\epsilon'_r$ in the paraelectric phase	Curie–Weiss law	Deviation from Curie–Weiss law
Thermal variation of $P_s$ , at $T_C$ (or $T_m$ ), on heating	Sharp (1st order trans.) or progressive (2nd order trans.) decrease at $T_C$ ; $P_s = 0$ if $T > T_C$	Progressive decrease with a polarisation tail for $T \geq T_m$

are lead-based ceramics such as PMN and derived compounds, or  $\text{Pb}(\text{M}'_{1/2}\text{M}''_{1/2})\text{O}_3$  ( $\text{M}' = \text{Sc, In}$ ;  $\text{M}'' = \text{Nb, Ta}$ ) with long-range polar order. However, these compounds have the obvious disadvantages associated with the volatility and toxicity of PbO. Therefore, much current research is directed towards more environmentally friendly Pb-free relaxor materials. The present chapter discusses some of the solid-state chemistry aspects of lead-free ferroelectric relaxors. The selected compounds belong to either perovskite or tetragonal tungsten bronze (TTB) families.

## 30.2 Lead-free relaxor ceramics derived from $\text{BaTiO}_3$

### 30.2.1 Relations between relaxor behaviour and ionic substitutions in solid solutions

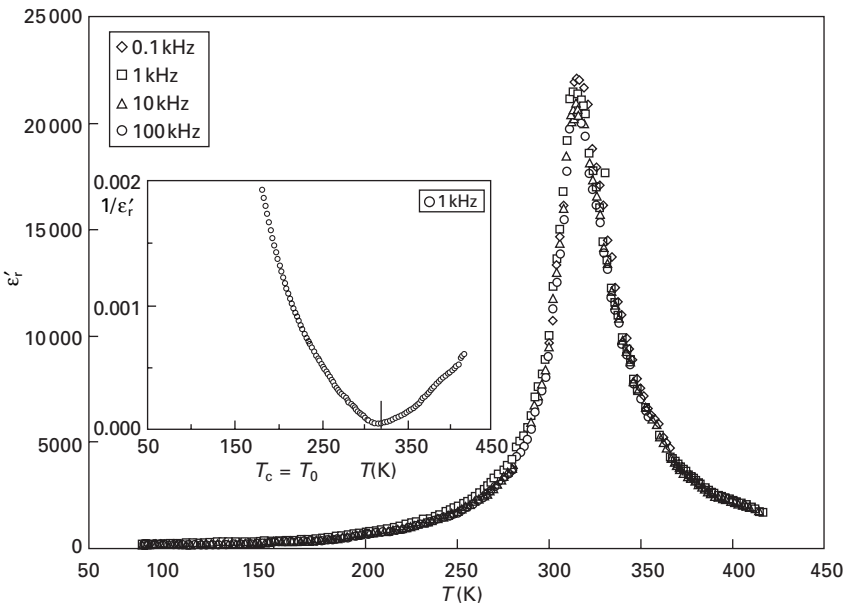
Barium titanate is of perovskite  $\text{AMX}_3$  type structure with a 12-CN (coordination number) site ( $\text{Ba}^{2+}$ ) and a 6-CN one ( $\text{Ti}^{4+}$ ). It presents three phase transitions:



The three low-temperature phases are ferroelectric. Numerous solid solutions can easily be made by either cationic or anionic substitutions [28, 29].

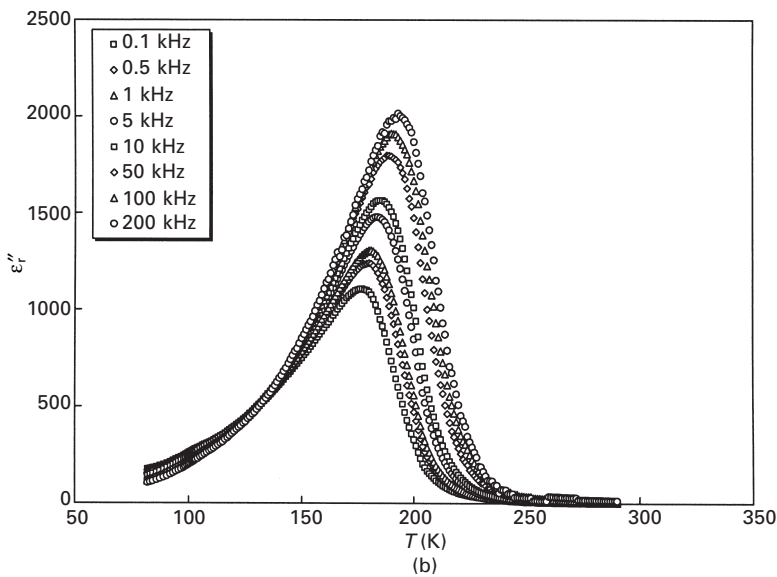
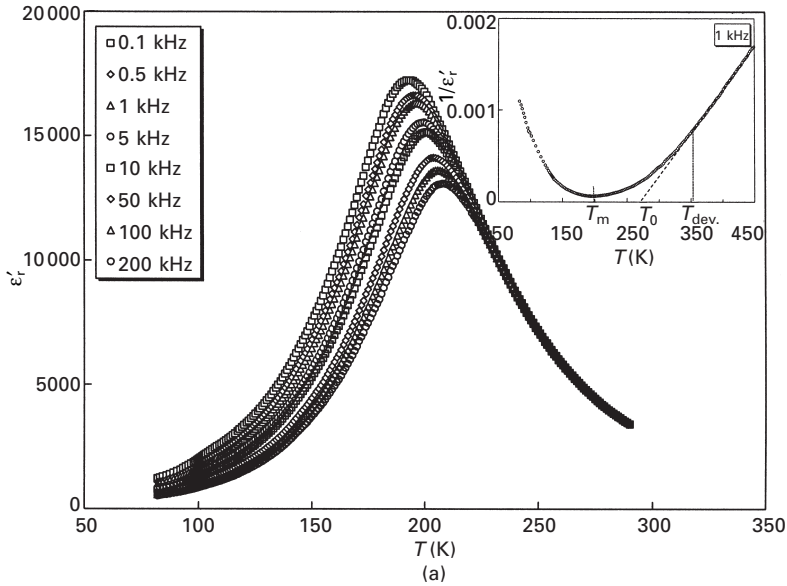
Depending on both the substitution and the composition, different types of behaviour were evidenced in binary systems:

- For homovalent substitutions on the A site (e.g.  $\text{Ba}_{1-x}\text{A}_x\text{TiO}_3$ ; A = Ca, Sr) or for compositions very close to BT whatever the type of substitution, a ferroelectric–paraelectric transition was observed at  $T_C$ . The three phase transitions were retained, as was the case for  $\text{BaTiO}_3$ .
- For homovalent substitutions on the M site (e.g.  $\text{Ba}(\text{Ti}_{1-x}\text{M}_x)\text{O}_3$ ; M = Zr, Sn, Ce) the transition sequence was the same as that of BT for low values of  $x$  (e.g.  $x \leq 0.10$ , M = Zr) [30–33]. For greater values of  $x$  (e.g.  $0.10 < x \leq 0.27$ , M = Zr) there was only one rhombohedral, ferroelectric  $T_C \rightarrow$  cubic, paraelectric transition after the disappearance of the orthorhombic and the tetragonal phases. The transition was second order for  $x = 0.20$  as  $T_C = T_0$  (Fig. 30.1). For the highest values of  $x$  (e.g.  $x > 0.27$ , M = Zr) there was only one broad peak of  $\epsilon'_r$  at  $T_m$  with a typical relaxor frequency dispersion. There was also a deviation from the Curie–Weiss law. Such properties are the dielectric attributes of a relaxor behaviour. As an example, Fig. 30.2 shows the temperature dependences of both  $\epsilon'_r$  and  $\epsilon''_r$  and the corresponding deviation from the Curie–Weiss law ( $T_0 > T_m$ ), for a ceramic with composition  $\text{Ba}(\text{Ti}_{0.65}\text{Zr}_{0.35})\text{O}_3$ . As  $x$  increases the value of  $T_{\text{dev.}} - T_m$  and the relaxor effect increase



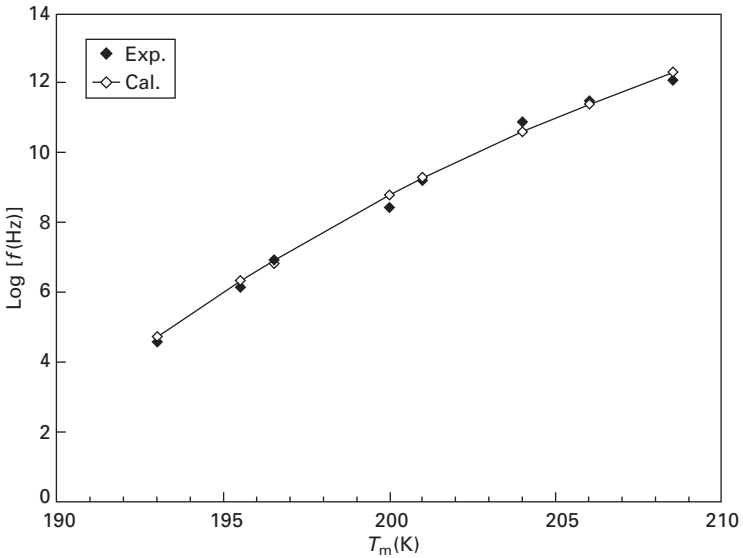
30.1 Temperature and frequency dependences of  $\epsilon'_r$  and temperature dependence of  $1/\epsilon'_r$ , for a ceramic with composition  $\text{Ba}(\text{Ti}_{0.80}\text{Zr}_{0.20})\text{O}_3$ .





30.2 Temperature and frequency dependences of  $\epsilon''$  (a) and  $\epsilon''$  (b) and temperature dependence of  $1/\epsilon'$  (a) for a ceramic with composition  $\text{Ba}(\text{Ti}_{0.65}\text{Zr}_{0.35})\text{O}_3$ .

( $T_{\text{dev.}}$ : temperature at which  $1/\epsilon'$  starts diverging from the Curie–Weiss law). Figure 30.3 illustrates how well the data  $\log f$  vs.  $T_m$  fit the Vogel–Fulcher law ( $T_{\text{VF}} = 154 \pm 10$  K). Scaling dielectric characteristics differ from those of lead complex perovskite relaxor [34].



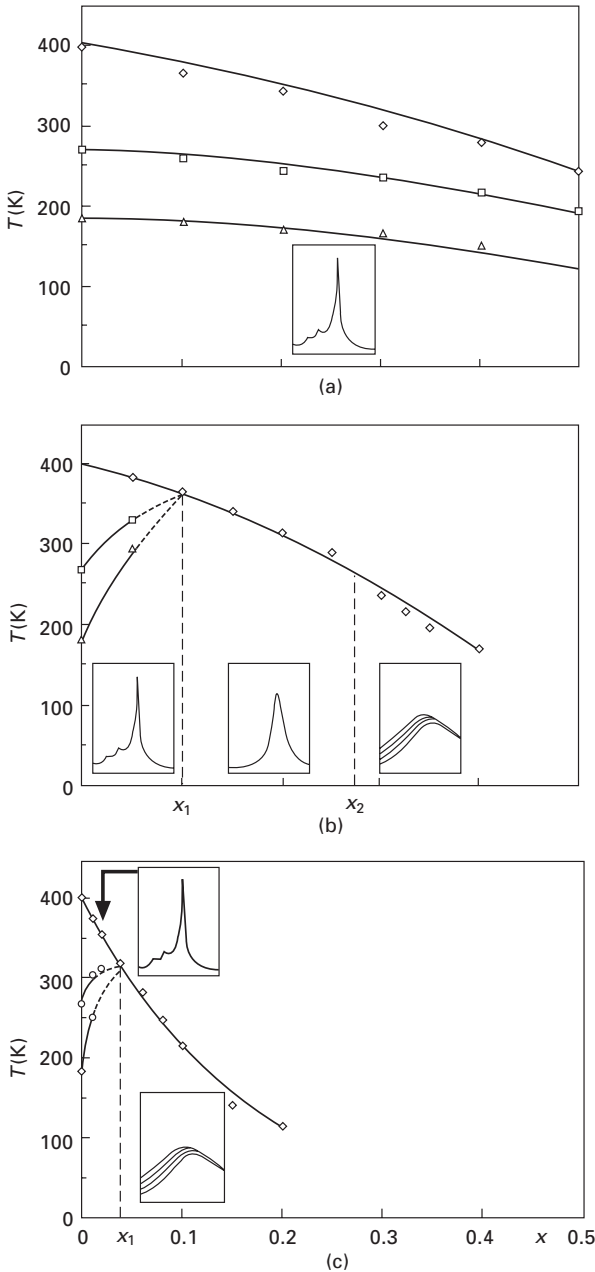
30.3 Variation of  $\log f$  with  $T_m$  for a ceramic with composition  $\text{Ba}(\text{Ti}_{0.65}\text{Zr}_{0.35})\text{O}_3$ .

- For homovalent substitutions in both A and M sites (e.g.  $\text{Ba}_{1-x}\text{Ca}_x(\text{Ti}_{1-x}\text{Zr}_x)\text{O}_3$ ), the sequence was similar to the previous one, but the composition limits of the various phase zones are of course different.
- For heterovalent substitutions in the A site (e.g.  $\text{Ba}_{1-x}(\text{La}_{x/2}\text{K}_{x/2})\text{TiO}_3$ ,  $\text{Ba}_{1-x}\text{A}_{2x/3}\square_{x/3}\text{TiO}_3$  ( $\text{A} = \text{La}, \text{Bi}$ )), the transition sequence was the same as that of BT up to relatively high values of  $x$  (e.g.  $x \leq 0.20$  for  $\text{Ba}_{1-x}(\text{La}_{x/2}\text{K}_{x/2})\text{TiO}_3$ ). For higher values of  $x$ , a relaxor behaviour was observed. The system  $x\text{BaTiO}_3-(1-x)\text{Na}_{1/2}\text{Bi}_{1/2}\text{TiO}_3$  shows a wide relaxor solid solution ( $0.20 \leq x \leq 0.80$ ). The value of  $T_m$  increases with  $x$ . However, the relaxor phase was reported to be tetragonal [35].
- For heterovalent substitutions in both A and M sites (e.g.  $\text{Ba}_{1-x}\text{K}_x(\text{Ti}_{1-x}\text{M}_x)\text{O}_3$ ,  $\text{Ba}_{1-x}\text{Na}_x(\text{Ti}_{1-x}\text{Nb}_x)\text{O}_3$ ) or in both M and X sites (e.g.  $\text{Ba}(\text{Ti}_{1-x}\text{Li}_x)\text{O}_{3-3x}\text{F}_{3x}$ ), the relaxor properties were observed from values of  $x$  as small as 0.05, i.e. for small substitution rates [32, 36–41].

Figure 30.4 shows the various types of behaviour depending on the type of ionic substitution from  $\text{BaTiO}_3$ .

### 30.2.2 Relaxor characteristics in solid solutions

The relaxor characteristics ( $\Delta T_m = T_m(100 \text{ kHz}) - T_m(0.1 \text{ kHz})$ ,  $\Delta \epsilon'_r / \epsilon'_r = [\epsilon'_r(0.1 \text{ kHz}) - \epsilon'_r(100 \text{ kHz})] / \epsilon'_r(0.1 \text{ kHz})$  (at  $T_m$ ) become more significant as the composition deviates from  $\text{BaTiO}_3$ . Moreover, the



**30.4** Composition dependence of the transition temperatures for homovalent substitutions in the A site (e.g.  $\text{Ba}_{1-x}\text{Sr}_x\text{TiO}_3$ ) (a), for homovalent substitutions in the B site (e.g.  $\text{BaTi}_{1-x}\text{Zr}_x\text{O}_3$ ) (b) and for heterovalent substitutions (e.g.  $\text{Ba}_{1-x}\text{K}_x(\text{Ti}_{1-x}\text{Nb}_x)\text{O}_3$ ) (c). The temperature dependences of  $\varepsilon_r'$  are shown on insets.

Table 30.2 Comparative values of  $x$  for the same shift of  $T_m$  ( $\Delta T_m = 10\text{K}$ ) and values of  $T_{\text{dev.}} - T_m$  (at 1 kHz)

Substitution	Sites	Solid solutions	$x$	$T_{\text{dev.}} - T_m$ (K)
Homovalent	M	$\text{Ba}(\text{Ti}_{1-x}\text{Zr}_x)\text{O}_3$	0.35	150
	A and M	$\text{Ba}_{1-x}\text{Ca}_x(\text{Ti}_{1-x}\text{Zr}_x)\text{O}_3$	0.225	130
Heterovalent	A	$\text{Ba}_{1-x}\text{K}_{x/2}\text{La}_{x/2}\text{TiO}_3$	0.30	100
		$\text{Ba}_{1-x/2}\square_{x/2}(\text{Ti}_{1-x}\text{Nb}_x)\text{O}_3$	0.10	120
	A and M	$\text{Ba}_{1-x}\text{K}_x(\text{Ti}_{1-x}\text{Nb}_x)\text{O}_3$	0.125	105
	M and X	$\text{Ba}(\text{Ti}_{1-x}\text{Li}_x)\text{O}_{3-3x}\text{F}_{3x}$	0.15	120

composition range of solid solutions showing the relaxor behaviour depends on the type of substitution. Table 30.2 gives comparative values of  $x$  for the same shift of  $T_m$  ( $\Delta T_m = 10\text{K}$ ):

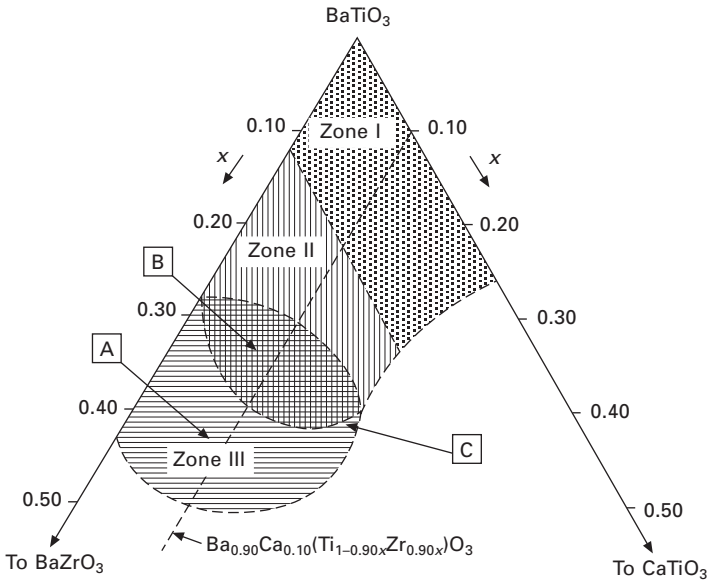
- For homovalent substitutions in the A site or for all compositions very close to  $\text{BaTiO}_3$ , no relaxor behaviour was detected.
- For homovalent substitutions in the M site, the equal charge of the cations (e.g.  $\text{Ti}^{4+}$  and  $\text{Zr}^{4+}$ ) requires a high substitution rate ( $x = 0.35$ ).
- Coupled homovalent substitutions in both A and M sites generate higher heterogeneity, leading to relatively lower values of  $x$  ( $x = 0.225$ ).
- Concerning heterovalent substitutions in the A site, the value of  $x$  is nevertheless high, because even for different charges, the relaxor effect is not enhanced by substitutions in such a site.
- For heterovalent substitutions in the M site, whatever the coupled substitutions in other sites A or X, in order to respect electrical neutrality, the values of  $x$  are the lowest. This implies that the relaxor effect is mainly dependent on heterovalent substitutions in this M site.

The values of  $T_{\text{dev.}} - T_m$  (see Fig. 30.2) which characterise the diffusivity of the transition and consequently the relaxor behaviour, are in the range 100–150K for the compositions listed in Table 30.2.

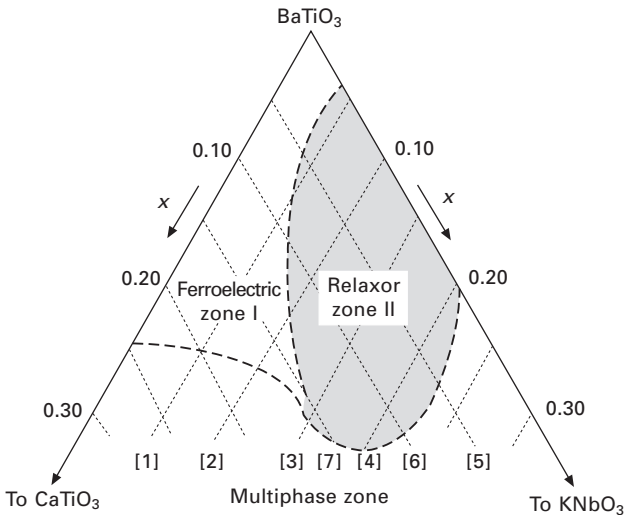
### 30.2.3 Relaxor compositions in some ternary systems

Large solid solution zones with compositions relatively close to  $\text{BaTiO}_3$  and with a derived perovskite structure were evidenced in some ternary systems:  $\text{BaTiO}_3$ – $\text{BaZrO}_3$ – $\text{CaTiO}_3$ ,  $\text{BaTiO}_3$ – $\text{KNbO}_3$ – $\text{CaTiO}_3$ ,  $\text{BaTiO}_3$ – $\text{BaZrO}_3$ – $\text{CaLiF}_3$ ,  $\text{BaTiO}_3$ – $\text{BaZrO}_3$ – $\text{BaLiF}_3$  and  $\text{BaTiO}_3$ – $\text{BaZrO}_3$ – $\text{La}_{2/3}\text{TiO}_3$  [34, 42–46]. Figures 30.5, 30.6 and 30.7 show, as examples, the ferroelectric or relaxor zones in the corresponding ternary diagrams.

In the  $\text{BaTiO}_3$ – $\text{BaZrO}_3$ – $\text{CaTiO}_3$  system (Fig. 30.5), zones I, II and III correspond to a ferroelectric zone with three phase transitions like  $\text{BaTiO}_3$ , a ferroelectric one with only a rhombohedral–cubic transition and a relaxor

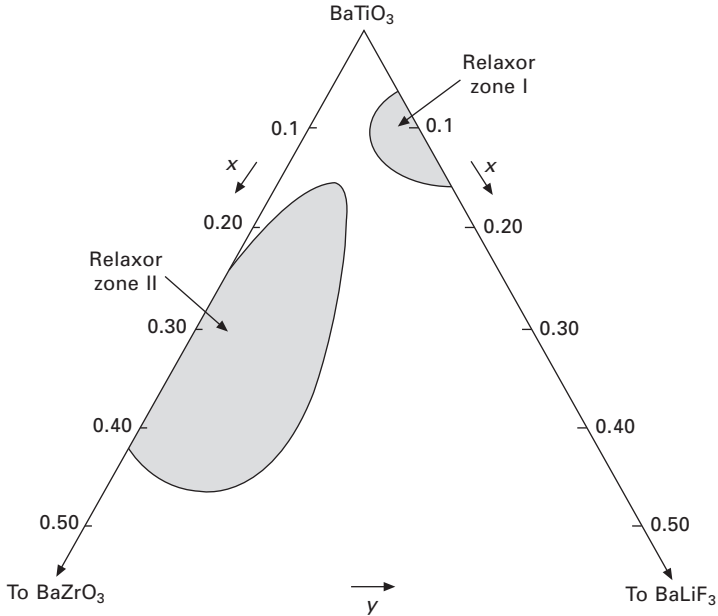


30.5 Schematic representation of the  $[\text{BaTiO}_3\text{-BaZrO}_3\text{-CaTiO}_3]$  ternary diagram.



30.6 Schematic representation of the  $[\text{BaTiO}_3\text{-KNbO}_3\text{-CaTiO}_3]$  ternary diagram.

one, respectively. The wide boundary between zones II and III represents a ferroelectric-relaxor transition; such a type of transition will be discussed in Section 30.4. In the  $\text{BaTiO}_3\text{-KNbO}_3\text{-CaTiO}_3$  system (Fig. 30.6), there is only one relaxor zone (zone II). In the  $\text{BaTiO}_3\text{-BaZrO}_3\text{-BaLiF}_3$  system (Fig. 30.7), zones I and II are both relaxor.



30.7 Schematic representation of the relaxor zones I and II in the [BaTiO<sub>3</sub>-BaZrO<sub>3</sub>-BaLiF<sub>3</sub>] ternary diagram. Filled circles represent the investigated compositions.

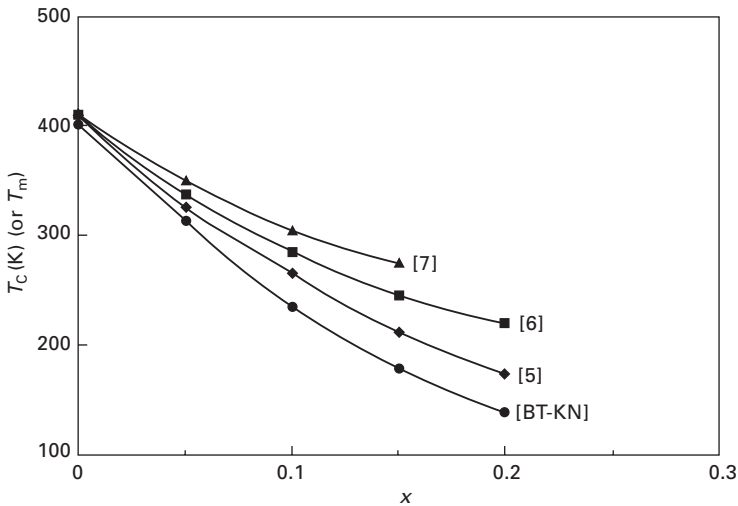
In all the cases, the relaxor zones develop from the relaxor solid solutions existing in the binary systems BaTiO<sub>3</sub>-BaZrO<sub>3</sub>, BaTiO<sub>3</sub>-KNbO<sub>3</sub> and BaTiO<sub>3</sub>-BaLiF<sub>3</sub>. There are always two types of ionic substitutions: (Ca<sup>2+</sup>-Ba<sup>2+</sup> and Zr<sup>4+</sup>-Ti<sup>4+</sup>), (K<sup>+</sup>-Ba<sup>2+</sup> and Nb<sup>5+</sup>-Ti<sup>4+</sup>) and (Li<sup>+</sup>-[Ti<sup>4+</sup>, Zr<sup>4+</sup>] and 3F<sup>-</sup>-3O<sup>2-</sup>). The presence of different cations in the same crystallographic site enhances the relaxor effect and the main dielectric relaxor characteristics. The values of  $T_m$ ,  $\Delta T_m$  and  $\Delta \epsilon'_r / \epsilon'_r$  (at  $T_m$ ) increase when the composition deviates from the binary system. An example is given in Table 30.3 for the BaTiO<sub>3</sub>-BaZrO<sub>3</sub>-CaTiO<sub>3</sub> system. Another example is illustrated by Figs 30.8 and 30.9 concerning the BaTiO<sub>3</sub>-KNbO<sub>3</sub>-CaTiO<sub>3</sub> system.

### 30.2.4 X-ray diffraction and Raman studies

An X-ray diffraction study performed on Ba(Ti<sub>0.65</sub>Zr<sub>0.35</sub>)O<sub>3</sub> showed that the dielectric peak at  $T_m$  does not correspond to any symmetry change: it remains cubic. Such a result has been reported for PMN relaxor. For a more complex substitution in Ba<sub>0.92</sub>Ca<sub>0.08</sub>(Ti<sub>0.75</sub>Nb<sub>0.25</sub>)O<sub>3</sub> the result is different, e.g. for Pb(Mg<sub>0.3</sub>Nb<sub>0.6</sub>Ti<sub>0.1</sub>)O<sub>3</sub>. It transforms spontaneously from a relaxor (cubic) into a microscopic ferroelectric (rhombohedral) state on cooling. Such a transition was in good agreement with dielectric and pyroelectric measurements.

Table 30.3 Variation of ferroelectric and relaxor characteristics with composition

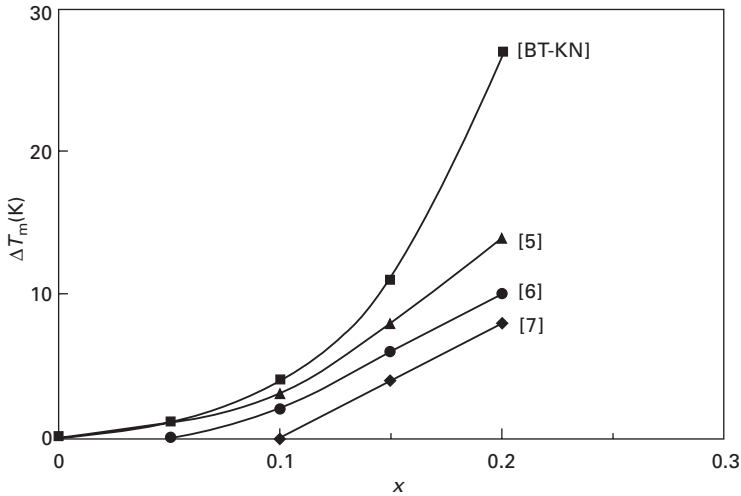
Compositions		$T_C$ (K) <sup>a</sup>	$T_m$ (K) <sup>a</sup>	$\Delta T_m$ (K) <sup>b</sup>	$\Delta\varepsilon'_r/\varepsilon'_r$ <sup>c</sup>
Ca <sup>2+</sup> -Ba <sup>2+</sup> substitution	BaTiO <sub>3</sub>	400			0.06
	Ba <sub>0.80</sub> Ca <sub>0.20</sub> TiO <sub>3</sub>	405			0.05
	Ba(Ti <sub>0.85</sub> Zr <sub>0.15</sub> )O <sub>3</sub>	340			0.07
	Ba <sub>0.85</sub> Ca <sub>0.15</sub> (Ti <sub>0.85</sub> Zr <sub>0.15</sub> )O <sub>3</sub>	347			0.03
	Ba(Ti <sub>0.63</sub> Zr <sub>0.37</sub> )O <sub>3</sub>		194	14	0.41
	Ba <sub>0.88</sub> Ca <sub>0.12</sub> (Ti <sub>0.63</sub> Zr <sub>0.37</sub> )O <sub>3</sub>		169	28	0.45
Zr <sup>4+</sup> -Ti <sup>4+</sup> substitution	BaTiO <sub>3</sub>	400			0.06
	Ba(Ti <sub>0.80</sub> Zr <sub>0.20</sub> )O <sub>3</sub>	314			0.05
	Ba(Ti <sub>0.60</sub> Zr <sub>0.40</sub> )O <sub>3</sub>		188	16	0.43
	Ba <sub>0.90</sub> Ca <sub>0.10</sub> TiO <sub>3</sub>	410			0.05
	Ba <sub>0.90</sub> Ca <sub>0.10</sub> (Ti <sub>0.90</sub> Zr <sub>0.10</sub> )O <sub>3</sub>	364			0.06
	Ba <sub>0.90</sub> Ca <sub>0.10</sub> (Ti <sub>0.70</sub> Zr <sub>0.30</sub> )O <sub>3</sub>		209	19	0.37

<sup>a</sup> at 1 kHz<sup>b</sup>  $\Delta T_m = T_m(10\text{ kHz}) - T_m(0.1\text{ kHz})$ <sup>c</sup>  $\Delta\varepsilon'_r/\varepsilon'_r = \varepsilon'_r(0.1\text{ kHz}) - \varepsilon'_r(200\text{ kHz})/\varepsilon'_r(0.1\text{ kHz})$ , at  $T_C$  (or  $T_m$ ) - 50 K30.8 Variation of  $T_C$  (or  $T_m$ ) with composition for coupled substitution of (Ba<sup>2+</sup>, Ti<sup>4+</sup>) for (K<sup>+</sup>, Nb<sup>5+</sup>) in the BaTiO<sub>3</sub>-KNbO<sub>3</sub>-CaTiO<sub>3</sub> diagram.

The numbers in brackets correspond to the various composition lines given in Fig. 30.6. The value of  $x$  represents the atomic ratio  $x = [K + Nb]/([Ba + Ti] + [K + Nb])$ .

This behaviour is due here to a supplementary local polarisation resulting from the Ca<sup>2+</sup> displacement in its crystallographic site because of its small size (1.36 Å) compared with that of Ba<sup>2+</sup> (1.61 Å) in 12-CN [47].

A Raman study was performed on barium titanate ceramics doped with either zirconium or niobium [48, 49]. These two Zr<sup>4+</sup> and Nb<sup>5+</sup> cations have



30.9 Variations of  $\Delta T_m = T_m(0.1 \text{ kHz}) - T_m(100 \text{ kHz})$  for some composition lines (see Fig. 30.6) corresponding to coupled substitution of  $(\text{Ba}^{2+}, \text{Ti}^{4+})$  for  $(\text{K}^+, \text{Nb}^{5+})$ .

been chosen because of their differences with titanium:  $\text{Zr}^{4+}$  is isovalent but larger in size by about 20% than  $\text{Ti}^{4+}$ , while  $\text{Nb}^{5+}$  has approximately the same size as  $\text{Zr}^{4+}$  but a different charge. It reinforces the general idea that electric random fields are more efficient in ferroelectric materials than elastic (dilatational) random fields in lowering the ferroelectric transition temperature and in inducing the relaxor behaviour, as was already demonstrated in a previous theoretical study [50], in which the nature of the complex defects expected from the inherent high concentration of barium vacancies in Nb-doped compositions was discussed in connection with photoluminescence spectra.

### 30.3 Perovskite-type relaxor not derived from $\text{BaTiO}_3$

A series of relaxor compositions were derived from the antiferroelectric  $\text{NaNbO}_3$  in several solid solutions such as  $\text{NaNbO}_3\text{-AMO}_3$  ( $\text{AMO}_3 = \text{NaTaO}_3, \text{CaTiO}_3, \text{SrTiO}_3$ , etc.),  $\text{NaNbO}_3\text{-Sr}_{0.5}\text{NbO}_3$ ,  $\text{NaNbO}_3\text{-MSnO}_3$  ( $\text{M} = \text{Ca}, \text{Ba}$ ), etc. The values of  $T_m$  are well below room temperature. However, the  $T_m$  values can be increased by Li or K-doping, leading to the formation of  $\text{NaNbO}_3\text{-ABO}_3\text{-LiNbO}_3$  ( $\text{KNbO}_3$ ) solid solution zones [51–57].

### 30.4 Crossover from a ferroelectric to a relaxor state

The aim of this section is to determine the crossover from ferroelectric to relaxor versus substitutions rate in lead-free ceramics. Indeed, the continuous



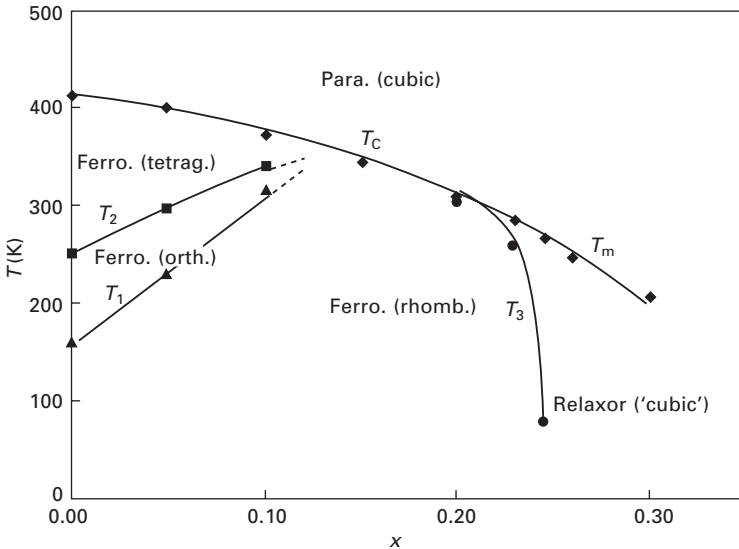
change from ferroelectric to relaxor behaviour is a unique feature of lead-free solid solutions. In lead-containing compounds, only well-defined compositions lead to a low-temperature relaxor state. In addition, the exact nature of the relaxor state in lead-free perovskites is still a matter of debate [58]. Investigating the gradual change from ferroelectric to relaxor behaviour is thus helpful to understand the physics of the latter. To this aim, it has been focused on the following compositions:  $\text{Ba}(\text{Ti}_{1-x}\text{Zr}_x)\text{O}_3$ ,  $\text{Ba}_{1-x/2}\square_{x/2}(\text{Ti}_{1-x}\text{Nb}_x)\text{O}_3$ ,  $\text{Ba}_{0.95x}\square_{0.05x}(\text{Ti}_{0.90}\text{Nb}_{0.10})\text{O}_{2.05+0.95x}$  and  $\text{Ba}(\text{Ti}_{1-x}\text{Li}_x)\text{O}_{3-3x}\text{F}_{3x}$  belonging to the various systems  $\text{BaO-TiO}_2\text{-ZrO}_2$ ,  $\text{BaO-TiO}_2\text{-Nb}_2\text{O}_5$  and  $\text{BaO-BaF}_2\text{-TiO}_2\text{-LiF}$  [59–63]. They correspond to homovalent and/or heterovalent cationic substitutions on the 6-CN site, anionic substitution and also non-stoichiometric compositions.

When the local strength of the substituted defects increases, the ferroelectric-relaxor crossover composition  $x_{f-r}$  decreases:

- for an homovalent substitution ( $\text{Zr}^{4+} \rightarrow \text{Ti}^{4+}$ ),  $x_{(f-r)} = 0.27$ ;
- for an heterovalent substitution ( $2\text{Nb}^{5+} + \square \rightarrow \text{Ba}^{2+} + 2\text{Ti}^{4+}$ ),  $x_{(f-r)} = 0.06$ ;
- for both anionic and cationic heterovalent substitutions ( $\text{Ti}^{4+} + 3\text{O}^{2-} \rightarrow \text{Li}^+ + 3\text{F}^-$ ),  $x_{(f-r)} = 0.045$ .

On this list, the homovalent  $\text{Zr}^{4+}$  ions are the softest defects while the coupled ions  $\text{Li}^{3+} + 3\text{F}^-$  are the strongest.

Figure 30.10 shows the composition dependence of transition temperatures for a ceramic with the  $\text{Zr}^{4+}\text{-Ti}^{4+}$  substitution. The solid solution starts from

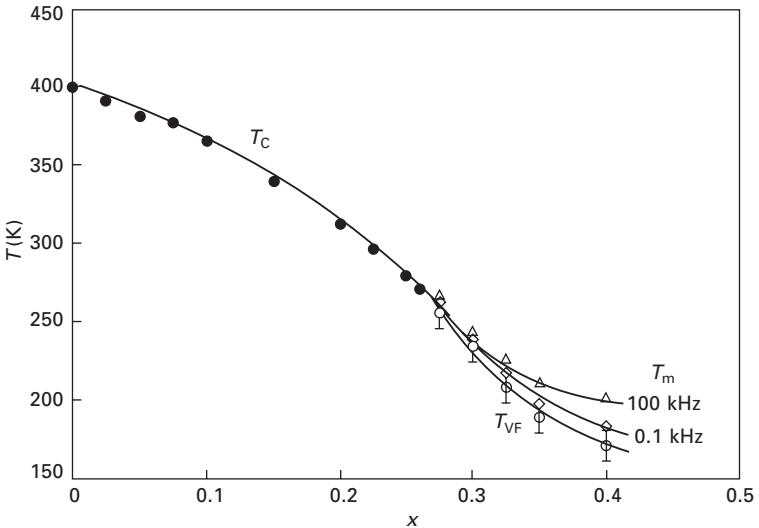


30.10 Variation of transition temperatures with composition for ceramics of  $(\text{Ba}_{0.90}\text{Ca}_{0.10})(\text{Ti}_{1-0.90x}\text{Zr}_{0.90x})\text{O}_3$  solid solution.

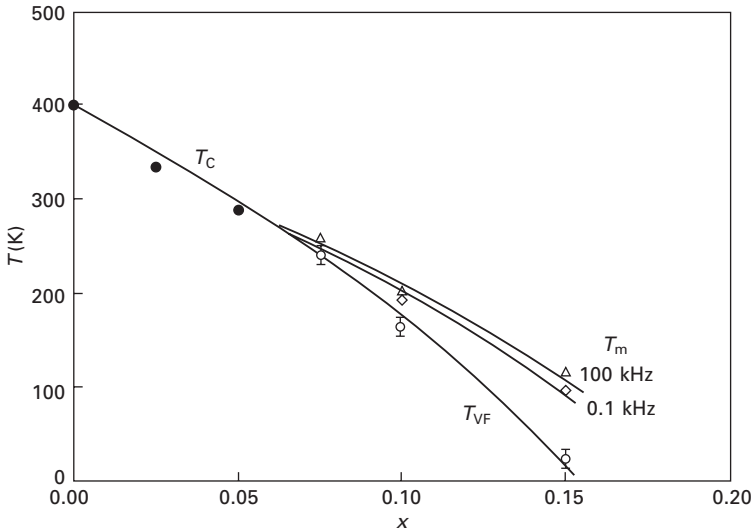
a composition of the  $\text{BaTiO}_3\text{--CaTiO}_3$  system,  $(\text{Ba}_{0.90}\text{Ca}_{0.10})\text{TiO}_3$ . There is first a progressive disappearance of the tetragonal and orthorhombic ferroelectric phases, leading to a rhombohedral, ferroelectric–cubic, paraelectric transition only. Secondly, as observed earlier, a relaxor phase appears with a transition from relaxor to ferroelectric at  $T_3$ , on cooling.

The shape of the phase diagrams displayed on Figs. 30.11 and 30.12 for  $\text{Ba}(\text{Ti}_{1-x}\text{Zr}_x)\text{O}_3$  and  $\text{Ba}_{1-x/2}\text{Ca}_{x/2}(\text{Ti}_{1-x}\text{Nb}_x)\text{O}_3$  respectively is also of interest. Indeed, for  $x < x_{f-r}$ , the paraelectric–ferroelectric transition temperature decreases on increasing  $x$ . When the crossover composition  $x_{f-r}$  is reached, this transition line splits because of the already mentioned dielectric dispersion in the relaxor state. The Vogel–Fulcher line can be considered, following equation [30.1], as the zero frequency extrapolation of the various  $T_m$  lines. The error bars that are drawn on Figs 30.11 and 30.12 take into account the limited accuracy of the Vogel–Fulcher fitting which mainly stems from the limited frequency range used. Nevertheless, it can be noted that in lead-containing relaxors, extended frequency ranges usually lead to similar Vogel–Fulcher temperatures. Keeping in mind these limitations, the Vogel–Fulcher line  $T_{VF} = f(x)$  ( $x > x_{f-r}$ ) is the best extrapolation of the ferroelectric line  $T_C = f(x)$  ( $x < x_{f-r}$ ). This is the main experimental feature that will be discussed in the following.

To confirm the dielectric results, X-ray diffraction and thermocurrent measurements were performed on the composition  $\text{Ba}_{0.92}\text{Ca}_{0.08}(\text{Ti}_{0.75}\text{Zr}_{0.25})\text{O}_3$  corresponding to point B in Fig. 30.5, i.e. in the wide boundary between



30.11 Variations of  $T_C$ ,  $T_m$  and  $T_{VF}$  with composition for ceramics of the  $\text{Ba}(\text{Ti}_{1-x}\text{Zr}_x)\text{O}_3$  system.



30.12 Variations of  $T_C$ ,  $T_m$  and  $T_{VF}$  with composition for ceramics of the  $\text{Ba}_{1-x/2}\square_{x/2}(\text{Ti}_{1-x}\text{Nb}_x)\text{O}_3$  system.

zones [II] and [III]. As stated above, there is a ferroelectric–relaxor transition at  $T_3 = 210$  K, and  $T_m = 255$  K, at 1 kHz. The temperature dependence of the symmetry and the cell parameters showed a rhombohedral–apparently cubic transition at  $T_3$ . The  $\alpha$  rhombohedral angle increases progressively from  $88.93^\circ$  at 93 K and reaches  $90^\circ$  at  $T_3$  [47]. No symmetry change was observed at  $T_m$ . The ceramic appeared to be pyroelectric from 80 to about 350 K [64]. Its polarisation could also be reversed, thus indicating a ferroelectric behaviour. A strong and sharp current peak around 200 K, close to  $T_3$ , which involved a steep decrease in spontaneous polarisation, was due to a decrease in the ferroelectric distortion. It corresponds to the ferroelectric–relaxor transition. At higher temperature, a progressive decrease in  $p$  occurred, resulting from a decrease in  $P_s$  with increasing temperature.

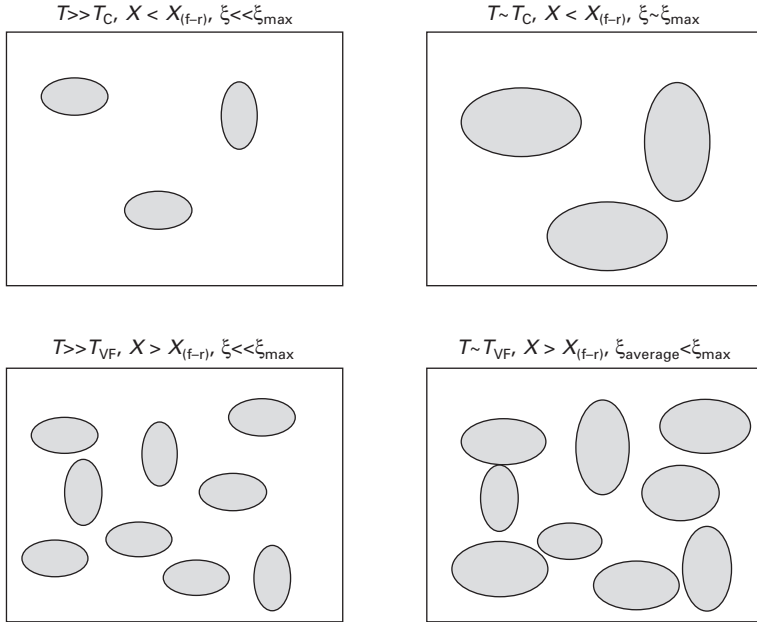
The Vogel–Fulcher line  $T_{VF} = f(x)$  ( $x > x_{f-r}$ ) and the ferroelectric transition line  $T_C = f(x)$  ( $x < x_{f-r}$ ) are aligned, calling for a possible link between the ferroelectric and relaxor transitions. This link is by no way obvious since these two states are very different in nature. In lead-containing relaxors, the interplay between ferroelectricity and relaxor state displays a wealth of different features. In PMN, the ferroelectricity is only field induced and the transition temperature lies well below the relaxor transition. In PST and PSN, the ferroelectricity is spontaneous in chemically ordered compounds and closely follows the relaxor transition.

Having established a link between the relaxor and ferroelectric lines in lead-free compounds, it is interesting to understand the possible origin of

this link. The ferroelectric transition ( $x < x_{f-r}$ ) follows a strong increase of the interaction (or correlation length) at  $T_C$ . In the following, this optimal ferroelectric correlation length will be called  $\xi_\infty$ . In the real world, this correlation length is not infinite as it should theoretically be. The possible occurrence of limited correlation length for  $T \gg T_C$ , well in the paraelectric state, is not discussed here. In the soft mode picture of BaTiO<sub>3</sub>, the infinite correlation length at  $T_C$  results from the condensation of a phonon mode which mainly includes the Ti–O bond oscillations. An alternative model takes into account the correlated Ti–O chains which are present at all temperatures [65]. In both cases, the Ti–O bonds are the key origin to ferroelectricity. These bonds are exactly what is disrupted on substituting Zr<sup>4+</sup> for Ti<sup>4+</sup>, 2Nb<sup>5+</sup> for Ba<sup>2+</sup>+2Ti<sup>4+</sup> and Li<sup>+</sup>–3F<sup>–</sup> for Ti<sup>4+</sup>–3O<sup>2–</sup>. The perturbation strength  $\Delta P$  increases in the order of the substitutions. As  $x$  increases, the ferroelectric line  $T_C = f(x)$  for  $x < x_{f-r}$  stems from a decrease of the maximal correlation length  $\xi_{\max}$  ( $\xi_{\max} \propto \xi_\infty/x\Delta P$ ). Formally, this equation means that there are two ways to decrease the ferroelectric correlation length and thus to decrease the ferroelectric transition temperature: increase of the number of substituted defects  $x$  and increase of the strength of perturbation of each defect  $\Delta P$ . The former parameter leads to the negative slope of  $T_C = f(x)$  and the latter increases the slope of this line. This is qualitatively consistent with the observations in the three studied families.

The next step is to consider that each substituted point defect perturbs a part of its surrounding host BaTiO<sub>3</sub> lattice. Because of the anisotropic nature of this lattice, such polarised clusters are expected to have an ellipsoid shape. Using the Ornstein Zernicke formalism, it can be thought that this perturbation is exponentially decreasing along the radii of these ellipsoids as  $\propto \Delta P \exp(-r/\xi)$  [66]. It is beyond the scope of the present section to exactly define this exponential decrease. What can be said is that the maximum size of these perturbed clusters is reached when  $\xi = \xi_{\max}$ , i.e. at  $T_C$ . This is the key point: not only the maximum correlation length  $\xi_{\max}$  drives the host matrix properties but it also sets the size of the perturbed clusters around each substituted defect. Since, in this assumption,  $\xi_{\max}$  decreases both with increasing  $x$  and  $\Delta P$ , the picture which arises is the following (Fig. 30.13):

- For  $x < x_{f-r}$ , the density of impurity-induced clusters is very small and the BaTiO<sub>3</sub> host matrix properties are kept only with a decrease of the maximal correlation length  $\xi_{\max}$ . At the same time, each cluster can reach its maximum size (Fig. 30.13, upper row).
- When  $x \sim x_{f-r}$ , small clusters start to interact with each other. In this model,  $x_{f-r}$  is the right point where all the macroscopic sample is filled by impurity-induced microscopic clusters. This interaction is the source for the observed dielectric dispersion.
- When  $x > x_{f-r}$ , the maximal correlation length cannot be reached and the



30.13 Sketch of the impurity-induced clusters in the  $\text{BaTiO}_3$  host lattice. On cooling to the transition temperature, the clusters can reach their maximum extension when their density is low leading to a ferroelectric state (upper row). When their density is high, this optimal size cannot be reached and a distribution of cluster size sets in, leading to a relaxor state (lower row).

Vogel–Fulcher temperature is the temperature where all clusters stop relaxing. The clusters can no longer reach their maximum size and, because of the interaction among clusters, a size distribution sets in (Fig. 30.13, lower row).

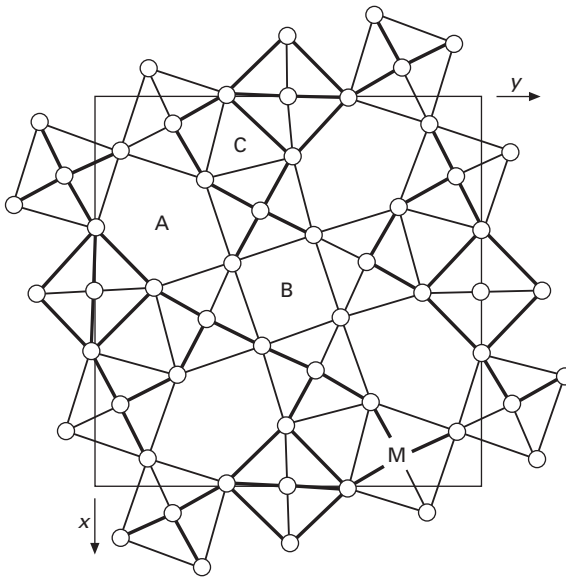
Without a quantitative evaluation of  $\Delta P$  and  $\xi(x)$ , it is not possible to go further in the quantitative description of the ferroelectric–relaxor crossover. It can, however, be explained why the ferroelectric and relaxor phase diagrams are aligned: this is simply because the  $\text{BaTiO}_3$  ultimate correlation length  $\xi_{\infty}$  appears in all the spatial parameters that were defined. In other words, the  $\text{BaTiO}_3$  correlation length imprints both the matrix and cluster properties; the Ti–O bond oscillations are the key mechanisms. This picture is consistent with the one which was drawn on the basis of high-pressure Raman scattering experiments and which uses the  $\text{BaTiO}_3$  correlation length [58]. Also, it can be recalled that the soft-mode related cluster sizes and the Ornstein Zernicke function were used in the case of lithium-substituted  $\text{KTaO}_3$  [67, 68]. From these pioneering works, several attempts have been made to transfer the cluster model to lead-containing relaxors. It seems that the continuous crossover

that was evidenced in lead-free compounds is in favour of the cluster model of relaxors. However, the comparison between lead-containing and lead-free relaxors is limited since:

- a number of features of lead-containing relaxors do not appear in lead-free relaxors (diffuse scattering, high-pressure-induced Raman lines,...);
- the electronic lone pair of lead leads to very peculiar Pb dynamics which is not present in Ba-based compounds;
- a continuous crossover from ferroelectric to relaxor states in Pb-based compounds is missing. There is perhaps one example of such crossover which is  $\text{PbTiO}_3 : \text{La}$  for which  $x_{\text{f-r}}$  is about 0.20. However, this is very different from the standard relaxors where the substitution has single discrete values (0.33/0.66 or 0.50/0.50).

### 30.5 Lead-free relaxors with tetragonal bronze (TTB) structure

Figure 30.14 shows a schematic representation of the TTB structure projection along the [001] direction. For a general formulation  $\text{A}_2\text{BC}_2\text{M}_5\text{X}_{15}$  ( $\text{X} = \text{O}, \text{F}$ ), large cations (e.g.  $\text{Na}^+$ ,  $\text{K}^+$ ,  $\text{Sr}^{2+}$ ,  $\text{Ba}^{2+}$ ,  $\text{Pb}^{2+}$ ,  $\text{La}^{3+}$ ,  $\text{Bi}^{3+}$ , ...) occupy the 15-CN (A) and the 12-CN (B) sites, small cations such as  $\text{Li}^+$  are in the 9-CN (C) sites and small and highly charged cations (e.g.  $\text{Nb}^{5+}$ ,  $\text{Ta}^{5+}$ , ...) are



30.14 Schematic projection of the anionic TTB structure along the 4-fold  $c$ -axis (A, B and C correspond to cationic sites with 15, 12 and 9 coordination number).

in the octahedral (M) site. The present section is devoted to selected lead-free relaxor compounds of TTB-type structure [69, 70].

The relaxor behaviour was demonstrated in various TTB compositions including niobates, tantalates, niobo-tantalates and niobo-titanates (Table 30.4) [25, 71, 72]. There was a typical relaxor temperature dependence of  $\epsilon'_r$  and  $\epsilon''_r$ . In addition, there was a deviation from the Curie–Weiss law and the shift of  $T_m$  to lower values for decreasing frequencies obeys the Vogel–Fulcher law [60, 73].

Table 30.4 Some lead-free TTB relaxor compositions

Relaxor compositions	$T_m$ ( $\pm 10$ K) (at 1 kHz)	$\Delta T_m$ (K)
$K_2LaNb_5O_{15}$	165	22
$K_2BiNb_5O_{15}$	220	80
$BaLa\Box Nb_5O_{15}$	203	55
$BaBi\Box Nb_5O_{15}$	295	75
$BaLa_{2/3}\Box_{1/3}NaNb_5O_{15}$	210	34
$BaLaNa(Nb_4Ti)O_{15}$	171	41
$BaLaK(Nb_4Ti)O_{15}$	146	13
$Ba_{1.5}La\Box_{0.5}(Nb_4Ti)O_{15}$	190	35
$Ba_{1.5}Bi\Box_{0.5}(Nb_4Ti)O_{15}$	255	65
$Ba_2La(Nb_3Ti_2)O_{15}$	185	20
$Ba_2Bi(Nb_3Ti_2)O_{15}$	270	25
$Sr_2NaTa_5O_{15}$	120	25
$Sr_2KTa_5O_{15}$	<80	*
$Ba_2NaTa_5O_{15}$	<80	*
$Ba_2KTa_5O_{15}$	<80	*
$K_3LiNb_5O_{14}F$	210	40
$Ba_{2.25}\Box_{0.75}Nb_5O_{14.5}F_{0.5}$	175	30
$SrK_2Nb_5O_{14}F$	112	16
$BaN_{a_2}Nb_5O_{14}F$	140	17
$Ba_{5/2}Bi_{5(1-x)}Nb_5O_{15}$ ( $0.52 \leq x \leq 0.80$ )	$257 \geq T_m \geq 251$	41 (0.52) to 81 (0.80)
$Sr_2Na(Nb_{1-x}Ta_x)_5O_{15}$ ( $0.40 \leq x \leq 1$ )	$222 \geq T_m \geq 120$	20 (0.40) to 25 (1)
$Sr_2K(Nb_{1-x}Ta_x)_5O_{15}$ ( $0.16 \leq x \leq 1$ )	$263 \geq T_m \geq 80$	21 (0.16) to * (1)
$Ba_2Na(Nb_{1-x}Ta_x)_5O_{15}$ ( $0.65 \leq x \leq 1$ )	$260 \geq T_m \geq 80$	6 (0.65) to * (1)
$Ba_{2-x}Na_{1+x}Nb_5O_{15-x}F_x$ ( $0.31 \leq x \leq 1$ )	$250 \geq T_m \geq 140$	40 (0.31) to 17 (1)
$Ba_2Na(Nb_{5-x}Ti_x)O_{15-x}F_x$ ( $0.31 \leq x \leq 0.50$ )	$265 \geq T_m \geq 168$	15 (0.31) to 30 (0.50)
$Sr_{2-x}Na_{1+x}Nb_5O_{15-x}F_x$ ( $0.075 \leq x \leq 0.35$ )	$320 \geq T_m \geq 222$	10 (0.075) to 20 (0.35)
$Sr_{2-x}K_{1+x}Nb_5O_{15-x}F_x$ ( $0.20 \leq x \leq 1$ )	$290 \geq T_m \geq 112$	15 (0.20) to 16 (1)
$Sr_{2.5(1-x)}Ba_{2.5x}\Box_{0.5}Nb_5O_{15}$ **	**	**

$\Delta T_m = T_m(10^5 \text{ Hz}) - T_m(10^2 \text{ Hz})$ . In the case of solid solutions, the given values of  $T_m$  correspond to the  $x$  limit values.

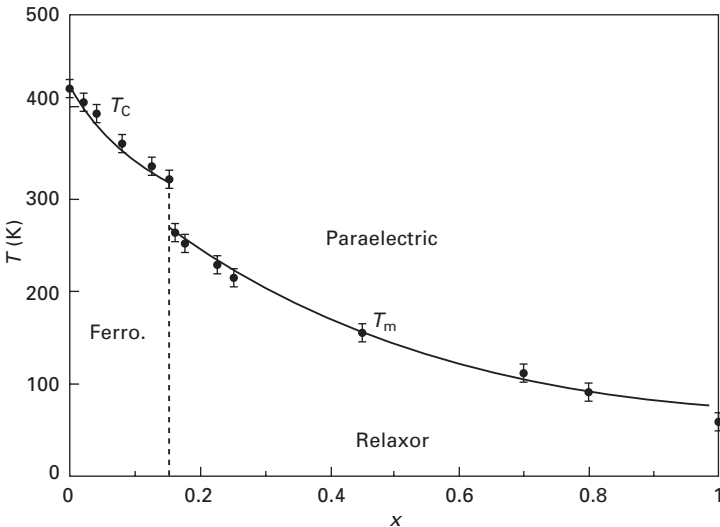
\* Unknown values due to the experimental low temperature limitation of our dielectric measurements.

\*\* A relaxor behaviour was announced by previous authors; due to some disagreements between them, the values of  $x$ ,  $T_m$  and  $\Delta T_m$  are not given here. This is due to the modulated distribution of  $Sr^{2+}$  and  $Ba^{2+}$  which can vary versus the different types of preparation between the various samples.

Some solid solutions situated between niobate oxide ferroelectric and relaxor were also studied. Such is the case with  $A_2B(Nb_{1-x}Ta_x)_5O_{15}$ . The relaxor behaviour occurs for the highest values of  $x$ . Figure 30.15 shows, as an example, the variations of  $T_C$  ( $0 \leq x < 0.16$ ) and  $T_m$  ( $0.16 \leq x \leq 1$ ) for ceramics with composition  $Sr_2K(Nb_{1-x}Ta_x)_5O_{15}$ . Both values decrease when the tantalum rate increases.

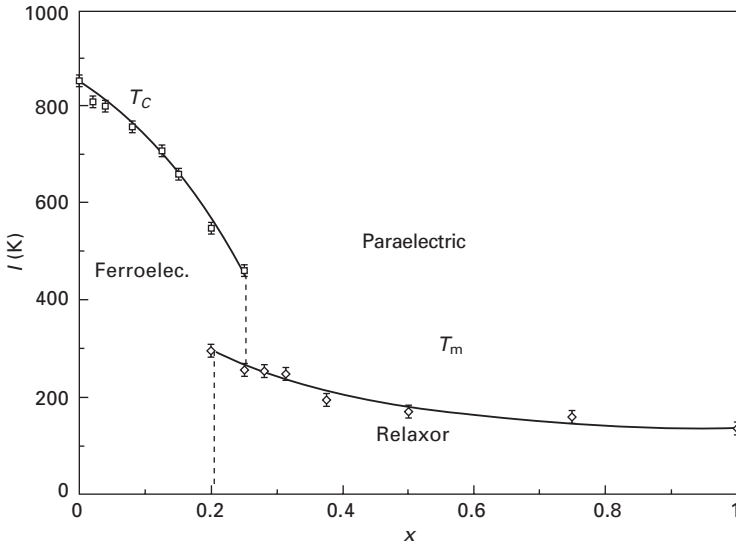
This is also the case with the  $Sr_2KNb_5O_{15}$ – $SrK_2Nb_5O_{14}F$  and  $Ba_2NaNb_5O_{15}$ – $BaN_2Nb_5O_{14}F$  systems; for the compositions close to the oxide, the behaviour is ferroelectric while it becomes relaxor when the fluorine rate and thus the sodium or potassium rate are high enough [74–76]. Figure 30.16 shows as an example the variations of  $T_C$  ( $0 \leq x \leq 0.25$ ) and  $T_m$  ( $0.20 \leq x \leq 1$ ) for the barium–sodium system. It is interesting to note that both relaxor and ferroelectric phases coexist for compositions ( $0.20 \leq x \leq 0.25$ ), giving rise to the transition sequence relaxor–ferroelectric–paraelectric on heating. Here also both values of  $T_C$  and  $T_m$  decrease when  $x$  increases. Elsewhere the frequency dependence of the permittivities of a ceramic with a composition  $BaN_2Nb_5O_{14}F$  clearly displays a frequency relaxation at 77 K, while it disappears at 300 K, i.e. for  $T > T_m$  ( $T_m = 140$  K at  $10^3$  Hz) (Fig. 30.17).

Figure 30.18 shows the temperature dependence of the pyroelectric coefficient  $p$  for a ceramic with composition  $Sr_{1.341}Ba_{1.097}Nb_{4.875}Sn_{0.125}O_{15}$  (SBNS). It shows a broad maximum around 240 K. Above 240 K, the pyroelectric signal decreases to values close to zero at approximately 350 K. The variation of  $P_s$  of the sample was obtained by integration of  $p$  vs.

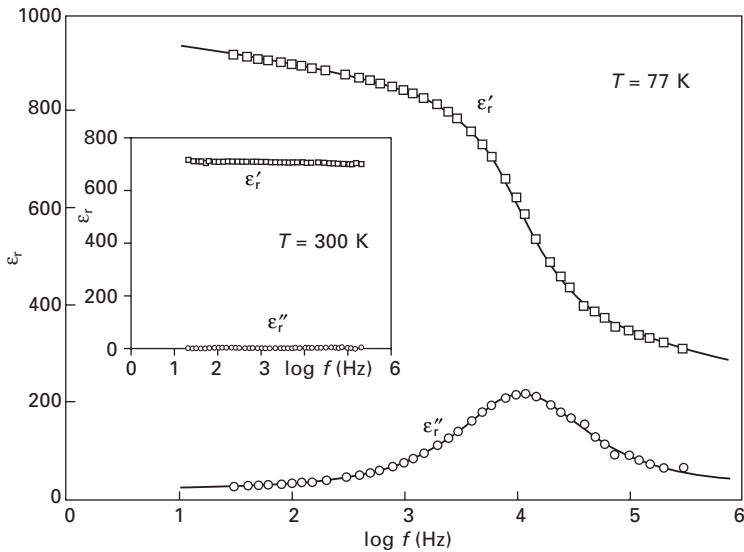


30.15 Variation of transition temperatures with  $x$  for ceramics with composition  $Sr_2K(Nb_{1-x}Ta_x)_5O_{15}$ .



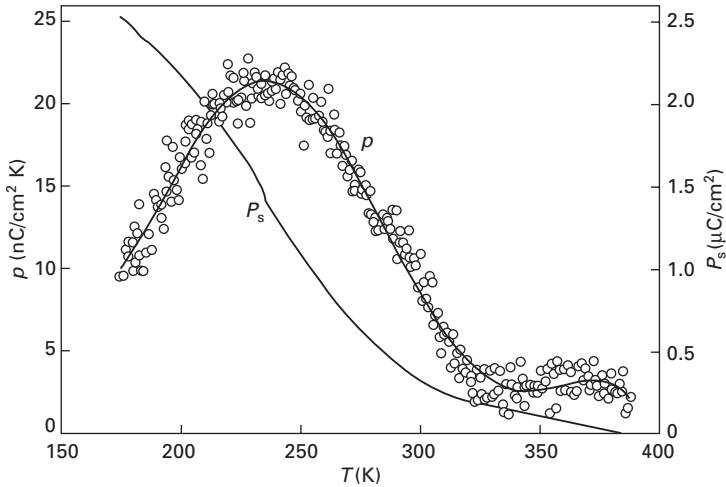


30.16 Variation of transition temperatures with  $x$  for ceramics with composition  $Ba_{2-x}Na_{1+x}Nb_5O_{15-x}F_x$ .



30.17 Frequency dependences of  $\epsilon'_r$  and  $\epsilon''_r$  for a ceramic with composition  $BaNa_2Nb_5O_{14}F$ .

temperature (Fig. 30.18). The slow decrease of the spontaneous polarisation associated to a very noisy pyroelectric signal should be considered as characteristic of a relaxor ferroelectric: the decrease of the polarisation is associated to a progressive relaxation of polar microdomains. The switching



30.18 Thermal variations of pyroelectric coefficient  $p$  and spontaneous polarization  $P_s$  in SBNS.

of the independent dipoles, isolated in this particular microstructure, occurs then randomly, giving rise to a very high noise level in the pyroelectric signal.

Some of these compositions were previously prepared and characterised. They were announced as ferroelectric, because the measurements had been performed only at one frequency (1 kHz) and not at various frequencies as required for the studies of relaxor properties. It was the automation of dielectric measurements performed with impedance analysers which allowed the relaxor behaviour to be revealed.

As in the perovskites, the relaxor behaviour appears in the TTB-type compounds when at least two ions occupy the same crystallographic site. The coexistence of cations seems to be as favourable on the A site as on the M site. In addition, at least one ferroelectrically active cation ( $\text{Ti}^{4+}$ ,  $\text{Nb}^{5+}$ ,  $\text{Ta}^{5+}$ ) must be present on the octahedral site.

The relaxor behaviour can be due to a cationic disorder on the A site, whatever the coupled substitution ensuring the electrical neutrality; this is the case with  $\text{BaLaNb}_5\text{O}_{15}$  when  $\text{Ba}^{2+}$  and  $\text{La}^{3+}$  occupy only the A site.  $\text{Ba}_2\text{NaNb}_5\text{O}_{15}$ , in which the same two  $\text{Ba}^{2+}$  cations occupy the A site and  $\text{Na}^+$  occupies the B sites, is a ferroelectric. On the contrary,  $\text{BaNa}_2\text{Nb}_5\text{O}_{14}\text{F}$  is a relaxor. The crystal structure of this last compound is in good agreement with the dielectric properties, i.e. the A-site is statistically occupied by equal quantities of  $\text{Ba}^{2+}$  and  $\text{Na}^+$ , thereby giving rise to a cationic disorder on the A site while the B site is filled by  $\text{Na}^+$  cations [77, 78]. In addition there is coexistence of  $\text{F}^-$  and  $\text{O}^{2-}$  on the anionic sites.

Concerning the Ta–Nb substitution, the replacement of  $\text{Nb}^{5+}$ , highly polarisable, by  $\text{Ta}^{5+}$  transforms the macroscopic polarisation into a local one. This results in a relaxor state as the long-range order is not induced by a local dipolar cationic order. The higher the associated cationic order in the A and B sites, the higher the Ta–Nb substitution rate leading to relaxor behaviour (Table 30.4): e.g.  $x = 0.16$  for  $\text{Sr}_2\text{K}(\text{Nb}_{1-x}\text{Ta}_x)_5\text{O}_{15}$  and  $x = 0.65$  for  $\text{Ba}_2\text{Na}(\text{Nb}_{1-x}\text{Ta}_x)_5\text{O}_{15}$ . In fact there is no ambiguity regarding the disordered distribution of the two small  $\text{Sr}^{2+}$  cations and the single large  $\text{K}^+$  one, nor regarding the ordered distribution of the two large  $\text{Ba}^{2+}$  cations and the single small  $\text{Na}^+$  ones, since both occur in two large A sites and in one smaller B one.

For oxyfluorides, the  $\text{F}^- - \text{O}^{2-}$  substitution is coupled with the cationic one in order to ensure electric neutrality. The origin of relaxor behaviour comes from cationic or/and anionic substitutions when there are two different cations on the same crystallographic site, e.g.  $\text{Ba}_{2-x}\text{Na}_{1+x}\text{Nb}_5\text{O}_{15-x}\text{F}_x$ , the A site being filled by both  $\text{Ba}^{2+}$  and  $\text{Na}^+$  and the X site by both  $\text{O}^{2-}$  and  $\text{F}^-$  for  $x > 0$  [79].

However, it seems that the relaxor behaviour can be attributed to the only anionic  $\text{F}^- - \text{O}^{2-}$  substitution in the lack of different cations on the same site, e.g.  $\text{K}_3\text{LiNb}_5\text{O}_{14}\text{F}$ : owing to their very different sizes, the  $3\text{K}^+$  and the  $\text{Li}^+$  cations occupy only the (2A + B) sites and the C site, respectively. The relaxor behaviour is induced by a dilution of the oxygen network leading to a local polarisation which breaks the long-range order usually at the origin of ferroelectric properties.

The influence of the heat treatments of the ceramics was studied with composition  $\text{BaNa}_2\text{Nb}_5\text{O}_{14}\text{F}$  (Table 30.5). The value of  $\Delta T_m$  increased from 9 to 60 when the sintering of the ceramics was followed by either slow cooling (favouring order) (50 K/h), medium cooling (300 K/h) or quenching in liquid nitrogen (favouring disorder). This result is in good agreement with the relationship between ionic disorder and relaxor behaviour. As a comparison, similar results were obtained on  $\text{Pb}(\text{Sc}_{1/2}\text{Ta}_{1/2})\text{O}_3$  (PST): the ceramic was a ferroelectric after a long annealing while it was a relaxor after quenching [80].

*Table 30.5* Values of  $T_m$  and  $\Delta T_m$  for ceramics with composition  $\text{BaNa}_2\text{Nb}_5\text{O}_{14}\text{F}$  obtained after different cooling treatments

	Slow cooling	Medium cooling	Quenching
$T_m$ (K) at 0.1 kHz	142	138	101
$T_m$ (K) at 1 kHz	143	141	111
$T_m$ (K) at 10 kHz	147	145	122
$T_m$ (K) at 100 kHz	151	155	161
$\Delta T_m$ (K)	9	17	60

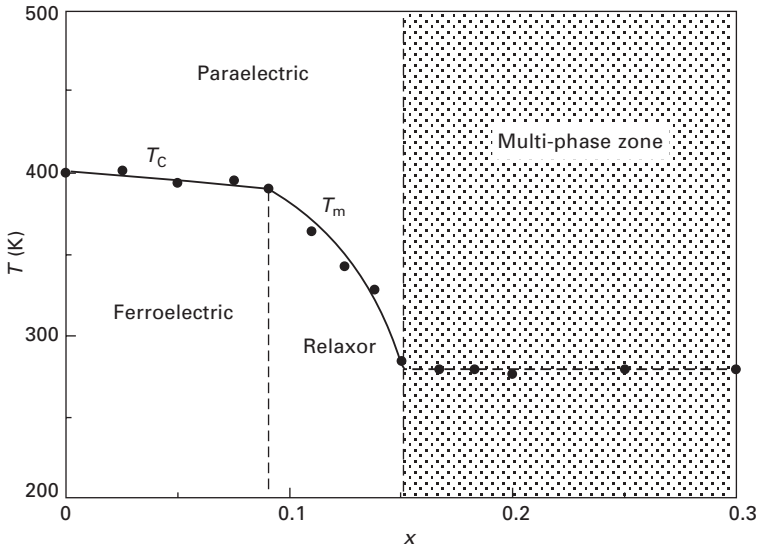
### 30.6 Ceramics containing bismuth

The aim of the present section is to discuss the relaxor properties of the ceramics containing bismuth. The  $\text{Na}_{0.5}\text{Bi}_{0.5}\text{TiO}_3$ -derived compositions are not considered here, nor is the perovskite-type solid solution between  $\text{ATiO}_3$  ( $A = \text{Ca}, \text{Sr}, \text{Ba}$ ) and  $\text{Na}_{1/2}\text{Bi}_{1/2}\text{TiO}_3$  [35, 81].

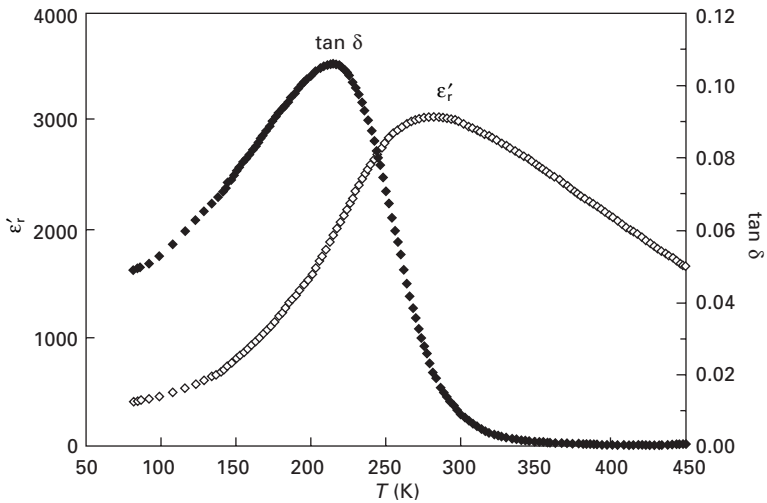
#### 30.6.1 Ceramics of perovskite type

The  $\text{Ba}_{1-x}\text{A}_{2x/3}\square_{x/3}\text{TiO}_3$  ( $A = \text{La}, \text{Bi}$ ) ceramics showed ferroelectric properties for compositions very close to  $\text{BaTiO}_3$  [82]. Relaxor behaviour occurred for values of  $x \geq 0.15$ . However, both the values of  $T_C$  or  $T_m$  were higher for Bi- than for La- substitution: e.g.  $T_m < 80\text{K}$  in  $\text{Ba}_{0.8}\text{La}_{0.4/3}\text{TiO}_3$ ,  $T_m = 165\text{K}$  in  $\text{Ba}_{0.8}\text{La}_{0.2/3}\text{Bi}_{0.2/3}\text{TiO}_3$  and  $T_m = 292\text{K}$  in  $\text{Ba}_{0.8}\text{Bi}_{0.4/3}\text{TiO}_3$ . This is not related to a steric effect, since the apparent cationic sizes are very close ( $r_{\text{La}^{3+}} = 1.16\text{\AA}$ ,  $r_{\text{Bi}^{3+}} = 1.17\text{\AA}$  in 8-CN; these values are given for 8-CN, although the cations are in the 12-CN site of the perovskite, because no corresponding value is given for  $\text{Bi}^{3+}$ ) [83]. The real cause is undoubtedly related to the lone pair, which leads to the non-spherical and strongly polarised  $\text{Bi}^{3+}$  cation. Such an effect is well known, for example, in the case of the influence of  $\text{Pb}^{2+}$  (also possessing a lone pair) on the  $T_C$  variation of  $\text{Ba}_{1-x}\text{Pb}_x\text{TiO}_3$ :  $T_C(\text{BaTiO}_3) = 400\text{K}$ ,  $T_C(\text{PbTiO}_3) = 763\text{K}$  [84–87].

For ceramics with composition  $\text{Ba}_{1-x}\text{Bi}_{2x/3}\text{TiO}_3$ , for  $0 \leq x < 0.09$ , i.e. in the ferroelectric region, the value of  $T_C$  decreases only very slowly as  $x$  increases (Fig. 30.19). Indeed, two antagonist effects are in competition. The replacement of the big  $\text{Ba}^{2+}$  cation by the smaller  $\text{Bi}^{3+}$  and the creation of cationic vacancies should lead to a decrease of  $T_C$  ( $r_{\text{Ba}^{2+}} = 1.42\text{\AA}$ ,  $r_{\text{Bi}^{3+}} = 1.17\text{\AA}$  in 8-CN) [83]. In contrast, the introduction of  $\text{Bi}^{3+}$  with its lone pair leads to an increase of  $T_C$ . The resultant of these two effects is probably responsible of the relative stability of  $T_C$  with  $x$ . For compositions  $0.09 \leq x \leq 0.15$ , the nanostructural disorder which characterises the relaxor behaviour is less sensitive to the local electronic configuration of  $\text{Bi}^{3+}$ , leading thus to a stronger decrease of  $T_m$  with  $x$  [1]. Figure 30.20 shows the temperature dependence of  $\epsilon'_r$  and the dissipation factor  $\tan \delta = \epsilon''_r/\epsilon'_r$  at 1 kHz for a ceramic with composition corresponding to  $x = 0.15$ . The main dielectric relaxor characteristics  $\Delta T_m$  and  $\Delta \epsilon'_r/\epsilon'_r$  increase as the  $2/3 \text{ Bi}^{3+}\text{-Ba}^{2+}$  substitution rate increases (Table 30.6). This is due of course to the strong composition heterogeneity that exacerbates the relaxor effect. This was typically the case in the lead perovskite relaxor PMN where local 1:1 order between niobium and magnesium atoms generated ordered regions surrounded by rich niobium polar regions. The heterogeneity thus created induced the relaxor behaviour commonly correlated with nanoscale spontaneous polarisation [1]. The present result is of great interest for obtaining relaxor compositions at temperatures close to 300K for use as lead-free capacitors, dielectrics or



30.19 Variation of  $T_C$  or  $T_m$  with  $x$  for ceramics of  $\text{Ba}_{1-x}\text{Bi}_{2x/3}\text{TiO}_3$  composition.



30.20 Temperature dependences of  $\epsilon'_r$  and  $\tan \delta$  for a ceramic with composition  $\text{Ba}_{0.85}\text{Bi}_{0.10}\text{TiO}_3$ , at 1 kHz.

actuators. The value of  $T_m$  corresponding to  $x = 0.15$  is 288 K (at 1 kHz), which can be compared with that of the well-known lead-containing PMN ( $T_m = 265$  K).

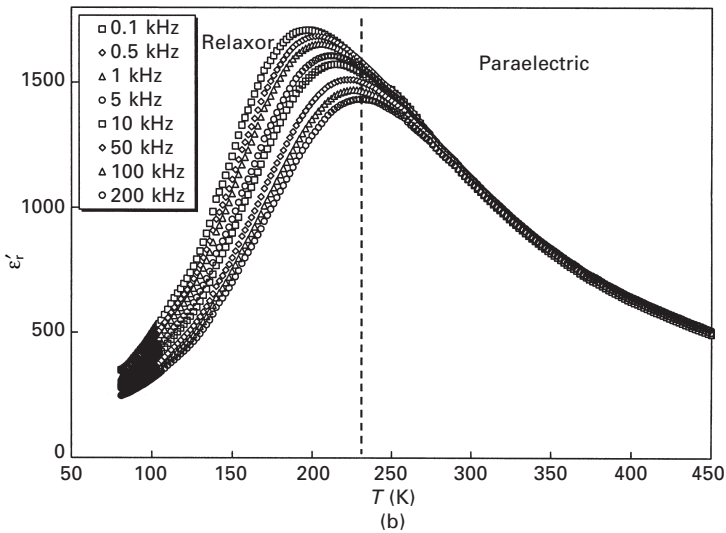
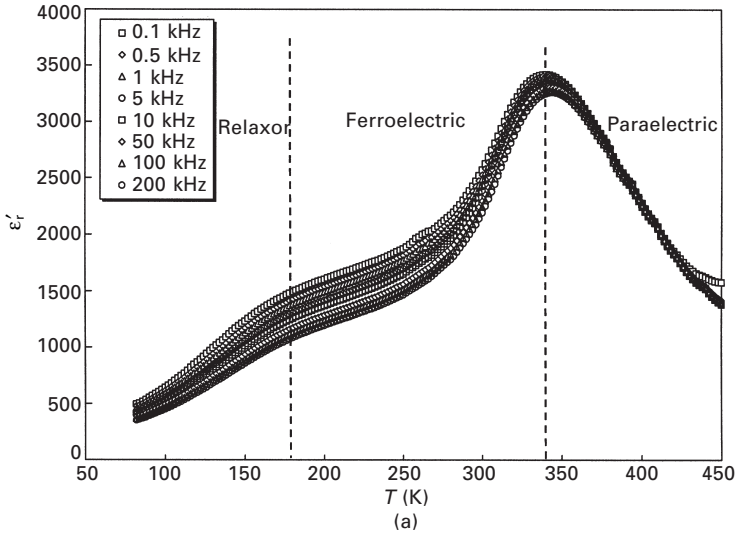
Another interesting study concerns ceramics with compositions  $\text{Ba}_{0.9}\text{Bi}_{0.067}\square_{0.033}(\text{Ti}_{1-x}\text{Zr}_x)\text{O}_3$ , i.e. with substitutions on both 6-CN and 12-

Table 30.6 Values of  $T_m$ ,  $\Delta T_m$  and  $\Delta\epsilon'_r/\epsilon'_r$  for ceramics with composition  $\text{Ba}_{1-x}\text{Bi}_{2x/3}\text{TiO}_3$

$x$	$T_m$ (K) at 1 kHz	$\Delta T_m$ (K)	$\Delta\epsilon'_r/\epsilon'_r$
0.090	390	2	0.050
0.110	365	5	0.045
0.135	328	10	0.120
0.150	288	26	0.325

CN cationic sites. Two different kinds of behaviour appeared in the thermal evolution of  $\epsilon'_r$  versus frequency. For  $0 \leq x < 0.075$ , there was one relatively sharp peak of  $\epsilon'_r$ , no dependence on frequency at  $T_C$  and a shoulder in the slope with a dispersion of  $\epsilon'_r$  and an increase of  $T'_m$  with frequency. As an example the result for a ceramic corresponding to  $x = 0.040$  is reported in Fig. 30.21: the behaviour is of ferroelectric type. For  $0.075 \leq x \leq 1$ , only one peak was observed, showing the typical relaxor  $\epsilon'_r = f(T, f)$  dependences. In addition, there was a deviation from the Curie–Weiss law and a strong dielectric dispersion was evidenced, leading to a Vogel–Fulcher behaviour [6, 88]. All these dielectric characteristics are typical of relaxor behaviour [1]. Figure 30.22 shows the variations in  $T_C$ ,  $T'_m$  and  $T''_m$  with the composition at 1 kHz.  $T''_m$  decreased from  $x = 0.075$  to  $x = 0.8$ . For  $0.8 < x \leq 1$ , the values of  $T''_m$  are not plotted, due to low-temperature experimental limitations.

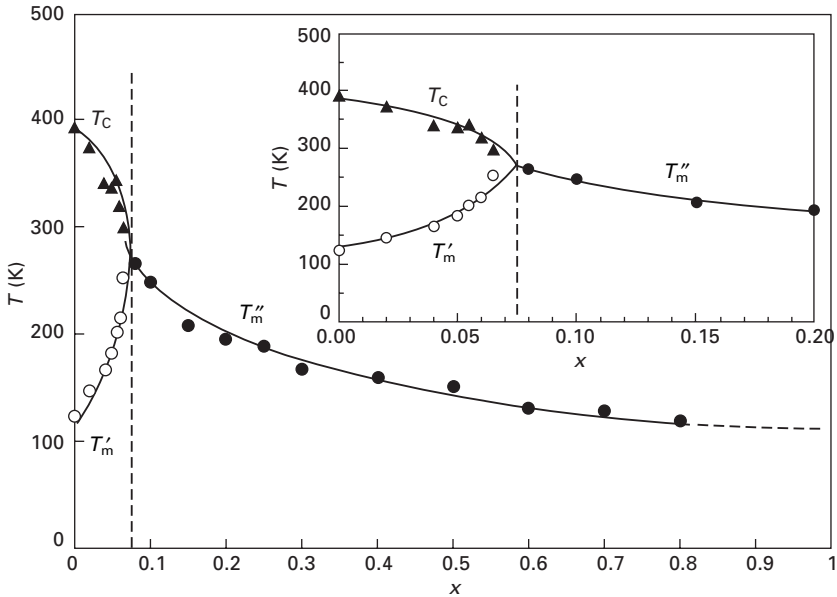
Examination of Fig. 30.22 shows that for a relatively low Zr–Ti substitution rate, the value of  $T_C$  is decreasing while that of  $T'_m$  is increasing up to a composition  $x \approx 0.07$ , beyond what remains a single effect at  $T''_m$  between a relaxor state and a paraelectric one. This value of  $T''_m$  slowly decreases to values close to 100 K when  $x$  further increases. The very peculiar features of the phase diagram displayed on Fig. 30.22 can be pointed out as follows. For compositions close to  $\text{Ba}_{0.9}\text{Bi}_{0.067}\text{TiO}_3$ , i.e.  $x \leq 0.07$ , the ceramics undergo two phase transitions on cooling. The first, at  $T_C$ , is from a paraelectric to the ferroelectric state similar to  $\text{BaTiO}_3$ . The second one, which occurs within the ferroelectric state, is of relaxor type. This is very unusual in relaxors where the succession of transitions is always in the thermodynamically favourable sequence on cooling: paraelectric  $\rightarrow$  relaxor  $\rightarrow$  ferroelectric. The latter ordering transition can be either electric field induced as in PMN [89, 90] or chemically driven as in PSN and PST [91]. The very peculiar behaviour of  $\text{Ba}_{0.9}\text{Bi}_{0.067}(\text{Ti}_{1-x}\text{Zr}_x)\text{O}_3$  is ascribed to the dual substitution on the A and B sites. The Bi substitution on the A site leads to the low-temperature relaxor state while the Zr substitution on the B site keeps the high-temperature ferroelectric state at low rates. This special chemistry explains the apparent contradiction of such results with thermodynamics which always calls for ordering on cooling. Detailed investigations of the possible segregation of



30.21 Temperature dependence of  $\epsilon'_r$  for a ceramic with composition  $\text{Ba}_{0.9}\text{Bi}_{0.067}(\text{Ti}_{0.96}\text{Zr}_{0.04})\text{O}_3$  (a) or  $\text{Ba}_{0.9}\text{Bi}_{0.067}(\text{Ti}_{0.85}\text{Zr}_{0.15})\text{O}_3$  (b).

both substituted cations on nanoscale are needed to clarify the microscopic origin of the transition sequence.

With a view to future applications in electronic components, attention was focused on the ceramics with composition  $\text{Ba}_{0.9}\text{Bi}_{0.067}(\text{Ti}_{0.92}\text{Zr}_{0.08})\text{O}_3$ . Its relaxor characteristics, reported in Table 30.7, show that high permittivities



30.22 Variations of  $T_C$ ,  $T_m'$  and  $T_m''$ , at 1 kHz, for ceramics with composition  $Ba_{0.9}Bi_{0.067}(Ti_{1-x}Zr_x)O_3$ .

Table 30.7 Some relaxor characteristics of a ceramic with composition  $Ba_{0.9}Bi_{0.067}(Ti_{0.92}Zr_{0.08})O_3$

$f$ (kHz)	$T_m''$ (K)	$\epsilon'_{rmax}$ at $T_m''$	FWHM (K)
0.1	255	3930	227
1	264	3810	224
10	275	3650	221
100	287	3470	219

FWHM: full width at half maximum.

are achieved close to room temperature for this composition. In addition, there is also a strong deviation from the Curie–Weiss law ( $T_m'' < T_0$ ) characteristic of dipole interactions responsible of some type of short range order. The large curvature of  $1/\epsilon'_r$  around  $T_m''$  is in good agreement with a strongly diffuse phase transition. The value of the frequency dispersion  $\Delta\epsilon'_r/\epsilon'_r$  at a normalised temperature  $T = T_m'' - 60$  K is about 0.091. The good fit of the  $\log f = f(T_m'')$  data to the Vogel–Fulcher law leads to the value  $T_{VF} = 238 \pm 10$  K. It appears that such a composition satisfies the criteria for applications:

- The value of  $T_m''$  is next to room temperature, allowing relaxor properties to be used in normal conditions.
- The values of  $\Delta T_m''$  and that of  $\Delta\epsilon'_r/\epsilon'_r$  are high ( $\Delta T_m = 32$  K,  $\Delta\epsilon'_r/\epsilon'_r =$



0.91); they are higher than those of PMN ceramics ( $\Delta T_m = 15$  K,  $\Delta \epsilon'_r / \epsilon'_r = 0.19$ ), usually used for applications.

- The value of  $\epsilon'_r$  lies between 3400 and 4000; these values are promising. Current studies will lead to an increase in these values, thanks to an optimisation of processing parameters.

Other compositions have also been studied in the BaO–Bi<sub>2</sub>O<sub>3</sub>–TiO<sub>2</sub> ternary system [92].

### 30.6.1 Ceramics of TTB type

From a crystallographic point of view, it is interesting to note the two compositions BaA□Nb<sub>5</sub>O<sub>15</sub> (A = La, Bi) from the TTB family (Table 30.4), in which only two over three of the large A and B sites (15 and 12-CN) are occupied [93]. Such a composition type is original since it has one vacancy in the (2A + B) sites and the two C sites of 9-CN are also empty compared with the general formulation A<sub>2</sub>BC<sub>2</sub>M<sub>5</sub>O<sub>15</sub>.

Table 30.8 shows the dielectric properties of some lanthanum and bismuth relaxor compositions in which the value of  $T_m$  increases systematically from lanthanum to bismuth. This increase becomes greater as the amount of A<sup>3+</sup> cation increases compared with that of Ba<sup>2+</sup>:

- BaLaNb<sub>5</sub>O<sub>15</sub> (205 K) and BaBiNb<sub>5</sub>O<sub>15</sub> (295 K) (there are as many A<sup>3+</sup> as Ba<sup>2+</sup> cations).
- Ba<sub>2</sub>La(Nb<sub>3</sub>Ti<sub>2</sub>)O<sub>15</sub> (195 K) and Ba<sub>2</sub>Bi(Nb<sub>3</sub>Ti<sub>2</sub>)O<sub>15</sub> (185 K) (there are fewer A<sup>3+</sup> than Ba<sup>2+</sup> cations).

The value of  $T_m$  decreases as the ratio A<sup>3+</sup>/Ba<sup>2+</sup> decreases but this also occurs simultaneously as the relative amount of Ti<sup>4+</sup> increases (it is thus difficult to attribute this phenomenon to one or the other type of composition replacement). When K<sub>2</sub>ANb<sub>5</sub>O<sub>15</sub> and BaANb<sub>5</sub>O<sub>15</sub> are compared, the value of  $T_m$  is found to decrease from the barium to the potassium compounds. This

Table 30.8 Relaxor characteristics of some TTB ceramics

	$T_m$ (K) at 1 kHz ( $\pm 10$ K)	$\Delta T_m$ (K)* ( $\pm 10$ K)
K <sub>2</sub> LaNb <sub>5</sub> O <sub>15</sub>	165	20
K <sub>2</sub> BiNb <sub>5</sub> O <sub>15</sub>	225	80
BaLa□Nb <sub>5</sub> O <sub>15</sub>	205	55
Ba <sub>1.5</sub> La□ <sub>0.5</sub> (Nb <sub>4</sub> Ti)O <sub>15</sub>	190	35
Ba <sub>2</sub> La(Nb <sub>3</sub> Ti <sub>2</sub> )O <sub>15</sub>	185	20
BaBi□Nb <sub>5</sub> O <sub>15</sub>	295	75
Ba <sub>1.5</sub> Bi□ <sub>0.5</sub> (Nb <sub>4</sub> Ti)O <sub>15</sub>	255	65
Ba <sub>2</sub> Bi(Nb <sub>3</sub> Ti <sub>2</sub> )O <sub>15</sub>	200	30

$$\Delta T_m = T_m(200 \text{ kHz}) - T_m(0.1 \text{ kHz})$$

is also accompanied by a decrease in the ratio from  $1A^{3+}/1Ba^{2+}$  to the ratio  $1A^{3+}/2K^{+}$ . All these results show the favourable influence of these  $A^{3+}$  cations on the highest value of  $T_m$ .

Of all the lead-free TTB compounds studied, the highest value of  $T_m$  was obtained for  $BaBiNb_5O_{15}$  ( $T_m = 295$  K, at 1 kHz). In addition, independently of the value of  $T_m$ , the bismuth compounds allow the highest values of  $\Delta T_m$ :  $\Delta T_m = 80$  and  $75$  K for the potassium and barium niobates, respectively. Such a result is in good agreement with that obtained for  $BaBiNb_5O_{15}$  [71].

### 30.7 Conclusions

In each lead-free family investigated, i.e. perovskite or TTB-type, the relaxor behaviour appears when at least two different cations occupy the same crystallographic site. This condition is necessary but not sufficient. The lack of relaxor effect in perovskite  $BaMg_{1/3}Nb_{2/3}O_3$  is a good example. One of the  $M^{n+}$  cations in the octahedral site has to be ferroelectrically active (e.g.  $Ti^{4+}$ ,  $Nb^{5+}$  or  $Ta^{5+}$ ). In any case, a local polarisation leads to a relaxor behaviour while a macroscopic one gives rise to a ferroelectric ordering.

Lead-free perovskites derived from  $BaTiO_3$  are solid solutions. The only local polarisation comes from dilution of the ferroelectric character. The relaxor effect is greater if the substitution affects the octahedral site. The higher the substitution rate, the greater the relaxor effect. For TTB-type compounds (not only solid solutions), the effect is due either to a cationic disorder in the A or B site or to a dilution of the ferroelectric character by cationic or anionic substitution, on any crystallographic sites.

The increase of substitution rate from either  $BaTiO_3$  or a TTB ferroelectric oxide leads to an increase of the main relaxor dielectric characteristics but also a decrease of  $T_C$ , then of  $T_m$ . A continuous change from ferroelectric to relaxor either driven by composition or temperature variation was evidenced. It reflects the ionic feature of lead-free solid solutions (contrary to lead-containing compounds). The corresponding studies were helpful to understand the physics of such relaxors.

Among all the compounds investigated, those containing bismuth possess simultaneously the highest value of  $T_m$  (close to room temperature) and the best relaxor characteristics. Such ceramics present a real interest for applications as a lead-free dielectric for capacitors or actuators.

### 30.8 References

1. Cross L.E., 'Relaxor ferroelectrics: an overview', *Ferroelectrics*, 1994 **151** 305–320.
2. Elissalde C., Ravez J. and Gaucher P., 'The low and high frequency relaxations in lead magnesium niobate ceramics', *Mat. Sci. Eng.*, 1993 **B 20** 318–323.

3. Vogel H., 'The law of the relation between the viscosity of liquids and the temperature', *Z. Phys.*, 1921 **22** 645–646.
4. Fulcher G., 'Analysis of recent measurements of the viscosity of glasses', *J. Am. Ceram. Soc.*, 1925 **8** 339–355.
5. Viehland D., Jang S.J. and Cross L.E., 'Freezing of the polarization fluctuations in lead magnesium niobate relaxors', *J. Appl. Phys.*, 1990 **68(6)** 2916–2921.
6. Glazounov A.E. and Tagantsev A.K., 'Direct evidence for Vogel–Fulcher freezing in relaxor ferroelectrics', *Appl. Phys. Letters*, 1998 **73(6)** 856–858.
7. Hornebecq V., Elissalde C., Weill F., Villesuzanne A., Menetrier M. and Ravez J., 'Study of disorder in a TTB ferroelectric relaxor: a structural approach', *J. Appl. Cryst.*, 2000 **33** 1037–1045.
8. Smolenski G.A. and Agranovskaya A., 'Dielectric polarization of a series of compounds of complex structure', *Fizika Tverdogo Tela*, 1959 **1(10)** 1562–1572.
9. Rolov B., 'The effect of composition fluctuations on spreading of ferroelectric phase transitions', *Sov. Phys. Solid State*, 1965 **6** 1976–1979.
10. Cross L.E., 'Relaxor ferroelectrics', *Ferroelectrics* 1987 **76** 241–267.
11. Randall C.A. and Bhalla A.S., 'Nanostructural–property relations in complex lead perovskites', *Jpn J. Appl. Phys.*, 1990 **29** 327–333.
12. Thomas N.W., 'A new framework for understanding relaxor ferroelectrics', *J. Phys. Chem. Solids*, 1990 **51** 1419–1431.
13. Husson E., Chubb M. and Morell A., 'Superstructure in lead magnesium niobate ( $\text{PbMg}_{1/3}\text{Nb}_{2/3}\text{O}_3$ ) ceramics revealed by high resolution electron spectroscopy', *Mater. Res. Bull.*, 1988 **23** 357–361.
14. De Mathan N., *PhD thesis*, Ecole Centrale, Paris, France 1991.
15. Rosenfeld H.D. and Egami E., 'A model of short and intermediate range atomic structure in the relaxor ferroelectric ( $\text{PbMg}_{1/3}\text{Nb}_{2/3}\text{O}_3$ )', *Ferroelectrics*, 1994 **158** 351–356.
16. Qian H. and Bursill L.A., 'Random-field Potts model for the polar domains of lead magnesium niobate and lead scandium tantalate', *Int. J. Mod. Phys.*, 1996 **B 10** 2027–2047.
17. Qian H., Peng J.L. and Bursill L.A., 'NNN-Ising model simulation of nanodomain textures in relaxor-type lead scandium tantalate', *Int. J. Mod. Phys.*, 1993 **B 7** 4353–4369.
18. Viehland D., Wuttig M. and Cross L.E., 'The glassy behaviour of relaxor ferroelectrics', *Ferroelectrics*, 1991 **120** 71–77.
19. Pirc R. and Blinc R., 'Spherical random-bond-random-field model of relaxor ferroelectrics', *Phys. Rev. B*, 1999 **60(19)** 13470–13478.
20. Westphal V., Kleeman W. and Glinchuk M.D., 'Diffuse phase transitions and random-field-induced domain states of the relaxor ferroelectric  $\text{PbMg}_{1/3}\text{Nb}_{2/3}\text{O}_3$ ', *Phys. Rev. Lett.*, 1992 **68** 847–850.
21. Glazounov A.E., Tagantsev A.K. and Bell A.J., 'Effect of the a-c electric field on the dielectric permittivity of lead magnesium niobate relaxor', *Ferroelectrics*, 1996 **184** 217–226.
22. Chen I.W. and Wang Y., 'A domain wall model for relaxor ferroelectrics', *Ferroelectrics*, 1998 **206–207** 245–263.
23. Egami T., Dmowski W., Teslic S., Davies P.K., Chen I.W. and Chen H., 'Nature of atomic ordering and mechanism of relaxor ferroelectric phenomena in PMN', *Ferroelectrics*, 1998 **206–207** 231–244.

24. Egami T., 'Microscopic model of relaxor phenomena in Pb containing mixed oxides', *Ferroelectrics*, 1999 **222** 421–428.
25. Ravez J. and Simon A., 'Some solid state chemistry aspects of lead-free relaxor ferroelectrics', *J. Solid State Chem.*, 2001 **162(2)** 260–265.
26. Ravez J., 'Ferroelectricity in solid state chemistry', *C.R. Acad. Sci. IIC*, 2000 **3** 267–283.
27. Uchino K., 'Relaxor ferroelectric devices', *Ferroelectrics*, 1994 **151** 321–330.
28. Simon A. and Ravez J., 'Relations between relaxor behaviour and cationic substitutions in lead-free BaTiO<sub>3</sub> derived ceramics', *Ferroelectrics*, 2000 **240** 335–342.
29. Ravez J. and Simon A., 'Lead-free ferroelectric relaxor ceramics derived from BaTiO<sub>3</sub>', *Euro. Phys. J. AP*, 2000 **11** 9–13.
30. Ravez J. and Simon A., 'Temperature and frequency dielectric response of ferroelectric ceramics with composition Ba(Ti<sub>1-x</sub>Zr<sub>x</sub>)O<sub>3</sub>', *Eur. J. Solid State Inorg. Chem.*, 1997 **34** 1199–1209.
31. Yasuda N., Ohwa H. and Asano S., 'Dielectric properties and phase transitions of Ba(Ti<sub>1-x</sub>Sn<sub>x</sub>)O<sub>3</sub> solid solution', *Jpn. J. Appl. Phys.*, 1996 **35** 5099–5103.
32. Yu Zhi, Ang Chen, Jing Zhi, Vilharino P.M. and Baptista J.L., 'Dielectric properties of Ba(Ti,Ce)O<sub>3</sub> from 10<sup>2</sup> to 10<sup>5</sup>Hz in the temperature range 85–700K', *J. Phys. Condens. Matter*, 1997 **9** 3081–3088.
33. Ravez J. and Simon A., 'Ferroélectriques classiques ou relaxeurs dérivés de BaTiO<sub>3</sub>', *C. R. Acad. Sci. IIB*, 1997 **325** 481–486.
34. Bokov A.A., Maglione M., Simon A. and Ye Z.G., 'Dielectric behaviour of Ba(Ti<sub>1-x</sub>Zr<sub>x</sub>)O<sub>3</sub> solid solution', *Ferroelectrics*, 2006 **337** 169–178.
35. Gomah Petry J.R., Marchet P., Simon A., Von Der Mühl R., Maglione M. and Mercurio J.P., *Integrated Ferroelectrics*, 2004 **61** 155–158.
36. Ravez J. and Simon A., 'Relaxor ferroelectricity in ceramics with composition Ba<sub>1-x</sub>K<sub>x</sub>(Ti<sub>1-x</sub>Nb<sub>x</sub>)O<sub>3</sub>', *Mater. Lett.*, 1998 **36** 81–84.
37. Lemanov V.V., Zaitseva N.V., Smirnova E.P. and Syrnikov P.P., 'BaTiO<sub>3</sub>–KTAO<sub>3</sub> solid solution – a new relaxor system', *Ferroelectric Lett.*, 1995 **19** 7–12.
38. Ravez J. and Simon A., 'Le premier relaxeur ferroélectrique oxyfluoré', *Phys. Stat. Sol.*, 1997 **159** 517–522.
39. Ravez J. and Simon A., 'New oxyfluoride ceramics derived from BaTiO<sub>3</sub> with either a relaxor or a classical ferroelectric behavior', *Eur. J. Solid State Inorg. Chem.*, 1997 **34** 331–342.
40. Khemakhem H., Simon A., Von Der Mühl R. and Ravez J., 'Relaxor or classical ferroelectric behavior in ceramics with composition Ba<sub>1-x</sub>Na<sub>x</sub>Ti<sub>1-x</sub>Nb<sub>x</sub>O<sub>3</sub>', *J. Phys.: Condens. Matter*, 2000 **12** 5951–5959.
41. Ravez J. and Simon A., 'New lead-free relaxor ceramics derived from BaTiO<sub>3</sub> by cationic heterovalent substitutions in the 12-CN crystallographic site', *Solid State Sci.*, 2000 **2(5)** 525–529.
42. Ravez J., Broustera C. and Simon A., 'Lead-free ferroelectric relaxor ceramics in the BaTiO<sub>3</sub>–BaZrO<sub>3</sub>–CaTiO<sub>3</sub> system', *J. Mater. Chem.*, 1999 **9** 1609–1613.
43. Ravez J. and Simon A., 'Classical or relaxor ferroelectric ceramics in the BaTiO<sub>3</sub>–KNbO<sub>3</sub>–CaTiO<sub>3</sub> system', *Solid State Sci.*, 1999 **1(1)** 25–35.
44. Aliouane K., Hamadene M., Guehria A., Simon A. and Ravez J., 'New oxyfluoride lead-free ferroelectric relaxors in the BaTiO<sub>3</sub>–BaZrO<sub>3</sub>–CaLiF<sub>3</sub> system', *J. Fluor. Chem.*, 2000 **105** 71–76.
45. Kerfah A., Taibi K., Guehria A., Simon A. and Ravez J., 'New oxyfluoride lead-free ferroelectric relaxors in the BaTiO<sub>3</sub>–BaZrO<sub>3</sub>–BaLiF<sub>3</sub> system', *Mater. Lett.*, 2000 **42** 189–193.

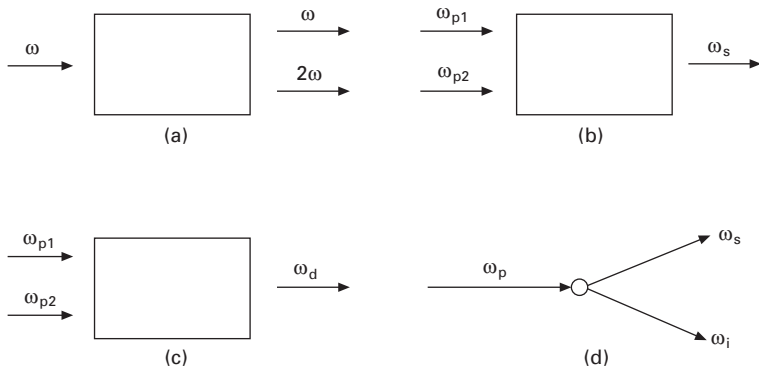
46. Aliouane K., Guehria A., Simon A. and Ravez J., 'Study of new relaxor materials in the BaTiO<sub>3</sub>-BaZrO<sub>3</sub>-La<sub>2/3</sub>TiO<sub>3</sub> system', *Solid State Sci.*, 2005 **7(11)** 1324-1332.
47. Sciau P., Calvarin G. and Ravez J., 'X-ray diffraction study in Ba(Ti<sub>0.65</sub>Zr<sub>0.35</sub>)O<sub>3</sub> and Ba<sub>0.92</sub>Ca<sub>0.08</sub>Ti<sub>0.75</sub>Zr<sub>0.25</sub>O<sub>3</sub> compositions: influence of electric field', *Solid State Commun.*, 2000 **113** 77-82.
48. Ravez J. and Simon A., 'Classical or relaxor ferroelectric ceramics in the BaTiO<sub>3</sub>-KNbO<sub>3</sub>-CaTiO<sub>3</sub> system', *Solid State Sci.*, 1999 **1(1)** 25-35.
49. Fahri R., El Marssi M., Dellis J.L., Yuzyuk Yui, Ravez J. and Glinchuck M.D., 'Raman scattering from relaxor ferroelectrics and related compounds', *Ferroelectrics*, 1999 **2356(1-4)** 9-17.
50. Fahri R., El Marssi M., Simon A. and Ravez J., 'Relaxor-like and spectroscopic properties of niobium modified barium titanate', *Eur. Phys. J. B.*, 2000 **18** 605-610.
51. Sakowsky A.C., Lukaszewicz K. and Megaw H.D., 'Structure of sodium niobate at room temperature, and the problem of reliability in pseudosymmetric structures', *Acta Crystallogr.*, 1969 **25** 851-865.
52. Hewat A.W., 'Neutron powder profile refinement of ferroelectric and antiferroelectric crystal structures', *Ferroelectrics*, 1974 **7** 83-85.
53. Aydi A., Khemakhem H., Boudaya C., Simon A. and Von Der Mühl R., 'X-ray and dielectric studies of ferroelectric or relaxor phases in the Ca<sub>1-x</sub>Na<sub>x</sub>Sn<sub>1-x</sub>Nb<sub>x</sub>O<sub>3</sub> system' *Solid State Sci.*, 2005 **7** 249-255.
54. Aydi A., Khemakhem H., Boudaya C., Von Der Mühl R. and Simon A., 'New ferroelectric and relaxor ceramics in the mixed oxide system NaNbO<sub>3</sub>-BaSnO<sub>3</sub>', *Solid State Sci.*, 2004 **6(3)** 333-337.
55. Raevski I.P. and Prosandeev S.A., 'A new lead-free family of perovskites with a diffuse phase transition: NaNbO<sub>3</sub>-based solid solutions', *J. Phys. Chem. Solids*, 2002 **63** 1939-1950.
56. Raevskaya S.I., Dellis J.L., Reznichenko L.A., Prosandeev S.A., Raevski I.P., Lisitsina S.O. and Jastrabik L., 'Lead-free relaxor ferroelectric ceramics in NaNbO<sub>3</sub>-Sr<sub>0.5</sub>NbO<sub>3</sub>-LiNbO<sub>3</sub> solid solution system', *Ferroelectrics*, 2005 **317** 241-243.
57. Raevski I.P., Reznichenko L.A., Malitskaya M.A., Shilkina L.A., Lisitsina S.O., Raevskaya S.I. and. Kuznetsova E.M., 'NaNbO<sub>3</sub>-based relaxor', *Ferroelectrics* 2004 **299** 95-101.
58. Kreisel J., Bouvier P., Maglione M., Dkhil B. and Simon A., 'High pressure Raman investigation of the peculiar lead-free relaxor BaTi<sub>0.65</sub>Zr<sub>0.35</sub>O<sub>3</sub>', *Phys. Rev. B*, 2004 **69(9)** 092104-092110.
59. Ravez J. and Simon A., 'Perovskite relaxor ferroelectrics free from lead', *J. Korean Phys. Soc.*, 1998 **32** S955-S956.
60. Ravez J. and Simon A., 'Non-stoichiometric perovskites derived from BaTiO<sub>3</sub> with a ferroelectric relaxor behaviour', *Phys. Stat. Solidi (a)*, 2000 **178** 793-797.
61. Kherfah A., Taibi K., Guehria-Laidoudi A., Simon A. and Ravez J., 'New oxyfluoride lead-free ferroelectric relaxors in the BaTiO<sub>3</sub>-BaZrO<sub>3</sub>-BaLiF<sub>3</sub> system', *Mater. Letters*, 2000 **42** 189-193.
62. Simon A. and Ravez J., 'New lead-free non-stoichiometric perovskite relaxor ceramics derived from BaTiO<sub>3</sub>', *Solid State Sci.*, 2004 **5** 1459-1464.
63. Ravez J. and Simon A., 'Spontaneous transition from relaxor to ferroelectric state in new lead-free perovskite ceramics', *Ferroelectrics*, 2000 **240** 313-320;
64. Ravez J., Von Der Mühl R., Simon A. and Sciau P., 'A perovskite ceramic of composition Ba<sub>0.92</sub>Ca<sub>0.08</sub>Ti<sub>0.75</sub>Zr<sub>0.25</sub>O<sub>3</sub> with both ferroelectric and relaxor properties', *J. Mater. Chem.*, 1999 **9** 2829-2832.

65. Comes R., Lambert M. and Guinier A., 'Chain structure of barium titanate and potassium niobate', *Solid State Comm.*, 1968 **6** 715–719.
66. Levanyuk A.P., Sigov A.S. and Sobyenin A.A., 'Modern problems in condensed matter sciences', in *Light Scattering Near Phase Transitions* Amsterdam (North Holland), editors H.Z. Cummins and A.P. Levanyuk, Ch. **3** Vol 5, 1983.
67. Vogt H., 'Hyper-Rayleigh scattering from the bulk of nominally pure potassium tantalate (KTaO<sub>3</sub>)', *Phys. Rev.*, 1990 **B 41** 1184–1193.
68. Vugmeister B.E. and Glinchuck M.D., 'Dipole glass and ferroelectricity in random-site electric dipole system', *Rev. Mod. Phys.*, 1990 **62**(4) 993–1026.
69. Ravez J. and Simon A., 'Lead-free relaxor ferroelectrics with TTB structure', *C. R. Acad. Sci.*, 2002 **5**(3) 143–148.
70. Ravez J. and Simon A., 'Solid state chemistry and non-linear properties in tetragonal tungsten bronze materials', *C. R. Chimie*, 2006 **9**(10) 1268–1276.
71. Ravez J., Perron-Simon A. and Hagenmuller P., 'Les phases de structure "bronzes de tungstène quadratiques"; règles cristallographiques et distorsions structurales', *Ann. Chim.*, 1976 **1** 251–268.
72. Woike T., Petricek V., Dusek M., Hansen N.K., Fertey P., Lecomte C., Arakcheeva A., Chapuis G., Imlau M. and Pankrath R., 'The modulated structure of Ba<sub>0.39</sub>Sr<sub>0.61</sub>Nb<sub>2</sub>O<sub>6</sub>. I. Harmonic solution', *Acta Cryst. B*, 2003 **59** 28–35.
73. Simon A., Ravez J. and Maglione M., 'The cross-over from a ferroelectric to a relaxor state in lead-free solid solution', *J. Phys. Condens. Matter*, 2004 **16** 963–970.
74. El Alaoui-Belghiti, Simon A., Elahtmani M., Reau J.M. and Ravez J., 'TKWB-type lead-free oxyfluoride relaxors derived from Ba<sub>2</sub>NaNb<sub>5</sub>O<sub>15</sub>', *Phys. Stat. Solidi (a)*, 2001 **187**(2) 549–556.
75. El Alaoui-Belghiti H., Von Der Mühl R., Simon A., Elahtmani M. and Ravez J., 'Relaxor or classical ferroelectric behaviour in ceramics with composition Sr<sub>2-x</sub>A<sub>1+x</sub>Nb<sub>5</sub>O<sub>15-x</sub>F<sub>x</sub> (A = Na, K)', *Mater. Lett.*, 2002 **55**(3) 138–144.
76. El Alaoui-Belghiti H., Simon A., Gravereau P., Villesuzanne A., Elahtmani M. and Ravez J., 'Ferroelectric and crystallographic properties of the Sr<sub>1-x</sub>K<sub>1+x</sub>Nb<sub>5</sub>O<sub>15-x</sub>F<sub>x</sub> solid solution', *Solid State Sci.* 2002 **4**(7) 933–940.
77. Ravez J., 'The inorganic fluoride and oxyfluoride ferroelectrics', *J. Phys. III*, 1997 **7** 1129–1144.
78. Von Der Mühl R. and Ravez J., 'Structure cristalline de BaNa<sub>2</sub>Nb<sub>5</sub>O<sub>14</sub>F', *Bull. Soc. Fr. Mineral. Cristallogr.*, 1975 **98** 118–120.
79. Ravez J., El Alaoui-belghiti H., Elahtmani M. and Simon A., 'Relations between ionic disorder and classical or relaxor ferroelectric behaviour in two lead-free TKWB-type ceramics', *Mater. Letters*, 2001 **47** 159–164.
80. Setter N. and Cross L.E., 'The role of B-site cation disorder in diffuse phase transition behavior of perovskite ferroelectrics', *J. Appl. Phys.*, 1980 **51** 4356–4360.
81. Gomah Pettry J.R., Salak A.N., Marchet P., Ferreira V.M. and Mercurio J.P., 'Ferroelectric relaxor behaviour of Na<sub>0.5</sub>Bi<sub>0.5</sub>TiO<sub>3</sub>-SrTiO<sub>3</sub> ceramics', *Phys. Stat. Solidi*, 2004 **241**(8) 1949–1956.
82. Bahri F., Khemakhem H., Simon A. and Ravez J., 'Classical or relaxor ferroelectric behaviour of ceramics with composition Ba<sub>1-x</sub>Bi<sub>2x/3</sub>TiO<sub>3</sub>', *Phys. Stat. Solidi (a)*, 2001 **184**(2) 459–464.
83. Shannon R.D., 'Revised effective ionic radii and systematic studies of interatomic distances in halides and chalcogenides', *Acta Cryst.*, 1976 **A32** 751–767.
84. Ravez J., Pouchard M. and Hagenmuller P., 'Chemical bonding and ferroelectric perovskite', *Eur. J. Solid State Inorg. Chem.*, 1991 **28** 1107–1123.

85. Smolenskii G.A., 'New seignettelectric substances', *Dokl. Akad. Nauk SSSR*, 1950 **70** 405–408.
86. Ravez J., Pouchard M. and Hagenmuller P., 'Chemical bonding, a relevant tool for designing new perovskite ferroelectric materials', *Ferroelectrics*, 1997 **197** 161–173.
87. Mitsui T. and Noumura S., *Ferroelectrics and Related Substances*, Landolt-Börnstein III Vol. **16**, Springer, Berlin 1981.
88. Viehland D., Jang S.J. and Cross L.E., Freezing of the polarization fluctuations in lead magnesium niobate relaxors', *J. Appl. Phys.*, 1990 **68(6)** 2916–2921.
89. Colla E.V., Yu Koroleva E., Nabereznov A.A. and Okuneva N.M., 'The lead magnesium niobate behaviour in applied electric field', *Ferroelectrics*, 1994 **151** 337–342.
90. Sommer R., Yushin N.K. and Van Der Klink J.J., 'Polar metastability and an electric-field-induced phase transition in the disordered perovskite lead magnesium niobium oxide ( $\text{PbMg}_{1/3}\text{Nb}_{2/3}\text{O}_3$ )', *Phys. Rev.*, 1993 **B 48** 13230–13237.
91. Stenger C.G.F. and Burgraaf A.J., 'Order–disorder reactions in the ferroelectric perovskite niobium oxide ( $\text{PbSc}_{1/2}\text{Nb}_{1/2}\text{O}_3$ ) and lead scandium tantalum oxide ( $\text{PbSc}_{1/2}\text{Ta}_{1/2}\text{O}_3$ ). II. Relation between ordering and properties', *Phys. Stat. Solidi (a)*, 1980 **61** 653–664.
92. Bahri F., Khemakhem H., Simon A., Von Der Mühl R. and Ravez J., 'Dielectric and pyroelectric studies on the  $\text{Ba}_{1-3a}\text{Bi}_{2a}\text{TiO}_3$ ', *Solid State Sci.* 2003 **5** 1235–1238.
93. Simon A. and Ravez J., 'Lead-free relaxors with TTB structure containing either lanthanum or bismuth', *Phys. Stat. Solidi a*, 2003 **199(3)** 541–545.

### 31.1 Introduction

Second harmonic generation (SHG) is described schematically in Fig. 31.1(a). A single pump wave, with fundamental frequency  $\omega$ , is incident on a nonlinear medium and generates a wave at the second frequency  $2\omega$ . Figure 31.1(b) illustrates the sum frequency generation (SFG). Two pump waves at frequencies  $\omega_{p1}$  and  $\omega_{p2}$  incident on a nonlinear medium combine to generate a wave at the sum frequency  $\omega_s = \omega_{p1} + \omega_{p2}$ . Third harmonic generation (THG) is obtained normally by two cascading  $\chi^{(2)}$  processes: SHG and SFG. Difference frequency generation (DFG), shown in Fig. 31.1(c) is similar to sum frequency generation, except that the two pump waves combine to produce a wave at the difference frequency  $\omega_d = \omega_{p1} - \omega_{p2}$ . The latter process is the same as that involved in optical parametric amplification and oscillation. Optical parametric



31.1 Schematic illustration of the frequency conversion and parametric processes discussed in this chapter. (a) Second harmonic generation (SGH). (b) Sum-frequency generation (SFG). (c) Difference-frequency generation (DFG). (d) Optical parametric process in which in pump photon of energy splits into two photons of signal and idler energy.



generation (OPG) is illustrated schematically in Fig. 31.1(d). A photon of frequency  $\omega_p$  is incident on a nonlinear medium and spontaneously splits into two lower-frequency photons. These are called the signal photon of frequency  $\omega_s$  and the idler photon of frequency  $\omega_i$ . This phenomenon is somewhat analogous to spontaneous Raman or Brillouin scattering with the exceptions that both particles created in the scattering are photons and not, for example, phonons. Another nonlinear  $\chi^{(2)}$  process is optical parametric amplification (OPA). A pump wave and a signal wave are incident on a nonlinear medium. Through the DFG process, the signal wave is amplified, and the idler wave is generated at the difference frequency. Basically the gain of an OPA is modest even for high pump intensities. The net gain can be increased by providing positive feedback of the signal. A convenient way of achieving this is to place the nonlinear crystal in a two-mirror resonator. When the optical parametric gain of the resonator exceeds its optical loss, oscillation occurs. Such a device is called an optical parametric oscillator (OPO). Above the threshold for oscillation, the signal and idler waves grow dramatically. It is well known that phase matching (PM) is necessary for efficient nonlinear processes (frequency conversion and parametric process). Three basic phase matching techniques are angle phase matching (scalar and vector), temperature phase matching and quasi-phase-matching (QPM). Armstrong *et al.* (1962) were the first to suggest ways to achieve QPM. The most common technique is described here. The nonlinear crystal is divided into segments each with a coherence length long. Each segment is then rotated relative to its neighbors by  $180^\circ$  about the axis of propagation. Such a structure with sign changing of nonlinear susceptibility is called dielectric superlattice (DSL) throughout this chapter.

Artificial superlattices are normally divided, according to their constituents, into several categories: semiconductor, metallic, dielectric, magnetic, etc. These new materials show many unusual properties, which are of fundamental interest in physics and have potential applications in microelectronics. For the past two decades, inspired by the success of the semiconductor superlattice and quasi-phase-matching (QPM) technique, the dielectric superlattice (DSL) has become a hot topic in material science and photoelectronics. It is expected that the material can provide a new means to control and manipulate light and ultrasound by means of its unique functions. As is well known, in dielectric crystals, the most important physical processes are the propagation and excitation of classical waves (optical and acoustic waves). The propagation of classical waves in a DSL (classical system) is similar to the electron motion in periodic potentials of crystal lattice (quantum system). Thus, some ideas in solid-state electronics, for example, the reciprocal space, Brillouin zone, dispersion relation, may be used in classical wave processes. On the other hand, DSL may consist of two kinds of dielectric materials or of dielectric and non-dielectric materials layer by layer alternatively, forming

so-called heterostructures. Most of them consist of the same kind of material, such as single ferroelectric crystals, in which the modulated structure is the ferroelectric domain. All physical properties associated with a third-rank tensor in such a superlattice will be modulated with the domain, whereas those associated with an even-rank tensor remain constant. It is the modulated physical properties that make the material different from the homogeneous single domain crystal, and specially favorable for applications in nonlinear optics and ultrasound.

In this chapter, an overview will be given of the studies on DSLs for nonlinear optical effects and acoustic devices. Since there are reviews of progress in periodic poling methods for second harmonic generation (SHG) (Houe and Townsend, 1995) and in QPM nonlinear interactions (Byer, 1997), much has been focused on the work done in our laboratory, especially on coupled nonlinear optical frequency conversion in quasi-periodic structures and the excitation of high-frequency ultrasound.

Preparation of DSLs can be realized by the modulation of microstructures, such as by the modulation of domain structures, phase structures, compositions, and by the modulation of crystallographic orientations and heteroepitaxy structures. The modern technology of crystal growth and micro-processing, the assembly of small dielectric spheres, the atomic-layer-controlled-epitaxy and heteroepitaxy (patterned growth by molecular beam epitaxy, metal-organic chemical-vapor deposition), or the use of acousto-optical effect, electro-optical effect or photorefractive effect make it possible to fabricate one-, two- and three-dimensional (1D, 2D, and 3D) DSLs. In the following sections we will describe the preparation of DSL by the modulation of ferroelectric domains and by photorefractive effect.

### **31.2 Preparation of DSLs by modulation of ferroelectric domains**

As mentioned above, most of a dielectric superlattice is fabricated by ferroelectric crystal, which is composed of  $180^\circ$  anti-parallel laminar domains. A variety of techniques for controlling domain patterns in ferroelectric crystals, either during or after growth, have been developed. Among them, growth striation technique (Feng *et al.*, 1980 and Ming *et al.*, 1982), field poling technique (Yamada *et al.*, 1993), electron writing (Ito *et al.*, 1991) and Corona poling are mainly used for bulk ferroelectric crystals, while chemical diffusion and substitution of impurities are used for waveguide materials (Webjorn *et al.*, 1989). In spite of making progress, many of these techniques remain semi-empirical in which the mechanisms of polarization reversal are poorly understood. Nevertheless, this does not prevent them from being practical methods to fabricate the various ferroelectric superlattices for different applications.

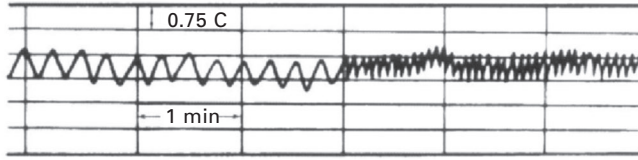
### 31.2.1 Growth striation technique

Fabrication of ferroelectric superlattice using the growth striation technique was first accomplished by Feng *et al.* (1980) and Ming *et al.* (1982) in a Czochralski system. The technique has been successfully used to grow  $\text{LiNbO}_3$  (LN) (Feng *et al.*, 1980 and Ming *et al.*, 1982),  $\text{LiTaO}_3$  (LT) (Feng *et al.*, 1986),  $\text{Ba}_2\text{NaNb}_5\text{O}_{15}$  (BNN) (Xu *et al.*, 1992), and TGS (triglycine sulphate) (Wang and Qi, 1986) superlattices. Feisst and Koidl (1985) and some other groups respectively, reported their works on fabricating LN superlattices using similar growth methods.

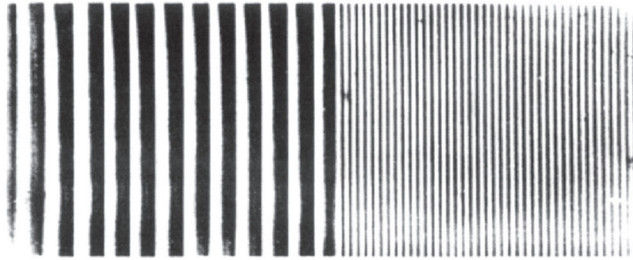
In the method the melt is doped with impurity, such as yttrium, indium or chromium for LN, with a concentration about 0.1 – 0.5 wt.% to control domain structure. Ming *et al.* (1982) found that a temperature fluctuation may be introduced into the solid–liquid interface, either through an off-axis rotation or through applying an alternating electric current. The temperature fluctuation causes a spatial modulation of the impurity or composition in crystal along the growth direction. The effect can form a space charge distribution, and in turn induce a local electric field in crystal. When cooling through the Curie point, the field plays a key role of causing *in situ* and local laminar domain. The modulated domain structure may automatically realize during the cooling process of crystal. Obviously the domain structures and the impurity distribution should have the equal period. The period or structure parameter of domain may be adjusted by choosing suitable pulling rate and rotation frequency or by changing the period of modulating electric current.

Figure 31.2 shows the measured temperature fluctuations at the solid–liquid interface (Fig. 31.2 (a)) and the formed growth striations (Fig. 31.2 (b)) for LN crystal. Ming *et al.* (1982) demonstrated the one-to-one correspondence between the growth striations and the laminar domain structure (Fig. 31.2(c) and (d)). The relationship between solute fluctuation and the ferroelectric domain structure has also been revealed with X-ray energy dispersive spectrum analysis. Figure 31.3 is the measured result of a LN crystal sample doped with yttrium. This figure shows domain walls are always situated at the places where the gradient of the Y dopant concentrations changes its sign from plus to minus or vice versa.

A significant progress was made by Magel *et al.* (1990), who used laser-heated pedestal growth to prepare an LN single crystal fiber. A domain pattern with 2–3.5  $\mu\text{m}$  period in the fiber of  $\sim 250 \mu\text{m}$  diameter was achieved by periodically modulating the heating power. The mechanism in the method is similar to that in the growth striation technique. Jundt *et al.* (1991) used a single crystal fiber with 1.24 mm in length and a 3.47  $\mu\text{m}$  domain period for a second harmonic green generation of 2 W from a 4 W, 1.064  $\mu\text{m}$  fundamental source. It was the first report of an LN superlattice being operated at average power at the watt level.

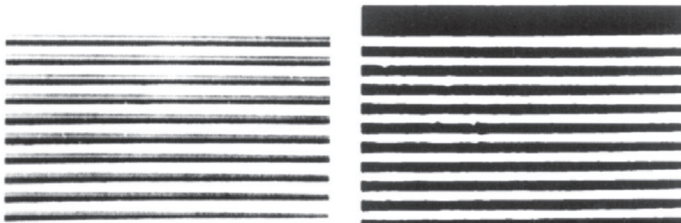


(a)



(b)

200 μm

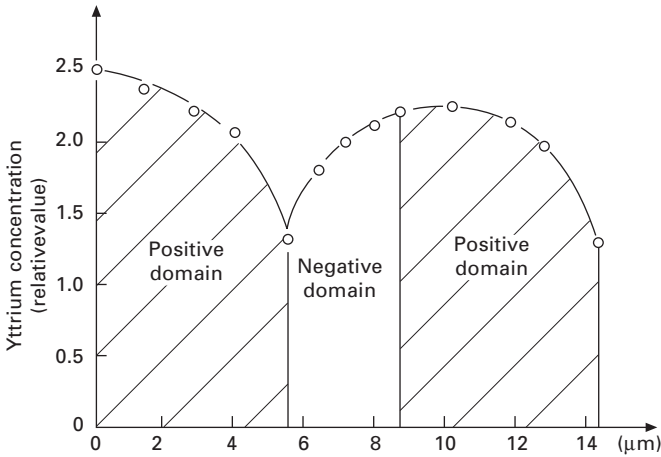


(c)

(d)

31.2 Temperature fluctuations measured on the solid–liquid interface (a) and the corresponding surface rotational growth striations in a LN crystal (b), while rotational rate was changed suddenly from 4 to 13 rpm in the experiment, surface rotational growth striations (c) and the corresponding interior laminar ferroelectric domain structures (d) (after Ming *et al.*, 1982).

An advantage of the growth striation technique is that the sample prepared has a large cross-section, which can avoid tight position alignment tolerance and results in a higher output in optical applications. Another advantage of the method is that it is easy to dope some laser active ions into the crystal during growth for the design of a multifunction laser device. Lu *et al.* (1996c) and Zheng *et al.* (1998) doped  $\text{Nd}^{3+}$  and  $\text{Er}^{3+}$  ions into the LN superlattice crystals, respectively. The nonlinear optical properties of substrate crystal and spectral properties of  $\text{Nd}^{3+}$  or  $\text{Er}^{3+}$  ions were combined in the same superlattice. The spectral structure (including absorption and fluorescence



**31.3** The yttrium concentration distribution and ferroelectric domain structures in rotational striations. The yttrium concentration measured using X-ray energy dispersive spectrum analysis, point by point, along the modulation direction of domain. It is worth noting the domain boundaries are situated at places where the gradient of yttrium concentration changes its sign (after Ming *et al.*, 1982).

spectra) of these superlattices is generally similar to those of doped crystals with single domain or glass fibers, verifying no obvious effect of domain wall for the excitation properties of doping ions.

### 31.2.2 Chemical diffusion

In 1979, Miyazawa (1979) discovered that the diffusion of element titanium (Ti) could give rise to the domain reversal on the  $+z$  surface of an LN crystal. Later, it was confirmed that proton or ion exchange followed by heat treatment could also produce domain reversal on the  $+z$  face of LN (Zhu Y.Y. *et al.*, 1995), and the  $-z$  faces of LT (Ahlfeldt, 1994) and  $\text{KTiOPO}_4$  (KTP) (Vanherzeel and Bierlein, 1992), respectively. Following these discoveries, the chemical diffusion and impurity ion exchange were exploited to fabricate the periodical domain reversal located within a few micrometers of the surfaces of the LN, LT and KTP crystals. These two methods were appropriate for guided wave interactions and surface acoustic wave devices. Their advantage is that the metal mask, defined by lithography, is deposited on the surfaces prior to Ti diffusion or proton exchange, which can lead to a well-defined domain period when domain reversal occurs. The disadvantage is that the shape of the reversed domain is either triangular (for Ti diffusion in LN) or semicircular (for proton exchange in LT). The shapes of reversed domains are not ideal for optical or acoustic applications; however, high conversion efficiencies were still obtained in waveguide devices due to long effective interaction length and tight confinement of beam in the geometry (Yamada *et al.* 1993).

A possible explanation to the domain reversal mechanism of Ti diffusion was given by Peuzin (1986) according to the earlier works of Thaniyavarn *et al.* (1985), Tasson *et al.* (1976) and Ming *et al.* (1982). Ming and Tasson had certified that an impurity concentration gradient in LN had the same poling property as an electric field (equivalent field). This mechanism might apply more generally for the chemical diffusion and heat treatment methods.

### 31.2.3 Electron beam writing

Electron beams have been used to induce a modulated domain structure in some ferroelectric crystals by writing on the negative polarity surfaces of these crystals directly. Keys *et al.* (1990) and Ito *et al.* (1991) first made progress in LN, whereafter, Hsu and Gupta (1992) in LT and Gupta *et al.* (1993) in KTP, respectively, using a scanning electron microscope (SEM). In a typical experimental geometry, the  $+c$  surface of the crystal was coated with 50–150 nm Au, Al, Cr or other metal film, and mounted on the SEM sample stage. The electron beam was focused and scanned on the uncoated  $-z$  face of the crystal. The acceleration voltage of the electron beam is sample dependent. It is 20–25 kV for a LN wafer with 0.5 mm thickness. The beam current and beam size fall on the surface of sample ranges within several pA–several nA and from 0.3–0.5  $\mu\text{m}$ , respectively, depending on the period of domain and scanning speed that is generally set from 0.02 to 0.1 mm/s. The penetration depth of the electron into treated samples depends on the electron energy and the nature of the material. It is estimated to be about a few micrometers for most ferroelectric crystals. The domain reversal can steadily extend across the sample wafer, under certain conditions, and the thickness can reach to 1 mm for LN crystal, which are several hundred times greater than the electron penetration depth. This method provides a domain wall perpendicular to the surface. The mechanism for the domain reversal by the electron beam is not very clear at this moment. However, a volume domain grating can be fabricated in the ferroelectric sample. LN, LT and KTP superlattices with period 3–7  $\mu\text{m}$  were fabricated by the method and highly efficient second harmonic green and blue lights were generated by the bulk and waveguide experimental geometry, respectively. Mizuuchi and Yamamoto (1994) reported that ion-beam writing induced the domain reversal in a LN or LT crystal wafer, and therefore can also be used to fabricate ferroelectric superlattices.

### 31.2.4 Electric field poling

Although electron and ion writing can be used in the fabrication of small periodic domain gratings, it is in practice limited by the slow writing speed and the complicated and expensive beam scan system. A definite goal for

practical applications is to find a technique that can mass-produce modulated domain materials at low cost. Yamada and his co-workers (Yamada *et al.*, 1993) realized a significant breakthrough along this direction. They successfully fabricated a periodic domain grating in a  $\sim 0.2$  mm thick LN thin wafer by applying a pulsed field at room temperature. The period of the domain structures was defined by the lithographically fabricated metal electrode. They also confirmed that the periodic electrode should be fabricated on the positive  $z$  face of LN, for the reversed domain nucleates more easily on the  $+z$  face than on the  $-z$  face. By using this technique, great progress has been made towards fabricating thicker samples as well as other ferroelectrics, such as LT, KTP and SBN. The details for field poling on LN, LT, KTP and SBN crystals at room temperature were described by Miller (1998), Zhu S.N. *et al.* (1995a,b), Rick and Lau (1996) and Zhu *et al.* (1998). In this method, the location of the reversed domains is defined by the lithographically fabricated electrode and the domain duty cycle is controlled by the spacing ratio of electrode and switch time  $t_s$ . The  $t_s$  should be selected according to the expression

$$Q = \int_0^{t_s} i dt = kP_s A$$

where  $Q$  is the total delivered charge,  $k$  a coefficient around 2.2–2.5 from experiential, and  $P_s$  and  $A$  are the spontaneous polarization and total area of reversed domain, respectively. If the period of a superlattice is  $\Lambda$  and the average width of the reversed domains is  $d$ , the duty cycle  $\rho = d/\Lambda$ . Miller (1998) proposed that domain reversal under periodic electrodes could be divided into several stages. First, domain nucleates along each strip electrode edges. Then, domain apex propagates toward the opposite face. Once the apex reaches the  $-z$  face, it extends rapidly and coalesces under the electrode and extends out of the area covered by electrode strips. The duty cycle of the domain is controlled by the electrode width, and amplitude and duration of the applied field. For small-period patterns ( $\Lambda < 10\mu\text{m}$ ), the width of the electrode is generally designed not to exceed  $\Lambda/4$  to avoid domain merging prior to coalescence and the field amplitude is set at the field with the value of highest nucleation site density. In conventional poling, in order to prevent the back-switching effect (Fatuzzo and Merz, 1967), the external field is ramped to zero over a duration of  $\sim$ several tens of milliseconds to stabilize the reversed domains, instead of removing it abruptly.

By far, most of the LN and LT superlattices are made of congruent composition crystals, because they are easy to grow and are available commercially with high quality and low price. Recent progress in the growth techniques makes it possible to grow LN and LT with stoichiometric properties. Gopalan *et al.* (1998) and Kitamura *et al.* (1998) found that the electric field for domain reversal in the stoichiometric crystals was much lower than that

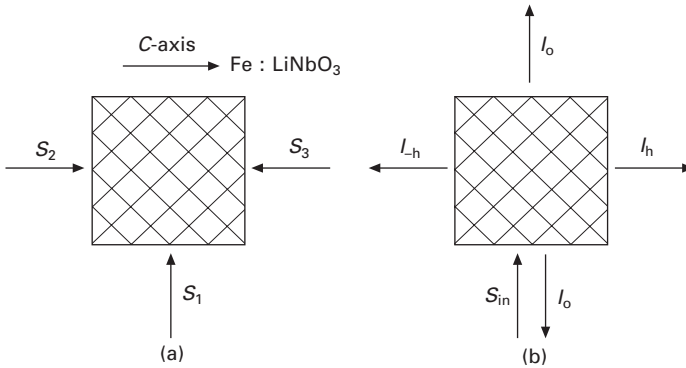
in the congruent crystals, and the values are about one-fifth for LN and one-thirteenth for LT, respectively. However, the spontaneous polarizations  $P_s$  and the Curie temperature were relatively insensitive to the non-stoichiometry. The internal fields in the congruent crystals, which were calculated from the asymmetry in the  $P_s$  versus electric field hysteresis, disappeared in stoichiometric crystals. These results further verify that the origin of the internal field and large changes in the poling fields of LN and LT appear to be largely dependent on the ratios of  $[\text{Li}]/[\text{Li}+\text{Nb}]$  and  $[\text{Li}]/[\text{Li}+\text{Ta}]$ , therefore, on non-stoichiometric point defects in these two crystals, respectively. Interest has been aroused about the stoichiometric crystals because lower poling field and better poling characteristic make them candidates for poling thicker samples (thicker than a few millimeters) to fabricate bulk devices for nonlinear optical application. Recently, Batchko *et al.* (1999) further improved the electric field poling technique that incorporates domain back-switching as a means for realizing high-fidelity short-period domain pattern essential for SHG of blue and ultra-violet (UV) light. A high-quality LT superlattice with period as short as  $1.7 \mu\text{m}$  was prepared for UV SHG (Mizuuchi *et al.*, 1997). LN (Burr *et al.*, 1997), SBN (Zhu Y.Y. *et al.*, 1997a,b) and KTP (Wang *et al.* 1998) superlattices with 1 mm thickness were fabricated successfully.

The superlattices with various domain gratings, such as chirped period (Loza *et al.*, 1999), quasi-period (Zhu S.N. *et al.*, 1997a,b; Zhu Y.Y. *et al.*, 1998), Thue-Morse structure and domain lens and prism array (Yamada *et al.*, 1996, Chiu *et al.*, 1996) were also fabricated using the above method. The poling properties of various doped LN, LT, SBN and KTP crystals have also been studied at room temperature and at low temperatures ( $\sim 170 \text{ K}$ ) (Rosenman *et al.*, 1998). These studies enable significant optimization of the process parameters.

### 31.3 Preparation of DSL by the photorefractive effect

Usually domain inversion does not change the dielectric constants of the material. In order to modulate the dielectric constants of DSL, other methods should be used, such as volume holographic record and thermal fixation. In this case, 1D, 2D or 3D DSL (or, say, photonic crystals) can be realized. In our experiments, we have used an oxidized Fe-doped LN (0.1 wt.% Fe) single domain crystal for the holographic recording. A beam of the blue line of an argon-ion laser is split into three nearly equal-intensity ones,  $S_1$ ,  $S_2$ , and  $S_3$ , which are recombined and interfered to cause spatial variations of the refractive index. Thus a 2D square periodic grating can be recorded into the crystal as shown in Fig. 31.4(a). The oxidized Fe : LN sample exhibits high resistance to relax and the grating remains stable after the writing beams are removed. If a beam of an argon-ion laser is split into four equal-intensity





31.4 (a) Optical geometry for recording a 2D refractive index grating into a Fe:LN single domain crystal. (b) Schematic diagram of four-wave diffraction.  $I_{in}$  is the incident wave satisfying the exact Bragg condition of four-wave diffraction.

ones and an  $S_4$  is applied parallel to the normal of the sheet of Fig. 31.4(b), a 3D cubic DSL may be formed (Xu and Ming, 1993a; Wang *et al.*, 1996a, b).

### 31.4 Application of DSLs in nonlinear parametric interactions

The concept of superlattice was initiated by Esaki and Tsu (1970). Since then, the study of superlattices has experienced three stages according to the symmetry of the superlattice. The first stage was began in the 1970s, which was devoted to the investigation of periodic superlattices. The second stage of the study of quasi-periodic superlattices was triggered by the discovery of quasi-crystals, with the periodic one still remaining a subject. The quasi-periodic structure is of increasing interest because it is intermediate between periodic and random. Recently, aperiodic and disorder structures have attracted considerable attention. Like semiconductor and metal superlattices, the structure of dielectric superlattices may be periodic, quasi-periodic, aperiodic and disorder, 1D or 2D, which show different physical properties.

#### 31.4.1 Wave vector conservation

Usually wave vector conservation plays an important role in interactions between electromagnetic waves and media, no matter whether the interactions are linear or nonlinear. One best known example is the Bragg condition in X-ray diffraction, where the wave vector conservation between the incident and diffracted X-rays is fulfilled with a reciprocal vector provided by the

crystal lattice. In optical range, more interesting phenomena exist related to the wave vector conservation.

In the linear interaction regime, when the light transmission in 1D DSL is considered, the Bragg condition is important for constructive interference to take place. The treatment can be extended to light transmission in 2D DSL. In that case, more than one Bragg condition, for example, two Bragg conditions can be fulfilled (Feng and Ming, 1989). It is noted that an X-ray can hardly satisfy two Bragg conditions at the same time in a crystal because the lattice periods are non-adjustable; whereas in 2D DSL, the reciprocal vectors can be adjusted to make the incident waves satisfy the two conditions simultaneously.

Among the nonlinear interaction regime, the most studied are optical frequency conversion and Kerr-form nonlinearity. The former one is related to the second-order nonlinear process, while the latter one is related to the third-order nonlinear process.

In the optical frequency conversion process, the wave vector conservation involves light waves with different wavelengths. In that case, the wave vector conservation is just the so-called phase-matching condition. In the SHG process, the phase mismatch between the fundamental and the second harmonic can be compensated either using the birefringence of the crystal (birefringence phase-matching (PM) method) or using the reciprocal vectors in DSL (QPM method). When optical bistability is discussed in 1D and 2D DSLs with Kerr-form nonlinearity, the situation becomes quite different. In 1D DSL, it is the change of the phase mismatch between the propagating wave vector and the reciprocal vector provided by the periodic structure that brings the incident wave from a forbidden transmission state to an allowed state, or from a low transmission state to a high transmission state. The bistability in 1D DSL is thus attributed to the phase-mismatch mechanism. Recent research work by present authors has revealed that a novel bistable mechanism, that is, the refractive index modulation (RIM) mechanism, which is characteristically different from the phase mismatch mechanism, exists in 2D DSL containing Kerr-form nonlinearity. It is well known that in 1D DSL the light transmission in the exact phase-matched condition (the incident wave vector satisfied the exact Bragg condition) corresponds to the forbidden state. However, in 2D DSLs, when the transmitting light satisfies the exact Bragg condition of multi-wave diffraction, whether the transmission state is located in the forbidden band or in the allowed band is determined by the value of a set of parameters which are defined as the RIM strengths of the 2D periodic structure. If the values of these parameters are arranged suitably, the light will propagate in the allowed band. Changes of these values will lead to high or low transmission states for each diffracted wave, since in the allowed band in the exact Bragg condition, the intensities of the multi-diffracted waves are oscillation functions of these parameters.

### 31.4.2 Nonlinear optical frequency conversion and optical parametric oscillation in 1D periodic DSL

Nonlinear optical frequency converters are attractive sources of coherent radiation in applications for which laser sources are unavailable or for which wide tunability is needed. One promising technique is QPM in periodic DSLs. A significant advantage of QPM is that any interaction within the transparency range of the material can be non-critically phase matched at any temperature, even the interactions for which birefringence phase matching is impossible (for example, LT crystals). Another benefit is that the interacting waves can be chosen so that coupling occurs through the largest element of the  $\chi^{(2)}$  tensor. In LN, QPM with all waves polarized parallel to the  $z$ -axis yields a gain enhancement over the birefringence phase-matched process of  $(2d_{33}/\pi d_{31})^2$ . Much work has been done on LN, LT, KTP, SBN and RbTiOAsO<sub>4</sub> (RTA) because of their large nonlinear optical coefficients. As early as 1980, we prepared for the first time a periodic DSL LN by the Czochralski method (Feng *et al.*, 1980). Later with the same method, we fabricated the first periodic DSL LT (Wang *et al.*, 1986). With these periodic DSLs, we verified the QPM theory proposed by Bloembergen *et al.* in 1962 (Armstrong *et al.*, 1962).

In 1985, Feisst and Koidl (1985) performed the experiment with LN DSL of less periods, prepared through the application of an alternating electric current during the growth process. Later, Magel *et al.* (1990) realized the blue light SHG in an LN fiber DSL. In 1990s, the QPM technique, spurred by the need for blue light laser sources for data storage, compact disk players, etc., has made great progress (Feng *et al.*, 1980; Yamada *et al.*, 1993; Miller *et al.*, 1997; Mizuuchi *et al.*, 1997; Zhu S.N. *et al.*, 1995a, b, 1997a, b; Byer 1994; Webjorn *et al.*, 1994; Chen and Risk, 1994; Myers *et al.*, 1995; Ito *et al.*, 1995; Karlsson *et al.*, 1996; Zheng *et al.*, 1998; Bierlein *et al.*, 1990; Arie *et al.*, 1998; Lu Y.Z. *et al.*, 1991, 1994, 1996a, b, c, d; Englander *et al.*, 1997; Myers *et al.*, 1996; Burr *et al.*, 1997; Missey *et al.*, 1998; Kartaloglu *et al.*, 1998; Reid *et al.*, 1997; Wang *et al.*, 1998; Karlsson *et al.*, 1996; Mizuuchi and Yamamoto, 1992; Hadi *et al.*, 1997; Arbore and Fejer, 1997; Serkland *et al.*, 1997; Kintaka *et al.*, 1997; Eger *et al.*, 1997; Arbore *et al.*, 1997; Reid *et al.*, 1998; Chou *et al.*, 1998; Landry and Maldonado, 1997; Qin *et al.*, 1998). A highly efficient QPM SHG has been demonstrated in LN DSL and KTP DSL in both continuous wave (CW) and pulsed regimes. For example, single-pass CW and quasi-CW SHG with efficiencies high as 42% (Miller *et al.*, 1997) and 65% (Pruneri *et al.*, 1996) were realized in LN DSLs, respectively. An internal conversion efficiency of 64% was achieved using a KTP DSL for single-pass SHG of high-repetition-rate, low-energy, diode-pumped lasers (Englander *et al.*, 1997). By placing a KTP DSL in an external resonant cavity, a conversion efficiency of 55% was obtained for a CW Nd : YAG laser. When used for optical parametric oscillator (OPO), DSLs show

advantages such as high gain, low threshold and engineerability of domain structures, thus making it possible to develop a robust, all solid-state, diode-pumped, miniaturized OPO (Myers *et al.*, 1996; Burr *et al.*, 1997; Missey *et al.*, 1998; Kartaloglu *et al.*, 1998; Reid *et al.*, 1997). For example, Batchko *et al.*, (1998) demonstrated a 532 nm CW pumped single-resonant OPO based on a 5.2 cm long first-order QPM LN sample with a 64% quantum efficiency and a threshold less than 1 W. With all these achievements, it is possible, by intracavity frequency doubling the outputs (signal and idler waves), to generate blue and red light for display applications. For more detailed discussions on the SHG and OPO with the DSL, interested readers are referred to a the review article by Byer (1997).

Usually, DSL LN and LT are limited to periods that are not very short and to thicknesses  $\leq 1$  mm because of the side growth of inverted domains. This inhibits the use of the DSL LN and LT in UV SHG and high-power pulsed OPOs. However, with the improvement of the poling technique and the use of new materials, this situation has been changed gradually. High-quality DSL LT with period as short as  $1.7 \mu\text{m}$  was prepared for UV SHG (Mizuuchi *et al.*, 1997). DSL LN (Burr *et al.*, 1997), SBN (Zhu Y.Y. *et al.*, 1997a, b) and KTP (Wang *et al.*, 1998) with 1 mm thickness were fabricated successfully. The low coercive field of RTA, which allows the poling of thick crystals (3 mm) (Karlsson *et al.*, 1996), together with its high damage threshold, low temperature dependence and high resistance to photorefractive damage, makes this material more suitable for high-power applications. Thus far in our laboratory, efficient pulsed SHG (including ns, ps and fs) has been obtained with periodic DSL LN, LT, SBN samples prepared by the room temperature poling technique (RTPT) or Czochralski method. We obtained experimental results for several samples by using a picosecond automatic tunable OPO as a fundamental source (Lu Y. L. *et al.*, 1996a). The CW 0.35 mW, 405 nm blue light and CW 1.34 mW, 489 nm blue light generations by directly doubling an 810 nm GaAlAs laser diode and a 978 nm InGaAs laser diode, respectively, have been reported (Lu Y. L. *et al.*, 1996a, b). Periodic DSL Nd : MgO : LN has been grown for self-frequency-doubling (Lu Y. L. *et al.*, 1996b). Visible dual-wavelength light generation through upconversion and QPM frequency doubling has been realized in erbium-doped periodic DSL LN (Zheng *et al.*, 1998).

### 31.4.3 Nonlinear optical frequency conversion in 1D quasi-periodic DSLs

Before 1984, research work on superlattices was mainly focused on periodic structures. The discovery of quasi-crystals has opened a new field in condensed matter physics and therefore attracted much attention (Steinhardt and Ostlund, 1997; Janot, 1992). Can this kind of material be of any practical use? It is well known that the key to QPM is to construct a 1D periodic structure that

provides a reciprocal vector to compensate the mismatch of wave vectors due to the dispersive effect of the refractive index. This 1D periodic structure can provide a series of reciprocal vectors, each of which is an integer times a primitive vector. In other words, the reciprocal vectors of a periodic DSL are determined by an integer and one structural parameter. It is the reciprocal vectors that make the optical parametric processes in the material phase matched. Compared with the periodic structure, a 1D quasi-periodic dielectric superlattice (QPDSL) has low space group symmetry, but its symmetry is higher than that of an aperiodic structure. Its reciprocal vectors are governed by two integers and two structural parameters rather than by one integer and one structural parameter as in the case of the periodic one. This fact makes the QPDSL more flexible in structure design. Therefore, a QPDSL can provide more reciprocal vectors to the QPM optical parametric process. Because of this, not only the QPM multi-wavelength SHG but also some coupled parametric processes, such as the third-harmonic generation (THG) and fourth-harmonic generation, can be realized with high efficiency (Feng *et al.*, 1990; Zhu and Ming, 1990, Zho Y.Y. *et al.*, 1997a, b, 1998; Qin *et al.*, 1999). This is an example of possible applications of quasiperiodic structure materials in nonlinear optics.

#### *The construction of QPDSL*

The QPDSL with Fibonacci sequence is constructed as follows. We first define two fundamental blocks A and B, which are arranged according to the production rule  $S_j = S_{j-1}S_{j-2}$  with  $j > 3$ ,  $S_1 = A$  and  $S_2 = AB$ . Each block is composed of one positive and one negative ferroelectric domain, so that the neighboring domains are interrelated by a dyad axis in the  $x$  direction. The thickness of the positive ferroelectric domain in blocks A and B are  $l_{A1}$  and  $l_{B1}$ , respectively. The thickness of the negative ferroelectric domain in block A is  $l_{A2}$  and that in block B is  $l_{B2}$ . Here,  $l_{A1}$  is chosen to be equal to  $l_{B1}$ , that is  $l_{A1} = l_{B1}$ . The details of the structure parameters can be seen in Fig. 31.5(a). The sequence of the blocks, ABAABABA . . . produces a QPDSL (see Fig. 31.5(b)).

The sample was fabricated by poling a  $z$ -cut LT single domain wafer at room temperature. In the sample of QPDSL for experiment, blocks A and B consist nominally of 11, 13  $\mu\text{m}$  and 11, 65  $\mu\text{m}$ , respectively. The sample is the 13 generation, 377 A and B blocks, with a total length of  $\sim 8$  mm and a thickness of  $\sim 0.5$  mm.

#### *Theoretical treatment of the nonlinear optical processes in QPDSLs*

Here, we consider a case in which a single laser beam with  $\omega_1 = \omega$  is incident from the left onto the surface of a QPDSL made from, for example, LN,



$$\begin{aligned} \kappa'_1 &= \frac{d_{33}}{2c} \sqrt{\frac{\omega_1^2 \omega_2}{n_1^2 n_2}} \\ \kappa'_2 &= \frac{d_{33}}{c} \sqrt{\frac{\omega_1 \omega_2 \omega_3}{n_1 n_2 n_3}} \\ \Delta k_1 &= k^{2\omega} - 2k^\omega \\ \Delta k_2 &= k^{3\omega} - k^{2\omega} - k^\omega \end{aligned}$$

Here  $f(x)$  can be Fourier transformed to (Birch *et al.*, 1990)

$$f(x) = \sum_{m,n} f_{m,n} \exp(iG_{m,n}x) \tag{31.3}$$

with the reciprocal vector

$$G_{m,n} = \frac{2\pi[m + \gamma(p)n]}{D} \tag{31.4}$$

and

$$f_{m,n} = \frac{2[1 + \gamma(p)]}{\gamma(p)l_A + l_B} \frac{\sin \frac{G_{m,n}(p)l}{2}}{\sin \frac{G_{m,n}(p)l}{2}} \frac{\sin(X_{m,n})}{X_{m,n}} \tag{31.5}$$

Here  $m$  and  $n$  are two integers and  $D = \gamma(p)l_A + l_B$ . In fact, only the Fourier component that is phase matched contributes significantly to the parametric interaction. If the non-phase-matched components are ignored, the coupled equations become:

$$\begin{aligned} \frac{dA_1}{dx} &= -2i\kappa_1 A_1^* A_2 \exp(-i\Delta k_1 x) - i\kappa_2 A_2^* A_3 \exp(-i\Delta K_2 x) \\ \frac{dA_2}{dx} &= -i\kappa_1 A_1^2 \exp(i\Delta k_1 x) - i\kappa_2 A_1^* A_3 \exp(-i\Delta K_2 x) \\ \frac{dA_3}{dx} &= -i\kappa_2 A_1 A_2 \exp(i\Delta K_2 x) \end{aligned} \tag{31.6}$$

with

$$\begin{aligned} \Delta K_1 &= k^{2\omega} - 2k^\omega - G_{m,n} \\ \Delta K_2 &= k^{3\omega} - k^{2\omega} - k^\omega - G_{m',n'} \end{aligned} \tag{31.7}$$

$$\begin{aligned} \kappa_1 &= f_{m,n} \kappa'_1 = \frac{d_{m,n}}{2c} \sqrt{\frac{\omega_1^2 \omega_2}{n_1^2 n_2}} \\ \kappa_2 &= f_{m',n'} \kappa'_2 = \frac{d_{m',n'}}{c} \sqrt{\frac{\omega_1 \omega_2 \omega_3}{n_1 n_2 n_3}} \end{aligned} \tag{31.8}$$

The equation can be solved analytically for the boundary conditions of  $A_2(0) = 0$  and  $A_3(0) = 0$  under a small signal approximation:

$$\begin{aligned}
 A_2 = & -\frac{\Delta k_2 + \sqrt{\Delta k_2^2 + 4\kappa_2^2 A_1^2}}{2\kappa_2 A_1} C_1 \exp\left[-i\frac{1}{2}(\Delta k_2 - \sqrt{\Delta k_2^2 + 4\kappa_2^2 A_1^2})L\right] \\
 & -\frac{\Delta k_2 - \sqrt{\Delta k_2^2 + 4\kappa_2^2 A_1^2}}{2\kappa_2 A_1} C_2 \exp\left[-i\frac{1}{2}(\Delta k_2 + \sqrt{\Delta k_2^2 + 4\kappa_2^2 A_1^2})L\right] \\
 & -\frac{\kappa_1 A_1^2 \Delta k_3}{\Delta k_1 \Delta k_3 - \kappa_2^2 A_1^2} \exp(i\Delta k_1 L)
 \end{aligned} \tag{31.9}$$

$$\begin{aligned}
 A_3 = & C_1 \exp\left[i\frac{1}{2}(\Delta k_2 + \sqrt{\Delta k_2^2 + 4\kappa_2^2 A_1^2})L\right] \\
 & + C_2 \exp\left[i\frac{1}{2}(\Delta k_2 - \sqrt{\Delta k_2^2 + 4\kappa_2^2 A_1^2})L\right] \\
 & + \frac{\kappa_1 \kappa_2 A_1^3}{\Delta k_1 \Delta k_3 - \kappa_2^2 A_1^2} \exp(i\Delta k_3 L)
 \end{aligned} \tag{31.10}$$

with 
$$C_1 = -\frac{\kappa_1 \kappa_2 A_1^3}{\Delta k_1 \Delta k_3 - \kappa_2^2 A_1^2} \frac{\Delta k_1 + \Delta k_3 + \sqrt{\Delta k_2^2 + 4\kappa_2^2 A_1^2}}{2\sqrt{\Delta k_2^2 + 4\kappa_2^2 A_1^2}}$$

and 
$$C_2 = \frac{\kappa_1 \kappa_2 A_1^3}{\Delta k_1 \Delta k_3 - \kappa_2^2 A_1^2} \frac{\Delta k_1 + \Delta k_3 - \sqrt{\Delta k_2^2 + 4\kappa_2^2 A_1^2}}{2\sqrt{\Delta k_2^2 + 4\kappa_2^2 A_1^2}}$$

$$\Delta k_3 = \Delta k_1 + \Delta k_2$$

where  $L$  is the length of crystal.

Under the QPM conditions

$$\Delta K_1 = k^{2\omega} - 2k^\omega - G_{m,n} = 0 \tag{31.11}$$

$$\Delta K_2 = k^{3\omega} - k^{2\omega} - k^\omega - G_{m',n'} = 0$$

Equations (9) and (10) can be simplified to

$$\begin{aligned}
 A_2 = & i\kappa_1 A_1^2 L \sin c(\kappa_2 A_1 L) \\
 A_3 = & -2\kappa_1 \kappa_2 A_1^3 L^2 \sin c^2\left(\frac{1}{2}\kappa_2 A_1 L\right)
 \end{aligned} \tag{31.12}$$

Using the following relation, we can get the harmonic intensity:

$$I_1 = \frac{1}{2} \sqrt{\frac{\varepsilon_1}{\mu_1}} \omega_1 |A_1|^2 \tag{31.13}$$

If the  $\kappa_2 A_1 L$  is very small, then we can get the conversion efficiency:

$$\eta_2 = \frac{8\pi^2 d_{m,n}^2 L^2}{n_1^2 n_2 c \varepsilon_0 \lambda^2} I_1$$



$$\eta_3 = \frac{144\pi^4 d_{m,n}^2 d_{m,n}'^2 L^4}{n_1^3 n_2^2 n_3 c^2 \epsilon_0^2 \lambda^4} I_1^2 \tag{31.14}$$

Usually under the small signal approximation, the second harmonic generated through the second-order nonlinear process and the third harmonic generated through the third-order nonlinear process are proportional to  $L^2$ . Here because of the coupling effect between the SHG and sum frequency generation (SFG) processes, the third harmonic generated through the second-order nonlinear process is proportional to  $L^4$ . Thus it is possible to obtain THG in a QPDSL with high efficiency. In addition, it can be seen clearly that the effective nonlinear optical coefficients play an important role in nonlinear parametric processes. Thus it is helpful to derive the expression for the effective nonlinear optical coefficients.

*Effective nonlinear optical coefficients*

For QPM SHG in a periodic DSL, the conversion efficiency is proportional to the square of the effective nonlinear optical coefficient, which is represented by

$$d_n = \frac{2d_{33}}{n\pi} \sin\left(n\pi \frac{l}{\Lambda}\right)$$

with  $l$  the length of the reverse domain (Fejer *et al.*, 1992).  $n = 1$  corresponds to the first-order QPM with the largest conversion efficiency. For QPM THG in a QPDSL, the situation becomes much more complex. In order to see the relationship, it is needed to obtain the expression of the effective nonlinear optical coefficient for QPDSL.

For the QPDSL, the modulated nonlinear coefficient  $d(x) = d_{33}f(x)$ . Then the effective nonlinear coefficient is

$$d_{m,n} = d_{33} f_{m,n} = d_{33} \frac{2[1 + \gamma(p)]}{\gamma(p)l_A + l_B} \frac{\sin \frac{G_{m,n}(p)l}{2}}{\sin \frac{G_{m,n}(p)l}{2}} \frac{\sin(X_{m,n})}{X_{m,n}} \tag{31.15}$$

where  $X_{m,n} = \pi D^{-1} [1 + \gamma(p)](ml_A - nl_B)$ . Obviously the value of  $d_{m,n}$  depends strongly on the adjustable structure parameters such as  $l$  and the ratio  $l_A/l_B$ . Note that when  $p = 1$ , the result is just one for the Fibonacci sequence. When  $l_A = l_B$ , the QPDSL turns back to a periodic DSL and  $d_{m,n}$  reduces to  $d_n = \frac{2d_{33}}{n\pi} \sin\left(n\pi \frac{l}{\Lambda}\right)$  with  $m = n$ , the effective nonlinear coefficient for the periodic DSL.

***QPM multi wavelength SHG*** (Zhu and Ming, 1990; Zhu S. N. et al., 1997b; Qin et al., 1999)

To verify the theoretical predictions, two types of QPDSL have been fabricated: one with  $p = 1$ , the so-called Fibonacci type, and the other one a generalized QPDSL with  $p = 2$ . The sample was fabricated by poling a z-cut LT single domain wafer at room temperature (Zhu S. N. et al., 1995a,b). The SHG spectrum of the QPDSL LT was measured with the fundamental tuned in the infrared. With the QPDSL samples, we obtained QPM second harmonic blue, green, red and infrared light output with conversion efficiencies up to ~5–20%. The measured and calculated results are in good agreement.

It is theoretically predicted and experimentally observed that the X-ray diffraction and Raman spectra of quasi-periodic superlattice exhibit self-similarity. However in the SHG spectra of the QPDSL, careful analysis of the measured spectrum show that the self-similarity no longer holds. This is due to the dispersive effect of the refractive index, although the reciprocal vector does in reciprocal space.

As pointed out, here the QPM multi-wavelength SHGs are wholly determined by the distribution of the reciprocal vectors of the QPDSL. Therefore with the aid of Fourier transformation, arbitrary wavelength-response functions can be obtained by design of appropriate DSL (Chou et al., 1999). The QPM structures with multiple phase-matching wavelengths can be used for wavelength-division-multiplexed wavelength conversion. Using the SH spectra obtained in QPDSL either with  $p = 1$  or  $p = 2$ , the dispersion relationship of the refractive index has been deduced (Zhu S. N. et al., 1997b; Qin et al., 1999).

***Direct third-harmonic generation*** (Feng et al., 1990; Zhu S. N. et al., 1997a; Zhu Y. Y. et al., 1998; Qin et al., 1999)

THG has a wide application as a means to extend coherent light sources to short wavelengths. The creation of the third harmonic directly from a third-order nonlinear process is of little practical importance because of the intrinsic low third-order optical nonlinearity. Conventionally, an efficient THG was achieved by a two-step process. Two nonlinear optical crystals are needed: the first for SHG and the second for SFG. In this regard, QPDSL has some advantages over the conventional method. Here only one crystal is needed and the harmonic generation can be realized using the largest nonlinear optical coefficient over the entire transparency range of the material with high efficiency. For the QPDSL, the QPM conditions for THG in a collinear interaction are given by equation 11. THG was tested with a tunable optical parametric oscillator. Several THGs have been detected; however, only one TH has a high conversion efficiency (>20%). Others are very weak. Theoretical

analysis has shown that the THG can be generated through the nearly QPM SFG with the SHG either QPM or mismatched. However, an efficient third harmonic can be generated only when both the SHG and SFG processes are quasi-phase matched. Recently, QPM THG has been demonstrated using a simple silica structure of six modulation periods through cubic nonlinearity ( $\chi_{ijkl}$ ) (Williams *et al.*, 1998). CW frequency tripling by simultaneous three-wave mixings has been realized in an LN crystal (Pfister *et al.*, 1997). In an LN waveguide, ultraviolet THG of 355nm has been observed (Kintaka *et al.*, 1997). With the aid of RTPT, we have performed a systematic study on QPDSL SBN related to SHG and THG (Zhu S. N. *et al.*, 1997a, b; Zhu Y. Y. *et al.*, 1998).

#### 31.4.4 Nonlinear optical frequency conversion in 2D DSLs

In 1998, Berger (Berger, 1998) extended the QPM study from 1D to 2D, and proposed the concept of an  $\chi^{(2)}$  photonic crystal in order to contrast and compare it with a regular photonic crystal having a periodic linear susceptibility. In a configuration proposed by Berger, a crystal has a 2D periodic modulation of nonlinear susceptibility, and a linear susceptibility that is a function of the frequency, but constant in space. It is an in-plane generalization of 1D QPM structures and can be realized in periodic poled LN or in GaAs. An interesting property of these structures is that new phase-matching processes appear in the 2D plane as compared with the 1D case. It is shown that these in-plane phase-matching resonances are given by a nonlinear Bragg law (Berger, 1998):

$$\lambda^{2\omega} = \frac{2\pi}{|G|} \sqrt{\left(1 - \frac{n^\omega}{n^{2\omega}}\right)^2 + 4 \frac{n^\omega}{n^{2\omega}} \sin^2 \theta} \quad 31.16$$

where  $\lambda^{2\omega}$  is the SH wavelength inside the material and  $2\theta$  the walk-off angle between  $k^{2\omega}$  and  $k^\omega$ . More generally, this equation gives the direction of coherent radiation at the wavelength  $\lambda^{2\omega}$  for a phased array of nonlinear dipoles having a phase relation fixed by the propagation of the pump. Nonlinear Bragg law is a generalization for nonlinear optics of the Bragg law. It gives the direction of resonant scattering at the wavelength  $\lambda^{2\omega}$  of a plane wave with vector  $k^\omega$  by a set of nonlinear dipoles. Since then, the concept of a  $\chi^{(2)}$  photonic crystal has been gradually accepted in the nonlinear optics community. Actually  $\chi^{(2)}$  photonic crystals can also be called 2D DSLs when  $\chi^{(2)}$  modulation is obtained by ferroelectric modulation in the 2D system. Recently several novel classes of nonlinear optical effects in 2D DSLs were discovered by researchers, such as second-order SHG in 2D square poled LN, tunable SHG in a tetragonal poled LN, and higher-order harmonic generation with cascaded

process in a hexagonally poled LN. In addition, in 2D DSLs, generation of a flat-top second-harmonic beam and nonlinear optical diffraction with transversely patterned QPM gratings have been realized by Fejer's group (Kurz *et al.*, 2002). Baudrier-Raybaut *et al.* (2004) investigated continuous SHG in 2D random domain structures.

In our laboratory, Xu *et al.* (2004) reported a novel nonlinear optical phenomenon – a conical second-harmonic (SH) beam, generated from 2D DSLs – a hexagonally poled LiTaO<sub>3</sub> (HPLT) crystal. The conical SH beam emerged when the HPLT was illuminated with a *z*-polarized fundamental beam with no special requirements. The conical beams were visualized as rings when projected onto a screen behind the crystal, and were presented in axial symmetry or mirror symmetry when the fundamental beam propagated along a symmetrical axis of the hexagonal structure. This reveals the presence of another type of nonlinear interaction – a scattering involved optical parametric generation. The interaction is greatly enhanced by a QPM process in the 2D DSLs; thus, the infrared scattering signal ( $\omega$ ) is converted to the visible band ( $2\omega$ ) through mixing with the incident wave ( $\omega$ ). Further study confirms that the conical beam records the spatial distribution of the scattering signal and reveals the structure information of the 2D DSLs.

The QPM approach can enhance not only the elastic scattering signal intensity but also the inelastic scattering signal intensity in a nonlinear medium. Raman scattering, as a sort of inelastic scattering, is always accompanied by frequency change. Raman scattering can be mediated by many different types of elementary excitations in a medium, such as transverse optical phonons, phonon polaritons or plasmons. Compared with elastic scattering, Raman scattering is much weaker, which is possibly enhanced by the QPM process in a  $\chi^{(2)}$  modulated medium. Xu *et al.* (2005) reported the experimental studies on QPM enhanced phonon–polariton (P–P) Raman scattering in artificial microstructure – an HPLT crystal. The QPM approach was first operated to generate two laser beams to drive an intense coherent (P–P) field in the HPLT crystal and was then used to amplify the generated Raman signals by parametric amplification, which resulted in the generation of a stimulated P–P Raman scattering. The anti-Stokes and Stokes spectrum with very low Raman shift down to  $2\text{cm}^{-1}$  and very high scattering order up to the 11th rank was detected from the medium. The resulting spectrum exhibits a comb-shaped structure with an equal frequency interval tunable by changing the frequency of excited polariton. The QPM approach was successfully introduced into the 2D DSLs medium for enhancement of inelastic scattering.

### 31.5 Application of DSLs in acoustics

It was well known that for an unpoled ferroelectric crystal, the resonances at low frequencies, which are related to the geometry and dimensions of the

measured sample, are absent. Only the resonance at a very high frequency, which is related to the domain structure in the sample, is observed. The position of the resonant peak and its bandwidth depend on the sizes of domains and their size distribution. For a single domain ferroelectric crystal, only the low frequency resonance related to the geometric sizes of the sample and its high-order harmonics can be detected, whereas high frequency resonance is absent. All resonances in a ferroelectric material, whether poled or unpoled, originate from the domains and are excited through piezoelectric effect. In a ferroelectric superlattice, piezoelectric coefficient  $h_{ijk}$ , as a third-rank tensor, is a periodic or quasi-periodic function of spatial coordinates, depending on the array of domains. The modulation of piezoelectric coefficient can result in some novel acoustic effects. It is the reason why ferroelectric superlattice sparks so much interest in the ultrasonic field. Since 1988 Zhu *et al.* (1988) have systematically studied the excitation and propagation of elastic waves in DSL and successfully fabricated various DSL devices (Zhu *et al.*, 1996). Owing to piezoelectricity, the discontinuity of the piezoelectric stresses at the domain walls may be produced under the action of an external electric field. The stress must be balanced by a strain  $S(u_m)$ , where  $u_m$  ( $m = 1, 2, \dots$ ) represent the positions of the domain walls. If the external field is an alternating field, the strain can propagate as an elastic wave:

$$S(u) = S(u_m) \cos(\omega t - ku) \quad 31.17$$

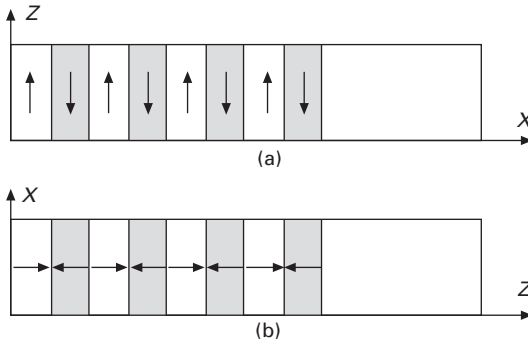
where  $\omega$ ,  $k$  and  $t$  are the angle frequency, wave vector and time, respectively. Every domain wall can be viewed as a  $\delta$  sound source. All domain walls in a DSL are arranged in a certain sequence forming an array. The elastic waves excited by this  $\delta$  sound source array will interfere with each other when certain frequency conditions are satisfied. Those satisfying the condition for constructive interference will appear as resonances. This is the physical basis for the ultrasonic excitation in DSL.

### 31.5.1 High-frequency resonance in DSLs

As an example, considering the case of Fig. 31.6 (b), an alternating voltage is applied on the  $z$  faces of the superlattice, thus a longitudinal planar wave propagating along the  $z$ -axis will be excited inside the sample. This situation is described by the wave equation:

$$\frac{\partial^2 u_3}{\partial z^2} - \left(\frac{1}{v^2}\right) \frac{\partial^2 u_3}{\partial t^2} = \left(\frac{2h_{33}D_3}{C_{33}^D}\right) \sum_m \delta(Z - Z_m) \quad 31.18$$

where  $u_3$  represents the particle displacement along the  $z$  direction,  $v$  is the velocity of sound,  $h_{33}$  and  $C_{33}^D$  are the piezoelectric and elastic coefficients, respectively, and  $D_3$  is the component of the electric displacement along the  $z$ -axis.



31.6 Periodic superlattice with the spontaneous polarization modulated along (a) the x-axis and (b) the z-axis.

For a DSL with periodic domain structure, by using the Green’s function method to solve the elastic wave equation, the electric impedance of the DSL can be derived, and then the resonance frequency can be obtained as follows:

$$f_n = \frac{n \cdot v}{(a + b)}, \quad n = 1, 2, 3, \dots \tag{31.19}$$

where  $v$  is the velocity of the longitudinal wave propagating along the  $z$ -axis,  $a$  and  $b$  are the thickness of positive and negative domains, respectively, and  $a + b$  is the period  $\Lambda$  of the DSL. It is obvious that the resonance frequency is determined only by the period of the DSL, i.e.  $a + b$ , not by the total thickness of the wafer. The thinner the laminar domains, the higher the resonance frequencies. As we know, the thickness of a resonator working at several hundred MHz is about several micrometers. An ordinary material with such a thickness is too thin to be fabricated by current mechanical processing methods and too thick to be deposited by film growth techniques. However, it is easy to grow by the Czochralski method (Zhu and Ming *et al.*, 1992a) or fabricated by poling (Chen *et al.*, 1997). In practice, a domain period with several micrometers has been achieved by using these two methods, which corresponds to resonance frequencies of hundreds MHz to several GHz (Zhu and Ming, 1992b).

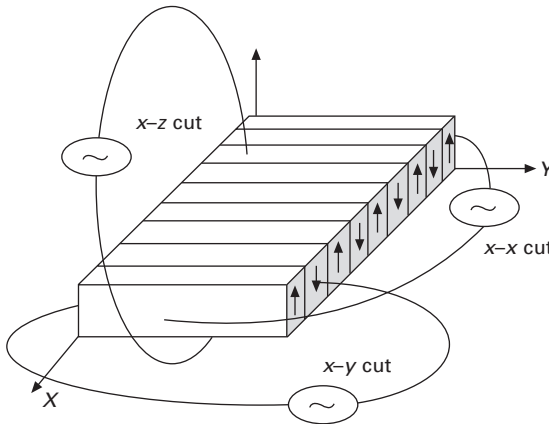
For a DSL with domain configuration like Fig. 31.6 (a), acoustic waves can be excited through two different schemes. One is an in-line scheme with the acoustic propagation vector parallel to the applied electric field. The other is a cross-field scheme, which is characterized by an electric field perpendicular to the propagation vector. A schematic diagram of the two kinds of schemes is shown in Fig. 31.7. Zhu and Ming (1992b) studied the two kinds of acoustic excitations in a DSL theoretically and Chen *et al.* (1997) experimentally confirmed their theory in the DSLs based on LT superlattices and fabricated a set of resonators operating in the range of several hundreds MHz. The devices made of DSLs can be divided into two

categories, resonator and transducer types, depending on their boundary conditions. For resonator, both electrode faces of DSL are free, whereas for transducer, one face is fully matched to a transmission medium. The insertion loss of transducer is an important parameter for an acoustic device. For transducers made of homogeneous piezoelectric materials, such as a single-domain LN wafer, the static capacitance is the main part of the impedance at the resonance frequency under high-frequency operation. As a result, the insertion loss of the transducer is very high. In DSL case, the impedance of transducer may be adjusted by choosing the number of periods  $N$  and the area of the electrode face  $A$ . As a example, an insertion loss of near 0 dB at 555 MHz was achieved in a  $50\ \Omega$  measurement system (Zhu *et al.*, 1988).

Acoustic excitation and propagation in a quasi-periodic superlattice have been studied both theoretically and experimentally (Zhu *et al.*, 1989). The excitation spectrum in a Fibonacci superlattice is expressed by the following equation:

$$H(k) \propto \sin(kL/2) \sum (\sin X_{m,n}/X_{m,n}) \delta\{k - 2\pi(m + n\tau)/D\} \quad 31.20$$

where  $X_{mn} = \pi\tau(m\tau - n)/(1 + \tau^2)$  and  $\tau = (1 + \sqrt{5})/2$  the golden mean. The self-similarity of the Fibonacci sequence in the reciprocal space was experimentally confirmed by the acoustic excitation spectrum.



31.7 A schematic diagram of the ultrasonic excitation in an acoustic superlattice made of a LT crystal in which the domains are arranged periodically along the  $x$ -axis, and the spontaneous polarization directions of these domains are parallel to the  $z$ -axis. The excitation by the electrodes coated on the  $x$  faces ( $x$ - $x$  cut) corresponds to the in-line scheme, while electrodes coated on the  $y$  faces ( $x$ - $y$  cut) and the  $z$  faces ( $x$ - $z$  cut) excite acoustic waves by the cross-field scheme (after Chen *et al.*, 1997).

### 31.5.2 Polariton excitation in DSLs

In a real crystal, coupling exists among the motions of electrons, photons and phonons. For example, infrared absorption and polariton excitation result from the coupling between lattice vibrations and electromagnetic waves in an ionic crystal. It is expected that the same coupling may occur in artificial materials with modulated domain structures. Lu Y. Q. *et al.* (1999b) considered the case of a ferroelectric superlattice with the ‘head to head’ configuration (Fig. 31.6(b)). This structure is similar to a 1D diatom chain with positive and negative ‘ions’ connected periodically. They called the superlattice an ionic-type phononic crystal (ITPC) and expected that a polariton excitation might occur in it.

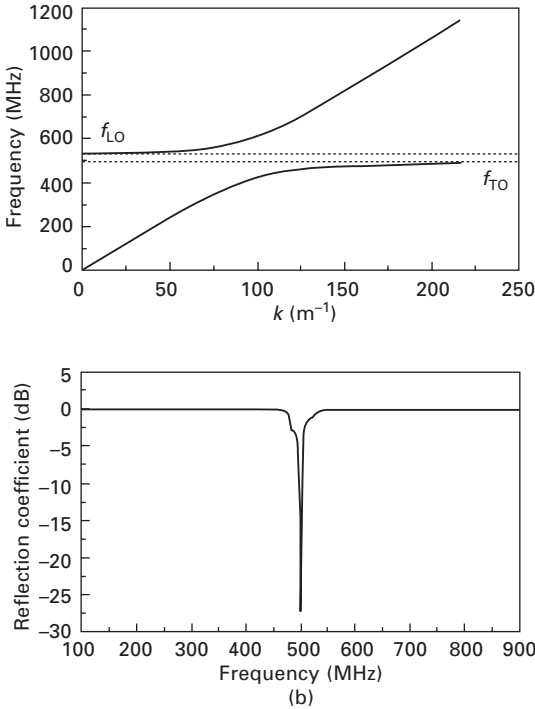
In a real ionic crystal, the polariton excitation originates from the coupling of electromagnetic wave and the lattice vibration of crystal, appearing within the infrared region. In an ITPC, this excitation may originate from the coupling between the superlattice vibration and electromagnetic wave. The piezoelectric effect leads to the vibration of superlattice when there is external electromagnetic field. The vibration frequency depends on the period and material constants of superlattice, so the polariton excitation in such a ferroelectric superlattice is expected to occur in the microwave region.

To verify the prediction, Lu Y. Q. *et al.* (1999b) prepared a LN superlattice with a period of  $7.2\mu\text{m}$  and a ‘head to head’ configuration by the growth striation method, and calculated its polariton dispersion curve. The measurement of dielectric spectrum confirmed that there was a gap between the calculated  $f_{\text{T0}}$  and  $f_{\text{L0}}$  where  $\epsilon < 0$  (Fig. 31.8), where an incident electromagnetic wave would be strongly reflected. The measured reflection coefficient as a function of frequency showed that there was an absorption peak ( $\sim 26$  dB) at 502 MHz. The results verified there was a polariton mode in the measured sample indeed. According to the above results, one can expect that other long-wavelength optical properties (such as Raman and Brillouin scattering) in a real ionic crystal also exist in such a ferroelectric superlattice. The only difference is that they occur in different frequencies, one in the infrared region (THz) and the other one in the microwave region (GHz).

## 31.6 Application of DSLs in electro-optic technology

In the linear optics regime, physics effects in a ferroelectric superlattice mainly involved in modulated electro-optic coefficient  $r_{ijk}$ . As a third-rank tensor, its elements have opposite signs in a positive and a negative domain. In the presence of an external field along some axis of the crystal, the modulation of electro-optic coefficient will accordingly lead to the modulation of refractive index, or the alternating rotation of the principle axis due to the

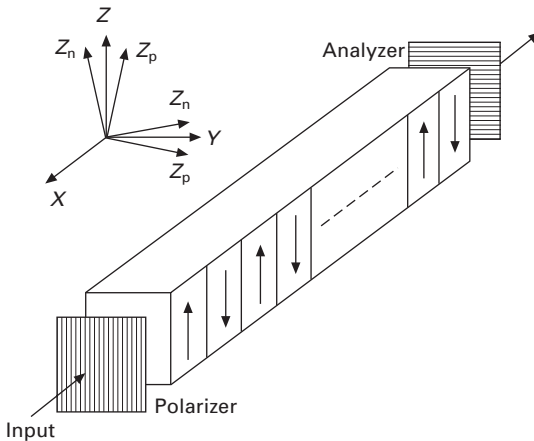




31.8 (a) Calculated polariton dispersion curve of an ionic-type phononic crystal with the period of 7.2 mm without consideration of damping. There is a frequency gap between  $f_{LO}$  and  $f_{TO}$  where no EM waves are permitted to propagate in the sample. (b) The measured reflection coefficient of the sample in the microwave band. The minimum of the reflection coefficient indicates that there is a strong microwave absorption peak at 502 MHz (after Lu *et al.*, 1999).

deformation of the refractive index ellipsoid in the superlattice. Lu *et al.* (2000) and Zhu and Ming (1992a) studied the electro-optic effects and the transmission spectra in a periodic and a quasi-periodic LN superlattice, respectively. Figure 31.9 shows the electro-optic effect in a LN superlattice. The electrodes are coated on the  $y$  surfaces of the superlattice. In the absence of an external electric field, the principal axes of the positive domains overlap with those of the negative domains and the dielectric tensor has only diagonal components with respect to the principal axes. The superlattice is homogeneous to the propagation of light in the linear optics regime. There is no refractive index modulation accompanying the domain modulation. In the presence of an external electric field, however, the dielectric tensor is perturbed because of the electro-optic effect, which results in a small dielectric modulation along the propagation direction of light. The new dielectric principal axes may no longer overlap because new off-diagonal components appear in their

original dielectric tensors. The new principal axes rotate from the original principal axes by an angle with opposite signs in positive and negative domains, respectively. The angles depend on the applied external field. In Fig. 31.9, the initial condition at  $x = 0$  which is determined by the polarizer is given by  $E_y(0) = 0$  and  $E_z(0) = 1$ , where  $E_y$  and  $E_z$  are the mode amplitudes for  $y$ -polarized and  $z$ -polarized light, respectively. According to the coupled-mode theory, Lu *et al.* (2000) and Zhu and Ming (1992a) considered the coupling effect of light beams with orthogonal polarization in a periodic and a quasi-periodic superlattice, respectively. They found that the energy could be transferred back and forth between these two orthogonal modes in this electro-optic system. At the analyzer ( $y$ -polarized), i.e.  $x = L$  (which is directly related to the number of domain blocks),  $E_z$  is extinguished, and the transmission of the  $y$ -component is wavelength dependent and is controllable by an applied electric field. Their results verify that the periodic and quasi-periodic superlattices are similar to adjustable Solc filters. Moreover, Lu *et al.* (2000) proposed an electro-optic tuning scheme to tune the output frequency of a QPM OPO. Compared to temperature tuning, the electro-optic tuning provides a faster response. The tuning rate was expected to exceed 3 nm/kV/mm. Recently Lu *et al.* (2000) proposed a high-frequency traveling-wave integrated electro-optic modulator based on a periodically poled LN. The traveling velocity of the optical wave and the electrical wave velocity in the waveguide can be quasi-matched due to the periodic structure. Using this design, a wide-bandwidth electro-optic modulator with several hundred GHz can be realized.



31.9 Schematic diagram of an DSL electro-optic system.  $X, Y, Z$  denote the principal axes of the unperturbed dielectric tensor, and  $Y_n, Z_n$  and  $Y_{pr}, Z_{pr}$  are the principal axes of the perturbed dielectric tensor of negative and positive domains, respectively.

The modulated anti-parallel ferroelectric domains with different geometric patterns have been used to focus, switch and deflect a light beam through the electro-optic effect. Yamada *et al.* (1996) and Chiu *et al.* (1996) prepared the electric-field induced cylindrical lens, switching and deflection devices composed of the inverted domain array. These micro-optical devices can align the light beam and yield high-quality optical systems at low cost, therefore, they are especially suitable for integrated optics fabricated in ferroelectric substrates.

### 31.7      Outlook

Superlattices have opened an area to the development of new synthetic materials that do not exist in nature. The flexibility in the choice of superlattice materials allows superlattices to exhibit a wide range of tailorable properties that are of interest for scientific and technological purposes. Recently, much interest has been aroused on new applications of DSLs, such as engineerable compression of ultrashort pulses in chirped-periodic DSL (Arbore *et al.*, 1997; Reid *et al.*, 1998), amplitude squeezing (Serkland *et al.*, 1997), wavelength-division-multiplexing (WDM) (Chou *et al.*, 1998) and cascaded nonlinearity (Landry and Maldonado, 1997; Qin *et al.*, 1998). Engineered QPM patterns also hold great promise for use in soliton systems. For example, soliton-based signal compression and shaping in QPM structures with longitudinal chirps has been proposed. (Torner *et al.*, 1998) Spatial switching between different output soliton state has been predicted in QPM geometries with dislocations, tilts and wells (Clausen *et al.*, 1999). More recently, quadratic spatial solitons have been observed in a DSL LN (Bourliaguet *et al.*, 1999). QPM also opens the search for better nonlinear media to new classes of materials, such as poled-polymer and fused-silica films, diffusion-bonded stacks of plates, laterally patterned semiconductors and asymmetric quantum wells (Byer, 1997). Among them, silica and other glasses are particularly attractive, since they are dominant materials in information technology and in the development of fiber laser sources. These glasses offer high transparency, low cost, a high optical damage threshold and straightforward integrability. Moreover, rare-earth doping of glass fibers has allowed the development of important laser devices, such as erbium-doped fiber amplifiers and high-power CW and pulsed fiber lasers. Unfortunately, the inversion symmetry of the glass matrix prevents the frequency conversion of coherent radiation through second-order parametric processes. The recent discovery that poling techniques can provide permanent and large second-order nonlinearity in silica made it possible to implement QPM in glass and glass waveguides and fibers. Periodically poled glass waveguides and fibers are ideal for a wide range of QPM processes, such as frequency conversion of fiber lasers, difference-frequency generation as a means for frequency conversion of

telecommunication wavelengths, generation of correlated photon pairs by parametric processes for quantum cryptography, and cascading of second-order nonlinearities to produce equivalent third-order effects (self- and cross-phase modulation) for all-optical switching (Pruneri *et al.*, 1999; Bonfrate *et al.*, 1999). Recently, greater than 20% efficient frequency doubling of 1532 nm nanosecond pulses has been realized in QPM germanosilicate optical fibers (Pruneri *et al.*, 1999).

The DSL can also be applied to beam control, beam focusing and beam steering (Chiu *et al.*, 1996; Yamada *et al.*, 1996). The ability to photolithographically pattern the DSL structure allows the consideration of prism and lens arrays for these applications. Beam deflection with prism arrays and focal length control, optical switching has been demonstrated successfully. These results show that the possibilities for extending the use of DSL to control optical beams are open for further exploration and development.

### 31.8 Acknowledgments

This work was supported by the State Key Program for Basic Research of China (Grant Nos. 2004CB619003 and 2006CB921804), by the National Natural Science Foundation of China (Grant Nos. 10523001, 10504013, 10674065 and BK2005076).

### 31.9 References and further reading

- Agranovich V M, Kiselev S A Mills D L (1991), 'Optical multistability in nonlinear superlattices with very thin layers', *Phys. Rev. B*, **44**, 10917
- Ahlfeldt H (1994), 'Single-domain layers formed in heat-treated LiTaO<sub>3</sub>', *Appl. Phys. Lett.*, **64**, 3213–3215
- Alvarez PL, Reid D T, Faller P, *et al.* (1999), 'Simultaneous femtosecond-pulse compression and second-harmonic generation in a periodically poled KTiOPO<sub>4</sub>', *Opt. Lett.*, **24**, 1071–1073
- Ando S, Chang S S, Fukui T (1991), 'Selective epitaxy of GaAs/AlGaAs on (111)B Substrates by MOCVD and applications to nanometer structure', *J. Cryst. Growth*, **115**, 69
- Arbore M A, Fejer M M (1997), 'Singly resonant optical parametric oscillation in periodically poled lithium niobate', *Opt. Lett.*, **22**, 151–153
- Arbore M A, Galvanauskas A, Harter D, Fejer M M (1997), 'Engineerable compression of ultrashort pulses by use of second-harmonic generation in chirped-period-poled lithium niobate', *Opt. Lett.*, **22**, 1341–1344
- Arie A, Rosenman G, Korenfeld A, *et al.* (1998), 'Efficient resonant frequency doubling of a cw Nd:YAG laser in bulk periodically poled KTiOPO<sub>4</sub>', *Opt. Lett.*, **23**, 28–30
- Armstrong J A, Bloembergen N, Ducuing J (1962), 'Interactions between light waves in a nonlinear dielectric'. *Physics Review*, **127**, 1918–1939

- Batchko R G, Weise D R, Fejer M M (1998), 'Continuous-wave 532-nm-pumped singly resonant optical parametric oscillator based on periodically poled lithium niobate', *Opt. Lett.*, **23**, 168
- Batchko R G, Fejer M M, Byer R L (1999), 'Continuous-wave quasi-phase-matched generation of 60mW at 465nm by single-pass frequency doubling of a laser diode in backswitch-poled lithium niobate', *Opt. Lett.*, **24**, 1293
- Batchko R G, Shur V Y, Fejer M M, Byer R L (1999), 'Backswitch poling in lithium niobate for high-fidelity domain patterning and efficient blue light generation', *Appl. Phys. Lett.*, **75**, 1673–1675
- Baudrier-Raybaut M, Haidar R, Kupecek Ph, Rosencher E (2004), 'Random quasi-phase-matching in bulk polycrystalline isotropic nonlinear materials', *Nature*, **432**, 374
- Berger V (1998), 'Nonlinear photonic crystals', *Phys. Rev. Lett.*, **81**, 4136–4139
- Bierlein J D, Laubacher D B, Brown J B (1990), 'Balanced phase matching in segmented  $\text{KTiOPO}_4$  waveguides', *Appl. Phys. Lett.*, **56**, 1725
- Birch J, Severin M, Wahlstrom U (1990), 'Structural characterization of precious-mean quasiperiodic Mo/V single-crystal superlattices grown by dual-target magnetron sputtering', *Phys. Rev. B*, **41**, 10398
- Bonfrate G, Pruneri V, Kazansky P G (1999), 'Parametric fluorescence in periodically poled silica fibers', *Appl. Phys. Lett.*, **75**, 2356
- Bourliaguet B, Couderc V, Barthelemy G (1999), 'Observation of quadratic spatial solitons in periodically poled lithium niobate', *Opt. Lett.*, **24**, 1410–1412
- Broderick N G R, Ross G W, Offerhaus H L (2000), 'Hexagonally poled lithium niobate: A two-dimensional nonlinear photonic crystal', *Phys. Rev. Lett.*, **84**, 4345
- Broderick N G R, Bratfalean R T, Monro T M (2002), 'Temperature and wavelength tuning of second-, third-, and fourth-harmonic generation in a two-dimensional hexagonally poled nonlinear crystal', *J. Opt. Soc. Am. B*, **19**, 2263
- Burr K C, Tang C L, Arbore M A (1997), 'Broadly tunable mid-infrared femtosecond optical parametric oscillator using all-solid-state pumped periodically poled lithium niobate', *Opt. Lett.*, **22**, 1458–1460
- Byer R L (1997), 'Quasi-phase-matched nonlinear interaction and device', *Journal Nonlinear Optical Physics & Materials*, **6**, 549–592
- Camlibel I (1969), 'Spontaneous polarization measurements in several ferroelectric oxides using a pulsed-field method', *J. Appl. Phys.*, **40**, 1690
- Chen J, Zhou Q, Hong J F (1989), 'Influence of growth striations on para-ferroelectric phase transitions: Mechanism of the formation of periodic laminar domains in  $\text{LiNbO}_3$  and  $\text{LiTaO}_3$ ', *J. Appl. Phys.*, **66**, 336
- Chen Q, Risk W P (1994), 'Periodic poling of  $\text{KTiOPO}_4$  using an applied electric field', *Electron. Lett.*, **30**, 1516
- Chen W, Mills D L (1987), 'Gap solitons and the nonlinear optical response of superlattices', *Phys. Rev. Lett.*, **58**, 160
- Chen Y B, Zhang C, Zhu Y Y (2001), 'Optical harmonic generation in a quasi-phase-matched three-component Fibonacci superlattice  $\text{LiTaO}_3$ ', *Appl. Phys. Lett.*, **78**, 577–579
- Chen Y F, Zhu S N, Zhu Y Y (1997), 'High-frequency resonance in acoustic superlattice of periodically poled  $\text{LiTaO}_3$ ', *Appl. Phys. Lett.*, **70**, 592–594
- Chiu Y, Stancil D D, Schlesinger T E (1996), 'Electro-optic beam scanner in  $\text{KTiOPO}_4$ ', *Appl. Phys. Lett.*, **69**, 3134–3136.
- Chou M H, Parameswaran K R, Arbore M A (1998), 'Conference on Lasers and Electro-

- Optics', 6 OSA Technical Digest Series (Optical Society of America, Washington, DC), 475
- Chou M H, Parameswaran K R, Fejer M M (1999), *Opt. Lett.*, **24**, 1157
- Chui H C, Woods G L (1995), 'Tunable mid-infrared generation by difference frequency mixing of diode laser wavelength in intersubband InGaAs/AlAs quantum wells', *Appl. Phys. Lett.*, **66**, 265–267
- Clausen C B, Torner L (1999), 'Spatial switching of quadratic solitons in engineered quasi-phase-matched structures', *Opt. Lett.*, **24**, 7–9
- Clausen C B, Kivshar Y S, Bang O, (1999), 'Quasiperiodic Envelope Solitons', *Phys. Rev. Lett.*, **83**, 4740–4743
- Cui Y *et al.* (1997), 'Widely tunable all-solid-state optical parametric oscillator for the visible and near infrared', *Opt. Lett.*, **18**, 122–124
- Delyon F, Levy Y E, Souillard B (1986), 'Nonperturbative Bistability in Periodic Nonlinear Media', *Phys. Rev. Lett.*, **57**, 2010
- Eger D, Oron M, Katz M (1997), 'Quasi-phase-matched waveguides in electric field poled, flux grown  $\text{KTiOPO}_4$ ', *Electron. Lett.*, **33**, 1548
- Englander A, Lavi R, Katz M (1997), 'Highly efficient doubling of a high-repetition diode-pumped laser with bulk periodically poled KTP', *Opt. Lett.*, **22**, 1598–1600
- Esaki L, Tsu R (1970), 'Superlattice and negative differential conductivity in semiconductors' *IBM J. Res. Dev.*, **14**, 61
- Espinosa F R M, Jimenez E, Torres M, 1998, 'Ultrasonic band gap in a periodic two-dimensional composite', *Phys. Rev. Lett.*, **80**, 1208
- Fatuzzo E, Merz W J (1967), *Ferroelectricity*, North-Holland Publishing Company, Amsterdam
- Feisst A, Koidl P (1985), 'Current induced periodic ferroelectric domain structures in  $\text{LiNbO}_3$  applied for efficient nonlinear optical frequency mixing', *Appl. Phys. Lett.*, **47**, 1125–1127
- Fejer M M, (1992), 'Nonlinear optical frequency conversion in periodically-poled ferroelectric waveguides', in *Guided Wave Nonlinear Optics*, Kluwer Academic Publishers, The Netherlands, 133–145
- Fejer M M, Magel G A, Jundt D H (1992), 'Quasi-phase-matched second harmonic generation: tuning and tolerances', *Journal Quantum Electronics*, **28**, 2631–2654
- Feng J, Ming N B (1989), 'Light transmission in two-dimensional optical superlattices', *Phys. Rev. A*, **40**, 7047
- Feng D, Ming N B, Hong J F (1980), 'Enhancement of second-harmonic generation in  $\text{LiNbO}_3$  crystals with periodic laminar ferroelectric domains', *Appl. Phys. Lett.*, **37**, 607–609
- Feng D, Wang W S, Zhou Q (1986), 'Second harmonic generation in  $\text{LiNbO}_3$  crystals with modulated structure', *Chinese Phys. Lett.*, **3**, 181
- Feng J, Zhu Y Y, Ming N B (1990), 'Harmonic generations in an optical Fibonacci superlattice', *Phys. Rev. B*, **41**, 5578
- Gellermann W, Kohmoto M, Sutherland B (1994), 'Localization of light waves in Fibonacci dielectric multilayers', *Phys. Rev. Lett.*, **72**, 633–637
- Gibbs H M, McCall S L, Venkatesan T N C (1976), 'Differential gain and bistability using a sodium-filled Fabry-Perot Interferometer', *Phys. Rev. Lett.*, **36**, 1135
- Gopalan V, Gupta M C (1996), 'Origin of internal field and visualization of  $180^\circ$  domains in congruent  $\text{LiTaO}_3$  crystals', *J. Appl. Phys.*, **80**, 6099
- Gopalan V, Mitchell T E, Furukawa Y (1998), 'The role of nonstoichiometry in  $180^\circ$  domain switching of  $\text{LiNbO}_3$  crystals', *Appl. Phys. Lett.*, **72**, 1981–1983

- Gu B Y, Dong B Z, Zhang Y (1999), 'Enhanced harmonic generation in aperiodic optical superlattices', *Appl. Phys. Lett.*, **75**, 2175–2177
- Gupta M C, Risk W P, Nutt A G (1993), 'Domain inversion in  $\text{KTiOPO}_4$  using electron beam scanning', *Appl. Phys. Lett.*, **63**, 1167–1169
- Hadi K E, Sundheimer M, Aschieri P (1997), 'Quasi-phase-matched parametric interactions in proton-exchanged lithium niobate waveguides', *J. Opt. Soc. Amer. B*, **14**, 3197
- Hadimioglu B, Comb L J, Wright D R (1987), 'High efficiency, multiple layer ZnO acoustic transducers at millimeter-wave frequencies' *Appl. Phys. Lett.*, **50**, 1642
- Harada A, Nihei Y (1996), 'Bulk periodically poled  $\text{MgO-LiNbO}_3$  by corona discharge method', *Appl. Phys. Lett.*, **69**, 2629
- He J, Cada M (1991), 'Optical bistability in semiconductor periodic structure', *IEEE J. Quantum Electron.* **27**, 1182
- Houe M, Townsend P D (1995), 'An introduction to methods of periodic poling for second-harmonic generation', *J. Phys. D: Appl. Phys.*, **28**, 1747
- Hsu W Y, Gupta M C (1992), 'Domain inversion in  $\text{LiTaO}_3$  by electron beam', *Appl. Phys. Lett.*, **60**, 1–3
- Hu W S, Liu Z G, Lu Y Q (1996), 'Pulsed-laser deposition and optical properties of completely (001) textured optical waveguiding  $\text{LiNbO}_3$  films upon  $\text{SiO}_2/\text{Si}$  substrates', *Opt. Lett.*, **21**, 946–948
- Hu Z W, Thomas P A, Snigirev A (1998), 'Phase-mapping of periodically domain-inverted  $\text{LiNbO}_3$  with cohehnt x-ray', *Nature*, **392**, 690
- Imeshev G, Proctor M, Fejer M M (1998), 'Lateral patterning of nonlinear frequency conversion with transversely varying quasi-phase-matching gratings' *Opt. Lett.*, **23**, 673
- Ito H, Takyu C, Inaba H (1991), 'Fabrication of periodic domain grating in  $\text{LiNbO}_3$  by electron beam writing for application of nonlinear optical processes', *Electronic Letters*, **27**, 1221–1222
- Janot C (1992), *Quasicrystals* (Clarendon Press, Oxford, UK)
- Joannopoulos J D, Meade R D, Winn J (1995), *Photonic Crystals*, Princeton University, Princeton, NJ
- Joannopoulos J D, Villeneuve P R, Fan S (1997), 'Photonic crystals :putting a new twist on light', *Nature*, **386**, 143
- John S (1987), 'Strong localization of photons in certain disordered dielectric superlattices', *Phys. Rev. Lett.*, **58**, 2486
- John S, Wang J (1990), 'Quantum electrodynamics near a photonic band gap: Photon bound states and dressed atoms', *Phys. Rev. Lett.*, **64**, 2418
- Jundt H D, Magel G A, Fejer M M (1991), 'Periodically poled  $\text{LiNbO}_3$  for high-efficiency second-harmonic generation', *Appl. Phys. Lett.*, **59** 2657–2659
- Karlsson H, Laurell F, Henriksson P (1996), 'Frequency doubling in periodically poled  $\text{RbTiOAsO}_4$ ', *Electron. Lett.*, **32**, 556
- Kartaloglu T, Koprulu K G, Aytur O (1998), 'Femtosecond optical parametric oscillator based on periodically poled  $\text{KTiOPO}_4$ ', *Opt. Lett.*, **23**, 61
- Keys R W, Loni A, *et al.* (1990), 'Fabrication of domain reversed gratings for SHG in  $\text{LiNbO}_3$  by electron beam bombardment', *Electronic Letters*, **26**, 188–190
- Kintaka K, Fujimura M, Suhara T (1997), 'Third harmonic generation of Nd:YAG laser light in periodically poled  $\text{LiNbO}_3$  waveguide', *Electron. Lett.*, **33**, 1459
- Kitamura K, Furukawa Y, Niwa K (1998), 'Crystal growth and low coercive field  $180^\circ$  domain switching characteristics of stoichiometric  $\text{LiTaO}_3$ ', *Appl. Phys. Lett.*, **73**, 3073

- Kolossovski K Y, Buryak A V, Sammut R A (1999), 'Quadratic solitary waves in a counter-propagating quasi-phase-matched configuration', *Opt. Lett.*, **24**, 835–837
- Kozhokin A, Kurizki G, (1995), 'Self-induced transparency in Bragg reflectors: gap solitons near Absorption Resonances', *Phys. Rev. Lett.*, **74**, 5020–5023
- Kurz J R, Schober A M, Hum D S, (2002), 'Nonlinear physical optics with transversely patterned quasi-phase-matching gratings', *IEEE J. Sel. Topics Quantum Electronics* **8**, 660
- Kushwaha M S, Halevi P (1994), 'Band-gap engineering in periodic elastic composites', *Appl. Phys. Lett.* **64**, 1085
- Landry G D, Maldonado T A (1997), 'Efficient nonlinear phase shifts due to cascaded second-order processes in a count-propagating quasi-phase-matched configuration', *Opt. Lett.*, **22**, 1400–1402
- Lifshitz R, Arie A, Bahabad A (2005), 'Photonic quasicrystals for nonlinear optical frequency conversion', *Phys. Rev. Lett.*, **95**, 133901
- Lim E J, Fejer M M, Byer R L, (1989), 'Second-harmonic generation of green light in periodically poled planar LiNbO<sub>3</sub> waveguide', *Electron. Lett.*, **25**, 174
- Liu H, Zhu Y Y, Zhu S N (2001), 'Aperiodic optical superlattices engineering for optical frequency conversion', *Appl. Phys. Lett.*, **79**, 728–730
- Loza A P, Reid D T, Faller P (1999), 'Simultaneous femtosecond-pulse compression and second-harmonic generation in aperiodically poled KTiOPO<sub>4</sub>', *Opt. Lett.*, **24**, 1071–1073
- Lu Y L, Cheng X F, Xue C C (1996a), 'Growth of optical superlattice LiNbO<sub>3</sub> with different modulating periods and its applications in second-harmonic generation', *Appl. Phys. Lett.*, **68**, 2781–2783
- Lu Y L, Lu Y Q, Chen X F (1996b), 'Formation mechanism for ferroelectric domain structures in a LiNbO<sub>3</sub> optical superlattice', *Appl. Phys. Lett.*, **68**, 2642
- Lu Y L, Lu Y Q, Xue C C (1996c), 'Growth of Nd<sup>3+</sup>-doped LiNbO<sub>3</sub> optical superlattice crystals and its potential applications in self-frequency doubling', *Appl. Phys. Lett.*, **68**, 1467–1469
- Lu Y L, Lu Y Q, Zheng J J (1996d), 'Efficient continuous wave blue light generation in optical superlattice LiNbO<sub>3</sub> by direct frequency doubling a 978 nm InGaAs diode laser', *Appl. Phys. Lett.*, **69**, 1660
- Lu Y L, Mao L, Ming N B (1991), 'Second-harmonic generation of blue light in LiNbO<sub>3</sub> crystal with periodic ferroelectric domain structures', *Appl. Phys. Lett.*, **59**, 516
- Lu Y L, L. Mao L, Ming N B (1994), 'Green and violet light generation in LiNbO<sub>3</sub> optical superlattice through quasiphase matching', *Appl. Phys. Lett.*, **64**, 3092
- Lu Y L, Wei T, Duewer F (1997), 'Nondestructive imaging of dielectric-constant profiles and ferroelectric domains with a scanning-tip microwave near-field microscope' *Science*, **276**, 2004
- Lu Y Q, Lu Y L, Luo G P (1996a), 'Frequency doubling a cw diode laser to generate 489nm blue in optical superlattice LiNbO<sub>3</sub>', *Electron. Lett.*, **32**, 336
- Lu Y Q, Lu Y L, Xue C C (1996b), 'Femtosecond violet light generation by quasi-phase-matched frequency doubling in optical superlattice LiNbO<sub>3</sub>', *Appl. Phys. Lett.*, **69**, 3155
- Lu Y Q, Zheng J J, Lu Y L (1999a), 'Frequency tuning of optical parametric generator in periodically poled optical superlattice LiNbO<sub>3</sub> by electro-optic effect', *Appl. Phys. Lett.*, **74**, 123–125
- Lu Y Q, Zhu Y Y, Chen Y F (1999b), 'Optical properties of an ionic-type phononic crystal', *Science*, **284**, 1822–1824



- Lu Y Q, Wan Z L, Wang Q (2000), 'Electro-optic effect of periodically poled optical superlattice LiNbO<sub>3</sub> and its applications', *Appl. Phys. Lett.*, **77**, 3719–3721
- Luo G Z, Zhu S N, He J L (2001), 'Simultaneously efficient blue and red light generations in a periodically poled LiTaO<sub>3</sub>', *Appl. Phys. Lett.*, **78**, 3006–3008
- Ma B, Wang T, Sheng Y, Cheng B, Zhang D, (2005), 'Quasi phase matched harmonic generation in a two-dimensional octagonal photonic superlattice', *Appl. Phys. Lett.*, **87**, 251103
- Magel G A (1990), 'Optical second harmonic generation in Lithium Niobate Fibers', PhD thesis, Stanford University
- Magel G A, Fejer M M, Byer R L (1990), 'Quasi-phase-matched second-harmonic generation of blue light in periodically poled LiNbO<sub>3</sub>', *Appl. Phys. Lett.*, **56**, 108
- McGowan C. *et al.* (1998), 'Femtosecond optical parametric oscillator based on periodically poled lithium niobate', *Journal of Optical Society of America B*, **15** 694–698
- Meyn J P, Klein M E, Woll D (1999), 'Periodically poled potassium niobate for second-harmonic generation at 463nm', *Opt. Lett.*, **24**, 1154
- Miller G D (1998), 'Periodically poled lithium niobate: modeling, fabrication, and nonlinear-optical performance', PhD thesis, Stanford University
- Miller G D, Batchko W M *et al.* (1997), '42%-efficient single-pass CW second-harmonic generation in periodically poled lithium niobate', *Opt. Lett.*, **22**, 1834–1836
- Mills, D L, Trullinger S E (1987), 'Gap solitons in nonlinear periodic structures', *Phys. Rev. B*, **36**, 947
- Ming N B, Hong J F, Feng D (1982), 'The growth striations and ferroelectric domain structures in Czochralski-grown LiNbO<sub>3</sub> single crystals', *Journal of Material Science*, **17**, 1663–1670
- Missey M J, Dominic V, McKay J (1998), *Conference on Lasers and Electro-Optics*, 1998 OSA Technical Digest Series, Optical Society of America, Washington DC, 540
- Miyazawa S (1979), 'Ferroelectric domain inversion in Ti-diffused LiNbO<sub>3</sub> optical waveguide', *J. Appl. Phys.*, **50**, 4599–4603
- Mizuuchi K, Yamamoto K (1992), 'Highly efficient quasi-phase-matched second-harmonic generation using a first-order periodically domain-inverted LiTaO<sub>3</sub> waveguide', *Appl. Phys. Lett.*, **60**, 1283
- Mizuuchi K and Yamamoto K (1994), 'Second-harmonic-generation in domain-inverted grating induced by focused ion beam', *Optical Review*, **1**, 100–102
- Mizuuchi K, Yamamoto K, Kato M (1997), 'Generation of ultraviolet light by frequency doubling of a red laser diode in a first-order periodically poled bulk LiTaO<sub>3</sub>', *Appl. Phys. Lett.*, **70** 1201–1203
- Myers L E, Miller G D, Eckardt R C (1995), 'Quasi-phase-matched 1064 nm pumped optical parametric oscillator in bulk periodically poled LiNbO<sub>3</sub>', *Opt. Lett.*, **20**, 52
- Myers L E, Eckardt R C, Fejer M M (1996), 'Multigrating quasi-phase-matched optical parametric oscillator in periodically poled LiNbO<sub>3</sub>', *Opt. Lett.*, **21**, 591
- Nassau K and Levinstein H J (1965), 'Ferroelectric behavior of lithium niobate', *Appl. Phys. Lett.*, **7**, 69
- Ni P, Ma B, Wang X (2003), 'Second-harmonic generation in two-dimensional periodically poled lithium niobate using second-order quasi-phase matching', *Appl. Phys. Lett.*, **82**, 4230
- Nishizawa J (1991), 'Molecular layer epitaxy and its fundamentals', *J. Cryst. Growth*, **115**, 69
- Normile D (1999), 'Cages for light go from concept to reality', *Science*, **286** 1500–1502

- Orlowski R, Kratzig E, Kurz H (1977), 'Photorefractive effects in LiNbO<sub>3</sub>:Fe under external electric field', *Opt. Commun.*, **20**, 171
- Peng L H, Hsu C C, Ng J, (2004), 'Wavelength tunability of second-harmonic generation from two-dimensional nonlinear photonic crystals with a tetragonal lattice structure', *Appl. Phys. Lett.*, **84**, 3250
- Peuzin J C (1986), 'Comment on "Domain inversion effects in Ti-LiNbO<sub>3</sub> integrated optical devices"', *Appl. Phys. Lett.*, **48**, 1104
- Pfister O, Wells J S, Hollberg L (1997), 'Greater than 20%-efficient frequency doubling of 1532-nm nanosecond pulses in quasi-phase-matched germanosilicate optical fibers', *Opt. Lett.*, **22**, 1211
- Pruneri V, Betterworth S D, Hanna D C (1996), 'Highly efficient green-light generation by quasi-phase-matched frequency doubling of picosecond pulses from an amplified mode-locked Nd:YLF laser', *Opt. Lett.*, **21**, 390–392
- Pruneri V, Bonfrate G, Kazansky P G (1999), 'Greater than 20%-efficient frequency doubling of 1532-nm nanosecond pulses in quasi-phase-matched germanosilicate optical fibers', *Opt. Lett.*, **24**, 208
- Qin Y Q, Zhu Y Y, Zhu S N (1998), 'Optical bistability in periodically poled LiNbO<sub>3</sub> induced by cascaded second-order nonlinearity and electro-optic effect', *Journal of Physics: Condensed Matter.*, **10**, 8939–8945
- Qin Y Q, Zhu Y Y, Zhu S N (1999), 'Nonlinear optical characterization of a generalized Fibonacci optical superlattice', *Appl. Phys. Lett.*, **75**, 448
- Reid D T, Penman Z, Ebrahimzadeh M (1997), 'Broadly tunable infrared femtosecond optical parametric oscillator based on periodically poled RbTiOAsO<sub>4</sub>', *Opt. Lett.*, **22**, 1397
- Reid D T, Loza A P, Ebrahimzadeh M (1998), *Conference on Lasers and Electro-Optics*, 6 OSA Technical Digest Series, Optical Society of America, Washington DC, 17
- Rick P W and Lau S D (1996), 'Periodic electric field poling of KTiOPO<sub>4</sub> using chemical patterning', *Appl. Phys. Lett.*, **69**, 3999–4001
- Robert G B, Fejer M M, Byer R L (1999), 'Continuous-wave quasi-phase-matched generation of 60 mW at 465 nm by single-pass frequency doubling of a laser diode in backswitched-poled lithium niobate', *Opt. Lett.*, **24**, 1293–1295.
- Rosenman G, Skliar A, Eger D (1998), 'Low temperature periodic electrical poling of flex-grown KTiOPO<sub>4</sub> and isomorphous crystals', *Appl. Phys. Lett.*, **73**, 3650–3652
- Scalora M, Dowling J P, Bowden C M (1994), 'Optical limiting and switching of ultrashort pulses in nonlinear photonic band gap materials', *Phys. Rev. Lett.*, **73**, 1368
- Serkland D K, Kumar P, Arbore M A (1997), 'Amplitude squeezing by means of quasi-phase-matched second-harmonic generation in a lithium niobate waveguide', *Opt. Lett.*, **22** 1497–1499
- Shen Y R (1984), *The Principles of Nonlinear Optics*, Wiley, New York
- Steinhardt, P J, Ostlund S (1997), *The Physics of Quasicrystals*, World Scientific, Singapore
- Sterke C M, Sipe J E (1989), 'Extensions and generalizations of an envelope-function approach for the electrodynamics of nonlinear periodic structures', *Phys. Rev. A*, **39**, 5163
- Tabata H, Kawai T (1997), 'Dielectric properties of strained (Sr,Ca)TiO<sub>3</sub>/(Ba,Sr)TiO<sub>3</sub> artificial lattices', *Appl. Phys. Lett.*, **70**, 321
- Tasson M, Legal H, Gay J C (1976), 'Piezoelectric study of poling mechanism in lithium niobate crystal at temperature close to the Curie point', *Ferroelectrics*, **13**, 479–484

- Thaniyavarn S, Findakly T, Booher D (1985), 'Domain inversion effects in Ti-LiNbO<sub>3</sub> integrated optical devices', *Appl. Phys. Lett.*, **46**, 933–935
- Torner L, Clausen C B, Fejer M M (1998), 'Adiabatic shaping of quadratic solitons', *Opt. Lett.*, **23**, 903–905
- Vanherzeel H, Bierlein J D (1992), 'Magnitude of the nonlinear-optical coefficients of KTiOPO<sub>4</sub>', *Opt. Lett.*, **17**, 982–984
- Wang S, Karlsson H, Laurell F (1998), *Conference on Laser and Electro-Optics*, 6 OSA Technical Digest Series, Optical Society of America, Washington, DC, 520
- Wang W S, Qi M (1986), 'Research on TGS single crystal growth with modulated structure', *Journal of Cryst. Growth*, **79**, 758–761
- Wang W S, Zhou Q, Geng Z H (1986), 'Study of LiTaO<sub>3</sub> crystals grown with a modulated structure I second harmonic generation in LiTaO<sub>3</sub> crystals with periodic laminar ferroelectric domains', *J. Cryst. Growth*, **79**, 706
- Wang Z L, Wu J, Yang Z J (1996a), 'Optical bistability and hysteresis in a two-dimensional periodic structure fabricated in Fe doped LiNbO<sub>3</sub>', *Solid State Commun.*, **98**, 1057
- Wang Z L, Wu J, Yang Z J (1996b), 'Observation of optical bistability in two-dimensional volume refractive index gating thermally fixed in LiNbO<sub>3</sub>:Fe crystal', *Chin. Phys. Lett.*, **13**, 440
- Wang Z L, Zhu Y Y, Xu N (1996c), 'Optical response in two-dimensional optical superlattices with Kerr nonlinearity', *J. Appl. Phys.*, **80**, 25
- Wang Z L, Zhu Y Y, Yang Z J (1996d), 'Gap shift and bistability in two-dimensional nonlinear optical superlattices', *Phys. Rev. B*, **53**, 6984
- Wang Z L, Yang Z J, Zhu Y Y (1996e), 'Bistable switching in two-dimensional nonlinear optical superlattices', *Opt. Commun.*, **123**, 649
- Wang Z L, Wu J, Liu X J (1997), 'Nonlinear transmission resonance in a two-dimensional periodic structure with photonic band gap', *Phys. Rev. B*, **56**, 9185
- Webjorn J, Laurell F, Arvidsson G (1989), 'Blue light generated by frequency doubling of laser diode light in a lithium niobate channel waveguide', *IEEE Photonics Technique Letters*, **11**, 316–318
- Webjorn J, Pruneri V, Barr J R M (1994), 'Quasi-phase-matched blue light generation in bulk lithium niobate, electrically poled via periodic liquid electrodes', *Electron. Lett.*, **30**, 894
- Wei Q H, Liu X H, Zhou C H (1993), 'In situ studies of colloidal aggregation induced by alternating electrical fields', *Phys. Rev. E*, **48**, 2786
- Wen W J, Wang N, Ma H R (1999), 'Field Induced Structural Transition in Mesocrystallites', *Phys. Rev. Lett.*, **82**, 4248
- Williams D L, West D P, King T A (1998), 'Quasi-phase matched third harmonic generation', *Opt. Commun.*, **148**, 208
- Winful H G, Marburger J H and Garmire E (1979), 'Theory of bistability in nonlinear distributed feedback structures', *Appl. Phys. Lett.*, **35**, 379
- Xu B and Ming N B (1993a), 'Experimental observation of bistability and instability in a two-dimensional nonlinear optical superlattice', *Phys. Rev. Lett.*, **71**, 3959–3962
- Xu B, Ming N B (1993b), 'Optical bistability in a two-dimensional nonlinear superlattice', *Appl. Phys. Lett.*, **71**, 1003–100.
- Xu H P, Jiang G Z, Mao L (1992), 'High-frequency resonance in an acoustic superlattice of barium sodium niobate crystals', *J. Appl. Phys.*, **71**, 2480–2482
- Xu P, Ji S H, Zhu S N (2004), 'Conical second harmonic generation in a two-dimensional photonic crystal: a hexagonally poled LiTaO<sub>3</sub> crystal', *Phys. Rev. Lett.*, **93**, 133904

- Xu P, Zhu S N, Yu X Q (2005), 'Experimental studies of enhanced Raman scattering from a hexagonally poled LiTaO<sub>3</sub> crystal', *Phys. Rev. B*, **72**, 064307
- Yablonovitch E (1987), 'Inhibited spontaneous emission in solid-state physics and electronics', *Phys. Rev. Lett.*, **58**, 2059
- Yamada M, Nada N, Saitoh M (1993), 'First-order quasi-phase-matched LiTaO<sub>3</sub> waveguide periodically poled by applying an external field for efficient blue second-harmonic generation', *Appl. Phys. Lett.*, **62**, 435–436
- Yamada M, Saitoh M, Ooki H (1996), 'Electric-field induced cylindrical lens, switching and deflection devices composed of the inverted domains in LiNbO<sub>3</sub> crystal', *Appl. Phys. Lett.*, **69**, 3659–3661
- Yariv A and Yeh P (1984), *Optical Waves in Crystals*, John Wiley & Sons, New York
- Yi S Y, Shin S Y, Jin Y S (1996), 'Second-harmonic generation in a LiTaO<sub>3</sub> waveguide domain-inverted by proton exchange and masked heat treatment', *Appl. Phys. Lett.*, **68**, 2943–2947
- Zhang C, Zhu Y Y, Yang S X (2000), 'Crucial effect of the coupling coefficients on quasi-phase-matched harmonic generation in an optical superlattice', *Opt. Lett.*, **25**, 436–438
- Zheng J J, Lu Y Q, Luo G P (1998), 'Visible dual-wavelength light generation in optical superlattice E<sub>r</sub>:LiNbO<sub>3</sub> through upconversion and quasi-phase-matched frequency doubling', *Appl. Phys. Lett.*, **72**, 1808–1810
- Zhu S N, Cao W W (1997), 'Direct observation of ferroelectric domains in LiTaO<sub>3</sub> using environmental scanning electron microscopy', *Phys. Rev. Lett.*, **79**, 2558
- Zhu S N, Zhu Y Y, Yang Z J (1995a), 'Second-harmonic generation of blue light in bulk periodically poled LiTaO<sub>3</sub>', *Appl. Phys. Lett.*, **67**, 320
- Zhu S N, Zhu Y Y, Zhang Z Y (1995b), 'LiTaO<sub>3</sub> crystal periodically poled by applying an external pulsed field', *J. Appl. Phys.*, **77**, 5481–5483
- Zhu S N, Zhu Y Y, Ming N B (1997a), 'Quasi-phase-matched third-harmonic generation in a quasi-periodic optical superlattice', *Science*, **278**, 843–846
- Zhu S N, Zhu Y Y, Qin Y Q (1997b), 'Experimental realization of second harmonic generation in a Fibonacci optical superlattice of LiTaO<sub>3</sub>', *Phys. Rev. Lett.*, **78**, 2752–2755
- Zhu Y Y, Ming N B (1990), 'Second-harmonic generation in a Fibonacci optical superlattice and the dispersive effect of the refractive index', *Phys. Rev. B*, **42**, 3676–3679
- Zhu Y Y, Ming N B (1992a), 'Electro-optic effect and transmission spectrum in a Fibonacci optical superlattice', *J. Phys.: Cond. Matt.*, **4**, 8073–8082
- Zhu Y Y and Ming N B (1992), 'Ultrasonic excitation and propagation in an acoustic superlattice', *J. Appl. Phys.*, **72**, 904–914
- Zhu Y Y, Ming N B, Jiang W H (1988), 'Acoustic superlattice of LiNbO<sub>3</sub> crystals and its applications to bulk-wave transducers for ultrasonic generation and detection up to 800 MHz', *Appl. Phys. Lett.*, **53**, 1381–1383
- Zhu Y Y, Ming N B, Jiang W H (1989), 'Ultrasonic spectrum in Fibonacci acoustic superlattices', *Phys. Rev. B*, **40**, 8536–8538
- Zhu Y Y, Zhu S N, Hong J F (1995), 'Domain inversion in LiNbO<sub>3</sub> by proton exchange and quick heat treatment', *Appl. Phys. Lett.*, **65**, 558–560
- Zhu Y Y, Zhu S N, Qin Y Q (1996), 'Further studies on ultrasonic excitation in an acoustic superlattice', *J. Appl. Phys.*, **79**, 2221
- Zhu Y Y, Fu J S, Xiao R F (1997a), 'Second harmonic generation in periodically domain-inverted Sr<sub>0.6</sub>Ba<sub>0.4</sub>Nb<sub>2</sub>O<sub>6</sub> crystal plate', *Appl. Phys. Lett.*, **70**, 1793–1795

Zhu Y Y, Xiao R F, Fu J S (1997b), 'Second-harmonic generation in quasi-periodically domain-inverted  $\text{Sr}_{0.6}\text{Ba}_{0.4}\text{Nb}_2\text{O}_6$  optical superlattices', *Opt. Lett.*, **22**, 1382

Zhu Y Y, Xiao R F, Fu J S (1998), 'Third harmonic generation through coupled second-order nonlinear optical parametric processes in quasi-periodically domain-inverted  $\text{Sr}_{0.6}\text{Ba}_{0.4}\text{Nb}_2\text{O}_6$  optical superlattices', *Appl. Phys. Lett.*, **73**, 432–434

## Dielectric and optical properties of perovskite artificial superlattices

---

T TSURUMI and T HARIGAI, Tokyo Institute of Technology, Japan

### 32.1 Introduction

One of the dreams of materials scientists is to make a material with an artificially designed structure that will provide the desired properties. Artificial superlattices, for which theoretical prediction was made by Esaki and coworkers in 1970s,<sup>1-3</sup> were realized by the subsequent progress of thin film growth technologies such as molecular beam epitaxy (MBE) and chemical vapor deposition (CVD) techniques. Compound semiconductor superlattices, such as GaAs/GaAlAs superlattices, have been formed by precise control of one atomic layer deposition. These superlattices are used for some practical devices. Artificial superlattices consisting of oxide compounds are current research topics for material and ceramic scientists because oxides have various physical properties, such as dielectric, piezoelectric, magnetic, optical and electron-transfer. Oxide superlattices may provide unknown material properties or significant enhancement of known properties. In particular, perovskite oxides are a treasure-house of interesting properties because ferroelectricity, piezoelectricity, high dielectricity, electron conductivity and other properties are obtained by changing constituent elements in the same perovskite structure.

A pioneer work of artificial superlattices of perovskite oxide, BaTiO<sub>3</sub> (BTO)/SrTiO<sub>3</sub> (STO), was carried out by Iijima *et al.*<sup>4,5</sup> in the early 1990s. They succeeded in the monolayer growth of BTO and STO using alternate evaporation of Ba or Sr and Ti as well as co-evaporation of these elements. The metal elements evaporated from electron-beam-heated or tungsten-wire-heated sources were oxidized in a high-vacuum chamber by partially ozonized oxygen. Their reactive evaporation process became the base of the MBE process currently used for the deposition of oxide superlattices. Other pioneer works of perovskite oxide artificial superlattice were reported by Koinuma and coworkers<sup>6-9</sup> and Tabata *et al.*<sup>10</sup> in the 1990s. Koinuma *et al.* developed a laser MBE system which enabled monolayer depositions of perovskite oxides. They also developed a process to make atomically flat surface on STO single crystal substrates, which is one of the most important techniques

required for atomic layer epitaxy of perovskite oxides. The enhancement of material properties in artificial superlattices was demonstrated by Tabata *et al.*,<sup>10</sup> who found the enhancement of the dielectric permittivity in the BTO/STO superlattice with a stacking periodicity of two unit cells/two unit cells. We started perovskite superlattice work in 1994 and published the first report on the formation of BTO/STO superlattices using computer-controlled atomic-layer-depositions of BaO, SrO and TiO<sub>2</sub>.<sup>11</sup>

After these works, perovskite artificial superlattices were prepared by several research groups using laser MBE process,<sup>12–21</sup> reactive MBE process<sup>22–24</sup> and radiofrequency (RF)-sputtering process.<sup>25–28</sup> Kim *et al.*<sup>12,13</sup> demonstrated the enhancement of dielectric properties in artificial BTO/STO superlattices by manipulating lattice strains in the superlattices. They observed large dielectric permittivity ( $\epsilon_r = 1230$ ) and extremely large dielectric nonlinearity in BTO/STO superlattice with a stacking periodicity of two unit cells/two unit cells. Christen *et al.*<sup>16</sup> prepared SrZrO<sub>3</sub> (SZO)/STO and BTO/STO superlattices using pulsed laser deposition (laser MBE) and indicated that the electric field-dependence of the permittivity of both types of structure had a different behavior from that observed in the corresponding solid solutions, and, especially, the data of the SZO/STO superlattices were consistent with the assumption that strain induced ferroelectricity in the STO films at room temperature. A constrained ferroelectricity was also found in the (001)-textured PbZrO<sub>3</sub>/BaZrO<sub>3</sub> superlattice films by Wu and Hung<sup>27</sup> and in the BTO/STO superlattices by Shimuta *et al.*<sup>29</sup> Superlattices of thin ferroelectric and non-ferroelectric perovskite layers, e.g. short-period BTO/STO, have been reported to exhibit enhancements of dielectric constant and remanent polarization. However, it should be noted that the movement of space charges in the superlattices can spuriously produce an apparent significant enhancement of dielectric permittivity as pointed out by O'Neill *et al.*<sup>30</sup> The dielectric properties of perovskite superlattices remain ambiguous.

As for the theoretical works on the perovskite superlattices, Neaton and Rabe<sup>31</sup> performed first-principle calculations on the BTO/STO superlattices and indicated that significant polarization enhancement could be achieved in perovskite oxide superlattices. This enhancement arose from the combined effects of strain, induced in the BTO layers by the epitaxial growth, and internal electric fields, associated with the superlattice geometry. The STO layers were found to be tetragonal and polar, possessing nearly the same polarization as the BTO layers. The first-principles calculation of Kim *et al.*<sup>32–34</sup> demonstrated that the BTO/STO superlattices under in-plane compressive state showed enhanced stability of tetragonal phase while the stability of monoclinic phase was enhanced under the in-plane tensile state. Yang *et al.*<sup>35</sup> also performed first-principles calculations on the SZO/STO superlattices and indicated that the lattice distortion from the lattice mismatch in the superlattices led to the formation of spontaneous polarization in the

superlattices, although neither SZO nor STO is ferroelectric. Lo and Jiang<sup>36</sup> employed Landau–Khalatnikov theory to demonstrate that enhanced dielectric permittivity occurred when the stacking periodicity was reduced to a few monolayers in the superlattices under in-plane interfacial strains. All of these works pointed out that the lattice distortion due to the in-plane stress is a key factor in explaining the enhancements of dielectric permittivity and remanent polarization in perovskite superlattices.

In our research on perovskite artificial superlattices, a modern MBE system was developed first and deposition process refined in 1990s. BTO/STO and SZO/STO artificial superlattices were prepared and their optical and dielectric properties evaluated. It was found from a series of our works that BTO/STO exhibited remarkable high dielectric permittivity above 30 000 in the in-plane direction and SZO/STO exhibited strain-induced ferroelectricity. The enhancement of the permittivity in BTO/STO superlattices was recently confirmed in the multilayered films prepared by the RF-sputtering process. These results have provided experimental evidence for the theoretical works.

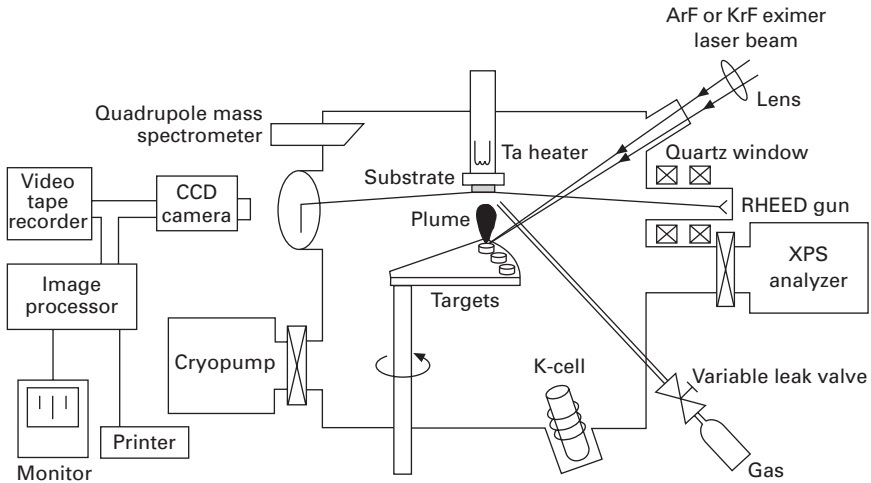
In this chapter, the deposition processes for the oxide artificial superlattices are reviewed first. The lattice distortions induced by the lattice mismatch between the film and substrate and between constituent layers in the superlattices were analyzed using high-resolution X-ray diffraction (XRD) equipment. The results obtained for the BTO/STO and SZO/STO superlattices are discussed in Section 32.3. The optical properties of the superlattices measured with a spectroscopic ellipsometer and the dielectric properties of the superlattices measured with planer electrodes are reviewed in Sections 32.4 and 32.5.

## 32.2 Preparation of artificial superlattices

### 32.2.1 Laser MBE system

Since the works of Koinuma *et al.*<sup>6–9</sup> and Tabata *et al.*,<sup>10</sup> the laser MBE system has been commonly used for the deposition of perovskite superlattices. A schematic drawing of a typical laser MBE system is shown in Fig. 32.1.<sup>6</sup> It is composed of three main parts: (1) a laser ablation chamber (base pressure of  $1 \times 10^{-10}$  torr), (2) a KrF excimer laser (248 nm), and (3) *in-situ* reflection high-energy electric diffraction (RHEED) (20 kV) and X-ray photoelectron spectrum (XPS) analyzer. A pulsed laser beam (typically, 10 ns, 2–10 Hz and  $1 \text{ J/cm}^2$ ) is focused onto a ceramic target to deposit the corresponding film on a substrate heated with a Ta heater under flushing of O<sub>2</sub> gas at  $10^{-8}$ – $10^{-5}$  torr. The *in-situ* RHEED pattern and its intensity at the specular beam spot and XPS can be monitored during the film growth. The deposition rate is about 0.5 nm/min for a laser frequency of 5 Hz. For the growth of artificial superlattices, the ceramic target is changed automatically with a computer-





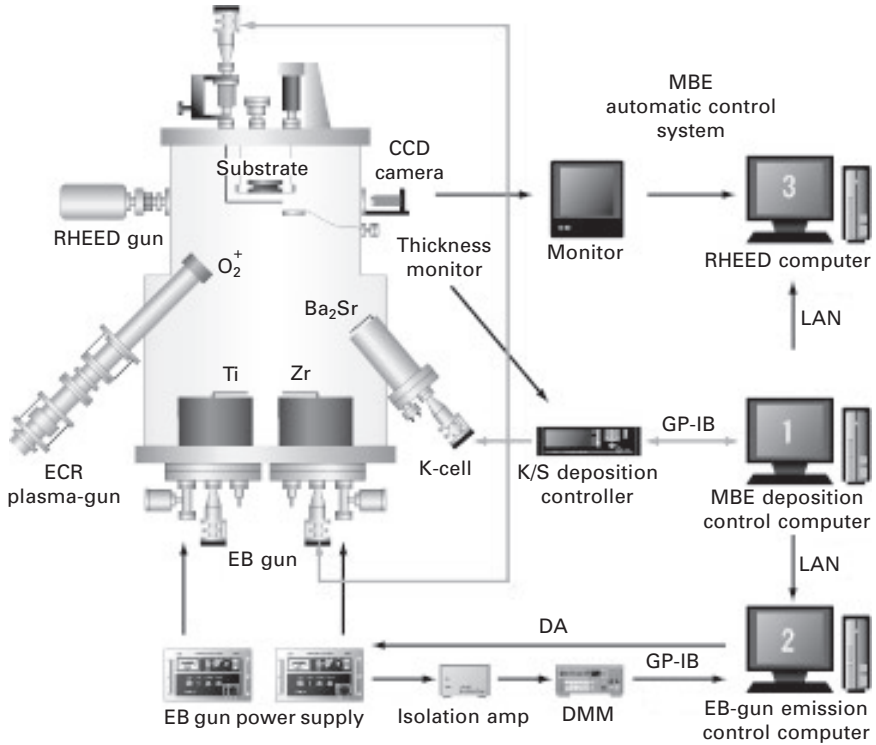
32.1 Laser MBE system with *in-situ* RHEED and XPS apparatus.<sup>6</sup>

controlled system. The thickness of one molecular layer deposition is controlled by monitoring RHEED intensity oscillations or simply by the number of laser pulse shots to the ceramic targets.

The advantage of the laser MBE process is relatively easy deposition of high-quality films without precise control of chemical composition. The target composition is copied to the film under optimum deposition conditions. Because of this advantage, various artificial superlattices of different material systems can be prepared without consuming time and manpower for optimizing deposition conditions. Another advantage of the laser MBE is a wide variation of deposition conditions. In particular, this process does not choose the oxygen partial pressure in the film deposition, which enables the deposition of oxide films at relatively high oxygen partial pressures to improve the properties of oxide films. On the other hand, the biggest disadvantage of the laser MBE is the restriction of substrate area. The deposition on a large area is not realistic as far as a normal system is used, which severely restricts this process for use as an industrial process. Moreover, the deposition of droplets, which is frequently observed in a film growth, considerably reduces the film quality. The laser MBE process is a quite useful process in basic research aimed at the discovery of useful and interesting material systems as well as their superlattice structures.

### 32.2.2 Reactive MBE system

Figure 32.2 shows the schematic illustration of an MBE system developed in our laboratory.<sup>11,37-39</sup> The MBE chamber (Ulvac Co., base pressure of  $1 \times 10^{-9}$  torr) is equipped with three Knudsen cells (K-cells), two electron-

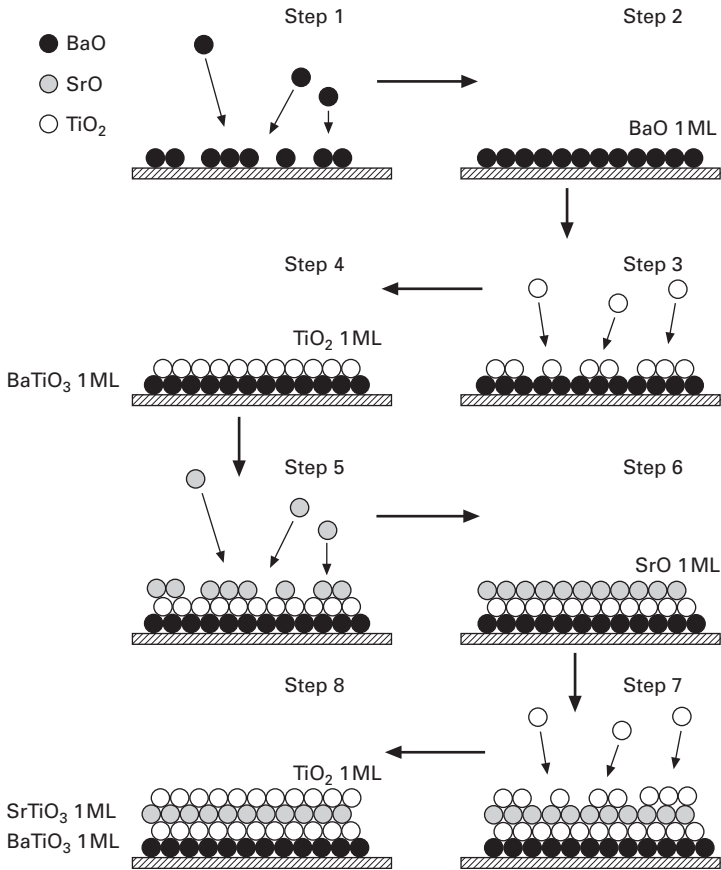


32.2 Schematic illustration of an MBE system.

beam-heated guns (EB guns), an RHEED gun and an electron cyclotron resonance gun (ECR gun). The vacuum pumping system of the chamber consists of a rotary pump, a turbo molecular pump and a titanium sublimation pump. The K-cells are used for the evaporation of Ba and Sr metals while Ti and Zr metals with relatively high melting temperatures are evaporated with the EB guns. The deposition process is controlled with three computers; the first and main computer reads the frequency of a quartz oscillator placed near the substrate, calculates the film thickness from the frequency change of the oscillator and outputs a signal to a deposition controller (Inficon, IC/5) which operates shutters of each evaporation gun. For the frequency stability of the quartz oscillator, distilled water at a constant temperature flows into the quartz oscillator holder. The second computer is used for stabilizing evaporation rate of the EB guns using proportional-integral-derivative (PID) feedback control. The third computer is monitoring the RHEED patterns and its intensity at the specular beam spot. These three computers are connected with a local area network (LAN) to enable synchronized controls. One of the most important points in the oxide film deposition with MBE system is the oxidation of metals at the film surface in a high vacuum chamber. We employed

an ECR gun for this purpose. The oxygen radicals and ions generated in the ECR gun are continuously irradiated to the film surface during the film deposition. The irradiation of oxygen ions ( $O^{2-}$ ) severely reduces the film quality. To avoid the  $O^{2-}$  irradiation to the film surface, a positive voltage is applied to the plasma electric discharge room of the ECR gun (acceleration voltage) and a negative voltage is applied to the substrate holder (bias voltage).<sup>38</sup>

Perovskite superlattices are deposited by an alternate deposition process. The deposition sequence of a BTO/STO superlattice is illustrated in Fig. 32.3. As the topmost atomic plane of STO single crystal substrates is a  $TiO_2$  layer,<sup>7</sup> the deposition starts from one molecular layer (ML) of BaO followed by one molecular layer of  $TiO_2$  to form one unit cell of BTO lattice. For the deposition of the BTO/STO and SZO/STO superlattices, BaO and  $TiO_2$  layers are respectively replaced with SrO and  $ZrO_2$  layers according to the design of superlattices. Typical deposition conditions of the BTO/STO and SZO/STO superlattices are as follows:



32.3 Deposition sequence for BTO/STO artificial superlattice.

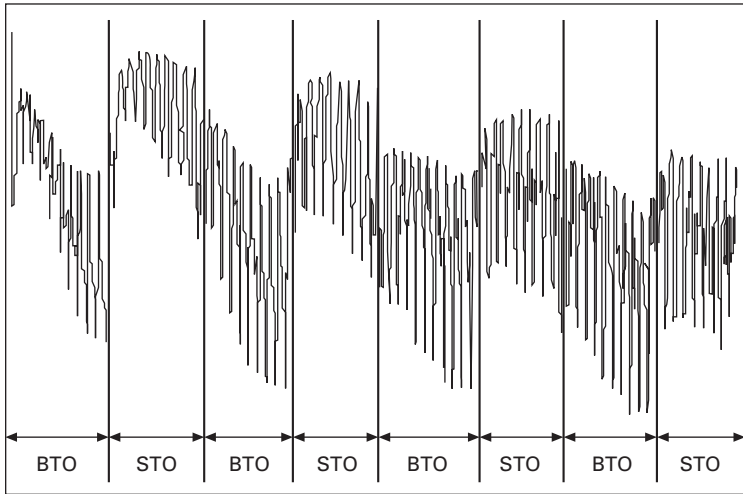
- Substrates: (001) STO single crystal (Shinkosha Co.)  
(001) Nb-doped STO single crystal (Shinkosha Co.)
- Substrate temperature: 600 °C
- Oxygen partial pressure:  $3.0 \times 10^{-6}$ – $5.0 \times 10^{-6}$  torr
- Temperature of K-cell (Ba): 540–580 °C
- Temperature of K-cell (Sr): 415–430 °C
- Emission current of EB gun (Ti): 14–20 mA
- Emission current of EB gun (Zr): 70–130 mA
- Acceleration voltage: +50 V
- Bias voltage: – 100 V

A typical RHEED pattern and its oscillations are shown in Fig. 32.4. The streak pattern of a deposited film and the RHEED oscillations indicates that the two-dimensional atomic-layer-epitaxy is achieved with the MBE system. Each oscillation of RHEED intensity corresponds to the deposition of one molecular layer. It should be noted that the RHEED intensity oscillations observed in the alternate deposition process are due to the difference of electron reflectivity of each molecular layer, which is different from that observed in a co-evaporation process such as the laser MBE, where the oscillation corresponds to the step growth of one molecular layer of perovskite lattice.

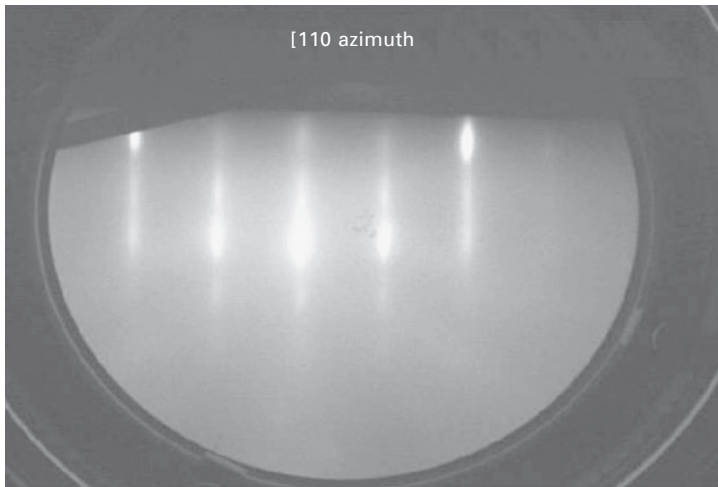
The advantages of the MBE process over other processes are film quality over a large area and controllability of the atomic layer deposition. Schlom *et al.*<sup>23</sup> succeeded in preparing almost perfect perovskite superlattices using adsorption-controlled growth with a reactive MBE system and purified ozone for the oxidation. The controlled synthesis of atomic-layered oxide heterostructures offers great potential for tailoring the dielectric and ferroelectric properties of materials. We have even made compositional-gradient artificial modulated structure using the MBE system, as shown in Fig. 32.2.<sup>37</sup> However, the deposition control and oxidation of metal sources in high vacuum still need a state-of-art technique and the deposition rate of the MBE process should be improved for industrial use of this process.

### 32.2.3 Sputtering system

Perovskite artificial superlattices can be formed using sputtering system. We have constructed two sputtering systems, an ion beam sputtering (IBS) and a conventional Rf-magnetron sputtering, for the growth of superlattices. Schematic drawings of the two systems are shown in Fig. 32.5. The IBS system uses a Kaufman-type ion beam gun to irradiate Ar ions to ceramic targets fixed at 100 mm from the gun. Oxygen radicals and ions generated with an ECR-gun are irradiated to the film surface to improve the crystallinity of oxide films. The film thickness is monitored with the quartz oscillator and



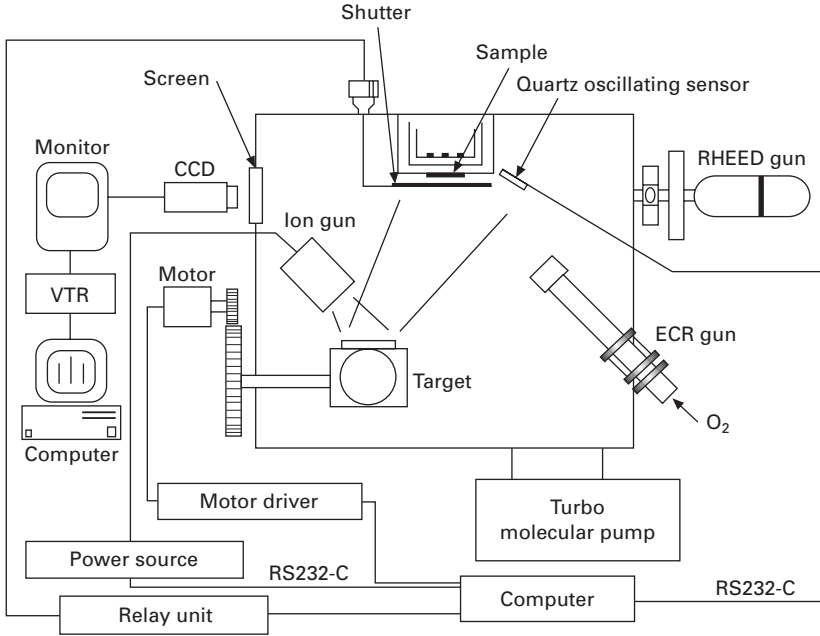
(a)



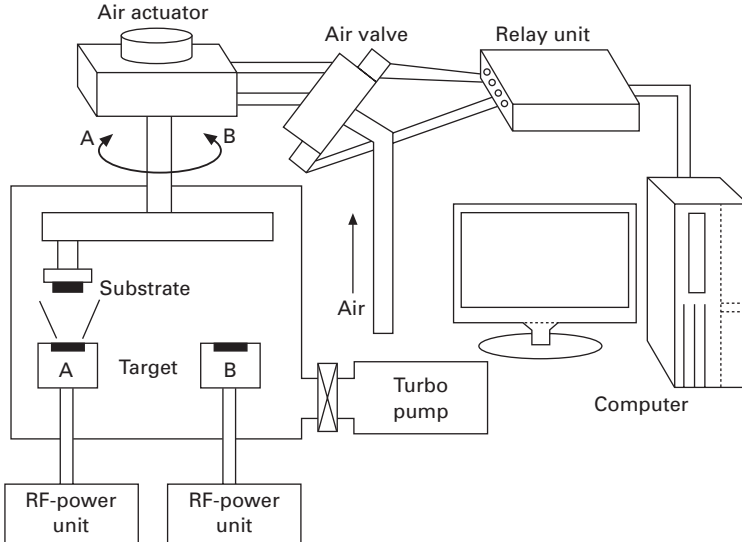
(b)

32.4 (a) RHEED intensity oscillation observed during the deposition of  $[\text{BTO}_{10}/\text{STO}_{10}]_4$  artificial superlattice and (b) an RHEED pattern of deposited film.

RHEED intensity oscillations. We have succeeded in making NiO/ZnO artificial superlattices using this system.<sup>40</sup> The IBS system with an oxidation assisting radical source is suitable to prepare multilayer films and even superlattices of simple oxide but the compositional deviation from the target restricts the application of this system to perovskite oxides. At present, it is difficult to find any advantage of the IBS process over the laser MBE system as far as the perovskite superlattices are concerned.



(a)



(b)

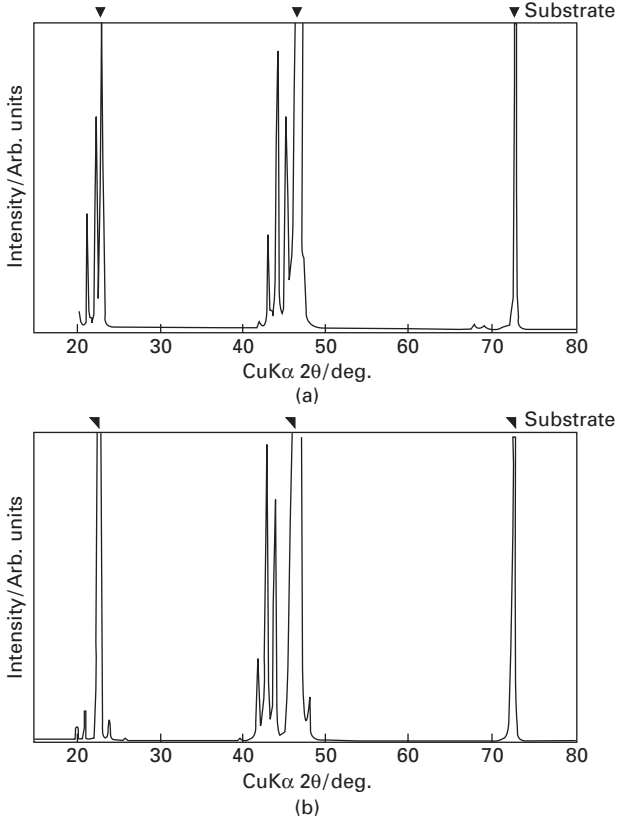
32.5 Schematic illustrations of (a) an ion beam sputtering system and (b) an RF-magnetron sputtering system used for the depositions of oxide superlattices.

Although the reactive MBE process produces perovskite superlattices of the highest quality, the deposition rate of the MBE process is still too slow to prepare perovskite superlattices for practical applications. Most of the industrial manufacturing processes of oxide thin films are still by simple and conventional RF-magnetron sputtering. Therefore, we tried to make BTO/STO superlattices using a simple sputtering system as shown in Fig. 32.5(b). A substrate is rotated with an air actuator to alternately face the RF-plasma of BTO (A) and STO (B) targets. The thickness of each layer is determined from the deposition time. Tsai *et al.*<sup>25</sup> prepared the BTO/STO superlattices and Wu and Hung<sup>27</sup> made the  $\text{PbZrO}_3/\text{BaZrO}_3$  superlattices using RF-magnetron sputtering systems. They confirmed the formation of superlattices from the satellite peaks in XRD profiles. Although the RF-sputtering is a promising process for practical applications, the quality of the superlattices must be improved to obtain the desired properties.

### 32.3 Lattice distortions in artificial superlattices

Figure 32.6 shows the XRD profiles of BTO/STO and SZO/STO superlattices made with the MBE system shown in Fig. 32.2. Clear satellite peaks indicate the formation of superlattices. XRD reciprocal-space-mapping measurements were performed using high-resolution XRD equipment (Bruker AXS, Discover8). Typical reciprocal-space-mappings obtained for BTO/STO superlattices are shown in Fig. 32.7. The highest peaks in the maps are the 002 diffractions of the STO substrates. Clear satellite peaks are observed in  $[\text{BTO}_{10}/\text{STO}_{10}]_4$  superlattices. The shift of diffraction spots to the  $x$ -direction ( $a^*$ -axis) in the maps indicates that the  $a$ -parameter (in-plane lattice parameter) of the epitaxial film changed from that of the substrate due to the relaxation of crystal lattices. In  $[\text{BTO}_{10}/\text{STO}_{10}]_4$  superlattices, all satellite peaks lie on the same  $a^*$  line as the substrate, indicating that the strained lattice is formed in the films without relaxation of crystal lattices. In this case, a large lattice distortion was induced by the lattice mismatch between BTO and STO in substrate and in superlattices. On the other hand, a diffraction spot of the  $[\text{BTO}_{40}/\text{STO}_{40}]_1$  is shifted in the  $x$ -direction from the substrate by the relaxation of crystal lattice.

The variations of the  $a$ - and  $c$ -parameters with the periodicity of BTO/STO and SZO/STO superlattices calculated from the diffraction angles of 002 peaks are shown in Fig. 32.8. It should be noted that all superlattices in one series have the same total thickness (80 perovskite unit cells) and the same chemical composition ( $\text{Ba} : \text{Sr} = 0.5 : 0.5$  and  $\text{Ti} : \text{Zr} = 0.5 : 0.5$ ). The dotted lines in Fig. 32.8 indicate the lattice parameters of bulk samples. In the case of BTO/STO superlattices, the  $a$ -parameters of superlattices with the periodicities of 10 and 20 unit cells are identical to that of STO substrate, indicating that almost completely strained lattices are formed in these

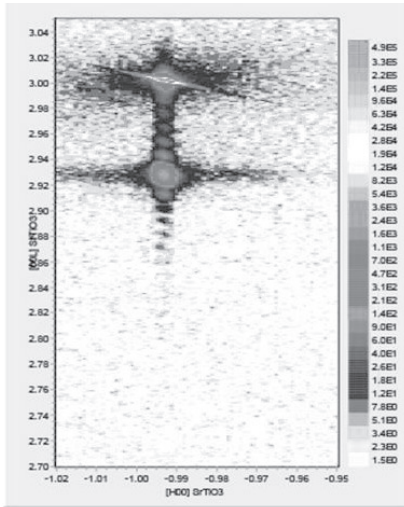


32.6 XRD profiles of (a)  $[BTO_{10}/STO_{10}]_4$  and (b)  $[SZO_{10}/STO_{10}]_4$  superlattices.

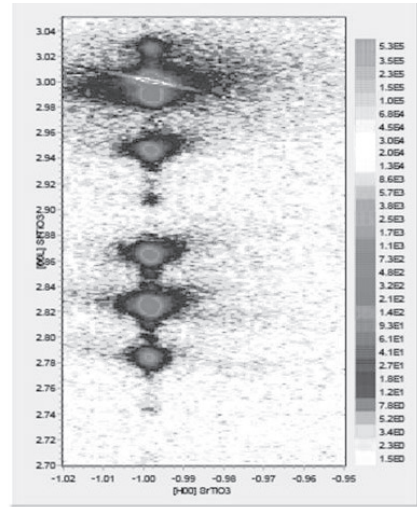
superlattices. The  $a$ -parameter was relaxed to a large value when the periodicity was increased to 40. The anisotropy of the crystal lattice has a maximum at the periodicity of 10. On the other hand, the  $a$ -parameter of SZO/STO superlattices increases with the periodicity. The  $c$ -parameter of the superlattice with the periodicity of 10 is consistent with that of the ideally strained lattice calculated from the unit cell volume of the bulk samples. The anisotropy of the crystal lattice has the maximum value in this superlattice. The lattice parameters of the superlattice with the periodicity of 40 are almost the same as bulk SZO ceramics because the diffraction from the STO layer in the relaxed superlattice is overlapped with that of the substrate and the lattice parameters are calculated from the diffraction only from the SZO layer in the superlattice.

The different behaviors in the variation of lattice parameters between BTO/STO and SZO/STO superlattices in Fig. 32.8 are attributable to the difference in the  $a$ -parameters of bulk samples of BTO (0.3994 nm) and SZO

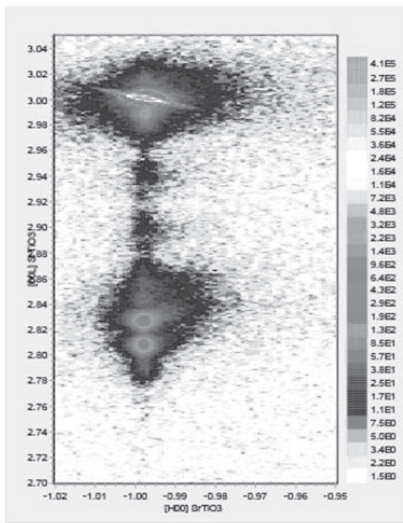




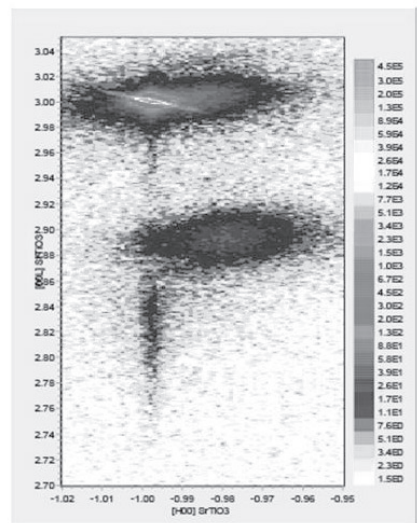
(a) [BTO<sub>1</sub>/STO<sub>1</sub>]<sub>40</sub>



(b) [BTO<sub>10</sub>/STO<sub>10</sub>]<sub>4</sub>



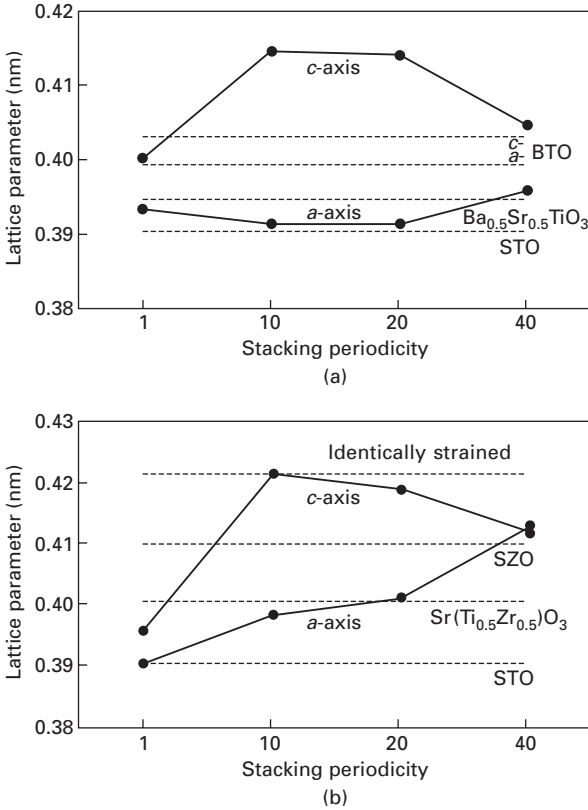
(c) [BTO<sub>20</sub>/STO<sub>20</sub>]<sub>2</sub>



(d) [BTO<sub>40</sub>/STO<sub>40</sub>]<sub>1</sub>

32.7 XRD reciprocal-space-mappings of BTO/STO superlattices.

(0.4100 nm). As the SZO has a large *a*-parameter, the in-plane compressive strain induced to the SZO layers from the STO substrate and the STO layers in the superlattices cannot be retained with the increase of the periodicity, giving rise to the relaxation of lattice strains, more easily than the case of BTO/STO superlattices. The lattice parameters of the superlattices with a periodicity of 1 have anomalous values, i.e. the *c*-parameters of the superlattices markedly shrink in both cases. The formation of solid solution films due to



32.8 Variations of lattice parameters with the stacking periodicity of (a) BTO/STO superlattices and (b) SZO/STO superlattices.

the interdiffusion of constituent elements is the reason for this phenomenon but the lattice volume shrinkage observed in the SZO/STO superlattice cannot be explained at present.

## 32.4 Optical property of artificial superlattices

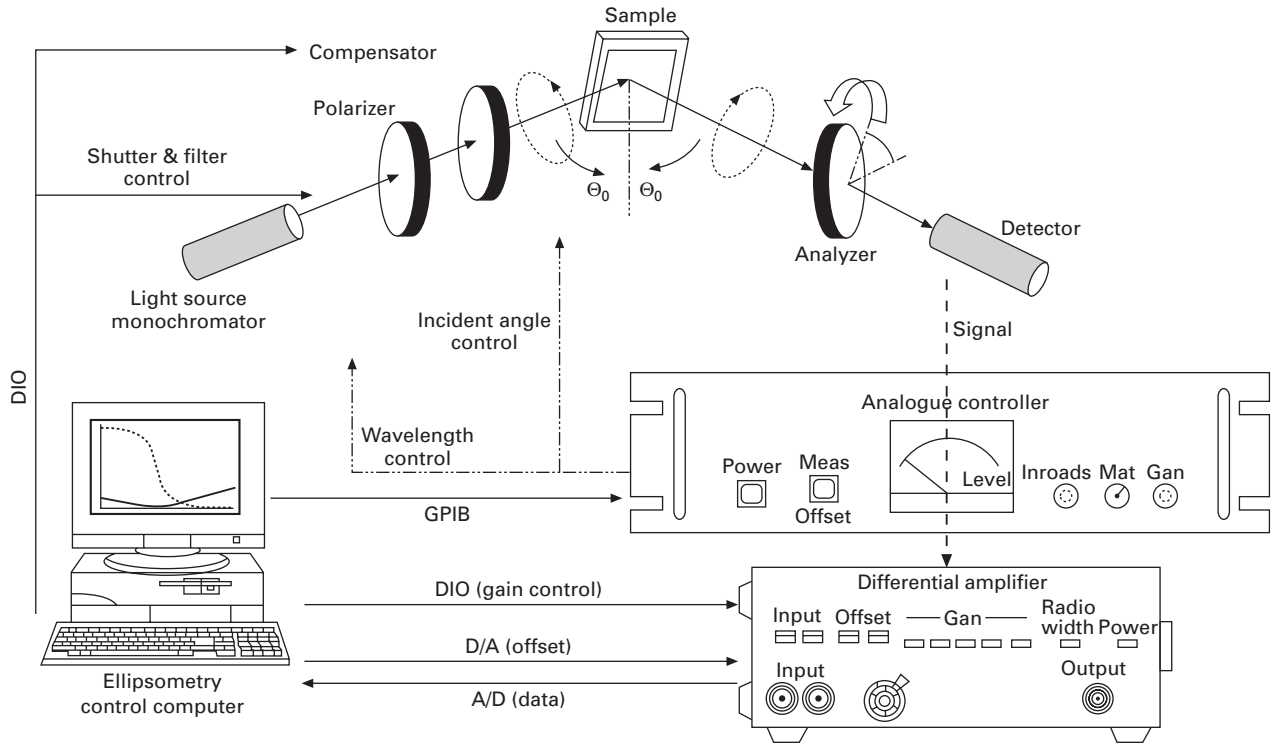
### 32.4.1 Spectroscopic ellipsometry

Ellipsometry is an optical technique that can evaluate the optical constant and film thickness of a thin film simultaneously. It is widely used for the characterization of thin films and *in-situ* observation of growth process of thin films.<sup>41–46</sup> The basic theory of ellipsometry was summarized in a book written by Azzam and Bashara.<sup>47</sup> There are some reports on the ellipsometry of semiconductor superlattices<sup>48–52</sup> but the studies on oxide artificial superlattices are extremely limited except for our work on NiO/ZnO superlattices prepared by the IBS process.<sup>53</sup>

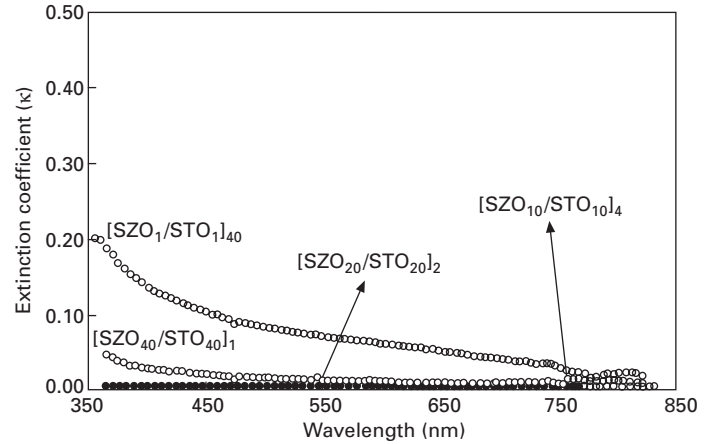
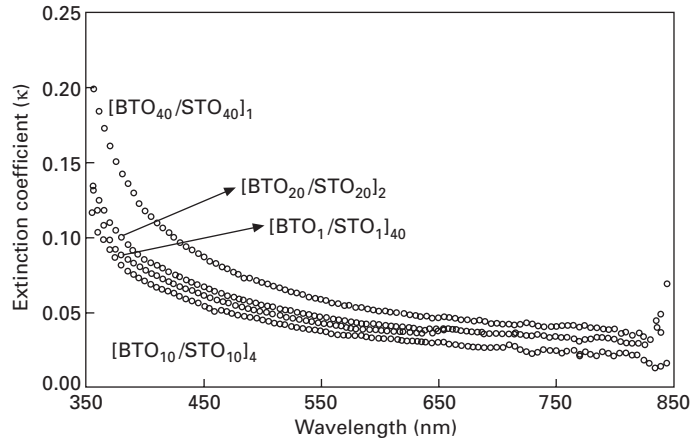
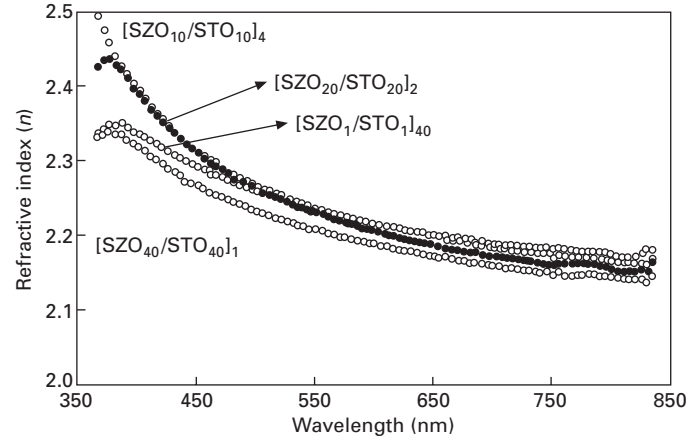
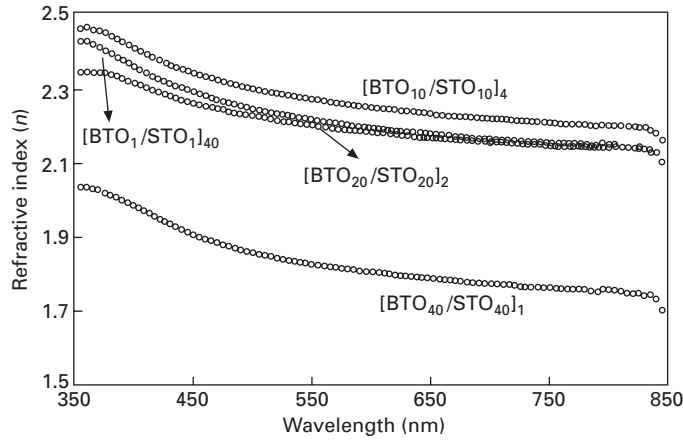
Figure 32.9 shows the rotating-analyzer type spectroscopic ellipsometer used for the evaluation of ellipsometer angles,  $\Psi$  and  $\Delta$ , of superlattices on substrates. Reflection ellipsometry is a technique based on the measurements of the states of polarization of the incident and reflected waves, leading to the determination of the ratio  $\rho$  of the complex Fresnel reflection coefficients. The ratio  $\rho$  is represented in terms of ellipsometer angles by  $\rho = \tan \Psi \exp(i\Delta)$ . The rotation-analyzer ellipsometer becomes inaccurate when  $\Delta < 10^\circ$  or  $\Delta > 170^\circ$ <sup>54</sup> which is frequently encountered in the measurements of transparent films.<sup>55-58</sup> To avoid this problem, a compensator (a quarter-wave retarder) is inserted after the polarizer to change the polarizing state of incident light. Polarized light from 350 to 850 nm in wavelength is provided from a Xe lamp (75 W) through a computer-controlled monochromator and an optical fiber. The incident angle is varied from  $50^\circ$  to  $80^\circ$ . The refractive indices of thin films were calculated using the three-phase model (ambient thin films substrate). In the analysis, the superlattices were regarded as uniform thin films along the thickness. The difficulty in the ellipsometric measurements of superlattices is that the refractive index of the substrate is very close to that of thin films. We measured the ellipsometer angles of STO substrates very accurately to prepare database used for the analysis of thin films. Nonlinear least-squares-fitting software was developed to determine the optical constant,  $n^* = n - i\kappa$ , where  $n$  is the refractive index and  $\kappa$  is the extinction coefficient, from the complex Fresnel reflection coefficients ( $\rho$ ) determined at different incident angles. No theoretical assumption was used to evaluate the wavelength dispersion of refractive index.

### 32.4.2 Optical constants of superlattices

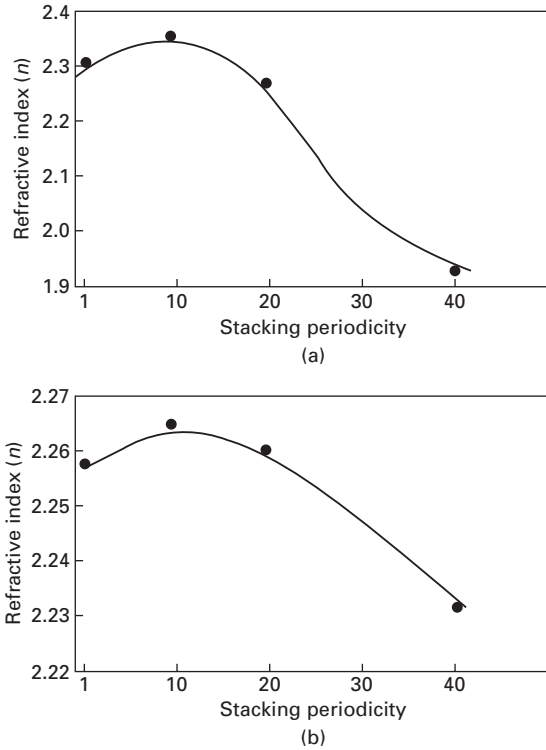
The refractive index ( $n$ ) and extinction coefficient ( $\kappa$ ) of the BTO/STO and SZO/STO superlattices determined by the ellipsometer system are shown in Fig. 32.10 as a function of light wavelength. The refractive index decreases with increasing wavelength for all specimens. High refractive indices at low wavelengths are due to the effect of the fundamental absorption below 350 nm. It was found that the BTO/STO and SZO/STO superlattices with the periodicity of 10 had higher refractive indices than those of the other superlattices over the whole wavelength range. The variation of refractive index at a wavelength of 500 nm with the stacking periodicity of the superlattices is shown in Fig. 32.11. The refractive index shows a maximum at the periodicity of 10 in both systems. The superlattices with a periodicity of 10 had the highest anisotropy of crystal lattice as shown in Fig. 32.8. The result in Fig. 32.11 indicates that the lattice distortions induced by the lattice mismatches change the electronic states affecting electronic polarizations in the superlattices, giving rise to the variation of refractive index even though the averaged chemical compositions of the superlattices are identical.



32.9 Schematic illustration of rotating-analyzer type spectroscopic ellipsometer.



32.10 Optical constant of (a) BTO/STO and (b) SZO/STO superlattices as a function of wavelength.

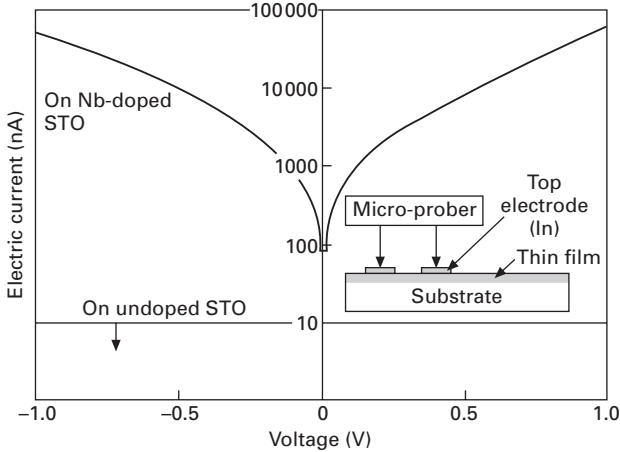


32.11 Refractive index of (a) BTO/STO and (b) SZO/STO superlattices measured at wavelength of 500 nm.

## 32.5 Dielectric properties of artificial superlattices

### 32.5.1 Electrodes and measuring principle and technique

The selection of substrate is extremely important for the growth of perovskite superlattices. The (001)-oriented STO single crystal is frequently used for the substrate of superlattice growth because of its high crystallinity and a small lattice mismatch with perovskite films. However, for the electric measurements, superlattices should be deposited on a conductive layer working as a bottom electrode. The easiest way to meet this demand is the usage of conductive Nb-doped STO single crystals. We have used this substrate at the beginning of the research but it gave a serious problem of high leakage current in the superlattices. Figure 32.12 shows the difference in the leakage currents between the BTO/STO superlattices deposited on undoped STO and on Nb-doped STO substrate. The leakage current was measured between two neighboring electrodes of In on the film surface as shown in the drawing in Fig. 32.12. The In electrode makes an ohmic contact with semiconductive oxides. The superlattice deposited on the Nb-doped STO substrate showed a



32.12 Leakage current of BTO/STO superlattices on STO and Nb-doped STO substrate.

higher leakage current although the substrate was not used as a bottom electrode. On the other hand, the leakage current of the superlattice on undoped STO was lower than the measuring limit of the electric current meter used for the measurement. The high leakage current observed in the superlattice on the the Nb-doped STO substrate could not be improved by annealing films in oxygen atmosphere or variation of the stoichiometry of the films. We believe that the high leakage current is due to the thermal diffusion of Nb into the film. It may be that some of anomalous dielectric behaviors reported for artificial superlattices on the Nb-doped STO substrates may be due to the Maxwell–Wagner polarization between electrodes with the Schottky barrier.

To avoid the problem of the high leakage current mentioned above, we tried to measure the dielectric properties of the superlattices on undoped STO using planar electrodes on the film. Farnell’s theory<sup>59</sup> is frequently used to evaluate the dielectric permittivity of films measured with interdigital electrodes. From this theory, the relation between the dielectric permittivity of a substance and the capacitance measured with interdigital electrodes is given by:

$$C_1 = K(\epsilon_s + 1)$$

$$K = 6.5\left(\frac{D}{L}\right)^2 + 1.08\left(\frac{D}{L}\right) + 2.37 \tag{32.1}$$

where  $C_1$  is the capacitance per unit length,  $\epsilon_s$  is the dielectric permittivity of the substance,  $D$  is the width of the finger and  $L$  is the distance between the center of two neighboring fingers in interdigital electrodes. The capacitance

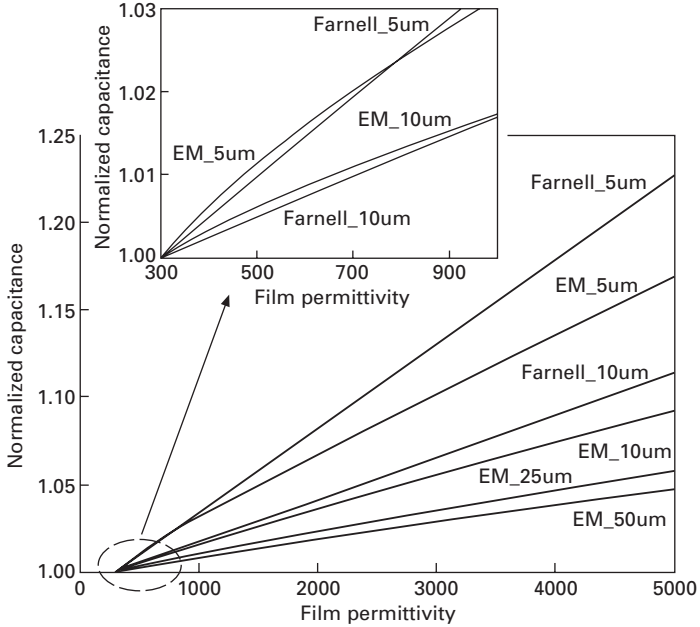
of a film on a substrate ( $C$ ) is represented by the capacitance due to the film  $C_F$  and that due to the substrate  $C_S$  as follows:

$$C = C_S + (C_F - C_S)[1 - \exp(-4.6h/L)] \quad 32.2$$

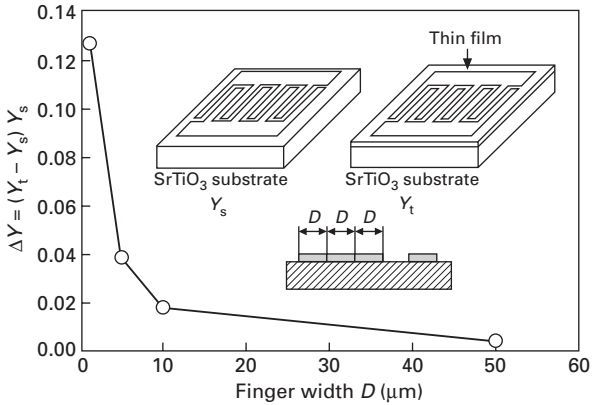
where  $h$  is the thickness of film. By combining Eqs. (32.1) and (32.2), the dielectric permittivity of the film is calculated from the capacitances  $C$  and the permittivity of the substrate  $\epsilon_s$ . However, Eqs. (32.1) and (32.2) are accurate only under the conditions that the permittivity of substrate and film is 50 or less, the finger width  $D$  and the space between fingers ( $L - D$ ) are equal and the ratio of the film thickness  $h$  to the space between fingers ( $D - L$ ) is 0.2 or more. These conditions cannot be satisfied in the case of superlattices with a thickness of about 32 nm (80 unit cells of the primitive perovskite lattice). Therefore, electromagnetic (EM) field analysis (Sonnet, EM) was employed to calculate the film permittivity from the capacitance measured with interdigital electrodes. The validity of Farnell's theory was simulated at first. The parameters used for the simulation are as follows: the dielectric permittivity of the substrate is 300 (STO), the film thickness ( $h$ ) is 32 nm, the finger-to-space ratio  $D/(L - D)$  is fixed at 0.5 and the finger width  $D$  is changed from 5 to 50  $\mu\text{m}$ . The thickness of the substrates and that of the air above the electrode were 0.5 mm and 10 mm, respectively. The results of the simulation using Farnell's theory and the EM analysis are compared in Fig. 32.13 where the capacitance is normalized to that simulated for the substrate without film. The normalized capacitance increases with decreasing finger width  $D$  in both Farnell's theory and the EM analysis. Although Farnell's theory gave a relatively good approximation when the film permittivity was low, the capacitance calculated from Farnell's theory became higher than that from the EM analysis as the dielectric permittivity of the film increased. This result indicates that Farnell's theory overestimates the permittivity of ultra-thin superlattices and that the EM analysis is indispensable to determine the dielectric permittivity of the superlattices with high dielectric permittivity.

The required finger width of interdigital electrodes for the measurements of superlattices was determined using EM analysis. In this analysis, the admittance calculated for a substrate ( $\epsilon_s = 300$ ) was compared with that calculated for the substrate with a film (30 nm,  $\epsilon = 1000$ ). The  $\Delta Y$  defined by  $\Delta Y = (Y_t - Y_s)/Y_t$ , where  $Y_s$  is the admittance of the substrate and  $Y_t$  is the admittance of the film and the substrate, is shown in Fig. 32.14 as a function of the finger width of interdigital electrodes. The  $\Delta Y$  increases with decreasing finger width, indicating that the contribution of the film to the admittance increases with decreasing finger width. The result in Fig. 32.14 shows that the finger width of interdigital electrodes should be less than 10  $\mu\text{m}$  to obtain reliable admittance data of the film. Based on this analysis, the finger width was determined to be 5  $\mu\text{m}$  in the final design and the simulation model as shown in Fig. 32.15.

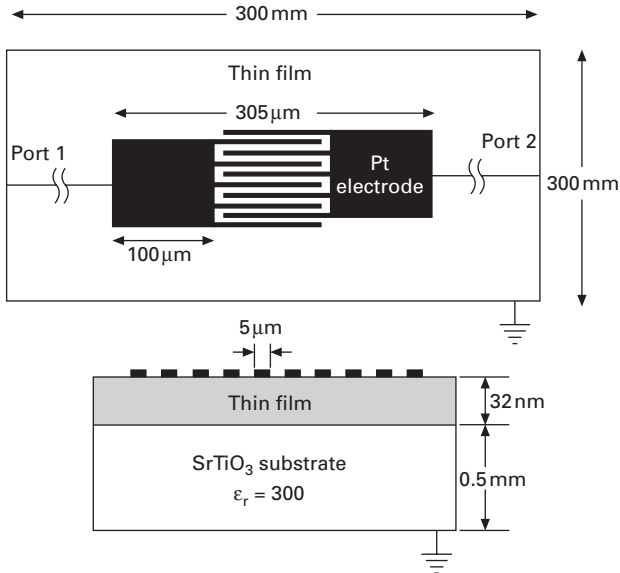




32.13 Capacitance variation with film permittivity and the finger width of interdigital electrodes calculated using Farnell’s theory and EM analysis. Capacitance in the y-axis is normalized to the capacitance calculated for substrate only (without the film). The notation of Farnell\_5um, for example, means the capacitance calculated from the Farnell’s theory for interdigital electrodes with a finger width of 5µm.



32.14 Change of  $\Delta Y = (Y_t - Y_s) / Y_s$  with the finger width  $D$  of interdigital electrodes obtained by the EM analysis.  $Y_s$  is the admittance of only substrate ( $\epsilon_s = 300$ ) and  $Y_t$  is the admittance of a film (30 nm,  $\epsilon = 1000$ ) with substrate.



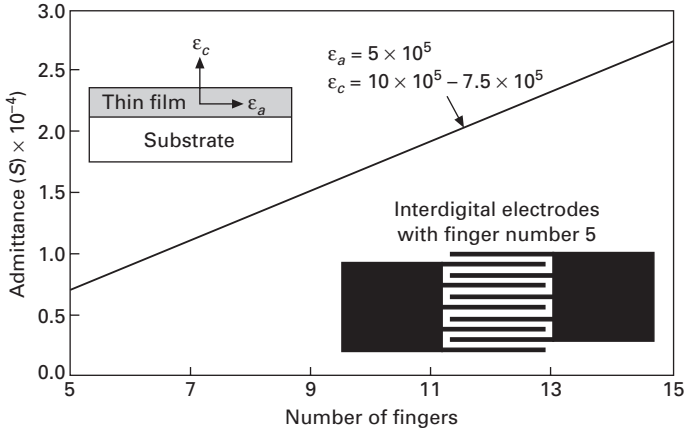
32.15 Final design and the model of the EM analysis of interdigital electrodes on superlattice films.

Another problem in the dielectric measurement of superlattices is the anisotropy of dielectric properties. The crystal lattices in the superlattices are distorted in one direction as shown in Fig. 32.8, indicating that the dielectric permittivity along the film plane ( $\epsilon_a$ ) and that along the film thickness ( $\epsilon_c$ ) must be different. Figure 32.16 shows the variation of admittance with the number of fingers in the interdigital electrodes (Fig. 32.15) obtained by the EM analysis. In this analysis, the relative dielectric permittivity along the film plane ( $\epsilon_a$ ) was fixed at  $5 \times 10^5$  and that along the film thickness ( $\epsilon_c$ ) was changed from  $1.0 \times 10^5$  to  $7.5 \times 10^5$ . The values of admittance calculated are identical in spite of the variation of  $\epsilon_c$  as shown in Fig. 32.16, leading to a very important conclusion that the permittivity measured for superlattices using interdigital electrodes in Fig. 32.15 is the permittivity along film plane ( $\epsilon_a$ ) of the superlattices.

### 32.5.2 Dielectric property

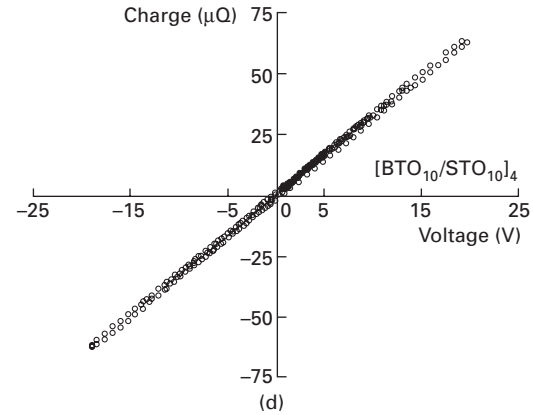
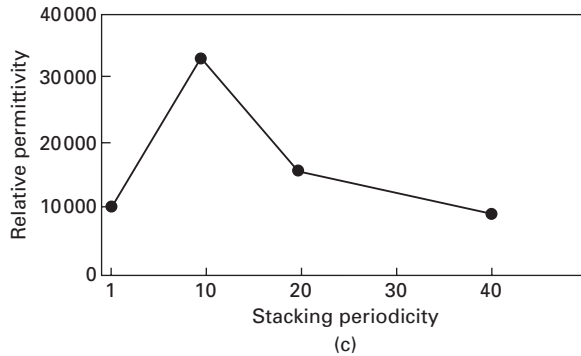
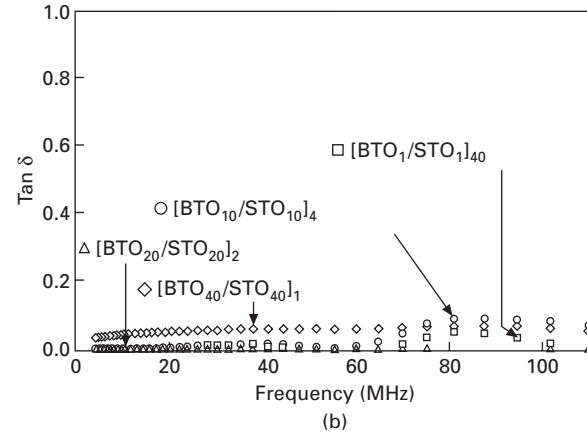
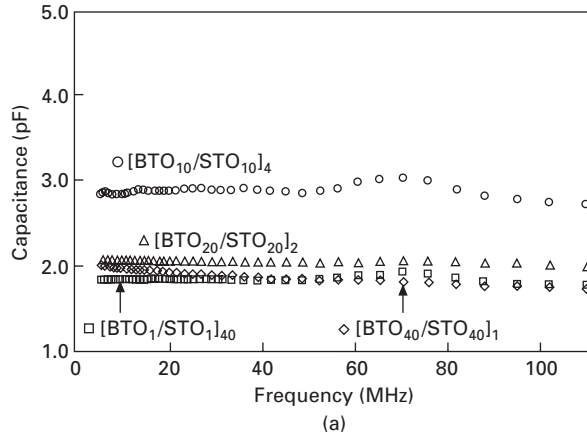
#### *Dielectric permittivity of BTO/STO superlattices*

The interdigital electrodes shown in Fig. 32.15 were formed on the film surface using electron beam lithography. The admittance between the fingers of the interdigital electrodes was measured using impedance analyzer (HP4294A) connected to a micro-prober system (Measure Jigu, WN365A1).



**32.16** Admittance as a function of the number of fingers in interdigital electrodes obtained by the EM analysis. In the analysis, the permittivity along the film plane ( $\epsilon_a$ ) was fixed at  $5 \times 10^5$  but that along the film thickness ( $\epsilon_c$ ) was varied from  $1.0 \times 10^5$  to  $7.5 \times 10^5$ . The admittance is independent of  $\epsilon_c$ .

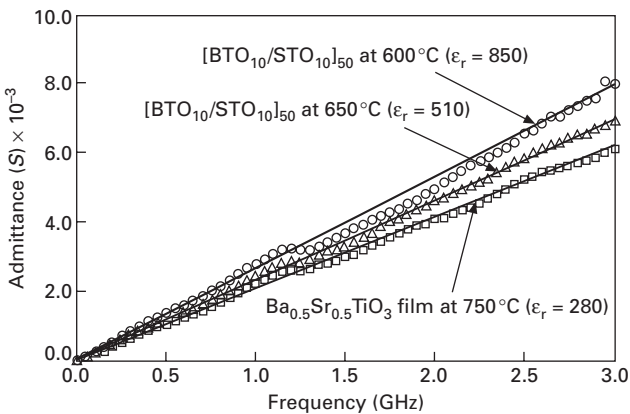
The dielectric properties of BTO/STO superlattices are shown in Fig. 32.17. The frequency dispersion of capacitance (Fig. 32.17a) indicates that the capacitance (dielectric permittivity) of the BTO/STO superlattices does not depend on frequency significantly and that the permittivity of  $[\text{BTO}_{10}/\text{STO}_{10}]_4$  superlattice is much higher than that of other superlattices. The dielectric loss tangents of all superlattices are several % or less (Fig. 32.17b). The dielectric permittivity of superlattices was calculated by fitting admittance calculated with the EM analysis to that observed. The EM analysis was repeated with changed permittivity of the superlattices until the best fit was obtained. The dielectric permittivity so obtained for the BTO/STO superlattices at 110 MHz is shown as a function of the stacking periodicity of the superlattices in Fig. 32.17(c). The BTO/STO superlattice with the stacking period of 10 unit cells of perovskite lattice shows the highest permittivity of 33 000 which is remarkably higher than those reported previously.<sup>10,12</sup> However, the highest permittivity was very sensitive to the quality of superlattices and it varied from 16 000 to 35 000 with a slight variation of the deposition conditions. The charge ( $Q$ ) vs. voltage ( $V$ ) curve of the  $[\text{BTO}_{10}/\text{STO}_{10}]_4$  superlattice measured with the interdigital electrodes at 132.5 Hz is shown in Fig. 32.17(d). A linear relation is observed in the  $Q - V$  curve. Bulk ceramics of the BTO-STO system also exhibit large dielectric permittivity with the relaxor or the diffuse phase transition behaviors. The high permittivity of the bulk ceramics is accompanied with the nonlinearity of the dielectric permittivity, and it can be explained by the electric-field-induced orientation of thermally fluctuating



32.17 Dielectric properties of BTO/STO superlattices: (a) frequency dispersion of capacitance; (b) frequency dispersion of loss tangent; (c) relative dielectric permittivity at 110 MHz as a function of stacking periodicity of superlattices; (d) charge vs. voltage curve of [BTO10/STO10]<sub>4</sub> superlattices.

spontaneous polarization in the polar nano-regions. This type of dipole polarization always shows nonlinear dielectricity and dielectric dispersion at relatively low frequencies. However, the high permittivity of the superlattices does not show any nonlinear behaviors, as shown in Fig. 32.17(d) and the dielectric relaxation is not observed at frequencies up to 110 MHz. We think that this is a truly remarkable and anomalous dielectric behavior of the superlattice.

The enhancement of the permittivity was also confirmed in the BTO/STO superlattices prepared with the RF-magnetron sputtering system shown in Fig. 32.5(b). The admittances measured with a planar electrode on the  $[\text{BTO}_{10}/\text{STO}_{10}]_4$  superlattices and on the  $\text{Ba}_{0.5}\text{Sr}_{0.5}\text{TiO}_3$  thin film are shown in Fig. 32.18 as a function of frequency. The planar electrode was designed to contact a ground-source-ground three terminal probe (Cascade Microtech.) for high-frequency measurements. The straight lines to fit the experimental data in Fig. 32.18 were obtained from the EM-analysis. The relative permittivity of the  $[\text{BTO}_{10}/\text{STO}_{10}]_{50}$  superlattices deposited at  $600^\circ\text{C}$  was determined to be 850, which was much higher than that of the  $\text{Ba}_{0.5}\text{Sr}_{0.5}\text{TiO}_3$  thin film deposited at  $750^\circ\text{C}$  ( $\epsilon_r = 280$ ). The relative permittivity of the  $[\text{BTO}_{50}/\text{STO}_{50}]_{10}$  superlattices was about 750, which was lower than the superlattice with the periodicity of 10. These results are consistent with those obtained for superlattices made with the MBE system, indicating that the formation of superlattices enhanced the permittivity and the degree of enhancement is enlarged in the superlattices with the periodicity of 10. It is also an important and anomalous behavior that the superlattice film deposited at a higher temperature of  $650^\circ\text{C}$  showed a lower permittivity ( $\epsilon_r = 510$ ) than that deposited at  $600^\circ\text{C}$  ( $\epsilon_r = 850$ ). This phenomenon can be interpreted by



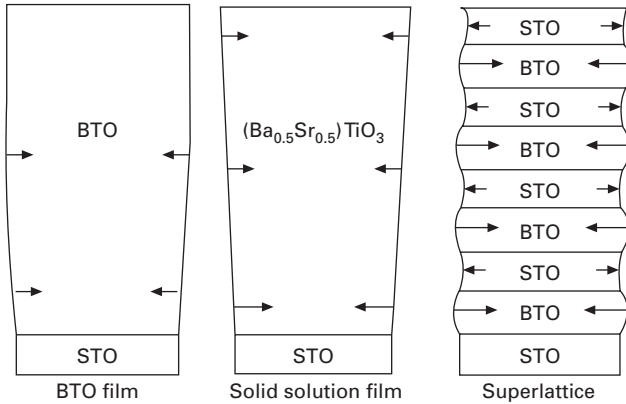
32.18 Admittance of BTO/STO superlattices and  $\text{Ba}_{0.5}\text{Sr}_{0.5}\text{TiO}_3$  thin film as a function of frequency. The solid lines were obtained by the EM analysis.

taking into account an interdiffusion of Ba and Sr at the boundary of each layer during the deposition at high temperatures. Although the enhancement of the permittivity was confirmed by the superlattices prepared with a different deposition process, the permittivity of RF-sputtered superlattices was much lower than that prepared with the MBE process. This is obviously due to the imperfection of superlattice structures in the sputter-derived films. We could not, in fact, observe clear satellite peaks in the XRD analysis of the sputter-derived films. The enhancement of the permittivity is sensitive to the quality of superlattices. However, the enhancement of the permittivity in the films deposited with a simple sputtering process has an important meaning for the practical applications of perovskite superlattices. Decoupling capacitors on Si-chips are currently demanded for the noise reduction and the stable electric-current supply to the LSI circuits. The BTO–STO thin films are regarded as one of the candidates for this application because of their relatively high permittivity with low loss, but the permittivity at low deposition temperatures still need to be enhanced at the present. The formation of superlattice-like structures using simple sputtering process may give a new solution to satisfy the requirements to the capacitor films.

#### *Mechanism of permittivity enhancement in BTO/STO superlattices*

Although the Maxwell–Wagner effects due to the electric conduction have been pointed out as a mechanism of dielectric enhancements in oxide superlattices,<sup>30</sup> we do not think that the anomalous dielectric behavior shown in Fig. 32.17 is due to these effects because the superlattices showed relatively low loss tangents, a linear  $Q$ – $V$  relation (leakage current gives round shape in the curve) and dielectric enhancement at high frequencies. It should be also be noted that the result of dielectric enhancement is consistent with the change of refractive index (Fig. 32.11) as well as the lattice distortions (Fig. 32.8).

The relaxation of crystal lattices and the stress directions in a BTO film, a  $\text{Ba}_{0.5}\text{Sr}_{0.5}\text{TiO}_3$  film and a BTO/STO superlattice on a STO substrate are depicted in Fig. 32.19. A large in-plane compressive stress is applied to the BTO films from the substrate because of the lattice mismatch between BTO and STO. The BTO lattices near the substrate are distorted to elongate its  $c$ -parameter (lattice parameter along the film thickness) while keeping the  $a$ -parameter (lattice parameter along the film plane) to achieve the lattice matching with the STO substrate. These strained lattices are relaxed with increasing film thickness by introducing dislocations. The similar stress should be applied to the  $(\text{Ba}_{0.5}\text{Sr}_{0.5})\text{TiO}_3$  film but the stress is lower than the case of BTO film because of the smaller lattice mismatch between  $(\text{Ba}_{0.5}\text{Sr}_{0.5})\text{TiO}_3$  and STO. Therefore, the strained lattices are remained thicker than the case of the BTO films. In the case of superlattices, the similar compressive stress is applied to the first BTO layer from the substrate to distort the crystal



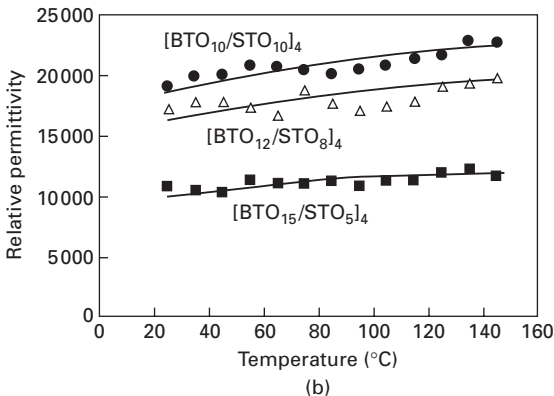
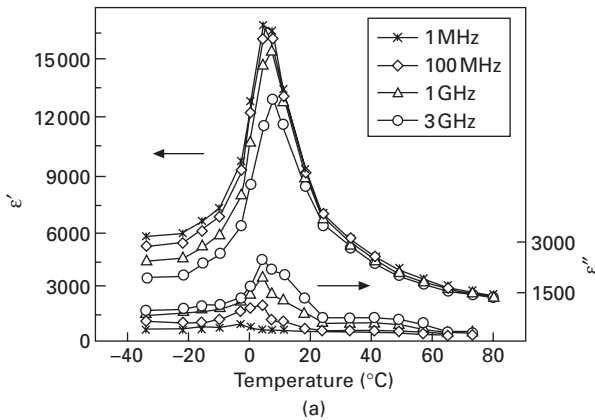
32.19 Models of lattice relaxation and the direction of stresses in films deposited on STO substrates.

lattices of the BTO, but these strained lattices of BTO are not relaxed because the next STO layers are deposited on the strained BTO lattices to give a new compressive stress. Owing to the stress induced by the STO layers in the superlattices, the strained BTO lattices remain up to the film surface. Although a large stress and a strain are thus induced into the BTO layers, the stress and strain in the STO layers in the superlattices should be very small because the stress is hardly induced to the STO layers from the strained BTO layers or the STO substrate with the same  $a$ -parameter.

The ideal cases of the strained lattice formation are observed in the BTO/STO superlattice with the periodicity of 10, where the  $a$ -parameter of the superlattice is consistent with that of STO (Fig. 32.8). As the stacking periodicity increases to 40, the strained lattices were relaxed as indicated by the change in the  $a$ -parameter. The elongation of  $c$ -parameter of BTO lattice stabilizes and/or enhances the spontaneous polarization of BTO layers along the film thickness. It should be recalled that the result of the EM analysis indicated that the permittivity measured with interdigital electrodes was that along the film plane. This means that the electric field applied in the dielectric measurements using interdigital electrodes is perpendicular to the direction of the spontaneous polarization of BTO layers, which is analogous with the permittivity measurement of a tetragonal BTO single crystal along its  $a$ -axis. It is known that the permittivity along the  $a$ -axis of the tetragonal BTO is much higher than that along the  $c$ -axis because of flat potential wells in the lattice and/or the rotation of spontaneous polarization with electric fields which contribute to the dipole polarizations. We believe that this is the mechanism of the enhancement of dielectric permittivity in the BTO/STO superlattices formed on the STO substrate. The permittivity observed in our study was much higher than previously reported because we only used planar electrodes in the permittivity measurements.

*Temperature dependence of permittivity of BTO/STO superlattices*

Temperature dependence of the dielectric permittivity provides important information for understanding the mechanism of the dielectric anomaly of the superlattices. The high permittivity of BTO-STO ceramics is accompanied by the phase transition at the Curie point. Even in the relaxors, the formation of polar nano-regions can be regarded as a precursor phenomenon of the phase transition. As far as the phase transition is concerned with the generation of high permittivity, the permittivity inevitably varies with temperature. Figure 32.20(a) shows the complex dielectric permittivity of  $\text{Ba}_{0.6}\text{Sr}_{0.4}\text{TiO}_3$  ceramics as a function of temperature.<sup>60</sup> The ceramics show a large permittivity peak at about  $5^\circ\text{C}$  corresponding to the first-order phase transition. The room temperature permittivity of about 6000 is due to the tailing of the peak, therefore the temperature stability of high permittivity cannot be expected in the ceramics. The real dielectric permittivity of the BTO/STO superlattices



32.20 Temperature dependence of dielectric permittivity; (a)  $\text{Ba}_{0.6}\text{Sr}_{0.4}\text{TiO}_3$  ceramics; (b) BTO/STO superlattices.

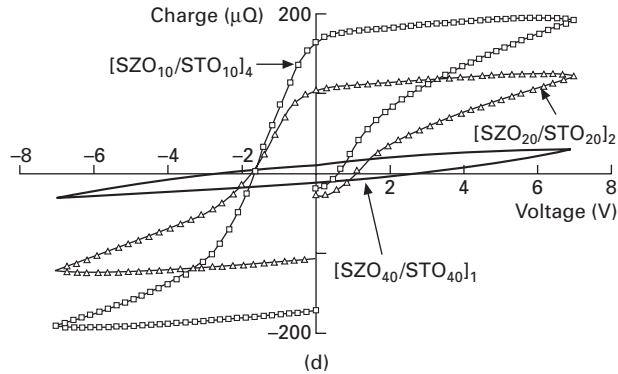
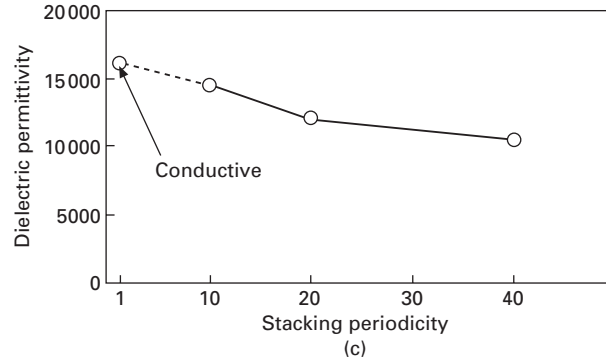
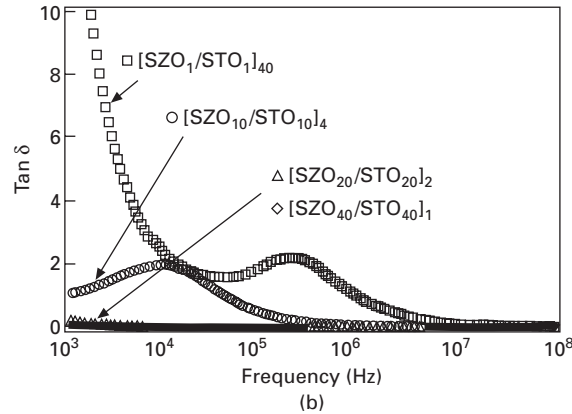
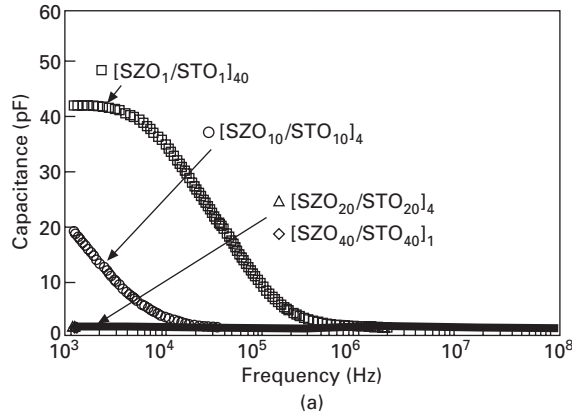


with different compositions is shown in Fig. 32.20(b) as a function of temperature. The permittivity of the  $[\text{BTO}_{10}/\text{STO}_{10}]_4$  superlattice is about 19000 at room temperature, which is lower than the result in Fig. 32.17. This discrepancy is due to the sensitivity of permittivity to the quality of the superlattices. The dielectric permittivity of the  $[\text{BTO}_{10}/\text{STO}_{10}]_4$  superlattices is higher than other superlattices, namely  $[\text{BTO}_{12}/\text{STO}_8]_4$  and  $[\text{BTO}_{15}/\text{STO}_4]_4$ . Again, the enhancement of the permittivity in the superlattices with a periodicity of 10 was confirmed. As for the temperature dependence of the permittivity, the permittivity increases in all superlattices with increasing temperature and no peak of the permittivity is observed in the temperature range up to 150 °C. These results strongly suggest that the high permittivity of the superlattices is not concerned with the phase transition but is caused by the temperature-stable lattice distortions induced by the lattice mismatch between STO and BTO.

#### *Artificial ferroelectricity in SZO/STO superlattices<sup>61</sup>*

Figure 32.21(a) and (b) shows capacitances and dielectric loss tangents of the SZO/STO superlattices. It is notable that a large dielectric relaxation was observed in the superlattices with the periodicity of 1 and 10, which was not observed in the BTO/STO superlattices in Fig. 32.17. The dielectric loss tangent of the  $[\text{SZO}_1/\text{STO}_1]_{40}$  superlattice steeply increases in the low-frequency region, which obviously indicates the effect of electric conduction. This superlattice also shows a high extinction coefficient in the optical frequencies (Fig. 32.10b). We believe that the high loss and high leakage current observed only in this superlattice are concerned with overlapping of electron clouds caused by the lattice shrinkage of this superlattice (see the result of the XRD analysis in Fig. 32.8b). A dielectric loss peak was also observed at 250 kHz in the  $[\text{SZO}_1/\text{STO}_1]_{40}$  superlattice. The dielectric loss peak indicates that a polarizing species with a relatively long relaxation time exists in this superlattice. A similar dielectric loss is observed in the  $[\text{SZO}_{10}/\text{STO}_{10}]_4$  superlattice but its frequency is lower than that of the  $[\text{SZO}_1/\text{STO}_1]_{40}$  superlattice. The dielectric loss of the  $[\text{SZO}_{20}/\text{STO}_{20}]_2$  superlattice slightly increases in the low-frequency region. This may be due to the tailing of the dielectric loss peak at lower frequencies. The peak frequency seems to decrease with increasing periodicity of superlattices.

The variation of the relative permittivity at 110 MHz with the periodicity of superlattices is shown in Fig. 32.21(c). The permittivity of the superlattice with a periodicity of 1 is not reliable because of its high leakage current. The permittivity decreased with increasing periodicity over the periodicity of 10, which is similar to the behavior of the BTO/STO superlattices, but the maximum permittivity of the SZO/STO superlattices is lower than that of the BTO/STO superlattices (Fig. 32.17c).



32.21 Dielectric properties of SZO/STO superlattices: (a) frequency dispersion of capacitance; (b) frequency dispersion of loss tangent; (c) relative dielectric permittivity at 110MHz as a function of stacking periodicity of superlattices; (d) Charge vs. voltage curve.

Figure 32.21(d) shows  $Q$ - $V$  curves of the SZO/STO superlattices measured at 132.5 Hz. It should be stressed that the  $[\text{SZO}_{10}/\text{STO}_{10}]_4$  superlattice shows a clear hysteresis loop in the  $Q$ - $V$  relation. The absolute value of the remanent polarization could not be determined because of the use of interdigital electrodes, but the  $Q$ - $V$  relations indicate that the remanent polarization decreases with increasing periodicity. The hysteresis loop was only observed around or below the frequency of the dielectric relaxation. The ferroelectricity in the SZO/STO superlattices is induced artificially by the lattice distortion because both materials do not have a ferroelectric nature. Abe and coworkers<sup>62,63</sup> also reported that the ferroelectricity of BTO-STO solid solution films was enhanced by the anisotropic lattice distortion. From the results of Figs 32.8 and 32.20, it is obvious that the artificial ferroelectricity depended on the anisotropic lattice distortion, i.e. the  $[\text{SZO}_{10}/\text{STO}_{10}]_4$  superlattice with the highest lattice distortion showed the largest remanent polarization with a clear hysteresis curve. It is interesting that the remanent polarization is not maintained after the measuring cycle in the artificially induced ferroelectricity. In the measurement using interdigital electrodes, the electric field is mainly applied along the film plane, which is perpendicular to that of lattice distortion along the  $c$ -axis. Therefore, the spontaneous polarization should rotate  $90^\circ$  in order to show the hysteresis loops. The  $90^\circ$  switching of the spontaneous polarization tends to relax after the electric field is removed, which may be the reason for the reduced remanent polarization after a measuring cycle. The dielectric loss peak with the Debye-like dielectric relaxation may be due to the rotation of the spontaneous polarization induced by the lattice distortions. The artificial ferroelectricity found in the artificial superlattices is unique because it is observed only in the low-frequency region accompanied with the dielectric relaxation. In normal ferroelectrics, dielectric relaxation is not observed up to the GHz region and ferroelectricity is retained up to much higher frequencies. The  $90^\circ$  switching of spontaneous polarization in the superlattices may have a limit of switching speed.

Considering the lattice parameters of bulk specimens, the stress induced in the SZO/STO superlattices must be larger than that induced in the BTO/STO superlattices as mentioned in Section 32.3. The artificial ferroelectricity was not observed in the BTO/STO superlattices. This indicates that the anisotropic lattice distortion is more effective at inducing the ferroelectricity than the ferroelectric nature of BTO. The BTO/STO superlattices showed a higher dielectric permittivity than the SZO/STO superlattices. It seems that a large lattice distortion enhances the ferroelectricity but reduces the dielectric permittivity in the perovskite superlattices, which is analogous with the behaviors of normal ferroelectrics and relaxors. The anisotropic lattice distortion induced by the lattice mismatch between the film and substrate and between the constituent layers in superlattices played an important role in giving rise to the high permittivity and the artificial ferroelectricity.

## 32.6 Conclusions and future trends

The aim of our study of perovskite artificial superlattices was to answer the following simple question: are the dielectric properties of perovskite artificial superlattices different from the thin films with the same composition and thickness? We can now say that the answer is 'yes'. In this chapter, important studies on the preparation and the properties of the perovskite artificial superlattices were introduced, and the advantage and disadvantage of deposition processes were discussed. As far as the film quality is concerned, the reactive MBE process seems to be superior to other processes. The quality and perfection of the superlattice structure are the most important factors for research into superlattices as pointed out by Shlom *et al.*<sup>23</sup> We have succeeded in preparing BTO/STO and SZO/STO superlattices using reactive MBE system but the films obtained still suffer from quality issues. The deposition of perfect superlattices containing metal elements with high melting temperatures requires further improvement of the whole system. The lattice distortion induced by the lattice mismatch between the film and substrate and also between the constituent layers in the superlattices is the origin of the dielectric anomalies observed in the superlattices. In both BTO/STO and SZO/STO superlattices, the highest anisotropic distortion was induced in the superlattices when the periodicity of the superlattices is 10. The refractive index of superlattices measured with a spectroscopic ellipsometer showed maximum values when the highest anisotropic distortion was induced into the superlattices. The permittivity of the superlattices was measured using interdigital electrodes and the EM analysis. The BTO/STO superlattices showed a marked enhancement of the permittivity when the superstructure periodicity was 10. The similar enhancement was confirmed in the superlattice prepared by the RF-sputtering process. The mechanism of the dielectric enhancement was discussed in terms of the anisotropic lattice distortion. Ferroelectricity was artificially induced in the SZO/STO superlattices with the highest anisotropic lattice distortion even though both compounds were non-ferroelectrics. This ferroelectricity was interpreted by 90° rotations of the spontaneous polarizations induced by the lattice distortion into the superlattices.

The future trend of this subject will be the manipulation of one molecular layer in the superlattices. The insertion of magnetic active layers in ferroelectric superlattices may produce a new interaction between magnetic and ferroelectric properties. The conductive layers in the dielectric superlattices may enhance the interfacial polarization to obtain high permittivity. The composition graduation in the superlattice is also a challenging topic for study. This kind of artificially modulated structures will produce special stress fields in the films, which may give additional enhancements of the properties.

The history of oxide superlattices is only 20 years old. In spite of the recent progresses in the deposition, characterization and property evaluation

techniques, the study of oxide superlattices is still the state of the art for most materials and ceramics scientists. We believe that the oxide superlattices have definitely opened a new field of materials science and nanotechnology, in which young or established materials scientists can make a significant impact. We hope this chapter provides them with useful guidance to investigate this challenging but very fruitful research field.

## 32.7 References

1. Esaki L and Tsu R (1970), 'Superlattice and negative differential conductivity in semiconductors', *IBM J Res Development*, **Jan.**, 61–65.
2. Tsu R and Esaki L (1973), 'Tunneling in a finite superlattice', *Appl Phys Lett*, **22**, 562–564.
3. Esaki L and Chang L L (1974), 'New transport phenomenon in a semiconductor superlattice', *Phys Rev Lett*, **33**, 495–498.
4. Iijima K, Terashima T, Bando Y, Kamigaki K and Terauchi I (1992), 'Atomic layer growth of oxide thin films with perovskite-type structure by reactive evaporation', *J Appl Phys*, **72**, 2840–2845.
5. Iijima K, Terashima T, Yamamoto K, Hirata K and Bando Y (1990), 'Preparation of ferroelectrics BaTiO<sub>3</sub> thin films by activated reactive evaporation', *Appl Phys Lett*, **56**, 527–529.
6. Ohkubo H, Kanda N, Yoshimoto M and Koinuma H (1993), 'Fabrication of high-quality perovskite oxide films by lateral epitaxy verified with RHEED oscillation', *Jpn J Appl Phys*, **32**, 689–691.
7. Yoshimoto M, Maeda T, Gonda S, Shomozono K, Koinuma H, Ishiyama O and Shomomura M (1994), 'Molecular layer epitaxy of perovskite-based oxides by laser MBE', *Mat Res Soc Symp Proc*, **341**, 133–138.
8. Kawasaki M, Takahashi K, Maeda T, Tsuchiya R, Shonohara M, Ishiyama O, Yonezawa T, Yoshimoto M and Koinuma H (1994), 'Atomic control of the SrTiO<sub>3</sub> crystal surface', *Science* **266**, 1540–1542.
9. Yoshimoto M, Maeda T, Ohnishi T, Lee G H and Koinuma H (1996), 'Atomic scale control of epitaxial growth and interface in oxide thin films for advanced oxide lattice engineering', *Mat Res Soc Symp Proc*, **401**, 21–31.
10. Tabata H, Tanaka H and Kawai T (1994), 'Formation of artificial BaTiO<sub>3</sub>/SrTiO<sub>3</sub> superlattices using pulsed laser deposition and their dielectric properties', *Appl Phys Lett*, **65**, 1970–1972.
11. Tsurumi T, Suzuki T, Yamane M and Daimon M (1994), 'Fabrication of barium titanate-strontium titanate artificial superlattice by atomic layer epitaxy', *Jpn J Appl Phys*, **33**, 5192–5195.
12. Kim J, Kim Y, Kim Y-S, Lee J, Kim L and Jung D (2002), 'Large nonlinear dielectric properties of artificial BaTiO<sub>3</sub>/SrTiO<sub>3</sub> superlattices', *Appl Phys Lett*, **80**, 3581–3583.
13. Kim L, Jung D, Kim J, Kim Y, Kim Y-S and Lee J (2003), 'Strain manipulation in BaTiO<sub>3</sub>/SrTiO<sub>3</sub> artificial lattice toward high dielectric constant and its nonlinearity', *Appl Phys Lett*, **82**, 2118–2120.
14. Kim J, Kim L, Jung D, Kim Y-S, Kim I-W, Je J-H and Lee J (2003), 'Thickness dependent dielectric property of BaTiO<sub>3</sub>/SrTiO<sub>3</sub> artificial superlattices', *Jpn J Appl Phys*, **42**, 5901–5903.

15. Guerville F De, Marssi M El, Raevski I P, Karkut M G and Yuzyuk Yu I (2006), 'Soft mode dynamics and the reduction of  $Ti^{4+}$  disorder in ferroelectric/relaxor superlattices  $BaTiO_3/BaTi_{0.68}Zr_{0.32}O_3$ ', *Phys Rev*, **B74**, 064107.
16. Christen H-M, Knauss L A and Harshavardhan K S (1998), 'Field-dependent dielectric permittivity of paraelectric superlattice structure', *Mater. Sci. Engineer.*, **B56**, 200–203.
17. Tong F O, Yu W X, Liu F, Zuo Y and Ge X (2003), 'Microstructural study of  $BaTiO_3/SrTiO_3$  superlattice', *Mater Sci Engineer*, **B98**, 6–9.
18. Qu B D, Evstigneev M, Johnson D J and Prince R H (1998), 'Dielectric properties of  $BaTiO_3/SrTiO_3$  multilayered thin films prepared by pulsed laser deposition', *Appl Phys Lett*, **72**, 1394–1396.
19. Katiyar R S, Yuzyuk Yu I, Das R R, Bhattacharya P and Gupta V (2005), 'Polarization Raman spectra of  $BaTiO_3/SrTiO_3$  superlattices', *Ferroelectrics*, **329**, 907–916.
20. Choi T and Lee J (2005), 'Dielectric properties of  $PbZrO_3/PbTiO_3$  artificial superlattices grown by pulse laser deposition', *Ferroelectrics*, **328**, 799–804.
21. Seo S S A, Lee H N and Noh T W (2005), 'Infrared spectroscopy of  $CaTiO_3$ ,  $SrTiO_3$ ,  $BaTiO_3$ ,  $Ba_{0.5}Sr_{0.5}TiO_3$ , thin films, and  $(BaTiO_3)_5/(SrTiO_3)_5$  superlattice grown on  $SrRuO_3/SrTiO_3(001)$  substrates', *Thin Solid Films*, **486**, 94–97.
22. Jiang J C, Pan X Q, Tian W, Theis C D and Schlom D G (1999), 'Abrupt  $PbTiO_3/SrTiO_3$  superlattices grown by reactive molecular beam epitaxy', *Appl Phys Lett*, **74**, 2851–2853.
23. Schlom D G, Haeni J H, Lettieri J, Theis C D, Tian W, Jiang J C and Pan X Q (2001), 'Oxide nano-engineering using MBE', *Mater Sci Eng*, **B87**, 282–291.
24. Tian W, Jiang J C, Pan X Q, Haeni J H, Li Y L, Chen L Q, Schlom D G, Neaton J B, Rabe K M and Jia Q X (2006), 'Structural evidence for enhanced polarization in a commensurate short-period  $BaTiO_3/SrTiO_3$  superlattice', *Appl Phys Lett*, **89**, 092905.
25. Tsai H-N, Liang Y-C and Lee H-Y (2005), 'Characteristics of sputter-deposited  $BaTiO_3/SrTiO_3$  artificial superlattice films on an  $LaNiO_3$ -coated  $SrTiO_3$  substrate', *J Cryst Growth*, **284**, 65–72.
26. Katiyar R S and Yuzyuk Yu I (2006), 'Stress relaxation effects in ferroelectric thin films and superlattices', *Ferroelectrics*, **334**, 487–491.
27. Wu T-B and Hung C-L (2005), 'Constrained ferroelectricity in the (001)-textured superlattices of  $PbZrO_3/BaZrO_3$ ', *Appl Phys Lett*, **86**, 112902.
28. Hung C-L, Chueh Y-L, Wu T-B and Chou L-J (2005), 'Characterization of constrained ferroelectricity in  $PbZrO_3/BaZrO_3$  superlattice films', *J Appl Phys*, **97**, 034105.
29. Shimuta T, Nakagawara O, Makino T, Arai S, Tabata H and Kawai T (2002), 'Enhancement of remanent polarization in epitaxial  $BaTiO_3/SrTiO_3$  superlattices with "asymmetric" structure', *J Appl Phys*, **91**, 2290–2294.
30. O'Neill D, Bowman R M and Gregg J M (2000), 'Dielectric enhancement and Maxwell–Wagner effects in ferroelectric superlattice structures', *Appl Phys Lett*, **77**, 1520–1522.
31. Neaton J B and Rabe K M (2003), 'Theory of polarization enhancement in epitaxial  $BaTiO_3/SrTiO_3$  superlattices', *Appl Phys Lett*, **82**, 1586–1588.
32. Kim L, Kim J, Jung D, Lee J and Waghmare U V (2005), 'Polarization of strained  $BaTiO_3/SrTiO_3$  artificial superlattice: first-principles study', *Appl Phys Lett*, **87**, 052903.
33. Kim L, Kim J, Waghmare U, Jung D and Lee J (2005), 'Lattice instability of  $BaTiO_3/SrTiO_3$  artificial superlattice', *Integrated Ferroelectrics*, **73**, 3–10.
34. Kim L, Kim J, Waghmare U, Jung D and Lee J (2005), 'Structural transition and

- dielectric response of an epitaxial strained BaTiO<sub>3</sub>/SrTiO<sub>3</sub> superlattice: a first-principles study', *Phys Rev*, **B72**, 214121.
35. Yang K, Wang C L, Li J C, Zhao M L and Wang X Y (2006), 'Strain induced ferroelectricity in the SrZrO<sub>3</sub>/SrTiO<sub>3</sub> superlattice: first principles study,' *Solid State Comm.*, **139**, 144–147.
  36. Lo V C and Jiang W (2006), 'Simulation of stress-induced enhanced dielectric permittivity in ferroelectric superlattice,' *Integrated Ferroelectrics*, **78**, 35–43.
  37. Tsurumi T, Miyasou T, Ohashi N and Ishibashi Y (1998), 'Preparation and dielectric property of BaTiO<sub>3</sub>/SrTiO<sub>3</sub> artificially modulated structures', *Jpn J Appl Phys*, **37**, 5104–5107.
  38. Ishibashi Y, Tsurumi T, Ohashi N and Fukunaga O (1998), 'Epitaxial growth of barium titanate thin films at low temperatures by low-energy positive oxygen ion assisting', *Solid State Ionics*, **108**, 91–97.
  39. Ishibashi Y, Ohashi N and Tsurumi T (2000), 'Structural refinement of x-ray diffraction profile for artificial superlattices', *Jpn J Appl Phys*, **39**, 186–191.
  40. Nishizawa S, Tsurumi T, Hyoudo H, Ohashi N and Fukunaga O (1997), 'Structural changes in ZnO/NiO artificial superlattice made by ion beam sputtering', *Thin Solid Films*, **302**, 133–139.
  41. Collins R W (1990), 'Automatic rotating element ellipsometers: calibration, operation and real-time applications', *Rev Sci Instrum*, **61**, 2029–2062.
  42. Shirafuji T, Motomura H and Tachibana K (2004), 'Fourier transform infrared phase-modulated ellipsometry for *in situ* diagnostics of plasma surface interactions', *J Phys*, **D37**, R49–R73.
  43. Tolmachev V A (1999), 'Adsorption-ellipsometry method of studying the optical profile, thickness, and porosity of thin films', *J Opt Tech*, **66**, 596–607.
  44. Jenkins T E (1999), 'Multiple-angle-of-incidence ellipsometry', *J Phys*, **D32**, R45–R56.
  45. Topcu S, Chassagne L and Alayli Y (2003), 'A new type of fiber-optic-based interferometric ellipsometer for *in situ* and real-time measurements', *Rev Sci Instrum*, **74**, 4442–4447.
  46. Lee J, Koh J and Collins R W (2001), 'Dual rotating-compensator multichannel ellipsometer: instrument development for high-speed Mueller matrix spectroscopy of surfaces and thin films', *Rev Sci Instrum*, **72**, 1742–1754.
  47. Azzam R M A and Bashara N M (1977), *Ellipsometry and Polarized Light*, Amsterdam, North Holland, Elsevier Science Publishers BV.
  48. Sik J, Schubert M, Leibiger G, Gottschalch V and Wagner G (2001), 'Band-gap energies, free carrier effects, and phonon modes in strained GaNAs/GaAs and GaNAs/InAs/GaAs superlattice heterostructures measured by spectroscopic ellipsometry', *J Appl Phys*, **89**, 294–305.
  49. Sik J, Schubert M, Leibiger G, Gottschalch V, Kirpal G and Humlicek J (2000), 'Near-band-gap optical functions spectra and band-gap energies of GaNAs/GaAs superlattice heterostructures measured by spectroscopic ellipsometry', *Appl Phys Lett*, **76**, 2859–2861.
  50. Logothetidis S, Kalfagiannis N, Sarakinos K and Patsalas P (2006), 'Investigation of bilayer period and individual layer thickness of CrN/TiN superlattices by ellipsometry and X-ray techniques', *Surf Coat Tech*, **200**, 6176–6180.
  51. Bellani V, Stella A, Chen C and Wang X (2005), 'Spectroscopic ellipsometry study of Cd<sub>1-x</sub>Mn<sub>x</sub>Te/CdTe superlattices', *J Appl Phys*, **98**, 103523.
  52. Losurdo M, Giuva D, Giangregorio M M, Bruno G and Brown A S (2004),

- 'Spectroscopic ellipsometry characterization of interface reactivity in GaAs-based superlattices', *Thin Solid Films*, **455–456**, 457–461.
53. Ma Y, Tsurumi T, Nishizawa S, Ohashi N and Fukunaga O (1998), 'Spectroscopic ellipsometry of NiO/ZnO artificial superlattice', *J Am Ceram Soc*, **81**, 2125–2129.
  54. Nijs J M M and Silfhout A (1988), 'Systematic and random errors in rotating-analyzer ellipsometry', *J Opt Soc Am*, **5**, 773–781.
  55. Kim S Y (1996), 'Simultaneous determination of refractive index, extinction coefficient, and void distribution of titanium dioxide thin film by optical methods', *Appl Opt* **35**, 6703–6707.
  56. Trolier-McKinstry S, Chindaudom P, Vedam K and Hiremath B V (1995), 'Characterization of optical thin films by spectroscopic ellipsometry', *J Am Ceram Soc*, **78**, 2412–2416.
  57. Chindaudom P and Vedam K (1992), 'Determination of the optical constants of an inhomogeneous transparent LaF<sub>3</sub> thin film on a transparent substrate by spectroscopic ellipsometry', *Opt Lett*, **17**, 538–540.
  58. Gustin K M (1987), 'Optical characterization of low-index transparent thin films on transparent substrates by spectroscopic ellipsometry', *Appl Opt*, **26**, 3796–3802.
  59. Farnell G W, Cermak I A, Silverster P and Wong S K (1970), 'Capacitance and field distributions for interdigital surface-wave transducers', *IEEE Trans. UFFC*, **SU-17**, 188–195.
  60. Li J, Kakemoto H, Wada S, Kawaji H and Tsurumi T (2006), 'Dielectric relaxation in GHz region and phase transition of BaTiO<sub>3</sub>-based ceramics', *J Appl Phys*, **100**, 024106.
  61. Tsurumi T, Harigai T, Tanaka D, Nam S-M, Kakemoto H, Wada S and Saito K (2004), 'Artificial ferroelectricity in perovskite superlattices', *Appl Phys Lett*, **85**, 5016–5018.
  62. Abe K, Komatsu S, Yanase N, Sano K and Kawakubo T (1997), 'Ferroelectric properties in heteroepitaxial Ba<sub>0.6</sub>Sr<sub>0.4</sub>TiO<sub>3</sub> thin films on SrRuO<sub>3</sub>/SrTiO<sub>3</sub> substrates', *Jpn J Appl Phys*, **36**, 5575–5579.
  63. Kawakubo T, Komatsu S, Abe K, Sano K, Yanase N and Fukushima N (1998), 'Ferroelectric properties of SrRuO<sub>3</sub>/(Ba, Sr)TiO<sub>3</sub>/SrRuO<sub>3</sub> epitaxial capacitor', *Jpn J Appl Phys*, **37**, 5108–5111.



## Crystal structure and defect control in $\text{Bi}_4\text{Ti}_3\text{O}_{12}$ -based layered ferroelectric single crystals

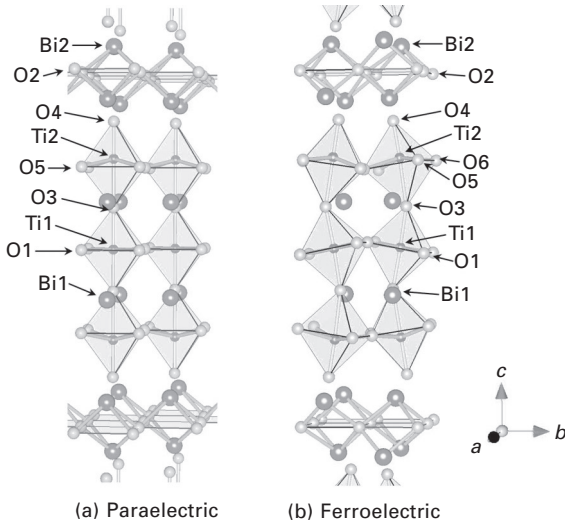
Y NOGUCHI and M MIYAYAMA,  
The University of Tokyo, Japan

### 33.1 Introduction

The study of ferroelectrics offers unparalleled opportunities to advance the fundamental physics and materials design of dielectric materials, and to develop innovative semiconductor-based applications such as nonvolatile memories, piezoelectric and electro-optic devices and uncooled infrared detectors [1]. Ferroelectric bismuth titanate ( $\text{Bi}_4\text{Ti}_3\text{O}_{12}$ , BiT) [2] has been regarded as a promising material because of its high Curie temperature ( $T_C$ ) of 675 °C [3], large spontaneous polarization ( $P_s$ ) of  $\sim 50 \mu\text{C}/\text{cm}^2$  [4, 5] and large electro-optic coefficient [6, 7].

In the crystal structure of BiT, the perovskite layers composed of three  $\text{TiO}_6$  octahedral layers with Bi at the A site are sandwiched between  $\text{Bi}_2\text{O}_2$  layers, as shown in Fig. 33.1. In the paraelectric state above  $T_C$ , BiT has a parent tetragonal structure with  $I4/mmm$  symmetry. The ferroelectric transition results in descending symmetry, and the crystals at room temperature exhibit a monoclinic distortion with  $B1a1$  space group [8]. Polarization measurements of BiT single crystals have revealed a  $P_s$  of  $50 \mu\text{C}/\text{cm}^2$  along the  $a$ -axis and of  $3\text{--}5 \mu\text{C}/\text{cm}^2$  along the  $c$  axis [4, 5]. Rae *et al.* [8] have clearly shown through single-crystal structural analysis at room temperature that the shape of  $\text{TiO}_6$  octahedra in the paraelectric state remains nearly intact in the ferroelectric state. The  $\text{TiO}_6$  octahedra rotate in the  $a$ - $b$  plane as well as incline away from the  $c$ -axis. The displacement of the  $\text{TiO}_6$  octahedra with respect to Bi ions along the  $a$ -axis mainly contributes to the ferroelectric polarization in the BiT system and off-center Ti displacements in the octahedra play a minor role in  $P_s$  [8]. These structural features of BiT are markedly different from the  $\text{ABO}_3$ -type ferroelectrics such as  $\text{BaTiO}_3$  and  $\text{PbTiO}_3$  where the ferroelectricity results from the relative displacements of A and B cations with respect to oxygen-octahedral cage.

It is recognized that defects are closely related to the leakage current and polarization properties of BiT [9–16]. Takahashi *et al.* [17, 18] have revealed the conduction mechanism of BiT single crystals and polycrystalline ceramics



33.1 Crystal structures of  $\text{Bi}_4\text{Ti}_3\text{O}_{12}$  of (a) the paraelectric phase at  $700^\circ\text{C}$  and (b) the ferroelectric phase at  $25^\circ\text{C}$ .

at high temperatures. The electrical conductivity along the  $a$ -axis is higher by several orders of magnitude than that along the  $c$ -axis. Oxide-ion migration ascribed to a large number of oxygen vacancies in the perovskite layers controls the high electrical conduction along the  $a$ -axis. With decreasing temperature, the contribution of oxide ions to the electrical conduction becomes less significant, and electron holes become the dominant carrier at low temperatures. Recently, Noguchi *et al.* [12, 19] have clarified the origin of the leakage current of BiT crystals at room temperature. Electron holes arising from the incorporation of oxygen from ambient at the oxygen vacancies act as detrimental carriers of leakage current up to high electric fields.

La- and Nd-substituted BiT (BLT and BNT) have received a great deal of attention since these substitutions led to better memory properties such as a large remanent polarization ( $P_r$ ), a high fatigue endurance and a superior insulating property [20–32]. These rare-earth (RE) elements have been reported to preferentially occupy the perovskite A site [33]. The presence of RE at the A site reduces lattice distortion in the perovskite layers [34–36] as well as providing an additional domain-nucleation site, an antiphase-domain boundary in the lattice [30]. Recently, considerable effort has been made to realize a ferroelectric memory using BLT and BNT, and the device technology related to processing and integration is being developed.

In this chapter, the polarization switching and leakage current properties of the single crystals of BiT and RE-substituted BiT are discussed in terms of the crystal structure, electronic structure, domain structure and defect structure. At first, the ferroelectric distortion and phase transition are viewed

from the electronic and structural features. Next, the defect structure in BiT is shown, and the vacancies of Bi at the A site and the adjacent oxygen vacancies (the resultant electron hole) are shown to dominate the overall polarization and leakage current properties of BiT crystals. The role of La and Nd at the A site is discussed from the structural and electronic points of view. Finally, a guiding principle of defect control in fabrication process for achieving high-performance BiT-based devices is proposed.

Here, the materials properties along the  $a$ -axis (the major polarization direction) are focused, and therefore the simplified crystal symmetry of orthorhombic  $B2cb$  instead of exact monoclinic  $B1a1$  is applied to discuss the structure–property relations in the BiT system.

## 33.2 Crystal structure

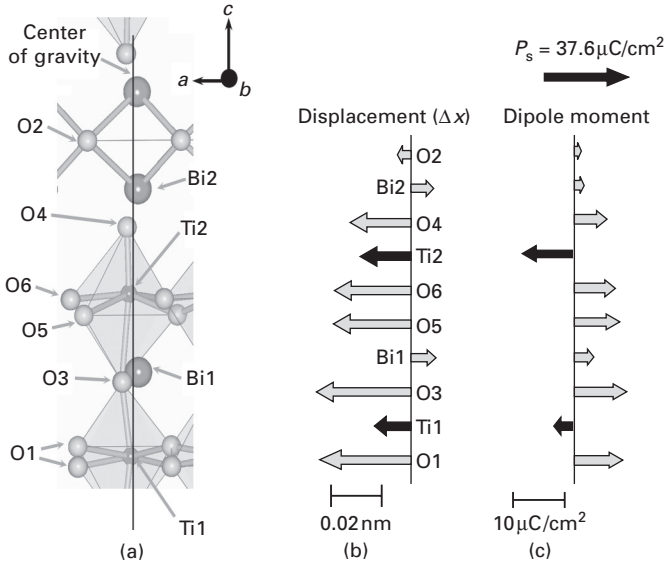
### 33.2.1 Ferroelectric distortion and spontaneous polarization

Figure 33.1 shows the crystal structure of BiT in (a) the paraelectric state (700 °C) and (b) the ferroelectric state (25 °C) determined by neutron diffraction study. The perovskite layers in the paraelectric state are composed of a regular stacking of three  $\text{TiO}_6$  octahedra with Bi at the A site, while a large structural distortion is stored in the crystal lattice in the ferroelectric state. The  $\text{TiO}_6$  octahedra rotate in the  $a$ – $b$  plane as well as incline away from the  $c$ -axis [8, 10, 34, 36–38]. These octahedral distortions are induced by the freezing of several kinds of displacive-type ferroelectric soft modes. The dipole moments caused by the ionic displacements along the  $b$ -axis are cancelled due to the presence of glide plane normal to the  $b$ -axis. Thus, the constituent ions are displaced cooperatively along the  $a$  and  $c$ -axes, leading to a spontaneous polarization ( $P_s$ ) along the both axes. It has been reported that the  $P_s$  along the  $a$ -axis is  $\sim 50 \mu\text{C}/\text{cm}^2$  [4, 5, 10], which is much larger than that along the  $c$ -axis ( $3\text{--}5 \mu\text{C}/\text{cm}^2$ ) [4]. Hereafter, we pay attention only to the  $P_s$  along the  $a$ -axis.

Assuming the constituent ions to have their formal charge (+3 for Bi, +4 for Ti, –2 for O), we can calculate the ionic spontaneous polarization ( $P_{s,\text{ion}}$ ) by the following equation:

$$P_{s,\text{ion}} = \sum_i (m_i \times \Delta x_i \times Q_i e) / \Omega \quad [33.1]$$

where  $m_i$  is the site multiplicity,  $\Delta x_i$  is the displacement along the  $a$ -axis from the corresponding position in the parent tetragonal ( $I4/mmm$ ) structure,  $Q_i e$  is the ionic charge for the  $i$ th constituent ion, and  $\Omega$  is the volume of the unit cell. Figure 33.2 depicts (a) the actual crystal structure at 25 °C projected along the  $b$ -axis, (b) the  $\Delta x_i$  along the  $a$ -axis and (c) the dipole moment ( $\Delta x_i \times Q_i e$ ). It is interesting to note that the three  $\text{TiO}_6$  octahedral layers move

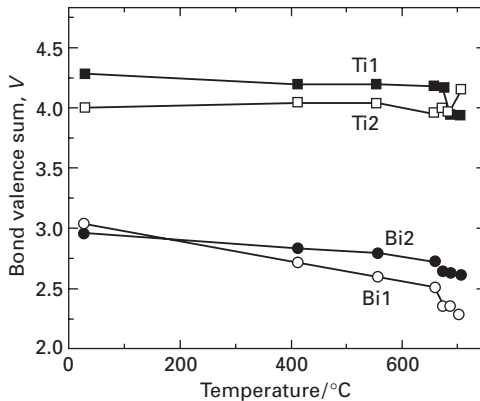


33.2 Detailed structural distortion at 25°C along the polarization direction (the  $a$ -axis): the actual crystal structure projected along the  $b$ -axis, (b) the atomic displacement ( $\Delta x$ ) along the  $a$ -axis from the corresponding position in the parent tetragonal ( $I4/mmm$ ) structure and (c) the dipole moment obtained from the  $\Delta x$  and formal charge. The  $P_s$  along the  $a$ -axis at 25°C is estimated to be  $37.6 \mu\text{C}/\text{cm}^2$ .

cooperatively along the  $a$ -axis with respect to Bi ions, which leads to a  $P_{s,\text{ion}}$  opposite to the  $a$ -axis. In our analysis,  $P_{s,\text{ion}}$  is estimated to be  $37.6 \mu\text{C}/\text{cm}^2$  at 25°C. This value is smaller than that of the experimental  $P_s$ , because the electronic contribution is not taken into account in the calculation of  $P_{s,\text{ion}}$  [39]. Although the relative displacements of Ti ions with respect to the  $\text{TiO}_6$  octahedral center are seen, the off-center Ti displacements play a minor role in  $P_{s,\text{ion}}$ . The entire shift of the  $\text{TiO}_6$  octahedra with respect to heavy Bi ions results in the large dipole moments of oxide ions in the perovskite layers, which gives the dominant contribution to the ferroelectric polarization in the BiT system (see Fig. 33.2c).

### 32.2.2 Bond valence analysis and the role of Bi in the ferroelectric phase transition

To understand the distorted structure in the ferroelectric phase, bond valence analysis [40, 41] has been used as a powerful approach, especially for understanding the crystal chemistry in layered ferroelectrics [38, 42, 43]. The bond valence sum ( $V_i$ ) is assumed to be the apparent valence of an atom in the crystal structure. Figure 33.3 shows the  $V_i$  of cations as a function of



**33.3** Temperature dependence of bond valence sum ( $V$ ) estimated from the structural data.  $V$  represents static charge of ions in crystals.

temperature calculated from the structural data determined by neutron diffraction study. The  $V_{\text{Ti}2}$  is 4.2 in the paraelectric state at 700 °C, and therefore Ti2 is overbonded in the octahedra. This indicates that the Ti2–O bonds are too short and that the  $\text{Ti}2\text{O}_6$  octahedra are under compressive stress. The ferroelectric phase transition results in the  $V_{\text{Ti}2}$  of approximately 4.0. This value is in good agreement with the nominal charge of  $\text{Ti}^{4+}$ , indicating that Ti2 is positioned in the crystallographically moderate environment in the  $\text{Ti}2\text{O}_6$  octahedra in the ferroelectric state. In contrast, the ferroelectric transition leads to an increase in  $V_{\text{Ti}1}$  from 4.0 (700 °C) to 4.3 (25 °C). Although the  $V_{\text{Ti}1}$  of 4.3 (25 °C) is slightly overbonded, the difference from the nominal charge (+4) is smaller than that of Bi.

The ferroelectric phase transition is found to result in a marked change in  $V_{\text{Bi}1}$  and  $V_{\text{Bi}2}$ . In the paraelectric state, Bi1 and Bi2 are characterized by strong underbonding. In particular, the underbonding of Bi1 is remarkable, since  $V_{\text{Bi}1}$  is only 2.3 at 700 °C. This is much lower than the nominal charge of  $\text{Bi}^{3+}$ . This bond valence analysis exhibits that Bi1 in the paraelectric state requires tighter bonding with oxide ions at the perovskite A site to satisfy bonding requirement. The ferroelectric transition leads to an increase in  $V_{\text{Bi}1}$  and  $V_{\text{Bi}2}$ . The values of  $V_{\text{Bi}1}$  and  $V_{\text{Bi}2}$  are 3.0 at 25 °C, which agrees well with the nominal charge of  $\text{Bi}^{3+}$ . While Bi1 cannot get a tight bonding with oxide ions in the paraelectric state due to the restricted movement only along the  $c$ -axis in the  $I4/mmm$  structure, the descending symmetry due to the ferroelectric transition provides a three-dimensional degree of freedom for the displacements of Bi1 and Bi2 to fulfill bonding requirement. The satisfactory bonding of Bi1 and Bi2 stabilizes the ferroelectric distortion in the crystal. It is strongly suggested that the loose bonding of Bi in the paraelectric state, especially the

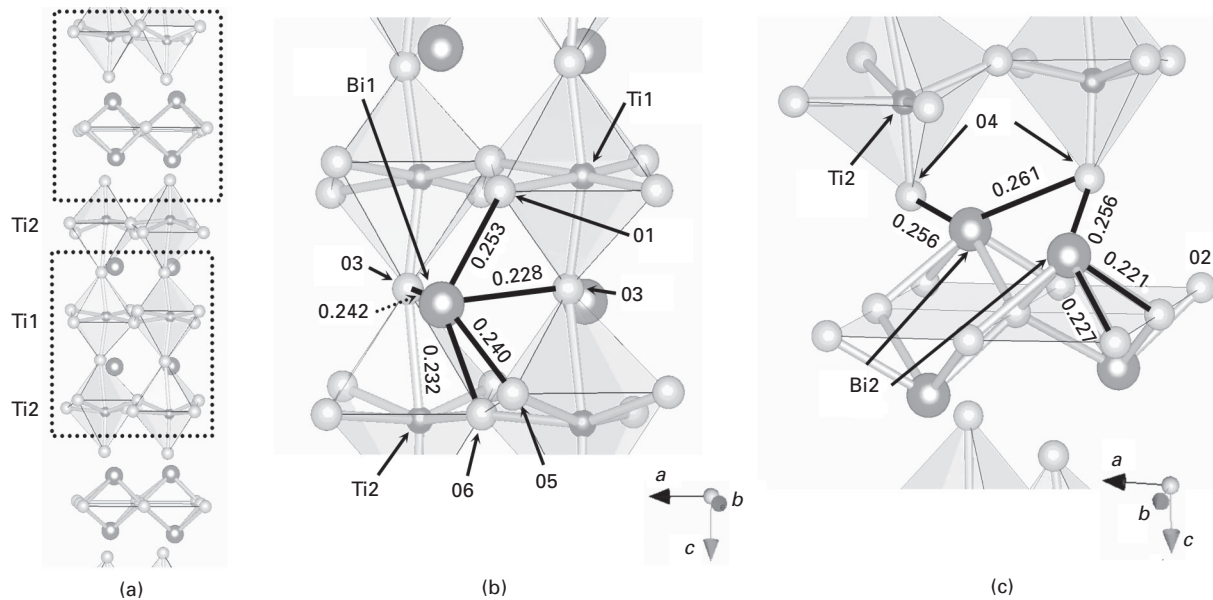
underbonded Bi1 at the A site acts as the structural trigger for the ferroelectric transition in the BiT system.

Figure 33.4 depicts the detailed bond length around Bi1 and Bi2 in the ferroelectric state at 25 °C. In the paraelectric state, Bi is located at the high-symmetry  $4e$  site. The ferroelectric transition leads to several short bonds as shown in Fig. 33.4(b), and the satisfactory bonding of Bi1 is established. The shortest bond is seen in bond length ( $l$ ) between Bi1 and O3 of 0.2284 along the  $a$ -axis, which is 0.0458 nm (17%) smaller than that in the paraelectric state. The strong bonding of Bi1–O3 plays an essential role in the ferroelectric polarization as well as in the appropriate bond valence of the Bi1 at the A site. The shorter bond is also found in  $l_{\text{Bi1-O3}} = 0.2418$  nm (12% shorter) along the  $b$ -axis and  $l_{\text{Bi1-O1}} = 0.2527$  nm (17% shorter), which are responsible for the large  $\text{TiO}_6$  octahedral rotation around the  $a$ -axis, as clearly seen in Fig. 33.1(b).

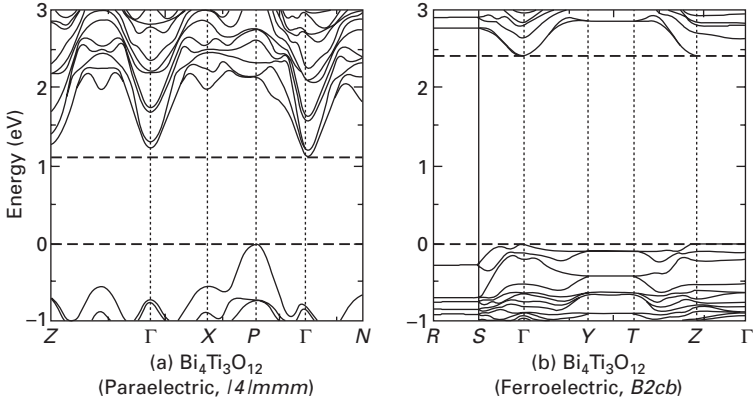
It is interesting to note that a marked change in bond length is also observed for Bi2–O. The smallest two bonds are observed in  $l_{\text{Bi1-O4}} = 0.2556$  nm (12% shorter) along the  $b$ -axis and  $l_{\text{Bi1-O4}} = 0.2614$  nm (10% shorter) along the  $a$ -axis. These bond lengths are relatively longer compared with  $l_{\text{Bi1-O3}}$ . Although the Bi2–O4 bonding contributes to the satisfactory bonding of Bi2 and to the stabilization of the alternate stacking of the  $\text{Bi}_2\text{O}_2$  layers and the perovskite layers, these bonds are suggested to play a minor role in the ferroelectricity in the BiT system.

### 33.3 Electronic band structure and density of states (DOS)

Figure 33.5 shows the electronic band structures for (a) the paraelectric (700 °C) and (b) the ferroelectric (25 °C) phases of BiT calculated from the structural data determined by the neutron diffraction study. The band dispersion for the paraelectric phase is larger than that for the ferroelectric phase, which is attributed to the ferroelectric displacements induced by the descending symmetry. In the paraelectric state, the fundamental band gap ( $E_g$ ) is indicated to be indirect (valence band maximum at  $P$  and conduction band minimum at Brillouin-zone center  $\Gamma$ ) [34], which is consistent with the calculation performed by Shimakawa *et al.* [34]. In contrast, our calculations suggest that the ferroelectric BiT has a direct band gap, with the valence band maximum and conduction band minimum lying at  $\Gamma$ . As is typical in the calculations using density functional theory (DFT) within generalized gradient approximation,  $E_{g(\text{DFT})}$  is underestimated in our calculations. The experimental  $E_g$  of 3.3 eV [35] at 25 °C is higher than the calculated  $E_{g(\text{DFT})}$  of 2.4 eV. The calculated  $E_{g(\text{DFT})}$  of the paraelectric phase is 1.1 eV. The values of  $E_{g(\text{DFT})}$  agree qualitatively with the results of the optical measurements of BiT crystals [35]. The electronic structure of the Nd-substituted BiT is discussed in Section 33.8.



33.4 Detailed bond length in the ferroelectric state at 25°C: (a) the crystal structure projected along the  $b$ -axis, the enlarged views of (b) around Bi1 at the perovskite A site and (c) around Bi<sub>2</sub> in the Bi<sub>2</sub>O<sub>2</sub> layers.



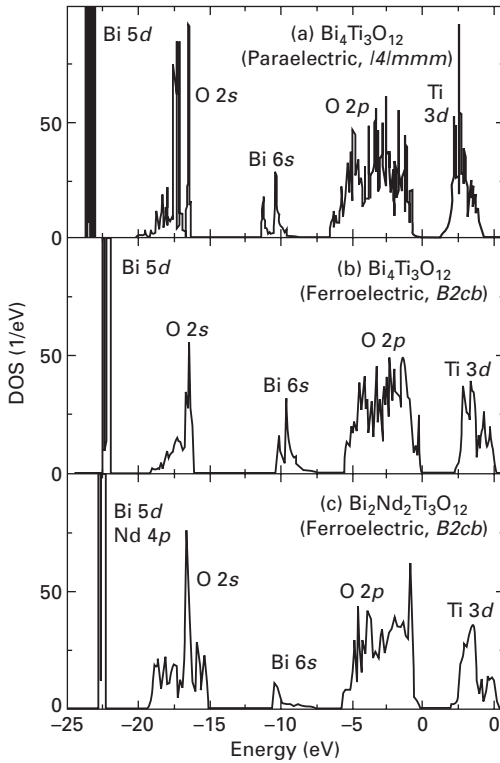
33.5 Band structures of  $\text{Bi}_4\text{Ti}_3\text{O}_{12}$  calculated from the structure data determined by the Rietveld analysis: (a) the paraelectric phase and (b) the ferroelectric phase.

Figure 33.6 presents the total electronic density of states (DOS) between  $-25$  and  $7.5$  eV, where the Fermi level ( $E_F$ ) is set at  $0$  eV. For both the paraelectric and ferroelectric phases, the Bi  $5d$  states are localized at a deep level ( $-22$  to  $-24$  eV). The O  $2s$  and Bi  $6s$  states appear at  $-17$  to  $-20$  eV and  $-7$  to  $-12$  eV, respectively. The valence band consists mainly of the O  $2p$  states, while the Ti  $3d$  states form the conduction band. The Bi  $6p$  states overlap with the Ti  $3d$  states in the conduction band.

Figure 33.7 depicts the total DOS and partial (ion decomposed and sphere projected) DOS (PDOS) of the constituent ions of the (a) paraelectric and (b) ferroelectric phases of BiT. The ionic model suggests that the Ti  $4d$  states are formed only in the conduction band, while significant PDOS of the Ti  $3d$  states is seen in the valence band in both the paraelectric and ferroelectric states. The presence of the Ti  $3d$  states in the valence band indicates that the orbital hybridization between the Ti  $3d$  and the O  $2p$  occurs in the BiT system. Although the hybridization of the Ti  $3d$ -O  $2p$  stabilizes the  $\text{TiO}_6$  octahedra, this orbital interaction does not play an important role in the ferroelectric phase transition, because the value of the Ti- $3d$  PDOS remains unchanged regardless the phase transition.

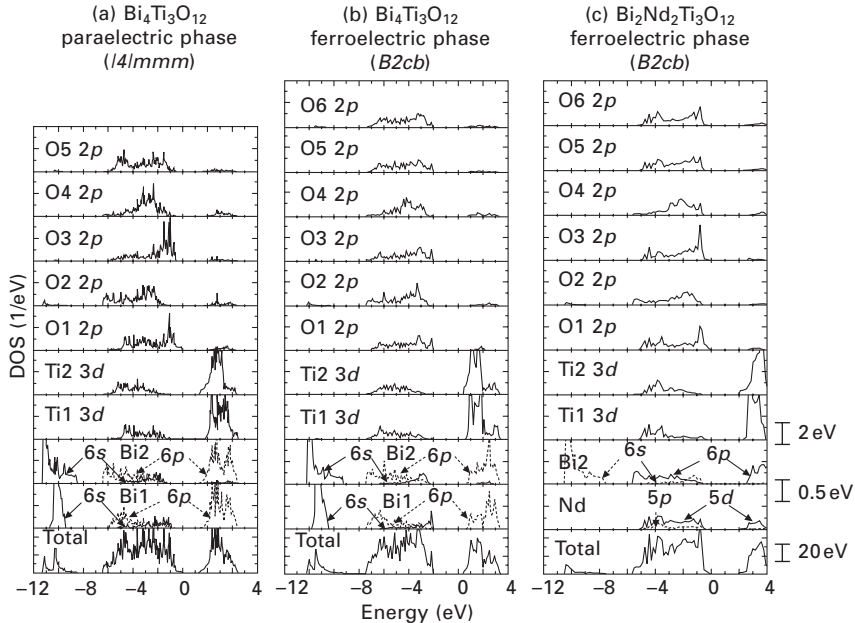
The PDOS analysis shows a marked change in the orbital interaction between Bi and O induced by the transition. The primary band of the Bi  $6s$  appears at around  $-10$  eV, while that of the Bi  $6p$  lies in the conduction band, which is consistent with the ionic model. The PDOS of the O  $2p$  is observed to some degree in the Bi  $6s$  band due to the hybridization of the Bi  $6s$ -O  $2p$ . Furthermore, the PDOS of the O  $2p$  is seen also in the Bi  $6p$  band caused by the Bi  $6p$ -O  $2p$  bonding and antibonding interactions. Thus, the PDOS of the O  $2p$  in these Bi bands can be regarded as a qualitative indicator of the degree of the orbital hybridization between Bi-O.





**33.6** Total electronic density of states (DOS) of (a) the paraelectric phase of  $\text{Bi}_4\text{Ti}_3\text{O}_{12}$ , (b) the ferroelectric phase of  $\text{Bi}_4\text{Ti}_3\text{O}_{12}$ , and (c) the ferroelectric phase of  $\text{Bi}_2\text{Nd}_2\text{Ti}_3\text{O}_{12}$ . In the calculations, the perovskite A site is assumed to be occupied only by Nd.

In the  $\text{Bi}_2\text{O}_2$  layers, the Bi2 6s is strongly hybridized with the O2 2p in both the paraelectric and ferroelectric states, and a large PDOS of the O2 2p is seen at the same energy level in the Bi2 6s main band. The Bi1 6s–O 2p hybridization is also recognized in both states. These results suggest that the traditional model [36, 38, 44] based on the stereoactive lone-pair electrons of  $\text{Bi}^{3+}$  is not sufficient to explain the structural distortion in the ferroelectric state. The phase transition leads to a marked increase in the PDOS of the O3 2p in the Bi1 6s and 6p main bands, which is consistent with the short bond length between Bi1 and O3 in the ferroelectric state. These electronic and structural analyses demonstrate that the hybridization of the Bi1 6s(*p*)–O3 2p acts as a trigger of the ferroelectric transition. This hybridization results in a satisfactory chemical bonding of Bi1 at the A site, and then the ferroelectric distortion is stabilized in the perovskite layers.



33.7 Partial (ion decomposed and sphere projected) DOS (PDOS) of (a) the paraelectric phase of  $\text{Bi}_4\text{Ti}_3\text{O}_{12}$ , (b) the ferroelectric phase of  $\text{Bi}_4\text{Ti}_3\text{O}_{12}$ , and (c) the ferroelectric phase of  $\text{Bi}_2\text{Nd}_2\text{Ti}_3\text{O}_{12}$ . In the calculations, the perovskite A site is assumed to be occupied only by Nd.

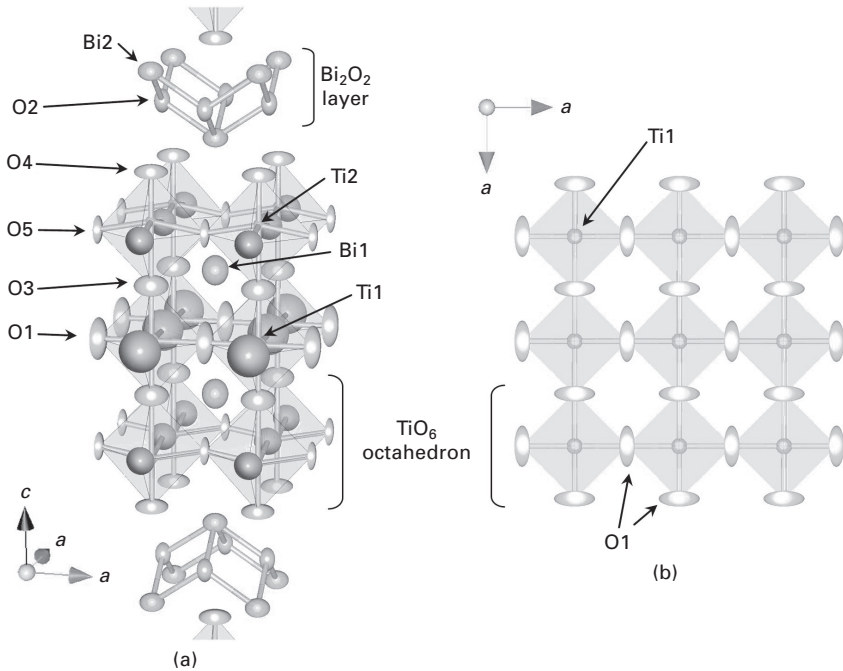
## 33.4 Defect structure

### 33.4.1 Neutron diffraction study

The information of oxygen vacancies in BiT has been obtained by the Rietveld analysis of the time-of-flight neutron powder diffraction data measured at  $700^\circ\text{C}$  in vacuum [19]. The refined crystal structure with the thermal ellipsoids (probability 80%) is depicted in Fig. 33.8. It is interesting to note that the thermal ellipsoid of O1 is large compared with those of other oxide ions and that the nuclear density of O1 spreads in the  $a$ - $a$  plane. This result strongly indicates that self-diffusion of oxide ions occurs through the O1 site at which a large number of oxygen vacancies ( $\text{V}_\text{O}^\bullet$ ) are present. Takahashi *et al.* [17] have demonstrated, through the high-temperature impedance spectroscopy study, that oxide ion is the dominant carrier for high electrical conduction along the  $a$ -axis in BiT crystals [19], which is consistent with the results of this neutron structural study.

### 33.4.2 *Ab initio* band structure calculations

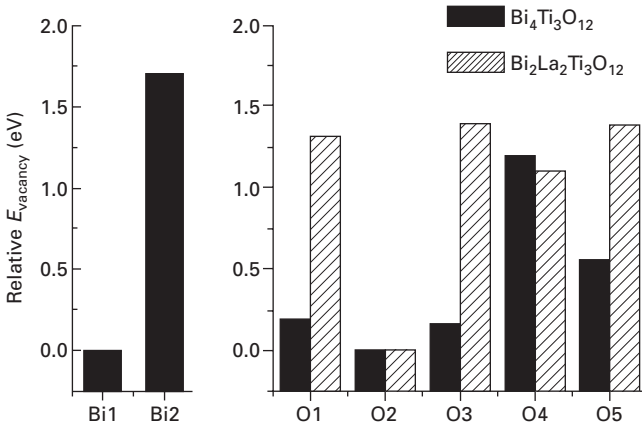
Vacancy formation energies of Bi and O in the paraelectric state in the BiT system obtained by *ab initio* band structure calculations have been reported



33.8 Refined crystal structure with thermal ellipsoids (probability 80%) of BiT at 700 °C by neutron diffraction Rietveld analysis.

[19]. The supercell method is adapted for estimating vacancy formation energy ( $E_{\text{vacancy}}$ ) to reduce vacancy–vacancy interaction. Figure 33.9 indicates the relative  $E_{\text{vacancy}}$  of Bi and O. Since Bi1 and O2 show the lowest  $E_{\text{vacancy}}$  in Bi and O, these values are set to be the standard for comparison. The calculations for BiT show that the  $E_{\text{vacancy}}$  of Bi1 is lower by about 2 eV than that of Bi2. The much lower  $E_{\text{vacancy}}$  of Bi1 indicates that Bi vacancies are created preferentially at the Bi1 site in the perovskite layers rather than at the Bi2 site in the  $\text{Bi}_2\text{O}_2$  layers. For oxygen vacancies, O1, O2 and O3 show similar  $E_{\text{vacancy}}$  within 0.2 eV, which is lower by about 0.4–0.6 eV than those of O4 and O5. It is concluded that Bi1 vacancies and O1 vacancies are primary ionic defects in BiT at high temperatures.

It is interesting to note that the presence of La at the perovskite A site increases  $E_{\text{vacancy}}$  of the adjacent oxygen atoms, O1, O3 and O5, by about 1 eV, as shown in Fig. 33.9. These results suggest that La substitution is effective for improving the chemical stability of oxygen in the perovskite layers. The total/partial DOS analysis of BLT ( $x = 2.0$ ) suggests that the La 5d is hybridized with the O 2p of the adjacent oxygen. The covalent bonding between La and O in the perovskite layers creates the DOS of the La 5d states in the valence band near the Fermi level (–5~0 eV), which is a possible origin of the high chemical stability of oxygen in BLT. The chemical



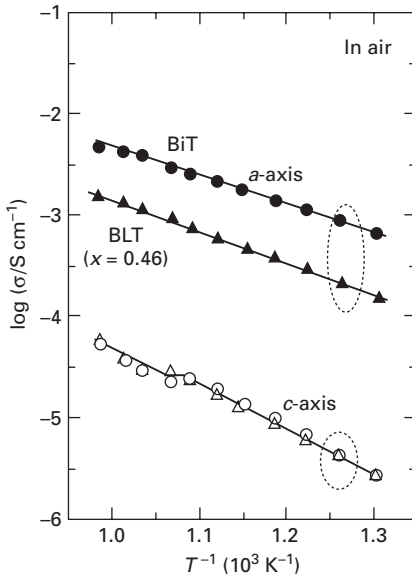
33.9 Relative difference in vacancy formation energy ( $E_{\text{vacancy}}$ ) in  $I4/mmm$  tetragonal symmetry calculated by *ab initio* band structure calculations. In the calculations for BLT, the perovskite A site is assumed to be occupied by La.

stability of oxide ions seen in BLT is confirmed also in BNT by *ab initio* calculations.

### 33.4.3 Electrical conductivity investigations by ac impedance spectroscopy

Figure 33.10 shows the temperature dependence of electrical conductivity ( $\sigma$ ). The  $\sigma$  along the  $a$ -axis of BiT was about two orders of magnitude higher than that along the  $c$ -axis. Takahashi *et al.* have revealed that the high  $\sigma$  along the  $a$  axis is attributed to oxide ion conduction in the perovskite layers [17, 18]. In contrast, the  $\text{Bi}_2\text{O}_2$  layers act as a barrier to oxide ion migration along the  $c$ -axis; hence this yields the low  $\sigma$  along the  $c$ -axis ( $h^\bullet$  conduction is dominant). The oxide ion migration is achieved through O1 vacancies, and oxide ions are suggested to move in the middle of the perovskite layers in the  $a$ - $a$  ( $a$ - $b$ ) plane.

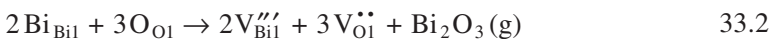
The  $\sigma$  along the  $c$ -axis of BLT ( $x = 0.46$ ) crystals was the same as that of BiT, while the La substitution decreases  $\sigma$  along the  $a$ -axis. In BLT ( $x = 0.46$ ), most La occupies the perovskite A site [33]. The same  $\sigma$  along the  $c$ -axis for BiT and BLT suggests that the  $\text{Bi}_2\text{O}_2$  layers play the same role for BiT and BLT in the electrical conduction along the  $c$ -axis. The lower  $\sigma$  along the  $a$ -axis of BLT strongly indicates that the La substitution is effective for decreasing ( $V_{\text{O}1}^{\bullet\bullet}$ ), which is essentially consistent with the results of the  $E_{\text{vacancy}}$  calculations. The relatively high oxide-ion conductivity observed for BLT ( $x = 0.46$ ) indicates that a certain amount of ( $V_{\text{O}1}^{\bullet\bullet}$ ) is present even in the lattice.



33.10 Electrical conductivity in air as a function of temperature observed for the crystals of BiT and  $\text{Bi}_{4-x}\text{La}_x\text{Ti}_3\text{O}_{12}$  (BLT,  $x = 0.46$ ).

### 33.4.4 Defect-formation mechanism

Here, a mechanism of vacancy formation in BiT at high temperatures is discussed. It has been shown that the Bi vacancy at the Bi1 site ( $V_{\text{Bi1}}'''$ ) is more easily generated than  $V_{\text{Bi2}}'''$ , where ' denotes one negative charge (Fig. 33.9). Furthermore, the nuclear-density analysis has revealed that oxygen vacancies preferentially reside at the O1 site ( $V_{\text{O1}}''$ ), where ' indicates one positive charge (Fig. 33.8). The vacancy formation of  $V_{\text{Bi1}}'''$  is likely to be the trigger for generating  $V_{\text{O1}}''$ . At high temperatures,  $V_{\text{Bi1}}'''$  is formed accompanied with the nearest-neighbor  $V_{\text{O1}}''$ , which is the origin of the defect formation in the BiT system. The high oxide-ion conduction observed in the BiT crystals is ascribed to the large number of  $V_{\text{O1}}''$  at the perovskite layers. The high oxide-ion conductivity also indicates that the electrical neutrality during the defect formation is satisfied through the generation of  $2V_{\text{Bi1}}'''$  accompanied with  $3V_{\text{O1}}''$  as follows:

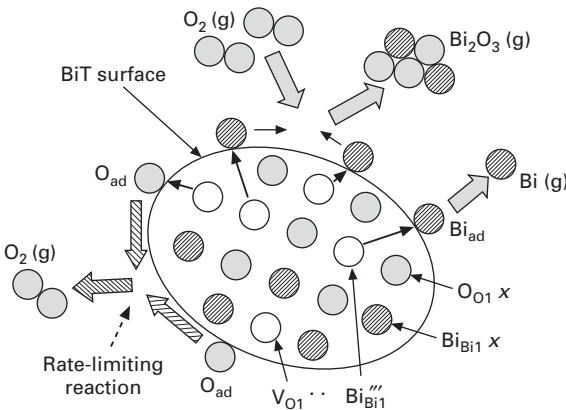


and the electron hole ( $h^\bullet$ ) plays a minor role in the high-temperature defect formation.

As a result of the thermogravimetric analysis of BiT powder under different oxygen partial pressures ( $P_{\text{O}_2}$ ) [19], the weight loss due to the vacancy formation was promoted in low- $P_{\text{O}_2}$  (reducing) atmosphere. The weight loss

due to the vacancy formation was observed above 1000 °C in air [19]. Annealing in air at 1000 °C for 5 h led to a 0.25% decrease in weight, while annealing in O<sub>2</sub> ( $P_{O_2} = 0.1$  MPa) at 1000 °C did not result in weight loss. The O<sub>2</sub> annealing at 1050 °C for 5 h resulted in a weight loss of 0.5%, which was much smaller than the annealing at 1050 °C for 5 h in air (1.2% loss). The  $P_{O_2}$  dependence of weight loss shows that the limiting factor of the vacancy formation is the surface reaction on BiT powder, and this result gives valuable information that the vacancy formation can be suppressed by heat treatment in high- $P_{O_2}$  atmosphere [19].

Thermogravimetric analysis allows us to propose the mechanism of reaction on the BiT surface that leads to the vacancy formation from the three possible models. In model 1, two lattice Bi1 ( $Bi_{Bi1}^x$ ) and three lattice O1 ( $O_{O1}^x$ ) migrate to the surface and react with each other to form Bi<sub>2</sub>O<sub>3</sub>. The resultant Bi<sub>2</sub>O<sub>3</sub> evaporates into the atmosphere, i.e. Bi<sub>2</sub>O<sub>3</sub>(g). This reaction, however, should be independent of  $P_{O_2}$  and thus does not explain the experimental results. In model 2, only  $Bi_{Bi1}^x$  moves from the lattice to the surface. Then, the adsorbed Bi ( $Bi_{ad}$ ) reacts with O<sub>2</sub> gas in the atmosphere, O<sub>2</sub>(g), and evaporates as Bi<sub>2</sub>O<sub>3</sub>(g). Although this reaction yields  $V_{Bi1}''$  and electron holes ( $h^*$ ), an increase in  $P_{O_2}$  should enhance the weight loss, i.e.  $V_{Bi1}''$  formation, which is not consistent with the experiments. In model 3, two  $Bi_{Bi1}^x$  and three  $O_{O1}^x$  migrate to the surface, but do not react with each other because of the low possibility of  $Bi_{ad}$  meeting  $O_{ad}$  on the surface (due to low vacancy concentrations), as schematically depicted in Fig. 33.11.  $Bi_{ad}$  reacts with O<sub>2</sub>(g) and evaporates as Bi<sub>2</sub>O<sub>3</sub>(g) at a relatively higher  $P_{O_2}$ , while  $Bi_{ad}$  detaches from the surface as Bi(g) or Bi clusters in reducing atmosphere.



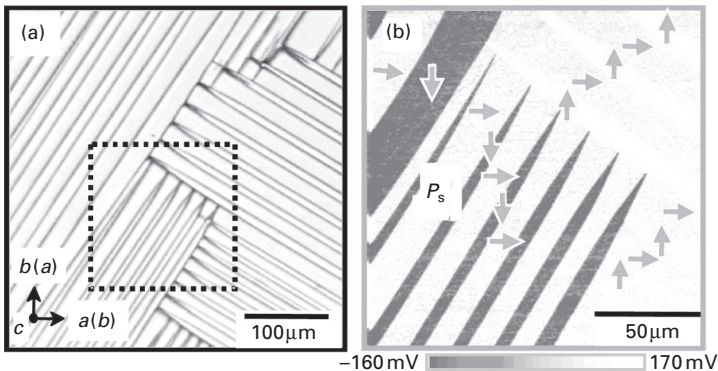
**33.11** Mechanism of vacancy formation in BiT at high temperatures.  $Bi_{Bi1}^x$  is Bi at the Bi1 site with no charge and  $O_{O1}^x$  denotes O at the O1 site with no charge.  $Bi_{Bi1}^x$  and  $O_{O1}^x$  migrate to the surface and then become adsorbed  $Bi_{ad}$  and  $O_{ad}$ . The limiting factor of the vacancy formation is the surface reaction related to  $O_{ad}$ .

These reactions proceed quickly and do not limit the vacancy formation reaction. In contrast,  $O_{ad}$  has to meet another  $O_{ad}$  on the surface to form an  $O_2$  molecule, which then diffuses into the atmosphere. The reaction related to  $O_{ad}$  that is suppressed at a higher  $P_{O_2}$  is the limiting factor of the vacancy formation for BiT. Therefore, only model 3 can account for the  $P_{O_2}$  dependence of weight loss. The formation of  $V_{Bi}''$  brings about  $V_{O1}^{\bullet}$  for charge compensation in the crystal as expressed by eq. (33.1). High- $P_{O_2}$  atmosphere inhibits the reaction on the crystal surface, and thereby further creation of  $V_{O1}^{\bullet}$  is restricted, which prevents  $V_{Bi}''$  generation. Thus, a high  $P_{O_2}$  during heating is effective for suppressing the vacancy formation in the lattice, i.e. synthesizing high-quality BiT crystalline samples [19].

### 33.5 Domain structure

Figure 33.12 shows the domain structure in the  $a$ - $b$  plane of a BiT crystal. In the optical micrograph (Fig. 33.12a), taken in the transmission mode, a striped  $90^\circ$  domain structure is clearly seen, similar to that reported for  $BaTiO_3$  single crystals [45] and PZT ceramics. Furthermore, a needle-like domain structure is also observed, and the needlepoints are terminated at domain walls. This kind of complex domain structure has been reported for  $PbTiO_3$  thin films [46] and predicted by Li *et al.* [47]. The striped domain structures are observed at temperatures below the Curie temperature ( $T_C = 675^\circ\text{C}$ ) and disappear above  $T_C$ .

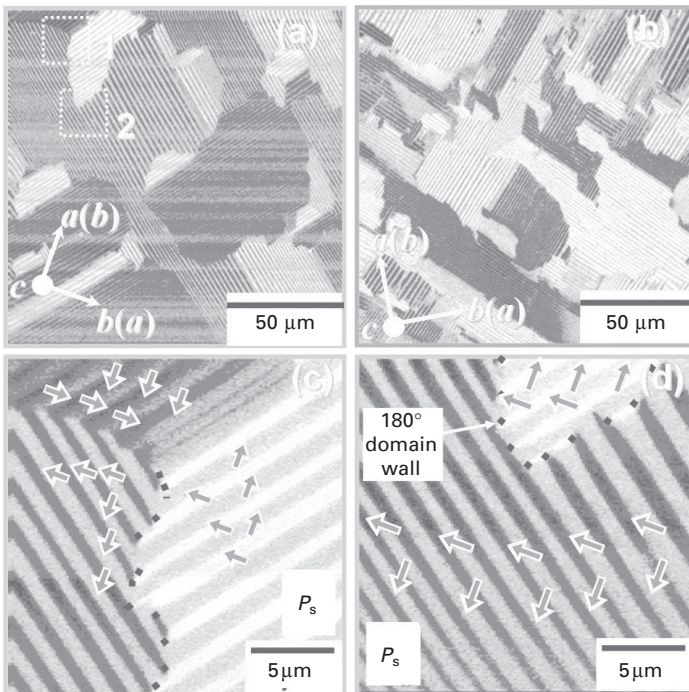
Figure 33.12(b) shows the piezoresponse-force microscope (PFM) image for the area indicated by the dashed square in Fig. 33.12(a). White (the strongest PFM signal) and black (the weakest one) areas have the domains with  $P_s$  oriented in upper and lower direction, respectively, while the gray



33.12 (a) Domain structure of a BiT crystal in the  $a$ - $b$  plane observed with optical microscopy, and (b) piezoelectric-force microscopic image of the area denoted by the dashed line in (a).

color indicates the domain with  $P_s$  oriented in the horizontal direction. The dark lines observed in the optical micrograph are  $90^\circ$  domain walls. In addition to the striped  $90^\circ$  domains,  $180^\circ$  domain walls with head-to-head and tail-to-tail configurations are seen in some of needle-like  $90^\circ$  domains. These ‘charged’ domain walls are known to strongly interact with  $V_O^{\bullet\bullet}$  [11, 19].

Figure 33.13 shows the PFM images of  $\text{Bi}_{4-x}\text{La}_x\text{Ti}_3\text{O}_{12}$  (BLT,  $x = 0.85$  and 1.2) crystals. La substitution led to a significant change in domain structure, and the domain size decreases with an increase in La content ( $x$ ). In contrast to BiT, gentle and irregular curvatures were found, and striped  $90^\circ$  domain structures are constructed in the area framed by the curvatures. The enlarged micrographs of the dashed square denoted by ‘1’ and ‘2’ in Fig. 33.13(a) are indicated in Fig. 33.13(c) and (d), respectively. Surprisingly, all the striped  $90^\circ$  domains are regularly terminated at the curvature, implying that not only do domains interact with the neighbors but also that a widespread interaction plays a crucial role in the formation of the domain structure in the BLT crystals.

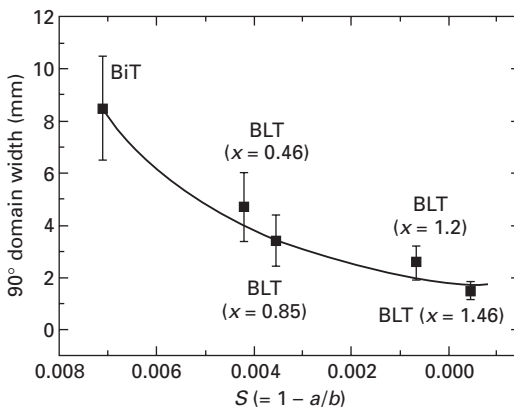


33.13 Piezoelectric-force microscopic images of BLT crystals: (a) BLT ( $x = 0.85$ ) and (b) BLT ( $x = 1.20$ ). The enlarged micrographs of the dashed square denoted by ‘1’ and ‘2’ in (a) are indicated in (c) and (d), respectively.



The curvature observed in the middle of Fig. 33.13(c) is composed of two different parts. One is the wall between the domains with upper- and lower-oriented  $P_s$ , showing a tail-to-tail  $180^\circ$  domain wall. The other between these  $180^\circ$  domain walls is the part with no change in PFM signal, indicating that the direction of  $P_s$  does not change regardless of the curvature. If striped  $90^\circ$  domains have a standard structural configuration with an alternative  $90^\circ$  rotation of the  $a$  and  $b$ -axes, the domains with the same PFM signal separated by the curvature should have the opposite  $b$ -axis distortion (the opposite  $\text{TiO}_6$  distortion along the  $b$ -axis, as discussed below). These domains can be superimposed on each other after a translation operation of  $[1/2 \ 1/2 \ 0]$ , suggesting that the other part of the curvature is an antiphase domain boundary (ADB), as observed in the ceramics of BLT [30] and  $\text{SrBi}_2\text{Ta}_2\text{O}_9$  [48]. Furthermore, on the upper left in Fig. 33.13(c), a head-to-head  $180^\circ$  domain wall as well as ADB is also observed.

Here, domain structures are discussed in terms of ferroelectric and ferroelastic distortions.  $90^\circ$  domains are formed to relieve mechanical stress induced by ferroelectric distortion with sacrificing elastic strain energy at domain walls. The formation of a new  $90^\circ$  domain wall requires the exchange of the axis between  $a$  and  $b$  in the  $a$ - $b$  plane. The strain energy is roughly proportional to spontaneous deformation ( $S$ ) expressed by  $S = a/b - 1$ . With increasing La content ( $x$ ),  $S$  decreases almost linearly from 0.007 (BiT) to 0.000 for BLT ( $x = 1.50$ ), and orthorhombic distortion becomes smaller. The close relation between  $S$  and the domain width of striped  $90^\circ$  domains is revealed (see Fig. 33.14), and a smaller  $S$  results in a narrower domain width, as can be clearly seen in Fig. 33.13. When  $S$  is lowered, the strain energy density of domain walls decreases. Thus, this increases the density of



33.14  $90^\circ$  domain width as a function of spontaneous deformation ( $S$ ). The value of  $S$  is calculated from the structural data obtained by the neutron diffraction Rietveld analysis.

90° domain walls to attain a lower total energy. It can be said that  $S$  governs 90° domain structure in the  $a$ - $b$  plane. However, the formation of ADB has generally no relation to strain energy, and  $S$  does not affect the configuration of ADB directly. Thus, we should consider local lattice distortion to elucidate the nature of ADB.

Neutron diffraction study has revealed that La substitution leads to a structural change in  $\text{TiO}_6$  distortion along the  $b$ -axis as well as in the ferroelectric distortion along the  $a$ -axis. While cooperative ionic displacements along the  $a$ -axis result in the  $P_s$ , the local dipole moments along the  $b$ -axis cancel each other owing to the presence of glide plane. Now the  $\text{TiO}_6$  rotation is focused as a reference of local lattice distortion. BiT has two kinds of  $\text{TiO}_6$  octahedron as shown in Fig. 33.1; one is the octahedron at the middle of the perovskite blocks ( $\text{TiO}_6$ ) and the other is the octahedron near  $\text{Bi}_2\text{O}_2$  layers ( $\text{Ti}_2\text{O}_6$ ). Here, only the octahedral distortion of  $\text{Ti}_2\text{O}_6$  is considered for simplicity. For BiT,  $\text{Ti}_2\text{O}_6$  rotates by 8.7° around the  $a$ -axis in the  $b$ - $c$  plane, while the rotation angle around the  $b$ -axis in the  $a$ - $c$  plane is only 2.4°. This indicates that the local  $\text{TiO}_6$  distortion is much larger in the  $b$ - $c$  plane than that in the  $a$ - $c$  plane. La substitution causes a smaller  $\text{TiO}_6$  rotation, and the rotation angle for BLT ( $x = 0.75$ ) is 8.2° in the  $b$ - $c$  plane and 1.6° in the  $a$ - $c$  plane.

In the single domain region, the phase of  $\text{TiO}_6$  rotation is opposite for adjacent octahedra that share oxide ions. The regular  $\text{TiO}_6$  rotation does not hold true at ADB, and the phase shift occurs by  $[1/2 \ 1/2 \ 0]$ . This irregular  $\text{TiO}_6$  rotation results in a large strain at ADB, and the strain energy becomes less for a smaller  $\text{TiO}_6$  rotation angle. The smaller  $\text{TiO}_6$  distortion for BLT seems to be a partial reason for the formation of ADB. The 90° domain structure surrounded by ADB strongly suggests that the 90° domain is constructed from ADB and the ADB acts as a nucleus of a new 90° domain, as suggested by Ding *et al.* [30]. However, the formation of ADB as well as 90° domain is closely related to the phase transition from parent tetragonal  $I4/mmm$  structure. Further study on the phase transition of BLT is required to clarify the domain structure and its role in polarization switching.

### 33.6 Leakage current

The impedance spectroscopic analysis has shown that  $h^\bullet$  is the dominant carrier for BiT crystals at relatively low temperatures [19]. During cooling or annealing at intermediate temperatures, the crystals absorb oxygen into the lattice, and the oxide ion occupies  $\text{V}_{\text{O}_1}^\bullet$  with the formation of  $h^\bullet$  according to the following reaction:

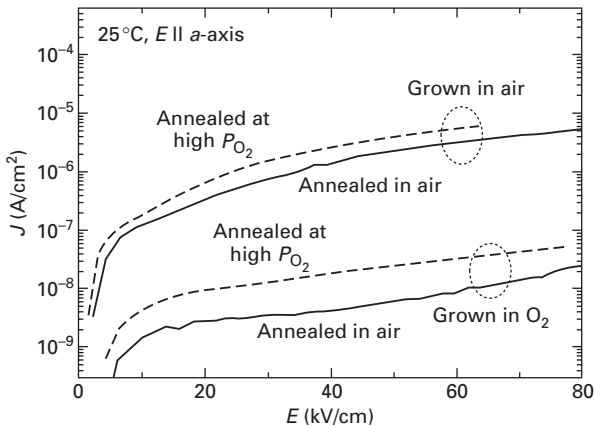


It has been reported that hole conduction becomes predominant over oxide-ion conduction at relatively low temperatures [19]. It is reasonable to consider

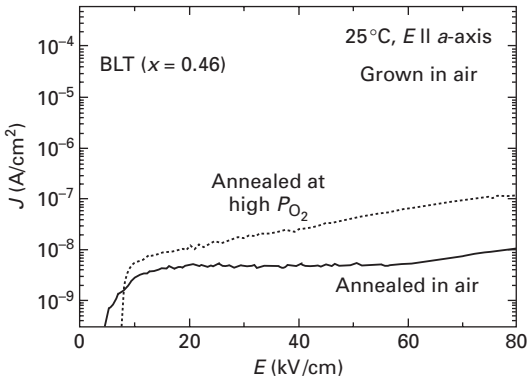
that hole conduction plays a detrimental role in leakage current at room temperature. Figure 33.15 shows the leakage current ( $J$ ) as a function of electric field applied along the  $a$ -axis of the poled BiT crystals. For the crystals grown in air, the ones annealed at  $700^\circ\text{C}$  in air had a relatively high  $J$  of the order of  $10^{-7}$  to  $10^{-6}$  A/cm<sup>2</sup>. Note that annealing at  $700^\circ\text{C}$  under a high  $P_{\text{O}_2}$  (35 MPa) atmosphere resulted in a higher  $J$  in spite of reducing oxygen vacancies. These results provide direct evidence that  $h^\bullet$  arising from oxygen absorption is the dominant carrier for leakage current and hence plays a detrimental role in the insulating properties of the BiT crystals at room temperature.

Surprisingly, crystals grown in  $\text{O}_2$  atmosphere ( $\text{O}_2$  crystals) exhibit a significantly lower  $J$  of the order of  $10^{-9}$  A/cm<sup>2</sup>, which is consistent with the results of La-substituted BiT thin films [49]. As described above, heat treatment at high temperatures inevitably creates  $V_{\text{O}_1}^{\bullet\bullet}$  as well as  $V_{\text{Bi}_1}^{\prime\prime}$  in the BiT lattice. Crystal growth under a higher  $P_{\text{O}_2}$  atmosphere suppresses the defect formation, and the  $\text{O}_2$  crystals have a smaller number of these vacancies compared with those grown in air. High- $P_{\text{O}_2}$  annealing ( $700^\circ\text{C}$ , 35 MPa) also increases  $J$  of the  $\text{O}_2$  crystals. This increase in  $J$  shows that the vacancies are present even in the  $\text{O}_2$  crystals; a further defect control could lead to a lower  $J$  in the BiT system.

Figure 33.16 shows the leakage current properties of BLT ( $x = 0.46$ ) crystals along the  $a$ -axis. The BLT crystals were grown in air. Note that BLT ( $x = 0.46$ ) crystals annealed in air at  $700^\circ\text{C}$  showed an extremely low  $J$  of the order of  $10^{-9}$  A/cm<sup>2</sup>. The high-pressure oxygen annealing ( $P_{\text{O}_2} = 35$  MPa) at



33.15 Leakage current density ( $J$ ) as a function of electric field ( $E$ ) applied along the  $a$ -axis at  $25^\circ\text{C}$  for the BiT crystals grown in air and  $\text{O}_2$  atmosphere. The annealing at  $700^\circ\text{C}$  under a high  $P_{\text{O}_2}$  of 35 MPa led to an increase in  $J$ .



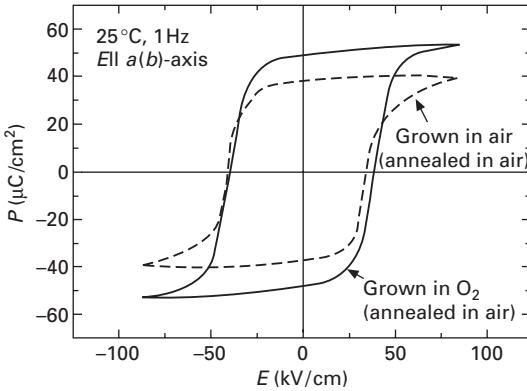
33.16 Leakage current density ( $J$ ) as a function of electric field ( $E$ ) applied along the  $a$ -axis at 25 °C for  $\text{Bi}_{4-x}\text{La}_x\text{Ti}_3\text{O}_{12}$  (BLT,  $x = 0.46$ ) crystals. The annealing at 700 °C under a high  $P_{\text{O}_2}$  of 35 MPa led to an increase in  $J$ .

700 °C increases  $J$ . Even though the oxygen annealing indeed decreases  $V_{\text{O}_i}^{\bullet\bullet}$ , the annealed crystals have a higher  $J$ . The oxygen annealing did not change the metal composition of the crystals. The fact of the high  $J$  caused by the oxygen annealing shows that the incorporation of oxygen into the lattice caused by the annealing generates  $h^{\bullet}$ , as expressed by Eq. (33.3). It is concluded that  $h^{\bullet}$  is the detrimental carrier in BLT crystals. The concentration of  $h^{\bullet}$  is determined by the excess oxygen that is absorbed from the ambient during annealing or cooling [19]. The La substitution reduces  $V_{\text{O}_i}^{\bullet\bullet}$  in the perovskite layers owing to the high chemical stability of oxide ions near La in the perovskite layers, and thus decreases  $h^{\bullet}$ . The chemical stabilization of oxide ions by La substitution is the origin of the high insulating property observed for the BLT crystals.

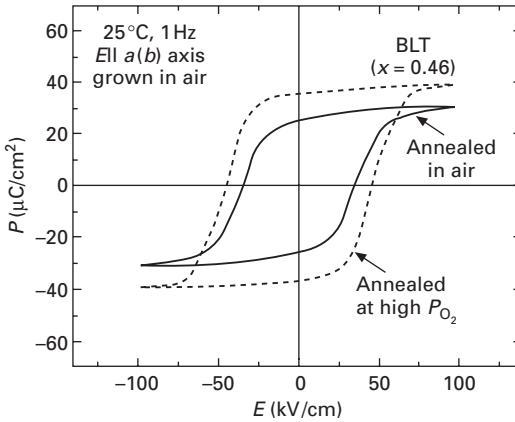
### 33.7 Polarization properties

Figure 33.17 shows the polarization hysteresis loops of the BiT crystals with air annealing (700 °C, 5 h) along the  $a(b)$ -axis. The air-grown crystals exhibit a  $P_r$  of 37  $\mu\text{C}/\text{cm}^2$  and a coercive field ( $E_c$ ) of 35–40 kV/cm. This  $P_r$  value is lower than those given in the previous reports [4, 5]. The  $\text{O}_2$  crystals consistently show a larger  $P_r$  of 48  $\mu\text{C}/\text{cm}^2$ . It is well known that a small  $P_r$  of BiT ceramics and thin films is a result of domain pinning caused by oxygen vacancies [11, 50]. The improvement of  $P_r$  observed for the  $\text{O}_2$  crystals is a result of domain depinning due to fewer  $V_{\text{O}_i}^{\bullet\bullet}$  associated with the high insulating property.

Figure 33.18 shows the polarization hysteresis loops of the BLT ( $x = 0.46$ ) crystals at 25 °C. The high- $P_{\text{O}_2}$  annealing ( $P_{\text{O}_2} = 35$  MPa, 700 °C, 10 h)



33.17 Polarization hysteresis loops along the *a*-axis measured at 25 °C for the BiT crystals.



33.18 Polarization hysteresis loops along the *a* axis measured at 25 °C for  $\text{Bi}_{4-x}\text{La}_x\text{Ti}_3\text{O}_{12}$  (BLT,  $x = 0.46$ ) crystals.

improves the rectangularity of the hysteresis and increases  $P_r$  from 25 to 36  $\mu\text{C}/\text{cm}^2$ . One of the reasons why the high- $P_{\text{O}_2}$  annealing leads to the larger  $P_r$  is a weak pinning of domains for the annealed crystals due to the small number of  $\text{V}_{\text{O}1}^{\bullet\bullet}$ . The air-annealed crystals still have a certain amount of  $\text{V}_{\text{O}1}^{\bullet\bullet}$  in the perovskite layers, and  $\text{V}_{\text{O}1}^{\bullet\bullet}$  acts as a pinning center of the domain wall. The oxygen annealing increases the number of switchable domains by applying an electric field. The high- $P_{\text{O}_2}$  annealing is demonstrated to be effective for improving polarization properties in the BLT system with a high insulating property.

### 33.8 Effects of La and Nd substitutions on the electronic band structure and chemical bonding

The electronic structure of BNT ( $x = 2.0$ ) was calculated for both the paraelectric  $I4/mmm$  and the ferroelectric  $B2cb$  structures. The calculated band structure of BNT ( $x = 2.0$ ) near  $E_F$  is almost the same as that of BiT (see Fig. 33.5a). The calculation for the paraelectric BNT ( $x = 2.0$ ) shows that the fundamental  $E_g$  is indirect (valence band maximum at  $P$  and conduction band minimum at  $\Gamma$ ), which is consistent with the result in the reported calculations [34]. In contrast, our calculations suggest that the ferroelectric BNT ( $x = 2.0$ ) has a direct band gap, with the valence band maximum and conduction band minimum lying at Brillouin-zone center  $\Gamma$ . Our calculation suggests that BNT ( $x = 2.0$ ) gives a narrower  $E_{g(\text{DFT})}$  of 2.4 eV compared with BiT ( $E_{g(\text{DFT})} = 2.6$  eV), which is in good agreement with the results of the optical measurements [35].

Figure 33.6(c) shows the total DOS between  $-25$  and  $7.5$  eV of BNT ( $x = 2.0$ ) with  $B2cb$  ferroelectric structure. In this calculations, Nd is assumed to occupy at the  $A$  site in the perovskite layers. The valence band consists mainly of the O  $2p$  states, while the Ti  $3d$  states form the conduction band. The width of the valence band was approximately 5.5 eV. Two kinds of Bi for BiT result in two localized states of Bi  $6s$  band near  $-10$  eV, whereas BNT has one peak of the Bi  $6s$  band attributed to the Bi in the  $\text{Bi}_2\text{O}_2$  layers. BiT and BNT indicate a similar low-lying O  $2s$  band ( $-19$  to  $-16$  eV), and the broad Nd  $5d$  states overlap with the O  $2p$  band for BNT.

Figure 33.7(c) presents the PDOS of BNT ( $x = 2.0$ ) with  $B2cb$  ferroelectric structure. For both BiT and BNT, the  $\text{Bi}_2\text{O}_2$  layers show similar electronic character, and the Bi2 and O2 in the  $\text{Bi}_2\text{O}_2$  layers do not have DOS near the Fermi energy ( $E_F$ ). Thus, the perovskite layers play an essential role in the electronic structure near the band gap, and  $E_g$  is determined by the orbital interaction in the perovskite layers. As in the case for BiT (see Fig. 33.7b), the electronic structure of BNT shows that the valence band maximum mainly consists of the O  $2p$  orbitals. The conduction band minimum is composed of the empty  $3d$  orbitals of Ti in the perovskite layers. There is a strong hybridization with Ti and Bi. This behavior reflects the strong hybridization of the Ti  $3d$  and O  $2p$  orbitals in the perovskite layers, as is common for  $\text{ABO}_3$  perovskites [51].

Interestingly, the Bi1 at the perovskite  $A$  site has a key role in the electronic structure of the valence band for BiT. The antibonding orbitals are composed of the  $6s$  of the Bi1 and the  $2p$  of the adjacent oxide ions form and constitute the large DOS just below the  $E_F$ . Furthermore, the orbital hybridization with O  $2p$  leads to considerable DOS of the Bi1  $6p$  states in the valence band. This behavior is unexpected in a simplified ionic picture, but has been demonstrated

also for  $\alpha$ -PbO [52, 53], PbTiO<sub>3</sub> [51] and BiScO<sub>3</sub>-PbTiO<sub>3</sub> solid solution [54]. The hybridization of the Bi1 6*p*-O 2*p* orbitals results in the bonding states in the valence band, and the occupation of the Bi 6*p* electrons in the valence band stabilizes the ferroelectric distortion in BiT.

Here, we discuss the role of Nd at the perovskite A site in view of electronic structure and oxygen stability. The Nd 5*d* states found in the valence band is a result of the orbital interaction with O 2*p* in the perovskite layers. Furthermore, the substitution of Nd causes a significant change in DOS just below the  $E_F$ . The oxide ions in the perovskite layers (O1, O3, O5, O6) have a large DOS near the  $E_F$  in BiT, which are the antibonding states caused by the Bi1 6*s*-O 2*p* hybridization. The Nd substitution decreases DOS near the  $E_F$  due to the lack of the Bi 6*s*-O 2*p* interaction and contributes to stabilizing the oxide ions in the perovskite layers. The total/partial density of states (DOS) analysis of BLT ( $x = 2.0$ ) suggests that the La 5*d* is hybridized with the O 2*p* of the adjacent oxygen. The covalent bonding between La and O in the perovskite layers creates the DOS of the La 5*d* states in the valence band near the Fermi level ( $-5\sim 0$  eV), which is a possible origin of the high chemical stability of oxygen in BLT.

Our calculations show that La and Nd substitutions at the perovskite A site lead to a decrease in oxygen vacancy. The lower concentration of oxygen vacancies is verified in BLT compared with BiT (see Fig. 33.10), which originates from the orbital interaction between La and O in the perovskite layers. The high stability of oxide ions are also expected for BNT, and this is consistent with the results of a leakage-current density of the order of  $10^{-9}$  A/cm<sup>2</sup> of BNT crystals [35]. Compared with BiT, BLT and BNT crystals exhibit a much lower leakage current, suggesting that defects such as oxygen vacancies and electron holes are lower in the BLT and BNT crystals. It is recognized that oxygen vacancies act as pinning site of domain wall and impedes polarization switching [11, 50]. The suppression of domain pinning results in a larger  $P_r$  and high fatigue endurance, which have been achieved for BNT thin films [24]. The results obtained in this study indicate that the substitution of La and Nd is effective for stabilizing oxide ions in the perovskite layers.

### 33.9 Summary

The crystal structures of Bi<sub>4</sub>Ti<sub>3</sub>O<sub>12</sub> in the ferroelectric and paraelectric states have been analyzed, and the ferroelectric distortion has been discussed in terms of ionic displacement of the constituent ions. The off-center Ti displacements in TiO<sub>6</sub> octahedra play a minor role in spontaneous polarization, while the entire shift of the TiO<sub>6</sub> octahedra with respect to heavy Bi ions results in a large spontaneous polarization along the *a*-axis. The bond valence analysis shows that the underbondings of Bi1 at the A site and Bi2 in the

$\text{Bi}_2\text{O}_2$  layers in the paraelectric state at  $700^\circ\text{C}$  is recovered to the satisfactory bonding by the ferroelectric transition. The analysis of partial density of states indicates that the ferroelectric transition originates from a strong hybridization between the  $\text{Bi}1$   $6s(p)$  and the  $\text{O}3$   $2p$  states.

The defect structure and the mechanism of leakage current at room temperature of  $\text{Bi}_4\text{Ti}_3\text{O}_{12}$ , and the role of La and Nb in  $\text{Bi}_4\text{Ti}_3\text{O}_{12}$  on the ferroelectric-related properties are discussed. La and Nd substitutions at the perovskite  $A$  site improve the chemical stability of the adjacent oxide ions and reduces the concentration of oxygen vacancies. The results of the leakage current properties of the single crystals reveal that electron holes arising from the incorporation of oxygen at oxygen vacancies in the perovskite layers act as detrimental carriers for leakage current at room temperature in the  $\text{Bi}_4\text{Ti}_3\text{O}_{12}$  system. A high insulating property at room temperature was obtained for the La- and Nb-substituted  $\text{Bi}_4\text{Ti}_3\text{O}_{12}$  crystals as a result of the small number of electron holes due to fewer oxygen vacancies.

The substitutions of La and Nd give rise to a smaller remanent polarization compared with  $\text{Bi}_4\text{Ti}_3\text{O}_{12}$ , which is in good qualitative agreement with the spontaneous polarization estimated from the structural data determined by neutron diffraction analysis. Electronic band structure calculations and the optical transmission data show direct band gap for the ferroelectric phases in the  $\text{Bi}_4\text{Ti}_3\text{O}_{12}$  system. The analysis of the electronic density of states of RE-substituted lattice indicates that the orbital interaction of the RE  $5d$  and O  $2p$  states stabilizes oxide ions in the perovskite layers, which is consistent with the much lower leakage current observed for the RE-substituted crystals.

The observations of domain structure show that striped  $90^\circ$  domain walls as well as head-to-head and tail-to-tail  $180^\circ$  domain walls are present in the  $\text{Bi}_4\text{Ti}_3\text{O}_{12}$  and La-substituted crystals. The substitution of La leads to a marked decrease in the  $90^\circ$  domain width. Piezoelectric-force microscope observations reveal that the antiphase domain boundary is formed only for La-substituted crystals. The antiphase domain boundary is suggested to play an important role in the formation of  $90^\circ$  domains.

### 33.10 Future trends

La and Nd substitutions into  $\text{Bi}_4\text{Ti}_3\text{O}_{12}$  are effective for improving chemical stability of oxide ions in the perovskite layers and thereby the leakage current is suppressed to a very low value of the order of  $\sim 10^{-9}\text{A}/\text{cm}^2$ . These substitutions, however, lead to a marked decrease in spontaneous polarization, and thus the superior leakage-current properties due to less oxygen vacancies are achieved by sacrificing the spontaneous polarization of  $\text{Bi}_4\text{Ti}_3\text{O}_{12}$ .

Here, a definite guide for achieving polarization switching as well as a low leakage current is proposed for the  $\text{Bi}_4\text{Ti}_3\text{O}_{12}$ -based devices. Although the processing temperature of the  $\text{Bi}_4\text{Ti}_3\text{O}_{12}$  films is about  $\sim 700^\circ\text{C}$  which is



much lower than that of crystal growth ( $\sim 1200^\circ\text{C}$ ), the extremely high surface energy of the films enhances defect formation in the films. A similar mechanism of the defect formation for the crystals could be used to control the vacancy formation in the films. A high  $P_{\text{O}_2}$  atmosphere suppresses the defect formation at high temperatures, while a moderate  $P_{\text{O}_2}$  atmosphere is preferable for achieving a low leakage current during subsequent cooling or annealing to avoid the incorporation of oxygen into the lattice that creates electron hole (carrier of the leakage current). Therefore, sintering under a high  $P_{\text{O}_2}$  atmosphere and subsequent annealing under a low  $P_{\text{O}_2}$  atmosphere would provide high-quality  $\text{Bi}_4\text{Ti}_3\text{O}_{12}$  films and crystals with a superior polarization-switching property as well as a low leakage current.

### 33.11 References

1. Wu, S Y, 'Optical switching characteristics of epitaxial bismuth titanate films for matrix-addressed displays', *Ferroelectrics*, 1976 **10** (1–4) 209–13.
2. Aurivillius, B, 'Mixed bismuth oxide with layer lattices II. Structure of  $\text{Bi}_4\text{Ti}_3\text{O}_{12}$ ', *Ark Kemi*, 1949 **1** (58) 499–512.
3. Subbarao, E C, 'Ferroelectricity in  $\text{Bi}_4\text{Ti}_3\text{O}_{12}$  and its solid solutions', *Phys Rev*, 1961 **122** (3) 804–7.
4. Cummins, S E, 'Electrical and optical properties of ferroelectric  $\text{Bi}_4\text{Ti}_3\text{O}_{12}$  single crystals', *J Appl Phys*, 1968 **39** (5) 2268–74.
5. Irie, H, 'Structure dependence of ferroelectric properties of bismuth layer-structured ferroelectric single crystals', *J Appl Phys*, 2001 **90** (8) 4089–94.
6. Joshi, P C, 'Structural and optical-properties of ferroelectric  $\text{Bi}_4\text{Ti}_3\text{O}_{12}$  thin-films by sol-gel technique', *Appl Phys Lett*, 1991 **59** (19) 2389–90.
7. Jo, W, 'Structural and electrooptic properties of laser ablated  $\text{Bi}_4\text{Ti}_3\text{O}_{12}$  Thin-Films on  $\text{SrTiO}_3(100)$  and  $\text{SrTiO}_3(110)$ ', *Appl Phys Lett*, 1992 **61** (13) 1516–18.
8. Rae, A D, *et al.* 'Structure refinement of commensurately modulated bismuth titanate,  $\text{Bi}_4\text{Ti}_3\text{O}_{12}$ ', *Acta Crystallogr, Sect B*, 1990 **46** 474–87.
9. Shimakawa, Y, 'Crystal structures and ferroelectric properties of  $\text{SrBi}_2\text{Ta}_2\text{O}_9$  and  $\text{Sr}_{0.8}\text{Bi}_{2.2}\text{Ta}_2\text{O}_9$ ', *Appl Phys Lett*, 1999 **74** (13) 1904–6.
10. Soga, M, 'Domain structure and polarization properties of lanthanum-substituted bismuth titanate single crystals', *Appl Phys Lett*, 2004 **84** (1) 100–102.
11. Noguchi, Y J, 'Defect control for large remanent polarization in bismuth titanate ferroelectrics doping effect of higher-valent cations', *Jpn J Appl Phys*, 2000 **39** (12B) L1259–L62.
12. Noguchi, Y, 'Oxygen stability and leakage current mechanism in ferroelectric La-substituted  $\text{Bi}_4\text{Ti}_3\text{O}_{12}$  single crystals', *Jpn J Appl Phys*, 2005 **44** (9B) 6998–7002.
13. Park, C H, 'First-principles study of the oxygen-vacancy in ferroelectric perovskites', *J Korean Phys Soc*, 1998 **32** S143–5.
14. Chan, N H, 'Defect chemistry of  $\text{BaTiO}_3$ ', *J Electrochem Soc*, 1976 **123** (10) 1584–5.
15. Chan, N-H, 'Nonstoichiometry in undoped  $\text{BaTiO}_3$ ', *J Am Ceram Soc*, 1981 **64** (9) 556–62.
16. Raymond, M V, 'Defect chemistry and transport properties of  $\text{Pb}(\text{Zr}_{1/2}\text{Ti}_{1/2})\text{O}_3$ ', *Integrated Ferroelectr*, 1994 **4** 145–54.

17. Takahashi, M, *et al.* 'Electrical conduction mechanism in  $\text{Bi}_4\text{Ti}_3\text{O}_{12}$  single crystal', *Jpn J Appl Phys*, 2002 **41** (11B) 7053–6.
18. Takahashi, M, *et al.* 'Electrical conduction properties of La-substituted bismuth titanate single crystals', *J Ceram Process Res*, 2005 **6** (4) 281–5.
19. Noguchi, Y, *et al.* 'Impact of defect control on the polarization properties in  $\text{Bi}_4\text{Ti}_3\text{O}_{12}$  ferroelectric single crystals', *Jpn J Appl Phys*, 2005 **44** (16–19) L570–2.
20. Soga, M, 'Domain structure and polarization properties of lanthanum-substituted bismuth titanate single crystals', *Appl Phys Lett*, 2004 **84** (1) 100–2.
21. Fujisaki, Y, 'Significant enhancement of  $\text{Bi}_{3.45}\text{La}_{0.75}\text{Ti}_3\text{O}_{12}$  ferroelectricity derived by sol-gel method', *Jpn J Appl Phys*, 2003 **42** (3B) L267–9.
22. Watanabe, T, 'Effect of cosubstitution of La and V in  $\text{Bi}_4\text{Ti}_3\text{O}_{12}$  thin films on the low-temperature deposition', *Appl Phys Lett*, 2002 **80** (1) 100–2.
23. Uchida, H, 'Approach for enhanced polarization of polycrystalline bismuth titanate films by  $\text{Nd}^{3+}/\text{V}^{5+}$  cosubstitution', *Appl Phys Lett*, 2002 **81** (12) 2229–31.
24. Kojima, T, 'Large remanent polarization of  $(\text{Bi},\text{Nd})_4\text{Ti}_3\text{O}_{12}$  epitaxial thin films grown by metalorganic chemical vapor deposition', *Appl Phys Lett*, 2002 **80** (15) 2746–8.
25. Kim, S H, 'Ferroelectric properties of Ta- and Mn-doped  $\text{Bi}_{3.3}\text{La}_{1.0}\text{Ti}_3\text{O}_{12}$  thin films', *Ferroelectrics*, 2002 **271** 1757–62.
26. Kang, B S, 'Retention characteristics of  $\text{Bi}_{3.25}\text{La}_{0.75}\text{Ti}_3\text{O}_{12}$  thin films', *Jpn J Appl Phys*, 2002 **41** (8) 5281–3.
27. Hayashi, T, 'Preparation and properties of  $\text{Bi}_{4-x}\text{La}_x\text{Ti}_3\text{O}_{12}$  ferroelectric thin films using excimer UV irradiation', *Jpn J Appl Phys*, 2002 **41** (11B) 6814–19.
28. Tokumitsu, E, 'Fabrication and characterization of metal-ferroelectric-metal-insulator-semiconductor (MFMS) structures using ferroelectric  $(\text{Bi},\text{La})_4\text{Ti}_3\text{O}_{12}$  films', *Jpn J Appl Phys*, 2001 **40** (9B) 5576–9.
29. Hou, Y, ' $\text{Bi}_{3.25}\text{La}_{0.75}\text{Ti}_3\text{O}_{12}$  thin films prepared on Si (100) by metalorganic decomposition method', *Appl Phys Lett*, 2001 **78** (12) 1733–5.
30. Ding, Y, *et al.* 'Why lanthanum-substituted bismuth titanate becomes fatigue free in a ferroelectric capacitor with platinum electrodes', *Appl Phys Lett*, 2001 **78** (26) 4175–7.
31. Chon, U, 'Degradation mechanism of ferroelectric properties in  $\text{Pt}/\text{Bi}_{4-x}\text{La}_x\text{Ti}_3\text{O}_{12}/\text{Pt}$  capacitors during forming gas annealing', *Appl Phys Lett*, 2001 **79** (15) 2450–52.
32. Park, B H, 'Lanthanum-substituted bismuth titanate for use in non-volatile memories', *Nature*, 1999 **401** (6754) 682–4.
33. Osada, M, 'Cation distribution and structural instability in  $\text{Bi}_{4-x}\text{La}_x\text{Ti}_3\text{O}_{12}$ ', *Jpn J Appl Phys*, 2001 **40** (9B) 5572–5.
34. Shimakawa, Y, *et al.* 'Crystal and electronic structures of  $\text{Bi}_{4-x}\text{La}_x\text{Ti}_3\text{O}_{12}$  ferroelectric materials', *Appl Phys Lett*, 2001 **79** (17) 2791–3.
35. Goto, T, 'Effects of Nd substitution on the polarization properties and electronic structures of bismuth titanate single crystals', *Mater Res Bull*, 2005 **40** (6) 1044–51.
36. Newnham, R E, 'Structural basis of ferroelectricity in bismuth titanate family', *Mater Res Bull*, 1971 **6** (10) 1029–39.
37. Dorrian, J F, 'Crystal-structure of  $\text{Bi}_4\text{Ti}_3\text{O}_{12}$ ', *Ferroelectrics*, 1971 **3** (1) 17–27.
38. Withers, R L, 'The crystal-chemistry underlying ferroelectricity in  $\text{Bi}_4\text{Ti}_3\text{O}_{12}$ ,  $\text{Bi}_3\text{TiNbO}_9$ , and  $\text{Bi}_2\text{WO}_6$ ', *J Solid State Chem*, 1991 **94** (2) 404–17.
39. Zhong, W, 'Giant LO-TO splitting in perovskite ferroelectrics', *Phys Rev Lett*, 1994 **72** (22) 3618–21.
40. Brown, I D, 'Bond-valence parameters obtained from a systematic analysis of the inorganic crystal-structure database', *Acta Crystallogr, Sect B*, 1985 **41** (Aug) 244–7.

41. Okeeffe., M, 'The prediction and interpretation of bond lengths in crystals', *Structure and Bonding*, 1989 **71** 161–90.
42. Thompson, J G, 'Revised structure of  $\text{Bi}_3\text{TiNbO}_9$ ', *Acta Crystallogr, Sect B*, 1991 **47** 174–80.
43. Hervoches, C H, 'Structural behavior of the four-layer Aurivillius-phase ferroelectrics  $\text{SrBi}_4\text{Ti}_4\text{O}_{15}$  and  $\text{Bi}_5\text{Ti}_3\text{FeO}_{15}$ ', *J Solid State Chem*, 2002 **164** (2) 280–91.
44. Frit, B, 'The crystal-chemistry and dielectric-properties of the Aurivillius family of complex bismuth oxides with perovskite-like layered structures', *J Alloys Compd*, 1992 **188** (1–2) 27–35.
45. Merz, W J, 'Domain formation and domain wall motions in ferroelectric  $\text{BaTiO}_3$  single crystals', *Phys Rev*, 1954 **95** (3) 690–98.
46. Goo, E K W, 'Transmission Electron-microscopy of  $\text{Pb}(\text{Zr}_{0.52}\text{Ti}_{0.48})\text{O}_3$ ', *J Am Ceram Soc*, 1981 **64** (9) 517–19.
47. Li, Y L, *et al.* 'Effect of electrical boundary conditions on ferroelectric domain structures in thin films', *Appl Phys Lett*, 2002 **81** (3) 427–9.
48. Ding, Y, 'Ferroelectric switching mechanism in  $\text{SrBi}_2\text{Ta}_2\text{O}_9$ ', *Appl Phys Lett*, 2001 **79** (7) 1015–17.
49. Kijima, T, 'Effect of high-pressure oxygen annealing on  $\text{Bi}_2\text{SiO}_5$ -added ferroelectric thin films', *Jpn J Appl Phys*, 2002 **41** (10B) L1164–6.
50. Noguchi, Y, 'Large remanent polarization of vanadium-doped  $\text{Bi}_4\text{Ti}_3\text{O}_{12}$ ', *Appl Phys Lett*, 2001 **78** (13) 1903–5.
51. Cohen, R E, 'Origin of ferroelectricity in perovskite oxides', *Nature*, 1992 **358** 136–8.
52. Watson, G W, 'Ab initio calculation of the origin of the distortion of  $\alpha$ - $\text{PbO}$ ', *Phys Rev B*, 1999 **59** (13) 8481–6.
53. Noguchi, Y, 'Chemical bonding and electronic states in  $\alpha$ - $\text{PbO}$ : analysis by an ab initio band calculation', *J Ceram Soc Jpn*, 2004 **112** (1) 50–56.
54. Iniguez, J, 'First-principles study of  $(\text{BiScO}_3)_{(1-x)}-(\text{PbTiO}_3)_x$  piezoelectric alloys', *Phys Rev B*, 2003 **67** (22) 224107.

- 
- (001) poling 106–7, 110, 369, 373  
  engineered domain configuration in  
    barium titanate 271, 272–3,  
    275–7  
  PMN–PT crystals 252, 253, 254–5  
    Bridgman growth 26, 32, 33, 35  
  PZN–PT crystals 248–54
- (011) poling  
  PMN–PT crystals 26–30, 32, 33–4,  
  35  
  PZN–PT crystals 256, 257
- (110) poling 370–3
- (111) poling  
  engineered domain configuration in  
    barium titanate 270–1, 273–4  
  PMN–PT crystals 258, 259  
  Bridgman growth 26, 27, 35
- ab initio* band structure calculations  
  1015–17
- abnormal grain growth (AGG) 159
- ac impedance spectroscopy 1017–18
- accommodation region 436
- acoustics 953–7  
  high-frequency resonance in DSLs  
    954–7  
  polariton excitation in DSLs 957, 958
- actuators 87–92  
  for cryogenic actuation 91–2  
  for deformable mirrors 88–90  
  MLCA 447  
  for rotorcraft flap control 90–1
- adaptive phase model 420–1, 775
- admittance 485–6, 991, 992  
  BTO/STO superlattices 991–2, 994
- amplitude squeezing 960
- anisotropic diffuse scattering 408, 409–10,  
  411
- anisotropy  
  dielectric and piezoelectric anisotropy  
    factors 314–16  
  and domain engineering 367–8  
  ferroelectric single crystals 367–8  
  of a free energy and piezoelectric  
    enhancement 317–26, 327  
  loss anisotropy 490–1, 492, 493
- annealing 612–13  
  and leakage current of BiT crystals  
    1023–5  
  and polarisation properties of BiT  
    crystals 1025–6
- antennas 527–9
- antiphase domain boundary (ADB)  
  1022–3
- artificial superlattices 559, 764, 765, 934,  
  971  
  dielectric *see* dielectric superlattices  
  perovskite *see* perovskite artificial  
    superlattices
- artificially produced nucleation sites  
  638
- atomic force microscopy (AFM)  
  nano-writing 545, 547  
  single crystalline films without  
    structural defects 711–13
- backswitched poling 649–52, 653
- backswitching, spontaneous 624, 625,  
  626, 640, 641, 644
- band structure *see* electronic band  
  structure
- bandwidth 94

- barium-sodium niobate oxide system 914, 915, 916
- barium titanate (BT or BTO) 205, 807–8, 879
  - BTO/STO artificial superlattices *see* BTO/STO artificial superlattices
  - concentration gradient 683–4, 685
    - improved control of interfaces 684–6, 687
  - engineered domain configuration 267, 269–300
    - (001) oriented single crystals 271, 272–3, 275–7
    - (111) oriented single crystals 270–1, 273–4
  - crystal structure and crystallographic orientation dependence 269–77
  - domain size dependence on electric field and temperature 278–80
  - domain size dependence of piezoelectric property using 31 resonators 281–4
  - domain size dependence of piezoelectric property using 33 resonators 284–6
  - future trends 300–1
  - intrinsic and extrinsic effects 298–300
  - patterning electrode 290–4, 300
  - piezoelectric properties measured under high electric field 272–5
  - piezoelectric properties measured under low ac electric field 275–7
  - role of non-180° domain wall region 286–90
  - uniaxial stress field 294–8, 299, 300
- lead-free relaxor ceramics derived from 897–906, 924
  - ferroelectric-relaxor crossover 906–12
- nanopowders 879
- polarisation rotation and anisotropy factors 314–16
- size effects 448–9
- thermally induced phase transitions and ‘rotator’ character 319–21
- thin films
  - domain evolution under electric field 586–91
  - domains in ultra-thin films 577–80
  - fully strained 779–81
  - strain relaxation and domain formation 783
  - under tensile strain 781–2
- barium titanate–barium zirconate–barium lithium fluoride system 903, 904
- barium titanate–barium zirconate–calcium titanate system 902–3, 904, 905
- barium titanate–potassium niobate–calcium titanate system 903, 904, 905, 906
- base–metal–electrode capacitors 555
- beam control, optical 961
- benders 87
- birefringence 358–9
- birefringent domains 198, 199, 200
- bismuth
  - bismuth-based perovskite single crystals *see* BSPT
  - bismuth-based pyrochlore ceramics *see* BZN-based pyrochlore ceramics
  - lead-free relaxors containing 918–24
    - perovskite type 918–23
    - TTB type 923–4
- bismuth ferrate 778–9
- bismuth lanthanum titanate *see* BLT
- bismuth layer-structured ferroelectrics (BLSF) 808–9, 818–51, 865, 869
  - future trends 847–9
  - grain orientation effects on electrical properties 823–47
    - dielectric properties 825–8, 829
    - hysteresis loops and remanent polarisation 833–6
    - microstructure 823–5
    - piezoelectric properties 836–41
    - pyroelectric properties 841–3
    - recent progress on bismuth titanate-based system 843–7
    - resistivities 828–33
  - grain orientation and hot-forging 822–3

- phase relation 821–2
- bismuth titanate (BiT or BIT) 543, 807, 818, 820, 821, 822, 1006–32
  - crystal structure 1006, 1007, 1008–11
    - bond valence analysis and role of bismuth in ferroelectric phase transition 1009–11, 1012
    - ferroelectric distortion and spontaneous polarisation 1008–9
  - defect structure 1015–20
    - ab initio* band structure calculations 1015–17
    - defect-formation mechanism 1018–20
    - electrical conductivity by ac impedance spectroscopy 1017–18
    - neutron diffraction 1015, 1016
  - domain structure 1020–3
  - effects of rare earth substitution on band structure and chemical bonding 1027–8
  - electronic band structure and density of states 1011–15
  - future trends 1029–30
  - grain orientation effects on electrical properties
    - crystalline structure 824–5
    - recent progress 843–7
    - resistivity 830–1, 832–3
  - leakage current 1023–5
  - novel sol-gel route to 873–6, 877
  - polarisation properties 1025–6
- BITN ceramics 843–7
- BITV ceramics 843–7
- blisters 738–9
- BLT (bismuth lanthanum titanate) 1007, 1029
  - band structure and chemical bonding 1027–8
  - defect structure 1016–18
  - domain structure 1021–3
  - leakage current 1024–5
  - novel sol-gel route to 875–6, 877, 878
  - polarisation properties 1025–6
- BNKT 803–7, 810, 811, 812
- BNT (neodymium-substituted BiT) 1007, 1014, 1015, 1029
  - band structure and chemical bonding 1027–8
  - bond valence analysis 1009–11, 1012
- boron oxides 40, 42–4, 48–50, 52, 53, 189–90
- Bragg condition 942–3
- branching 655
- Bridgman growth 4–37, 97, 104–5, 135, 158, 166
  - apparatus 9–12
  - data for selection of crystals 31–5
  - future trends 30–1
  - imperfections 13–15
  - interface control 13
  - optimisation of cut directions 25–30
  - phase equilibrium 6
  - PIMNT and PSMNT single crystals 216–26
  - platinum crucible leakage and lead oxide chemistry 6–9
  - procedures 12–13
  - property characterisation 15–25
    - interrelationship of properties 21–5
    - property variations 17–21
  - recent progress for PMN–PT crystal 74–81
- BSPT 425
  - high Curie temperature crystals 134, 141–5, 146, 148, 149, 150, 174
- BST
  - BST/BZN thin films 524–5
  - BST/MgO and BST/MgTiO<sub>3</sub> ceramic composites 675–83
  - thin films 521–3
- BTN 820
- BTO/STO artificial superlattices 559, 971–3, 1001
  - dielectric permittivity 991–5
    - mechanism of permittivity enhancement 995–6
    - temperature dependence of permittivity 997–8
  - lattice distortions 980–3
  - optical constants 984–7
  - reactive MBE system 976–7, 978
- BTT 821, 822
- bubble domains 582, 584–5, 586, 590
- buffer layer 738–9
- bulk screening 635, 659–60

- butterfly-type diffuse scattering 408, 409–10, 411
- BZN-based pyrochlore ceramics 503–38
- crystal structures in BZN system 504–9
    - cubic pyrochlore 505–7
    - monoclinic zirconolite-like structure 507, 508
    - non-stoichiometric pyrochlores and local crystal chemistry 507–9
  - dielectric properties 514–25
    - basic properties 514–15
    - dielectric relaxation 520–1
    - dielectric tunability in thin films 521–5
  - effect of ion substitution 515–16, 517
  - microwave and infrared dielectric response 516, 518–19
  - future trends 531–3
  - phase equilibrium and phase relation 509–14
    - melting behaviour 511–13
    - phase diagram 509, 510
    - phase formation of cubic and monoclinic pyrochlores 509–11, 512
    - phase transition and phase relation 513–14
  - potential RF and microwave applications 525–31
- BZT SSCG 159, 160, 162–3, 170
- dielectric and piezoelectric properties 163–5
- $\text{CaCu}_3\text{Ti}_4\text{O}_{12}$  674
- calcined compact 803, 804, 805
- capacitive microfabricated ultrasound transducer (cMUT) 101, 125–6
- capacitors
- base–metal–electrode 555
  - BZN and tunable capacitors 523, 525, 526, 527
  - MLCC 447, 503, 504, 686, 879
  - nano-capacitors on carbon nanotubes 545
- carbon nanotubes 545, 550
- with piezoelectric/pyroelectric PZT tips 562
- cascaded nonlinearity 960
- charge coefficient 93, 94
- charge screening 634–5, 761–2
- charge-voltage curves 992, 993, 999, 1000
- charged boundaries 672–4
- charged defects 671–4
- chemical bonding 1027–8
- chemical diffusion 935, 938–9
- chemical inhomogeneity regions (CIRs) 425–9, 436, 438, 450–1
- chemical solution deposition (CSD) 601
- chemically ordered regions (CORs) 394, 403–8, 425, 438, 450–1
- interaction with PNRs 408–12
  - see also* chemical inhomogeneity regions (CIRs)
- chirped-periodic DSL 960
- circular domains 553–4
- cluster nucleation 49
- coalescence of residual domains *see* merging
- cobaltous ferrite magneto-electric composite 545, 547
- coercive field 145, 147
- SBT from soft chemical methods 870, 875
- complete screening 636, 640
- component count ratio 532
- composite coating process 724, 725–9
- composite films *see* thick films
- compositional gradients 764–6
- interface control 683–6, 687
- compositional segregation 40, 44, 75–7, 81, 193–4
- compositional variation
- compositionally induced phase transitions 322, 323
  - PIMNT crystal 218–19
  - PMN-PT crystals 106
    - field dependent domain structures 349–57
    - field poling effect on optical properties 357–9
    - thermal stability and field poling 341–9
  - PSMNT crystal 219
- self-consistency of full-set data 242–4

- size effects on macroscopic properties of PMN-PT 453–66
- compound semiconductor superlattices 971
- compressive strain
  - domains in nanodots and nanowires 593–7
  - domains in PZT ultra-thin films 574, 575, 577–9, 585
- compressive stresses 312
- concentration profile 105–6
- conductivity 475, 830–2, 1017–18
  - see also* resistivity
- congruent LN (CLN) 627–8
- congruent LT (CLT) 627–8
- conical second-harmonic (SH) beam 953
- constitutive models 383
- continuous phase transitions 366
- conversion efficiency 949–50
- cooling treatments 917
- copper-electrode-embedded multilayer transformers 498–500
- co-precipitation method 852, 854–5
  - SBT 866–73, 874, 875
- core-shell structure 677–9, 680, 683–4, 685
  - improved control of interfaces 684–6, 687
- corner nucleation 46, 49–50
- correlated nucleation 645–9
- correlation length 910–11
- coupled-mode theory 959
- cracks
  - flux growth 55–6
  - microcracking 351, 352, 354, 355, 357
- critical thickness 761, 779
- cross-field acoustic wave excitation 955–6
- crosshatched (tweedlike) domains 464, 465
- crosslinking 857
- cryogenic actuation 91–2
- crystal cuts
  - field poling and PMN-PT single crystals
  - field-dependent domain structures 349–57
  - optical properties 357–9
  - thermal stability 341–8
  - optimisation of cut directions 25–30
  - polarising microscopy applied to perovskite structure crystals 336–41
- crystal deformation, under external fields 305–17
  - polarisation rotation and monoclinic phases 305–12
  - polarisation rotation vs polarisation extension 313–17
- crystal growth
  - Bridgman growth *see* Bridgman growth
  - flux growth *see* flux growth
  - for medical ultrasonic transducers 102–5
  - PSN and PSN–PT 185–91
    - growth mechanism 188–91
  - SSCG *see* solid-state single crystal growth
  - zone-melting growth 81–3
- crystal structures
  - BiT 1006, 1007, 1008–11
  - in BZN system 504–9
  - grain orientation and in BLSF 823–5
- crystal symmetry 237
  - novel crystal symmetries in fully strained films 779–81
- crystal thickness, and domain walls 543–4
- crystal variant-based modelling 367–8
- crystallisation temperature 604–5
- crystallographic shear 706
- cubic pyrochlore 504, 505–7
  - melting behaviour 511–13
  - phase formation 509–11, 512
  - phase transition and phase relations 513–14
- Curie temperature 112, 131–2, 133, 173–4
  - BLSF 828, 829, 842
  - BITN and BITV ceramics 843–4
  - Bridgman growth 18–19, 20
  - ceramics containing bismuth 918, 919, 920, 921
  - flux growth 46, 47
  - mapping of Curie temperature 50–2



- high Curie temperature *see* high Curie temperature
- Curie-Weiss law 896
- cut directions, optimisation of 25–30
  - see also* crystal cuts
- dash-like domains 653–4
- 'dead layer' model 762–4
- dealcoholation 854
- deep reactive ion etching (DRIE) 734
- defects
  - BiT and RE-substituted BiT single crystals 1015–20
    - defect-formation mechanism 1018–20
  - Bridgman growth 13–15
  - extended structural defects and ferroelectric properties of single crystalline PZT films 695–723
  - interface defects and dielectric properties 671–4
  - nano-islands and registration 609–10
- deformable mirrors 88–90
- degree of orientation (orientation factor)
  - BLSF 823, 825
    - BITN and BITV 845, 847
    - remanent polarisation 835
  - and RTGG process 809
- dehydration 854
- dendrite domains 642, 643–5
- densification rate 809–10
- density of states (DOS) 1011–15
- depolarisation field 572–3, 585, 633–5, 643, 659, 660
  - thin films
    - ferroelectric size effect 757–62
    - fully strained films 779–81
- diabetes 561–2
- diaphragm-type pMUT 733–6
  - see also* piezoelectric micromachined ultrasonic transducer (pMUT)
- dicing process 114, 228
- dielectric anisotropy factor 314–16
- dielectric constants 245
  - barium titanate-derived lead-free ceramics 898–9
  - BLSF 825–7, 842
  - BZN pyrochlores 514, 515
  - ceramics containing bismuth 918, 919, 920, 921
  - PIMNT ceramics 209, 211
    - Bridgman-grown crystals 220, 222, 223
    - flux-grown crystals 215
  - PMN-PT single crystals 16, 18, 78–9, 80, 110
    - complete set material properties 252, 253, 254–6, 258
    - covariation with piezoelectric constant 22–3
    - temperature dependence 112, 113
  - PSN-PT 184, 186
    - from sol-gel method 858–60
  - PZN-PT single crystals 248–54, 256, 257
  - PZT single crystalline films 716–17
  - SBT from soft chemical methods 870, 873
  - SSCG single crystals 163, 165, 166–7, 168, 169, 170
- dielectric losses 478–9, 480–3
  - BLSF 825, 827, 842
  - BTO/STO superlattices 992, 993
  - BZN-based pyrochlores 516, 519
  - ceramics containing bismuth 918, 919 and dc bias 84–5, 86
  - interdiffusion in ceramic composites 677–8, 679, 682, 683
  - PIMNT crystals 215
  - PYNT single crystal 138, 139
  - SZO/STO superlattices 998, 999
- dielectric permittivity
  - bismuth-based perovskite single crystals 143
  - BNZ-based pyrochlores 516, 517, 518
  - Farnell's theory 988–9, 990
  - grain boundary enhancement 674
  - perovskite artificial superlattices 988–1000
    - BTO/STO superlattices 991–5
    - permittivity enhancement in BTO/STO superlattices 995–6
    - temperature dependence in BTO/STO superlattices 997–8
    - SZO/STO superlattices 998–100
  - PMN 392, 393
  - PMN-PT 450

- and dc bias 84–5, 86
- and frequency 83–4
- size effects 455–8, 459, 461–2, 463
- thermal stability 341, 342, 344–6, 347
- PSN crystals 191–2
- PSN–PT crystals 180, 181, 192–4
- PYNT single crystal 138, 139
- size effects and 448–9, 455–8, 459, 461–2, 463
- tungstic oxide–doped PMN–PT crystals 348
- dielectric relaxation
  - BZN-based pyrochlores 520–1
  - interface defects 672, 673
- dielectric size effect 762–4
- dielectric superlattices (DSLs) 933–70
  - application in acoustics 953–7, 958
  - application in electro-optic technology 957–60
  - application in nonlinear parametric interactions 942–53
  - future trends 960–1
  - preparation by modulation of ferroelectric domains 935–41
  - preparation by photorefractive effect 941–2
- dielectric tunability 521–5, 532
- difference frequency generation (DFG) 933
- differential scanning calorimetry (DSC) 180–2, 183, 196
- differential thermal analysis (DTA) 863–4
- diffuse scattering 393–4, 401, 402
  - interaction between CORs and PNRs 408–12
- diffusion
  - chemical diffusion technique for preparation of DSLs 935, 938–9
  - direction and RTGG method 811–13
- Dion-Jacobson phase 885, 886
- dipole-dipole interaction energy 579
- directivity 747–9
- discontinuous grain growth 159
- discontinuous phase transitions 366
- dislocations 15
  - misfit dislocations *see* misfit dislocations
  - nano-islands 611–12, 614–18, 619
  - PZT single crystalline films 695, 697–8, 700–7
  - threading dislocations 695, 697–8, 700–7
- distorted 90° domain wall region 286–90
- domain engineering 228, 235–65, 266, 328
  - anisotropy and 367–8
  - characterisation of domain engineered crystals 237–48
  - complete set material properties 248–56, 257
  - engineered domain configuration *see* engineered domain configuration
  - enhancement of functional properties 260–3
  - ferroelectric single crystals 367–8
  - nano- and micro-domain engineering 622–69
    - artificially produced nucleation sites 638
    - backswitch poling 649–52, 653
    - dendrite domain structures 642, 643–5
    - domain observation in LN and LT 629–31
    - domain shape evolution during merging 641–2, 643
    - elementary nucleation processes 632–8
    - experimental conditions 627–31
    - future trends 663–4
    - growth of isolated domains 638–41
    - loss of domain wall shape stability 642–4
    - modern tricks 649–57
    - oriented quasi-regular domain rays 652–7
    - polarisation reversal in relaxors 657–62
    - self-assembled nanoscale domain structures 645–9
    - stages of domain structure evolution during polarisation reversal 624–6

- visualisation of nano-domain structure 662
  - polarisation rotation vs polarisation extension 313–17
  - principle of property enhancement 256–60, 261, 262
- domain size (domain wall density) 278–86
- domain structure
  - BiT and RE-substituted BiT crystals 1020–3
  - field-dependent in PMN-PT single crystals 349–57
  - PMN-PT crystals 106, 108, 109
  - PSN crystals 198–9
  - PSN-PT crystals 198–200
  - symmetry in multi-domain single crystals 236, 237–41
- domain tip propagation (forward growth) 624, 625–6
- domain wall dynamics 382
- domain wall pinning model 495
- domain walls 785
  - formation 616–18, 619
  - fragile 56–7
  - loss of shape stability 642–4
  - motion 381–2, 475
  - thickness 286–8, 761
- domain width 543–4
  - equilibrium domain width 575, 577
- domains
  - electrostatic domain-domain interaction 656–7
  - ferroelectric nanostructures 543–5, 570–99
    - BTO ultra-thin films 577–80, 586–91
    - domain evolution under electric field 580–91
    - methods 572–3
    - nanodots and nanowires 591–7
    - PZT ultra-thin films 573–7, 579–80, 581–6
    - thin films 573–91
    - toroidal and circular ordering 553–4
  - ferroelectric size effect 758–61
  - modulation to produce DSLs 935–41
  - strain effects on ferroelectric thin films and domain formation 783
- domes 604–5
- doping
  - and flux growth 63
  - and growth striation technique 937–8
  - modification of PMN-PT single crystals 134, 135–6, 150
  - tungstic oxide-doped PMN-PT crystals 348–9
  - see also* ion substitution
- dot-type domains 653–4
- dry etching 740–1
- dynamic RAMs (DRAMs) 541, 561, 877
- e-beam lithography 561, 562
- edge nucleation 49–50
- effective distribution coefficient 188
- effective Hamiltonian approach 572–3
  - domains in ferroelectric thin films 573–91
  - domains in nanodots and nanowire 591–7
- effective nonlinear optical coefficient 950
- effective symmetries 236, 237–41
- elastic compliance constants 244, 245–6, 248
  - PMN-PT crystals 17, 18–21, 22, 252, 253, 254–6, 258
  - PZN-PT single crystals 249–54, 257
- elastic loss 478–9, 480–3
- elastic stiffness constants 244, 245, 248
  - PMN-PT and PZN-PT single crystals 249–56, 257, 258
- elastic strain energy 248
- electric field 267
  - barium titanate crystals with engineered domain configurations
    - domain size dependence 278–80
    - patterning electrodes 291–2, 293–4
  - piezoelectric properties under high electric field 272–5
  - piezoelectric properties under low ac electric field 275–7
  - uniaxial stress field 297–9
- coercive field 145, 147, 870, 875
- depolarisation field *see* depolarisation field

- domain evolution in ferroelectric nanostructures 580–91
  - BTO ultra-thin films 586–91
  - PZT ultra-thin films 581–6
- effects on MPB phases 429–30
- effects on properties of piezoelectric crystals 130–2, 133, 134
  - dielectric behaviour 84–5, 86
  - piezoelectric behaviour 85–7, 130–1, 133
- energy analysis of field-induced phase transitions 366–88
- inducement of domain structures and phase transitions in PMN-PT single crystals 333–65
- inducement of piezoelectric property enhancement 322–6, 327
- local field and nano- and micro-domain engineering 633, 635, 648–9
  - polarisation rotation 307–12
- electric field poling *see* field poling
- electrically erasable read-only memories (EEPROMs) 541, 561
- electrocaloric cooling 555–7
- electrodes
  - bottom electrode of pMUT 738–9
  - interface with ferroelectric nanostructures 557–8
  - patterning electrodes 290–4, 300
  - perovskite artificial superlattices 987–91
- electromagnetic bandgap structures (EBGs) 530–1
- electromagnetic (EM) field analysis 989–91
- electromechanical coupling factors 110, 244–5, 246, 248, 480–1
  - barium titanate crystals with engineered domain configurations 275–7
  - bismuth-based perovskite single crystals 143–5
  - BLSF 837–8
    - BITN and BITV 844, 845, 847
  - orientation effect 260, 262
  - PIMNT ceramics 209, 212, 213
    - Bridgman-grown crystals 219, 220, 221, 223, 224
    - PMN–PT crystals 17, 18–21, 22, 130, 131, 132, 133
      - complete set material properties 252, 253, 254–6, 258, 259
    - pMUT 749, 750
    - PSN–PT crystal 198
    - PYNT single crystal 139–41, 142
    - PZN–PT single crystals 249–54, 256, 257
    - SSCG single crystals 165, 167, 168, 170
  - electron beam writing 935, 939
  - electron cyclotron resonance (ECR) gun 975–6
  - electron emission 554–5
  - electron probe microanalyser (EPMA) 218–19
  - electronic band structure, BiT 1011–15
    - ab initio* calculations 1015–17
    - effects of rare earth substitution 1027–8
  - electronic lone pair 397–9
  - electro-optic effect 631, 957–60
  - electrophoretic deposition 753
  - electrostatic domain-domain interaction 656–7
  - ellipsometry 983–4, 985
  - end-effect 13, 14
  - energy analysis of phase transitions 366–88
    - energy-based modelling 373–4
    - equations of energy equilibrium 374–5
    - future trends 382–3
    - irreversible work and hysteresis loss 378–81
    - work-energy analysis 376–8, 379, 380
      - see also* effective Hamiltonian approach; free energy
  - engineered domain configuration 266–303, 770, 801
    - crystal structure and crystallographic orientation dependence 269–77
      - piezoelectric properties under high electric field 272–5
      - piezoelectric properties under low ac electric field 275–7
    - domain size dependence 278–86
      - on electric field and temperature 278–80

- piezoelectric property using 31
  - resonators 281–4
- piezoelectric property using 33
  - resonators 284–6
- effect on piezoelectric property 268–9, 270
- future trends 300–1
- history of 267–8
- intrinsic and extrinsic effects 298–300
- patterning electrode 290–4, 300
- role of non-180° domain wall region
  - on piezoelectric properties 286–90
- uniaxial stress field 294–8, 299, 300
- epitaxial thin films
  - with extended structural defects 697–709
  - see also* molecular beam epitaxy (MBE)
- equilibrium domain width 575, 577
- equivalent circuits
  - parameters for pMUT 749–50, 751
  - piezoelectric resonance 486–7
- error amplification factors 242, 243
- error propagation 245–8
- etching
  - DRIE 734
  - PZT thick film 740–2
- ethylene glycol 866, 868, 876
- exaggerated grain growth 159
- extended structural defects 695–723
- ‘extender’ ferroelectrics 313–17
- extensive losses 478–81
  - experimental example 481–2
  - physical meaning 482–4
- external screening 634–5
- extinction coefficient 984, 986
- extrinsic contributions 262–3
- extrinsic effects 298–300
- Farnell’s theory 988–9, 990
- fatigue 865
- ferroelectric correlation length 910–11
- ferroelectric-ferromagnetic materials 553
- ferroelectric-gate field effect transistor (FET) 549
- ferroelectric nanostructures 541–69
  - base-metal-electrode capacitors 555
  - domains in *see* domains
  - electron emission 554–5
  - electrocaloric cooling for mainframes and MEMs 555–7
  - focal-plane arrays 559
  - future trends 561–2
  - interfacial phenomena 557–8
  - magnetolectrics and magnetoelectric devices 551–3
  - phased-array radar 558
  - self-patterning 549–51, 562
  - superlattices 559
  - toroidal and circular ordering of domains 553–4
  - ultra-thin single crystals 559–61
- ferroelectric-relaxor crossover 906–12
- ferroelectric size effect 757–62
- ferroelectric superlattices 559
- ferroelectric thin films *see* thin films
- Fibonacci superlattices 946, 947, 951, 955–6
- field cooling technique 61
- field-cooling-zero-field-heating (FC-ZFH) 335
- field poling 333–65
  - and domain structures 349–57
  - effect on optical properties 357–9
  - Landau free energy analysis 359–62
  - preparation of DSLs 935, 939–41
  - and thermal stability 341–9
- figures of merit 93, 94
  - pyroelectric properties of BLSF ceramics 841, 842
- film thickness
  - PZT ultra-thin films and domains 577, 585
  - size and distribution of nano-islands 602–4
- fine pitch phased array transducers 115–16, 117–21
- finger domains 642, 643–4, 646
- finger width of interdigital electrodes 989–91
- finite element analysis (FEA) 736
- finite element code 383
- first-principles-based methods 571–2
  - domains in ferroelectric nanostructures 572–3
- flap control 90–1
- ‘flash’ EEPROMs 541, 561

- flexoelectric effect 766
- flexensional actuators 87
- flow velocity gradient 801
- fluorite 511–13
- flux density 736
- flux growth 38–72, 74, 135, 158, 166
  - commonly encountered problems 52–7
  - effect of flux composition 42–4
  - future trends 62–4
  - high PT content 47–52, 53
  - low PT content 44–7
  - PIMNT single crystals 212–15
  - properties of crystals 57–60
    - comparison with reported property values 60–2
  - PSN and PSN-PT crystals 186–91
  - set-up and growth results 40–2
- flux-to-solute ratio 44
- flux trappings 55
- focal-plane arrays 559
- focused ion beams (FIBs) 547, 548, 560
- forward growth (domain tip propagation) 624, 625–6
- Fox-Scott mechanism 552
- fractal patterns 653, 654–5
- fragile domain walls 56–7
- FRAMs 541, 542, 548–9, 560, 561, 877, 878
- free energy
  - anisotropy of a free energy and piezoelectric enhancement 317–26, 327
  - compositionally induced phase transitions 322, 323
  - electric field and stress-induced piezoelectric enhancement 322–6, 327
  - thermally induced phase transitions 319–21
- electric field-induced domain structures and phase transitions in PMN-PT single crystals 359–62
- Gibbs free energy 318–19, 375, 376, 377–8, 379, 381, 481
  - per unit surface of crystal 758
  - see also* energy analysis of phase transitions
- frequency
  - dielectric properties and 83–4
  - high-frequency resonance in DSLs 954–7
  - multiplication of domain patterns 650–1, 652
- frequency constant 223–4
- full-set material properties 235–65
  - correlation between single domain and multi-domain properties 256–60, 261, 262
  - PMN–PT multidomain crystals poled along (001) 252, 253, 254–5
  - PZN–PT multidomain crystals
    - poled along (001) 248–54
    - poled along (011) 256, 257
- technical challenges and characterisation methods 237–48
  - effective symmetries of multi-domain single crystal systems 236, 237–41
  - experimental procedure and error analysis 244–8
  - factors affecting self-consistency of full-set data 236, 242–4
- fundamental lattice loss portion 475
- gallium orthophosphate 147–9
- generic phase diagram 130, 132
- Gibbs free energy 318–19, 375, 376, 377–8, 379, 381, 481
- Gibbs loss tangents 491, 492
- Ginzburg-Landau theory 571
- glasses 960–1
- Goldschmidt tolerance factor 135–6
- gradients, compositional 683–6, 687, 764–6
- Graham-Charlier expansion 395–7, 398
- grain boundaries 674
- grain orientation 819, 869
  - BLSF 818–51
    - effects on electrical properties 823–47
    - by hot-forging 823
- grain-oriented ceramics along engineered domain direction 301
- SBT from soft chemical methods 869–70, 872

- grain orientation factor *see* degree of orientation
- grain size effects *see* size effects
- green compacts 802, 803, 804
- growth direction
  - control and flux growth 63
  - and property variations of PMN-PT crystals 22, 24–5
- growth striation technique 935, 936–8
- half-loop dislocations 700, 701, 702, 703, 709
- hard PZT 266, 491–5
  - origin 495–7
  - semi-hard 497–8, 499
- harmonic imaging 116, 118, 120–1
- harmonic imaging transducer 94–5
- heat generation 379
  - loss mechanisms 488–90
- Helmholtz free energy 481
- heterogeneous thin films 764–7
- heterolayered BST/BZN thin films 524–5
- heterophase structure 657–8
- heterostructures 934–5
- hexagon domains 647–8
- hexagonally poled LT (HPLT) crystal 953
- high Curie temperature
  - high-performance piezoelectric crystals 130–57
    - crystal growth 135
    - modification of single crystals 135–6
  - bismuth-based perovskite single crystals 141–5, 146, 147, 148, 149, 174
  - future trends 150–1
  - non-perovskite single crystals 145–9
  - relaxor-PT systems with high Curie temperature 137–41
- MPB systems 467
- PIMNT system *see* PIMNT system
- high-energy ball milling 726
- high-frequency linear array transducers 116, 118
- high-frequency resonance, in DSLs 954–7
- high-*K* dielectrics 531
- high-power piezoelectric ceramics 491–500
  - high-power components 498–500
  - origin of 495–7
  - semi-hard PZT-based ceramics 497–8
  - very hard PZT-based ceramics 491–5
- high-resolution transmission electron microscopy (HRTEM)
  - analysis of defects in PZT single crystalline films 702–7
  - nano-islands 611–12
- hole conduction 1007, 1023–5
- hopping dipoles model 523
- hot-forging 801, 869
  - BLSF 818–51
- hot pressing 452–3, 454, 455, 801
- hydrolysis 853, 854
- hydrothermal method 887
- hysteresis
  - energy analysis of phase transitions 378–81
  - loss mechanisms *see* loss mechanisms
- hysteresis loops 477
  - micro- and nano-domain engineering 658–60
  - nano-islands 614
  - PMN-PT 460, 461, 464, 465–6, 860–2
  - polarisation–electric field loops *see* polarisation–electric field hysteresis loops
  - PZT single crystalline films 716, 717, 718
  - SZO/STO artificial superlattices 999, 1000
- impedance
  - ac impedance spectroscopy 1017–18
  - barium titanate crystals with engineered domain configurations 282, 283, 298
  - frequency dependence for BLSF ceramics 839, 840
    - BITN and BITV 844–5, 846, 847
  - multilayer/composite single crystal phased array 124, 125
  - multilayer single crystal probe 121, 122
- pMUT 749, 750, 751

- imperfections *see* defects
- impurity-induced clusters 910–11
- in-line acoustic wave excitation 955–6
- in-plane actuators 87
- in-situ* reflection high-energy electric diffraction (RHEED) 973–4, 975, 977, 978
- incommensurate systems 421
- incomplete screening 636, 637, 640
- ineffective screening 636
- inelastic scattering 953
- infrared dielectric response 516, 518–19
- inkjet printers 562
- instabilities
  - domain pattern-induced 263
  - free energy and piezoelectric enhancement 317–26, 327
- insulin inhaler 561
- integrated circuits (IC) 531, 532, 533
- intensive losses 476–8, 480–1
- interdiffusion 674–86
  - in BST-based ceramic composites 675–83
  - concentration gradients in ceramics 683–6, 687
- interdigital capacitor (IDC) 526, 527
- interdigital electrodes 988–91, 992
- interface control
  - Bridgman growth 13, 14
  - ferroelectric nanocomposites 670–91
    - concentration gradients 683–6, 687
    - future trends 686–7
    - improved in ceramic composites 677–9
    - improved in ceramics with compositional gradient 684–6, 687
- interface defects 671–4
- interface engineering 618–20
- interfacial phenomena 557–8
- internal bias electric field 497
- internal energy 374–5, 376, 377, 378, 379, 380–1
- intrinsic effects 298–300
- ion beam sputtering (IBS) 977–80
- ion exchangeable layered perovskite 885–7
- ion substitution
  - BZN-based pyrochlore ceramics 515–16, 517
  - lead-free relaxors
    - ferroelectric-relaxor crossover 906–12
    - relaxor behaviour and in barium titanate-based ceramics 897–900, 901
    - modification of PMN-PT single crystals 134, 135–6, 150
  - ionic complexes 49–50
  - ionic-type phononic crystal (ITPC) 957, 958
  - iron chromate 855
  - irreversible work 378–81
  - isolated domains, growth of 638–41
  - Kay–Dunn law 544
  - Kerr-form nonlinearity 943
  - Kittel's law 543–4, 758–61, 785
  - Kolmogorov–Avrami (K–A) approach 660–1
  - KTP superlattices 938–41
  - lamellar domains 464, 465
  - Landau–Ginzburg–Devonshire (LGD) theory 305
    - free energy and piezoelectric effect enhancement 317–26, 327
  - Landau-type free energy analysis 359–62
  - langasite 145–7
  - lanthanum-substituted BiT *see* BLT
  - LAO substrates 601, 605–6
  - laser ablation 656, 696
  - laser MBE system 973–4
  - lattice distortions
    - BiT 1008–9
    - BLT and domain structure 1022–3
    - perovskite artificial lattices 980–3
  - lattice mismatch 605–7
  - lattice relaxation 995–6
  - lattice softening 770, 775–6
  - layered perovskite  $K_2NbO_3F$  884–95
    - potassium niobate nanoparticles 885–9, 890, 891
    - conversion to nanosheets in water 887–8
    - ion exchangeability 886–7



- re-stacking of nanosheets 888–9, 890, 891
    - potassium niobate thin film 889–94
  - lead-free materials 328, 467, 848–9, 884
  - lead-free relaxors 896–929
    - ceramics containing bismuth 918–24, 924
    - perovskite type 918–23
    - TTB type 923–4
  - derived from barium titanate 897–906, 924
    - relations between relaxor
      - behaviour and ionic substitutions in solid solutions 897–900, 901
    - relaxor characteristics in solid solutions 900–2
    - relaxor compositions in ternary systems 902–4, 905, 906
    - X-ray diffraction and Raman studies 904–6
  - ferroelectric-relaxor crossover 906–12
  - perovskite-type relaxor not derived from barium titanate 906
  - with tetragonal bronze structure 912–17, 923–4
- lead magnesium niobate *see* PMN
- lead oxides
  - chemical behaviour 8–9, 10
  - flux growth 40, 42–4
- lead titanate (PT or PTO) 333
  - electric field and stress-induced enhancement of piezoelectric properties 324–6, 327
  - nano-islands 602, 603–4
  - polarisation rotation and anisotropy factors 314–16
  - PT-rich surface layer in flux growth 56–7
  - PT/STO system 616
  - single crystalline films free from extended structural defects 709–14, 715
  - thin films and strain effects 781–2, 783
- lead zinc niobate-lead titanate *see* PZN–PT
- lead zirconate titanate *see* PZT
- leakage current 558
- BiT crystals 1006–7, 1023–4
- BTO/STO superlattices 987–8
- density for thick films 733
- RE-substituted BiT crystals 1024–5
- light deflection at domain boundaries 631
- linear electro-optic effect 631, 957–60
- lines 653, 654
- lithium niobate (LN) 145, 266
  - nano- and micro-domain engineering
    - in single crystals 622–69
  - superlattices 559, 936–42
- lithium tantalate (LT) 266
  - nano- and micro-domain engineering
    - in single crystals 622–69
  - superlattices 936, 938–41
- lithographic patterning 623
- LN *see* lithium niobate
- local field 633, 635
  - self-assembled nanoscale domain structure 648–9
- lone pair, electronic 397–9
- loss anisotropy 490–1, 492, 493
- loss mechanisms 475–502
  - experimental example 481–2
  - future trends 501
  - heat generation in piezoelectrics 488–90
  - high-power piezoelectric ceramics 491–6
    - origin of 495–8
  - high-power piezoelectric components 498–500
  - physical meaning of extensive losses 482–4
  - piezoelectric resonance 484–8
    - losses as a function of vibration velocity 487–8
  - theoretical formulas 476–81
    - see also* dielectric losses
- low-symmetry ferroelectric phases 771–6
- low-temperature co-fired ceramic (LTCC) devices 503–4, 529
- LT *see* lithium tantalate
- macroscopic polarisation 591–2, 594–5
- magnesium oxide substrates 601, 605, 606, 607–8
- magnetoelectric composite 545, 547

- magnetolectrics/magnetolectric devices 551–3, 562
- mainframe computers 555–7
- martensitic transformation 421
- Maxwell-Wagner effect 764, 765
- maze domain structure 661, 662
- mechanical quality factor 475, 484
  - BLSF 839
  - high-power piezoelectric ceramics 494, 495–6
  - losses at a piezoelectric resonance 484, 486, 487–8
- mechanical softening 24
- mechanochemical activation/
  - mechanosynthesis 452–3, 454, 455
- medical nanostructure devices 561–2
- medical ultrasonic transducers 101–29, 227–8
  - commercialisation of single crystal transducers 112–21
  - future for single crystals 121–5, 126
  - future trends 125–6
  - piezoelectric single crystals 92–5, 102–7
    - characterisation 105–7, 108, 109, 110, 111
    - crystal growth 102–5
    - PIMNT crystals 222–5, 227–8
    - single crystals vs conventional PZT ceramics 107–12, 113
- melt growth 61–2
- melting behaviour 511–13
- merging (coalescence of domains) 624, 625, 626
  - domain shape evolution during 641–2, 643
- metal alkoxides 853–4
- metal–insulator–metal (MIM) thin film capacitors 531
- metal–oxygen–metal (M–O–M) networks 853–4
  - (1-*x*)PMN-*x*PT using THOME 863–4
- methanol 866, 867
- 2-methoxyethanol 865
- microcracking 351, 352, 354, 355, 357
- microelectromechanical systems (MEMS)
  - electrocaloric cooling 555–7
  - piezoelectric thick films for 724–55
    - soft chemical methods and 877–8
- microfluidic transport 561–2
- micromechanics models 383
- microstructure
  - grain orientation and 823–5
  - loss portion 475
  - spin-coated thick films 729–31
- microwaves
  - applications of BZN-based pyrochlores 525–31
  - dielectric response of BZN-based pyrochlores 516, 518–19
  - tunable microwave devices 526–7, 681–3
- misfit dislocations
  - critical thickness for PTO films 710
  - nano-islands 611–12
    - and domain wall formation 616–18, 619
    - impact on ferroelectric switching 614–16
  - PZT single crystalline films 695, 697–8, 703
  - see also* dislocations
- mode coupling 244
- modelling of MPB phase diagrams 421–5
- molecular beam epitaxy (MBE)
  - laser MBE system 973–4
  - reactive MBE system 974–7, 978, 980
- molten salt synthesis 801–2
- monoclinic phases 339
  - adaptive phase 420–1
  - BZN-based pyrochlore and zirconolite-like structure 507, 508
    - melting behaviour 511–13
    - phase formation 509–11, 512
    - phase transition and phase relations 513–14
  - low-symmetry phases in ferroelectric thin films 771–6
- PMN-PT 415, 451
  - polarisation rotation and 305–12, 412–20
- PSN-PT 178, 180, 182–3, 184, 417–20
- monodomains 582, 585, 590–1
- morphotropic phase boundary (MPB) 130, 132, 173–4, 180, 181, 207

- compositionally induced phase transitions 322, 323
- ferroelectric thin films 767–9
- MPB systems 391–446
  - CIRs 425–9
  - concentration evolution 438–40
  - future trends 432–40
  - modelling of MPB phase diagrams 421–5
  - monoclinic phase as adaptive phase 420–1
  - polarisation rotation via monoclinic phase 412–20
  - stability of MPB phases under external and internal fields 429–32, 433, 434
  - substitution of titanium 412–29
- PIMNT 211
- PMN–PT 362, 451, 855–6
- PSN–PT 176, 201
  - morphotropic phase diagram 182–4
- morphotropic phase region (MPR) 438–40
- morphotropic phase transition
  - temperature 130, 132, 173–4, 207
  - PIMNT 215, 221–2
  - PSN–PT 183–4
- MRAMs 548–9, 561
- multi-crucible Bridgman growth system 9–12, 30
- multi-domain single crystal systems 235–65
  - correlation between single domain and multi-domain properties 256–60, 261, 262
  - effective symmetries 237–41
  - PMN–PT crystals poled along (001) 252, 253, 254–5
  - PZN–PT crystals
    - poled along (001) 248–54
    - poled along (011) 256, 257
- multi-field-induced phase transitions 368–73
- multilayer ceramic actuators (MLCA) 447
- multilayer ceramic capacitors (MLCC) 447, 503, 504, 686, 879
- multilayer copper-embedded transformers 498–500
- multilayer/polymer composite single crystal phased array 123–5, 126
- multilayer/polymer composite transducer 110
- multilayer single crystal probe 121–3
- multiple nucleation 53–4
- multi-step deposition 607–9
- nano-array of platinum nanowires/PZT 545–7, 561
- nanodots 591–7
- nano-islands 550–1, 600–21
  - future trends 618–20
  - physical properties 610–18
    - dislocations and domain wall formation 616–18, 619
    - ferroelectric properties 613–14
    - growth mechanism 612–13
    - misfit dislocations and ferroelectric switching 614–16
    - structural investigation 610–12
  - preparation 601–10
    - control of size and distribution 602–4
    - effect of lattice mismatch 605–7
    - influence of crystallisation temperature 604–5
    - multi-step deposition 607–9
    - registration 609–10
- nanoparticles, potassium niobate 885–9, 890, 891
- nano-powders 878–9
- nanoscale domain arrays 645–6
- nanosheets 884–95
  - preparation of nanoparticles from 885–9
    - conversion of  $K_2NbO_3F$  to 887–8
    - re-stacking 888–9, 890, 891
  - preparation of thin films 889–94
- nano-spheres 550
- nano-toroids 547–8
- nano-trenches 561
- nanotubes
  - carbon 545, 550, 562
  - ferroelectric 545, 546, 550
- nano-twinning 775
- nanowires 591–7

- nano-writing 545, 547
- NBT 818, 820–1, 826
- NCBT 821, 825, 826, 848
  - piezoelectric properties 837–9
  - pyroelectric properties 841–3
- neodymium-substituted BiT *see* BNT
- neutron diffraction 1015, 1016
- niobate oxide systems 914–17
- niobium-doped STO substrate 987–8
- non-180° domain walls 286–90
- non-conventional sintering 679–83
- non-crystallographic crystal faces 45
- nonlinear Bragg law 952
- nonlinear parametric interactions 933–4, 942–53
  - optical frequency conversion
    - 1D periodic DSL 944–5
    - 1D quasi-periodic DSLs 945–52
    - 2D DSLs 952–3
  - wave vector conservation 942–3
- non-perovskite piezoelectric single crystals 134, 145–9, 150
- non-planar nanoferroelectrics 784
- non-stoichiometric BZN-based pyrochlores 507–9
- non-volatile random access memories (FRAMs) 541, 542, 548–9, 560, 561, 877, 878
- nucleation 624–5, 632
  - artificially produced nucleation sites 638
  - elementary nucleation processes 632–8
  - flux growth 46, 49–50
    - multiple nucleation 53–4
    - side-wall nucleation 41, 54
  - nano- and micro-domain engineering relaxors and polarisation reversal 661
- NXBT system 828
- one-dimensional (1D) DSLs 943
  - periodic 944–5
  - quasi-periodic 945–52
- optical beam control 961
- optical constants 984–7
- optical extinction angles 337–41
- optical frequency conversion 933–4, 943, 944–53
  - in 1D quasi-periodic DSLs 945–52
  - in 2D DSLs 952–3
  - and optical parametric oscillation in 1D periodic DSL 944–5
- optical parametric amplification (OPA) 934
- optical parametric generation (OPG) 933–4
- optical parametric oscillators (OPOs) 934, 944–5
- optical transmission 357–8
- optimisation of cut directions 25–30
- organic thin-film transistors (OTFT) 531, 532, 533
- orientation effect 256, 259–60, 261, 262
- orientation factor *see* degree of orientation
- orthorhombic phase 307, 309, 310
- out-of-phase boundaries (OPBs) 706
- output sound pressure level (SPL) 745–7
- overpoling 58, 59, 60, 61–2
- oxide superlattices 971
  - see also* perovskite artificial superlattices
- oxyborate crystals 149
- oxyfluorides 917
- oxygen deficiency 14–15
- oxygen deficiency diffusion model 497
- oxygen-titanium bond oscillations 910–11
- parasitic crystals 41, 54
- partial density of states (PDOS) 1013–15
- partial dislocations 700, 702, 703
- patterning electrodes 290–4, 300
- PBN 818, 820
- PBT 821
- Pechini method 856–7
- periodic DSLs 944–5
- periodically poled crystals 559
- perovskite artificial superlattices 971–1005
  - dielectric properties 987–1000
    - BTO/STO superlattices 991–8
    - electrodes and measuring 987–91
    - SZO/STO superlattices 998–1000
  - future trends 1001–2
  - lattice distortions 980–3
  - optical property 983–7
    - optical constants 984–7

- spectroscopic ellipsometry 983–4, 985
- preparation 973–80
  - laser MBE system 973–4
  - reactive MBE system 974–7, 978, 980
  - sputtering system 977–80, 994–5
- perovskite structure 304–32
  - anisotropy of a free energy and piezoelectric enhancement 317–26
  - compositionally induced phase transitions 322, 323
  - electric field and stress-induced enhancement 322–6, 327
  - Gibbs free energy 318–19
  - thermally induced phase transitions 319–21
- BSPT 134, 141–5, 146, 148, 149, 150, 174, 425
- crystal deformation under external fields 305–17
  - polarisation rotation and monoclinic phases 305–12
  - polarisation rotation vs polarisation extension 313–17
- piezoelectric property enhancement by texture formation 799–801
  - see also* reactive templated grain growth method
- perovskite-type lead-free relaxors
  - containing bismuth 918–23
  - derived from barium titanate 897–906, 924
    - ferroelectric-relaxor crossover 906–12
  - not derived from barium titanate 906
- perturbation strength 910–11
- Pfizer 561
- phase angle 271, 274, 282, 283
- phase coexistence 767–70
- phase diagrams
  - barium titanate crystals with engineered domain configuration 291, 292
  - BZN pyrochlores 509, 510
  - generic phase diagram for relaxor-PT crystal systems 130, 132
  - modelling of MPB phase diagrams 421–5
  - PIMNT system 209
  - PMN-PT 103–4, 207, 415, 416
  - PSN-PT 175, 176, 182–4, 201, 417–20
  - PZN-PT 207, 415–17
  - PZT 413–15
  - relaxor compositions in ternary systems 902–4
- phase equilibrium
  - BZN pyrochlores 509
  - PMN-PT 6, 7, 8
- phase field theory 382, 783
- phase formation 509–11, 512, 513
- phase matching (PM) 622–3, 934, 943
- phase relation
  - BLSF 821–2
  - BZN pyrochlores 513–14
- phase segregation 40, 44, 75–7, 81, 193–4
- phase-shifted model 403
- phase shifter 526
- phase stability 368
  - MPB phases under external and internal fields 429–32, 433, 434
- phase transitions
  - barium titanate-derived lead-free relaxor ceramics 897–900, 901
  - BZN-based pyrochlores 513–14
  - compositionally induced 322, 323
  - electric field-induced 322–6, 327
    - PMN-PT single crystals 333–65
  - energy analysis of field-induced transitions *see* energy analysis of phase transitions
  - multi-induced 368–73
  - role of bismuth in ferroelectric phase transition of BiT 1009–11, 1112
  - stress-induced 322–6, 327
  - thermally induced 319–21
- phase velocities 244, 245
- phased-array radar 558
- phased-array transducers 115–16, 117–21
- phonon-polariton (P-P) Raman scattering 953
- photonic arrays 562
- photorefractive effect 941–2
- piezoelectric anisotropy factor 314–16

- piezoelectric coefficients 245, 246–8, 769–70
  - barium titanate crystals with engineered domain configurations 271, 272, 273, 274, 275–7
  - domain size dependence 282–3, 284, 285
  - non-180° domain wall regime 287–90
  - uniaxial stress field 297–8, 299
- bismuth-based perovskite single crystals 143–5
- orientation effect 260, 261
- PIMNT ceramics 209–10, 213
  - Bridgman-grown 225, 226
  - flux-grown 215
- PMN-PT single crystals 77–9, 80, 110, 130–1, 133, 252, 253, 254–6, 258, 259
  - Bridgman-grown 16, 17, 20, 21
  - covariation with dielectric constant 22–3
  - dc bias 86, 87
  - flux-grown 59, 60
  - measured vs calculated 21–2
  - small increase in 23–4
- pMUT 743–4
- PSN-PT 184, 186
- PYNT single crystal 139–41, 142
- PZN-PT single crystals 59, 60, 110, 248–54, 257
- SSCG single crystals 165, 167, 168, 170
- thick films 731, 732
- piezoelectric loss 479, 480–3
- piezoelectric micromachined ultrasonic transducer (pMUT) 733–53
  - microfabrication 737–42
    - buffer layer of bottom electrode 738–9
    - etching of PZT thick film 740–2
    - polyimide layer 739–40, 741
  - performances 742–51
    - directivity of 2D pMUT array 747–9
    - electromechanical coupling coefficient 749, 750
    - equivalent circuit parameters 749–50, 751
    - output sound pressure level 745–7
    - piezoelectric response and simulated properties 742–5
    - size dependence of resonance frequency 750–1, 752
    - structure 733–6
- piezoelectric nanotubes/carbon nanowire hybrids 551
- piezoelectric resonance 484–8
  - equivalent circuit 486–7
  - losses as a function of vibration velocity 487–8
  - vibration 484–6
- piezoelectric thick films *see* thick films
- piezomagnetism 551
- piezomotors 87
- piezoresponse force microscopy (piezoforce microscopy) (PFM) 613–14, 629, 630
  - investigations of PZT single crystalline films 707–9, 717
- PIMNT (PIN-PMN-PT) system 31, 205–31
  - future trends 227–8
  - properties of ceramic 208–12, 213
  - single crystals 212–26
    - grown by Bridgman method 216–26
    - grown by flux method 212–15
- PINT 207, 208
  - high Curie temperature 134, 137–8, 146, 147
- platinum
  - crucible leakage 6–9
  - inclusions 56
- PLZT 628
- PMN (lead magnesium niobate) 333, 392–4, 909
  - structure 395–412
    - chemical order 403–8
    - interaction between CORs and PNRs 408–12
    - polar order 395–403
    - temperature evolution of structure 437, 438
- PMN-PT (or PMNT) (lead magnesium niobate-lead titanate) 205–7, 208, 316

- chemical inhomogeneity regions
  - 425–9
- nanopowders and MLCC 879
- PEG-based sol-gel route 855–65, 878
- phase diagram 103–4, 132, 134, 207, 415, 416
- single crystals 3–100, 130–4, 173–4, 878
  - actuators 88–92
  - Bridgman growth *see* Bridgman growth
  - challenges in growth of large crystals 4
  - complete set material properties 252, 253, 254–5, 256, 258, 259
  - data useful in selection of crystals 31–5
  - dynamic performance 83–7
  - effective symmetry 237–41
  - electric field-induced domain structures and phase transitions 333–65
  - field-dependent domain structures 349–57
  - field poling effect on optical properties 357–9
  - flux growth *see* flux growth
  - future trends 30–1, 62–4, 97–8
  - growth 102–5, 135
  - high PT content 47–52, 53
  - imperfections 13–15
  - innovative zone-melting growth 81–3
  - modification by doping 134, 135–6, 150
  - multi-field-induced phase transitions 371–3, 378, 379, 380
  - optimisation of cut directions 25–30
  - poled along (001) 252, 253, 254–5
  - poled along (111) 258, 259
  - properties of flux-grown crystals 57–62
  - properties of SSCG-grown crystals 166–7
  - property characterisation 15–25, 105–7, 108, 109, 110, 111
  - SSCG 161–2, 163, 164, 170
  - thermal stability 341–9
  - transducers 92–7
  - tungstic oxide doped 348–9
- size effects 447–71
  - 0.65PMN–0.35PT 461–6
  - 0.8PMN–0.2PT 453–61, 462
  - future trends 466–7
  - nature of 450–1
  - processing of submicrometre and nanostructured PMN-PT ceramics 452–3, 454, 455, 456
- PMN–PZT SSCG 161–2, 170
  - dielectric and piezoelectric properties 167–70
- PNC 827
  - resistivity 829–30, 831
- point defects 704–5
- Poisson ratio 777
- polar nano-regions (PNRs) 334–5, 393–4, 401–3, 436, 437, 438, 450
  - interaction with CORs 408–12
- polar order 395–403, 464
  - see also* polar nano-regions
- polarisation–electric field hysteresis loops 477
  - BiT and BLT 1025–6
  - field-dependent domain structures of PMN–PT crystals 350–1, 352–3
  - grain orientation and electrical properties of BLSF 833–6
  - high-power piezoelectric ceramics 496–7
  - PMN–PT 460, 461
    - PEG-based sol-gel route to 860–2
    - size effects 464
  - PMN–PZT SSCG 168, 169
  - PSN crystals 196–7
  - PSN–PT 184, 185, 196–7
  - PYNT crystals 138–9
  - PZT single crystalline films 716
  - SBT from soft chemical methods 870, 874
  - thick films 731, 732
  - tungstic oxide-doped PMN–PT crystals 348, 349
- polarisation extension 313–17
- polarisation reversal (switching)
  - BiT-based devices 1029–30
  - dipoles in BTO thin films 587–90

- domain structure evolution during 624–6
- ferroelectric nanostructures 544–5
- free energy piezoelectric enhancement 322–6, 327
- misfit dislocations and in nano-islands 614–16
- PZT single crystalline films 707–9
- in relaxors 657–62
  - hysteresis loops 658–60
  - switching by rectangular pulses 660–1
  - visualisation of nano-domain structure 662
- polarisation reversal/reorientation model 483–4
- polarisation rotation 305–17
  - and monoclinic phases 305–12, 412–20
  - vs polarisation extension 313–17
  - in thin films 432, 434, 770–1
- polarisation rotation angle 307–8, 313–14
- polarisation–stress hysteresis curves 477
- polarising microscopy 630–1
  - perovskite structure crystals 336–41
- polariton excitation 957, 958
- polydomains 699
- polyethylene glycol (PEG)
  - co-precipitation method for SBT 866, 867
  - sol-gel method for PMN–PT 855–65
- polyimide 739–40, 741
- polymeric ferroelectrics 562
- polymeric precursor method 856–7
- polyvinylidene fluoride (PVDF) 562
- potassium niobate 274–5, 277, 300–1, 884–95
  - future trends 894
  - nanoparticles 885–9, 890, 891
  - thin film 889–94
- predetermined nucleation 636–7
- pressure, external 431
- property characterisation methods 237–48
  - see also* full-set material properties
- property matrices 64
- proton exchange 938
- pseudo-cubic morphology 188, 190–1
- PSMNT 137
  - single crystals grown by Bridgman method 216–26
- PSN 174, 201, 909
  - crystal growth 185–91
    - growth mechanism 188–91
  - properties of single crystals 191–200
    - calorimetric analysis 196
    - dielectric properties 191–2
    - domain structure 198–200
    - ferroelectricity 196–7
    - piezoelectricity 198
  - structure 395–412
    - chemical order 403–8
    - interaction between CORs and PNRs 408–12
    - polar order 395–403
    - temperature evolution of structure 437, 438
- PSN–PT (PSNT) 173–204, 207–8, 417–20
  - chemical inhomogeneity regions 425–9
  - crystal growth 185–91
    - growth mechanism in single crystals 188–91
  - dielectric properties 180, 181
  - ferroelectric and piezoelectric characterisations 184–5
  - future trends 201–2
  - high Curie temperature crystals 134, 137, 146, 147
  - phase diagram 175, 176, 182–4, 201, 417–20
  - properties of single crystals 191–200, 201–2
    - dielectric properties 192–6
    - domain structure 198–200
    - ferroelectricity 196–7
    - piezoelectricity 198
  - structural analysis and X-ray spectra 177–80
  - synthesis 177
  - thermal analysis by DSC 180–2, 183
- PST 909
- PSZNT 137
- PT *see* lead titanate; PMN–PT; PSN–PT; PZN–PT
- PT/STO system 616
- pulsed-laser deposition (PLD) 696–7, 705–6, 709–11
- pulsed-laser interval deposition 697



- pulsed ultraviolet (UV) laser irradiation  
652–7
- PYbN-PMN-PT 31
- PYNT 207
  - high Curie temperature crystals 134, 137, 138–41, 142, 146, 147
- pyramids 604–5
- pyrochlores
  - pyrochlore crystals in flux growth 41, 54–5
  - pyrochlore phase 177, 188
  - BZN-based *see* BZN-based pyrochlore ceramics
  - crystal structure 504, 505
- pyroelectric coefficient 841–3, 914–15, 916
- PZBT 821
- PZN–PT (or PZNT) (lead zinc niobate–lead titanate) 3, 73, 130, 173–4, 205–7
  - effective symmetry 237–41
  - engineered domain configuration 267–8
  - flux growth 38–72, 74
    - common problems 52–7
    - future trends 62–4
    - low PT content 44–7
    - properties 57–60
    - properties compared with reported property values 60–1
  - growth 102–4, 135
  - multi-domain crystals
    - poled along (001) 248–54
    - poled along (011) 256, 257
  - multi-field-induced phase transitions 370–1
  - phase diagram 207, 415–17
- PZT (lead zirconate titanate) 168, 205, 543, 865
  - high-power piezoelectric ceramics 491–8
    - origin 495–7
    - semi-hard PZT-based ceramics 497–8, 499
    - very hard PZT-based ceramics 491–5
  - nanodots and nanowires 591–7
  - nano-islands *see* nano-islands
  - phase diagram 413–15
  - piezoelectricity and phase coexistence 767–9
  - single crystalline films *see* single crystalline PZT films
  - single crystals vs conventional PZT ceramics for medical ultrasound imaging 107–12, 113
  - texture development in BNKT–PZT solid solutions 812, 813
  - thin films 878
    - domain evolution under electric field 581–6
    - domains 573–7, 579–80
- PZT xerogel 725–6
- quartz 145
- quasicrystal systems 421
- quasi-periodic DLSS (QPDSLs) 942, 945–52
  - construction 946
  - direct THG 951–2
  - effective nonlinear optical coefficients 950
  - QPM multi wavelength SHG 951
  - theoretical treatment of nonlinear optical processes in 946–50
- quasi-phase matching (QPM) 934, 943, 944–53, 960–1
- quasi-regular domain rays 652–7
- r*-phase 780
- radiofrequency (RF) applications of BZN-based polychlores 525–31
- radiofrequency (RF)-magnetron sputtering 977–80, 994–5
- Raman scattering, P–P 953
- Raman spectroscopy 426–8
  - lead-free relaxors derived from barium titanate 905–6
- random bond–random field model 412
- random field models 394, 411–12
- rare-earth (RE)-substituted BiT 1006–32
  - defect structure 1016–18
  - domain structure 1021–3
  - effects of rare earth substitution on electronic band structure and chemical bonding 1027–8
  - leakage current 1024–5
  - polarisation properties 1025–6

- reactive MBE system 974–7, 978, 980
- reactive templated grain growth (RTGG)
  - method 799–817
  - application to solid solutions 811–13
  - factors determining texture
    - development 809–11, 812
    - future trends 813–14
    - selection of reactive templates 807–9
- rectangular pulses, switching by 660–1
- reflection effect 654, 655, 656–7
- reflection high-energy electric diffraction (RHEED) 973–4, 975, 977, 978
- refractive index
  - effect of field poling 358–9
  - perovskite artificial superlattices 984–7
- refractive index modulation (RIM) 943
- registration 546–7
  - nano-islands 609–10
- relaxor compounds 391–446, 628–9, 896–7
  - energy analysis of field-induced phase transitions in single crystals 366–88
  - future trends 432–40
  - historical context 392–5
  - lead-free *see* lead-free relaxors
  - polarisation reversal and nano- and micro-domain engineering 657–62
  - structure of archetypal relaxors PMN and PSN 395–12
    - chemical order 403–8
    - interaction between CORs and PNRs 408–12
    - polar order 395–403
  - temperature evolution of structure 435–8, 439, 440
- relaxor–PT materials 130–4, 167, 168, 205, 206
  - growth 135
  - with high Curie temperature 134, 137–41, 142, 150
  - piezoelectric constant and Curie temperature 225, 226
  - see also under individual materials*
- remanent polarisation
  - BiT and BLT crystals 1025–6
  - BLSF 833–6
  - PMN–PT crystals 341, 342, 347
  - PZT single crystalline films 716
  - SBT from soft chemical methods 870–3, 875
- residual depolarisation field 635, 643
- resistivity 828–33
- resonance
  - DSLs 953–4
    - high-frequency resonance 954–7
  - losses at a piezoelectric resonance 484–8
  - method for complete set material properties 242, 244
  - resonance frequency and pMUT 742–3
    - displacement and phase frequency properties 744–5
    - size dependence 750–1, 752
- resonator-type DSL devices 956
- re-stacking of nanosheets 888–9, 890, 891
- rhombohedral phase 130, 132, 773, 774
  - crystals for medical transducers 106–7, 108, 110
  - electric field and polarisation rotation 307, 309–12
- Rietvald analysis 460–1, 462, 464
- ring-shaped BZT crystal 162–3
- rotating-analyser type spectroscopic ellipsometer 984, 985
- rotation angles 25–6
- 'rotator' ferroelectrics 313–17
  - compositionally induced phase transitions 322, 323
  - thermally induced phase transitions 319–21
- rotorcraft flap control 90–1
- Ruddlesden-Popper phase 885, 886
- Samsung 555
- satellite crystals 41, 53–4
- SBN 940–1
- SBNS 914–16
- SBT (strontium bismuth tantalate) 543, 821, 822
  - soft chemical methods 865–73, 874, 875, 878
- SBTT ceramics 821, 848
  - Curie temperature 828, 829
  - piezoelectric properties 839–41

- remnant polarisation 836
- resistivity 832–3
- scandium cations 400
- screening 634–5, 761–2
- screening coefficient 572–3, 574, 575, 585
- screening effectiveness 636, 640
- second harmonic generation (SHG) 933, 943
  - QPDSLs 950, 951–2
  - QPM multi wavelength SHG 951
- seeded polycrystal conversion (SPC) 849
- selective chemical etching 629–30
- self-assembled nanoscale domain structures
  - nano- and micro-domain engineering 663–4
- self-consistency of full-set data 236, 242–4
- self-patterning 549–51, 562, 600–1, 784–5
- semi-hard PZT-based ceramics 497–8, 499
- shape, crystal 162–3, 164
- shear stresses 312
- Shchukin-Williams theory 604–5
- side-wall nucleation 41, 54
- sideways domain growth (spreading) 624, 625, 626, 633
- silica 960–1
- single crystalline PZT films 695–723
  - comparison of properties of films with and without structural defects 714–17, 718
  - pulsed-laser deposition 696–7
  - with extended structural defects 697–709
    - PFM investigations 707–9
    - TEM and HRTEM analyses 699–707
  - without extended structural defects 709–14, 715
- single domain-multi-domain correlation of properties 256–60, 261, 262
- sintered compacts 802–3, 804, 805, 806, 807
- sintering, non-conventional 679–83
- size effects
  - ferroelectric thin films 757–64
  - dielectric size effect 762–4
  - ferroelectric size effect 757–62
- in ferroelectrics 448–50
- grain size effects and macroscopic properties of PMN–PT 447–71
  - future trends 466–7
  - 0.65 PMN–0.35 PT 461–6
  - 0.8 PMN–0.2 PT 453–61, 462
  - processing of submicrometre and nanostructured PMN–PT ceramics 452–3, 454, 455, 456
- grain size reduction and MPB phase stability 431–2, 433
- skeletons 189
- sodium niobate, relaxors derived from 906
- soft chemical methods 852–83
  - co-precipitation method 852, 854–5
  - for ferroelectric SBT 865–73, 874, 875, 878
  - future trends 876–9
  - PEG-based sol-gel route to PMN–PT 855–65, 878
  - sol-gel process 852, 853–4
  - sol-gel route to BiT and BLT ceramics 873–6, 877
- soft PZT 266, 447, 449
- sol-gel process 852, 853–4
  - BiT 873–6, 877
  - BLT 875–6, 877, 878
  - PEG-based route to PMN–PT 855–65, 878
  - SBT 865, 866–73, 874, 875, 878
- solid solutions
  - lead-free relaxor characteristics in 900–2
  - RTGG method 811–13
- solid-state single crystal growth (SSCG) 135, 151, 158–72, 228
  - BZT single crystals 163–5
  - future trends 170
  - PMN-PT single crystals 166–7
  - PMN-PZT single crystals 167–70
  - process 159–63
- soliton systems 960
- sonar transducers 95–7
- sound pressure level (SPL) 745–7
- space charge 671–4
  - relaxation 672, 673

- spark plasma sintering (SPS) 681, 682
- spectroscopic ellipsometry 983–4, 985
- spherical model 360
- spin coating 728–9
  - characterisation of spin-coated thick films 729–33
- spindle-like domains 199, 200
- spontaneous backswitching (flip-back) 624, 625, 626, 640, 641, 644
- spontaneous nucleation 187, 188
- spontaneous polarisation 424
  - BiT single crystals 1008–9
  - perovskite structure and texture formation 799–801
- spreading (sideways domain growth) 624, 625, 626, 633
- sputtering systems 977–80, 994–5
- SRO 710
- stack actuators 87
  - for deformable mirrors 88–90
- stacking faults 703–4, 705
- static polar nanoregions (SPNRs) 438
- step generation and growth 632, 633, 636–8, 639
- STO substrates 601, 605, 606, 607–8
  - niobium-doped 987–8
- stochastic nucleation 636
- stoichiometric DSLs 940–1
- stoichiometric LN (SLN) 627–8
- stoichiometric LT (SLT) 627–8
- stoichiometric melt 4–6
  - see also* Bridgman growth
- stored energy 477–8
- strain
  - compressive *see* compressive strain
  - effects on ferroelectric thin films 776–83
    - fully strained films 779–81
    - lead titanate under tensile strain 781–2
  - strain relaxation and domain formation 783
  - piezoelectric property enhancement and texture 800–1
  - PMN–PT solid solution and grain size 465–6
  - remnant strain 380–1
  - tensile *see* tensile strain
  - unipolar 85–7
- strain-electric field relation 184, 185, 198, 465–6, 477
- strain gradients 765–6
- stress-strain curve 477
- stresses
  - BTO/STO superlattices 995–6
    - energy analysis of field-induced phase transitions 366–88
    - inducement of piezoelectric property enhancement 322–6, 327
    - polarisation rotation 312
    - uniaxial stress field 294–8, 299, 300
- stripe domains
  - BTO ultra-thin films 577–80
    - evolution under electric field 586–90
  - fully strained films 781
    - under tensile strain 781–2
  - nanodots and nanowires 595–7
  - PZT ultra-thin films 574–7
    - evolution under electric field 581–6
  - single crystal films of barium titanate 759–60
- strontium acetate 866, 868
- strontium bismuth tantalate *see* SBT
- strontium-potassium niobate oxide system 914
- strontium titanate (STO)
  - BTO/STO artificial superlattices *see* BTO/STO artificial superlattices
  - SZO/STO artificial superlattices *see* SZO/STO artificial superlattices
- structural distortion 1008–9
- sum frequency generation (SFG) 933, 951–2
- superdomes 604–5
- superlattices 559, 764, 765, 934, 971
  - dielectric *see* dielectric superlattices
  - perovskite *see* perovskite artificial superlattices
- surface structure 757, 758
- switching *see* polarisation reversal
- symmetry
  - and ferroelectric thin films 756, 767–76
    - low-symmetry ferroelectric phases 771–6
  - piezoelectricity and phase coexistence 767–70

- polarisation rotation 770–1
  - multi-domain single crystal systems 236, 237–41
  - novel crystal symmetries in fully strained films 779–81
- SZO/STO artificial superlattices 972–3, 976–7, 1001
  - dielectric properties 998–1000
  - lattice distortions 980–3
  - optical constants 984–7
- tantalum–niobium substitution 917
- temperature
  - crystallisation temperature 604–5
  - Curie temperature *see* Curie temperature
  - dependence of dielectric permittivity of BTO/STO superlattices 997–8
  - domain size dependence in barium titanate crystals with engineered domain configurations 278–80
  - evolution of structure of relaxors 435–8, 439, 440
  - morphotropic phase transition
    - temperature *see* morphotropic phase transition temperature
  - thermally induced phase transitions 319–21
- temperature usage range 145, 147
- templated crystal growth (TCG) 228
- templated grain growth (TGG) 802–3, 849
  - see also* reactive templated grain growth (RTGG) method
- tensile strain
  - domains in nanodots and nanowires 593, 594–5
  - domains in PZT ultra-thin films 574, 575, 576
  - lead titanate thin films under 781–2
- tensile stresses 312
- Tera-bit/in<sup>2</sup> PZT nano-array on platinum nanowires 545–7, 561
- ternary systems, relaxor compositions in 902–4, 905, 906
- tetragonal bronze (TTB) lead-free relaxors 912–17, 924
  - ceramics containing bismuth 923–4
- tetragonal phase 106, 130, 132
  - domain patterns 106, 109
  - electric field and polarisation rotation 307, 308–9
  - PSN–PT 178, 180, 183, 184
- texture
  - enhancement of piezoelectric properties by texture formation 799–801
  - see also* reactive templated grain growth method
- thermal loading 373–82
- thermal stability 341–9
- thermally induced phase transitions 319–21
- thermogravimetric (TG) analysis 863–4
- thick films 724–55
  - characterisation 729–33
    - ferroelectric and piezoelectric properties 731–2
    - leakage current density and dielectric properties 733
    - microstructure 729–31
  - composite coating process 724, 725–9
  - future trends 753
  - pMUT 733–53
    - microfabrication 737–42
    - performances 742–51, 752
- thin films
  - BZN and dielectric tunability 521–5
  - fabrication of potassium niobate thin film 889–94
  - ferroelectric nanostructures 545–6, 561
    - domains in *see* domains
  - ferroelectric thin films 756–95
    - future trends 783–5
    - gradients 764–7
    - heterogeneous 764–7
    - size effects 757–64
    - symmetry and ferroelectric properties 767–76
    - strain effects 776–83
  - polarisation rotation 432, 434, 770–1
  - single crystalline PZT films *see* single crystalline PZT films
  - soft chemical methods 877–8
- third harmonic generation (THG) 933
- QPDSLs 950, 951–2

- threading dislocations 695, 697–8, 700–7
- three-dimensional nanoferroelectrics 784
- three-ray stars 654, 655
- titanium 75–7, 82–3
  - cations 400
  - chemical diffusion and DSLs 938–9
  - substitution and MPB systems 412–29
- titanium isopropoxide 725
- titanium oxide 738–9
- titanium-oxygen bond oscillations 910–11
- tolerance factor 135–6
- tonpitz transducers 95–6
- top-seeded solution growth 39
- toroidal domains 553–4
- total energy 572
- towed sonary arrays 96, 97
- transducer-type DSL devices 956
- transducers 92–7
  - medical *see* medical ultrasonic transducers
  - pMUT *see* piezoelectric micromachined ultrasonic transducer
  - sonar 95–7
- transmission electron microscopy (TEM) 611–12
  - single crystalline films with defects 699–707
  - single crystalline films without defects 711, 713, 714
- transparency 77
- transverse acoustic (TA) phonon mode 403
- transverse optic (TO) phonon mode 403
- 1,1,1-tris(hydroxy)methylethane (THOME) 857–65
- tunability
  - dielectric tunability in BZN thin films 521–5, 532
  - tunable microwave devices 526–7, 681–3
- tungstic oxide doped PMN–PT crystals 348–9
- tunnelling 543
- twin wall nano-islands 616–18
- twinned nanodomains 421
- two-dimensional DSLs 943, 952–3
- two-dimensional electromagnetic bandgap structures (2D EBGs) 530–1
- two-mode behaviour 428–9
- ultrasonic pulse-echo method 244
- ultrasonic transducers *see* medical ultrasonic transducers
- ultra-thin films
  - domains in 573–91
    - barium titanate 577–80, 586–91
    - domain evolution 580–91
    - PZT 573–7, 579–80, 581–6
    - microstructural instability 601
    - see also* nano-islands; thin films
- ultra-thin single crystals 559–61
- uniaxial stress field 294–8, 299, 300
- uniform slurry 726–7
- uniformity
  - PMN–PT crystals 107, 111
  - single crystal transducers 114–15
- unipolar strain 85–7
- unmanned solar systems 96, 97
- vacancy formation
  - energy 1015–17
  - mechanism 1018–20
- vibration 484–8
- vibration velocity
  - high-power piezoelectric ceramics 491–5
  - losses as a function of 487–8
  - pMUT frequency response 743
- Vogel-Fulcher (VF) relationship 455, 458, 460, 896, 908, 909
- voltage tunable devices 526–7
- volume fraction of distorted domain wall region 286–8
- volumic ratio of ordered regions 406
- vortex dipole structures 591, 593, 595
- vortex domains 553–4
- waterfall effect 403
- wave vector conservation 942–3
- wavelength-division-multiplexing (WDM) 960
- wedge-type domains 464, 465
- wet etching 741–2
- work 374

- irreversible work and hysteresis loss 378–81
- work-energy analysis 376–8, 379, 380
- X phase 432
- X-ray diffraction (XRD) 106, 107
  - BiT 824–5
    - from soft chemical methods 876, 877
  - BITN and BITV 844, 845
  - BLT from soft chemical methods 876, 877
  - Bragg condition 942–3
  - layered perovskite  $K_2NbO_3F$  886, 887
  - lead-free relaxors derived from
    - barium titanate 904–5
    - nano-islands 610–11
  - perovskite artificial lattices 980, 981, 982
  - PIMNT ceramics 208–9, 210
  - PMN–PT
    - crystals 106, 107, 342–4, 346
    - powders 452, 453, 454
  - potassium niobate 886, 887
    - thin films 892, 893
  - PSN–PT 177–80
    - crystals 194–6
    - powders 452–3, 454
  - SBT from soft chemical methods 870, 871
- X-ray diffraction reciprocal space mapping (XRD-RSM) 713, 715, 980, 982
- xerogel 725–6
- Young's modulus 455, 459, 460
  - see also* elastic compliance constants
- zero-field-cooling (ZFC) 335
- zero-field-heating (ZFH) 335
- zinc oxide thin film transistor (TFT) 531, 533
- zirconium oxide 684
- zirconolite-like structure 507, 508
- zone levelling 9–12, 30, 81–2
- zone-melting growth 81–3